

MASSACHUSETTS INSTITUTE OF TECHNOLOGY

The RESEARCH LABORATORY *of* ELECTRONICS

PROGRESS REPORT

NO. 138

JANUARY 1–DECEMBER 31, 1995



DISCLAIMER NOTICE



**THIS DOCUMENT IS BEST
QUALITY AVAILABLE. THE
COPY FURNISHED TO DTIC
CONTAINED A SIGNIFICANT
NUMBER OF PAGES WHICH DO
NOT REPRODUCE LEGIBLY.**

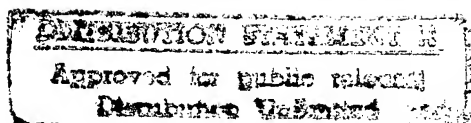
RLE Progress Report

No. 138

January 1 - December 31, 1995

Submitted by

Professor Jonathan Allen
Professor Daniel Kleppner



The RESEARCH LABORATORY *of* ELECTRONICS

MASSACHUSETTS INSTITUTE of TECHNOLOGY

CAMBRIDGE, MASSACHUSETTS 02139-4307

DTIC QUALITY INSPECTED 3

19961127 009

RLE Progress Report Number 138

Cover and title page:

RLE at 50. Pictured are Building 20, former home of MIT's Radiation Laboratory (1940-1945) and original home of RLE, on the right and the Karl Taylor Compton Laboratories (Building 26), headquarters of RLE until 1973, on the left. RLE rose to new heights with the dedication of the Sherman Fairchild complex in 1973 when Building 36 (to the rear) became the current base of the Laboratory.

The ten-foot parabolic antenna silhouetted against the sky atop Building 26 stands like a sentry as it has since 1963; it was the first antenna installed by RLE's Radio Astronomy Group. Nestled in the foreground is Michael Steiner's approximately ten foot by ten foot corten steel piece, *Niagara*; science and art at the crossroads of history. (Photo and caption by John F. Cook)

Our special thanks to the following staff members of the RLE Communications Group: Mary J. Ziegler for her exceptional organizational skills, editing, formatting, and graphics scanning and processing; John F. Cook for his outstanding photography and design of the cover, title, and divider pages; Michelle M. Scheer for her excellent formatting and technical typing; and Rita C. McKinnon for proofreading. We also want to thank David W. Foss, Manager of the RLE Computer Facility, for his time and invaluable technical assistance, and Mary S. Greene and Snow C. Sudduth for inputting information for the publications chapter.

We thank the faculty, staff, and students of RLE for their generous cooperation.

Editor:	Barbara Passero
Associate Editor:	Mary J. Ziegler
Design and photography:	John F. Cook
Logo design:	Everett Design, Boston, Massachusetts
Printer:	ZBR Publications, Haverhill, Massachusetts
Typesetting:	This report was produced with IBM's BookMaster Software.

Copyright © 1996 by the Massachusetts Institute of Technology. All rights reserved. ISSN 0163-9218

Table of Contents

The Research Laboratory of Electronics	1
PART I SOLID STATE PHYSICS, ELECTRONICS AND OPTICS	
Section 1 Materials and Fabrication	5
Chapter 1 Compound Semiconductor Materials and Devices	7
<i>Professor Clifton J. Fonstad, Jr.</i>	
• 1.1 Epitaxy-on-Electronics Integration Technology	7
• 1.2 High Peak-to-Valley Ratio Resonant Tunneling Diodes on GaAs Substrates	8
• 1.3 Monolithic Enhancement of MESFET Electronics with Resonant Tunneling Diodes	8
1.4 Integrated InGaAsP/GaAs Light Emitting Diodes and Surface-Emitting Laser Diodes	9
1.5 Integrated Photodetector Standard Cells	10
1.6 Microwave Characterization of Optoelectronic Devices	11
1.7 Growth of Distributed Bragg Reflector and Multiple Quantum Well Heterostructures at Reduced Temperature	12
1.8 Monolithic Integration of Self-Electrooptic-Effect Devices on Very Large Scale Integrated GaAs Electronics	12
1.9 Compact Integrated Optics Structures for Monolithic Integration	13
1.10 The OPTOCHIP Project and other Multigroup OEIC Chips	15
1.11 Normal Incidence Single- and Dual-Band Quantum-Well Intersubband Photodetectors	16
1.12 Integrated Quantum-Well Intersubband Photodetector Focal Plane Arrays	16
1.13 Intersubband Transitions in Narrow Quantum Wells	17
1.14 Kinetic Beam Etching of Semiconductor Nanostructures	18
• 1.15 Publications	18
Chapter 2 Physics of Hemterostructure Field-Effect Transistors	21
<i>Professor Jesús A. del Alamo</i>	
• 2.1 Introduction	21
• 2.2 A New Physical Model for the Kink Effect on InAlAs/InGaAs HEMTs	21
• 2.3 Publications	27
Chapter 3 Gas Source Molecular Beam Epitaxy of Compound Semiconductors	29
<i>Professor Leslie A. Kolodziejwski</i>	
• 3.1 Introduction	29
• 3.2 Gas Source Molecular Beam Epitaxy of ZnSe, ZnSe:Cl and ZnSe:N	29
3.3 Novel Epitaxial III-V Buffer Layers for Wide Bandgap II-VI Visible Sources	33
• 3.4 The Growth and Characterization of ZnSe/GaAs Heterostructures	35
3.5 Low Temperature Growth of (In,Ga)P/(In,Ga)As Lasers and LEDs for Optoelectronic-VLSI	38
3.6 InP-Based Devices for Optical Communication Networks	40
3.7 Integrated Optical Filters and Circuits in InP	41
3.8 Photonic Bandgap Structures	42

Section 2	Quantum-Effect Devices	45
Chapter 1	Statistical Mechanics of Quantum Dots	47
	<i>Professor Boris L. Altshuler</i>	
• 1.1	Project Description	47
• 1.2	Publications	48
Chapter 2	Artificial Atoms	49
	<i>Professor Marc A. Kastner</i>	
• 2.1	Goals and Objectives	49
• 2.2	Summary of Recent Work	49
• 2.3	Fabrication	51
• 2.4	Results	52
• 2.5	Publications	53
Chapter 3	Coulomb Blockade in Single And Double Quantum Dots	55
	<i>Professor Patrick A. Lee</i>	
• 3.1	Project Description	55
• 3.2	Transport Through a Single Quantum Dot	55
• 3.3	Transport Through Double Quantum Dots	56
• 3.4	Publications	57
Chapter 4	Superconducting and Quantum-Effect Devices	59
	<i>Professor Terry P. Orlando</i>	
4.1	Nonlinear Dynamics of Discrete Josephson Arrays	59
4.2	Resonance Splitting in Inductively Coupled Arrays	59
4.3	Flux Flow and Self Field Effects	60
4.4	Triangular Arrays of Josephson Junctions	60
4.5	One-dimensional Parallel Josephson-junction Arrays as a Tool for Diagnostics	61
4.6	Quantum Device Simulations	61
4.7	Publications	62
Chapter 5	Nanostructures, Technology, Research, and Applications	65
	<i>Professor Henry I. Smith</i>	
• 5.1	Nanostructures Laboratory	65
• 5.2	Scanning Electron Beam Lithography	65
• 5.3	Spatial-Phase-Locked Electron-Beam Lithography	66
• 5.4	X-Ray Nanolithography	68
• 5.5	Improved Mask Technology for X-Ray Lithography	69
• 5.6	A High-Precision Mask Alignment and Gapping System with Immunity to Overlayers	72
• 5.7	Interferometric Lithography	73
• 5.8	Ion-Beam Lithography	75
• 5.9	High-Performance, Self-aligned Sub-100 nm MOSFETs Using X-ray Lithography	75
• 5.10	Single and Dual-Gate SOI Devices	76
• 5.11	Fabrication of T-gate Devices using X-ray Lithography	77
• 5.12	Studies of Coulomb Charging Effects and Tunneling in Semiconductor Nanostructures	79
• 5.13	Fabrication and Transport Studies of Lateral Surface Superlattices in	

	GaAs/AlGaAs Modulation Doped Field-Effect Transistors	82
• 5.14	Single-Electron Transistor Research	83
• 5.15	Distributed-Feedback Lasers Fabricated by X-Ray Lithography	84
• 5.16	Fabrication of Integrated Quarter-Wave Shifted Distributed Bragg Gratings for Wavelength Division Multiplexing Applications	86
• 5.17	Design of a Grating-Based Matched Filter for Optical Communications	90
5.18	High-Dispersion, High-Efficiency Transmission Gratings for Astrophysical X-ray Spectroscopy	91
• 5.19	Submicrometer-Period Transmission Gratings for X-ray and Atom-Beam Spectroscopy and Interferometry	92
• 5.20	Publications	93
Chapter 6	Single-Electron Spectroscopy	95
	<i>Professor Raymond C. Ashoori</i>	
• 6.1	Goals and Objectives	95
• 6.2	High-Resolution Scanning Capacitance Spectroscopy of Semiconductor Structures	96
• 6.3	Single Electron Transistors for Studying Quantum Dots and other Nanoscale Objects	97
• 6.4	Time Domain Capacitance Spectroscopy	99
• 6.5	Use of High Sensitivity Electrometry to Study the Quantum Hall Effect	102
• 6.6	Publications	102
Section 3	Optics and Devices	103
Chapter 1	Optics and Quantum Electronics	105
	<i>Professor Hermann A. Haus, Professor Erich P. Ippen, Professor James G. Fujimoto, Professor Peter L. Hagelstein, Dr. Brett E. Bouma</i>	
• 1.1	Fiber Ring Lasers	105
1.2	Fiber Storage Rings	107
1.3	Long-Distance Fiber Communications	108
1.4	Laser Noise and Squeezing	110
1.5	Optical Waveguide Filters	111
1.6	Integrated Optical Filters and Circuits	115
• 1.7	High-Power and Frequency-Doubled Stretched-Pulse Fiber Laser	116
• 1.8	Femtosecond Pulse Amplification and Continuum Generation at 1.55 μm	118
• 1.9	Wavelength Shifting in Passive Semiconductor Waveguides	120
• 1.10	Visible and Near IR Femtosecond Pump-Probe Studies on C_{60} and Alkali-doped C_{60} Films	121
• 1.11	Characterization of ZnSe/GaAs Heterojunctions	122
• 1.12	Wavelength-Tunable Femtosecond Diagnostic Methods for Characterizing Photonic Bandgap Device Performance	123
• 1.13	Ultrashort Pulse Generation in Solid-State Lasers	124
• 1.14	Ultrafast Phenomena in Materials and Devices	126
1.15	Laser Medicine	128
1.16	EUV and Soft X-ray Laser Research	138
1.17	Elastic and Inelastic Neutron Hopping	143
1.18	Many-photon Configuration Space Theory and Applications	150
Chapter 2	Optical Propagation and Communication	159
	<i>Professor Jeffrey H. Shapiro, Dr. Ngai C. Wong</i>	

Table of Contents

2.1	Introduction	159
2.2	Nonlinear and Quantum Optics	159
2.3	Multiresolution Laser Radar Range Imaging	161
2.4	Optical Frequency Division and Synthesis	161
Chapter 3	High-Frequency (> 100 GHz) and High-Speed (< 10 ps) Electronic Devices	165
	<i>Professor Qing Hu</i>	
3.1	Introduction	165
3.2	Micromachined Millimeter-wave Devices	166
3.3	Far-infrared and Picosecond Time-resolved Transport Studies of Quantum-effect Devices	168
3.4	Intersubband Transitions in Coupled Multiple Quantum-well (MQW) Structures	174
3.5	Millimeter-wave, THz, and Subpicosecond Facilities	177
3.6	Publications	177
Section 4	Surfaces and Interfaces	179
Chapter 1	Synchrotron X-Ray Studies of Surface Disordering	181
	<i>Professor Robert J. Birgeneau</i>	
• 2.1	Introduction	181
• 1.2	Stability of Vicinal Si(111) Surfaces Under Sublimation and Electromigration	181
• 1.3	Monolayer Melting	184
• 1.4	Publication	184
Chapter 2	Semiconductor Surface Studies	185
	<i>Professor John D. Joannopoulos</i>	
• 2.1	Introduction	185
• 2.2	Mechanical Hysteresis on an Atomic Scale	185
• 2.3	Heteroepitaxial Growth	187
• 2.4	Publications	189
Chapter 3	Step Structures and Epitaxy on Semiconductor Surfaces	191
	<i>Professor Simon G.J. Mochrie</i>	
• 3.1	Introduction	191
• 3.2	Self-assembly of Nanoscale Gratings on Silicon	191
• 3.3	Self-assembly of Quantum Dots	194
• 3.4	Publications	196
PART II	APPLIED PHYSICS	
Section 1	Atomic, Molecular and Optical Physics	199
Chapter 1	Quantum Optics and Photonics	201
	<i>Professor Shaoul Ezekiel, Dr. Selim M. Shahriar, Dr. Stephen P. Smith</i>	
1.1	Classical and Quantum Noise Suppression in Distortion-Free Phase Conjugation Using Coherent Population Trapping	201
1.2	Unbounded Cooling Force in Traveling Waves Excitation of a Four-Level System	206

1.3	Evidence of Collective Atomic Recoil Lasing in a High-Density Sodium Atomic Beam ...	207
1.4	Applications of Porous Glass Based Thick Holograms for Optical Data Storage and WDM Demultiplexing	211
1.5	Distributed Fiberoptic Sensor for Quench Detection in Superconducting Tokamak Magnets	214
1.6	Demonstration of an Optical Mass Flow Meter	215
Chapter 2	Basic Atomic Physics	217
	<i>Professor Daniel Kleppner, Professor David E. Pritchard, Professor Wolfgang Ketterle</i>	
• 2.1	Studies in Quantum Chaos: Rydberg Atoms in Strong Fields	217
• 2.2	Determination of the Rydberg Frequency	221
• 2.3	Precision Mass Spectrometry of Ions	226
• 2.4	Atom Interferometry	229
2.5	Cooling and Trapping Neutral Atoms	235
Section 2	Plasma Physics	241
Chapter 1	Plasma Dynamics	243
	<i>Professor George Bekefi, Professor Abraham Bers, Professor Bruno Coppi, Professor Miklos Porkolab, Professor Jonathan S. Wurtele, Dr. Stefano Migliuolo, Dr. Abhay K. Ram, Dr. Linda E. Sugiyama, Ivan Mastovsky</i>	
1.1	MIT Microwiggler for Free Electron Laser Applications	243
1.2	Plasma Wave Interactions††RF Heating and Current Generation	247
1.3	Physics of Thermonuclear Plasmas	265
Section 3	Electromagnetics	275
Chapter 1	Electromagnetic Wave Theory and Applications	277
	<i>Professor Jin Au Kong, Dr. King Hau Ding, Dr. Robert T. Shin, Dr. Y.-C. Eric Yang</i>	
1.1	SIR-C Polarimetric Radar Image Simulation and Interpretation	277
1.2	Polarimetric Passive Remote Sensing	278
1.3	Theoretical Models for Microwave and Millimeter Wave Integrated Circuits with Anisotropic Materials	279
1.4	Three-Dimensional Time-Domain Analysis of Microstrip and Monolithic Millimeter/Submillimeter Wave Integrated Circuits	279
1.5	Electromagnetic Modeling of Snow with Microstructures	280
1.6	Study of SAR Interferometry	280
1.7	Inversion of Sea Ice Parameters	280
1.8	Study of Radio Interference on ILS Category III Operations	281
1.9	MMW Model for Three-Dimensional Radar Scattering from Targets and Background	281
• 1.10	Electromagnetic Waves in Complex Media	282
• 1.11	Publications	282
Section 4	Radio Astronomy	285
Chapter 1	Radio Astronomy	287
	<i>Professor Bernard F. Burke, Professor David H. Staelin, Dr. Philip W. Rosenkranz</i>	
1.1	Extragalactic Radio Source Studies	287
1.2	Algorithms for Advanced Microwave Sounding Unit Operational Use	289
1.3	Earth Observing System: Advanced Microwave Sounding Unit	289
1.4	High-Resolution Passive Microwave Imaging of Atmospheric Structure	290
1.5	Reduction of Variation	290

PART III SYSTEMS AND SIGNALS**Section 1 Computer-Aided Design 295****Chapter 1 Custom Integrated Circuits 297**

*Professor Jonathan Allen, Professor John L. Wyatt, Jr., Professor Jacob White,
Professor Srinivas Devadas, Professor Anantha P. Chandrakasan,
Dr. Ichiro Masaki*

1.1	Custom Integrated Circuit Design	297
1.2	Cost-Effective Hybrid Vision Systems for Intelligent Highway Applications	298
1.3	Computer-Aided Design Techniques for Embedded System Design	303
1.4	VLSI Design for Low-Power Dissipation	307
1.5	Parallel Algorithms for Device Simulation	309
1.6	Numerical Simulation of Short Channel MOS Devices	310
1.7	Coupled Simulation Algorithms for Microelectromechanical CAD	310
1.8	Numerical Techniques for Simulating Josephson Junction Arrays	311
1.9	Efficient 3-D Interconnect Analysis	312
1.10	Adaptive Gridding Techniques for Multipole-Accelerated Solution of Integral Equations	313
1.11	Coupled Circuit-Interconnect/ Packaging Analysis	314
1.12	Simulation Algorithms for Communication Circuits	315

Chapter 2 Computer-Integrated Design and Manufacture of Integrated Circuits 319

Professor Donald E. Troxel

2.1	Research Goals and Objectives	319
2.2	Operating High Variability Manufacturing Systems	320
2.3	A Distributed Discrete Event Simulation	321
2.4	QUAN: A Language for the Schedule Of Repetitive Manufacturing Systems	322
2.5	Microsystems Factory Representation	323
2.6	Run-by-Run: Interfaces, Implementation, and Integration	324
2.7	Remote Fabrication of Integrated Circuits	324
2.8	Message Passing Tools for Software Integration	325
2.9	Remote Microscope for Inspection of Integrated Circuits	326
2.10	Semiconductor Manufacturing Process Flow Representation	326
2.11	Computer-Aided Technology Design	327
2.12	Modeling of Advanced Device Structures	328
2.13	Semiconductor Process Repository	329
2.14	Process Capabilities Database	330
2.15	National Infrastructure for Networked Design and Prototyping	330
2.16	Metal Reliability and Electromigration	331
2.17	RTFM: A Digital Design Lab Expert	332
2.18	Publications	332

Section 2 Digital Signal Processing 335**Chapter 1 Digital Signal Processing Research Program 337**

*Professor Alan V. Oppenheim, Professor Arthur B. Baggeroer, Professor Gregory W.
Wornell*

1.1	Introduction	337
1.2	Digital Audio Filter Design Using Frequency Transformations	338
1.3	Channel Equalization for Self-Synchronizing Chaotic Systems	338
1.4	Techniques for Enhancing the Performance of Communication Systems Employing	

1.5	Spread-Response Precoding	338
1.6	Active Noise Cancellation in Automobiles	339
1.7	Single Mode Excitation in the Shallow Water Acoustic Channel	339
1.8	Efficient Communication Using Chaotic Systems	340
1.9	Signal Transmission and Recovery in Self-Synchronous Chaotic Systems	340
1.10	Algorithmic Structures for Signal Processing in Relation to the Rapid Prototyping of Application Specific Signal Processors	341
1.11	Algebraic and Probabilistic Structure in Fault-Tolerant Computation	341
1.12	Signal Processing Applications of Chaotic Dynamical Systems	342
1.13	Multiscale Signal Processing with Fractal Renewal Processes	342
1.14	Low-Complexity Receivers for Code Division Multiple Access Systems	343
1.15	Approximate Signal Processing	343
1.16	Tools for Decentralized Decision and Control with Application to Multiple Access Communications	344
1.17	Analysis and Applications of Systems Exhibiting Stochastic Resonance	344
1.18	Distributed Digital Signal Processing Architectures for Approximate Processors	344
1.19	Sinusoidal Analysis-Synthesis	345
1.20	Signal Processing and Communication with Solitons	345
1.21	Environmental Robustness in Automatic Speech Recognition	346
1.22	Oceanographic Signal Processing	346
1.23	Acoustic Thermometry of Ocean Climate	347
1.23	Publications	348
Chapter 2	Advanced Television and Signal Processing Program	351
	<i>Professor Jae S. Lim</i>	
2.1	Introduction	351
2.2	Signal Representations for Very-low-bit-rate Video Compression	352
2.3	Optimal Transform Coefficient Selection for Images	352
2.4	Biorthogonality in Lapped Transforms: A Study in Audio Compression	353
2.5	Multistage Video Compression	353
2.6	Video Source Coding for High-Definition Television	354
2.7	Improvement of MPEG by Position-dependent Encoding	355
2.8	HDTV Transmission Format Conversion and the HDTV Migration Path	355
2.9	Removing Degradations in Image Sequences	355
2.10	Speech Enhancement	356
Chapter 3	Combined Source and Channel Coding for High-Definition Television	357
	<i>Professor William F. Schreiber</i>	
3.1	Project Description	357
3.2	Technology	358
3.3	Current Status	358
3.4	Publications	359
PART IV	BIOELECTRONICS	
Section 1	Genetic Analysis	363
Chapter 1	Genosensor Technology Development	365
	<i>Dr. Mark A. Hollis, Dr. Daniel J. Ehrlich</i>	
1.1	Introduction	365
1.2	Development of Genosensor Arrays for DNA Decoding	365
1.3	Microdetection Technology for Automated DNA Sequencing	368
1.4	Advanced MEMS for High-Throughput DNA Sequencing	371

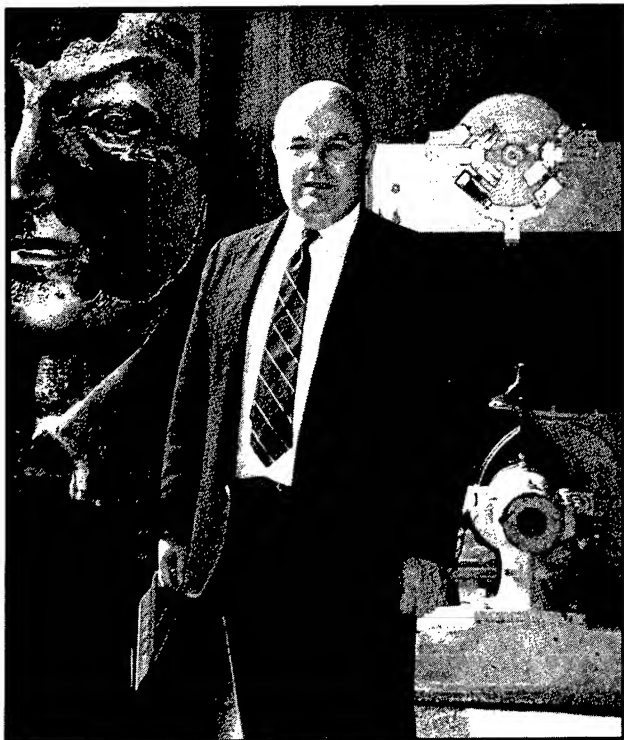
PART V LANGUAGE, SPEECH AND HEARING

Section 1	Speech Communication	375
Chapter 1	Speech Communication	377
	<i>Professor Kenneth N. Stevens, Dr. Joseph S. Perkell, Dr. Stefanie Shattuck-Hufnagel</i>	
1.1	Studies of Normal Speech Production	378
1.2	Speech Research Relating to Special Populations	379
1.3	Studies of the Acoustics, Perception, and Modeling of Speech Sounds	381
1.4	Models of Lexical Representation and Lexical Access	382
1.5	Speech Production Planning and Prosody	383
1.6	Development of Computer and Data Processing Facilities	383
1.7	Publications	384
Section 2	Sensory Communication	387
Chapter 1	Sensory Communication	389
	<i>Professor Louis D. Braid, Nathaniel I. Durlach, Dr. William M. Rabinowitz, Dr. Charlotte M. Reed, Dr. Mandayam A. Srinivasan, Dr. Thomas E.v. Wiegand, Dr. David Zeltzer, Dr. Patrick M. Zurek</i>	
1.1	Introduction	389
1.2	Hearing Aid Research	389
1.3	Enhanced Communication for Speechreaders	393
1.4	Cochlear Implants	396
1.5	Tactile Communication of Speech	397
1.6	Multimicrophone Hearing Aids	399
1.7	Hearing-Aid Device Development	400
1.8	Binaural Hearing	400
1.9	Virtual Environment Technology for Training	401
1.10	Training for Remote Sensing and Manipulation	408
1.11	Human and Robot Hands: Mechanics, Sensorimotor Functions and Cognition	408
1.12	Role of Skin Biomechanics in Mechanoreceptor Response	414
1.13	Peripheral Neural Mechanisms of Haptic Touch	416
1.14	Inertial Head Tracking	417
1.15	Supernormal Auditory Localization for Improved Human-Machine Interfaces	419
1.16	Auditory Cues to Combat Spatial Disorientation	421
Section 3	Auditory Physiology	423
Chapter 1	Signal Transmission in the Auditory System	425
	<i>Professor Lawrence S. Frishkopf, Professor Nelson Y.S. Kiang, Professor William T. Peake, Professor William M. Siebert, Professor Thomas F. Weiss, Professor Dennis M. Freeman, Dr. Bertrand Delgutte, Dr. Donald K. Eddington, Dr. John J. Guinan, Jr., Dr. John J. Rosowski</i>	
1.1	Introduction	425
1.2	Middle and External Ear	425
1.3	Auditory Neural Processing of Speech	433
1.4	Binaural Interactions in Auditory Brainstem Neurons	434
1.5	Electrical Stimulation of the Auditory Nerve	435
1.6	Cochlear Efferent System	436
1.7	Interactions of Middle-Ear Muscles and Olivocochlear Efferents	438
1.8	Cochlear Implants	438

Section 4	Linguistics	443
Chapter 1	Linguistics	445
	<i>Professor Noam Chomsky, Professor Morris Halle</i>	
1.1	Introduction	445
1.2	Abstracts of Doctoral Dissertations	445
 APPENDICES		
Appendix A	RLE Publications and Papers Presented	453
A.1	Meeting Papers	453
A.2	Journal Articles	465
A.3	Books/Chapters in Books	472
A.4	RLE Publications	473
A.5	RLE Theses	474
Appendix B	Current RLE Personnel	477
Appendix C	Milestones	483
C.1	New Faculty and Staff	483
C.2	Promotions	483
C.3	Retirements	484
C.4	Tenure	484
C.5	Awards and Honors	484
Appendix D	RLE Research Support Index	485
 Project Staff and Subject Index		 489

The Research Laboratory of Electronics

The Research Laboratory of Electronics (RLE) was established in 1946 as the Institute's first interdepartmental laboratory. Originally organized under the joint sponsorship of the Departments of Physics and Electrical Engineering, RLE has broadened its interests to cover a wide range of research.



Professor Jonathan Allen, Director, Research Laboratory of Electronics (Photo by John F. Cook)

RLE's 50th Anniversary

In November 1996, RLE will celebrate 50 years of technological impact and innovation with a technical conference, special exhibit, activities for alumni, and other events. Two special issues of *RLE currents* will describe the achievements of 20 of RLE's entrepreneurial alumni. For more information on this event, look at RLE's 50th anniversary page on the World Wide Web (see next column) or contact RLE Headquarters, telephone: (617) 253-4653; fax (617) 253-1301.

RLE Progress Report

RLE Progress Report Number 138 describes research programs at RLE for the period January 1 through December 31, 1995. Each chapter of the *Progress Report* includes a summary of research efforts for research projects listed. Faculty, research staff, students and others who participated in these projects are identified at the beginning of each project, along with sources of funding.

There are four appendices at the end of the report: Appendix A is a bibliography of RLE publications and papers presented by RLE staff during 1995; Appendix B is a roster of current RLE staff; Appendix C is a list of RLE faculty and staff milestones and honors received during 1995; and Appendix D is an index of RLE sponsors. The Project Staff and Subject Index provides additional access to the information in this report.

RLE on the World Wide Web

RLE has a presence on the World Wide Web (<http://rleweb.mit.edu>). RLE web pages include an introduction to RLE research and services; information about RLE's history, research groups, staff, and publications along with news of RLE events, and a history of the Radiation Laboratory (1940-1945).

RLE Publications

RLE also publishes *RLE currents*, a biannual newsletter which focuses on RLE research interests; a technical report series; *Speech Group Working Papers*; and other information related to the Laboratory. The *RLE Brochure*, published in 1991 for RLE's 45th anniversary, is also available at no charge.

For more information, write Massachusetts Institute of Technology, Research Laboratory of Electronics, Communications Office, Room 36-412, 77 Massachusetts Avenue, Cambridge, Massachusetts 02139-4307, Tel. (617) 253-2566, Fax (617) 258-7864.

Part I Solid State Physics, Electronics and Optics

Section 1 Materials and Fabrication

Section 2 Quantum-Effect Devices

Section 3 Optics and Devices

Section 4 Surfaces and Interfaces

Section 1 Materials and Fabrication

Chapter 1 Compound Semiconductor Materials and Devices

Chapter 2 Physics of Heterostructure Field-Effect
 Transistors

Chapter 3 Gas Source Molecular Beam Epitaxy of
 Compound Semiconductors

Chapter 1. Compound Semiconductor Materials and Devices

Academic and Research Staff

Professor Clifton G. Fonstad, Jr.

Visiting Scientists and Research Affiliates

Norio Iisuka,¹ Dr. Sheila Prasad,² Masami Tachikawa,³ Praveen T. Viadyanathan²

Graduate Students

Rajni J. Aggarwal, Joseph F. Ahadian, Isako Hoshino, Paul S. Martin, Janet L. Pan, Steven G. Patterson, Yakov Royter, Krishna V. Shenoy, Hao Wang

Technical and Support Staff

Charmaine A. Cudjoe-Flanders, Angela R. Odoardi

1.1 Epitaxy-on-Electronics Integration Technology

Sponsors

Defense Advanced Research Projects Agency/
National Center for Integrated Photonics
Technology
Fannie and John Hertz Foundation
Graduate Fellowship
Joint Services Electronics Program
Grant DAAH04-95-1-0038
National Science Foundation
Graduate Fellowship

Project Staff

Joseph F. Ahadian, Yakov Royter, Steven G. Patterson, Hao Wang, Praveen T. Viadyanathan, Paul S. Martin, Rajni J. Aggarwal, Krishna V. Shenoy, Gale S. Petrich, Professor Leslie A. Kolodziejski, Professor Clifton G. Fonstad, Jr., J.M. Mikkelsen⁴

Epitaxy-on-electronics (EoE) is a monolithic, heterojunction device, very-large-scale-integration (VLSI) technology. In the EoE technique, device heterostructures are grown by molecular beam epitaxy (MBE) in dielectric growth windows (DGWs)

on foundry-processed GaAs MESFET integrated circuit chips. Manufactured by Vitesse Semiconductor, these circuits are known to withstand extended temperature cycles of up to 470 degrees C without significant change in electronic performance. Using gas source molecular beam epitaxy (GSMBE), high-performance LED and laser diode material has been grown within the EoE time-temperature envelope. Using solid source MBE multiquantum well modulators and SEED structures, and resonant tunneling diodes have also been grown under these conditions. Through an interactive foundry service begun by our group known as the OPTOCHIP Project, eight university research teams now have the opportunity to design optoelectronic integrated circuits (OEICs) incorporating LEDs, photodetectors, and VLSI-density enhancement and depletion-mode GaAs MESFET logic gates. Because the OPTOCHIP Project requires a robust EoE process and well characterized optoelectronic devices, development of this technology has been our goal.

A major advance in EoE technology in the past year has been the development of an effective DGW preparation method. DGW formation is complicated by the need to etch through the thick ($> 6 \mu\text{m}$), highly nonuniform dielectric stack without

¹ Toshiba Corporation Ltd., Kawasaki, Japan.

² Northeastern University, Boston, Massachusetts.

³ NTT, Atsugi, Japan.

⁴ Vitesse Semiconductor Corporation, Camarillo, California.

damaging the underlying GaAs substrate. Prior attempts using reactive ion etching alone resulted in undesirable damage to the GaAs substrate, while wet etching frequently damaged nearby electronics. A new procedure utilizing directional dry etching to a metal etch-stop layer roughly $0.5\ \mu\text{m}$ above the surface and a combination of wet and plasma etching to the substrate, is now used to obtain an undisturbed GaAs surface without affecting the electronic circuitry.

Another major advance was made in the area of in situ surface cleaning prior to epitaxy. In earlier work, we had used a hydrogen plasma to remove the oxides on the surface of GaAs wafers at temperatures as low as 350 degrees C (normal thermal oxide desorption is done at 600 degrees C). However, a hydrogen plasma source is expensive, and the energetic ions involved in the process may cause surface damage. Recently, we have shown that atomic hydrogen, obtained in situ using an economical, high-temperature cracker cell installed on Professor Kolodziejski's GSMBE works equally well. A similar cell will soon be installed on the solid-source MBE.

Work in 1996 will focus on (1) gaining a better understanding of the consequences of doing epitaxy on the ion-implanted, semi-insulating substrates intrinsic to the EoE process, (2) quantifying and controlling the lateral infringement of defects from the DGW edges into the epitaxial regions, (3) obtaining statistical data on defects and yield, and (4) refining and improving the post-epitaxy processing sequences.

1.2 High Peak-to-Valley Ratio Resonant Tunneling Diodes on GaAs Substrates

Sponsor

Joint Services Electronics Program
Grant DAAH04-95-1-0038

Project Staff

Rajni J. Aggarwal, Professor Clifton G. Fonstad, Jr.

Resonant tunneling diodes have traditionally had relatively low peak-to-valley current ratios (PVCRs) when grown on GaAs. Resonant tunneling diodes relying on lattice-matched and/or pseudomorphic heterostructures on GaAs have achieved PVCRs as high as seven at room temperature, whereas pseudomorphic heterostructures on InP have achieved values as high as 50. Based on these observations, a number of research groups have grown high-indium-fraction heterostructures on GaAs in attempts to obtain some of the improve-

ments seen using InP substrates and have achieved a limited amount of success, achieving PVCRs as high as 9.3 at room temperature. Still, these recent results fall short of the PVCr of ten or more needed to make development of many RTD circuit applications attractive. We have taken an approach that can be viewed as combining features of several recent reports and have achieved PVCRs on GaAs as high as 13 at room temperature. The idea was to use (1) fully relaxed buffer layers and x-ray studies to confirm that the layers are indeed fully relaxed; (2) an increased In fraction, but not more indium than can be accommodated by the buffer layer composition steps; and (3) pseudomorphic AlAs barriers, rather than metamorphic layers.

Strain-relaxed $\text{In}_x\text{Ga}_{1-x}\text{As}$ step buffers were used in the present work. The structure was grown by solid-source molecular beam epitaxy (MBE) system using $\langle 100 \rangle$ GaAs n^+ substrates. Mesa diodes with areas ranging from $25\ \mu\text{m}^2$ to $90\ \mu\text{m}^2$ were processed using standard photolithography and wet etching techniques. The I-V characteristics of the devices were measured at room temperature and 77 K. The maximum peak current density was $22.8\ \text{kA/cm}^2$. The maximum PVCr measured was 13:1 at room temperature and 27.5:1 at 77 K.

The good intrinsic performance of the devices indicates that resonant tunneling structures are robust and can withstand the presence of some dislocations within active layers, although care clearly must be taken to keep their density down. The devices were grown under conditions compatible with epitaxy on commercial GaAs VLSI. With reduction of their series resistance, they will be suitable, for example, for realizing high-density, low-power static random access memory arrays.

1.3 Monolithic Enhancement of MESFET Electronics with Resonant Tunneling Diodes

Sponsor

Joint Services Electronics Program
Grant DAAH04-95-1-0038

Project Staff

Rajni J. Aggarwal, Professor Clifton G. Fonstad, Jr., in collaboration with Professor Eugene A. Fitzgerald and M.T. Bulsara

Using the epitaxy-on-electronics (EoE) integration technique, we have monolithically integrated relaxed-buffer InGaAs/AlAs resonant tunneling diodes (RTDs) with GaAs MESFET VLSI circuits to

build static random access memory (SRAM) cells. We have performed material characterization and electrical characterization of the integrated RTDs, and our results show that RTD heterostructure material grown on GaAs VLSI circuits is comparable in quality to that grown on epi-ready GaAs substrates. We also evaluated the critical RTD parameters for this application (i.e., the peak and valley voltages and current densities) over a 25 mm² integrated circuit to quantitatively establish circuit design rules. Finally, in the past year we have demonstrated the first RTD memory cells monolithically integrated on GaAs integrated circuits.

The lack of a compact, low-power memory cell has been an important limitation of GaAs MESFET integrated circuit (IC) technology. Because of large junction leakage currents, dynamic memory cells of the type widely used in silicon integrated circuits are not viable in GaAs ICs, and designers are forced to use static cells based on flip-flop circuits. These cells involve many transistors (a minimum of six, but more typically ten), consume a great deal of power, and occupy a lot of chip space. A compact, low-power static memory cell formed with two tunnel diodes and a single transistor has been proposed as an alternative by several groups. Other groups have proposed integrating tunnel diodes with resonant hot electron transistors (RHETs) and heterojunction bipolar transistors (HBTs) to produce low-power III-V logic circuits.

A major problem with these proposals is that they would require the development of an entire VLSI technology to be implemented. It is in this aspect of the problem that the EoE technology offers its solution. By building on the multimillion dollar, multithousand man-year investment in technology development made by such companies as Motorola and Vitesse Semiconductor in developing their commercial GaAs VLSI production facilities, the EoE process leapfrogs the basic issue of developing a VLSI technology and focuses on the issues involved in complementing that technology with monolithic heterostructure devices, in the present case, with resonant tunneling diodes.

The uniformity of device performance across an integrated circuit chip of EoE RTDs and the similarity of that data to that of RTDs formed on bulk material, has important implications for optoelectronic device integration as well. Figure 1, for example, compares the forward characteristics of roughly 50 devices measured on an integrated circuit, and the same number on an epi-ready substrate. The spreads in peak and valley current and voltage levels in each case is comparable; this is very good. On the other hand, there is a difference in the current levels, which are consistently a factor

of two lower on the integrated circuit. A possible explanation is that defects originating from the ion implanted DGWs on the IC deplete portions of the RTD heterostructure, reducing the active area by two, but not otherwise affecting device performance.

The next issues to address in this program will be the minimum size of a growth well and the ultimate packing density of RTD memory cells. These issues are also being addressed with respect to optoelectronic integration.

1.4 Integrated InGaAsP/GaAs Light Emitting Diodes and Surface-Emitting Laser Diodes

Sponsors

Defense Advanced Research Projects Agency/
National Center for Integrated Photonics
Technology
National Science Foundation
Graduate Fellowship

Project Staff

Joseph F. Ahadian, Steven G. Patterson, Praveen T. Viadyanathan, Dr. Gale S. Petrich, Professor Leslie A. Kolodziejski, Professor Clifton G. Fonstad, Jr.

The epitaxy-on-electronics (EoE) integration technique allows for the growth of optical devices in foundry-opened dielectric growth windows (DGWs) on fully processed GaAs MESFET integrated circuits. But to prevent the degradation of the electronic circuit performance, epitaxy must be done at temperatures below 470 degrees C. InGaAsP, which can be grown by gas-source molecular beam epitaxy (GSMBE) and solid-source molecular beam epitaxy (SSMBE) at these temperatures, is preferred over InGaAlAs for EoE emitter applications. We are actively researching the fabrication of light emitting diodes (LEDs) and surface emitting laser diodes (SELs) in this materials system.

LEDs utilizing InGaP/GaAs double heterostructures have been grown and characterized (electroluminescent efficiencies are typically 3 μ W/mA), with recent efforts directed toward improving their electrical and optical performance. Various doping profiles have been implemented to reduce device bulk resistivity and to improve the current spreading in order to obtain more uniform optical emission. Incorporated into the LED design have been various etch-stop layers to permit selective etching of mesa type structures. A wet-etch process has been developed on campus using these etch stops,

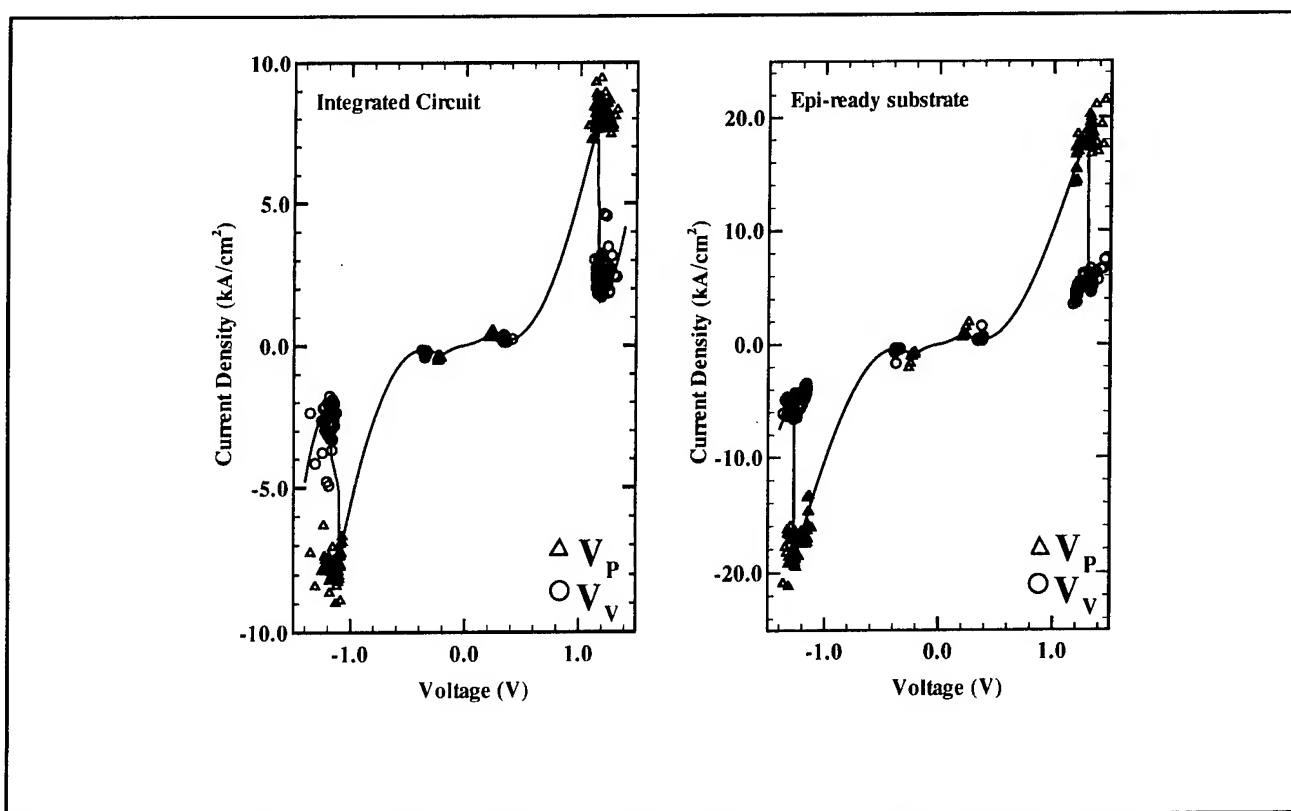


Figure 1. The variations in peak and valley current and voltage measured on fifty resonant tunneling diodes on an integrated circuit (left) and on an epi-ready GaAs substrate (right). Based on these results, we conclude that EoE integration yields devices with uniformity comparable to bulk growth. For proper operation, an integrated memory cell using the $n = 1$ resonance must accommodate up to a 9 percent variation in peak current, and one that uses the $n = 2$ resonance must accommodate a 15 percent variation.

and our collaborator, Dr. William Goodhue at MIT Lincoln Laboratory, has recently developed a dry-etch process for these materials using ion-beam assisted etching, and we will be applying this technique to mesa LEDs soon. A variety of top contacts have also been investigated, including indium tin oxide, transparent metals, and "finger" patterns.

Efforts have also been directed on several fronts at the development of SELs for integration. Broad-area, in-plane lasers grown at 470 degrees C show current thresholds of 200 A/cm², and our immediate goal is to use such material to fabricate in-plane surface-emitting lasers (IPSELs). To this end, we are collaborating with Dr. Goodhue and Professor Steve Forrest at Princeton University to adapt their respective IPSEL processes to this materials system.

Ultimately, we hope to develop a vertical-cavity, surface-emitting laser (VCSEL) integration technology. We are collaborating with Professor Dan Dapkus at the University of Southern California on oxidation of AlAs to form distributed Bragg reflec-

tors (DBRs). A 33-pair InGaP/AlAs DBR fabricated in our laboratory displayed a reflection coefficient spectrum that closely matched theoretical calculations, and oxidation of AlAs layers has been successfully accomplished, thereby enabling the fabrication of highly reflective DBRs with fewer reflector periods. Recognizing that the performance of future VCSELs depends strongly on the DBR quality and strict cavity length control, an in situ spectroscopic ellipsometer will be utilized during the fabrication of future DBR heterostructures.

1.5 Integrated Photodetector Standard Cells

Sponsors

Defense Advanced Research Projects Agency/
National Center for Integrated Photonics
Technology
National Science Foundation
Graduate Fellowship
NTT Corporation

Project Staff

Masami Tachikawa, Joseph F. Ahadian, Professor Clifton G. Fonstad, Jr.

In the epitaxy-on-electronics (EoE) optoelectronic integration process, it is desirable to use photodetectors fabricated utilizing the basic MESFET process, rather than epitaxially, so that the epitaxial heterostructures can be reserved and optimized exclusively for emitters. Consequently, we have begun to design, process through MOSIS, and characterize various photodetector structures. These studies involve individual photodetectors, as well as photodetectors with associated electronics (e.g., transimpedance amplifiers), which taken together can be viewed as optical bond pads for inputting signals optically to chips.

Three types of cells involving detectors fabricated during the standard MOSIS/Vitesse HGaAs₃ process have been investigated to date: (1) optically-sensitive field effect transistors (OPFETs), (2) OPFETs with depletion-mode field-effect transistor (DFET) loads, and (3) metal-semiconductor-metal (MSM) photo-detectors. The spectral response of these devices was measured and found to match closely the absorption spectrum of gallium arsenide. The measured output current of the MSM detectors is linear as a function of input light power, while the OPFETs show a logarithmic dependance of their voltage on the input current level, as predicted by the theory of a floating gate OPFET. The current response is 7.5 A/W at 880 nm and increases to over 400 A/W at wavelengths shorter than 800 nm. The MSM response is 0.1 A/W at these shorter wavelengths.

Measurements of the dynamic response of the detectors is still underway, and improvements need to be made in our system to permit measurements at higher frequencies. To date, the devices have been mounted in 40-pin integrated circuit packages along with chip preamplifiers to provide enough signal with a high speed light emitting diode as the input. The OPFETs are found to be relatively slow, with response times of several tens of microseconds. This is consistent with earlier work done on these devices by our collaborators at CalTech, and represents the gain-bandwidth trade-off inherent in these devices. The MSM devices, on the other hand, are much faster detectors; presently we are limited by our measurement system in characterizing MSMs to response times of 0.1 μ s.

Our immediate objective is to improve our measurement system to perform high-frequency characterization, evaluate the effects of backgating on OPFET and MSM response, and develop and eval-

uate high-performance transimpedance amplifiers for use with MSM detectors.

1.6 Microwave Characterization of Optoelectronic Devices

Sponsors

Defense Advanced Research Projects Agency/
National Center for Integrated Photonics
Technology
National Science Foundation
Graduate Fellowship

Project Staff

Praveen T. Viadyanathan, Dr. Sheila Prasad, Professor Clifton G. Fonstad, Jr.

The investigation of the high-frequency and high-speed performance of optoelectronic devices and integrated circuits has been initiated. The optical and electrical components will be characterized separately, afterward the entire optoelectronic integrated circuit (OEIC) will be characterized. There are certain significant issues arising in optoelectronic integration that directly affect the high-frequency/high-speed performance of the OEICs. These issues are to be explored in the course of the investigation.

A scattering (S) parameter measurement facility has been designed and implemented for the high frequency characterization of the optical components of the OEIC. This facility permits the characterization of individual photonic devices and subsequently the characterization of the full OEIC.

The set-up consists of Hewlett-Packard 8510B automatic network analyzer equipped with an S-parameter test set, a modified Cascade Microtech on-wafer probe station, and a New Focus high speed photodetector. This is a broadband photodetector (400-1650 nm) operating from DC to 26 GHz, 17 ps rise time and 5 V/W. The responsivity of this photodetector is approximately 0.2 A/W over the entire wavelength. It is planned the make measurement of laser diodes and light emitting diodes over this frequency range. On wafer probing eliminates problems with packaging parasitics, and the Cascade microwave probe station has been modified so that it is suitable for the constant temperature probing of both edge and surface emitting devices. Future modifications for the probing of photodetecting devices such as photodiodes and MSM detectors are being designed.

Simultaneously, the issue of novel methods of instrument calibration is being addressed. Calibration techniques which take into account the optical components such as the fibers are under investigation for the optimization of accuracy. This calibration will be equivalent to the electrical open-short-line method used for electrical calibration.

This facility will permit the full characterization of optical and electrical devices as well as the circuits. Measurements will be performed for the extraction of model parameters and equivalent circuits to design optimized devices.

1.7 Growth of Distributed Bragg Reflector and Multiple Quantum Well Heterostructures at Reduced Temperature

Sponsors

Defense Advanced Research Projects Agency/
National Center for Integrated Photonics
Technology
National Science Foundation
Graduate Fellowship

Project Staff

Hao Wang, Professor Clifton G. Fonstad, Jr.

Growth of optical devices on commercially available VLSI GaAs electronic circuits via the epitaxy-on-electronics (EoE) integration technique employing molecular beam epitaxy (MBE) requires growth temperatures below 470 degrees C to avoid deterioration of the underlying circuitry. Furthermore, a growth temperature even lower than 470 degrees C is required to grow thick, and therefore lengthy growth sequences of optical devices such as vertical cavity surface emitting lasers (VCSELs) and self electro-optic effect device (SEED) modulators.

An important issue to be addressed is whether the reduced-temperature MBE growth can produce high quality optical devices and how the optical quality at low-growth temperatures can be optimized. We are currently investigating lowered-temperature growth of distributed Bragg reflectors (DBRs) and multiple quantum wells (MQWs), which are constituent elements of VCSELs and SEEDs. We are also growing complete VCSELs and SEEDs. The growth temperature constraint does not allow fully optimized quantum well formation and ideal

interfacial quality in superlattices during conventional MBE. Therefore, we are exploiting alternative methods of low-temperature epitaxy, such as atomic layer epitaxy (ALE) via MBE, pulsed-arsenic MBE, and stoichiometric (unity group III to group V flux ratio) MBE. By reducing the arsenic overpressure while still staying above unity V/III flux ratio, we have demonstrated (Al, Ga)As DBRs with growth-temperature independent reflectivity down to a growth temperature as low as 400 C (see figure 2).

In addition to high optical quality mirrors, low modulation-voltage MQWs are also essential for integration with low-voltage digital circuits which typically have 0 V and -2.0 V rails. SEED devices grown at 500 degrees C have been fabricated and function well with an 8 V voltage swing. Asymmetric integrated with enhancement- and depletion-mode MESFET VLSI circuits, which were designed as a part of the EoE multiproject chip, to produce dual-rail digital optical logic circuits which will effectively compete with depletion-mode only MESFET-SEED technology.

1.8 Monolithic Integration of Self-Electrooptic-Effect Devices on Very Large Scale Integrated GaAs Electronics

Sponsors

Defense Advanced Research Projects Agency/
National Center for Integrated Photonics
Technology
National Science Foundation

Project Staff

Hao Wang, Krishna V. Shenoy, Professor Clifton G. Fonstad, Jr., Professor Cardinal Warde, in collaboration with Jiafu Luo and Dr. Demetri Psaltis⁵

Benefiting from the novel epitaxy-on-electronics (EoE) optoelectronic integration technique, the pursuit of integrating self-electrooptic-effect devices (SEEDs) with both enhancement- and depletion-mode MESFET VLSI circuits has become feasible.

Dedicated SEED MESFET VLSI circuits have been designed and fabricated as part of the MIT EoE multiproject chips, which includes optical logic gates such as a SEED receiver, NOR gate, transmitter, and more complicated logic combinations. In addi-

⁵ California Institute of Technology, Pasadena, California.

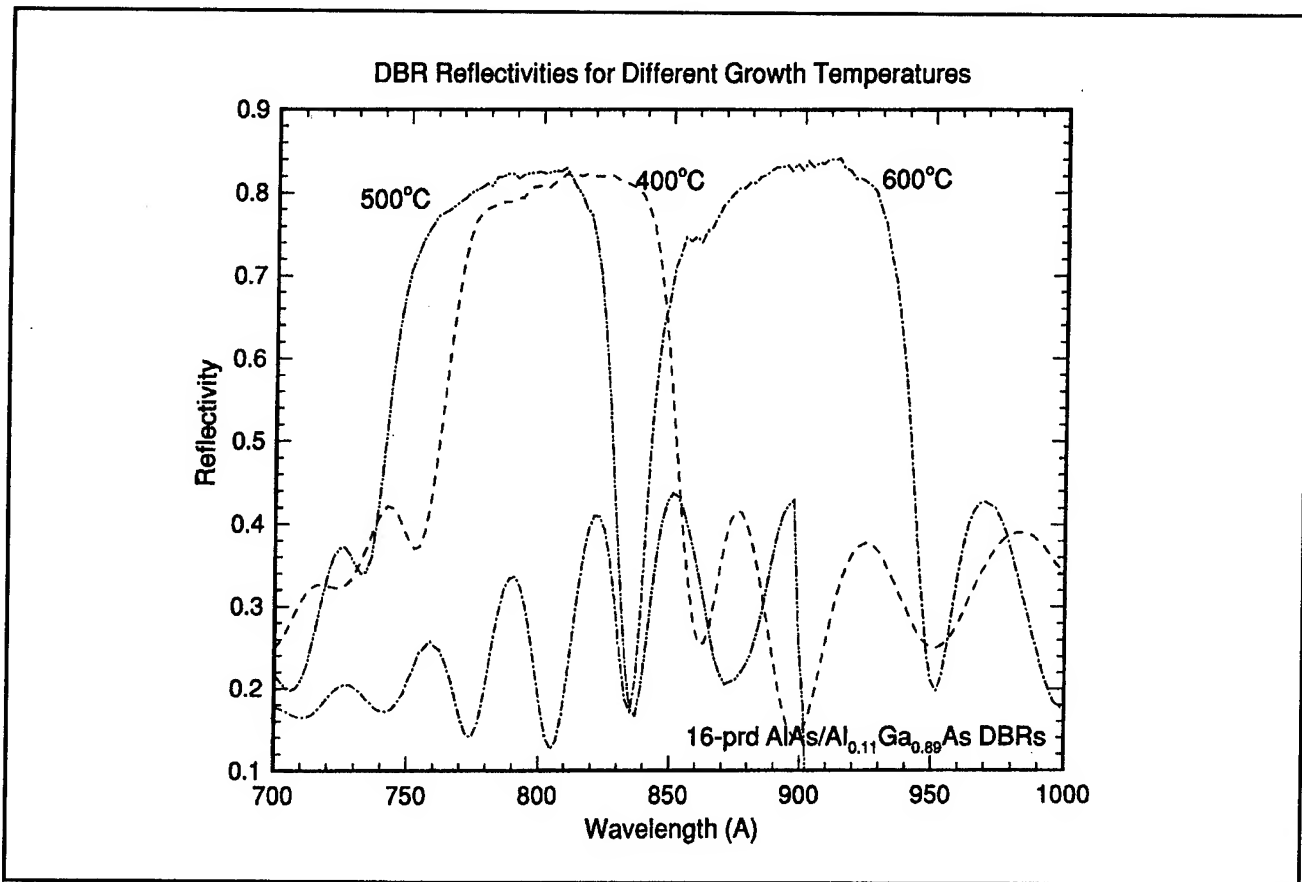


Figure 2. Reflectivities of 16 periods' AlAs/Al_{0.11}Ga_{0.89}As DBRs grown at temperatures ranging from 600 degrees C down to 400 degrees C. The shift in wavelength of the pass band is due to a calibration error and is not related to the growth temperature differences.

tion, a 10 x 10 SEED optical bump circuit array has been designed by our collaborators at Caltech. After several SEED growth/fabrication efforts, the first working low-temperature integrated SEED has been demonstrated on a chip. A useful contrast ratio of 2.2:1 was obtained for a monolithically integrated device while even a better contrast ratio of 3.27:1 was obtained for the bulk monitor at 10V bias (see figure 3). Further improvements of regrowth crystal quality are currently under investigation.

One very important issue addressed in our research is how to achieve low-temperature substrate cleaning prior to molecular-beam epitaxy growth. The EoE integration technique demands that we not expose the VLSI chip to a temperature higher than 470 degrees C to avoid degradation of the underlying circuitry. However, conventional MBE growth involves thermal oxide removal at 580 degrees C prior to epitaxy, which poses serious problems for the survival of the electronics. Our current research is exploiting alternative methods of low-temperature oxide removal, such as in situ chemical etching of GaAs substrates by gaseous

HCl, or GaAs substrate cleaning using atomic hydrogen. With these efforts, fully functioning high density optoelectronic SEED circuitry will soon be achieved with performance superior to current depletion-mode-only FET-SEED technology.

1.9 Compact Integrated Optics Structures for Monolithic Integration

Sponsors

Defense Advanced Research Projects Agency/
National Center for Integrated Photonics
Technology

Project Staff

Yakov Royter, Professor Clifton G. Fonstad, Jr., in collaboration with Dr. William D. Goodhue

Recently, due to the fiberoptic telecommunications boom, much work has been done on integrating semiconductor optical devices, such as modulators, detectors, and lasers, with driving electronics made up of MESFETs, MODFETs, or HBTs. However,

the necessity to optimize both the optical and electronic devices simultaneously makes the progress slow. Our project is to integrate mature GaAs electronic ICs with integrated optics components by selectively growing (MBE) our optical devices on open areas of commercial GaAs IC chips. This epitaxy-on-electronics (EoE) technique has already been successfully achieved for integrating LED arrays with driver circuits. Our goal is to demonstrate a working integrated optics circuit fabricated on and integrated with a GaAs IC chip. The basic optical components of this system are passive waveguides, phase modulators, and detectors. The electronics will consist of driving and amplifying circuit for the modulators, and detectors, as well as signal processing and control digital circuits. Since the area of the GaAs VLSI chip is expensive, the conventional gradual bends, necessary to change the propagation direction of guided light will be replaced by abrupt 90 degree bends with deep etched total internal reflection (TIR) mirrors (see figure 4).

In our first attempts at EoE integrated optics, we have used lowered temperature AlGaAs/GaAs heterostructures, grown at 500 degrees C, so that drastic deterioration of the IC performance is not

caused. However, the material quality of AlGaAs is poor: we have measured waveguide losses greater than 20 dB/cm. Therefore, lattice matched InGaP/GaAs heterostructures will be used since InGaP grown at 470 degrees C is higher quality. Currently, etching techniques for InGaP material are being investigated. In particular, dry etching methods for creating deep openings with smooth vertical walls in InGaP/GaAs heterostructures are being developed. Such smooth vertical walls are necessary for the low loss TIR mirror waveguide bends.

In addition to optical device design, circuit design is also being carried out. Several versions of modulator driver circuits have been designed, fabricated at the Vitesse MOSIS foundry, and tested. These circuits are able to drive the modulators with a 10 V swing output with DCFL inputs of 0-0.6 V, and speeds of up to 5 MHz driving external circuit board lines. Since the HSPICE simulation suggests 200 MHz performance, we expect a drastic improvement in performance for these circuits driving on chip interconnections. (The simulations were done using Vitesse HSPICE device parameters.) Complementing the modulator driver design, such fundamental issues for high voltage MESFET

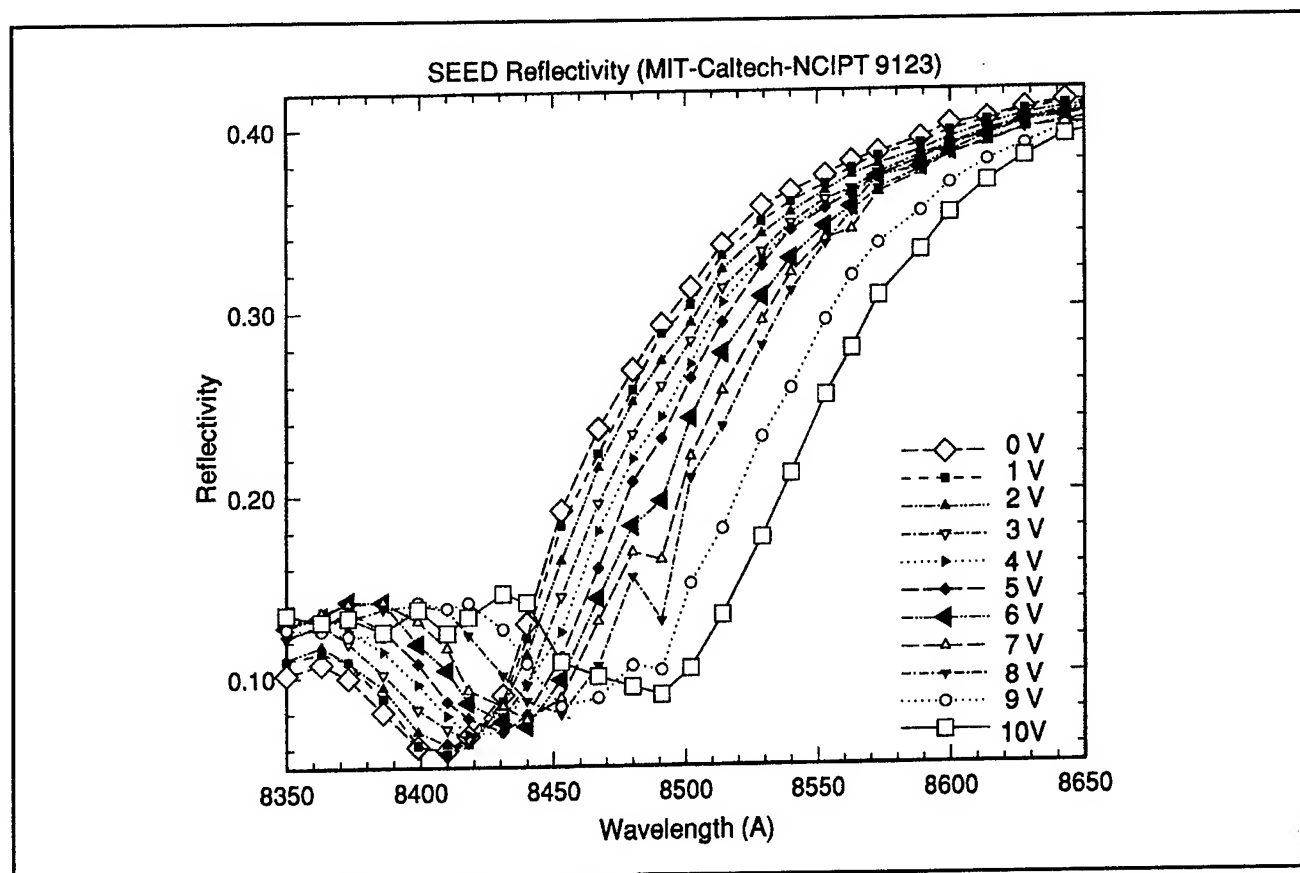


Figure 3. The measured reflectivity spectrum between 835 and 865 nm of a SEED modulator at selected voltages between 0 and 10 volts.

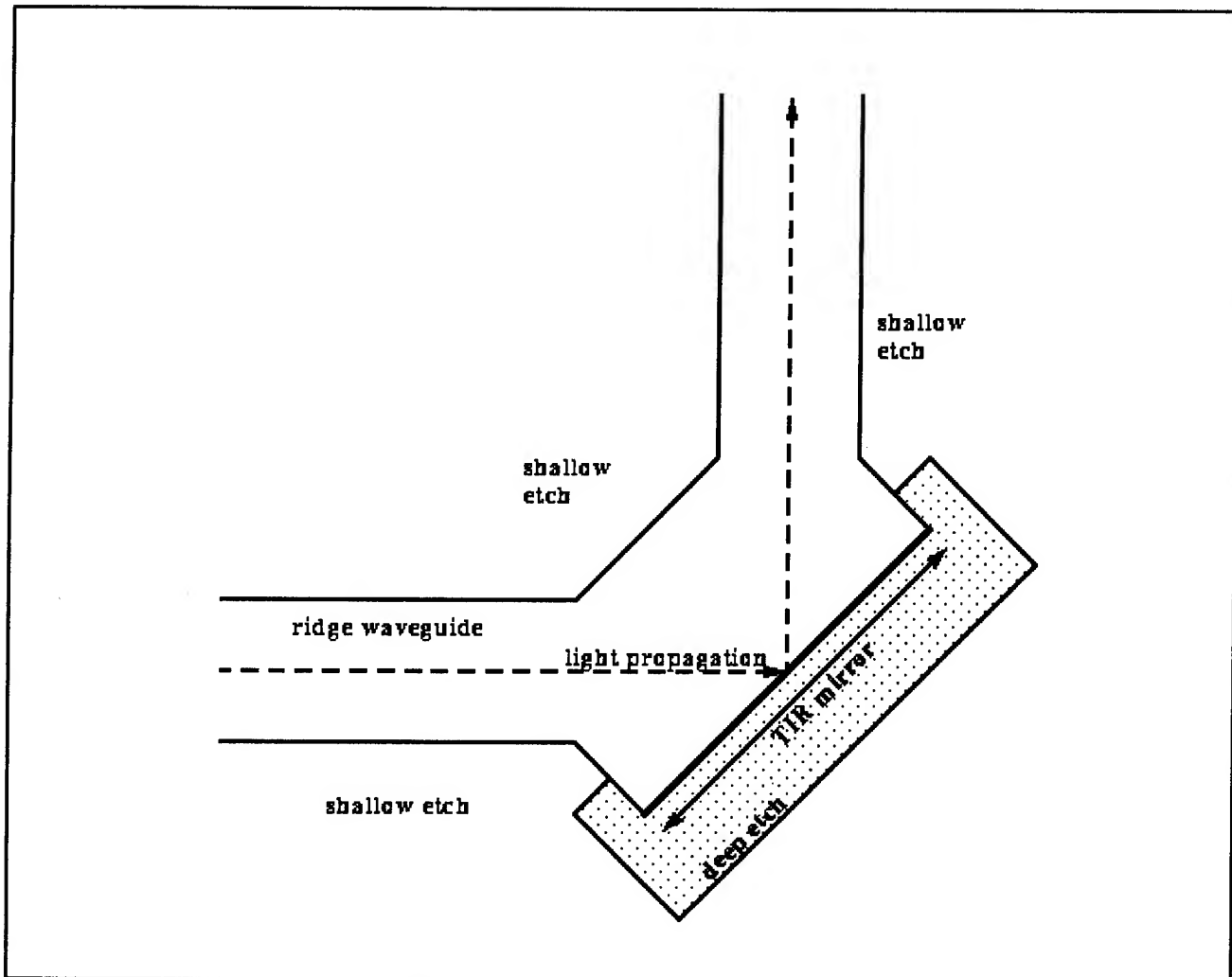


Figure 4. Waveguide bend with total internal reflection (TIR) mirror.

circuit design such as backgating and gate breakdown are being investigated. Structures with depleted isolation barriers have been shown to eliminate backgating. Finally, a library of digital circuit cells is being compiled for the control logic needed in the demonstration project.

1.10 The OPTOCHIP Project and other Multigroup OEIC Chips

Sponsors

Defense Advanced Research Projects Agency/
National Center for Integrated Photonics
Technology

Project Staff

Joseph F. Ahadian, Steven G. Patterson, Yakov Royter, Praveen T. Viadyanathan, Masami Tachikawa, Dr. Gale S. Petrich, Professor Leslie A.

Kolodziejski, Professor Clifton G. Fonstad, Jr., and J.M. Mikkelsen

The OEIC Platforms Project is a directed technology project within NCIPT focused on developing an optoelectronic integration technology based on commercially available gallium arsenide integrated circuits. This technology, named epitaxy-on-electronics (EoE), involves the epitaxial growth of optoelectronic device heterostructures on fully metallized GaAs MESFET VLSI electronics. In addition to developing this OEIC technology, the project has the goal of making this technology available to the broad academic and research communities.

Progress has continued in all major areas of the OEIC Directed Project: (1) continued work on reduced-temperature epitaxy (RTE) of low-threshold InGaAsP laser diodes (GS-MBE growth), (2) use of atomic hydrogen to prepare surfaces for epitaxy at 350 C, (3) demonstration of the first monolithically

integrated SEED and other window modulator structures, (4) initiation of integrated optics (fiber-coupled geometry) projects, (5) realization of the second multiproject OEIC chip, and (6) inauguration of the OPTOCHIP project.

The NCIPT multiproject OEIC chips are our vehicle for involving many NCIPT groups and members of the outside community epitaxy-on-electronics OEIC chips. These chips, of which there are now two generations, involve OEIC and test cell designs (over 50 in total) from five universities. Included are cell designs for both smart pixel (i.e., surface-normal configuration) OEICs and integrated optics (i.e., in plane, fiber-coupled configuration) OEICs. The chips are being used as the foundation for epitaxial growth and device processing for a variety of device types and structures and for realization of a wide variety of OEICs.

The OPTOCHIP Project was launched in Fall 1995 to involve the smart pixel community in an epi-on-electronics multiproject OEIC chip through a foundry-like mechanism. A total of eight diverse groups have been selected to participate from over twice that number of applicants. The offering will involve LEDs, detectors, and MESFETs. Chips designs will be completed in May 1996, and chips will be returned to participants in October 1996.

1.11 Normal Incidence Single- and Dual-Band Quantum-Well Intersubband Photodetectors

Sponsors

National Science Foundation
U.S. Navy - Office of Naval Research

Project Staff

Paul S. Martin, Janet L. Pan, Professor Clifton G. Fonstad, Jr., and P. Kannam

Quantum-well intersubband photodetectors (QWIPs) are attractive devices to compete with HgCdTe for use in focal plane arrays. QWIPs can take advantage of the established technology for growing and processing GaAs optical devices to improve device uniformity and array yield.

We have demonstrated the first TE-active normal incidence QWIPs based on InGaAs/AlGaAs quantum wells grown pseudomorphically strained on GaAs. Our best devices consist of five 45 Å quantum wells of In_{0.13}GaAs doped n-type at $5 \times 10^{17} \text{ cm}^{-3}$ and separated by 510 Å of unintentionally doped Al_{0.30}GaAs. The measured responsivity is shown in figure 5. The peak signal to noise ratio of

680 occurred for a bias of 3.2 V giving a peak wavelength of 6.4 μm , a peak responsivity of 200,000 V/W (25 mA/W) and a D_λ of $6 \times 10^9 \text{ cm} - \text{Hz}^{1/2}/\text{W}$ for a 100 μm square mesa device measured at 77 K. The FWHM of the response is 1.0 μm typical of bound to quasi-bound intersubband signals and very attractive for potential multi-band QWIP applications. The D_λ of $6 \times 10^9 \text{ cm} - \text{Hz}^{1/2}/\text{W}$ for this unoptimized device is within a factor of two of the value at which uniformity of the QWIP array and not D^* becomes the limiting factor in performance as measured by NEDT. This highlights our emphasis on TE active devices which eliminate the need for additional processing to implement gratings for other TM coupling mechanisms and removes the additional processing nonuniformity these TM couplers cause.

We are currently working to improve the responsivity of our detectors and to integrate a second detector on top of another vertically. Because no gratings are needed to couple the normally incident light into the active detectors, these dual band detectors are relatively simple to design and emphasize the advantages of the simple TE mode device design.

1.12 Integrated Quantum-Well Intersubband Photodetector Focal Plane Arrays

Sponsor

U.S. Navy - Office of Naval Research

Project Staff

Paul S. Martin, Janet L. Pan, Professor Clifton G. Fonstad, Jr., P. Kannam

The monolithic integration on GaAs circuits of normal-incidence-active (TE-mode) quantum well infrared photodetector (QWIP) focal plane arrays (FPAs) is expected to increase the yield and processing simplicity of infrared photodetector FPAs. This is very important because QWIP and other infrared photodetector FPAs are currently limited by the uniformity of the performance over an entire FPA and not by detectivity of each pixel in the array.

Monolithic integration means that there is no thermal mismatch between different substrate materials, as there is in a hybridized technology of GaAs QWIPs bump bonded to Si circuits. Processing is also simplified because intricate and expensive In bump bonding is not needed. Normal incidence active QWIPs do not require gratings to be coupled to the normally incident radiation. The use of GaAs

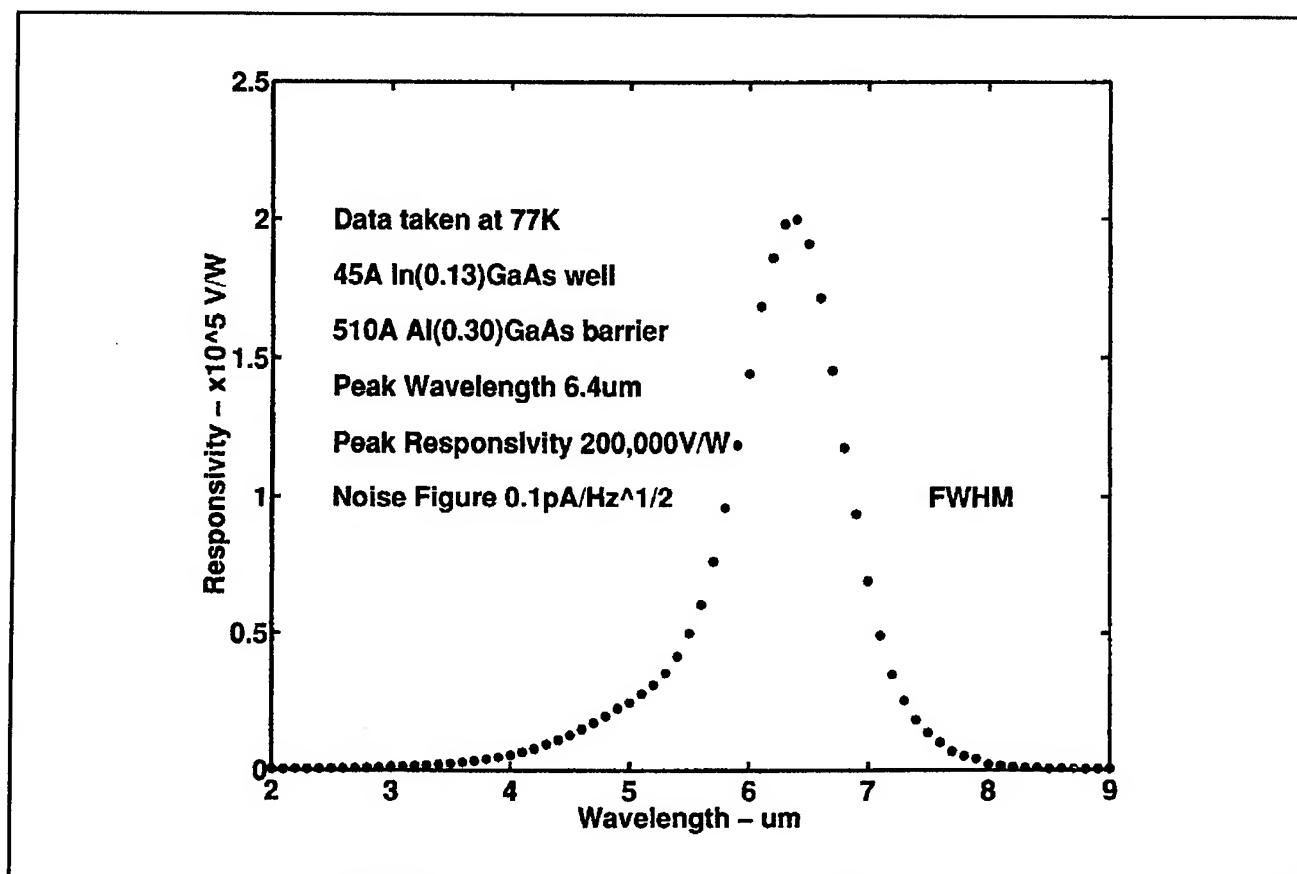


Figure 5. The normal incidence responsivity measured at 77K for a pseudomorphic InGaAs QWIP consisting of five periods of 4.5 nm of $\text{In}_{0.13}\text{Ga}_{0.87}\text{As}$ and 51 nm of $\text{Al}_{0.3}\text{Ga}_{0.7}\text{As}$.

as the substrate material offers advantages of: (1) a mature processing technology; (2) the existence of large, low cost, highly uniform and reliable substrates, as compared with mercury cadmium telluride detectors; and (3) the intrinsic radiation hardness of GaAs, as compared with Si. The elimination of In bump bonding and grating fabrication, as well as the use of a GaAs substrate, allows for high yield and low cost QWIP FPAs.

In addition to the simplified processing steps discussed above, the cost of using QWIP FPAs can be lowered by increasing the QWIP operating temperature. We are investigating two possible approaches to doing this. First, band gap engineering will be used to design QWIPs whose upper state lifetimes are greatly increased. This would increase the detectivity, and thus the temperature of the background limited performance, of each QWIP. Second, microlenses will be used to increase the ratio of the photocurrent to the dark current at a given QWIP size by concentrating more of the incident photon flux onto each QWIP pixel. Microlenses increase the detectivity at a given QWIP

size, as well as allowing more of the space between QWIP pixels to be used for circuits.

1.13 Intersubband Transitions in Narrow Quantum Wells

Sponsors

National Science Foundation
Toshiba Corporation

Project Staff

Norio Iisuka, Professor Clifton G. Fonstad, Jr.

Intersubband transitions are very attractive phenomena because they are applicable to lasers, photodetectors, optical modulators and other novel photonic devices. In this project, we focus our effort on research on quantum wells in which the intersubband wavelength is $1.55 \mu\text{m}$ shorter, which is optimal for optical communication. To achieve such intersubband transitions, we are growing $\text{In}(\text{Ga})\text{As}/\text{AlAs}$ quantum well structures where on InP or GaAs substrates the well width is as narrow as a few monolayers.

The well width in these structures is so narrow that the quality of interface between the barrier and the well is critical. Interface roughness will cause the transition energy to shift. To achieve good quality of interface, we are trying to adapt migration enhanced epitaxy (MEE) to this problem. Another material problem is that the critical thickness of a barrier layer or a well layer is very small because of the large difference in the lattice constants of the barrier and the well materials. Consequently, it is difficult to grow multiple-quantum-well structures which give the light and quantum wells more time to interact than a single quantum well structure does. To overcome this difficulty, the strain compensated structure, which consists of InAs and AlAs on InP substrate, will be tested.

In actual materials, absorption due to undesirable energy levels such as a surface level are sometimes confused with absorption due to intersubband transitions. We have found that there is the specific region of cap layer thickness in which the effect of surface states can be eliminated in absorption measurements made on the waveguide configuration. With this thickness of the cap layer, very little of the incident light exists in the cap layer, which is confirmed by calculating the distribution of the light intensity. A self-consistent electronic state calculation program is also being developed. The calculation will give us information about what the quantum well structure is like, what the subband levels are, and how many electronics populate the well region. Accordingly, it will become a useful tool for the design of novel devices using intersubband transitions.

1.14 Kinetic Beam Etching of Semiconductor Nanostructures

Sponsors

Defense Advanced Research Projects Agency/
National Center for Integrated Photonics
Technology
AT&T Bell Laboratories
Graduate Fellowship

Project Staff

Isako Hoshino, Professor Clifton G. Fonstad, Jr.

Since it became necessary to grow compound semiconductor epitaxial layers upon an already existing integrated circuit, it became crucial to minimize or eliminate surface damages caused by conventional etching techniques using plasma sources. To find a solution to the problem of process-induced damage, we have begun a project investigating the use of molecular-beam (hot neutral

beam, also known as kinetic beam) techniques to etch and clean III-V substrates and heterostructures with a minimum of surface damage and allowing maximum flexibility in attaining various etch profiles. Depending on the gas combination, it is anticipated that low energy (0.1 to 10 eV) kinetic beams can be used to (1) both directionally and isotropically etch-pattern III-V heterostructure wafers with no damage; (2) clean surfaces allowing epitaxial growth on wafers that have been removed from the UHV environment for external processing; and (3) selectively remove masking materials and clean surfaces suitable for subsequent overgrowth.

A differentially pumped UHV kinetic beam etch (KBE) system design to use a methane-hydrogen gas mixture using a supersonic beam has been designed and constructed. The initial function tests of the KBE system are currently underway. Subsequently, a full-scale characterization of the ability of the KBE system will be performed, mainly concentrating on etch rate, etch profile, and surface damage assessment. The extent of surface damage, if any, will be determined through electrical and optical characterizations of heterostructure devices grown by solid-source MBE. Once the KBE system is fully characterized, it will be connected to the existing MBE system through a UHV transfer tube.

1.15 Publications

Aggarwal, R.J., and C.G. Fonstad. "High Peak-to-valley Current Ratio InGaAs/AlAs RTSs on GaAs using Relaxed InGaAs Buffers." *Electr. Lett.* 31: 75-76 (1995).

Aggarwal, R.J., K.V. Shenoy, and C.G. Fonstad, Jr. "A Technology for Monolithic Integration of High-indium-fraction Resonant-tunneling Diodes with Commercial MESFET VLSI Electronics." *Proceedings of the Seventh International Conference on Indium Phosphide and Related Materials*, Sapporo, Japan, May 9-13, 1995.

Braun, E.K., K.V. Shenoy, and C.G. Fonstad. "Elevated Temperature Stability of GaAs Digital Integrated Circuits." *IEEE Elect. Dev. Lett.* Forthcoming.

Martin, P.S., J.C. Chen, C.G. Fonstad, and H.A. Haus. "Application of the Spectral Index Method to Laser Diode Design." *IEEE J. Lightwave Technol.* 13: 569-574 (1995).

Peng, L.H., and C.G. Fonstad. "Multiband Coupling Effects on Electron Quantum Well Intersubband Transitions." *J. Appl. Phys.* 77: 747-754 (1995).

Peng, L.H., and C.G. Fonstad. "Spatial Confinement Effects on Type II Quantum Well Intersubband Transitions." *Appl. Phys. Lett.* 66: 1806-1808 (1995).

Peng, L.H., and C.G. Fonstad, Jr. "Intersubband Transitions in Conduction Band Quantum Wells: The Role of Energy Band Gaps and Band Offsets." *Proceedings of the Seventh International Conference on Indium Phosphide and Related Materials*, Sapporo, Japan, May 9-13, 1995.

Shenoy, K.V., C.G. Fonstad, A.C. Grot, and D. Psaltis. "Monolithic Optoelectronic Circuit Design and Fabrication by Epitaxial Growth on Commercial VLSI GaAs MESFETs." *IEEE Photon. Tech. Lett.* 7: 508-510 (1995).

Smet, J.H., C.G. Fonstad, and Q. Hu. "Intrawell and Interwell Intersubband Transitions in Single and Multiple Quantum Well Heterostructures for IR

and FIR Coherent Sources." *J. Appl. Phys.* Forthcoming.

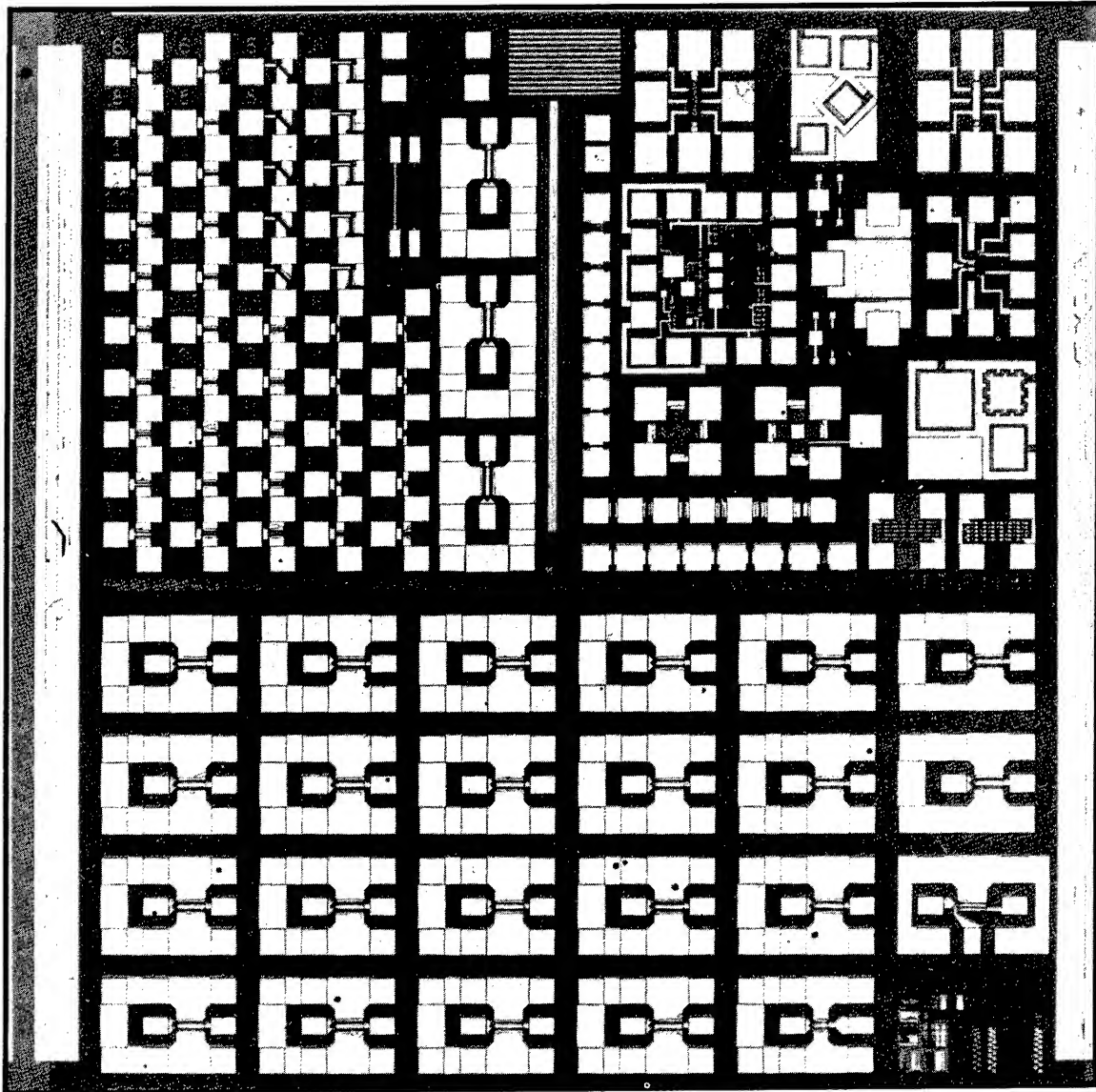
Theses

Aggarwal, R.J. *Design of Resonant-Tunneling Diodes for a GaAs Integrated SRAM*. Ph.D. diss. Dept. of Electr. Eng. and Comput. Sci., MIT, 1995.

Ahadian, J F. *Phosphide-based Optical Emitters for Monolithic Integration with GaAs MESFETs*. S.M. thesis. Dept. of Electr. Eng. and Comput. Sci., MIT, 1995.

Braun, E. *Elevated Temperature Stability of Gallium Arsenide Integrated Circuits*. S.M. thesis. Dept. of Electr. Eng. and Comput. Sci., MIT, 1995.

Shenoy, K.V. *Monolithic Optoelectronic VLSI Circuit Design and Fabrication for Optical Interconnects*. Ph.D. diss. Dept. of Electr. Eng. and Comput. Sci., MIT, 1995.



Photomicrograph of InAlAs/InGaAs High-Electron Mobility Transistor test chip fabricated at MIT.

Chapter 2. Physics of Heterostructure Field-Effect Transistors

Academic and Research Staff

Professor Jesús A. del Alamo

Graduate Students

Mark H. Somerville

Undergraduate Students

Alexander N. Ernst

Technical and Support Staff

Lisa Zeidenberg

2.1 Introduction

Sponsors

Joint Services Electronics Program

Contract DAAH04-95-1-0038

Texas Instruments

Agreement dated 11/23/94

The goal of this project is to develop InAlAs/InGaAs heterostructure field-effect transistors suitable for millimeter-wave high-power applications. This is a key missing component for millimeter-wave radar and communication systems.

Our team has been involved on research of high-power InAlAs/InGaAs heterostructure field-effect transistors for several years. Two key contributions in the past have been (1) the demonstration that the use of AlAs-rich InAlAs pseudoinulators substantially improves the breakdown voltage¹ and (2) the demonstration of selective recessed-mesa sidewall isolation to reduce gate leakage current.² We also recently identified the detailed physical mechanisms responsible for breakdown in InAlAs/InGaAs HFETs.³

In the last period of performance, we have studied in detail the physical origin of the "kink effect" in InAlAs/InGaAs HFETs.⁴ This important anomaly in the operation of these transistors deleteriously affects their power performance. Our physical understanding has culminated in the proposal of a new equivalent circuit model that successfully captures the kink. This will enable first-pass success in the design of future millimeter-wave systems based on these devices.

2.2 A New Physical Model for the Kink Effect on InAlAs/InGaAs HEMTs

InAlAs/InGaAs high electron mobility transistors (HEMTs) show significant promise for low-noise and high-power millimeter-wave applications. A significant anomaly in their behavior is the *kink effect*, a sudden rise in the drain current at a certain drain-to-source voltage that results in high drain conductance and reduced voltage gain. Conventional wisdom suggests that traps are responsible for the kink. Most theories incorporating traps suggest that high fields and/or impact-ionization-generated holes

¹ S.R. Bahl, W.J. Azzam, and J.A. del Alamo, "Strained-Insulator In_xAl_{1-x}As/n⁺-In_{0.53}Ga_{0.47}As Heterostructure Field-Effect Transistors," *IEEE Trans. Electr. Dev.* 38: 1986 (1991).

² S.R. Bahl and J.A. del Alamo, "Elimination of Mesa-Sidewall Gate-Leakage in InAlAs/InGaAs Heterostructures by Selective Sidewall Recessing," *IEEE Electr. Dev. Lett.* 13: 195 (1992).

³ S.R. Bahl and J.A. del Alamo, "Physics of Breakdown in InAlAs/n⁺-InGaAs Heterostructure Field-Effect Transistors," *IEEE Trans. Electr. Dev.* 41: 2268 (1994); S.R. Bahl, J.A. del Alamo, J. Dickmann, and S. Schildberg, "Off-State Breakdown in InAlAs/InGaAs MODFETs," *IEEE Trans. Electr. Dev.* 42: 15 (1995).

⁴ M. Somerville, J.A. del Alamo, and W. Hoke, "A New Physical Model for the Kink Effect on InAlAs/InGaAs HEMTs," *International Electron Devices Meeting*, Washington, D.C., December 10-13, p. 201, 1995.

charge traps either in the buffer⁵ or in the insulator,⁶ leading to a shift in the threshold voltage. Such a theory, while plausible, is of little predictive value because of the large number of variables involved. It is therefore important to search for other physical origins of the kink that might be amenable to simple modeling in these devices.

Recent experiments have provided indirect evidence linking the kink and impact ionization;⁷ however, it remains unclear how the two phenomena are connected. Using a specially-designed sidegate structure, we have carried out extensive characterization of the kink effect in a double-heterostructure InAlAs/InGaAs HEMT. Our measurements provide direct evidence linking the kink with impact ionization, while at the same time clearly showing that impact ionization current alone is not responsible for the kink. Careful analysis leads us to postulate a new mechanism of *barrier-induced hole pile-up* at the source to explain the kink and to propose a simple equivalent circuit description of the phenomenon.

A cross-section of the MBE-grown, double-heterostructure HEMT used in this study is presented in figure 1. The channel sheet carrier concentration is $3.5 \times 10^{12} \text{ cm}^{-2}$. Fabrication consists of device isolation via a mesa etch with a sidewall recess, a PECVD Si_3N_4 layer for liftoff assistance, Au/Ge ohmic contacts, a selective gate recess, and Pt/Ti/Au gates and interconnects. Devices with gate lengths between $0.6 \mu\text{m}$ and $2 \mu\text{m}$ were characterized. The devices exhibit $I_{\text{D,max}} = 520 \text{ mA/mm}$, $g_{\text{m,max}} = 440 \text{ mS/mm}$, and $\text{BV}_{\text{DS(off)}} \approx 8 \text{ V}$.

A relationship between the kink and impact ionization has previously been postulated based on simulation results⁸ as well as light emission and

channel-engineering experiments.⁷ However, these experiments only provided an indirect view of impact ionization. By using a specially designed sidegate structure,⁹ we have succeeded in *directly* tracking impact ionization in the device without perturbing its behavior. The sidegate structure consists of an ohmic contact on a $40 \mu\text{m} \times 15 \mu\text{m}$ mesa located $15 \mu\text{m}$ from the device under test. In the measurement, the sidegate is held at a large negative potential with respect to the source ($V_{\text{SG-S}} = -20\text{V}$). This allows the sidegate to collect a small fraction of the holes generated by impact ionization, as sketched in the inset of figure 2. Thus, the sidegate current should approximately track the impact ionization generation rate. Such behavior is observed in figure 2, where the ratio of the net sidegate current to the drain current is plotted as a function of $1/(V_{\text{DS}} - V_{\text{DS(sat)}})$ for typical values of V_{GS} . Throughout the device's range of operation, I_{SG} follows classical exponential impact ionization behavior.

Using I_{SG} , we can now explore the relationship between impact ionization and the kink effect. In figure 3, we examine I_{D} and I_{SG} for $V_{\text{GS}} = 0 \text{ V}$. The kink is clearly visible in I_{D} starting at $V_{\text{DS}} \approx 1 \text{ V}$. The onset of the kink coincides with the appearance of I_{SG} . We have found that this is the case for other values of V_{GS} . This is clearly seen in figure 4, which shows I_{D} , I_{G} , and I_{SG} as a function of V_{DG} for different V_{GS} values. This figure illustrates a number of key characteristics of the kink: the kink in I_{D} occurs approximately at constant $V_{\text{DG}} \approx 1.2 \text{ V}$; the size of the kink appears to increase with increasing V_{GS} ; and the onset of the kink coincides with the appearance of I_{SG} and with a prominent rise in I_{G} , presumably due to hole collection by the gate. These facts unequivocally establish the connection between the kink and impact ionization.

-
- ⁵ A.S. Brown et al., "AlInAs-GaInAs HEMTs Utilizing Low-temperature AlInAs Buffers Grown by MBE," *IEEE Electr. Dev. Lett.* 10: 565 (1989); T. Zimmer et al., "Kink Effect in HEMT Structures: a Trap-related Semi-quantitative Model and an Empirical Approach for Spice Simulation," *Sol. State Electr.* 35: 1543 (1992).
- ⁶ Y. Hori and M. Kuzuhara, "Improved Model for Kink Effect in AlGaAs/InGaAs Heterojunction FETs," *IEEE Trans. Electr. Dev.* 41: 2262 (1994).
- ⁷ G.G. Zhou, A.F. Fischer-Colbrie, and J.S. Harris, "I-V Kink in InAlAs/InGaAs MODFETs Due to Weak Impact Ionization in the InGaAs Channel," *Sixth International Conference on InP and Related Materials*, Santa Barbara, California, March 1994, pp.435.
- ⁸ K. Kunihiro, H. Yano, N. Goto, and Y. Ohno, "Numerical Analysis of Kink Effect in HJFET with a Heterobuffer Layer," *IEEE Trans. Electr. Dev.* 40: 493 (1993).
- ⁹ A.A. Moolji, S.R. Bahl, and J.A. del Alamo, "Impact Ionization in InAlAs/InGaAs HFETs," *IEEE Electr. Dev. Lett.* 15: 313 (1994).

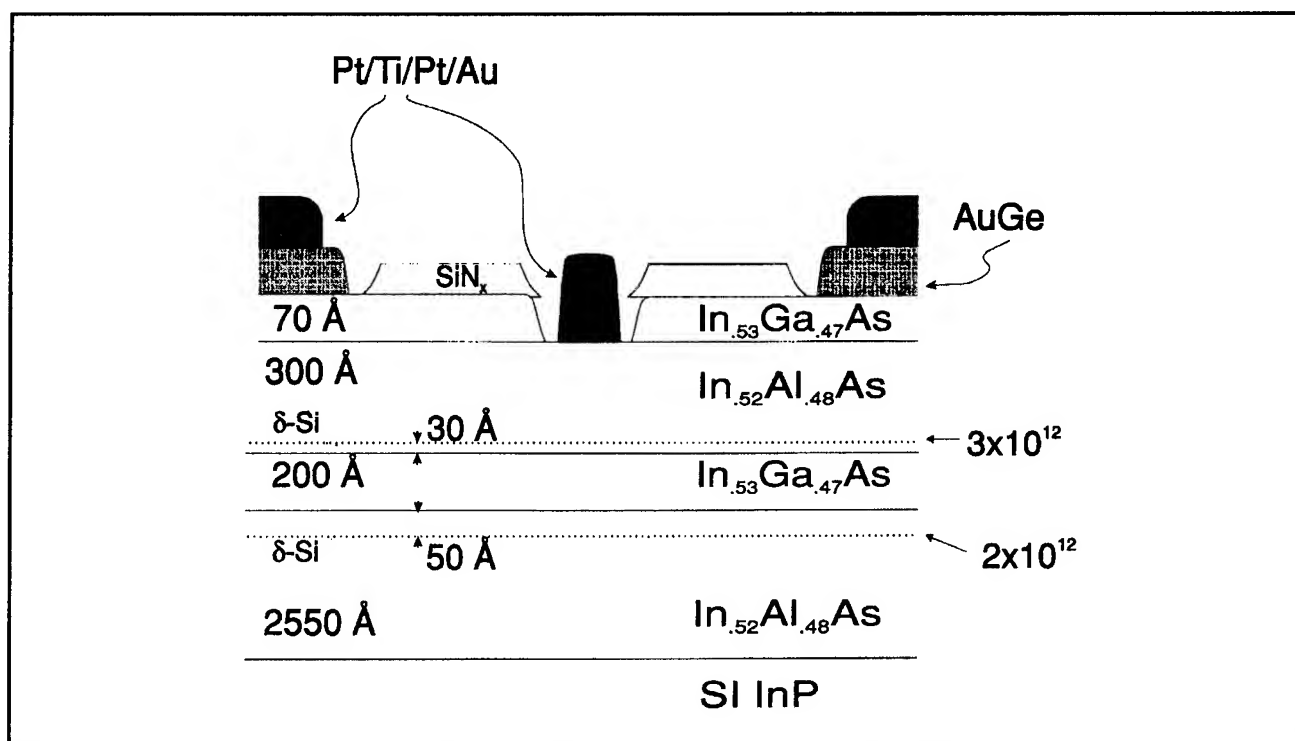


Figure 1. Schematic cross-section of InAlAs/InGaAs double-heterostructure HEMT used in this work.

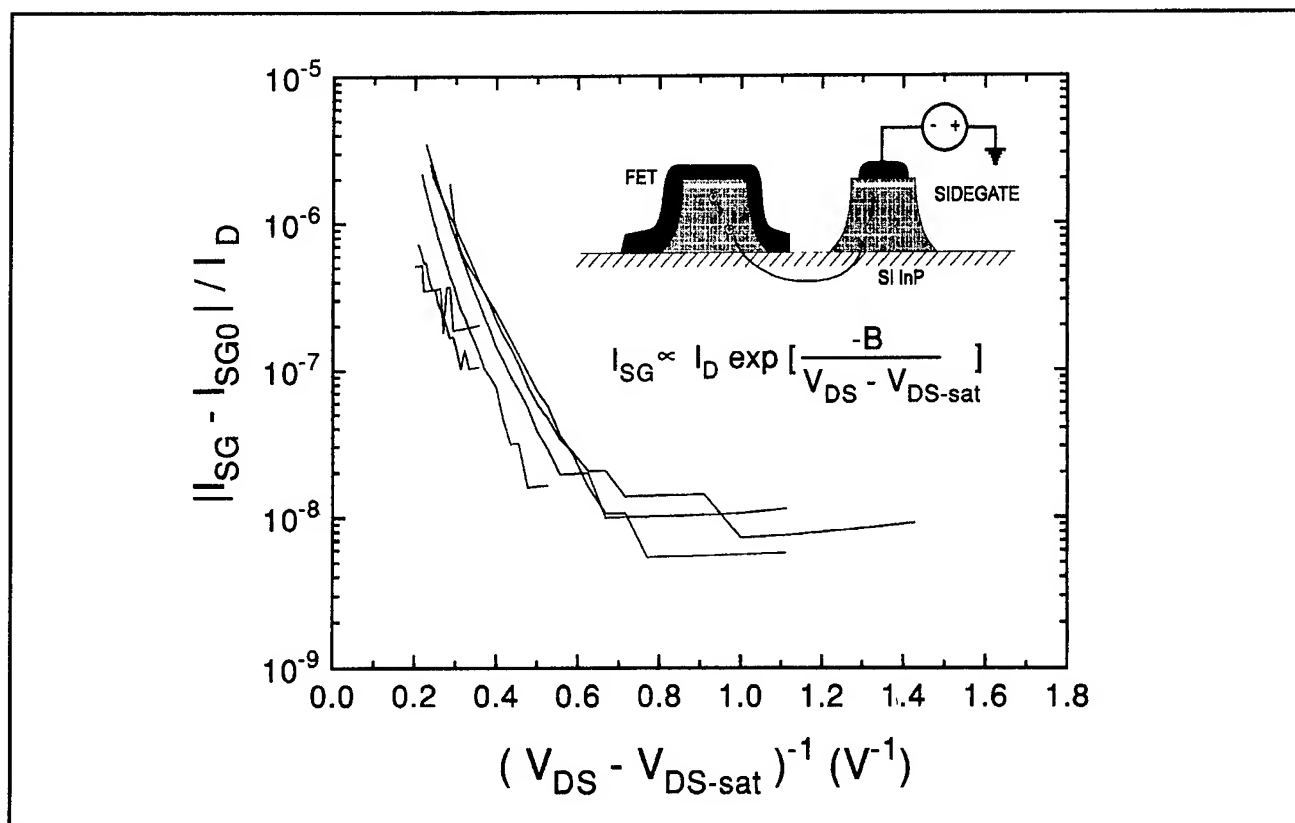


Figure 2. Semilog graph of $|I_{SB} - I_{SG0}|/I_0$ versus $1/(V_{DS} - V_{DS(sat)})$. The approximately exponential behavior at small $1/(V_{DS} - V_{DS(sat)})$ confirms the onset of impact ionization. $V_{SG-S} = -20$ V, $L_G = 2$ μ m, $T = 300$ K.

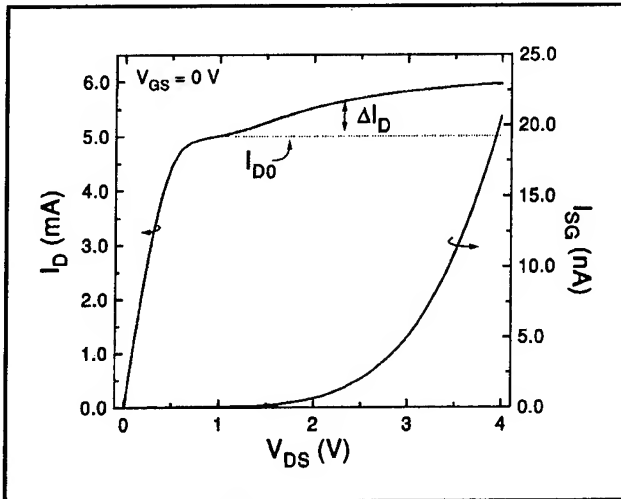


Figure 3. Drain and sidegate current at $V_{GS} = 0$. Note the saturation of the kink, in contrast with the exponential growth of the sidegate current. $L_G = 2 \mu\text{m}$, $T = 280 \text{ K}$.

Pure impact ionization has been proposed as an explanation for excess output conductance in InAlAs/InGaAs HEMTs.¹⁰ In this model, additional drain current originates from the impact ionization generated holes and electrons. Such an explanation of the kink is not consistent with our experiments. If impact ionization alone were responsible for the kink, the shape of the kink would closely track the shape of the sidegate current. However, as seen in figure 3, the kink saturates while the sidegate current grows strongly with V_{DS} . Clearly some other effect must be at work.

The kink effect in SOI MOSFETs is known to be a result of impact ionization generated holes flowing through the p-type buffer into the n^+ source.¹¹ This hole current forward biases the buffer-source p-n junction, thereby providing additional drive to the transistor. While such a hypothesis may be appropriate in some HEMT designs,¹² two facts make this explanation unlikely for current InAlAs/InGaAs HEMT designs. First, the presence of a significant valence band discontinuity (0.2 eV) between the channel and the buffer should confine most holes to the narrow channel. In addition, the fact that the

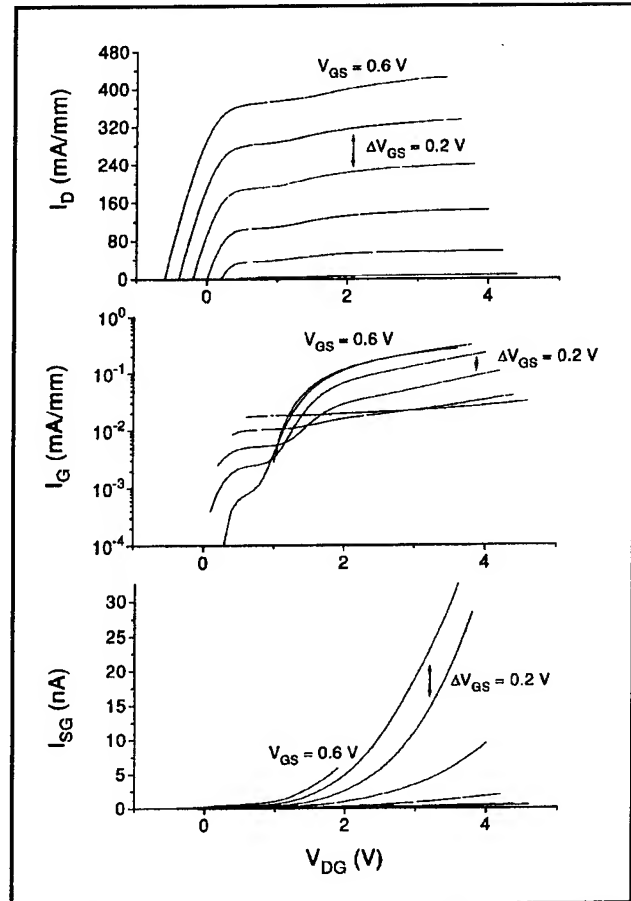


Figure 4. Drain, gate, and sidegate currents for different values of V_{GS} . The onset of the kink directly corresponds with the onset of the sidegate current and a significant increase in gate current. $L_G = 2 \mu\text{m}$, $T = 300 \text{ K}$.

channel and the buffer are undoped makes a parasitic bipolar effect less plausible.

Simulation results have recently suggested another possible explanation for the kink, source resistance reduction.¹³ In this model, holes drift into the low field source-gate region, where they diffuse and recombine. To maintain quasi-neutrality, the electron concentration must be increased, resulting in reduced source resistance. If this were the case, the excess current would be of the form

¹⁰ M. Chertouk et al., "Metamorphic InAlAs/InGaAs HEMTs on GaAs Substrates with Composite Channels and f_{max} of 350 GHz," *Seventh International Conference of InP and Related Materials*, Sapporo, Japan, 1995, p. 737.

¹¹ K. Kato, T. Wada, and K. Taniguchi, "Analysis of Kink Characteristics in SOI MOSFETs Using Two Carrier Modeling," *IEEE Trans. Electr. Dev.* ED-32: 458 (1985).

¹² K. Kunihiro, H. Yano, N. Goto, and Y. Ohno, "Numerical Analysis of Kink Effect in HJFET with a Heterobuffer Layer," *IEEE Trans. Electr. Dev.* 40: 493 (1993); B. Brar and H. Kroemer, "Influence of Impact Ionization on the Drain Conductance of InAs/AlSb Quantum Well HFETs," in press.

¹³ T. Enoki, T. Kobayashi, and Y. Ishii, "Device Technologies for InP-based HEMTs and their Applications to ICs," *IEEE GaAs IC Symposium*, 337-339, 1994.

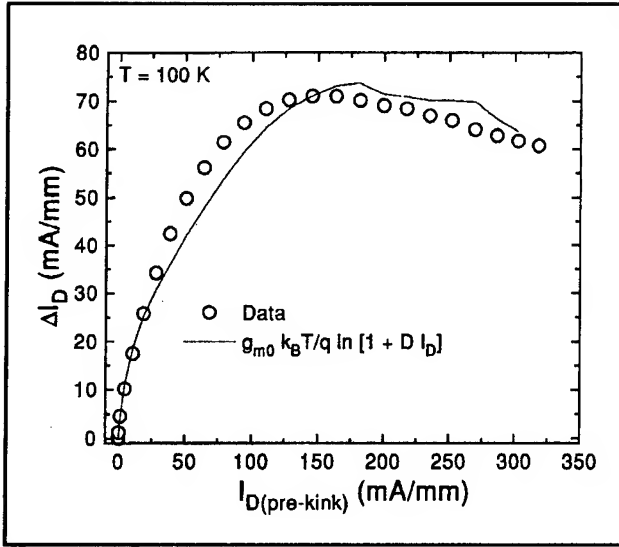


Figure 5. Kink magnitude extracted for $V_{DS} - V_{DS(sat)} = 3$ V at low temperature as a function of I_D . The solid line theoretical fit is discussed later in the text. $L_a = 0.8 \mu\text{m}$.

$$\Delta I_D = g_{m0} I_D \Delta R \quad (1)$$

where g_{m0} and I_D are "pre-kink" values, and ΔR is the drop in source resistance brought about by the hole accumulation. Since $|\Delta R|$ should increase with increasing I_D , the kink current ΔI_D would be superlinear in I_D according to this hypothesis. In order to evaluate this hypothesis, we plot in figure 5 the magnitude of the kink, extracted for constant $V_{DS} - V_{DS(sat)} = 3$ V, versus I_D . This measurement clearly indicates that the kink has a sublinear I_D dependence, which is inconsistent with source resistance reduction.

Although simple source resistance reduction does not appear to explain our results, recent reports of light emission from the extrinsic source¹⁴ and kink suppression by means of a buried p-layer¹⁵ motivate us to explore further the possible significance of holes in the kink effect. As the source-resistance reduction model suggests, holes can drift through the channel and invade the extrinsic source. Particularly effective hole pile-up might arise if there is a potential barrier at the source. Such a barrier can occur between the ohmic contact's n⁺-region and the channel, or at the transition between the capped and uncapped portions. If this is the case,

the ohmic drop in conjunction with the barrier creates a triangular well where holes can accumulate. Any pile-up of holes reduces the ohmic drop in the region immediately adjoining the barrier (figure 6). This provides an extra gate drive, V_{kink} , to the transistor.

A simple first-order analysis of this hypothesis provides a number of key dependences in the behavior of the kink that can be tested. An additional drive on the gate results in increased current:

$$\Delta I_D = g_{m0} V_{\text{kink}} \quad (2)$$

The kink voltage is to first order determined by the excess hole concentration at the barrier:

$$V_{\text{kink}} \propto \frac{k_B T}{q} \ln \left(\frac{n_0 + p}{n_0} \right) \quad (3)$$

In the classical description of impact ionization, the ionization rate is proportional to the exponential of the inverse of the field in the high field region. The excess hole concentration at the barrier will be proportional to the impact ionization generation rate, so

$$p \propto I_{\text{impact}} \propto I_D \exp \left(\frac{-B}{V_{DS} - V_{DS(sat)}} \right) \quad (4)$$

where B is a constant. Plugging (4) into (3) and (2), we obtain

$$\Delta I_D \propto$$

$$g_{m0} \frac{k_B T}{q} \ln \left[1 + A I_D \exp \left(\frac{-B}{V_{DS} - V_{DS(sat)}} \right) \right] \quad (5)$$

where A is another constant.

In examining (5), we note first that when the hole accumulation is large with respect to the pre-kink electron concentration, the exponential term dominates, so that at large V_{DS} values,

$$\Delta I_D |_{\text{large } V_{DS}} \propto \frac{-1}{V_{DS} - V_{DS(sat)}} \quad (6)$$

¹⁴ N. Shigekawa, T. Enoki, T. Furuta, and H. Ito, "Electroluminescence of InAlAs/InGaAs HEMTs Lattice-matched to InP Substrates," in press.

¹⁵ B. Brar and H. Kroemer, "Influence of Impact Ionization on the Drain Conductance of InAs/AlSb Quantum Well HFETs," in press; T. Suemitsu, T. Enoki, Y. Ishii, "Body Contacts in InP-based InAlAs/InGaAs HEMTs and Their Effects on Breakdown Voltage and Kink Suppression," *Electr. Lett.* 31: 758 (1995).

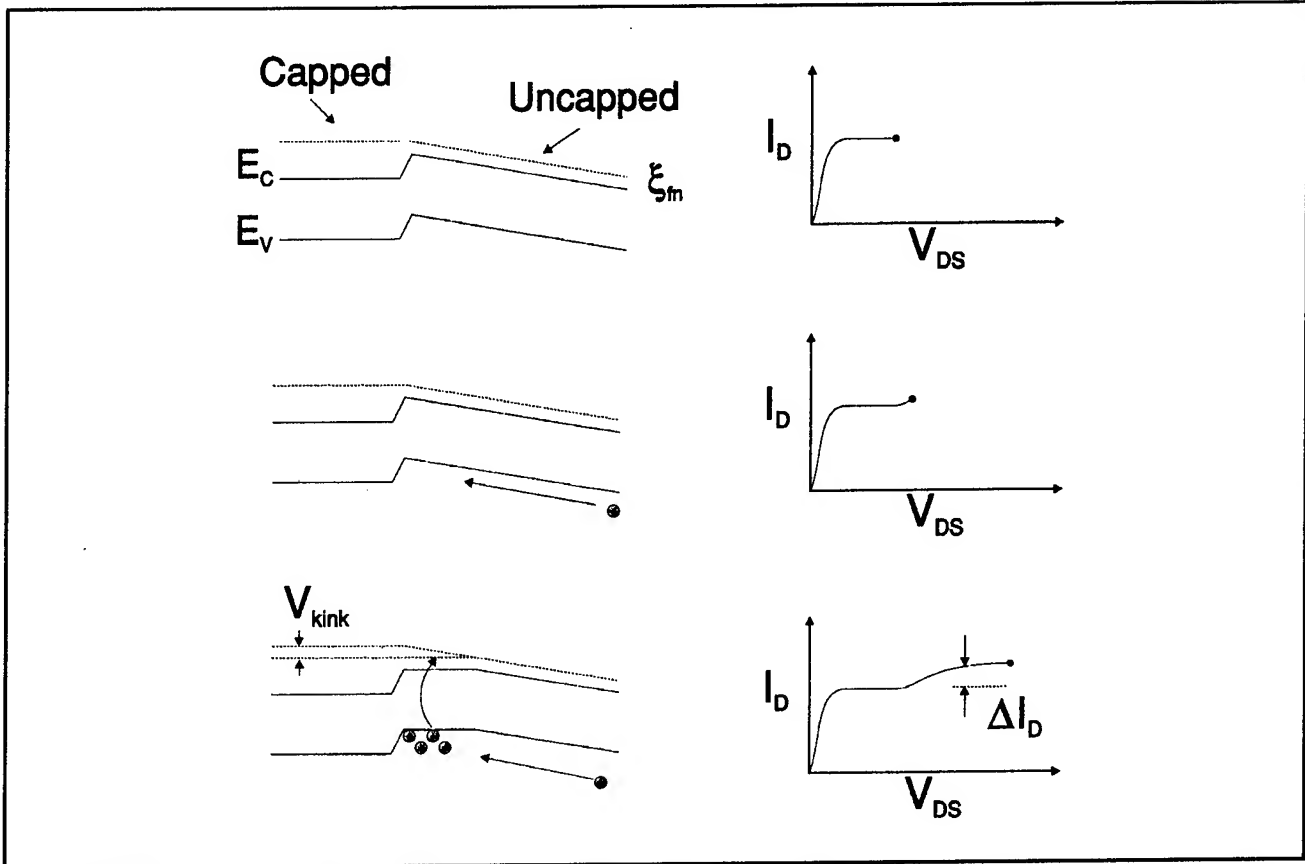


Figure 6. Postulated kink mechanism. Holes generated by impact ionization drift into the extrinsic source and accumulate in the well formed by the barrier and the ohmic drop. The resulting reduction in extrinsic voltage results in increased drive to the transistor.

Such a dependence is observed in our experiments, as shown in figure 7.

The direct relationship between the sidegate current and impact ionization generation rate further implies that the kink should be predicted by the sidegate current. In particular, from (4) and (5),

$$\Delta I_D \propto g_{m0} \frac{k_B T}{q} \ln [1 + C I_{SG}] \quad (7)$$

with C another constant. We observe this in figure 8.

Finally, if $V_{DS} - V_{DS(sat)}$ is held constant, the kink should be a simple function of g_{m0} and I_D :

$$\Delta I_D \propto g_{m0} \frac{k_B T}{q} \ln [1 + D I_D] \quad (8)$$

with D also a constant. Such a dependence explains our experimental observation of figure 5.

The understanding provided by this physical model allows us to build a simple equivalent circuit model description of the kink. A new model element needs

to be added in series with the intrinsic source of the FET (figure 9) that represents the additional drive provided by the hole pile-up. This element is a voltage source that is controlled by V_{DS} and I_D . Only two parameters are required to fit completely the characteristics of the transistor (figure 10).

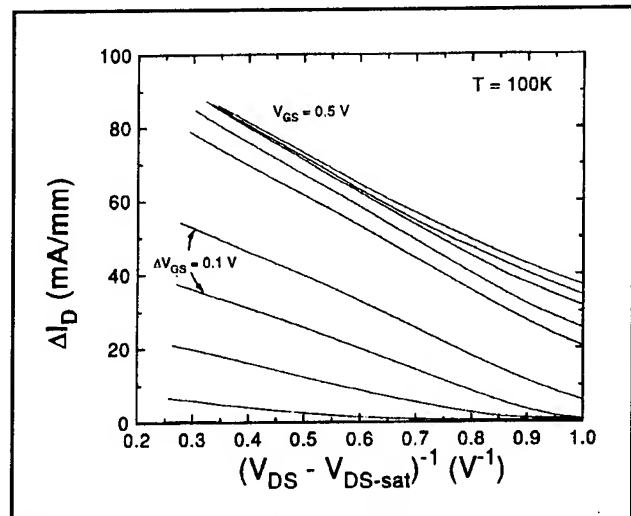


Figure 7. Kink magnitude vs. $V_{DS} - V_{DS(sat)}$. $L_G = 0.8 \mu\text{m}$.

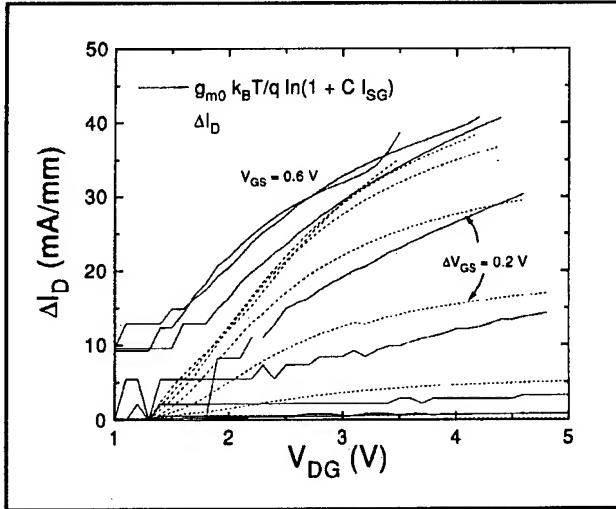


Figure 8. Comparison of the kink current, ΔI_D , with the kink predicted by the sidegate current. $L_G = 2 \mu\text{m}$, $T = 280 \text{ K}$.

Although the form of this model is very similar to those used in SOI MOSFETs, the physics at play are significantly different.

In conclusion, we have postulated a new physical model for the kink effect in InAlAs/InGaAs HEMTs. The kink arises from hole pile up at a potential barrier in the source of the device that brings about a reduction of the ohmic drop at the source. This results in extra gate drive to the transistor. Our findings have allowed us to formulate a simple equivalent model description of the kink effect in these devices.

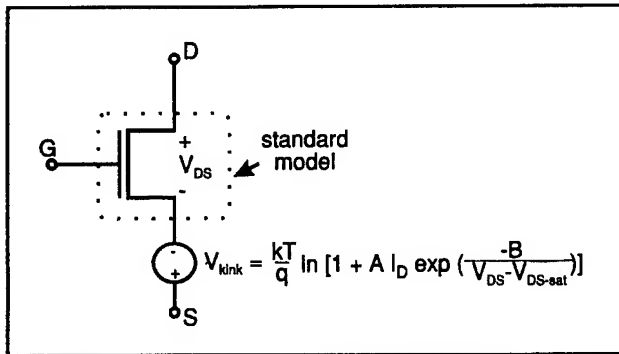


Figure 9. Proposed equivalent circuit model. A new element with only two bias-independent parameters is required to model the kink completely.

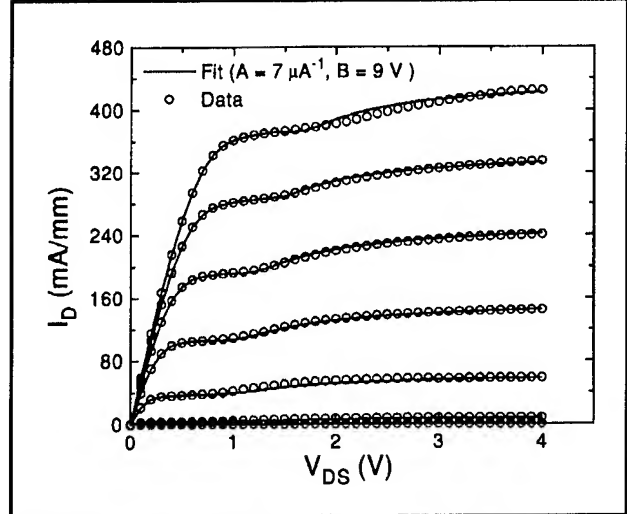


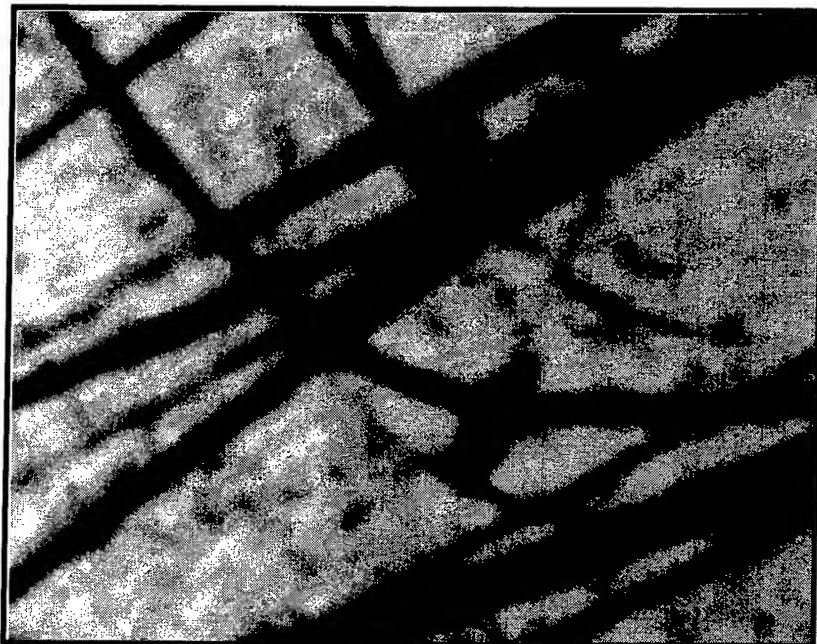
Figure 10. Comparison of model predictions for the kink with measured device characteristics. $L_G = 2 \mu\text{m}$, $T = 280 \text{ K}$.

2.3 Publications

Bahl, S.R., J.A. del Alamo, J. Dickmann, and S. Schildberg. "Off-State Breakdown in InAlAs/InGaAs MODFETs." *IEEE Trans. Electr. Dev.* 42: 15-22 (1995).

Berthold, S., E. Zanoni, C. Canali, M. Pavesi, M. Pecchini, M. Manfredi, S.R. Bahl, and J.A. del Alamo. "Impact Ionization and Light Emission in InAlAs/InGaAs Heterostructure Field-Effect Transistors." *IEEE Trans. Electr. Dev.* 42: 752-759 (1995).

Somerville, M.H., J.A. del Alamo, and W. Hoke. "A New Physical Model for the Kink Effect on InAlAs/InGaAs HEMTs." *Proceedings of the International Electron Devices Meeting*. Washington, D.C., December 1995, p. 221.



A cathodoluminescence micrograph from a 1 μm -thick ZnSe layer on a Zn-exposed, (2x4) reconstructed, 8 monolayer thick GaAs layer on a 4 μm graded InGaP layer. The surface was imaged at the ZnSe wavelength at a magnification of 1700x using a probe current of 32 nA and an acceleration voltage of 20 kV. The sample was grown in the Chemical Beam Epitaxy Laboratory which is under the direction of Professor Leslie A. Kolodziejski.

Chapter 3. Gas Source Molecular Beam Epitaxy of Compound Semiconductors

Academic and Research Staff

Professor Leslie A. Kolodziejwski, Dr. Gale S. Petrich

Graduate Students

Joseph F. Ahadian, Jay N. Damask, Easen Ho, Jody L. House, Kuo-Yi Lim, Elisabeth A. Marley, Jeremy M. Milikow, Steven G. Patterson, Xiao-feng Tang, Emily L. Warlick

Undergraduate Students

Anna Lopatnikova

Technical and Support Staff

Charmaine A. Cudjoe-Flanders, Angela R. Odoardi

3.1 Introduction

The emphasis of the research program which utilizes the chemical beam epitaxy laboratory revolves primarily around the epitaxial growth of a wide variety of compound semiconductors (both II-VI and III-V), as well as multilayered structures composed of II-VI/II-VI, II-VI/III-V and III-V/III-V heterostructures. The chemical beam epitaxy laboratory consists of two gaseous source epitaxy reactors (II-VI-dedicated and III-V-dedicated) interconnected to several smaller chambers which are used for sample introduction and *in-situ* surface analysis and metallization. Such a multichamber epitaxy system allows the fabrication of the aforementioned heterostructures to be accomplished within a continuous ultrahigh vacuum environment. The interconnected reactors enable an additional degree of freedom in device design by providing the ability to integrate the II-VI and III-V material families into a single device. For example, structures containing only III-V epilayers or only II-VI epilayers are grown in a single reactor, or in the case of II-VI/III-V heterostructures and quantum wells both reactors are used.

The III-V gas source molecular beam epitaxy (GSMBE) reactor uses solid elemental sources of Ga, In, Al, Si, and Be and gaseous hydride sources of arsenic and phosphorus. The II-VI reactor currently uses solid elemental sources of Zn and Se, as well as gaseous hydrogen selenide, in addition to a nitrogen plasma source and a solid ZnCl_2 source to achieve p- and n-type doping, respectively. The plasma source is also used with a high purity hydrogen/argon mixture for hydrogen plasma cleaning of GaAs and ZnSe substrates.

In the next section, we will describe our progress in the growth and doping of ZnSe using gas source molecular beam epitaxy and solid source molecular beam epitaxy to examine the role of hydrogen during epitaxy. The II-VI effort is complemented by a program investigating the growth of ZnSe on epitaxial (In,Ga,Al)P buffer layers. An additional II-VI/III-V effort involves the fabrication of ZnSe/GaAs quantum well structures, focusing on the formation of the ZnSe/III-V heterovalent structure and its resultant properties. The III-V GSMBE system is also utilized for the fabrication of (In,Ga)(As,P) waveguide-based devices and light emitters that operate at 1.55 μm , which is the wavelength used for optical fiber communication. Additional III-V-based projects include the fabrication of optoelectronic devices on premetallized GaAs MESFET integrated circuits for optoelectronic integrated circuits, and the fabrication of photonic bandgap crystals utilizing an air bridge microcavity structure. A final project consists of the fabrication of three-dimensional photonic bandgap crystals.

3.2 Gas Source Molecular Beam Epitaxy of ZnSe, ZnSe:Cl and ZnSe:N

Sponsors

Defense Advanced Research Projects Agency
Subcontract 284-25041

Joint Services Electronics Program
Contract DAAL04-95-1-0038

National Center for Integrated Photonic Technology
Contract 542-381

U.S. Army Research Office/ AASERT
Contract DAAH04-93-G-0175

Project Staff

Professor Leslie A. Kolodziejski, Dr. Gale S. Petrich, Easen Ho, Jody L. House, Emily L. Warlick, Anna Lopatnikova

Under the University Research Initiative (URI) program sponsored by ARPA through the Office of Naval Research, Professor Kolodziejski is a co-principal investigator along with Professor R.L. Gunshor, Purdue University, and Professor A.V. Nurmikko, Brown University. The focus of the URI is aimed towards achieving continuously operating, room temperature, short wavelength, visible light emitters operating in the blue and blue/green spectral ranges based on wide bandgap II-VI semiconductors. As the research effort continues toward eliminating the various technological barriers prohibiting the achievement of viable, commercial "blue" laser diodes, the heterostructures are becoming increasingly complex, requiring the use of advanced epitaxial growth techniques.

Gas source molecular beam epitaxy (GSMBE) is an alternative epitaxial growth method that replaces the high vapor pressure elements in molecular beam epitaxy (MBE) with hydride sources that are amenable to regulation using a precision mass flow controller. For example, AsH_3 , PH_3 , and H_2Se are used in place of elemental As, P, and Se, respectively, thus greatly reducing the associated problem of flux control. Lower vapor pressure elements such as Ga, In, and Zn are used in effusion sources. GSMBE retains most of the ultrahigh vacuum advantages of MBE while avoiding the use of metalorganic precursors and thus circumvents the issue of carbon incorporation. In addition, the use of a hydride gas cracker introduces an additional degree of freedom in controlling the form of the precursors provided to the growing surface. Several tradeoffs, however, are involved when using the GSMBE method, such as the high toxicity of the hydride gases and the increased pumping requirements compared to typical MBE apparatuses.

Another unique aspect of GSMBE is the copious and unavoidable generation of H_2 and sub-hydride species (such as As-H and Se-H) that are generated. Whether these H_2 and sub-hydride species are beneficial or deleterious depends on the material system involved. In the growth of III-V mate-

rials, the presence of hydrogen radicals have been postulated to aid in the removal of residual carbon inadvertently introduced into the vacuum system.¹ However, electrical passivation of both intentional and unintentionally introduced dopants has been frequently observed in the growth of Si and III-V compound materials. Our previous results² have shown that while the activation of chlorine donors in n-type ZnSe is not affected by the use of the H_2Se precursor, nitrogen-doped ZnSe is strongly passivated by hydrogen and leads to epitaxial layers that are electrically insulating. Secondary ion mass spectrometry (SIMS) analysis of both the chlorine-doped and nitrogen-doped ZnSe further confirmed the preferential electrical passivation of nitrogen by hydrogen. While the hydrogen concentration, [H], and chlorine concentration, [Cl], were found to behave independently of each other in the chlorine-doped samples, the clear synergy between the hydrogen concentration [H] and the nitrogen concentration [N] were observed in SIMS depth profiling (see figure 1).

An important question that remains to be answered concerns the passivation that is observed during the GSMBE growth of ZnSe doped with a nitrogen plasma source, i.e., is the *dominant* source of electrical passivation derived from molecular hydrogen that is produced by cracking, or from hydrogen radicals still attached to the Se precursor? In order to quantify the role of molecular hydrogen in the passivation mechanism of nitrogen acceptors, experiments were undertaken where various amounts of hydrogen were introduced into the chamber during conventional MBE growth. Figure 2 shows a SIMS profile of a structure containing intentionally hydrogenated regions (lined regions in the structure schematic) where different amounts of molecular hydrogen were introduced; the layer also contains undoped regions (shaded regions) as well as a doped region that was not exposed to a flux of hydrogen. The main features to note in figure 2 are as follows: (1) similar to GSMBE-grown ZnSe:N, [H] is seen to closely track [N], with both impurities decreasing to near their background levels in all of the undoped regions; (2) a clear increase in [H] coincident with the addition of 1 SCCM H_2 (from the schematically indicated ZnSe:N region to the ZnSe:N + 1.0 SCCM H_2 region) indicates that *nitrogen-induced hydrogen incorporation* has occurred; and (3) the [N]/[H] ratio in the ZnSe:N +

¹ Y. Okada, T. Sugaya, O. Shigeru, T. Fujita, and M. Kawabe, "Atomic Hydrogen-assisted GaAs Molecular Beam Epitaxy," *Jpn. J. Appl. Phys.* 34(2B): L238-L244 (1995); M. Sato, "Effect of Plasma-generated Hydrogen Radicals on the Growth of GaAs using Trimethylgallium," *Jpn. J. Appl. Phys.* 34(1B): L93-L96 (1995).

² E. Ho, P.A. Fisher, J.L. House, G.S. Petrich, L.A. Kolodziejski, J. Walker, and N.M. Johnson, "Hydrogen Passivation in Nitrogen and Chlorine-doped ZnSe Films Grown by Gas Source Molecular Beam Epitaxy," *Appl. Phys. Lett.* 66(9): 1062-1064 (1995).

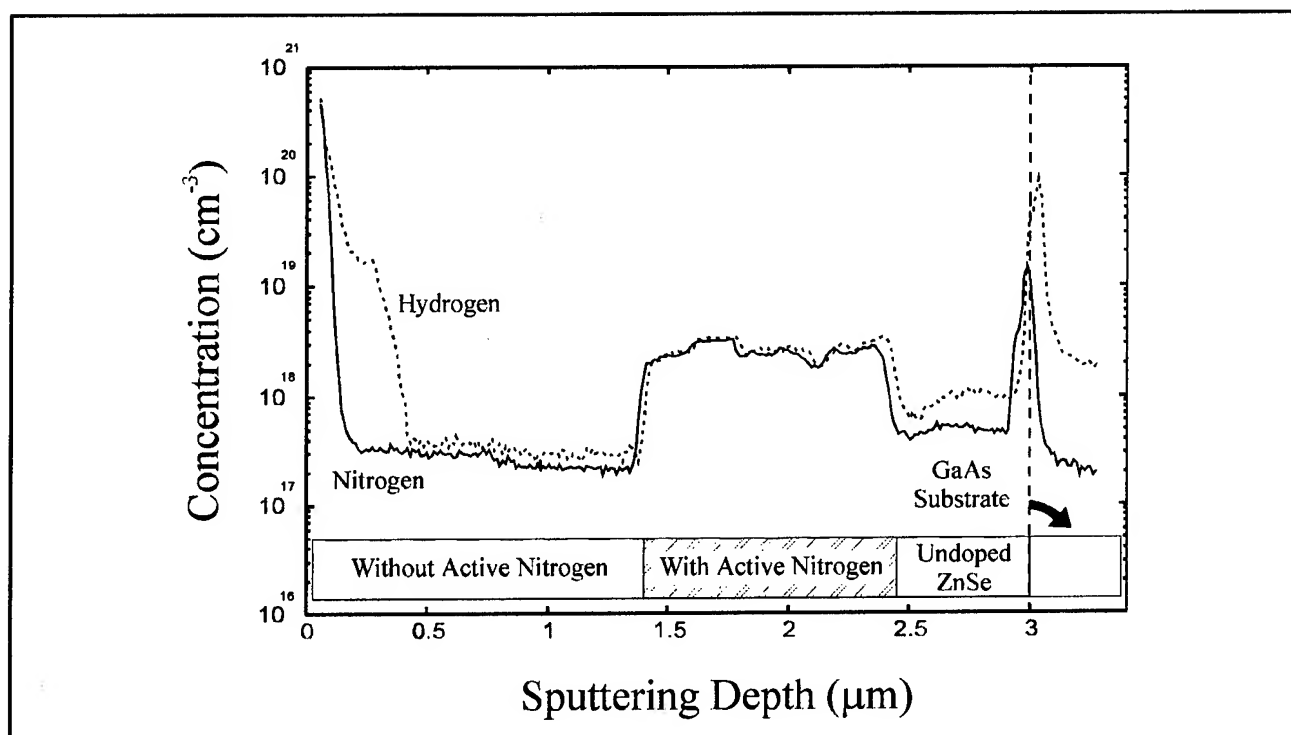


Figure 1. SIMS profile of a layered structure with designed nitrogen concentration variations to demonstrate the tracking behavior of [H] with [N]. The abrupt increases in the [H] and [N] near the ZnSe/GaAs interface were artifacts of the data normalization procedure and should be ignored.

1.0 SCCM region appears to be greater than the [N]/[H] in the ZnSe:N + 3.5 SCCM H₂ region which is consistent with the assumption that the observed increase in [H] is directly related to the amount of injected H₂.³

A comparison of capacitance-voltage (C-V) measurements performed on unhydrogenated ZnSe:N films (reference films without H₂) and intentionally hydrogenated films (ZnSe:N + various amounts of H₂) lends further support to our hypothesis that molecular hydrogen acts to passivate the nitrogen acceptors in MBE using a nitrogen plasma cell. Several series of nitrogen-doped films were grown by MBE, both with and without intentional hydrogen, using identical growth and doping conditions. C-V measurements were subsequently performed on all of the samples to measure the net acceptor concentration $[N_A - N_D]$. With a target $[N_A - N_D]$ of $\sim 2 \times 10^{17} \text{ cm}^{-3}$ for the unhydrogenated reference samples (typical MBE growth), it was generally found that a significant decrease in $[N_A - N_D]$ occurred for films that were grown with injected hydrogen. As an example of the magnitudes of

passivation that were observed, 25 percent and 60 percent passivation were measured for flow rates of 1 and 2 SCCM of H₂, respectively, as compared to the reference (unhydrogenated) MBE-grown samples (where the passivation was taken to be the 0 percent reference). This particular set of hydrogenation runs were grown at 280°C, under slightly Se-rich conditions with the following RF source parameters: 400 W of power and 2.2×10^{-5} Torr chamber background N₂ pressure. The precise amount of passivation was found to depend on the growth, doping conditions, as well as the hydrogen flow rates that were used. Figure 3 shows a *normalized percent passivation* (normalized by the nitrogen doping parameter defined as the product of *power * pressure*) as a function of the hydrogen flow rate used during the hydrogenation experiments. The positive slope in figure 3 highlights a result that we would reasonably expect: more hydrogen present at the surface for a given amount of active nitrogen species gives rise to a larger degree of observed passivation. Note that it is the relative amount of passivation that is of interest here and not the absolute magnitudes. The

³ The apparent increase in [H] at the interface of undoped ZnSe and ZnSe:N regions is due to residual levels of hydrogen in the shared hydrogen/nitrogen gas manifold that feeds the RF plasma cell. Therefore, some background level of passivation exists for this particular experiment even though H₂ is not intentionally introduced via the cracker.

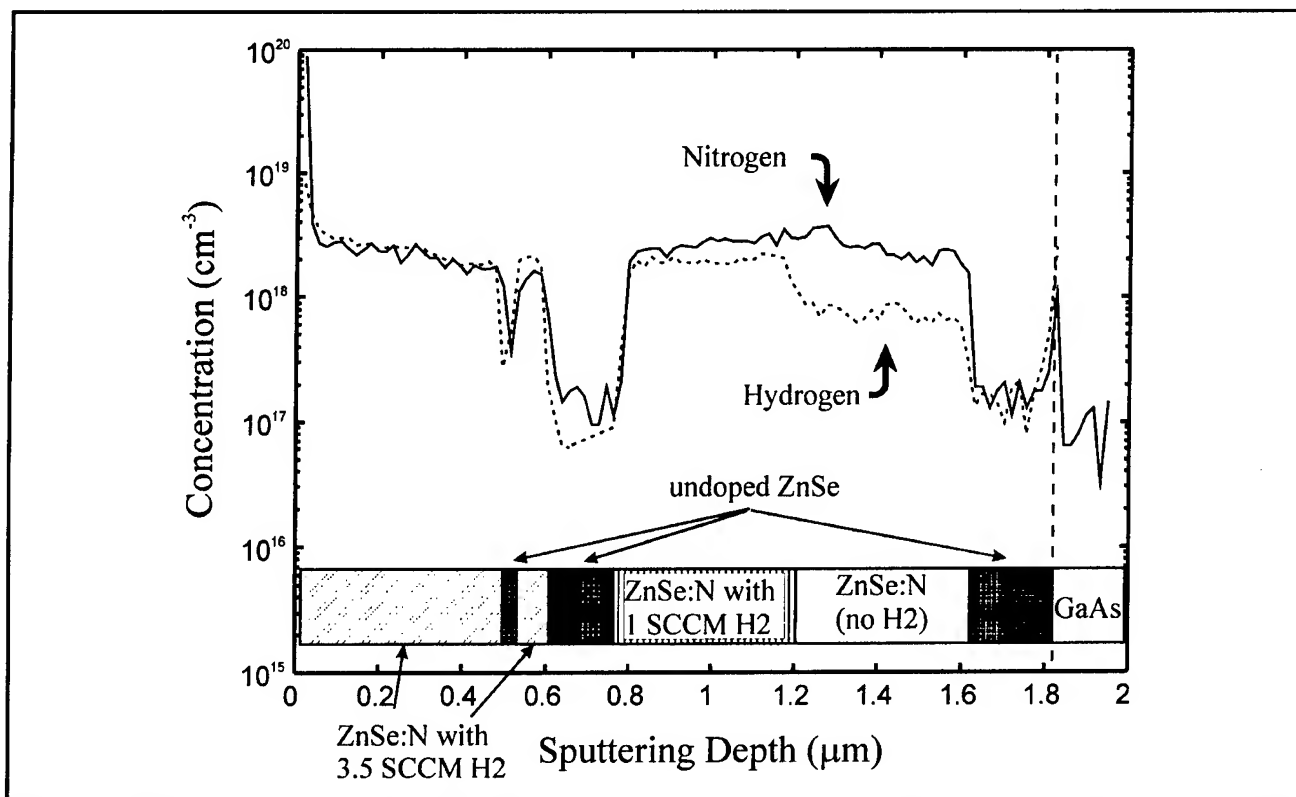


Figure 2. SIMS profile of a ZnSe:N layer grown by MBE on an undoped ZnSe buffer layer (on GaAs). As the depth into the ZnSe layer increases, various amounts of H₂ were introduced to the growth front, with two undoped regions as indicated. The undoped regions serve as markers for the background [H] and [N] concentrations. Variations in the H₂ flow are as indicated in the figure.

result of figure 3 can also be stated in a corollary manner: the amount of electrical passivation depends on the amount of active nitrogen present *for a given flow of hydrogen*. These results and postulates advanced above are consistent with the recent data on the thermal annealing of MOVPE-grown ZnSe:N films obtained by Ogata et al.,⁴ where annealing ZnSe:N epilayers (possessing an initial net acceptor concentration of $2.0 \times 10^{17} \text{ cm}^{-3}$) in an H₂ ambient at 350°C was found to provide significant electrical passivation of the nitrogen acceptors. More detailed studies are required to quantitatively understand the passivating relationship between the active nitrogen species and the H₂ present at the growing surface.

Cracking experiments with H₂Se revealed that 2 SCCM of injected H₂ provides a background hydrogen signal (as detected using a quadrupole mass spectrometer) that is approximately equal to that normally encountered during normal GSMBE growth. Since the degree of electrical passivation

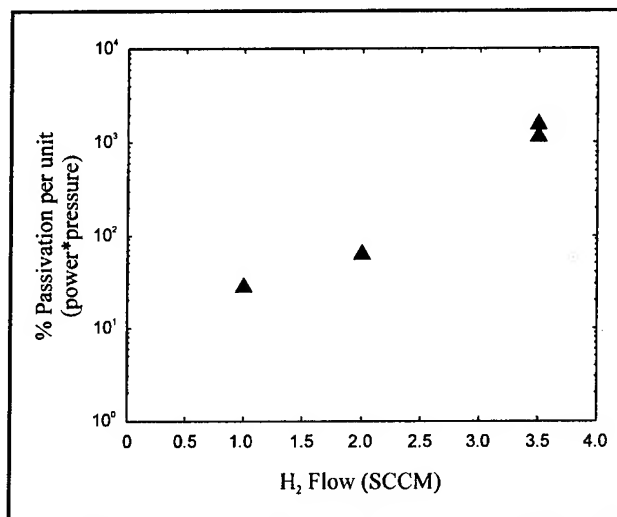


Figure 3. The percent of acceptor passivation (normalized by the doping parameter defined as the product of *power * pressure*) as a function of the intentionally injected H₂ flow rate.

⁴ K. Ogata, D. Kawaguchi, T. Kera, Sz. Fujita, and Sg. Fujita, paper presented at the Seventh International Conference on II-VI Compounds and Devices, Edinburgh, Scotland, August 13-18, 1995.

of GSMBE-grown ZnSe:N samples is found to be much more significant than that measured for the MBE + H₂ counterparts exposed to similar H₂ background levels, we speculate that an equally important mechanism for nitrogen acceptor passivation is related to incompletely cracked Se-H fragments. It is expected that hydrogen passivation during GSMBE growth can be *minimized* by cracking the H₂Se precursor as completely as possible. However, our results seem to indicate that some passivation is inevitable due to the presence of H₂ under normal growth and stoichiometry conditions. This reasoning might also play a part in reconciling our present results with other seemingly contradictory results,⁵ where hydrogen passivation has been reported to be absent in GSMBE-grown ZnSe using the same precursors. We believe that the hydrogenation behavior described here has significant implications for the GSMBE, as well as MOVPE growth of ZnSe:N where multiple pathways for hydrogen incorporation may exist. Further experiments are currently underway to study the effect of growth and surface stoichiometry conditions on hydrogen incorporation under both MBE and GSMBE growth conditions. It is our belief that further and fundamental understanding of the surface kinetic reactions that occur with hydrogen during GSMBE and MOVPE will ultimately dictate the usefulness of GSMBE and MOVPE for achieving practical and reproducible p-type conductivity in wide bandgap II-VIs with nitrogen acceptors.

3.2.1 Publications

Fisher, P.A., E. Ho, J.L. House, G.S. Petrich, L.A. Kolodziejski, J. Walker, and N.M. Johnson. "P- and N-type Doping of ZnSe: Effects of Hydrogen Incorporation." Eighth International Conference on Molecular Beam Epitaxy, Osaka, Japan, August 29-September 2, 1994; In *J. Cryst. Growth* 105(1-4): 729-733 (1995).

Ho, E., P.A. Fisher, J.L. House, G.S. Petrich, L.A. Kolodziejski, J. Walker, and N.M. Johnson. "Hydrogen Passivation in Nitrogen- and Chlorine-Doped ZnSe Films Grown by Gas Source Molecular Beam Epitaxy." *Appl. Phys. Lett.* 66(9): 1062-1064 (1995).

Ho, E., G.S. Petrich, and L.A. Kolodziejski. "Comparison of Hydrogen Passivation of ZnSe:N

Using Gas Source and Conventional Molecular Beam Epitaxy." Paper presented at the Seventh International Conference on II-VI Compounds and Devices, Edinburgh, Scotland, August 13-18, 1995; *J. Cryst. Growth*. Forthcoming.

3.3 Novel Epitaxial III-V Buffer Layers for Wide Bandgap II-VI Visible Sources

Sponsors

Defense Advanced Research Projects Agency
Subcontract 284-25041
National Center for Integrated Photonic Technology
Contract 542-381
National Science Foundation
Grant DMR 92-02957

Project Staff

Professor Leslie A. Kolodziejski, Dr. Gale S. Petrich, Easen Ho, Jody L. House, Emily L. Warlick

At present, most research into II-VI light emitting devices involves the use of GaAs substrates. GaAs is less expensive and more readily available than bulk ZnSe substrates, and allows for the eventual integration of II-VI optical devices onto GaAs-based electronics. Light-emitting diodes are described by the basic concepts of a forward biased pn-junction diode. By forward biasing the pn-junction, holes that are injected from the p-type region into the n-type region, recombine with electrons, resulting in photon emission. However, several mechanisms reduce the amount of radiative recombination due to the use of GaAs substrates, including non-radiative recombination due to misfit dislocations that are generated because of the 0.27 percent lattice-mismatch between ZnSe and GaAs, and the difficulty of injecting holes into the II-VI layers due to the large valence band discontinuity between the two semiconductors.

The lattice-mismatch between the ZnSe epilayer and the GaAs substrate causes a high density of misfit dislocations to form when the ZnSe epilayer thickness exceeds the critical layer thickness (150 nm for ZnSe on GaAs). The presence of misfit dislocations and stacking faults that occur at the II-VI/III-V interface causes the formation of new defects which propagate within the device and act

⁵ M. Imaizumi, Y. Endoh, K. Ohstuka, T. Isu, and M. Nunoshita, "Active-nitrogen Doped P-type ZnSe Grown by Gas Source Molecular Beam Epitaxy," *Jpn. J. Appl. Phys.* 32(12A): L1725-L1727 (1994); M. Imaizumi, Y. Endoh, K. Ohstuka, M. Suita, T. Isu, and M. Nunoshita, "Blue Light Emitting Laser Diodes Based on ZnSe/ZnCdSe Structures Grown by Gas Source Molecular Beam Epitaxy," *Jpn. J. Appl. Phys.* 33(1A): L13-L14 (1994).

as nonradiative recombination centers.⁶ The formation of the new nonradiative recombination centers leads to the degradation of the device. By varying the mole fraction of In, (In,Ga)P can be designed to be lattice-matched to ZnSe as opposed to GaAs, thus minimizing the strain-induced misfit dislocations between the ZnSe and the (In,Ga)P.⁷

The second problem with a GaAs substrate is the valence band offset between the ZnSe and the GaAs. The valence band discontinuities between ZnSe and GaAs, InGaP, and InAlP are 0.96 eV, 0.67 eV, and 0.34 eV, respectively. The reduction of the heterobarrier with an intermediate (In,Ga)P buffer layer has been found to lead to an enhancement of the hole thermionic emission,⁸ which in turn improved the electrical characteristics of the device.

At present, structures of the form ZnSe/(In,Ga,Al)P/GaAs are being studied, as shown in figure 4. The specific buffer layers studied include InGaP, InAlP, and graded layers of In(Ga,Al)P. As shown schematically in the upper part of figure 4, by varying the Ga to Al ratio in In(Ga,Al)P, the valence band offset between the ZnSe and the III-V epilayer can be decreased as the (In,Ga,Al)P bandgap energy increases. This can be accomplished independent of the lattice

constant. The lattice constant of the epilayers were either equal to the lattice constant of ZnSe or graded from the GaAs lattice constant to the lattice constant of ZnSe during the growth of the epilayer as shown in the bottom of figure 4. In doing so, the lattice mismatch between the III-V epilayer and the ZnSe layer can be minimized. The III-V buffer layers were transferred *in-situ* to the II-VI chamber. In the III-V GSMBE reactor, the In(Ga,Al)P buffer layers were grown with cracked arsine (AsH₃) and phosphine (PH₃) as the anion species, and elemental In, Ga, and Al as the cation species. The 4 μm thick buffer layers were grown at 490°C on an epitaxial 0.5 μm thick GaAs buffer layer, which was grown at 600°C. The 1 μm thick ZnSe layers were grown using elemental Zn and Se as source materials at a temperature around 300°C.

Several characterization techniques have been employed to investigate these epitaxial In(Ga,Al)P/ZnSe heterostructures, including *in-situ* reflection high energy electron diffraction (RHEED), Nomarski microscopy, x-ray diffraction (XRD), photoluminescence (PL), and cathodoluminescence (CL). XRD yielded information about the lattice matching as well as the dislocation density from the width of the diffraction peaks.⁹ The (400) diffraction rocking curves indicated that all of the (In,Ga,Al)P

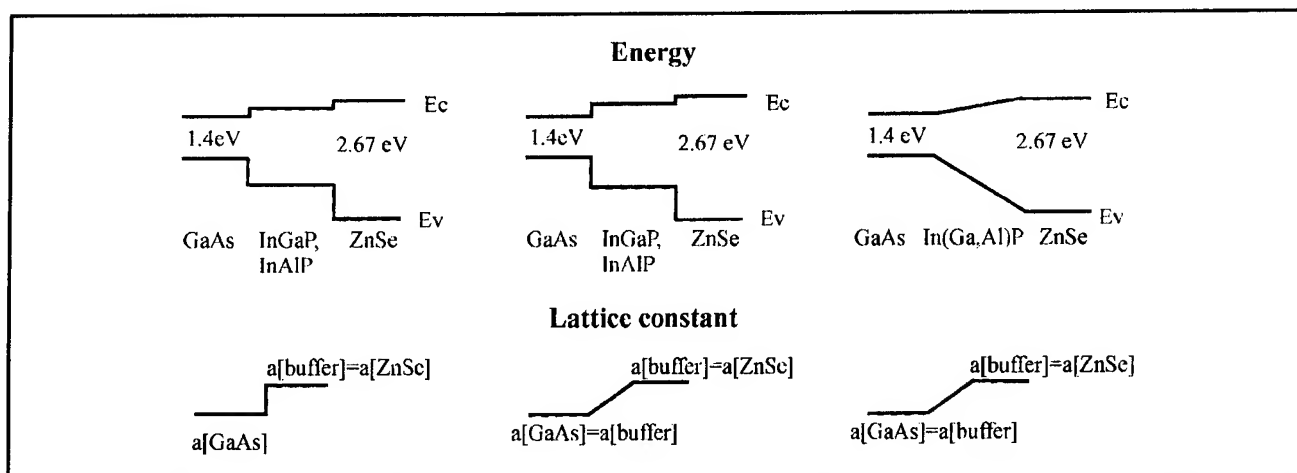


Figure 4. Schematic diagrams of the energy bands and lattice-constants of the In(Ga,Al)P/ZnSe heterostructures.

⁶ S. Guha, J.M. DePuydt, M.A. Haase, J. Qiu, and H. Cheng, "Degradation of II-VI Based Blue-green Light Emitters," *Appl. Phys. Lett.* 63(23): 3107-3109 (1993); S. Guha, H. Cheng, M.A. Haase, J.M. DePuydt, J. Qiu, B.J. Wu, and G.E. Hoffer, "<100> Dark Line Defect in II-VI Blue-green Light Emitters," *Appl. Phys. Lett.* 65(7): 801-803 (1994).

⁷ K. Lu, J.L. House, P.A. Fisher, C.A. Coronado, E. Ho, G.S. Petrich, and L.A. Kolodziejski, "(In,Ga)P Buffer Layers for ZnSe-Based Visible Emitters," *J. Cryst. Growth* 138(1-4): 1-7 (1994).

⁸ M. Onomura, M. Ishikawa, Y. Nishikawa, S. Saito, P.J. Parbrook, K. Nitta, J. Rennie, and G. Hatakoshi, "Blue-green Laser Diode Operation of CdZnSe/ZnSe MQW Structures Grown on InGaP Band Offset Reduction Layers," *Electron. Lett.* 29(24): 2114-2115 (1993).

⁹ R.L. Gunshor, N. Otsuka, and A.V. Nurmikko, "Blue Lasers on the Horizon," *IEEE Spectrum* 30(5): 28-33 (1993).

buffer layers were lattice-matched to ZnSe to within an average of 100 arcseconds. CL provides a spatial image of the luminescence of the semiconductor. In imaging of defects, the CL contrast is generally due to the enhanced nonradiative recombination at dislocations in the crystal. In undoped semiconductors used in this study, threading dislocations appear as very dark dots.¹⁰ These can clearly be seen in figure 5.

Currently, work is underway to image the defects in the structures using transmission electron microscopy (TEM) in order to determine the relative prominence of various forms of dislocations and faults. These results will enhance our understanding of the specific effects of lattice-matching. Eventually, the structures will be doped p-type with an n-type layer of ZnSe on top to perform I-V measurements and to evaluate the electrical capabilities of the diodes.

3.4 The Growth and Characterization of ZnSe/GaAs Heterostructures

Sponsors

Joint Services Electronics Program
Grant DAAL04-95-1-0038
National Science Foundation
Grant DMR 90-22933
Grant DMR 92-02957

Project Staff

Professor Erich P. Ippen, Professor Leslie A. Kolodziejski, Dr. Gale S. Petrich, David J. Dougherty, Jody L. House

The integration of II-VI and III-V semiconductors into a single II-VI/III-V heterojunction device enables the exploitation of the many similarities, as well as the many differences, in material properties (energy bandgap, lattice constant, dielectric constant, etc.) to create new devices exhibiting unique optical and electronic properties. As a specific example, the epitaxial growth of dielectric quantum wells (QWs) composed of ZnSe ($E_g=2.67\text{eV}$) and GaAs ($E_g=1.42\text{eV}$) is under investigation. ZnSe and GaAs have very similar lattice constants (0.27 percent lattice

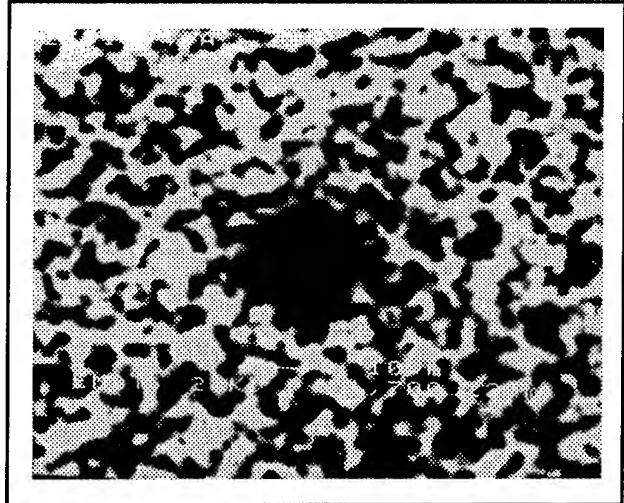


Figure 5. Room-temperature cathodoluminescence image of ZnSe/InAlP/GaAs, where the InAlP was lattice-matched to ZnSe. The image was taken at the peak wavelength of 460 nm. The bright regions are luminescent; the dark spots show points of nonradiative recombination, due primarily to threading dislocations.

mismatch) which enable the materials to be grown epitaxially to form a heterostructure.

A quantum well consisting of a thin layer of GaAs (1 - 100 nm) surrounded by ZnSe barriers has a large potential well ($\sim 1\text{ eV}$) in the valence band for holes and a smaller potential well ($\sim 0.2\text{ eV}$) in the conduction band for the electrons. Such a large potential barrier for the holes results in a number of possible confined hole energy states in the GaAs quantum well. When such a ZnSe/GaAs quantum well is excited, either electrically or optically, the transitions of holes between these confined levels (intersubband transitions) in the valence band can be detected. Furthermore, from a ZnSe/GaAs multiple quantum well structure, the density of intersubband transitions for the holes can be engineered to achieve a large signal at the optical communications wavelength of $1.3\text{ }\mu\text{m}$. In addition, the large variation in the other optical properties of GaAs and ZnSe (including a variation in the index of refraction of ~ 1) makes the mixed II-VI/III-V heterostructure a candidate for high-speed optical switching devices (switching times of less than 1 picosecond).¹¹

¹⁰ B.G. Yacobi and D.B. Holt, "Cathodoluminescence Scanning Electron Microscopy of Semiconductors," *J. Appl. Phys.* 59(4): R1-R24 (1986).

¹¹ H. Buhmann, L. Mansouri, J. Wang, P.H. Beton, L. Eaves, and M. Henini, "High Efficiency Submicron Light-emitting Resonant Tunneling Diodes," *Appl. Phys. Lett.* 65(26): 3332-3334 (1994); O.E. Raichev, "Theory of Hole Conductivity in Semiconductor Superlattices," *Phys. Rev. B* 50(8): 5382-5391 (1994); M. Kumagai and T. Takagahara, "Excitonic and Nonlinear-optical Properties of Dielectric Quantum-well Structures," *Phys. Rev. B* 40(18): 12,359-12,381 (1989); J. Moores, K. Bergman, H.A. Haus, and E.P. Ippen, "Optical Switching Using Fiber Ring Reflectors," *J. Opt. Soc. B* 8(3): 594-601 (1991); K. Kitayama and S. Wang, "Optical Pulse

A heterostructure intended for device purposes needs to have well-defined characteristics. In the ZnSe and GaAs case, there are two issues which affect the properties of the heterointerfacial regions. First, the GaAs and ZnSe are composed of elements with different valences. As one material is formed on top of the other, the bonding of the four different elements can have several orientations. For example, a theoretically abrupt interface can be formed where there are no interfacial layers of Ga, Zn, Se, and As. In this instance, an electronic imbalance results, and the associated electric field creates a depletion region for stability. In the instance when a few transitional monolayers exist, the heterostructure is no longer entirely ZnSe and GaAs. One goal of this study is to determine which of these two extremes is the best from a device perspective. There has been a great deal of work to date in defining the electronic structure of the ZnSe on GaAs heterostructure. Theoretically, the valence band-offset between the ZnSe and the GaAs has been shown to vary from 0.7 eV to 1.59 eV, depending on the ZnSe/GaAs interface formation.¹² However, little is known about the far-reaching effects of these different interfaces.

The second issue affecting the properties of the ZnSe/GaAs QW structure is the formation of the heterovalent interfaces, particularly the formation of the inverted interface formed by GaAs nucleated on a ZnSe epitaxial surface. The stoichiometry of each interface is engineered by using various growth techniques. Due to the severe mismatch in the optimal growth temperatures for the two material systems (600°C for GaAs and 300°C for ZnSe), additional emphasis has been placed on the reduced temperature growth of GaAs on ZnSe.

The nucleation of GaAs on ZnSe has been optimized utilizing a monolayer by monolayer growth procedure. The substrate temperature was increased from 250°C to 350°C while the V-III flux ratio was decreased from 12 to approximately one

during the deposition of the first ten monolayers. This approach has resulted in a defect-free heterointerface as exhibited in cross-sectional TEM micrographs (figure 6a). *In situ* monitoring of the GaAs nucleation on ZnSe with reflection high energy electron diffraction has shown a reconstructed c(4x4) surface within six monolayers of GaAs, indicating a smooth As-rich GaAs surface. For comparison, MBE-like nucleation conditions that were employed for the nucleation of GaAs on ZnSe (where the substrate temperature was 370°C and the V-III flux ratio was approximately five) resulted in a heterointerface riddled with a high density of stacking faults which propagate through the GaAs material as shown in figure 6b. The RHEED pattern for the MBE-like nucleation of GaAs on ZnSe exhibited a spotty bulk-like diffraction pattern indicative of a rough surface.

Optical characterization has been implemented to assess the quality of the reduced temperature GaAs and the ZnSe/GaAs double heterostructures. Multiple quantum well heterostructures composed of (In,Ga)P barriers and GaAs wells exhibit low temperature photoluminescence from the first confined state of GaAs grown at temperatures as low as 300°C. The optical properties of the ZnSe/GaAs double heterostructure on both GaAs and InGaP buffer layers are under investigation with photoluminescence, photorefectance, and photocurrent measurements. In addition, to examine the role of II-VI/III-V heterointerface, asymmetric quantum wells utilizing ZnSe and InGaP as barrier material, are also being investigated.

3.4.1 Publications

House, J.L., D.J. Dougherty, G.S. Petrich, L.A. Kolodziejski, E.P. Ippen, and G.-C. Hua. "Growth and Characterization of ZnSe/GaAs Single Quantum Well Structures." *Appl. Surf. Sci.* Forthcoming.

Compression by Nonlinear Coupling," *Appl. Phys. Lett.* 43(1): 17-19 (1983); N.M. Islam, *Ultrafast Fiber Switching Devices and Systems* (Cambridge, England: Cambridge University Press, 1992).

- ¹² G. Bratina, R. Nicolini, L. Sorba, L. Vanzetti, G. Mula, X. Yu, and A. Franciosi, "ZnSe-GaAs Heterojunction Parameters," *J. Cryst. Growth* 127(1-4): 387-391 (1993); G. Bratina, L. Vanzetti, R. Nicolini, L. Sorba, X. Yu, A. Franciosi, G. Mula, and A. Mura, "Microscopic Control of ZnSe-GaAs Heterojunction Band Offsets," *Physica B* 185(1-4): 557-565 (1993); G. Bratina, L. Vanzetti, L. Sorba, G. Biasiol, A. Franciosi, M. Peressi, and S. Baroni, "Lack of Band-offset Transitivity for Semiconductor Heterojunctions with Polar Orientation: ZnSe-Ge(001), Ge-GaAs(001), and ZnSe-GaAs(001)," *Phys. Rev. B* 50(16): 723-729 (1994); A. Kley and J. Neugebauer, "Atomic and Electronic Structure of the GaAs/ZnSe(001) Interface," *Phys. Rev. B* 50(12): 8616-8628 (1994); R. Nicolini, L. Vanzetti, G. Mula, G. Bratina, L. Sorba, A. Mura, J.E. Angelo, W.W. Gerberich, and A. Franciosi, "Local Interface Composition and Band Offset Tuning in ZnSe-GaAs(001) Heterostructures," *Phys. Rev. Lett.* 72(2): 294-297 (1994).

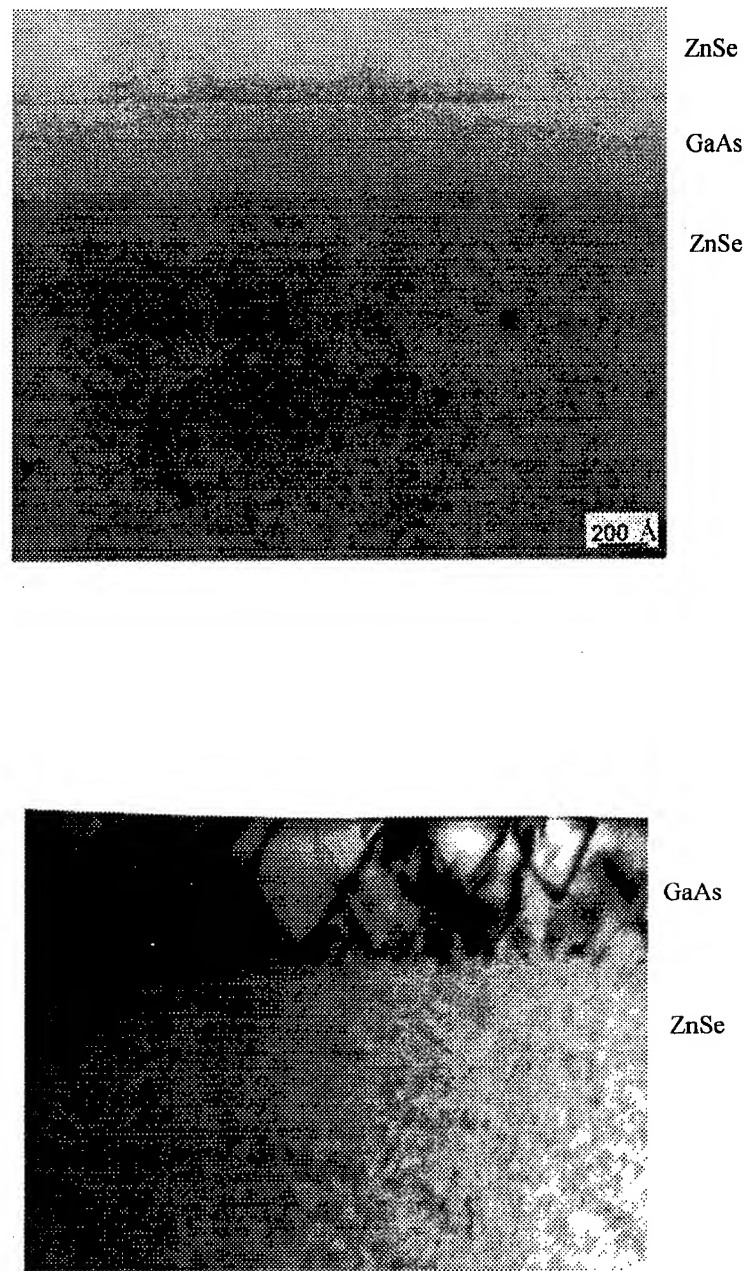


Figure 6. Cross-sectional transmission electron micrographs of GaAs nucleated on an epitaxial ZnSe surface. (a) (top) A ZnSe/GaAs quantum well structure (500 Å ZnSe/ 400 Å GaAs /ZnSe substrate) that was formed using monolayer-controlled deposition. (b) (bottom) A 2500 Å GaAs layer that was nucleated on a ZnSe epilayer using typical MBE growth techniques.

3.5 Low Temperature Growth of (In,Ga)P/(In,Ga)As Lasers and LEDs for OptoElectronic-VLSI

Sponsor

National Center for Integrated Photonic Technology
Contract 542-381

Project Staff

Professor Clifton G. Fonstad, Jr., Professor Leslie A. Kolodziejski, Dr. Gale S. Petrich, Joseph F. Ahadian, Steven G. Patterson, Dr. Krishna V. Shenoy

We are investigating the regrowth of (In,Ga)As quantum well lasers and light emitting diodes (LEDs) onto premetallized GaAs-based VLSI circuits. Our approach involves the use of (In,Ga)P cladding layers with (In,Ga)As active regions (all lattice-matched to GaAs). Following the design of the VLSI MESFET circuits, Vitesse Corporation completes the fabrication including all levels of metalization of the electronic portion of the circuit using the MOSIS foundry. The last process step carried out by Vitesse involves the removal of the various layers of dielectric material from the growth window in order to create a region for the epitaxial regrowth of the optical components (lasers and LEDs); the samples are then forwarded to MIT for regrowth and optical device processing.

We are emphasizing the gas source molecular beam epitaxial growth of lasers, LEDs, and dielectric Bragg reflecting mirrors with the requirement that all of the growth and subsequent device processing is carried out at temperatures below 500°C. Temperatures greater than 500°C have been found to significantly degrade the upper level metal on the various electronic components within the VLSI circuitry. Initial GSMBE experiments involved the growth on both bulk GaAs substrates as well as in the growth window of the GaAs-based VLSI circuits. However, early results indicated that the processing steps that were used to remove the dielectric material from the growth window resulted in an unacceptable surface for the regrowth of high quality GaAs. The "regrown" material was found to be heavily defective and exhibited a very rough surface morphology. Subsequent device design and further processing experiments were required to modify the steps necessary to prepare the growth windows for epitaxy. A significant effort within Professor Fonstad's group has been expended to alleviate this surface preparation problem. While this surface preparation problem was being addressed, we initiated a parallel effort to determine the growth parameters necessary to fabricate the various optical components of interest onto bulk GaAs sub-

strate material. The results from these initial growth, characterization, and prototype device fabrication experiments will provide the optical device operating characteristics to our collaborators as part of the OPTOCHIP project. With the current-voltage, light output-current, threshold current and threshold voltage characteristics, further OE-VLSI designs will be implemented by our OPTOCHIP collaborators. In addition, these initial device results will provide a baseline for the optical components that are integrated with the OE-VLSI circuits. Material has also been forwarded to Lincoln Laboratory and to Professor Steve Forrest (Princeton University) to begin experiments to identify the processing chemistry necessary to form chemically-etched 45° folded cavity mirrors with reactive ion etching (Princeton) and parabolic mirrors using chemically-assisted ion beam etching (Lincoln Laboratory) for the final fabrication of in-plane surface emitting lasers fully integrated with the OE-VLSI circuits.

Using the integrated modular GSMBE reactors, we have eliminated the need to remove the native GaAs oxide by raising the substrate temperature to 650°C for several minutes prior to the initiation of growth. This is accomplished within the II-VI reactor by using atomic hydrogen from a plasma source for the low temperature removal of the GaAs oxide. The oxide is removed at 300°C in conjunction with a 15-30 minute exposure to atomic hydrogen. Since this initial success with the plasma source in the II-VI reactor, a source of atomic hydrogen has been added to the III-V reactor to enable the oxide removal to be carried out with an arsenic ambient to further reduce the difficulty of Ga-droplet formation due to the excess evaporation of arsenic.

For use in vertical cavity surface emitting laser structures (VCSELs) and high efficiency LEDs, we have grown various Bragg mirrors having both large and small index of refraction discontinuities. The structures consist of AlAs/(In,Ga)P, which exhibits a small index of refraction difference (figure 7), and Al_xO_y /(In,Ga)P which exhibits a large index difference. The lattice-matched Bragg mirrors exhibit high optical reflectivity at the wavelength of interest for the optical devices under consideration, but exhibit poor electrical characteristics. The low temperature (470°C) growth of the AlAs layer is speculated to contribute to the high electrical resistivity of the Bragg mirrors, thus negating the expected improvement in the efficiency of the LEDs. For the Al_xO_y /(In,Ga)P Bragg mirrors, we have established the oxidation conditions necessary to complete the oxidation of the AlAs/(In,Ga)P Bragg mirrors following the approach of Professor Dan Dapkus (University of Southern California). A fully functioning oxidation furnace has been assembled at MIT and

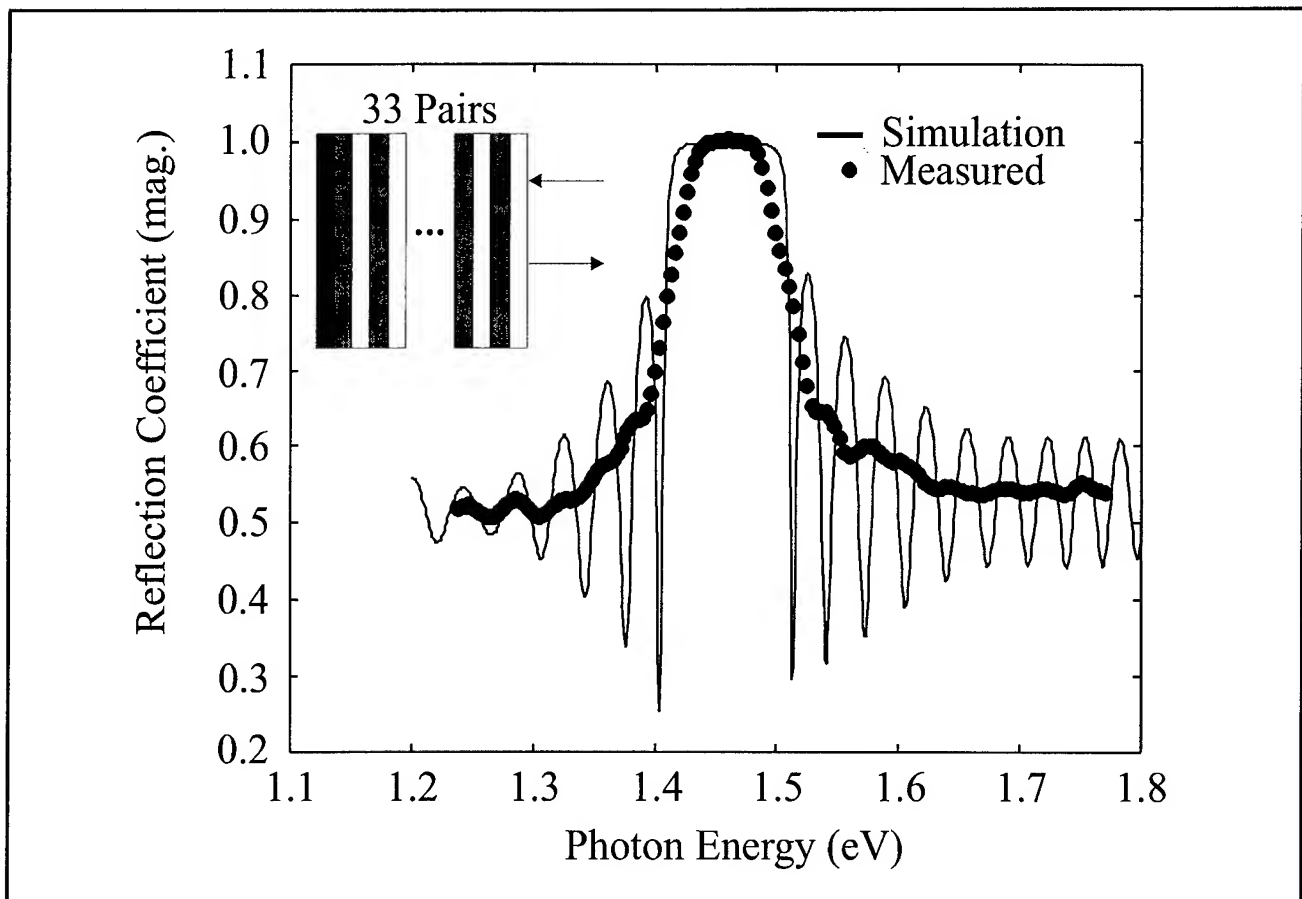


Figure 7. Measured and simulated reflection coefficient of a 33 pair InGaP/AlAs distributed Bragg reflector grown at 470°C on a GaAs substrate.

has been calibrated for the proper oxidation conditions. However, the oxidation temperature still needs to be reduced as the most successful oxidation conditions occur at 500°C, which exceeds the maximum allowable temperature during the processing of the optical devices with the integrated circuits.

A significant number of LEDs have been grown, fabricated, and characterized, each having various modifications to the layer design, doping characteristics, presence of etch stop layers, etc., to optimize the light emission from the optical device. The use of an AlAs etch stop layer was implemented to facilitate the chemical etching of the various sized mesas in order to minimize the leakage currents under a small forward bias.

To maximize the amount of light emitted from the LED structures, we are investigating various methods to increase the degree of current spreading underneath a top metal contact. Doping profile simulations of LED structures are being utilized to guide the growth experiments. In addition, we are investigating the use of alternative metal contacts, including transparent metal contacts, such

as Ti:Au in conjunction with current confining apertures, and transparent indium tin oxide contacts.

Thus far, various mask sets have been designed in order to vary the ratio of metal contact to surface area to maximize the light emission, but device fabrication is still required for proof of concept. In addition, the progress in fabricating LEDs using InGaP cladding layers, has been hampered by the wet chemical etching of the InGaP surfaces using $\text{H}_3\text{PO}_4/\text{HCl}/\text{H}_2\text{O}$. This etchant creates an etched surface with a rough morphology. We are currently investigating the use of $\text{CH}_3\text{COOH}/\text{HCl}/\text{H}_2\text{O}_2$. This etchant produces a smooth etched surface but causes process complications due to the presence of the organic acid.

Promising results have been demonstrated with regard to the cleaning steps necessary to prepare the growth windows for epitaxial regrowth. The new process involves a simple etch step by Vitesse to remove the various layers of dielectric down to a layer of Al that is placed near the final GaAs surface. Once the sample arrives at MIT, the aluminum layer is removed and the sample is then dipped in HF. The surface appears to be free of

the residue plaguing the earlier circuits, but still requires additional surface examination to determine the efficacy of this new surface cleaning process.

3.6 InP-Based Devices for Optical Communication Networks

Sponsors

MIT Lincoln Laboratory
National Center for Integrated Photonic Technology
Subcontract 542-383

Project Staff

Professor Leslie A. Kolodziejski, Dr. Gale S. Petrich, Dr. Katherine L. Hall,¹³ Dr. Joseph Donnelly,¹³ Elisabeth A. Marley, Jeremy M. Milikow

As communication networks continue to increase in speed and bandwidth, the semiconductor industry must continue to strive to provide network designers with devices that will meet their needs. One of the more critical requirements is the need for optical devices that operate with little or no drive current so that they may operate, or cause another optical source to operate, at extremely high pulse rates.

Devices operating at wavelengths of 1.55 μm and 1.3 μm are the standard for optical communication networks because the low loss and zero dispersion propagation wavelengths for commonly used optical fiber are 1.55 μm and 1.3 μm , respectively. These wavelength requirements can be met using the III-V materials system, specifically (In,Ga)(As,P). The growth method used for this project is gas source molecular beam epitaxy. GSMBE combines the flexibility and the use of gaseous group V hydrides (AsH_3 , PH_3) with the conventional molecular beam epitaxy control of the solid group III elements (In,Ga,Al). This combination lends itself to the growth of multi-layered structures, such as multiple quantum well (MQW) lasers and saturable Bragg reflectors (SBRs).

MQW lasers have become the preferred laser for communication networks due to the fact that they require a fewer number of injected carriers to operate than do separate confinement heterostruc-

ture (SCH) lasers.¹⁴ For this reason, the threshold current of MQW lasers is lower than that of other lasers. By manipulating the doping levels in the laser as well as accurately controlling the heterojunctions, the threshold current can be decreased even further. In conjunction with Dr. Joseph Donnelly of MIT Lincoln Laboratory, the current design is a broad area laser that contains three quantum wells and a lightly doped upper InP cladding layer, e.g., approximately 5×10^{17} Be atoms/ cm^2 , in order to minimize the free carrier loss. The net gain versus current density and the device structure are shown in figure 8. This structure has yielded threshold current densities of 190 A/ cm^2 for 3000 μm devices and a transparency current density of 165 A/ cm^2 . Current work on this topic includes fabricating and testing ridge waveguide lasers and tapers as well as designing future MQW laser structures.

Saturable Bragg reflectors (SBRs) are also of use in optical networks. SBRs are passive devices that are essentially distributed Bragg reflectors (DBRs). The SBR is designed as a conventional DBR, with a reflectivity bandwidth dependent upon the refractive indices and the thicknesses of the layers. The only difference is the incorporation of a single quantum well in one of the quarter-wave layers. The reflected intensity of this device, at the quantum well emission wavelength, can be varied based on the position of the quantum well within the DBR structure, e.g., the reflected intensity is highest if the quantum well is placed in the first quarter-wave layer, and decreases as the quantum well is placed further into the device. This quantum well should have an emission wavelength within the DBR reflectivity bandwidth in order to maximize the nonlinear reflectivity of the SBR due to the nonlinear effects caused by the quantum well. By placing the SBR in a low-gain solid-state laser cavity, its nonlinear reflectivity will mode-lock the laser, with the result being self-starting, stable, ultrashort optical pulses.¹⁵

SBRs have been demonstrated in the 0.85 μm wavelength range by Tsuda, et al.,¹⁵ but this wavelength is not usable in standard optical networks, thus, the need for SBRs that operate at 1.3 μm and 1.55 μm . In order to accomplish this, a material system such as (In,Ga)(As,P) lattice-matched to InP must be used. The disadvantage of this material

¹³ MIT Lincoln Laboratory, Lexington, Massachusetts.

¹⁴ P.S. Zory, Jr., ed., *Quantum Well Lasers*, (New York: Academic Press, 1993).

¹⁵ S. Tsuda, W.H. Knox, E.A. de Souza, W.Y. Jan, and J.E. Cunningham, "Low-loss Intracavity AlAs/AlGaAs Saturable Bragg Reflector for Femtosecond Mode Locking in Solid-state Lasers," *Opt. Lett.* 20(12): 1406-1408 (1995).

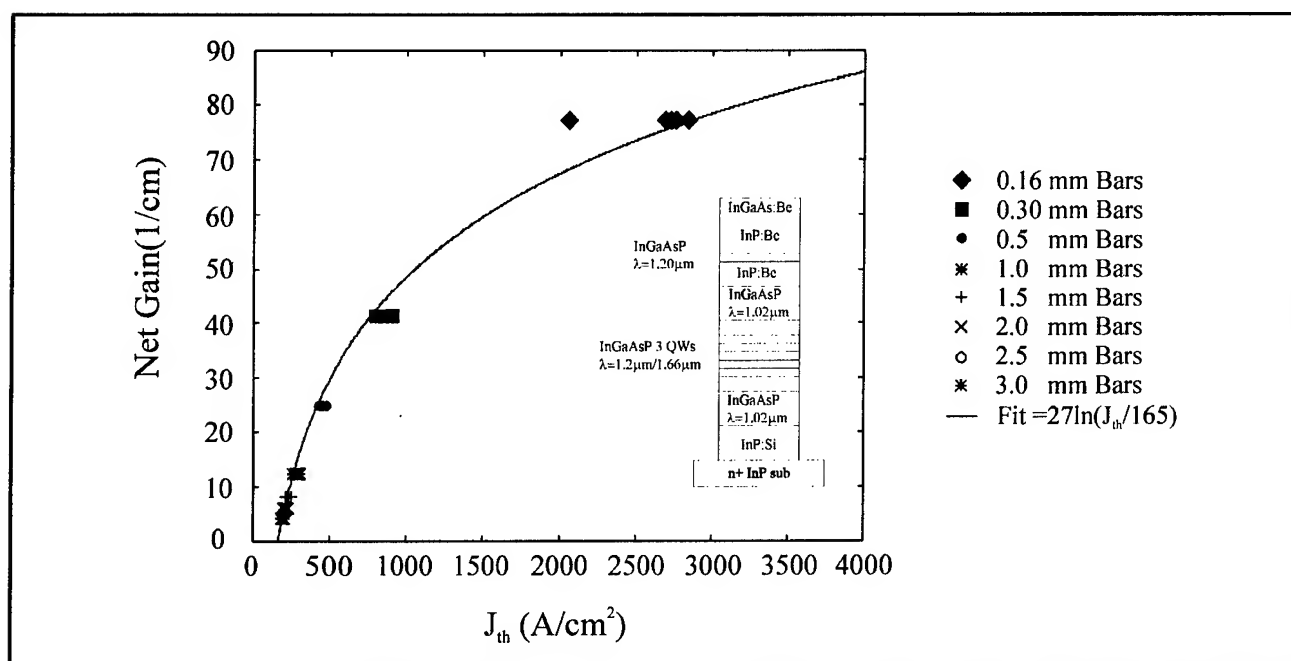


Figure 8. Net gain versus current density for 3 quantum well broad area lasers of various cavity lengths. The inset depicts the laser structure.

system is the small refractive index difference between (In,Ga)(As,P) and InP. To compensate for this, the SBR must contain on the order of 30 pairs of layers so as to achieve a reasonable reflectance. Due to the thickness requirements of each layer, this structure requires 15 or more hours for the GSMBE growth alone. When dealing with GaAs-based devices, it is possible to increase the difference in refractive indices by oxidizing AlAs. This increase in the difference between the high and low refractive indices in the DBR stack causes an increase of the stack reflectivity with fewer layers. For the InP system, the Al-containing compounds that are lattice-matched to InP are InAlAs and InAlAsP, which, when unoxidized, have a refractive index comparable to InGaAsP. Current work on this topic involves the oxidation of InAlAs(P) in a DBR-type structure.

3.7 Integrated Optical Filters and Circuits in InP

Sponsors

MIT Lincoln Laboratory
National Center for Integrated Photonic Technology
Subcontract 542-383

Project Staff

Professor Hermann A. Haus, Professor Leslie A. Kolodziejewski, Professor Henry I. Smith, Dr. Gale S.

Petrich, Jay N. Damask, Elisabeth A. Marley, Jeremy M. Milikow

As the designs for the integrated-resonant channel-dropping filter (CDF) have matured over the last year, increasing emphasis has been placed on the structural properties and integrity of the waveguides and gratings. In particular, an "ideal" CDF, made in the (In,Ga)(As,P)/InP material system, uses a quaternary alloy with a dilute concentration of Ga and As ($\text{In}_{0.93}\text{Ga}_{0.07}\text{As}_{0.15}\text{P}_{0.85}$), a rib height of about $1.5 \mu\text{m}$, and a grating depth of about $0.7 \mu\text{m}$ which, at a 244 nm period, translates to a grating aspect ratio on the order of 6:1. These waveguide dimensions and core alloy concentration were derived from trading off the core-to-clad index contrast with feature size. Such a trade-off maintains the grating strength and the modal confinement required by the channel-dropping filters while decreasing the polarization dependence by over a factor of six from the previous designs and increasing the circularity of the mode which, in turn, increases the fiber-to-chip coupling. Moreover, the waveguides with the aforementioned parameters are channel guides, which means that the tolerance on the rib etch depth is no longer an issue because the rib can be etched to any depth into the lower cladding without changing the optical properties.

The primary drawback to the current design is the high aspect ratio gratings. Such gratings will pose challenges to the etching, the thermal cleaning process, and the overgrowth steps that are required for fabrication. Reactive-ion etching is a popular

method to anisotropically etch high aspect ratio features, but optimizations to the process will have to be undertaken to insure that the grating tooth profile has straight side walls. After feature definition, the wafer must be returned to the GSMBE reactor for the growth of the upper InP cladding layer. Conventionally, in order to remove the native oxide and other contaminants from the surface, the wafer is thermally cleaned in the reactor. However, such treatment will likely cause some degree of reflow of the gratings which will dramatically degrade the spectral response of the CDF filter. In order to circumvent the thermal desorption of the oxide, a new atomic hydrogen source has been installed into the growth reactor. The atomic hydrogen species can remove the oxygen and carbon containing contaminants on the wafer surface at temperatures around 300°C. This cleaning treatment will likely pave the way in order to retain the structural integrity of the grating features.

Nucleation and full overgrowth of the grating features, with their 6:1 aspect ratios, has not been investigated. In order to understand the effects that influence the growth process, electron-beam lithography will be used to directly write features of various periods, duty cycles, and crystalline orientations. After each overgrowth on a patterned wafer, a focused-ion-beam tool will be used to create cross-sections of the grating with overgrowth for closer inspection.

In order to control the core alloy concentration in real time during the course of the film growth, an *in situ* ellipsometer is being installed on the GSMBE system. The feedback from the ellipsometer will be used to insure that the film composition is uniform and that the target thicknesses of the core and etch-stop layers are met to within ± 0.5 percent.

The combination of atomic hydrogen surface cleaning, *in situ* composition and thickness control, and focused-ion-beam work, in addition to waveguide designs, layout and nanolithographies, will, at the very least, offer a wide range of possible solutions to meet the specifications of the "ideal" channel-dropping filter design.

3.7.1 Publications

Damask, J.N. "Practical Design of Side-Coupled Quarter-Wave Shifted Distributed-Bragg Resonant Filters." Submitted to *J. Lightwave Tech.*

Damask, J.N. "Design of Synchronous Integrated-Optical Side-Coupled Resonators." Submitted to *J. Lightwave Tech.*

3.8 Photonic Bandgap Structures

Sponsor

National Science Foundation
DMR 94-00334

Project Staff

Professor John D. Joannopoulos, Professor Leslie A. Kolodziejski, Professor L. Rafael Reif, Dr. Gale S. Petrich, Dr. Pierre Villeneuve, Kuo-Yi Lim, Shanhui Fan, Jerry C. Chen, Xiao-feng Tang

A photonic crystal is a periodic dielectric structure that presents a range of frequencies within which photons fail to propagate. This forbidden band of frequencies translates into a photonic bandgap (PBG), analogous to an electronic bandgap in a semiconductor crystal. A defect state can also be introduced in the photonic bandgap when the dielectric periodicity of a photonic crystal is broken by the selective removal or addition of dielectric material. This defect results in the spatial localization of the defect mode to within a volume of approximately one cubic wavelength, yielding a high-Q electromagnetic microcavity. The realization of such a microcavity holds promises of vastly reducing spontaneous emission and zero point fluctuations within an energy band.

The main problem with the microfabrication of a three-dimensional photonic crystal originates from the rather sophisticated geometry and intricate arrangement of holes and rods needed to open a bandgap. These complex structures do not easily lend themselves to fabrication at submicron lengthscales. For example, the three dimensional PBG structure that is under investigation, is made of three materials (Si, SiO₂, and air) and consists essentially of a layered structure in which a series of cylindrical air holes are etched at normal incidence through the top surface of the structure. Furthermore, most applications for photonic bandgap structures require bandgaps larger than 10 percent which in turn require the use of materials with large index contrasts such as in the case of Si and SiO₂. In the structure under fabrication, the photonic bandgap is as large as 14 percent of the midgap frequency using Si, SiO₂, and air; and 23 percent using Si and air (after the SiO₂ is etched away). Until now, three-dimensional PBG crystals have been constructed for operation in the millimeter

wave region,¹⁶ and the fabrication of a two-dimensional photonic bandgap nanostructure has been reported.¹⁷

Several difficulties arose during the fabrication of the three-dimensional photonic bandgap structures. The first difficulty was creating Si trenches with the correct geometry. This problem was alleviated by using a low temperature oxide (LTO) as a hard mask as opposed to a photoresist mask and by the use of a special Cl_2 plasma etch. The second difficulty was the creation of voids in the SiO_2 that was subsequently deposited into the Si trenches using a LTO or SiO_2 that was deposited by plasma-enhanced chemical vapor deposition. Using $1\text{ }\mu\text{m}$ of boron phosphide silicate glass along with $1\text{ }\mu\text{m}$ of LTO, the Si trenches were completely filled with SiO_2 after the chemical/mechanical polishing step. Figure 9 shows the completed first layer. The third difficulty that arose was in the creation of a reproducible $1\text{ }\mu\text{m}$ shift between the second layer Si trenches and the first layer Si trenches. Future work includes the completion of the ten layers that are needed in the three-dimensional photonic crystal and the verification of the photonic bandgap.

The photonic bandgap air-bridge microcavity is essentially a one-dimensional photonic crystal made of III-V compound semiconductor material (refractive index, $n \sim 2.9\text{--}3.3$) surrounded by air ($n=1.0$). The one-dimensional crystal comprises of a semiconductor bridge that is punctuated with holes that are periodically spaced along the length of the bridge. A defect is introduced into the crystal by removing one of the holes. In *Progress Report No. 137*, we reported the successful fabrication of these structures using both silicon-based and III-V semiconductor material. Since that report, we have proceeded to design and fabricate devices coupled with single-mode waveguides for measurement purposes. These photonic bandgap air-bridge devices have been designed to exhibit a photonic bandgap centered at a wavelength of $4.5\text{ }\mu\text{m}$.

A typical device consists of a photonic bandgap air-bridge with waveguides feeding into and leading out of the air-bridge. The air-bridge material is GaAs and the structure is typically $14\text{ }\mu\text{m}$ long, $1.8\text{ }\mu\text{m}$ wide and $0.4\text{ }\mu\text{m}$ thick. The holes are $1.0\text{ }\mu\text{m}$ in diameter and are separated by $0.8\text{ }\mu\text{m}$. (The period of the holes is $1.8\text{ }\mu\text{m}$.) The defect is 2.6

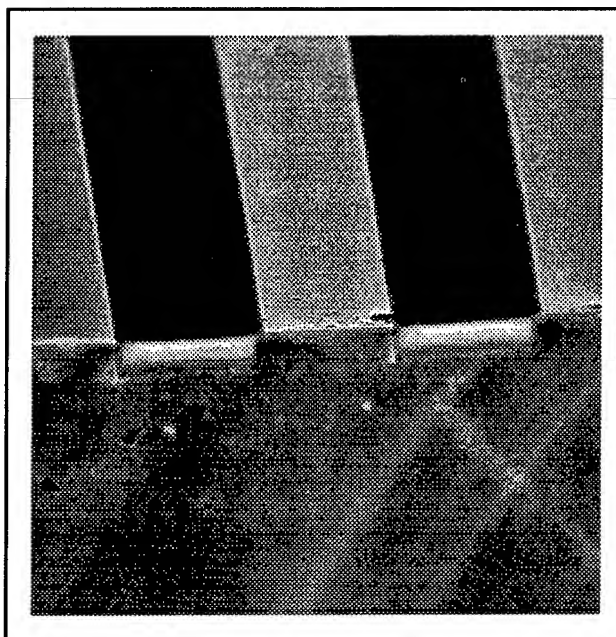


Figure 9. Scanning electron micrograph of the completed first layer of a three-dimensional photonic bandgap structure. The Si trenches are $1.8\text{ }\mu\text{m}$ wide and $1\text{ }\mu\text{m}$ deep.

μm wide (measured center-to-center of the two holes bordering the defect). The waveguide material is also GaAs, but has an upper cladding layer of $\text{Al}_{0.3}\text{Ga}_{0.7}\text{As}$ and a lower cladding layer of $\text{Al}_{0.7}\text{Ga}_{0.3}\text{As}$. The material configuration is designed to enhance the coupling of both the input beam from free space into the input waveguide, and from the input waveguide into the photonic bandgap air-bridge. Typically, the upper cladding is $0.4\text{ }\mu\text{m}$ thick and the lower cladding is $0.4\text{ }\mu\text{m}$ thick, and the tri-layer waveguide structure sits on a $4\text{ }\mu\text{m}$ $\text{Al}_{0.9}\text{Ga}_{0.1}\text{As}$ layer on top of the GaAs substrate.

The initial compound semiconductor material for the photonic bandgap air-bridge structure is grown by gas-source molecular beam epitaxy in the Chemical Beam Epitaxy Laboratory. A series of high-resolution photolithography, reactive ion etching and wet chemical etching steps are then performed to fabricate the bridge and waveguide structures. These processing steps utilize the facilities in both the Microsystems Technology Laboratory and the Center for Material Science and Engineering Microelectronics Fabrication Laboratory. We have successfully fabricated these devices and a scanning

¹⁶ E. Özbay, E. Michel, G. Tuttle, R. Biswas, K.M. Ho, J. Bostak, and D.B. Bloom, "Double-etch Geometry for Millimeter-wave Photonic Band-gap Crystals," *Appl. Phys. Lett.* 65(13): 1617-1619 (1994).

¹⁷ P.L. Gourley, J.R. Wendt, G.A. Vawter, T.M. Brennan, and B.E. Hammons, "Optical Properties of Two-dimensional Photonic Lattices Fabricated as Honeycomb Nanostructures in Compound Semiconductors," *Appl. Phys. Lett.* 64(6): 687-689 (1994).

electron micrograph of such a device is shown in figure 10.

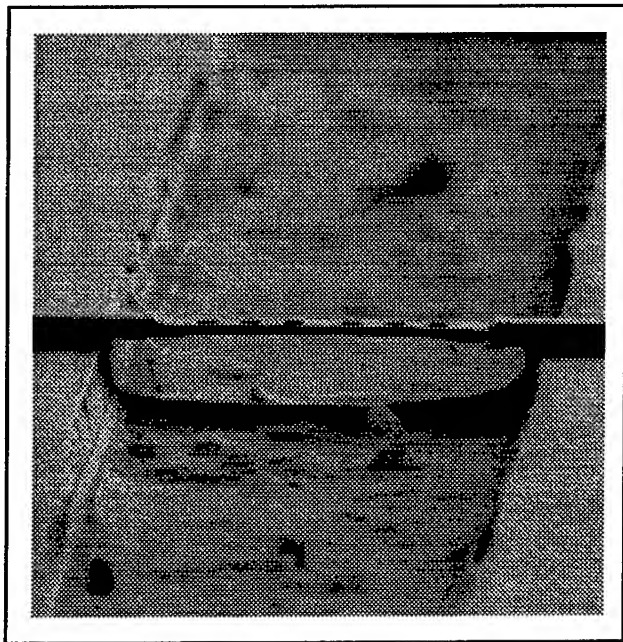


Figure 10. Scanning electron micrograph of a photonic bandgap air-bridge device coupled with input and output waveguides. The air-bridge is $1.8\ \mu\text{m}$ wide, $0.4\ \mu\text{m}$ thick and approximately $14\ \mu\text{m}$ long. The holes are $1.0\ \mu\text{m}$ in diameter and are separated by $0.8\ \mu\text{m}$. The defect region, in the middle of the air-bridge, is $2.6\ \mu\text{m}$ wide (center to center). The $0.4\ \mu\text{m}$ thick upper cladding layer of the waveguide (absent from the bridge) is clearly visible.

An experimental optical setup to measure and characterize the photonic bandgap air-bridge structure is under construction and measurements will be performed in the near future in conjunction with Professor Erich Ippen's group.

3.8.1 Publications

Villeneuve, P.R., S. Fan, J.D. Joannopoulos, K.Y. Lim, G.S. Petrich, L.A. Kolodziejski, and R. Reif. "Air-Bridge Microcavities." *Appl. Phys. Lett.* 67(2) 167-169 (1995).

Section 2 Quantum-Effect Devices

Chapter 1 Statistical Mechanics of Quantum Dots

Chapter 2 Artificial Atoms

Chapter 3 Coulomb Blockade in Single and Double Quantum Dots

Chapter 4 Superconducting and Quantum-Effect Devices

Chapter 5 Nanostructures Technology, Research, and
Applications

Chapter 6 Single-Electron Spectroscopy

Chapter 1. Statistical Mechanics of Quantum Dots

Academic and Research Staff

Professor Boris L. Altshuler, Dr. Nobuhiko Taniguchi

Graduate Students

Anton V. Andreev

1.1 Project Description

Sponsor

Joint Services Electronics Program
Grant DAAL04-95-1-0038

In 1995, the main objective of our research was the nonuniversal properties of quantum dots. Typical behavior of these closed systems of large but finite number of electrons is usually called quantum chaos.¹ This means something opposite to behavior of quantum integrable systems where spectra can be characterized by a set of quantum numbers. Quantum chaos can be caused either by disorder or by geometry of a quantum dot or by interactions between electrons. It was intensively studied for several years.² Probably the most popular characteristics of *chaotic* quantum systems are the statistics of energy spectra. The statistics that describe distribution of eigenstates in energy and parameter space were found for systems with well developed chaos to be universal with a pretty high accuracy. This means, e.g., that the correlation functions at small energies, after proper rescaling, become independent from the particular features of the quantum system and particular perturbation. Earlier, we evaluated these functions explicitly.³

The global properties of the spectra (i.e., correlation functions at higher energies), are different for different systems. We have solved the long time problem in the field of quantum chaos by expressing these features through the properties of the underlying classical system.

First, we considered disordered quantum dots.⁴ Using a nonperturbative approach, we have evaluated the large frequency ω asymptotics of the two-point correlation function

$$R(\omega) = \langle \sum_{ij} \delta(\varepsilon_i - \varepsilon_j) \delta(\varepsilon_i + \omega - \varepsilon_j) \rangle \quad (1)$$

where ε_i and ε_j denote the eigenstates of our system (quantum dot) measured in units of the mean level spacing and $\langle \dots \rangle$ stands for the averaging. We found that this function for systems with broken T-invariance (quantum dot in a magnetic field) can be presented as

$$R(\omega) = \delta(\omega) - R_{\text{smooth}}(\omega) + R_{\text{osc}}(\omega) \cos(2\pi\omega). \quad (2)$$

The functions $R_{\text{smooth}}(\omega)$ and $R_{\text{osc}}(\omega)$ are not universal: they depend on the shape of the quantum dot, its conductance, etc. In the universal limit,

$$R_{\text{smooth}}(\omega) = R_{\text{osc}}(\omega) 1/(4\pi^2\omega^2) \quad (3)$$

is very important for the understanding of the connection between classical and quantum problems; these functions are completely determined by the properties of classical diffusion in the system. Namely, $R_{\text{osc}}(\omega)$ is the spectral determinant of the diffusion operator and $R_{\text{smooth}}(\omega)$ is the Green's function of the same operator. As a result they are connected as

$$R_{\text{smooth}}(\omega) = - (1/4\pi^2) \partial \{ \ln [R_{\text{osc}}(\omega)] \} / \partial \omega^2. \quad (4)$$

¹ M.C. Gutzwiller, *Chaos in Classical and Quantum Mechanics* (New York: Springer-Verlag, 1990).

² M.V. Berry, in *Chaos in Quantum Physics*, eds. M.-J. Giamonni, A. Voros, and J. Zinn-Justin, Les Houches, Session LII, 1989 (Amsterdam: North Holland, 1991), p. 251.

³ For complete discussion see B.L. Altshuler and B.D. Simons, "Universalities: from Anderson Localization to Quantum Chaos," in *Mesoscopic Quantum Physics*, eds. E. Akkermans, G. Montambaux, J.-L. Pichard, and J. Zinn-Justin, Les Houches, Session LXI, 1994 (Amsterdam: North Holland, 1996), p. 1.

⁴ A.V. Andreev and B.L. Altshuler, "Spectral Statistics beyond Random Matrix Theory," *Phys. Rev. Lett.* 75: 902-905 (1995).

This relation is universal even for quantum dots without any disorder.⁵ We have been able to show that, in a very general case, there is a classical operator whose spectrum completely determines the spectral statistics of the quantum dot. This operator describes the time evolution of the classical counterpart of our quantum dot. It is crucial for the whole theory of quantum chaos that this operator corresponds to the *time irreversible* classical dynamics. This understanding allowed us to prove a conjecture proposed long ago by Bohigas, Giannoni and Schmit⁶ for a certain class of quantum systems. By making use of numerical studies, these authors found that the spectral statistics even for *simple* chaotic systems are very close to universal Wigner-Dyson statistics. From our calculations,⁵ it follows that this is true for systems with exponential relaxation. By making use of the nonperturbative approach, we can also evaluate nonuniversal corrections to this universal behavior, given the set of the relaxation times. This connection between quantal behavior of the quantum dot and irreversible classical dynamics of its classical counterpart is of a particular fundamental importance for the theory of both classical and quantum complex systems.

To complete our study of the universal properties of quantum dots, we evaluated the statistics of the oscillator strengths, starting from the Wigner-Dyson hypothesis.⁷ These statistics provide a characterization of quantum chaos which complements the usual energy level statistics. This theory can be applied to quantum dots and also to systems like the hydrogen atom in a strong magnetic field. Without additional assumptions, we have evaluated exactly the correlation function of oscillator strengths at different frequencies and different mag-

netic fields. We have also discovered an unexpected differential relation between the density of states statistics and those of the oscillator strengths.

Using the mathematical similarity between quantum particles in one dimension and energy levels, we have obtained important results that can be applied for better understanding of the quantum dots with interactions between electrons. In particular, we have discovered a novel relationship between equal time current and density correlations in the model known as Calogero-Sutherland model, where the interaction between one dimensional fermions is inverse proportional to the distance between them.⁸ This relationship exists in addition to the usual Ward identities.

1.2 Publications

Agam, O., B.L. Altshuler, and A.V. Andreev. "Spectral Statistics: From Disordered to Chaotic Systems." *Phys. Rev. Lett.* 75: 4389 (1995).

Andreev, A.V., and B.L. Altshuler. "Spectral Statistics beyond Random Matrix Theory." *Phys. Rev. Lett.* 75: 902-905 (1995).

Taniguchi, N., A.V. Andreev, and B.L. Altshuler. "Statistics of Oscillator Strength in Chaotic Systems." *Europhysics Lett.* 29: 515 (1995).

Taniguchi, N., B.S. Shastri, and B.L. Altshuler. "Random Matrix Model and Calogero-Sutherland Model: A Novel Current-Density Mapping." *Phys. Rev. Lett.* 75: 37 (1995).

⁵ O. Aham, B. Altshuler, and A.V. Andreev, "Spectral Statistics: From Disordered to Chaotic Systems," *Phys. Rev. Lett.* 75: 4389 (1995).

⁶ O. Bohigas, M.J. Giannoni, and C. Schmidt, *Phys. Rev. Lett.* 52: 1 (1984).

⁷ N. Taniguchi, A.V. Andreev, and B.L. Altshuler, "Statistics of Oscillator Strength in Chaotic Systems," *Europhysics Lett.* 29: 515 (1995).

⁸ N. Taniguchi, B.S. Shastri, and B.L. Altshuler, "Random Matrix Model and Calogero-Sutherland Model: A Novel Current-Density Mapping," *Phys. Rev. Lett.* 75: 37 (1995).

Chapter 2. Artificial Atoms

Academic and Research Staff

Professor Marc A. Kastner, Dr. Olivier Klein

Visiting Scientists and Research Affiliates

Theodore M. Lyszczarz,¹ Paul M. Mankiewich,² David C. Shaver,¹ Shalom Wind³

Graduate Students

David Abusch-Magder, David J. Goldhaber-Gordon, Nicole Y. Morgan

2.1 Goals and Objectives

Sponsors

Joint Services Electronics Program

Grant DAAH04-95-1-0038

National Science Foundation

Grant ECS 92-03427

U.S. Army Research Office

Grant DAAH04-94-G-0119

When electrons are confined to a small particle of metal or a small region of semiconductor, both the energy and charge of the system are quantized. In this way such nanometer-sized systems behave like artificial atoms.⁴ The quantization of energy is familiar: The solutions of the Schrodinger equation in an isolated region have discrete energies. In some ways, however, the quantization of charge is more mysterious. We are quite comfortable with the idea that the charge of a collection of electrons is discrete. However, the charge in any small volume of a large sample of conductor is *not* discrete because the electronic wavefunctions are extended over the entire sample. Only when the states are localized is the charge quantized.

Artificial atoms have been constructed using metals and semiconductors, and they have been given a variety of names: single-electron-tunneling transistor, quantum dot, single-electron transistor, and zero-dimensional electron gas. The physics of all these devices is the same, although the limits in

which they operate may be quite different. The goal of our research is to better understand the physics of these devices in order to optimize their performance so that circuit design may commence.

2.2 Summary of Recent Work

Our work this year has been successful in two arenas. First, we have followed up our studies, reported one year ago,⁵ showing that electrons in a single-electron transistor in GaAs undergo phase transitions as a function of magnetic field. We have recently reported the observation of low energy excitations which correspond to the critical fluctuations of these transitions. Second, we have recently fabricated metal oxide silicon SETs (MOSSETs) which show single electron phenomena up to 20 K. We concentrate here on the latter research.

A single-electron transistor (SET) is an island of charge which is coupled to leads by tunnel barriers. There are two energies that are encountered in changing the electronic state of the SET: the energy required to add an electron to the island, U , and the energy required to excite the electrons already on the island, ΔE . Both these energies increase as the size of the island is diminished. Since the resolution of single electron phenomena is limited by the temperature of the electrons, we may increase the operating temperature by

¹ MIT Lincoln Laboratory, Lexington, Massachusetts.

² AT&T Bell Laboratories, Short Hills, New Jersey.

³ IBM Corporation, Thomas J. Watson Research Laboratories, Yorktown Heights, New York.

⁴ M.A. Kastner, "Artificial Atoms," *Phys. Today* 46(1): 24 (1993).

⁵ O. Klein, C. de C. Chamon, D. Tang, D.M. Abusch-Magder, S.-G. Wen, M.A. Kastner, and S.J. Wind, "Exchange Effects in an Artificial Atom at High Magnetic Fields," *Phys. Rev. Lett.* 74: 785 (1995).

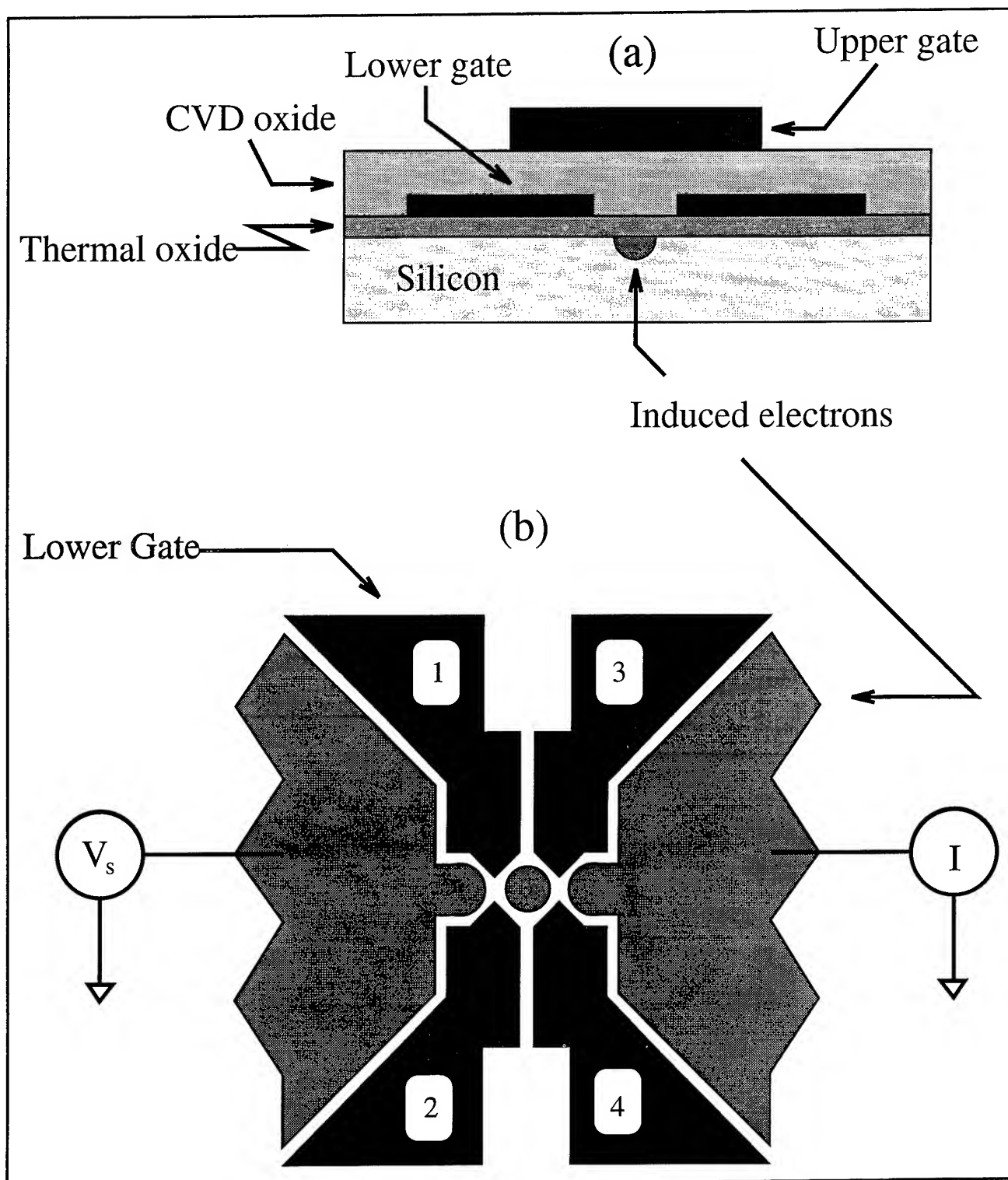


Figure 1. Schematic of the device: (a) The cross section shows the p-silicon substrate with 20 nm thermal SiO₂, lower metal gate patterned by electron beam lithography and liftoff, chemical vapor deposited SiO₂, and upper gate. In standard operation, the upper gate is held at a voltage above the inversion threshold while the voltages on the lower gates are kept below threshold. Electrons are then induced at the Si-SiO₂ interface where the lower gate does not screen the field of the upper gate. (b) Sketch of a top view of our device with an isolated island of electrons coupled to two leads by tunnel junctions. The lead on the left is the source and is biased at V_s ; the lead on the right, called the drain, is connected through an ammeter to ground. Our measurements are made by biasing the source and measuring the current that flows to the drain.

reducing the size of the SET. The purpose of our work is to fabricate small SETs and, in addition to achieving higher operating temperatures, to exploit the improved relative resolution to explore coherent interaction between the electrons in the leads and the electrons on the island.

An island of charge can be created by electrostatic depletion of a two-dimensional electron gas (2DEG). By changing the voltages on metallic gates which lie a short distance above a 2DEG, the electrostatic fields can be adjusted; in this way, both the number of electrons on the island and the size of the tunnel barriers may be varied. The size of the island is limited by the depletion width, which decreases as the gates are brought closer to the 2DEG; a small depletion width allows the possibility of a small island. Thus, to make small SETs one needs a material system in which the gates can be brought close to the 2DEG. The Si-SiO₂ MOS system is ideal for this purpose because SiO₂ is a robust insulator; layers as thin as 10 nm have low leakages, high breakdown voltages, and are easily fabricated. We have therefore chosen to fabricate SETs in the silicon MOS system, rather than in the more extensively studied GaAs-AlGaAs system. Previously observed coulomb blockade (CB) effects in electrostatically patterned MOS structures have resulted from impurities. More recent work⁶ has achieved CB in a Si-SiO₂ system using pattern-dependent oxidation. However, our studies are the first showing well-defined CB phenomena in lithographically defined MOSSETs where the tunnel barriers are created by gate electrodes.

2.3 Fabrication

Standard silicon fabrication techniques have been used in combination with electron beam lithography to fabricate MOSSETs, thus taking advantage of existing technology. Figure 1a shows the basic layer structure of our devices. We start with a lightly doped p-silicon substrate (25-45 Ω cm) and grow a 20 nm thick dry thermal oxide on its surface. Using electron beam lithography, we pattern a 50 nm layer of PMMA, which then serves as a lift-off mask for our lower metal gate, a 20 nm layer of chromium. A scanning electron micrograph of a typical lower metal gate pattern is shown in figure 2. After chemical vapor deposition of 85 nm of SiO₂ on top of the gate structure, we anneal our sample at 900 degrees C for 30 seconds in dry nitrogen. The upper metal gate and interconnects are then

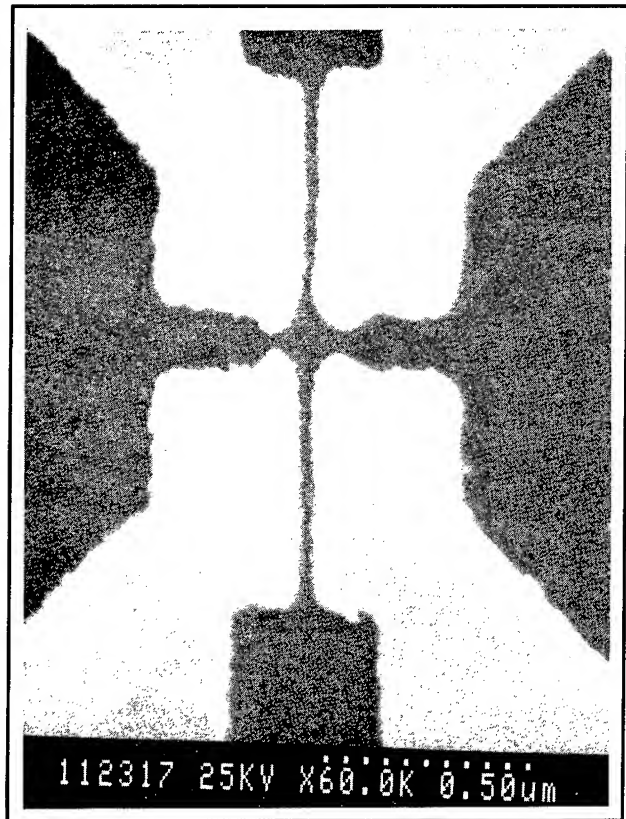


Figure 2. A scanning electron micrograph is shown of one of our SETs. Note that the gap between gates 1 and 3 is 25 nm. The full diameter of the gap between the lower gates is 120 nm. The measurements discussed in this paper were made on a larger SET whose diameter is about twice as large.

deposited by sputtering aluminum and are patterned photolithographically. Ohmic contact to the inversion layer is made by degenerately doped n⁺ implants.

In standard operation, the upper metal gate is held at a voltage above the inversion threshold while the voltages on the lower metal gates are kept below threshold. Electrons collect at the Si-SiO₂ interface in regions where the upper gate potential is not screened by the lower metal gates (see figure 1b); in this way, it is possible to pattern the 2DEG into an isolated island of electrons coupled to leads by tunnel junctions. Because this device uses SiO₂, which is a robust insulator, we can apply large voltages to the gates: > 20 V can be applied to the lower gates, while 50 V can be applied between the upper and lower gates. The relative transmission of the tunnel barriers can be tuned by applying a

⁶ Y. Takahashi, M. Nagase, H. Namatsu, K. Kurihara, K. Iwadate, Y. Nakajima, S. Horiguchi, K. Murase, and M. Tabe, "Fabrication Technique for Si Single-Electron Transistor Operating at Room Temperature," *Electron. Lett.* 31: 136 (1995).

voltage difference of up to 2 V between left and right lower gates.

2.4 Results

We have observed periodic conductance oscillations resulting from CB in a MOSSET, with an addition energy $U = 15$ meV, which corresponds to temperature $T = U/k_B = 175$ K. Figure 3 shows the conductance as a function of upper gate voltage for several temperatures in a MOSSET whose lithographic diameter is approximately 250 nm. We see the periodic peaks in conductance typical of CB with a spacing of 200 mV. One of the most striking features of our data is that the conductance peaks persist to high temperatures: the traces in figure 3 are taken at 0.315 K, 6 K, and 20 K with an offset added for clarity. The peaks are still well resolved

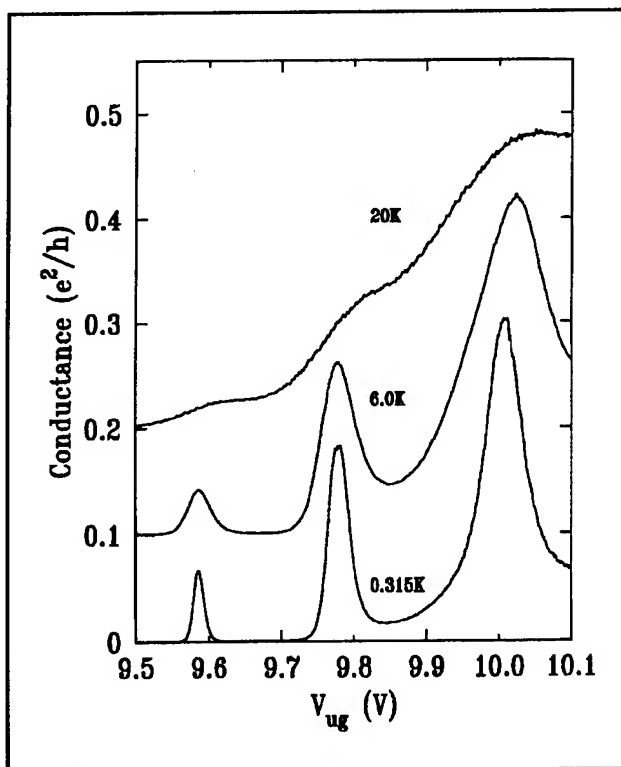


Figure 3. The conductance as a function of upper gate voltage is shown here for three different temperatures. Note that the conductance peaks are still sharp at 6 K, while a periodic modulation of the conductance is still present even at 20 K. This is consistent with a charging energy corresponding to 175 K. The measurement was made using standard lock-in techniques at 8.7 Hz with an excitation voltage of 65 μ V for the traces at 6 K and 20 K and an excitation voltage of 20 μ V for the trace at 0.315 K. The excitation voltage in all our measurements was chosen to be less than $k_B T/e$ so that we measure the linear response of the system. The curves at 6 K and 20 K are offset by $0.1e^2/h$ and $0.2e^2/h$ for clarity; the curve at 6 K is shifted by 0.06 V to the left.

at 6 K, and there is a clear periodic modulation of the conductance which persists up to 20 K, consistent with a CB charging energy of 175 K.

There are four important energy scales that determine the transport in CB: ΔE is the typical excitation energy of the island with a fixed number of electrons; Γ is the lifetime broadened natural line width resulting from tunneling between the island and the leads; U is the charging energy of the island; and $k_B T$ is the temperature of the SET. To observe well-separated CB peaks, $k_B T < U/5$. Past studies of SETs have been restricted to two different regimes, both of which have $k_B T > \Gamma$. For metal SETs, where $k_B T > \Delta E$, theory predicts that a conductance peak has full width at half maximum $\text{FWHM} = 4.2 k_B T/\alpha$, where $\alpha = C_g/C_\Sigma$, the ratio of the gate capacitance to the total capacitance. The amplitude is predicted to be independent of temperature. In the other previously studied regime, $k_B T < \Delta E$, and the transport is dominated by tunneling through a single quantum state. Again the FWHM is linear in temperature, but is now given by $3.5 k_B T/\alpha$, while the peak amplitude varies as $1/T$. Thus, by examining both the amplitude and width of the peaks as a function of temperature we may determine both the transport regime and the factor α .

In our data, we find that the width of the peak at 9.8 V is linear in temperature (figure 4a). However, in contrast to the prediction of the simplest model, the width extrapolates to a finite value at $T=0$. This result suggests that our MOSSET is operating in the regime where $\Gamma > k_B T$. In this regime, we expect the line shape to be a convolution of the natural line shape of the zero-temperature conductance resonance with the derivative of the Fermi-Dirac distribution function. If the line shape is Lorentzian with $\text{FWHM} = \Gamma$, the width is predicted to be linear in temperature, with a finite intercept: $\text{FWHM} = (3.5k_B T + \Gamma)\alpha$, which agrees well with the behavior seen in figure 4a. As discussed below, we find that $\Gamma = 1.3$ meV, corresponding to a temperature of 15 K, for the peak at 9.8 V. Furthermore, in this regime the amplitude is expected to have a $1/T$ dependence for $k_B T > \Gamma$, and below this temperature the amplitude is expected to saturate. Figure 4b shows such a crossover in the amplitude of the peak at 9.8 V, providing further evidence that the finite intercept in figure 4a is due to a large natural line width.

From the slope of the peak width versus temperature (figure 4a), we estimate $\alpha = 0.08$. The physical meaning of α is simple: when the gate potential is changed by ΔV_g , the potential of the electron island is changed by $\alpha \Delta V_g$. We thus use α to convert the gate voltage periodicity of CB peaks to an energy scale: $U = e\alpha\Delta V_g = 15$ meV, or $U/k_B =$

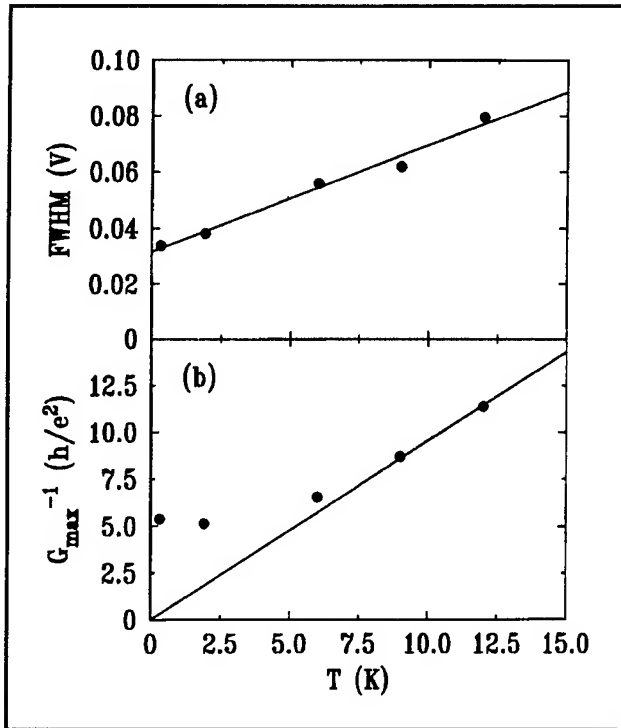


Figure 4. The full width at half maximum (a) and the inverse of the peak height (b) are shown as functions of temperature for the conductance peak at an upper gate voltage of 9.8 V (see figure 3). Notice that the width does not have a zero intercept, while the inverse of the maximum conductance saturates at low temperature. This behavior is results from the large natural line width G of the state. The line in (a) is a fit to all the points, while the line in (b) fits the high temperature points with a zero intercept.

175 K. Similarly, we use α to convert the peak widths and find Γ s of 500 μeV , 1.3 meV, and 3.3 meV for the three peaks in figure 3, in order of ascending gate voltage.

We have also measured the differential conductance dI/dV_s as a function of V_s the source voltage, which we call the tunneling spectrum. This spectrum (shown in figure 5) is proportional to the

density of single-particle states on the island which couple to the leads. The first feature to notice in figure 5 is the CB gap around zero bias. In addition, there are several features whose spacing is reproducible; these are marked with arrows. We associate these features in the density of states with excited states of the artificial atom (SET). The first peak in the spectrum on the right of the plot (arrow labeled gs N) is the current contribution from the ground state of the island with N electrons, while additional features (arrow labeled exc) are due to excited states of the N -electron island. Similarly, the peak on the left of the plot (arrow labeled gs $N-1$) is due to current through the ground state of the $N-1$ -electron island.

The typical energy spacing of bound states in the SET is ~ 4 meV; we have converted the voltage axis in figure 5 into an energy scale by accounting for the capacitive coupling between the lead and the island. This large value reflects the very small spatial extent of the electron droplet. Furthermore, this direct measurement of ΔE confirms that $k_B T < \Delta E$, as we have seen in the temperature dependence data.

2.5 Publications

Kastner, M.A. "Mesoscopic Physics with Artificial Atoms." *Comments on Condensed Matter Physics*. Forthcoming.

Kastner, M.A., O. Klein, C. de C. Chamon, D. Tang, D.M. Abusch-Magder, U. Meirav, X.-G. Wen, and S.J. Wind. "Exchange Effects in Artificial Atoms." *Jpn. J. Appl. Phys.* 34: 16 (1995).

Klein, O., C. de C. Chamon, D. Tang, D.M. Abusch-Magder, S.-G. Wen, M.A. Kastner, and S.J. Wind. "Exchange Effects in an Artificial Atom at High Magnetic Fields." *Phys. Rev. Lett.* 74: 785 (1995).

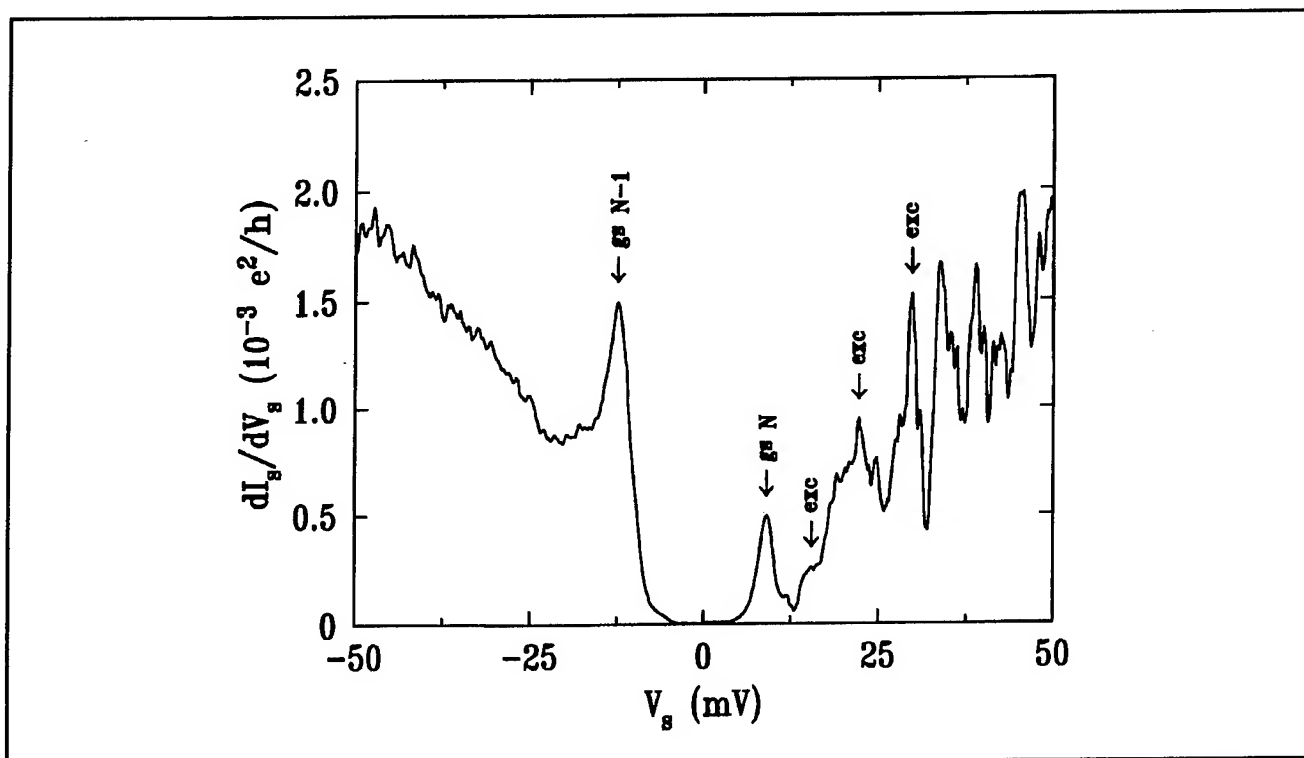


Figure 5. Tunneling spectrum of the SET at $T = 0.315$ K. The peaks correspond to variations in the density of states of the island. Peaks marked gs are due to tunneling through the ground state, while those marked exc are due to tunneling through excited states. The measurement was made using a lock-in amplifier at 8.7 Hz with an excitation voltage of 26 μ V.

Chapter 3. Coulomb Blockade In Single And Double Quantum Dots

Academic and Research Staff

Professor Patrick A. Lee, Dr. Akira Furusaki, Dr. Konstantin Matveev

Technical and Support Staff

Margaret O'Meara

3.1 Project Description

Sponsor

Joint Services Electronics Program
Grant DAAH04-95-1-0038

A few years ago, Professor Kastner's research group discovered that the conductance through a quantum dot weakly coupled to the leads shows periodic peaks as a function of the voltage on a gate electrode.¹ This behavior was attributed to the phenomenon of Coulomb blockade: to add an electron to the dot, the system must have an energy equal to the electrostatic energy of a dot charged by one electron. Most of the theoretical and experimental work on Coulomb blockade is devoted to the case when the quantum dot is separated from the leads by very high tunnel barriers, which ensure the discreteness of charge in the dot. A recent experiment² indicates that as the height of the barriers is lowered, the Coulomb blockade peaks are smeared and transformed into small oscillations. Apparently, as one lowers the barriers between the dot and the leads, the discreteness of the charge of the dot is smeared, and the Coulomb blockade is suppressed. An important theoretical problem is to find the conditions at which a dot strongly coupled to the reservoirs can exhibit the Coulomb blockade.

Our preliminary studies³ showed that a quantum dot connected to a lead by a single contact should demonstrate the Coulomb blockade oscillations of the dot's charge as long as the transmission coefficient of the contact T is less than unity. Experimentally, it is difficult to measure charge and in the

past year our research group worked on the theory of the transport through quantum dots.

3.2 Transport Through a Single Quantum Dot

The system we study is shown in figure 1.⁴ The quantum dot is coupled to the reservoirs (leads) by two quantum point contacts controlled by the corresponding gate voltages. Inside the electrostatically created constrictions, the potential changes adiabatically as the electrons move along the channel, which enables us to describe the transport by a one-dimensional model. We study the linear conductance through the quantum dot as a function of the gate voltage in the regime where the transmission through one or both contacts is almost perfect: the transmission coefficient T is close to 1. The results are as follows:

1. In agreement with the experiments, we found that the Coulomb blockade oscillations of the conductance disappear when the transmission through at least one contact is perfect, $T=1$. If neither of the contacts is in the regime of perfect transmission, the conductance shows weak periodic oscillations as a function of the gate voltage.
2. An unexpected result was obtained: unlike the oscillations of the average charge of the dot, the amplitude of the oscillations of conductance grows as the temperature is decreased (figure 2). At very low temperatures, the oscillations are no longer weak, and to find the conduc-

¹ M.A. Kastner, *Rev. Mod. Phys.* 64: 849 (1992).

² N. C. van der Vaart et al., *Physica* 189B: 99 (1993).

³ K.A. Matveev, *Phys. Rev. B* 51: 1743 (1995).

⁴ A. Furusaki and K.A. Matveev, *Phys. Rev. Lett.* 75: 709 (1995); A. Furusaki and K.A. Matveev, *Phys. Rev. B* 52: 16676 (1995).

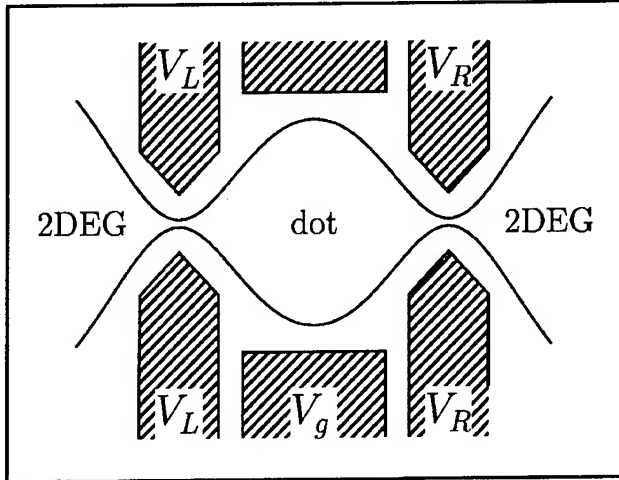


Figure 1. Schematic view of a quantum dot connected to two bulk 2D electrodes. The dot is formed by applying negative voltage to the gates (shaded). Solid line shows the boundary of the 2D electron gas (2DEG). Electrostatic conditions in the dot are controlled by the voltage applied to the central gates. Voltage $V_{L,R}$ applied to the auxiliary gates controls the transmission probability through the left and right constrictions.

tance a non-perturbative solution is required. Such a solution was found for several cases, and we discovered that in the low-temperature regime the weak oscillations of conductance are transformed into sharp peaks.

3. The conductance in the centers of the peaks is of the order of the conductance quantum e^2/h if the barriers are identical, and proportional to the temperature in the asymmetric case. Between the peaks, the conductance is always proportional to the square of the temperature.

Our theoretical description of the problem is applicable in a wide range of temperatures between the charging energy of the dot and the quantum level spacing. We believe that the results can be easily tested in the experiments.

3.3 Transport Through Double Quantum Dots

In a recent experiment,⁵ the Coulomb blockade oscillations of conductance through a system of two quantum dots (figure 3) were studied.⁶ In the experiment the contacts between the quantum dots and the leads were in the weak tunneling regime, with transmission coefficients $T_{l,r} \ll 1$. On the other

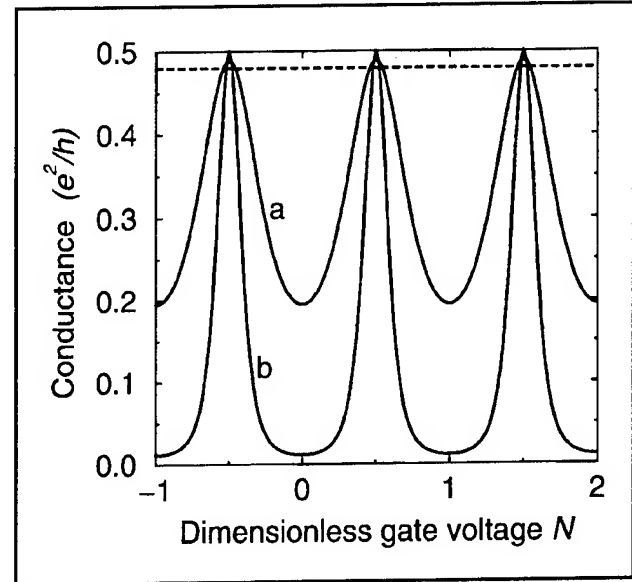


Figure 2. Conductance through a quantum dot as a function of the dimensionless gate voltage N for the case when the transmission coefficients for both contacts are 0.96. The dashed line represents the conductance in the high-temperature limit. The curves a) and b) are for the temperature equal to 0.04 and 0.005 in units the charging energy.

hand, the contact between the dots was tuned by adjusting the gate voltage V_0 in such a way that the corresponding transmission coefficient T_0 scanned the whole region from 0 to 1. As a result, a series of the dependences of the conductance on the gate voltage at different values of T_0 were measured. The experiment showed that as the transmission through the constriction between the dots is increased, the periodic peaks in the conductance split into doublets. The distance between the components of the doublets grows with T_0 , and at $T_0 = 1$ the periodicity is restored, but with a period which is smaller by a factor of two.

Some features of the experiment are easily explained on the basis of conventional theories of the Coulomb blockade. For instance, the change of the period by the factor of 2 is due to the fact that when the two dots are strongly coupled, they form a large single dot with a doubled capacitance. On the other hand, the splitting of the peaks when the transmission coefficient T_0 is between 0 and 1 cannot be explained with the usual electrostatic approach. The goal of this project is to develop a quantum theory of transport through the double dot system.

⁵ F.R. Waugh et al., *Phys. Rev. Lett.* 75: 705 (1995).

⁶ K.A. Matveev, L.I. Glazman, and H.U. Baranger, *Phys. Rev. B* 53: 1034 (1996).

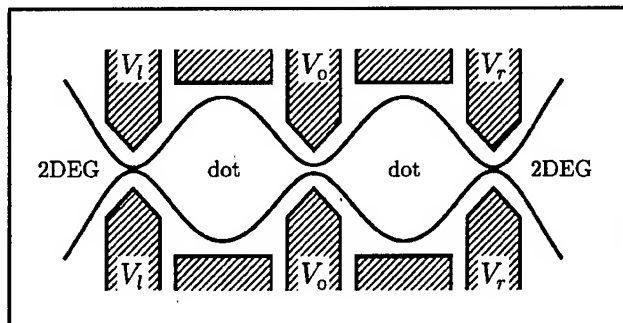


Figure 3. Schematic view of the double quantum dot system. The dots are formed by applying negative voltage to the gates (shaded); the solid line shows the boundary of the 2D electron gas (2DEG). V_l and V_r create tunnel barriers between the dots and the leads while V_0 controls the transmission coefficient through the constriction connecting the dots.

We start with the theory of the positions of the peaks in conductance as a function of the gate voltage. When the tunneling between the quantum dots is weak, an electron added to the double dot system can occupy two energetically equivalent positions on either the left or right dot. As a result, there is a double degeneracy of the peak positions. As the barrier between the two dots becomes more transparent, the degeneracy of the two states is lifted due to the hybridization of the two quantum states. Thus, the splitting of the peaks at $T_0 > 0$ is proportional to the decrease of the ground state energy of the double dot system due to the quantum fluctuations of the charge between the dots. We have been able to find the peak splitting in the both limiting cases of the transmission coefficient T_0 close to 0 and 1. At small T_0 , the splitting of the peaks is linear in T_0 ; at T_0 near 1, the deviation of the peak positions from the equidistant positions is proportional to $(1 - T_0) \ln(1 - T_0)$. The results are summarized and compared with the experiment in figure 4.

We have also investigated the temperature dependence of the peak heights. In the conventional theories of the Coulomb blockade, the heights of the peaks in conductance are temperature-independent. This result applies to the double-dot system in the regime of very weak coupling between the dots. However, as the coupling between the dots becomes stronger, the peaks acquire a power-law temperature dependence. The origin of this temperature dependence is similar to

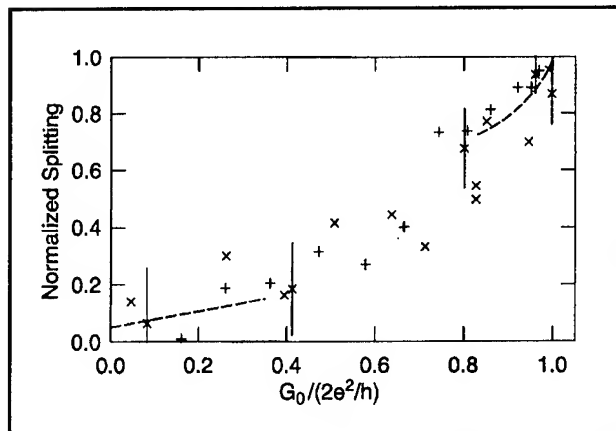


Figure 4. The normalized splitting of the Coulomb blockade peaks as a function of the inter-dot conductance. Our theoretical results (dashed lines) are in good agreement with the experiment (crosses and pluses). The splitting is normalized by the period of the peaks in the strong tunneling limit.

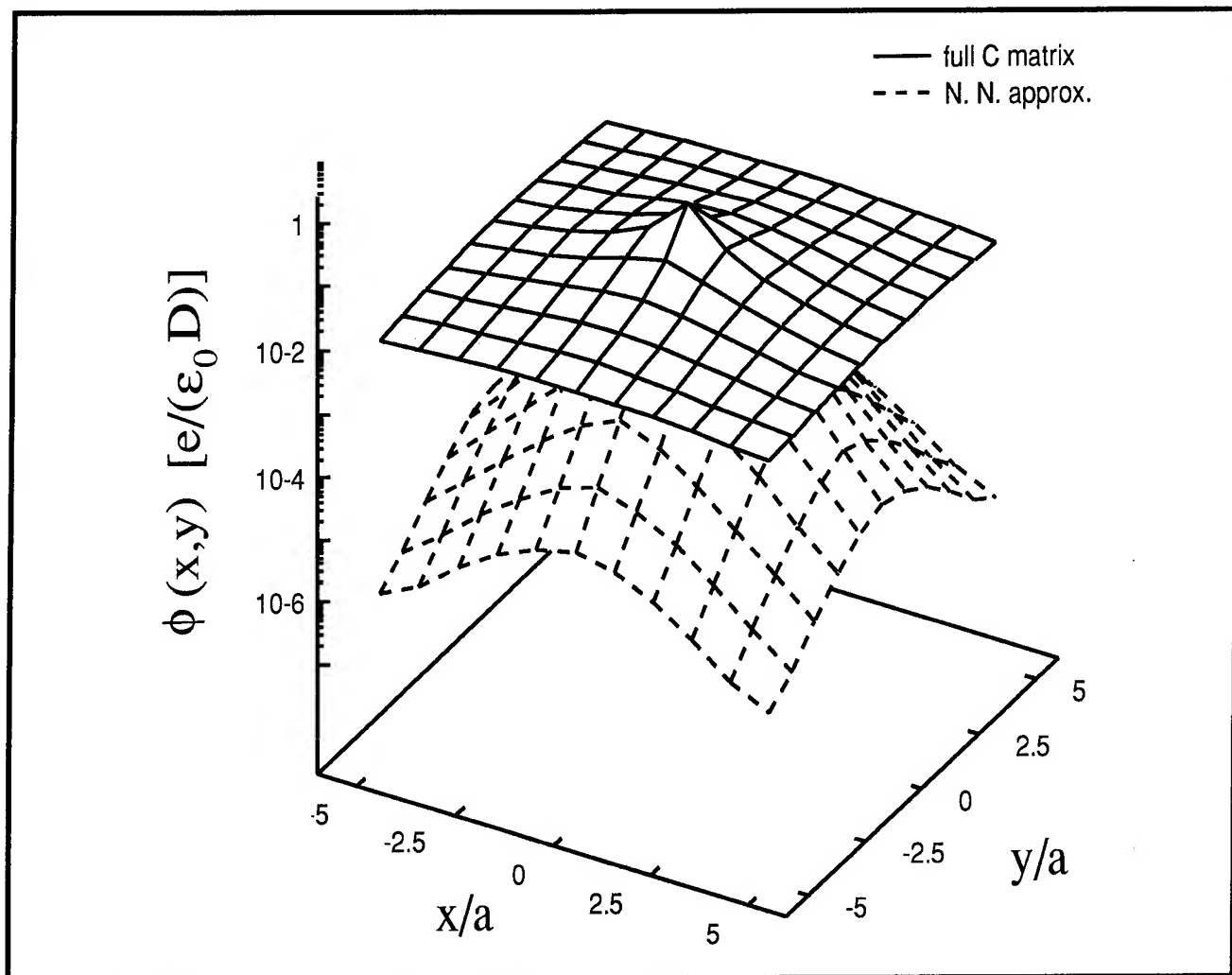
the well known "orthogonality catastrophe." When an electron tunnels from the left lead into the left dot, the right dot is also affected: to achieve the lowest possible energy, one-half of the charge of the added electron must be transferred to the right dot. Thus, the system must significantly modify its ground state in order to accommodate an additional electron. This effect shows up as a power-law suppression of the tunneling rates at low temperatures. In the case of nearly symmetric dots, we found that the conductance peaks are suppressed as power $5/4$ of the temperature. We expect that this result can be easily tested in our experiments.

3.4 Publications

Furusaki, A., and K.A. Matveev. "Coulomb Blockade Oscillations of Conductance in the Regime of Strong Tunneling." *Phys. Rev. Lett.* 75: 709 (1995).

Furusaki, A., and K.A. Matveev. "Theory of Strong Inelastic Cotunneling." *Phys. Rev. B* 52: 16676 (1995).

Matveev, K.A., L.I. Glazman, and H.U. Baranger. "Tunneling Spectroscopy of Quantum Charge Fluctuations in the Coulomb Blockade." *Phys. Rev. B* 53: 1034 (1996).



"Soliton" potential distribution in a 11x11 2D quantum-dot array, computed using the full capacitance matrix (solid line mesh) and the nearest neighbor approximation (dashed line mesh). The soliton is located at the center of the array ($x = y = 0$). (see section 4.6)

Chapter 4. Superconducting and Quantum-Effect Devices

Academic and Research Staff

Professor Terry P. Orlando, Dr. Chagarn B. Whan

Visiting Scientists and Research Affiliates

Dr. Herre S.J. van der Zant

Graduate Students

Martin Burkhardt, David J. Carter, Janet A. Cutro, Amy E. Duwel, Arvind Kumar, Mark R. Schweizer, Ilia Sokolinski, Enrique Trías

Undergraduate Students

Vjekoslav Svilan

Technical and Support Staff

Charmaine A. Cudjoe-Flanders, Angela R. Odoardi

4.1 Nonlinear Dynamics of Discrete Josephson Arrays

Sponsor

National Science Foundation
Grant DMR 94-02020

Project Staff

Dr. Herre S.J. van der Zant, Professor Terry P. Orlando, S. Watanabe, S. Strogatz

We have studied the dynamics of circular one-dimensional arrays of underdamped Josephson junctions connected in parallel. In these Josephson rings, a single vortex can be trapped and studied experimentally without complications caused by reflections off boundaries. We find that a propagating vortex can become phase-locked to linear waves excited in its wake. In the I-V curve, resonant steps are observed indicative of this phase-locking. Numerical simulations indicate that, at least in principle, an infinite number of these steps is possible. Resonant steps also occur in the I-V curves for higher voltages in the return path of the subgap region. These resonant steps have a completely different origin and occur at voltages where the periodic whirling solution undergoes an instability parametrically amplified by the linear modes in the system. Only $N/2$ steps are possible with N the number of junctions in the ring. Despite the presence of linear modes, our numerical studies show that a single propagating vortex can, for a certain range of parameters, be viewed as a particle with a long mean free path. This almost free vortex prop-

agation makes discrete Josephson rings ideal systems for further quantum vortex experiments.

4.2 Resonance Splitting in Inductively Coupled Arrays

Sponsor

National Science Foundation
Fellowship MIP 88-58764
Grant DMR 94-02020

Project Staff

Amy E. Duwel, Enrique Trías, Professor Terry P. Orlando, Dr. Herre S.J. van der Zant, S. Watanabe, S. Strogatz

Coupled arrays of one- and two-dimensional Josephson junctions have received renewed attention as model systems for high-temperature superconducting thin films of BSCCO and TBCCO, showing coupling of the discrete layers. These arrays are also of interest since phase locking between the coupled rows decreases the linewidth of the radiation emitted by oscillators made of these arrays.

We have observed that, in long inductively coupled arrays of niobium Josephson junctions, two Eck steps appear in the current-voltage (I-V) characteristic. These steps correspond to arrays of vortices traveling through the system. The wave is composed of nearly a single harmonic with a well-defined amplitude and dispersion relation. We have found that the lower step corresponds to an anti-

symmetric state where the voltages are oscillating out of phase between the two rows. However, the upper step corresponds to a symmetric state, where the oscillating voltages are in-phase. We have found an analytical ansatz for the voltage states which is close to numerical observations. We can analytically predict the DC voltages of these resonant states and numerically predict the amplitude of the AC voltages.

The upper step can have important technological implications. When the system is biased in this state, the AC voltages add, increasing the power output. The two-row device will also have higher output impedance than its continuous, stacked junction counterpart. These qualities make this device desirable for oscillator applications. As in a single row of a discrete array, the frequencies can be tuned with a control current and are stable for a relatively wide range of bias currents. Although the bandwidth is approximately the same as for the single row, a larger output resistance may increase the linewidth. However, phase locking between the two rows is expected to reduce the linewidth, and such measurements will be helpful.

4.3 Flux Flow and Self Field Effects

Sponsor

National Science Foundation
Fellowship MIP 88-58764
Grant DMR 94-02020

Project Staff

Enrique Trías, Dr. Herre S.J. van der Zant, Professor Terry P. Orlando

Measurements and numerical studies of the self-induced magnetic field effects on flux flow in two-dimensional arrays of niobium Josephson junctions have been performed. It was found that the flux-flow resistance becomes larger as the penetration depth of the array decreases. A phenomenological model, which agrees qualitatively with the experiments and simulations, has been developed to explain the self-field effects on flux flow. The main conclusion is that both the mass of the vortex and the array viscosity decrease due to the smaller spatial extent of the vortex current caused by the self-fields.

Vortices in the flux-flow region are localized and, because of the electrical energy in the junctions,

can be treated as massive particles. The applied field specifies the density of vortices present in the array. With this density, the driving force, and the viscosity, we model the dependence of the flux-flow resistance in terms of the array parameters, λ_{\perp} and β_c and applied magnetic field, f . A linear dependence of the flux-flow resistance R_{ff} versus f is found.

It has also been shown that R_{ff} is dependent on both λ_{\perp} and β_c . The dependence on β_c follows from spin-wave damping while the λ_{\perp} dependence is a result of a reduction of the viscosity caused by the decreasing physical size of traveling vortices as λ_{\perp} decreases. This simple phenomenological model gives a qualitative as well as a semi-quantitative description of the dynamics. The effects can also be seen in numerical simulations that take into account all the mutual inductances between cell pairs.

However, the flux-flow region appears to be richer in its dynamics than the presented model can account for. For small arrays, there is a spatial dependence of the flux-flow region which we have measured and also seen in simulations. Different rows have different flux-flow slopes and the outer rows closest to the edge appear to have almost no flux-flow associated with them. Though these deviations do not diminish the useful and intuitive results from the phenomenological model, they do point to further research on flux flow.

4.4 Triangular Arrays of Josephson Junctions

Sponsors

U.S. Air Force - Office of Scientific Research
Grant F30602-96-1-0059
Rome Laboratory

Project Staff

Amy E. Duwel, Professor Terry P. Orlando, S. Yukon¹

Superconducting arrays of Josephson junctions are important devices for coherent sources of low-power radiation in millimeter and sub-millimeter regime. One- and two-dimensional arrays of Josephson junctions are of particular importance because the phase-locking among the junctions overcomes many of the problems of low impedances and power levels of a single junction.

¹ U.S. Air Force, Rome Laboratory, Rome, New York.

Coherent microwave radiation has been observed in square arrays of Josephson junctions.

In novel geometries based on triangular rather than square arrays, numerical simulations and calculations show a novel and technologically important dynamical state. This state has junctions which generate microwave current and radiation without "going over the top" and producing a DC power loss.

We are developing techniques for designing triangular arrays of Josephson junctions within standard superconducting foundry capabilities. These arrays are predicted to generate AC current without a DC component, and we will explore the feasibility of making microwave measurements on these and other types of Josephson arrays.

4.5 One-dimensional Parallel Josephson-junction Arrays as a Tool For Diagnostics

Sponsor

Defense Advanced Research Projects Agency/
Consortium for Superconducting Electronics
Contract MDA 972-90-C-0021

Project Staff

Dr. Herre S.J. van der Zant, Professor Terry P. Orlando, in collaboration with A. W. Kleinsasser²

We propose and demonstrate the use of underdamped, one-dimensional parallel arrays of Josephson junctions as a tool for circuit diagnostics. By measuring the Fiske modes and the critical current in a magnetic field, we determined the self and nearest-neighbor inductances as well as the capacitances of single junctions. We have used this technique to find the capacitance of Nb-Al₂O_x-Nb junctions for critical current densities of 0.3 - 20 kA/cm². We find that the specific capacitance increases by about a factor of two over this range. This increase has important consequences for the design of single-flux-quantum circuits and SQUIDs. Measurement of the junction capacitance for critical current densities of 100 kA/cm² is possible, but requires submicrometer junctions with dimensions of the order of 0.3 μ m.

4.6 Quantum Device Simulations

Sponsor

National Science Foundation
Grant DMR 94-02020

Project Staff

Dr. Chagarn B. Whan, Professor Jacob K. White, Professor Terry P. Orlando

We numerically calculated the full capacitance matrices for both one-dimensional (1-D) and two-dimensional (2-D) quantum-dot arrays. We find that it is necessary to use the full capacitance matrix in modeling coupled quantum dots due to weaker screening in these systems in comparison with arrays of normal metal tunnel junctions. The static soliton (a fundamental electronic charge in the entire array) potential distributions in both 1-D and 2-D arrays are well approximated by the unscreened (1/r) coulomb potential, instead of the exponential fall-off expected from the often used nearest-neighbor approximation. In terms of dynamics, we compare the current-voltage (I-V) characteristics of voltage biased 1-D arrays using either the full capacitance matrix or its nearest-neighbor approximation. The I-V curves show clear differences and the differences become more pronounced when larger arrays are considered.

For quantum dot arrays made by electrostatic confinement of two-dimensional electron gas (2DEG) in GaAs/AlGaAs heterostructures, the array forms a co-planar structure with all dots residing in the 2DEG plane. The co-planar capacitors are far less effective than the parallel plates in terms of confining electric field. Therefore, in comparison with tunnel junction arrays, the field lines originating from one of the quantum dots are much less confined and can reach out to dots that are much further apart. A model that considers only the nearest-neighbor capacitive coupling is unlikely to be accurate in this situation. We now give a more quantitative analysis of this problem.

In our model, the quantum dots (small puddles of a 2DEG) are treated as thin circular shaped conducting plates, with diameter $D = 1 \mu$ m. The plates are arranged to form either 1-D or 2-D arrays with lattice constant $a = D + d = 1.1 \mu$ m, where $d = 0.1 \mu$ m is the closest separation between adjacent dots (or the tunnel barrier width). We believe these values are reasonable for arrays in the classical charging regime with weak inter-dot tunneling (i.e.,

² Jet Propulsion Laboratory, California Institute of Technology, Pasadena, California.

the tunneling resistance, $R_T \gg R_Q = h/e^2$). Once the array geometry is specified, we compute the full capacitance matrix C of the 1-D and 2-D arrays using FASTCAP, an efficient capacitance extraction tool.

We have calculated the potential distribution due to a soliton being located at the center of a 21×1 series array, using both the full capacitance matrix and its nearest neighbor approximation. The nearest neighbor approximation gives an exponentially decaying soliton potential as expected. However, the soliton potential distribution that result from the full capacitance matrix decays much slower. We find that the soliton potential follows the simple $1/r$ law almost exactly over the entire array, except at the origin where the Coulomb potential is singular.

We have also computed current-voltage (I-V) characteristics of 1-D quantum dot arrays, which is experimentally more relevant. The I-V curves are calculated with both the full capacitance matrix and the nearest-neighbor approximation. The resulting I-V curves show many differences. The threshold voltages are not exactly the same, and the fine structures are different and become more pronounced when we consider larger arrays. At high voltage, the two curves merge and become nearly linear. Hence, we see that the full capacitance matrix is necessary in the dynamical simulation of these arrays.

4.7 Publications

Burkhardt, M., H.I. Smith, D.A. Antoniadis, T.P. Orlando, M.R. Melloch, K.W. Rhee, and M.C. Peckerar. "Fabrication Using X-ray Nanolithography and Measurement of Coulomb Blockade in a Variable-Sized Quantum Dot." *J. Vac. Sci. Technol. B* 12: 3611-3613 (1994).

Burkhardt, M., D.J.D. Carter, D.A. Antoniadis, T.P. Orlando, H.I. Smith, M. Melloch, K.W. Rhee, and M.C. Peckerar. "Measurement of a Double Quantum Dot." Submitted to *J. Appl. Phys.*

Delin, K.A. and T.P. Orlando. "Superconductivity." In *The Engineering Handbook*. Ed. R.C. Dorf. Boca Raton, Florida: CRC Press, 1996.

Duwel, A.E., E. Trías, T.P. Orlando, H.S.J. van der Zant, S. Watanabe and S. Strogatz. "Resonance Splitting in Discrete Planar Arrays of Josephson Junctions." Submitted to *J. Appl. Phys.*

Orlando, T.P., H.S.J. van der Zant, J. White, E. Trías, and A. E. Duwel. "Measurements of Self-

Field Effects in Arrays of Josephson Junctions." In *Macroscopic Quantum Phenomena and Coherence in Superconducting Arrays*. Eds. C. Giovannella and M. Tinkham. World Scientific, 1995.

Smith, H.I., M.L. Schattenburg, S.D. Hector, J. Ferrera, E.E. Moon, I.Y. Yang, and M. Burkhardt. "X-ray Nanolithography: Extension to the Limits of the Lithographic Process." *Nanotechnology* (Special Issue of *Microelectronic Engineering*). Forthcoming.

Trías, E., T.P. Orlando, and H.S.J. van der Zant. "Flux Flow in Two-dimensional Arrays of Nb Josephson Junctions." Submitted to *Phys. Rev. B*.

Trías, E., J.R. Phillips, H.S.J. van der Zant, and T.P. Orlando. "Self-field Effects in Two Dimensional Nb Josephson-junction Arrays." *IEEE Trans. Appl. Superconduct.* 5: 2707 (1995).

van der Zant, H.S.J., T.P. Orlando, and A.W. Kleinsasser. "One-dimensional Parallel Josephson-junction Arrays as a Tool for Circuit Diagnostics." *IEEE Trans. Appl. Superconduct.* 5: 3333-3336 (1995).

van der Zant, H.S.J., T.P. Orlando, S. Watanabe and S.H. Strogatz. "Kink Propagation in a Highly Discrete System: Observation of Phase Locking to Linear Waves." *Phys. Rev. Lett.* 74: 174-177 (1995).

van der Zant, H.S.J., T.P. Orlando, S. Watanabe, and S.H. Strogatz. "Nonlinear Dynamics of Discrete Josephson Rings." In *Macroscopic Quantum Phenomena and Coherence in Superconducting Arrays*. Eds. C. Giovannella and M. Tinkham. World Scientific, 1995.

Watanabe, S., H.S.J. van der Zant, S. Strogatz, and T.P. Orlando. "Dynamics of Circular Arrays of Josephson Junctions and the Discrete Sine-Gordon Equation." Submitted to *Phys. Rev. D*.

Watanabe, S., S. H. Strogatz, H.S.J. van der Zant, and T. P. Orlando. "Resonant Steps in Parallel Josephson-junction Arrays: Parametric Instabilities of Whirling Modes." *IEEE Trans. Appl. Superconduct.* 5: 2698-2701 (1995).

Watanabe, S., S.H. Strogatz, H.S.J. van der Zant, and T.P. Orlando. "Whirling Modes and Parametric Instabilities in the Discrete Sine-Gordon Equation: Experimental Tests in Josephson Rings." *Phys. Rev. Lett.* 74: 379-382 (1995).

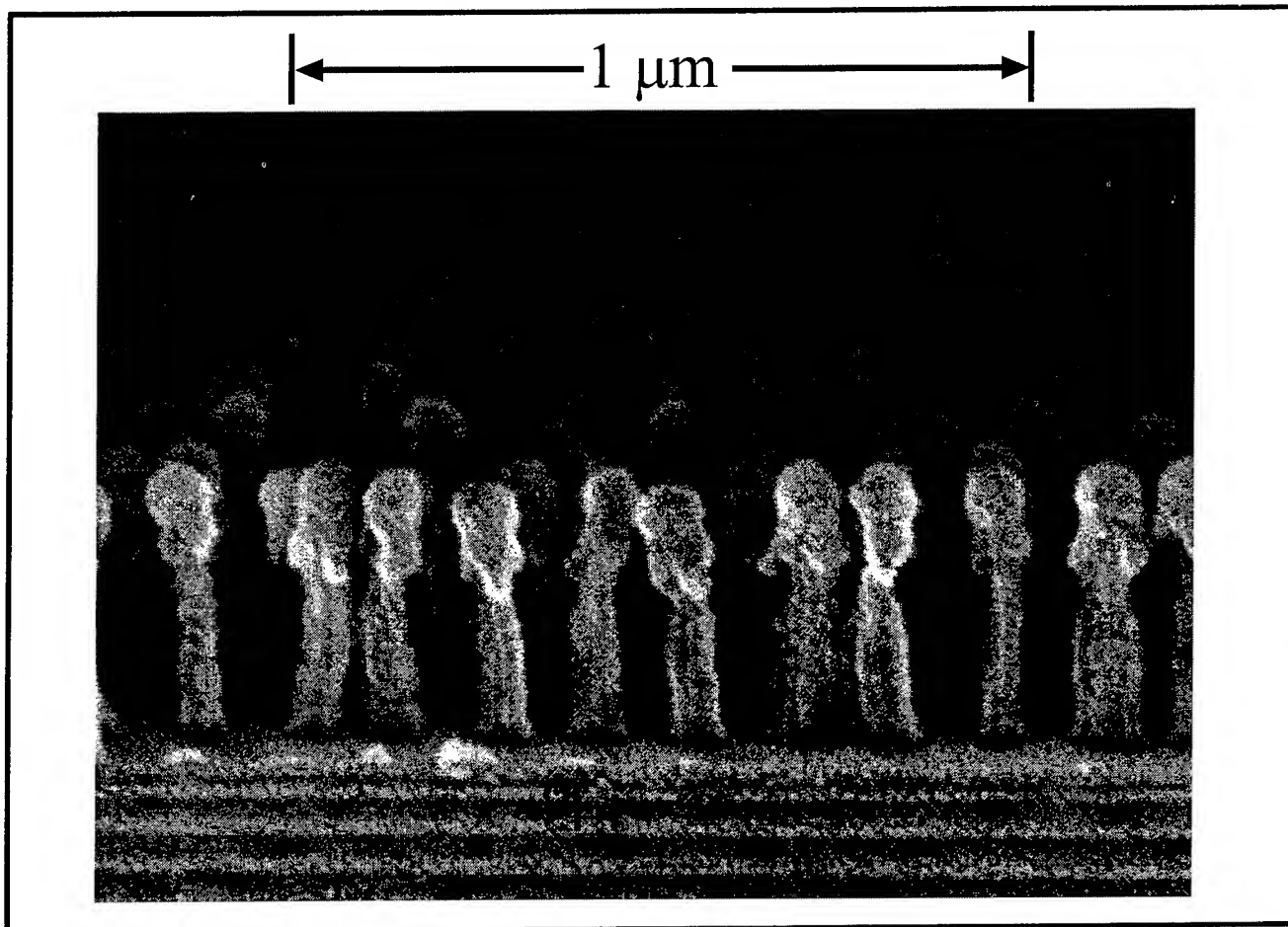
Whan, C.B., J. White, and T.P. Orlando. "Full Capacitance Matrix of Coupled Quantum Dot Arrays: Static and Dynamical Effects." Submitted to *Appl. Phys. Lett.*

Trías, E. *Inductance Effects in Two-Dimensional Arrays of Josephson Junctions*. S.M. thesis, Dept. of Electr. Eng. and Comput. Sci., MIT, 1995.

Theses

Burkhardt, M. *Fabrication Technology and Measurement of Coupled Quantum Dot Devices*. Ph.D. diss., Dept. of Electr. Eng. and Comput. Sci., MIT, 1995.

Duwel, A.E. *Underdamped Vortex Flow Devices*. S.M. thesis, Dept. of Electr. Eng. and Comput. Sci., MIT, 1995.



At the debutante's ball, young nano-women gather in their finery at the edge of the stage to weep because the nano-boys won't dance with them.

An array of 50-nm-wide posts with a periodicity of 100 nm. The posts consist of PMMA on top of an antireflection coating (ARC). The substrate consists of a 250-nm-thick layer of silicon nitride on silicon. The PMMA was exposed using achromatic interferometric lithography. After development of the PMMA, an O₂ reactive ion etch was used to etch through the ARC. SEM viewing caused some melting and charging which resulted in the large gathering of nanopeople. The melting problem was solved by imaging at low voltage.

Timothy A. Savas, a graduate student in RLE's Quantum-Effects Devices Group, submitted this micrograph, which won in the most bizarre category at the Electron Ion Photon Beam Technology and Nanofabrication Conference, Scottsdale, Arizona, in June 1995.

Chapter 5. Nanostructures Technology, Research and Applications

Academic and Research Staff

Professor Henry I. Smith, Dr. Mark L. Schattenburg, Dr. Anne Pepin, Richard J. Aucoin, James M. Carter, Robert C. Fleming, Euclid E. Moon, Scott E. Silverman

Visiting Scientists and Research Affiliates

Patrick N. Everett

Graduate Students

David Berman, Martin Burkhardt, David J. Carter, Jay N. Damask, Juan Ferrera, James S. Foresi, Andrea E. Franke, Marc Hill, Keith M. Jackson, Michael H. Lim, Mitchell W. Meinhold, Thomas E. Murphy, Timothy A. Savas, Satyen Shah, Ilia Sokolinski, Vincent V. Wong, Isabel Y. Yang, Anto Yasaka

Technical and Support Staff

Mark K. Mondol, Edward Murphy, Jeanne M. Porter, Margaret A. Flaherty, Lisa Zeidenberg

5.1 Nanostructures Laboratory

The Nanostructures Laboratory (NSL) at MIT develops techniques for fabricating surface structures with feature sizes in the range from nanometers to micrometers and uses these structures in a variety of research projects. The NSL includes facilities for lithography (photo, interferometric, electron beam, ion beam, and x-ray), etching (chemical, plasma and reactive-ion), liftoff, electroplating, sputter deposition and e-beam evaporation. Much of the equipment, and nearly all of the methods, utilized in the NSL are developed in house. Generally, commercial processing equipment designed for the semiconductor industry cannot achieve the resolution needed for nanofabrication, is inordinately expensive, and lacks the required flexibility.

The research projects within the NSL fall into three major categories: (1) development of submicron and nanometer fabrication technology; (2) short-channel semiconductor devices, quantum-effect electronics, and optoelectronics; (3) periodic structures for x-ray optics, spectroscopy, atomic interferometry, and nanometer metrology.

5.2 Scanning Electron Beam Lithography

Sponsors

Joint Services Electronics Program
Grant DAAH04-95-1-0038

Semiconductor Research Corporation
Contract 95-LJ-550

Project Staff

Scott E. Silverman, Juan Ferrera, Professor Henry I. Smith

Figure 1 is a photograph of the scanning-electron-beam lithography (SEBL) system (VS-PL) located in Room 38-185. This instrument was obtained as a donation from IBM Corporation in November 1993. It is an experimental system based on many years of IBM technology development in SEBL. In 1994, a digital pattern generator was implemented, based on a commercial high performance array processor, which utilizes dual RISC processors. In 1995, the capabilities of the pattern generator hardware were augmented. New shape primitives were incorporated into its software. Also, it is now possible to expose large mask designs composed of many stitched fields. Complementary to the pattern generator development was the implementation of conversion software, which allows a CAD data file to be fractured and translated prior to exposure by the electron-beam tool.

The VS-PL system is the cornerstone of a facility for high performance electron-beam lithography. The goals of the facility are to provide the MIT research community with an in-house SEBL capability for writing directly on experimental device substrates; to advance the state-of-the-art in SEBL, particularly with regard to pattern placement accuracy and long-range spatial-phase coherence; and

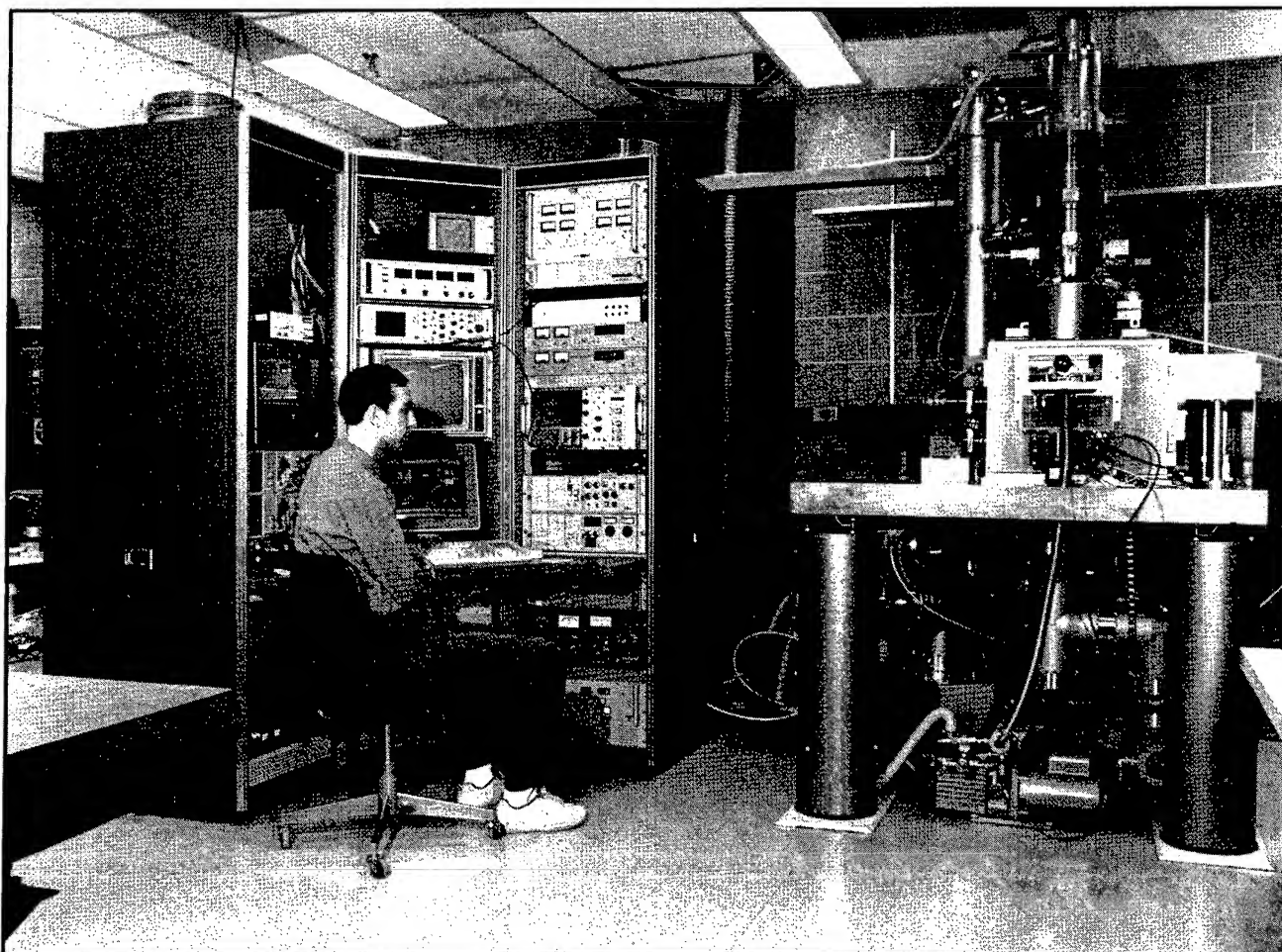


Figure 1. Photograph of the VS-PL scanning-electron-beam lithography system. The operator is Scott Silverman.

to pattern x-ray nanolithography masks for in-house use.

Figure 2 shows a region of an x-ray mask, patterned by the VS-PL tool with the gate level for deep-submicron silicon-on-insulator devices. This mask was then used in a mix-and-match scheme to fabricate the actual devices. Other projects include direct-write experiments on GaAs substrates oriented towards the fabrication of Coulomb-blockade devices; fabrication of photonic-bandgap resonator structures; and studies of MBE overgrowth of InP on patterned substrates for DFB lasers and optical filters.

5.3 Spatial-Phase-Locked Electron-Beam Lithography

Sponsors

Joint Services Electronics Program
Grant DAAH04-95-1-0038

National Science Foundation
Grant ECS 94-07078
Semiconductor Research Corporation
Contract 95-LJ-550
U.S. Army Research Office
Grant DAAH04-95-1-0564

Project Staff

James M. Carter, Juan Ferrera, Scott E. Silverman,
Professor Henry I. Smith

It is well known that scanning-electron-beam lithography can write extremely fine lines, ~ 10 nm in thin PMMA and ~ 1 nm in AlF_3 . However, because writing fields in electron-beam lithography are quite small ($\sim 10^4$ beam steps), large-area patterns must be created by stitching together the small fields, using a laser interferometer to provide X-Y positioning information. However, it is often overlooked that, due to instability, drift and a variety of other problems, the precision with which this can be done is much poorer than the resolution. Typically, stitching errors of 30 to 100 nm are observed at field boundaries.

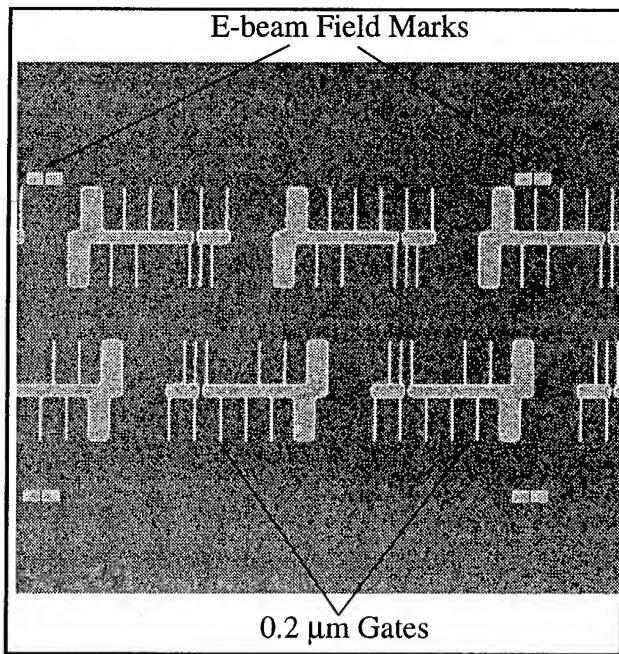


Figure 2. Scanning electron micrograph of a portion of an x-ray mask patterned with the VS-PL e-beam system, showing the gate level for deep-submicron silicon-on-insulator devices.

To solve this problem, we are developing a technology we call spatial-phase-locked electron-beam lithography (SPLEBL), which will provide pattern placement accuracy and precision finer than the resolution. The basic idea behind SPLEBL is to create on the substrate a fiducial grid and conduct all e-beam lithography with reference to it. The fiducial grid is produced by interferometric lithography (IL) to ensure long-range spatial-phase coherence.

We are investigating two modes of implementation: the global fiducial grid and the segmented grid. In the latter approach, the grid is transferred onto the substrate only in small regions ($2 \times 2 \mu\text{m}$ square) at the corners of each e-beam scan field. Spatial-frequency-domain techniques are used to achieve sub-pixel alignment and scaling. In the latter approach the fiducial grid is transparent to the exposing e-beam and covers the entire top of the resist film. By collecting the emitted secondary electrons, a computer will keep track of the e-beam position at all times and correct for any drift or spurious displacement.

SPLEBL was used to pattern x-ray masks with gratings for the fabrication of integrated optical filters, in collaboration with IBM's T.J. Watson Research Center. Gratings with multiple quarter-wave phase shifts and duty cycle variations are needed to fabricate filters whose performance exceeds that of single quarter-wave-shifted

resonators. For these applications, the flexibility of e-beam patterning is essential, while spatial-phase locking eliminates the pattern placement errors, which would have a significant deleterious impact in the performance of the devices.

The suitability of fiducials produced by interferometric lithography for pattern placement with nanometer precision is being investigated. The grid must be characterized with precision equal or better than the pattern placement desired. We are developing techniques to measure the fidelity of gratings and grids fabricated by interferometric lithography. Figure 3 shows a schematic of the system used to fabricate fiducials. Two spherical waves, which emanate from the spatial filters, are overlapped at the substrate plane to produce a grating image in resist. This grating has a nonlinear phase progression, i.e., a "chirp". The phase deviation from linearity can be calculated from the geometrical parameters of the interferometric system. To confirm the validity of this model, we use a self-reference technique: a substrate is exposed in the IL system and displaced by a known distance; it is then exposed again. Thus, two identical grating images have been exposed, which are shifted with respect to each other. The nonlinearities in the phase progression of the gratings cause them to beat in and out of phase. Upon development, a moiré pattern appears on the surface of the sample, which is, in effect, a map of the difference in phase between the two gratings (see figure 4). The moiré qualitatively matches a theoretical phase map, indicating that no distortion larger than a fraction of the grating period (200 nm) is present. Work is under way to extend this technique to enable the quantitative measurement of phase distortions.

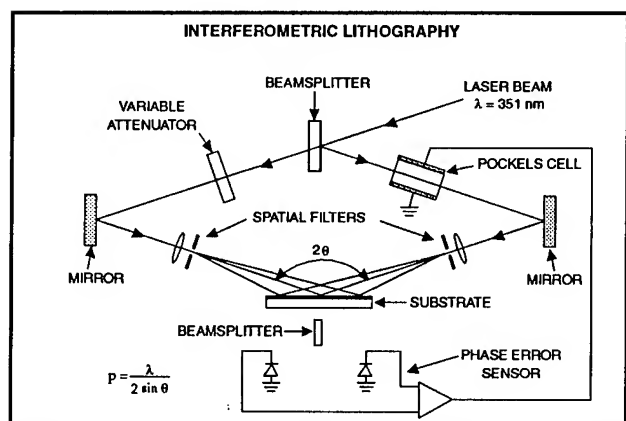


Figure 3. Schematic of the Interferometric Lithography (IL) system used to fabricate fiducial gratings and grids for spatial-phase locking. Mutually coherent spherical waves emanate from the spatial filters and are combined at the substrate to form a grating in resist. A grid is made of two gratings exposed at right angles to one another.

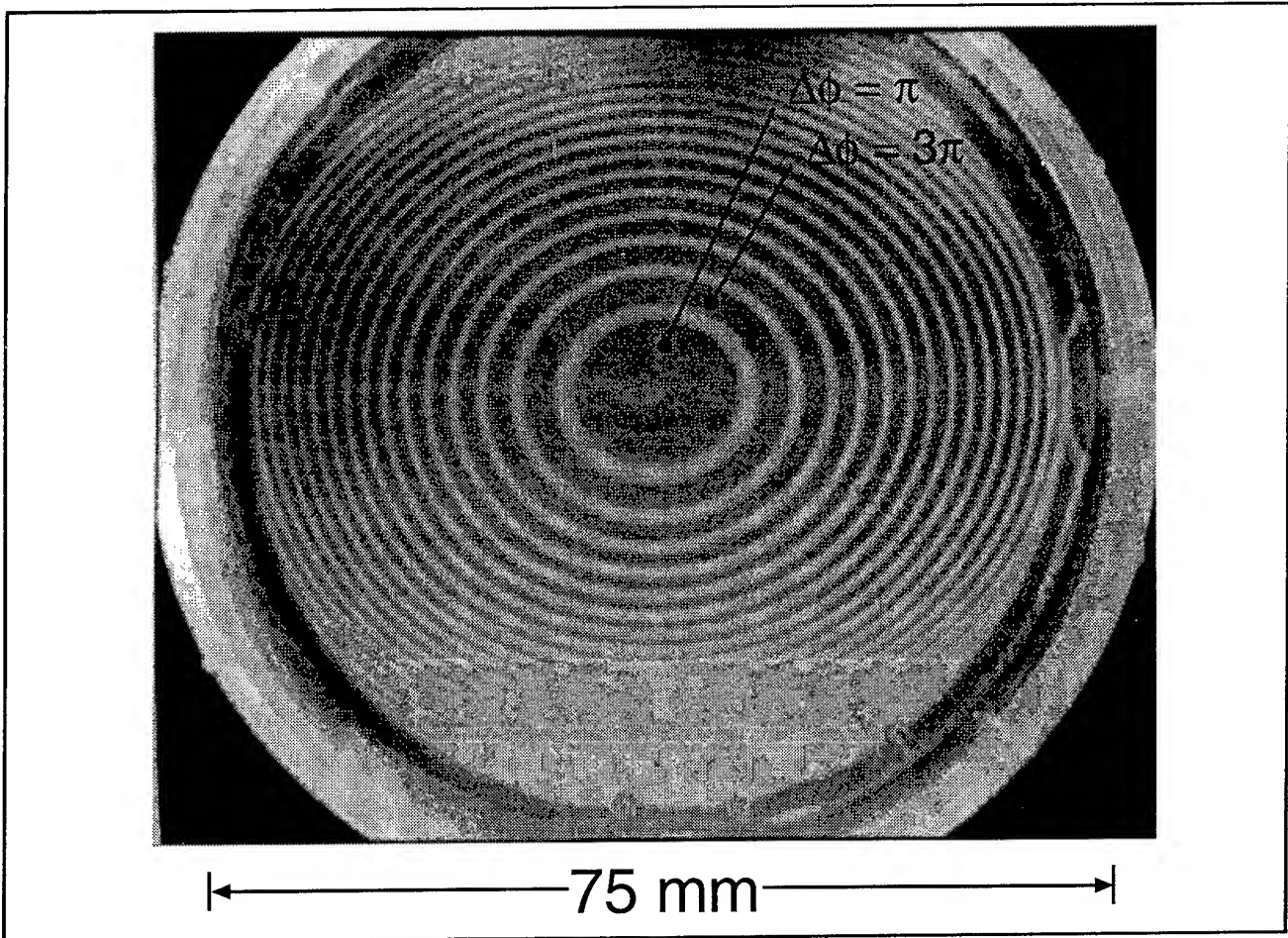


Figure 4. Photograph of a moiré pattern on a wafer, obtained by exposing two 200 nm-period gratings, with the substrate shifted laterally in between the two exposures. The moiré fringes denote the phase difference between the two exposures.

5.4 X-Ray Nanolithography

Sponsors

Defense Advanced Research Projects Agency/
Naval Air Systems Command
Contract N00019-95-K-0131
Joint Services Electronics Program
Grant DAAH04-95-1-0038

Project Staff

James M. Carter, Michael H. Lim, Euclid E. Moon,
Vincent V. Wong, Isabel Yang, Professor Henry I.
Smith

For several years, we have been developing the tools and methods of x-ray nanolithography (i.e., sub-100 nm features). We have explored the theoretical and practical limitations, and endeavored to make its various components (e.g., mask making, resists, electroplating, sources, alignment, etc.) reliable and "user friendly". Because of the critical

importance of the x-ray mask technology we discuss this separately in section 5.5.

Our sources for x-ray nanolithography are simple, low-cost electron-bombardment targets, typically Cu_L ($\lambda = 1.32$ nm), separated by a $1.4 \mu\text{m}$ -thick SiN_x vacuum windows from a helium-filled exposure chambers. In the future, we hope to replace the Cu_L sources with higher flux sources.

For most applications that require multiple mask alignment, we currently use a simple microscope-based system which provides about $0.3 \mu\text{m}$ superposition precision. We are also developing a high-precision mask alignment system (see section 5.6) that should provide overlay approaching 1 nm.

In earlier research, we showed that for x-ray wavelengths longer than ~ 0.8 nm, the range of the photoelectron emitted when an x-ray photon is absorbed in resist does not limit the resolution. Down to feature sizes ~ 20 nm, diffraction is the major concern. By means of accurate electromagnetic calculations, taking into account the vectorial

character of the electromagnetic field and the dielectric properties of the absorber, we have shown that when source spatial coherence is optimized, diffraction does not limit resolution as severely as had been predicted by simple Fresnel diffraction calculations. Figure 5 plots the maximum mask-to-sample gap, G , versus minimum feature size, W , for two values of the parameter α which connects gap and feature size: $G = \alpha W^2/\lambda$. Modeling and experiment verify that α can be between 1 and 1.5 while retaining good process latitude.

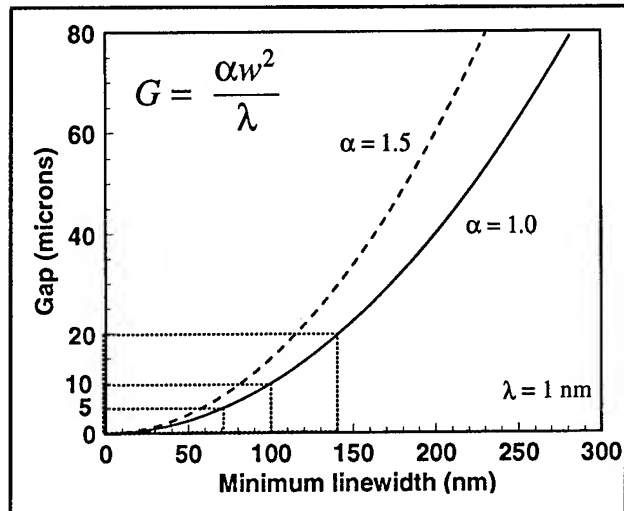


Figure 5. Plot of maximum mask-sample gap, G , versus minimum feature size, W , for two values of the parameter α .

For gaps below $10\ \mu\text{m}$, the mask and substrate must be optically flat (see section 5.5) and dust particles must be detected and eliminated. To accomplish this, a jet of frozen CO_2 micropellets impinging on the substrate or mask at a low angle can be used. The pellets knock off adhering dust particles while leaving no residue, and the CO_2 gas also tends to remove thin layers of organic contamination.

For the linewidth range from 70 to 20 nm, mask-substrate gaps must be below $5\ \mu\text{m}$. This is not a problem in a research setting. With wafer type substrates, we use small studs on the perimeter of the mask to achieve the required gap. On substrates that are smaller than the mask area (e.g., fragments of high-mobility, modulation-doped GaAs substrates), we use a specially designed apparatus that brings the mask membrane to zero gap without damaging either mask or substrate. In manufacturing, however, studs on the mask and mask contact are not acceptable, and for this reason we are investigating the feasibility of using arrays of

Fresnel zone plates for projection imaging with x rays of either 4.5 nm or about 1.0 nm wavelength.

5.5 Improved Mask Technology for X-Ray Lithography

Sponsors

Defense Advanced Research Projects Agency/
U.S. Navy - Naval Air Systems Command
Contract N00019-95-K-0131
Joint Services Electronics Program
Grant DAAH04-95-1-0038

Project Staff

Martin Burkhardt, James M. Carter, Andrea E. Franke, Michael H. Lim, Mark K. Mondol, Edward Murphy, Vincent V. Wong, Isabel Y. Yang, Professor Henry I. Smith

At feature sizes of 100 nm and below, the mask-to-sample gap, G , must be less than $\sim 10\ \mu\text{m}$ (see figure 5). We have developed a mask configuration compatible with this requirement in which the mask membrane is flat to $\sim 100\ \text{nm}$, as shown in figure 6. A novel, low-gradient furnace was developed to achieve such high levels of mask flatness.

Our mask technology is based on low-stress, Si-rich silicon nitride, SiN_x . This material is produced in the Integrated Circuit Laboratory at MIT in a vertical LPCVD reactor. The resulting films are clean and uniform, and x-ray mask membranes made from them are extremely robust. They can be cleaned and processed in conventional stations. Radiation hardness remains a problem at dose levels corresponding to production (i.e., millions of exposures). For research purposes, however, the material is fully acceptable.

For absorber patterns we use both gold, Au, and tungsten, W. The gold is electroplated onto the membrane after resist exposure and development using a specially designed apparatus. The stress of the gold, which affects the in-plane distortion, is controlled via the plating conditions. We generally try to achieve a stress below $10^7\ \text{Mpa}$. The W is sputter deposited and patterned by reactive-ion etching. In order to ensure uniform W stress over an entire membrane, a He-backside temperature-homogenization apparatus is used. This produces stress that is uniform to within about 5 Mpa over most of the membrane, but higher near the edges. The edge deviation is attributed to inadequate heat flow control. We are currently investigating schemes to fully homogenize the stress over the entire membrane.

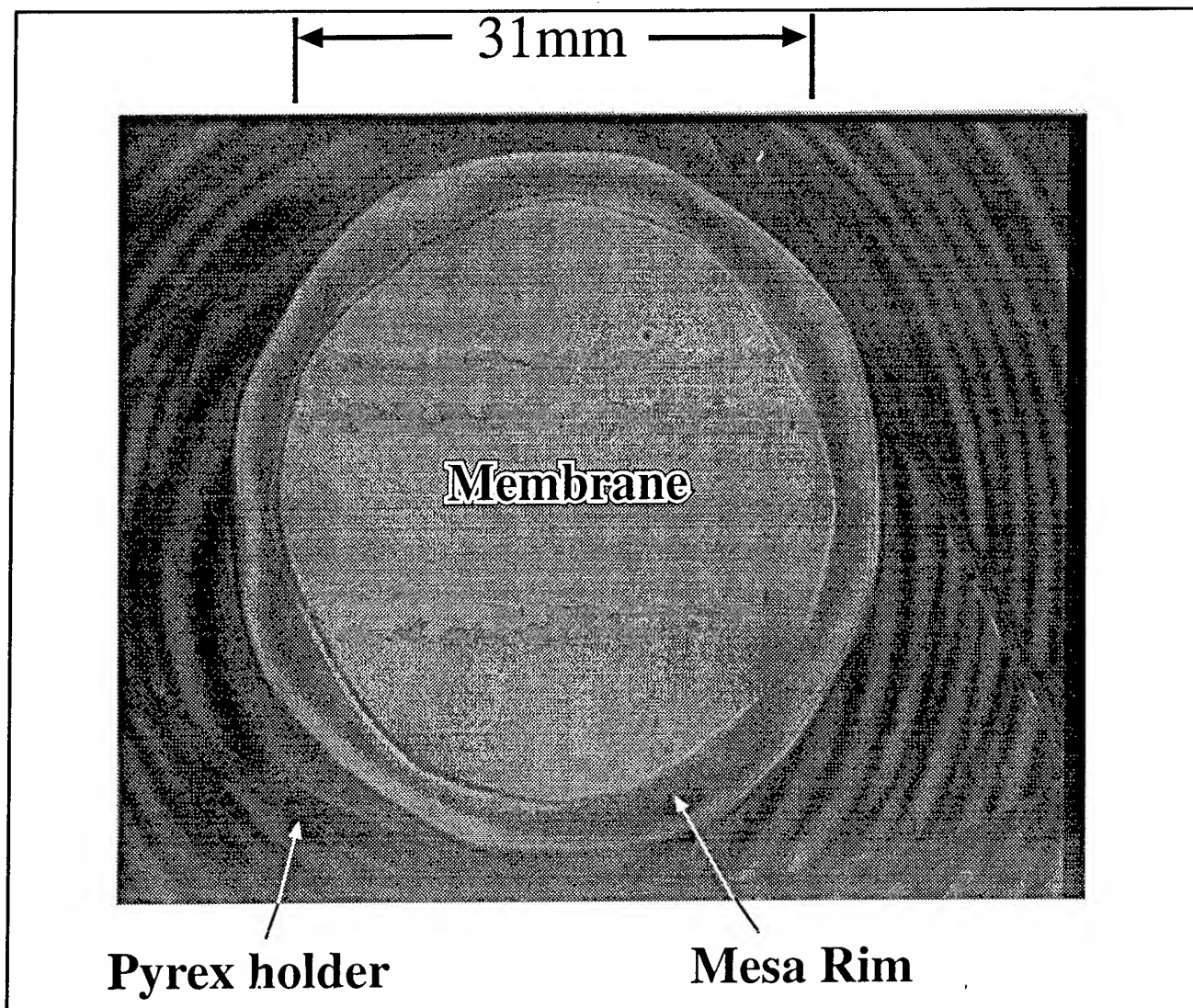


Figure 6. Fizeau interferogram of the top surface of an x-ray mask fabricated with the low gradient oven. There are no fringes visible over the membrane area indicating a flatness ~ 100 nm. The mesa rim deviates from perfect flatness by ~ 300 nm. The area outside the mesa rim is a pyrex frame, whose deviation from flatness is of no significance.

We are investigating a scheme for edge reinforcement, illustrated in figure 7. The overhang of B-doped Si, several micrometers thick, provides a transition between the rigid Si mesa rim, and the thin membrane. Along the edge of the Si mesa rim there are often sharp asperities due to the etching process. These sharp, rigid points increase the probability of accidental membrane breakage. The overhang should prevent this, making the masks more suitable for a production environment.

For periodic structures, patterning of x-ray masks is done by interferometric lithography (IL) but for patterns of arbitrary geometry, it is done by e-beam lithography, either in the MIT e-beam facility or in collaboration with NRL or IBM. We use CAD tools at MIT and convert the data into formats compatible with the e-beam exposure systems. Data is

shipped to NRL or IBM over the internet. After e-beam exposure, masks are shipped back to MIT by express mail where development and Au electroplating are carried out. This collaboration has already demonstrated that patterning x-ray masks by e-beam can be done remotely.

The recently acquired Digital Instruments STM/AFM was found it to be highly effective in inspecting x-ray masks, providing information on defects not apparent by other means. This is illustrated in figure 8.

For etching W absorber patterns on x-ray masks, a reactive-ion-etching process is required, which puts considerable power into the membrane substrate. Since membranes have very low thermal mass and conductivity, we use He-backside cooling in a reac-

tive ion etcher. Membranes can be cooled to below -20 C. At such low temperatures the isotropic etching component is suppressed leading to highly directional etching.

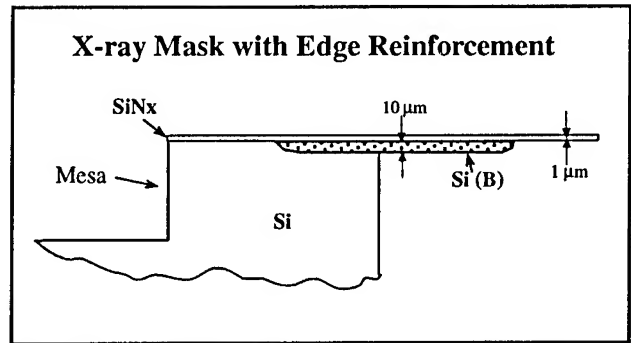


Figure 7. Schematic cross section of the edge reinforcement scheme being investigated to improve the robustness of x-ray masks. The overhang of B-doped Si, several micrometers thick, provides a transition between the rigid mesa rim and the 1-μm-thick membrane.

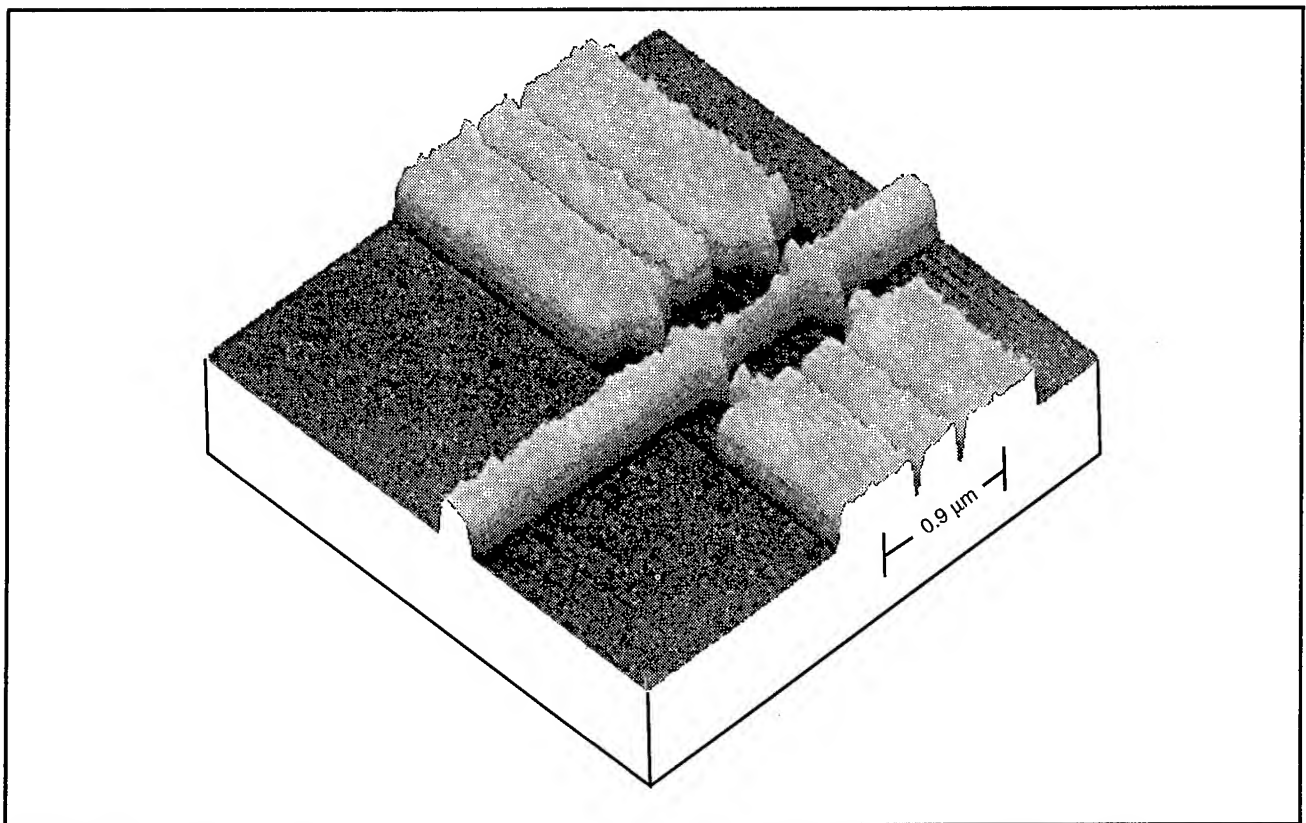


Figure 8. Inspection of an x-ray mask using the newly acquired Digital Instruments atomic-force microscope (AFM). This micrograph revealed that the plated gold in this pattern of a quantum-effect device was only 100 nm instead of the required 200 nm. This thickness deficiency was not apparent by SEM analysis.

5.6 A High-Precision Mask Alignment and Gapping System with Immunity to Overlayers

Sponsors

Defense Advanced Research Projects Agency/
Naval Air Systems Command
Contract N00019-95-K-0131
Joint Services Electronics Program
Grant DAAH04-95-1-0038

Project Staff

Patrick N. Everett, Euclid E. Moon, Professor Henry I. Smith

A novel x-ray lithographic alignment scheme termed interferometric broad-band imaging (IBBI) has been implemented and tested with a variety of wafer overlayers, such as resist, aluminum, and polysilicon. IBBI alignment employs grating and grid type alignment marks on mask and substrate, respectively, which are viewed through the mask from outside the x-ray beam at a Littrow angle with $f/10$

optics and a 110 mm working distance. Each mark consists of two gratings. When aligned, a grating period p_1 on mask is exactly above a grating period p_2 on wafer, with adjacent pair of gratings vice-versa. Gratings on wafer are "hatched" to enable Littrow diffraction in a plane parallel to the grating lines. This allows the optics to be offset in that plane to not obstruct the x-rays. Diffraction perpendicular to the grating-lines results in moiré fringes in the image plane. Using a CCD camera, misalignment is measured from two identical sets of moiré fringes (~ 50 mm period) that move in opposite directions as the mask is moved relative to the substrate. Alignment corresponds to matching the spatial phases of the two sets of fringes.

To demonstrate the insensitivity to overlayers, an alignment mark was partially covered with an overlayer. The resulting moiré pattern is shown in figure 9. Alignment was measured in each half of the image (i.e., with and without the overlayer) and the difference plotted in figure 10. With each of these overlayers, the mean alignment error between the regions is shown to be 0.2 nm or less.

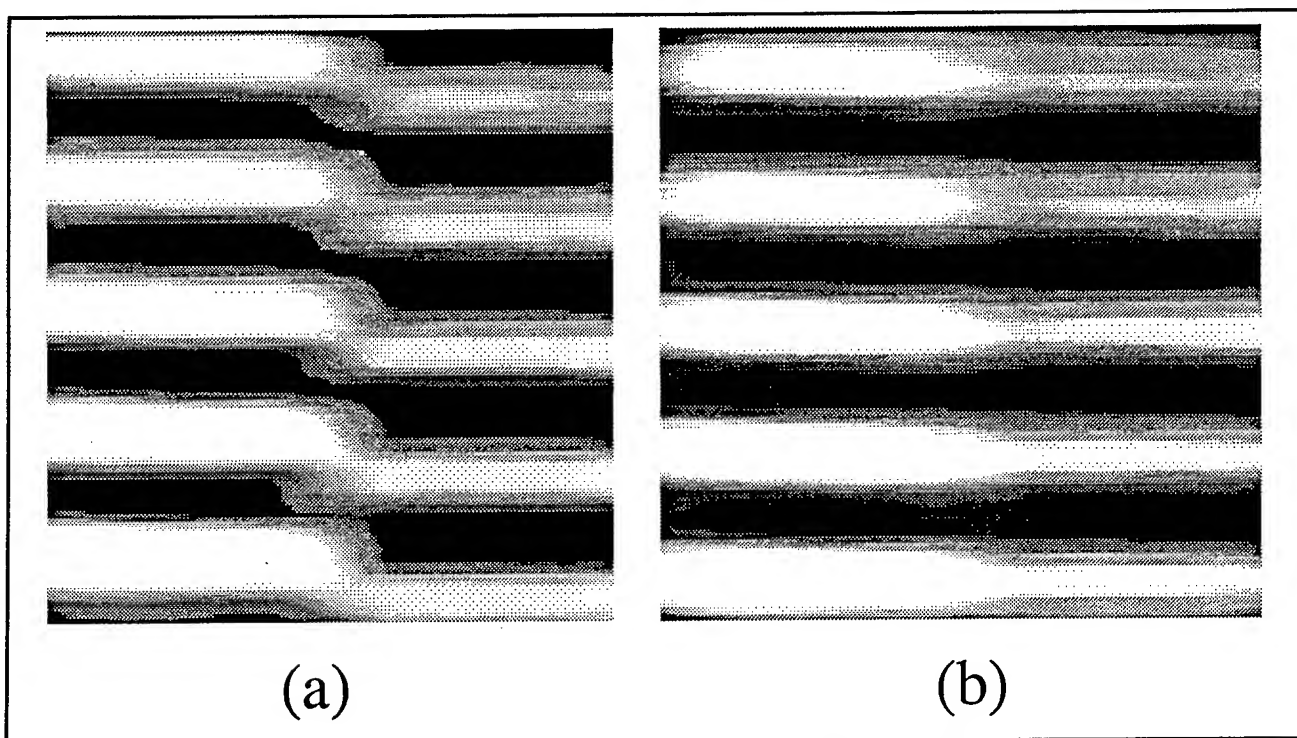


Figure 9. Interference fringes (moiré pattern) as seen by CCD camera in (a) misaligned and (b) aligned positions.

Gap is an important parameter in x-ray lithography, both to avoid mask-wafer contact and to ensure control of feature linewidth. To detect gap to high precision we have developed an interferometric gap detection scheme. This scheme uses the same marks and optics as employed in alignment, but viewed from a direction perpendicular to the grating

lines. When viewed (and illuminated) in this orientation, the mask mark acts as a quasi-Michelson interferometer, with the grating being the beamsplitter, and the arms being the thickness of the mask membrane and the gap between the mask and wafer. No corresponding mark is required on the wafer. Illuminating the mask mark

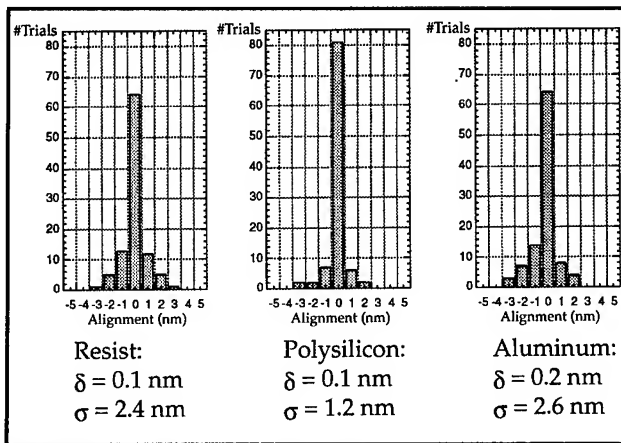


Figure 10. Effect of overlayers on alignment. For each overlayer, a histogram of 100 measurements is shown of the difference in spatial phase discontinuity between the half of the alignment mark with the overlayer and the half without the overlayer.

with polychromatic light results in an intensity variation as a function of gap. During a limited scan of gap, a beat pattern is obtained on each of the two sides of the mark. Since the beat periods are determined by the periods of the gratings, comparing these beat patterns yields an unambiguous measure of gap. The gap sensitivity of this method is better than 100 nm, which is sufficient for sub-100 nm lithography.

An x-ray source is being constructed to complete the prototype IBBI stepper/exposure system (figure 11). The nanometer-level alignment precision of this system will be essential in the fabrication of novel devices such as SOI-MOSFET devices with gates both above and below the Si channel.

5.7 Interferometric Lithography

Sponsors

Joint Services Electronics Program
Grant DAAH04-95-1-0038
National Aeronautics and Space Administration
Contract NAS8-38249
Grant NAGW-2003

Project Staff

James M. Carter, Juan Ferrera, Robert C. Fleming,
Timothy A. Savas, Dr. Mark L. Schattenburg,
Satyen Shah, Professor Henry I. Smith

Interferometric (also called holographic) lithography schemes are preferred for the fabrication of periodic

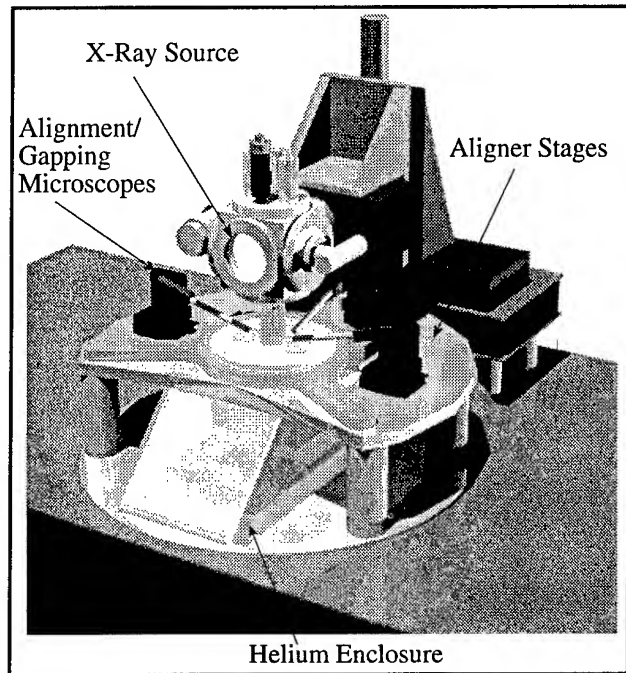


Figure 11. Interferometric broad-band imaging mask alignment/exposure system.

and quasi-periodic patterns that must be spatially coherent over large areas, and free of phase errors. For spatial periods down to 200 nm, an argon ion laser is used in a Mach-Zehnder configuration with a unique fringe-locking feedback system. This produces large area (10 cm diameter) gratings with long-range spatial-phase coherence, free of phase errors or detectable distortion. The fringe locking ensures reproducibility of exposure. A multiple exposure moire techniques is used to verify freedom from distortion (see section 5.3).

For spatial periods below 200 nm, bright light sources with wavelengths below 200 nm must be used. Such sources have limited temporal coherence, and thus one is forced to employ an achromatic scheme such as shown in figure 12. The source is an ArF laser (193 nm wavelength). A collimating lens, polarizer, and a scanning system are interposed between the source and the interferometer in order to achieve reasonable depth-of-focus and large exposure areas. We also use a white light interference principle to ensure equal path lengths in the two interferometer arms. Using this system, gratings and grids of 100 nm period (nominally 50 nm lines or posts) are obtained in PMMA on top of a specially designed antireflection coating. Figure 13 shows a 100 nm period grid etched into Si following achromatic interferometric lithography.

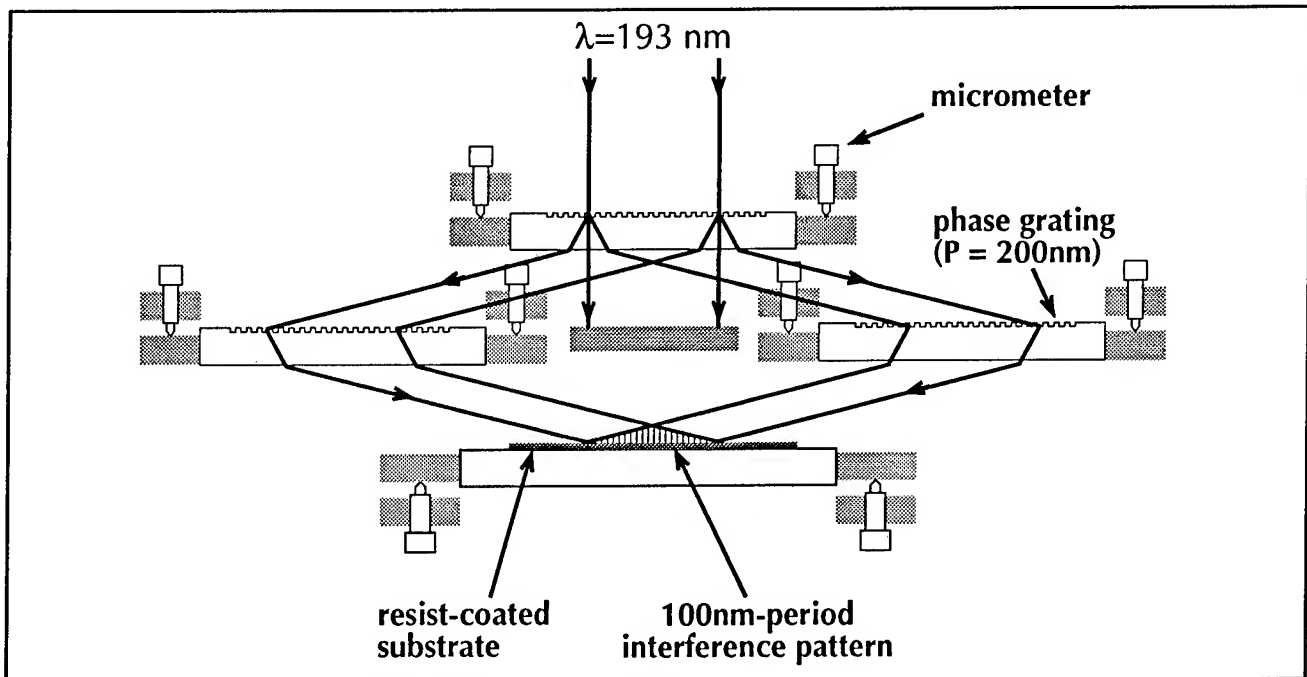


Figure 12. Achromatic interferometric lithography (ALL) configuration.

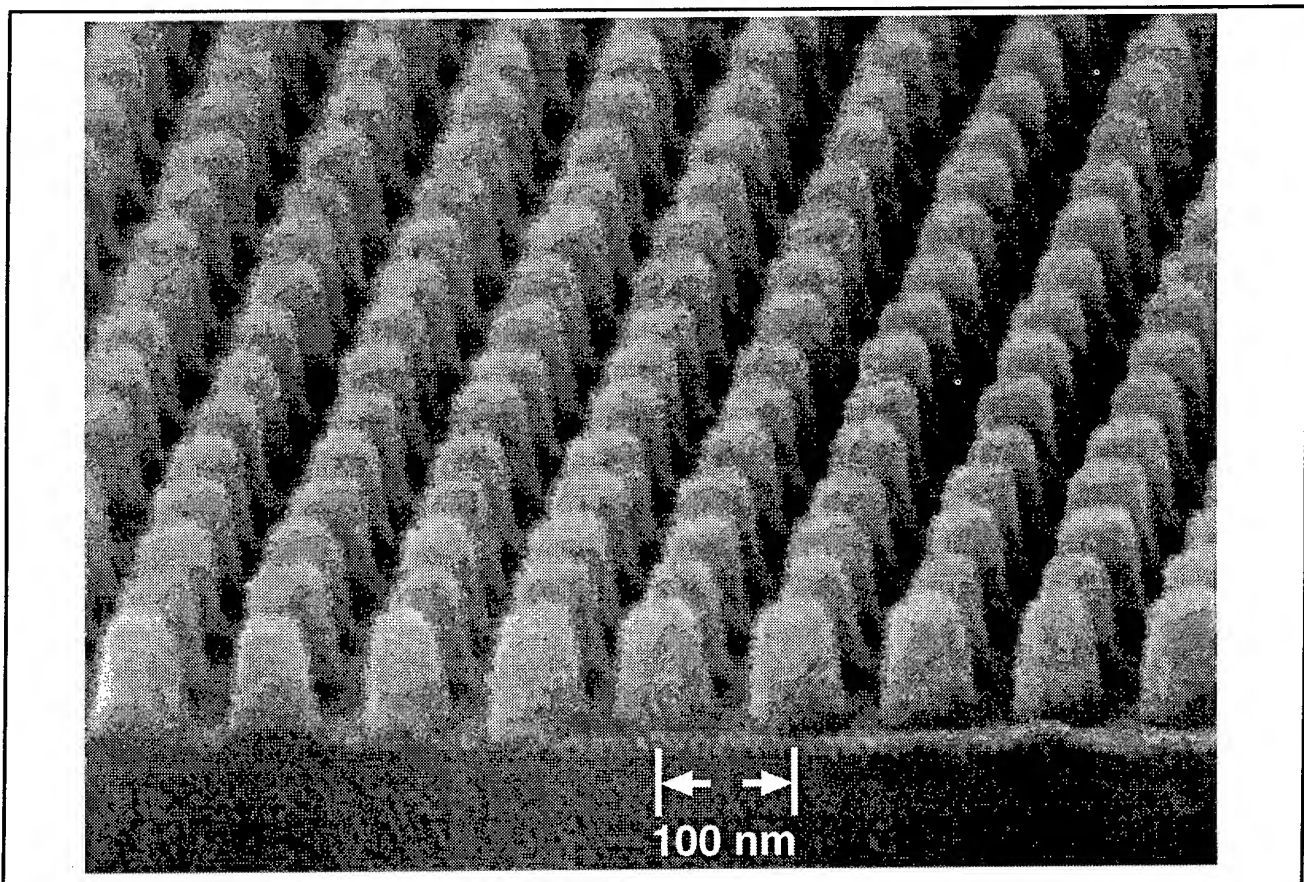


Figure 13. Scanning electron micrograph of a 100 nm period grid, exposed in PMMA on top of a specially designed antireflection coating, and transferred into Si by reactive ion etching.

Grids such as shown in figure 13 are of interest in a number of applications including high-density magnetic information storage and flat-panel displays based on field emission. At present, we use interferometric lithography to produce grid exposures of 200 and 320 nm period for a flat-panel-display program at MIT Lincoln Laboratory. In the future, we expect to provide similar grids for Professor Akinwande who also conducts research on flat-panel displays.

5.8 Ion-Beam Lithography

Sponsor

Joint Services Electronics Program
Grant DAAH04-95-1-0038

Project Staff

Scott E. Silverman, Professor Henry I. Smith, Professor Carl V. Thompson, Anto Yasaka

Yields of FIB-induced secondary electron from Si, Al, and PMMA targets have been measured to investigate the feasibility of spatial-phase-locked FIB lithography. The results indicate that Al has very high secondary electron yield ranging from 5.7 to 6.9 electrons per ion for 120-240 keV Si^{2+} incidence, and PMMA has very low secondary yield, ranging from 1.0 to 1.5 electrons per ion for the same ion irradiation conditions. These results lead to the conclusion that a fiducial grid fabricated on a substrate will be imaged with sufficient contrast by detecting FIB-induced secondary electrons. Furthermore, the image obtained by FIB will have a much better signal-to-noise ratio than the image obtained by electron beams because of the fact that ion bombardment produces almost no back-scattering electrons. The required ion dose to detect the fiducial-grid signal with appropriate contrast was calculated. This value is much lower than the ion dose required to expose resist. Thus, it is possible to detect the grid signal without disturbing the writing. It seems reasonable to conclude that spatial-phase-locked FIB lithography will be a promising tool to produce nanometer range resolution lithography with high accuracy and precision.

Secondary electron yields as a function of ion irradiation time were also measured. When plotting the results of the secondary yields versus time, considerable differences in the tendency of the curves are observed depending on the target materials. An explanation of the observed results was attempted in terms of two competing processes: sputtering by incident ions and oxidation by residual gases. For a Si target, the results can be illustrated quite naturally as due to the two processes. That

is, removal of native oxide by sputtering results in a decrease of secondary yield with time for high current density, and for low current density the surface remains oxidized due to reaction of residual gases and the surface atoms and thus the secondary yield shows little change with time. For an Al target, however, this model cannot explain all of the observed results. In some cases, an increase of the secondary yields with time has been observed.

5.9 High Performance Self-aligned Sub-100 nm MOSFETs using X-ray Lithography

Sponsors

Defense Advanced Research Projects Agency/
Naval Air Systems Command
Contract N00019-95-K-0131
IBM Corporation
Contract 1622
Joint Services Electronics Program
Grant DAAH04-95-1-0038
U.S. Navy- Office of Naval Research
Grant N00014-95-1-1297

Project Staff

James M. Carter, Keith M. Jackson, Isabel Y. Yang, Professor Dimitri A. Antoniadis, Professor Henry I. Smith

We have fabricated sub-0.1 μm N-channel MOSFET devices on bulk Si using x-ray lithography. Extremely well controlled short-channel effects were achieved through appropriate channel and source/drain engineering. Figure 14 shows the device schematic. The retrograde channel doping profile was accomplished using shallow indium and deep boron implants. The source/drain halo extensions were formed using a low energy arsenic implant with indium preamorphization and counter-doping. The self-aligned polysilicon gates were fabricated using x-ray nanolithography and an anisotropic etching process. The aligned microgap x-ray exposures were carried out using mesa-etched SiN_x x-ray masks with Au absorber pattern. Hot Carrier Degradation of the 0.1 μm N-channel MOSFETs devices has been examined with results suggesting that a V_{dd} of around 1.6 V gives a lifetime of 10 years for 0.1 μm devices fabricated in this lot.

Current work on sub-0.1 μm devices on bulk Silicon is focusing on N-channel MOSFETs designed to work at 77 K where further improvement of device characteristics occurs. Measurements show that the devices turn on and off more sharply (the sub-

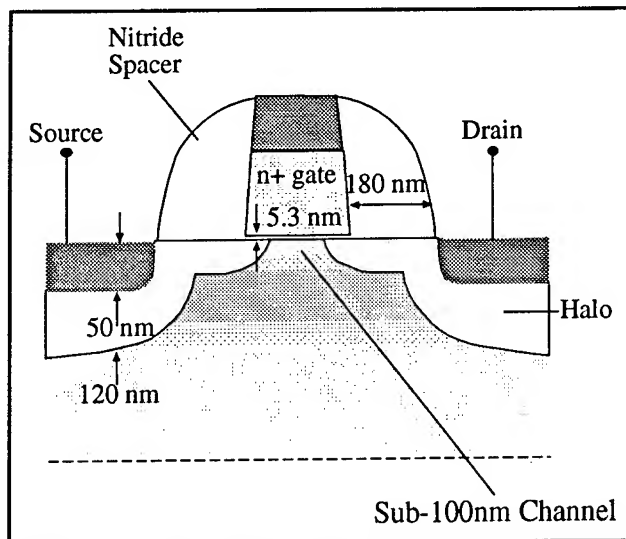


Figure 14. Schematic of 0.1 μm channel-length self-aligned NMOSFET.

threshold slope improves from 80 to 24 mV/decade) and the transconductances are at least 50 percent higher at 77 K, see figure 15. Future work will address fabrication of devices optimized for low temperature operation, performance improvements, and hot carrier reliability.

5.10 Single and Dual-Gate SOI Devices

Sponsors

Defense Advanced Research Projects Agency/
Naval Air Systems Command
Contract N00019-95-K-0131
IBM Corporation
Contract 1622
Joint Services Electronics Program
Grant DAAH04-95-1-0038
U.S. Navy- Office of Naval Research
Grant N00014-95-1-1297

Project Staff

James M. Carter, Keith M. Jackson, Isabel Y. Yang,
Professor Dimitri A. Antoniadis, Professor Henry I. Smith

Our current work aims to extend the 100 nm device technology to a full CMOS line, on bulk as well as on SOI substrates. Two different device structures are explored on the SOI substrates. One is the conventional structure on SOI, and the other is the double-gated structure (SOIAS) with a top gate having deep-submicron length, and a wider bottom gate.

Our first effort is to get a fundamental understanding of these devices in DC; i.e., short channel

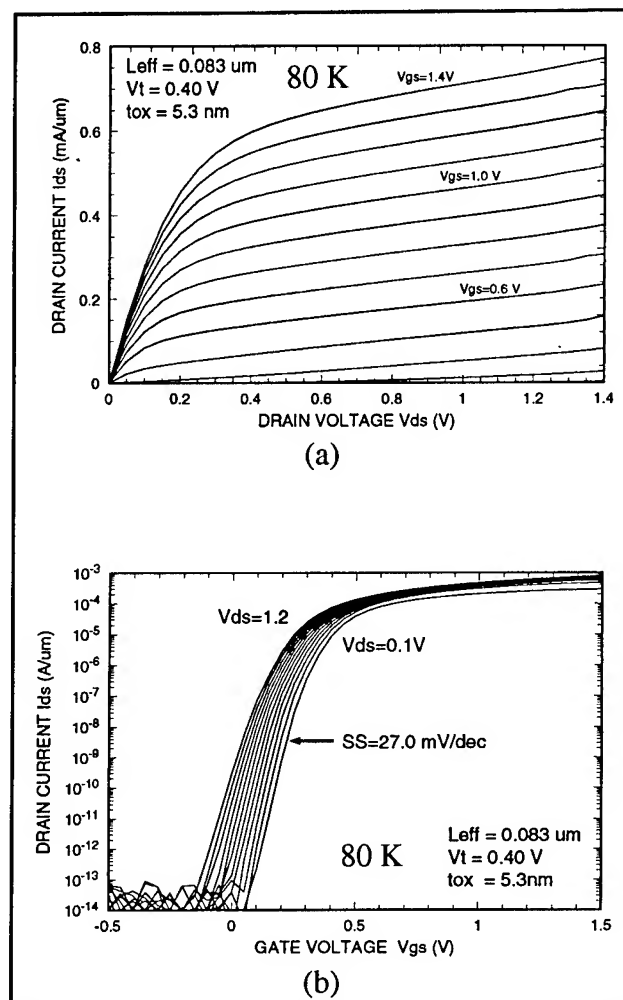


Figure 15. I-V characteristics of an 83 nm-channel-length NMOSFET cooled to 80 K.

effects, drain-induced barrier lowering (DIBL), coupling of the backgate to the front gate, etc. Currently, the backgate is defined by ion implantation through the top using optically exposed thick resist as the mask. The top gate is then aligned over this bottom gate via x-ray lithography. The technology issue here is the mixing and matching of the optical stepper to the e-beam tool which writes the patterns on the x-ray masks.

We have developed a technique to do this matching that also saves e-beam writing time. Figure 16 shows this process in which the coarse patterns, e.g., pads and e-beam field alignment marks, are first transferred onto a chrome coated quartz wafer using the optical stepper. The pattern is then transferred into chrome by a wet etch. A one-to-one pattern transfer of the coarse features onto the x-ray mask is then done using proximity 240 nm UV exposure. The coarse patterns and the field alignment marks are then plated up in Au and sent to the e-beam for fine pattern writing. The final pat-

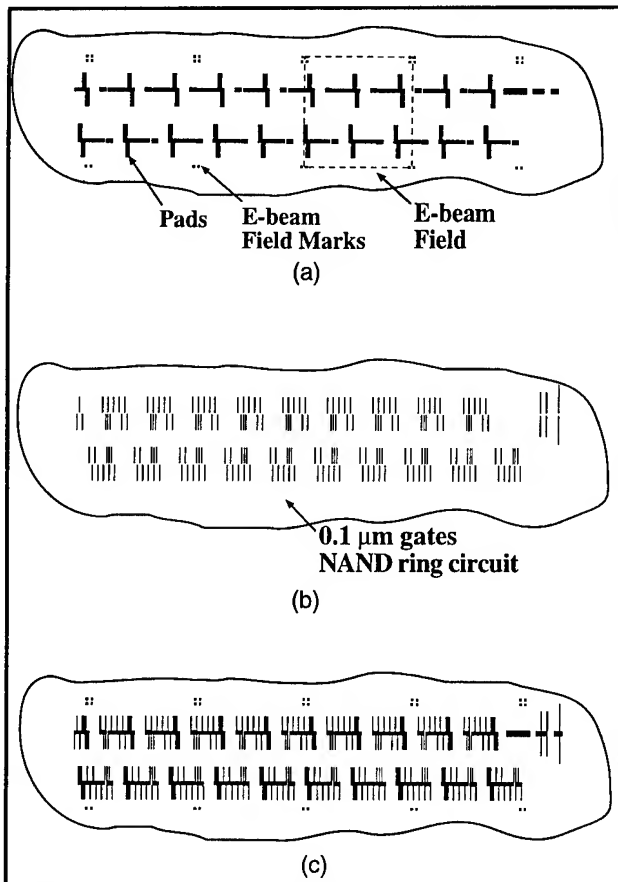


Figure 16. Sketch of a small portion of the chip showing: (a) a pattern of coarse features (pads) transferred onto the x-ray mask by deep UV lithography; (b) fine features written by e-beam lithography; (c) composite of fine and coarse features on the x-ray mask. The pattern is a nand ring circuit.

terns on the mask will have coarse features patterned by UV proximity printing and fine features written by e-beam lithography, as depicted in figure 16c.

We were able to fabricate CMOS devices on bulk, SOI and SOIAS substrates with this mix-and-match scheme with device lengths of $0.2\ \mu\text{m}$. Figure 17 shows the subthreshold characteristics of a back-gated device made on SOIAS substrate. The back-gate can control the NMOS and PMOS threshold voltages independently from the front-gate and from each other. Thus, making dynamic control of threshold voltage for low power applications possible.

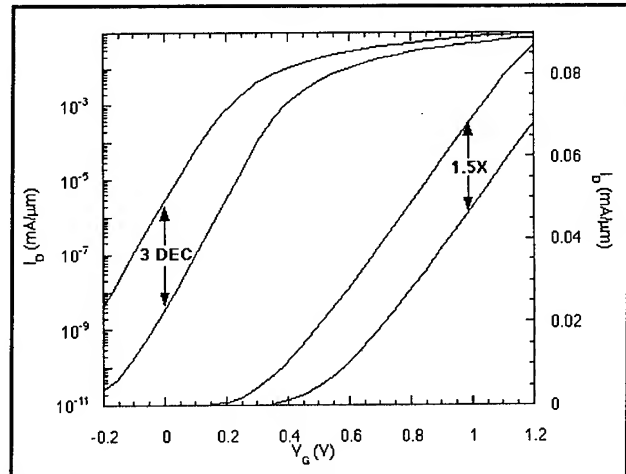


Figure 17. Subthreshold characteristics of an $L_{\text{eff}}=0.2\ \mu\text{m}$ device on linear and log scale showing 3 decade reduction in off current and 1.5 times increase in drive current when the threshold voltage is switched.

5.11 Fabrication of T-gate Devices using X-ray Lithography

Sponsor

U.S. Army Research Office
Grant DAAH04-94-G-0377

Project Staff

Mitchell W. Meinhold, Professor Henry I. Smith

Monolithic microwave integrated circuits (MMICs) have potential applications in automobile navigation, collision-avoidance, and wireless communication systems. The high-speed MODFET devices of such circuits require very short gate lengths, while preserving low resistance. Large gate widths are required for high current drive. To meet these conflicting demands so-called "T-gate" and "gamma-gate" processes are used in which the base or stem of the gate is very short ($\sim 100\ \text{nm}$) while the upper part is large, overlapping the stem, similar to a mushroom, or the letters T or Γ . Although such structures can be achieved using direct-write electron-beam lithography in double-layer resists, the technology is expensive, slow, and unlikely to meet future production needs. For these reasons, we are developing a process for fabricating T-gates using x-ray lithography.

The fabrication sequence is shown in figure 18. The first layer defines the stem of the gate, a critical parameter for a field-effect device. After exposing and developing the first layer, a second layer of resist is deposited and the pattern corresponding to the upper part of the gate exposed.

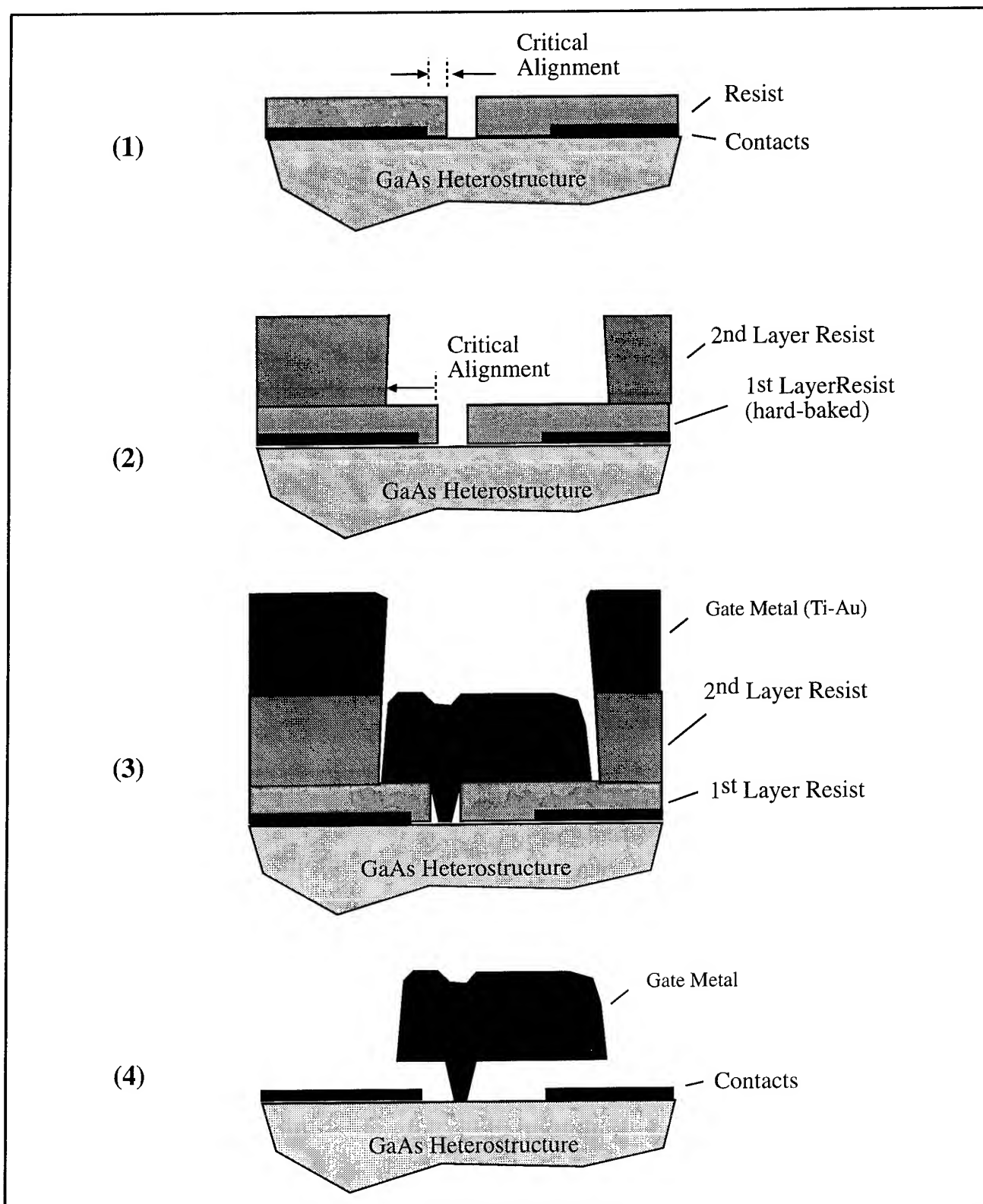


Figure 18. Depiction of the T-gate process steps: (1) Resist is deposited over existing contact metal. Alignment and exposure takes place. (2) After hardening the first layer, a second layer is deposited. The second pattern alignment and exposure takes place. (3) Gate metal is deposited. (4) Liftoff (resist removal)

At this point, gate metal can be deposited forming the T-gate. There are two challenges to achieving this process. First, it must be possible to align the x-ray masks to within 100 nm. Second, if the masks do not share a common coordinate system, features such as the gate stem and mushroom will not align properly. Also, without precision mask alignment it would not be possible to get the gate stem very close to the source. Therefore, the three x-ray masks required in the process depicted in figure 18 must be written with reference to a coordinate system that is common to all the masks. To meet the first challenge, we have put alignment marks on the masks that are compatible with the high precision, IBBI alignment system (see Section 5.6). We anticipate no difficulty in achieving sub-100 nm alignment with the IBBI system.

To meet the second challenge, x-ray masks are prepared with a grid array of reference marks located at the corners of fields measuring 0.1 x 0.1 mm, the field size of the e-beam lithography system. These reference marks were transferred to each x-ray mask with DUV lithography using the same optical mask, thereby guaranteeing a common coordinate system for all three x-ray masks. Upon registration to these marks, the e-beam lithography system should be able to place patterns with a precision well below 100 nm.

There are a number of interesting directions that may be followed once a reliable, high latitude process is established. For manufacturable MMIC systems, both MESFETs and HEMTs are required for low-noise and power applications. Initially, relatively simple GaAs MESFETs will be studied, followed by GaAs and InP HEMTs of varying degrees of complexity. Further studies could include low-temperature-grown GaAs MESFETs for high breakdown voltages, self-aligned devices, or gate materials other than Au such as W.

5.12 Studies of Coulomb Charging Effects and Tunneling in Semiconductor Nanostructures

Sponsors

Joint Services Electronics Program
Grant DAAH04-95-1-0038
U.S. Air Force - Office of Scientific Research
Grant F-49-620-92-J-0064

Project Staff

Martin Burkhardt, David J. Carter, Ilia Sokolinski, Professor Dimitri A. Antoniadis, Michael R. Melloch,¹ Professor Terry P. Orlando, Professor Henry I. Smith

Quantum-effect devices, whose minimum feature sizes are comparable to the Fermi wavelength (about 50 nm in a typical inversion layer), have promising potential in novel electronics applications. Quantum-dot devices have drawn particular attention. In such devices an electron gas is confined electrostatically in all three dimensions, forming a small "island" of electrons ~100 nm, bounded on all sides by potential walls. This small electron "island" resembles an atom because there can be only an integer number of electrons, and these electrons can occupy only certain discrete energy levels. If two dots are coupled, a structure resembling a molecule is obtained. The conductance of the dot, when connected to leads through tunneling barriers, exhibits strong oscillations as the voltage of the gate is varied. Each successive conductance maximum corresponds to the addition of a single electron to the dot. At temperatures in the mK range, the conductance decreases by orders of magnitude in between adjacent conductance maxima because there is a large energy cost for an electron in the lead to enter the dot. This energy cost can be removed by changing the gate voltage, resulting in the observed periodic dependence of the conductance on gate voltage. This depends on how fast the chemical potential within the dots is changed for a change in gate voltage. For two arbitrary dot sizes and very low temperature, the conditions for conductance through the dots are arbitrary, and conductance events are expected to be stochastic.

Figure 19 is a schematic of a coupled-quantum-dot device. The dots are formed in a two-dimensional electron gas (2DEG) in an MBE-grown GaAs/Al-GaAs heterostructure. The 2DEG is approximately 60 nm below the surface of the material. The 2DEG is contacted electrically with ohmic contacts, depicted in the corners, and the 2DEG is confined laterally with Schottky gates which repel the electrons underneath. The areas where the 2DEG exists are shown in light grey. The two quantum dots (the isolated "islands") are connected to the 2DEG leads by quantum point contacts (QPCs) and to each other by a thin tunnel barrier.

¹ Purdue University, West Lafayette, Indiana.

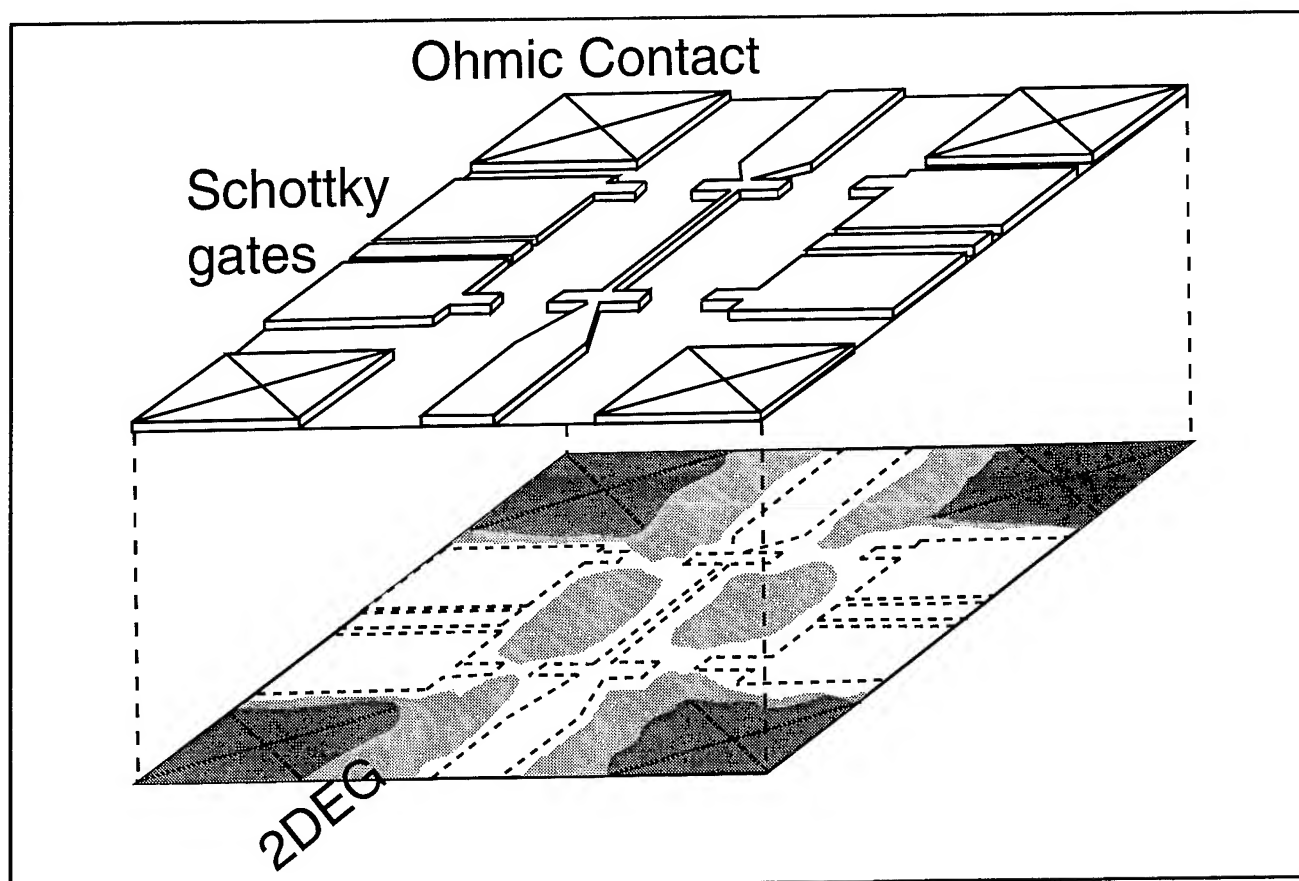


Figure 19. Schematic of a coupled-quantum-dot device. The two-dimensional electron gas (2DEG) is approximately 60 nm below the surface of a GaAs/AlGaAs heterostructure. Ohmic contacts, shown in dark grey, make electrical contact to the 2DEG and Schottky gates on the surface electrostatically create lateral confinement. Regions where the 2DEG exists after biasing the Schottky gates are shown in light grey.

The most critical aspect of quantum dot device fabrication in GaAs heterostructures is the nanolithography. We have been pursuing both direct-write electron-beam lithography and x-ray lithography. X-ray lithography has the advantage of producing more electrostatically robust devices, since thicker resist allows deposition of thicker gate metal and liftoff. It is also more compatible with future manufacturing than is electron-beam lithography.

Figure 20 is a scanning-electron micrograph of the gate structure of a coupled quantum dot device fabricated with electron-beam lithography. Each of the two quantum dots is connected to the outside world via three QPCs. Two QPCs allow tunneling of electrons to the 2DEG reservoirs, and the third QPC allows tunneling between the two dots. This structure will allow investigation of the coupled quantum dots in both parallel and series current flow configurations. We are also investigating devices in which a thin tunnel barrier is formed by a fine line (less

than 40 nm) between the two quantum dots instead of by a quantum point contact. (see Section 5.14) We plan to investigate the differences between the two structures as the voltage on the middle Schottky gate is varied and the dots go from being well-separated to being continuous.

We have also designed a one-dimensional quantum-dot-array structure. Figure 21 is a design layout of one of the arrays consisting of seven quantum dots defined by eight quantum point contacts (QPCs). Impurities in the semiconductor strongly affect the characteristics of QPCs. It is essential for our experiments that the tunneling conductance of each QPC in the array be the same. Therefore, each QPC is controlled by a separate voltage source. The device will be fabricated on a back-gated GaAs/AlGaAs heterostructure. The back-gate will allow independent control over the electron density in the 2DEG.

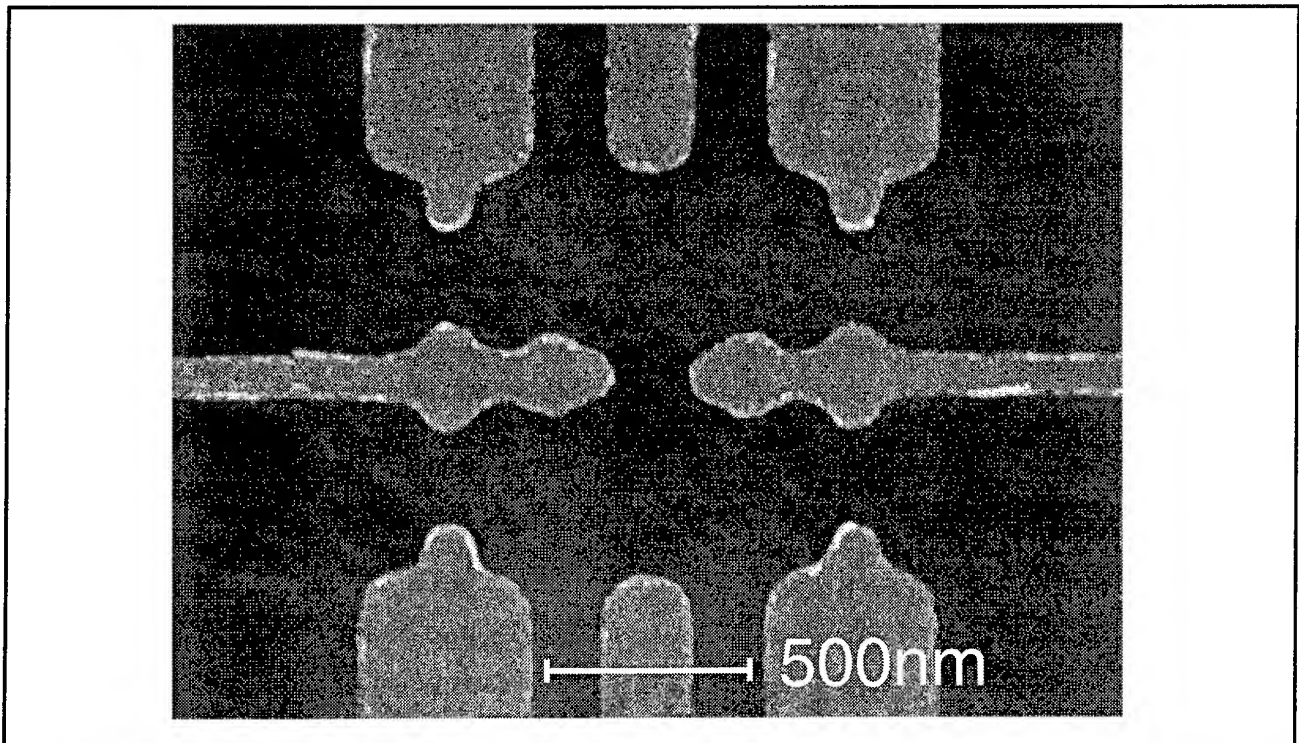


Figure 20. SEM micrograph of a coupled-quantum-dot device on a GaAs/AlGaAs heterostructure, produced by direct-write electron-beam lithography.

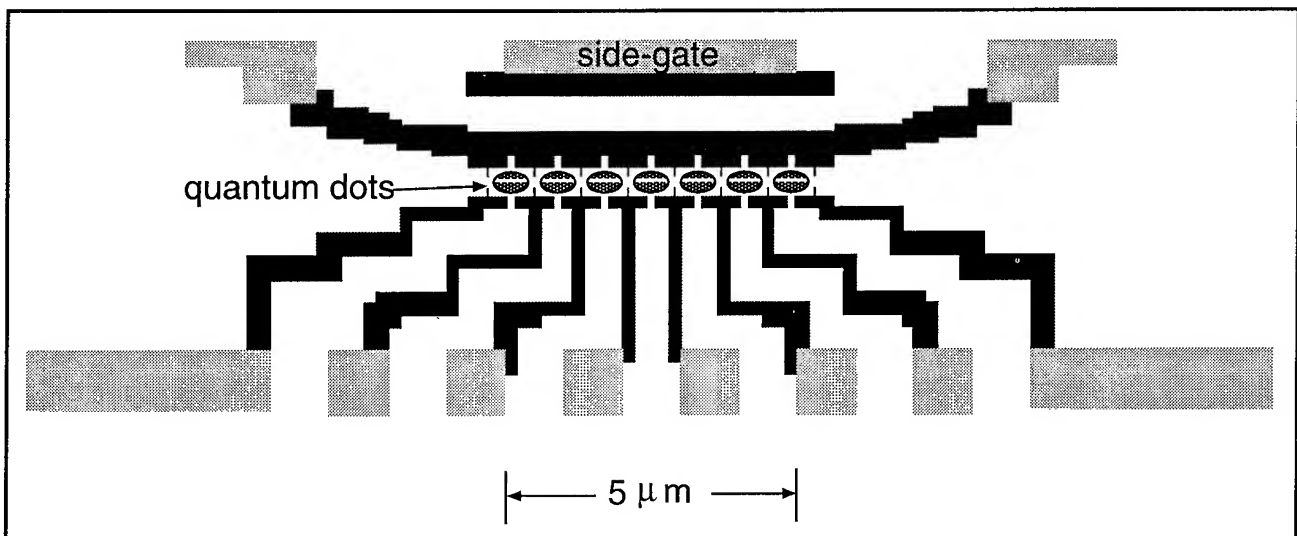


Figure 21. Layout of a series array of seven quantum dots. The eight quantum point contacts are independently controlled to ensure array uniformity.

5.13 Fabrication and Transport Studies of Lateral Surface Superlattices in GaAs/AlGaAs Modulation Doped Field-Effect Transistors

Sponsor

U.S. Air Force- Office of Scientific Research
Grant F-49-620-95-1-0311

Project Staff

Professor Dimitri A. Antoniadis, Michael R. Melloch,¹ Professor Terry P. Orlando, Dr. Anne Pepin, Mark R. Schweizer, Professor Henry I. Smith

Figure 22 depicts a lateral surface superlattice (LSSL) in a GaAs/AlGaAs modulation-doped field-effect transistor (MODFET). When a negative voltage is applied to the gate, the two-dimensional electron gas (2DEG), located at the AlGaAs/GaAs interface approximately 60 nm under the sample surface, is depleted under the gate fingers. A periodic modulation of the charge concentration is therefore introduced in the 2DEG. As a result, elec-

trons flowing from source to drain are subjected to a two-dimensional superlattice potential (i.e., a two-dimensional array of coupled quantum dots, in the case of the grid-gate shown in figure 22). The strength of the modulation can be adjusted by varying the gate bias.

Evidence of quantum superlattice effect (electron back-diffraction) was clearly observed in 200 nm-period and 60 nm-linewidth grid-gated structures. In the high field regime (high source-to-drain bias), negative differential conductance was also measured in various devices and primarily attributed to sequential resonant tunneling.

Although a wide variety of alternative techniques have since been investigated to induce LSSLs and several studies on magnetotransport measurements in LSSLs have been reported, none of the early transport results obtained at MIT could be reproduced. These objects are of great experimental and theoretical interest, and we have therefore chosen to further investigate electron transport in such structures. New grid-gated and grating-gated GaAs/AlGaAs MODFETs of different periods

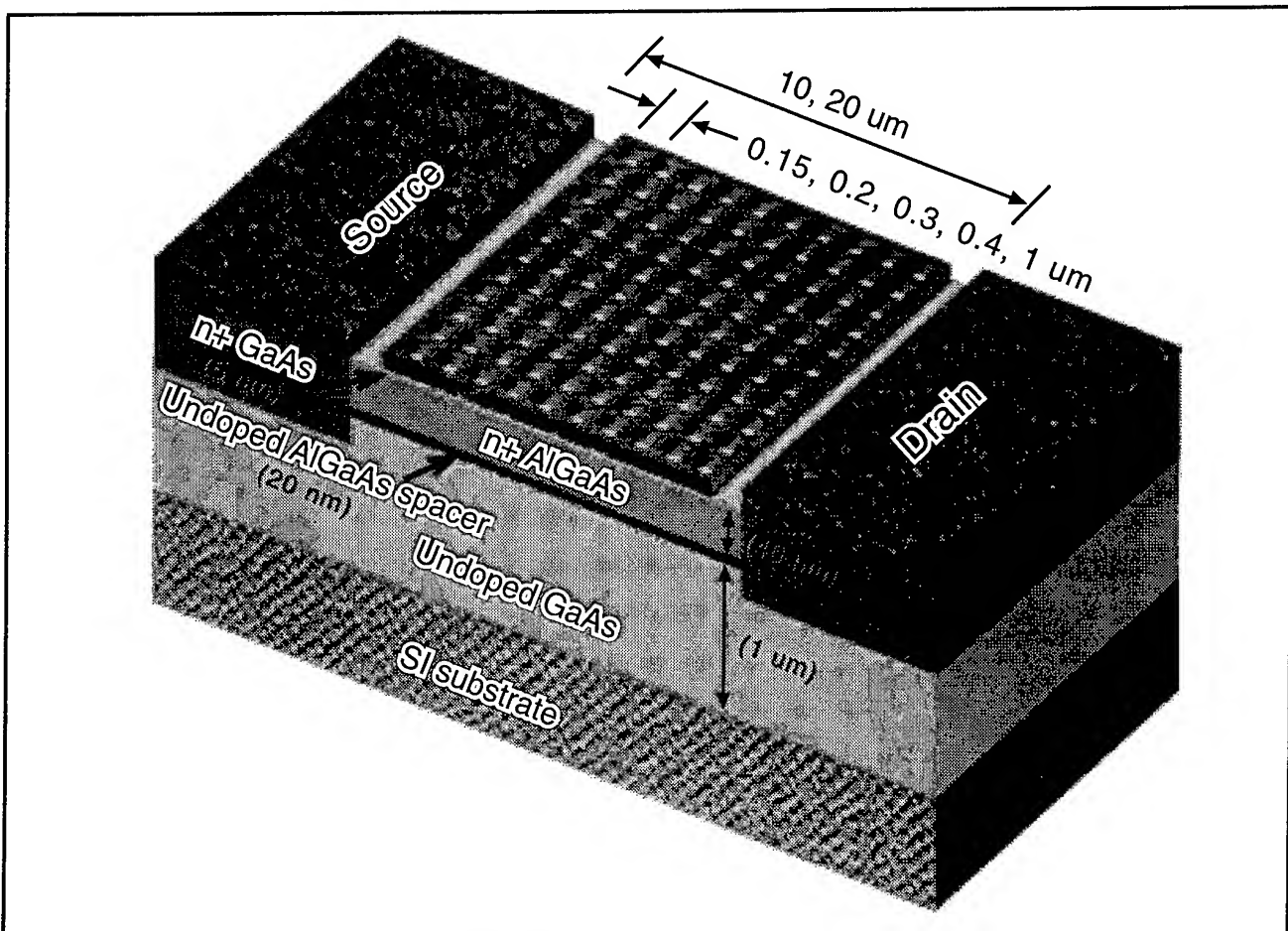


Figure 22. Cross section of the grid-gated MODFET.

(150, 200, 300, 400 nm and 1 μm) and gate lengths (10, 20 μm) are being fabricated. A cross-section of our structure is shown schematically in figure 22. X-ray nanolithography and subsequent metal lift-off are being used to define these structures. Figure 23 displays a scanning electron micrograph of a portion of a 200 nm-period Au grid-gate obtained on an x-ray mask. The gold pattern

was obtained on the 1 μm -thick silicon nitride x-ray mask after e-beam nanolithography and subsequent electroplating of 200 nm-thick gold. Linewidths as narrow as 38 nm achieved on x-ray masks should allow us to fabricate high performance devices. Low temperature transport measurement, particularly in the high field regime, will be carried out.

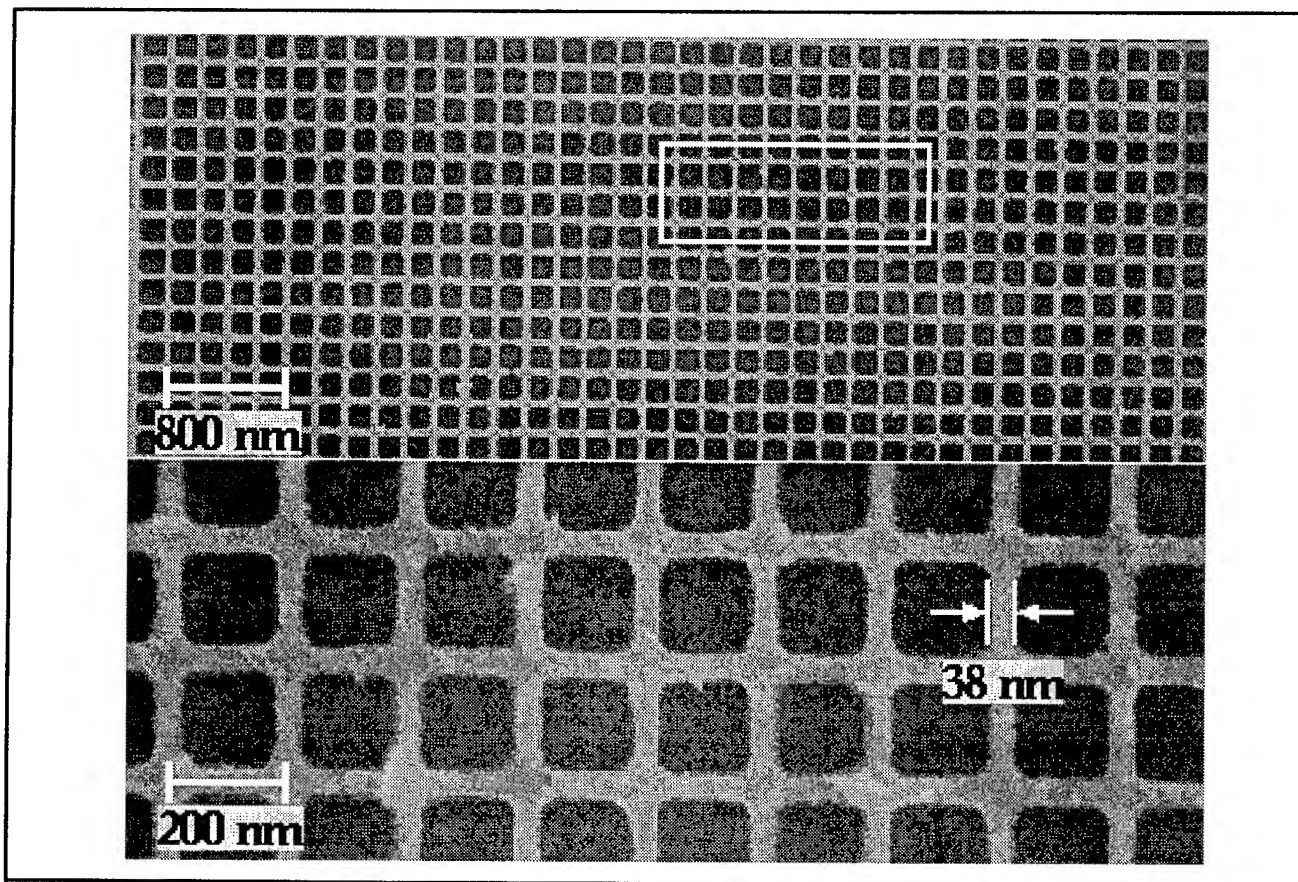


Figure 23. Scanning-electron micrograph of a 200 nm-period and 38 nm-linewidth Au grid-gate obtained on an x-ray mask.

5.14 Single-Electron Transistor Research

Sponsor

Joint Services Electronics Program
Grant DAAH04-95-1-0038

Project Staff

David Berman, Professor Raymond C. Ashoori,
Professor Henry I. Smith

The single-electron transistor (SET) has the highest charge sensitivity of any man-made device. In many respects, it is the electrical analog of the SQUID, which is the most sensitive detector of magnetic field. The SET is very well suited for applications

where one needs to measure small fluctuations of charge without disturbing the system under study. An example of such a system is a quantum dot.

Figure 24 shows a scanning-electron micrograph of one of our devices. The SET consists of a metal island connected to the source and drain electrodes by two small tunnel junctions. Fabrication of the tunnel junctions is done using a shadow evaporation method.

Operation of the SET depends on the fact that the central island has a very small capacitance, and the energy that it takes for electrons to charge this island is quite large. For example, if the device is cooled to temperatures below 1 K, the electron thermal energy becomes less than the charging

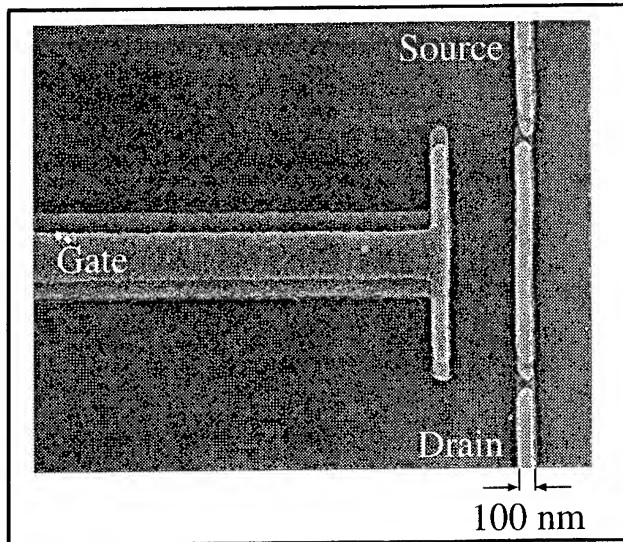


Figure 24. Scanning electron micrograph of a single-electron transistor, made of Al, in which the two tunnel barriers are produced by a two-angle shadow evaporation process.

energy. This means that without a significant source-drain voltage bias, the electrons cannot travel through the central island. This effect is known as the Coulomb blockade. The Coulomb blockade is manifested as a zero current region in the current-voltage dependence of the SET. This effect is shown in figure 25. The addition of gate voltage can alter the size of the Coulomb blockade region, thus we can use this device as a transistor.

5.15 Distributed-Feedback Lasers Fabricated by X-Ray Lithography

Sponsors

Joint Services Electronics Program
Grant DAAH04-95-1-0038
U.S. Army Research Office
Grant DAAH04-95-1-0564

Project Staff

Vincent V. Wong, Michael H. Lim, Elisabeth A. Marley, Thomas E. Murphy, James M. Carter, Juan Ferrera, Professor Leslie A. Kolodziejski, Professor Henry I. Smith

Distributed feedback (DFB) lasers are essential components in future wavelength-division-multiplexed systems. These systems require tunable transmitters that oscillate in a single longitudinal mode with narrow linewidths; the transmitters must also be integrable with electronic circuitry such as detectors and field-effect transistors. There are two basic DFB laser structures (figure 26), each with its own fabrication challenges. The fabrication

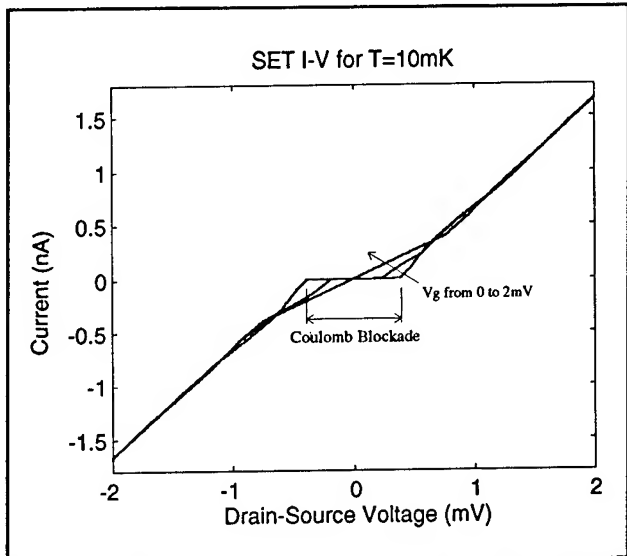


Figure 25. Current-voltage characteristic of a single-electron transistor taken at 10 mK, for three values of gate voltage. The Coulomb blockade is maximum at zero gate bias.

of the vertically-coupled DFB laser requires an epitaxial regrowth step carried out on top of the grating. This etch back step makes the coupling constant after epitaxial regrowth difficult to predict, lowering the yield on these devices. In the laterally-coupled DFB laser structure, gratings are etched on both sides of the ridge waveguide. This structure eliminates the need for regrowth and maximizes the utility of ridge-waveguide devices.

To achieve high enough contra-directional coupling for laser action to occur in the laterally-coupled DFB structure, as well as reliable control of coupling from device-to-device, the lateral gratings should run right up to the ridge sidewall since the coupling decreases as the lateral gratings move away from the ridge sidewall. This decrease is attributable to the decreased overlap between the optical field and the grating. For reasonable values of k ($\sim 20 \text{ cm}^{-1}$), the lateral gratings must be within 100 nm of the ridge sidewall. Lateral gratings that reside closer to the ridge sidewall also relax the tolerance on the grating duty cycle. However, spinning a thin coat of resist onto a wafer with a high ridge-waveguide results in a buildup next to the sidewall of the ridge; at thicknesses of greater than 1 μm this poses problems even for x-ray lithography. This buildup of resist prevents the gratings from running all the way up to the ridge sidewall.

We have developed a process, that uses ion implantation (figure 27) to overcome this problem. Once the ridge waveguides are defined, a 4.3 μm -thick planarizing layer of PMMA is spun onto the substrate. Next, three ion implantation/development steps are performed: (1) boron

700 keV; 10^{13} cm^{-2} ; 1:2 MIBK:IPA at 21° C for 150 seconds; (2) boron 120 keV; 10^{13} cm^{-2} ; 1:2 MIBK:IPA at 21° C for 150 seconds; (3) boron 80 keV; 10^{13} cm^{-2} ; 1:2 MIBK:IPA at 21° C for 150 seconds. After these steps, a $0.6 \mu\text{m}$ film of PMMA remains. Into this film, x-ray lithography defines a uniform 406 nm-period grating that runs up to the ridge waveguide sidewalls. The grating is then etched in a CH_4/H_2 plasma. Figure 28 shows the

results, lateral gratings that run right up to the edge of the ridge-waveguide.

The challenges of fabricating high quality vertically-coupled DFB laser are quite different than those of a laterally coupled DFB laser. Because of the geometries of the VC-DFB, high quality regrowth on a grating is the primary concern. In 1996, we will investigate such regrowth as a function of grating aspect ratio.

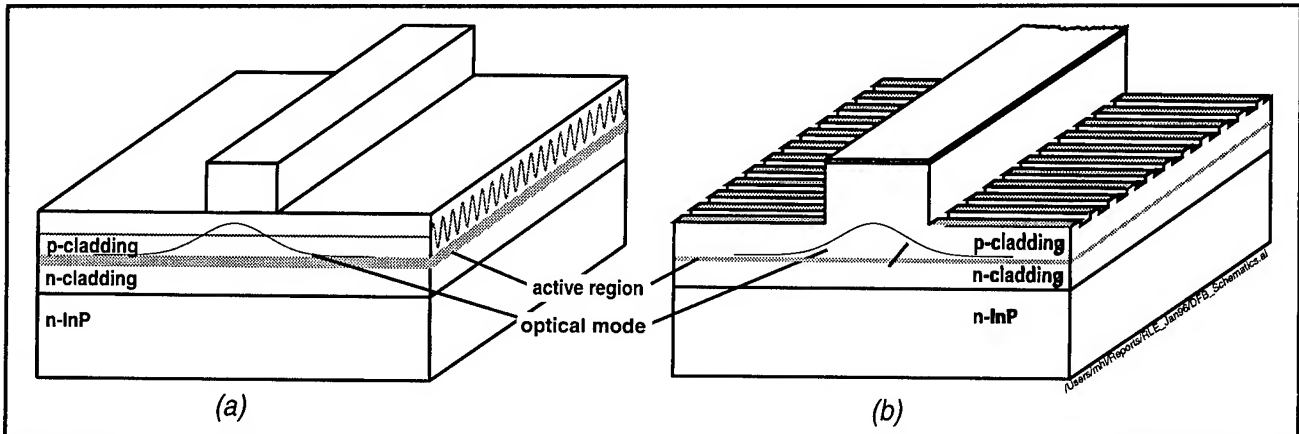


Figure 26. (a) A schematic of a DFB laser that relies on coupling vertically to the corrugation region above the gain region; (b) schematic of a laterally-coupled DFB laser that relies on coupling laterally to the corrugation regions on the side of the ridge waveguide. For adequate contra-directional coupling to occur, the distance from the sidewall of the ridge to the beginning of the grating must be less than 100 nm.

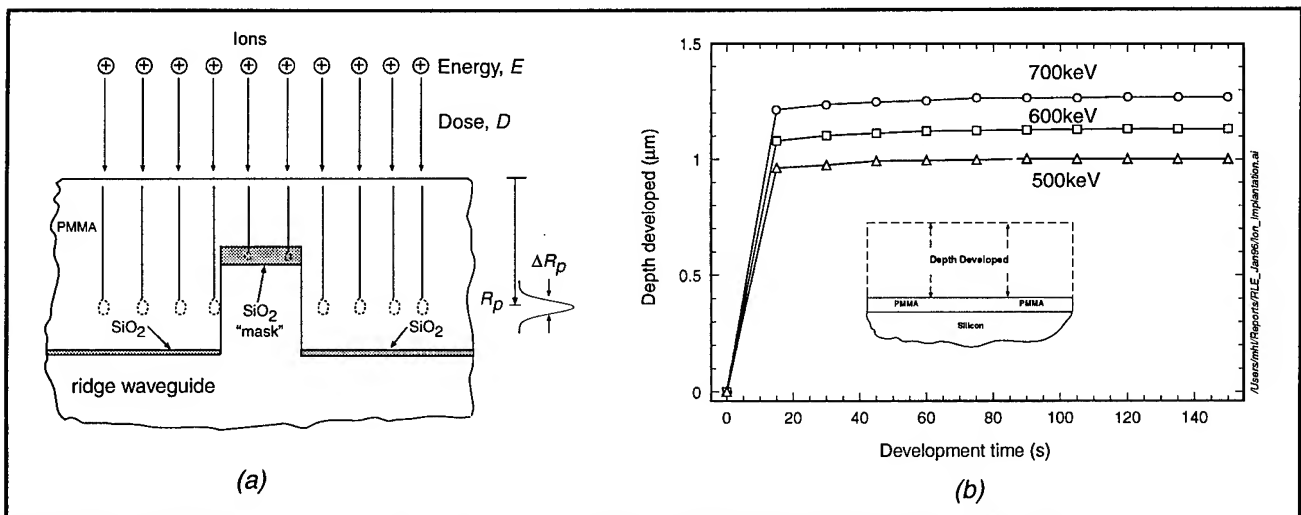


Figure 27. (a) When high energy ions are implanted, the majority of the ions stop at a particular depth governed by the energy of the ion. This allows one to develop the thick PMMA down to a thin film for x-ray exposure; (b) the depth of the developed PMMA saturates at a particular depth dependent on the energy of the implanted ion. The ion dose was $1 \times 10^{13} \text{ cm}^{-2}$. The PMMA was developed in a solution of 1:2 MIBK:IPA at 21° C .

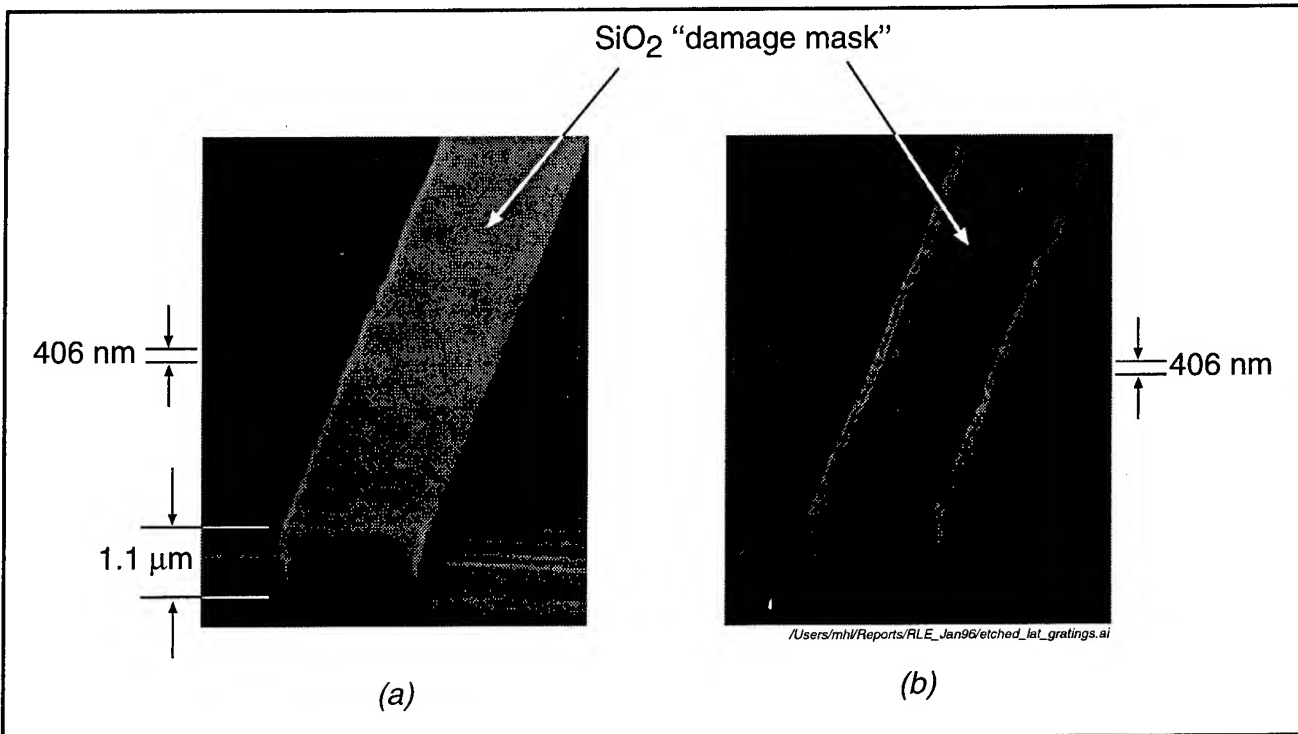


Figure 28. Lateral gratings defined on a 1.1 μm -high InP/InGaAlAs/InGaAsP ridge-waveguide. The grating has a period of 406 nm, which corresponds to a 2nd-order DFB laser operating at 1.3 μm wavelength. The silicon dioxide damage mask serves both as an RIE etch mask as well as an ion implantation damage mask. (a) scanning electron micrograph of a 406 nm-period lateral grating exposed in PMMA by x-ray lithography; (b) scanning electron micrograph of lateral gratings defined by CH_4/H_2 RIE.

5.16 Fabrication of Integrated Quarter-Wave Shifted Distributed Bragg Gratings for Wavelength Division Multiplexing Applications

Sponsor

Joint Services Electronics Program
Grant DAAH04-95-1-0038

Project Staff

Jay N. Damask, Juan Ferrera, Michael H. Lim, Thomas E. Murphy, Vincent V. Wong, Professor Hermann A. Haus, Professor Henry I. Smith

In order to best utilize the bandwidth available for optical communications systems, it is advantageous to transmit several communications signals in a single optical fiber, each modulated with a different carrier frequency. One key component in the implementation of such wavelength division multiplexed (WDM) systems is a narrow-band optical filter that can separate or "drop" one channel from a waveguide, leaving the other channels undisturbed.

Quarter-wave shifted Bragg gratings provide a compact, flexible filter for WDM applications. Insertion of an abrupt quarter-wave shift in an oth-

erwise coherent distributed Bragg grating gives rise to a single narrow resonance at the Bragg wavelength. The small spatial periods required for these grating filters (~ 510 nm in SiO_2 materials and ~ 250 nm in InP materials) necessitates the use of advanced nanolithography techniques in their fabrication.

The integrated resonant channel dropping filter (figure 29) is comprised of two quarter-wave shifted gratings, each evanescently side-coupled to a bus waveguide. The function of the filter is to spatially separate, or drop, just one channel from the bus waveguide without terminating or otherwise disturbing the remaining channels. The WDM bitstream is carried along the middle waveguide. Only that channel, or wavelength band, that excites the side-coupled resonators is removed from the bus to the upper waveguide. The remaining channels travel through undisturbed.

The Lorentzian filter response of a quarter-wave shifted grating is limited to a filter roll-off of -10 dB/decade away from the resonant frequency. In order to improve the filter roll-off, several such resonators can be cascaded along a single waveguide, producing a so-called multiple-pole filter, as shown in figure 30.

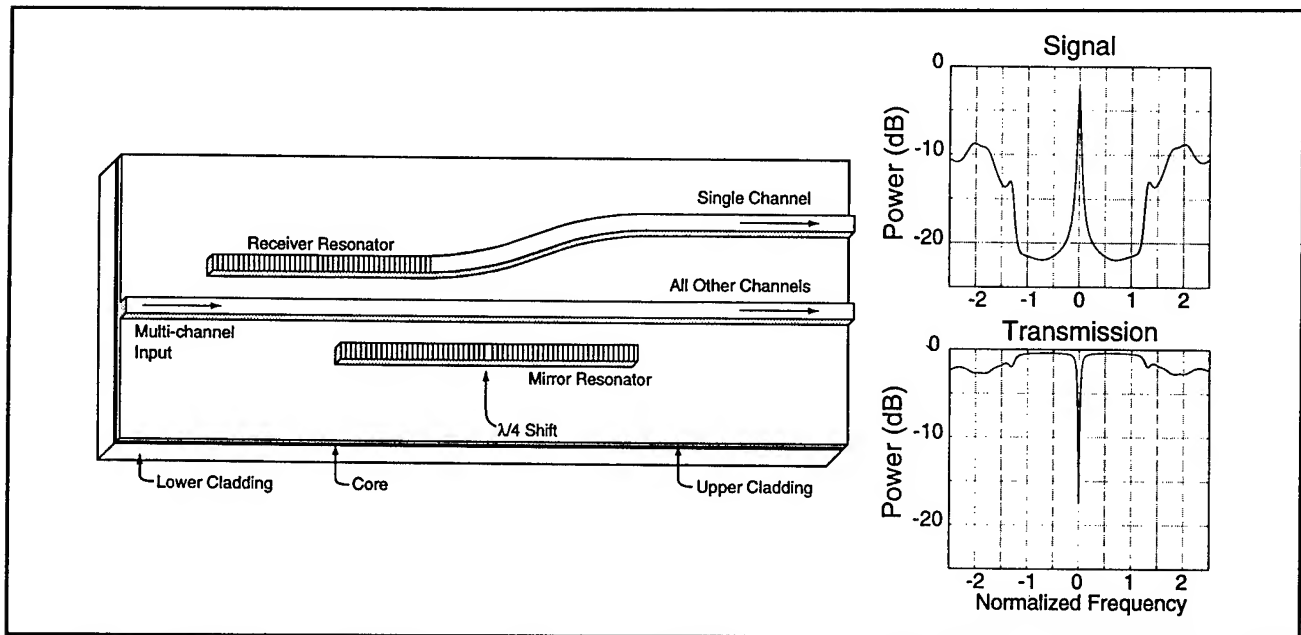


Figure 29. A schematic diagram of the integrated resonant channel-dropping filter, and the associated filter spectral response.

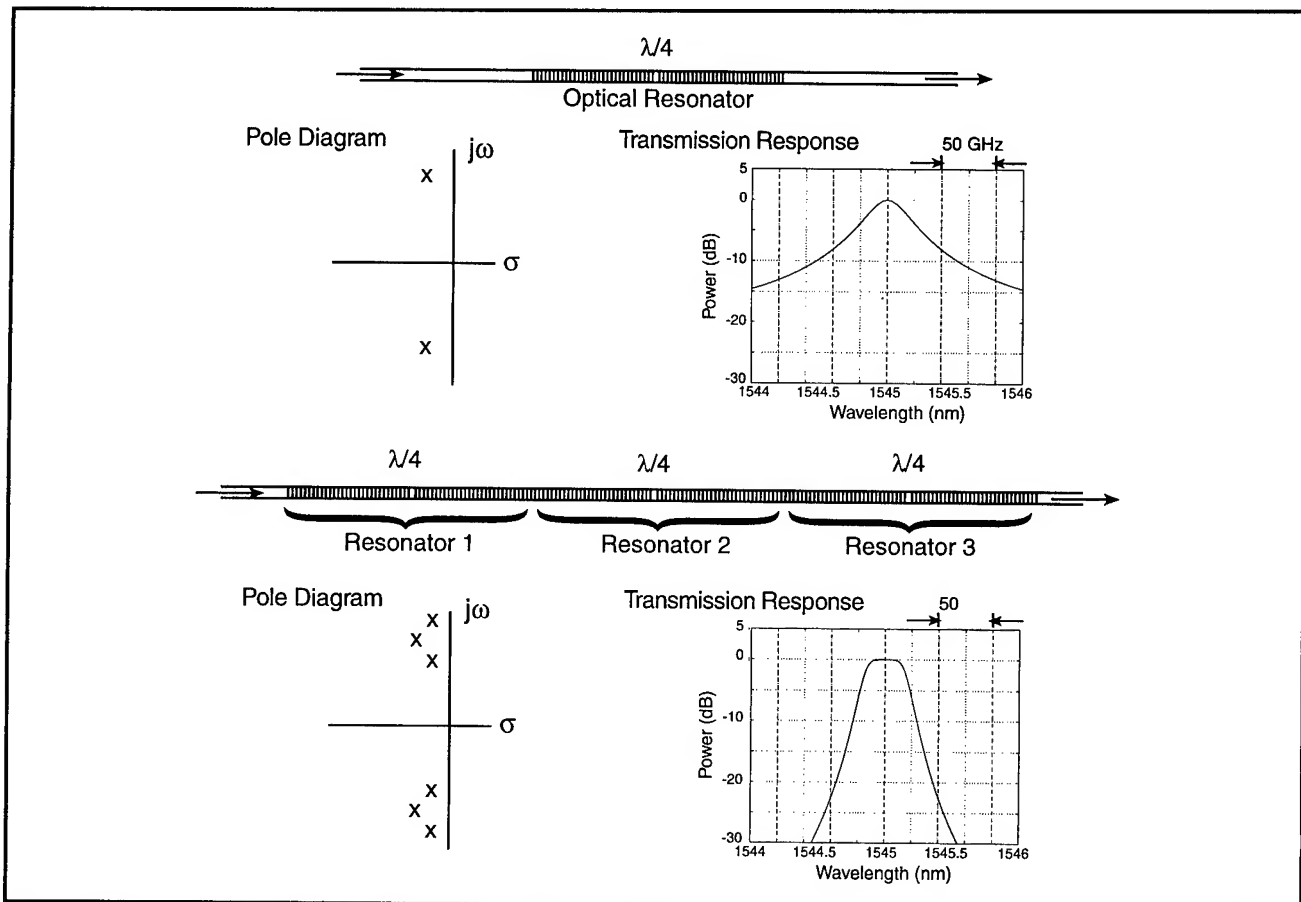


Figure 30. A comparison of the response of a single-pole Lorentzian filter to that of a properly designed multiple-pole filter.

We are developing the techniques to design and fabricate integrated resonant channel-dropping filters and higher-order cascaded quarter-wave shifted Bragg filters. We describe here our progress towards this goal, which includes the design of quarter-wave shifted filters, device fabrication using a combination of spatial-phase-locked e-beam, optical and x-ray lithographies, and finally device measurement and characterization.

The initial waveguide geometry consists of a 4 mm thick SiO_2 lower cladding layer, a 154 nm thick Si_3N_4 core region, topped by another SiO_2 cladding layer of thickness 340 nm. The guiding structure was constructed by optical lithography and reactive ion etching of the top cladding region to form a rib waveguide. After reactive-ion etching, chromium was deposited and a liftoff step performed, resulting in a layer of chromium covering all but the top of the rib waveguide. This layer of chrome acts as an etch mask in subsequent processing of the Bragg gratings, thereby ensuring that the gratings reside only on the top of the rib.

Fabrication of coherent quarter-wave-shifted gratings presents challenges to conventional lithography techniques. While long coherent gratings can be generated using interferometric lithography, quarter-wave-shifted gratings require the use of electron beam lithography (EBL). Since the grating lengths required by these types of filters extend beyond one EBL field, the grating patterns must be composed by stitching together several fields. In order to eliminate interfield stitching errors, which can ruin the coherence of the grating and adversely effect the filter performance, spatial phase locked e-beam lithography (SPLEBL) is used to pattern the gratings. To increase the throughput of the fabrication process, making the device more commercially viable, the gratings are e-beam written only once onto an x-ray mask, which is subsequently used to transfer the gratings to the waveguides.

The chemically amplified positive resist, ESCAP, was used for patterning of the Bragg gratings with x-ray lithography. An alignment step was necessary to place the gratings on the optical waveguides with the correct orientation and at the correct position. Note, however that because the chrome mask automatically confines the gratings to the tops of the rib waveguides, alignment of the gratings in the lateral direction is not critical, provided that the grating patterns are wide enough to cover the waveguides.

The gratings were etched to a target depth of 150 nm using reactive ion etching. In order to achieve a high degree of control for the grating etch depth, a two step etching technique was developed in which the sample is measured at an intermediate point during the etch process to determine the etching rate.

Figure 31 shows the optical transmission response of a single-pole filter, consisting of a quarter-wave shifted grating which spans nine e-beam fields. Figure 32 presents the optical transmission measurements of first-, third-, fifth-, and seventh-order Gaussian multiple pole filters, consisting of one or more cascaded quarter-wave shifted Bragg resonators fabricated by the methods described above. The 0.1 nm resolution of the spectrum analyzer used for the measurements limits the degree to which we can measure the filter roll-off as the filter order is increased.

Our continuing work in this area includes the design and fabrication of more complex device structures such as side-coupled resonators and ultimately integrated channel-dropping filters. We are also investigating other grating based devices such as apodized grating filters where the grating strength varies continuously along the length of the grating. Such devices are predicted to have very low sidelobe levels compared to conventional gratings. Additionally, we plan to construct grating based devices in the $\text{InP}/\text{InGaAsP}$ material system, in the process investigating and developing techniques for reliably regrowing high quality material over etched grating regions.

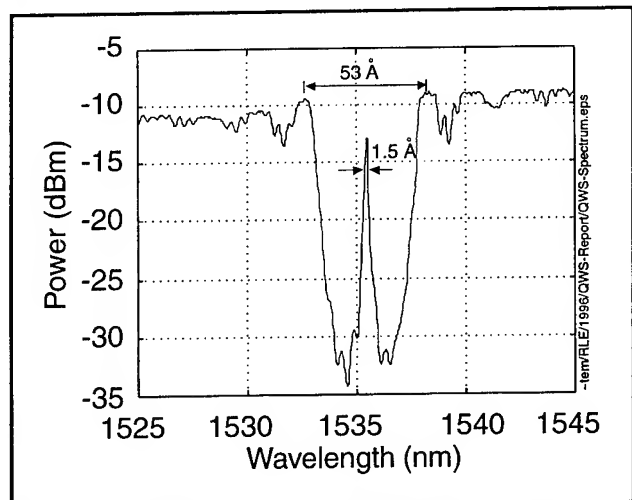


Figure 31. Measured optical transmission response of a single-pole quarter-wave shifted Bragg grating, spanning nine e-beam lithography fields.

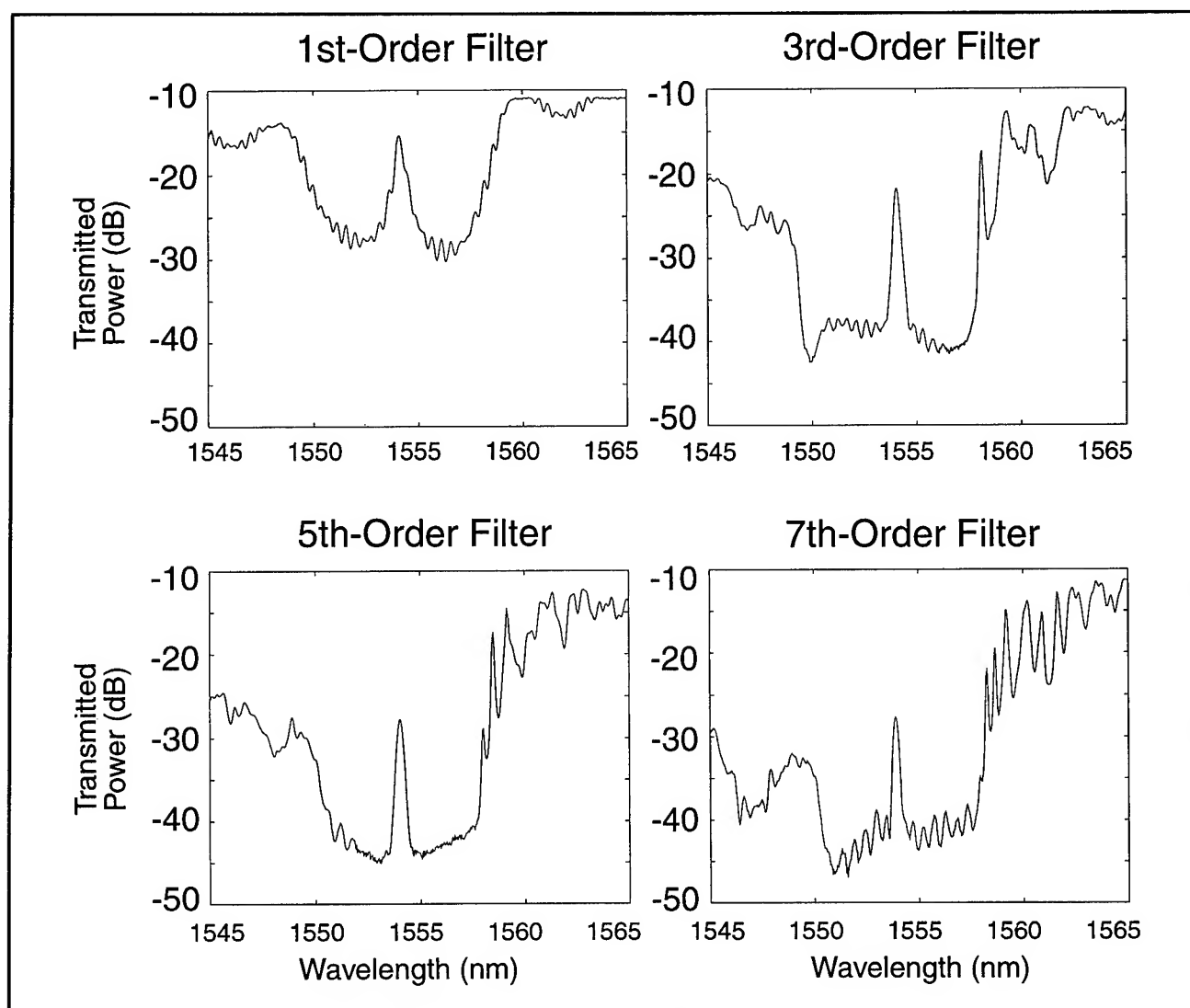


Figure 32. Measured optical transmission response of first-, third-, fifth-, and seventh-order Gaussian multiple pole filters. The shape of the filter response near resonance is not well resolved by the optical spectrum analyzer, but the sidelobes on the long-wavelength side are indicative of a Gaussian multiple-pole filter response.

5.17 Design of a Grating-Based Matched Filter for Optical Communications

Sponsor

Joint Services Electronics Program
Grant DAAH04-95-1-0038

Project Staff

Jay N. Damask, Thomas E. Murphy, Professor
Hermann A. Haus, Professor Henry I. Smith

In any long-distance optical-communications system, broadband noise is introduced during optical amplification. Optical filters are needed to improve the signal-to-noise ratio before the amplified signal is detected. The optimal filter is one that matches the spectrum of the original noise-free signal. Such a matched filter gives the largest possible signal-to-noise ratio when the filtered signal is sampled.

Figure 33 depicts a typical 10 Gb/s optical signal, consisting of a sequence of square pulses 100 ps in duration, each representing a single bit. The corresponding signal spectrum has the characteristic $\text{sinc}(\Delta\omega T)/\Delta\omega T$ shape, centered at the optical carrier wavelength of 1.55 μm .

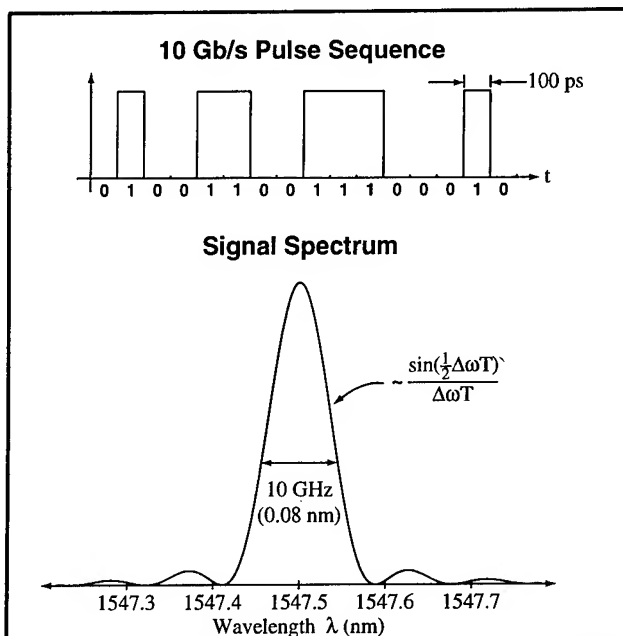


Figure 33. A typical 10 Gb/s binary encoded optical signal, and the corresponding signal spectrum. Note that only the slow 10 GHz amplitude modulation is depicted in the pulse diagram. The rapid oscillations associated with optical carrier frequency are not shown.

The reflection spectral response of a properly designed weak Bragg grating can match the spectrum of the incident pulse stream, thereby providing a convenient way to realize a matched filter. In order for the grating to have the desired spectral width, the grating length must be chosen such that the down and back propagation time of light in the grating is equal to one pulse duration. For SiO_2 -based waveguides, this corresponds to a grating length of ~ 1 cm. In order for the grating spectrum to be centered at a free-space wavelength of 1.55 μm (commonly used in optical communications), the period of the Bragg grating must be approximately 530 nm.

The weak grating filter operates as a single pass filter where the grating reflects a small portion of the signal back into the input port. The reflection spectrum of the weak grating has the same $\text{sinc}(\Delta\omega T)$ shape as an incident pulse stream. However, this response comes at the expense of a decreased power return, because much of the incident signal passes through the grating without being reflected. If the grating is made stronger, to try to increase the power return, the response no longer resembles a sinc function but rather has a characteristic plateau response associated with a strong Bragg grating.

Figure 34 depicts a weak Bragg grating filter, constructed in a Mach-Zehnder interferometer. The Mach-Zehnder configuration provides a means of spatially separating the reflected signal from the input signal. In this device, two identical grating filters are placed in opposite arms of a Mach-Zehnder interferometer. Light is launched in the upper port of the device and a codirectional coupling region transfers half of the signal to the lower waveguide. A portion of the light in each arm of the interferometer is reflected by the two identical weak gratings. The reflected signals recombine in the 50 percent coupling region and emerge in the lower port of the device.

Because one function of the device is to filter out broadband noise introduced during optical amplification, it is counterproductive to reamplify the filtered signal, as this would only reintroduce noise. Consequently, it is important to minimize the total insertion loss of the device. Sources of loss include material loss, bending-induced loss, and fiber-coupling loss. In design of the device, we have investigated each of these loss factors in an attempt to minimize the total insertion loss without compromising the device performance.

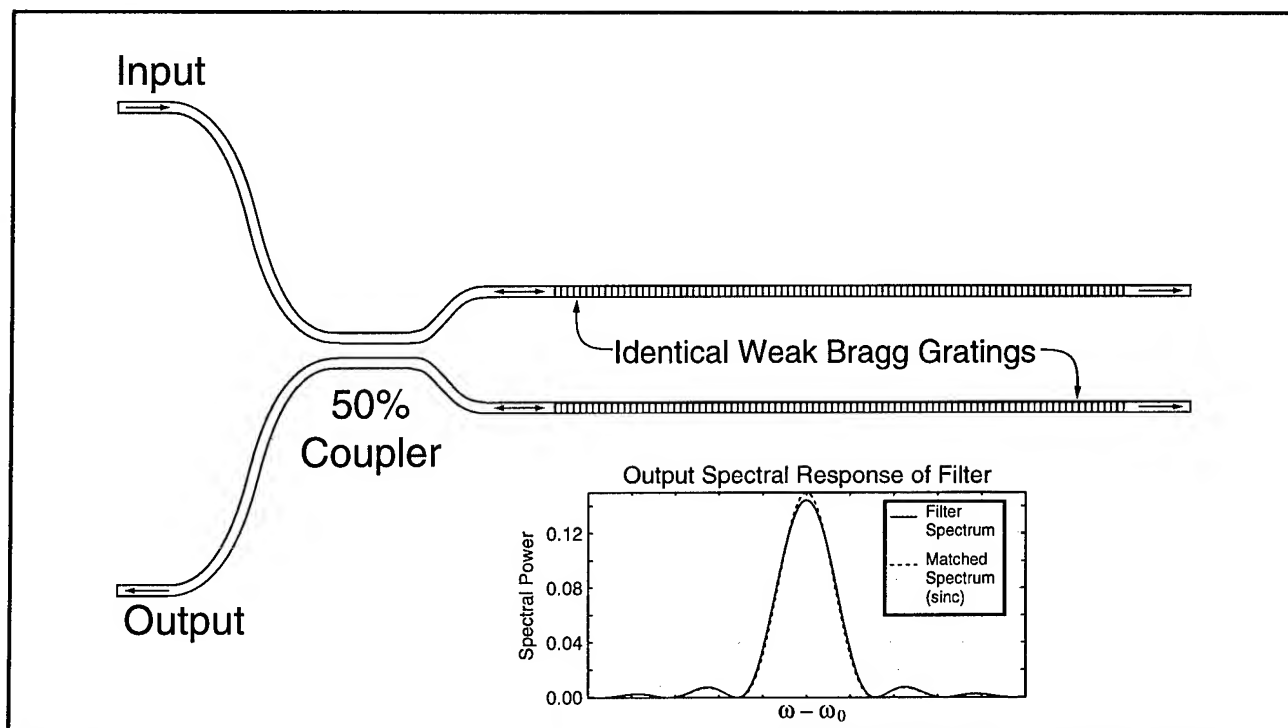


Figure 34. Two identical weak Bragg gratings, constructed in a Mach-Zehnder configuration. The Mach-Zehnder configuration provides spatial separation of the input signal and the filtered signal.

The waveguides will be fabricated from commercially available Ge doped SiO_2 slab waveguides. This material system has been shown to have low material loss, and favorable device dimensions. Because the index of refraction of SiO_2 is comparable to that found in most optical fibers, the device allows for good fiber coupling. Additionally, Ge doped SiO_2 has been shown to have photorefractive properties: irradiating the Ge doped core region with UV light can induce a small, permanent index change in the material. This effect could be used to adjust the relative phase between the two arms of the interferometer.

We plan to use optical lithography and reactive ion etching to construct the optical waveguides for this device. Interferometric lithography will be used to generate the long, spatially coherent gratings on an x-ray mask. The grating patterns can then be transferred to the waveguides using x-ray lithography, and reactive ion etched to form the grating corrugations.

We have completed the design of these filters and are presently fabricating them. The technologies required to build these filters should prove useful in the future for design and fabrication of related grating based devices, such as strong-grating filters and apodized grating filters, which could find important applications in wavelength division multiplexing.

5.18 High-Dispersion, High-Efficiency Transmission Gratings for Astrophysical X-ray Spectroscopy

Sponsor

National Aeronautics and Space Administration
Contract NAS8-38249
Grant NAGW-2003

Project Staff

Richard J. Aucoin, Robert C. Fleming, Dr. Mark L. Schattenburg, Professor Claude R. Canizares, Professor Henry I. Smith

Through a collaboration between the Center for Space Research (CSR) and the Nanostructures Laboratory (NSL), transmission gratings are provided for the Advanced X-ray Astrophysics Facility (AXAF) x-ray telescope, scheduled for launch on the NASA Space Shuttle in 1998. Many hundreds of large area, gold transmission gratings of 200 nm and 400 nm periods are required. In order to achieve spectrometer performance goals, the gratings need to have very low distortion. The gratings will provide high resolution x-ray spectroscopy of astrophysical sources in the 100 eV to 10 keV band.

The need for high grating quality and an aggressive production schedule require the development of a robust, high-yield manufacturing process. We have adopted a scheme involving interference lithography with tri-level resist, followed by cryogenic reactive-ion etching and gold electroplating. A chemical etching step then yields membrane-supported gratings suitable for space use. The gratings undergo extensive testing before being released for use in the spectrometer.

The Space Microstructures Laboratory, a new cleanroom fabrication facility, on the fourth floor of Building 37 (adjacent to the Gordon Stanley Brown Building) has been constructed in order to fabricate AXAF gratings. The proximity of the new lab to the Microsystems Technology Laboratory (MTL) has allowed the lab to share many MTL services such as DI and process water, nitrogen, process vacuum, and waste drains. The laboratory space includes 1700 square feet of Class 100 and associated support areas. Production of flight gratings is underway.

5.19 Submicrometer-Period Transmission Gratings for X-ray and Atom-Beam Spectroscopy and Interferometry

Sponsors

Joint Services Electronics Program
Grant DAAH04-95-1-0038
National Aeronautics and Space Administration
Contract NAS8-38249
Grant NAGW-2003

Project Staff

James M. Carter, Jeanne M. Porter, Timothy A. Savas, Dr. Mark L. Schattenburg, Professor Henry I. Smith

Transmission gratings with periods of 100-1000 nm are finding increasing utility in applications such as x-ray, vacuum-ultraviolet, and atom-beam spectroscopy and interferometry. Over 20 laboratories around the world depend on MIT-supplied gratings in their work. For x-ray and VUV spectroscopy, gratings are made of gold and have periods of 100-1000 nm and thicknesses ranging from 100-1000 nm. They are most commonly used for spectroscopy of the x-ray emission from high-

temperature plasmas. Transmission gratings are supported on thin ($1\text{ }\mu\text{m}$) polyimide membranes or made self supporting ("free standing") by the addition of crossing struts (mesh). For short x-ray wavelengths membrane support is desired, while for the long wavelengths a mesh support is preferred in order to increase efficiency. Fabrication is performed by interferometric lithography combined with reactive-ion etching and electroplating. Progress in this area tends to focus on improving the yield and flexibility of the fabrication procedures.

Another application is the diffraction of neutral atom and molecular beams by mesh supported gratings. Lithographic and etching procedures have been developed for fabricating free-standing gratings in thin silicon nitride (SiN_x) supported in a Si frame. Figure 35 shows a free-standing 100 nm period grating in 1000 Å-thick silicon nitride.

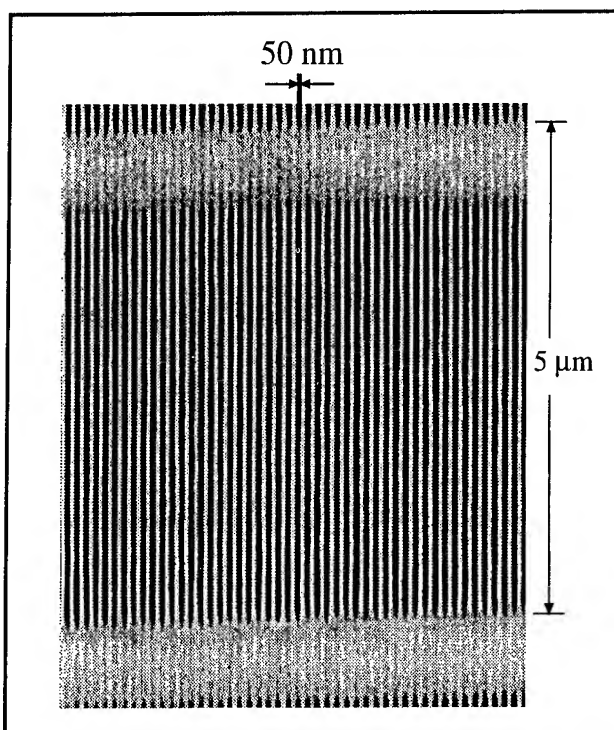


Figure 35. Scanning electron micrograph of a free-standing 100 nm period grating in a silicon nitride membrane of area $500\text{ }\mu\text{m}$ by $5\text{ }\mu\text{m}$.

We have established a collaboration with the Max Planck Institute in Goettingen, Germany which will utilize our gratings of 100 nm period in diffraction and interferometer experiments using He atom beams.

5.20 Publications

5.20.1 Journal Articles

- Aucoin, R.J., and M.L. Schattenburg. "Optically-Matched Tri-Level Resist Process for Nanostructure Fabrication." *J. Vac. Sci. Technol. B* 13: 3007-3011 (1995).
- Grayson, M., D.C. Tsui, and M. Shayegan. "Far-infrared Emission from Hot Quasi-One-Dimensional Quantum Wires in GaAs." *Appl. Phys. Lett.* 67: 1564 (1995).
- Moon, E.E., P.N. Everett, and H.I. Smith. "Immunity to Signal Degradation by Overlayers Using a Novel Spatial-Phase-Matching Alignment System." *J. Vac. Sci. Technol. B* 13: 2648-2652 (1995).
- Savas, T.A., S.N. Shah, M.L. Schattenburg, J.M. Carter, and H.I. Smith. "Achromatic-Interferometric Lithography for 100 nm-Period Gratings and Grids." *J. Vac. Sci. Technol. B* 13: 2732-2735 (1995).
- Smith, H.I. "100 Years of X-rays: Impact on Micro- and Nanofabrication." *J. Vac. Sci. Technol. B* 13: 2323-2328 (1995).
- Smith, H.I. "X-ray Lithography for Microelectronics." Jubilee Symposium, *X-rays in Natural Science and Medicine*, Uppsala University, Sweden, March 23-24 1995; *Physica Scripta*. Forthcoming.
- Smith, H.I., M.L. Schattenburg, S.D. Hector, J. Ferrera, E.E. Moon, I.Y. Yang, and M. Burkhardt. "X-ray Nanolithography: Extension to the Limits of the Lithographic Process." *Nanotechnology*, Special Issue of *Microelectron. Eng.* Forthcoming.
- Wong, V.V., A. Yasaka, and H.I. Smith. "Resist Planarization over Topography using Ion Implantation." *J. Vac. Sci. Technol. B* 13: 2797-2800 (1995).
- Wong, V.V., J. Ferrera, J.N. Damask, T.E. Murphy, and H.I. Smith. "Distributed Bragg Grating Integrated Optical Filters; Synthesis and Fabrication." *J. Vac. Sci. Technol. B* 13: 2859-2864 (1995).
- Yang, I.Y., J.M. Carter, S.E. Silverman, S. Rishton, D.A. Antoniadis, and H.I. Smith. "Combining and Matching Optical, E-beam and X-ray Lithographies in the Fabrication of Si CMOS Circuits with 0.1 and Sub-0.1 μm Features." *J. Vac. Sci. Technol. B* 13: 2741-2744 (1995).
- Zhao, Y., D.C. Tsui, M.B. Santos, and M. Shayegan. "Grating-Induced Cyclotron-Resonance Anomaly in GaAs/Al_{1-x}Ga_xAs Heterostructures." *Phys. Rev. B* 51: 174 (1995).

5.20.2 Conference Proceedings

- Burkhardt, M., S. Silverman, H.I. Smith, D.A. Antoniadis, K.W. Rhee, and M.C. Peckerar. "Gap Control in the Fabrication of Quantum-Effect Devices Using X-Ray Nanolithography." *Microelectron. Eng.* 27: 307-310 (1995).
- Choi, W.-Y., V.V. Wong, J.C. Chen, H.I. Smith, and C.G. Fonstad. "Design and Fabrication using X-Ray Lithography of Ridge-Waveguide Distributed Feedback Structures on InP." *International Conference on InP and Related Compounds*, Santa Barbara, California March 1994.
- Ferrera, J., M.L. Schattenburg, and H.I. Smith. "Analysis of Distortion in Interferometric Lithography." Submitted to *40th International Symposium on Electron Ion and Photon Beam Technology and Nanofabrication*.
- Moon, E.E., P.N. Everett, and H.I. Smith. "Simultaneous Measurement of Gap and Superposition in a Precision Aligner for X-ray Nanolithography." Submitted to *40th International Symposium on Electron Ion and Photon Beam Technology and Nanofabrication*.
- Rooks, M.J., R.C. Tiberio, M. Chapman, T. Hammond, E. Smith, A. Lenef, R. Rubenstein, D. Pritchard, S. Adams, J. Ferrera, and H.I. Smith. "Coherence and Structural Design of Free-Standing Gratings for Atom-Wave Optics." Presented at the *MicroProcess Conference*, Sandai, Japan, July 1995. Submitted to *Jap. J. App. Phys.*
- Savas, T.A., M.L. Schattenburg, J.M. Carter, and H.I. Smith. "Large-Area Achromatic Interferometric Lithography for 100 nm-Period Gratings and Grids; With Novel Applications." Submitted to *40th International Symposium on Electron Ion and Photon Beam Technology and Nanofabrication*. Symposium on Elect. Ion and Photon Beam Technol. and Nanofab.
- Smith, H.I. "A Maskless X-ray Projection Pattern Generator." *40th International Symposium on*

Electron Ion and Photon Beam Technology and Nanofabrication.

Yang, I.Y., D.A. Antoniadis, and H.I. Smith. "Fabrication of Back-gated CMOS Devices Using Mixed and Matched Optical and X-ray Lithographies." Submitted to *40th International Symposium on Electron Ion and Photon Beam Technology and Nanofabrication.*

5.20.3 Theses

Burkhardt, M. "Fabrication Technology and Measurement of Coupled Quantum Dot Devices." Ph.D diss. Dept. of Electr. Eng. and Comput. Sci., MIT, 1995.

Shah, S. "Free-standing 100 nm Period Gratings Produced by Achromatic Holographic Lithography." M.E. thesis. Dept. of Electr. Eng. and Comput. Sci., MIT, 1995.

Wong, V.V. "Fabrication of Distributed Feedback Devices Using X-ray Lithography." Ph.D. diss. Dept. of Electr. Eng. and Comput. Sci., MIT, 1995.

Yasaka, A. "Feasibility Study of Spatial-Phase-Locked Focused-Ion-Beam Lithography." S.M. thesis. Dept. of Mat. Sci. and Eng., MIT, 1995.

Chapter 6. Single-Electron Spectroscopy

Academic and Research Staff

Professor Raymond C. Ashoori, Dr. Stuart Tessmer, Dr. Nikolai Zhitenev

Graduate Students

David Berman, Mikhail G. Brodsky, Ho Bun Chan, Paul I. Glicofridis

Undergraduate Students

William M. LeBlanc, Aaron S. Cohen, Daniel M. Silevitch

6.1 Goals and Objectives

Several years ago, we developed a technique known as single-electron capacitance spectroscopy (SECS). We showed that a very sensitive electrometer could detect the motion of a single remote electron inside of a solid, and capacitance-voltage characteristics of very small structures could be performed. For small objects such as quantum dots, a spectrum of electron additions as a function of a gate bias can be clearly observed. We have produced quantum dots containing as few as one electron and up to 60 electrons. Additionally, electrons can be observed to enter different types of traps. Electron spectra for single impurity atoms have been determined this way.

SECS allows us to observe and manipulate single electrons to a previously unimagined degree. The main aim of our work is to advance and utilize these methods. All our work utilizes our specialized techniques for measuring very small amounts of electrical charge. The effort is divided into four projects which, while distinct, use considerably overlapping methods.

Our most significant advance in SECS will lie in our ability to perform the technique in a scanning fashion. By scanning a fantastically sensitive charge sensor, we are attempting to do something that is well beyond the capabilities of ordinary scanning tunneling microscopy: we will be able to "look" underneath surfaces. Further development of the method will allow scanning tunneling microscopy and spectroscopy of insulating surfaces.

A second key advance lies in our time domain SECS technique. We have developed a method which allows us to record, in the time domain, the motion of charge within a sample. This technique allows us to determine the nonlinear response of a

sample to which we cannot make electrical contacts. So far, we have used the method to study the characteristics of electron tunneling between a two-dimensional electron gas and a three-dimensional electron gas. This measurement was not possible before. Our plan is to eventually apply this technique to the study of single traps containing single electrons.

Presently, SECS is a difficult technique to employ. We have used HEMT transistors to measure very small amounts of charge. Typically, electron motion in our samples results in a small fraction of one electron charge appearing at the gate of this transistor. There is just barely enough sensitivity to detect this charge, and large amounts of signal averaging are required. We plan to change this by using single-electron transistors (SETs). SETs will greatly improve our capacitance spectroscopy measurements. We expect signal to noise levels to increase by a factor of 100 compared to our measurements using field effect transistors. We now have functioning aluminum-aluminum oxide SETs.

Finally, we are extending the charge sensitivity that we have developed for the SECS technique to study other systems. Until our recent experiments, sensitive charge sensors had never been used to study transport in semiconductors. There is a wealth of experiments for which they may be employed to greatly enhance sensitivity. HEMT transistors and FETs will allow us to measure unprecedentedly small conductances in objects such as lateral quantum dots, point contacts, and tunnel junctions. They also allow study of the quantum Hall effect in a fundamentally new way. We have developed a capacitance experiment which we feel gives the clearest picture to date regarding the nature of edge states in the quantum Hall effect.

6.2 High-Resolution Scanning Capacitance Spectroscopy of Semiconductor Structures

Sponsors

David and Lucille Packard Foundation
Joint Services Electronics Program
Grant DAAH04-95-1-0038
U.S. Navy - Office of Naval Research
Grant N00014-93-1-0633

Project Staff

Dr. Stuart Tessmer, Aaron S. Cohen, Daniel M. Silevitch, William M. LeBlanc, Professor Raymond C. Ashoori

The first SECS measurements in a disordered 1 micron diameter quantum dot revealed that there exists a fascinating diversity of quantum states in this system. The magnetic field evolution of the spectra indicated states in which single electrons were trapped on (1) potential fluctuations, (2) single silicon impurities, and (3) strange sites which bound two electrons at precisely the same energy in spite of the Coulomb repulsion between electrons (Negative-U centers). The latter states have been of significant theoretical interest recently. Despite all

of the information in the spectra, one gnawing question persists: What do the states "look" like? This kind of question can only be answered using a scanning probe technique. This probe will also help to answer critical questions related to localization in the quantum Hall effect, the structure of quantum Hall edge states, and the nature of dangling bonds in the Si-SiO₂ interface.

We have constructed a scanning tunneling microscope (STM), presently functioning at room temperature, which we are preparing to cool down to 300 mK. The room temperature STM works in a mode which is entirely different from a typical scanning tunneling microscope. Rather than detecting a current from electron tunneling between a scanning tip and the sample, our STM is sensitive to the induced charge in the vicinity of the tip. This means that the STM can be used to study *insulating* surfaces and to do spectroscopy on *buried* traps and surfaces. We are now taking our first images using the new method. It is our hope that this method will vastly expand the utility of STM. Shown in figure 1 is a scanning tunneling image (a) and a scanning capacitance image (b) taken with our microscope. Remarkably, the scanning capacitance image was taken with the tip at a distance of 700 Å from the sample surface.

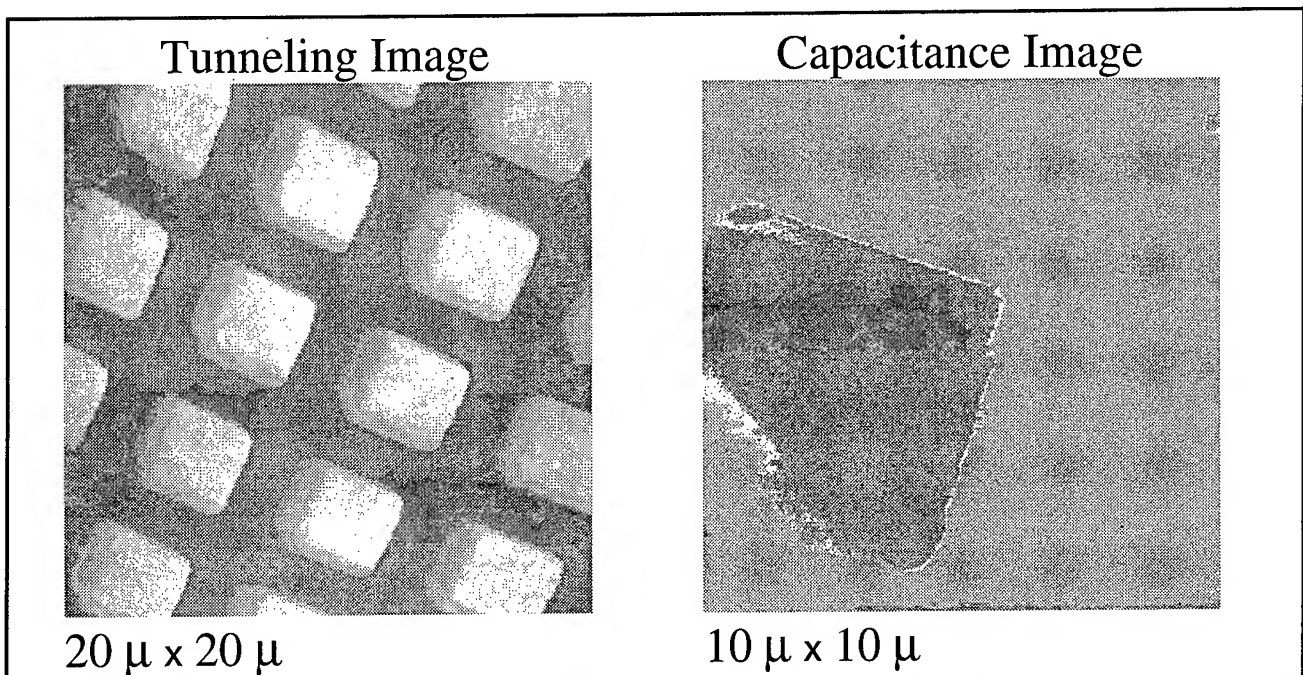


Figure 1. Scanned images of a microfabricated Au sample. The tunneling image of the surface topography shows an array squares of height 480 Å. It was acquired with the use of feedback, so that the tip maintained a 5 Å distance from the surface. Conversely, the capacitance image was acquired without feedback using a tip-sample distance of roughly 500 Å. The contrast reflects both the geometrical capacitance between the tip and surface and the impedance of an individual square with respect to the substrate.

6.3 Single Electron Transistors for Studying Quantum Dots and other Nanoscale Objects

Sponsors

Joint Services Electronics Program
Grant DAAH04-95-1-0038
National Science Foundation
Young Investigator Award
U.S. Navy - Office of Naval Research
Grant N00014-93-1-0633

Project Staff

David Berman, Professor Raymond C. Ashoori,
Professor Henry I. Smith

The major research thrust of our group is the study of the motion of small amounts of charge. In our experiments in capacitance spectroscopy, charges from a quantum dot sample are coupled to an amplifier. It is extremely important that the amplifier is located as close to the sample as possible to reduce the capacitance of the gate electrode, since the signal at the amplifier is inversely proportional to the gate electrode capacitance. This capacitance includes the coupling capacitance to the quantum dot, the gate capacitance of the transistor (the amplifier is usually a HEMT transistor), and all stray capacitance to the rest of the world. We are using the single-electron transistor (SET) as an ultra-sensitive electrometer in this application because it has a much smaller gate capacitance than the HEMT transistor. Also the SET can be fabricated in very close proximity to the quantum dot, thus reducing stray capacitance.

To further increase the sensitivity of our measurement, we will couple our signals into the central island of a SET with a gate. We will bias this gate separately with a specially designed low capacitance resistive element. In previous experiments with SET electrometers, the central island of the SET was directly coupled to the device being measured. By capacitively coupling a gate to the quantum dot, we hope to gain a threefold advantage. First, the size of the Coulomb blockade region is independent of the length of the gate wire and the size of the quantum dot, since it is capacitively coupled. Second, the potential on the coupling electrode is not affected by the SET itself, since the tunnel junctions are decoupled from this electrode. Third, we have greater control over the biasing of the amplifier circuit. We can bias the gate electrode with a resistor, as we have done in our circuits employing HEMT transistors. This would give us the ability to bias the gate of the SET at the optimum position. In addition, since we have a back contact to the quantum dot, we would also be

able to set the voltage across the quantum dot exactly.

Our single-electron transistors are composed of aluminum. Tunnel junctions, which establish most of the operational characteristics of the SET are formed by a small overlap of two layers of metal with a thin dielectric layer in between. This dielectric layer is formed by oxidizing the surface of the bottom layer of metal and then introducing the top layer. The thickness of this oxide layer is only a few atomic spacings, so it is very important to ensure that it is very uniform and pure.

The tunnel junctions have a capacitance mostly determined by the area of the metal overlap. In order for SET to operate properly, this overlap area must be less than $0.01 \mu\text{m}^2$. Electron beam lithography is used to pattern our devices. It is performed on a JEOL 6400 scanning electron microscope which we modified to be able to do lithography. The Ashoori group installed a pattern generation system on the SEM to control and scan the beam of the SEM. Using this system, we have been successful in patterning 60 nm features in electron-beam resist.

We form the metal layers in an e-beam metal evaporator. The high degree of directionality of the evaporated metal gives us more control over the patterning of the metal. Both layers of metal of the transistor are evaporated in one vacuum cycle, to prevent the bottom layer, which must be oxidized to form the tunnel barrier, from being exposed to oxygen-rich air, which would prevent us from controlling the thickness of the barrier. Double-angle evaporation, or shadow evaporation, is the method which we use to fabricate both layers so that the small overlap between them forms the tunnel junctions. Figure 2 shows a schematic of the shadow evaporation technique.

The electron-beam resist which we use in the shadow evaporation method plays a crucial role in the success of the process. In addition to the usual planar pattern, we must also engineer the profile of the patterned resist. As depicted in figure 1, the resist consists of two layers. The lower layer, MAA copolymer, is more sensitive to electron-beam bombardment than the top layer, PMMA. Thus, during development, MAA is dissolved more rapidly than PMMA. The result is that we get a large degree of undercut in the pattern profile. The result of this undercut is that we can get a suspended bridge in the PMMA by placing two lines in close proximity. In fact, we use a two-step development process to increase the extent of undercut. First, we develop the sample in a solution of methyl isobutyl ketone (MIBK) and isopropyl alcohol, which develops exposed regions of PMMA and MAA.

Then, we develop in a solution of poly glycol methyl ether acetate (PGMEA) and ethanol, which develops only the MAA copolymer layer. This technique allows us to increase the degree of undercut without affecting the linewidth. This process is shown in figure 3.

After its development, the sample is placed in a metal evaporator on a tilting stage. In order to form tunnel junctions, we perform two separate evapor-

ations at two different angles, as shown in figure 4. The oxide barrier is formed by introducing a controlled amount of oxygen gas into the chamber after the first metal evaporation.

We have recently produced our first SETs for measuring single quantum dots on a GaAs sample. Our first measurements using these devices are presently underway.

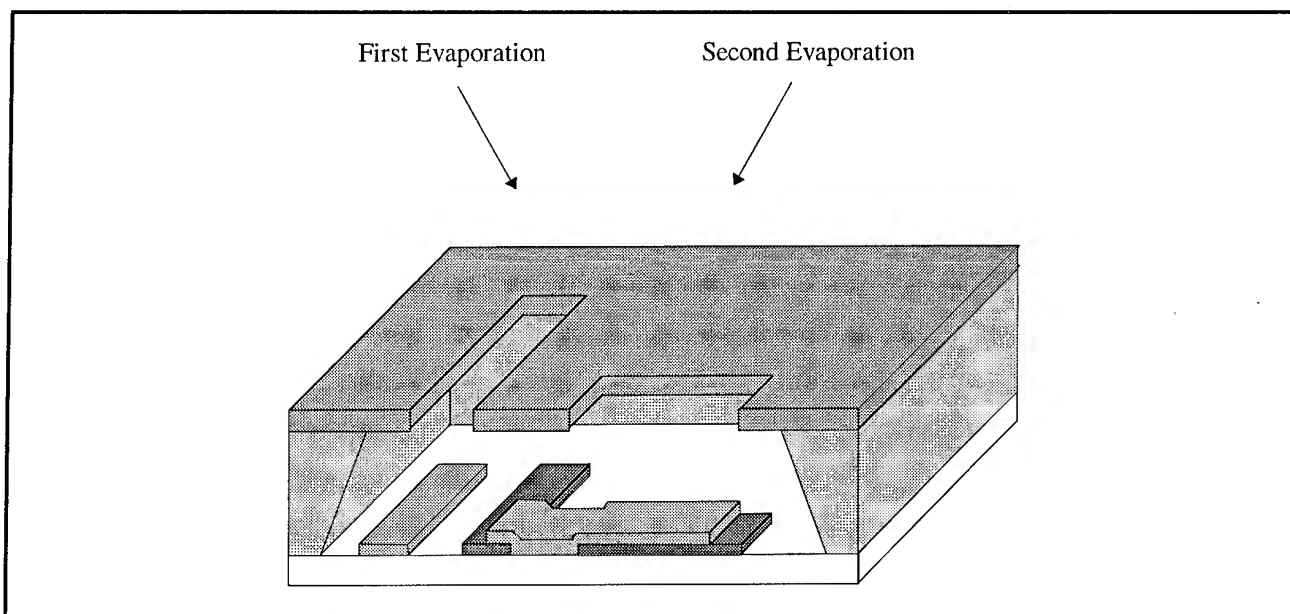


Figure 2. Double-angle evaporation schematic.

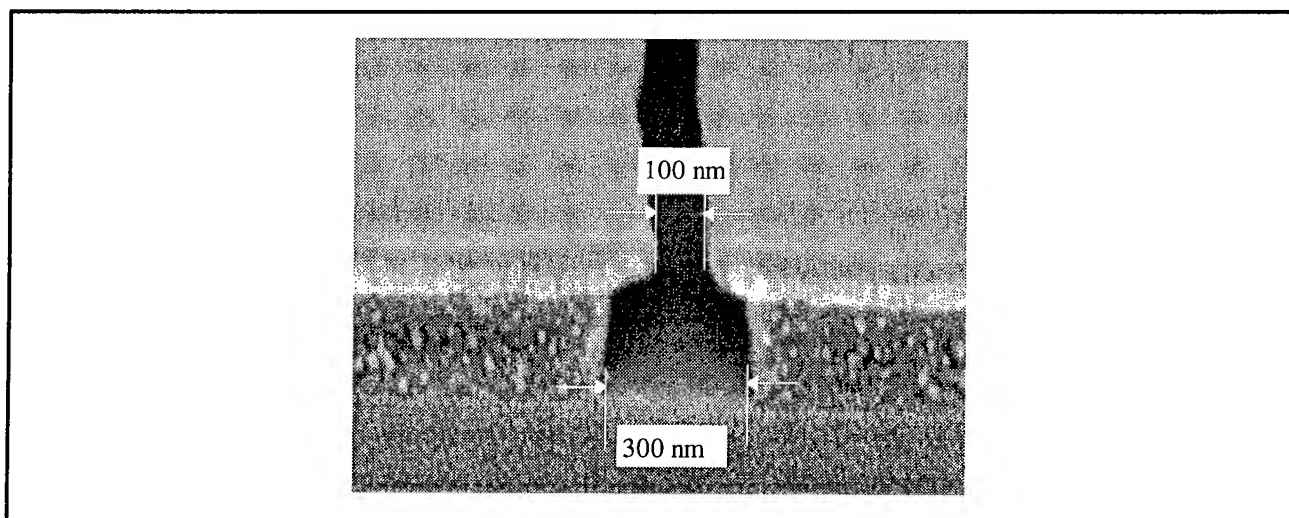


Figure 3. A 100 nm line drawn in PMMA and copolymer resists using the PGMEA process.

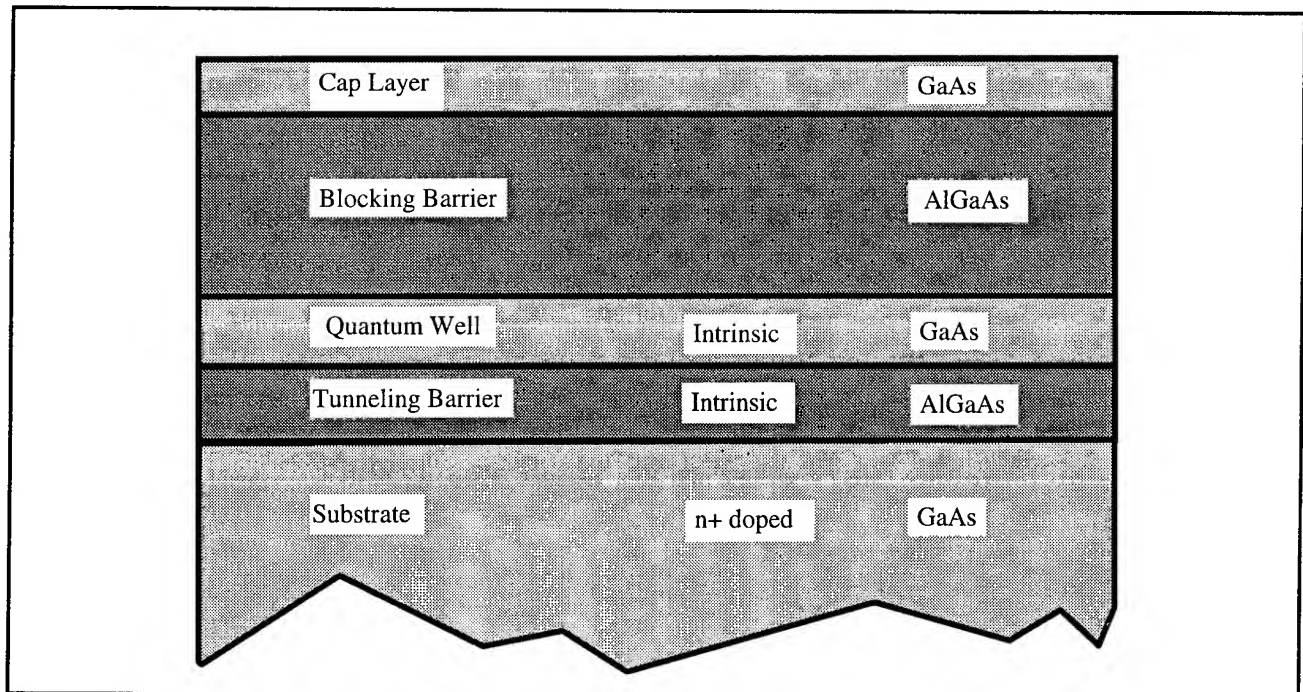


Figure 4. Structure for magnetocapacitance measurements of the 2DEG.

6.4 Time Domain Capacitance Spectroscopy

Sponsors

Joint Services Electronics Program
Grant DAAH04-95-1-0038
National Science Foundation
Young Investigator Award
U.S. Navy - Office of Naval Research
Grant N00014-93-1-0633

Project Staff

Ho Bun Chan, Professor Raymond C. Ashoori

We have developed a method which allows us to record, in the time domain, the motion of charge within a sample. This technique permits the determination of the nonlinear response of a sample to which we cannot make electrical contacts. So far, we have used the method to study the characteristics of electron tunneling between a two-dimensional and a three-dimensional electron gas. This measurement was not possible previously. We are now working to apply this technique to the study of single traps containing single electrons.

6.4.1 Motivation

One of the chief limitations of SECS measurements have been that they only probe the ground electronic states of quantum dots, impurities, and other charge traps. We have devised a method for using SECS to probe excited states. We expect that this will be a very powerful probe, capable of determining excitation spectra for single traps of many sorts. We decided to first try the technique on samples which would create much larger signals than would quantum dots. Our first experiments using this new technique have been carried out on a two-dimensional electron gas sample. We will describe these measurements first and then discuss how the measurement can be extended to be used on quantum dot samples.

We have been using magnetocapacitance measurements to study zero bias tunneling into a two-dimensional electron gas (2DEG). A magnetic field induced energy gap is observed in the tunneling spectrum of the 2DEG at low temperatures. This suppression of tunneling is believed to be a many body phenomena and is interpreted as a manifestation of a Coulomb gap.

Our experiment is performed on a GaAs tunneling capacitor (figure 4) grown by molecular beam epitaxy. The bottom electrode consists of an n+ doped GaAs region. Above this an AlGaAs tunnel barrier is grown followed by a GaAs quantum well defining the 2DEG. After the quantum well, there is a thick AlGaAs blocking barrier which prevents

electrical conduction between the quantum well and the top electrode. A DC bias is applied at the top electrode to control the number density of electrons in the quantum well. Sinusoidal excitations are used to measure the equilibrium tunneling conductivity. The Fermi energies on both sides of the tunnel barrier are kept within kT of each other. Time domain experiments yield a much clearer picture of the tunneling than our previous frequency domain measurements. The chief reason is that, using the time domain, we can easily determine the I-V characteristic for tunneling. Capacitance measurements are only useful for the tunneling resistance for $V=0$.

In this new experiment, we start with the 2DEG in equilibrium with the n^+ substrate. A sudden voltage step is then applied to create an offset in the Fermi energies between the two sides of the tunnel barrier (figure 5). As the electrons tunnel, this offset in Fermi energies equilibrate to zero. The amount of charge induced on the top gate is recorded in real time as electrons tunnel into the 2DEG. If the tunneling conductance is independent of the excitation amplitude, a familiar RC decay will be observed. The situation is different when the magnetic field reduces the tunneling density of states at the Fermi energy of the 2DEG. The tunneling conductance becomes voltage dependent and the signal deviates from a pure exponential decay.

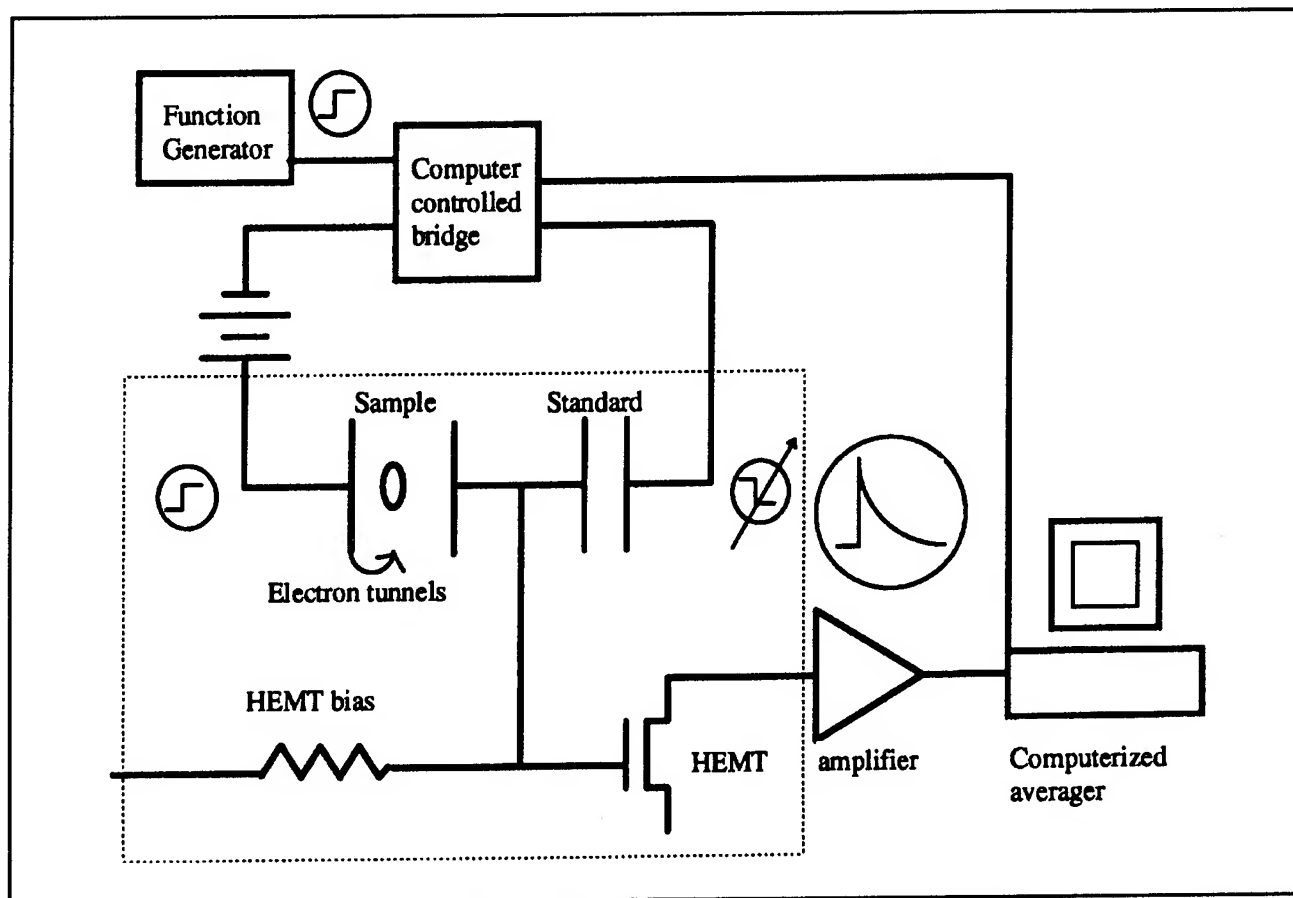


Figure 5. Schematic of the time domain experiment. Presently, the sample is a "tunnel capacitor" containing a 2DEG. In the future, it will be a quantum dot. Components enclosed in box sit inside cryostat.

This new technique of time-resolved capacitance measurement has a number of advantages compared to the frequency domain technique. In the frequency domain measurement, electrons tunnel into and out of the 2DEG with a frequency of the sinusoidal excitation. It is not possible to distinguish between tunneling of electrons into the 2DEG from the n^+ substrate or from the 2DEG into the n^+ substrate. In the time domain experiment, tunneling in both directions can be measured separately by

using steps of opposite polarity. Preliminary data indicate that an asymmetry of the tunnel gap does exist between electrons tunneling into and out of the 2DEG. The degree of asymmetry seems to depend strongly on the filling factor in the 2DEG. Even in the absence of a magnetic field, we have been able to detect the effect of momentum conservation on electrons tunneling into and out of the 2DEG. Consider the case where we increase the density of electrons in the 2DEG so that the two-

dimensional Fermi disk has a larger diameter than the three-dimensional Fermi sphere in the n^+ substrate. The tunneling rate for electrons entering the 2DEG will be suppressed because all the states which satisfy momentum conservation are already filled. On the other hand, such suppression does not exist for electrons tunneling out of the 2DEG since the states in the 3D substrate are empty. Our preliminary data demonstrate clearly the effect of this 2D-3D momentum conservation.

This voltage stepping technique has other advantages over the sinusoidal technique. In the frequency domain experiment, small excitations are

used so that the system is very close to equilibrium. Results from larger excitations are difficult to interpret because of the oscillating energy configuration in the sample. In the time domain experiment, the excitation is in the form of a voltage step. The energy configuration of the sample immediately after the voltage step can easily be determined. We can easily and precisely map out the excitation dependence of electron tunneling, a feat that is impossible using sinusoidal excitations. We will directly extend this technique for studying excited states in quantum dots using the method depicted in figure 6.

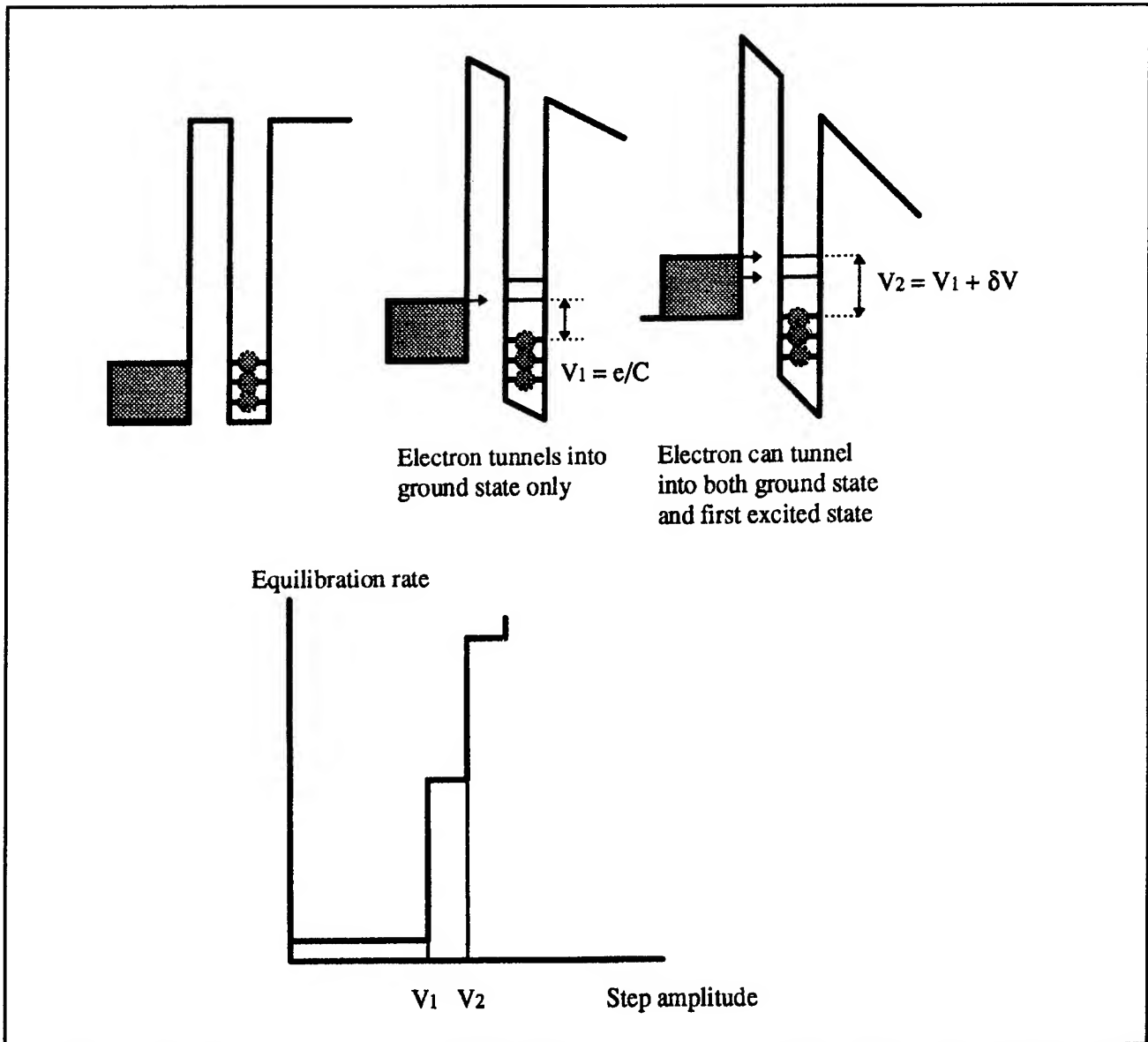


Figure 6. (top) Schematic of the use of the stepping technique to study quantum dots. (bottom) The expected change in the equilibration rate as tunneling is permitted for higher lying states of the dot.

6.5 Use of High Sensitivity Electrometry to Study the Quantum Hall Effect

Sponsor

David and Lucille Packard Foundation
 Joint Services Electronics Program
 Grant DAAH04-95-1-0038
 National Science Foundation
 Young Investigator Award
 U.S. Navy - Office of Naval Research
 Grant N00014-93-1-0633

Project Staff

Dr. Nikolai Zhitennev, Mikhail G. Brodsky, Professor
 Raymond C. Ashoori

We have developed a new technique for direct investigation of the resistance of incompressible strips adjoining edge channels under quantum Hall effect conditions. We measure the frequency dependence of the capacitance of a small gate covering the edge and part of a 2DEG from 100 Hz to 20 MHz, employing an ac cryogenic bridge. Geometrical capacitances are 0.01-1 pF, depending on the size of the gate. Varying the gate bias changes the character of the electron gas underneath the gate. While the portion of the electron gas nearest to the edge remains compressible (edge channel), the remainder evolves from compressible, to incompressible, and then to compressible encircled by incompressible as the electron concentration is enhanced by the gate bias.

The latter situation of a compressible puddle surrounded by an incompressible strip (IS) is realized when $\nu_g > \nu_s \geq \nu_b$. Here ν_g and ν_b are filling factors under the gate and in the bulk; ν_s is the integer filling factor of the IS. To charge the puddle, electrons must tunnel from the edge channel through the IS. Typical capacitance versus gate voltage traces, measured on a sample with gate dimensions $32 \mu\text{m}$ (along the edge) \times $5 \mu\text{m}$ (perpendicular) at 100 kHz, are shown in the figure (curves for different fields are shifted vertically). Peaks seen in the capacitance correspond to conductance resonances for electrons tunneling through the edge IS.

There is a striking similarity of the resonance spectrum observed for samples with vastly different gate

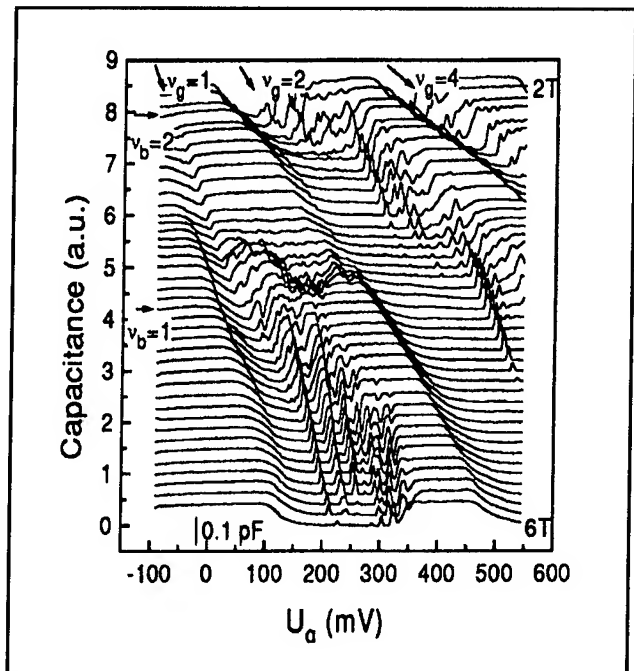


Figure 7. Capacitance versus gate bias scans for a small gate over the edge of a two-dimensional electron gas. The different scans are for different magnetic field values varying from 2-6 Tesla. Note the resonances.

lengths along the edge ($1\text{-}170 \mu\text{m}$). The resonances are no broader and appear no more frequently in samples with longer gates. This fact, as well as the character of the temperature dependence of the peaks, excludes impurity-assisted tunneling as the origin of the resonances.

We speculate that the resonances arise from abrupt transitions in structure in or near edge incompressible strips. The sharpness of the resonances in the case of long gates indicates an unusual ubiquity of the transitions, despite the expected inhomogeneity of the sample edge. There appears to be an underlying phenomenon which forces large regions of the edge to behave as a single structure.

6.6 Publications

Ashoori, R.C. "A New Class of Resonances at the Edge of the Two Dimensional Electron Gas." Submitted to *Phys. Rev. Lett.*

Ashoori, R.C. "Electrons in Artificial Atoms." *Nature* 379: 413-419 (1996).

Section 3 Optics and Devices

Chapter 1 Optics and Quantum Electronics

Chapter 2 Optical Propagation and Communication

Chapter 3 High-Frequency (> 100 GHz) and High-Speed
 (< 10 ps) Electronic Devices

Chapter 1. Optics and Quantum Electronics

Academic and Research Staff

Professor Hermann A. Haus, Professor Erich P. Ippen, Professor James G. Fujimoto, Professor Peter L. Hagelstein, Dr. Brett E. Bouma

Visiting Scientists and Research Affiliates

Dr. Mark E. Brezinski,¹ Dr. Brent E. Little, Dr. Shu Namiki, Dr. Viktor P. Mikhailov,² Dr. Martin H. Muendel,³ Dr. Shu Namiki, Dr. Günter Steinmeyer, William Hodge⁴

Graduate Students

Igor P. Bilinsky, Luc Boivin, Stephen A. Boppart, Jerry C. Chen, Patrick Chou, Leo Chun, Jay N. Damask, Ali M. Darwish, David J. Dougherty, Siegfried B. Fleischer, Marc Fleury, Boris Golubovic, James G. Goodberlet, Matthew Grein, Michael R. Hee, David J. Jones, Sumanth Kaushik, Mohammed J. Khan, Farzana I. Khatri, Gadi Lenz, Lynn E. Nelson, Timothy A. Savas, Guillermo J. Tearney, Eric R. Thoen, Constantine Tziligakis, William S. Wong, Charles Yu

Technical and Support Staff

Mary C. Aldridge, Donna L. Gale, Cynthia Y. Kopf

1.1 Fiber Ring Lasers

Sponsors

Defense Advanced Research Projects Agency/
MIT Lincoln Laboratory
Contract MDA972-92-J-1038
Joint Services Electronics Program
Grant DAAH04-95-1-0038
National Science Foundation
Grant ECS 94-23737
U.S. Air Force - Office of Scientific Research
Contract F49620-95-1-0221

Project Staff

Professor Hermann A. Haus, Professor Erich P. Ippen, Matthew Grein, David J. Jones, Lynn E. Nelson, William S. Wong

In the past several years, we have constructed and improved the operation of mode-locked fiber ring lasers in general, stretched pulse fiber ring lasers operating at 1.5 μm wavelength, in particular. The fiber ring lasers are modelocked via intensity-

dependent polarization rotation followed by an analyzer, resulting in an effective saturable absorber action. This mechanism is now known as polarization additive-pulse modelocking (P-APM). In the stretched pulse laser, two segments of fiber are used, one of positive dispersion, the other of negative dispersion, the net dispersion being close to zero. The pulse stretches and contracts alternately as it propagates around the loop. Its average intensity is much lower than its peak intensity, and thus the nonlinear effects in the fiber are greatly reduced. Since excessive nonlinearity leads to pulse instabilities, this design of the laser is able to produce much shorter pulses of much higher intensity than any other all-fiber laser. When the polarizer is replaced by a polarization beam splitter (see figure 1), the power normally absorbed in a polarizer, is available as output power. Since up to 50 percent of the power ends up in this polarization, very large output powers can be achieved this way. The output of a stretched pulse laser operated in this manner is two orders of magnitude higher than that of a regular all-fiber ring laser. The pulse shape and spectrum, while not as clean as that in the

¹ Massachusetts General Hospital, Boston, Massachusetts.

² International Laser Center, Minsk, Belarus.

³ Polaroid Corporation, Cambridge, Massachusetts.

⁴ High Energy Laser Associates, Oakland, California.

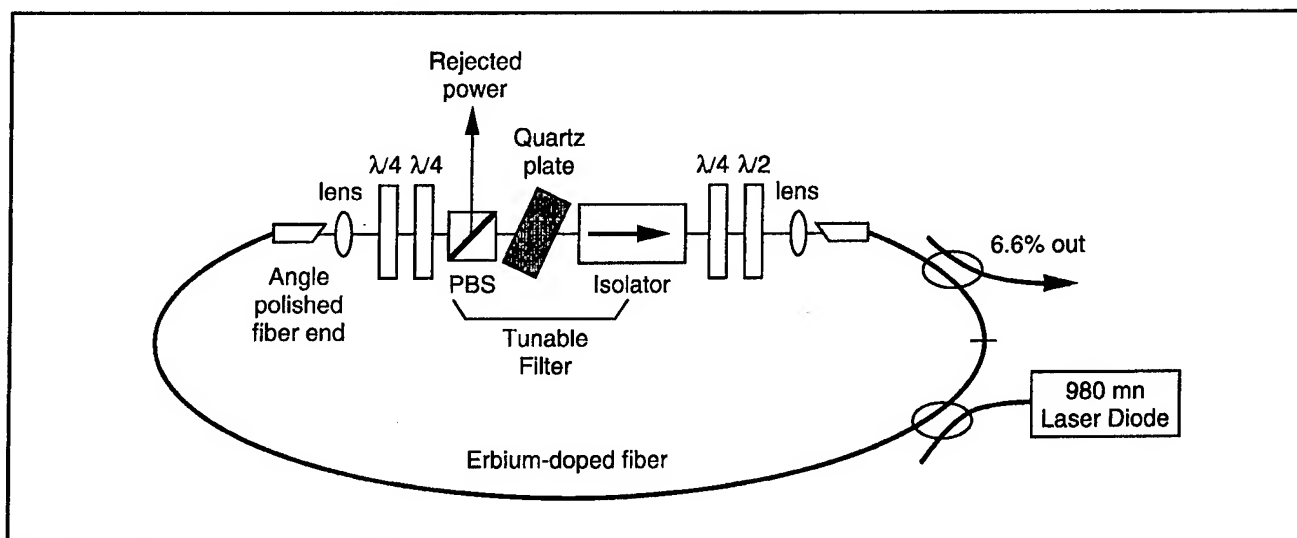


Figure 1. Schematic of stretched pulse laser with bulk output coupler.

dominant polarization, is adequate for most applications.⁵

In order to show that the P-APM modelocking scheme is not unique to the erbium doped system, we designed and operated a thulium doped fiber laser,⁶ which operates near 1.8 μm . Draper Laboratories has expressed interest in this wavelength regime for fiber gyro applications, and there are possible applications in medicine and eye-safe laser radar. The laser produced sub-500 fs pulses that were broadly tunable from 1798 nm to 1902 nm, with continuous tuning of 50 nm possible by filter adjustment only. Both the thulium-doped fiber and the passive fiber have large negative dispersion in this wavelength region, thus forcing the laser to operate in the soliton regime where the shortest pulse width is limited by continuum generation. Future work may include improved filtering to smooth the pulse spectrum and attempting to stretch the pulse in order to avoid the soliton regime.

Graduate student C.R. Doerr discovered a new actively modelocked system, the asynchronously modelocked fiber ring laser running near 1 GHz, during the previous year. Under normal circumstances (synchronous modelocking), the RF drive to the modulator in the fiber ring laser must be precisely a harmonic of the roundtrip frequency. In the asynchronous laser the phase modulator is detuned 15-30 kHz from a cavity harmonic. The soliton nature of the pulses enable them to survive this detuned modulation. The value of the asynchronous system is that it needs no stabilization of the cavity length with respect to the modelocking drive. With extensive numeric simulations confirmed by both analytic theory and experimental results, we have gained a thorough understanding of the asynchronous modelocking process.⁷ In particular, we have found it possible to implement asynchronous modelocking in polarization maintaining (PM) fiber for increased environmental stability. For this reason, it is our intent in the coming year to develop both asynchronous and passively modelocked versions of fiber lasers using PM fiber.

⁵ K. Tamura, E.P. Ippen, and H.A. Haus, "Pulse Dynamics in Stretched-Pulse Fiber Lasers," *Appl. Phys. Lett.* 67: 158 (1995); H.A. Haus, K. Tamura, L.E. Nelson, and E.P. Ippen, "Stretched-Pulse Additive Pulse Mode-Locking in Fiber Ring Lasers: Theory and Experiment," *IEEE J. Quant. Electron.* 31: 591 (1995); G. Lenz, K. Tamura, H.A. Haus, and E.P. Ippen, "All-Solid-State Femto-second Source at 1.55 μm ," *Opt. Lett.* 20: 1289 (1995).

⁶ L.E. Nelson, E.P. Ippen, and H.A. Haus, "Broadly Tunable Sub-500 fs Pulses from an Additive-Pulse Mode-Locked Thulium-Doped Fiber Ring Laser," *Appl. Phys. Lett.* 67: 19 (1995).

⁷ H.A. Haus, D.J. Jones, E.P. Ippen, and W.S. Wong, "Theory of Soliton Stability in Asynchronous Modelocking," *J. Lightwave Technol.*, forthcoming.

1.1.1 Publications

Haus, H.A., K. Tamura, L.E. Nelson, and E.P. Ippen. "Stretched-Pulse Additive Pulse Mode-Locking in Fiber Ring Lasers: Theory and Experiment." *IEEE J. Quant. Electron.* 31: 591 (1995).

Haus, H.A., D.J. Jones, E.P. Ippen, and W.S. Wong. "Theory of Soliton Stability in Asynchronous Modelocking." *J. Lightwave Technol.* Forthcoming.

Lenz, G., K. Tamura, H.A. Haus, and E.P. Ippen. "All-Solid-State Femtosecond Source at 1.55 μm ." *Opt. Lett.* 20: 1289 (1995).

Nelson, L.E., E.P. Ippen, and H.A. Haus. "Broadly Tunable Sub-500 fs Pulses from an Additive-Pulse Mode-Locked Thulium-Doped Fiber Ring Laser." *Appl. Phys. Lett.* 67: 19 (1995).

Tamura, K., E.P. Ippen, and H.A. Haus. "Pulse Dynamics in Stretched-Pulse Fiber Lasers." *Appl. Phys. Lett.* 67: 158 (1995).

necessity.⁸ With this purpose in mind, we are working on the storage of bits in optical fiber rings. The fiber storage ring demonstrated last year operated at 1 GHz, which required electro-optic amplitude modulation to provide timing stability. A data pattern of 66 bits (ones and zeros) loaded into the ring could be maintained for at least 30 minutes inside the ring.

Graduate student William Wong, working with MIT Lincoln Laboratory researchers, extended the data rate to 20 Gb/s.⁹ All-optical long-term storage at 10 Gb/s has also been demonstrated using cross-gain saturation in a semiconductor amplifier to provide the optical modulation.¹⁰

Using the new technique of rational-harmonic modelocking, where the ratio of the fundamental modulation frequency to the cavity fundamental frequency is rational (nonintegral), 3.8-kbit packets of data can be stored at 50 Gb/s.¹¹ This method offers the advantage of achieving storage at bit rates a few times that of the modelocking drives. In the near future, we shall attempt to scale the operation to even higher frequencies and to produce streams as well as patterns of ones and zeros.

1.2 Fiber Storage Rings

Sponsors

Defense Advanced Research Projects Agency/
MIT Lincoln Laboratory
Contract MDA972-92-J-1038
U.S. Air Force - Office of Scientific Research
Contract F49620-95-1-0221

Project Staff

Professor Hermann A. Haus, Professor Erich P. Ippen, William S. Wong

For high bit-rate optical communications, storage and buffering of data at communication nodes is a

1.2.1 Publications

Hall, K.L., J.D. Moores, K.A. Rauschenbach, W.S. Wong, E.P. Ippen, and H.A. Haus. "All-Optical Storage of a 1.25 kb Packet at 10 Gb/s." Paper published in the *Conference on Lasers and Electro-Optics*. OSA Technical Digest Series. Washington, D.C.: Optical Society of America, 1995, paper CPD16.

Hall, K.L., J.D. Moores, K.A. Rauschenbach, W.S. Wong, E.P. Ippen, and H.A. Haus. "All-Optical Storage of a 1.25 kb Packet at 10 Gb/s." *IEEE Photon. Technol. Lett.* 7: 1093 (1995).

⁸ K. Rauschenbach, K. Hall, J. Moores, E. Swanson, M. Haner, H.A. Haus, and W. Wong, "Broadband Optical Local Area Network Technologies," in *Digest of IEEE LEOS'94 7th Annual Meeting* (New York: Institute of Electrical and Electronics Engineers, 1994), paper UO4.1; K.A. Rauschenbach, K.L. Hall, J.D. Moores, S.G. Finn, R.A. Barry, W. Wong, H.A. Haus, E.P. Ippen, and M. Haner, "Technologies for Ultra-High-Bit-Rate Time-Division-Multiplexed Networks," *OSA Photonics in Switching Digest '95* 12: 45 (1995).

⁹ J.D. Moores, K.L. Hall, S.M. LePage, K.A. Rauschenbach, W.S. Wong, H.A. Haus, and E.P. Ippen, "20-GHz Optical Storage Loop-Laser using Amplitude Modulation, Filtering, and Artificial Fast Saturable Absorption," *IEEE Photon. Technol. Lett.* 7: 1096 (1995).

¹⁰ K.L. Hall, J.D. Moores, K.A. Rauschenbach, W.S. Wong, E.P. Ippen, and H.A. Haus, "All-Optical Storage of a 1.25 kb Packet at 10 Gb/s," in *Conference on Lasers and Electro-Optics*, OSA Technical Digest Series (Washington, D.C.: Optical Society of America, 1995), paper CPD16; K.L. Hall, J.D. Moores, K.A. Rauschenbach, W.S. Wong, E.P. Ippen, and H.A. Haus, "All-Optical Storage of a 1.25 kb Packet at 10 Gb/s," *IEEE Photon. Technol. Lett.* 7: 1093 (1995).

¹¹ J.D. Moores, W.S. Wong, and K.L. Hall, "50 Gb/s Optical Pulse Storage Ring Using Novel Rational-Harmonic Modulation," *Opt. Lett.* 20: 2547 (1995).

Moore, J.D., K.L. Hall, S.M. LePage, K.A. Rauschenbach, W.S. Wong, H.A. Haus, and E.P. Ippen. "20-GHz Optical Storage Loop/Laser using Amplitude Modulation, Filtering, and Artificial Fast Saturable Absorption." *IEEE Photon. Technol. Lett.* 7: 1096 (1995).

Rauschenbach, K.A., K.L. Hall, J.D. Moore, S.G. Finn, R.A. Barry, W. Wong, H.A. Haus, E.P. Ippen, and M. Haner. "Technologies for Ultra-High-Bit-Rate Time-Division-Multiplexed Networks." *OSA Photonics in Switching Digest* 12: 45 (1995).

1.3 Long-Distance Fiber Communications

Sponsors

Defense Advanced Research Projects Agency
MIT Lincoln Laboratory
Contract MDA972-92-J-1038
National Science Foundation
Grant ECS 94-23737

Project Staff

Professor Hermann A. Haus, Farzana I. Khatri, William S. Wong

We continue to pursue theory and numerical simulation of phenomena occurring in long-distance soliton communications. We developed a simple theory of continuum generation by soliton disturbances (such as lumped gain, lumped Kerr effect, lumped filtering).¹² The continuum can affect another soliton in a bit-stream formed of soliton ONEs and ZEROs (a ZERO is a gap with no soliton pulse present). Quantitatively, we have evaluated the amount of displacement caused by a wave packet of low intensity colliding with a soliton.¹³ For example, in figure 2 we show the timing shift as a function of distance due to a soliton colliding with an asymmetric Hermite Gaussian wave packet (shown in figure 2 inset). Theory and simulation are shown by solid and dashed lines, respectively.

In 1995, Professor Haus spent two months at AT&T Bell Laboratories as part of his one-term sabbatical. In collaboration with Drs. W.H. Knox and D.A.B.

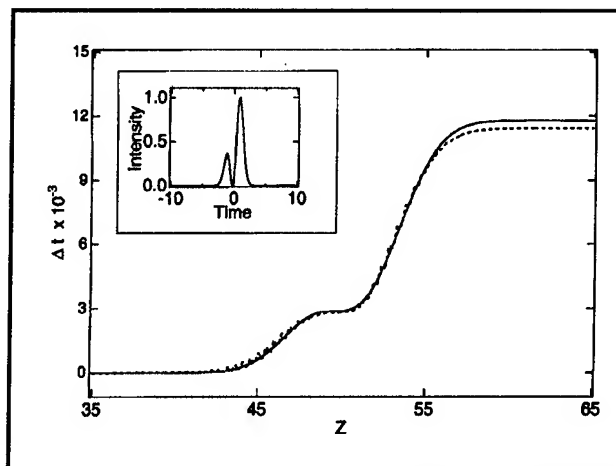


Figure 2. The timing shift due to a collision between a soliton and a low-intensity, asymmetric Hermite Gaussian wave packet. Solid and dashed lines represent theory and simulation, respectively. The inset shows the initial perturbation as a function of time.

Miller, a scheme was developed that would replace the sliding-frequency guiding filters for soliton stabilization which have been proposed and demonstrated by Mollenauer and Gordon. The disadvantage of sliding-guiding filters is the requirement that each undersea amplification "pod" be equipped with a filter tuned to a different frequency. Our new scheme acts as an effective saturable absorber with all its pods identical. A patent application has been filed.

Another issue confronting long distance soliton communication vis á vis the successfully deployed non-return to zero (NRZ) systems is line monitoring (LM), or supervisory control. In an NRZ system, a low-intensity, low-bit-rate modulation is applied to the high bit-rate pulse stream. A very small fraction of the signal is tapped off at each amplifier stage and returned in the opposite direction. This signal is then processed in order to determine the location of faulty amplifiers or fiber breaks. The NRZ LM scheme is, however, incompatible with nonlinear soliton communications, since low level signals are automatically suppressed.

A soliton LM scheme was developed by Professor Haus, in collaboration with Drs. Stephen Evangelides and Bruce Nyman of AT&T Bell Laborato-

¹² H.A. Haus, W.S. Wong, and F.I. Khatri, "Continuum Generation by Perturbation of Soliton," submitted to *J. Opt. Soc. Am. B*.

¹³ H.A. Haus, F.I. Khatri, W.S. Wong, K.R. Tamura, and E.P. Ippen, "Interaction of Soliton with Sinusoidal Wave Packet," *J. Quantum Electron.*, forthcoming; H.A. Haus, F.I. Khatri, and W.S. Wong, "Soliton Interaction with Continuum," paper presented at the Conference on Ultrafast Transmission Systems in Optical Fibres, Trieste, Italy, February 1995; H.A. Haus, E.P. Ippen, W.S. Wong, F.I. Khatri, and K.R. Tamura, "Pulse Self-Ordering in Soliton Fiber Lasers," Conference on Lasers and Electro-Optics, Baltimore, Maryland, May 1995, paper JTua7.

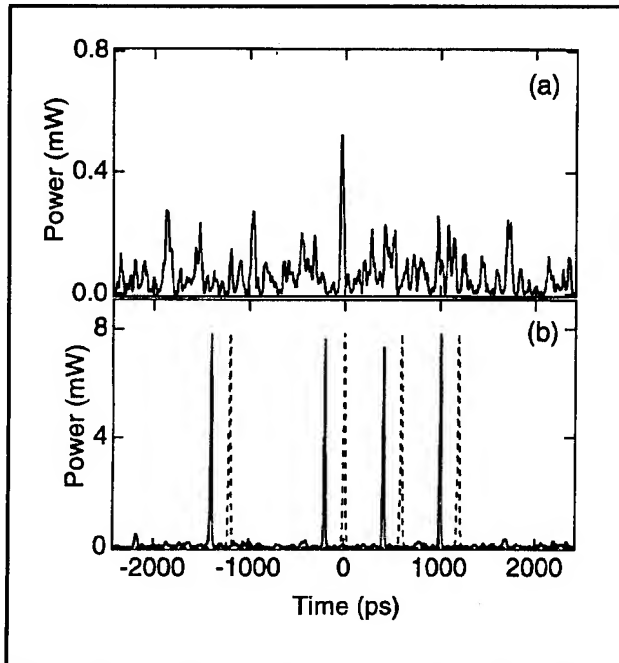


Figure 3. (a) and (b) show simulation results for loop-back "1" and "2." Shown in (b) are the input (dashed) and output (solid) pulse power versus time. Note that we have time shifted loop-back "2" for aesthetic purposes.

ries and graduate student Farzana Khatri.¹⁴ In our scheme, the LM is a separate channel which employs a low-bit-rate wavelength division multiplexed (WDM) channel of soliton pulses encoded with a pseudorandom bit pattern. The couplers employed are stronger than their NRZ counterpart and are located so that the gain is maximized. In addition, the fiber dispersions may be arranged so that the LM experiences "reflective gain" on the return and so that the east- and west-going data channels are spectrally separated, eliminating crosstalk. Results from a simulation of our LM scheme are shown in figure 3. Figure 3a shows the LM signal returning from a degraded amplification stage, while figure 3b shows the LM signal

returning from a normal amplification stage. A patent application has been filed.

1.3.1 Publications

Haus, H.A., W.S. Wong, and F.I. Khatri. "Continuum Generation by Perturbation of Soliton." Submitted to *J. Opt. Soc. Am. B*.

Haus, H.A., F.I. Khatri, and W.S. Wong. "Soliton Interaction with Continuum." Paper presented at the Conference on Ultrafast Transmission Systems in Optical Fibres, Trieste, Italy, February 1995.

Haus, H.A., E.P. Ippen, W.S. Wong, F.I. Khatri, and K.R. Tamura. "Pulse Self-Ordering in Soliton Fiber Lasers." Conference on Lasers and Electro-Optics, Baltimore, Maryland, May 1995, paper JTUA7.

Haus, H.A., W.S. Wong, and F.I. Khatri. "Continuum Generation by Perturbation of Soliton." Submitted to *J. Opt. Soc. Am. B*.

Khatri, F.I., S.G. Evangelides, P.V. Mamyshev, B.M. Nyman, and H.A. Haus. "A Line-Monitoring System for Undersea Soliton Communication Systems with Sliding-Frequency Guiding Filters." Paper presented at the Optical Fiber Communication Conference '96, San Jose, California, February 1996, paper ThH6.

Khatri, F.I., S.G. Evangelides, P.V. Mamyshev, B.M. Nyman, and H.A. Haus. "A Line-Monitoring System for Undersea Soliton Communication Systems with Sliding-Frequency Guiding Filters." Submitted to *IEEE Photon. Technol. Lett.*

Haus, H.A., F.I. Khatri, W.S. Wong, K.R. Tamura, and E.P. Ippen. "Interaction of Soliton with Sinusoidal Wave Packet." *J. Quantum Electron.* Forthcoming.

¹⁴ F.I. Khatri, S.G. Evangelides, P.V. Mamyshev, B.M. Nyman, and H.A. Haus, "A Line-Monitoring System for Undersea Soliton Communication Systems with Sliding-Frequency Guiding Filters," paper ThH6, Optical Fiber Communication Conference '96, San Jose, California, February 1996; F.I. Khatri, S.G. Evangelides, P.V. Mamyshev, B.M. Nyman, and H.A. Haus, "A Line-Monitoring System for Undersea Soliton Communication Systems with Sliding-Frequency Guiding Filters," submitted to *IEEE Photon. Technol. Lett.*

1.4 Laser Noise and Squeezing

Sponsors

National Science Foundation
Grant ECS 94-23737
U.S. Navy - Office of Naval Research
Grant N00014-95-1-0715

Project Staff

Professor Hermann A. Haus, Professor Erich P. Ippen, Luc Boivin, Dr. Shu Namiki, Charles Yu

The eventual goal of our squeezing experiments is to develop an all-fiber squeezing system compatible with a fiber gyro for improved gyro sensitivity. Squeezing experiments were performed with GHz rate pulses from a compact Ti:Sapphire laser in the positive dispersion regime of the fiber. The GHz rate is required to suppress the effect of guided acoustic wave Brillouin scattering (GAWBS).¹⁵ The sub-shot noise level was inadequate, mainly due to the amplitude fluctuations of the source. Future work requires better control of the fluctuations of the pulses emitted from a modelocked laser.

In an attempt to develop low-noise sources of modelocked pulses, we have begun a theoretical and experimental study of noise in fiber ring lasers. If used for squeezing experiments, they would be an ideal source for soliton squeezing in the 1.5 μm wavelength regime. We found that timing jitter in these lasers is quantum limited, i.e., due solely to the spontaneous emission noise of the laser amplifier. It is the first demonstration of a quantum limited modelocked operation.¹⁶ The amplitude fluctuations were also found to be lower (0.2 percent) than reported in any other laser system.

The use of short and intense pulses to generate squeezed light in optical fibers is very attractive since large nonlinear shifts can then be achieved using very short fibers. Pulses shorter than about 1

ps are, however, affected by stimulated Raman scattering. The impact of Raman noise on short pulse squeezing was analyzed at zero dispersion¹⁷ and was shown to be surmountable.¹⁸

In order to design the positive dispersion Ti:sapphire squeezer, a numerical code based on the symmetrized split-step method was developed to evolve both the pump and the quantum noise. Some of our results were published¹⁸ and show that large degrees of squeezing can be achieved over a few centimeters using typical modelocked Ti:sapphire systems.

A possible approach to squeezed fiber gyro makes use of optical solitons. In one of our theoretical projects, we calculated the degree of squeezing for fundamental solitons without using the small quantum noise approximation. This analysis, based on the exact time dependence of the Bethe eigenstates for the quantized nonlinear Schrödinger equation, confirms the results of the linearized theory and establishes its domain of validity.¹⁹ The fluctuations of the position and of the phase of a fundamental soliton were also shown to be limited by the lower bound of the Heisenberg uncertainty relations.

We proposed a new method to generate squeezed light using an optical fiber.²⁰ Contrary to previous approaches using the self-phase modulation experienced by intense pulses in these waveguides, the new method relies on cross-phase modulation between pulses with orthogonal polarizations. As the squeezed vacuum and the pump are not degenerate in polarization, they can be easily separated without using a Sagnac interferometer. This feature of the new squeezer leads to a simpler design.

The ultimate limit of noise suppression in squeezing experiments is set by the quantum efficiency of the photo-detectors. If the quantum efficiency is 90 percent, the maximum shot noise suppression pos-

¹⁵ R.M. Shelby, M.D. Levenson, S.H. Perlmutter, R.G. DeVoe, and D.F. Walls, *Phys. Rev. Lett.* 54: 691 (1986); K. Bergman, H.A. Haus, and M. Shirasaki, "Analysis and Measurement of GAWBS Spectrum in a Nonlinear Fiber Ring," *Appl. Phys. B* 55: 242 (1992).

¹⁶ S. Namiki, C.X. Yu, and H.A. Haus, "Observation of Nearly Quantum-Limited Timing Jitter in an All-Fiber Ring Laser," submitted to *J. Opt. Soc. Am. B*.

¹⁷ J.H. Shapiro and L. Boivin, "Raman Noise Limit for Four-Wave Mixing," *Opt. Lett.* 18: 925 (1994); L. Boivin, "Sagnac Loop Squeezer at Zero Dispersion with a Finite Response Time for Kerr Nonlinearity," *Phys. Rev. A* 52: 754 (1995).

¹⁸ L. Boivin, C.R. Doerr, K. Bergman, and H.A. Haus, "Quantum Noise Reduction Using a Sagnac Loop with Positive Dispersion," in *Quantum Communications and Measurement*, eds. V.P. Belavkin, O. Hirota, and R.L. Hudson (New York: Plenum Press, 1995), pp. 489-496.

¹⁹ F.X. Kärtner and L. Boivin, "Quantum Noise of the Fundamental Soliton," *Phys. Rev. A* 53 (1996), forthcoming.

²⁰ L. Boivin and H.A. Haus, " $\chi^{(3)}$ -Squeezed Vacuum Generation Without a Sagnac Interferometer," *Opt. Lett.* 21 (1996), forthcoming.

sible is 10 dB. Hence, one may raise the question whether there are ways to overcome this limit. Since phase sensitive amplification can be made noise-free in the ideal limit, we investigated the possibility of phase sensitive preamplification in the spirit of a quantum nondemolition measurement of the twin beams detected in the balanced detector.²¹ We found that it is possible to use preamplification, with realistic pump power levels and fiber lengths, to overcome the limits set by the detector quantum efficiency.

1.4.1 Publications

Boivin, L., and H.A. Haus. " $\chi^{(3)}$ -Squeezed Vacuum Generation Without a Sagnac Interferometer." *Opt. Lett.* 21 (1996). Forthcoming.

Boivin, L. "Sagnac Loop Squeezer at Zero Dispersion with a Finite Response Time for Kerr Nonlinearity." *Phys. Rev. A* 52: 754 (1995).

Boivin, L., C.R. Doerr, K. Bergman, and H.A. Haus. "Quantum Noise Reduction Using a Sagnac Loop with Positive Dispersion." In *Quantum Communications and Measurement*. Eds. V.P. Belavkin, O. Hirota, and R.L. Hudson. New York: Plenum Press, 1995, pp. 489-496.

Kärtner, F.X., and L. Boivin. "Quantum Noise of the Fundamental Soliton." *Phys. Rev. A* 53 (1996). Forthcoming.

Namiki, S., C.X. Yu, and H.A. Haus. "Observation of Nearly Quantum-Limited Timing Jitter in an All-Fiber Ring Laser." Submitted to *J. Opt. Soc. Am. B*.

1.5 Optical Waveguide Filters

Sponsors

MIT Center for Material Science and Engineering
National Center for Integrated Photonics
Technology
Contract DMR 94-00334

National Science Foundation
Grant ECS 94-23737

Project Staff

Professor Hermann A. Haus, Jerry C. Chen, Mohammed J. Khan, Dr. Brent E. Little

For some years, we have been developing the theory and perfecting the fabrication of filters using passive waveguide gratings. Active filters, while more difficult to fabricate, have many desirable properties. For instance, suppression of undesirable modes is more effective in active filters. A detailed theory of active filters has been published.²²

We have started to investigate traveling-wave ring resonators as alternatives to quarter-wave-shifted grating resonators for filtering applications. The basic idea originated with Marcatilli²³ in 1969. Since then, fabrication has advanced to a point where adequate Qs can be expected. A ring resonator placed between two waveguides is capable of transferring all the power from one waveguide to another waveguide at a particular wavelength. This is not possible using a single resonator with standing wave resonances. Figure 4 shows a ring resonator and its characteristic narrow band response.²⁴ Utilizing the Vernier effect of two resonators of different dimensions with one coincident resonator frequency, the free spectral range can be extended. Figure 5 shows such a Vernier filter using rings of different radii. Cascading of ring resonators can lead to the synthesis of desirable filter characteristics, such as Butterworth and Chebyshev response.

Waveguides with large index discontinuities similar to that of photonic bandgap materials can provide large filter bandwidths and large free spectral ranges compatible with optical communication channels of 10 Gbit and 100 GHz spacings. For this reason, we are investigating the design of waveguide-resonator structures that suppress radiation adequately, an unavoidable effect in such compact, open (unshielded) resonator structures.

²¹ F.X. Kärtner and H.A. Haus, "QND - Measurement of Twin Beams," submitted to *J. Opt. Soc. Am. B*.

²² H.A. Haus and M.J. Khan, "Gain-Distributed Feedback Filters," *J. Lightwave Technol.* 13: 261-274 (1995).

²³ E.A.J. Marcatilli, "Bends in Optical Dielectric Waveguides," *Bell Syst. Tech. J.* 14: 2103 (1969).

²⁴ B.E. Little, S.T. Chu, and H.A. Haus, "Micro-Ring Resonator Channel Dropping Filters," *IEEE/LEOS Annual Meeting*, San Francisco, California, 1995, paper WDM 2.3.

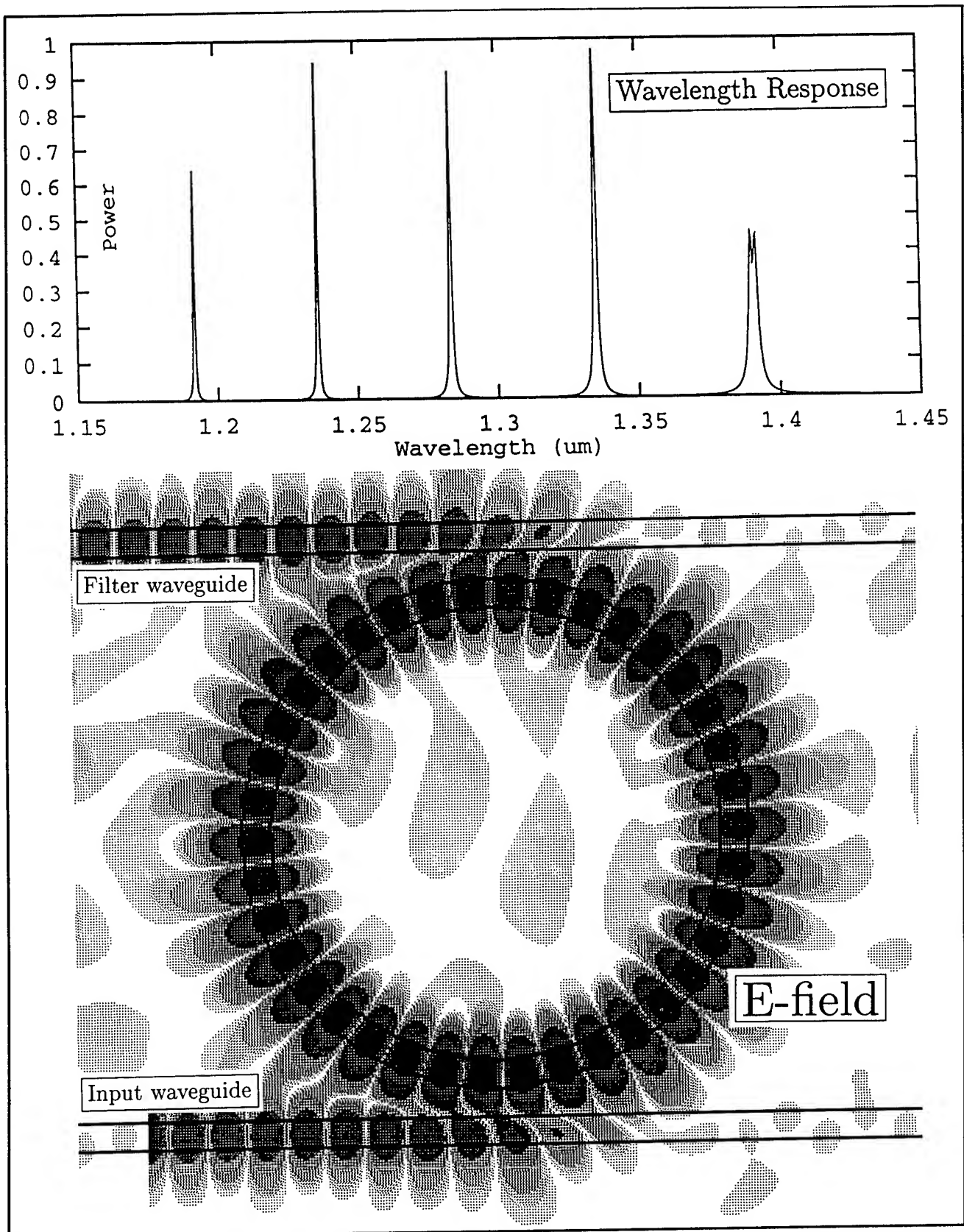


Figure 4. Wavelength response of a single-ring resonator. The upper graph shows the sharp, narrow band peaks at the channel dropping wavelengths. The lower graph is a plot of electric field intensity in the micro-ring resonator at a particular resonator wavelength.

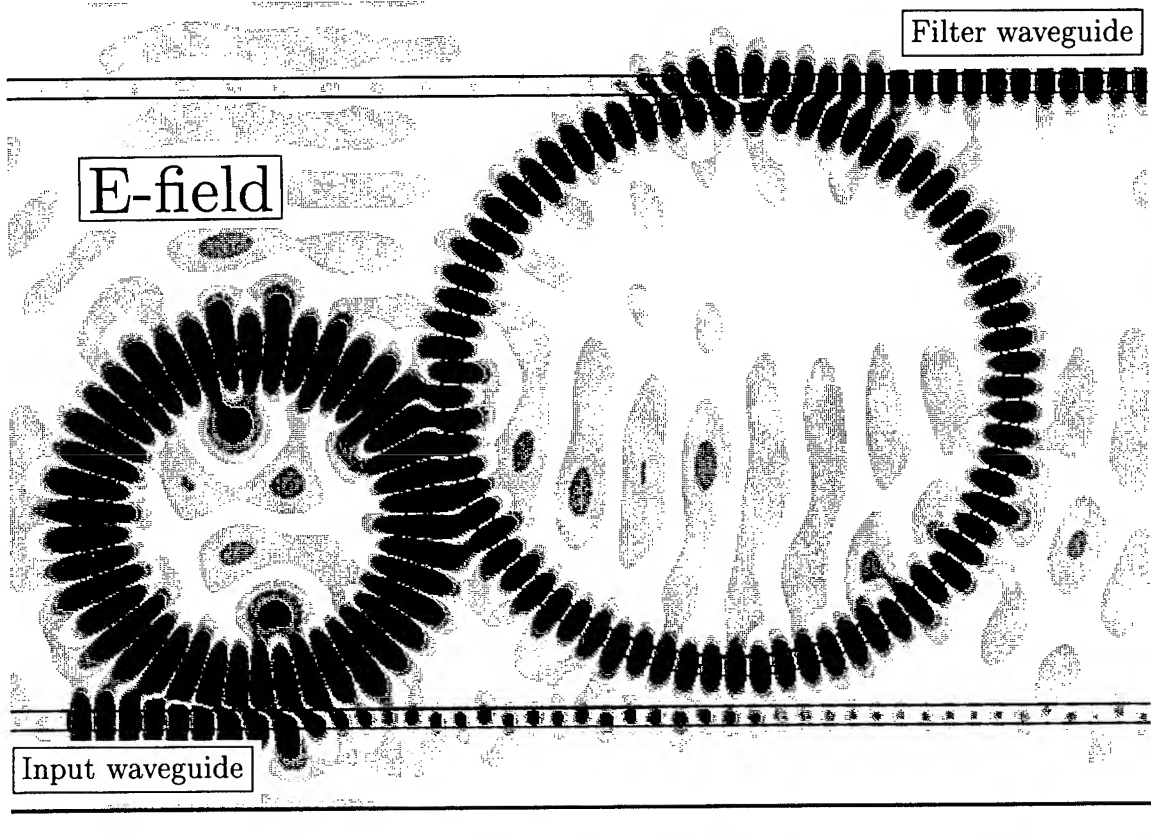
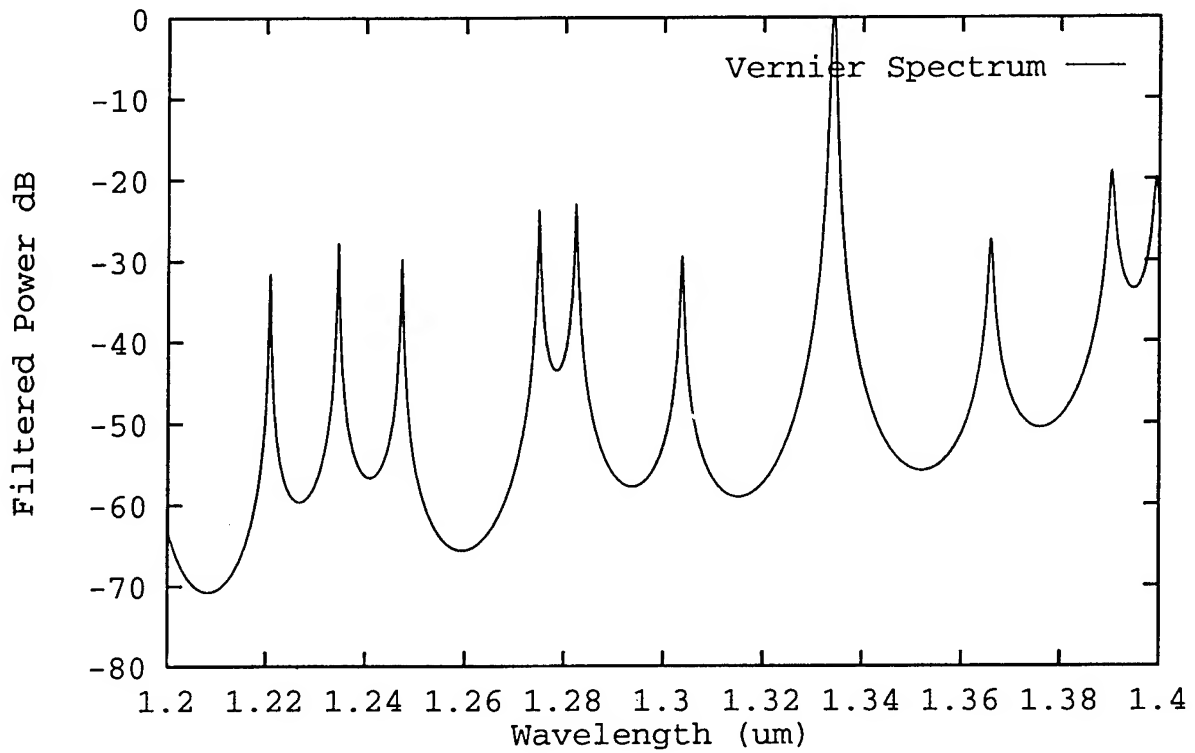


Figure 5. Vernier ring resonator using two dissimilar rings. The upper graph shows the wavelength response. Of the multiple resonator peaks shown, only one at $\lambda = 1.334 \mu\text{m}$ is completely extracted by the filter. Other peaks are suppressed by -25 dB by the Vernier effect. The lower graph shows the electric field intensity in the filter.

We have developed designs for 1.5 μm applications that provide a Q as high as 24,000 in structures that are only 18 μm long²⁵ (see figure 6). An analytic theory has been developed to take into account higher order effects in deeply etched gratings, such as resonator frequency shifts and radiation loss.²⁶

1.5.1 Publications

Chen, J.C., H.A. Haus, S. Fan, and J.D. Joannopoulos. "Optical Filters from Photonic Band Gap Air Bridges." European Conference on Integrated Optics, Delft, The Netherlands, 1995, paper ThC3.

Chen, J.C., H.A. Haus, S. Fan, P.R. Villeneuve, J.D. Joannopoulos, K. Li, and R.T. Shin. "Optical Filters from Photonic Band Gap Air Bridges." *Proceedings of the Photonics Society of the Chinese-Americans Annual Meeting* Baltimore, Maryland, 1995.

Chen, J.C., H.A. Haus, J. N. Winn, S. Fan, and J.D. Joannopoulos. "Wide Stop Band Optical Filters from Photonic Band Gap Air Bridges," in *Guided-Wave Optoelectronics: Device Characterization, Analysis, and Design*. New York: Plenum Press, 1995, pp. 477-483.

Chen, J.C., and K. Li. "Quartic Perfectly Matched Layers for Dielectric Waveguides and Gratings." *Microwave Opt. Technol. Lett.* 10: 319 (1995).

Chen, J.C., H.A. Haus, S. Fan, P.R. Villeneuve, and J.D. Joannopoulos. "Optical Filters from Pho-

tonic Band Gap Air Bridges." Submitted to *J. Lightwave Technol.*

Chen, J.C., P.R. Villeneuve, H.A. Haus, and J.D. Joannopoulos. "Narrow-Band Transmission Filters from Highly Resonant Gratings." Submitted to the *Topical Meeting on Integrated Photonics Research*.

Fan, S., J.N. Winn, A. Devenyi, J.C. Chen, R.D. Meade, and J.D. Joannopoulos. "Guided and Defect Modes in Periodic Dielectric Waveguides." *J. Opt. Soc. Am. B* 12: 1267 (1995).

Haus, H.A., and M.J. Khan. "Gain-Distributed Feedback Filters." *J. Lightwave Technol.* 13: (1995).

Little, B.E. "A Variational Coupled-Mode Theory Including Radiation Loss for Grating-Assisted Couplers." *IEEE J. Lightwave Technol.* 14 (1996).

Little, B.E., and H.A. Haus. "A Variational Coupled-Mode Theory for Periodic Waveguides." *IEEE J. Quantum Electron.* 31: 2258 (1995).

Villeneuve, P.R., S. Fan, I. Kurland, J.C. Chen, and J.D. Joannopoulos. "Photonic Band Gap Structures and Devices." *Quantum Electronics and Laser Science Conference*. Baltimore, Maryland, 1995, paper QWH1.

Villeneuve, P.R., S. Fan, J.D. Joannopoulos, K.-Y. Lim, J.C. Chen, G.S. Petrich, L.A. Kolodziejski, and R. Reif. "Microcavities in Channel Waveguides." *Proceedings of a NATO Advanced Studies Institute of Photonic Band Gap Materials*, Elounda, Greece, 1995.

²⁵ J.C. Chen, H.A. Haus, S. Fan, and J.D. Joannopoulos, "Optical Filters from Photonic Band Gap Air Bridges," European Conference on Integrated Optics, Delft, Netherlands, 1995, paper ThC3; J.C. Chen, H.A. Haus, S. Fan, P.R. Villeneuve, J.D. Joannopoulos, K. Li, and R.T. Shin, "Optical Filters from Photonic Band Gap Air Bridges," *Proceedings of the Photonics Society of the Chinese-Americans Annual Meeting* Baltimore, Maryland, 1995; P.R. Villeneuve, S. Fan, I. Kurland, J.C. Chen, and J.D. Joannopoulos, "Photonic Band Gap Structures and Devices," *Quantum Electronics and Laser Science Conference*, Baltimore, Maryland, 1995, paper QWH1; P.R. Villeneuve, S. Fan, J.D. Joannopoulos, K.-Y. Lim, J.C. Chen, G.S. Petrich, L.A. Kolodziejski, and R. Reif, "Microcavities in Channel Waveguides," *Proceedings of a NATO Advanced Studies Institute of Photonic Band Gap Materials*, Elounda, Greece, 1995; S. Fan, J.N. Winn, A. Devenyi, J.C. Chen, R.D. Meade, and J.D. Joannopoulos, "Guided and Defect Modes in Periodic Dielectric Waveguides," *J. Opt. Soc. Am. B* 12: 1267 (1995); J.C. Chen, H.A. Haus, J. N. Winn, S. Fan, and J.D. Joannopoulos, "Wide Stop Band Optical Filters from Photonic Band Gap Air Bridges," in *Guided-Wave Optoelectronics: Device Characterization, Analysis, and Design* (New York: Plenum Press, 1995), pp. 477-483; J.C. Chen and K. Li, "Quartic Perfectly Matched Layers for Dielectric Waveguides and Gratings," *Microwave Opt. Technol. Lett.* 10: 319 (1995); J.C. Chen, H.A. Haus, S. Fan, P.R. Villeneuve, and J.D. Joannopoulos, "Optical Filters from Photonic Band Gap Air Bridges," submitted to *J. Lightwave Technol.*; J.C. Chen, P.R. Villeneuve, H.A. Haus, and J.D. Joannopoulos, "Narrow-Band Transmission Filters from Highly Resonant Gratings," submitted to the *Topical Meeting on Integrated Photonics Research*.

²⁶ B.E. Little, "A Variational Coupled-Mode Theory Including Radiation Loss for Grating-Assisted Couplers," *IEEE J. Lightwave Technol.* 14 (1996); B.E. Little and H.A. Haus, "A Variational Coupled-Mode Theory for Periodic Waveguides," *IEEE J. Quantum Electron.* 31: 2258 (1995).

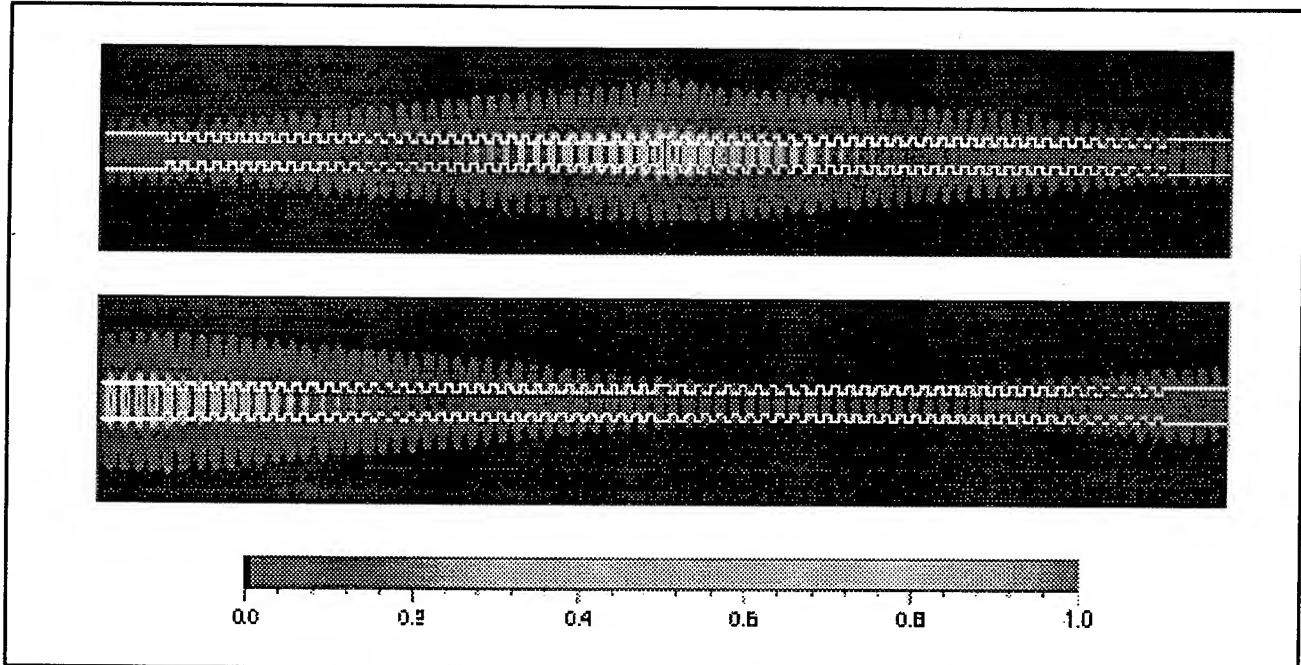


Figure 6. Electric and magnetic field propagating through air bridge filter. Frequency is close to the transmission resonance.

1.6 Integrated Optical Filters and Circuits

Sponsor

National Center for Integrated Photonics
Technology

Project Staff

Professor Hermann A. Haus, Professor Leslie A. Kolodziejski, Professor Henry I. Smith, Jay N. Damask, Juan Ferrera, Mohammed J. Khan, Michael H. Lim, Dr. Brent E. Little, Thomas E. Murphy

The integrated optics program that spans the Optics, Nanostructures, and Chemical-Beam Epitaxy Groups at MIT has significantly expanded this year in both numbers of research staff and in devices being developed. Moreover, the requisite software and theoretical tools have been developed. Waveguide designs can be quickly analyzed, and waveguide device patterns can be automatically laid out and fractured onto an e-beam grid.

The integrated optical devices currently under design and construction include the familiar channel-dropping filter, a matched filter for NRZ-encoded optical data, a co-directional wave-

guide coupler with a flat wavelength response, and novel optical circuits. One set of these circuits implement a reconfigurable add/drop switch with a Mach-Zehnder (MZ) interferometer and two channel-dropping filters and the other implements a spectrally-isolated multiple-pole filter. We work with the InGaAsP/InP material system, in collaboration with Professor Leslie A. Kolodziejski and her group, and the Ge-doped SiO₂ system, which can be purchased from PIRI. We are tailoring our filters and couplers for the all-optical network group and space-based communications group at MIT Lincoln Laboratories, the fiber gyro group at RLE (Professor Haus), and the medical imaging group at RLE (Professor Fujimoto).

To lay out the waveguides that are designed for fabrication, a significant amount of code was written within the group. We needed to unambiguously specify with the least amount of input the shape of the waveguides, so that the computer could calculate the remaining dimensional parameters and then fracture the mathematical line onto a grid suitable for e-beam writing. Figure 7 shows the required specification of a waveguide pair and a closeup of the fractured waveguide.

Work this year will focus on the development of the InP and glass material systems to suit the various optical designs and implement most of the current filter and coupler designs.

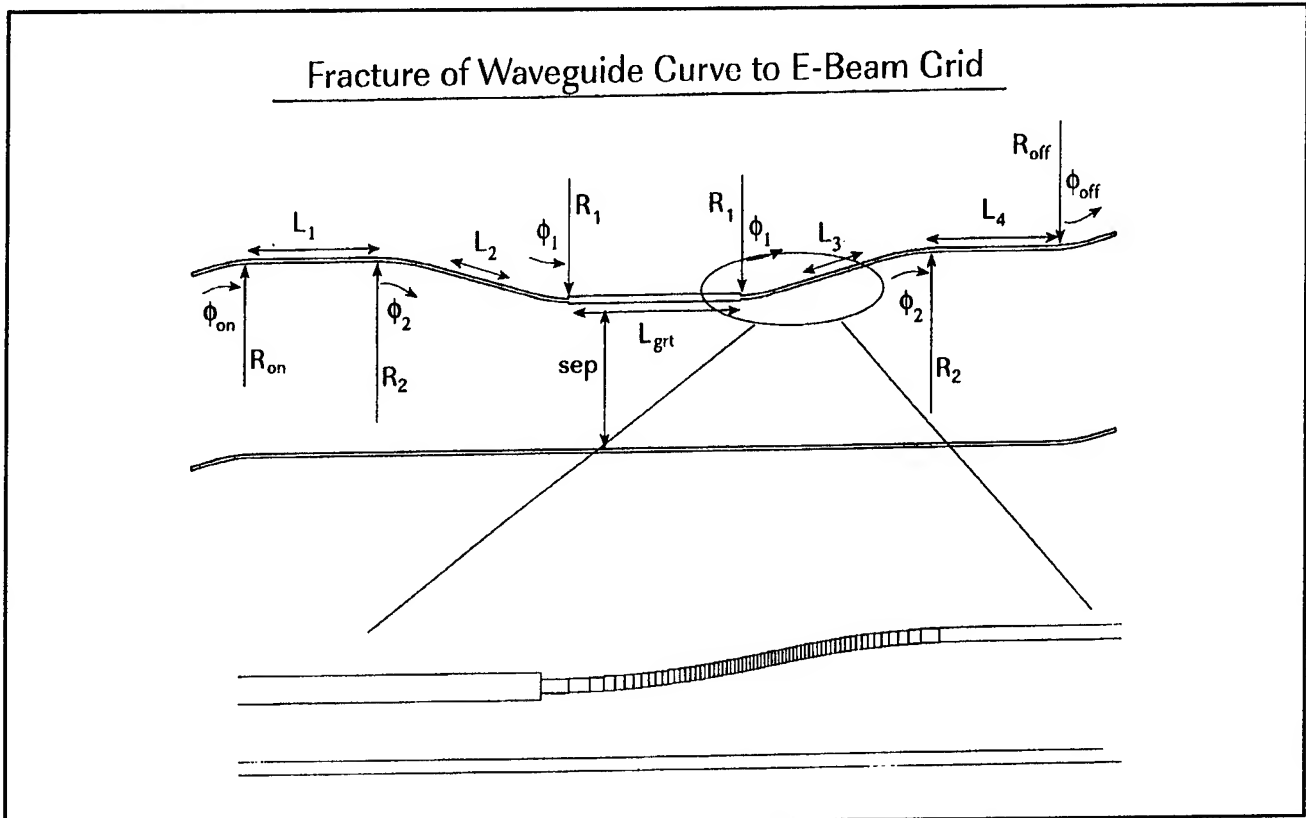


Figure 7. Fracture of waveguide curve to E-beam grid.

1.7 High-Power and Frequency-Doubled Stretched-Pulse Fiber Laser

Sponsors

Joint Services Electronics Program
Grant DAAH04-95-1-0038
National Center for Integrated Photonics
Technology
U.S. Air Force - Office of Scientific Research
Contract F49620-95-1-0221

Project Staff

Professor Erich P. Ippen, Lynn E. Nelson, Siegfried B. Fleischer, Gadi Lenz, David J. Dougherty

Our group's recent work on stretched-pulse additive-pulse mode-locked (SP-APM) fiber lasers has led to a generation of ultrashort pulses (100 fsec) with energies comparable to those of color-center lasers.²⁷ By using the APM rejection port as the output port, pulse energies of over 2 nJ have been achieved with average powers of > 90 mW. One application for these high power pulses is as a

seed for a Ti:Sapphire regenerative amplifier. The output pulses from the fiber laser at 1.55 μm are compressed and passed through a nonlinear crystal to generate pulses at 775 nm which can then seed the amplifier. This frequency-doubled SP-APM fiber laser is an inexpensive, compact seeding source for regenerative amplifiers and could replace the argon-pumped Ti:Sapphire laser.

Our goal has been to optimize the efficiency of the second harmonic generation and the quality of the frequency-doubled pulse width, rather than the fundamental pulse width and quality. By operating the SP-APM laser with a large net positive dispersion and backwards pumping a long piece of erbium-doped fiber, we obtained average output powers of > 95 mW at 35.2 MHz. The highly stretched 1 psec pulses have a 70 nm bandwidth and are compressed with silicon Brewster prisms to 100 fsec pulses with 85 mW of average power.

By focusing the compressed fundamental pulses into a 1 cm-long (uncoated) BaB_2O_4 (BBO) crystal, frequency-doubled powers as high as 7.5 mW can be achieved. These correspond to an 8.5 percent

²⁷ K. Tamura, C.R. Doerr, L.E. Nelson, H.A. Haus, and E.P. Ippen, "Technique for Obtaining High-energy Ultrashort Pulses from an Additive Pulse Mode-locked Erbium-doped Fiber Ring Laser," *Opt. Lett.* 19: 46 (1994).

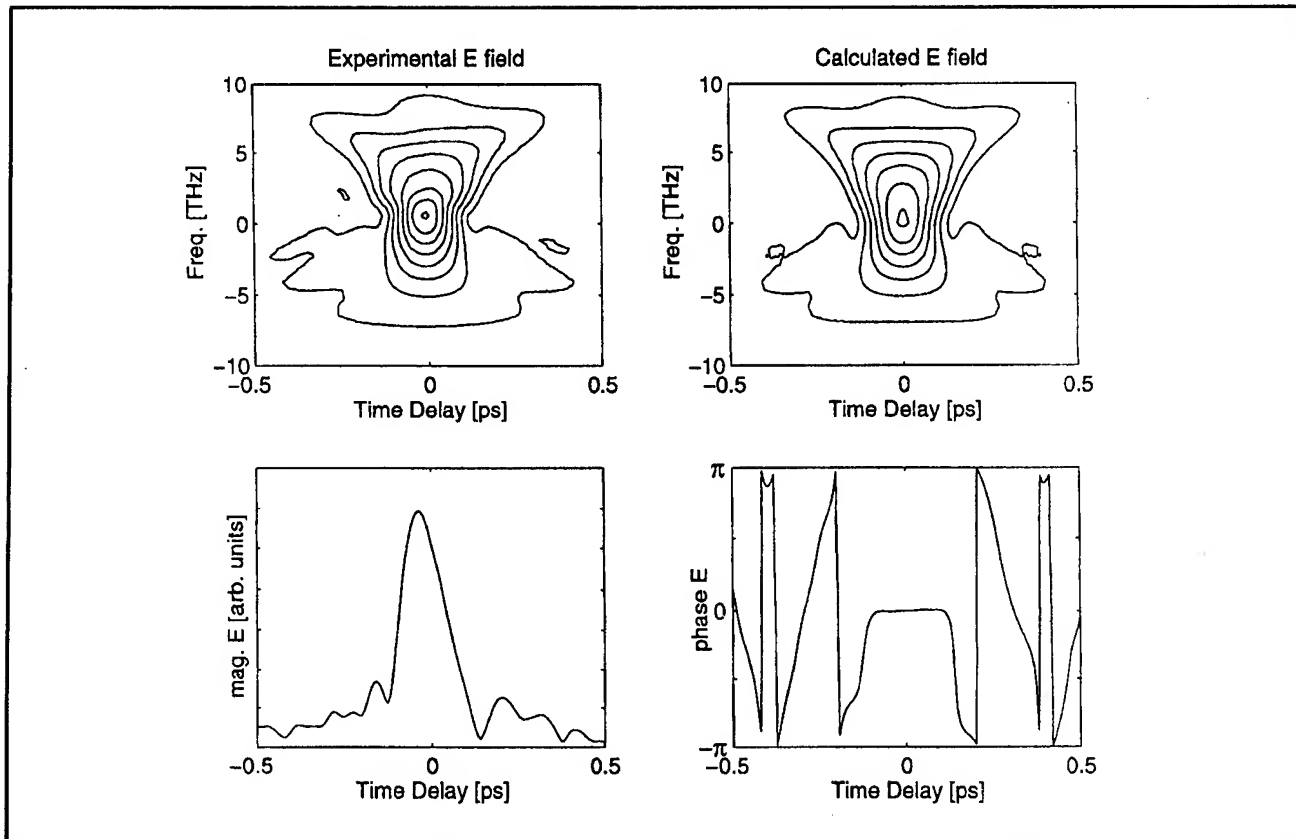


Figure 8. FROG data on the fundamental pulse: experimental data (top left), calculated fit (top right), derived pulse amplitude (bottom left), and derived pulse phase profile (bottom right).

conversion efficiency and pulse energies of up to 210 pJ. The frequency-doubled pulse width is 73 fsec and the spectrum is 8.5 nm wide centered at 774 nm, resulting in a time-bandwidth product of 0.31, which is near transform-limited assuming secant hyperbolic pulse shapes. Pulse energies on this order are required to seed high-repetition-rate regenerative amplifiers to avoid amplified spontaneous emission background.²⁸

In order to better characterize both the fundamental and frequency-doubled pulses, we used frequency-resolved optical gating (FROG), which allows the direct determination of the intensity and phase of an ultrashort pulse.²⁹ FROG data on the fundamental pulse was taken by measuring the spectrum of the second harmonic generation (SHG) as the pulse delay was changed in a background-free autocorrelation configuration. An iterative Fourier transform

algorithm was then used to derive the pulse amplitude and phase profiles, which are shown in figure 8 along with the SHG FROG trace from the calculated field. The phase is flat across the central portion of the pulse and indicates that the linear chirp has been compensated by the prisms in this region, whereas in the pulse wings, the phase varies rapidly, indicating nonlinear chirp. The high-pulse quality of the frequency-doubled output was confirmed by performing an SHG FROG measurement on this pulse using another background-free autocorrelation setup. The FROG trace was round and smooth, indicating that the phase was flat across the entire pulse. Efficient frequency-doubling at the peak of the fundamental pulse thus selects that part of the pulse which is unchirped, resulting in a visible red beam of transform-limited pulses which may be used for aligning and seeding a Ti:sapphire regenerative amplifier.

²⁸ T.B. Norris, "Femtosecond Pulse Amplification at 250 kHz with a Ti:Sapphire Regenerative Amplifier and Application to Continuum Generation," *Opt. Lett.* 17: 1009 (1992).

²⁹ D.J. Kane and R. Trebino, "Characterization of Arbitrary Femtosecond Pulses Using Frequency-resolved Optical Gating," *IEEE J. Quantum. Electron.* 29: 571 (1993); J. Paye, M. Ramaswamy, J. Fujimoto, and E.P. Ippen, "Measurement of the Amplitude and Phase of Ultrashort Light pulses from Spectrally Resolved Autocorrelation," *Opt. Lett.* 18: 1946 (1993).

1.8 Femtosecond Pulse Amplification and Continuum Generation at 1.55 μm

Sponsors

Joint Services Electronics Program
Grant DAAH04-95-1-0038
National Center for Integrated Photonics
Technology
U.S. Air Force - Office of Scientific Research
Contract F49620-95-1-0221

Project Staff

Professor Erich P. Ippen, Gadi Lenz, David J. Dougherty, Dr. Günter Steinmeyer, Werner Gellermann³⁰

High-power femtosecond pulses are needed for a variety of time-resolved spectroscopy applications. They provide intense excitation and make it possible to generate new wavelengths. Particularly useful for the latter process is a phenomenon known as continuum generation, in which a focused pulse produces a broadband femtosecond flash with synchronized spectral components over a wide wavelength range. Most previous sources providing this capability, notably amplified dye and Ti:sapphire systems, have been centered at near-visible and visible wavelengths. We have been working on a system for use in the longer wavelength 1.5 μm band of importance to optical communications. One such source was demonstrated previously: an additive-pulse-modelocked (APM) NaCl:OH⁻ color-center laser followed by a six pass NaCl:OH⁻ amplifier.³¹ This has not been pursued further because of difficulties with oscillator stability, the need for continuous multilaser illumination of the color-center crystals, and poor gain and beam quality in the amplifier. Instead, we have developed a different source using a very stable, diode-pumped femtosecond fiber laser oscillator and a high-gain KCl:Ti⁺ amplifier. With a kilohertz-rep-rate Q-switched Nd:YAG pump for the amplifier pump, only two passes are needed to amplify the fiber laser pulses to 10 $\mu\text{J/pulse}$. The output beam quality is excel-

lent, and a broadband continuum can be generated in a variety of materials.³²

The experimental arrangement is shown in figure 9. The diode-pumped stretched-pulse APM erbium-doped fiber laser³³ puts out highly chirped, 1.5-ps pulses with energies of about 2 nJ, at a rep-rate of 40 MHz. Single pulses are selected from this beam, by a LiTaO₃ modulator, at a 1 KHz rep-rate to match that of the Q-switched Nd:YAG laser. Relative timing between the selected pulse and peak amplifier gain can be adjusted with a countdown circuit. Single pass gain through the 2-cm-long KCl amplifier is about 1000 for Nd:YAG pumping of 1.5 mJ/pulse. After only two passes, the pulses have been amplified by a total factor of more than 10⁴, to energies on the order of 10 μJ . These pulses are then chirp compensated by a pair of silicon prisms to 200-fs durations and used to generate continuum. The limitation on pulse duration is due to mismatch between the fiber laser spectrum and amplifier gain spectrum which narrows the output spectrum to 20 nm.

Broadband continuum generation was observed in several different materials. Figure 10 shows typical spectra, observed by focusing into commercially available, 3-mm-thick samples of SF56 glass and ZnSe. In addition to the plotted spectrum limited by the InGaAs photodiode array in our multichannel analyzer, components extending all the way to the visible were apparent. Techniques for performing differential time-resolved spectroscopy with the entire continuum, and for selecting wavelength tunable pulses over the 1.4 to 1.7 μm range, are now being pursued.

1.8.1 Publication

Lenz, G., W. Gellerman, D.J. Dougherty, K. Tamura, and E.P. Ippen. "Femtosecond Fiber Laser Pulses Amplified by a KCl:Ti⁺ Color-center Amplifier for Continuum Generation in the 1.5- μm Region." *Opt. Lett.* 21: 137 (1996).

³⁰ Department of Physics, University of Utah, Salt Lake City, Utah.

³¹ G. Sucha, S.R. Bolton, and D.S. Chemla, "Generation of High-Power Femtosecond Pulses Near 1.5 μm Using a Color-Center Laser System," *IEEE J. Quantum Electron.* 28: 2163 (1992).

³² G. Lenz, W. Gellerman, D.J. Dougherty, K. Tamura, and E.P. Ippen, "Femtosecond Fiber Laser Pulses Amplified by a KCl:Ti⁺ Color-center Amplifier for Continuum Generation in the 1.5- μm Region," *Opt. Lett.* 21: 137 (1996).

³³ K. Tamura, E.P. Ippen, H.A. Haus and L.E. Nelson, "77-fs Pulse Generation From a Stretched-Pulse Mode-Locked All-Fiber Ring Laser," *Opt. Lett.* 18: 1080-1082 (1993).

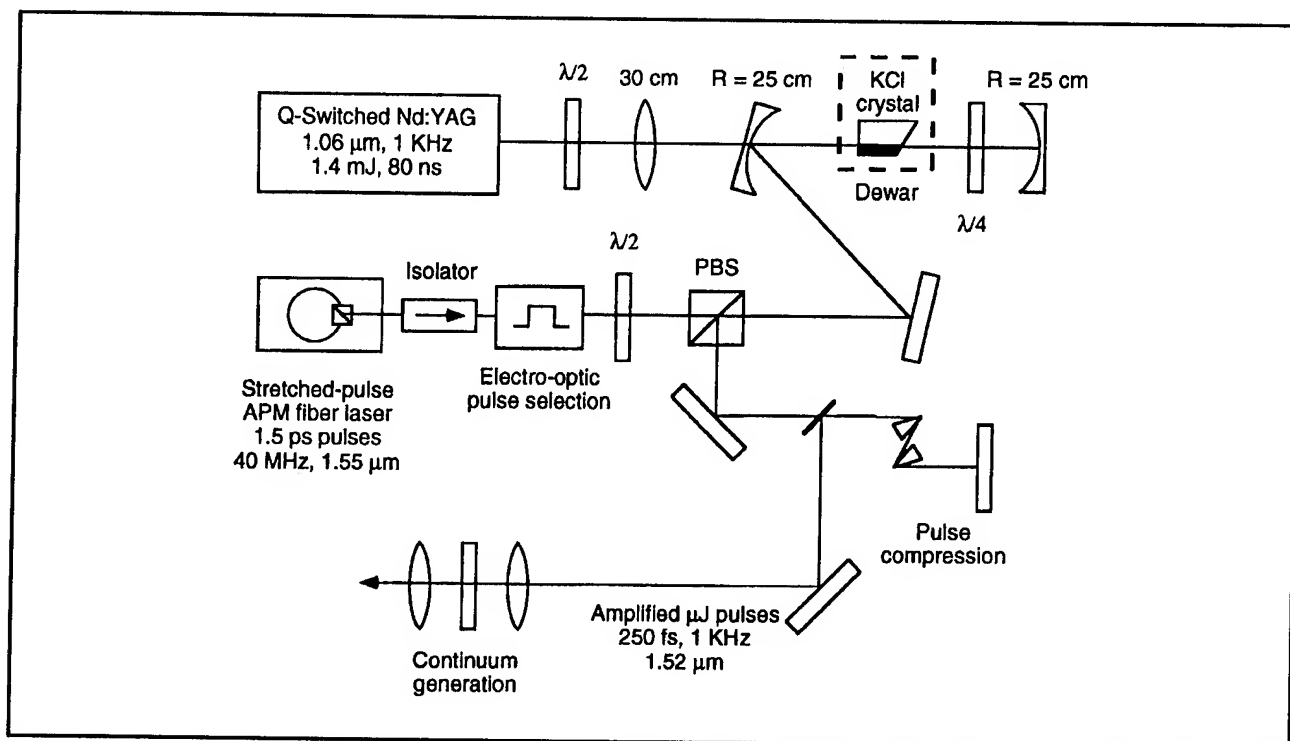


Figure 9. Experimental setup of the amplified fiber laser. $\lambda/2$ s, half-wave plates; $\lambda/4$, quarter-wave plate; PBS, polarizing beam splitter.

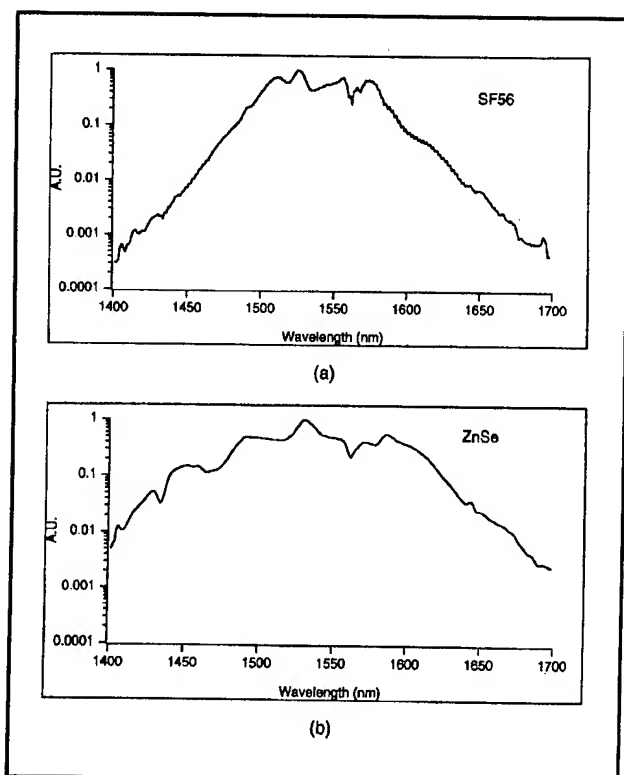


Figure 10. Continuum generated (a) in SF56 glass and (b) in ZnSe. The spectrum is displayed on a log axis normalized to the spectrum maximum and covers a spectral range of 1400-1700 nm.

1.9 Wavelength Shifting in Passive Semiconductor Waveguides

Sponsors

Joint Services Electronics Program
Grant DAAH04-95-1-0038
National Center for Integrated Photonics
Technology
U.S. Air Force - Office of Scientific Research
Contract F49620-95-1-0221

Project Staff

Professor Erich P. Ippen, Ali M. Darwish

Nondegenerate four-wave mixing (FWM) is a parametric process for frequency conversion in wavelength division multiplexing systems. We study FWM at $\lambda = 1.5 \mu\text{m}$ in passive InGaAsP/InP waveguides since in passive waveguides the nonlinearity relies on virtual transitions and is therefore ultrafast. Our preliminary picosecond³⁴ and CW³⁵ experimental results are promising. In a 7.5-mm-long passive InGaAsP/InP single quantum well waveguide, a conversion efficiency of -11 dB was accomplished for a wavelength shift of 25 nm (3.3 THz) with picosecond pulses. Figure 11 shows a typical output spectrum for this case. A conversion efficiency of -20 dB, with a wavelength shift of 20 nm, was also achieved with CW light. To assess the suitability of InGaAsP/InP waveguides for communication systems, we measured the fundamental parameters of the waveguides. For example, we measured group velocity dispersion using FWM phase matching nulls, linear loss coefficient using Fabry-Perot techniques, and two photon absorption (TPA) coefficient using a power saturation technique.

Nonlinear loss mechanisms such as TPA can place fundamental limitations on the FWM conversion efficiency. We investigated the effect of nonlinear loss by solving a system of coupled first-order differential equations. The analysis indicates the presence of a geometry-independent maximum conversion efficiency equal to $e^{-2}|\chi^{(3)}/\text{Im}\{\chi^{(3)}\}|^2$. The analysis allows us to find the optimum device length and operating conditions and to understand some important issues in short pulse FWM. We are verifying the theoretical results with picosecond pulse FWM experiments.

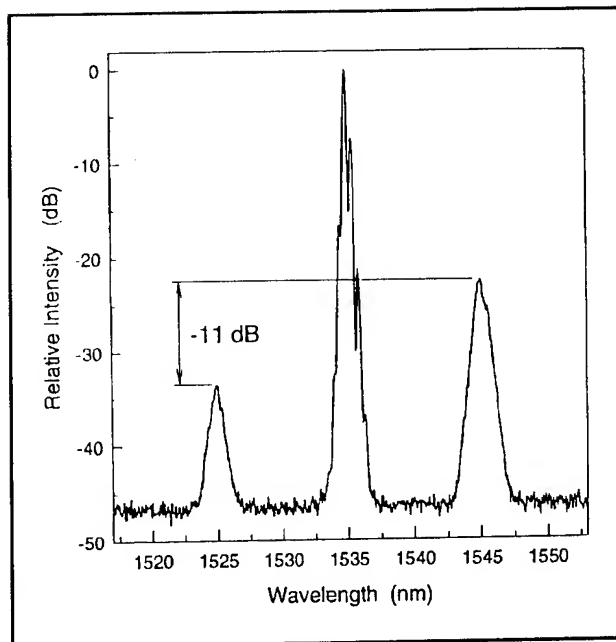


Figure 11. A conversion efficiency of -11 dB is achieved for a wavelength shift of 20 nm with high-peak power picosecond pulses.

Since the FWM process is phase sensitive, nonlinear index changes are expected to play an important role. Hence, we extended the FWM analysis to the case where nonlinear index changes dominate (e.g., a material with good nonlinear index switching figure of merit) and to the general case where both nonlinear index and loss mechanisms participate. The analysis indicates the presence of an improved geometry-independent maximum conversion efficiency that approaches unity as the nonlinear index changes dominate. In addition, the conversion efficiency has an oscillatory behavior with pump power since the nonlinear index changes drive the FWM process in- and out-of-phase. Compared to the case where nonlinear loss dominates, the optimum pump intensity and device length become significantly smaller when nonlinear index participate. While this is desirable for the CW case, it places serious restrictions on pump power for the short-pulse case. Finally, phase distortions due to nonlinear index changes lead to very complicated temporal pulse shaping at high pump powers.

This work is being carried out in collaboration with H. Le, J.P. Donnelly, S. Groves and E.A. Swanson at MIT Lincoln Laboratories. New multiple-

³⁴ A.M. Darwish, E.P. Ippen, H.Q. Le, J.P. Donnelly, S.H. Groves, and E.A. Swanson, "Short Pulse Wavelength Shifting by Four Wave Mixing in Passive InGaAsP/InP Waveguides," *Appl. Phys. Lett.*, forthcoming.

³⁵ J.P. Donnelly, H.Q. Le, E.A. Swanson, S.H. Groves, A. Darwish, and E.P. Ippen, "Nondegenerate Four-Wave Mixing Wavelength Conversion in Low-Loss Passive InGaAsP/InP Quantum-Well Waveguides," *Photonics Technol. Lett.*, forthcoming.

quantum-well structures are being designed with their collaboration for enhanced nonlinearity.

1.9.1 Publications

Darwish, A.M., E.P. Ippen, H.Q. Le, J.P. Donnelly, S.H. Groves, and E.A. Swanson. "Short Pulse Wavelength Shifting by Four Wave Mixing in Passive InGaAsP/InP Waveguides." *Appl. Phys. Lett.* Forthcoming.

Donnelly, J.P., H.Q. Le, E.A. Swanson, S.H. Groves, A. Darwish, and E.P. Ippen. "Nondegenerate Four-Wave Mixing Wavelength Conversion in Low-Loss Passive InGaAsP/InP Quantum-Well Waveguides." *Photonics Technol. Lett.* Forthcoming.

1.10 Visible and Near IR Femtosecond Pump-Probe Studies on C_{60} and Alkali-doped C_{60} Films

Sponsors

Joint Services Electronics Program
Contract DAAH04-95-1-0038
U.S. Air Force - Office of Scientific Research
Contract F49620-95-1-0221

Project Staff

Professor Erich P. Ippen, Siegfried B. Fleischer

Many novel photonic materials, such as C_{60} , are first available as thin films, since this is the easiest way to fabricate them. The nonlinear effects obtained from such sub-micron films are, however, many orders of magnitude smaller than for millimeter-size potential devices. It is thus important to detect very small signal modulations. In some cases, such as the present, high sensitivity is even more important because the samples are known to undergo long-lived photo-transformation under optical pumping.

At low chopping frequencies in pump-probe experiments, the signal-to-noise, and thus the lowest detectable signal, is in generally determined by intensity fluctuations of the femtosecond laser source. This requires the use of relatively high pump excitations for measurements of nonlinear properties. But at modest power levels (~ 1 mW), most laser sources with a sufficiently high

repetition-rate are shot-noise-limited at radio frequencies (RF). We implemented a RF modulation and heterodyne detection system for our pump-probe measurements that allows us to do shot-noise-limited-detection from 1 mW down to $2 \mu\text{W}$ detected power (at 800 nm). The modulation is done with an AOM at 10 MHz, and for the detection, we used a tuned detector to obtain a noise-equivalent power of about $1 \text{ pW}/\sqrt{\text{Hz}}$ at 10 MHz. The RF modulation also makes it possible to eliminate slow thermal background signals interfering with the picosecond or subpicosecond nonlinear response. Modulating both pump and probe eliminates scattered pump light and radiative RF pickup.

With this high sensitivity, we performed low-excitation-intensity pump-probe measurements on C_{60} thin films to study the ultrafast initial relaxation processes in the excited state. Pump excitation wavelengths throughout the visible spectrum and near UV and a variety of probe wavelengths in the visible and near IR were used. The signal, idler and pump beams of a Ti:Sapphire-pumped optical parametric oscillator (OPO) served as the femtosecond pulse source. Second harmonic generation and other mixing processes were used to generate quasi-continuously tunable light in the visible. An initial ultrafast response given by a step-response without any ultrafast decay on a picosecond or subpicosecond time-scale was observed. These results are in contrast to previously reported nonexponential decays obtained with higher fluence levels. We attribute those earlier results to laser induced changes in sample structure. Our experiments show further that the simple step response we observe at low powers changes to a more complicated, non-exponential response at higher pump fluence.³⁶ This effect is pronounced for shorter wavelength excitation. An average excitation fluence as low as 5 W/cm^2 at 460 nm was necessary to avoid it.

We also performed similar pump-probe studies on superconducting alkali-doped C_{60} films. Potassium- and rubidium-doped films were studied. The superconducting transition temperatures were measured for the samples used in this work and correspond to the 18 K and 33 K reported for K_3C_{60} and Rb_3C_{60} . Besides an instantaneous and a long-lived response, we observe two different decay processes with time-constants about 0.3 ps and 1 ps which we attribute to electronic scattering and vibrational relaxation. Our collaborators on this

³⁶ S.B. Fleischer, B. Pevzner, D.J. Dougherty, M.S. Dresselhaus, and E.P. Ippen, "Visible and Near-IR Femtosecond Low-excitation Pump-Probe Studies on C_{60} and Alkali-doped C_{60} Films," MRS Fall Meeting, Boston, Massachusetts, November 1995.

topic are Boris Pevzner and Professor Mildred S. Dresselhaus. Investigations of the superconducting films are continuing.

1.10.1 Publication

Fleischer, S.B., B. Pevzner, D.J. Dougherty, M.S. Dresselhaus, and E.P. Ippen. "Visible and Near-IR Femtosecond Low-excitation Pump-Probe Studies on C_{60} and Alkali-doped C_{60} Films." MRS Fall Meeting, Boston, Massachusetts, November 1995.

1.11 Characterization of ZnSe/GaAs Heterojunctions

Joint Services Electronics Program
Contract DAAH04-95-1-0038
U.S. Air Force - Office of Scientific Research
Contract F49620-95-1-0221

Project Staff

Professor Erich P. Ippen, David J. Dougherty, Professor Leslie A. Kolodziejski, Jody L. House

The investigation of the III-V/II-VI heterojunction formed between GaAs and ZnSe is important for several optoelectronic applications such as reliable blue laser diodes, and for linear and nonlinear optical communication devices.³⁷ By using a new technique which is a combination of photoreflectance (PR) and internal photo-emission (IPE) spectroscopies, we obtained an estimate of 200 meV for value of the conduction band offset. This is different from the commonly accepted value of 300 meV. We also have determined the magnitude and sign of the interface charge and trap densities for our sample.

The usual diagnostic tools for semiconductor characterization such as photoluminescence, Hall effect, and capacitance voltage measurements are either not specific to the interface, or cannot be used in this case because the films must be kept thin ($< 0.15 \mu\text{m}$) to avoid dislocations. Photoreflectance (PR) spectroscopy, a form of modulation spectroscopy which detects built-in electric fields, can be used to measure interface trap and charge densities and is thus well suited to characterizing

heterointerfaces. The bottom four traces in figure 12 (left) show PR spectra taken with different pump lasers for a $0.12 \mu\text{m}$ ZnSe film on an n-type GaAs buffer layer. The oscillation at 2.6 eV is the ZnSe bandgap signal, and the signals at 2.9 eV and 3.1 eV are due to the GaAs E1 and E1 + Δ_1 signals. These E1 and E1 + Δ_1 features were previously considered to be caused by spatially indirect cross over transitions and were used to deduce the currently accepted value of 300 meV for the ZnSe/GaAs conduction band offset.³⁸ Our data for a bare GaAs substrate, shown in the top trace, clearly demonstrate that the 2.9 eV signal originates from the GaAs alone and make the value of the conduction band offset an open question.

Analysis of the lineshapes of these signals as well as the signal from the GaAs bandedge (not shown) indicates the presence of a large ($1.8 \times 10^{12} \text{ cm}^{-2}$) surface charge density on the interface while the pump saturation intensities indicate a much smaller surface trap density of approximately 10^{10} to 10^{11} cm^{-2} . The bottom three traces in figure 12 (left) were taken with pump photon energies well below the ZnSe bandgap but still above the GaAs bandedge. The GaAs features are still present since electrons and holes are created in the GaAs, but a small signal at the ZnSe edge is also apparent. In a slab charge one-dimensional model of the electrostatics of the interface, carriers confined to the GaAs cannot screen fields in the ZnSe, so this signal must originate from electrons skipping over the barrier and into the ZnSe. This explanation accounts for the sign change as well as the drastically increased saturation intensity observed for this signal.

Tuning further towards the GaAs band edge eventually reduces the ZnSe signal as electrons do not have enough energy to enter the ZnSe. Figure 12 (right) shows the dependence on the ZnSe signal (hollow circles) amplitude as compared to the GaAs E1 signal (filled circles) as the pump wavelength is tuned from 840 nm to 688 nm corresponding to an energy range of 65 meV to 340 meV above the GaAs bandedge. The quadratic increase of the ZnSe signal above 160 meV is strikingly similar to internal emission photoconductivity results in other semiconductor heterojunctions.³⁹ In this experiment, tuning above the barrier results in a quadratic increase in current as described by Fowler-Nordheim emission theory. In our technique, the

³⁷ J.L. House, D.J. Dougherty, G.S. Petrich, L.A. Kolodziejski, and E.P. Ippen, *Appl. Surf. Sci.*, forthcoming.

³⁸ L. Kassel, H. Abad, J.W. Garland, M. Raccach, J.E. Potts, M.A. Haase, and H. Cheng, *Appl. Phys. Lett.* 56: 42 (1990).

³⁹ H.K. Yow, P.A. Houston, and M. Hopkinson, *Appl. Phys. Lett.* 66: 2852 (1995).

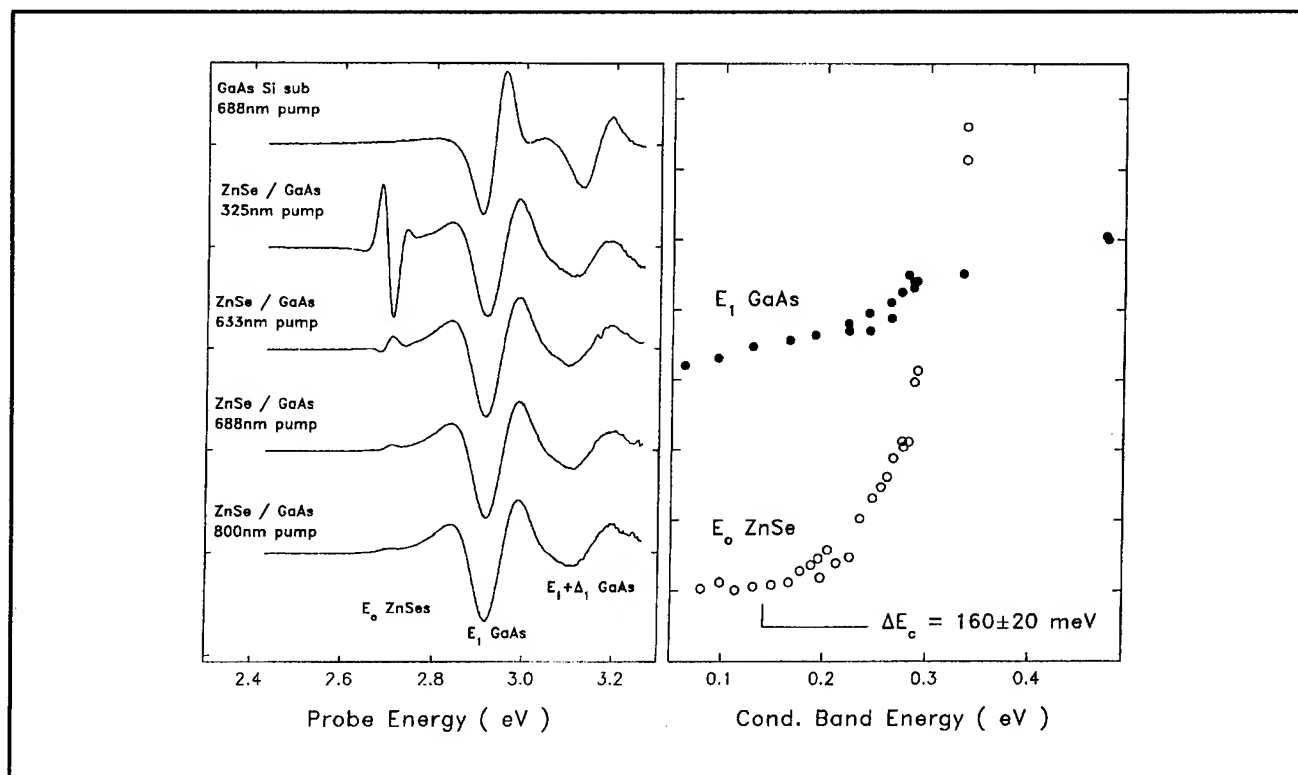


Figure 12. (left) PR spectra for a GaAs:Si substrate and a ZnSe/GaAs heterostructure taken with different pump sources. The features at 2.9 eV and 3.2 eV are due to transitions from the valence band to the L valley in GaAs. The signal at 2.67 eV is due to the ZnSe bandedge. (right) Signal amplitudes as a function of pump photon energy measured as electron conduction band energy in the GaAs. The threshold in the E_0 curve denotes the minimum electron energy necessary to escape into the ZnSe from the GaAs.

arrival of the electrons in the ZnSe is detected by the Franz-Keldysh effect rather than as photocurrent, making it an equivalent noncontact technique. Note that the E_1 GaAs signal, which remains relatively constant over this range, is, in fact, a measure of the absorption spectrum of the GaAs in a manner similar to photoluminescence excitation spectroscopy. The 160 meV threshold energy can be combined with a solution of Poisson's equation to arrive at a value for conduction band offset of 200 meV.

With this technique, we can measure surface charge and trap densities as well as the fundamental band alignment of semiconductor heterostructures. Relating these parameters to MBE growth and layer nucleation conditions should lead to improved understanding of semiconductor interfaces and interesting new materials such as ZnSe/GaAs quantum wells.

1.11.1 Publications

House, J.L., D.J. Dougherty, G.S. Petrich, L.A. Kolodziejski, and E.P. Ippen. *Appl. Surf. Sci.* Forthcoming.

Yow, H.K., P.A. Houston, and M. Hopkinson. *Appl. Phys. Lett.* 66: 2852 (1995).

1.12 Wavelength-Tunable Femtosecond Diagnostic Methods for Characterizing Photonic Bandgap Device Performance

Sponsors

Joint Services Electronics Program
Contract DAAH04-95-1-0038

National Science Foundation
Grant ECS 94-23737

U.S. Air Force - Office of Scientific Research
Contract F49620-95-1-0221

Project Staff

Professor Erich P. Ippen, Constantine Tziligakis, Gadi Lenz, Siegfried B. Fleischer, Dr. Günter Steinmeyer

A major area of potential applications for photonic bandgap materials is in the development of new devices with improved characteristics in the optical regime. Submicron structures are being fabricated for the near-infrared wavelengths by Professor Kolodziejski's group, and we are developing wavelength-tunable-femtosecond (WTF) techniques to investigate the actual device characteristics.

For that purpose, we are building a WTF experimental setup for characterizing one dimensional air-bridge photonic bandgap devices in the 3-5 micron range. These devices, currently being fabricated, consist of a dielectric waveguide periodically punctuated with holes and suspended in air, thus forming an air-bridge structure which exhibits an optical bandgap in the 3-5 micron wavelength range. The introduction of an appropriate defect region (absence of a hole) in the middle of the periodic structure creates a microcavity characterized by a high Q resonance placed inside the bandgap. In the fabrication of the structures, GaAs is used for the waveguide and $\text{Al}_x\text{Ga}_{1-x}\text{As}$ for the underlying substrate. The experimental setup we are using to test these structures takes advantage of the unique features of femtosecond Ti:sapphire lasers and optical parametric oscillators (OPOs). By synchronously pumping an OPO with a Ti:sapphire laser, two well-synchronized femtosecond pulse trains are obtained with tens of milliwatts average power tunable in the 1-2 micron wavelength range. Femtosecond pulses at longer wavelengths are then obtained by difference frequency generation in a LiIO_3 nonlinear crystal. Wavelength conversion of femtosecond pulses to the 3-5 micron regime is possible with an average powers of hundreds of microwatts available for coupling into the photonic bandgap structures. Reflecting microscope objectives couple the infrared pulses into the waveguides and provide imaging of the output. With the output light coupled into a spectrometer, we take advantage of the very wide spectrum of the femtosecond pulses to obtain essentially single-shot measurement of the device bandgap and filtering character-

istics. In preliminary work these diagnostics are being applied to test waveguide structures.⁴⁰

1.12.1 Publication

Tziligakis, C., K.Y. Lim, J.C. Chen, G.S. Petrich, L.A. Kolodziejski, E.P. Ippen, S. Fan, P.R. Villeneuve, and J.D. Joannopoulos. "Wavelength-Tunable Femtosecond Diagnostic Methods for Characterizing Photonic Bandgap Device Performance." *NATO Advanced Studies Institute of Photonic Bandgap Materials*, Elounda, Greece, June 18-30, 1995.

1.13 Ultrashort Pulse Generation in Solid-State Lasers

Sponsors

Joint Services Electronics Program
Grant DAAH-04-95-1-0038
U.S. Air Force - Office of Scientific Research
Contract F49620-95-1-0221
U.S. Navy - Office of Naval Research (MFEL)
Contract N00014-94-1-0717

Project Staff

Dr. Brett E. Bouma, Igor P. Bilinsky, Boris Golubovic, Dr. Viktor P. Mikhailov, Professor James G. Fujimoto

1.13.1 Compact Ultrashort Pulse Sources

Advances in signal processing, high-speed communications, and the investigation of ultrafast nonlinear processes in semiconductor devices and materials may be facilitated through the development of compact ultrashort pulse laser sources. Generally, these sources must be technologically simple, robust, and cost effective. While solid state gain media are well suited to meet these criteria, their relatively low-gain cross-sections have required the use of fast saturable absorption for modelocking. During the last few years, significant advances have been made in the development of fast saturable absorbers utilizing the electronic Kerr effect. Kerr

⁴⁰ C. Tziligakis, K.Y. Lim, J.C. Chen, G.S. Petrich, L.A. Kolodziejski, E.P. Ippen, S. Fan, P.R. Villeneuve, and J.D. Joannopoulos, "Wavelength-Tunable Femtosecond Diagnostic Methods for Characterizing Photonic Bandgap Device Performance," *NATO Advanced Studies Institute of Photonic Bandgap Materials*, Elounda, Greece, June 18-30, 1995.

lens modelocking (KLM),⁴¹ in fact, has allowed the generation of the shortest pulses ever produced directly from a laser oscillator.⁴² A theoretical understanding of Kerr effect modelocking has been developed by Professors Eric P. Ippen and Hermann A. Haus in conjunction with our group.⁴³

In the past year, we have applied our theoretical model of KLM to facilitate optimization of mode-locking performance and allow the extension of this simple pulse-forming mechanism to novel resonator geometries. Two Ti:Al₂O₃ KLM lasers in our laboratory, currently producing pulses of ~ 10 fs duration, are the direct result of the accuracy of our modeling.

KLM lasers utilize self-focusing in the presence of soliton-like pulse shaping arising from self-phase modulation and net negative intracavity group-velocity dispersion (GVD) to generate chirp-free ultrashort pulses. Negative GVD is most commonly achieved in KLM lasers by use of an intracavity prism pair; however, this places constraints on laser geometry and size. To date, KLM lasers have almost exclusively used a folded X- or Z-cavity geometry with the prism pair in one arm of the laser. Repetition rates have not exceeded the 100 MHz range.

In the past year, we have advanced our theoretical understanding of KLM to include novel compact laser geometries. We have demonstrated that alternative Kerr-lens mode-locked resonator designs can simultaneously reduce overall laser size and complexity while actually enhancing functionality.⁴⁴ These new resonator designs enable the self-starting generation of 100 fs pulses at repetition rates of 1 GHz. These lasers have important implications for compact, all-solid-state, femtosecond laser technology, especially because it can readily be extended to the modelocking of diode-pumped lasers.

1.13.2 Flashlamp Pumped Ti:Al₂O₃ Laser Modelocking

Simple and affordable high-power, short-pulse laser sources are important for numerous applications such as optical frequency conversion including harmonic generation and parametric generation, studies of nonlinear optical properties of materials, materials processing, and laser surgery. To date, the most common approach to obtaining short pulses in the microjoule to millijoule range from modelocked Ti:Al₂O₃ lasers is by using multipass or regenerative amplifier systems. Such systems achieve excellent performance, however they are relatively complex and costly. A simple, alternative method for the generation of high-power, picosecond pulses directly from a single laser oscillator is the use of flashlamp pumped, modelocked systems.⁴⁵

In collaboration with Dr. Victor Mikhailov at the International Laser Center in Minsk, Belarus, we have extended our previous work by investigating the applications of new materials capable of providing passive saturable absorber action in the near infrared. We have explored the spectroscopy and absorption dynamics of materials such as CuIn_{2-x}Se_x nanoparticles in glass, CuS and Fe ion films, and V³⁺:YAG. The relative simplicity of these materials allows the inexpensive fabrication of laser quality samples. Our preliminary studies have indicated that these materials may be appropriate for the passive modelocking of flashlamp pumped Ti:Al₂O₃.

1.13.3 Broad Spectrum Solid-State Laser Development

Numerous studies, including the investigation of ultrafast carrier relaxation processes in semiconductors and semiconductor devices and biomedical imaging, require the availability of broad spectral coverage in the infrared and near infrared wave-

⁴¹ D.K. Negus, L. Spinelli, N. Goldblatt, and G. Feugnet, "Sub-100 fs Pulse Generation by Kerr Lens Modelocking in Ti:Al₂O₃," Postdeadline paper presented at the Topical Meeting on Advanced Solid State Lasers, Optical Society of America, Washington, DC, May 1991.

⁴² J. Zhou, G. Taft, C-P. Huang, M.M. Murnane, H.C. Kapteyn, and I.P. Christov, "Pulse Evolution in a Broad-Band Ti:Sapphire Laser," *Opt. Lett.* 19: 1149 (1994).

⁴³ H.A. Haus, J.G. Fujimoto, and E.P. Ippen, "Structures for Additive Pulse Modelocking," *J. Opt. Soc. Am. B* 8: 2068 (1991); H.A. Haus, J.G. Fujimoto, and E.P. Ippen, "Analytic Theory of Additive Pulse and Kerr Lens Mode Locking," *IEEE J. Quant. Electron.* 28: 2086 (1992).

⁴⁴ B.E. Bouma and J.G. Fujimoto, "Compact Kerr-lens Mode-locking Resonators," *Opt. Lett.* 21: 256 (1996).

⁴⁵ B.E. Bouma, A. Gouveia-Neto, J. A. Izatt, J. Russel, R. Sierra, U. Keller, and J. G. Fujimoto, "Hybrid Mode Locking of a Flash-Lamp-Pumped Ti:Al₂O₃ Laser," *Opt. Lett.* 19: 1858 (1994).

length range. Several broad bandwidth, tunable solid state sources have been developed, most notably $\text{Ti:Al}_2\text{O}_3$ (titanium sapphire), $\text{Cr:Mg}_2\text{SiO}_4$ (Cr:Forsterite), and Cr:YAG. The combination of these three sources alone can, in principle, cover the entire range from $.65\ \mu\text{m}$ to $1.65\ \mu\text{m}$. However, of these sources only titanium sapphire has been demonstrated to tune throughout its fluorescent emission range. This fact is largely due to the presence of excited state absorption, parasitic absorption, and poor figure of merit in the Chromium doped crystals.

During the past year, we have explored two approaches to enhancing the wavelength coverage of the three laser crystals listed above. The first approach involves the development of novel pumping strategies which allow the use of shorter laser crystals and thereby reduce the deleterious effects of excited state and parasitic absorption. The second approach has explored new crystal growth procedures which may allow the development of more strongly doped and higher figure of merit crystals.

Fluorescent emission from Cr:Forsterite suggests the possibility of producing modelocked laser pulses in the wavelength range of $1.05\ \mu\text{m}$ to $1.35\ \mu\text{m}$. However, an overlap with the absorption band on the short wavelength end of the spectrum and the presence of water absorption lines near $1.35\ \mu\text{m}$ have limited the tuning range for modelocked operation. The convenience of pumping with the standard $1.06\ \mu\text{m}$ Nd:YAG lasers, where the absorption of Cr:Forsterite is relatively weak, dictates the use of long laser crystals which preclude tuning below $1.18\ \mu\text{m}$. We have constructed a Nd:YAG pumped KLM Cr:Forsterite laser and have demonstrated tuning over the range $1.18\ \mu\text{m}$ to $1.32\ \mu\text{m}$. This laser produces modelocked pulse durations of 30 fs and is currently being used for short coherence length biomedical imaging.

In collaboration with the International Laser Center, in Minsk, Belarus, we have investigated new crystal growth procedures which may allow the development of more strongly doped Cr:Forsterite crystals. Higher doping will allow the use of shorter laser crystals than previously used and should result in both greater tuning range and the production of shorter modelocked pulse durations. During the

past year, we have investigated the spectroscopy and laser action of Cr:Forsterite crystals grown along the crystallographic c-axis, comparing their performance to the standard crystal growth which progresses along the a-axis. Our preliminary investigation focused on crystals from the two growth procedures having equivalent concentrations of chromium ions and indicated that this new crystal growth process can produce laser gain media with performance comparable to that of the standard crystals. Future work will explore the spectroscopy and laser performance of highly doped c-axis grown Cr:Forsterite crystals.

1.13.4 Publication

Bouma, B.E., and J.G. Fujimoto. "Compact Kerr-lens Mode-locking Resonators." *Opt. Lett.* 21: 256 (1996).

1.14 Ultrafast Phenomena in Materials and Devices

Sponsors

Joint Services Electronics Program
Grant DAAH-04-95-1-0038
U.S. Air Force - Office of Scientific Research
Contract F49620-95-1-0221
U.S. Navy - Office of Naval Research (MFEL)
Grant N00014-94-1-0717

Project Staff

Igor P. Bilinsky, Boris Golubovic, Dr. Brett E. Bouma, Professor James G. Fujimoto, Dr. Christopher Stanton,⁴⁶ Dr. Norman Tolk⁴⁷

1.14.1 Carrier Dynamics in InGaAs Strained Layer Diodes

Nonlinear gain and transient carrier dynamics in diode lasers play important roles in laser line width, modulation bandwidth, amplification, and short pulse generation. Previous studies by our group⁴⁸ have used a new heterodyne multiple wavelength pump-probe technique to investigate nonlinear gain dynamics in InGaAs/AlGaAs graded-index single-

⁴⁶ University of Florida, Gainesville, Florida.

⁴⁷ Vanderbilt University, Nashville, Tennessee.

⁴⁸ C.-K. Sun, B. Golubovic, J.G. Fujimoto, H.K. Choi, and C.A. Wang, "Heterodyne Nondegenerate Pump-Probe Measurement Technique for Guided Wave Devices," *Opt. Lett.* 20: 210-212 (1995).

quantum-well diode lasers. To our knowledge, preceding this work, no multiple wavelength gain and transient carrier dynamics measurements were reported. We were able to map the femtosecond gain dynamics at a range of wavelengths for a fixed excitation pulse. The transient measurements showed a pump-induced transmission decrease in both the gain and loss regions. Around zero time delay, a sharp transmission decrease was observed with a spectral peak around the pump wavelength and a time-resolution limited recovery. This transient may be attributed to a combination of two-photon absorption, spectral hole burning, and coherent artifacts. Shortly after the pump pulse, a thermalized carrier distribution with higher temperature and lower concentration is established. Gain depletion throughout the investigated spectral region was observed. For time delays longer than 1 ps, the gain partially recovers as the temperature reaches equilibrium with the lattice. The residual gain changes are produced by the decrease in the carrier population and recover on a much longer time scale.

In collaboration with theoretical physicists at the University of Florida, Gainesville, detailed theoretical models for the gain dynamics for InGaAs strained layer diodes were developed. Calculations of the femtosecond gain dynamics in InGaAs/AlGaAs strained layer single-quantum-well diode lasers were compared to experiments which used a multiple-wavelength pump probe technique.⁴⁹ In the model developed, transient gain and differential transmission are computed in a multiband effective mass model including biaxial strain, valence subband mixing, and scattering both within and between subbands. The transient photogeneration of electron-hole pairs by the pump pulse and subsequent relaxation of carriers by both polar optical phonon scattering and carrier-carrier scattering are calculated within a Boltzmann equation framework. A relaxation approximation for the carrier-carrier scattering is made and the coupled Boltzmann equation is solved using an adaptive Runge-Kutta technique.⁵⁰ This formalism aids the full understanding of the obtained experimental results and may aid future device design.

1.14.2 Multiwavelength Studies of The Nonlinear Index of Refraction in Narrow Bandgap Semiconductors

The nonlinear optical properties of semiconductor materials are of great interest because of their role as components of various optical semiconductor devices. The dominant nonlinear contribution to the index of refraction is the third order nonlinear response of the material. It is important for various applications including optical limiting, all optical switching and modulation as well as for frequency modulation behavior of diode lasers.

Theory predicts the scaling of nonlinear index with semiconductor bandgap, E_g , as E_g^{-4} .⁵¹ For this reason, narrow bandgap semiconductor materials, such as InAs, GaSb, etc., are of particular importance. To date, most previous investigations of nonlinear index effects have used fixed wavelength or narrowly tunable laser sources and inferred the scaling behavior and wavelength dependence by performing experiments in different materials systems. Tunability constraints have been especially severe for these experiments which require high-intensity, short laser pulses. Using the Vanderbilt Free Electron Laser (FEL) as a broadly tunable, high-intensity source, we have initiated the first systematic study of wavelength dependence of nonlinear index in narrow gap semiconductors.

There are several techniques for measuring the nonlinear index. One of the simplest and most sensitive is Z-scan.⁵¹ It uses nonlinear propagation in order to measure the integrated nonlinear index. A high intensity laser beam is focused onto a material and the position of the material is scanned in the axial or Z direction. Scanning the Z position varies the focusing parameters of the beam in the nonlinear material and changes the propagation of the beam in the far field. Changes in the divergence of the beam are measured by measuring the transmission through an aperture positioned in the far field region behind the sample. From these transmission changes, the sign and magnitude of the nonlinear index can be calculated.

⁴⁹ G.D. Sanders, C.-K. Sun, B. Golubovic, J.G. Fujimoto, and C.J. Stanton, "Carrier-carrier Scattering in the Gain Dynamics of InGaAs/GaAs Diode Lasers," submitted to *Phys. Rev. B*; G.D. Sanders, C.J. Stanton, C.-K. Sun, B. Golubovic, and J.G. Fujimoto, "Theory of Carrier Gain Dynamics in InGaAs/GaAs Strained-layer Single-quantum-well Lasers," paper presented at the Eighth International Conference on Superlattices Microstructures and Microdevices, Cincinnati, Ohio, August 20-25, 1995.

⁵⁰ G.D. Sanders, C.-K. Sun, B. Golubovic, J.G. Fujimoto, and C.J. Stanton, "Hot Carrier Effects in Femtosecond Gain Dynamics of InGaAs/AlGaAs Quantum Well Lasers," paper presented at the Ninth International HCIS Conference, Chicago, August 1995.

⁵¹ M. Sheik-Bahae, A.A. Said, T.-H. Wei, D.J. Hagan, and E.W. Van Stryland, *J. Quant. Electron.* 26: 760 (1990).

In collaboration with Professor Norman Tolk's group at Vanderbilt University, we have used the Vanderbilt FEL to perform Z-scan experiments in InAs, GaSb and Ge. The Vanderbilt FEL is a high intensity laser source continuously tunable in the wavelength region from 2 to 10 microns which is relevant for narrow bandgap semiconductors. The Z-scan experiments were performed in the region from 4 to 6.5 microns which allowed us to observe both the bound and free carrier contributions to the nonlinear index as well as the two photon absorption coefficients as a function of wavelength. The measured values of the components of the nonlinear index are in fair agreement with ones obtained from theoretical predictions. By utilizing a pulse selection mechanism, it should be possible to eliminate thermal effects and further separate the bound and free carrier components of the nonlinear index. Thus the sensitivity and accuracy of the measurements will be increased.

1.14.3 Publications

Sanders, G.D., C.-K. Sun, B. Golubovic, J.G. Fujimoto, and C.J. Stanton. "Carrier-carrier Scattering in the Gain Dynamics of InGaAs/GaAs Diode Lasers." Submitted to *Phys. Rev. B*.

Sanders, G.D., C.J. Stanton, C.-K. Sun, B. Golubovic, and J.G. Fujimoto. "Theory of Carrier Gain Dynamics in InGaAs/GaAs Strained-layer Single-quantum-well Lasers." Paper presented at the Eighth International Conference on Superlattices Microstructures and Microdevices, Cincinnati, Ohio, August 20-25, 1995.

Sanders, G.D., C.-K. Sun, B. Golubovic, J.G. Fujimoto, and C.J. Stanton. "Hot Carrier Effects in Femtosecond Gain Dynamics of InGaAs/AlGaAs Quantum Well Lasers." Paper presented at the Ninth International HCIS Conference, Chicago, Illinois, August, 1995.

Sun, C.-K., B. Golubovic, J.G. Fujimoto, H.K. Choi, and C.A. Wang. "Heterodyne Nondegenerate Pump-Probe Measurement Technique for

Guided Wave Devices." *Opt. Lett.* 20: 210-212 (1995).

1.15 Laser Medicine

Sponsors

National Institutes of Health
Grant 9-R01-EY11289
U.S. Air Force - Office of Scientific Research
Grant F49620-95-1-0221
U.S. Navy - Office of Naval Research (MFEL)
Contract N00014-94-1-0717

Project Staff

Stephen A. Boppart, Dr. Brett E. Bouma, Professor James G. Fujimoto, Dr. Mark E. Brezinski, Michael R. Hee, Guillermo J. Tearney, Professor James G. Fujimoto, Eric A. Swanson,⁵² Dr. Cynthia A. Toth,⁵³ Dr. Reginald Birngruber,⁵⁴ Dr. Clarence P. Cain,⁵⁵ Gary D. Noojin,⁵⁵ Dr. W.P. Roach,⁵⁶ Dr. Cheryl D. DiCarlo⁵⁶

1.15.1 Optical Coherence Tomography Technology

Optical biopsy, or micron scale, cross-sectional, optical imaging of tissue microstructure in situ, would aid the diagnosis and clinical management of many diseases. Optical coherence tomography (OCT) is a new optical imaging technique that uses low coherence interferometry to perform high-resolution, cross-sectional imaging in biological systems. OCT is analogous to ultrasound B mode imaging except that it uses an infrared light source and low coherence interferometry to perform micron resolution ranging and imaging. For an interferometric signal to be detected, the optical path lengths of the object and reference beam must be matched to within the coherence length of the source. Since multiply scattered photons from the object have traveled different optical path lengths than the reference beam, multiple scattering effects are minimized in the OCT image. Tissue reflectance is obtained axially by varying the reference arm delay and digitizing the magnitude of the inter-

⁵² MIT Lincoln Laboratory, Lexington, Massachusetts.

⁵³ Duke University Eye Center, Durham, North Carolina.

⁵⁴ Medizinisches Laserzentrum, Lubeck, Germany.

⁵⁵ TASC, San Antonio, Texas.

⁵⁶ Armstrong Laboratory, Brooks Air Force Base, Texas.

ference. A cross-sectional image is produced by recording axial reflectance profiles while the beam on the tissue specimen is scanned.

OCT has been extensively applied in ophthalmology to provide tomographic images of the transparent structures in the eye.⁵⁷ Clinical studies have shown that OCT provides high resolution, cross-sectional images of the retina and can be used to diagnose a wide range of retinal macular diseases.⁵⁸ OCT imaging in other human tissues is made difficult due to optical scattering. However, recent *in vitro* studies have shown that OCT can image architectural morphology in highly optically scattering tissues.

An important application of OCT is imaging the vascular system to identify atherosclerotic lesions that are prone to rupture.⁵⁹ OCT has ten times greater resolution than state-of-the-art catheter-based ultrasonography, intravascular ultrasound (IVUS). Additional research has shown that OCT can perform high-resolution imaging of other organ systems such as the gastrointestinal and urinary tracts.⁶⁰

Research in this laboratory, performed to advance optical coherence tomography technology, has yielded significant improvements in image resolution, acquisition speed, and the development of endoscopic imaging techniques. One of the key technological areas which greatly enhances the performance of OCT is the development of high power, ultrashort coherence length light sources. Recently, OCT imaging with axial resolutions of 2 to 4 μm have been demonstrated using broad bandwidth, short pulse femtosecond laser sources which have a short coherence length.⁶¹

Improvement in image acquisition times have also been recently demonstrated. The image acquisition times of OCT systems used in previous studies (60 seconds) is adequate for *in vitro* imaging but is insufficient for *in vivo* imaging because of motion artifacts. The development of higher power sources is critical to increasing image acquisition speed since the image acquisition rate directly trades off against detection sensitivity. To achieve image acquisition times below one second, alternatives to mechanical reference arm scanning technologies must also be developed. Recent work using these new technologies have achieved an acquisition rate of up to four images per second.⁶²

Another technology which is necessary to apply OCT to imaging of internal organ systems is a catheter/endoscope which can deliver, focus, scan, and collect a single spatial mode optical beam. The catheter must be flexible and have a small diameter to facilitate its entry into internal channels such as coronary arteries, pancreatic or biliary ducts. A single mode fiber optic scanning OCT catheter/endoscope prototype has been developed during the past year.⁶³ This device is an enabling technology for developing a wide range of endoscopes and will permit OCT imaging of the *in vivo* gastrointestinal tissues.

This work is an ongoing collaboration with researchers at MIT, MIT Lincoln Laboratories, Massachusetts General Hospital's Cardiology Department, Pathology Department, and the Wellman Laboratories of Photomedicine. MIT Lincoln Laboratories has provided much of the OCT technology and equipment for use in ophthalmic and multiply scattering tissue studies. Massachusetts General Hos-

⁵⁷ G.D. Sanders, C.-K. Sun, B. Golubovic, J.G. Fujimoto, and C.J. Stanton, "Hot Carrier Effects in Femtosecond Gain Dynamics of InGaAs/AlGaAs Quantum Well Lasers," paper presented at the Ninth International HCIS Conference, Chicago, Illinois, August 1995.

⁵⁸ C.A. Puliafito, M.R. Hee, C.P. Lin, E. Reichel, J.S. Schuman, J.S. Duker, J.A. Izatt, E.A. Swanson, and J.G. Fujimoto, "Imaging of Macular Diseases with Optical Coherence Tomography," *Ophthalmol.* 102: 217-229 (1995).

⁵⁹ M.E. Brezinski, G.J. Tearney, B.E. Bouma, J.A. Izatt, M.R. Hee, E.A. Swanson, J.F. Southern, and J.G. Fujimoto, "Optical Coherence Tomography for Optical Biopsy: Properties and Demonstration of Vascular Pathology," *Circulation*, forthcoming.

⁶⁰ G.J. Tearney, M.E. Brezinski, M.R. Hee, B. Bouma, J.A. Izatt, E.A. Swanson, J.F. Southern, and J.G. Fujimoto, "Optical Biopsy in Human Tissue using Optical Coherence Tomography and Microscopy," paper presented at the Conference on Lasers and Electro-Optics, Optical Society of America, May 1995; G.J. Tearney, M.E. Brezinski, B.E. Bouma, J.F. Souther, and J.G. Fujimoto, "High Resolution Imaging of Gastrointestinal Tissue using Optical Coherence Tomography," Annual Meeting of the American Gastrointestinal Association, May 1996.

⁶¹ B.E. Bouma, G.J. Tearney, S.A. Boppart, M.R. Hee, M.B. Brezinski, and J.G. Fujimoto, "High Resolution Optical Coherence Tomographic Imaging Using a Modelocked Ti:Al₂O₃ Laser Source," *Opt. Lett.* 20(13): 1486-1488 (1995).

⁶² G.J. Tearney, B.E. Bouma, S.A. Boppart, B. Golubovic, E.A. Swanson, and J.G. Fujimoto, "High Speed Optical Coherence Tomography," paper to be presented at the Conference on Advances in Photon Migration, Orlando, Florida, March 1996.

⁶³ G.J. Tearney, S.A. Boppart, B.E. Bouma, M.E. Brezinski, N. Weissman, J.F. Southern, and J.G. Fujimoto, "Scanning Single Mode Fiber Optic Catheter/Endoscope for Optical Coherence Tomography," *Opt. Lett.*, forthcoming.

pital has been instrumental in providing the tissue samples and pathology and performing research aimed at evaluating the potential for OCT to obtain micron level "optical biopsies" of human tissue.

1.15.2 High-Resolution Optical Coherence Tomography

Chromium doped Forsterite is a new tunable solid-state laser material with a broad emission band near $1.2\ \mu\text{m}$. Cr:Forsterite has been modelocked using KLM, and pulse durations as short as 25 fs have been achieved. The peak output power from this laser is sufficient to generate significant spectral broadening within optical fiber. The zero dispersion point of standard single mode fiber overlaps with the spectral output of the Cr:Forsterite laser. This coincidence results in a strongly modulated spectral output inappropriate for biomedical imaging. We have avoided this problem by using dispersion shifted fiber and can obtain high resolution, high contrast coherence gating. The high average output power provided by this source enables high image acquisition speeds at high sen-

sitivities since speed, sensitivity, and optical source power directly trade off against each other.

Coherence ranging is performed with the self-phase modulated spectral source using a fiber optic Michelson interferometer. Wavelength flattened splitters were used to preserve the spectral extent of the source as it was routed to the scanning reference arm mirror, the biological sample, and back to the detectors. Dual balanced heterodyne detection enabled near shot-noise limited detection.

An image of human adipose tissue, shown in figure 13, demonstrates the high resolution imaging capability of this system. For this image, the transverse resolution, determined by the numerical aperture of the focusing objective, matches the measured longitudinal resolution of 5.7 microns.

Ultrahigh resolution OCT imaging using mode locked solid state lasers is a powerful technology for performing optical biopsy which can be applied for diagnosis, interoperative guidance, and clinical management in a wide range of medical applications.

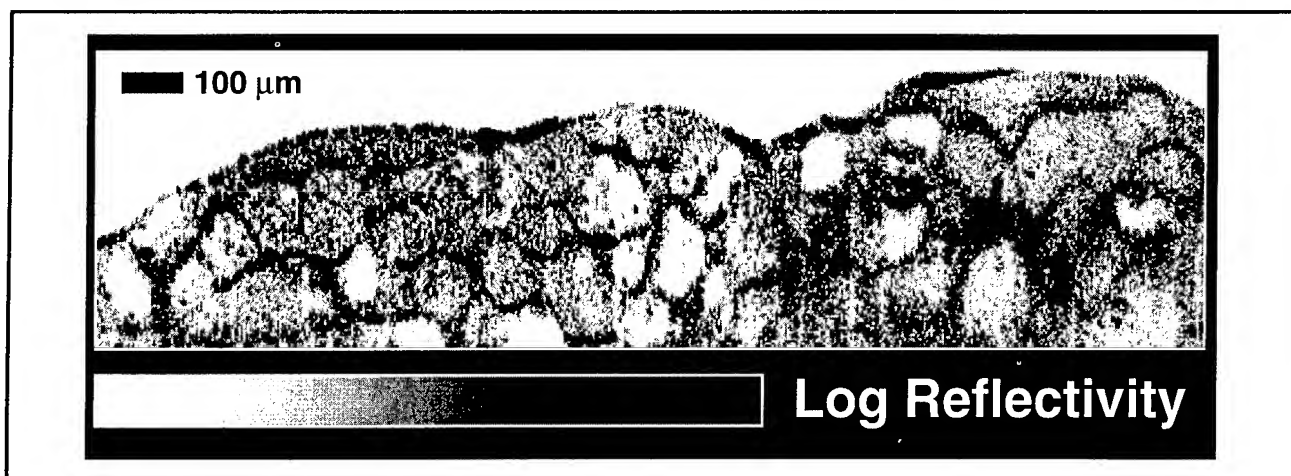


Figure 13. High-resolution OCT image of human adipose tissue.

1.15.3 High-Speed Optical Coherence Tomography

Currently, typical OCT systems used to image human tissue are implemented using superluminescent diodes (SLD) with center wavelengths of 850 or 1300 nm. These OCT systems have free space axial resolutions of 20-40 μm , a sample arm power of 50-150 μW , and signal-to-noise ratios (SNR) ranging from 90 to 110 dB. The image acquisition times of these systems (5 to 60 seconds) make difficult their application to *in vivo* imaging because of motion artifacts. To achieve image acquisition times below one second, alternative technologies to mirror translation scanning must

be developed. Because a high SNR is necessary for imaging to significant depths within turbid media, any increase of image acquisition rate must be accompanied by a commensurate increase in source optical power. We have constructed a novel OCT system which addresses both of these concerns and achieves an acquisition rate of four images per second. Each image consists of 292 x 250 pixels covering a sample area of 3 mm x 2.5 mm.

Previous OCT systems have utilized a mechanically translated reference arm mirror to enable axial scanning. The mirror velocity is typically in the range of 30 mm/s corresponding to a Doppler fre-

quency of 50 kHz. To enable image acquisition rates of two frames per second the Doppler frequency must be increased ~ 100 fold to 5 MHz. This would necessitate a reference mirror velocity of 3 m/s. Additionally, this velocity must be held constant over distances of 3-5 mm and repetition rates of ~ 0.5 kHz. Because no cost effective translator meeting these specifications is currently available, we have developed an alternative technology that uses piezo-electric transducers to induce stretch in an optical fiber. 40 m of single mode optical fiber is wrapped under constant tension about a piezo-electric modulator (PZM). As the PZM expands, the fiber is stretched inducing temporal delay on the light propagating within it. The long length of the fiber allows the small expansion of the PZM to be magnified to a length of approximately 3 mm. The deleterious effects of static and dynamic birefringence incurred in the fiber are compensated using Faraday rotators placed in the free space region of the interferometer arms. A triangle wave voltage tailored to minimize hysteresis

To maintain the high SNR necessary for deep imaging into turbid media such as human tissue, the decrease in image acquisition time must be matched by an increase in optical power. To enable high-speed, high-SNR imaging, we have employed the Cr:Forsterite laser source discussed above. At the high modulation frequency induced by the fast scanning piezo delay line, the noise due to amplitude fluctuation in the mode locked laser is low, but prevents Shot noise limited detection. Heterodyne dual balanced detection is used to reduce the laser noise below the Shot noise level and allows for OCT imaging with a SNR of 112 dB. This dynamic range is sufficient to allow OCT imaging to depths of greater than 2 mm within human tissue

1.15.4 Scanning Catheter/Endoscope for Optical Coherence Tomography

In order to apply OCT for imaging of internal organ systems, a flexible, small diameter, catheter/endoscope which is capable of delivering, focusing, scanning, and collecting a single spatial mode optical beam must be constructed. In the past year, we have developed a prototype single mode fiber optic scanning OCT catheter with a diameter

of 1 mm. The OCT catheter consists of a drive motor at its proximal end, a single mode fiber running the length of the catheter, and optical focusing and beam directing elements at the distal end. During image acquisition, the catheter is inserted into an internal tissue channel and the focused beam is scanned perpendicular to the axis of the catheter. An OCT image is acquired as the beam angle of rotation is varied over some range (usually 360 degrees). The speed of imaging depends on the speed of the rotation and the OCT unit acquisition speed. Preliminary images have been acquired using a superluminescent diode based OCT system.

To demonstrate imaging with the catheter, we have performed OCT of an *in vitro* human saphenous vein (figure 14A). The intact specimen was taken postmortem and imaged with the catheter in the center of the lumen of the vessel. The rectangular raw data image array was displayed in polar coordinates using a linear interpolation algorithm. The image was also processed to correct for the depth dependent exponential power loss caused by the optical attenuation of the tissue. A 30 MHz Intravascular Ultrasound image of the vein is displayed adjacent to the OCT image (figure 14B). As demonstrated by the figure, the OCT image shows a significant enhancement in resolution and capability to differentiate tissue morphology.

While many engineering issues still must be addressed in order to perform OCT imaging *in vivo*, the key enabling technologies required to achieve this objective have been developed and demonstrated by this laboratory. Improvement in image resolution, acquisition time, and the development of a fiber optic endoscope have been shown to be technically feasible. We believe that the results of this research will accelerate progress towards performing *in vivo* optical biopsies and should have a significant impact on medical diagnosis and the management of disease.

1.15.5 Ophthalmic Imaging and Diagnosis With Optical Coherence Tomography

In collaboration with MIT Lincoln Laboratory, we have developed a clinically effective, ophthalmic imaging OCT system.⁶⁴ A compact superluminescent diode (SLD) light source is utilized to provide approximately 500 μ W of 840 nm light onto

⁶⁴ M.E. Hee, J.A. Izatt, E.A. Swanson, D. Huang, C.P. Lin, J.S. Schuman, C.A. Puliafito, and J.G. Fujimoto, "Optical Coherence Tomography of the Human Retina," *Arch. Ophthalmol.* 113: 325-332 (1995); M.R. Hee, J.A. Izatt, E.A. Swanson, D. Huang, J.S. Schuman, C.P. Lin, C.A. Puliafito, and J.G. Fujimoto, "Optical Coherence Tomography for Micron-resolution Ophthalmic Imaging," *IEEE Eng. Med. Bio.* 14: 67 (1995).

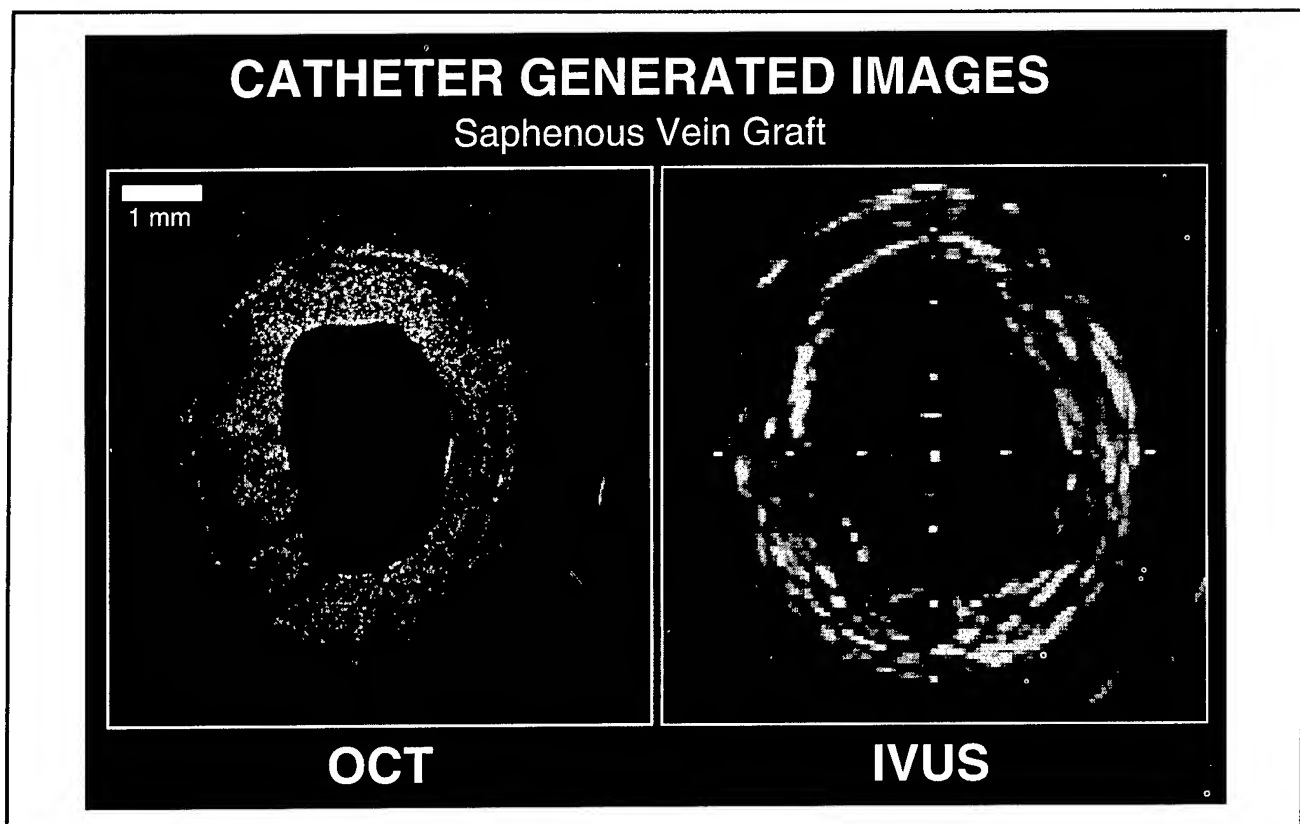


Figure 14. OCT and IVUS image of human saphenous vein graft.

the retina with a longitudinal resolution of $10\ \mu\text{m}$. The OCT system is integrated with a conventional ophthalmic slit-lamp biomicroscope using fiber-optics. Imaging of the retina occurs through a +78 diopter condensing lens mounted in front of the slit-lamp. A infrared sensitive video camera provides a view of the scanning probe beam on the fundus so that the location of each scan on the retina can be monitored. The operator is able to simultaneously view this video image and a false-color OCT tomogram on a computer monitor, which is updated in real time every 2.5 seconds. The system is fully computer controlled to allow fast positioning of a variety of scanning patterns at different locations on the retina. Imaging of different retinal regions occurs by translating either the patient's fixation point or the location of the scanning beam on the fundus, both under computer control. The fixation target provided in the ipsilateral eye allows the position of each OCT image relative to fixation to be automatically recorded, and permits follow-up scans to be accurately placed on the retina.

Image processing algorithms have been developed to minimize the effects of longitudinal patient eye motion during scanning and to automatically extract the thickness of various retinal layers directly from the OCT images. Longitudinal eye motion is accounted for by cross-correlating pairs of adjacent A-scans which form the tomogram to create an estimate of the retinal contour. The contour estimate is then digitally filtered to remove high frequency variations corresponding to patient motion. Quantitative measurements of retinal and retinal nerve fiber layer thickness are potentially useful in the diagnosis and monitoring of ocular diseases such as glaucoma and macular edema. These measurements may be performed using standard edge-detection image processing techniques.

Approximately 2000 patients with a variety of macular diseases and diseases of the optic nerve head have been examined at the New England Eye Center, Tufts University School of Medicine. In patients with macular pathology, OCT images have been correlated with the conventional clinical techniques of slit-lamp biomicroscopy and fluorescein

angiography.⁶⁵ We have found that the cross-sectional view of OCT is effective in the diagnosis and monitoring of macular holes, retinal detachment, macular edema, epiretinal membrane, and age-related macular degeneration. In patients with glaucoma, the ability of OCT to directly measure retinal nerve fiber layer thickness with micron scale resolution may lead to the first truly objective diagnostic for the presence or progression of this degenerative disease.

Macular hole is a frequently encountered retinal disease that is often difficult to diagnose accurately because there are a number of ophthalmoscopically similar appearing lesions. The disease progresses to involve a complete loss of the retina directly in the fovea leading to a devastating reduction in visual acuity. However, surgical intervention can often prevent or correct vision loss. OCT greatly facilitates the diagnosis and staging of macular holes, ensuring appropriate treatment. OCT is diagnostically useful in separating macular holes from other ophthalmoscopically similar appearing lesions and evaluating the stage of macular hole progression and the risk of hole formation in the second eye of patients who already have a unilateral macular hole. This information is useful in considering candidates for surgical treatment. Furthermore, OCT has been able to provide information on the pathogenesis of hole formation and the conditions which lead to the development of macular holes which may eventually lead to better treatment of this disease.⁶⁶

OCT is superior to conventional slit-lamp biomicroscopy in evaluating retinal detachments, such as those occurring with central serous chorioretinopathy.⁶⁷ In a series of patients with this disease, OCT was effective in objectively quantifying the extent of neurosensory and pigment epithelial detachment many of which were undetected at the slit-lamp. Longitudinal OCT measurements were successful in monitoring the resolution of subretinal fluid. The ability of OCT to objectively and quantitatively monitor these detachments over time is useful in evaluating the necessity or effectiveness of treatment.

Diabetic retinopathy is the second leading cause of blindness in the United States. The development of macular edema is a major treatable cause of vision loss in patients with diabetic retinopathy. Macular edema is also common manifestation of a variety of other retinal diseases including epiretinal membranes, uveitis, and retinal vascular occlusions. Macular edema is traditionally evaluated by assessing (1) retinal thickening with slit-lamp biomicroscopy and (2) leakage of fluorescein dye from blood vessels into the retina, a relatively poor indicator of vision loss. OCT was used to measure retinal thickness in 72 eyes with the clinical diagnosis of nonproliferative or proliferative diabetic retinopathy, 34 eyes in diabetic patients who had no evidence of retinopathy, and 59 healthy control eyes. The mean \pm SD central foveal thickness measured by OCT was $146\pm 22\ \mu\text{m}$ in healthy eyes and $150\pm 24\ \mu\text{m}$ in diabetic eyes without evidence of retinopathy. In patients with diabetic retinopathy, OCT could objectively monitor the development and resolution of macular edema following treatment with $10\ \mu\text{m}$ precision. In these patients, the central foveal thickness was $172\pm 35\ \mu\text{m}$ in the 49 eyes without macular edema as assessed by slit-lamp biomicroscopy, and $339\pm 101\ \mu\text{m}$ in the 23 eyes with macular edema. Central foveal thickness correlated with best corrected visual acuity in eyes with nonschemic retinopathy. These results show that OCT is a more sensitive indicator of retinal thickening due to macular edema than either slit-lamp biomicroscopy or fluorescein angiography, useful in objectively tracking the resolution of edema following laser therapy, and may be effective as a screening tool for the development of retinal edema in these patients.⁶⁸

Current diagnostic techniques for epiretinal membranes in the macular region include slit-lamp biomicroscopy and fluorescein angiography. OCT images are useful in confirming the diagnosis of faint, diaphanous membranes, and in providing a cross-sectional assessment of factors contributing to vision loss, such as membrane opacity, retinal distortion or tractional detachment, and macular edema. The amount of foveal distortion,

⁶⁵ M.R. Hee, J.A. Izatt, E.A. Swanson, D. Huang, J.S. Schuman, C.P. Lin, C.A. Puliafito, and J.G. Fujimoto, "Optical Coherence Tomography of the Human Retina," *Arch. Ophthalmol.* 113: 325-332 (1995).

⁶⁶ C.A. Puliafito, M.R. Hee, C.P. Lin, E. Reichel, J.S. Schuman, J.S. Duker, J.A. Izatt, E.A. Swanson, and J.G. Fujimoto, "Imaging of Macular Diseases with Optical Coherence Tomography (OCT)," *Ophthalmol.* 102: 217-229 (1995).

⁶⁷ M.R. Hee, C.A. Puliafito, C. Wong, J.S. Duker, E. Reichel, J.S. Schuman, E.A. Swanson, and J.G. Fujimoto, "Optical Coherence Tomography of Macular Holes," *Ophthalmol.* 102: 748-746 (1995).

⁶⁸ M.R. Hee, C.A. Puliafito, C. Wong, J.S. Duker, E. Reichel, J.S. Schuman, E. A. Swanson, and J.G. Fujimoto, "Optical Coherence Tomography of Central Serous Chorioretinopathy," *Am. J. Ophthalmol.* 120: 65-74 (1995).

detachment, or edema provides an indication of the severity of the membrane. The thickness and reflectivity of the membrane on the OCT tomogram gives information on membrane opacity. Many studies have attempted to define prognostic indicators, such as membrane thickness or the presence of pre-operative cystoid macular edema, to predict eventual visual outcome after epiretinal membrane surgery. OCT provides a means to evaluate the cross-sectional characteristics of an epiretinal membrane, allowing a quantitative measurement of retinal thickness, membrane thickness, and the separation between the membrane and inner retina. These measurements may eventually prove useful for pre-operative characterization of surgical prognosis.

Age-related macular degeneration is the leading cause of blindness in the United States. Vision loss in this disease is often due to the formation of choroidal neovascularization (CNV). However, many eyes with CNV lack the fluorescein angiographic features required for treatment eligibility according to the Macular Photocoagulation Study guidelines and OCT may represent a new technique for visualizing such occult CNV. We have found that OCT is effective in the identification and quantification of subretinal and intraretinal fluid, and is particularly useful in evaluating possible foveal involvement of fluid accumulation or CNV. Measurements of retinal thickness with OCT provide an objective means of following edema and subretinal fluid in a patient through successive examinations. In patients with untreated exudative AMD, OCT was compared with fluorescein angiography in the classification of CNV. CNV could be morphologically divided into three categories on OCT: well-defined, poorly-defined, and fibrovascular pigment epithelial detachment (PED). CNV classified as well-defined or fibrovascular PED on OCT had well demarcated boundaries and might be potentially treatable. These membranes included most angiographically classic CNV and a subset of angiographically occult CNV which would not be traditionally eligible for treatment. OCT was also useful in monitoring CNV before and after laser photocoagulation. These studies suggest that OCT may have potential in defining the boundaries of a subset of occult CNV, leading to the possibility of more effective treatment delivery in these cases.

Glaucoma is the third leading cause blindness in the United States. The clinical evaluation of this pervasive disease is presently difficult. Current

diagnostic techniques such as stereoscopic visualization of the optic nerve, nerve fiber layer photography, and evaluation of the cup-to-disc ratio are subjective with variation occurring even among experienced observers. Glaucoma is a disease of insidious onset, often leading to significant losses in peripheral vision that may not be immediately noticed by the patient. Quantitative visual field testing can provide early identification of these visual defects; however, up to 50 percent of the retinal nerve fiber layer may be lost before detection by standard clinical techniques. The ability of OCT to directly measure nerve fiber layer thickness may lead to an objective, early diagnostic for the onset of glaucoma, and a sensitive indicator of glaucomatous progression.

OCT provides a quantitative method of directly measuring the thickness of the retina and retinal nerve fiber layer (NFL) with high resolution as a potential early glaucoma diagnostic.⁶⁹ In a series of patients with and without glaucoma, NFL thickness as measured by OCT correlated well with the functional status of the optic nerve as measured by traditional visual field examination, and correlated better with visual field loss than either cupping or neuroretinal rim area. There was a highly significant difference in NFL thickness measured by OCT between normal and glaucomatous eyes. Longitudinal studies of measurement reliability indicate that retinal nerve fiber layer thickness measurements with OCT are reproducible to within 10 to 20 μm . These studies indicate that OCT is potentially able to detect the onset of glaucoma or glaucomatous progression before significant and irreversible damage to the retina occurs.

1.15.6 Cardiovascular Imaging Using Optical Coherence Tomography

Acute myocardial infarction (AMI), commonly referred to as "heart attack", is the leading cause of death in the industrialized world. AMI represents the abrupt loss of blood flow to a region of the heart resulting in tissue death. The cessation of blood flow results from the rupture of small to moderate sized cholesterol laden lesions in the arteries of the heart (coronary arteries), followed by clot formation and vessel occlusion. The current inability to identify these plaques prospectively is due to inadequacies of existing imaging techniques in defining plaque composition. Our hypothesis is that OCT, a new method of fiber optic based micron scale

⁶⁹ M.R. Hee, C.A. Puliafito, C. Wong, J.S. Duker, E. Reichel, B.K. Rutledge, J.S. Schuman, E.A. Swanson, and J.G. Fujimoto, "Quantitative Assessment of Macular Edema with Optical Coherence Tomography," *Arch. Ophthalmol.* 113: 119-129 (1995).

tomographic imaging, can be developed as a method of high-resolution vascular imaging to ultimately address these limitations in cardiac diagnostics. We have demonstrated with initial *in vitro* studies that OCT identifies plaques which are structurally unstable with a resolution, between 4 and 20 μm , superior to that of any clinically available imaging technology. In addition, OCT was capable of generating high contrast between tissue microstructure, and imaging could be performed through even the most heavily calcified samples. We also directly compared OCT with high frequency ultrasound, the current imaging technology with the highest resolution (110 μm). OCT consistently identified tissue microstructure which was not seen in the ultrasound images. Finally, an imaging catheter was developed which will be used for *in vivo* imaging. The catheter is less than 1 mm in diameter and no transducer was present within it, resulting in a relatively low cost in construction. Future studies will focus on catheter based imaging and optimizing the system for patient imaging. The latter will include improved data acquisition rates, optimizing the wavelength of the incident source, and combination with spectroscopy.

1.15.7 Histological Correlation of Laser-Induced Retinal Lesions with OCT Images

With an increase in the medical technologies using lasers, a thorough understanding of laser-tissue interactions is necessary. In particular, interactions with sensitive ocular structures have been of interest for both clinical medical applications and for laser safety. Much of the laser-tissue interaction data obtained from ocular structures has relied on the use of (1) *in vivo* ophthalmoscopic or fluorescein angiographic examination,⁷⁰ or (2) post-mortem histological preparations to assess effects and extent of possible damage.⁷¹

In the past year, we have correlated results obtained in our investigation of laser-induced retinal injury using OCT to the corresponding histological preparations. OCT is a new imaging technique which utilizes fiber optic based low-coherence interferometry along with a super luminescent diode laser source to provide micron scale cross-sectional

tomographic images of retinal structure. In contrast to conventional histopathology techniques, OCT is noninvasive, and thus it is possible to image laser induced retinal lesions at different time intervals ranging from immediately after laser exposure to several days. This provides a direct tomographic measurement of the formation and healing response to laser retinal exposure. Comparative OCT studies were performed at Brooks Air Force Base in Texas, using cw argon, nanosecond, picosecond, and femtosecond, laser-induced lesions. Histopathology was acquired at selected time points for comparisons with OCT images.

Direct comparisons between OCT images and corresponding histology reveal consistent tissue morphology in addition to several types of artifacts that result from histological processing. Because OCT images represent the *in vivo* orientation of the microstructure, preparation artifacts can be identified. In addition, with the clinical ophthalmic implementation of OCT, our histological correlations provide a more definitive explanation of what retinal structures are represented by the differential optical backscatter measured with the OCT instrument.

These studies are the first *in vivo* microstructural measurements which document the formation and healing response of retinal laser exposure. The histological evidence confirms the observations made using OCT and improves our understanding of laser-tissue interactions by enhancing visualization of retinal structure. These results have important implications for ophthalmic laser surgery as well as establishing laser retinal injury standards.

1.15.8 Optical Coherence Tomographic Investigation of Developing Embryonic Morphology

Recent advances in molecular biology techniques have permitted the site-specific insertion of predetermined mutations into embryos for the investigation of normal and abnormal development. Not only does this have fundamental scientific interest, but also has the potential for the study, understanding, and possible cure for genetic diseases. Currently, there are several imaging modalities available to observe the expression of genetic

⁷⁰ J.S. Schuman, M.R. Hee, C.A. Puliafito, C. Wong, T. Pedut-Kloizman, C.P. Lin, E. Hertzmark, J.A. Izatt, E.A. Swanson, and J.G. Fujimoto, "Quantification of Nerve Fiber Layer Thickness in Normal and Glaucomatous Eyes using Optical Coherence Tomography: A Pilot Study," *Arch. Ophthalmol.* 113: 586-596 (1995).

⁷¹ R. Birngruber, V.-P. Gabel, and F. Hillenkamp, "Threshold Criteria and Derivation of Safe Levels for Laser Radiation," in *Current Concepts in Ergophthalmology*, eds. B. Tengroth, D. Epstein, A. Anseth, A. Hedin, A.H. Keeney, M.J. Roper-Hall, and D.H. Sliney (The Hague, The Netherlands, 1978).

mutations including light, confocal, and electron microscopy, but these typically require small, transparent, or fixed specimens. Progress has also been made to reimplement the clinical magnetic resonance imaging, computed-tomography, and ultrasound technologies as high-resolution, microscopic imaging modalities. High-resolution MRI,⁷² CT,⁷³ and ultrasound backscatter microscopy⁷⁴ have achieved resolutions on the order of 15-50 μm . These techniques, however, still present limitations in acquisition time, resolution, cost, or complexity. Optical coherence tomography (OCT) offers the ability to image *in vivo* developing morphology in many of the animal models used for genetic studies. In addition, OCT has the potential to rapidly and repeatedly acquire optical histology to assess development and to identify the expression of normal and abnormal genes.

We have acquired OCT images of *in vivo* developing morphology from several developmental biology animal models (leopard frog, African frog, zebra fish) which demonstrate that numerous anatomical features can be distinguished with high resolution (figure 15). Images correlate strongly with corresponding histology. Optical histology performed with OCT preserves the *in vivo* orientation of the morphology and can be used to identify normal and abnormal morphology. Images can be acquired from single specimens throughout development thereby allowing longitudinal studies to be performed rather than acquiring multiple time-points from multiple specimens. Cross-sectional images can also be acquired at spatial intervals and later used to reconstruct a three-dimensional representation of the specimen. From this 3D data set, arbitrary section planes can be repeatedly obtained to highlight specific anatomy. This is in contrast to the one-time orientation with histological sectioning.

Optical coherence tomography offers numerous possibilities for the investigation of *in vivo* embryonic morphology and for developmental biology in general. Utilizing solid-state laser sources, cellular resolutions of 4 μm have already been demonstrated.⁷⁵ This high-resolution instru-

ment has potential for the microscopic investigation of normal and abnormal developing biology.

1.15.9 Publications

Bouma, B.E., G.J. Tearney, S.A. Boppart, M.R. Hee, M.B. Brezinski, and J.G. Fujimoto. "High Resolution Optical Coherence Tomographic Imaging Using a Modelocked Ti:Al₂O₃ Laser Source." *Opt. Lett.* 20(13): 1486-1488 (1995).

Brezinski, M.B., G.J. Tearney, B.E. Bouma, J.A. Izatt, M.R. Hee, E.A. Swanson, J.F. Southern, and J.G. Fujimoto. "Optical Coherence Tomography for Optical Biopsy: Properties and Demonstration of Vascular Pathology." *Circulation*. Forthcoming.

Hee, M.R., J.A. Izatt, E.A. Swanson, D. Huang, J.S. Schuman, C.P. Lin, C.A. Puliafito, and J.G. Fujimoto. "Optical Coherence Tomography for Micron-resolution Ophthalmic Imaging." *IEEE Eng. Med. Bio.* 14: 67 (1995).

Hee, M.R., J.A. Izatt, E.A. Swanson, D. Huang, J.S. Schuman, C.P. Lin, C.A. Puliafito, and J.G. Fujimoto. "Optical Coherence Tomography of the Human Retina." *Arch. Ophthalmol.* 113: 325-332 (1995).

Hee, M.R., C.A. Puliafito, C. Wong, J.S. Duker, E. Reichel, J.S. Schuman, E.A. Swanson, and J.G. Fujimoto. "Optical Coherence Tomography of Macular Holes." *Ophthalmol.* 102: 748-746 (1995).

Hee, M.R., C.A. Puliafito, C. Wong, J.S. Duker, E. Reichel, J.S. Schuman, E.A. Swanson, and J.G. Fujimoto. "Optical Coherence Tomography of Central Serous Chorioretinopathy." *Am. J. Ophthalmol.* 120: 65-74 (1995).

Hee, M.R., C.A. Puliafito, C. Wong, J.S. Duker, E. Reichel, B.K. Rutledge, J.S. Schuman, E.A. Swanson, and J.G. Fujimoto. "Quantitative

⁷² B. Lorentz, "Morphologic Changes of Chorioretinal Argon Laser Burns during the First Hour Post Exposure," *Lasers in Life Sci.* 2(3): 207-226 (1988).

⁷³ R.E. Jacobs and S.E. Frase, "Magnetic Resonance Microscopy of Embryonic Cell Lineages and Movements," *Sci.* 263: 681-684 (1994).

⁷⁴ E.J. Morton et al., "Three-dimensional X-ray Microtomography for Medical and Biological Applications," *Phys. Med. Biol.* 35: 805-820 (1990).

⁷⁵ B.E. Bouma, G.J. Tearney, S.A. Boppart, M.R. Hee, M.B. Brezinski, and J.G. Fujimoto, "High Resolution Optical Coherence Tomographic Imaging Using a Modelocked Ti:Al₂O₃ Laser Source," *Opt. Lett.* 20(13): 1486-1488 (1995).

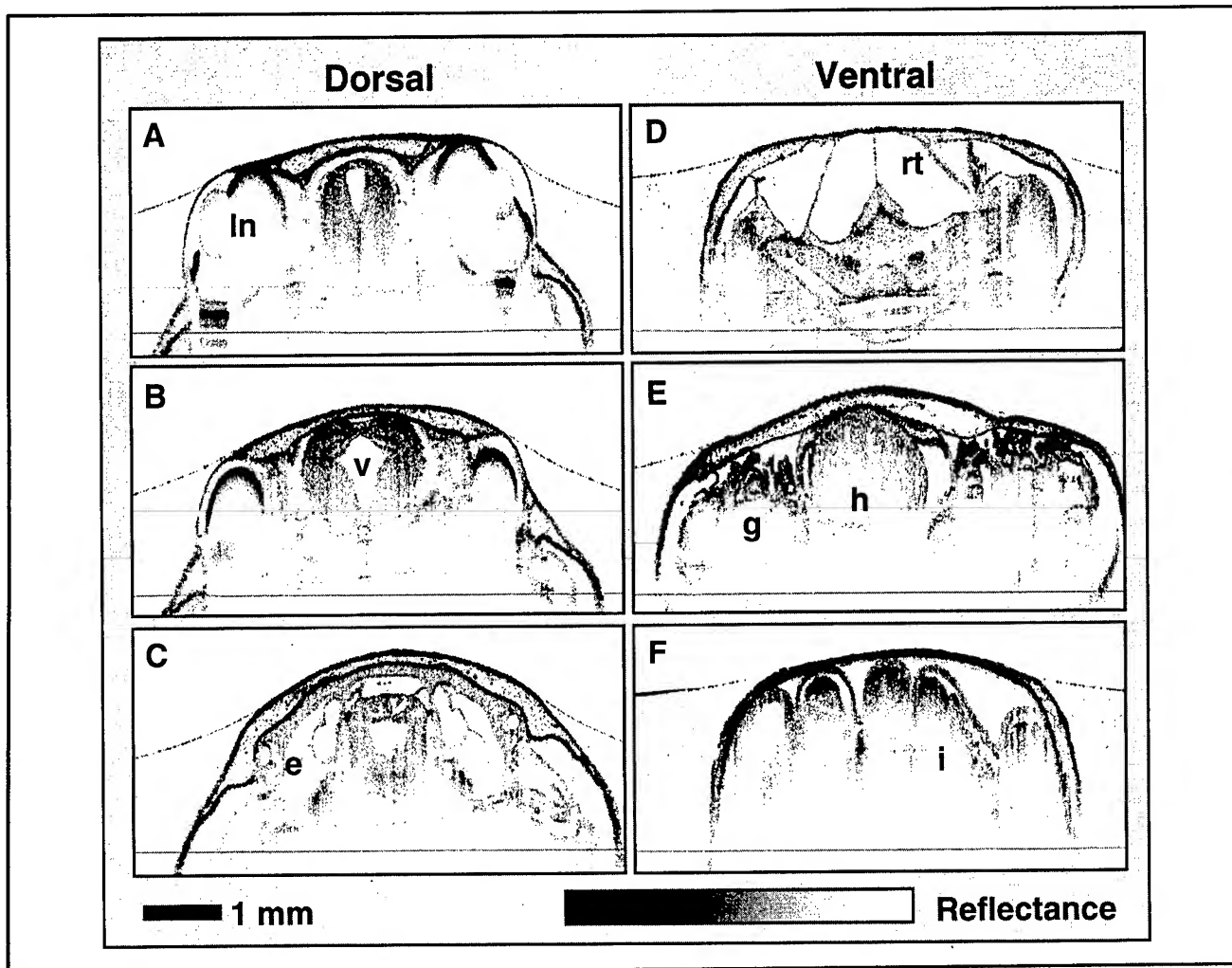


Figure 15. Cross-sectional OCT images of an *in vivo* leopard frog tadpole. Images were acquired from the dorsal (A-C) and the ventral (D-F) sides of the specimen to highlight particular anatomical features. Abbreviations: e = ear, g = gills, h = ventricle of heart, i = intestine, ln = lens of eye, rt = respiratory tract, v = fourth ventricle of brain.

Assessment of Macular Edema with Optical Coherence Tomography." *Arch. Ophthalmol.* 113: 119-129 (1995).

Hee, M.E., J.A. Izatt, E.A. Swanson, D. Huang, C.P. Lin, J.S. Schuman, C.A. Puliafito, and J.G. Fujimoto. "Optical Coherence Tomography of the Human Retina." *Arch. Ophthalmol.* 113: 325-332 (1995).

Puliafito, C.A., M.R. Hee, C.P. Lin, E. Reichel, J.S. Schuman, J.S. Duker, J.A. Izatt, E.A. Swanson, and J.G. Fujimoto. "Imaging of Macular Diseases with Optical Coherence Tomography (OCT)." *Ophthalmol.* 102: 217-229 (1995).

Puliafito, C.A., M.R. Hee, C.P. Lin, E. Reichel, J.S. Schuman, J.S. Duker, J.A. Izatt, E.A. Swanson, and J.G. Fujimoto. "Imaging of Macular Dis-

eases with Optical Coherence Tomography." *Ophthalmol.* 102: 217-229 (1995).

Schuman, J.S., M.R. Hee, C.A. Puliafito, C. Wong, T. Pedut-Kloizman, C.P. Lin, E. Hertzmark, J.A. Izatt, E.A. Swanson, and J.G. Fujimoto. "Quantification of Nerve Fiber Layer Thickness in Normal and Glaucomatous Eyes using Optical Coherence Tomography: A Pilot Study." *Arch. Ophthalmol.* 113: 586-596 (1995).

Tearney, G.J., M.E. Brezinski, M.R. Hee, B. Bouma, J.A. Izatt, E.A. Swanson, J.F. Southern, and J.G. Fujimoto. "Optical Biopsy in Human Tissue using Optical Coherence Tomography and Microscopy." Paper presented at the Conference on Lasers and Electro-Optics, Optical Society of America, May 1995.

Tearney, G.J., M.E. Brezinski, B.E. Bouma, J.F. Souther, and J.G. Fujimoto. "High Resolution Imaging of Gastrointestinal Tissue using Optical Coherence Tomography." Annual Meeting of the American Gastrointestinal Association, May 1996.

Tearney, G.J., B.E. Bouma, S.A. Boppart, B. Golubovic, E.A. Swanson, and J.G. Fujimoto. "High Speed Optical Coherence Tomography." Paper presented at the Conference on Advances in Photon Migration, Orlando, Florida, March 1996.

Tearney, G.J., S.A. Boppart, B.E. Bouma, M.E. Brezinski, N. Weissman, J.F. Southern, and J.G. Fujimoto. "Scanning Single Mode Fiber Optic Catheter/Endoscope for Optical Coherence Tomography." *Opt. Lett.* Forthcoming.

Turnbull, D.H., et al. "Ultrasound Backscatter Microscope Analysis of Early Mouse Embryonic Brain Development." *Proc. Nat. Acad. Sci.* 92: 2239-2243 (1995).

1.16 EUV and Soft X-ray Laser Research

Sponsor

MIT Lincoln Laboratory
Contract BX-5098

Project Staff

Professor Peter L. Hagelstein, James G. Goodberlet, Marc Fleury,⁷⁶ Dr. Martin H. Muendel,⁷⁷ William Hodge,⁷⁸ Shourov Chattevj

Significant amplification in the EUV and soft x-ray regime was first demonstrated in 1984 at Lawrence Livermore National Laboratories (LLNL) and Princeton University. Since that time, short wavelength laser research has been explored at a large number of laboratories in the U.S. and around the world. When we began our efforts at MIT, it was thought that kilojoule pump lasers were required to drive short wavelength lasers using the collisional scheme. Recombination lasers could be studied at much lower energy, but these lasers have historically been plagued with difficulties in achieving a

high total gain length. We set out to try to develop EUV lasers using a table-top facility in order to pump collisional lasers at the joule level instead of at the kilojoule level.

Since that time, many things have occurred. We succeeded in developing a laboratory for studying laser-produced plasmas relevant to short wavelength lasers, and we have tested a number of laser schemes. In 1992, we demonstrated apparent gain in Ni-like Nb at 204 Å using a pump energy later estimated to be 2-3 joules. Later on, experiments on recombining H-like boron plasmas indicated the presence of somewhat higher gain.

Elsewhere, laser plasma experiments on the Ne-like and Ni-like sequences have provided systematic demonstrations of gain in a wide variety of neon-like ions from S to Mo and in the nickel-like sequence from Sn to Au.

Significant gain has been detected in neon-like ions with somewhat less than 100 J pump energy being required for the observation of gain in Ti. The field has been stimulated by a number of notable recent results including: the demonstration of significant gain in recombining Li at 135 Å pumped by a femtosecond laser; the development of a saturated neon-like argon laser in a capillary discharge; the demonstration of very high gain in neon-like titanium pumped using a few joule nanosecond pulse to create a plasma and then a few joule picosecond pulse to heat it; and the demonstration of optical field ionization for creating a plasma for collisional excitation in Pd-like Xe.

During the past few years, U.S. funding in this area has been very low outside of LLNL; one hopes that this will change. The advent of short wavelength lasers will stimulate research in a number of areas: nonlinear spectroscopy will be extended into the EUV and soft x-ray regimes; new EUV and x-ray optical instruments and techniques have come into existence; and short wavelength lasers have been successfully applied to the problem of imaging of dense plasmas and biological systems. Some think that these lasers will find applications in the semiconductor industry for use either in fabrication or inspection of devices.

In the following sections, we discuss recent developments in our effort at MIT.

⁷⁶ Graduate student, Ecole Polytechnique, Paris, France.

⁷⁷ Polaroid Corporation, Cambridge, Massachusetts.

⁷⁸ High Energy Laser Associates, Oakland, California (Sponsor: National Science Foundation SBIR Grant 90-06960).

1.16.1 Constant Dose Gain Measurements

Amplified spontaneous emission in long, narrow lasers has been of interest for many years in laser science; it is especially important in short wavelength laser research since the reflectivity of the best mirrors in this regime (which are multilayer mirrors) is poor. If the gain is assumed to be constant, then the laser intensity exponentiates according to

$$I(\lambda) = I_0(e^{\alpha(\lambda)L} - 1)$$

along rays that traverse the full length of the laser L . The laser linewidth is usually quite narrow $\lambda/\Delta\lambda \sim 10^4$, so that the observed intensity for a wavelength averaged diagnostic is

$$\langle I \rangle = I_0 \int (e^{\alpha(\lambda)L} - 1) d\lambda$$

This integral depends weakly on the details of the gain lineshape α ; it is typically approximated by the Linford expression

$$\langle I \rangle \sim \frac{(e^{\alpha L} - 1)^{3/2}}{(\alpha L e^{\alpha L})^{1/2}}$$

An experimental determination of the presence of gain or loss in short wavelength laser experiments is usually done by measuring the wavelength averaged intensity versus the laser length L , and then fitting the results to the Linford curve to determine α . For a high-gain system, αL can be more than 10, and it is obvious that the laser works as a laser. For smaller values of αL , it is possible to fit the Linford curve to estimate the gain coefficient α , but the accuracy of the resulting estimate will depend on the linearity of the detection system and its geometry.

One way to minimize the nonlinearities associated with the detection system is to use a constant dosage measurement scheme.⁷⁹ In such a scheme, the experiments are carried out to produce approximately the same signal at the detector for different conditions. To measure gain, values of the wavelength averaged intensity are needed at different lengths L ; if the gain is low, then the signal will be

approximately proportional to the length. In order to develop a constant dosage scheme for such a measurement, the signal at the detector must somehow be doubled for a measurement at length $L/2$ to compare with a measurement at length L . This was accomplished in our laboratory by using film to sum up the results from several shots and then scaling the number of shots taken according to the inverse of the length. For example, four shots summed at length L can be compared in a constant dosage measurement with eight shots summed at length $L/2$, and so forth.

In our previous experiments on a possible recombination laser in H-like B, fitting the wavelength averaged I from streak camera measurements at different lengths L yielded an apparent result of several gain lengths in H-like B at 262 Å.⁸⁰ A confirmation of this result was attempted taking advantage of the constant dose measurement scheme. It was found that for the same experimental conditions that the signal grew linearly as measured with the constant dosage technique as shown in figure 16. The previous measurements are believed to be in error and can be attributed to nonlinearities in the detection system.

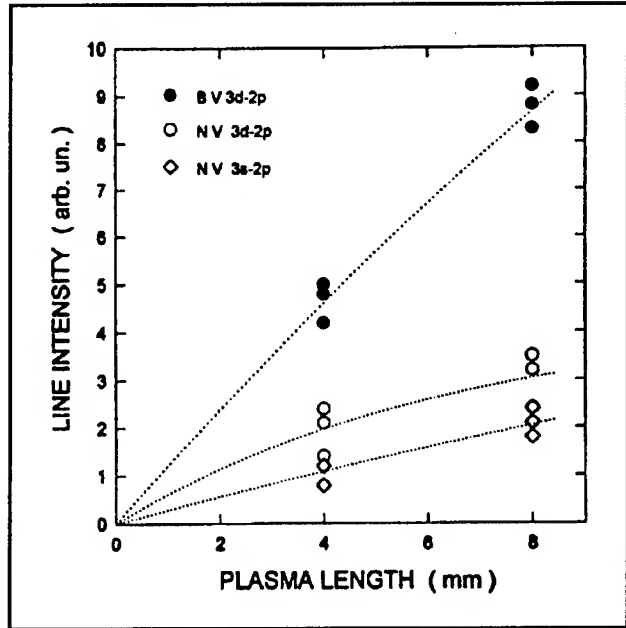


Figure 16. Wavelength averaged intensity I versus length L for H-like B.⁷⁹

⁷⁹ J. Goodberlet, *An Experimental Investigation of a Table-Top, Laser Drive Extreme Ultraviolet Laser*, Ph.D. diss., Dept. of Electr. Eng. and Comput. Sci., MIT, 1996.

⁸⁰ J. Goodberlet et al., "Observation of Gain in a Recombining H-like Boron Plasma," *J. Opt. Soc. Am. B* 12: 980 (1995).

1.16.2 Survey of Recombination Laser Schemes

Our earlier experimental efforts on recombination lasers focused on the 3d-2p transition at 262 Å in H-like B. This work was stimulated by number of reports of the observation of significant gain on the same transition in H-like C at low energy. The absence of detectable gain in our experiments as discussed above is a relatively recent result, the explanation of which is a current research question. It was decided to explore experimentally other recombination laser schemes with our facility, including the He-like 3d-2p, Li-like 4f-3d and 5g-4f, and Na-like 5g-4f schemes.

The motivation for these experiments comes from a number of considerations. Gain on many of these transitions has been studied in laser plasma experiments at other laboratories, in many cases with low pump laser energy. Additionally, the experimental requirements for the development of gain at longer wavelengths tend to be less demanding. One other consideration included the issue of radiation trapping; while radiation trapping is expected to impact many of the recombination laser schemes (and has the potential to spoil the gain). The Li-like 5g-4f scheme will not be affected as much by radiation trapping and has been shown to give high gain in related experiments.

Representative of the results is the case of the 4f-3d transition in Li-like F at 381.8 Å. The observation and identification of the candidate laser line was reasonably straightforward, which is typical of recombination lasers in the EUV and soft x-ray regimes. Using a CaF₂ target, the candidate laser line was observed to be the dominant feature locally in the spectrum⁸¹ (see figure 17). Intensity versus length experiments showed a linear growth of intensity with length; no detectable gain was observable (see figure 18).⁸¹

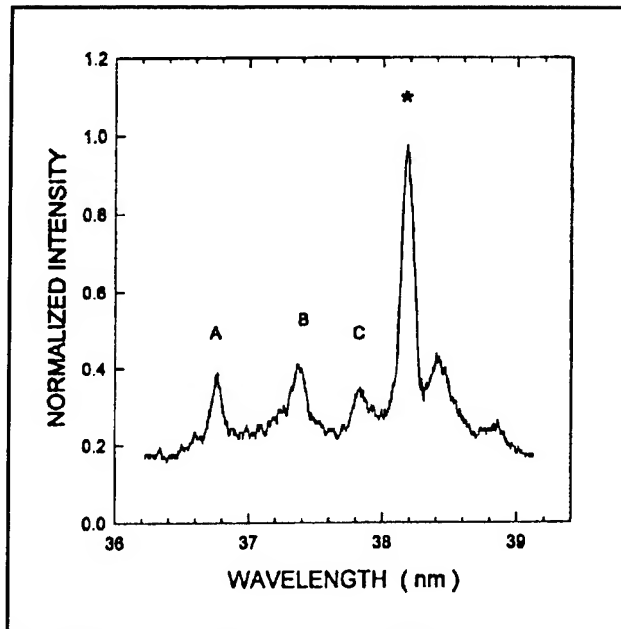


Figure 17. Li-like F spectrum. Line identifications are: * - Li-like F 4f-3d (381.8 Å); A - Li-like F 4d-3p (367.9 Å); B - Mg-like Ca (373.9 Å); C - Mg-like Ca (378.1 Å).⁸¹

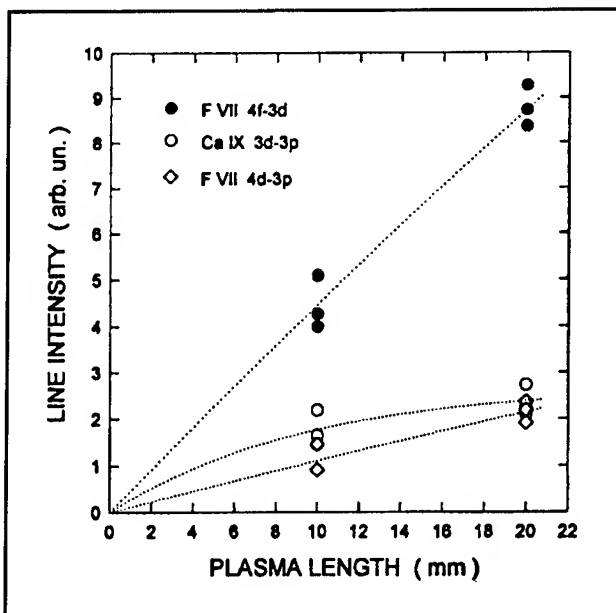


Figure 18. Li-like F spectrum intensity versus length measurement.⁸¹

⁸¹ J. Goodberlet, *An Experimental Investigation of a Table-Top, Laser Drive Extreme Ultraviolet Laser*, Ph.D. diss., Dept. of Electr. Eng. and Comput. Sci., MIT, 1996.

Experiments were performed additionally on: He-like $1s3d\ ^1D - 1s2p\ ^1P$ transition in He-like C at 267.2 Å, the 5g-4f transition in Li-like Mg at 404.3 Å, and the 5g-4f transition in Na-like Ca at 401.6 Å (see figure 19).⁸²

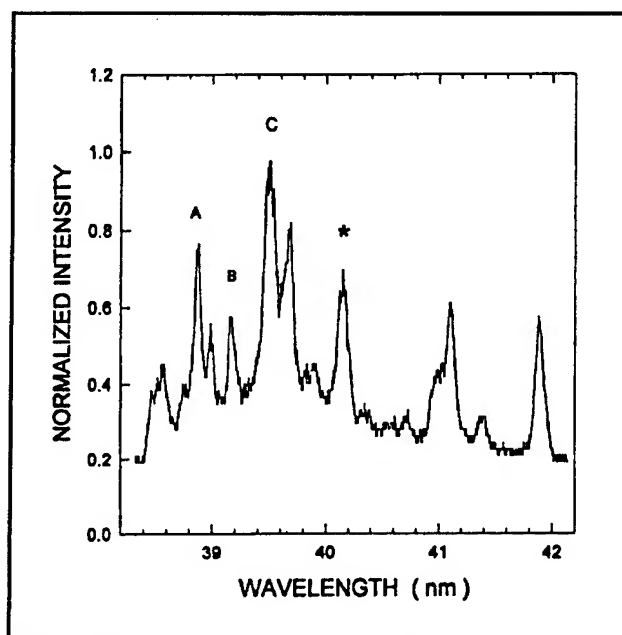


Figure 19. Na-like Ca spectrum. Line identifications are: * - Na-like Ca 5g-4f (401.6 Å); A - Mg-like Ca (388.8 Å); B - Li-like F (291.8 Å); C - Mg-like Ca (395.0 Å).⁸² The observation of the candidate laser line in Na-like Ca may be the first time that this line has been identified.

1.16.3 Survey of Collisional Excitation Laser Schemes

The first experimental campaign to detect gain conducted on our laser facility focused on a candidate laser line in Ni-like Nb,⁸³ as reported in previous *RLE Progress Reports*. In this work, a strong line appeared at 204 Å and based on a number of considerations, this line was identified as the $J=0$ 4d-4p laser transition showing weak gain. The arguments supporting this included: (1) the line was within a few tenths of an Angstrom of the expected wave-

length from isoelectronic interpolation; (2) it appeared to be significantly brighter than the nearby Cu-like lines under conditions where the highest gain was expected; (3) the line showed a strong threshold behavior with intensity, consistent with what would be expected of a transition within an excited state manifold; (4) an intensity versus length measurement showed weak exponentiation. One problem with this result is that the streak data showed the emission from the candidate laser line to typically last longer than would be possible if pumped by collisional excitation alone (although short temporal emission of this line was observed in the presence of a long background on occasion).

The development of the constant dose measurement technique has indicated that nonlinearities in detector and film response can mimic the presence of gain in an intensity versus length experiment as described above. While much effort went into the calibration of the nonlinear response of the measurement system in these experiments, we now consider that the intensity versus length measurement for this experiment may also suffer from similar problems. Consequently, the present experiment results weakens the previous claims. This experiment needs to be repeated using a constant dosage measurement scheme. Such an experiment was attempted, but it was not possible to reproduce the pumping conditions of the experiment with the existing laser set up (we are not able safely to reach the same intensity levels as required for these experiments as discussed in previous *RLE Progress Reports*).

There have been numerous recent reports of gain in low-Z, Ne-like ions, such as argon, calcium, and titanium. Gains in the range of a few per centimeter have been observed in a number of laboratories under a wide range of conditions. We attempted to observe the candidate $J=0$ laser line in Ne-like Ca and Ne-like Ti. Numerous experiments were performed using both line pumping and a spot focus. We were unable to obtain a clear observation of the laser line, although in Ca some emission was observed in the vicinity of the expected wavelength (see figure 20).

⁸² J. Goodberlet, *An Experimental Investigation of a Table-Top, Laser Drive Extreme Ultraviolet Laser*, Ph.D. diss., Dept. of Electr. Eng. and Comput. Sci., MIT, 1996.

⁸³ S. Basu et al., "Amplification in Ni-like Nb at 20.4 nm Pumped by a Table-top Laser," *Appl. Phys. B* 57: 303 (1993).

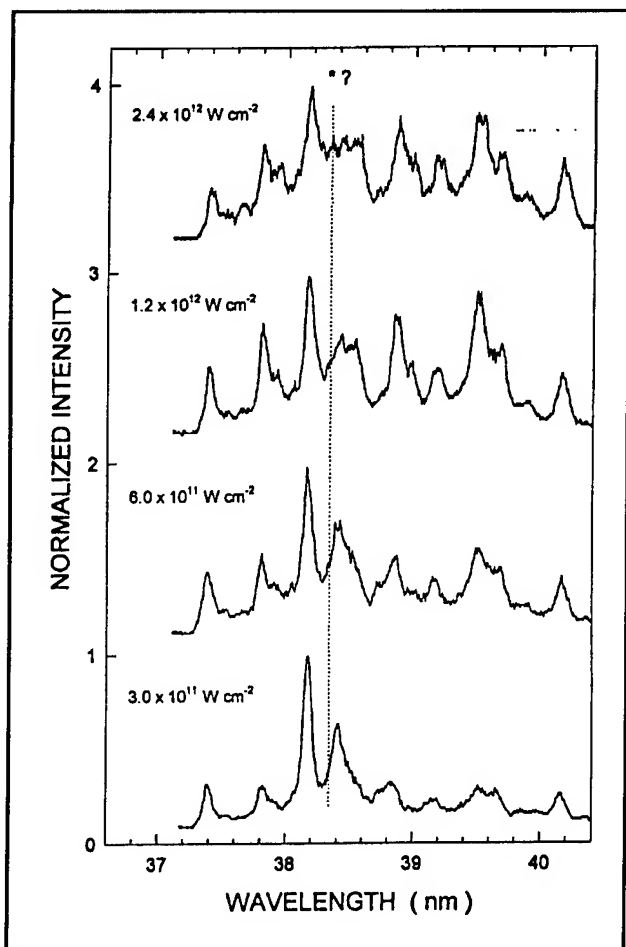


Figure 20. Ca spectra for increasing pump-laser intensity. The pump-laser intensity was increased for a 5 mm long plasma. A spectral feature was observed at the location of the candidate Ne-like Ca 3p-3s lasing line, marked with the dotted line.

1.16.4 Axicon and Tube Experiments

The efficiency of EUV and soft x-ray lasers as demonstrated at various laboratories around the world is typically quite low, on the order of 10^{-6} conversion of incident pump laser light to output laser radiation. For EUV lasers to be applied, we need to develop more efficient designs. In laser-plasma experiments, usually a high-intensity laser ablates plasma from material that is initially a solid. In the course of

the irradiation, much of the thermal energy that is deposited is converted into kinetic energy that drives the ablation. Much of the remaining energy drives ionization in nearby high-density material, and some is lost to radiation. Eventually, a small fraction of the energy is used to populate the upper laser state, but at the high-electron density that maximizes the laser gain, most of this upper state population is lost to collisional deexcitation.

From these considerations, it is easy to see why such short wavelength lasers are inefficient. To improve significantly the overall efficiency, a way must be found to reduce the loss for each of the individual mechanisms. To this end, we proposed some time ago the possibility of using a low-density plasma to develop an efficient short wavelength laser. The collisional scheme at low density can be made to be quite efficient (the intrinsic efficiency of the kinetics can approach 10 percent). The basic problem then is how to create and heat such a plasma efficiently. Inverse bremsstrahlung absorption becomes inefficient at low density, and it is not possible to absorb a significant fraction of the incident pump energy into such a plasma using a single pass. We proposed the use of an axicon and tube to provide a way to re-use the pump laser light. Another approach to this problem is to use optical field ionization instead of inverse bremsstrahlung absorption to create a plasma and to couple energy to the plasma; this approach was recently demonstrated at Stanford University.⁸⁴

An axicon and tube was recently designed⁸⁵ and fabricated at the Lawrence Livermore National Laboratory⁸⁶ using diamond turning on oxygen-free copper. This optic was designed to focus an incident-collimated pump laser beam at 1.0μ into a line using a reflective axicon, and the tube re-focuses the light four times to produce a plasma roughly 6 cm in length. The optic was constructed with a surface figure precision on the order of a micron and with a local surface smoothness on the order of 25 \AA . Preliminary experiments are currently being performed with this optic, and a plasma has been generated in argon.⁸⁷ Intense focusing of the light to a line within the axicon and tube on the micron scale is predicted, and plasma formation observed with single-pulse irradiation is consistent.

⁸⁴ B.E. Lemoff et al., "Demonstration of a 10-Hz Femtosecond-pulse-driven XUV Laser at 41.8 nm in Xe IX," *Phys. Rev. Lett.* 74: 1574 (1995).

⁸⁵ M. Fleury, Ph.D. diss., *Ecole Polytechnique*, forthcoming.

⁸⁶ The optic was built by Tony Demeris of LLNL during the spring of 1995.

⁸⁷ M. Muendel, M. Fleury, S. Chatterji, and P. Hagelstein, presented at the 1996 *International X-ray Laser Conference*, Lund, Sweden.

1.17 Elastic and Inelastic Neutron Hopping

Sponsors

Electric Power Research Institute
Contract RP3170-25
ENECO

Project Staff

Professor Peter L. Hagelstein with contributions from Steve Crouch-Baker and Michael McKubre

For several years, a number of anomalies have been reportedly observed in metal hydrides. The claims of excess heat production, if correct, are perhaps the most important. In PdD, the largest excess power production claimed so far is a factor of about three over the input power; many laboratories claim observations of smaller effects. The total energy claimed to have been generated involves on the order of a hundred times the chemical energy that would be released if the cathode were replaced by an explosive and detonated. Recent claims have also been made by a few individuals of the observation of power gains on the order of 50 or more in NiH electrolysis experiments, with considerably larger energy production per cathode atom. If this larger effect proves to be real, then it would perhaps follow that commercial applications are not far off; such a strategy is currently being pursued by a company, Clean Energy Technologies, Inc.

Claims have also been made for the generation of tritium and other radioactive isotopes, and neutron generation has been reported. If these effects are real, then they are clearly secondary processes compared to whatever primary process is responsible for heat production.

Currently, neither heat production nor any of the other claimed effects is generally accepted by the scientific community. These results, if real, indicate the presence of a new physical effect that allows nuclear reactions to take place in a way very different from that which have been studied in nuclear physics for more than 60 years. Most physicists do not believe in such a possibility and simply reject all claims.

From our perspective, the key experiments relating to heat production in PdD appear to be reproducible at a number of laboratories; they work with different types of calorimetry; they show similar dependencies on loading and current at different laboratories;

and the effects seem to be correlated with the average rate of exothermic desorption. If there is a new physical effect, then according to the experimental claims it is a very big effect; a primary goal of our research is to try to understand theoretically what is the basic effect.

We have found during the past several years two new physical mechanisms that may be relevant: (1) neutron hopping and (2) anomalous energy transfer by phonon frequency shifting. Elastic neutron hopping is proposed to be analogous with electron hopping as a second order process. This effect is found to be maximized in deuterated vacancy phase NiH and PdH. Anomalous energy transfer requires the presence of a phonon laser and would allow neutron hopping to occur between inequivalent nuclei. Inelastic neutron hopping is proposed to be responsible for excess heat and tritium production. These and related issues are discussed in the following sections.

1.17.1 The Neutron Mixed Valence Model

The premise of neutron hopping theory is that there exists a finite coupling between bound neutron states and continuum neutron states. The origin of this process is ultimately in correlation effects associated with the nuclear structure problem.⁸⁸ For example, in a multiconfigurational Hartree-Fock description of a nucleus, configurations including both bound and free neutrons should be included. Strong force interaction matrix elements will lead to a coupling between configurations with bound neutrons and with free neutrons.

The largest effects are expected to occur when the free neutron has no net angular momentum (the centripetal potential keeps a slow neutron away from the nucleus in the case of non-zero angular momentum); stable isotope pairs that would be described by this theory occur in the elements H, He, Si, Cd, Sn, Te and Xe. The first such example that we studied was the coupling between ground state ^{29}Si and ground state ^{28}Si plus a free s-wave neutron.

In the crudest single configuration description, ^{29}Si can be thought of as a ^{28}Si core plus an outer 2s valence neutron. Mixing between the ^{29}Si ground state and the ionized system would involve a single neutron excitation. From Brillouin's theorem, it is known that in the Hartree-Fock description, direct coupling between such states is forbidden; conse-

⁸⁸ P.L. Hagelstein, "Neutron Hopping in Crystals," submitted to *Phys. Rev. B*.

quently, we must go to second order to obtain matrix elements of the type required. One can use perturbation theory to include correlation effects

$$\langle \Psi_0 | H | \Phi_k \rangle = \sum_n \frac{\langle \Phi_0 | V_s | \Phi_n \rangle \langle \Phi_n | V_s | \Phi_k \rangle}{E_0 - E_n} + \dots$$

The resulting matrix elements are expected to be on the order of the characteristic strong force potential (MeV) weighted by the square root of the ratio of nuclear to atomic volumes

$$\langle \Psi_0 | H | \Phi_k \rangle \sim v_s \sqrt{\frac{V_n}{V_a}}$$

which is on the order of 100 meV. We have examined the second order coupling in detail in the case of ^{29}Si and ^2H ; in the case of ^{29}Si , the numerical results from summing over several hundred configurations are consistent with such an estimate.

In the case of ^2H , the intermediate states are isobaric deuteron configurations (corresponding to internal proton and neutron excitations), and the resulting nuclear matrix element is estimated to be on the order of 500 meV. There is a significant uncertainty in this number originating from the current uncertainty in isobaric content of the deuteron. We estimate the interaction matrix element to be linear in the isobaric deuteron fraction according to

$$\langle \Psi_0 | H | \Phi_k \rangle \sim 500 p_{\text{iso}}(\%) \text{ meV}$$

A 1 percent deuteron isobar content corresponds to a 500 meV interaction matrix element. Theoretical estimates for the total isobaric content of the deuteron in the literature are in the range of a few percent.

In the case of isolated nuclei, the coupling discussed above leads to minor corrections in the nuclear energy and very little else. For a collection of nuclei in a lattice, it seems appropriate to adopt models that have been successful to describe analogous effects for electrons. The relevant model in this case is a version of the periodic Anderson model, which might be termed a neutron mixed valence model;⁸⁸ the associated Hamiltonian is

$$\begin{aligned} \hat{H} = & \sum_{k, \sigma} \epsilon_k \hat{c}_{k, \sigma}^\dagger \hat{c}_{k, \sigma} + \sum_{i, \lambda} \epsilon_\lambda \hat{X}_{\lambda\lambda}(i) + \sum_{i, \mu} \epsilon_\mu \hat{X}_{\mu\mu}(i) \\ & + \frac{1}{\sqrt{N}} \sum_i \sum_{k, \sigma\lambda, \mu} \\ & [V_{\lambda\sigma\mu}(k) e^{-ik \cdot \hat{R}_i} \hat{c}_{k, \sigma}^\dagger \hat{X}_{\lambda\mu}(i) + V_{\mu\sigma\lambda}(k) e^{ik \cdot \hat{R}_i} \hat{X}_{\mu\lambda}(i) \hat{c}_{k, \sigma}] \end{aligned}$$

This Hamiltonian includes the valence neutron energy, the free neutron energy, and the coupling between bound and free neutrons. The physical content of this model is minimal; it describes basic configuration interaction effects for a collection of nuclei in a lattice. This Hamiltonian differs from the electron mixed valence Hamiltonian in two respects: (1) phonon interactions are more important since neutrons are much heavier than electrons, and (2) the valence and conduction bands are widely separated (by MeV in the neutron model). We have assumed in our work a harmonic lattice, which is suppressed in the above Hamiltonian.

1.17.2 Predicted Neutron Hopping Rates

The neutron mixed valence model can be used to examine the possibility of elastic neutron hopping from one site to a neighboring site. For two nuclei in isolation, this probability is calculated from this model to be exponentially small due to extreme destructive interference among the different free neutron states. In a lattice, the model predicts that resonant Bragg scattering causes a relatively small number of free neutron states to avoid this destructive interference, which gives rise to a small probability of the valence neutron being delocalized on the atomic scale. If the delocalized neutron is resonantly captured by a neighboring nucleus, then a neutron hopping event will have occurred.

We can calculate neutron hopping rates directly from second order perturbation theory⁸⁸

$$\Gamma = - \left[\frac{2}{\hbar} \right] \times$$

$$\text{Im} \langle \hat{V} [E - \hat{H}_0]^{-1} \hat{V}^\dagger [E - \hat{H}_0]^{-1} \hat{Q} \hat{V} [E - \hat{H}_0]^{-1} \hat{V}^\dagger \rangle$$

where the transition operator \hat{V} is taken from the neutron mixed valence Hamiltonian

$$\hat{V} = \frac{1}{\sqrt{N}} \sum_{\mathbf{k}} \sum_{\sigma, \lambda} \sum_{\mu} v_{\mu\sigma\lambda}(\mathbf{k}) e^{-i\mathbf{k} \cdot \hat{\mathbf{R}}_i} \hat{\chi}_{\mu\lambda}(i) \hat{c}_{\mathbf{k}, \sigma}$$

The operator \hat{Q} is a projection operator.

Elastic neutron hopping rates for a variety of crystals are shown in figure 21. In the high temperature limit, the Mössbauer contribution to the neutron hopping rate is proportional to an exponential factor

$$\Gamma_0 \sim e^{-\Delta\epsilon_{ij}/kT}$$

The effective barrier energy $\Delta\epsilon_{ij}$ for neutron hops from site i to site j within a unit cell is approximately

$$\Delta\epsilon_{ij} = \frac{1}{2} M \omega_0^2 |\Delta\mathbf{R}_{ij}|^2$$

where M is the mass of the nucleus after a neutron hop, where $|\Delta\mathbf{R}_{ij}|$ is the atomic site separation in a unit cell, and where ω_0 is the classical frequency associated with the nucleus consistent with the experimentally observed Debye-Waller factor.

Some interesting physics can be seen in the predicted hopping rates. Considerable destructive interference among the free neutron Bragg states occurs, and finite neutron hopping rates are pre-

dicted only when this effect is minimized. To minimize the destructive interference, the number of Bragg states must be minimized; this is predicted to occur at high temperature in materials where phonons are generated via recoil most easily. To maximize neutron hopping, we seek crystals with "soft" inter-atomic potentials. The potentials for hydrogen in metal hydrides, especially PdH, are predicted to be superior in this regard to all monatomic crystals. The largest neutron hopping rates are predicted to occur in metal hydrides that have extreme host lattice metal vacancy content (as can be seen in figure 21), because the local hydrogen potential in such materials is even softer.

1.17.3 Predicted Gamma Emission Rates

We computed neutron hopping rates that result from a bound neutron developing a small probability of being delocalized by resonant Bragg scattering in a lattice. A bound neutron that is delocalized may be captured by a neighboring nucleus if the capture process is exothermic. This neutron capture event would be expected to be accompanied by the emission of a gamma, which could then be observed. We have proposed this as a way to indirectly demonstrate experimentally that elastic neutron hopping occurs.⁸⁸

In the case of virtual neutrons originating from deuterium, neutron capture is energetically allowed (since the neutron is most weakly bound on deuterium of all stable nuclei). The gamma capture

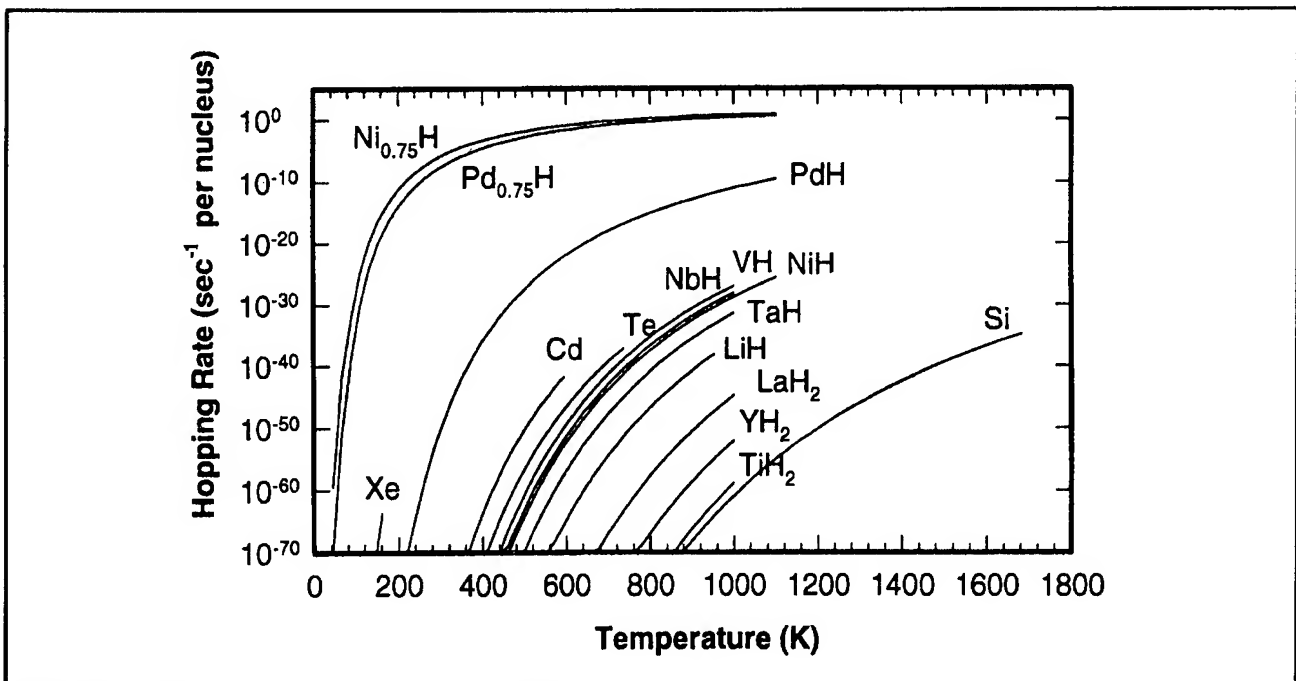


Figure 21. Predicted neutron hopping rates in various crystals assuming an optimum isotopic mix.

rate can be estimated from the neutron mixed valence model by adding a complex potential due to (n, γ) absorption to the Hamiltonian

$$\hat{H}_0 + \hat{V} \rightarrow \hat{H}_0 + \hat{V} - i\hat{U}$$

from which the gamma emission rate can be computed to be⁸⁸

$$\Gamma_\gamma = - \left[\frac{2}{\hbar l_n^3} \right] \text{Re} \langle \hat{U} \hat{V} \hat{U}^\dagger [E - \hat{H}_0]^{-1} \hat{V} \hat{V}^\dagger \rangle$$

$$- \left[\frac{2}{\hbar l_n^3} \right] \text{Re} \langle \hat{V} \hat{V}^\dagger [E - \hat{H}_0]^{-1} \hat{U} \hat{U}^\dagger \rangle$$

Gamma emission can come about in a metal hydride through capture by deuterium nuclei or through capture by the host metal nuclei. While the cross section for virtual neutron capture is expected to be much larger for the host metal nuclei, the probability that a virtual neutron will be at the site of

a host metal lattice has been computed and is quite small. Consequently, the dominant decay process is expected to be gamma capture by deuterium, leading to the emission of a 4.0 MeV gamma. The associated gamma emission rate for this type of process is shown in figure 22. The largest gamma emission rates are predicted for deuterated vacancy phase nickel hydride and palladium hydride. The gamma emission rate for vacancy phase deuterated nickel hydride is shown in figure 23.

1.17.4 Thermodynamics of Vacancy Phase NiH and PdH

An experimental demonstration of elastic neutron hopping according to the predictions of the neutron mixed valence model outlined above requires the production of vacancy phase metal hydrides in cubic centimeter-sized samples. Fukai and Okuma demonstrated recently that extreme vacancy production occurs thermodynamically in NiH and PdH at high temperature at a rate limited by vacancy diffusion from the surface.⁸⁹

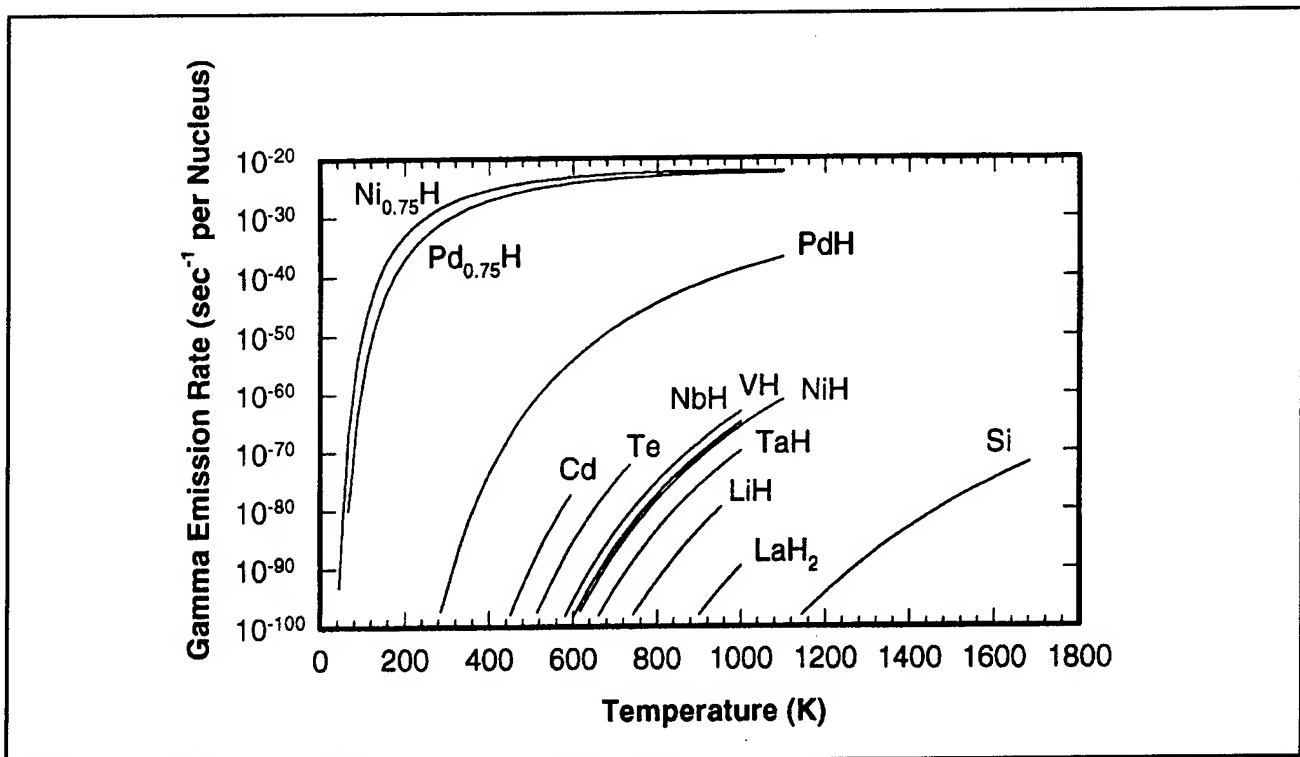


Figure 22. Gamma emission rates estimated in the high temperature limit for a variety of materials. Gamma emission due to same-element capture is assumed in all cases (consistent with 4.0 MeV emission in the deuterated metal hydrides).

⁸⁹ Y. Fukai and N. Okuma, "Evidence of Copious Vacancy Formation in Ni and Pd under High Hydrogen Pressure," *Jpn. J. Appl. Phys.* 32L: 1256 (1993); Y. Fukai and N. Okuma, "Formation of Superabundant Vacancies in Pd Hydride under High Hydrogen Pressures," *Phys. Rev. Lett.* 73: 1640 (1994).

We have recently examined a simple model for the thermodynamics of vacancy phase PdH and NiH. The equilibrium vacancy concentration x_v can be determined from the entropy S_k and enthalpy h_f of vacancy formation through

$$\frac{x_v}{1 - x_v} = e^{S_k/k} e^{-h_f/kT}$$

The entropy of point defect formation S_k is known for a variety of materials at low concentration, and according to Fukai and Okuma is of the order of $2.5k$ (we follow Fukai and Okuma and use $e^{S_k/k} = 10$ here for both Ni and Pd).

The enthalpy of formation h_f has been studied theoretically using density functional theory, and from experiment. At high loading, the enthalpy of formation is approximately linear in the hydrogen concentration. If we define x_c to be the hydrogen concentration referenced to the number of host metal atom sites (and independent of the number of vacancies), then

$$h_f \approx h_f^0 + x_c \frac{dh_f}{dx_c}$$

We can then determine the hydrogen loading x_c required to establish an equilibrium vacancy concentration x_v ; we obtain

$$x_c = - \left[\frac{dh_f}{dx_c} \right]^{-1} \left\{ h_f^0 - kT \left[\frac{S_k}{k} - \ln \frac{x_v}{1 - x_v} \right] \right\}$$

We have plotted in figure 24 results from this model for a variety of specified vacancy concentrations.

This model predicts that the vacancy phase is thermodynamically favored at high loading under normal conditions; both NiH and PdH are unstable against spontaneous vacancy phase formation at high loading, rate limited only by the vacancy diffusion rate. This provides the basis for possible routes for vacancy phase sample generation: We could in principle generate internal sources of vacancies (by electron or ion bombardment), and then transiently heat the sample. Alternatively, we could attempt to grow vacancy phase NiH or PdH on a highly loaded vacancy phase substrate.

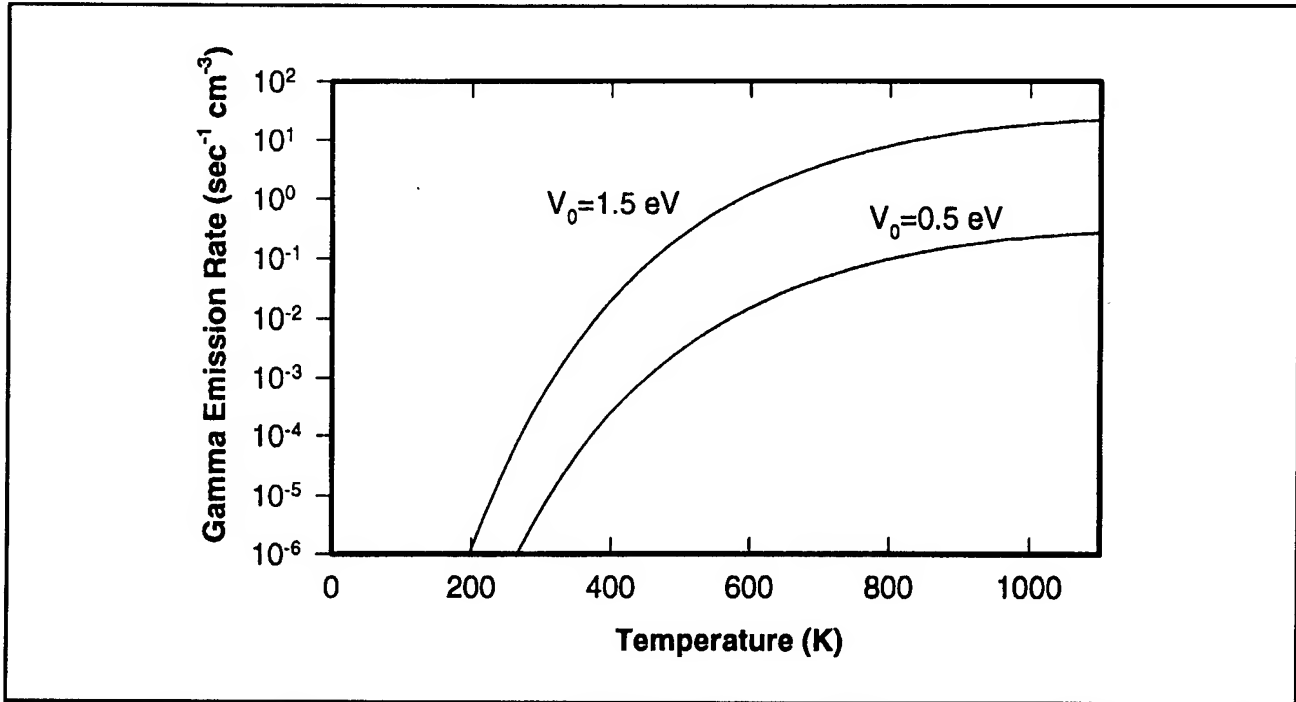


Figure 23. Gamma emission rate for deuterated nickel hydride $\text{Ni}_{0.75}\text{H}_{0.33}\text{D}_{0.67}$ as a function of temperature. Significant uncertainties exist in the nuclear transition matrix element. We have included predictions for what we consider to be a conservative estimate ($V_0 = 0.5$ eV, corresponding to 1 percent deuteron total isobar content) and also for a less conservative estimate ($V_0 = 1.5$ eV, corresponding to 3 percent total isobar content) that is representative of isobar content values found in the literature.

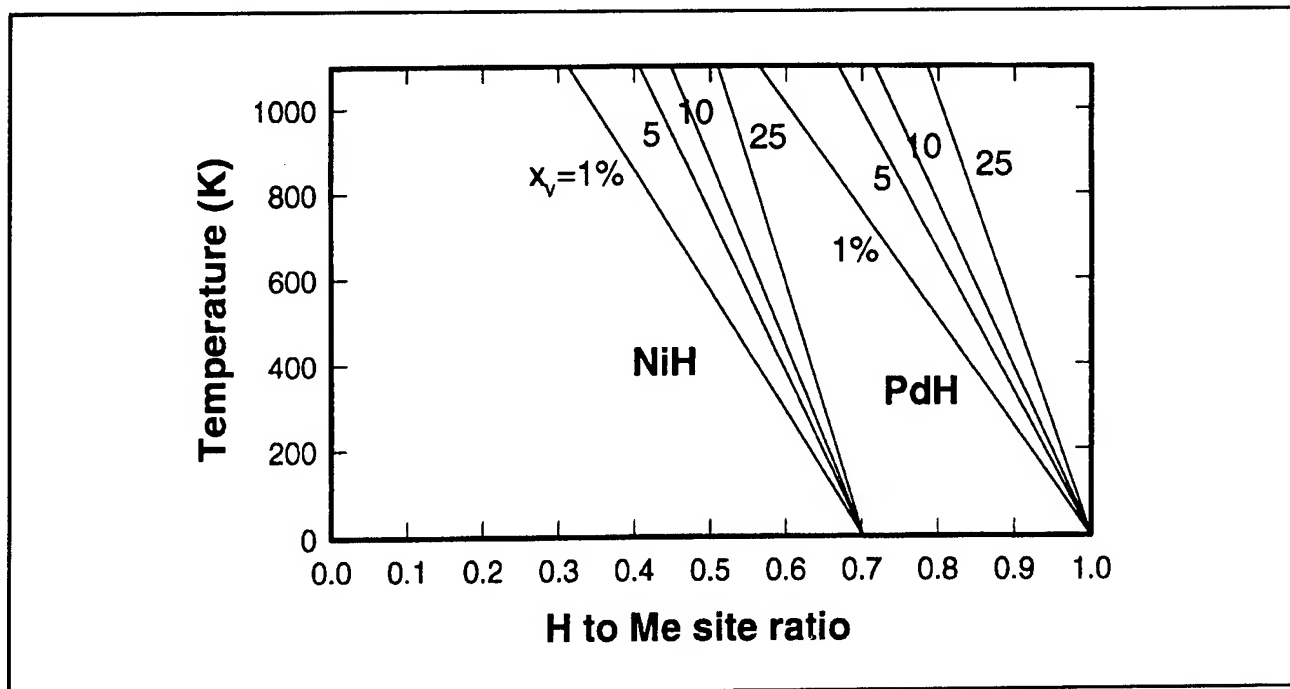


Figure 24. Estimated temperature and hydrogen loading required for the production of vacancy phase Pd_{1-x}H and Ni_{1-x} .

1.17.5 Inelastic Neutron Hopping

The possibility of neutron hopping as an elastic process has been discussed above; here we consider the possibility of inelastic neutron hopping, in which a neutron hops from one nucleus to an inequivalent nucleus, and the excess energy is dissipated. One motivation for our interest in this possibility comes from numerous reports of excess heat, tritium, neutrons, and significant induced radioactivity in electrochemical experiments involving palladium and from reports of excess heat in NiH experiments. While these experiments are not currently accepted by the scientific community, many of these effects have been reproduced numerous times in different laboratories. Should these experiments eventually be accepted as being fundamentally correct, then an explanation will be required; inelastic neutron hopping is one candidate explanation.

The basic idea is as follows: Inelastic neutron hopping would involve the transfer of a neutron from a nucleus to an inequivalent nucleus, with the energy difference transferred elsewhere. It is not difficult to show that such a large energy cannot be transferred through a general interaction that

creates large numbers of low energy quanta. Instead, we have examined the possibility that such an energy transfer can proceed through a minor frequency shift of a macroscopic oscillator that is highly excited.

It has been known for decades (and now discussed in textbooks) that a small number of phonon modes of a lattice can jump across a phonon band gap due to a modification of the mass or force constants associated with an atom at one site in the lattice.⁹⁰ In molecular physics, the effect is known as the Duschinsky effect⁹¹ when the molecular force constants are altered due to an electronic transition. A prototypical example of a lattice version of this effect is the case of hydrogen and deuterium impurities in a dilute metal hydride.⁹² If initially there are N_H hydrogen atoms and N_D deuterons in a metal lattice, then there will be $3N_H$ phonon modes near the hydrogen resonant frequency ω_0 and $3N_D$ phonon modes near the deuterium resonant frequency $\omega_0/\sqrt{2}$. A neutron capture by a proton causes these numbers to change neutron capture. There are $N_H - 1$ hydrogen atoms with $3(N_H - 1)$ associated phonon modes at ω_0 , and $N_D + 1$ deuterons with $3N_D + 1$ associated phonon modes

⁹⁰ P.G. Dawber and R.J. Elliott, "The Vibrations of an Atom of Different Mass in a Cubic Crystal," *Proc. Phys. Soc.* 81: 483 (1963).

⁹¹ F. Duschinsky, "Zur Deutung der Elektronenspektren mehratomiger Molekule," *Acta Physicochemica* (URSS) 7: 521 (1937).

⁹² P.L. Hagelstein, "Possibility of Mössbauer Effect in Neutron Capture," *Hyperfine Interact.* 92: 1059 (1994).

at $\omega_0\sqrt{2}$. In this example, the phonon modes are impurity continuum modes within a band, and it is the three lowest energy phonon modes of the hydrogen impurity band that jump to form three new highest modes of the deuteron band.

It can also be shown that, to within a reasonable approximation, that the phonons originally in a mode that jumps undergo a frequency shift according to the frequency shift of the phonon mode. The total associated energy transfer is then⁹²

$$\Delta E = n_{ph} \hbar \delta \omega$$

where n_{ph} is the number of phonons initially in the modes that jump, and $\delta \omega$ is the associated frequency shift. In the limit that the number of phonons n_{ph} is great, then the resulting energy transfer will be large. For example, phonon lasers were developed soon after the advent of the optical laser; with a phonon laser it is possible to achieve a very high number of phonons in a mode. Phonon lasers have been demonstrated up to 0.87 THz by optical pumping of impurity atoms in a crystal.⁹³ We have developed and published a model for the anomalous broadening and shifting of the gamma transition associated with neutron capture by protons in a dilute metal hydride due to frequency shifts of thermally generated and phonon laser produced phonons.⁹²

Consequently, a mechanism that enables an inelastic neutron hopping effect may exist, provided that an appropriate phonon band gap is present, and that in addition a phonon laser is operating. We have begun an investigation of a model for inelastic neutron hopping mediated by phonon exchange through the frequency shift of a large number of phonons. Within the framework of the neutron mixed valence model, the associated inelastic hopping rate can be computed from⁹⁴

$$\Gamma = - \left[\frac{2}{\hbar l_n^2} \right] \text{Im} \langle \hat{V}_{bc} V_{cb}^2 [E - \hat{H}_0]^{-1} \hat{V}_{b'c} \hat{V}_{cb} \rangle$$

where the index b refers to orbitals of the donor nuclei, where c refers to the continuum, and where b' refers to orbitals of the acceptor nuclei. This theory is formally closely related to the elastic

neutron hopping theory discussed above. For an exothermic neutron hopping reaction, if the energy is transferred to the lattice, then there exists the possibility that the lattice will decay. The basic theory for this has been developed and published earlier;⁹⁵ the primary lattice decay modes are likely to be Coulomb mediated electronic and atomic recoils that alter the number of vacancies. If we assume that this is so, then the resulting reaction rate for inelastic neutron hopping in the high temperature limit is⁹⁴

$$\Gamma \sim \left[\frac{V_D^2 V_A^2 N_A N_D N}{2 l_D^2} \right] \times \sum_{i,j} f_{\mu}^{(i)} f_{\lambda}^{(j)} \frac{e^{-\Delta E_{ij}/kT}}{\det^{1/2} M_{ij}} \frac{1/\tau_L}{(I_D - I_A)^2 + (\hbar/2\tau_L)^2}$$

In this formula, V_D and V_A are the associated nuclear interaction matrix elements discussed previously; N_D and N_A here are the number of contributing Brillouin zones for the donor and acceptor nuclei, respectively; I_D and I_A are the donor and acceptor neutron binding energies; ΔE_{ij} is the associated effective barrier energy for neutron hopping (it can be of a similar magnitude as in the case of elastic neutron hopping). In this expression, τ_L is the time associated with the lattice decay, within the framework of a model in which real energy transfer to the lattice occurs (as opposed to this being a virtual process). This type of model predicts reaction rates for inelastic neutron hopping that can occur at a nontrivial fraction of the elastic hopping rate in the presence of a suitable phonon laser.

Such a theory is naïve relative to the energy exchange with the phonons. Energy transfer to a lattice by phonon modes frequency shifting upward results in a final state lattice with the excess energy distributed over a large number of phonon modes on the high energy side of the phonon band gap. If the phonon band gap is associated with vacancies (specifically, if a change in the number of vacancies causes phonon modes to jump the band gap), then the lattice can decay through electronic or atomic recoil (as long as it changes the number of vacancies). The lattice decay time for this type of

⁹³ P. Hu, "Stimulated Emission of 29-cm⁻¹ Phonons in Ruby," *Phys. Rev. Lett.* 44: 417 (1980).

⁹⁴ P.L. Hagelstein, "New Lattice-nucleus Coupling Mechanisms and Possible Energy Production," *Proceedings of the Symposium on Fusion Engineering (SOFE '95)*, forthcoming.

⁹⁵ P.L. Hagelstein, "Lattice-Induced Atomic and Nuclear Reactions," *Trans. Fusion Tech.* 26: 461 (1994).

process is computed to be extremely short—so short that perturbation theory is not appropriate.⁹⁵

Consequently, an inelastic neutron hop within this theory would occur by virtual energy transfer to the lattice and subsequent decay by a large number of low energy recoil events. That the process is virtual appears to be extremely important within the theory, because it means that a much smaller number of phonons is required to be present in the mode for the overall process to occur. In essence, the lattice only has to have the possibility of accommodating a relatively small amount of energy in order to mediate the decay by recoil of a large amount of energy.⁹⁴

1.18 Many-photon Configuration Space Theory and Applications

Project Staff

Professor Peter L. Hagelstein

We describe in the following sections some ideas that have been developed recently relating to light propagation in nonlinear fibers, and possible applications of the resulting theory. The motivation for much of this work came about from a series of discussions at the MIT Laboratory of Computer Science during the summer of 1994 concerning the possibility of quantum computation, and the application of quantum optics techniques to the problem.⁹⁶

The premise of quantum computation seemed to require the use of single photons, in order to generate interference effects equivalent to the prerequisite quantum superposition. Yet it is very difficult to arrange for useful nonlinear interactions between single photons, because the associated fields are so weak. We would have liked to use optical pulses for fast switching, but single photon interference patterns resulting from the optical pulses would not produce the correct probability distributions needed for quantum computation.

The brainstorm that evolved in these meetings was to think about the quantum soliton itself as a single quantum object and consider the possibility of designing a new class of optical elements that would switch optical solitons as quantum objects. For example, an optical soliton incident on a beamsplitter would be fractionated into two optical pulses with partial energy depending on the reflection and transmission coefficients. This would not be appropriate for our purposes; we require a

beam divider that would switch the soliton either one way or another as an intact quantum object in order to implement our vision of a quantum computer.

Unfortunately, the quantum radiation theory that is currently used for nonlinear optics problems is not particularly well-adapted for the treatment of such problems. The essential reason for this is that the questions posed above are configuration space questions, while the radiation theory is cast in terms of a second quantization formulation. To make progress, we require a configuration space description for quantum nonlinear optics. Such a project had never been attempted and ultimately proved to be quite a significant task. In the sections that follow, we provide a summary of some of the issues, results, and applications.

1.18.1 Photon Configuration Space Theory

To explain what a configuration space Schrödinger equation is for a photon, it is perhaps simplest to think first about the more familiar problem of what is the configuration space equation for a particle. The Schrödinger equation in configuration space for a nonrelativistic particle in quantum mechanics is

$$\hat{E}\psi(r, t) = \left[\frac{|\hat{p}|^2}{2m} + V(r) \right] \psi(r, t)$$

with $\hat{E} = i\hbar \frac{\partial}{\partial t}$ and $\hat{p} = -i\hbar \nabla$. This equation is used to describe the time evolution of the probability amplitude ψ relevant for the calculation of quantum effects (interference, tunneling, etc.).

Problems in quantum optics are presently not treated with configuration space models; instead, such problems are typically formulated using a second quantized theory. In the case of particles, a second quantized model is developed through the quantization of the wavefunction ψ to give

$$\hat{E}\Psi = \int \hat{\psi}^\dagger \left[\frac{|p|^2}{2m} + V(r) \right] \hat{\psi} d^3r \Psi$$

This we recognize as a Schrödinger equation in second quantization. Here $\hat{\psi}$ and $\hat{\psi}^\dagger$ are field operators. This type of theory would appear as part of a description of the probability amplitude for a collection of noninteracting particles (or consist of

⁹⁶ P.L. Hagelstein, N. Margolus, and M. Biafore, "Towards an Optical Quantum Computer Project," unpublished (1994).

probabilities that the collection contains different numbers of noninteracting particles). Second quantized models of particles are of considerable use in many-body quantum physics applications.

Quantum radiation problems are usually formulated using an underlying description of the radiation field that derives from a second quantized Hamiltonian of the form

$$\hat{E}\Psi = \int \frac{1}{2} \epsilon_0 |\hat{E}|^2 + \frac{1}{2} \mu_0 |\hat{H}|^2 d^3r \Psi$$

where $|\hat{E}|^2$ and $|\hat{H}|^2$ are quantum squared electric and magnetic field operators. In this type of theory, the probability amplitude Ψ describes the radiation field, that will be in general a superposition of states each with a different number or different distribution of photons. Modern quantum optics research is described ultimately in terms of this type of theory (augmented with matter interactions, and typically cast in terms of a Heisenberg picture, instead of a Schrödinger picture).

In the case of particles, problems can be formulated and worked either in first quantization or in second quantization. The first quantization approach tends to be mathematically simpler; the second quantization approach tends to solve harder problems when the quantum problems can be solved. In the case of photons, quantum mechanical problems are uniformly worked using second quantization techniques; first quantization methods have not been applied to quantum radiation problems to any significant degree. The reason for this concerns difficulties associated with the photon configuration space, which has been said by some noted authors not to exist.

We have recently applied quantum field theory techniques developed for the analogous relativistic electron quantum theory to the photon problem⁹⁷ and have obtained a configuration space photon equation of the form

$$\hat{E}\psi(r, t) = \hat{\Lambda}_{++} [\alpha_M \cdot c\hat{p} + \hat{V}_\epsilon] \hat{\Lambda}_{++} \psi(r, t)$$

In this theory, ψ is a 6×1 column vector, α_M is a 6×6 spin-1 matrix, and V_ϵ is a 6×6 nonlocal operator that includes the effect of matter from linear response theory applied directly to QED. The Λ_{++}

operators are projection operators that restrict interactions to the positive energy spectrum of possible quantum states.

The resulting configuration space theory suffers from a variety of problems that are well known in the literature: For example, the configuration space theory is not covariant, photons cannot be localized (so that all interactions with matter or other photons are inherently nonlocal), and $|\psi|^2$ cannot be interpreted as a probability density. While these problems are serious, the method that we used to develop photon configuration space equations maps the configuration space problem onto an equivalent second quantized QED problem, which is free of the problems which plague the configuration space theory.

Consequently, it is now possible to apply the configuration space theory systematically to quantum radiation problems, such as occurs in quantum nonlinear optics, to obtain formulations that are fundamentally simpler. In addition, the configuration space method provides additional insights and analogs to well known configuration space particle problems that may be obscured in a second quantized formulation.

1.18.2 Photon Configuration Space Description of Soliton Propagation

One of the most basic quantum problems of interest in quantum optics is quantum soliton propagation along an optical fiber. This problem has been analyzed by numerous authors, using formulations in second quantization. The results of these models indicate that the solitons largely behave as classical solitons with quantum fluctuations appearing in the center of mass location and in the relative phases of the component number states. We have applied the configuration space theory to this problem in order to benchmark the theory, and to understand quantum soliton propagation from a configuration space viewpoint.⁹⁸

A soliton in a fiber from a photon configuration space point of view is a collection of photons that are bound around a photonic center of mass (photons do not have mass, but the concept of a center of mass is convenient here). The photons interact with other photons with an attractive approximate delta function interaction potential, forming a collective photonic ground state, that is a

⁹⁷ P.L. Hagelstein, "Many-Photon Configuration Space Equations," submitted to *Phys. Rev. A*.

⁹⁸ P.L. Hagelstein, "Application of Photon Configuration Space Equations to Optical Soliton Propagation," *Phys. Rev. A*, forthcoming.

bosonic analog to a nuclear ground state. In the case of the nuclear states, it is possible in the non-relativistic approximation to exactly separate center of mass and relative mass coordinates; we seek an equivalent separation for the photon configuration space wavefunction.

The configuration space theory in one dimension leads to a soliton number state wavefunction Ψ_n that can be written as a product

$$\Psi_n = \psi(x, t) \Phi(\xi_1, \dots, \xi_{n-1})$$

where $\psi(x, t)$ is a wavefunction for the soliton center of mass, and where $\Phi(\xi_1, \dots, \xi_{n-1})$. The Schrödinger equation for the photonic center of mass in a moving frame can be written

$$i\hbar \frac{\partial}{\partial t} \psi(x, t) = -\frac{\hbar^2}{2m} \frac{\partial^2}{\partial x^2} \psi(x, t)$$

where m here is a parameter that is related to the fiber dispersion. This Schrödinger equation is the same as that for a free particle; consequently, the configuration space analogy for soliton center of mass propagation is that of a free quantum particle. If the center of mass is initially localized, then the associated probability amplitude will spread; the spread in time is found from

$$\Delta x^2(t) = \Delta x_0^2 + \frac{\Delta p_0^2}{4m^2} t^2$$

When the relevant parameters are computed for the quantum soliton, it is found that this formula gives correctly the quantum fluctuations computed from the second quantized models. In this case, the underlying origin of the effect is perhaps simpler to understand.⁹⁸

1.18.3 Soliton Configuration Space Position-Phase Wavefunctions

The second quantized theories naturally include states with different photon number, and it is of interest to compute the phase shifts and fluctuations in phase that occur for soliton propagation.

This problem is well known in the quantum soliton literature, and the computation of the spread in phase has been computed using second quantized techniques. We decided to attempt a computation of this effect using the configuration space approach.

We introduced the Fourier transform of the center of mass wavefunction weighted by the Fock space mixing coefficients;⁹⁸ for example, we define

$$\psi(x, \theta, t) = \sum_n a_n \psi_n(x, t) e^{in\theta}$$

The inverse transform is

$$a_n \psi_n(x, t) = \int_0^{2\pi} \frac{d\theta}{2\pi} \psi(x, \theta, t) e^{-in\theta}$$

The function $\psi(x, \theta, t)$ is termed a position-phase wavefunction. Although it could be argued that $\psi(x, \theta, t)$ is not really a wavefunction at all, it was found to behave very much like a wavefunction. The time evolution of $\psi(x, \theta, t)$ is given by

$$\psi(x, \theta, t) = \sum_n \int \frac{dk}{2\pi} a_n \psi(k) e^{ikx} e^{in\theta} e^{-iE_n(k)t/\hbar}$$

The energy $E_n(k) = \hbar\omega_n(k)$ is made up of the center of mass kinetic energy and the soliton binding energy. The dependence of energy on soliton number and center of mass momentum leads to a frequency of the form

$$\omega_n(k) =$$

$$\omega_0 + (n - n_0) \frac{\partial \omega}{\partial n} + \frac{1}{2} (n - n_0)^2 \frac{\partial^2 \omega}{\partial n^2} + \frac{1}{2} k^2 \frac{\partial^2 \omega}{\partial k^2}$$

The evolution equation for the position-phase wavefunction is then

$$i \frac{\partial}{\partial t} \psi(x, \theta, t) = \left[\omega_0 + \frac{\partial \omega}{\partial n} \left(-i \frac{\partial}{\partial \theta} - n_0 \right) + \frac{1}{2} \frac{\partial^2 \omega}{\partial n^2} \left(-i \frac{\partial}{\partial \theta} - n_0 \right)^2 - \frac{1}{2} \frac{\partial^2 \omega}{\partial k^2} \frac{\partial^2}{\partial x^2} \right] \psi(x, \theta, t)$$

This equation is simplified if we transform into a moving frame in θ ; we obtain⁹⁸

$$i \frac{\partial}{\partial t} \psi(x, \theta, t) = \left[-\frac{1}{2} \left(\frac{\partial^2 \omega}{\partial n^2} \right) \frac{\partial^2}{\partial \theta^2} - \frac{1}{2} \left(\frac{\partial^2 \omega}{\partial k^2} \right) \frac{\partial^2}{\partial x^2} \right] \psi(x, \theta, t)$$

Using Ehrenfest's theorem, we obtain exact evolution equations for the fluctuations in both x and θ that are solved to yield

$$\Delta x^2(t) = \Delta x_0^2 + \frac{\Delta p_0^2}{4\hbar^2} \left(\frac{\partial^2 \omega}{\partial k^2} \right) t^2$$

$$\Delta \theta^2(t) = \Delta \theta_0^2 + \frac{\Delta n_0^2}{4} \left(\frac{\partial^2 \omega}{\partial n^2} \right) t^2$$

After substituting in the appropriate parameters specific to soliton propagation, these formulas are found to agree with the equivalent results obtained from second quantized models. Moreover, the evolution of the squeezing factor is also in agreement between the two models; this allows for a particularly simple physical interpretation of soliton squeezing as spreading of an initially localized free-particle wavefunction in θ -space.⁹⁸

1.18.4 Quantum Soliton Center of Mass Interferometry

Configuration space wavefunctions are naturally adapted for the calculation of interference phenomena. While we are familiar with single photon interference effects, much less is currently understood about many photon interference effects. Such interference effects could be observed in principle with an interferometer of the type illustrated in figure 25. In this case, the configuration space soliton wavefunction at the detector is composed of two contributions from the different paths through the interferometer

$$\Psi = \Psi_1 + \Psi_2$$

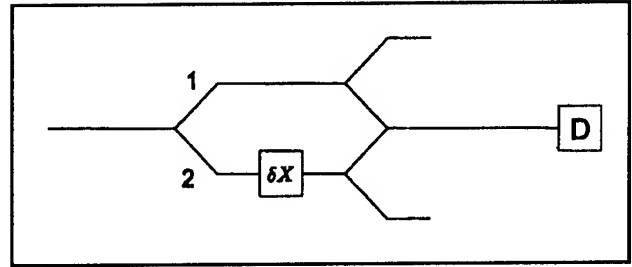


Figure 25. Soliton center of mass interferometer. The soliton is assumed to be switched as a quantum object by quantum beam dividers (normal beamsplitters would fractionate the soliton).

The probability of detection is then proportional to

$$p_D = |\Psi_1|^2 + |\Psi_2|^2 + \langle \Psi_1 | \Psi_2 \rangle + \langle \Psi_2 | \Psi_1 \rangle$$

We can develop formulas in terms of the soliton center of mass position-phase wavefunctions for such calculations; it can be shown that the expectation value of a many-photon configuration space operator can be expressed in terms of the center of mass position-phase wavefunction as

$$\langle \hat{Q} \rangle = \langle \psi(x, \theta, t) | \hat{Q} | \psi(x, \theta, t) \rangle$$

The "transformed" operator \hat{Q}' can be related formally back to the matrix elements of \hat{Q} ; we find

$$\hat{Q}' = \sum_{nm} \int \frac{d\theta'}{2\pi} e^{i(n\theta' - m\theta)} \langle \Phi_n | \hat{Q} | \Phi_m \rangle e^{i(\theta' - \theta)} \frac{\partial}{\partial \theta}$$

The classical state position-phase wavefunction for soliton propagation is⁹⁹

$$\psi(x, \theta, t) = [2\pi\Delta x_0\Delta\theta_0[1 + i\Phi_x(t)][1 + i\Phi_\theta(t)]]^{-\frac{1}{2}} \times e^{ik_0x} e^{in_0\theta} e^{-i\omega_0 t} e^{-\frac{(x - \langle x \rangle)^2}{4\Delta x_0^2[1 + i\Phi_x(t)]}} e^{-\frac{(\theta - \langle \theta \rangle)^2}{4\Delta\theta_0^2[1 + i\Phi_\theta(t)]}}$$

This solution is characterized by eight basic parameters: the mean position $\langle x \rangle$ and phase $\langle \theta \rangle$; the center of mass momentum k_0 and the photon number n_0 ; the initial spread in center of mass position Δk and phase $\Delta\theta$; the dispersion of the center of mass position and phase as parameterized by the corresponding angles $\Phi_x(t)$ and $\Phi_\theta(t)$. The

⁹⁹ P.L. Hagelstein, "Application of Photon Configuration Space Equations to Optical Soliton Propagation," *Phys. Rev. A*, forthcoming; P.L. Hagelstein, "Application of Photon Configuration Space Equations to Optical Soliton Center of Mass Interferometry," submitted to *Phys. Rev. A*.

expectation values of position and phase evolve according to

$$\langle x \rangle = x_0 + \frac{\partial \omega}{\partial k} t$$

$$\langle \theta \rangle = \theta_0 + \frac{\partial \omega}{\partial n} t$$

The initial center of mass spread Δx_0 and phase spread $\Delta \theta_0$ are in general arbitrary. However, for soliton propagation beginning with a classical soliton state the initial spread in center of mass position is related to the single photon spread through

$$\Delta x_0^2 = \frac{\langle x^2 \rangle}{n}$$

in a sector of Fock space, and the initial spread in phase is due to the spread in photon number

$$\Delta \theta_0^2 = \frac{1}{4n_0^2}$$

The remaining time evolution of the wavefunction is accounted for in the increase in the angles Φ_x and Φ_θ , which are given by

$$\Phi_x(t) = \frac{1}{2} \frac{\partial^2 \omega}{\partial k^2} \frac{\Delta k}{\Delta x} t$$

$$\Phi_\theta(t) = \frac{1}{2} \frac{\partial^2 \omega}{\partial n^2} \frac{\Delta n}{\Delta \theta} t$$

We can use these results to computer the detection probability for various center of mass interferometry schemes. For example, if the interferometer produces a relative position delay with no accompanying phase delay or squeezing, then the detection probability is¹⁰⁰

$$p_D = \frac{1}{2} \left[1 + e^{-\frac{\delta x^2}{8\Delta x_0^2}} \cos \frac{2\pi n_0 \delta x}{\lambda} \right]$$

If the interferometer produces a relative phase delay with no accompanying position delay or squeezing, then the detection probability is

$$p_D = \frac{1}{2} \left[1 + e^{-\frac{\delta \theta^2}{8\Delta \theta_0^2}} \cos(n_0 \delta \theta) \right]$$

The configuration space theory can be used systematically to evaluate soliton center of mass interferometers, with arbitrary combinations of delays in position and in phase, momentum and photon number, as well as the degree of squeezing in either position or in phase. These results are new. Currently there exists no interferometers of this type; it is not presently certain that they can even be constructed. The motivation for pursuing such interferometry is the potential for obtaining λ/n interference fringes with light of wavelength λ .¹⁰¹

1.18.5 Possible Adiabatic Quantum Switching of a Soliton Center of Mass

We have applied the configuration space photon theory to nonlinear directional couplers and fiber Y-dividers.¹⁰² While the development of a general quantum theory for such devices using a second quantization formulation has not yet been reported, the configuration space model has been applied directly with no particular difficulty. The immediate goal of our effort was the design of a quantum beam divider that could put a "macroscopic" quantum soliton into a superposition of two states. From the results of the analysis, we would be able to determine whether such a device could be developed.

The configuration space many-photon equations for a nonlinear coupler can be separated approximately into a center of mass equation and a relative coordinate equation; the approximate separation is implemented through the use of a Born-Oppenheimer type product wavefunction

$$\Psi(R, \{\xi\}, t) = \psi(R, t) \Phi_R(\{\xi\})$$

¹⁰⁰ P.L. Hagelstein, "Application of Photon Configuration Space Equations to Optical Soliton Center of Mass Interferometry," submitted to *Phys. Rev. A*.

¹⁰¹ P.L. Hagelstein, "Many-Photon Configuration Space Equations," submitted to *Phys. Rev. A*; P.L. Hagelstein, "Application of Photon Configuration Space Equations to Optical Soliton Propagation," *Phys. Rev. A*, forthcoming; P.L. Hagelstein, "Application of Photon Configuration Space Equations to Optical Soliton Center of Mass Interferometry," submitted to *Phys. Rev. A*.

¹⁰² P.L. Hagelstein, "Application of Photon Configuration Space Equations to Optical Soliton Center of Mass Switching," submitted to *Phys. Rev. A*.

The center of mass dynamics is described by a Schrödinger equation of the form

$$\left[i\hbar \frac{\partial}{\partial t} - v_{gr} P_x \right] \psi(R, t) = \left[\frac{P_x^2}{2M_{||}} + \frac{|P_T|^2}{2M_{\perp}} + V_{\xi}(R) \right] \psi(R, t)$$

The effective potential $V_{\xi}(R)$ seen by the center of mass wavefunction is given by

$$V_{\xi}(r) = \langle \Phi_R | H_{\xi} + V(R, \{\xi\}) | \Phi_R \rangle$$

which is simply the relative coordinate Hamiltonian averaged over the relative coordinate wavefunction. This method of separating the center of mass and relative coordinates is in some ways like a Born-Oppenheimer approximation.

This method of approximation corresponds to a physical picture: A quantum soliton that propagates along a fiber may execute a weak transverse

motion. When the transverse center of mass moves off center, it does so because the single photon states have developed an admixture from higher order fiber modes, which have a corresponding higher frequency. The total soliton energy is then greater, and this corresponds to a net dynamical motion of the transverse soliton center of mass. This transverse energy is split up in this picture into a kinetic contribution as defined within the framework of the paraxial approximation, and a potential contribution due to the presence of linear and nonlinear dielectric.

This model has been applied to the design of a quantum nonlinear Y-coupler and a nonlinear quantum directional coupler. Our initial effort focused on the design of a Y-coupler that would switch a quantum soliton initially in a single fiber into a superposition of two states corresponding to soliton propagation down one (or the other) of two exit fibers. The results of the analysis (figure 26) demonstrated clearly conditions for which adiabatic switching could produce such states in an ideal lossless coupler. Real fibers are lossy, and it was found that the characteristic switching length was greater than the single photon loss length. In prin-

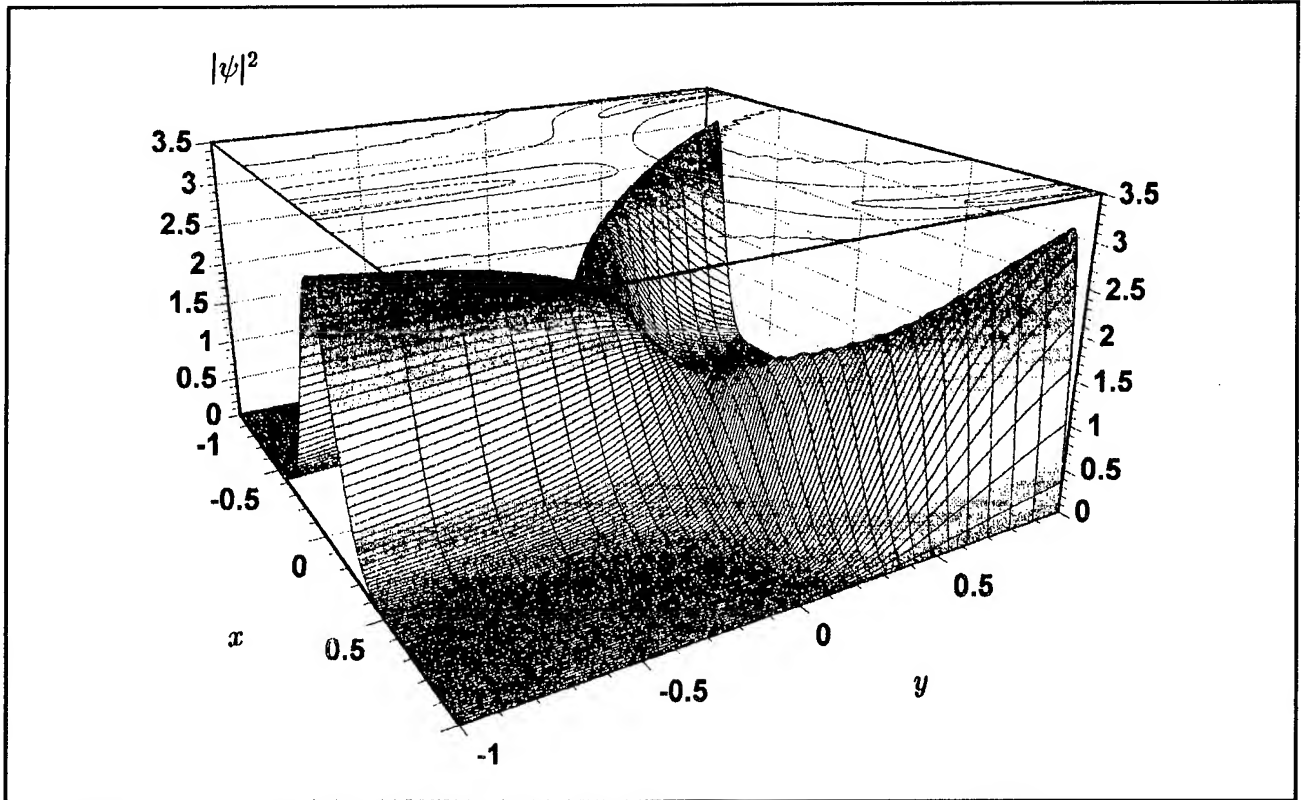


Figure 26. Wavefunction for the transverse center of mass for a quantum optical soliton in a Y-coupler in the adiabatic limit. The x-axis gives a normalized distance between the two fibers; the y-axis is a normalized measure of the strength of the nonlinear coupling relative to the splitting of the lowest modes (which corresponds to distance along the Y-coupler). On the left, the soliton is initially fractionated between the two couplers so that the center of mass is in the middle; on the right, the soliton is in a superposition of states of being mostly in one fiber or the other.

ciple, this implies that the desired superposition that would be required for the development of an interferometer could probably not be obtained. But even this conclusion is to some degree premature, as the question of the presence of an interference effect is known to depend on whether the results of the photon loss can be determined from a measurement. This problem is subtle; its resolution will ultimately require a combination of theoretical developments and an associated experimental effort.

A superior route towards resolution comes from consideration of the design of a quantum nonlinear directional coupler. In this case, the quantum soliton would switch by center of mass tunneling from one fiber to another, which can be accomplished much more easily than splitting the center of mass wavefunction between two fibers as in the case of the quantum nonlinear Y-coupler. The results of the configuration space model indicate that an ideal directional coupler can be readily designed that produces a quantum superposition for a macroscopic soliton. Once again, the switching length is found to exceed the single photon loss length.

While these initial results are either to be expected (since macroscopic quantum effects are at best elusive) or disappointing (since such a device would be extremely interesting), there are a number of variations of the initial approach that are of interest: (1) While it may not be possible to switch the soliton completely within a single photon loss length, it is certainly possible to generate other states that correspond to fractional splitting (like 60/40) which would show λ/n interference effects; (2) It is quite likely that the loss of a single or of a few photons will not destroy an interference pattern, as long as the loss is not measurable. Such questions will be of extreme interest if this field develops. (3) Much more relaxed constraints are obtained on the design of such optical elements if short pulses are used that are not solitons. It is not obvious whether the resulting states will exhibit quantum interference, but clearly there are interesting possibilities.

1.18.6 Application to Quantum Computation

There has been a growing realization that quantum computation, long considered to be highly speculative, is likely to have practical applications that are potentially important. The premise of quantum computation schemes is that extreme parallelism can be obtained by creating a computer that can be put into a quantum superposition of states. The computer then calculates and adjusts relative phases based on the results of the calculation. The result of the calculation is determined from a measurement of the state of the computer, and the answer will be probabilistic, reflecting the results of the calculations that were done in each state of the quantum superposition. The advantage of the approach over classical computation is that a single quantum computer can in principle be put into a superposition of perhaps 10^{100} states and perform computations that ultimately depend on the results of computations performed in each of these states. A highly parallel classical computer could not achieve equivalent computational power. The applications for such quantum computers, assuming that they can be developed, may be in the areas of factorization of large numbers and modeling of complex quantum systems (we will inevitably expect to see a new class of computer games).

We have been interested in the use of optical solitons and short optical pulses for a possible implementation of a quantum computer.¹⁰³ Nonlinear optical techniques can be used for fast switching, and low loss optical fibers are useful for applications in high bandwidth communications. Most current proposals for quantum computation involve the manipulation of electronic or nuclear spins or use of cavity QED techniques, both of which are very slow in comparison with optical switching. These proposals have the advantage that (1) they are based on experimentally demonstrated technology, (2) they provide an implementation of quantum computation on discrete bit, and (3) the associated phase coherence times are sufficiently long to allow on the order of perhaps 10^6 or more coherent quantum computations. Quantum computation with optical solitons could not achieve a competitive number of coherent quantum computations (intrinsic fiber loss produces an upper limit of about 10^3 coherent quantum computations in an ideal optical system).¹⁰⁴

¹⁰³ P.L. Hagelstein, N. Margolus, and M. Biafore, "Towards an Optical Quantum Computer Project," unpublished (1994).

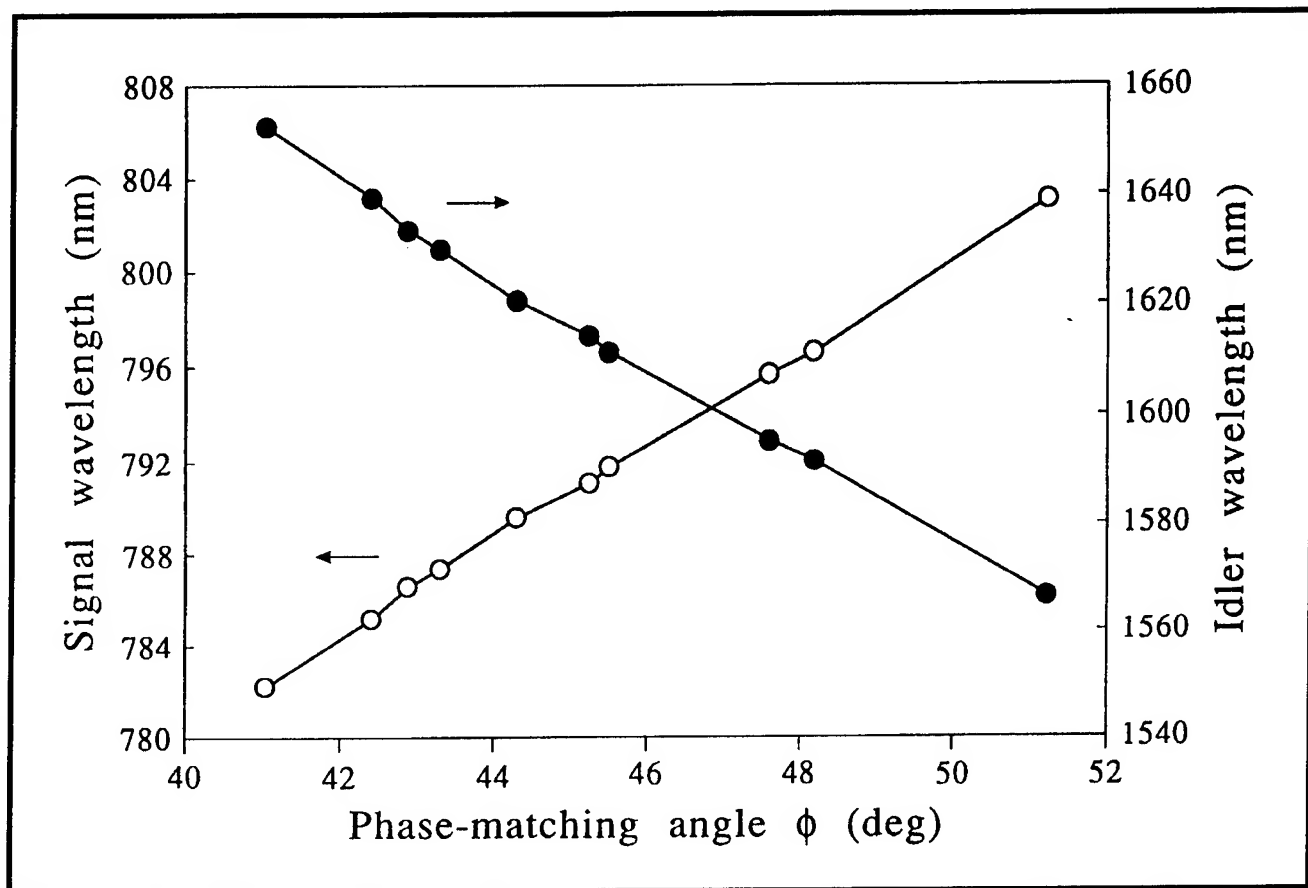
¹⁰⁴ P.L. Hagelstein, "Possibility of Quantum Computation Using Optical Pulses in Fibers," invited talk at the *First Japanese International Conference on Quantum Computation*, Osaka, Japan, December 1995.

Consequently, quantum computation based on optical pulses in fibers would not be competitive against the other leading approaches if the measure of quantum computational power is total number of coherent operations possible. There has been some exploratory discussion of the possibility of quantum error correcting schemes for quantum computation, which are at this point speculative relative the proposed applications. Should quantum error correction algorithms prove to be viable for quantum computation, then the the total number of coherent quantum computations would no longer be the dominant measure; instead, the rate at which quantum computation can be done will be more important. In this case, quantum computation based on optical technology has the potential to be faster by many orders of magnitude than the conventional approaches.¹⁰⁴

Even if quantum error correction were shown not to be viable, there would still be an important reason to explore optical quantum computation. This is because the optical system is fundamentally a continuum quantum system, where groups of spins or two-state atomic systems constitute a discrete quantum system. The potential capabilities of discrete versus continuum quantum computers will be very different; the class of quantum problems that could be modeled using a continuum quantum computer represents a different class of problems than the class that can be modeled using a discrete quantum computer.¹⁰⁴

1.18.7 Publications

- Goodberlet, J., et al. "Observation of Gain in a Recombining H-like Boron Plasma." *J. Opt. Soc. Am. B* 12: 980 (1995).
- Hagelstein, P.L. "Application of Photon Configuration Space Equations to Optical Soliton Propagation." *Phys. Rev. A*. Forthcoming.
- Hagelstein, P.L. "Application of Photon Configuration Space Equations to Optical Soliton Center of Mass Interferometry." Submitted to *Phys. Rev. A*.
- Hagelstein, P.L. "Application of Photon Configuration Space Equations to Optical Soliton Center of Mass Switching." Submitted to *Phys. Rev. A*.
- Hagelstein, P.L. "New Lattice-nucleus Coupling Mechanisms and Possible Energy Production." *Proceedings of the Symposium on Fusion Engineering* (SOFE '95). Forthcoming.
- Hagelstein, P.L. "Possibility of Quantum Computation Using Optical Pulses in Fibers." Invited talk at the *First Japanese International Conference on Quantum Computation*, Osaka, Japan, December 1995.
- Hagelstein, P.L. "Many-Photon Configuration Space Equations." Submitted to *Phys. Rev. A*.



Tunable 1.6 μm source: Plot of input signal and output idler wavelengths versus internal CTA crystal phase matching angle ϕ for $\theta=90^\circ$ and a pump wavelength of 531 nm.

Chapter 2. Optical Propagation and Communication

Academic and Research Staff

Professor Jeffrey H. Shapiro, Dr. Robert H. Rediker, Dr. Ngai C. Wong

Graduate Students

Jeffrey K. Bounds, L. Reginald Brothers, Donald R. Greer, Dicky Lee, Gilbert Leung, Elliott J. Mason, Phillip T. Nee, Steven G. Patterson, Asif Shakeel

Undergraduate Students

Patrick Grayson

2.1 Introduction

The central theme of our programs has been to advance the understanding of optical and quasi-optical communication, radar, and sensing systems. Broadly speaking, this has entailed: (1) developing system-analytic models for important optical propagation, detection, and communication scenarios; (2) using these models to derive the fundamental limits on system performance; and (3) identifying and establishing through experimentation the feasibility of techniques and devices which can be used to approach these performance limits.

2.2 Nonlinear and Quantum Optics

Sponsor

Maryland Procurement Office
Contract MDA 904-93-C4169
Contract MDA 903-94-C6071

Project Staff

Professor Jeffrey H. Shapiro, Dr. Ngai C. Wong, Jeffrey K. Bounds, Elliott J. Mason, Phillip T. Nee, Steven G. Patterson, Asif Shakeel

2.2.1 Quantum Optical Tap

It has been predicted that a gain-saturated optical parametric amplifier (OPA) can offer an improvement in the large-signal signal-to-noise ratio over a conventional phase-insensitive optical amplifier.¹ This unique characteristic can lead to a better

photodetection system and is potentially useful in coherent optical communication networks.

As a prelude to demonstrating the preceding quantum optical tap concept, we have set up an ultralow loss optical parametric oscillator (OPO) for the study of quantum noise correlation. High quality mirrors and a potassium titanyl phosphate (KTP) crystal have permitted stable cw operation of the OPO with a threshold of 30 mW. With a longer crystal, a two-piece lower-loss design, and a 2.7 percent output coupler, the OPO threshold was 150 mW. It is expected that this higher-threshold OPO should yield an intensity correlation between the signal and idler outputs of 80-90 percent and allow us to study the mean-field characteristics, gain saturation, and quantum-noise spectra of an injection-seeded OPA.²

Instead of using a large-frame krypton ion laser as a green pump source, we have recently generated over 300 mW of 532 nm light using resonant second harmonic generation of a 500-mW 1.06 μm diode-pumped YAG laser. This cw green source has been utilized to pump a KTP OPO for increased mechanical stability. The system is used for investigating the possibility of self-phase locking in a type-II phase matched OPO using an intracavity quarter-wave plate. The wave plate mixes the two orthogonally polarized subharmonic outputs and provides a means for signal injection for both subharmonics. When the OPO is operated near frequency degeneracy, it is expected that this mutual signal injection should induce self-phase locking, similar to that observed in type-I phase

¹ N.C. Wong, "Squeezed Amplification in a Nondegenerate Parametric Amplifier," *Opt. Lett.* 16(21): 1698-1700 (1991).

² K.X. Sun, *Classical and Quantized Fields in Optical Parametric Interactions*, Ph.D. diss., Dept. of Physics, MIT, 1993.

matched OPO.³ Self-phase locking is of interest in the study of squeezed states and in precision measurements.

2.2.2 Quasi-Phase Matched Nonlinear Optics

We have initiated a study of quasi-phase matching (QPM)⁴ in lithium niobate with the goal of fabricating QPM nonlinear optical devices that can be operated at any user specified wavelength within the transparency window of lithium niobate, such as in the 1.5 μm optical communication window. Nonlinear optical devices that are fabricated using QPM are potentially useful in many applications such as optical frequency conversion and amplification for optical communication networks. By employing the electric field poling technique,⁵ we have successfully obtained domain reversal in a bulk 6-mm-long 240- μm -thick lithium niobate sample with a periodicity of 21.5 μm . We are in the process of testing the QPM material in a three-wave mixing experiment with inputs of 782 nm from a Ti:sapphire laser and 1064 nm from a diode-pumped YAG laser. Improvements in the QPM fabrication process are also in progress in order to obtain more uniform and longer gratings.

2.2.3 Squeezed-State Generation in Optical Fiber

In theoretical work, we have been establishing the limits on squeezed-state generation in optical fiber. We have shown that the Raman noise which accompanies the noninstantaneous Kerr effect sets a new limit on the degree of quadrature-noise squeezing that can be obtained from continuous-

wave (cw) four-wave mixing (fwm) in optical fiber with a spectrum-analysis homodyne measurement.⁶ For pulsed squeezed-state generation in fiber, we have shown that local-oscillator (LO) selection is the key to observing the full squeezing generated when the nonlinear interaction is pumped by a transform-limited Gaussian pulse.⁷ We have developed a general theory for optimal LO selection for quadrature-noise measurements of arbitrary spatio-temporal quantum states.⁸ Using this theory, in conjunction with a single-resonance model for the non-instantaneous Kerr response of single-mode fiber, we have shown that previously suggested LO selections—the bright-fringe LO from a Sagnac interferometer squeezer, a weak-signal fwm LO from a Sagnac interferometer, and a pulse-compressed LO—are all sub-optimum.⁹ Furthermore, our general theory has revealed a new squeezing mode for cw-source fiber experiments, namely Raman squeezing.⁹ Here, the output from a cw-pumped fiber is homodyned with a LO comprised of two unequal-amplitude, optimally-phased optical frequencies separated by a frequency difference comparable to that of the peak Raman gain.

2.2.4 Publications

Patterson, S.G. *Quantum Intensity Noise Correlation in a Type-II Phase Matched Optical Parametric Oscillator*. S.M. thesis, Dept. of Electr. Eng. and Comput. Sci., MIT, 1995.

Shakeel, A. *Enhanced Squeezing in Homodyne Detection via Local-Oscillator Optimization*. S.M. thesis, Dept. of Electr. Eng. and Comput. Sci., MIT, 1995.

-
- ³ C.D. Nabors, S.T. Yang, T. Day, and R.L. Byer, "Coherence Properties of a Doubly Resonant Monolithic Optical Parametric Oscillator," *J. Opt. Soc. Am. B* 7(5): 815-820 (1990).
 - ⁴ M.M. Fejer, G.A. Magel, D.H. Jundt, and R.L. Byer, "Quasi-Phase-Matched Second Harmonic Generation: Tuning and Tolerances," *IEEE J. Quantum Electron.* 28(11): 2631-2654 (1992).
 - ⁵ M. Yamada, N. Nada, M. Saitoh, and K. Watanabe, "First-Order Quasi-Phase Matched LiNbO₃ Waveguide Periodically Poled by Applying an External Field for Efficient Blue Second-Harmonic Generation," *Appl. Phys. Lett.* 62(5): 435-436 (1993).
 - ⁶ J.H. Shapiro and L. Boivin, "Raman-Noise Limit on Squeezing in Continuous-Wave Four-Wave Mixing," *Opt. Lett.* 20(8): 925-927 (1995).
 - ⁷ L.G. Joneckis and J.H. Shapiro, "Enhanced Fiber Squeezing via Local-Oscillator Pulse Compression," *Proceedings of Nonlinear Optics: Materials, Fundamentals and Applications*, Waikaloa, Hawaii, July 24-29, 1994.
 - ⁸ A. Shakeel, *Enhanced Squeezing in Homodyne Detection via Local-Oscillator Optimization*, S.M. thesis, Dept. of Electr. Eng. and Comput. Sci., MIT, 1995.
 - ⁹ J.H. Shapiro and A. Shakeel, "Optimizing Homodyne Detection of Quadrature-Noise Squeezing via Local Oscillator Selection," submitted to *J. Opt. Soc. Am. B*.

Shapiro, J.H. "Phase Conjugate Quantum Communication with Optical Heterodyne Detection." *Opt. Lett.* 20(9): 1059-1061 (1995).

Shapiro, J.H., and L. Boivin. "Raman-Noise Limit on Squeezing continuous Wave Four-Wave Mixing." *Opt. Lett.* 20(8): 925-927 (1995).

Shapiro, J.H. "On the Holographic Generation of Squeezed States." *Opt. Lett.* Forthcoming.

Shapiro, J.H., and A. Shakeel. "Optimizing Homodyne Detection of Quadrature-Noise Squeezing via Local Oscillator Selection." Submitted to *J. Opt. Soc. Am. B*.

2.3 Multiresolution Laser Radar Range Imaging

Sponsor

U.S. Air Force - Office of Scientific Research
Grant F49620-93-1-0604

Project Staff

Professor Jeffrey H. Shapiro, Donald R. Greer, Gilbert Leung

This effort is part of a collaboration on automatic target detection and recognition, with Professors Alan S. Willsky (from MIT's Laboratory for Information and Decision Systems) and W. Eric L. Grimson (from MIT's Artificial Intelligence Laboratory) and their students. The unifying theme of the collaboration is the use of multiresolution (wavelet) methods at every stage—from sensor front-end processing, through feature extraction, to the object recognition module—in an overall system. We have been developing the use of wavelet-based maximum-likelihood (ML) estimation for laser radar range imaging.¹⁰ The importance of the ML approach lies in its ability to suppress the range anomalies caused by laser speckle, while simultaneously providing a physically-motivated, data-dependent route to optimally terminating a coarse-to-fine resolution progression. The practicality of the ML approach derives from the utility of the expectation-maximization (EM) algorithm for this problem together with the special properties of the Haar wavelet basis.¹¹ ML/EM range processing of typical

128 × 128 raw imagery with an arbitrary multiresolution basis is prone to both an untenable computational burden and numerical sensitivity. With the Haar basis, however, we have developed a fast ML/EM processor that is orders of magnitude faster than the general-wavelet formulation, numerically robust, and fully parallelizable. We have demonstrated the key properties of the fast ML/EM algorithm on real laser radar data, and we are now proceeding to apply this algorithm as a front-end processor to a model-based object recognition module.

2.3.1 Publications

Greer, D.R. *Multiresolution Laser Radar Range Profiling of Real Imagery*. M.Eng. thesis, Dept. of Electr. Eng. and Comput. Sci., MIT, 1996.

Greer, D.R., I. Fung, and J.H. Shapiro. "Maximum-Likelihood Multiresolution Laser Radar Range Imaging." Submitted to *IEEE Trans. Image Process*.

2.4 Optical Frequency Division and Synthesis

Sponsors

MIT Lincoln Laboratory
Advanced Concepts Program
Contract CX-16335
U.S. Army Research Office
Grant DAAH04-93-G-0399
Grant DAAH04-93-G-0187

Project Staff

Dr. Ngai C. Wong, L. Reginald Brothers, Dicky Lee, Patrick Grayson

Frequency division and synthesis in the optical domain play an important role in modern optical precision measurements, optical frequency standards, and coherent optical communication. The focus of this program is to build an optical frequency counter based on a parallel network of phase locked optical parametric oscillators (OPOs) and to apply it to precision measurements. An OPO-based optical frequency counter can be used

¹⁰ I. Fung and J.H. Shapiro, "Multiresolution Laser Radar Range Profiling with the Expectation-Maximization Algorithm," *Proceedings of the Joint ATR Systems and Technology Conference IV*, Monterey, California, November 14-18, 1994.

¹¹ D.R. Greer, *Multiresolution Laser Radar Range Profiling of Real Imagery*, M.Eng. thesis, Dept. of Electr. Eng. and Comput. Sci., MIT, 1996; D.R. Greer, I. Fung, and J.H. Shapiro, "Maximum-Likelihood Multiresolution Laser Radar Range Imaging," submitted to *IEEE Trans. Image Process*.

to measure, compare, and synthesize frequencies from optical to microwave, with high precision and accuracy. Our research includes the development of a number of enabling technologies such as wideband optical frequency comb generation,¹² tunable cw OPOs,¹³ and techniques for operating a parallel network of OPOs.

2.4.1 Terahertz Optical Frequency Comb Generation

In order to facilitate difference frequency measurements in the terahertz range, we have developed an optical frequency comb generator based on an efficient electro-optic phase modulator design. By incorporating a microwave waveguide resonator structure in a LiNbO₃ electro-optic modulator, the phase velocities of the microwave and optical fields can be matched to maximize the electro-optic modulation at a user-specified microwave frequency. The modulation is further enhanced by placing the modulator inside an optical cavity that is resonant for the input optical beam and the generated sidebands. For 1 W of microwave power at 17 GHz, we have obtained an optical frequency comb with a 3-THz span.¹² We have found that the span is limited by the group velocity dispersion of the lithium niobate electro-optic material.

In order to overcome the dispersion limitations, we employed dispersion compensating prism pair, similar to its usage in ultrafast mode-locked lasers. Preliminary results show that indeed the span of the comb can be extended beyond the dispersion limit. However, because of increased intracavity losses of the prism pair, the span is only 3.5 THz. We are now working on replacing the current 1-W microwave amplifier with a 20-W amplifier that should clearly show a greatly enhanced modulation and a larger span. We expect that a 5-10 THz span should be feasible.

2.4.2 Quantum Phase Diffusion Noise of an Optical Parametric Oscillator

It is well known theoretically that the phase between the subharmonic outputs of an optical parametric oscillator undergoes phase diffusion similar to that of a laser.¹⁴ In order to observe this phase diffusion noise, it is necessary to have a stable and constant frequency difference between the two outputs, as in our phase locked KTP OPO. We have made measurements of such a phase locked system with the OPO beat frequency set at 30 MHz. The beat signal was demodulated to yield both the in-phase and quadrature-phase noise spectra. Preliminary results show that the observed noise spectra have the same qualitative behavior as our theoretical model. Quantitatively, the noise powers were higher than expected, due probably to the excess noise from the pump laser. We plan to improve the OPO system to eliminate most of the excess noise in order to obtain the first measurement of the phase diffusion noise of an OPO. This noise measurement is important to optical frequency counting because phase coherence between the optical frequency and the microwave frequency standard is crucial.

2.4.3 Optical Frequency Division

A key element of the optical frequency counter is a 3:1 optical frequency divider in which the input to output frequency ratio is 3:1. The first step is to generate an approximate ratio of 3:1 by three-wave mixing of the inputs $3f$ and $2f + \delta$ to yield a difference frequency of $f - \delta$. A second step involves a second-stage three-wave mixing of the input $2f + \delta$ and the output $f - \delta$ to yield a second output at $f + 2\delta$. By measuring the beat frequency between the two outputs at 3δ and setting δ to zero, an exact 3:1 frequency ratio is obtained.

We have previously used the nonlinear optical crystal cesium titanyl arsenate (CTA) for generating ~3:1 frequency ratio by three-wave difference frequency mixing.¹⁵ More recently, we have tested the crystal lithium borate (LBO) and obtained similar results. The LBO crystal has been well character-

¹² L.R. Brothers, D. Lee, and N.C. Wong, "Terahertz Optical Frequency Comb Generation and Phase Locking of Optical Parametric Oscillator at 665 GHz," *Opt. Lett.* 19(4): 245-247 (1994).

¹³ D. Lee and N.C. Wong, "Tunable Optical Frequency Division using a Phase-Locked Optical Parametric Oscillator," *Opt. Lett.* 17(1): 13-15 (1992).

¹⁴ R. Graham and H. Haken, "The Quantum Fluctuations of the Optical Parametric Oscillator," *Z. Physik* 210: 276-302 (1968).

¹⁵ B. Lai, N.C. Wong, and L.K. Cheng, "Continuous-Wave Tunable Light Source at 1.6 μm by Difference-Frequency Mixing in CsTiOAsO₄," *Opt. Lett.* 20(17): 1779-1781 (1995).

ized and has very good optical properties compared with the CTA crystal. However, its nonlinear coefficient is a few times smaller than that of CTA. We are currently preparing the second three-wave mixing step using another CTA crystal with a different crystal cut.

2.4.4 Publications

Brothers, L.R., and N.C. Wong. "Optical Frequency Comb Generation for Terahertz Difference-Frequency Measurements." *Proceedings of the SPIE Laser Frequency Stabilization and Noise Reduction Conference*, San Jose, California, February 9-10, 1995.

Lai, B., N.C. Wong, and L.K. Cheng. "Continuous-Wave Tunable Light Source at 1.6 μm by Difference-Frequency Mixing in CsTiOAsO_4 ." *Opt. Lett.* 20(17): 1779-1781 (1995).

Lee, D., and N.C. Wong, "Quantum Phase Diffusion Noise Measurements in a cw Optical Parametric Oscillator." *Proceedings of the 7th Rochester*

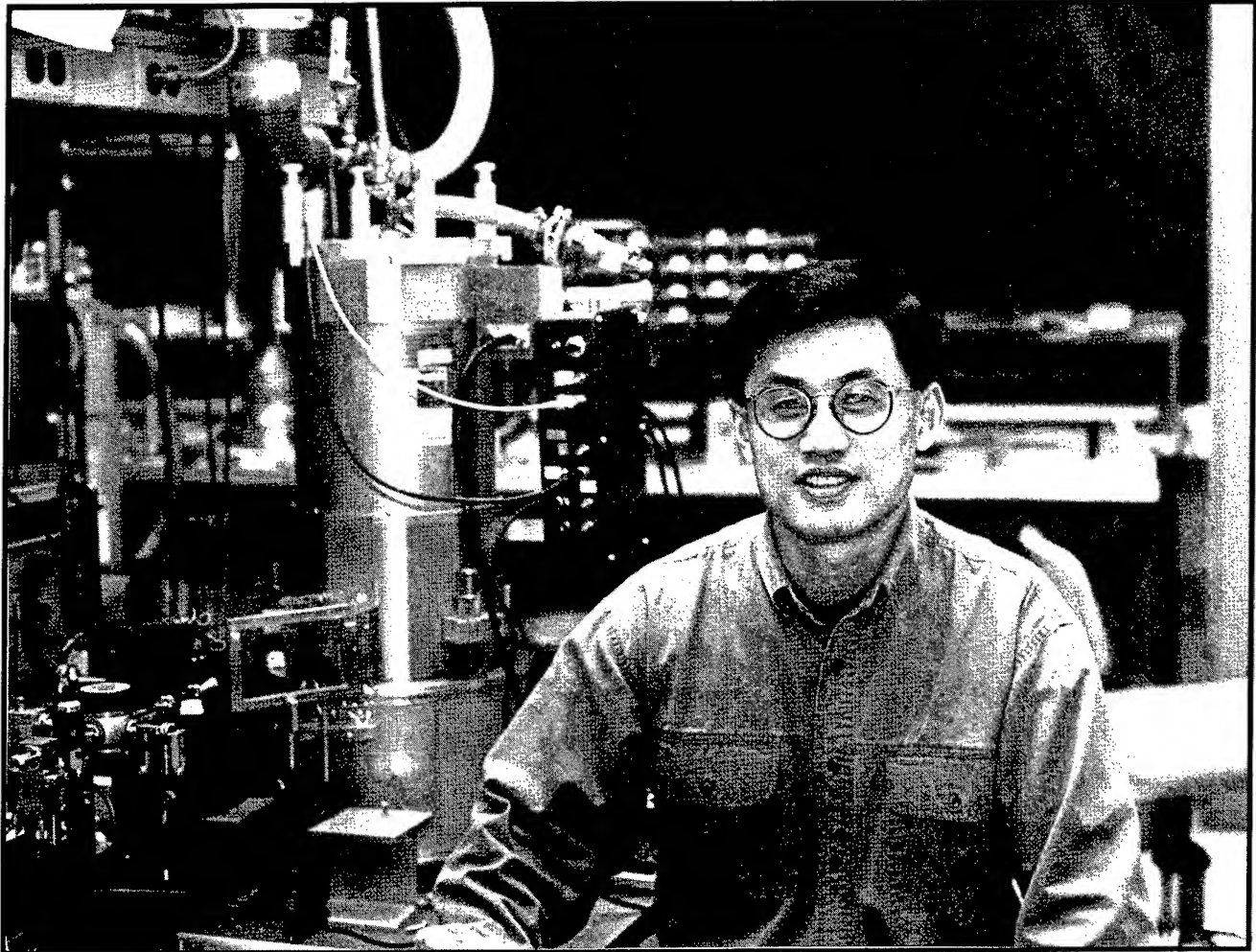
Conference on Coherence and Quantum Optics, Rochester, New York, June 7-10, 1995.

Lee, D., and N.C. Wong, "Tuning Characteristics of a cw Dual-Cavity KTP Optical Parametric Oscillator." Paper presented at SPIE Solid State Lasers and Nonlinear Crystals, San Jose, California, February 5-7, 1995.

Wong, N.C. "Optical-to-Microwave Frequency Chain Utilizing a Two-Laser-Based Optical Parametric Oscillator Network." *Appl. Phys. B* 61: 143-149 (1995).

Wong, N.C., B. Lai, P. Nee, and E. Mason. "Experimental Progress toward Realizing a 3:1 Optical Frequency Divider." *Proceedings of the Fifth Symposium on Frequency Standards and Metrology*, Woods Hole, Massachusetts, October, 15-19, 1995.

Wong, N.C. "New Applications of Optical Parametric Devices." Invited paper presented at SPIE Solid State Lasers and Nonlinear Crystals, San Jose, California, February 5-7, 1995.



Professor Qing Hu

Chapter 3. High-Frequency (>100 GHz) and High-Speed (<10 ps) Electronic Devices

Academic and Research Staff

Professor Qing Hu, Dr. Gerhard de Lange, Dr. Simon Verghese

Graduate Students

Erik Duerr, Ilya Lyubomirsky, Arifur Rahman, Farhan Rana, Rolf A. Wyss, Bin Xu, Noah D. Zamdmer

3.1 Introduction

Millimeter-wave and far-infrared frequencies ($f > 100$ GHz) remain one of the most underdeveloped frequency ranges, even though there are great numbers of potential applications in remote sensing, spectroscopy, plasma diagnostics, and communications. This is because the millimeter wave and far-infrared frequency range falls between two other frequency ranges in which conventional semiconductor devices are usually operated, the microwave frequency range and the near-infrared and optical frequency range. Semiconductor devices which utilize the classical diffusive transport of electrons, such as diodes and transistors, have a high frequency limit. This limit is set by the time electrons take to travel a certain distance. Currently, electron mobility and the smallest feature size which can be fabricated by lithography limit the frequency range to below several hundred GHz. Semiconductor devices based on quantum mechanical interband transitions, however, are limited to frequencies higher than those corresponding to the semiconductor energy gap, which is higher than 10 THz for most bulk semiconductors. Therefore, a large gap exists from 100 GHz to 10 THz in which very few devices are available.

Semiconductor quantum-effect devices (which can be loosely termed "artificial atoms"), including both vertically grown quantum-well structures and laterally confined mesoscopic devices, are human-made quantum mechanical systems in which the energy levels can be chosen by changing the sizes of the devices. Typically, the frequency corresponding to the intersubband transitions is in the millimeter-wave to THz range ($\Delta E \sim 1$ -4 meV) for the lateral quantum-effective devices, and above one THz for the vertical quantum wells. It is therefore appealing to develop ultrahigh-frequency devices, such as radiation detectors and mixers, THz lasers, and parametric frequency down converters utilizing the intersubband transitions in these devices. Furthermore, the study of the interaction between photons (with energies comparable to the intersubband spacings) and the quantum-effect

devices (artificial atoms) is analogous to optical spectroscopy in atomic physics. Naturally, this study will literally shine "new light" on these devices, and new information can be obtained that cannot be extracted from dc transport measurements. It is also clear that devices with THz characteristic frequencies will have picosecond speed response. Such ultrahigh-speed devices could be useful in easing the electronic "bottleneck" in the current fiber optical communication systems, in which only a small fraction of the 20-THz bandwidth of optical fibers are utilized because of the slow speed of electronic devices.

In addition to new physical concepts, novel technologies must also be developed to meet the challenges at these high frequencies. Conventional mechanically machined horn antennas integrated with waveguide cavities have been the workhorse at microwave and millimeter-wave frequencies since they were first implemented more than 50 years ago during World War II. Very high antenna gain and essentially perfect antenna efficiency can be achieved using these structures. However, they are expensive, bulky, and incompatible with arrays. In order to overcome these problems, there have been new developments in micromachining to fabricate the horn antenna structures. In these structures, the active elements and their planar antennas are fabricated on a free-standing thin (~ 1 micron) SiN membrane, which is suspended over a silicon pyramidal horn that is formed by anisotropic etching or micromachining. The side walls of this micromachined structure can then be coated with Au to form a horn antenna. Compared to conventional waveguide horn antennas, this micromachined structure has several major advantages. It is easier to fabricate fine three-dimensional structures by using photolithography. Horn antennas with micron precision can be easily defined and inexpensively mass produced. They are made on Si or GaAs wafers and compatible with thin-film technology. Thus, active elements, such as RF and IF amplifiers, mixers and video detectors, local oscillators, and post-detection signal processors, can be integrated monolithically with the antenna structures to form

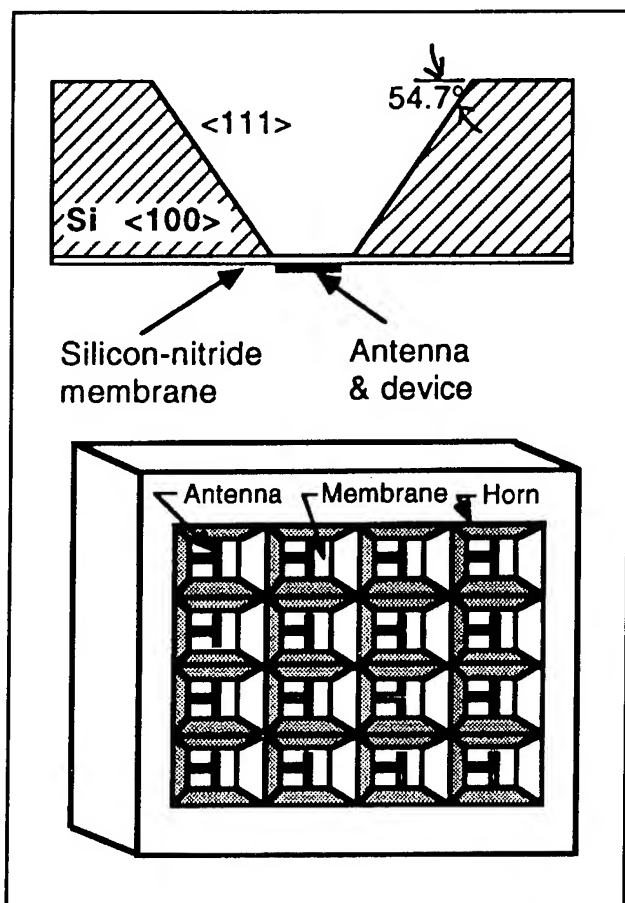


Figure 1. (a)(top) Example of a micromachined horn antenna structure that is made by anisotropically etching a <100> silicon wafer. (b)(bottom) Schematic of a focal-plane array on a single wafer made using micromachining.

monolithic transmitter/receiver systems which are light-weight and compact. The most attractive feature of the micromachined structure is that focal-plane arrays can be fabricated easily on a single wafer, as illustrated in figure 1b. Such systems will yield a significantly improved spatial resolution in remote sensing and a much greater antenna gain when implemented with phased arrays.

In our group, we are systematically investigating physical and engineering issues that are relevant to high-frequency and high-speed devices. Specifically, we are working on micromachined millimeter- and submillimeter-wave devices, far-infrared and picosecond time-resolved transport studies of lateral quantum-effect devices, and development of far-infrared lasers, photodetectors, and optical parametric amplifiers using multiple quantum-well structures.

3.2 Micromachined Millimeter-wave Devices

Sponsors

Defense Advanced Research Projects Agency
Contract MDA972-90-C-0021
National Aeronautics and Space Administration
Grant NAGW-4691
Grant 959705
National Science Foundation
Grant AST 94-23608

Project Staff

Dr. Gerhard de Lange, Arifur Rahman, Erik Duerr,
Professor Qing Hu, Dr. Richard Ralston¹

3.2.1 Micromachined Millimeter-wave SIS Receivers

Superconductor-insulator-superconductor (SIS) heterodyne receivers have been demonstrated to be the most sensitive receivers throughout 30-840 GHz frequency range. The challenge in the SIS receiver technology is to extend their operating frequency into the THz range and to develop focal-plane arrays in order to improve the efficiency of data acquisition. In order to achieve these goals, we are currently developing a scheme to couple the millimeter-wave and submillimeter-wave signals to the superconducting devices by using a micromachined horn antenna and a planar antenna supported by a thin (~1 micron) membrane, as shown in figure 1a. As stated in the introduction, this novel micromachined antenna structure can be produced with a high precision using photolithography, and it can be utilized in focal-plane arrays, as shown in figure 1b.

Following our initial success in fabricating high-quality and high-current-density SIS junctions on free-standing SiN membranes, we have further improved our micromachining techniques for whole-wafer fabrication, higher yield, and better qualities side walls that are critical for the antenna performance. Recently, we have constructed and tested W-band (75-110 GHz) micromachined SIS receiver. Figure 2 shows the pumped I-V characteristic of an SIS receiver in a micromachined antenna structure. It also shows the response to a hot (the curved marked as 300 K) and a cold (at 77 K) blackbody

¹ Group 86, MIT Lincoln Laboratory.

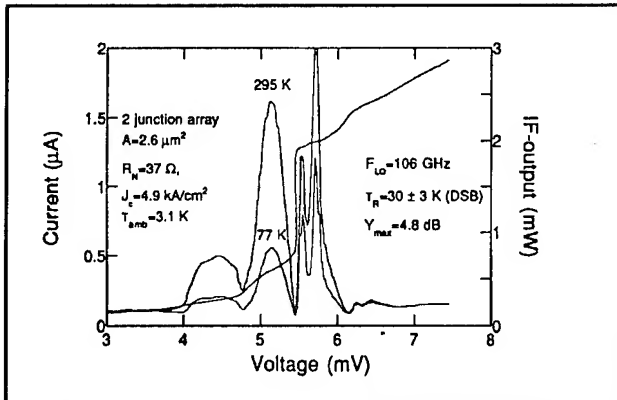


Figure 2. Pumped I-V characteristic of an SIS device in a micromachined antenna structure. The curve marked 300 K corresponds to the IF response when a hot (300 K) blackbody radiator is placed in front of the receiver, while the curve marked 77 K is with a cold load.

radiator at the intermediate frequency (IF). The 4.8-dB difference between the two curves corresponds to a double-sideband (DSB) noise temperature of 30 K (without any corrections). This result is comparable to the lowest receiver noise temperatures from the best waveguide systems that have been developed in the last 15 years. Our work has thus firmly established the micromachined receiver system as a competitive alternative to the conventional waveguide systems. We are currently designing and constructing 3×3 focal-plane array receivers using this technology, which should be tested in the coming year.

3.2.2 Micromachined Room-temperature Millimeter-wave Sensors

Due to a millimeter-wave's (especially around the 94-GHz atmospheric window) great penetration in foggy, dusty, and smoky environments and to its much better spatial resolutions compared to the longer wavelengths at microwave frequencies, sensitive room-temperature millimeter-wave devices are very useful in imaging and object identification and tracking. They are important for both military and commercial applications, such as motor vehicle collision avoidance radars. Based on our recent remarkable success in the development of micromachined SIS receivers, we are currently developing room-temperature millimeter-wave sensors using the micromachining technology.

We have used microbolometers (whose dimension is approximately several microns as illustrated in figure 3) in our micromachined systems. Microbolometers are easy to make (in fact, they are much easier to make than the superconducting tunnel junctions), robust, and sensitive. In addition, our micromachined millimeter-wave structure is ideal for

bolometric detectors in such a way that the thin SiN membrane provides a natural thermal isolation that a sensitive bolometer requires.

The dominating noise source in bolometric detectors is the $1/f$ noise associated with the resistive element (which is usually made out of semimetal materials, such as Bi, to achieve a high resistance value for impedance matching). Recently, it was discovered in the field of superconducting electronics that a commonly used superconducting material, Nb, has an order of magnitude lower level of $1/f$ noise (at room-temperature) than Bi while still providing sufficiently high resistivity for impedance matching. Assuming we operate the microbolometers above the $1/f$ noise frequency region, the NEP (noise equivalent power) of the microbolometers is limited by the temperature fluctuation, i.e., the phonon noise. Using realistic parameters for thermal conductance, a room-temperature Nb microbolometer can achieve an NEP of $6 \times 10^{-12} \text{ W}/(\text{Hz})^{1/2}$. This is more than one order of magnitude lower than that of pyroelectric detectors, which are the commonly used room-temperature millimeter-wave sensors. This level of reduction in NEP will significantly improve the sensitivity of the detectors and reduce the required integration time by at least a factor of 100 for the same signal/noise ratio.

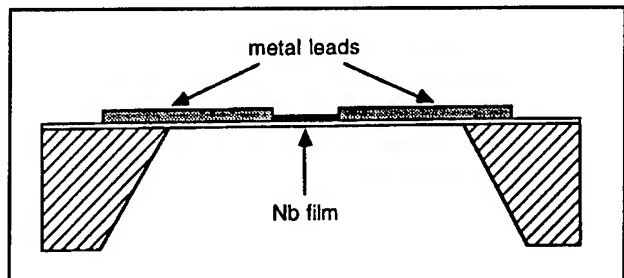


Figure 3. Schematic of a microbolometer supported by a thin membrane, which provides a good thermal insulation.

We have fabricated and tested several batches of Nb microbolometers with micromachined horn antennas. Figure 4 shows the speed and the noise performance of a microbolometer. Because of the low thermal mass associated with its small dimensions, a microbolometer has a roll-off frequency much higher than that of a conventional "macro" bolometer. This high speed may make the microbolometers useful in radar applications as well as in passive radiometry sensing. The left curve in figure 4 indicates the roll-off frequency of our microbolometer to be on the order of 10 kHz. The measured overall frequency dependence of the voltage responsivity agrees well with our theoretical calculations, which is shown as the dashed line. The noise equivalent power of this microbolometer is measured to be $4 \times 10^{-10} \text{ W}/(\text{Hz})^{1/2}$ at frequencies

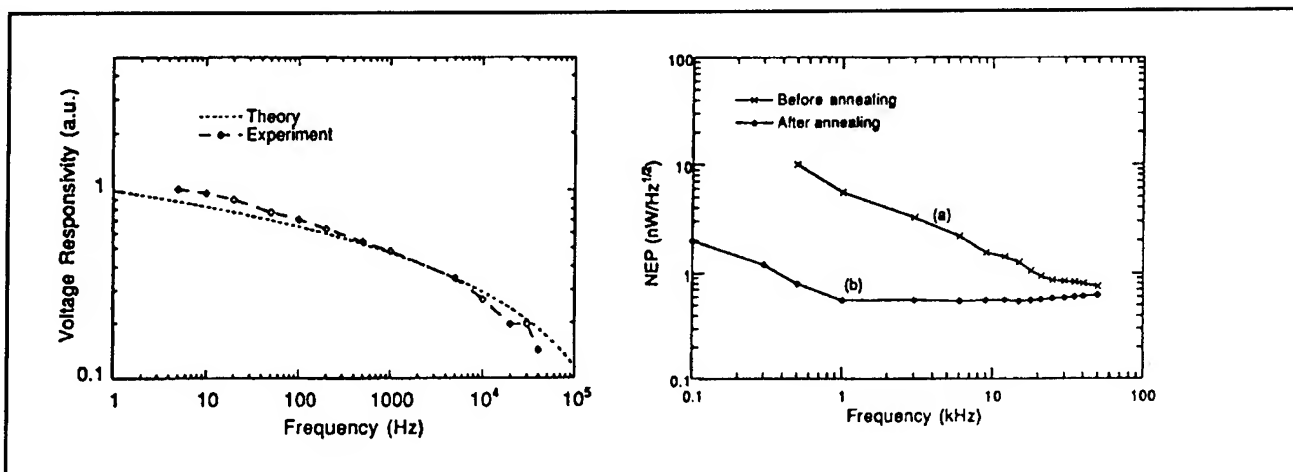


Figure 4. Left: Measured and calculated voltage responsivity as functions of the modulation frequency. Right: Noise equivalent power as a function of the frequency.

where the $1/f$ noise is not dominant. This result is already better than those for room-temperature pyroelectric detectors. With further improvements by optimizing the geometry of the SiN membrane, we should be able to reduce the NEP by another order of magnitude, which will make these microbolometers with micromachined antennas most sensitive uncooled millimeter-wave sensors.

3.3 Far-infrared and Picosecond Time-resolved Transport Studies of Quantum-effect Devices

3.3.1 Far-infrared Studies of Antenna-coupled Quantum Point Contacts

Sponsor

National Science Foundation/MRSEC
Grant DMR 94-00334

Project Staff

Rolf A. Wyss, Farhan Rana, Professor Qing Hu, Jesús A. del Alamo, Dr. Michael R. Melloch,² Dr. Michael J. Rooks³

Quantum transport has been one of the most active fields in solid-state physics in recent years. Advances in material preparation have made quantum phenomena profound in electron transport for many semiconductor quantum devices such as

quantum point contacts, quantum dots, quantum wires, quantum wells, superlattices, etc. In clean samples and at low temperatures, electrons can travel through the whole sample without suffering phase-destructive scattering. Extensive work has been done to study various features of such phase-coherent quantum transport. However, most of the experiments reported so far are limited to measurements using dc transport and far-infrared spectroscopy.

It is well known in the field of superconducting tunneling that photons can assist the tunneling process, provided the tunneling is elastic. In a broad sense, elastic tunneling is a phase-coherent quantum transport process in a classically forbidden region. Therefore, all the results of photon-assisted tunneling can be applied to the study of photon-assisted quantum transport in semiconductor devices. This will provide a new dimension to study the exciting quantum transport phenomena. Novel long-wavelength optoelectronic devices may also emerge from this research.

In this project, we intend to study the interaction between far-infrared photons and ballistic electrons in quantum point contact devices. We have fabricated several antenna-coupled, quantum point contact devices using a combination of optical and electron-beam lithography. The dc transport measurement of the drain/source transport showed high quality of the devices. Under coherent far-infrared radiation at 285 GHz, a pronounced photon-induced drain/source current is produced throughout the

² Purdue University, West Lafayette, Indiana.

³ Cornell National Nanofabrication Facility, Ithaca, New York.

gate voltage range in which the device exhibits the behavior of a one-dimensional electron system. This photon-induced current is attributed to a bolometric effect as described in the previous report.

In addition to the photoconductive effect, we have recently discovered a pronounced photovoltaic effect in several antenna-coupled quantum point contacts irradiated from 280 GHz to 2.5 THz. Figure 5a shows the drain/source current of an irradiated quantum point contact *without* external drain/source bias. This induced current tracks the subband structure in a very regular manner that is similar to the transconductance of the device measured without radiation. We have identified this photovoltaic effect as a result of thermopower due to an asymmetric heating of the source and drain. This analysis is supported by experimental evidence that by shifting the focal spot of the radiation, we can reverse the polarity of the photon-induced current, as shown in figure 5.

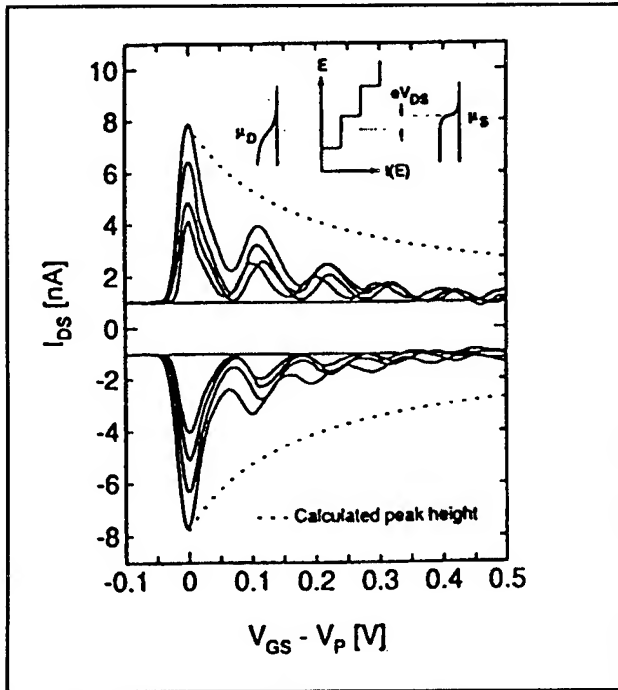


Figure 5. Measured photocurrents (at zero bias voltage) at different radiation power levels. (top) Positive currents correspond to beaming toward the source region, while (bottom) negative currents correspond to beaming toward the drain region.

3.3.2 Direct Simulation of Photon-assisted Transport

Sponsor

National Science Foundation/ MRSEC
Grant DMR 94-00334

Project Staff

Professor Qing Hu, Dr. Kou Yakubo,⁴ Dr. Shechao Feng⁴

In spite of the straightforward analogy with the photoemission phenomenon, however, our experimental investigations have failed to provide evidence for photon-assisted transport. We have carried out extensive measurements over a broad frequency range from 90 GHz to 2.5 THz (corresponding to $\hbar\omega = 0.3 - 10$ meV), with the radiation electric field polarization both along and perpendicular to the drain/source conductance path, which have yielded nothing but bolometric signals. It is natural to ask why such a simple process (which is analogous to so many well-established phenomena, such as photoemission in metals, photo-ionization of atoms, photon-excited bound-to-extended-state transitions in quantum-well structures, and photon-assisted tunneling in superconducting tunnel junctions) has not been observed in quantum-point-contact devices.

In this work, we solve time-dependent Schrödinger's equation numerically in order to investigate the conditions that could lead to a pronounced effect of photon-assisted transport. Our main finding is that the selection rule, which is the mathematical statement of the momentum conservation of the electron/photon systems, determines whether the electron transport is adiabatic or photon-excited. Mathematically, in order to achieve an appreciable photon-excited transition probability, the dipole-moment integration must be truncated to a region that is not much greater than the coherence length $1/\Delta k$, where Δk is equal to the momentum difference between the electrons before and after photon absorption/emission. This truncation can be achieved experimentally by either a localized electron state or a localized photon-field profile. Physically, this spatial localization of the electron or photon field provides the momentum spread that is necessary for the photon excitation process. Figure 6a shows a wave function (in k -space) in the presence of an ac field. The main peak at $k = 0$ corresponds to the wave function in a free space without radiation. The satellite peaks

⁴ University of California, Los Angeles, California.

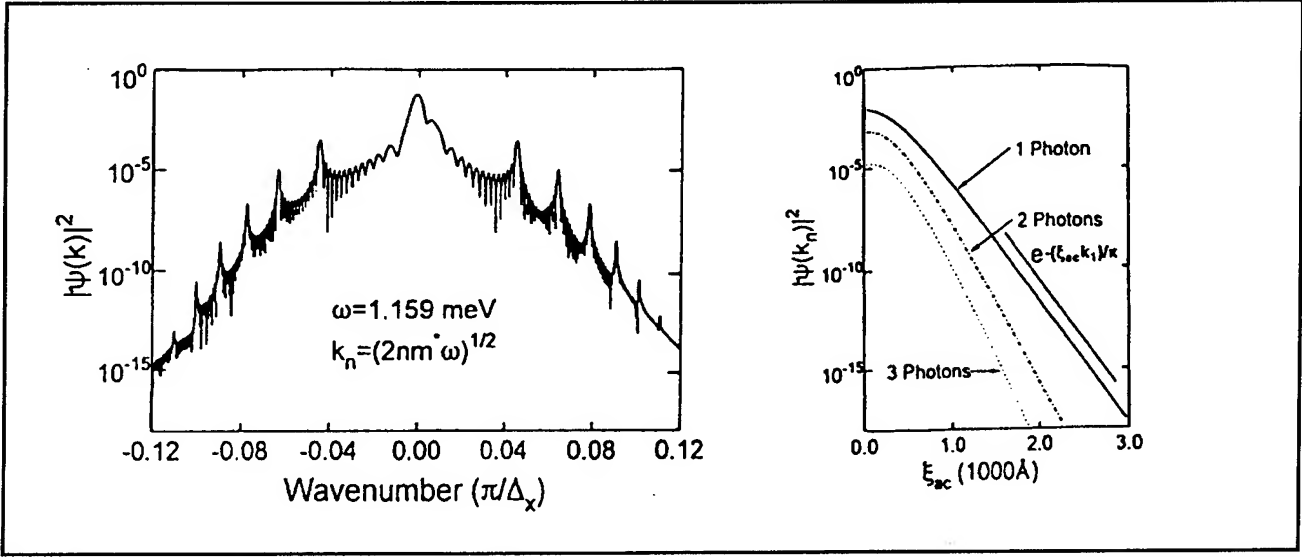


Figure 6. (left) Square of a wave function of free electrons (in k -space) under the irradiation of an ac field. The satellite peaks correspond to photon emission. (right) Values of photon-excited states as functions of the width of the ac field.

correspond to photon emissions. Figure 6b shows the amplitudes of these peaks as functions of the ac-field spatial width ξ_{ac} . Clearly, the photon-excitation process decreases exponentially as the ac-field spatial confinement loosens.

Our simulation indicates that the selection rule requires a spatially confined ac field if the photon-excited transition is between two extended electronic states, such as the case for quantum point contact devices. This can be achieved by bringing the antenna terminals very close to the central region. Photon excitation can also be achieved by using double- or multiple-barrier structures to create quasibound electronic states. The spatially localized nature of these quasibound states provide the momentum spread for the photon-assisted process. Our simulations have provided positive evidence to support this understanding.

The curve in figure 7 shows the enhanced transmission coefficient T^* (defined as $(T_{ac} - T_{dc})/T_{dc}$, where T_{ac} is the transmission coefficient with a radiation field and T_{dc} is the one without) through a double-barrier structure as a function of the width of the ac field ξ_{ac} . In great contrast to the curve in figure 6, T^* decreases algebraically with ξ_{ac} . This algebraic decrease is simply due to a decrease of the ac electric field strength in the active region between the two barriers as ξ_{ac} increases. This

result differs qualitatively from that in figure 6, in which the interaction vanishes exponentially as ξ_{ac} increases because of the selection rule.

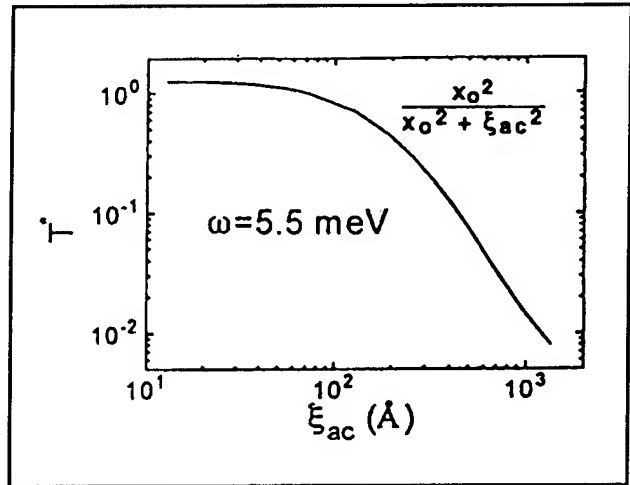


Figure 7. Radiation-enhanced transmission coefficient through an asymmetric double-barrier structure as a function of the width of an ac field ξ_{ac} . The parameters used in the simulation are: The left barrier has a height of 10.9 meV and width of 118 Å, the right barrier has a height of 12.2 meV and a width of 205 Å, the separation of the two barriers is 378 Å. The energy of the incident electrons is at the same level of the quasibound state at 9.2 meV, and the radiation frequency is 5.5 meV.

3.3.3 Photon-assisted Transport in Lateral Dual-gate Devices

Sponsors

MIT Lincoln Laboratory
Advanced Concept Program
Grant BX-5464
National Science Foundation/ MRSEC
Grant DMR 94-00334

Project Staff

Dr. Simon Verghese, Rolf A. Wyss, Dr. Thomas Schäpers, Professor Qing Hu, Arno Föster,⁵ Dr. Michael J. Rooks⁶

As our direct simulation of photon-assisted transport indicates, photon absorption requires a momentum transfer of $\Delta k \sim m^* \omega / \hbar k_i$ for an electron with a wavevector $\sim k_i$ to absorb a photon with $k \approx 0$. This momentum transfer can be achieved by either localizing (1) the photon field to within the coherence length $1/\Delta k$, or (2) the electron wavefunctions. The devices described here supply Δk mainly by localizing the electron wavefunction in one dimension that is parallel to the photon's polarization. A similar scheme has been successfully implemented in mid-infrared ($\lambda \sim 10 \mu\text{m}$) photon detectors using vertically grown quantum-well structures. These devices absorb photons when a 1D-localized electron in a bound state is excited into the continuum. In order to maintain a steady-state operation, the depleted electron in the quantum wells are supplied by thermionic electrons from the emitter over the barriers. In our case, the depleted electrons are supplied by tunneling injection from the source. Consequently, the eigenstates are quasibound states with lifetimes much greater than the modulation period of the ac field.

In figure 8b and 8c are shown the measured radiation-induced current as functions of the drain/source bias voltage V_{ds} (curves labeled by i). The two sets of curves are taken with radiation frequencies at 90 GHz (in b) and 270 GHz (in c). The radiation power level at both frequencies is approximately the same. It is very clear that the two sets of curves exhibit distinctively different features at the two radiation frequencies. The ones at 90 GHz show much sharper modulations of the radiation-induced current, while the ones at 270 GHz have

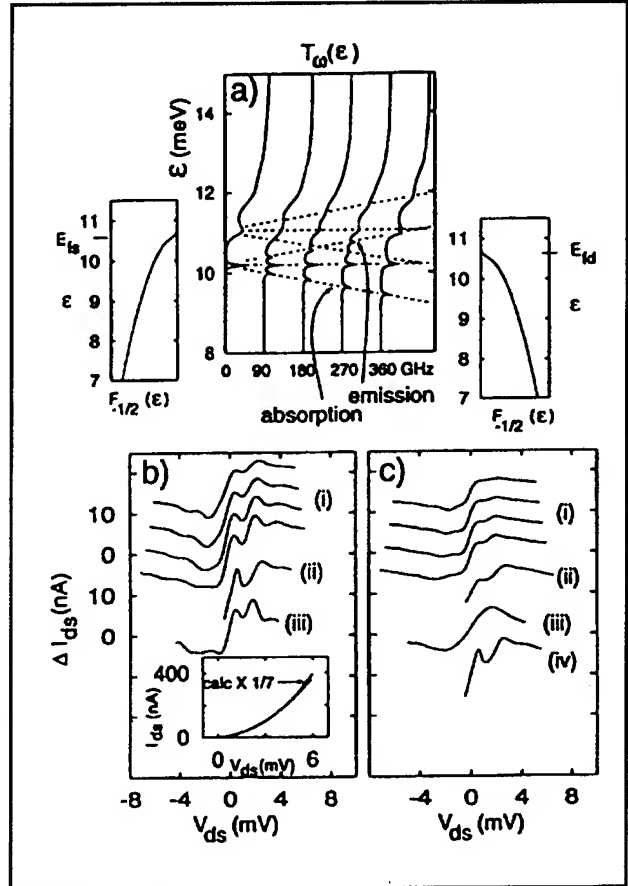


Figure 8. (a) Effective transmission coefficient that includes the effect of photon absorptions and emissions. (b) and (c) Curves (i): measured radiation-induced current at 90 GHz (b) and 270 GHz (c). Curves (ii): calculated radiation-induced current based on the model of photon-assisted transport. Curve (iv): calculated radiation-induced current based on heating model.

much smoother features. This is due to the overlap of photon subbands at this high frequency, as illustrated in figure 8a. This frequency-dependent feature is the strongest evidence that the radiation-induced current is a photonic effect that depends on the energy of an individual photon. The curves labeled (ii) in figure 8b and 8c are calculated photocurrent based on the model of photon-assisted transport. They agree with the experimental results quite well. In comparison, the calculated radiation-induced current based on a bolometric model (labeled iv) is frequency independent and cannot explain the experimental results taken at 270 GHz.

⁵ Forschungszentrum Jülich, Jülich, Germany.

⁶ Cornell National Nanofabrication Facility, Ithaca, New York.

3.3.4 Picosecond Dynamical Studies of Quantum-effect Devices

Sponsors

MIT Lincoln Laboratory
Advanced Concept Program
Grant BX-5464
National Science Foundation/MRSEC
Grant DMR 94-00334

Project Staff

Dr. Simon Verghese, Noah D. Zamdmer, Professor Qing Hu, Dr. Elliot Brown,⁷ Dr. Michael R. Melloch,⁸ Dr. Michael J. Rooks⁹

Modern solid-state physics and electrical engineering communities are witnessing a trend in which electronic devices are becoming smaller and faster. This is driven by modern society's insatiable appetite for an increased capacity of information processing and transmission. In this project, we use ultrafast probes to study the dynamics of ultrasmall devices.

We are pursuing two types of measurements. The first one involves a far-infrared spectrometer pumped by a mode-locked Ti:Sapphire laser which we recently constructed, as shown in figure 9. In this set up, two antenna-coupled Auston switches are pumped by a Ti:Al₂O₃ pulsed laser. The THz electrical pulses are launched into free space and then combined by a beam splitter. The combined beam is a superposition of two coherent subpicosecond electrical pulses whose relative time delay can be varied. These combined pulses will then be focused onto an antenna-coupled quantum device to generate a dc electrical current in the device through the photon-assisted transport/tunneling process. Effectively, the generated electrical current is proportional to the time autocorrelation function of the whole system, whose Fourier transform will give the frequency response of the system. We have constructed such a spectrometer and reported its THz performance in a previous report.

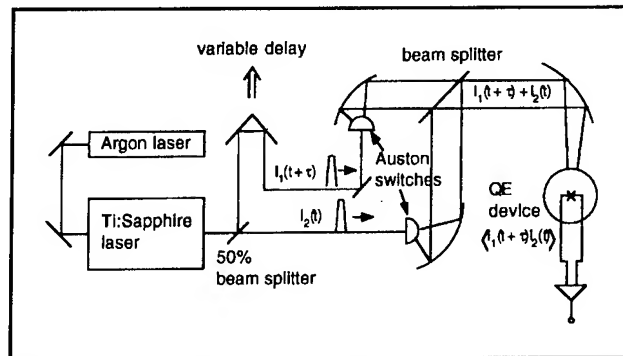


Figure 9. Schematic of an interferometer pumped by a pulsed Ti:Sapphire laser.

The second type of experiment involves a pump-and-probe method by integrating two Auston switches *monolithically* with the quantum-effect devices, as shown in figure 10. One switch will be used to apply a short electric pulse on the input, and the second one will be used to probe the output electrical current in a time-resolved fashion. This scheme differs from the first one in that the pump and probe beams are focused on *different* spots. In this way, we can measure the time scale of the transport process from the input to the output, as well as the spectroscopic information of the system. In order to achieve a high speed from the Auston switches, lattice-matched low-temperature-grown (LTG) GaAs materials will be used which have subpicosecond recombination time.

We have constructed a cryogenic system in which subpicosecond optical pulses are brought into the cryogenic stage through single-mode optical fibers. The schematic of this system, along with the measurement results, is shown in figure 11. The measurement shows the THz electrical pulse after propagating along a 2-mm long coplanar transmission line. Clearly, the signal-to-noise ratio improves as the temperature is lowered from the room temperature to 4.2 K. Also, the pulse width is reduced due to a lower loss of the transmission line at cryogenic temperatures. The time resolution of the current system is about five picosecond, which is mainly limited by the dispersion of the optical fibers. By using shorter fibers and longer optical pulses (picosecond instead of femtosecond) to minimize dispersion broadening, we are confident to be able to improve the time resolution to approximately one picosecond.

⁷ MIT Lincoln Laboratory, Lexington, Massachusetts.

⁸ Purdue University, West LaFayette, Indiana.

⁹ Cornell National Nanofabrication Facility, Ithaca, New York.

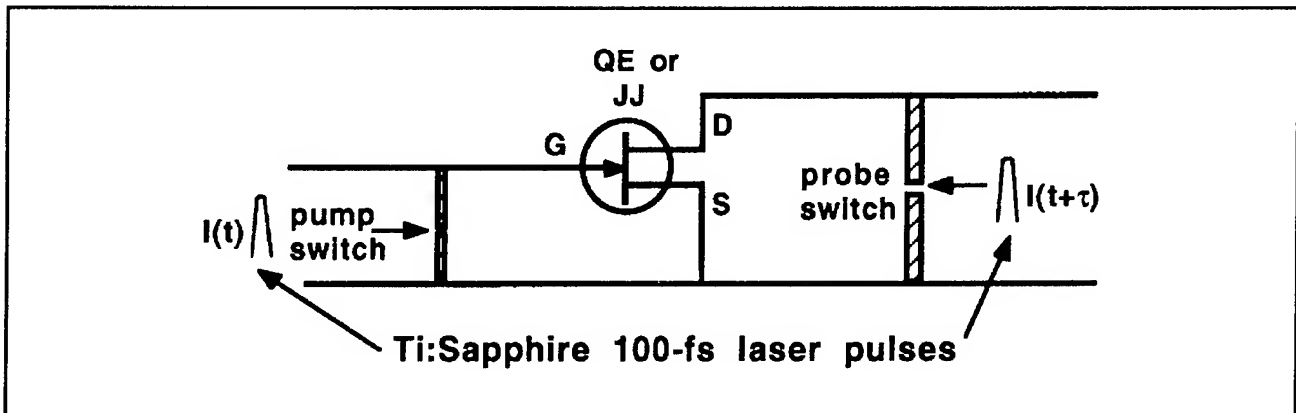


Figure 10. Schematic of a three-terminal (QE or Josephson) device pumped by a subpicosecond electrical pulse at the input, and the induced output current can be time-resolved by another time-delayed probe beam.

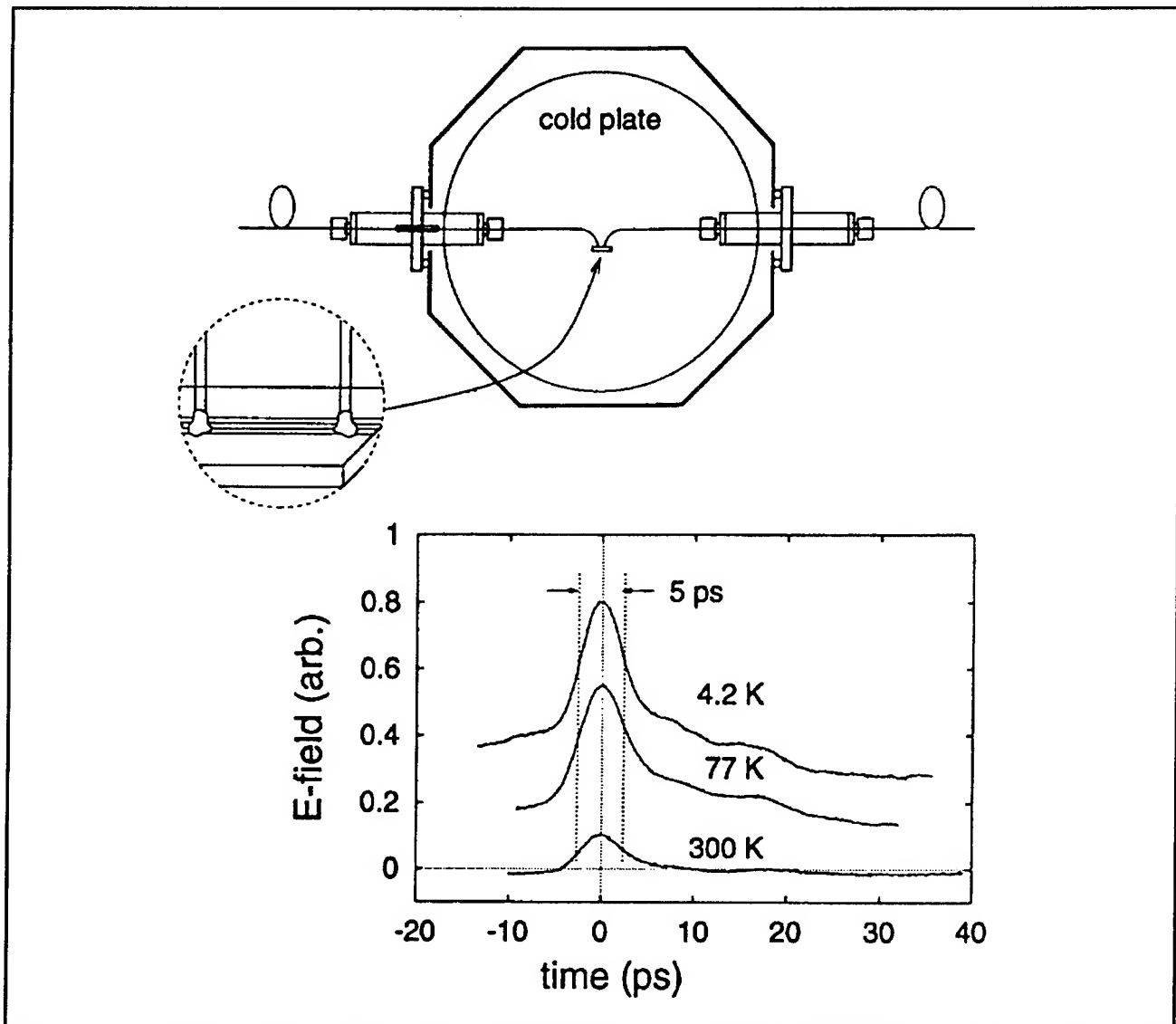


Figure 11. Top: Schematic of a fiber-coupled cryostat. Bottom: Time-resolved measurement of electrical pulses propagating through a 2-mm long coplanar transmission line.

3.3.5 Optical Correlators Using Low-temperature-grown GaAs (LTG) Photoconductors

During our investigation of picosecond time-resolved transport studies, we made an interesting discovery that may have potential applications in laser diagnostics and ranging. Since useful information is often contained in modulations of the intensity envelope of optical pulses, it is an important experimental task to measure the intensity-intensity autocorrelation function of the pulses $\langle I(t)I(t+\tau) \rangle$. Traditionally, this is done by using a nonlinear crystal to double the frequency and then measure the autocorrelation function of the second harmonic. We have discovered that a photoconductor connected to a transmission line has a nonlinear response to the optical signal simply due to a voltage dividing between the photoconductor and the characteristic impedance Z_0 of the transmission line. This nonlinear response can be utilized to measure the second order correlation function $\langle I(t)I(t+\tau) \rangle$. This concept is illustrated in figure 12a. Figure 12b shows the second-order nonlinear responsivity $S_i^{(2)}$ as a function of the incident power $I(t)$. For the best contrast ratio, the incident power should be in the range that the photoconductance

is comparable to $1/Z_0$. This corresponds to a power level of 0.01 mW, which is much lower than that required for conventional autocorrelators (typically $\gg 1$ mW). Since the LTG correlator does not require the use of a nonlinear crystal and all the components for phase matching, it is very compact, low cost, and sensitive. Figure 12c shows the measured results of fiber-broadened optical pulses (which preserve the spectral bandwidth). As the length of the fiber is increased, the pulse width increases noticeably as measured using our LTG correlator.

3.4 Intersubband Transitions in Coupled Multiple Quantum-well (MQW) Structures

Coupled MQWs are simply voltage tunable two-level or multilevel systems. Therefore, under specific bias conditions for carefully designed and fabricated MQWs, the devices can generate far-infrared radiation (when the initial state is higher than the final state), or detect far-infrared radiation (when the initial state is lower than the final state); or perform nonlinear optical functions such as parametric amplifications.

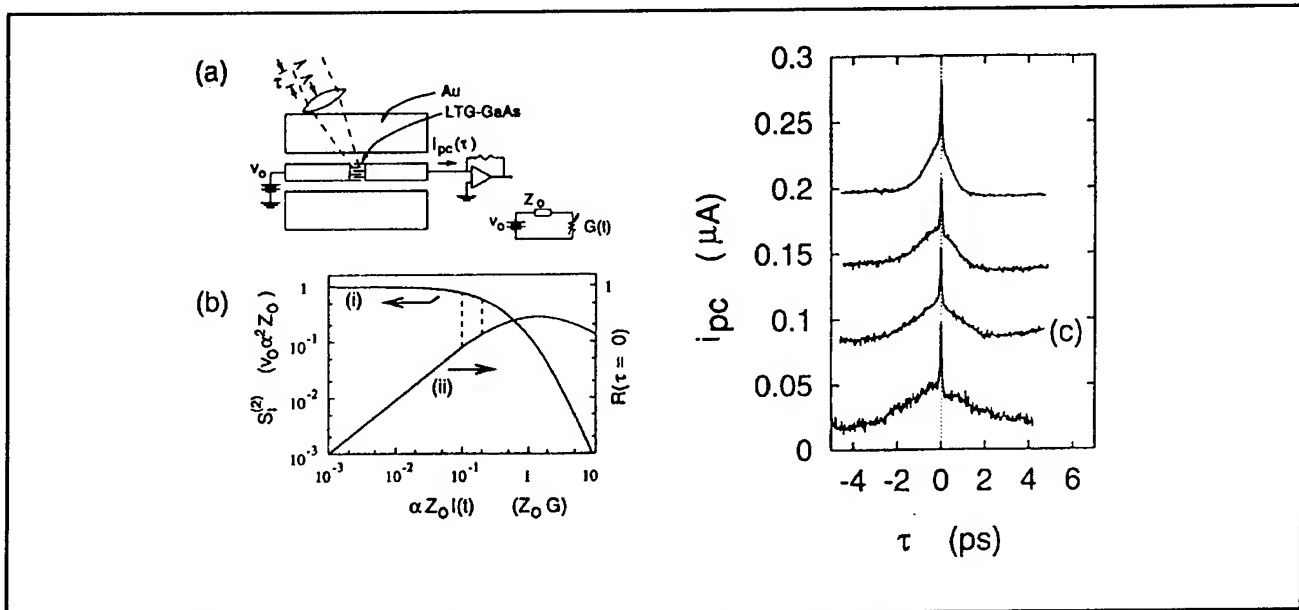


Figure 12. (a) Schematic diagram of the LTG-GaAs photoconductor embedded in a co-planar transmission line. The equivalent circuit models the high-frequency response of the LTG correlator to an intensity pulse $I(t)$. (b) (i) Calculation of the second-order nonlinear current responsivity plotted in dimensionless units versus the normalized intensity $\alpha Z_0 I(t)$. (ii) Calculation of the contrast ratio plotted versus $\alpha Z_0 I(t)$. The shaded region indicates the optimum range of operation for the LTG correlator. (c) Output signal of the LTG correlator versus time delay τ for two optical pulses that were dispersed by propagating through 30, 50, 70, and 9 cm of fiber.

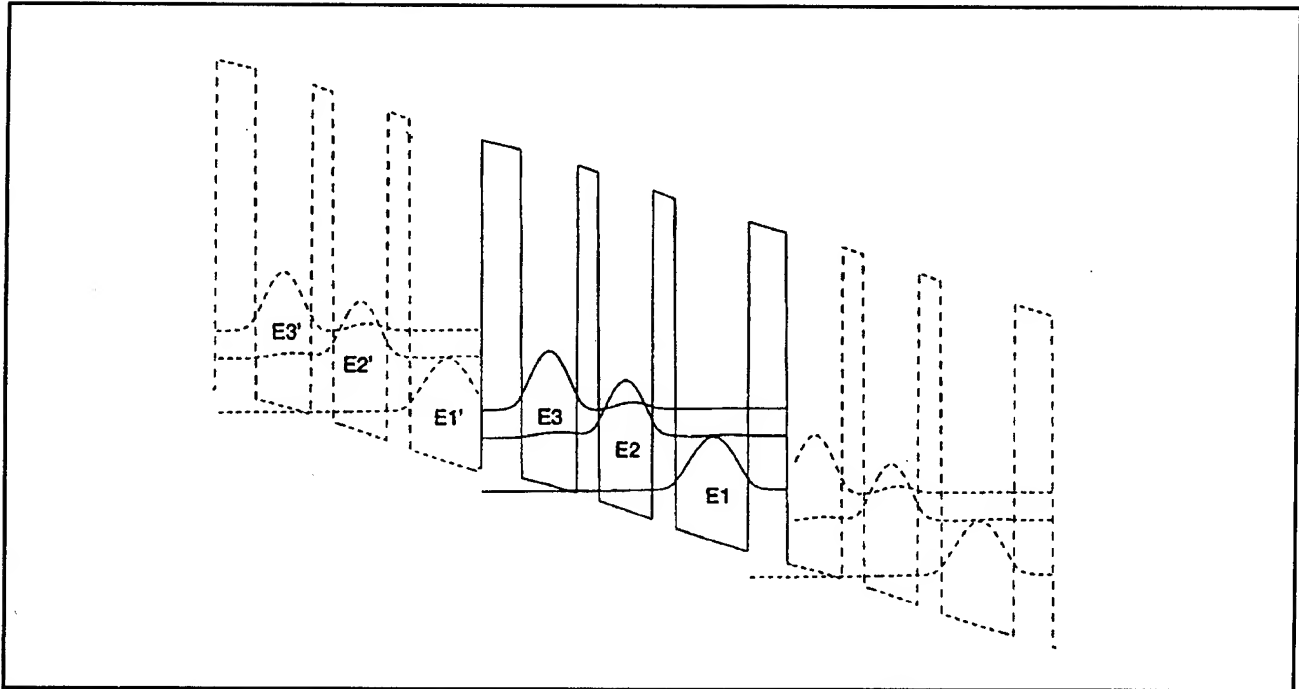


Figure 13. Conduction band profile and the square of wavefunctions for a MQW structure under the bias condition that the intersubband transition from E_3 to E_2 will generate radiation at 5 THz.

3.4.1 Far-infrared Lasers and Detectors Using MQW Structures

Sponsor

U.S. Army Research Office
Grant DAAH04-95-1-0610

Project Staff

Bin Xu, Professor Qing Hu, Dr. Michael R. Melloch¹⁰

The schematic of a single MQW module (sketched with solid lines) is shown in figure 13. The conduction band profile, subband structures, and carrier densities are calculated self-consistently from Schrödinger and Poisson equations, after typical five iterations. The lasing transition takes place between the subbands E_3 and E_2 . The energy difference for this particular structure is designed to be 20 meV, which corresponds to 5 THz radiation frequency. The third quantum well on the collector side is used to improve injection efficiency by preventing electrons in E_3 to propagate to the collector. The energy difference between E_2 and E_1 is designed to be 36 meV, which is the LO phonon energy. Thus, the fast LO-phonon emission process

will keep the E_2 level empty, maintaining an inverted population between E_3 and E_2 . Our detailed calculation yields the following time scales for various relaxation processes: $\tau_{32} \sim 17$ ps (mainly due to electron-electron scattering), $\tau_{21} = 2.8$ ps (due to LO-phonon emission), and $\tau_{31} = 38$ ps (due to LO-phonon emission). These relaxation rates will easily produce an inverted population with an injection efficiency greater than 50 percent.

The most important parameter that determines the radiation properties (due to the 3→2 intersubband transition) of this MQW structure is the dipole moment $\langle 3|z|2 \rangle$, or equivalently, the oscillator strength f_{32} , which is the ratio of the quantum mechanical radiative decay rate over that of a classical Hertzian dipole at the same frequency. We have chosen the barrier thickness that yields an oscillator strength of 0.25. This choice is made with a trade-off between a high oscillator strength and an acceptable rate of electron-electron scattering. With this design and by using 100 identical MQW modules (other modules are shown with the dashed lines in figure 13), the threshold carrier density will be approximately $3 \times 10^{10}/\text{cm}^2$. Consequently, lasing threshold can be reached at $e\Delta n/\tau_{32} \sim 1$ kA/cm² current density, which is quite feasible.

¹⁰ Purdue University, West Lafayette, Indiana.

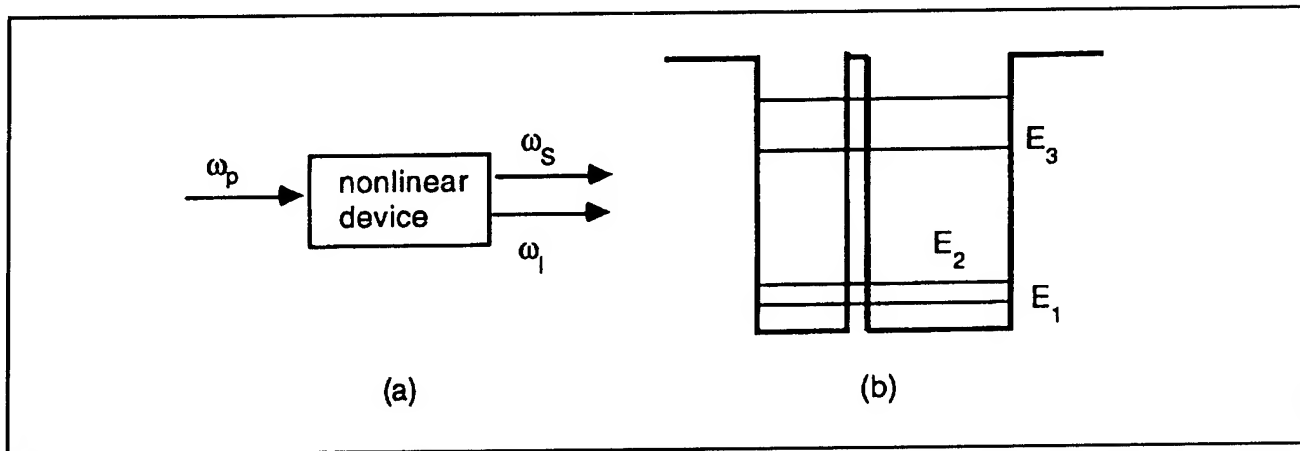


Figure 14. (a) Illustration of parametric amplification process, which converts a photon with a frequency ω_p into two photons with frequencies ω_l and ω_s , with $\omega_l + \omega_s = \omega_p$. (b) An asymmetric DQW structure that could produce a large $\chi^{(2)}$ at mid- and far-infrared frequencies.

3.4.2 Far-Infrared Optical Parametric Amplifiers Using MQWs

Sponsors

Hertz Foundation Fellowship
U.S. Army - Office of Scientific Research
Grant DAAH04-94-G-0167

Project Staff

Ilya Lyubomirsky, Professor Qing Hu, Dr. Ben Streetman¹¹

It is well known in the field of nonlinear optics that the nonlinear susceptibility $\chi^{(2)}$ is large near a resonant frequency for a system that is lack of inversion symmetry. Such a large $\chi^{(2)}$ has been widely used in second harmonic generation, second frequency generation, and parametric frequency down conversion at optical and near-infrared frequencies, where coherent sources at pump frequencies are readily available. As far as its optical properties are concerned, a quantum-well device acts like a giant atom, whose resonant frequencies are in the mid- to far-infrared frequencies. Naturally, if we design a QW structure so that it has resonances at mid-infrared frequency ($\lambda \sim 10$ microns) and far-infrared frequencies, we can use easily available CO₂ lasers as a pump source to parametrically generate far-infrared radiations. This nonlinear photon conversion process is illustrated in figure 14a.

However, a single quantum well has inversion symmetry, and therefore has a vanishing $\chi^{(2)}$. This

problem can be solved easily by using a coupled DQW structure with asymmetric well widths, as shown in figure 14b. In this structure, the energy difference between levels 3 and level 1 is close to 120 meV (corresponding to a wavelength of 10 microns). This intersubband transition energy corresponds to the pump frequency. The energy difference between level 3 and 2 is approximately 20 meV, corresponding to the far-infrared signal frequency. The nonlinear susceptibility $\chi^{(2)}$ is proportional to the product of three dipole moments, $\langle Z_{12} \rangle \langle Z_{13} \rangle \langle Z_{23} \rangle$. By careful design, each dipole moment can be as large as several 10Å, which is at least one order of magnitude larger than that at optical frequencies for atomic systems. Using the doubly resonant structure shown in figure 14b, we estimate $\chi^{(2)}$ to be as large as 10^{-6} m/V, which is four orders of magnitude greater than the value for bulk GaAs materials. This extraordinarily large $\chi^{(2)}$ can be used for efficient parametric amplifications. The challenging issue of phase-matching can be solved by using Stark effect (changing the resonant conditions by applying a bias voltage) to control $\chi^{(2)}$ in selected regions to set up a periodic $\chi^{(2)}$, as shown in figure 15. In this structure, V_1 is tuned to be on resonance while V_2 , off resonance. The length under the electrodes V_1 and V_2 are approximately one coherence length. This periodic nonlinear structure will provide conditions for quasi-phase-matching, thus approximately half of the total length will contribute to the parametric down conversion process.

¹¹ University of Texas, Austin, Texas.

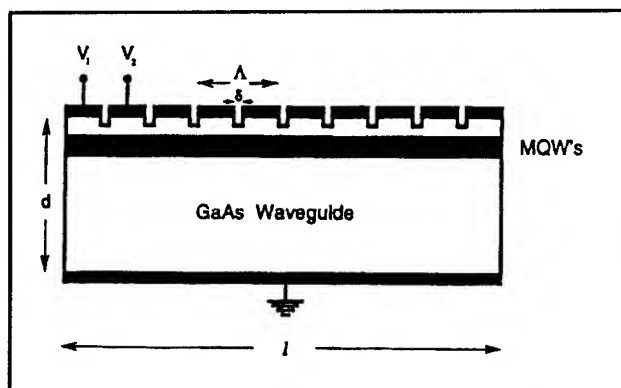


Figure 15. Periodic waveguide structure for quasi phase matching of the OPO.

3.5 Millimeter-wave, THz, and Subpicosecond Facilities

Professor Hu's laboratory is equipped with various millimeter-wave and infrared sources which can generate coherent and incoherent radiation from 75 GHz up to 30 THz. These include: Gunn oscillators at W-band frequencies (75-110 GHz); a frequency doubler, tripler, and quadrupler using Schottky diodes at 200, 300, and 400 GHz; an optically pumped far-infrared laser which generates coherent radiation from 245 GHz to 8 THz; and an infrared Fourier transform spectrometer which is capable in performing linear spectroscopy from 45 GHz to 30 THz and beyond. This laboratory is also equipped with various cryogenic millimeter-wave and infrared detectors. These include: Si composite bolometers, InSb hot-electron bolometers, superconductor-insulator-superconductor (SIS) receivers, and room-temperature microbolometers. Recently, with support from AT&T, a mode-locked Ti:sapphire laser that can generate optical pulses as short as 70 femtosecond was purchased and installed.

3.6 Publications

3.6.1 Journal Articles

de Lange, G., B.R. Jacobson, and Q. Hu. "A Low-noise Micromachined Millimeter-wave Heterodyne Mixer with Nb Superconducting Tunnel Junctions." *Appl. Phys. Lett.* Forthcoming.

de Lange, G., B.R. Jacobson, and Q. Hu. "Micromachined Millimeter-wave SIS Mixers." *IEEE Trans. Appl. Supercond.* 5: 1087 (1995).

Hu, Q., S. Verghese, R.A. Wyss, T. Schäpers, J. del Alamo, S. Feng, K. Yakubo, M.J. Rooks, M.R. Melloch, and A. Förster. "High-frequency (f

~ 1 THz) Studies of Quantum-effect Devices." Submitted to *Semicond. Sci. and Tech.*

Lyubomirsky, I., and Q. Hu. "Optical Parametric Oscillators Without Phasematching." Submitted to *Opt. Lett.*

Rahman, A., G. de Lange, and Q. Hu. "Micromachined Room-temperature Microbolometers for Millimeter-wave Detection." *Appl. Phys. Lett.* Forthcoming.

Smet, J.H., C.G. Fonstad, and Q. Hu. "Intrawell and Interwell Intersubband Transitions in Multiple Quantum Wells." Submitted to *J. Appl. Phys.*

Verghese, S., R.A. Wyss, T. Schäpers, A. Förster, M.J. Rooks, and Q. Hu. "Photon-assisted Transport Through Quantized Energy States in a Lateral Dual-gate Device." *Phys. Rev. B* 52: 14834 (1995).

Verghese, S., N. Zamdmer, E.R. Brown, A. Foerster, and Q. Hu. "An Optical Correlator using a Low-temperature-grown GaAs Photoconductor." Submitted to *Appl. Phys. Lett.*

Wyss, R.A., C.C. Eugster, J.A. del Alamo, Q. Hu, M.J. Rooks, and M.R. Melloch. "Far-infrared Radiation-induced Thermopower in a Quantum Point Contact." *Appl. Phys. Lett.* 66: 1144 (1995).

Yakubo, K., S. Feng, and Q. Hu. "Direct Simulation of Photon-assisted Quantum Transport." Submitted to *Phys. Rev. B.*

3.6.2 Conference Presentations

de Lange, G., B.R. Jacobson, and Q. Hu. "A Low-noise Micromachined Millimeter-wave Heterodyne Mixer with Nb Superconducting Tunnel Junctions." Paper published in the *Proceedings of the European Space Agency (ESA) Workshop on Millimeter Waves Technology and Applications*, Noordwijk, the Netherlands, December 1995, p. 231.

de Lange, G., B.R. Jacobson, A. Rahman, and Q. Hu. "Micromachined Millimeter-wave SIS Mixers." Paper published in the *Proceedings of the Sixth International THz Conference*, Pasadena, March 1995, p.372.

del Alamo, J.A., C.C. Eugster, Q. Hu, M.R. Melloch, and M.J. Rooks. "Electron Waveguide Devices." Invited paper published in the *Proceedings of the Eighth International Conference on*

Superlattices, Microstructures and Microdevices (ICSMM-8), Cincinnati, Ohio, August 1995. Forthcoming.

Hu, Q. "FIR Studies of Mesoscopic Devices." Invited paper presented at the *First Frontiers In Electronic Low-Dimensional Systems (FIELDS) Workshop on High Frequency Experiments on Low-Dimensional Systems*, Weizmann Institute of Science, Israel, November 1995.

Hu, Q. "High-frequency ($f \sim$ THz) Studies of Quantum-effect Devices." Invited paper presented at *NATO Advanced Research Workshop on Future Trends in Microelectronics*, Ile de Bendor, France, July 1995.

Hu, Q., J. Smet, B. Xu, and I. Lyubomirsky. "Far-infrared (THz) Lasers and Parametric Oscillators Using Coupled Double Quantum-well Structures." Invited paper presented at the *International Conference on Intersubband Transitions in Quantum Wells: Physics and Applications*, Kibbutz Ginosar, Israel, October 1995.

Hu, Q., S. Verghese, R.A. Wyss, Schäpers, J. del Alamo, S. Feng, K. Yakubo, M.J. Rooks, M.R. Melloch, and A. Förster. "High-frequency ($f \sim 1$ THz) Studies of Quantum-effect Devices." Invited paper published in the *Proceedings of the International Semiconductor Device Research Symposium*, Charlottesville, Virginia, December 1995, p. 337.

Lyubomirsky, I., B. Xu, and Q. Hu. "THz Parametric Oscillators Using Coupled Double Quantum

Wells." Paper published in the *Proceedings of the International Semiconductor Device Research Symposium*, Charlottesville, Virginia, December 1995, p. 623.

Rahman, A., G. de Lange, and Q. Hu. "Micro-machined Room-temperature Microbolometers for Millimeter-wave Detection." Paper published in the *Proceedings of the International Semiconductor Device Research Symposium*, Charlottesville, Virginia, December 1995, p. 463.

Verghese, S., N. Zamdmer, E.R. Brown, A. Förster, and Q. Hu. "Correlation of Optical Pulses with a Low-Temperature-Grown GaAs Photoconductor." Paper published in the *Proceedings of the International Semiconductor Device Research Symposium*, Charlottesville, Virginia, December 1995, p. 433.

3.6.3 Patents

Verghese, S., E.R. Brown, and Q. Hu. "Low Temperature-Grown GaAs Correlator (LTGGC)." Filed for patent application, October 1995.

3.6.4 Thesis

Wyss, R.A. *Far-infrared Radiation Response of Antenna-coupled Quantum-effect Devices*. Ph.D. diss. Dept. of Elect. Eng. and Comput. Sci., MIT, 1995.

Section 4 Surfaces and Interfaces

Chapter 1 Synchrotron X-Ray Studies of Surface Disordering

Chapter 2 Semiconductor Surface Studies

Chapter 3 Step Structures and Epitaxy on Semiconductor
Surfaces

Chapter 1. Synchrotron X-ray Studies of Surface Disordering

Academic and Research Staff

Professor Robert J. Birgeneau, Dr. Barry Wells

Graduate Students

Monte J. Ramstad, Michael J. Young

Technical and Support Staff

Debra L. Martin

1.1 Introduction

Sponsor

Joint Services Electronics Program
Grant DAAH04-95-1-0038

In this research program, we use modern x-ray scattering techniques to study structures and phase transitions in thin films and on surfaces. We have two principal experimental facilities, one at MIT and the other at the National Synchrotron Light Source at Brookhaven National Laboratory. At MIT, we have four high-resolution, computer-controlled x-ray spectrometers. The angular resolution can be made as fine as 1.8 seconds of arc, which enables us to probe the development of order from distances of the order of the x-ray wavelength, 1 Å, up to 30,000 Å. The sample temperature can be varied between 2 K and 500 K, with a relative accuracy of 2×10^{-3} K. At the National Synchrotron Light Source, in collaboration with IBM, we have three fully instrumented beam lines. Two of these beam lines allow us to make studies with photons varying in energy between 3 and 12 keV; the third has a fixed energy of 17 keV.

We are currently designing an undulator-based beam line which will be implemented at the Advanced Photon Source at Argonne National Laboratory. This facility will make possible a new generation of x-ray experiments with unprecedented precision. In collaboration with Professor Simon G.J. Mochrie, we have designed, built, and commissioned a second-generation x-ray surface facility which is extremely versatile, allowing a wide range of surface scattering experiments.

Our basic scientific objective is to understand the morphologies and microscopic structures of simple semiconductor and metal surfaces at high temperatures. Possible phase changes include surface roughening, surface reconstruction, melting, amorphization, and dilution.

Semiconductor surfaces exhibit rich structural and morphological behavior in both equilibrium and non-equilibrium steady-state conditions. Equilibrium structures and phase transitions of high-symmetry facets are often closely related to important models in two-dimensional statistical mechanics. The physics of stepped (vicinal) surfaces, even in equilibrium, is subtle and poorly understood. For example, stepped surfaces should always be rough because of the freedom of the steps to wander. Step structures and spacing should be profoundly affected by any nearby high-symmetry surface reconstruction. Their association bears on issues of faceting and equilibrium crystal shapes. The steps themselves may exhibit phase transitions that involve dislocations and/or bunching in the step lattice as well as step-height changes. Changes in the morphology, especially those involving vacancy aggregates, should be strongly affected by nearby steps.

Semiconductor surface physics involves fundamental issues in statistical mechanics that are important to a broad spectrum of other problems. Furthermore, elucidating the factors that control the morphology and perfection of vicinal semiconductor surfaces can be expected to lead to improved electronic device processing and ultimately improve semiconductor device performance and lifetime.

1.2 Stability of Vicinal Si(111) Surfaces Under Sublimation and Electromigration

The morphological instabilities of vicinal Si(111), caused by a DC electric current and a 7×7 reconstruction, have been studied using a variety of diffraction and imaging techniques. The current induced instabilities, which occur at sublimation temperatures or under conditions of step-flow, produce morphological features on length scales appropriate for optical studies, 5 to 50 μ . Optical microscopy, a laser diffraction technique atomic force microscopy (AFM) and high resolution x-ray

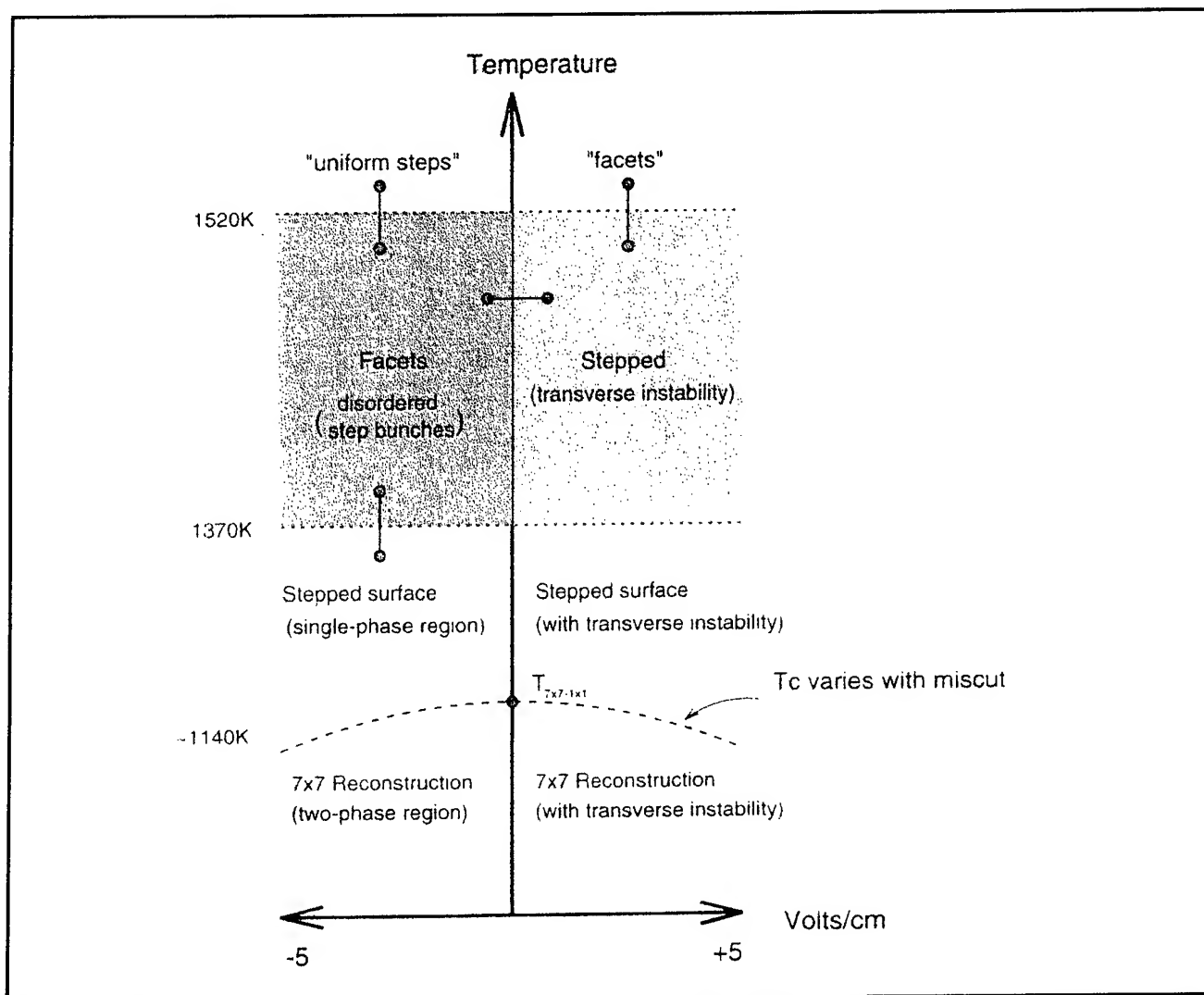


Figure 1. Stepped regions refer to single height (bilayer) steps. Bars indicate reversible transitions studied in experiment. At fixed current, the voltage is not a controllable parameter in our experiment.

diffraction have been applied to these surfaces. In addition to the step bunching instabilities reported by others, these techniques reveal a transverse instability in the step profiles for current flowing in the step-down direction at all temperatures between 700°C and 1300°C (see figure 1). For the same current direction, the step bunching instability is observed below $1025^{\circ}\pm 15^{\circ}\text{C}$ and above $1230^{\circ}\pm 15^{\circ}\text{C}$ up to at least 1300°C . On the other hand, for current flowing in the step-up direction, the step profiles are stabilized and the step bunching instability is observed between $1025^{\circ}\pm 15^{\circ}$ and $1230^{\circ}\pm 15^{\circ}$. Stoyanov's theory of the current driven step-bunching instabilities has been extended to explain the step wandering instabilities by modifying the boundary conditions of a diffusion equation at the step edges. Measurements of the rate of growth of the transverse instability indicate an activation energy of $2.7 \pm 0.1\text{eV}$. Near the 7×7 reconstruction temperature,

$T_c = 870^{\circ}\text{C}$, a faceting transition occurs. We have investigated the time and temperature dependence of the spinodal decomposition of step bands and the approach to the equilibrium crystal shape. The equilibrium shape profile exhibits critical behavior $z \sim x^{\alpha}$ where $\lambda = \alpha/(\alpha - 1) = 3.0 \pm 0.1$ which is consistent with a Pokrovsky-Talapov transition.

Studies of the step behavior on vicinal Si(111) have also been conducted on surfaces misoriented by 4 and 8° toward (1,1,-2). An investigation of the effect of current reversal on the dynamics of step bunching and debunching was completed at 1376 K, 1420 K, and 1470 K for the 8° sample, and at 1418 K for the 4° sample. The phase diagram (figure 1) shows the relevant temperature regions. The dashed line around 1140 K simply represents the orientational dependence of the reconstruction driven faceting transition. The applied voltage is

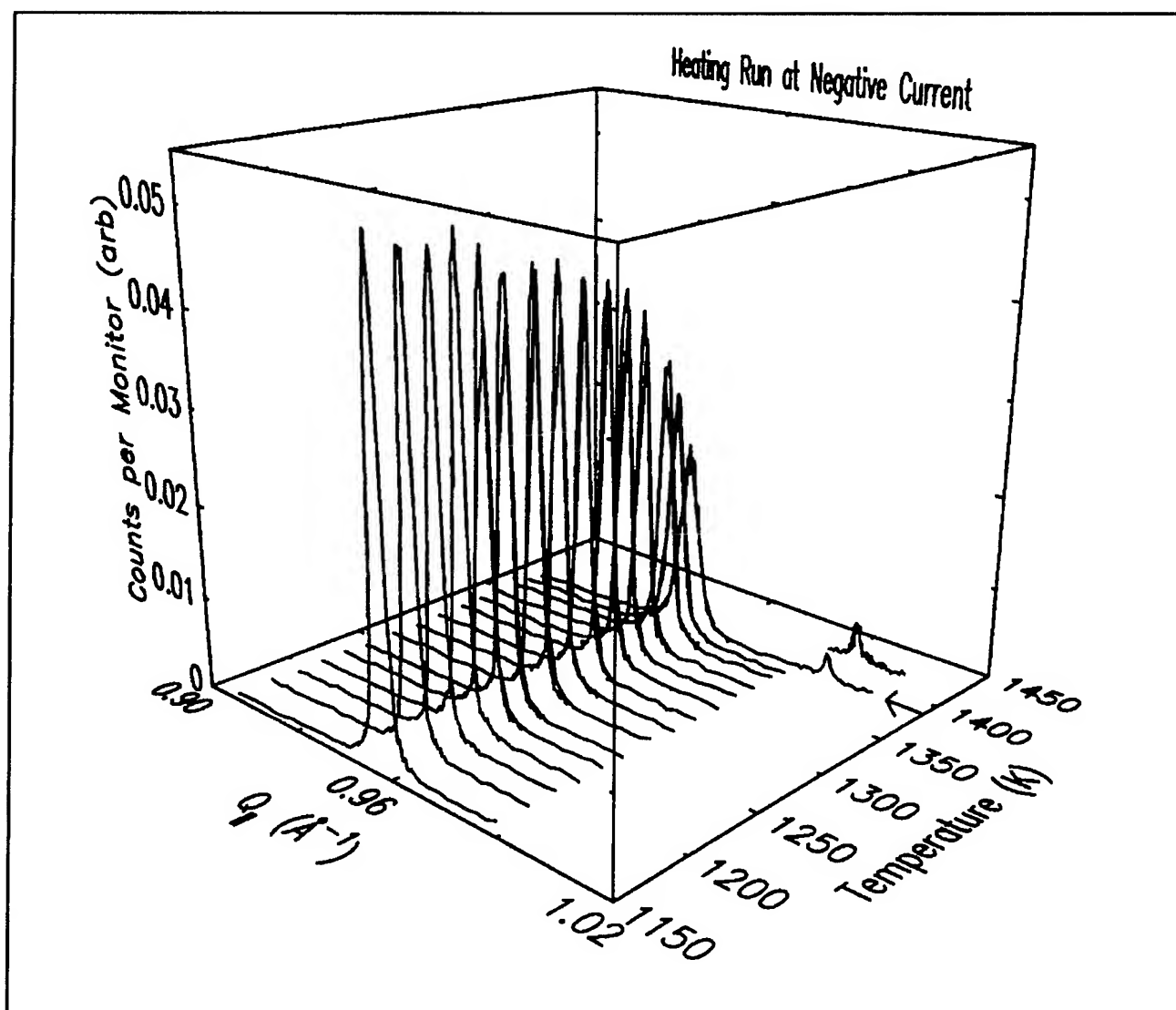


Figure 2. Temperature dependence of the step peak at negative current above the 7×7 reconstruction. Note coexistence of the (1,0) peak and the step peak at 1376 K (indicated by arrow).

not an independently controllable parameter in this phase diagram. Between 1370 K and about 1470 K, the time evolution was slow enough to permit independent measurements of the q -dependence of the scattering at the integer order facet peak (1,0) and at the step peak without significant distortion in the scattering profiles over periods ranging up to 200 minutes. The surface morphologies at these temperatures were essentially completely reversible, except after very long times at fixed current direction where either faceting or transverse step wandering could become saturated. Thus, a determination of the time dependence of the step correlation lengths, facet size, and integrated intensities was made for these temperatures over a substantial time range. The lower bound step-facet transition at ~ 1370 K was also studied on heating from the single phase stepped region at negative current

(see figure 2). In addition, a series of studies showing the time-dependence of the (1,0) peak were made on the 8° sample after quenching from above 1520 K (an unfaceted surface) to 1406 K and 1376 K at negative current showing a continual development of the morphology over periods of up to 150 minutes. In some cases facets as large as $0.7 \times 2.5 \mu^2$ were observed.

The scattering in the vicinity of the order-disorder transition at approximately 1520 K (see figure 1) was also examined for current both parallel and anti-parallel to (1,1,-2), i.e., positive and negative current, respectively. This transition temperature was found to be independent of miscut for both current directions to within the experimental error. True "step-ordering" above 1520 K at negative current was not observed at both current directions

for both the (1,0) peak and the step peak. Ex-situ optical microscopy revealed that large facets developed on samples quenched from above 1520 K at positive current and indicated a transverse instability consistent with that previously seen in other experiments on smaller miscut samples.

1.3 Monolayer Melting

We have investigated the melting transition of near-monolayer xenon at three temperatures: 121 K, 140 K and 145 K. Xenon on graphite is widely regarded as a model system for the investigation of two-dimensional melting in the presence of a weak orientational field. It may represent an example in which melting occurs continuously through the unbinding of topological defects in a way analogous to the Kosterlitz-Thouless transition in superfluids. Recent electron diffraction studies are consistent with a two-stage melting process in this system with an intermediate aligned liquid or hexatic phase between the solid and quasi-isotropic liquid phases. We have carried out isothermal high-resolution

synchrotron x-ray diffraction measurements of the transition from a finite-size limited 2D solid to a well correlated (~ 100 Å) orientationally ordered 2D liquid. Our investigation confirms that at 140 K and 145 K there is continuous evolution of the length scale of the positional fluctuations up to approximately 1000 Å. At 121 K, despite no discernable evolution of the correlation length, the transition is found to be no sharper in reduced units than at the higher temperatures. The exponent characterizing the decay of the order parameter corresponding to a finite-sized 2D crystal is found to be consistent with values reported for finite-sized two-dimensional magnets undergoing Kosterlitz-Thouless-like (2D-XY) continuous transitions.

1.4 Publication

Nuttall, W.J., D.Y. Noh, B.O. Wells, and R.J. Birgeneau. "Isothermal Melting of Near-monolayer Xenon on Single Crystal Graphite at 140K. *J. Phys. Condens. Matter* 7: 4337 (1995).

Chapter 2. Semiconductor Surface Studies

Academic and Research Staff

Professor John D. Joannopoulos, Dr. Kyeongjae Cho, Dr. Pierre Villeneuve

Graduate Students

Rodrigo B. Capaz, Shanhui Fan, Ickjin Park

Technical and Support Staff

Margaret O'Meara

2.1 Introduction

Sponsor

Joint Services Electronics Program
Grant DAAH04-95-1-0038

Understanding the properties of surfaces of solids and the interactions of atoms and molecules with surfaces is extremely important both from the technological and academic points of view. The advent of ultrahigh vacuum technology has made microscopic studies of well-characterized surface systems possible. The way atoms move to reduce the energy of the surface, the number of layers of atoms involved in this reduction, the electronic and vibrational states that result from this movement, and the final symmetry of the surface layer are all of utmost importance in arriving at a fundamental and microscopic understanding of the nature of clean surfaces, chemisorption processes, and the initial stages of interface formation.

The theoretical problems associated with these systems are quite complex. However, we are currently at the forefront of solving the properties of real surface systems. In particular, we are continuing our efforts to develop new techniques for calculating the total ground-state energy of a surface system from "first principles," so that we can provide accurate theoretical predictions of surface geometries and behavior. Our efforts in this program have concentrated on the areas of surface growth, surface reconstruction geometries, structural phase transitions, and chemisorption.

2.2 Mechanical Hysteresis on an Atomic Scale

Hysteresis is generally associated with two (or more) different pathways connecting two macroscopic equilibrium states. A classic example is a ferromagnetic system of spins in a uniform external magnetic field, where one can cycle repeatedly between two equilibrium points by varying the magnetic field. This is a macroscopic collective phenomenon. One can also envision a *microscopic* hysteresis phenomenon if it were possible to construct a *local* magnetic field that couples to only one spin of the system. Since a microscopic hysteresis involves a single spin, even a pure antiferromagnet, which exhibits no macroscopic hysteresis, could exhibit a microscopic hysteresis.

However, it has not been proved possible to generate a magnetic field which couples to only one spin of the system, and consequently this novel phenomenon of microscopic hysteresis has not been observed. There are, on the other hand, systems which are not magnetic but nevertheless belong to the same universality class as magnetic systems for which observation of a microscopic hysteresis may be possible. One particularly interesting example is the (100) surface of silicon which can be mapped onto a two-dimensional antiferromagnetic spin system. Such a mapping has been used to study the phase transition of the Si (100) surface in which each asymmetric surface dimer is associated with a single spin degree of freedom. What is interesting about this system is that if one were now to bring a sharp tip near the surface, as in atomic force microscopy, the force field between the tip and surface dimers would act like a local external magnetic field for the corresponding magnetic system.

To investigate the possible existence of a microscopic hysteresis effect in Si (100), we performed *ab initio* total energy calculations which describe the surface system in the presence of a tungsten tip

typically used in AFM experiments. The coupling strength and sign of the force between the AFM tip and a surface dimer is controlled by moving the tip up and down. The response of the dimer to the change of the external field is monitored by studying the changes in geometric structure and energy of the dimer configuration as a function of the tip height.

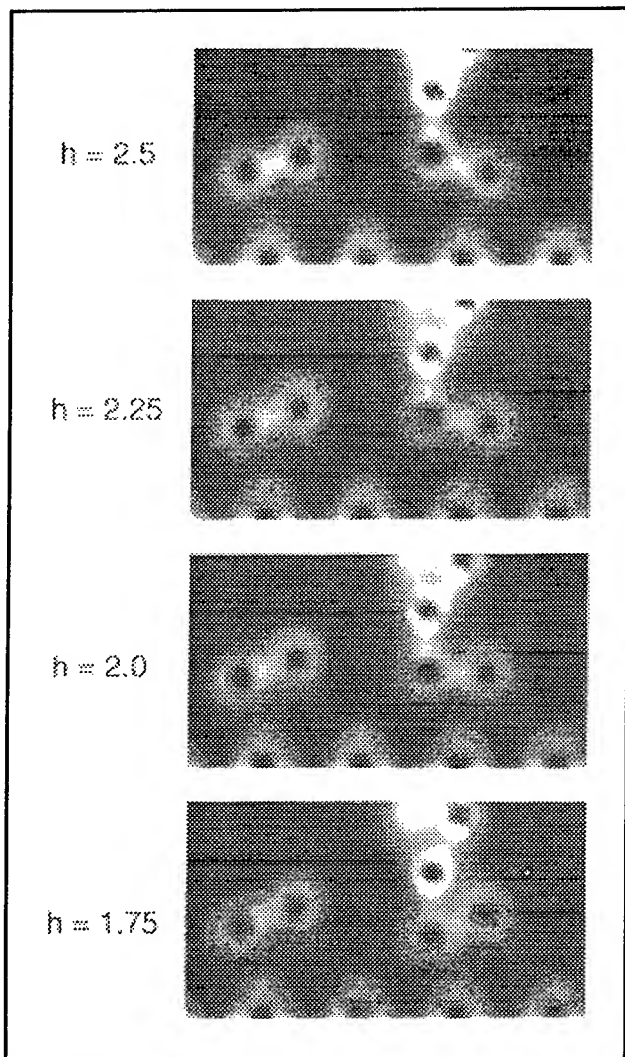


Figure 1. The sequence of charge density cross sections (from bottom to top) as the tip pushes down and flips the dimer. h is the tip-surface distance in Å defined as the distance of the top apex atom and the upper dimer atom before relaxation.

The four panels in figure 1 correspond to the sequence of decreasing the tip-surface distances, 2.5, 2.25, 2.0, and 1.75 Å. This sequence shows that as the AFM tip moves down, it *pushes down and flips* the surface dimer. The first three panels show a gradual decrease of the dimer angle (17°, 12°, and 2°), but the change of the equilibrium

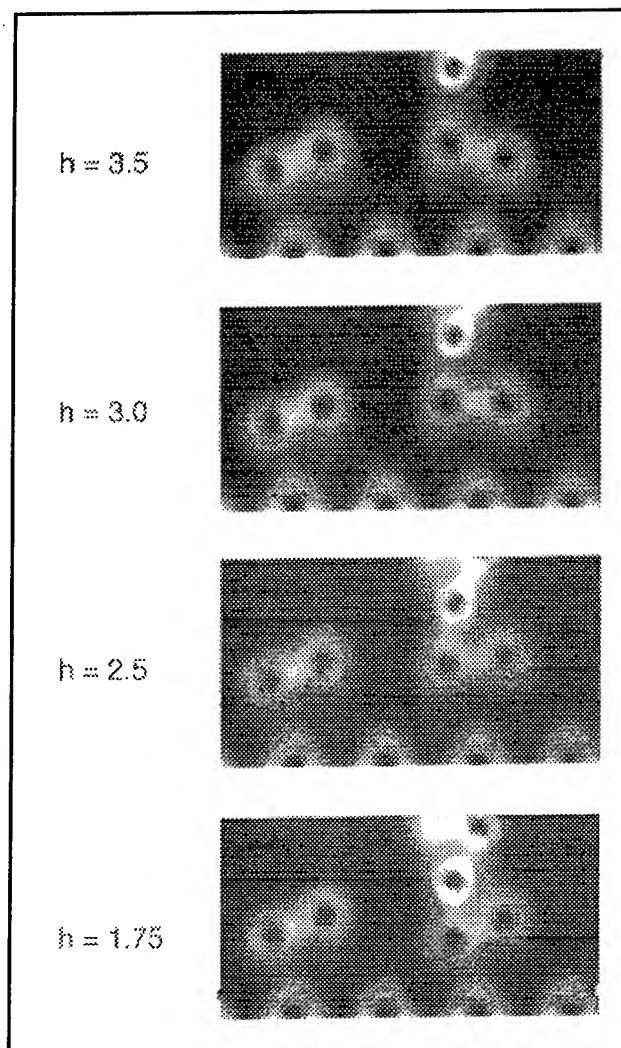


Figure 2. The sequence of charge density cross sections (from top to bottom) as the tip pulls up and flips the dimer. Same convention for h as in figure 1.

dimer-angle between the third panel and the fourth panel appears *discontinuous* (from 2° to -24°).

However, as the AFM tip moves up, the dimer configuration changes continuously as shown in figure 2. From the sequence of bottom to top, the tip-surface distance increases from 1.75 to 2.5 Å to 3.0 to 3.5 Å, and the dimer-angle increases gradually. This different behavior of dimer geometry clearly indicates that the dimer configuration follows two different local minimum energy paths as the tip moves down and up. The continuous up-path corresponds to a continuous transition in the Landau theory as illustrated in the right-hand sequence of figure 2. Therefore, the dimer configuration shows not only a quantitative difference but also a qualitative difference in the down-up cycle.

In order to make direct contact with AFM experiments for this system, we have calculated the force

on the tip for the two different pathways corresponding to lowering and raising the tip. The results are shown in figure 3. We note that the force-distance hysteresis loop exhibits a rather complex behavior. As the tip approaches the surface between 5.0 and 3.5 Å along the down-path, the force on the tip becomes more attractive and reaches a maximum at 3.5 Å. This corresponds to an inflection point in the interaction energy curve between the tip and surface. From 3.5 to 2.25 Å, one approaches a metastable equilibrium geometry for "adsorption" of the tip on the surface. At 2.25 Å the force is zero and the interaction energy is at its minimum. As the tip approaches closer to the surface, the force now becomes repulsive and at a distance of slightly less than 2 Å the dimer has flipped with a discontinuous change in its equilibrium angle. This corresponds to a process of overcoming a kink in the interaction energy. At this point the force is large and attractive since the tip would prefer to get closer to the down-dimer atom. This corresponds ultimately to the global adsorption energy minimum geometry.

As we now raise the tip from a distance of 1.75 to 3 Å, the force initially becomes slightly less attractive up to 2.5 Å and then reverts to becoming slightly more attractive from 2.5 to 3 Å. This corresponds directly to the tip atom being allowed to relax more during the first phase (1.75 → 2.5 Å). At 3 Å, the dimer angle has just changed sign. As the tip-surface distance increases further, the dimer gradually reverts to its original flipped geometry, and the force on the tip approaches zero.

This investigation leads to the prediction that the Si(100) surface in the presence of a tungsten AFM tip does indeed provide a potentially observable

example of mechanical hysteresis on a microscopic or atomic scale.

2.3 Heteroepitaxial Growth

Understanding epitaxial growth is a long-standing unsolved problem in condensed matter physics. An atomistic, theoretical approach is extremely difficult because the many different physical processes, such as adsorption, diffusion, re-evaporation, are complex and occur simultaneously at high temperatures. Computer simulations such as Monte-Carlo or molecular-dynamics are the obvious way to describe these phenomena. However, large-scale simulations can only be done for a restricted class of materials that can be accurately described by empirical or semi-empirical interatomic potentials.

One very important technological system involving heteroepitaxial growth is GaN on (0001) 6H-SiC, and for this system an *ab initio* treatment is required. In this work we have applied our *ab initio* techniques to investigate the nature of the initial stages of heteroepitaxial growth in this system. Since both SiC and GaN are partly ionic and partly covalent bonded materials with different degrees of ionicity and bond strengths, it is not obvious which bonding configuration will prevail at the interface. Although fundamental for the understanding of the growth process in these materials, very little attention has been given in the literature to the issue of GaN polarity on SiC substrates. Thus, total energies of four different types of interfaces were calculated, corresponding to Si-terminated or C-terminated substrates and Ga-terminated or N-terminated epilayers.

Contour plots of the total valence charge density and schematic ball-and-stick models for the four types of interfaces are displayed in figure 4. The plane of cut for all the figures is the hexagonal (10 $\bar{1}$ 0) plane, which contains two of the four bonds of the tetrahedrally coordinated atoms. The ball-and-stick models superimposed on each charge density plot give faithful description of the bond lengths and bond angles for each structure. Notice that the C and N atoms are surrounded by regions of high density of contours, reflecting the displacement in the bond maximum density towards these two atoms with higher electronegativity. Accordingly, Si and Ga atoms correspond to regions of depletion of valence charge density and "look smaller" compared to C and N. Let us denote by E_a , E_b , E_c and E_d the total energies of the four interfaces displayed in figures 4a, 4b, 4c and 4d, respectively. Figure 4a corresponds to a Si-terminated substrate and ideally Ga-terminated film. Notice that the Si and N atoms at the interface form

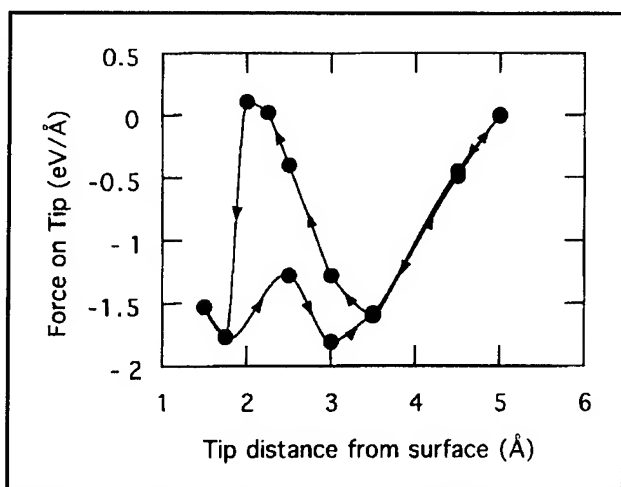


Figure 3. The hysteresis loop of the force on the AFM tip as the tip moves down (left arrows) and up (right arrows).

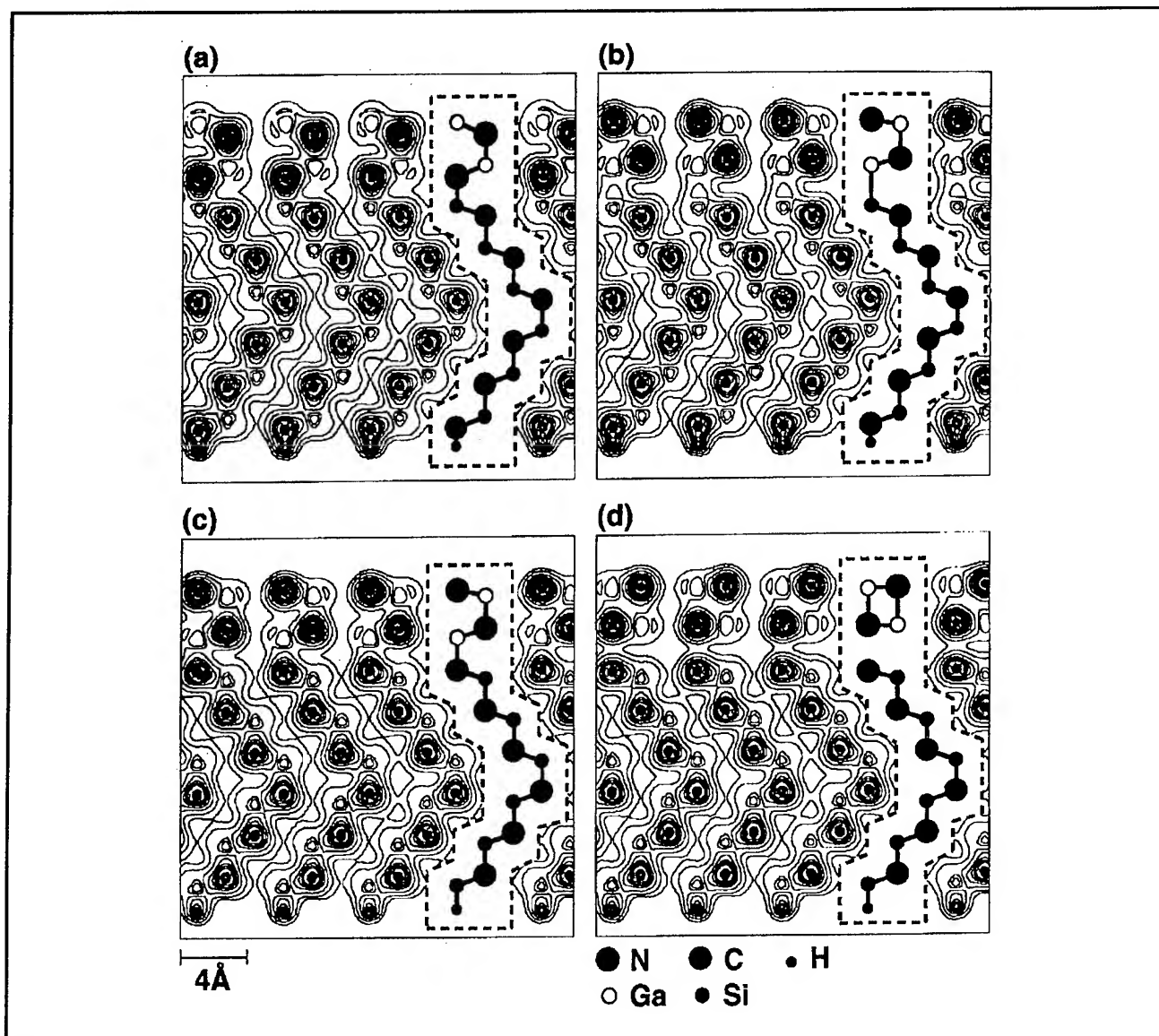


Figure 4. Contour plots of electronic density for four interfaces. Twelve evenly spaced contours from 0.4 to 3.7 (in units of electrons/Å³) are used. Two additional contours at 0.1 and 0.2 help to map the low charge density regions. Ball-and-stick models are superimposed for each case. Balls are placed at the actual atomic positions and differ by shade and size according to the atomic types.

a partly covalent, partly ionic bond. The Si-N bond distance is 1.77 Å. The remaining bond lengths and angles do not change significantly from the bulk values and the initial epilayers of the film look like a smooth continuation of the substrate. Figure 4b still corresponds to a Si-terminated substrate, but the film is now ideally N-terminated. A covalent bond is formed between Si and Ga at the interface (the bond distance is 2.43 Å). However, this bond is very weak since most of the charge remains concentrated around the C and N atoms. Subtraction of E_b from E_a gives us $E_a - E_b = -1.08\text{eV}$, indicating that for Si-terminated substrates, the ideally Ga-terminated film with Si-N bonds at the interface is energetically favorable.

A similar situation occurs for C-terminated substrates (figures 4c and 4d). In figure 4c, the ideally N-terminated film with C-Ga bonds at the interface is shown, and the charge density contours resemble very much those of figure 4a with inverted polarity. A strong covalent and ionic bond between C and Ga (bond length 1.99 Å) is formed at the interface. However, for ideally Ga-terminated films (figure 4d) the situation is surprisingly distinct from all the previous cases. The N atoms at the interface prefer to make bonds along the c-axis to the nearby Ga atoms (bond distance 2.22 Å) than to the C atoms on the substrate, yielding a very weakly coupled film-substrate system. The angles

between all the Ga-N bonds shown in the figure are very close to 90° , indicating sp^2 hybridization of the epilayers. Although carbon and nitrogen form strong covalent bonds in a large variety of situations, the presence of the surrounding atoms seems to make polarization effects very crucial, and the C and N atoms behave almost like two repelling negative charges. The total energy difference, $E_c - E_d = -1.07\text{eV}$, suggests that for C-terminated substrates, the ideally N-terminated film with C-Ga bonds at the interface is energetically favorable.

The results above suggest that the importance of the strength of covalent bonds is diminished by the polarization induced by the surrounding atoms and the ionic component of the bonds prevails. Thus our findings can be described in terms of a very simple rule of polarity matching at the surface. The lowest energy interfaces are those on which "positive" substrate ions bind to "negative" film ions, and vice-versa. Therefore the GaN films will grow with the same polarity as the SiC substrates. Besides being intuitively appealing, this picture is strongly supported by the fairly big energy differences ($\sim 1\text{eV}$ per surface atom) we found in our calculations. We believe that it is also robust enough to describe other possible microscopic processes during the initial stages of growth (for example, replacement of substrate ions by film ions at the interface should also satisfy polarity matching).

2.4 Publications

Capaz, R., K. Cho, and J.D. Joannopoulos. "Signatures of Bulk and Surface Arsenic Antisite Defects in GaAs(110)." *Phys. Rev. Lett.* 75: 1811 (1995).

Capaz, R., H. Lim, and J.D. Joannopoulos. "Ab initio Studies of GaN Epitaxial Growth on SiC." *Phys. Rev. B* 51: 17755 (1995).

Chen, J., H. Haus, J. Winn, S. Fan, and J.D. Joannopoulos. "Wide Stop Band Optical Filters from PBG Air Bridges." In *Guided-Wave Optoelectronics*. Eds. Tamir, Bertoni, and Greffell. New York: Springer Verlag, 1995.

Chen, J., H. Haus, S. Fan, and J.D. Joannopoulos. "Optical Filters from PBG Air-Bridges." Paper published in the *Proceedings of the European Conference on International Optics*, The Netherlands, 1995.

Cho, K., and J.D. Joannopoulos. "Tip-induced Modifications in Scanning Tunneling Microscopy and Atomic Force Microscopy." *Scan. Microscopy* 9: 381 (1995).

Cho, K., and J.D. Joannopoulos. "Mechanical Hysteresis on an Atomic Scale." *Surf. Sci.* 328: 320 (1995).

Fan, S., P. Villeneuve, and J.D. Joannopoulos. "Theoretical Investigation of Fabrication-Related Disorder on the Properties of Photonic Crystals." *J. Appl. Phys.* 78: 1415 (1995).

Fan, S., A. Devenyi, R. Meade, and J.D. Joannopoulos. "Guided Modes in Periodic Dielectric Materials." *J. Opt. Soc. Am. B* 12: 1267 (1995).

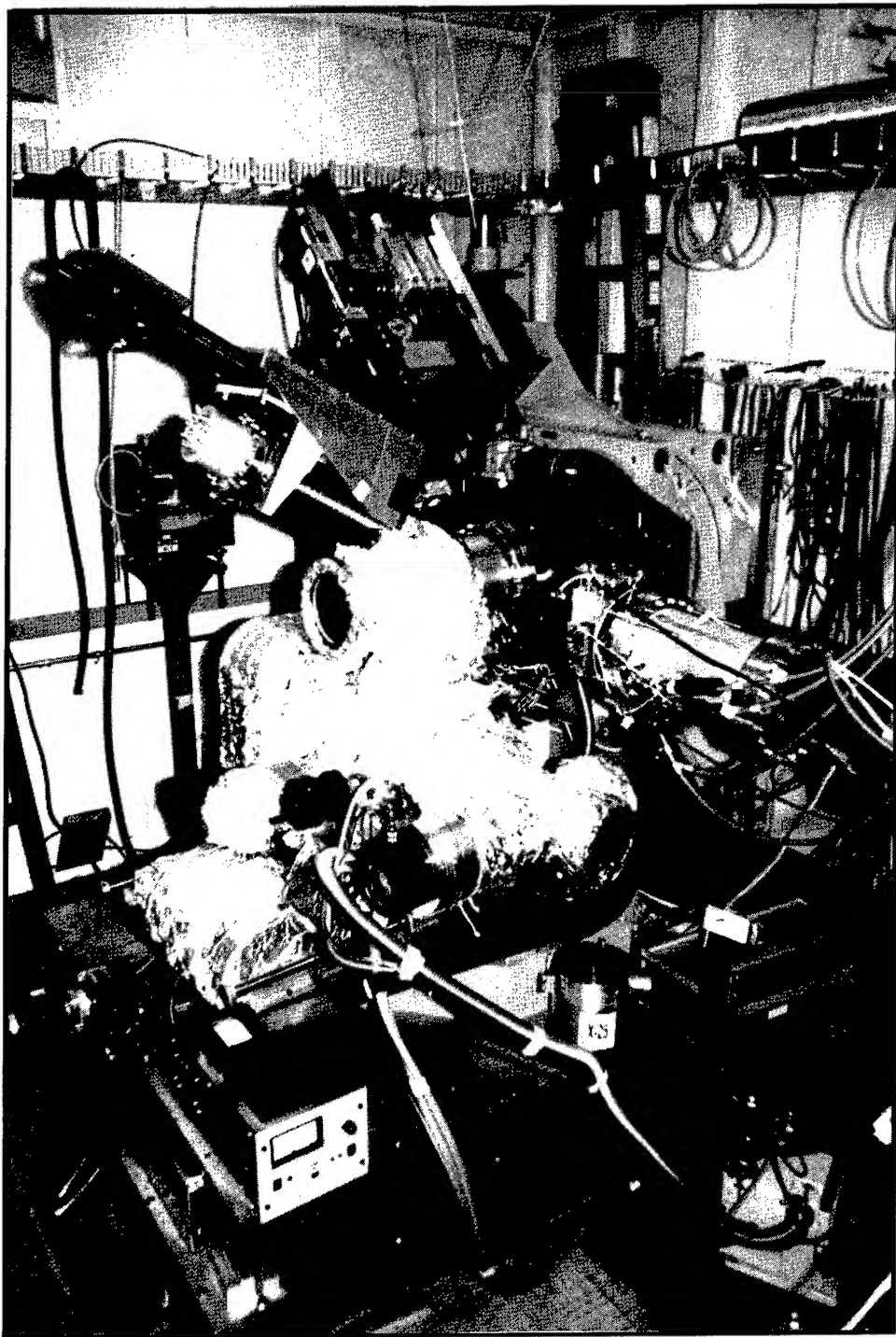
Joannopoulos, J.D. "An Introduction to Photonic Crystals." Paper published in the *Proceedings of NATO ASI*, Crete, 1995.

Joannopoulos, J.D. "The Almost-Magical World of Photonic Crystals." Paper published in the *Proceedings of the Seventh Brazilian Workshop on Semiconductor Physics*, Rio de Janeiro, Brazil, 1995.

Villeneuve, P.R., and J.D. Joannopoulos. "Tricks of the Light." *New Sci.* 147(1992): 26 (1995).

Villeneuve, P., S. Fan, J.D. Joannopoulos, K. Lim, G. Petrich, L. Kolodziejski, and R. Reif. "Air-Bridge Microcavities." *Appl. Phys. Lett.* 67: 167 (1995).

Villeneuve, P.R., S. Fan, I. Kurland, J.C. Chen, and J.D. Joannopoulos. "Photonic Bandgap Structures and Devices." *QELS Tech. Digest Series* 15 (1995).



The MIT ultra-high vacuum apparatus for surface x-ray scattering in the hutch of the X25 beamline at the National Synchrotron Light source at Brookhaven National Laboratory.

Chapter 3. Step Structures and Epitaxy on Semiconductor Surfaces

Academic and Research Staff

Professor Simon G.J. Mochrie

Graduate Students

Seunghoon Song, Mirang Yoon

3.1 Introduction

Sponsors

Joint Services Electronics Program

Grant DAAH04-95-1-0038

National Science Foundation

Grant DMR 94-23641

At present, there is considerable effort directed towards the fabrication and utilization of nanoscale semiconductor objects. This is, in part, to investigate the behavior of electrons within structures of sufficiently small dimensions to produce quantum confinement. Such so-called *quantum dots* and *quantum wires* have dimensions of typically a few hundred Angstroms. In addition, quantum dots and wires have been proposed as a route to develop many new device applications.¹

Recently, it has emerged that nanoscale structures on certain semiconductor surfaces may spontaneously self-assemble into more or less ordered patterns. Over the last year, we have been pursuing investigations of two examples of this remarkable phenomenon. Our goal is to achieve a microscopic and predictive understanding of the factors that determine the nanostructure. We also want to understand how it may be controlled and exploited in the creation of novel nanoscale surface structures, for example, by decoration schemes to create chemically heterogeneous surfaces. Specifically, we have pursued studies of the self-assembly of nanoscale grooves on stepped silicon surfaces. In addition, we have initiated a study of Ge quantum dots on Si.

3.2 Self-assembly of Nanoscale Gratings on Silicon

We have found that certain stepped silicon surfaces spontaneously form a remarkable mesoscopically grooved morphology. One side of each groove is a step-free (113) facet and the other side is a step bunch. Individual grooves are a few hundred Angstroms across and exceed one micron in length. The grooves self-assemble to form a nearly-periodic nanoscale grating. Associated with this grating are first-order diffraction peaks. The peak locations are determined by the grating periodicity and the peak widths by the degree of order of the grating. Figure 1 shows typical scattering profiles obtained at several times up to 1200 s, following a temperature quench from 1248 K, where surface steps are uniformly separated, to 1171 K, where step bunches form, in turn forming grooves. The peak at $Q_y = 0$ corresponds to specular reflection (zeroth-order diffraction peak). The two peaks, symmetrically located about the specular peak, constitute first-order diffraction peaks from the grooves. With increasing time, these peaks grow in intensity, shift to smaller wavevectors, corresponding to an increase in the groove period, and become narrower, corresponding to an increasingly ordered structure.

The peak positions and widths (HWHM) of the first-order diffraction peaks are shown on a log-log scale versus time for three representative final temperatures in figure 2. The variation of the peak position versus time is consistent with a $1/6$ power-law behavior for times between one and several hundred seconds. This result has inspired a theory of the growth of grooves, which reproduces the $1/6$ power-law and identifies the rate-limiting step as the close approach of neighboring step bunches.² However, at longer times the position approaches a

¹ C. Weisbuch and G. Vinter, *Quantum Semiconductor Structures* (Boston: Academic Press, 1991).

² S.T. Milner (unpublished).

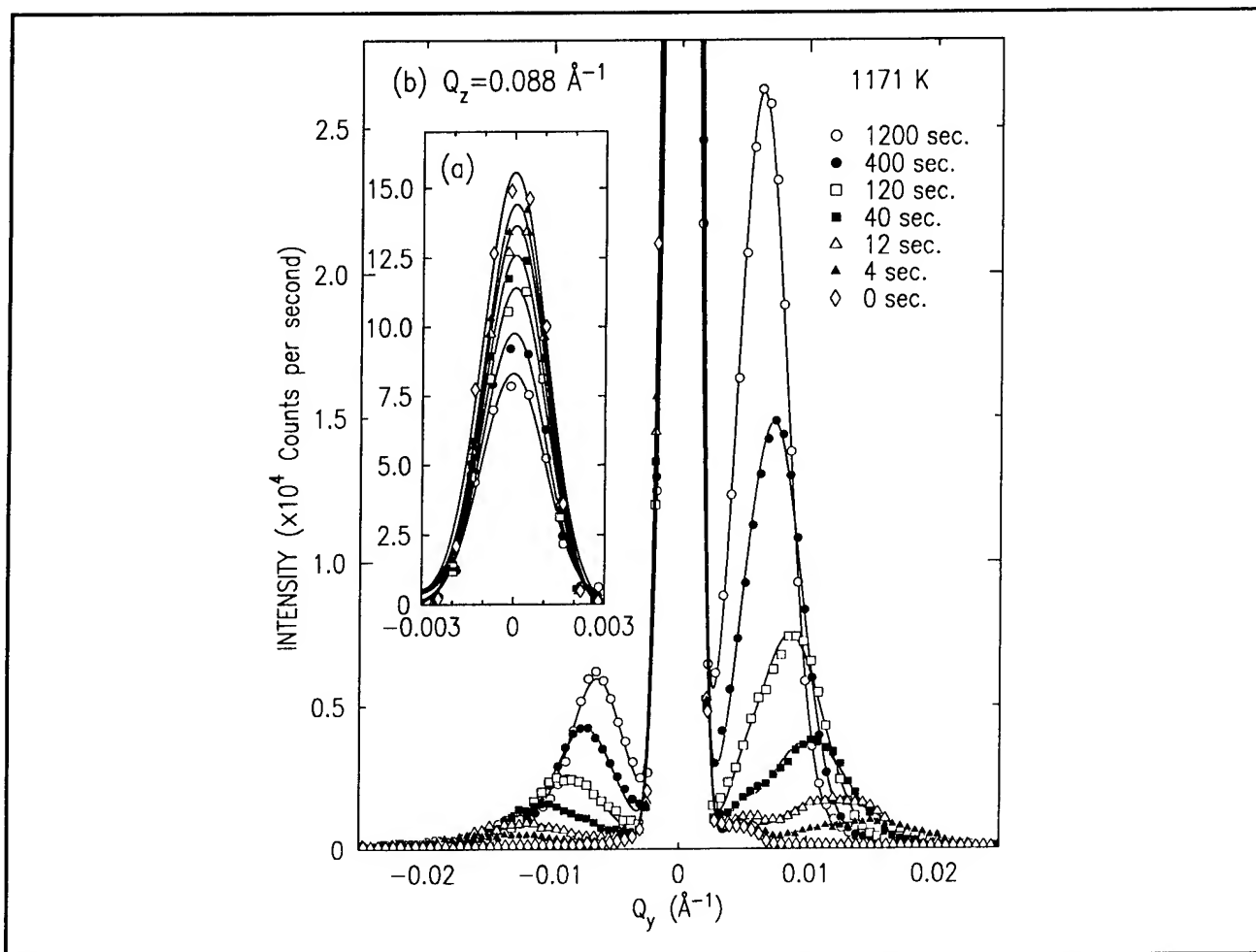


Figure 1. Time evolution of the first-order diffraction peaks of the groove superstructure, following a temperature quench from 1248 to 1171 K.

constant value, corresponding to a limiting groove size. By contrast, the peak width continues to decrease even at long times, indicating that the surface morphology evolves to an ordered equilibrium state. Notice that, by a second quench to room temperature, we may prepare a surface with any periodicity between 300 and 1200 Angstroms at will.

Shown in figure 3 is the limiting facet size plotted versus the angle between the sides of the groove for two samples with different misorientations. It seems especially surprising that the limiting facet size depends nonmonotonically on the angle. However, this may be understood qualitatively on the basis of the work done by Marchenko³ and Alerhand,⁴ where it is proposed that the lowest

energy configuration of a faceted surface corresponds to a periodically grooved morphology. The special stability of the grooved structure originates in a reduction of surface-stress-induced elastic energy in the bulk that occurs for mesoscopic facets as compared to macroscopic facets. The period is determined by balancing the reduction in elastic energy against the energetic cost of maintaining edges between the coexisting phases. The theory predicts that the groove period is minimized when the angles between each side of the groove and the macroscopic surface are equal, as found experimentally for the two differently misoriented samples. Thus, we have achieved an in-depth understanding of the mechanism responsible for nanoscale grooves on stepped Si(113) surfaces. As a result, it may become possible to engineer the

³ V.I. Marchenko, *Zh. Eksp. Teor. Fiz.* 81: 1141 (1981); *Sov. Phys. JETP* 54: 605 (1981).

⁴ O.L. Alerhand, D. Vanderbilt, R. Meade, and J.D. Joannopoulos, *Phys. Rev. Lett.* 61: 1973 (1988).

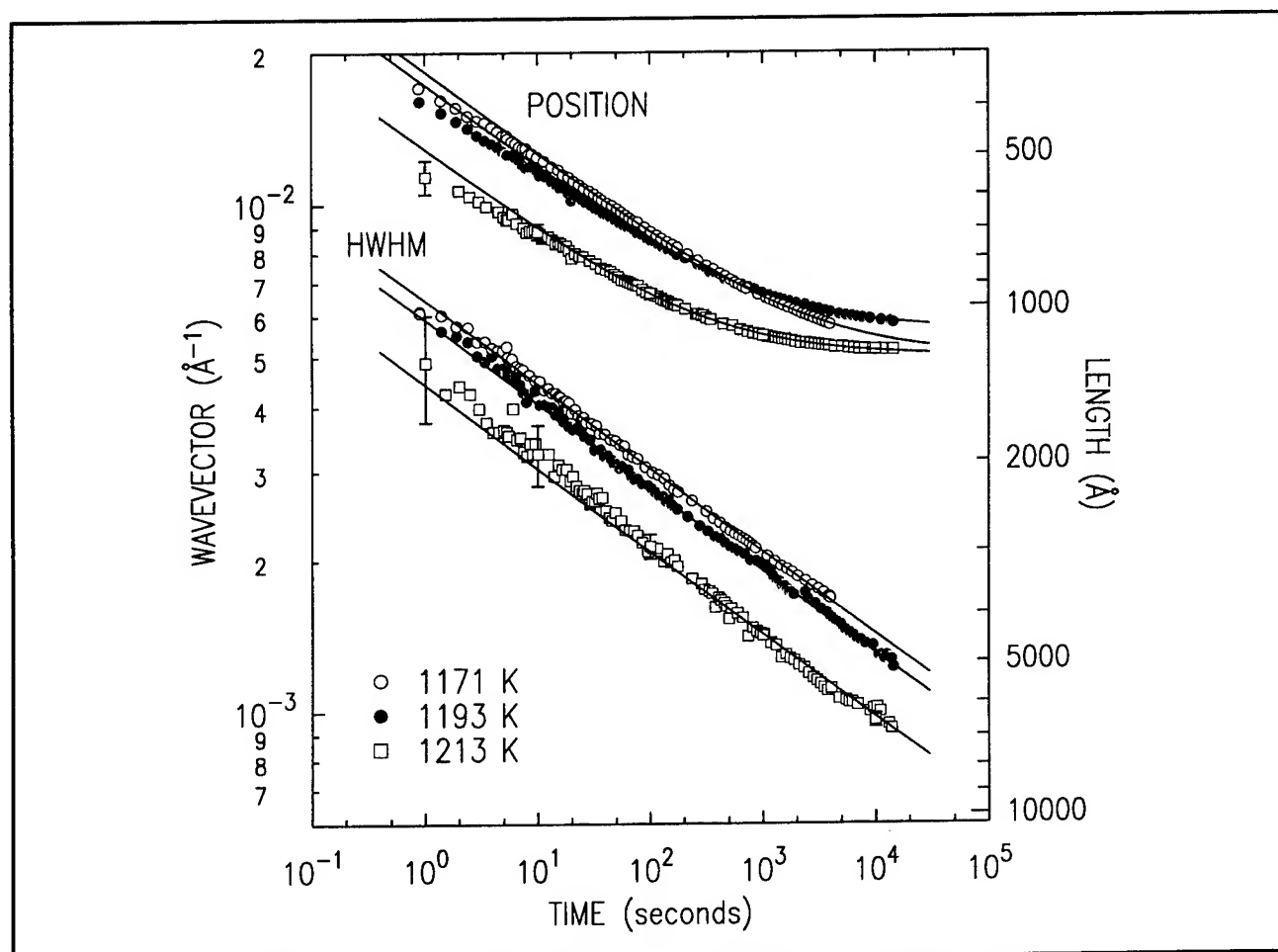


Figure 2. Log-log plot of the position and HWHM for three representative quench temperatures.

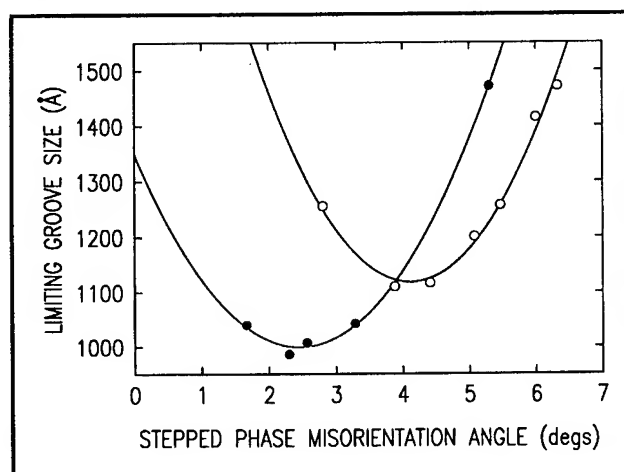


Figure 3. Limiting groove size vs. the groove angle.

equilibrium groove size. For example, an adsorbed species might lower the edge energy, allowing us to tune the groove periodicity with coverage.

The results described in this section refer to a single azimuthal orientation of the steps. In this case the surface is tilted away from (113) towards (001). We plan to investigate the behavior for other azimuthal orientations. In particular, we have initiated studies of surfaces tilted towards $(1\bar{1}0)$ (90° -rotated with respect to the surfaces studied previously by 90°). Figure 4 shows an AFM image of this surface, which was quenched to 300 K after equilibration at 900 K. The surface morphology for the azimuth of figure 4 is evidently more complicated than simple linear grooves. Specifically, straight steps are not stable; instead, there are kinks between two stable step orientations, giving rise to a two-dimensionally patterned substrate. Further AFM measurements of this surface quenched from other temperatures and x-ray measurements versus temperature are called for to further elucidate this behavior.

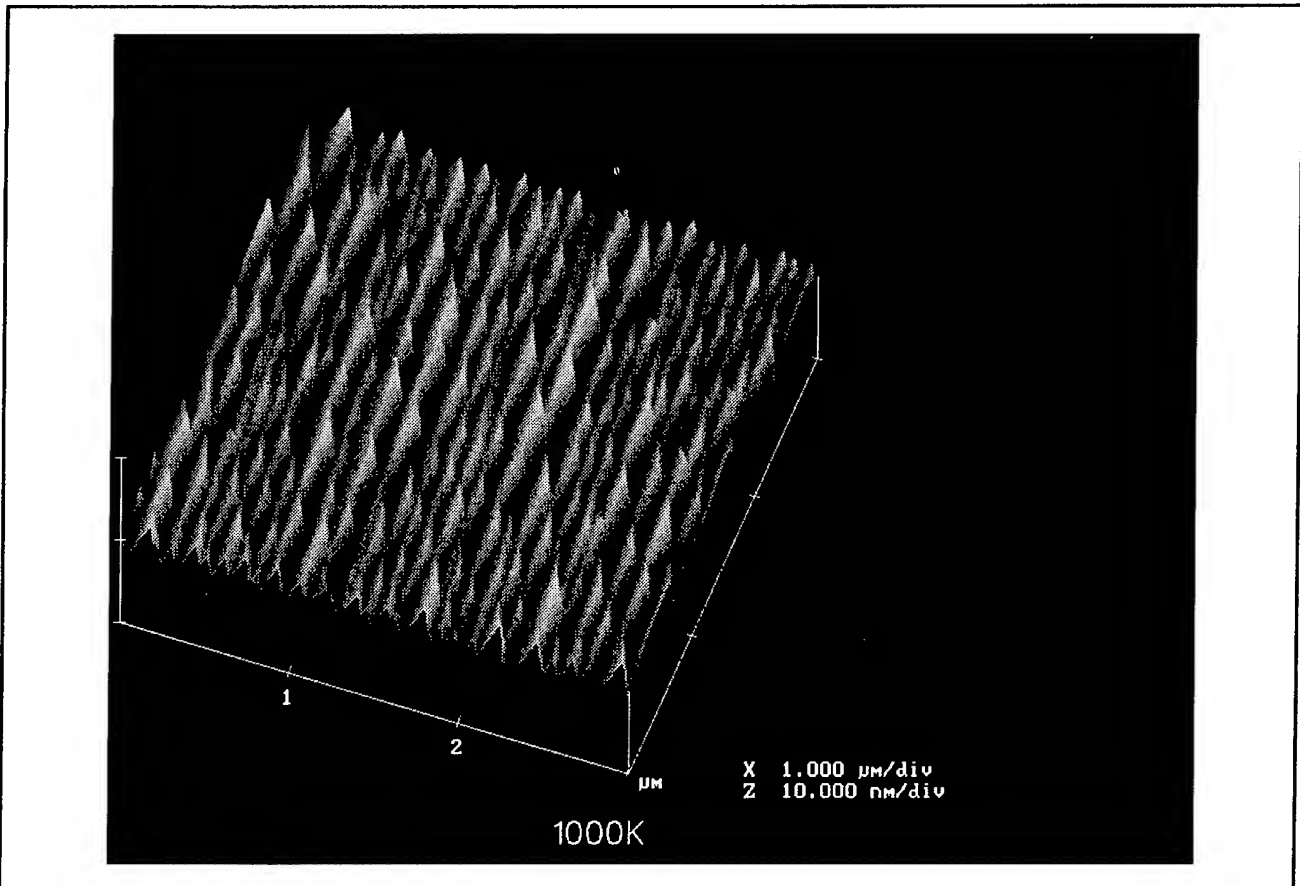


Figure 4. AFM image of the surface morphology of a stepped Si(113) surface tilted towards $(1\bar{1}0)$, quenched from 900 K.

3.3 Self-assembly of Quantum Dots

The manufacture of nanostructure semiconductor objects is exceedingly difficult, because these structures are tiny. For example, it is difficult to achieve the requisite sizes with lithography. Schemes which directly build quantum-sized objects during growth are possible alternatives. Such schemes may include cluster formation in the gas phase and subsequent cluster deposition and growth on patterned substrates such as stepped surfaces.

An especially promising and interesting approach is the self-assembly of a nanostructure during strained heteroepitaxial growth on a flat substrate. Strained heteroepitaxial growth, involving a large lattice mismatch, generally proceeds via the formation of islands after the initial growth of a few flat layers. Recently, Krishnamurthy et al.,⁵ Leonard et al.,⁶ and

Moison et al.⁷ have found that it is possible to prepare near-uniformly sized and spaced islands of dislocation-free Ge on Si(001), InGaAs on GaAs(001), and InAs on GaAs(001), respectively. It is this apparent self-organization of defect-free quantum dots that is so exciting, both from technological and scientific viewpoints. However, a fundamental understanding of quantum dot formation—whether it is kinetic or thermodynamic in origin—is presently lacking.

In the earlier studies, it was not possible to examine *in-situ* island formation during the deposition and annealing processes. By contrast, we have initiated an *in-situ* investigation of the self-assembly of quantum dots of germanium on silicon as it occurs. We are using both synchrotron x-ray scattering techniques to monitor how the surface morphology develops in real-time and the atomic force micro-

⁵ M. Krishnamurthy, J. Drucker, and J.A. Venables, *J. Appl. Phys.* 69: 6461 (1991).

⁶ D. Leonard et al., *J. Vac. Sci. Technol. B* 12: 1063 (1994).

⁷ J.M. Moison et al., *Appl. Phys. Lett.* 64: 196 (1994).

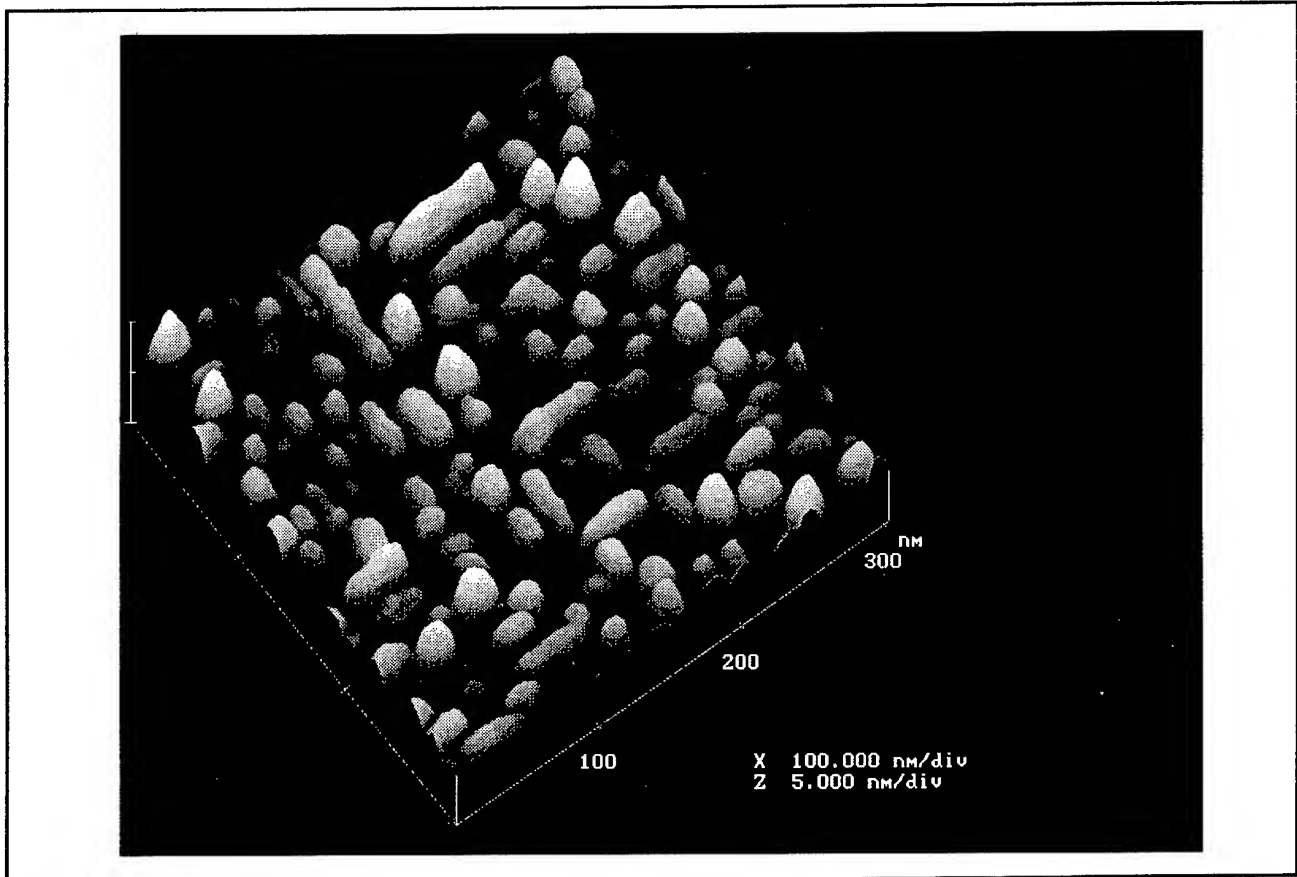


Figure 5. AFM image of Ge quantum dots on Si(001).

scope to definitively determine “snap shots” of the surface morphology by means of rapid temperature quenches. In this way, we will achieve a microscopic and predictive understanding of the factors that determine the final morphology. As result, we expect to learn how to control the nanostructure.

We have chosen to study initially the Ge-on-Si system, in part, because of the earlier work of Krishnamurthy et al., and also because of the potential utility of Ge-Si heterostructures in device applications. In addition, the topic of the present research was inspired by the detailed understanding of the role of elasticity in promoting nanoscale self-assembly. We have gained this knowledge from our own measurements (made within the Joint Services Electronics Program at MIT) of the self-assembly of a nanoscale grating on stepped silicon surfaces described above.⁸

Figure 5 illustrates an AFM image of a surface upon which is deposited the equivalent of approxi-

mately eight monolayers of Ge at a substrate temperature of 300 K, which we obtained. Three monolayers grow in a layerwise fashion, but subsequent deposition occurs in the form of three-dimensional islands, i.e., quantum dots, which may be clearly seen in the image more or less uniformly spaced across the surface. This figure demonstrates that we can prepare quantum dots for study. As may be seen, some of the dots are elongated along two orthogonal directions, which are high symmetry directions of the substrate. This interesting aspect is not understood.

The development of the morphology seen in figure 5 may be monitored *in situ* and in real time using synchrotron x-ray scattering. In this way, we will investigate the evolution of the surface morphology versus time at different deposition temperatures and for different Ge coverages and temperatures subsequent to deposition. Our goal is to gain a quantitative microscopic understanding of Ge quantum dots on Si(001) and how they form. On the basis of the

⁸ S. Song and S.G.J. Mochrie, *Phys. Rev. Lett.* 73: 995 (1994); S. Song and S.G.J. Mochrie, *Phys. Rev. B* 51: 10068 (1995); S. Song, S.G.J. Mochrie, and G.B. Stephenson, *Phys. Rev. Lett.* 74: 5240 (1995).

behavior observed for stepped Si(113), we are lead to speculate that Ge quantum dots on Si may themselves self-assemble under the right conditions into a *periodic* superlattice as a result of elastic effects. It would then be possible to grow Si on top of such a structure. Following on from layered superlattices, such a three-dimensionally patterned material would be very interesting.

3.4 Publications

Mochrie, S.G.J., S. Song, M. Yoon, and D.L. Abernathy. "Faceting of Stepped Si(113) Surfaces: Self-assembly of Nanoscale Gratings." *Physica B*. Forthcoming.

Song, S., M. Yoon, and S.G.J. Mochrie. "Faceting, Tricriticality, and Attractive Interactions Between Steps in the Orientational Phase Diagram of Silicon Surfaces Between [113] and [5 5 12]" *Surf. Sci.* 334: 153 (1995).

Song, S., S.G.J. Mochrie, and G.B. Stephenson. "Faceting Kinetics of Stepped Si(113) Surfaces: A Time-Resolved X-ray Scattering Study." *Phys. Rev. Lett.* 74: 5240 (1995).

Song, S., and S.G.J. Mochrie. "Attractive Step-step Interactions, Tricriticality, and Faceting in the Orientational Phase Diagram of Silicon Surfaces Between [113] and [114]." *Phys. Rev. B* 51: 10068 (1995).

Part II Applied Physics

Section 1 Atomic, Molecular and Optical Physics

Section 2 Plasma Physics

Section 3 Electromagnetics

Section 4 Radio Astronomy

Section 1 Atomic, Molecular and Optical Physics

Chapter 1 Quantum Optics and Photonics

Chapter 2 Basic Atomic Physics

Chapter 1. Quantum Optics and Photonics

Academic and Research Staff

Professor Shaoul Ezekiel, Dr. Selim M. Shahriar, Dr. Stephen P. Smith, Dr. Timothy Grove,
Dr. Venkatapuram S. Sudarshanam

Visiting Scientists and Research Affiliates

Dr. Philip R. Hemmer,¹ Dr. Mara G. Prentiss,² John D. Kierstead¹

Graduate Students

John J. Donoghue,³ Daniel P. Katz,⁴ Juliet Mervis⁴

1.1 Classical and Quantum Noise Suppression in Distortion-Free Phase Conjugation Using Coherent Population Trapping

Sponsor

U.S. Air Force - Electronic Systems Division
Contract F19628-92-K-0013

We have observed greater than 10 dB classical noise correlations and indirect evidence of equally strong quantum noise suppression using distortion-free, four-wave mixing in optically dense sodium vapor under conditions of high gain (up to 50). To achieve such a performance in a strongly absorbing medium, it is necessary to suppress unwanted absorption effects while enhancing index modulation. We accomplish this via a process analogous to coherent population trapping (or electromagnetically induced transparency) in a pseudo-four-level, closed-loop system. This type of quantum noise suppression may be useful for broadband image squeezing in optical computers.

Four-wave mixing (FWM) has numerous potential applications to image processing, aberration correction and amplification. In addition, FWM is a natural choice for the generation of spatially broadband squeezed light for sub-shot noise

imaging applications. In general, however, these applications require a FWM mechanism that can deliver high gain without propagation distortion or excessive scattered light generation. Moreover, for sub-shot noise imaging applications, the FWM should be optimized for low intensity cw signals.

Recently, electromagnetically induced transparency (EIT) was shown to eliminate propagation distortion and even self-focusing via coherent population trapping (CPT) in optically dense media.⁵ Noise correlation via CPT has also been studied, and strong classical noise correlations observed. In a previous paper, we demonstrated high gain at low pump intensity in optically dense sodium vapor using FWM and CPT in a pseudo-double- Λ system (i.e., a three- or four-level system, excited by four fields in a closed-loop geometry, as shown in figure 1).⁶ Here, we report noise suppressions and signal propagation effects in this novel pseudo-double- Λ system.

Figure 1 shows the basic excitation scheme as well as the atomic configuration for realizing FWM via CPT in a pseudo-double- Λ system. As shown, the forward and backward pump beams, F and B respectively, excite opposite legs of separate Λ -subsystems. The input probe beam, P, completes the subsystem excited by F, and the conjugate beam, C, completes the other, as shown.

¹ Rome Laboratory, Hanscom Air Force Base, Bedford, Massachusetts.

² Professor, Department of Physics, Harvard University, Cambridge, Massachusetts.

³ Electro-optics Center, Tufts University, Medford, Massachusetts.

⁴ Department of Physics, Harvard University, Cambridge, Massachusetts.

⁵ M. Jain, A.J. Merriam, A. Kasapi, G.Y. Yin, and S.E. Harris, *Phys. Rev. Lett.* 75: 4385 (1995).

⁶ P.R. Hemmer, D.P. Katz, J. Donoghue, M. Cronin-Golomb, M.S. Shahriar, and P. Kumar, *Opt. Lett.* 20: 982 (1995).

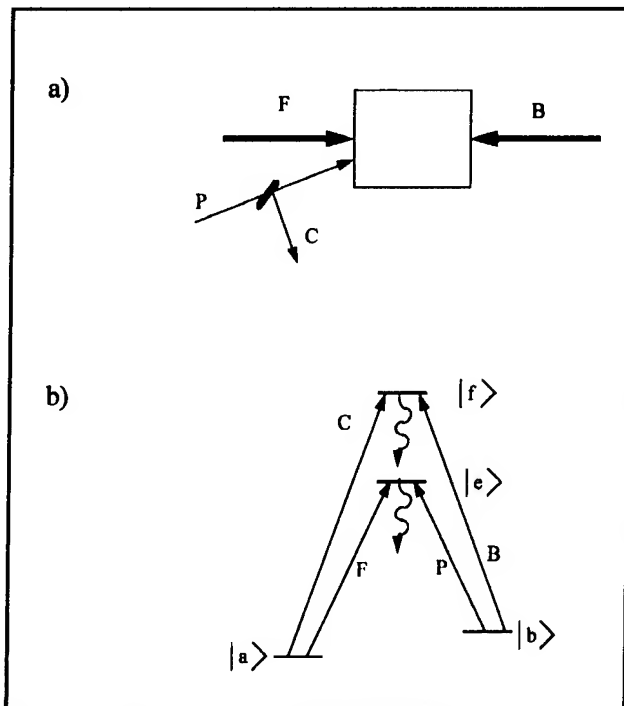


Figure 1. (a) basic four wave mixing scheme where F is the forward pump, B is the backward pump, P is the input probe beam, and C is the conjugate. (b) double lambda atomic system with lasers F, B, P, and C.

In analogy to EIT,⁷ it is possible to view FWM in this system as a two-step process. In the first step, F and P write a grating in the ground state coherences via CPT. In the second step, beam B diffracts off this grating to produce C. This simple picture is valid in the limit of weak B and C. However, for applications, it is more realistic for the pumps F and B to be strong with P and C initially weak. In this case, it is clear that conventional CPT or EIT is not possible, since the two Λ subsystems have conflicting transparency conditions. Nonetheless, it is still possible to interpret the pseudo-double- Λ system in terms of CPT concepts by considering the four-level closed-loop transparency condition.

The transparency condition for a closed-loop, double- Λ system is more restrictive than in a single- Λ system. In addition to the requirement for properly phased atomic ground states, there are also restrictions on the relative phases and magnitudes of the four fields. The FWM geometry, shown in figure 1, automatically satisfies the phase constraint. However, the field magnitude condition is not satisfied in general. This condition requires a

relation between Rabi frequency ratios $F/P = C/B$, and is clearly far from being satisfied when P and C are weak. Still, it is possible to understand the evolution of this system in analogy with CPT. Recall that in the case of a single- Λ system an arbitrary initial atomic state can be written as a superposition of a dark state and a set of bright states. CPT causes the system to evolve into the dark state by decay. Similarly, in the double- Λ system, an arbitrary configuration of atomic and field states can be expressed as a linear combination of a closed loop dark state (for which $F/P = C/B$) and one or more bright states. Again the tendency is to evolve toward the transparent state. However, in the closed loop system, this will involve the rearrangement of both atomic and field populations (i.e., there will be optical loss and/or gain).

For example, if F and B are strong and P and C are weak, then, for opportune choices of parameters, transparency may be approached most rapidly by attenuation of F and B and gain in P and C. In addition, if F and B have initially similar strengths, it is reasonable to expect nearly equal amounts of energy to be transferred into both P and C, resulting in noise correlations. Finally, as the transparency condition is approached, the resonant nonlinear refractive index is expected to be suppressed, thereby reducing self-focusing and other propagation aberrations as in EIT.

Of course, the physical explanation just given is an oversimplification. For example, in cw FWM using the counter-propagating geometry shown in figure 1, the transparency condition is only approximately approached near the center of the cell. In this case, the nonlinear refractive index suppression is probably not mediated by EIT. Rather, experimental observations suggest that the refractive index may be controlled by canceling the nonlinear refractive index changes by spatially varying two-photon Stark shifts. These Stark shifts can produce nonlinear refractive index changes of either sign via steep refractive index variations in the neighborhood of the two-photon Raman resonance.

Figure 2 illustrates typical experimental conditions. The $3^2S_{1/2}$ ground state (hyperfine $F=1$ and $F=2$) and the $3^2P_{1/2}$ hyperfine levels ($F=1$ and $F=2$) compose the sodium system used in this report. Two dye lasers tuned near the D1 line provide the F and B beams (FWHM approximately 1.4 mm and 100 mW power). The two pumps have nearly identical beam diameters and are collimated to within 1

⁷ S.E. Harris, *Phys. Rev. Lett.* 70: 552 (1993); S.E. Harris, *Phys. Rev. Lett.* 72: 52 (1994); S.E. Harris, J.E. Field, and A. Kasapi, *Phys. Rev. A* 46: R29 (1992).

mrad. To generate the weak probe beam, P, an acousto-optical modulator shifts the frequency of a small portion of the F beam by -1.77 GHz (as shown in figure 2). This probe beam has a FWHM of approximately 0.9 mm and 1 mW of power. Figure 2 shows the typical detuning of each beam. The angles between the F and P (and B and C) are kept below 4 mrad in order to maintain a good beam overlap in the sodium cell. The sodium cell is a heat pipe oven at approximately 180°C . At this temperature, the sodium density is high enough that the near-resonant probe beam absorption is greater than 95 percent (when blocking both pump beams). Photodiodes and/or video cameras, marked as detectors in figure 2, measure the power and/or beam profiles of beams exiting the sodium cell.

Figure 3 shows the measured probe beam profiles exiting the cell. In particular, figure 3a shows the

profile for an unamplified probe (frequency tuned outside the Doppler profile). This beam is slightly larger than the 0.9 mm FWHM in the cell (the beam diffracts over the 1.2 m distance from cell to camera). Figure 3b shows an amplified probe cross section for a probe power gain of 10. The smaller FWHM diameter in this case is probably due to slight residual self focusing and is noticeable only because of the large cell to camera distance. Figure 3c illustrates the case of gain of 50, showing the onset of distortion effects. Such distortion becomes more severe for gains in excess of 100 (the largest observed gain is in excess of 1000). In both figures 3b and 3c, pump depletion effects are significant. In fact, higher gain is achieved by attenuation of the input probe power (10 dB in figure 3c).

The four-wave mixing process in the pseudo-double- Λ system is expected to yield quantum

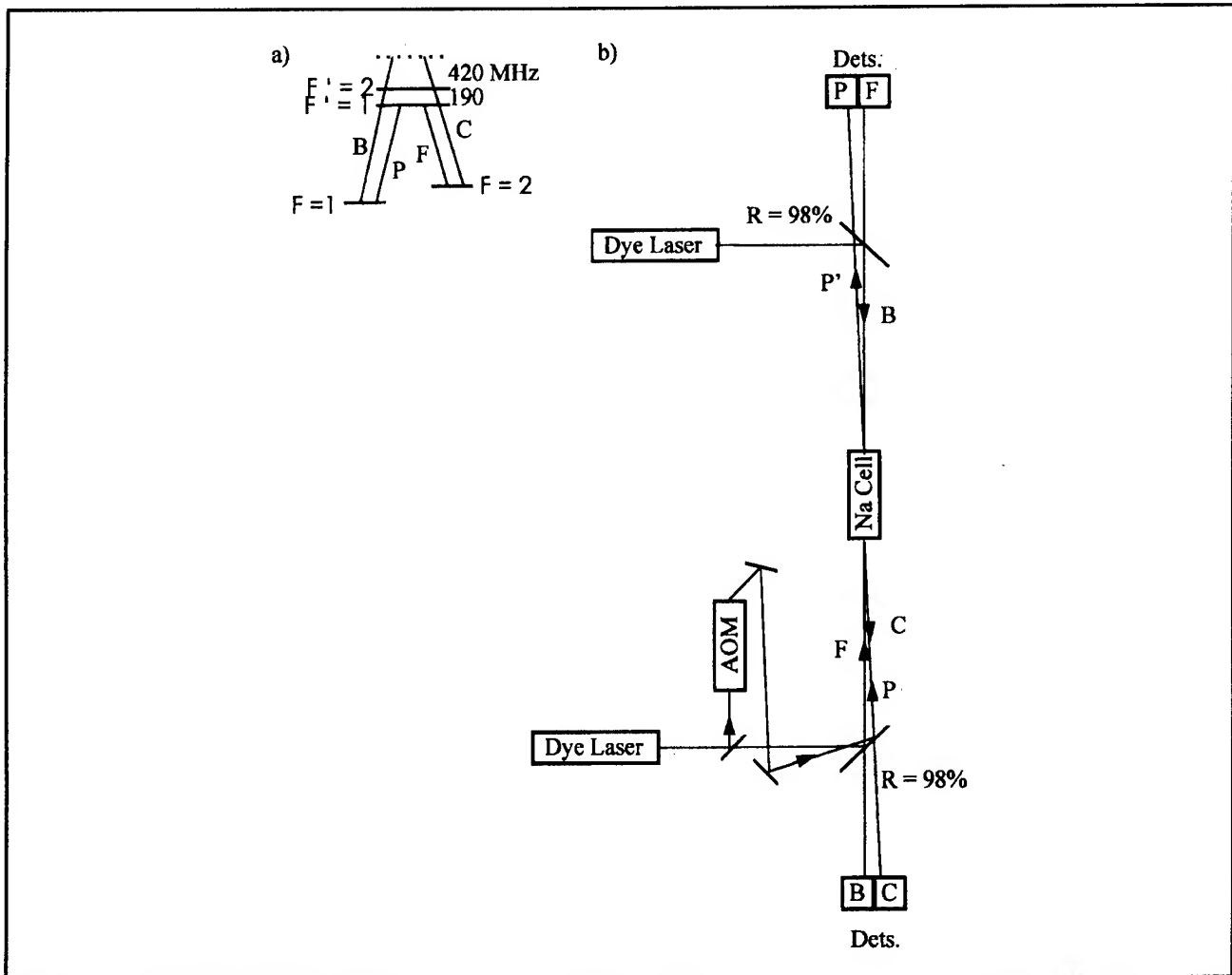


Figure 2. (a) Experimental double lambda system. Ground states consist of the $3^2S_{1/2}$ levels $F=1$ and $F=2$. Excited states consist of the $3^2P_{1/2}$ levels $F=1$ and $F=2$. Approximate detunings are given. (b) Experimental set-up showing the generation of each beam.

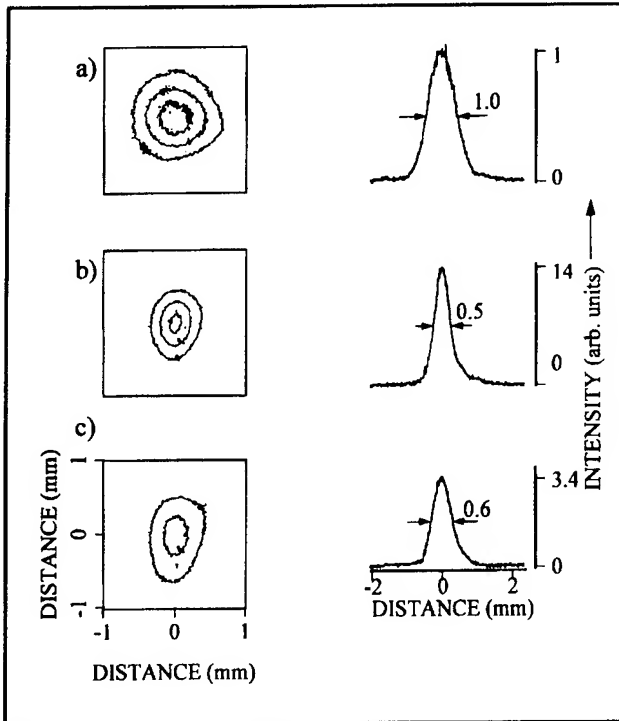


Figure 3. Contour and horizontal profiles of the probe beam and the amplified probe beam under various conditions. a) Unamplified probe, b) gain=10 amplified probe, c) gain=50 amplified probe.

noise suppression. In particular, we have shown⁸ that the conjugate and amplified probe are twin beams, with noise correlations substantially (> 10 dB) below the shot-noise limit, as illustrated in figure 4. Figure 4a shows the degree of twin beam squeezing as a function of the probe/conjugate detuning. For the case of 10 dB squeezing, the probe and conjugate are almost 10 dB quantum noise correlated (i.e., twin beams), and the correlation is illustrated using numerically computed joint photon probability distribution in figure 4b.

This correlation can be observed in the current difference of a photodiode detecting the amplified probe, and another photodiode detecting the conjugate. As usual, the calculation assumes that quantum noise of the pumps can be ignored. In addition, the two pumps (F and B) are assumed to be generated from the same laser, so that any classical noise (i.e., fluctuation in the mean intensity) is not expected to affect the probe-conjugate quantum noise correlation to first order.

However, in our experiment, two independent lasers generate the two pump beams, so that the classical noises in F and B are uncorrelated. Such a situation is extremely difficult to take into account in quantum noise correlation calculations. Nonetheless, it is possible to estimate the effects of the uncorrelated classical noises of the pump beams. Assuming ideal wave mixing (i.e., loss free), it is well known that the degree of quantum noise correlation is proportional to the gain of the probe beam.⁹ By a classical noise analysis, it is easy to show that the same conclusion applies to the classical noise correlation between the conjugate and the amplified probe in the presence of classical pump noise.

Figure 5 shows the measured intensity noise correlations between the amplified probe beam and the conjugate beams (P' and C). The dashed line in all traces of figure 4 corresponds to the arbitrary level of -117 dBm on our spectrum analyzer. The annotated noise in each trace corresponds to the extra noise above the -117 dBm level at a noise frequency of 300 kHz. Figures 5b and 5c show the conjugate and amplified probe noise (respectively) versus noise frequency. Here (figures 5b and 5c) the noise is larger than a coherent beam of equal power (see figures 5e and 5f). Subtracting the conjugate and amplified probe signal greatly reduces the noise (see figure 5d). In fact, the subtracted noise signal is almost at the electronic noise level (see figure 5a). The unamplified probe noise (not shown) is smaller than the electronic noise. This demonstrates that the probe and conjugate are intensity noise correlated. Figures 5e, 5f, and 5g show that the backward and forward pump noises are uncorrelated. In particular, figure 5e is the noise in B; figure 5f is the noise in F; and figure 5g is the B-F signal which shows larger noise than in either F or B alone (expected for uncorrelated noise sources). For comparison, the F and B noise traces were made after attenuation of F and B to the same power levels of P and C. This shows the excess noise generated by the amplification process.

These observations, coupled with our theoretical calculations, provide indirect evidence of at least 10dB of quantum noise suppression. For direct observation of squeezing, it is necessary to suppress the classical noise to a level below the shot-noise limit. This can be achieved, for example, by reducing the classical noise in each pump by servo-stabilization of the laser intensities.

⁸ M.S. Shahriar and P.R. Hemmer, submitted to *Phys. Rev. A*.

⁹ O. Aytur and P. Kumar, *Phys. Rev. Lett.* 65: 1551 (1990).

In conclusion, we have demonstrated a high-gain, low-pump power medium that yields distortion-free propagation. Furthermore, there is a high degree of classical as well as quantum noise correlation between the amplified probe signal and the conju-

gate signal. Quantum noise suppression achieved this way may be useful in sub-shot-noise imaging applications such as parallel processors in optical computers.

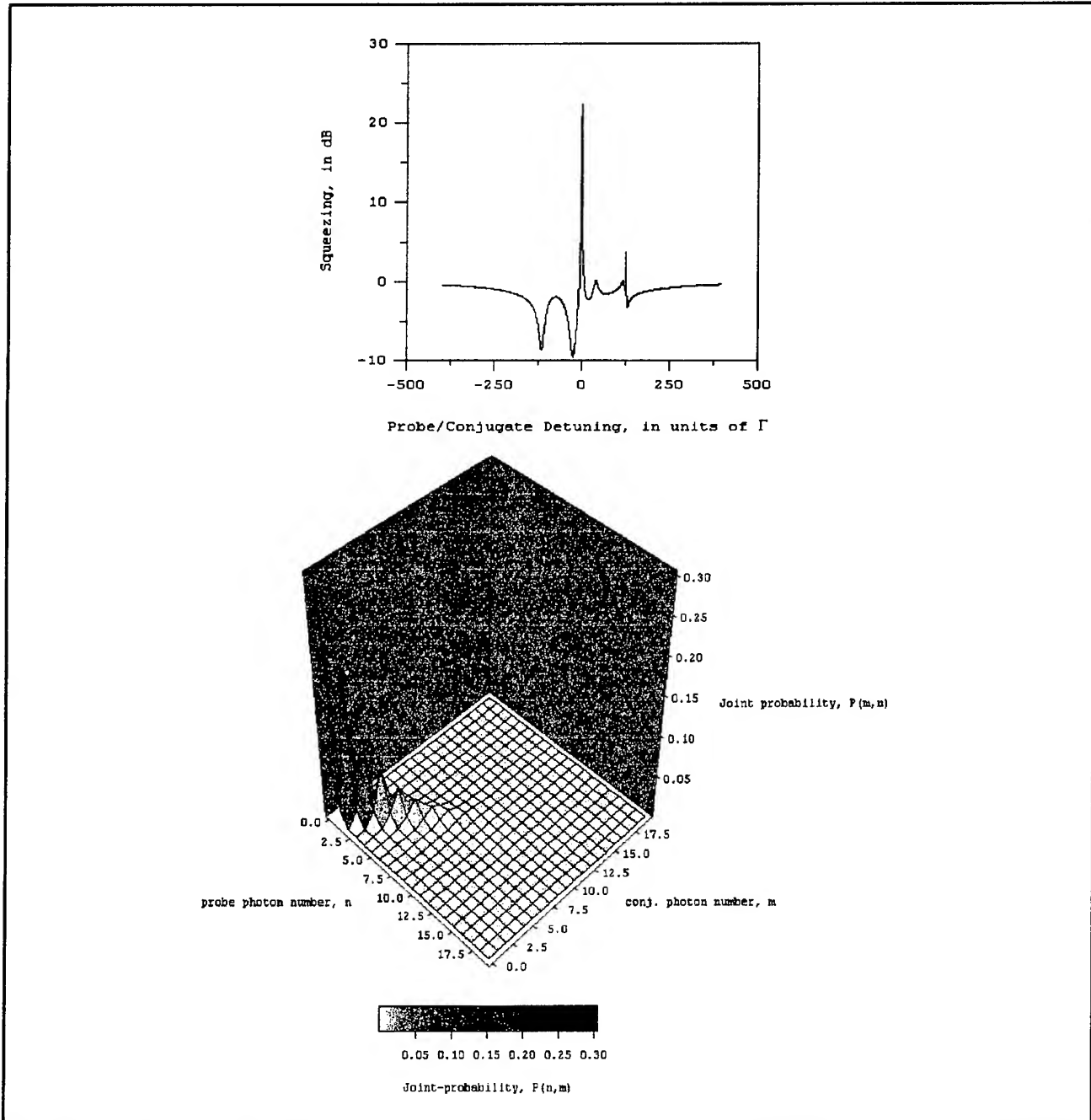


Figure 4. Theoretical predictions of quantum noise squeezing: (a) Quadrature squeezing, as a function of probe or conjugate detuning; and (b) the joint photon probability distribution for 10 dB twin beam squeezing, corresponding to the condition for maximum quadrature squeezing.

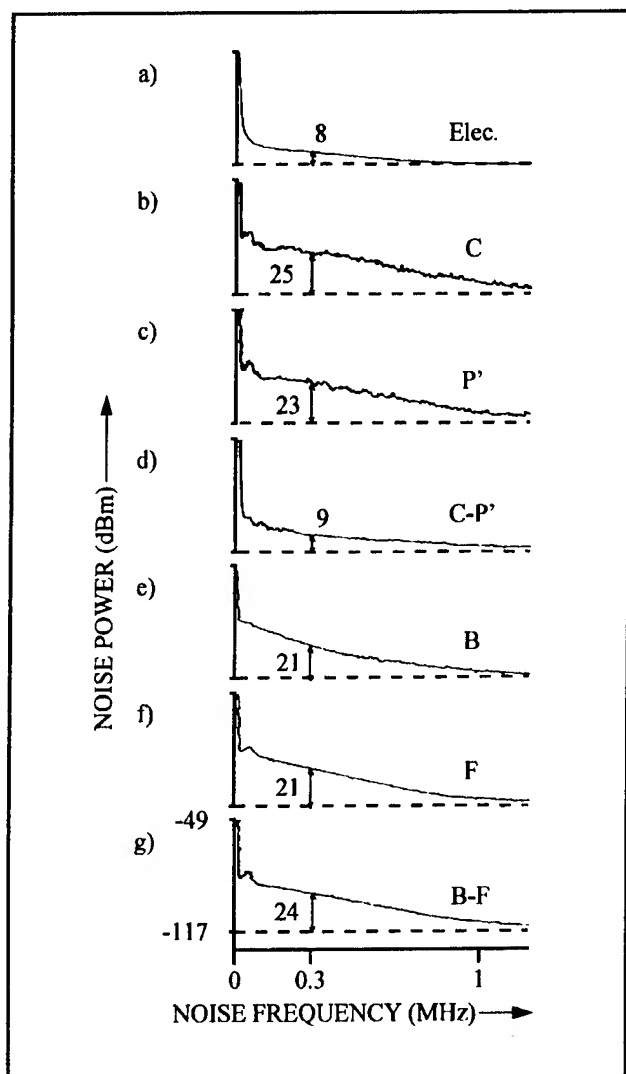


Figure 5. Noise versus frequency for a variety of conditions. The background noise level is marked with a dotted line (-117 dBm), and the noise at 300 kHz is tracked throughout. (a) Electronic noise of a pair of crossed photodiodes (the current produced in one photodiode opposes the current produced in the other). (b) The conjugate noise (one photodiode blocked). (c) The amplified probe noise (one photodiode blocked). (d) Subtraction of the conjugate and the amplified probe. Note that the noise is nearly equivalent to the electronic noise level. (e) Backward noise after it emerges from the four-wave mixer and attenuated to the power of the conjugate (one photodiode blocked). (f) Forward noise after it emerges from the four-wave mixer and attenuated to the power of the amplified probe (one photodiode blocked). (g) Subtraction of the backward and forward beams. Note that there is no noise reduction indicating that the backward and forward beam are not phase correlated.

1.2 Unbounded Cooling Force in Traveling Waves Excitation of a Four-Level System

Sponsor

U.S. Navy - Office of Naval Research
Grant N0014-91-J-1808

We have found a novel type of cooling mechanism using traveling wave excitation of a four-level system. This process yields cooling forces much larger than the spontaneous force, without intensity gradients. The force scales linearly with the Rabi frequency, as long as the laser detunings are also varied proportionately, and may be of use in open system (molecular) cooling. Unlike stimulated mechanisms of cooling, this process does not suffer from Doppleron resonances that heat other atoms while cooling only one velocity group.

In a two-level system under traveling wave excitation, the cooling force is bounded by the spontaneous force, given by the product of the photon momentum and the excited state decay rate. This is because the force in such a scheme originates from absorption of directed photons followed by emission of spontaneous photons in random directions. In the case of a standing wave excitation, this limit no longer holds. The atoms can in principle absorb photons from one direction, while emitting coherent photons in the other direction via stimulated emission. This process, known as stimulated cooling, requires symmetry breaking, leading to effects such as Doppleron cooling, which occur for specific combinations of velocities, Rabi frequencies, and detunings.¹⁰ For small variations in velocity, for example, the force can turn from heating to cooling. As a result, the standing wave cooling is not convenient for slowing down a thermal beam with a broad velocity spread.

It is generally held that the stimulated cooling requires the presence of intensity gradients. However, we have found a system where the stimulated redistribution of photons can occur even without the presence of any intensity gradients. Specifically, this scheme employs a four-level system, with two ground and two excited levels (the double Λ system). We find that the cooling force obeys very simple resonance conditions, and does not change sign over a large range of velocities. Moreover, this force scales linearly with the Rabi frequency, without bound (in the limit of rotating wave and electric dipole approximations). There-

¹⁰ M.G. Prentiss and A. Cable, *Phys. Rev. Lett.* 62: 1354 (1989).

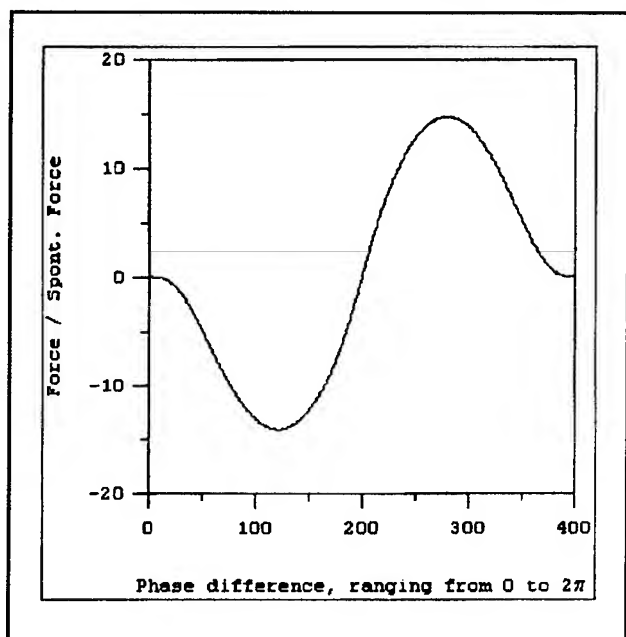


Figure 6. The resonant cooling force as a function of the closed loop phase, ϕ .

fore, this process may be used to provide very strong cooling over a short period of time and over a broad range of velocities. These properties makes this scheme a very attractive candidate for cooling open systems such as molecules.

Figure 1 shows schematically the level structure and the fields. Here, the fields F and P are traveling waves, propagating in the z direction, while B and C are traveling waves propagating in the opposite direction. The fields are assumed to have each the same Rabi frequency, g , and can be detuned independently, with the constraint (the so-called closed loop condition) that the two-photon detuning, Δ , (of F and P) matches the same for B and C. In addition, we limit ourselves to the condition that the average detuning, δ , of F and P is one-third that of B and C. One other parameter of interest is the (time independent) phase difference between the beat of F and P and that of B and C, denoted by ϕ . We find that when $\Delta=0$, $g=4\delta$, and $\phi = \pi/2$, the force is much larger than the spontaneous force, as illustrated in figure 6. Note that the force varies sinusoidally with ϕ . Moreover, if the Rabi frequencies and detunings are scanned while maintaining this ratio, the peak force scales linearly with the Rabi frequency, as shown in figure 7.

Briefly, this force results from a properly phased, symmetry-broken cycling of the atoms through the closed loop, with consecutive absorptions and stimulated emissions. Note that this force is fundamentally different from force rectification studied earlier under standing wave excitations of two¹¹ or three¹² level atoms. The rectified forces were only valid for zero velocity atoms, and are useful primarily for deflection. In contrast, the force considered here can be useful in deflection as well as cooling. For the later, one would have to chirp the frequencies and the intensities simultaneously, thus slowing down atoms, starting from the high velocity group, and sweeping all the atoms to a low velocity, much like the Zeeman slower, but much faster.

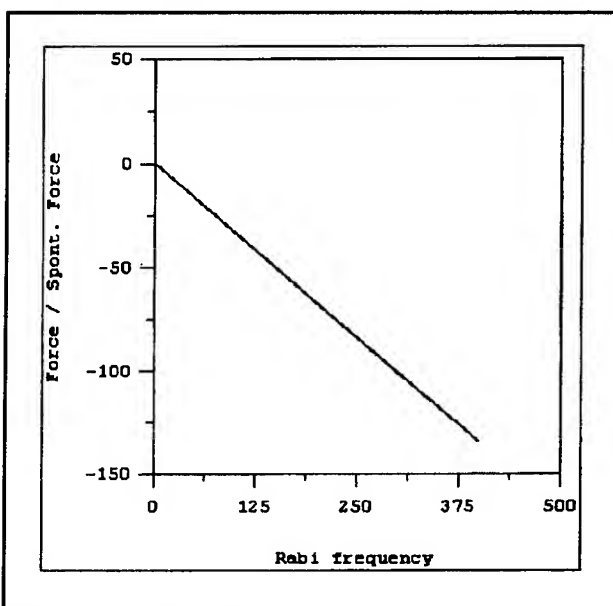


Figure 7. The maximum resonant cooling force for $\phi = \pi/2$, as a function of Rabi frequency, while the resonance condition is maintained.

1.3 Evidence of Collective Atomic Recoil Lasing in a High-Density Sodium Atomic Beam

We have observed that as atomic density is increased, strongly driven sodium atoms in a Doppler broadened system exhibit simultaneous gain and grating formation in the presence of a strong probe beam. This grating is properly oriented to deflect light from the pump into the probe, and is strong enough to significantly influence the

¹¹ R. Grimm, Y.B. Ovchinnikov, A.I. Sidorov, and V.S. Letokhov, *Phys. Rev. Lett.* 65: 1415 (1990).

¹² P.R. Hemmer, M.S. Shahriar, M.G. Prentiss, D.P. Katz, K. Berggren, J. Mervis, and N.P. Bigelow, *Phys. Rev. Lett.* 68: 3148 (1992).

probe gain. This positive feedback between the probe gain and the grating formation leads to exponential growth of the probe for a density exceeding a critical value. This observation is an apparent evidence of collective atomic recoil lasing (CARL),¹³ a process which may lead to coherent X-ray generation from relativistic particle beams using a low frequency pump.

Applications such as coherent X-rays generation from relativistic particle beams require the efficient direction reversal of coherent radiation. Currently, this is accomplished by back-diffraction from relatively weak bunched-particle gratings. However, it has been suggested¹³ that the efficiency of such gratings can be greatly enhanced by using internal states of the particles. Specifically, the CARL process proposes using the optical forces generated by the pump and probe beams to enhance bunching and therefore diffraction efficiency, which in turn amplifies the probe, creating positive feedback. Here, we show that efficient atomic gratings are formed in Doppler broadened sodium when a pump and relatively strong probe are present, and that at high atomic densities, these gratings can have a significant effect on the observed gain.

The experimental setup for observing the grating and its effect on the gain is shown schematically in figure 8. The Doppler broadened sodium source is an uncollimated atomic beam, excited immediately at the output of a 5 mm diameter effusive multi-collimator. This multi-collimator consists of a length of ridged nickel foil, rolled into a circular shape. The average channel is about $50\ \mu\text{m} \times 250\ \mu\text{m}$ with a length of 1.3 cm. At the oven temperatures used (from 300°C to 500°C), the mean free path of sodium is generally longer than the channel width, but shorter than its length. Under these conditions, the atom density in the beam is a fixed fraction of that in the oven, but the beam transverse velocity distribution is significantly broadened, compared to an ideal effusive multi-collimator.¹⁴ The measured Doppler width of the beam (at low oven temperature) is about 1.0 GHz, which is to be compared with the 1.5 GHz Doppler width of sodium vapor. The atomic density in the beam is estimated at about 110 times smaller than that in the oven,

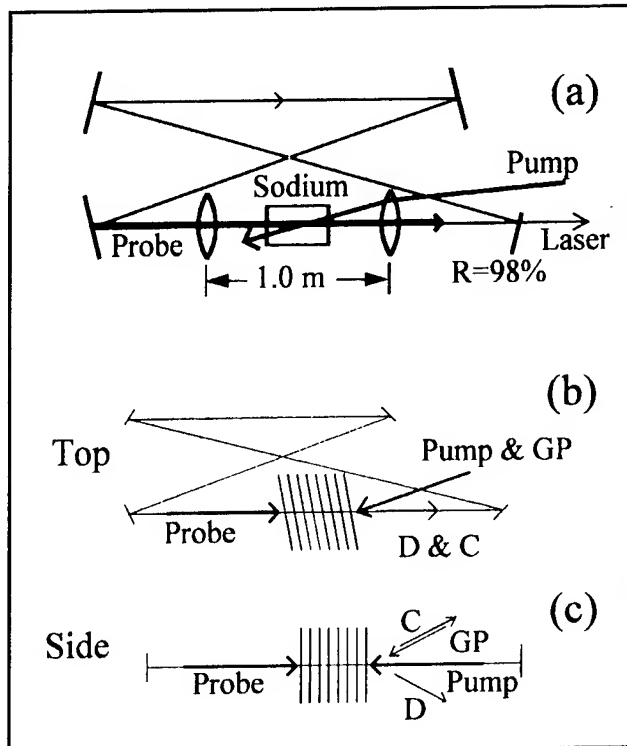


Figure 8. Schematic of experimental setup. (a) Setup for generating a strong back-propagating probe beam using a ring laser. (b) and (c) Top and side view, respectively, of setup for measuring grating diffraction efficiency.

based on geometric considerations and low temperature absorption measurements. The back-propagating probe beam is either supplied by a separate dye laser or else is generated by a back-propagating oscillation in a ring resonator which uses the sodium as an active medium.¹⁵ This second case is shown in figure 8a. Both pump and probe are focused to about 0.3 mm (FWHM) at the interaction region, using two 50 cm focal length lenses. The pump and probe are aligned about 10 mrad away from exactly counter-propagating for experimental convenience. Pump beam intensities range from $100\ \text{W/cm}^2$ to $1000\ \text{W/cm}^2$, while the (intra-cavity) probe beam is up to 12 percent as intense as the pump. Typically, the pump is circularly polarized and is resonant with the sodium D_2 line.

¹³ R. Bonifacio, L. DeSalvo, L. M. Narducci, and E.J. D'Angelo, "Exponential Gain and Self-bunching in a Collective Atomic Recoil Laser," *Phys. Rev. A* 50: 1716-24 (1994).

¹⁴ H. Pauly, "Other Low-energy Beam Sources," in *Atomic and Molecular Beam Methods*, Vol. 1, Ed. G. Scoles (New York: Oxford University Press, 1988) pp. 83-123.

¹⁵ J.S. Kane, P.R. Hemmer, J. Donoghue, and M. Cronin-Golomb, "Bidirectional Oscillation and Phase Conjugation in a Sodium-vapor Ring Resonator," in *Quantum Electronics and Laser Science Conference*, 1992 OSA Technical Digest Series, Vol. 13 (Washington, DC: Optical Society of America, 1992) pp. 272-3; P.R. Hemmer, D.P. Katz, N.P. Bigelow, M.S. Shahriar, R. Bonifacio, and L. DeSalvo, *Phys. Rev. Lett.*, forthcoming.

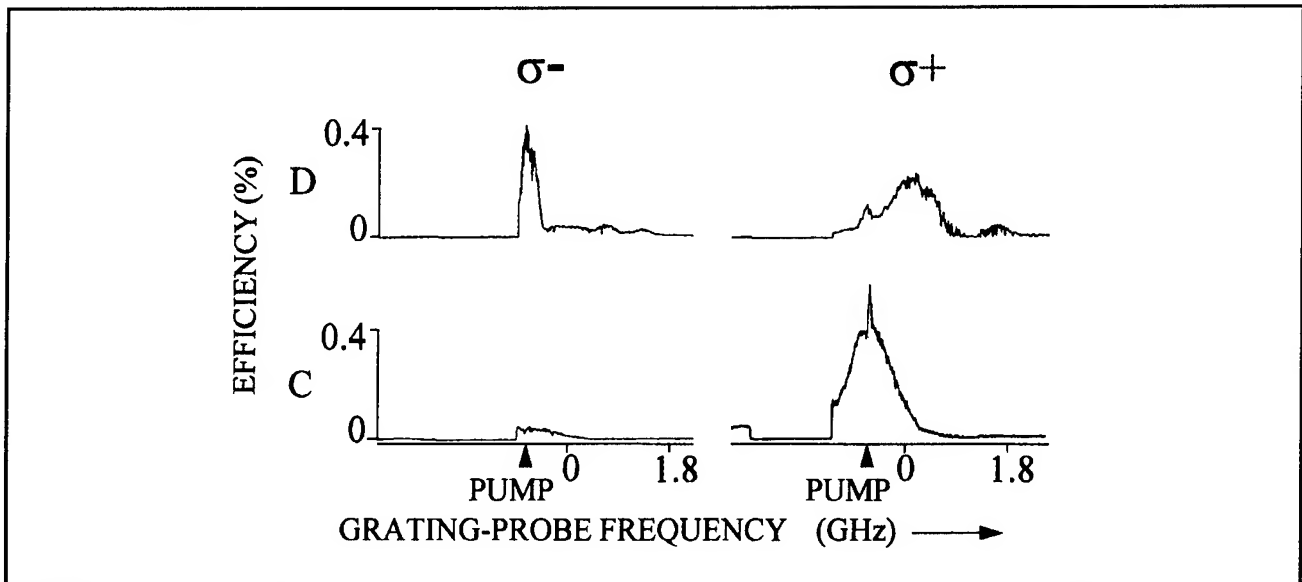


Figure 9. Grating diffraction (denoted by D) and conjugate (denoted by C) efficiencies versus grating-probe frequency. Here, σ^+ denotes a grating-probe with (circular) polarization identical to that of the pump, and σ^- denotes the orthogonal grating-probe polarization. The efficiencies are referenced to the grating-probe input power.

To observe the grating, an additional laser beam, called the grating-probe, is also focused into the interaction region, as shown in figure 8b and 8c. This grating-probe beam is typically from 4 percent to 25 percent as intense as the pump and is incident at an angle of about 10 mrad out of the pump/probe plane, but is approximately co-propagating with the pump when projected into this plane. The backscattered (or diffracted) portion of the grating-probe beam exits the interaction region in the same out-of-plane direction as the grating-probe, but the same in-plane direction as the back-propagating probe, as shown. Under some conditions, a phase conjugate beam is also observed, which is exactly counter-propagating with the grating-probe beam in all planes.

Typical diffraction and conjugate efficiencies as a function of grating-probe frequency and polarization are shown in figure 9. Here, the pump and back-propagating (intra-cavity) probe frequencies are held fixed. To accomplish this, the grating-probe is derived from an independent dye laser. The column labeled σ^+ in the figure denotes a (circular) grating-probe polarization which is identical to that of the pump, whereas σ^- denotes the orthogonal grating-probe polarization. As shown, in the case of a σ^- grating-probe, a diffracted beam is observed when the grating-probe is tuned to within 250 MHz (FWHM) of the pump frequency. For comparison, the calculated pump Rabi frequency is about 1.5 GHz, which is based on an input pump intensity of 280 W/cm² and the matrix elements for the $F = 2, m_F = 2 \leftrightarrow F = 3, m_F = 3$ sodium transition. For the data in figure 9, the (intra-cavity)

back-propagating probe intensity is about 0.8 W/cm² (or 0.3 percent of the pump), the grating-probe intensity is 10 W/cm², and the peak diffracted beam intensity is about 40 mW/cm² (or 0.4 percent of the grating-probe).

At peak diffraction efficiency, the intra-cavity, back-propagating probe is observed to be a factor of 2 weaker (not shown), which signifies a reduction in gain. To determine whether this gain reduction is due to perturbation of the grating or optical pumping, the experiment is repeated with the grating-probe tuned to the sodium D_1 transition, but all other conditions identical. Since the D_1 transition is 0.5 THz away from the D_2 transition, the grating-probe will no longer be Bragg matched to diffract from the grating. However, the optical pumping rate out of the $F=2, m_F=2$ ground state sublevel is about 2 times faster for σ^- excitation on D_1 , compared to D_2 , so that optical pumping effects are enhanced. When the grating-probe is tuned to be resonant with the same velocity group as the pump beam (which is analogous to peak diffraction condition in figure 9, σ^- case), no diffracted beam or intra-cavity probe attenuation are observed.

For identically (σ^+) polarized grating-probe and pump beams, a conjugate is observed when the grating-probe frequency is within 800 MHz (FWHM) of the pump frequency, as shown in figure 9. Diffraction is also observed, but its peak is a factor of 2 smaller than in the σ^- case and corresponds to a blue-shifted grating-probe. Attenuation of the back-propagating intra-cavity probe is also less (about 30 percent at peak diffraction). The 800 MHz linewidth of conjugate (and diffraction) efficien-

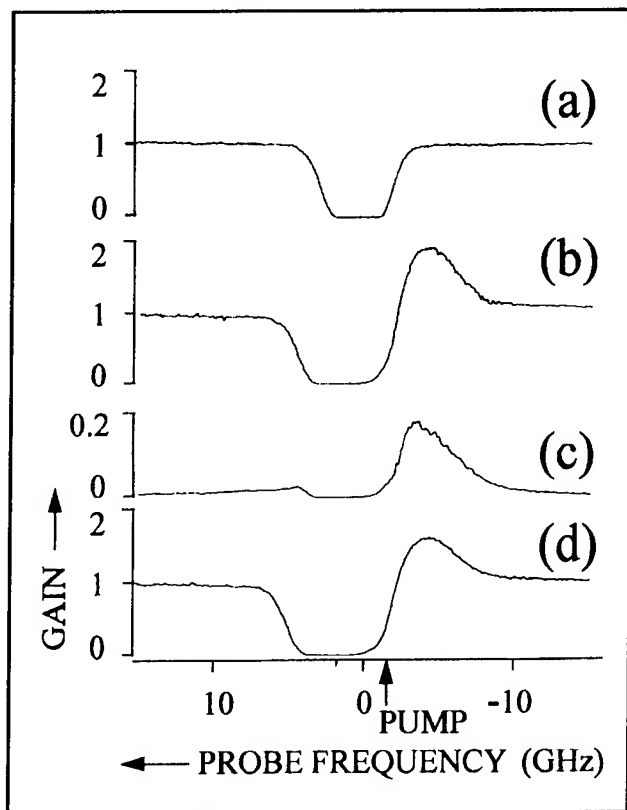


Figure 10. Gain versus back-propagating probe frequency. (a) Probe absorption in the absence of pump beams. (b) and (d) Probe gain spectrum in the absence and presence of a grating-probe, respectively. (c) Diffracted beam corresponding to (d).

cies in the σ^+ case is about 3.2 times the diffraction efficiency linewidth in the σ^- case. The reason for this is not clear. However, it is interesting to note that the ratio of summed optical transition probabilities for σ^+ versus σ^- transitions, starting from the $F=2$, $m_F=2$ sodium ground sublevel, is 3:1. Finally, the narrow spike in conjugate efficiency occurs when the pump and grating-probe frequency separation is comparable to the two-laser beat linewidth.

Figure 10 shows more clearly, the competition between gain and grating-probe diffraction. Here, figure 10a shows the probe absorption in the absence of a pump, figure 10b and 10d show the probe gain spectrum without and with the grating-probe, respectively, and figure 10c shows the diffraction efficiency. Clearly, the gain is reduced when light is diffracted from the grating. Moreover, the loss in output probe power is approximately equal to the power in the diffracted beam. For this

data, the ring cavity is blocked and the back-propagating probe beam derived from a second dye laser, which allows the probe frequency to be independently scanned. The grating-probe is derived from the same dye laser as the pump, but is orthogonally (σ^-) polarized. In order to achieve a high signal to noise ratio for this data, the gain is increased by increasing the pump intensity. Since the maximum dye laser output power is 300 mW, this is accomplished by replacing the 50 cm lenses by 30 cm lenses, separated by 60 cm. This reduces the pump (and probe) spot sizes to about 0.18 mm. The pump intensity is 800 W/cm², the probe intensity is 15 W/cm², and the grating-probe is 200 W/cm². Finally, with the shorter focal length lenses, it is found that the grating-probe and diffracted beams must be less than 5 mrad away from colinear to achieve high efficiencies.

Other measurements made on the diffracted beam include frequency, polarization, response time, and sensitivity probe beam propagation direction. When the grating-probe is derived from the pump beams, and therefore has exactly the same frequency, the diffracted beam is at the frequency as the probe. This is also true when the probe is generated by laser oscillation, except that in this case they both have the same spectrum, since the lasing is multi-mode. The rise time of the diffracted beam (when the back-propagating probe is chopped) is less than 20 nsec, the measurement being limited by the acousto-optic shutter response time. A grating is also observed when the back-propagating probe replaced by a forward-propagating one. Moreover, diffracting off this forward-scattering grating reduces the forward probe gain, in analogy with the back-propagating probe case. However, forward-propagating probe, measurements are complicated by forward-scattering and self-defocusing of the pump beam, and will not be discussed further.

The competition between gain and grating-probe diffraction is very sensitive to atomic density. This is shown graphically in figure 11. Here, figure 11b shows the back-propagating probe gain as a function of atomic density, with and without the grating-probe present. Figure 11a shows the diffracted beam power, referenced to the input probe power. For these plots, the atomic density in the interaction region is estimated by dividing the calculated oven density (at each temperature) by the factor of 110 discussed earlier. Clearly, as atomic density is increased, the grating can have a significant effect on the gain.

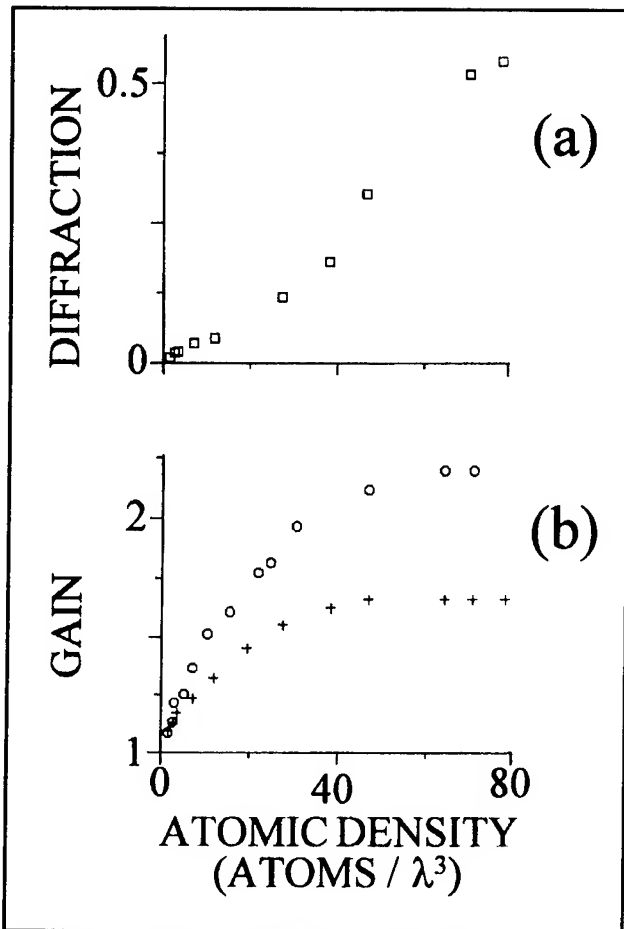


Figure 11. Peak gain and diffraction efficiency versus atomic density (units of atoms/ λ^3). (a) Diffraction efficiency in units of input back-propagating probe power. (b) Back-propagating probe gain in the absence (circles) and presence (+s) of a grating-probe beam.

In summary, we have shown that efficient gratings can be formed in high density sodium in the presence of a pump and a strong probe. We also show that this grating can significantly influence the probe gain. This interdependence of gain and gratings is one of the necessary conditions for effects such as CARL. Finally, it is interesting to note that the atomic density for which this interdependence becomes significant is about 40 atoms/ λ^3 . This is close to the CARL threshold density of 100 atoms/ λ^3 , which is calculated by equating the CARL bandwidth¹³ of the relevant sodium transition to the measured inhomogeneous linewidth.

1.4 Applications of Porous Glass Based Thick Holograms for Optical Data Storage and WDM Demultiplexing

Sponsor

Ballistic Missile Defense Organization
Grant NG0921-94-C-0101

We have observed ultra-high Bragg selectivity in a new type of thick hologram, made using a novel material called Photopolymer with Diffusion Amplification (PDA). This material is very stable against temperature variation and does not suffer from differential shrinkage during development. As a result, holograms can be made as thick as 1 cm, which is nearly two orders of magnitude thicker than the thickest photopolymer based holograms currently in use. This opens up the possibility of using these holograms for enhancing the volume holographic data storage density by at least one order of magnitude. In addition, we can use a stack of these holograms to build an individual channel tunable demultiplexer for a wavelength division multiplexing (WDM) network.

Dynamic holograms, commonly known as phase conjugators, have flourished in many areas such as image processing, photon echo data storage, rectification of wavefront distortion, stable laser cavity designs, and so on. Static holograms, in comparison, have been somewhat limited in applications. One reason for this limitation is that it is difficult to produce thick static holograms. Consider, for example, a hologram made of dichromated gelatins. Typically, the gelatin is first deposited on a substrate of glass, followed by exposure to the image and write beams. During the post-exposure processing, the gelatin suffers from nonuniform shrinkage, which limits hologram thickness to no more than 100 microns. Recently, we, in collaboration with a company (Northeast Photosciences, Hollis, NH) and a group of scientists in Russia, have developed technologies to circumvent this problem, and have been able to produce inexpensive holograms that are a few millimeters thick, with a very high degree of Bragg selectivity.¹⁶

The advantages of thick holograms are numerous.¹⁷ For example, they possess high diffraction efficiency, they allow reconstruction of holograms from a fragment of a whole hologram (associative memory), and they are characterized by high

¹⁶ J.E. Ludman, J.R. Riccobono, H.J. Caulfield, J.M. Fournier, I.V. Semenova, N.O. Reinhand, P.R. Hemmer, and S.M. Shahriar, in *Proceedings of IS and T Conference*, San Jose, California, February 1995.

¹⁷ H. Kogelnik, *Bell Syst. Tech. J.* 48: 2909 (1969).

angular and spectral selectivity, which allow for recording multiple holograms at the same location. As such, these holograms are useful for enhancement of holographic storage density. Holograms with a thickness of $100\text{ }\mu\text{m}$ are currently used in commercially available volume holographic optical storage units.¹⁸ A 1 cm thick hologram will enhance the storage density of this proven technology by as much as two orders of magnitude.

Another very important application of thick holograms is in the development of individual channel tunable filters for a WDM network. Wavelength division demultiplexers are key elements in planned all-optical terabit computer networks linking supercomputers. Next generation wavelength multiplexers are expected to consist of laser arrays of up to 10 elements with precise 2 nm wavelength increments. The multiplexing operation is currently performed by waveguide combiners, even though these are somewhat lossy, because they are tolerant to wavelength errors. Demultiplexing is currently performed by curved diffraction gratings which can be fabricated either mechanically or holographically (thin holograms). Although adequate wavelength selectivity can be achieved with such devices, they are not tolerant to offsets or drifts in the operating wavelengths of the laser sources. While it is possible to compensate for wavelength errors common to all lasers in an array by temperature tuning, channel to channel offsets cannot be easily compensated for in curved grating structures. However, manufacturing tolerances or thermal crosstalk can result in channel to channel drifts on the order of 1 nm or more in a large, ten-element array. Thermal crosstalk is a potentially more serious problem since it occurs in real time, in response to individual lasers being turned on and off. Clearly, a device which is capable of compensating for channel to channel wavelength errors in real time while still maintaining high efficiency and the necessary frequency selectivity would be ideal for both multiplexing and demultiplexing operations.

It is well known that thick holograms can have sub-nanometer wavelength selectivity.¹⁹ For example, at a design wavelength of $1.5\text{ }\mu\text{m}$ a 2 mm thick hologram has a wavelength selectivity of better than 1 nm (Much more precise selectivity can be achieved using near-backward reflection geometry; however, 1 nm selectivity is typically warranted for WDM applications in order to allow signal modulation). The problem arises when it is desired to

simultaneously diffract more than one wavelength. Because of Bragg selectivity, multiple beam diffraction requires multiple holograms. If multiple exposures of a single substrate are used to write the required holograms, the diffraction efficiency for each individual hologram decreases rapidly as more holograms are written. The solution is therefore to use multiple substrates. To simultaneously diffract multiple beams, the individual holographic substrates are stacked. Since thick holograms that are not Bragg matched have very small diffraction efficiency, the light passes through most of the stack with minimal losses and is diffracted with high efficiency from the Bragg matched hologram. Typical efficiencies of 2 mm thick, phase holograms are about 95 percent for light near $1.5\text{ }\mu\text{m}$ optical wavelength. In contrast, non-Bragg matched diffraction is theoretically less than 5 percent on the strongest side-mode, so that much of the expected loss is due to incidental causes such as scattering in the substrate or surface reflections (which can be controlled by anti-reflection coatings). Thus, even a stack of 10 holograms would be expected to have an overall efficiency of greater than 50 percent. Of course, for a very large number of holograms (greater than 10 or 20), the stack concept becomes less practical, due to low overall diffraction efficiency and large physical size. However, most near term WDM systems do not anticipate using more than 10 wavelengths (limited by the required bandwidth for each channel, and the bandwidth of the Erbium doped fiber amplifier) and hence the stack concept becomes very competitive.

The basic setup for wavelength demultiplexing using a stack of thick holograms is illustrated figure 12. As shown, the output from an optical fiber is collimated with a microlens and directed through the stack. In each case, the diffracted light is collected by a lens and focused onto a single element of a photodetector array. To allow real time adjustment of the Bragg angle, each hologram is mounted on a separate flexure mount with a piezoelectric actuator. A 2 mm sized mount with an inexpensive, commercially available actuator capable of $1\text{ }\mu\text{m}$ displacement is adequate to provide the maximum anticipated 1 mrad tilt angle. Since the piezoelectric element is charge driven, it consumes essentially no power in the steady state. This sample device, consisting of eight holograms, would have an overall physical length of less than 2 cm.

¹⁸ H. Yu, S. Li, and D. Psaltis, *J. Opt. Soc. Amer. A* 12: 1902 (1995).

¹⁹ F.H. Mok, *Opt. Lett.* 18: 915 (1993).

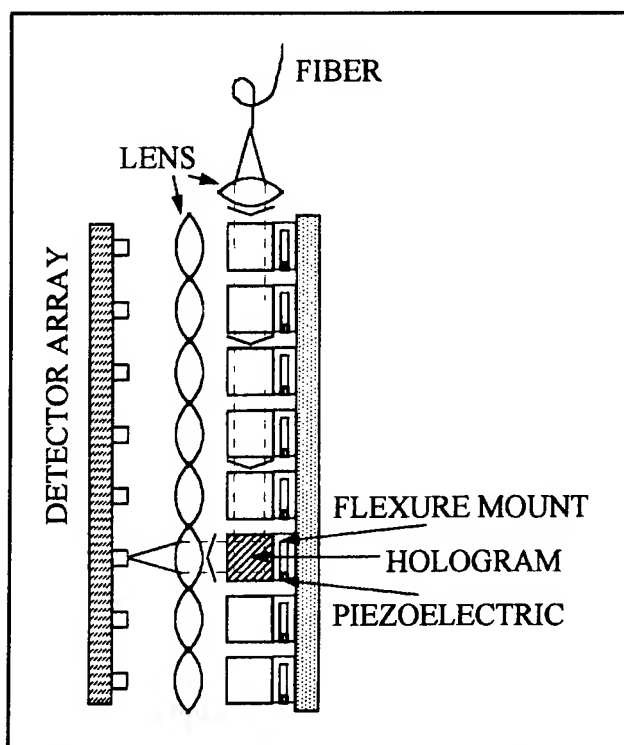


Figure 12. Schematic of an 8-wavelength fiber demultiplexer. Each wavelength is diffracted by only one hologram as illustrated.

With our collaborators in Russia, we have recently developed two novel materials for thick holographic data storage as well as WDM demultiplexing. These are (1) a thick porous glass substrate which can be embedded with a host of materials such as photopolymers or dichromated gelatin, and (2) a thick PolyMethylMethAcrylate (PMMA) based system called Photopolymer with Diffusion Amplification (PDA).

Consider first the porous glass system. A typical unit is a quartz porous glass matrix containing pores of about 10 to 30 nm in size. These pores are interconnected with a continuous network of capillaries. The photo-reactive materials (such as dichromated gelatin or a dye solution) can be introduced into the pores, aided by the strong capillary force (about 20 to 30 atm for 20 nm diameter capillaries). After the suspension liquid is dried off, the active molecules form a coating on the inner walls of the pores. The advantages of this substrate over amorphous polymer surface are numerous: (1) The porous glass is made of quartz, and can have a very high quality surface, and (2) The structure is very rigid, robust against thermal

stresses and fluctuations, and virtually immune to differential shrinkage. As a result, it should easily be possible to make high quality holograms as thick as 1 cm.

In collaboration with scientists from Russia, we have already demonstrated 1 and 2 mm thick holograms in porous glass, with dichromated gelatin as the embedded photo-reactive material. We have written plane wave fringes in order to use these holograms as nonspatial filters of laser noise. The observed Bragg selectivity and efficiency are consistent with the theory for thick holograms.¹⁷ While this material has the distinct advantage that it does not suffer from differential shrinkage during the post-exposure development of the holograms, there is room for further improvement in performance. For example, the density of pores in this glass are not uniform over the whole volume. This limits the quality of the output beam in applications such as Nonspatial Filtering. Recently, we have identified a new material, also developed by the same institute in Russia, that out-performs the porous glass in general, and solves the problem of nonuniformity in particular.²⁰

This material, known as PDA, consists of phenanthraquinone embedded in PMMA. This medium uses the novel principle of diffusion amplification of holograms on polymeric recording media. Briefly, photoexposure of this system results in writing of two out-of-phase periodic structures that partially compensate each other. One of these is formed by a concentration distribution of chromophore groups combined into macromolecules, while the other is formed by free molecules. As a result of diffusion of the free molecules, the corresponding grating degrades, and the resulting grating is amplified *without additional processing*. The surviving grating is stored in macromolecules that do not diffuse.

As stated above, the PDA thick holograms compare favorably with thick holograms made using porous glass. To start with, due to the immobility of the macromolecules that hold the final hologram, the PDA thick holograms are as robust as the porous glass ones. However, the PDA holograms do not suffer from any systematic variation in the concentration of the macromolecules. As a result, light diffracted from a plane wave PDA hologram shows a single Gaussian peak. In contrast, the density of pores in the porous glass is not uniform over the entire volume. Therefore, the diffracted spot in this

²⁰ A.V. Veniaminov, V.F. Goncharov, and A.P. Popov, *Opt. Spectrosc. (USSR)* 70: 505 (1991); A.V. Veniaminov et al., *Opt. Spectrosc. (USSR)* 60: 87(1991).

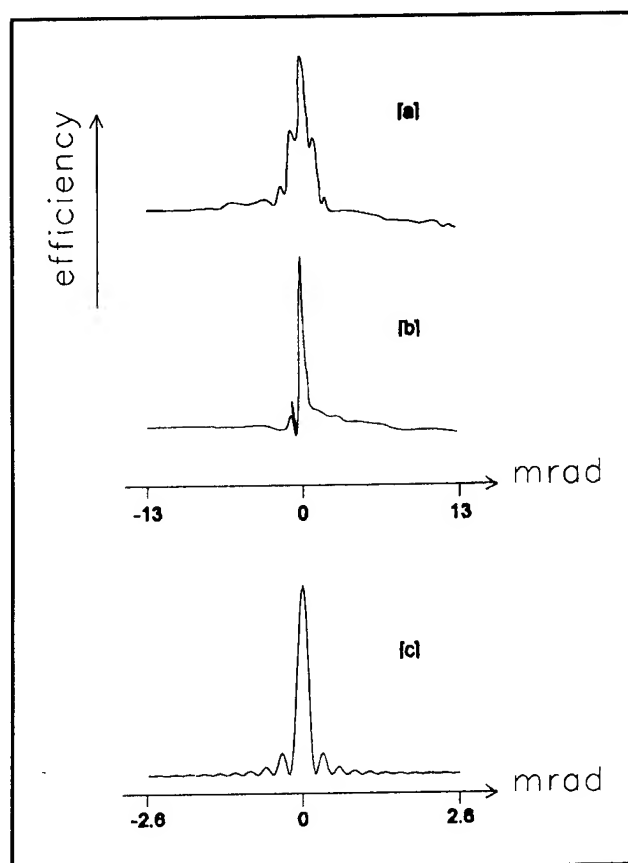


Figure 13. Experimentally observed angular selectivity of thick holograms, for (a) photopolymer embedded in porous glass (b) PDA. The theoretical plot (c) is for an ideal thick hologram, illuminated by a plane wave (note the difference in scale). When the Gaussian profiles and the corresponding divergence of the read and write beams are taken into account, the small sidelobes in (c) wash out, agreeing well with the output of PDA. The strong sidelobes in (b) represent the Fourier transform of the nonuniformity of pore densities. The sharp but small feature in (b) is an artifact, and the efficiency in each plot is normalized.

case shows additional sidebands, corresponding to the Fourier transform of the pore density nonuniformity. We have observed this distinction experimentally¹⁶ as illustrated in figure 13. As can be seen, the diffracted spot of the PDA thick hologram show a single peak (ignoring the experimental glitch), while the diffracted spot of the porous glass thick hologram has strong side-lobes. The observed Bragg selectivity of 1 mrad, along with the elimination of sidelobes, makes PDA very suitable for both thick holographic data storage and for WDM demultiplexing.

1.5 Distributed Fiberoptic Sensor for Quench Detection in Superconducting Tokamak Magnets

Sponsor

MIT Plasma Fusion Center

The next generation magnetic confinement fusion machines (tokamaks) will use superconducting, rather than conventional, magnets for confining and heating the plasmas. These magnets can be longer than a kilometer and typically are cooled using a forced flow of liquid helium through the conduit which surrounds the superconducting cable. The detection of a quench, i.e., a section of the magnet going normal, is very important since the local heating due to an undetected quench could lead to permanent magnet damage. Thus, a quick and reliable way of detecting such quenches is very important.

One novel method for detecting quenches in such a magnet is to include an optical fiber with the superconducting cable inside the conduit. Since the optical fiber is in close contact with the cable, any local heating of the cable also causes heating of the fiber, which can be detected interferometrically.

This technique has been successfully demonstrated in laboratory scale experiments²¹ and an experiment with a 100 meter cable is currently underway. This experiment, called ITER, is a part of an international scientific collaboration on fusion research between the United States, Japan, the European Union, and the Russian Federation. The test cable was made in Japan; the sensors were provided by the U.S.; and final preparations are underway for testing in Switzerland.

For this latest experiment, techniques had to be developed for embedding the fiber inside the superconducting cable and withstanding the numerous manufacturing steps required to build the sample, including a heat treatment with a temperature above 600° C for over 200 hours, and also cooling to 4 K during the experiment.

In order to survive the heat treatment, single mode optical fiber with a copper jacket instead of a conventional plastic jacket was selected. For additional mechanical protection, this fiber was covered with a

²¹ S. Pourrahimi, W.C. Guss, J.V. Minervini, D.B. Montgomery, N.T. Pierce, J.H. Schultz, S.P. Smith, and S. Ezekiel, "U.S. Contributions to the Development and Calibration of Quench Detectors for the ITER QUELL," *Proceedings of the Applied Superconductivity Conference*, Boston, Massachusetts, October 17-20, 1994.

glass braid and then encased in a stainless steel capillary tube.

Using this arrangement the optical fiber has survived the entire manufacturing process including sample cabling, insertion into the conduit, compaction, winding and heat treatment. Further, the fiber has now survived the cooling of the sample to liquid helium temperatures in preparation for testing.

1.6 Demonstration of an Optical Mass Flow Meter

Sponsor

MIT Plasma Fusion Center

The accurate measurement of liquid helium flow is important in a number of experiments and applications involving superconducting magnets. Conventional measurement techniques, such as venturis and orifice plates, have a number of drawbacks including a small dynamic range, constriction of the flow, poor bidirectional response, poor transient response and the need to measure several thermodynamic quantities to find the mass flow rate.

A new optical technique is being investigated for the measurement of the flow rate in an unseeded liquid helium flow. This technique has the advantages of a very large dynamic range, high accuracy, inherent bidirectionality, and virtually no constriction or disruption of the flow. In addition, the output of this sensor is proportional to the mass flow rate over a very wide range of thermodynamic conditions.²²

This flow measurement technique is based on the change in the speed of light in a moving medium, referred to as Fresnel drag. The relativistic calculation gives the speed of light in a moving medium, c_m , as,

$$c_m = \frac{c_0/n + v}{1 + v/nc_0} \approx \frac{c_0}{n} + \left(1 - \frac{1}{n^2}\right)v$$

where c_0 is the speed of light in vacuum, n is the index of refraction of the medium, and v is the velocity of the flow along the direction of light propagation. Thus, for a 1 m/s flow in liquid helium, the fractional optical path length change, $\Delta L/L$, resulting from this change in the speed of light is only about 2×10^{-10} .

One method of measuring this small effect uses a Sagnac interferometer, shown in figure 14.²³ Light from a source is coupled into a single mode optical fiber and is then split into two beams by a fiber coupler, C, and the beams are then sent in opposite directions around a fiber ring. The beams are then recombined using the same coupler C and the resulting intensity is measured using detector D. However, in contrast with either a Michelson or Mach-Zehnder interferometer, since both beams travel along the same path, any change in optical path length, for example due to fiber temperature changes or strain changes, is the same for both beams, i.e., the effect is reciprocal, and results in no change in the output intensity. Only effects which are nonreciprocal, i.e., different for the two directions of propagation, will result in a change in the output intensity.

Fresnel drag, as discussed above, is one such non-reciprocal effect. As shown schematically in figure 14, the light in the clockwise (CW) direction experiences a copropagating flow while the light in the counterclockwise (CCW) direction experiences a counterpropagating flow. Thus, the flow will cause a difference in the optical path length for the two beams, resulting in a phase shift between the two beams.

Figure 15 shows an initial demonstration of this flow meter using an unseeded water flow. For this experiment a 25 cm long flow cell was used with a maximum water flow velocity of about 27 cm/sec. As seen in the figure, this sensor detected both the magnitude and direction of the water flow. For comparison, the observed phase shift is equivalent to the phase shift expected for a 2.5 m/s flow of liquid helium in the same flow cell due to the much smaller index of refraction of liquid helium.

²² R.T. de Carvalho and J. Blake, "Slow-flow Measurements and Fluid Dynamics Analysis Using Fresnel Drag Effect," *Appl. Opt.* 33: 6073-6077 (1994); G.A. Sanders and S. Ezekiel, "Measurement of Fresnel Drag in Moving Media Using a Ring-Resonator Technique," *J. Opt. Soc. Am. B* 5: 674-678 (1988).

²³ J.L. Davis and S. Ezekiel, "Closed-loop, Low-noise Fiber-optic Rotation Sensor," *Opt. Lett.* 6: 505-508 (1981).

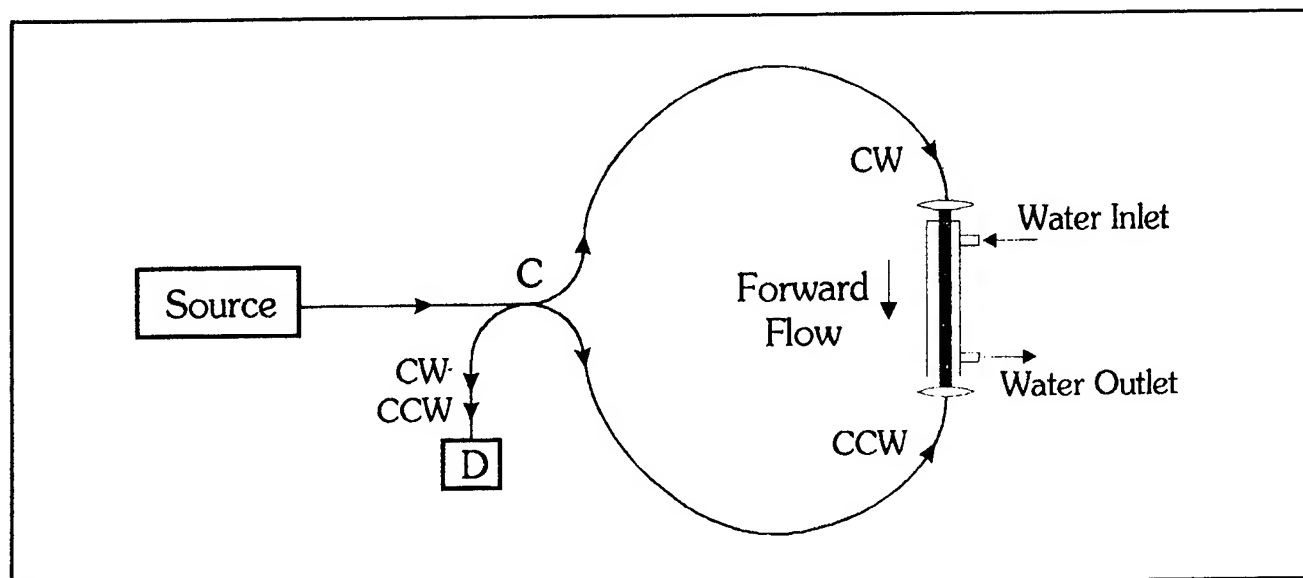


Figure 14.

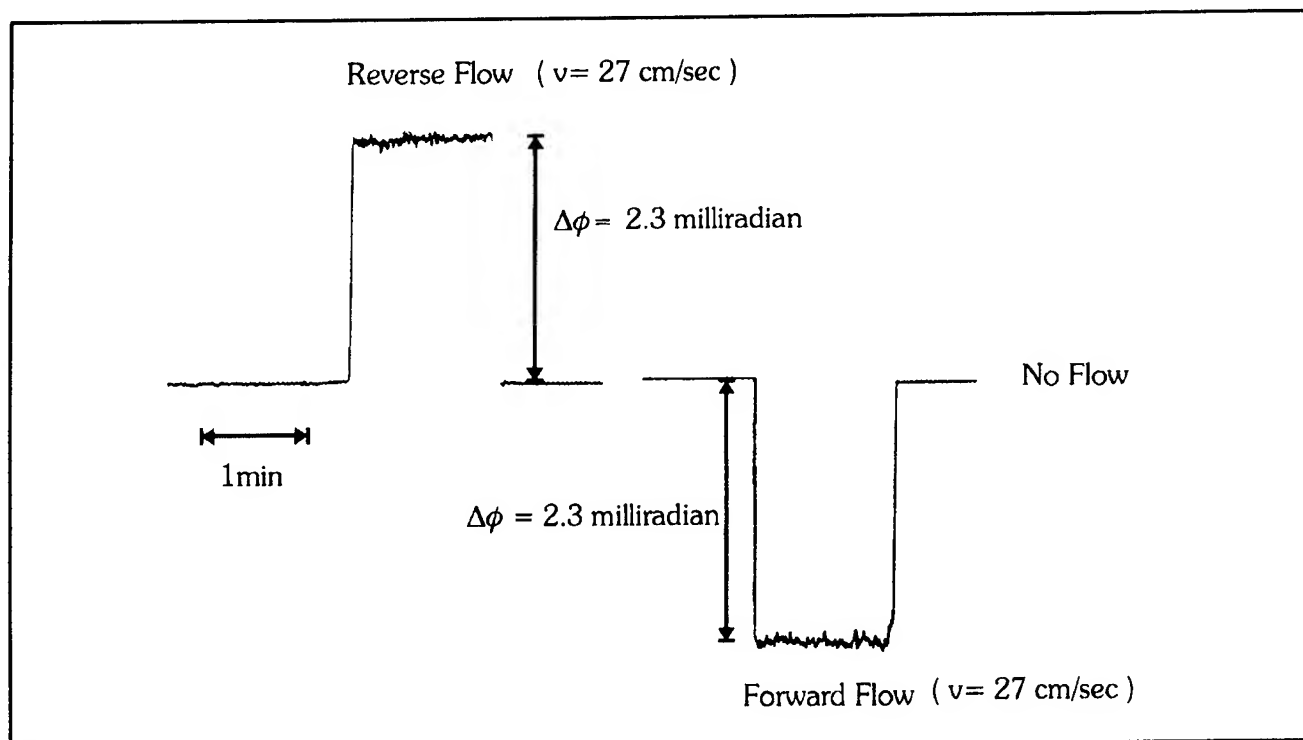


Figure 15.

An important feature of this flow meter is that the observed phase shift is not just proportional to the velocity of the flow, but, over a wide range of conditions, is proportional to the velocity of the medium times the density of the medium. Thus the sensor can be used to directly measure mass flow. The calculated mass flow rate sensitivity of this meter for a helium flow at a variety of pressures between

1 and 20 bars and a temperature range between 2 K and 1000 K only changes about ± 1 percent.

Thus, this sensor has the promise of yielding a mass flow output directly. In addition, it is inherently bidirectional, virtually immune to electromagnetic interference, insensitive to temperature and mechanical perturbations, as well as having a very high dynamic range and a very low sensitivity to magnetic fields.

Chapter 2. Basic Atomic Physics

Academic and Research Staff

Professor Daniel Kleppner, Professor David E. Pritchard, Professor Wolfgang Ketterle, Dr. Alan L. Lenef, Dr. Fred L. Palmer, Dr. Nicolaas J. van Druten

Visiting Scientists and Research Affiliates

Dr. John R. Brandenberger,¹ Dr. Theodore W. Ducas,² Dr. Marek L. Czachor,³ Dr. Bernd S. Rohwedder,⁴ Dr. H. Jörg Schmiedmayer⁵

Graduate Students

Michael R. Andrews, Michael P. Bradley, Michael S. Chapman, Michael W. Courtney, Kendall B. Davis, Joel C. DeVries, Frank DiFilippo, Dallin S. Durfee, Troy D. Hammond, Jeffrey R. Holley, Ljubomir M. Ilic, Hong Jiao, David A. Kokorowski, Dan M. Kurn, Robert I. Lutwak, Marc-O. Mewes, Daniel Ripin, Richard A. Rubenstein, Edward T. Smith, Neal W. Spellmeyer

Undergraduate Students

Ilya Entin, David Garrison, Philip M. Hinz, Everest W. Huang, Amrit R. Pant, Till P. Rosenband, Szymon M. Rusinkiewicz, Charles K. Sestok, Stanley H. Thompson, Peter S. Yesley

Technical and Support Staff

Carol A. Costa

2.1 Studies in Quantum Chaos: Rydberg Atoms in Strong Fields

Sponsors

Joint Services Electronics Program
Grant DAAH04-95-1-0038
National Science Foundation
Grant PHY 92-21489
U.S. Navy - Office of Naval Research
Grant N00014-90-J-1322

Project Staff

Michael W. Courtney, Hong Jiao, Neal W. Spellmeyer, Dr. John R. Brandenberger, Professor Daniel Kleppner

The goal of this research is to understand the structure and dynamics of atomic systems in external fields that are comparable to the interior fields and

in which the classical motion may be irregular. Rydberg atoms are central to this research because laboratory fields can be comparable to their atomic fields. In addition, the classical counterparts of these systems often undergo a transition from order to chaos as the field or energy is varied. Consequently, Rydberg atoms in applied fields provide a natural testing ground for studying the (1) connections between quantum mechanics and classical dynamics and (2) quantum behavior of chaotic systems. Our understanding of this system has been advanced by high resolution spectroscopy, development of efficient quantum calculations for atoms in electric and magnetic fields, and theoretical advances in classical dynamics.

Periodic orbit theory provides a unifying principle for relating a quantum spectrum to the periodic orbits of the corresponding classical system in the semi-classical limit. According to periodic orbit theory,

¹ Professor, Lawrence University, Appleton, Wisconsin.

² Professor, Physics Department, Wellesley College, Wellesley, Massachusetts.

³ Fulbright fellow, Warsaw, Poland.

⁴ Universidad Catolica de Chile.

⁵ Professor, Physics Department, Innsbruck University, Innsbruck, Austria.

each periodic orbit produces a sinusoidal modulation in the density of states. A spherical wave sent out from the origin will recur (overlap with the original outgoing wave) at times corresponding to the periods of the periodic orbits of the classical system. The magnitude of this overlap gives the strength of the spectrum modulation.

In our laboratory, we have recently studied lithium in parallel electric and magnetic fields.⁶ In this work, we were concerned with only the low action orbits and ignored differences between hydrogen and lithium caused by the lithium core.⁷

The Hamiltonian of hydrogen in parallel electric and magnetic fields is

$$H = \frac{1}{2} p^2 - \frac{1}{r} + \frac{1}{8} B^2 \rho^2 - Fz.$$

This can be rescaled using the substitutions $\tilde{r} = B^{2/3} r$, $\tilde{p} = B^{-1/3} p$, $\tilde{t} = Bt$, and $\tilde{f} = FB^{-4/3}$. The scaled Hamiltonian

$$\tilde{H} = \frac{1}{2} \tilde{p}^2 - \frac{1}{\tilde{r}} + \frac{1}{8} \tilde{\rho}^2 - \tilde{f}\tilde{z}$$

depends only on the scaled energy $\tilde{H} = \varepsilon = EB^{-2/3}$ and scaled field $\tilde{f} = FB^{-4/3}$. Consequently, the classical dynamics also depends only on these two parameters, not on E , F , and B separately. In the limit of large \tilde{f} , this is just the hydrogen Stark system for which the classical motion is regular. As \tilde{f} approaches zero, the system evolves into diamagnetic hydrogen, which is strongly chaotic for $\varepsilon > -0.1$. An examination of the system at intermediate values of \tilde{f} should reveal the system becoming chaotic. We experimentally measured the recurrence spectrum at a scaled energy of $\varepsilon = 0$. At this energy, the system is in the continuum and the motion is unbound.

The scaled action of a particular closed orbit, $\tilde{S}_k = B^{1/3} S_k$, depends only on ε and \tilde{f} . If the spectrum is recorded while the field and the energy are

varied simultaneously to keep ε and \tilde{f} constant, the classical dynamics remains the same. This approach has been used previously,⁸ but this is its first experimental application to the parallel fields system. An orbit's scaled action and recurrence strength can be obtained directly from the Fourier transform of the spectrum. This Fourier transform is called the recurrence spectrum because *each* peak is located at the scaled action of a periodic orbit, and the height of each peak is proportional to that orbit's recurrence strength.

Our experiment employs a lithium atomic beam that travels along the axis of a split-coil superconducting magnet. A pair of field plates provides an electric field parallel to the atomic beam. Laser beams intersect the atomic beam at a right angle. A 735 nm laser excites the $2S \rightarrow 3S$ two-photon transition, and a second laser polarized parallel to the applied fields excites $m=0$ continuum states that rapidly ionize. The ions are detected by a micro-channel plate. To generate a scaled-energy spectrum, the magnetic field is ramped between 0.5 T and 3.0 T while the electric field is varied to maintain \tilde{f} constant. In general, the laser frequency must also be varied to maintain constant ε , but by choosing $\varepsilon = 0$, we could operate at fixed laser frequency. The fractional uncertainty in scaled energy and scaled field are 0.15 percent and 0.2 percent, respectively.

Understanding the experimental spectrum requires a good understanding of the classical dynamics. The traditional tool for studying chaos is the Poincaré surface of section. However, this is not well suited to the continuum where phase space is unbounded and the trajectories rapidly ionize. As an alternative, we have found that the concept of classical ionization time provides a useful signature of the transition from regular to chaotic behavior. Following Main and Wunner,⁹ we define the classical ionization time T_{ion} to be the time that an electron excited near the nucleus at an initial angle θ_0 relative to the z axis requires to reach the electric field saddle point. Figure 1 shows how T_{ion} varies with θ_0 for $\tilde{f} = 1.0, 0.4$, and 0.05 .

⁶ H. Jiao, *Experimental and Theoretical Aspects of Quantum Chaos in Rydberg Atoms in Strong Fields*, Ph.D. diss., Dept. of Physics, MIT, 1996.

⁷ U. Eichmann, K. Richter, D. Wintgen, and W. Sander, *Phys. Rev. Lett.* 61: 2438 (1988); M. Courtney, H. Jiao, N. Spellmeyer, and D. Kleppner, *Phys. Rev. Lett.* 73: 1340 (1994).

⁸ U. Eichmann, K. Richter, D. Wintgen, and W. Sander, *Phys. Rev. Lett.* 61: 2438 (1988); T. van der Veldt, W. Vassen, and W. Hogervorst, *Europhys. Lett.* 21: 9 (1993); A. Holle, J. Main, G. Wiebusch, H. Rottke, and K.H. Welge, *Phys. Rev. Lett.* 61: 161 (1988).

⁹ J. Main and G. Wunner, *Phys. Rev. Lett.* 69: 586 (1992).

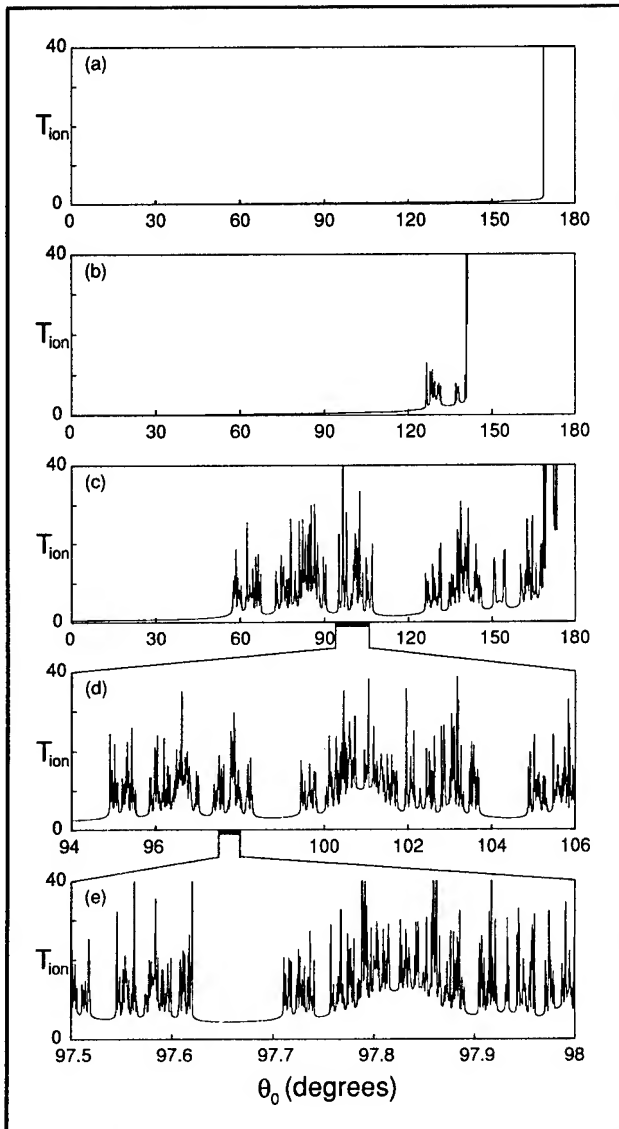


Figure 1. The classical ionization time T_{ion} (in units of scaled time) as a function of the initial angle θ_0 at $\varepsilon = 0$ for various values of f . (a) $f = 1.0$, (b) $f = 0.4$, (c) $f = 0.05$. (d) and (e) successive blowups of regions indicated.

In the pure Stark problem, the only periodic orbit is the "uphill" orbit, along the axis with $\theta_0 = 180$ degrees. At other angles, the electron leaves essentially immediately. This behavior is seen in figure 1a, except that T_{ion} remains large down to 170 degrees due to the stabilizing effect of the magnetic field. At $f = 0.4$ (figure 1b), the stable region extends down to about 140 degrees, but below this angle T_{ion} varies erratically for about 15 degrees. At $f = 0.05$ (figure 1c), the erratic behavior extends to below 60 degrees, with the system displaying wild and random fluctuations. Successive magnifications (figures 1d and 1e) show that the randomly varying pattern extends to ever finer scales: fractal behavior is evident. Similar behavior has been observed in nuclear scattering from model potentials, where the phenomenon has been dubbed chaotic scattering.¹⁰ Following Main and Wunner, we adopt the term *chaotic ionization* to describe the ionization process.

The chaotic ionization process is intimately linked to the existence of closed orbits in the system. Figure 2 shows the locations of closed orbits with scaled action up to $\tilde{S} = 10$, and T_{ion} as functions of θ_0 . The fractal structures appear to be localized near the closed orbits. The closed orbits seem to exert a trapping effect on nearby trajectories: the sensitivity of these trajectories to θ_0 is the source of the fractal behavior in T_{ion} .¹¹ Because chaotic ionization develops as f approaches zero, we expect to see the development of new closed orbits in the recurrence spectrum of the system. This is what we observe experimentally.

¹⁰ B.P. Koch and B. Bruhn, *J. Phys. A* 25: 3945 (1992).

¹¹ B. Eckhardt and C. Jung, *J. Phys. A* 19: L829 (1986); C. Jung and H.J. Scholz, *J. Phys. A* 20: 3607 (1987).

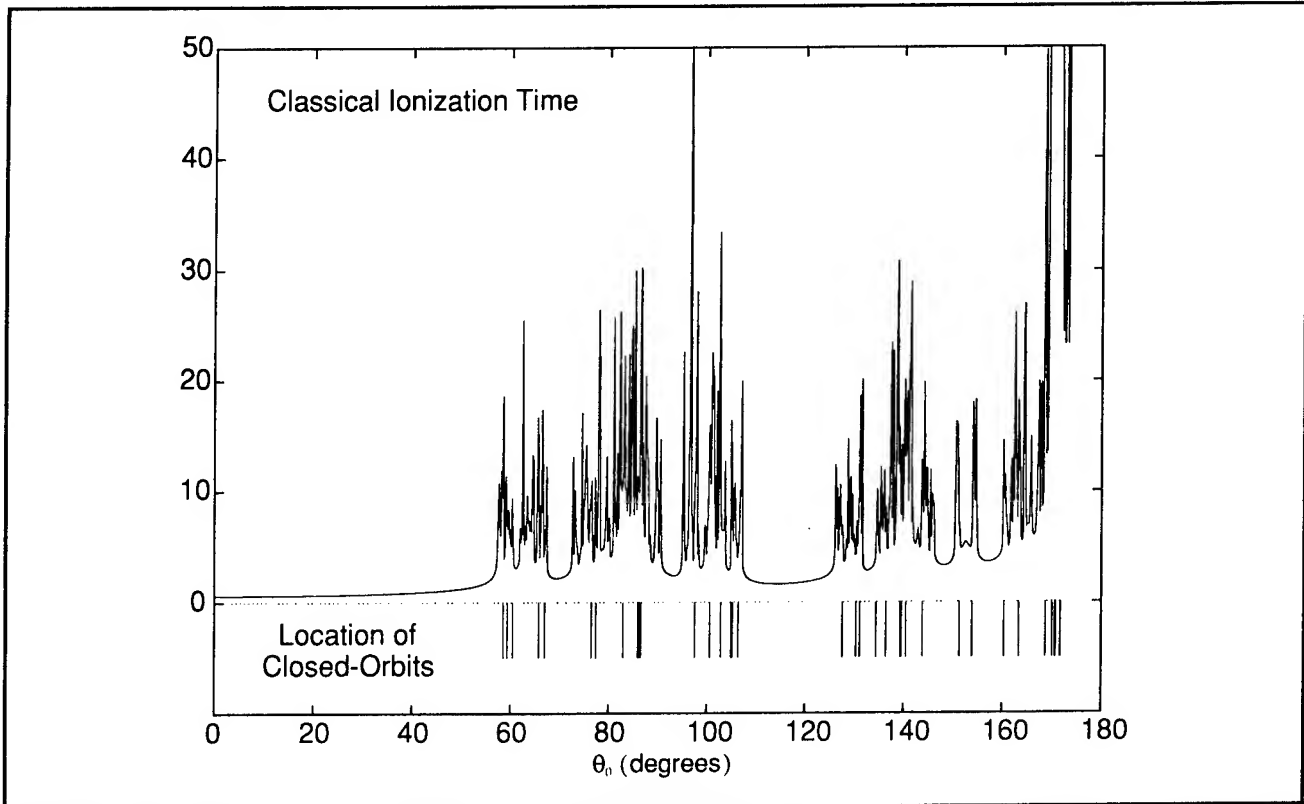


Figure 2. Above: the classical ionization time (in units of scaled time) at $\varepsilon = 0$ and $f = 0.05$. Below: location of closed orbits with $\tilde{S} \leq 10$.

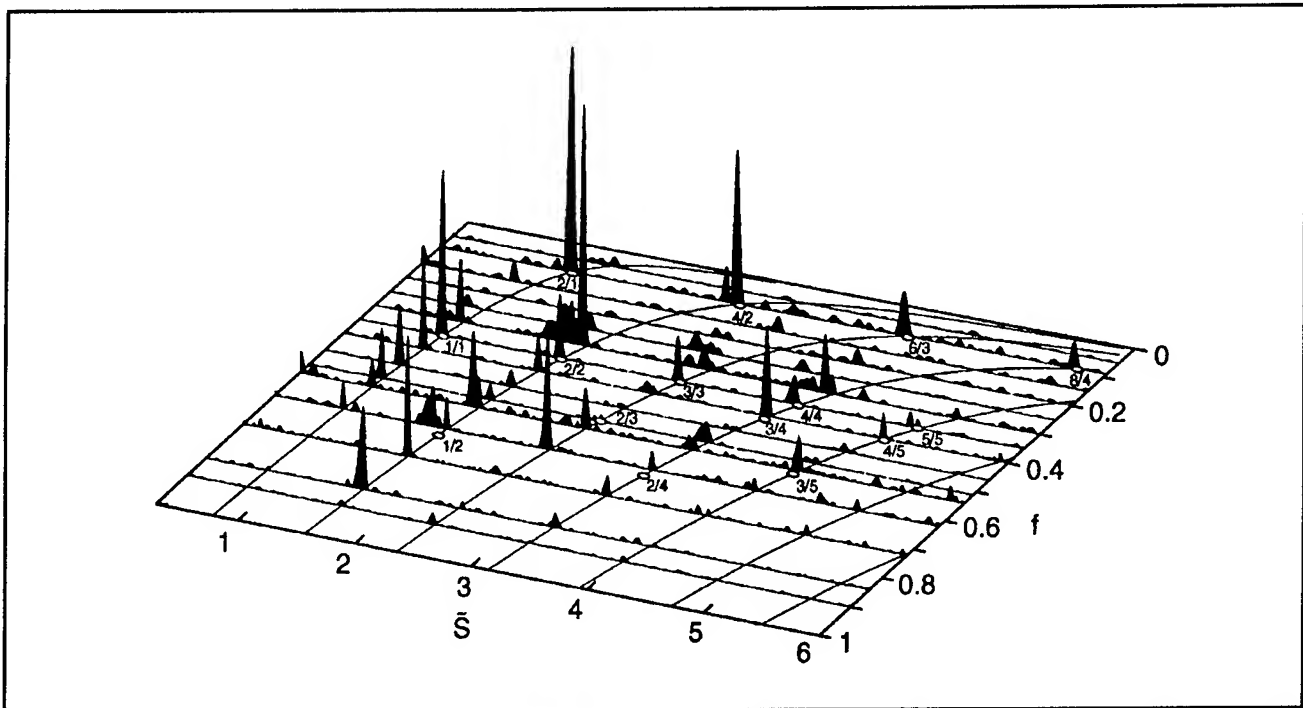


Figure 3. Experimental recurrence spectra at $\varepsilon = 0$ for scaled fields ranging from $f = 0.05$ to $f = 1$. The curved lines are the calculated scaled actions of the parallel orbit and its repetitions. Locations of bifurcations are marked with small ovals.

Figure 3 shows experimental recurrence spectra for values of f between 1.0 and 0.05. At large f , the recurrences are those of the parallel "uphill" orbit and its repetitions. As f is reduced, new recurrences become visible. These are created by bifurcations of the parallel orbit and its repetitions. Near the bifurcation points, the orbits often generate large recurrences. This enhancement, caused by the focusing effects of nearby orbits, has been described quantitatively.¹²

In summary, we have shown that one can characterize classical chaos in the continuum through the concept of chaotic ionization, and we have demonstrated that closed-orbit theory provides a natural way to interpret the continuum spectra of a chaotic system. These results help to establish a useful connection between the classical and quantum descriptions of an unbound chaotic system.

In the coming year, we plan to approach this problem in a fundamentally new way: by applying a resonant RF field, we anticipate being able to manipulate individual classical closed orbits in the system. Work is now under way.

2.1.1 Publications

Courtney, M., N. Spellmeyer, H. Jiao, and D. Kleppner. "Classical, Semiclassical, and Quantum Dynamics in the Lithium Stark System." *Phys. Rev. A* 51: 3604 (1995).

Courtney, M., H. Jiao, N. Spellmeyer, D. Kleppner, and J.B. Delos. "Closed Orbit Bifurcations in Continuum Stark Spectra," *Phys. Rev. Lett.* 74: 1538 (1995).

Courtney, M., H. Jiao, N. Spellmeyer, and D. Kleppner. "Long-period Orbits in the Stark Spectrum of Lithium." *Phys. Rev. Lett.* 73: 1340 (1994).

Courtney, M., H. Jiao, N. Spellmeyer, and D. Kleppner. "Quantum Chaos and Rydberg Atoms in Strong Fields." *Proceedings of the Drexel Conference*. Forthcoming.

Shaw, J.A., J.B. Delos, M. Courtney, and D. Kleppner, "Recurrences Associated with Clas-

sical Orbits in the Nodes of Quantum Wavefunctions." *Phys. Rev. A* 52: 3695 (1995).

Theses

Courtney, M. *Rydberg Atoms in Strong Fields: A Testing Ground for Quantum Chaos*. Ph.D. diss., Dept. of Physics, MIT, 1995.

Jiao, H. *Experimental and Theoretical Aspects of Quantum Chaos in Rydberg Atoms in Strong Fields*. Ph.D. diss., Dept. of Physics, MIT, 1996.

2.2 Determination of the Rydberg Frequency

Sponsors

Joint Services Electronics Program
Grant DAAH04-95-1-0038
National Science Foundation
Grant PHY 92-21489

Project Staff

Joel C. DeVries, Dr. Theodore W. Ducas, Jeffrey R. Holley, Robert I. Lutwak, Professor Daniel Kleppner

The Rydberg constant, R_∞ , relates the wavelengths of the spectrum of atomic hydrogen to practical laboratory units. As such, R_∞ is the natural unit for measurements of atomic energies, and appears as an auxiliary constant in many spectroscopic measurements. Recent advances in optical wavelength metrology have made possible measurements of R_∞ with accuracy approaching 2 parts in 10^{11} .¹³ The Rydberg frequency, cR_∞ , similarly relates the atomic unit of frequency to laboratory units. Although the speed of light c is an exactly defined quantity, the relation between the Rydberg constant and the Rydberg frequency is not merely formal. The precision with which a frequency can be measured is limited in principle to the precision of atomic clocks, which currently exceeds 1 part in 10^{14} and is expected to grow even larger. In contrast, wavelength metrology appears to have reached its limit of precision, somewhat less than 1 part in 10^{11} .

To make full use of the precision of lasers and modern laser spectroscopy and for applications in communications, control, and metrology, we need

¹² M. Courtney, H. Jiao, N. Spellmeyer, D. Kleppner, J. Gao, and J.B. Delos, *Phys. Rev. Lett.* 74: 1538 (1995).

¹³ T. Andreae et al., "Absolute Frequency Measurement of the Hydrogen 1S-2S Transition and a New Value of the Rydberg Constant," *Phys. Rev. Lett.* 69(13): 1923-1926 (1992); F. Nez et al., "Precise Frequency Measurement of the 2S-8S/8D Transitions in Atomic Hydrogen: New Determination of the Rydberg Constant," *Phys. Rev. Lett.* 69(16): 2326-2329 (1992).

to develop general techniques for measuring the frequency of light. As part of this effort, we propose to help establish an atomic optical frequency scale by measuring the Rydberg frequency directly.

The goals of our experiment are three-fold. First is the re-evaluation of R_∞ itself, providing an independent check, in a different regime and using a totally different technique from previous measurements. Second is the determination of the ground state Lamb shift. Because our method employs high angular momentum states for which the Lamb shift is extremely small and effectively exactly known, our results may be compared with optical measurements of transitions between low-lying states to yield an improved measurement of the Lamb shift. Third is to provide a frequency calibration of the spectrum of hydrogen, enabling the creation of a comprehensive frequency standard extending from the radio frequency regime to the ultraviolet.

Our approach involves measuring the frequency of transitions in atomic hydrogen in a regime where the frequency can be synthesized directly from an atomic clock. The experiment explores transitions between highly excited "Rydberg" states of atomic hydrogen in the neighborhood of $n=29$. The transition $n=29 \rightarrow 30$ occurs at approximately 256 GHz.

The experiment employs an atomic beam configuration to reduce Doppler and collisional perturbations. Atomic hydrogen is excited to the low angular momentum $n=29, m=0$ state by a two-step process. The excited atoms are then transferred to the longer lived $n=29, m=28$ circular state by absorption of circularly polarized radio frequency radiation.¹⁴ The atoms enter a region of uniform electric field in which the frequency of the transition $(n=29, m=28) \rightarrow (n=30, m=29)$ is measured by the method of separated oscillatory fields. The final state distribution is analyzed by a state-sensitive electric field ionization detector. The resonance signal appears as a transfer of atoms from the $n=29$ state to the $n=30$ state as the millimeter-wave frequency is tuned across the transition.

Figure 4 illustrates the main features of the apparatus. Atomic hydrogen or deuterium is dissociated from H_2 or D_2 in a radio frequency discharge. The beam is cooled by collisions with a cryogenic thermalizing channel in order to slow the atoms and thereby increase the interaction time. After the beam is collimated, the atoms pass through two layers of magnetic shielding and an 80 K cryogenic shield before entering the 4 K interaction region. The interaction region is logically divided into three

sections: the circular state production region, the separated fields region, and the detection region. These are described briefly below.

In the circular state production region, the hydrogen atoms are excited from the $1s$ ground state to the $2p_{3/2}$ state, and then to one of the $n=29, m=0$ states. This takes place in an electric field to provide selective population of one particular $n=29, m=0$ Stark sub-level. The electric field is then rapidly reduced to an intermediate value as the atoms pass through the center of a circle of four electrodes. These form two pairs of antennas which are fed by a 2 GHz RF source with a 90 degree phase offset. This creates a circularly polarized field that drives the atoms into the $n=29, m=28$ circular state by the absorption of 28 photons. A pulsed electric field ionization (EFI) detector in the circular state production region monitors the efficiency of the optical excitation and angular momentum transfer processes.

After the atoms are prepared in the $n=29$ circular state, the beam enters the millimeter-wave separated fields region. Because Rydberg atoms interact strongly with external fields, accurate measurement of the energy level structure requires careful control of the interaction environment. Thermal radiation is reduced by cooling the interaction region to ~ 4 K with a liquid helium flow system. The ambient magnetic field is reduced by the double-wall high-permeability shields. To define the quantization axis, a small electric field is applied with high uniformity by field plates above and below the atomic beam. The millimeter-waves intersect the atomic beam at two locations separated by 50 cm. The millimeter-wave optical system was described in the 1990 *RLE Progress Report*.

The state distribution of the atoms emerging from the interaction region is analyzed by a state-selective electric field ionization detector. Within the detector, the atoms enter a region of increasing electric field produced by a pair of symmetric ramped plates held at constant potential. Atoms in different states are selectively ionized at different fields and the charged nuclei are detected at different positions. The detection electronics record the state and arrival time of each atom to reach the detector. Because the laser system is pulsed, the time resolution of the ionization signal allows contributions to the resonance pattern from each velocity class to be analyzed individually, providing a valuable check on possible systematic errors.

A preliminary resonance measurement was presented in the 1992 *RLE Progress Report*. The pre-

¹⁴ R. Hulet and D. Kleppner, "Rydberg Atoms in 'Circular' States," *Phys. Rev. Lett.* 51(16): 1430-1433 (1983).

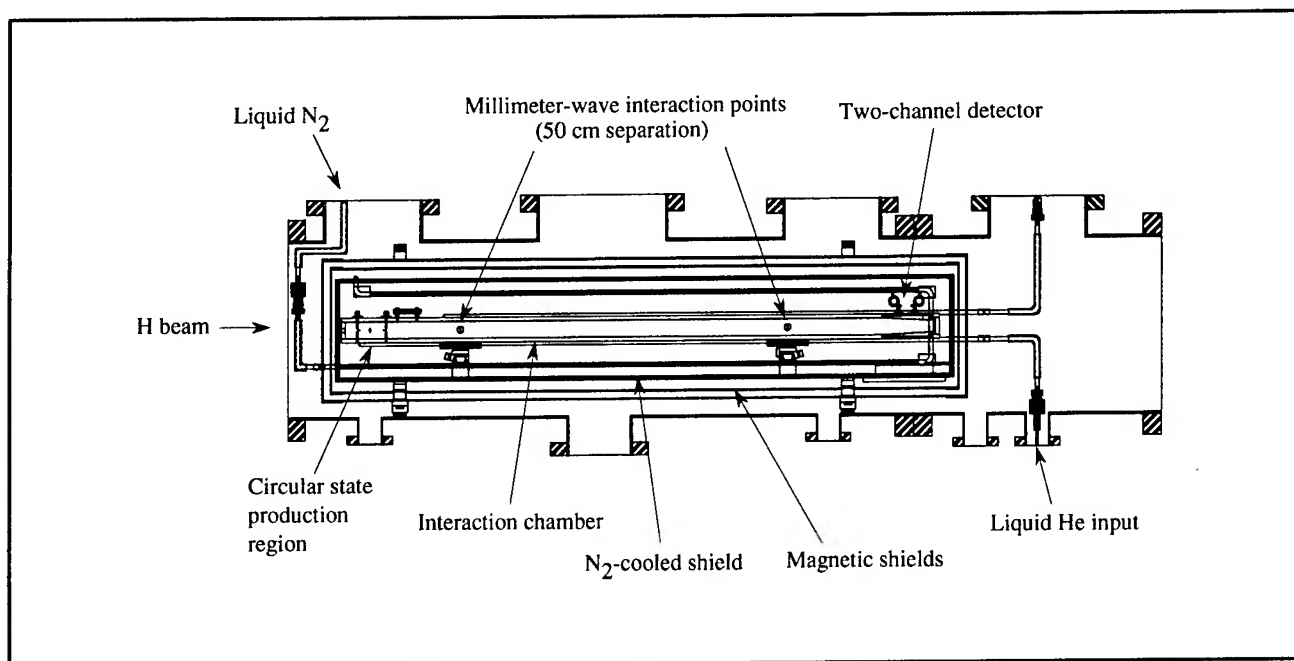


Figure 4. Main chamber of the atomic beam apparatus.

cision of that measurement was limited by low signal levels. Since that time, we have built a second-generation version of the apparatus designed to improve the signal-to-noise ratio by several orders of magnitude. We have completed the new apparatus and have recently begun taking data.

Two accomplishments this year have brought us to the point where we are now beginning to explore the systematics of the new apparatus. The first was the completion and installation of the cryogenically-cooled interaction region. The design of the interaction region was discussed in last year's *RLE Progress Report*, and construction and assembly brought few surprises. The second achievement was the development of the laser system, which is depicted schematically in figure 5.

The laser system consists of two high-power narrow-linewidth dye lasers. The heart of each dye laser is the tunable oscillator, which is shown in figure 6. The gain medium is a quartz cell through which a fluorescent dye (DMQ dissolved in P-Dioxane) flows at roughly 3 l/min. The dye is

excited by the excimer laser beam which is focused to a line with cylindrical optics. The oscillator cavity is basically of the grazing incidence design,¹⁵ with the addition of an intra-cavity etalon and additional line-narrowing components. The grating-tuning mirror combination acts as a narrow-band mirror, which along with the 60 percent output coupler, defines a plane-parallel Fabry-Perot cavity. The four-prism anamorphic achromatic beam expander provides expansion of 25 times in the horizontal plane which ensures that the 3600 line/mm grating is uniformly illuminated, providing a linewidth of about 0.15 cm^{-1} . The oscillator linewidth is further reduced to about 0.04 cm^{-1} by the intra-cavity etalon. The solid quartz plane-parallel etalon has a free spectral range of 1.3 cm^{-1} . Because the etalon linewidth increases with the divergence of the incident beam, several steps were taken to reduce divergence within the cavity. The prism beam expander reduces the horizontal divergence by a factor of 25 and the pinhole aperture eliminates high order cavity modes. The oscillator frequency is tuned by rotating the grating and the etalon simultaneously along a trajectory which maintains the centering of the etalon mode on the grating line.

15 M. Littman and H. Metcalf, "Spectrally Narrow Pulsed Dye Laser Without Beam Expander," *Appl. Opt.* 17(14): 2224-2227 (1978).

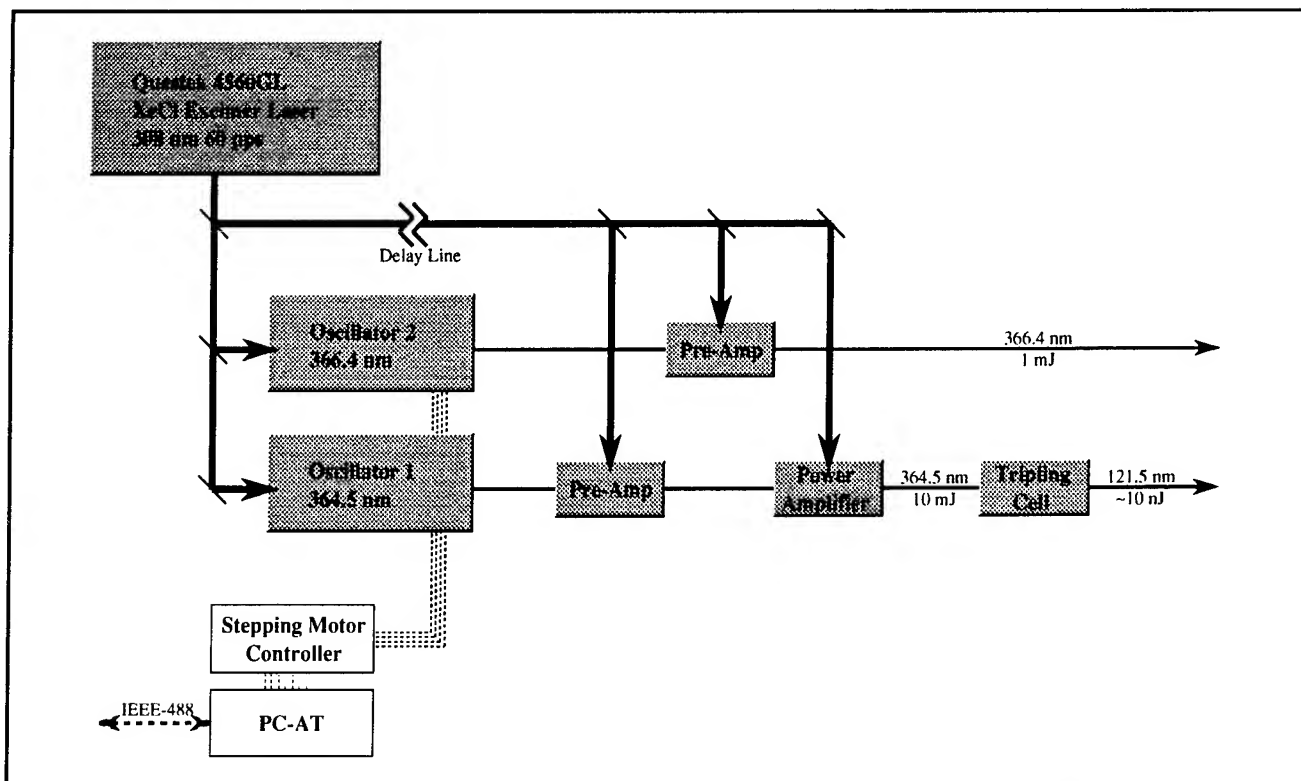


Figure 5. Schematic of the high power ultraviolet laser system.

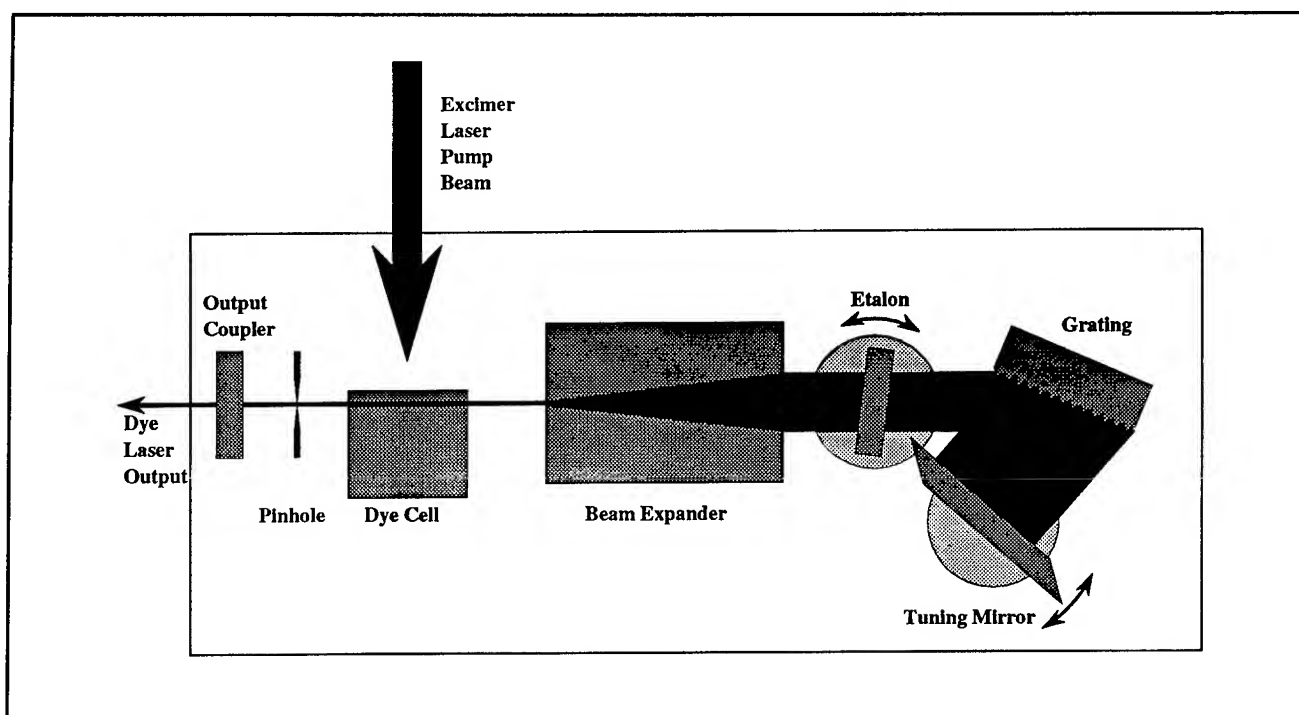


Figure 6. Narrow band tunable dye laser oscillator cavity with intra-cavity etalon.

In order to maintain stability, all fixed oscillator components are rigidly attached to a one-inch thick aluminum base. The tunable components are mounted on double-row high precision industrial

bearing sets which are fixed into the base. Because the grating and etalon are quite sensitive to temperature changes, the cavity is enclosed in a plexiglass box and the sensitive components are

actively stabilized to ± 5 mK. The rotating components are driven by 100-pitch lead screws, which push against extended lever arms. An additional 100:1 anti-backlash worm and gear set is incorporated in the grating drive mechanism. The lead screws are turned by stepping motors with 400 steps per revolution, which are driven by the stepping-motor controller. The angular resolution of the drive system is $10 \mu\text{rad}$ for the etalon and 100 nano-rad for the grating. An AT-compatible personal computer which operates the stepping-motor controller through its parallel printer port maintains the synchronous tuning of the grating and etalon. The controlling software allows for keyboard manipulation of the tuning curves as well as an IEEE-488 interface for remote control of the laser tuning.

The oscillator is pumped by 25 mJ of excimer laser energy and produces roughly $250 \mu\text{J}$ of tunable radiation around 364 nm. The tunable radiation is then amplified to 1 mJ in a preamplifier, pumped by an additional 25 mJ of excimer power which is delayed by 5 ns to allow for the oscillator start-up

delay. This 1 mJ is sufficient for the $2p \rightarrow n=29$ laser at 365 nm. The Lyman- α radiation for the $1s \rightarrow 2p$ transition is generated by four-wave mixing of a signal from a laser that is tuned to one-third of the Lyman- α frequency. This signal passes through a second amplifier stage, which is pumped with roughly 150 mJ of excimer power, to produce a 10 mJ pulse at 364.5 nm. The radiation is then focused into a high-purity gas cell containing a phase-matched mixture of krypton and argon gas, where the 364.5 nm radiation is tripled by degenerate four-wave mixing to produce the 121.5 nm Lyman- α radiation.

A typical scan of the Lyman- α laser is presented in figure 7. For this scan the second laser was tuned to the $n=70$ state of hydrogen. A 10 V/cm electric field was applied to wash out the resonant structure of the upper state. The Lyman- α radiation was then tuned through the $2p_{1/2}$ and $2p_{3/2}$ states while the excited state population was monitored by the pulsed electric field ionization detector located in the circular state production region.

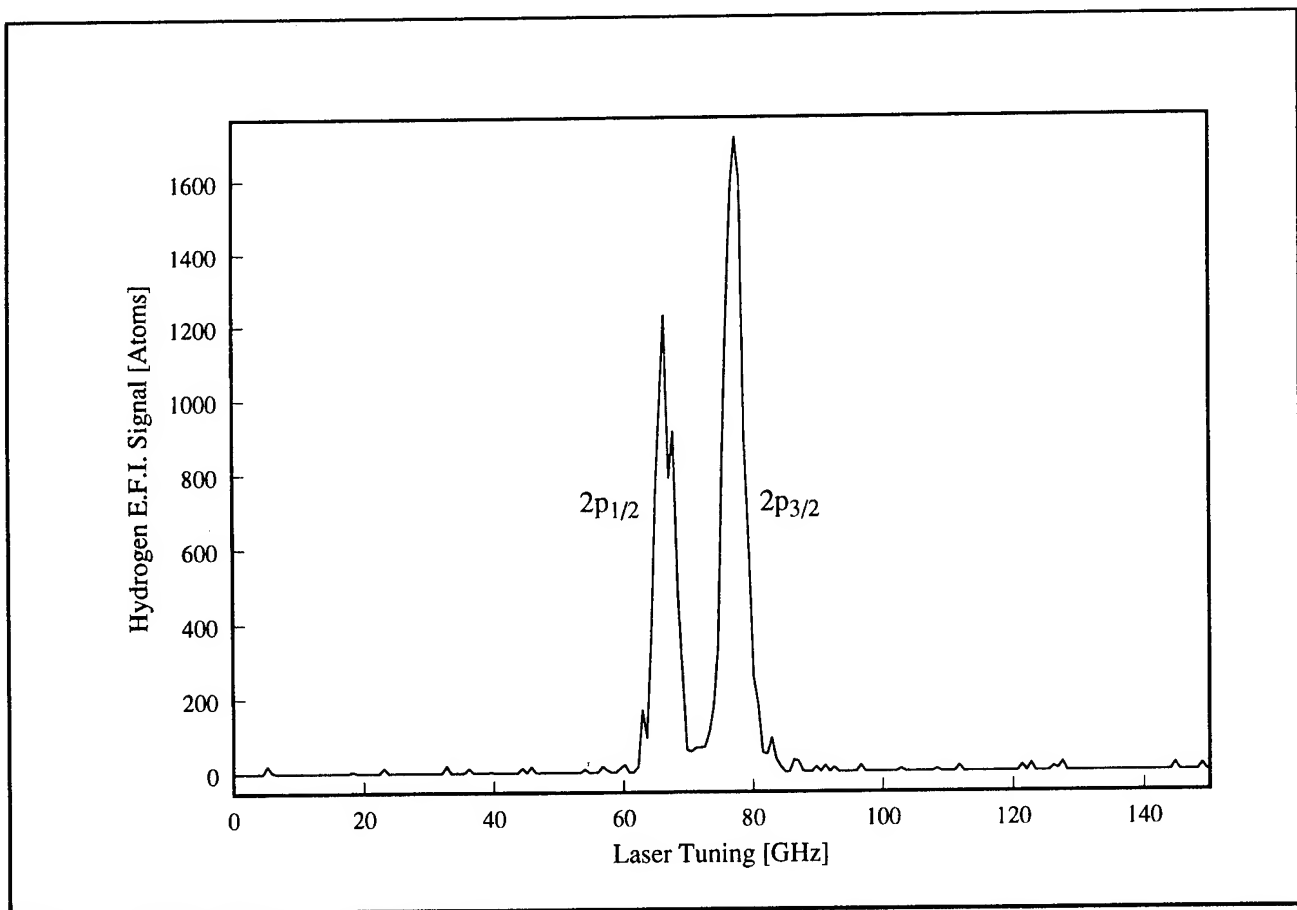


Figure 7. EFI spectrum of the $2p$ states of atomic hydrogen obtained by two-photon excitation of the $n=70$ Rydberg state.

Currently, we are fine-tuning the process of transferring the atoms from the $n=29$, $m=0$ laser-excited state to the $n=29$, $m=28$ circular state. We expect to begin circular-state spectroscopy and to make measurements below the 10^{-10} level this year.

Conference Proceedings

Lutwak, R., J. Holley, J. DeVries, and D. Kleppner, "Millimeter-Wave Measurement of the Rydberg Frequency." *Proceedings of the Symposium on Frequency Standards and Metrology*, Woods Hole, Massachusetts, October 1995.

2.3 Precision Mass Spectrometry of Ions

Sponsors

Joint Services Electronics Program
Grant DAAH04-95-1-0038
National Science Foundation
Grant PHY 92-22768

Project Staff

Michael P. Bradley, David Garrison, Ljubomir M. Ilic, Dr. Fred L. Palmer, Daniel Ripin, Szymon M. Rusinkiewicz, Professor David E. Pritchard

In 1995, we published papers which confirmed that our atomic mass measurements are the most accurate in the world.¹⁶ Our mass table consists of ten atomic masses of particular importance to physics or metrology.¹⁷ The accuracy of these masses, typically 10^{-10} , represents one to three orders of magnitude improvement over previously accepted values. Furthermore, a wide variety of self consistency checks has allowed us to virtually eliminate the possibility of unknown systematic errors. These results contribute to several important experiments in both fundamental and applied physics, including:

- Recalibration of the current x-ray wavelength standard by weighing the energy differences associated with the neutron capture gamma rays of ^{14}N , which are widely used as calibration lines; and
- Determination of the atomic weight of ^{28}Si , part of a program to replace the artifact kilogram

mass standard by a crystal of pure silicon, in effect creating an atomic standard of mass.

We have also developed several new techniques that will improve the accuracy and versatility of our apparatus. These include methods for loading a wider variety of ions into the trap, hardware and software for directly controlling the amplitude and phase of the the ions' magnetron orbits, the demonstration of a technique for dramatically improving the accuracy of our mass comparisons by comparing two simultaneously trapped ions (to eliminate the problems due to field drift), and the demonstration of a squeezing technique to reduce the influence of thermal noise on the measurements. These advances open the door to another dramatic improvement in mass resolution that would allow:

- Determination of excitation and binding energies of atomic and molecular ions by weighing the associated small decrease in mass, $\Delta m = E_{\text{bind}}/c^2$ (we must reach our ultimate goal of a few times 10^{-12} to make this a generally useful technique);
- Determination of the molar Planck constant $N_A \hbar$ by weighing neutron capture γ -rays of silicon or sulphur, whose wavelengths will be measured by a NIST group; this will also provide an independent determination of the fine structure constant;
- Measurement of the $^3\text{H} - ^3\text{He}$ mass difference, important in ongoing experiments to determine the electron neutrino rest mass;
- Improvement of some traditional applications of mass spectrometry resulting from our orders of magnitude improvement in both accuracy and sensitivity; and
- Determination of the molar Planck constant $N_A \hbar$, by measuring the atomic mass and recoil velocity of an atom that has absorbed photons of known wavelength.

Our experimental approach is to measure ion cyclotron resonance on a single molecular or atomic ion in a Penning trap, a highly uniform magnetic field in which confinement along the magnetic field lines is provided by much weaker electric fields. We monitor the ion's axial oscillation by detecting the currents induced in the trap electrodes using ultrasensitive superconducting electronics

¹⁶ F. DiFilippo, V. Natarajan, M. Bradley, F. Palmer, and D.E. Pritchard, *Physica Scripta* T59: 144-54 (1995); F. DiFilippo, V. Natarajan, M. Bradley, F. Palmer, and D.E. Pritchard, in *Atomic Physics 14* (New York: American Institute of Physics, 1995).

¹⁷ F. DiFilippo, V. Natarajan, K. Boyce, and D. E. Pritchard, *Phys. Rev. Lett.* 73: 1481 (1994).

developed for this application.¹⁸ This work in trapping and precision resonance draws on Nobel Prize (1989) winning techniques developed by Dr. Hans Dehmelt at the University of Washington and Dr. Norman Ramsey at Harvard University.

We have developed techniques for driving, cooling, and measuring the frequencies of all three normal modes of ion motion in a Penning trap. Thus we can manipulate the ion position reproducibly to within 30 microns of the center of the trap, correcting for electrostatic shifts in the cyclotron frequency to great accuracy. We use a π -pulse method to coherently swap the phase and action of the cyclotron and axial modes.¹⁹ Therefore, although we detect only the axial motion directly, we can determine cyclotron frequency by measuring the phase accumulated in the cyclotron motion in a known time interval. We can measure the phase of the cyclotron motion to within 10 degrees, leading to a precision of 10^{-10} for a one minute measurement. Our entire ion-making

process is fully automated, and the computer can cycle from an empty trap to having a cooled single ion in about three minutes under optimal conditions.

Careful shimming of the electric and magnetic fields allows us to keep our systematic errors well below 5×10^{-11} , but unfortunately, the typical statistical fluctuation in our magnetic field between measurements is 2.4×10^{-10} . Thus even with the ability to achieve ~ 20 alternate loadings of two different ions in one night, our overall accuracy is at best 8×10^{-11} (see figure 8). We have found that the distribution of field variation is not Gaussian, but rather has too many outlying points. This has led us to use a generalization of least squares fitting called robust statistics in which a Hampel estimate is used to deweight outlying points in a manner determined by the observed excess number of outliers. This has eliminated arbitrary decisions about dropping "bad points" from our data sets and has increased the stability of our fits.

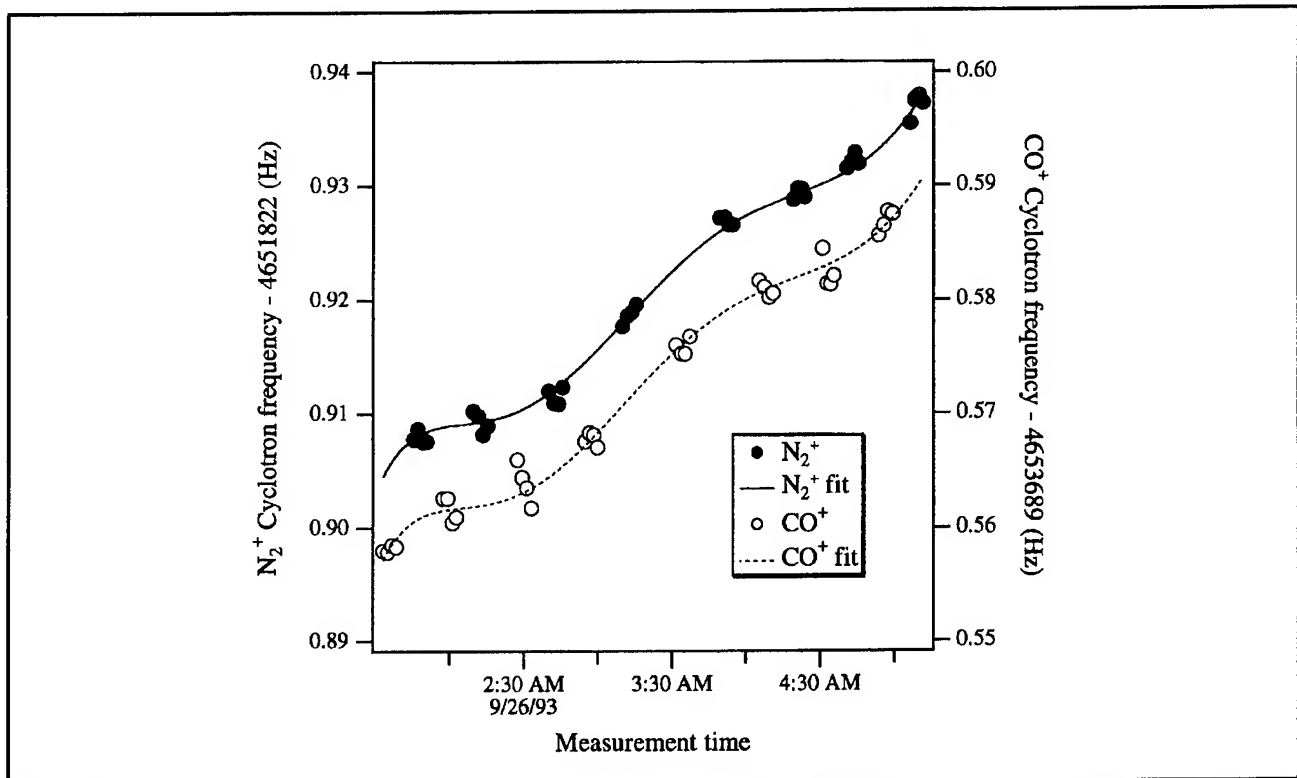


Figure 8. Cyclotron frequency as a function of time for alternate N_2^+ and CO^+ ions in our Penning trap. The frequencies are obtained after a 50s integration of cyclotron phase (see text). The solid line is a polynomial fit to the drift in the field common to both ions.

¹⁸ R. Weisskoff, G. Lafyatis, K. Boyce, E. Cornell, R. Flanagan, Jr., and D.E. Pritchard, *J. Appl. Phys.* 63: 4599 (1988).

¹⁹ E.A. Cornell, R.M. Weisskoff, K. Boyce, and D.E. Pritchard, *Phys. Rev. A* 41: 312 (1992).

We have performed a wide variety of stringent checks for systematic errors. In fact, every mass in the table has been obtained from at least two independent sets of mass ratios. Several of the checks employ our new technique for comparison of non-doublets,²⁰ pairs of ions whose nominal mass to charge ratios are unequal. This technique represents a significant advance in precision mass spectrometry since it allows us to obtain absolute masses by direct comparison to carbon, which is defined to have an atomic mass of exactly 12. It also provides an absolute check of our accuracy by allowing measurements that should verify known ratios such as N_2^+/N^+ and Ar^+/Ar^{++} . We have compared CD_4^+ and CD_3^+ to C to obtain two independent determinations of the atomic weight of deuterium. The results are consistent with the values for the hydrogen masses we obtained from conventional doublet measurements. An extensive series of checks using only doublet ratios was also performed. These include repeated checks of identical ratios (some interspaced by a significant reduction of our field inhomogeneities), checks of circular ratios (eg., A/B , B/C , and C/A), and checks of related ratios (e.g., CO/N_2 and CO_2/N_2O). The consistency of all these checks practically guarantees that our errors are within the quoted limits.

We have made major advances toward our long term goal of improving our accuracy by more than an order of magnitude, which will be achieved by measuring the cyclotron frequencies of two ions trapped in the same field at the same time to eliminate the problem of field fluctuations, and by using squeezing techniques to reduce thermal noise. We have modified our apparatus to allow excitation and detection of two ions at the same time, and demonstrated the capability of two ion measurements to reduce the effects of field fluctuations (figure 9). We have expanded our previous theoretical understanding²¹ of two ion dynamics to include the effects of minute imperfections in the trapping fields, identified particular magnetron orbits where these effects are minimized, and developed hardware and software to place ions in those orbits.

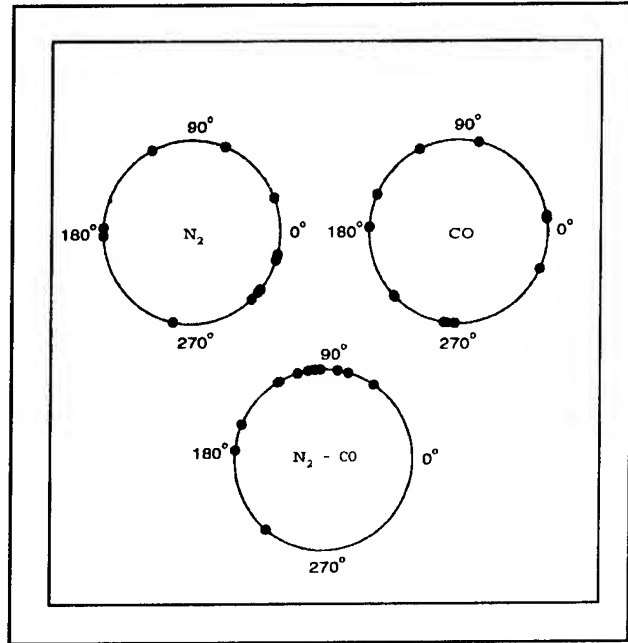


Figure 9. Each dot represents one measured cyclotron phase of simultaneously trapped single N_2^+ and CO^+ ions 16 seconds after excitation. Daytime field fluctuations have virtually randomized the phases of the individual ions but the phase difference between the two remains well defined.

We have also studied the possibility of placing two ions in adjacent traps in case unexpected problems occur when placing them in the same trap. We have evaluated the leading sources of error and designed an arrangement of superconducting coils that will prevent the magnetic fields in the two traps from fluctuating independently.

With either two-ion scheme, the primary source of measurement noise will be the special relativistic mass shift due to thermal fluctuations in cyclotron amplitude. We have proposed several methods of classical squeezing with parametric drives to reduce amplitude fluctuations²² and demonstrated the simplest of these,²³ reducing thermal noise by about a factor of two.

We have also improved the efficiency and versatility of our basic apparatus. We have built a specialized loader for alkali atoms, as well as an external ion loader with associated ion optics to guide ions into the trap. We have implemented a new signal pro-

²⁰ V. Natarajan, K. Boyce, F. DiFilippo, and D.E. Pritchard, *Phys. Rev. Lett.* 71: 1998 (1993).

²¹ E.A. Cornell, K. Boyce, D.L.K. Fyngenson, and D.E. Pritchard, *Phys. Rev. A* 45: 3049 (1992).

²² F. DiFilippo, V. Natarajan, K. Boyce, and D.E. Pritchard, *Phys. Rev. Lett.* 68: 2859 (1992).

²³ V. Natarajan, F. DiFilippo, and D.E. Pritchard, *Phys. Rev. Lett.* 74: 2855 (1995).

cessing algorithm that quickly detects unwanted ions in the trap, and a new data analysis routine that more accurately extracts mass ratios from the

data. Finally, we have begun construction of a new detector based on a DC SQUID that will increase our sensitivity by a factor of three or more.

Table 1. Atomic mass table. The center column lists the atomic masses determined from our experiment, and the right column lists the accepted atomic masses from the 1983 evaluation.

Atom	Mass (amu)	Accepted values (amu)
^1H	1.007 825 031 6 (5)	1.007 825 035 0 (120)
n	1.008 664 923 5 (23)	1.008 664 919 0 (140)
^2H	2.014 101 777 9 (5)	2.014 101 779 0 (240)
^{13}C	13.003 354 838 1 (10)	13.003 354 826 0 (170)
^{14}N	14.003 074 004 0 (12)	14.003 074 002 0 (260)
^{15}N	15.000 108 897 7 (11)	15.000 108 970 0 (400)
^{16}O	15.994 914 619 5 (21)	15.994 914 630 0 (500)
^{20}Ne	19.992 440 175 4 (23)	19.992 435 600 0 (22000)
^{28}Si	27.976 926 532 4 (20)	27.976 927 100 0 (7000)
^{40}Ar	39.962 383 122 0 (33)	39.962 383 700 0 (14000)

2.3.1 Publications

DiFilippo, F., V. Natarajan, M. Bradley, F. Palmer, and D.E. Pritchard. "Accurate Atomic Mass Measurements from Penning Trap Mass Comparisons of Individual Ions." *Physica Scripta* T59: 144-54 (1995).

DiFilippo, F., V. Natarajan, M. Bradley, F. Palmer, and D.E. Pritchard. "Accurate Atomic Mass Measurements from Penning Trap Mass Comparisons of Individual Ions." In *Atomic Physics 14*. New York: American Institute of Physics, 1995.

Natarajan, V., F. DiFilippo, and D.E. Pritchard. "Squeezed States of Classical Motion in a Penning Trap." *Phys. Rev. Lett.* 74: 2855 (1995).

2.4 Atom Interferometry

Sponsors

Charles S. Draper Laboratory
Contract DL-H-4847759
Joint Services Electronics Program
Grant DAAH04-95-1-0038
U.S. Army - Office of Scientific Research
Grant DAAL03-92-G-0229
Grant DAAL01-92-6-0197
U.S. Navy - Office of Naval Research
Grant N00014-89-J-1207

Project Staff

Michael S. Chapman, Troy D. Hammond, Dr. Alan L. Lenef, Edward T. Smith,²⁴ Richard A. Rubenstein, Dr. H. Jörg Schmiedmayer,²⁵ David A. Kokorowski, Dr. Marek L. Czachor, Bernd S. Rohwedder, Allen Jordan, Professor David E. Pritchard

²⁴ Partially supported by a National Science Foundation Fellowship.

²⁵ Partial support from the University of Innsbruck and an APART Fellowship of the Austrian Academy of Sciences.

Atom interferometers, in which atom or molecular de Broglie waves are coherently split and then recombined to produce interference fringes, have opened up exciting new possibilities for precision and fundamental measurements with complex particles. The ability to accurately measure interactions that displace the de Broglie wave phase has led to qualitatively new measurements in atomic and molecular physics, fundamental tests of quantum mechanics, and new ways to measure acceleration and rotation:

- Atom interferometers permit completely new investigations of ground state properties of atoms and molecules including precision measurements of atomic polarizabilities to test atomic structure models, determination of long range forces important in cold collisions and Bose-Einstein condensation, and measurements of molecular polarizability tensor components.
- Atom interferometers can make fundamental measurements in quantum mechanics. These include measurements of topological and geometric phases, loss of coherence from a reservoir, quantum measurement, and investigations of multiparticle interferometry and entanglement.
- The large mass and low velocities of atoms makes atom interferometers especially useful in inertial sensing applications, both as precision accelerometers and as gyroscopes. They have

a potential sensitivity to rotations $\sim 10^{10}$ greater than in optical interferometers of the same area.

- Atom interferometers may have significant applications to condensed matter physics, including measurements of atom-surface interactions and lithography using coherently manipulated fringe patterns that are directly deposited onto substrates.

Our group has pioneered many of these areas, including the first (and only) atom interferometry experiments that employ physically separated paths to make precision measurements. Several major papers have been published this year on a variety of topics underscoring the versatility and usefulness of our interferometer. These topics include quantum coherences,²⁶ atomic polarizability measurements,²⁷ index of refraction of matter waves,²⁸ near field imaging (atomic Talbot effect),²⁹ molecule optics and interferometry,³⁰ and a new velocity selection scheme for precision measurements.³¹ The investigations have proved to be of widespread general interest to the scientific community and have received many write-ups in the popular scientific press.³²

During 1995, we made significant improvements to our interferometer's performance, completed experiments in quantum measurement theory, and undertook an experiment demonstrating the high inertial sensitivity of atom interferometers.

²⁶ M.S. Chapman, T.D. Hammond, A. Lenef, J. Schmiedmayer, R.A. Rubenstein, E.T. Smith, and D.E. Pritchard, "Photon Scattering from Atoms in an Atom Interferometer: Coherence Lost and Regained," *Phys. Rev. Lett.* 75: 3783 (1995).

²⁷ C.R. Ekstrom, J. Schmiedmayer, M.S. Chapman, T.D. Hammond, and D.E. Pritchard, "Measurement of the Electric Polarizability of Sodium with an Atom Interferometer," *Phys. Rev. A* 51: 3883 (1995).

²⁸ J. Schmiedmayer, M.S. Chapman, C.R. Ekstrom, T.D. Hammond, S. Wehinger, and D.E. Pritchard, "Index of Refraction of Various Gases for Sodium Matter Waves," *Phys. Rev. Lett.* 74: 1043 (1995).

²⁹ M.S. Chapman, C.R. Ekstrom, T.D. Hammond, J. Schmiedmayer, B.E. Tannian, S. Wehinger, and D.E. Pritchard, "Near Field Imaging of Atom Diffraction Gratings: the Atomic Talbot Effect," *Phys. Rev. A* 51: R14 (1995).

³⁰ M.S. Chapman, C.R. Ekstrom, T.D. Hammond, R. Rubenstein, J. Schmiedmayer, S. Wehinger, and D.E. Pritchard, "Optics and Interferometry with Molecules," *Phys. Rev. Lett.* 74: 4783 (1996).

³¹ T.D. Hammond, D.E. Pritchard, M.S. Chapman, A. Lenef, and J. Schmiedmayer, "Multiplex Velocity Selection for Precision Matter Wave Interferometry," *Appl. Phys. B* 60: 193 (1995).

³² Articles on recent work performed by our interferometer group have appeared in several journals: J. Maddox, *Nature* February (1995); I. Peterson, *Sci. News*, 147: 116 (1995); P. Yam, *Sci. Am.* 272(4): 30-31 (1995); R. Pool, *Sci.* 268: 1129 May (1995); S. Werner, *Phys. World*, 8(6): 25 (1995); B. Levi, *Phys. Today*, 48(7): 17-18 (1995); P.F. Schewe and B. Stein, *AIP Phys. Bull. on Phys. News*, January 4, 1996; M. Browne, "It's a Molecule. No, It's More Like a Wave," *New York Times Science Section*, August 15, 1995.

2.4.1 Improvements to the Apparatus

This year, we have increased the sensitivity of our apparatus through an improved fabrication process for the 200 nm period de Broglie wave transmission gratings that are its most important component. In collaboration with the Cornell Nanofabrication Facility, where we make our gratings, we have developed a novel registration technique that is capable of producing gratings with phase uniformity over five times the usable area of our old gratings.³³ With the new gratings, we achieve an atom count rate of 200 kcount/sec and a contrast of 17 percent, giving a shot noise limited sensitivity of 5 millirad/ $\sqrt{\text{min}}$. We have also fabricated 140 nm and 160 nm period gratings which will further improve sensitivity and allow for separated beam experiments with more massive atoms and molecules. Currently, efforts are underway in the NanoStructures Laboratory here at MIT to develop 100 nm large scale silicon nitride (1 cm^2) gratings with unprecedented phase uniformity using achromatic interferometric (optical) lithography.³⁴

2.4.2 Quantum Interference and Coherence

We have investigated the loss of coherence between the two separated de Broglie wave components of our interferometer by scattering resonant photons, λ , in an optically pumped sodium beam. This experiment realized a which-path gedanken experiment contemplated by Feynman³⁵ and quantifies the transition between coherence and loss of coherence in an interferometer. We measured the fringe contrast due to scattering as a function of separation between the two paths and found that it decreased significantly when the separation exceeded $\lambda/4$, in accordance with the expectations of Bohr's complementarity principle. Contrast at larger separations, however, exhibited strong revivals (figure 10a), as predicted by our theory. The phase shift of the fringes was also measured and suffered predicted discontinuities (figure 10b).

In an extension of this decoherence experiment, we explicitly showed that scattered photons do not necessarily destroy coherence between the two de Broglie wave components of the interferometer. By using a highly collimated beam and reducing the acceptance angle of our detector, we were able to observe atoms which experienced a photon recoil confined to a small scattering range. For these atoms, we found that the fringe contrast persists over significantly larger path separations than in the previous experiment where all scattering events were detected.

2.4.3 Rotation Sensing

Experiments have been performed to measure both the interferometer's response to rotations as well as its rotational noise, demonstrating the inherent sensitivity of matter-wave interferometers to inertial effects.³⁶ Small rotations of a few earthrates (earthrate, $\Omega_e = 7.3 \times 10^{-5} \text{ rad/sec}$) or less were applied to the apparatus, and the resulting interferometer phase measured (figure 11). Since the interferometer has a linear phase response to rotations, a rotation rate was easily inferred and compared to the rotation rate determined from two accelerometers attached to the vacuum housing of our apparatus. A comparison was then made for rotation amplitudes ranging from -4 to $+4 \Omega_e$, and plotted in figure 12a.

We have shown the response to have better than 1 percent agreement with theory, and directly observed rotations below $50 \text{ m}\Omega_e$ with 20 second integration times. Rotational noise was shot-noise limited for short times (less than two seconds) and was measured to be $13 \text{ m}\Omega_e$ in 80 seconds (figure 12b). These results are three orders of magnitude more sensitive than previous measurements of rotation using atom interferometers and demonstrate the promise of using atom interferometers for inertial navigation systems.

³³ M.J. Rocks, R.C. Tiberio, M.S. Chapman, T.D. Hammond, E.T. Smith, A. Lenef, R.A. Rubenstein, D.E. Pritchard, and S. Adams, "Coherence of Large Gratings and Electron-beam Fabrication Techniques for Atom-Wave Interferometry," *J. Vac. Sci. Technol. B* 13: 2745 (1995); M.J. Rocks, R.C. Tiberio, M.S. Chapman, T.D. Hammond, E.T. Smith, A. Lenef, R.A. Rubenstein, D.E. Pritchard, and S. Adams, "Coherence and Structural Design of Free-standing Gratings for Atom-Wave Optics," submitted to the *Jap. J. Appl. Phys.*

³⁴ T.A. Savas, S.N. Shah, M.L. Schattenburg, J.M. Carter, and H.I. Smith, "Achromatic Interferometric Lithography for 100 nm-Period Gratings and Grids," *J. Vac. Sci. Technol. B* 13: 2732 (1995).

³⁵ R. Feynman, R. Leighton, and M. Sands, "The Feynman Lecture Notes," vol. 3 (Boston: Addison-Wesley, 1966).

³⁶ A. Lenef, et al, "Rotation Sensing with an Atom Interferometer," to be submitted.

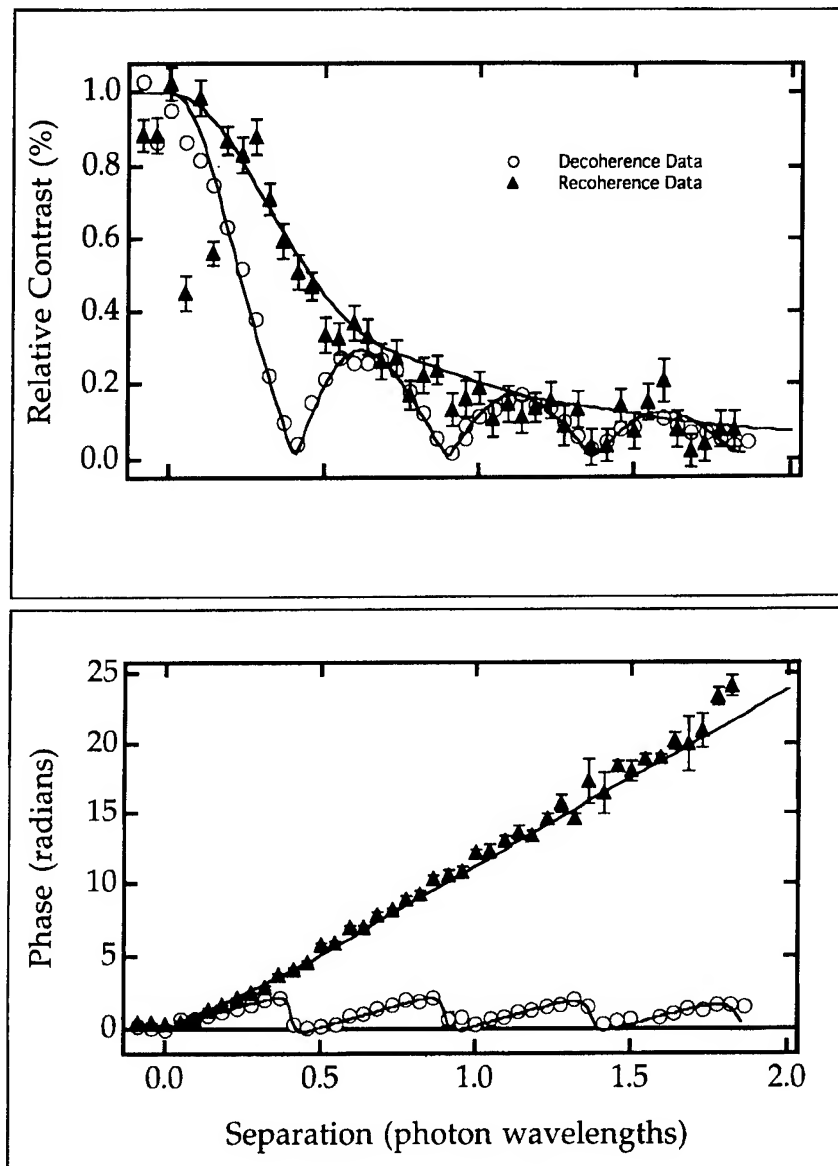


Figure 10. Results of light scattering experiment. (a) Contrast versus separation between de Broglie wave components in units of optical wavelengths. Decoherence data (circles) shows fringe contrast decreasing rapidly, but with revivals. Recoherence data (triangles) show a more gradual decrease in fringe contrast from sub-photon recoil momentum resolved detection of atoms. (b) Phase versus separation between de Broglie wave components in units of optical wavelengths for decoherence data (circles) and recoherence data (triangles).

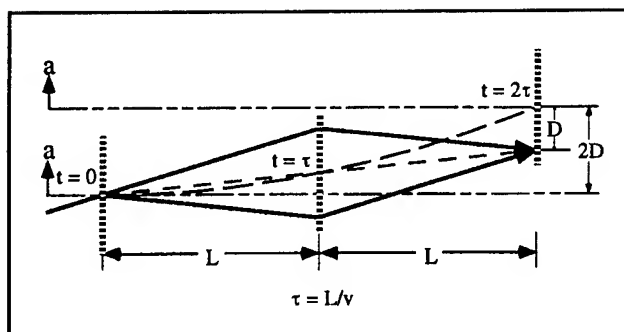


Figure 11. The interferometer in motion under the influence of a transverse acceleration. The atomic beam travels from left to right in the laboratory frame but interacts with the progressively displaced gratings of the moving apparatus. Because a center-line (short dash) between the atom beam paths passes through the middle of the first grating at $t = 0$, and is offset by a transverse velocity $v_t = 1/2\tau$, it also passes through the middle of the displaced second grating at $t = \tau$. The dashed curve (long dash) represents the displacement of the interferometer due to acceleration. The center-line of the accelerating interferometer is shown (short/long dash) at $t = 0$, and $t = 2\tau$ where fringes have a relative displacement of $-D$.

2.4.4 Ongoing Investigations

Longitudinal Momentum Correlations

Recent advances in atom optics and interferometers exploit the transverse coherence of atom sources. Longitudinal coherence is possible, but since atoms with different (but correlated) velocities have different kinetic energies, it is an inherently time dependent phenomenon. Currently, we are pursuing theory with time varying potentials to understand ways to measure, create, and manipulate the longitudinal coherences in our beam.

Understanding and being able to manipulate these coherences will allow us to employ our apparatus to perform studies of a wide range of intriguing time-dependent interactions, including forces which differentially alter the momentum of the atoms in the two legs of the interferometer. One of these, the Anandan force,³⁷ that arises when a quantum dipole passes through a region of uniform electric and magnetic field, is the subject of considerable theoretical debate.

Velocity Dependent Index of Refraction of a Gas

The refractive index of a gas to passage of a sodium de Broglie wave arises from the collision-induced phase shift between the ground state sodium atoms of the beam and the molecules in the gas cell through which they pass. We plan to extend our recent experiment by varying the incident beam energy, providing a powerful means for further exploration of the intermolecular potentials involved in the collisions.

Dedicated Rotation Sensing Device

The impressive results of our rotation response and noise measurements have motivated the study of a dedicated inertial sensing device based on a high flux atom interferometer with fabricated gratings. Such a device using an effusive Cs beam would produce detected fluxes of about 10^{10} atoms/sec and have a shot noise limited sensitivity of $5 \times 10^{-8} \Omega_e / \sqrt{\text{hr}}$.

Velocity Selection through Velocity-multiplexing

The strength of applied potentials in atom interferometry is typically limited because the resulting dispersive phase shifts wash out the interference pattern. In velocity-multiplexing, the velocity distribution of the atomic beam is chopped into a series of narrow peaks such that the velocity dependence of the phase shifts result in rephasing of the interference signal for certain strengths of applied potential. The technique overcomes limitations due to wide and/or poorly known velocity distributions and thus allows a more precise determination of the applied interaction with complete independence from the initial velocity distribution of the beam. We plan to use this scheme to perform experiments requiring precision beyond the 0.1 percent level.

Geometric Phases

Precision measurements of the Aharonov-Casher (AC) phase are planned. This will allow a study of the dependence on the interfering particle's dipole orientation for the first time. Modifications made to our interaction region (a device which allows different potentials to be applied to either arm of the interferometer) to introduce spatially varying magnetic fields will permit investigation of Berry's phase as well.

³⁷ J. Anandan, *Phys. Rev. Lett.* 48: 1660 (1982).

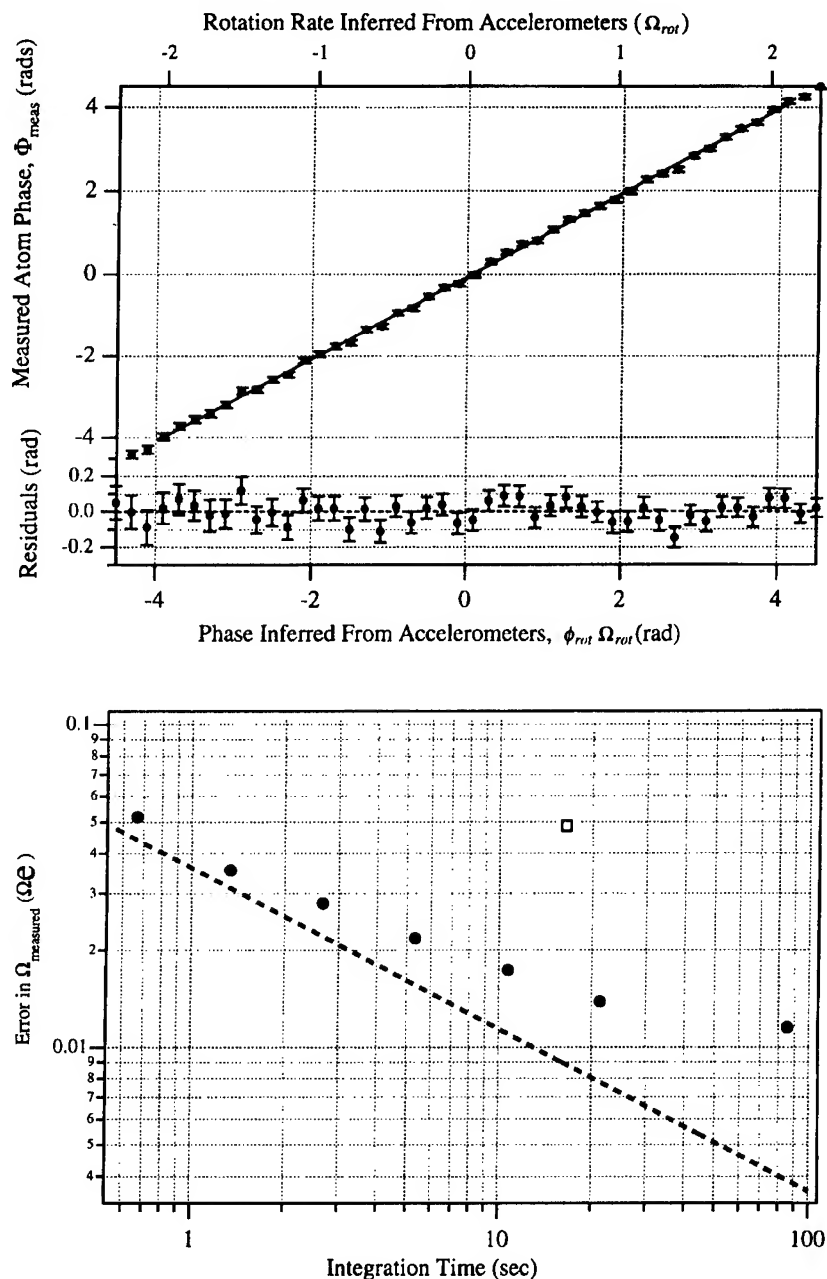


Figure 12. (a) A plot of the measured interferometer phase, ϕ_{meas} , versus the inferred phase from the accelerometer readings, ϕ_{rot} , from a combination of 20 second runs totaling approximately 400 seconds of data (~ 10 sec of data per point). There is a 0.8 percent difference between these measurements with a total error of 1 percent. (b) Reproducibility of the interferometer measurement when driven by a 4.6 Hz sinusoidal motion. The standard deviation of the fluctuations in the measured rotation of the 4.6 Hz spectral peak is plotted versus integration time (circles). This is compared to the shot noise limited error versus integration time (dashed line).

2.4.5 Publications

Chapman, M.S., C.R. Ekstrom, T.D. Hammond, R. Rubenstein, J. Schmiedmayer, S. Wehinger, and D.E. Pritchard. "Optics and Interferometry with Molecules." *Phys. Rev. Lett.* 74: 4783 (1995).

Chapman, M.S., T.D. Hammond, A. Lene, J. Schmiedmayer, R.A. Rubenstein, E.T. Smith, and D.E. Pritchard. "Photon Scattering from Atoms in an Atom Interferometer: Coherence Lost and Regained." *Phys. Rev. Lett.* 75: 3783 (1995).

Schmiedmayer, J., et al, "Atom and Molecule Interferometry with Separated Beams." In *Atom Interferometry*. Ed. Paul R. Berman, New York: Academic Press. Forthcoming.

Thesis

Chapman, M.S. *Photon Induced Coherence Loss in Atom Interferometry*. Ph.D. diss., Dept. of Physics, MIT, 1995.

2.5 Cooling and Trapping Neutral Atoms

Sponsors

Alfred P. Sloan Foundation
National Science Foundation
Grant PHY 95-01984
U.S. Army Research Office
Contract DAAL01-92-C-0001
U.S. Navy - Office of Naval Research
Grant N00014-90-J-1642
Grant N00014-94-1-0807

Project Staff

Professor Wolfgang Ketterle, Dr. Nicolaas J. van Druten, Michael R. Andrews, Kendall B. Davis, Dallin S. Durfee, Ilya A. Entin, Philip M. Hinz, Everest W. Huang, Dan M. Kurn, Marc O. Mewes, Till P. Rosenband, Charles K. Sestok, Stanley H. Thompson, Peter S. Yesley

2.5.1 Introduction and Summary

Cooling and trapping of neutral atoms offers exciting new possibilities. Many are related to the fact that the deBroglie wavelength increases with decreasing temperature T as $1/\sqrt{T}$. When the deBroglie wavelength is comparable to atomic dimensions (range of the interaction potential), collisions can no longer be treated classically. They are dominated by weak long-range interactions. Dramatic effects happen at even colder temperatures and higher densities, when the deBroglie wavelength becomes comparable to the interatomic spacing. In this case, the atomic waves overlap, and a novel type of highly correlated quantum matter is observed. Fermions would form a correlated Fermi sea where collisions and light scattering are suppressed if most of the final states for these processes are already occupied.

Einstein predicted in 1925 that a gas of bosonic particles will undergo a phase transition into a Bose-Einstein condensate (BEC) if they are cooled to a very low temperature.³⁸ This new phase is characterized by a macroscopic population of the lowest energy levels. Bose-Einstein condensation is therefore a macroscopic quantum phenomenon like superfluidity and superconductivity. It is distinguished by the coherence of atoms; all atoms in the condensate are indistinguishable and behave identically.

The observation of Bose-Einstein condensation has been one of the major goals in atomic physics in the last few years. This goal has been achieved recently by three groups using different atoms and different techniques.³⁹ The successful production of Bose condensates is the starting point for a thorough study of this long-sought novel form of matter. The study of Bose-Einstein condensation is important because:

- Bose-Einstein condensation is a paradigm of quantum statistical physics that was predicted more than 70 years ago.³⁸
- It becomes possible to perform crucial tests of theories on the weakly interacting Bose condensate. In contrast to other macroscopic quantum phenomena like superconductivity and superfluidity, Bose condensation in atomic gases can be studied at such low densities that

³⁸ A. Einstein, *Sitzungsber. Preuss. Akad. Wiss.* 18 (1925).

³⁹ M.H. Anderson, J.R. Ensher, M.R. Matthews, C.E. Wieman, and E.A. Cornell, *Sci.* 269: 198 (1995); C.C. Bradley, C.A. Sackett, J.J. Tollet, and R.G. Hulet, *Phys. Rev. Lett.* 75: 1687 (1995); K.B. Davis, M.-O. Mewes, M.R. Andrews, N.J. van Druten, D.S. Durfee, D.M. Kurn, and W. Ketterle, *Phys. Rev. Lett.* 75: 3969 (1995).

perturbative approaches and mean-field theories are accurate.⁴⁰ A detailed theoretical understanding of Bose condensation based on first principles might advance our understanding of more complex systems like liquid helium or high-T_c superconductors.

- A Bose condensate is the ultimate source of ultracold atoms. The kinetic energy of a Bose condensate is on the order of tens of nanokelvin. Such ultracold atoms are ideal for precision experiments (determination of fundamental constants, tests of fundamental symmetries) because the slow motion eliminates most systematic effects. Furthermore, such samples of atoms have potential applications in the field of atom optics, such as the creation of microscopic structures by direct-write lithography or atom microscopy. Structures as small as 65 nm were obtained recently by laser-focused atomic deposition,⁴¹ mainly limited by the transverse collimation and the thermal velocity spread of the atomic beam. Improvements by an order of magnitude should be possible. With ultracold atoms, one could realize the ultimate resolution in focusing atoms. This is analogous to the diffraction limit in optics. A Bose condensate would also find application in metrology, improving frequency standards and atom interferometry. Cesium clocks using microkelvin atoms might improve the accuracy of the current frequency standard by two orders of magnitude.⁴² Nanokelvin atoms would offer additional improvements.
- A Bose condensate consists of coherent atoms. Such a state of matter has many analogies with coherent photons or laser light and can be regarded as the first realization of an atom laser. The accumulation of atoms in the Bose condensate can be interpreted as stimulated emission of matter waves. The study of coherent matter waves might become an exciting new subfield of atomic physics.
- A Bose condensate is a novel form of matter with many unknown properties. The ideal (non-interacting) case is well understood, but does not include even the qualitative features

of real, weakly interacting systems.⁴⁰ In the wake of the progress of the last few years, many theories have been developed on the formation of a condensate, and its collisional and optical properties. Most theories are approximate and have to be tested experimentally. Some theories even lead to contradictory conclusions.

- When a new regime of ultracold temperatures is explored, there is always the hope of finding something completely unexpected!

Despite the rapid progress in laser cooling over the last few years, the closest approach towards BEC was still missing four to five orders of magnitude in phase space density. Laser cooling is limited in the lowest temperature by heating due to spontaneous emission and in density by absorption of scattered light and excited state collisions. Current research activities try to push the limits of laser cooling even further.⁴³

Our approach is to use laser cooling as a first step and then continue with evaporative cooling which does not involve light and therefore does not suffer from the above mentioned limitations. The cooling is accomplished by selectively removing atoms with the highest energy from a magnetic trap and then allowing the rest of the sample to rethermalize through elastic collisions. In 1994, we were able to realize for the first time this combination of laser cooling and evaporative cooling.⁴⁴ The cooling was limited by trap loss (Majorana flops) in the magnetic trap. In 1995, we could eliminate the trap loss in a novel trap, the optically plugged magnetic quadrupole trap, and cool sodium atoms to Bose-Einstein condensation.

2.5.2 Optically Plugged Magnetic Quadrupole Trap

In 1995, we demonstrated a novel atom trap which consists of a combination of magnetic fields and far-off-resonant light. This trap offers a superior combination of large trapping volume and tight confinement. It allowed us to obtain samples of ultracold atoms at unprecedented densities (10^{14} cm^{-3})

⁴⁰ K. Huang, *Statistical Mechanics*, 2nd ed. (Wiley, New York, 1987), pp. 286-302.

⁴¹ J.J. McClelland, R.E. Scholten, E.C. Palm, and R.C. Celotta, *Sci.* 262: 877 (1993).

⁴² K. Gibble and S. Chu, *Metrologia* 29: 201 (1992).

⁴³ J. Lawall, S. Kulin, B. Saubamea, N. Bigelow, M. Leduc, and C. Cohen-Tannoudji, *Phys. Rev. Lett.* (1995), forthcoming.

⁴⁴ K.B. Davis, M.-O. Mewes, M.A. Joffe, M.R. Andrews, and W. Ketterle, *Phys. Rev. Lett.* 74: 5202 (1995).

and to evaporatively cool atoms to Bose-Einstein condensation.⁴⁵

Evaporative cooling requires an atom trap which is tightly confining and stable. So far, magnetic and optical dipole traps have been used. Optical dipole traps provide tight confinement, but have only a very small trapping volume (10^{-8} cm^3). The tightest confinement in a magnetic trap is achieved with a spherical quadrupole potential (linear confinement); however, atoms are lost from this trap due to non-adiabatic spinflips as the atoms pass near the center where the field rapidly changes direction. This region constitutes a hole in the trap of micrometer dimension. The recently demonstrated TOP trap suppresses this trap loss, but at the cost of lower confinement.⁴⁶

We suppressed the trap loss by adding a repulsive potential around the zero of the magnetic field, literally plugging the hole. This was accomplished by tightly focusing an intense blue-detuned laser that generated a repulsive optical dipole force. The optical plug was created by an argon ion laser beam (514 nm) of 3.5 W focused to a diameter of $30 \mu\text{m}$. Heating due to photon scattering was suppressed by using far-off-resonant light, and by the fact that the atoms are repelled from the region where the laser intensity is highest.

The total potential experienced by the atoms is a combination of the dipole potential, the quadrupole trapping potential and the rf dressed atom potential. The latter can be understood qualitatively with a simple argument. At the point where atoms are in resonance with the rf, the trapped state undergoes an avoided crossing with the untrapped states, and as a result the trapping potential bends over. The total potential orthogonal to the propagation direction of the blue detuned laser is depicted in figure 13.

At temperatures above $15 \mu\text{K}$, the observed trapped clouds were elliptical with an aspect ratio of 2:1 due to the symmetry of the quadrupole field (figure 14). At the position of the optical plug, there was a hole, which was used for fine alignment. A misalignment of the optical plug by $\sim 20 \mu\text{m}$ resulted in increased trap loss and prevented us from cooling below $50 \mu\text{K}$. This is evidence that the Majorana spin flips are localized in a very small region around the center of the trap. At temperatures below $15 \mu\text{K}$, the cloud separated into two

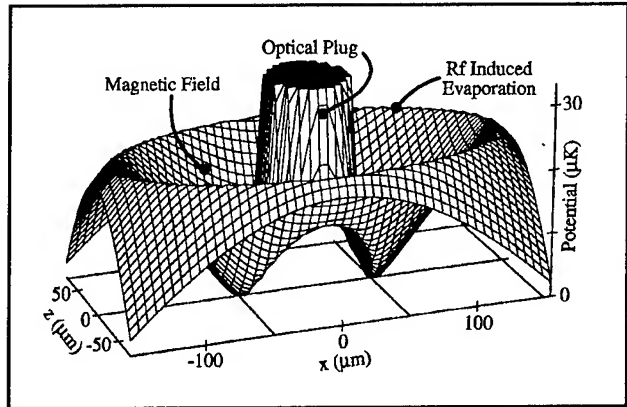


Figure 13. Adiabatic potential due to the magnetic quadrupole field, the optical plug, and the rf. This cut of the three-dimensional potential is orthogonal to the propagation direction (y) of the blue detuned laser. The symmetry axis of the quadrupole field is the z -axis.

pockets (see figure 14b) at the two minima in the potential of figure 13.

2.5.3 Bose-Einstein Condensation of Sodium Atoms

We have recently observed Bose-Einstein condensation in a dilute gas of sodium atoms.⁴⁵ The atoms were trapped in the optically plugged magnetic quadrupole trap and cooled by evaporation. The essential condition for evaporative cooling is that the collision rate be sufficiently high for many collisions to occur within the lifetime of the atoms in the trap. Beside high initial density and long trapping times, evaporative cooling requires a method for selectively removing hot atoms from the trap. In rf induced evaporation, atoms are spin-flipped to an untrapped state when they are in resonance with an applied rf field (figure 15). Since this resonance frequency is a function of magnetic field B , atoms are selectively removed at a specific value of B . In the case of transitions between magnetic sublevels m_F , the resonance frequency is $\omega_{rf} = g \mu_B B / \hbar$, where g is the g -factor and μ_B the Bohr magneton. Since the trapping potential is given by $m_F |g| \mu_B B(r)$, only atoms which have a total energy $E > \hbar \omega_{rf} |m_F|$ will evaporate. Evaporative cooling is forced by lowering the rf frequency. Within seven seconds, this reduced the temperature by a factor of 100, and increased the phase space density by six orders of magnitude, leading to Bose-Einstein condensation of the remaining atoms.

⁴⁵ K.B. Davis, M.-O. Mewes, M.R. Andrews, N.J. van Druten, D.S. Durfee, D.M. Kurn, and W. Ketterle, *Phys. Rev. Lett.* 75: 3969 (1995).

⁴⁶ W. Petrich, M.H. Anderson, J.R. Ensher, and E.A. Cornell, *Phys. Rev. Lett.* 74: 3352 (1995).

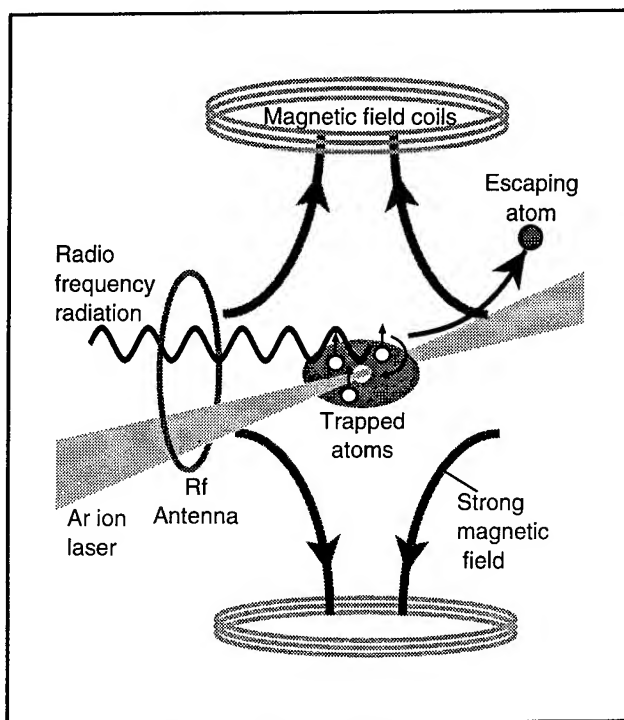


Figure 14. Absorption images of atom clouds trapped in the optically plugged trap. Cloud (a) is already colder than was attainable without the plug (Ar ion laser beam). Cloud (b) shows the break-up of the cloud into two pockets in the two minima of the potential in figure 13. The size of cloud (c) reaches the optical resolution of the imaging system ($< 10 \text{ mm}$) still absorbing 90 percent of the probe light. This sets an upper bound on temperature ($< 10 \mu\text{K}$) and a lower bound on density ($5 \times 10^{12} \text{ cm}^{-3}$).

Condensates contained up to 5×10^5 atoms at densities exceeding 10^{14} cm^{-3} . The striking signature of Bose condensation was the sudden appearance of a bimodal velocity distribution when the sample was cooled below the critical temperature of $\sim 2 \mu\text{K}$. The distribution consisted of an isotropic thermal distribution and an elliptical core attributed to the expansion of a dense condensate (figure 16).

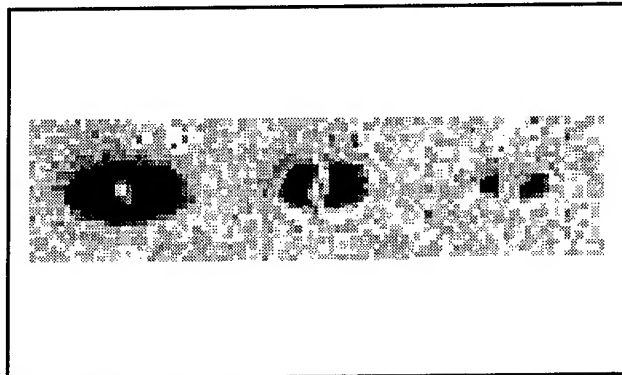


Figure 15. Experimental setup for cooling atoms to Bose-Einstein condensation. Sodium atoms are trapped by a strong magnetic field, generated by two coils. In the center, the magnetic field vanishes, allowing the atoms to spin-flip and escape. Therefore, the atoms are kept away from the center of the trap by a strong (3.5 W) π laser beam (optical plug) which exerts a repulsive force on the atoms. Evaporative cooling is controlled by radio-frequency radiation from an antenna. The rf selectively flips the spins of the most energetic atoms. The remaining atoms rethermalize (at a lower temperature) by collisions among themselves. Evaporative cooling is forced by lowering the rf frequency.

This experiment was one of three independent approaches which succeeded in creating BEC in the last few months.⁴⁷ Our results on sodium are distinguished by a production rate of Bose condensed atoms which is three orders of magnitude larger than in the two previous experiments. Densities higher than $10^{14} \text{ atoms/cm}^3$ exceed previous results by more than a factor of ten and are promising for the study of collisions and interactions of dense ultracold atoms.

We are currently preparing experiments to study the shape, stability, and optical properties of the condensate. Of special interest are experiments which might reveal the coherent nature of the atoms. Such experiments could be coherent excitations of the condensate by modulating the trapping potential,⁴⁸ and interference between two condensates.⁴⁹

⁴⁷ M.H. Anderson, J.R. Ensher, M.R. Matthews, C.E. Wieman, and E.A. Cornell, *Sci.* 269: 198 (1995); C.C. Bradley, C.A. Sackett, J.J. Tollett, and R.G. Hulet, *Phys. Rev. Lett.* 75: 1687 (1995); K.B. Davis, M.-O. Mewes, M.R. Andrews, N.J. van Druten, D.S. Durfee, D.M. Kurn, and W. Ketterle, *Phys. Rev. Lett.* 75: 3969 (1995).

⁴⁸ P.A. Ruprecht, M.J. Holland, K. Burnett, and M. Edwards, *Phys. Rev. A* 51: 4704 (1995).

⁴⁹ J. Javanainen and S.M. Yoo, *Phys. Rev. Lett.* 76: 161 (1996).

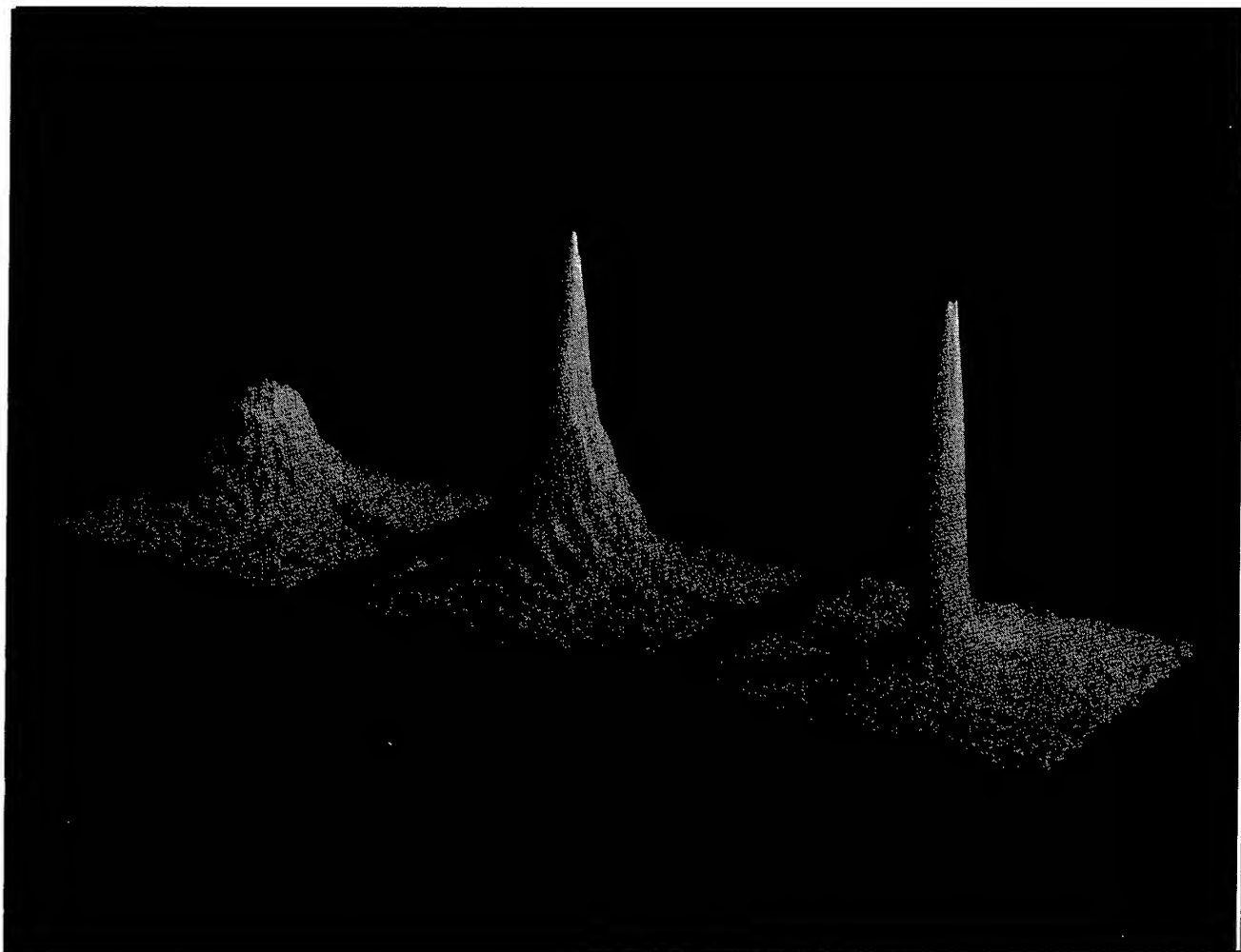


Figure 16. Two-dimensional probe absorption images, after 6 ms time of flight, showing evidence for BEC. (a) is the velocity distribution of a cloud cooled to just above the transition point, (b) just after the condensate appeared, (c) after further evaporative cooling has left an almost pure condensate. The figure shows the difference between the isotropic thermal distribution and an elliptical core attributed to the expansion of a dense condensate. The width of the images is 0.87 mm.

2.5.4 Publications

Davis, K.B., M.-O. Mewes, M.R. Andrews, N.J. van Druten, D.S. Durfee, D.M. Kurn, and W. Ketterle. "Bose-Einstein Condensation in a Gas of Sodium Atoms." *Phys. Rev. Lett.* 75: 3969-3973 (1995).

Davis, K.B., M.-O. Mewes, M.A. Joffe, M.R. Andrews, and W. Ketterle. "Evaporative Cooling of Sodium Atoms." *Phys. Rev. Lett.* 74: 5202 (1995); Erratum: *Phys. Rev. Lett.* 75: 2909 (1995).

Davis, K.B., M.-O. Mewes, and W. Ketterle: "An Analytical Model for Evaporative Cooling of Atoms." *Appl. Phys. B* 60: 155-159 (1995).

Conference Contributions with Published Abstracts

Davis, K.B., M.-O. Mewes, M.A. Joffe, M.R. Andrews, and W. Ketterle. "Evaporative Cooling of Sodium Atoms." In *Research Conference on Bose-Einstein Condensation*, Mont Ste. Odile, June 1995, *Book of Abstracts*, p. 53.

Ketterle, W. "Evaporative Cooling of Magnetically Trapped Sodium." *Bull. Am. Phys. Soc.* 40: 1269 (1995).

Theses

Davis, K.B. *Evaporative Cooling of Sodium Atoms*. Ph.D. diss., Dept. of Physics, MIT, 1995.

Entin, I.A. *Magnetic Trapping of Neutral Sodium Atoms*. S.B. thesis, Dept. of Physics, MIT, 1995.

Thompson, S.H., Jr. *Radio Frequency Induced Evaporative Cooling of Magnetically Trapped Neutral Sodium Atoms*. S.B. thesis, Dept. of Physics, MIT, 1995.

Yesley, P.S. *The Design and Testing of Novel, Spin-Flip, Zeeman Slowing Technique*. S.B. thesis, Dept. of Physics, MIT, 1995.

Section 2 Plasma Physics

Chapter 1 Plasma Dynamics

Chapter 1. Plasma Dynamics

Academic and Research Staff

Professor George Bekefi,¹ Professor Abraham Bers, Professor Bruno Coppi, Professor Jonathan S. Wurtele, Dr. Chiping Chen, Dr. Stefano Migliuolo, Dr. Abhay K. Ram, Dr. Richard Stoner,² Dr. Linda E. Sugiyama, Ivan Mastovsky

Visiting Scientists and Research Affiliates

Dr. Augusta Airoidi, Dr. Giuseppe Bertin, Dr. Francesca Bombarda, Franco Carpignano, Dr. Giovanna Cenacchi, Dr. Paolo Detragiache, Dr. Matteo Erba, Dr. Vladimir Fuchs,³ Dr. Riccardo Maggiora, Dr. Francesco Pegoraro, Marco Riccitelli, Dr. Suraj Salihu, George M. Svolos, Dr. Motohiko Tanaka, Dr. Joachim Theilhaber,⁴ Dr. Ian Wilson,⁵ Dr. Walter Wuensch⁵

Graduate Students

Palmyra E. Catravas, William S. Daughton, Darin R. Ernst, Felicisimo W. Galicia, Steven D. Schultz, Gregory E. Penn, Darren M. Pierre, Caterina Riconda, Luigi Vacca

Undergraduate Students

Gianmarco M. Felice, MöH Kuang, Kevin Lewis, Evan Reich, Jeremy Roy

Technical and Support Staff

Felicia G. Brady, Marika Contos, Laura von Bosau, Miriam Weiner

1.1 MIT Microwiggler for Free Electron Laser Applications

Sponsor

U.S. Navy - Office of Naval Research
Grant N00014-90-J-4130

Project Staff

Professor George Bekefi, Professor Hermann A. Haus, Professor Jonathan S. Wurtele, Dr. Richard Stoner, Ivan Mastovsky, Palmyra E. Catravas, Marcus Babzien,⁶ Ken Batchelor,⁶ Dr. Ilan Ben-Zvi,⁶ Jimmy Fang,⁶ Dr. Alan Fisher,⁶ Dr. William Graves,⁶ Dr. Zvi Şegalov,⁶ Joe Qiu,⁶ Dr. Xi-Jie Wang⁶

A microwiggler-based FEL permits operation at shorter wavelengths with a reduction in the size and cost of the device. Reduction in the period of the wiggler from the typical 3-10 cm to below 1 cm permits operation of FELs at shorter wavelengths for a given beam energy. The MIT microwiggler is a pulsed ferromagnetic-core electromagnet with 70 periods of 8.8 mm each which generates an on-axis peak magnetic field of 4.2 kG. The pulse repetition rate is 0.5 Hz with FWHM 0.5 msec. The microwiggler is characterized by extensive tunability. We employed a novel tuning regimen through which the rms spread in peak amplitudes was reduced to 0.08 percent, the lowest ever achieved in a sub-cm period magnetic field. The microwiggler is a serviceable scientific apparatus. Spontaneous emission has been observed for wavelengths of 500-800 nm using a 40-50 MeV

¹ Deceased August 17, 1995.

² Smithsonian Astrophysical Observatory, Cambridge, Massachusetts.

³ Centre Canadien de Fusion Magnétique (CCFM), Québec, Canada.

⁴ IBM Corporation, Waltham, Massachusetts.

⁵ CERN, SL-RFL, CH-1211, Geneva 23, Switzerland.

⁶ Accelerator Test Facility, Brookhaven National Laboratory, Long Island, New York.

beam from the Accelerator Test Facility LINAC at BNL.

High field precision in short-period wigglers is difficult to achieve. Mechanical tolerances and other coil-to-coil variations become sufficiently large on the scale of the wiggler period that they translate easily into field errors of harmful amplitude. The severity of the problem compounds with wiggler length, and curtails the FEL efficiency through dele-

terious increases in electron beam walk-off and energy spread. Various microwiggler designs have been investigated to address these technical challenges.⁷ (see table 1) We have employed a novel approach to reducing wiggler field errors in which extensive tunability is controlled through a rigorous tuning procedure. The high performance of the microwiggler makes it well-suited for the development of a linac-based FEL in the visible and UV wavelengths.

GROUP	TECHNOLOGY AND STATUS	N_w	$\lambda_w, \text{mm} / \text{G, mm}$	B_w, kG	PEAK RMS ERROR	POLE INT. ERROR
Stoner <i>et al.</i> , MIT	Pulsed ferroc core electromagnet	70	8.8/4.2	4.2	0.08%	0.14%
Huang <i>et al.</i> , Stanford	Staggered ferroc core array in solenoid	50	10.0/2.0	10.8	1.2%	Not reported
Warren and Fortgang LANL	Permanent magnet	73	13.6/1.5	6.5	0.3%	Not reported
Tecimer and Elias CREOL	Hybrid	62	8/Not reported	1.0	0.2%	0.6%
Ben-Zvi <i>et al.</i> , BNL	Superconducting ferroc core electromagnet	68	8.8/4.4	>5.5	*	*

* Phase shake and walk-off ($\pm 22 \mu\text{m}$) reported in lieu of peak amplitude and pole integral spread.

Table 1. Comparison of some short period wigglers.

⁷ I. Kimel and R. Elias, "Micro-undulator Fields," *Nucl. Instr. and Meth. A* 296: 611-618 (1990); G. Ramian, L. Elias, and I. Kimel, "Micro-undulator FELs," *Nucl. Instr. and Meth. A* 250: 125-133 (1986); J.H. Booske, W.W. Destler, Z. Segalov, D.J. Radack, E.T. Rosenbury, J. Rodgers, T.M. Antonsen, Jr., V.L. Granatstein, and I.D. Mayergoyz, "Propagation of Wiggler Focused Relativistic Sheet Electron Beams," *J. Appl. Phys.* 64: 6-11 (1988); V.A. Papadichev and O.A. Smith, "Helical Microundulators of the P.N. Lebedev Physical Institute," *Nucl. Instr. and Meth. A* 318: 803-808 (1992); R.W. Warren, D.W. Feldman, and D. Preston, "High-Field Pulsed Microwigglers," *Nucl. Instr. and Meth. A* 296: 558-562 (1990); C.M. Fortgang and R.W. Warren, "Measurement and Correction of Magnetic Fields in Pulsed Slotted-tube Microwigglers," *Nucl. Instr. and Meth. A* 341: 436-439 (1994); R.W. Warren and C.M. Fortgang, "Fabrication of High-Field Short-period Permanent Magnet Wigglers," *Nucl. Instr. and Meth. A* 341: 444-448 (1994); Y.C. Huang, H.C. Wang, R.H. Pantell, J. Feinstein, and J. W. Lewellen, "A Staggered-Array Wiggler for Far-Infrared, Free-Electron Laser Operation," *IEEE J. Quant. Electron.* 30(5): 1289-1294 (1994). N. Ohigashi, K. Mima, Y. Tsunawaki, S. Ishii, N. Ikeda, K. Imasaki, M. Fujita, S. Kuruma, A. Murai, C. Yamanaka, and S. Nakai, "Development of an Electromagnetic Helical Microwiggler," *Nucl. Instr. and Meth. A* 341: 426-430 (1994); I. Ben-Zvi, R. Fernow, J. Gallardo, G. Ingold, W. Sampson and M. Woodlee, "Performance of a Superconducting, High Field Subcentimeter Undulator," *Nucl. Instr. and Meth. A* 318: 781-788 (1992); G. Ingold, I. Ben-Zvi, L. Solomon, and M. Woodlee, "Fabrication of a High-Field Short-period Superconducting Undulator," submitted to *Proceedings of the 17th International Free Electron Laser Conference*, New York, 1995; M. Tecimer and L.R. Elias, "Hybrid Microundulator Designs for the CREOL Compact cw-FEL," *Nucl. Instr. and Meth. A* 341: ABS126-ABS127 (1994); R. Stoner, S.-C. Chen, and G. Bekefi, "A Planar Electromagnet Microwiggler for Free Electron Lasers," *IEEE Trans. Plasma Sci.* 18: 387-391 (1990).

PARAMETER	VALUE
on-axis magnetic field, B_w	4.2 kG
wiggler period, λ_w	8.8 mm
wiggler parameter, a_w	0.34
wiggler gap, G	4.2 mm
number of periods, N_w	70
rms spread in peak amplitudes, $(\delta B/B)_{\text{RMS}}$	0.08%
rms spread in pole integrals, $(\delta I/I)_{\text{RMS}}$	0.14%
repetition rate	0.5 Hz

Table 2. MIT Microwiggler parameters.

1.1.1 Microwiggler Field Characteristics

Table 2 summarizes the microwiggler parameters. Wiggler design, construction and tuning algorithm are detailed in Stoner and Bekefi.⁸ The measurements of field characteristics described here are for the full 70 periods (excluding tapered end effects) and for a repetition rate of 0.5 Hz. Each half period in the wiggler is created by a pair of magnets connected electrically in parallel, which are mounted on either side of a stainless steel bore in a precisely formed aluminum matrix (see figure 1). Current flows independently to each pair of magnets and is controlled by a variable series resistance. In order to completely characterize the microwiggler field characteristics, a comprehensive battery of field measurements was performed.

The Measurement System

An automated control system monitors the field profile, in which a B-dot loop is pulled through the bore and recorded. Peak amplitudes and peak axial positions are extracted from curve fits to the data. The control system includes feedback to maintain the wiggler total current at a constant level. Complete field scans are repeated from 5-15 times and averaged, so that a single field profile contains the information of over 10,000 field amplitude data points.

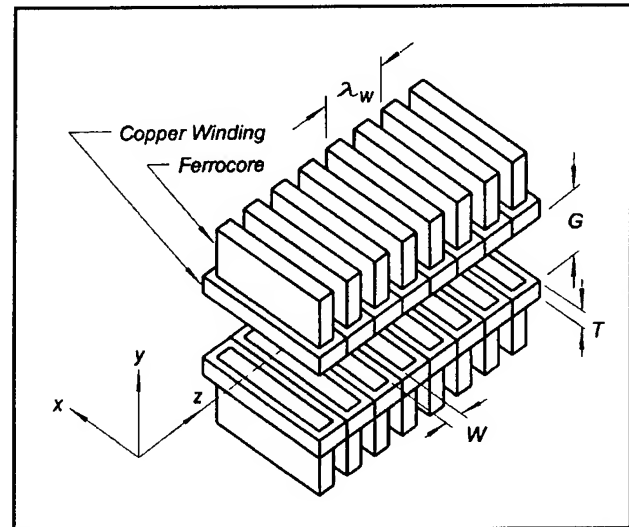


Figure 1. Schematic of the wiggler geometry.

The untuned field profile was dominated by the effects of small inhomogeneities in the wiggler construction and had an rms spread of 4 percent (figure 2). From a consecutive sequence of field profile measurements, tuning iterations reduced the spread in peak amplitudes to 0.08 percent or better, an improvement of nearly two orders of magnitude. This is an outstanding level of uniformity for a sub-cm period wiggler and illustrates the power of our tuning algorithm in controlling the field.

⁸ R. Stoner and G. Bekefi, "A 70-Period High-Precision Microwiggler for Free Electron Lasers," *IEEE J. Quant. Electron.* 31: 1158-1165 (1995).

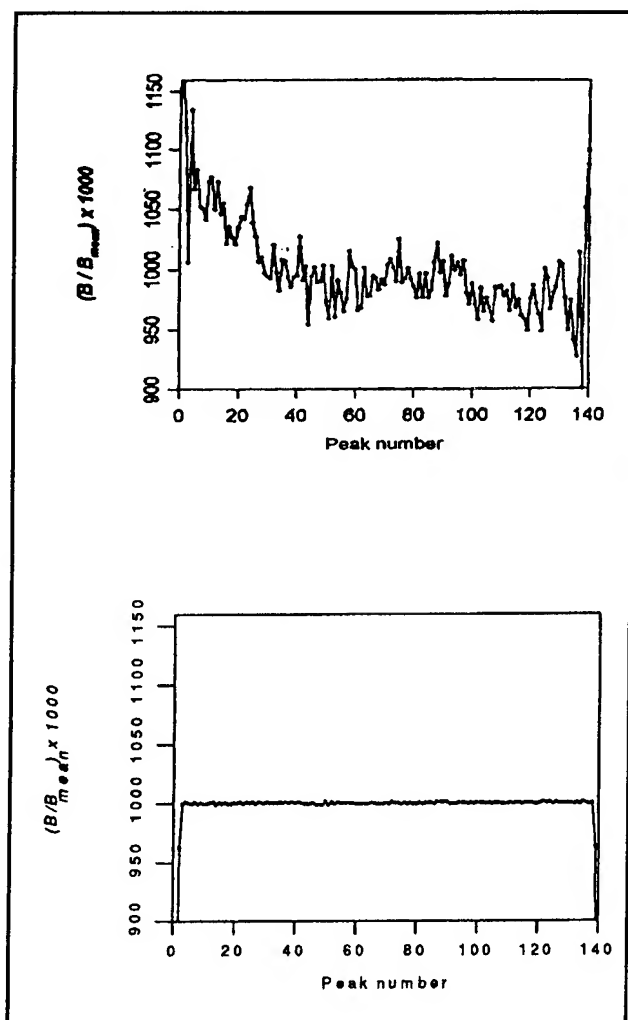


Figure 2. Peak amplitude profile: untuned profile (rms spread 4 percent) and tuned profile (0.08 percent).

A high level of purity in the wiggler field harmonic spectrum was measured and provides an independent confirmation of the peak amplitude uniformity. Furthermore, it is important that the design of the wiggler gap dimension, which must be small for large field amplitudes, does not result in field harmonics, since the high frequency harmonic emissions can damage optical coatings during lasing. Measurements show that the third harmonic is down by more than five orders of magnitude from the fundamental, the fifth harmonic is just above the noise level, and the other harmonics are not measurable.

1.1.2 Spontaneous Emission Measurements

We have been working in collaboration with researchers at the Accelerator Test Facility at Brookhaven National Laboratory to lase at 532 nm with the MIT Microwiggler in a linac-based FEL. Work in the past year has included the setup of a 3.67 m cavity around the wiggler, and the development of system alignment techniques.

Systematic measurements of spontaneous emission as a function of beam parameters are underway, to investigate how the emissions reflect the characteristics of the machine. Appropriate dependence of emissions with electron beam energy (figure 3), energy spread, emittance, and wiggler field strength have been observed. The potential for the wiggler emissions to provide information on beam alignment has been experimentally demonstrated. Single-shot spectra for 20 micropulses and even as low as a single micropulse have been recorded using a CCD camera on the output of the spectrometer. Ringdown of the spontaneous emission in the cavity has been recorded, as well as spontaneous emission trains during full macropulse operation.

1.1.3 Discussion

The high precision field profile of the MIT Microwiggler will permit the generation of coherent radiation at wavelengths ranging from the visible to ultraviolet. With our typical observations of an rms spread of 0.08 percent in peak amplitudes and 0.14 percent in pole integrals, the MIT Microwiggler currently provides the world's most uniform periodic field for any sub-cm period wiggler and is a unique tool for FEL research.

1.1.4 Publications

Babzien, M., I. Ben-Zvi, P. Catravas, J. Fang, A. Fisher, W. Graves, X.-Z. Qin, Z. Segalov and X.-J. Wang. "Optical Diagnostics for the ATF Microundulator FEL." Submitted to the *Proceedings of the 17th International Free Electron Laser Conference*, New York, 1995.

Catravas, P., R. Stoner, J. Blastos, D. Sisson, I. Mastovsky, G. Bekefi, A. Fisher, and X.-J. Wang. "MIT Microwiggler for Free Electron Laser Applications." Paper presented at the Particle Accelerator Conference, Dallas, Texas, 1995.

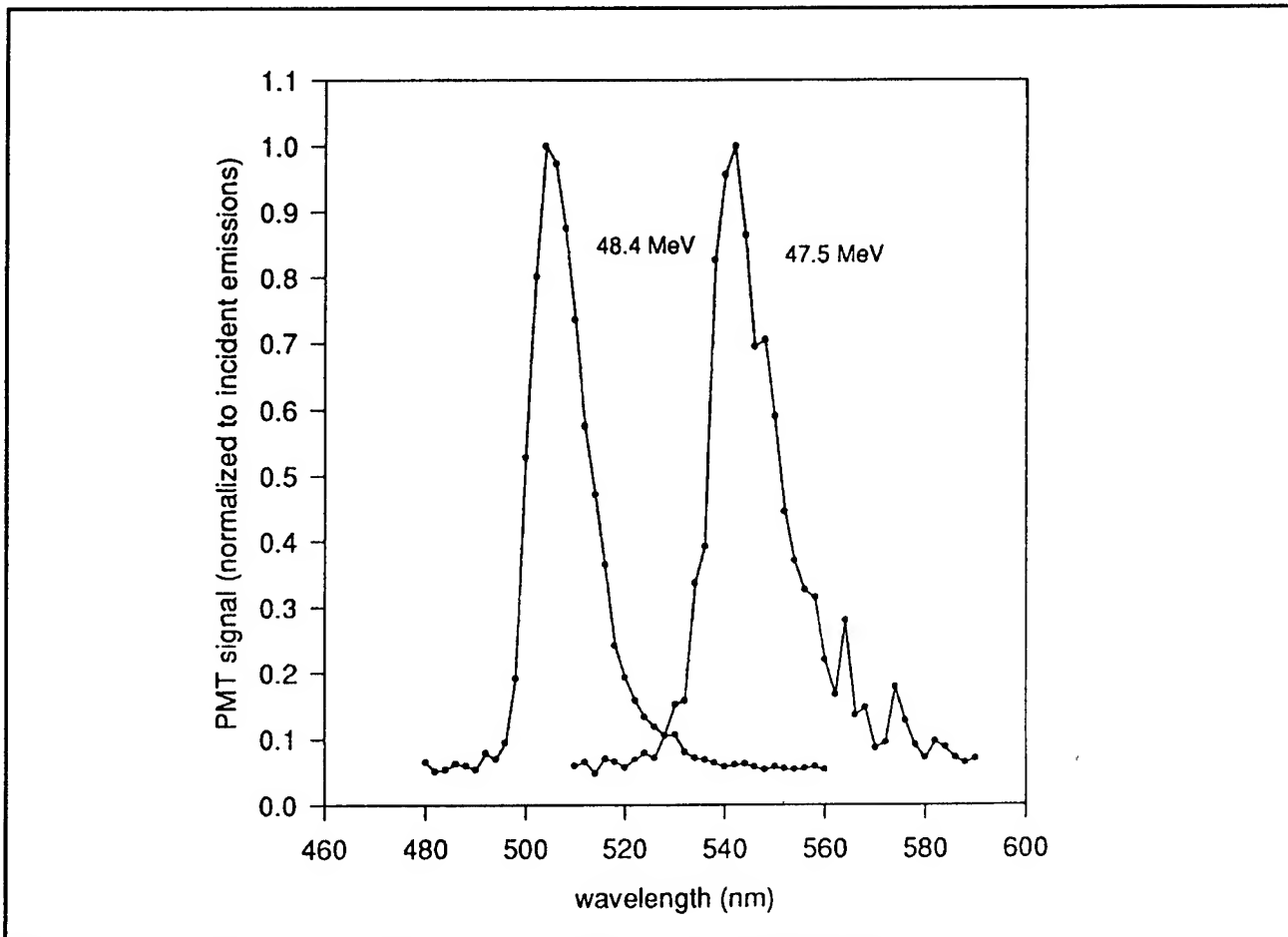


Figure 3. Spontaneous emission spectra for beam energies of 47.5 and 48.4 MeV.

Catravas, P., R. Stoner, and G. Bekefi. "Characteristics of the MIT Microwiggler for Free Electron Laser Applications." Submitted to the *Proceedings of the 17th International Free Electron Laser Conference*. New York, 1995.

Stoner, R., and G. Bekefi. "A 70-Period High-Precision Microwiggler for Free Electron Lasers." *IEEE J. Quantum Electron.* 31(6): 1158-1165 (1995).

1.2 Plasma Wave Interactions—RF Heating and Current Generation

1.2.1 Introduction

The research of this group is concerned with both basic and applied problems in the electrodynamics of plasmas. Attention is directed toward understanding the nonlinear dynamics of plasmas driven by high-frequency electromagnetic fields (such as in laser-plasma interactions or RF heating and current

drive of magnetically confined plasmas), the generation and propagation of unstable radiations from anisotropic electron distributions in space and astrophysical plasmas, and the energization of ions to the magnetosphere.

The first two reports describe our progress in the analysis of mode conversion from fast Alfvén waves to ion-Bernstein waves in tokamak confined plasmas. Recent experiments (TFTR at Princeton, Tore Supra in Cadarache, France, and Alcator C-MOD at MIT) have shown that mode-converted ion-Bernstein waves are effective in producing localized electron heating. Very recent experiments on TFTR have also produced localized plasma currents with such waves, and this may prove to be an important means for significantly enhancing the quality and operation of tokamak plasmas. The third report describes our continuing effort at exploring a possible synergism between RF driven currents and the bootstrap current for steady state confinement of tokamak plasmas. The fourth report describes an evaluation of a new transport mechanism of minority ion energy loss in tokamak plasmas intensely heated by ion-cyclotron RF

power. Finally, the last report takes a new look at induced stochasticity in ion dynamics in an electrostatic wave propagating across the magnetic field. This study is aimed at exploring its possible application toward understanding the transverse acceleration of O^+ and H^+ ions from the ionosphere to the magnetosphere where they are observed.

1.2.2 Mode Conversion of Fast Alfvén Waves to Ion-Bernstein Waves

Sponsors

Princeton University/Tokamak Physics Experiment
Grant S-03688-G
U.S. Department of Energy
Grant DE-FG02-91-ER-54109

Project Staff

Dr. Abhay K. Ram, Professor Abraham Bers, Dr. Vladimir Fuchs, Steven D. Schultz

A successful way of delivering radio frequency power for heating a tokamak plasma has been through fast Alfvén waves (FAW), excited by antennas on the low-field side of a tokamak, in the ion-cyclotron range of frequencies (ICRF). In a plasma consisting of at least two ion species with different charge-to-mass ratios, the ion-ion hybrid resonance can be present in the plasma if the frequency of the RF wave is chosen appropriately. In the vicinity of this resonance, the FAW can mode convert to the ion-Bernstein wave (IBW), which then propagates away from the resonance towards the high-field side of the tokamak. In our previous progress report,⁹ we described this mode conversion process in the presence of the high-field side, right-hand cutoff of the FAW. We presented a physical model, based on a modified Budden-type analysis that included the right-hand cutoff, which showed that the power mode-conversion coefficient to IBWs could be a maximum of 100 percent. The mode-conversion coefficient depended on the phase difference between the FAW incident on the right-hand cutoff and the FAW reflected from this cutoff. We have since formulated the technique for calculating this phase for more realistic representations of the FAW dispersion relation. This is described below in detail.

In a simple, one-dimensional (equatorial plane) description, the approximate cold-plasma dispersion relation for the FAW is:

$$n_{\perp}^2 = \frac{(L - n_{\parallel}^2)(R - n_{\parallel}^2)}{S - n_{\parallel}^2} \quad (1)$$

where all the symbols and their significance are described in last year's progress report.⁹ The propagation of the FAW through the resonance and the cutoffs is thus described by a differential equation:

$$\frac{d^2 E}{d\xi^2} + Q(\xi)E = 0 \quad (2)$$

where E is the poloidal component of the electric field, $\xi = \omega x/c$ is the normalized spatial coordinate along the equatorial plane, and $Q(\xi)$ is the "potential" function, which for a cold plasma is equal to the right-hand side of (1).

For the propagation of FAW incident on the left-hand cutoff ($L = n_{\parallel}^2$) and propagating through the resonance ($S = n_{\parallel}^2$) to the high-field side right-hand cutoff ($R = n_{\parallel}^2$), the model potential in (2) is taken to be given by:

$$Q(\xi) = \begin{cases} \gamma - \frac{\beta}{\xi}, & \text{if } \xi > 0 \\ \alpha\xi + \tilde{\gamma} - \frac{\beta}{\xi}, & \text{if } \xi \leq 0 \end{cases} \quad (3)$$

and α , β , γ , and $\tilde{\gamma}$ are parameters that are determined from a fit to the local fast wave dispersion relation. For $\xi > 0$, (3) gives the usual Budden potential with $\gamma > 0$ and $\beta > 0$. The right-hand cutoff is given by $Q(\xi) = 0$ for $\xi < 0$. We will assume that near the right-hand cutoff $|\beta/\xi|$ is very small compared to $|\alpha\xi|$ and $\tilde{\gamma}$, so that this cutoff is approximately given by $\xi_R = -\tilde{\gamma}/\alpha$. Since for $\xi < \xi_R$ we assume that the solutions to (2) are evanescent, it follows that $\alpha > 0$ and $\tilde{\gamma} > 0$. A model $Q(\xi)$ plotted in figure 4 shows characteristics very similar to those of the FAW dispersion relation between the high-field side cutoff and the left-hand cutoff.

⁹ A. Bers, A.K. Ram, C.C. Chow, V. Fuchs, K.P. Chan, S.D. Schultz, and L. Vacca, "Plasma Wave Interactions—RF Heating and Current Generation," *RLE Progress Report* 137: 229-237 (1994).

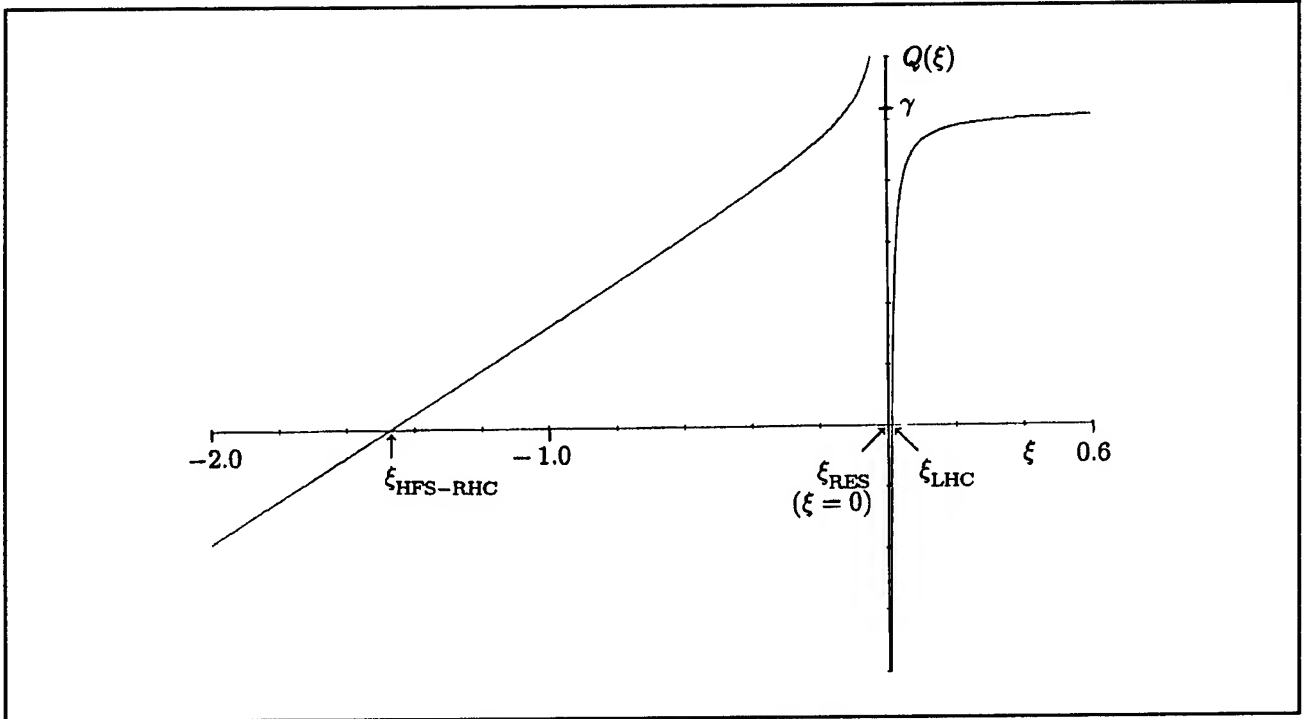


Figure 4. The model potential of equation (3) for $\alpha = 351$, $\beta = 5$, and $\gamma = \tilde{\gamma} = 513.6$. The locations of the high-field side right-hand cutoff, the ion-ion hybrid resonance, and the left-hand cutoff are denoted by $\xi_{\text{HFS-RHC}}$, ξ_{RES} , and ξ_{LHC} , respectively.

The solution to (2) and (3) is obtained by determining the solutions for $\xi < 0$ (referred to as Region I) and for $\xi > 0$ (Region II) and matching them across $\xi = 0$. In Region II, the solutions are given by the usual Whittaker functions. In Region I, there does not exist a closed form solution in terms of known functions. However, by subdividing Region I into three subregions and doing uniform asymptotic matching¹⁰ across these three subregions, we obtain an approximate solution in Region I. The matching conditions at $\xi = 0$ are:

$$E_{\text{II}}(\xi) \Big|_{\xi \rightarrow 0^+} = E_{\text{I}}(\xi) \Big|_{\xi \rightarrow 0^-}$$

$$\frac{dE_{\text{II}}(\xi)}{d\xi} \Big|_{\xi \rightarrow 0^+} = \frac{dE_{\text{I}}(\xi)}{d\xi} \Big|_{\xi \rightarrow 0^-} + i\pi\beta E(0) \quad (4)$$

where 0^+ or 0^- indicates that ξ tends to zero from the positive or the negative side, respectively. The

jump condition for the derivative of E can be easily derived since near $\xi = 0$ the potential function is of the form $-\beta/\xi$.

The high-field cutoff ξ_R ensures that the power transmission coefficient is zero. The solution to (2) and (3) will determine the power reflection coefficient R . The mode-conversion coefficient will be $C = 1 - R$. The solution in Region II can be written as:

$$E_{\text{II}}(x) = c_{\text{II}} W_{\kappa, 1/2}(z) + d_{\text{II}} W_{-\kappa, 1/2}(-z) \quad (5)$$

where c_{II} and d_{II} are constants determined by the boundary conditions, $W_{\kappa, 1/2}(z)$ and $W_{-\kappa, 1/2}(-z)$ are the Whittaker functions,¹¹ and:

$$z = -2i\sqrt{\gamma}\xi, \quad \kappa = -\frac{i}{2} \frac{\beta}{\sqrt{\gamma}} = -\frac{i}{2} \eta \quad (6)$$

¹⁰ C.M. Bender and S.A. Orszag, *Advanced Mathematical Methods for Scientists and Engineers* (New York: McGraw-Hill, 1978).

¹¹ M. Abramowitz and I.A. Stegun, *Handbook of Mathematical Functions* (New York: Dover Publications, 1970).

Using the asymptotic forms of the Whittaker functions,¹² the power reflection coefficient can be expressed as:

$$R = \left| \frac{c_{||}}{d_{||}} - (1 - e^{\pi\eta})e^{-2i\theta} \right|^2 e^{-2\pi\eta} \quad (7)$$

where θ is the phase of $\Gamma(-i\eta/2)$. The ratio $c_{||}/d_{||}$ is determined by matching to the solution in Region I. In Region I, as $\xi \rightarrow 0^-$, the solution to (2) and (3) is:

$$\lim_{\xi \rightarrow 0^-} E_I(\xi) = c_I W_{\tilde{\kappa}, 1/2}(\tilde{z}) + d_I W_{-\tilde{\kappa}, 1/2}(-\tilde{z}) \quad (8)$$

where c_I and d_I are constants, and

$$\tilde{z} = -2i\sqrt{\tilde{\gamma}} \xi, \quad \tilde{\kappa} = -\frac{i}{2} \frac{\beta}{\sqrt{\tilde{\gamma}}} = -\frac{i}{2} \tilde{\eta} \quad (9)$$

From the matching conditions in (4) at $\xi=0$, and using the properties of the Whittaker functions near $\xi=0$,¹³ we find:

$$\frac{c_{||}}{d_{||}} = e^{-2i\theta} \frac{\frac{c_I}{d_I} e^{2i\tilde{\theta}} \left\{ A + i\pi + i\pi \coth\left(\frac{\pi\eta}{2}\right) \right\} - \left\{ A + i\pi \coth\left(\frac{\pi\eta}{2}\right) - i\pi \coth\left(\frac{\pi\tilde{\eta}}{2}\right) \right\}}{\frac{c_I}{d_I} e^{2i\tilde{\theta}} A - \left\{ A - i\pi - i\pi \coth\left(\frac{\pi\tilde{\eta}}{2}\right) \right\}} \quad (10)$$

where

$$A = \frac{1}{2} \ln\left(\frac{\tilde{\gamma}}{\gamma}\right) + \psi_R\left(\frac{i\tilde{\eta}}{2}\right) - \psi_R\left(\frac{i\eta}{2}\right) + i\frac{\pi}{2} \left\{ \coth\left(\frac{\pi\tilde{\eta}}{2}\right) - \coth\left(\frac{\pi\eta}{2}\right) \right\} \quad (11)$$

$\tilde{\theta}$ is the phase of $\Gamma(-i\tilde{\eta}/2)$, and ψ_R is the real part of the Psi function.¹¹

An approximate solution in Region I is obtained by uniform asymptotic matching.¹⁰ We find:

$$\frac{c_I}{d_I} = -i \left(\frac{\alpha}{8i\tilde{\gamma}^{3/2}} \right)^{-i\tilde{\eta}} \exp\left(\frac{\pi\eta}{2}\right) \exp\left(\frac{4i}{3\alpha} \tilde{\gamma}^{3/2}\right) \quad (12)$$

Since from (12) $|c_I/d_I| = 1$, it can be shown that, from (10), $|c_{||}/d_{||}| = 1$. Thus, we can express $c_{||}/d_{||} = \exp[i(\pi + \phi)]$ where the expression for ϕ can be determined from (10) and (12). Thus, the phase ϕ mentioned in *Progress Report No. 137* is now completely determined for a realistic model of the potential function describing the propagation of FAWs. Substituting (12) into (7) completely determines the reflection coefficient. With this representation, the power mode-conversion coefficient is:

$$C = 4T_B(1 - T_B) \cos^2\left(\frac{\phi}{2} + \theta\right) \quad (13)$$

where $T_B = \exp(-\pi\eta)$.

In the special case when $\tilde{\gamma} = \gamma$, we find from (10) and (12) that the phase ϕ is given by:

$$\begin{aligned} \phi &= \frac{4}{3\alpha} \gamma^{3/2} + \eta \ln\left(\frac{8\gamma^{3/2}}{\alpha}\right) + \frac{\pi}{2} \\ &= \frac{4\sqrt{\gamma}}{3|\xi_R|} + \eta \ln\left(\frac{8\sqrt{\gamma}}{|\xi_R|}\right) + \frac{\pi}{2} \end{aligned} \quad (14)$$

where $\xi_R < 0$ is the location of the right-hand cutoff. Thus, the phase introduced by the right-hand cutoff is related to the distance between the resonance

¹² J. Heading, *J. Math. Soc. (London)* 37: 195 (1962).

¹³ H. Buchholz, *The Confluent Hypergeometric Function* (New York: Springer Verlag, 1969).

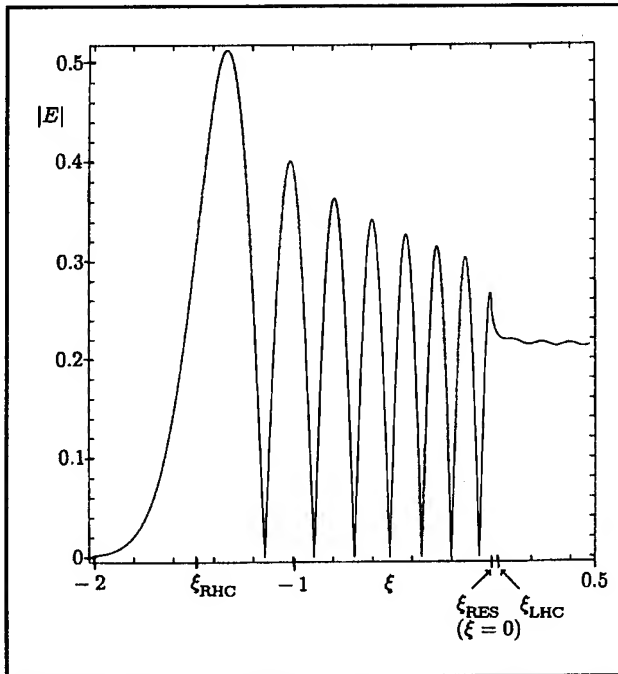


Figure 5. The field solution, $|E|$, to equation (2) for the $Q(\xi)$ given in figure 4. The parameters chosen were such that the reflection coefficient is almost zero and the entire incoming FAW power is mode converted.

and the right-hand cutoff normalized to the FAW wavelength.

The above analysis implies that the triplet system can be viewed as forming an internal plasma resonator which contains resonant absorption. The resonator is intrinsic to the plasma because it does not require a structure external to the plasma—it is formed by features (the cutoffs) that are intrinsic to the plasma. The fast Alfvén wave incident from the low-field side is coupled to the resonator at the left-hand cutoff. This coupling is mainly determined by η which enters into T_B in (13). The resonator is naturally specified by the phases ϕ and θ . However, due to the intrinsically inhomogeneous plasma, these phases are not simply related to some integer multiple of half-wavelengths between the left-hand cutoff and high-field side right-hand cutoff. The dissipation in this resonator occurs at the ion-ion hybrid resonance layer. In the cold plasma model, this is exhibited as resonant absorption; a kinetic description of the ion-ion hybrid resonance layer shows that this is mode conversion of the incident fast Alfvén wave to an ion-Bernstein wave which damps on electrons.¹⁴ The condition for 100 percent mode conversion corresponds to the situation in which the incident fast Alfvén wave is

critically coupled to this resonator. Then there is no reflection of the fast Alfvén wave towards the low-field side, and the incident wave power is totally absorbed. Figure 5 shows an example of the internal resonator effect where we have chosen parameters such that $\eta \sim 0.22$. Here there is no reflection, so that the mode-conversion efficiency is nearly 100 percent, and the fields are localized between the resonance and the high-field cutoff.

1.2.3 Mode Conversion to Ion-Bernstein Waves of Fast Alfvén Waves With Finite Poloidal Wavenumber

Sponsors

National Science Foundation

Grant ATM 94-24282

U.S. Department of Energy

Grant DE-FG02-91-ER-54109

Project Staff

Steven D. Schultz, Professor Abraham Bers, Dr. Abhay K. Ram

In *Progress Report No. 137* and in the preceding section, we described ongoing theoretical work on the mode conversion of fast Alfvén waves (FAW) at the ion-ion hybrid resonance. The fraction of power mode converted to ion Bernstein waves was calculated using a resonant absorption model, with the plasma shape near the ion-ion hybrid resonance approximated as a slab which has a uniform magnetic field in the z direction and which is also uniform in the y direction. In order to more accurately apply the preceding theory to tokamak experiments, we have extended the mode conversion problem to a new slab geometry which more closely matches the magnetic field and geometry features of a toroidally-shaped plasma. The most important change was to give the FAW a nonzero poloidal wavenumber, since the incident FAW does not have an infinite extent in the poloidal direction. Additionally, we have included a poloidal magnetic field, which changes as the wave propagates.

The mode conversion region is approximately described by a set of Cartesian coordinates, with the x direction chosen along the equatorial plane of the torus and the y and z directions corresponding to the poloidal and toroidal directions, respectively. In this model, the density and magnetic field of the plasma will still vary only in the x direction. Since a real tokamak has both a toroidal and poloidal mag-

¹⁴ A.K. Ram and A. Bers, *Phys. Fluids* B3: 1059 (1991).

netic field, the magnetic field vector lies in the y-z plane, forming an angle $\alpha(x)$ with the z axis. To calculate the dispersion relation for fast Alfvén waves, we rotate the coordinate frame into the direction of the magnetic field, so that at each point x the coordinates must be rotated by $\alpha(x)$.

The electric field of the FAW is assumed to have the form

$$\vec{E} = \hat{E}(x) \exp(ik_y y + ik_z z - i\omega t) \quad (1)$$

where k_y and k_z correspond to the poloidal and toroidal wavenumbers, respectively. Each wave-number is treated as a constant in the vicinity of the mode conversion region. Then, in the rotated coordinate system, the wavenumbers become

$$k_{\parallel} = k_y \sin \alpha + k_z \cos \alpha \quad (2)$$

$$k_{\perp} = k_y \cos \alpha - k_z \sin \alpha \quad (3)$$

The dispersion relation of the fast Alfvén wave is then calculated from cold plasma theory, using the approximation that for a low frequency wave, the electric field in the direction of the equilibrium magnetic field will be shorted out. Under these conditions, the propagation of the FAW is described by a second-order differential equation for $E = E_{\perp}$, of the form

$$\frac{d^2 E}{d\xi^2} + p(\xi) \frac{dE}{d\xi} + q(\xi) E = 0 \quad (4)$$

with the potential functions

$$p(\xi) = \frac{d}{d\xi} \ln \left(\frac{S - n_{\parallel}^2}{S - n_{\parallel}^2 - n_{\perp}^2} \right) \quad (5)$$

and

$$q(\xi) = S - n_{\parallel}^2 - n_{\perp}^2 - (\alpha')^2 \quad (6)$$

$$- \frac{D^2 - n_{\perp} D' - \alpha' n_{\parallel} D + \alpha'' n_{\parallel} n_{\perp}}{S - n_{\parallel}^2} - \frac{S'(n_{\perp} D - \alpha' n_{\parallel} n_{\perp})}{(S - n_{\parallel}^2)(S - n_{\parallel}^2 - n_{\perp}^2)}$$

In this notation, ξ is once again $(\omega/c)x$, and the primes all indicate differentiation with respect to ξ . S and D are the usual cold plasma tensor elements.

In our previous mode conversion analysis, all resonant dissipation occurred at the ion-ion hybrid resonance, which is the point at which $S - n_{\parallel}^2 = 0$. The most interesting feature of this new theory is the appearance of a second singularity in the functions p and q , at the point in space where $S - n_{\parallel}^2 - n_{\perp}^2 = 0$. This has been observed in other mode conversion theories with similar features.¹⁵ For comparison to our theory of the preceding section, consider the change of variables

$$E(\xi) = \exp \left(-\frac{1}{2} \int p(\xi) d\xi \right) W(\xi) \\ = \sqrt{\frac{S - n_{\parallel}^2 - n_{\perp}^2}{S - n_{\parallel}^2}} W(\xi) \quad (7)$$

which results in the equation

$$\frac{d^2 W}{d\xi^2} + Q(\xi) W = 0 \quad (8)$$

where $Q(\xi) = q(\xi) - (1/2)p(\xi)' - (1/4)p(\xi)^2$. In figure 6, the new potential function Q is plotted and compared to the potential for $n_{\perp} = 0$.

¹⁵ R.B. White and F.F. Chen, *Plasma Phys.* 16: 565 (1974); T.H. Stix, *Waves in Plasmas* (New York: American Institute of Physics, 1992), pp. 369-379.

In this more complicated problem, numerical integration of the equation (4) is used to compare to the much simpler Budden mode conversion solution.¹⁶ For comparison, the functions (5) and (6) were fit to simpler expressions in a few parameters:

$$p(\xi) = \frac{1}{\xi} - \frac{1}{\xi - \xi_r} \quad (9)$$

$$q(\xi) = \gamma - \frac{\beta}{\xi} + \frac{\delta}{\xi(\xi - \xi_r)}. \quad (10)$$

These parameters were chosen to fit the features of TFTR during mode-conversion heating experiments.¹⁷

Figure 7 shows the numerically calculated values of the power mode-conversion coefficient, for increasing values of k_+ . It is observed that for k_+ greater than 8 m^{-1} , the fraction of wave power dissipated in the resonant region increases significantly, to well beyond the Budden limit of 25 percent. For comparison, we also graph the predicted mode conversion from Budden theory, which is $T(1-T)$, where T is the power transmitted through the resonant region.

In order to understand the nature of this additional dissipation, we can check the conservation of wave power directly from the numerically integrated solution of (4). The results are plotted in figure 8 in the region of the resonances. For $k_+ = 4 \text{ m}^{-1}$, there is only one point where FAW power has a significant change, at the usual ion-ion hybrid resonance $S - n_{\parallel}^2 = 0$. However, for $k_+ = 15 \text{ m}^{-1}$, there is also power lost from the FAW at the second resonant point where $S - n_{\parallel}^2 - n_{\perp}^2 = 0$. This appears to indicate that the increased power dissipation which is observed in figure 7 occurs at the second resonance. This result may mean that the additional power may be lost to some process other than

mode conversion to IBWs. We are currently trying to understand this new result.

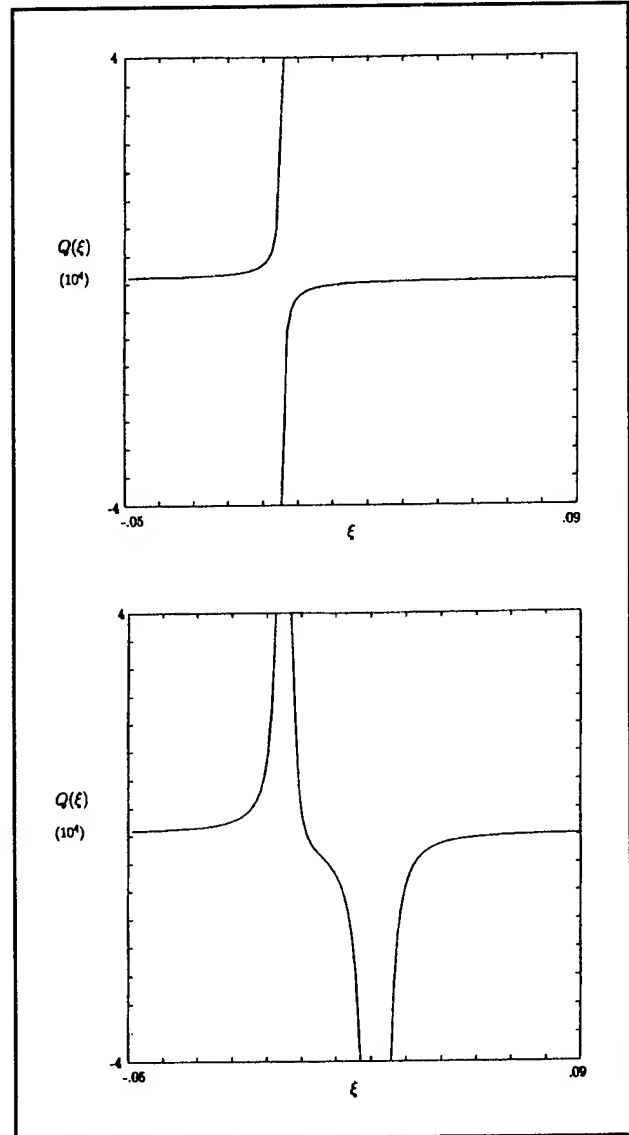


Figure 6. $Q(\xi)$ in vicinity of mode-conversion region for (a) $k_+ = 0$ and (b) $k_+ = 15 \text{ m}^{-1}$.

¹⁶ K.G. Budden, *The Propagation of Radio Waves* (Cambridge: Cambridge University Press, 1985), pp. 596-602.

¹⁷ R. Majeski et al., in *Proceedings of the 11th Topical Conference on RF Power in Plasmas*, Palm Springs, California, 1995, ed. R. Prater and V.S. Chan (New York: American Institute of Physics Conference Proceedings 355, 1995), p. 63.

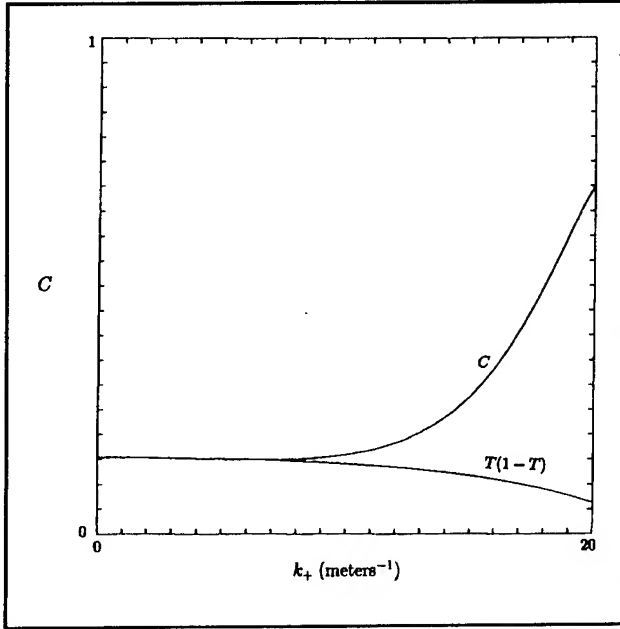


Figure 7. Fraction of FAW power dissipated (C) and Budden prediction [$T(1 - T)$] as a function of k_+ for TFTR parameters.

1.2.4 Enhancement of the Bootstrap Current in Tokamaks Using RF Waves

Sponsors

National Science Foundation
Grant ATM 94-24282
U.S. Department of Energy
Grant DE-FG02-91-ER-54109

Project Staff

Steven D. Schultz, Professor Abraham Bers, Dr. Abhay K. Ram, Dr. Joachim Theilhaber

In *Progress Report No. 137*, we began considering the use of radio frequency (RF) waves to enhance the bootstrap current to create a sustained plasma current in tokamak devices. This analysis used kinetic theory to determine the effects of a toroidal shape (see figure 9) and quasilinear diffusion on the velocity-space distribution of electrons.

The current carried by electrons (including bootstrap current) can be found by taking a moment of their distribution function f ,

$$J_{\parallel} = -e \int d^3v v_{\parallel} f. \quad (1)$$

We take f to be at steady state, averaged over the magnetic gyromotion, and independent of the toroidal angle ϕ by axisymmetry. Under these

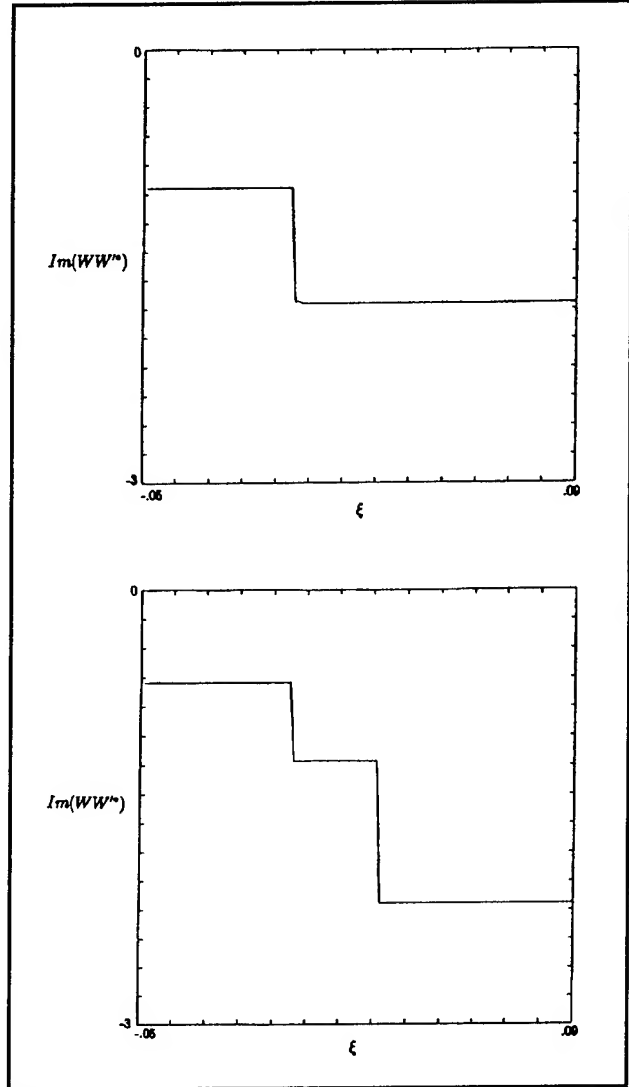


Figure 8. FAW power as a function of ξ in the mode-conversion region, showing changes at the resonances.

assumptions, f can be written as a function of the guiding center coordinates r and θ and two constants of the motion, the electron's energy E and magnetic moment μ . Then f satisfies the *drift kinetic equation* (DKE)

$$v_{\parallel} \frac{B_{\theta}}{B} \frac{1}{r} \frac{\partial f}{\partial \theta} + v_{D_r} \frac{\partial f}{\partial r} = C(f) + Q(f). \quad (2)$$

where $C(f)$ is the collision operator, and $Q(f)$ is the quasilinear operator for diffusion due to RF waves.

In *Progress Report No. 137*, we showed one way of solving (2) through expansion in small parameters. The result was

$$f = f_0^{(0)} - \frac{m}{eB_0} v_{\parallel} \frac{\partial f_0^{(0)}}{\partial r} + \tilde{f}_1^{(0)} \quad (3)$$

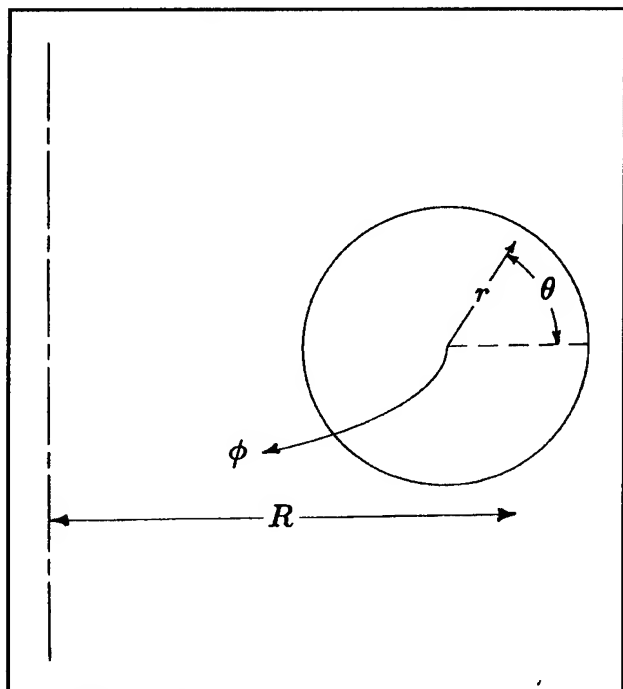


Figure 9. Toroidal coordinate system.

The modified electron distribution due to RF effects only was the solution to

$$\{C(f_0^{(0)}) + Q(f_0^{(0)})\} = 0 \quad (4)$$

where the braces indicate averaging over a bounce orbit. Inclusion of guiding center drifts gives the higher order equations found in *Progress Report No. 137*. Their solution gives the second quantity in (3) as well as the bounce-averaged quantity $\bar{f}_1^{(0)}$, which is found to be the solution to

$$\{C(\bar{f}_1^{(0)}) + Q(\bar{f}_1^{(0)})\} = S \quad (5)$$

with the "source term"

$$S = \left\{ C \left(\frac{m}{eB_0} v_{\parallel} \frac{\partial f_0^{(0)}}{\partial r} \right) + Q \left(\frac{m}{eB_0} v_{\parallel} \frac{\partial f_0^{(0)}}{\partial r} \right) \right\} \quad (6)$$

Since the remainder of a quantity after bounce averaging is generally smaller by a factor of r/R_0 (the ratio of minor radius to major radius), the θ -dependent contribution $f_0^{(1)}$ (described in *Progress*

Report No. 137) has been neglected in subsequent derivations.

The kinetic solution for the bootstrap current is thus dependent upon our ability to find solutions $f_0^{(0)}$ and $\bar{f}_1^{(0)}$ for the similar equations (4) and (5). Analysis of this type of quasilinear/Fokker-Planck equation has been important in RF current drive theory. Due to the complexity of the Fokker-Planck collision operator, numerical solutions have proved to be very useful in this analysis.¹⁸ In our work, we have used a simple Fokker-Planck computer code which makes use of a linear collision operator with only pitch angle collisions. This limited operator is sufficient for bootstrap analysis, since it is the deflection of the electrons' path with respect to the magnetic field which moves them into and out of trapped orbits, transferring momentum to the passing electrons and producing the bootstrap current.

This type of collisional/quasilinear code requires a large amount of storage space and run time. Optimization of the code has therefore been an important task. The use of parallel processing machines is also being considered to allow the use of more complicated Fokker-Planck operators or, as a more advanced problem, to solve the DKE (2) in four dimensions without resorting to the small-parameter expansion discussed above.

While this kinetic analysis is useful for its approach to RF velocity-space diffusion, it is important to consider the approach to the bootstrap current used in neoclassical transport theory.¹⁹ In particular, the diffusion of plasma across the magnetic field as the driving source of the bootstrap current must be considered. As shown in these theories, the friction force felt by particles moving parallel to the magnetic field is directly related to both cross field neoclassical transport and the bootstrap current. An important consideration in our enhancement of the current may be a possible effect on plasma confinement due to increased diffusion. The transport theories¹⁹ are all based on the approximation that the distributions of all species are close to a Maxwellian, which may not be accurate in the case of RF-modified plasmas. So we have considered the generalization of transport theories to non-Maxwellian plasmas as a future step in this problem.

Once the proper codes have been developed or adapted to solve the problem, the quasilinear oper-

¹⁸ J. Killeen, G.D. Kerbel, M.G. McCoy, and A.A. Mirin, *Computational Methods for Kinetic Models of Magnetically Confined Plasmas* (New York: Springer-Verlag, 1986).

¹⁹ S.P. Hirshman and D.J. Sigmar, *Nucl. Fusion* 21: 1079 (1981); F.L. Hinton and R.D. Hazeltine, *Rev. Mod. Phys.* 48: 239 (1976).

ator can be changed to model any of the well-known types of RF waves (lower hybrid, fast Alfvén, electron cyclotron, or ion-Bernstein). By changing the frequency and wavenumber characteristics of these waves, the velocity-space diffusion of the distribution function can be controlled. Comparison of the numerically generated results of the code will be used to find a RF wave scheme which can produce enhanced values of the bootstrap current.

1.2.5 ICRF-Heated Trapped Particles and Banana Widening Transport

Sponsor

U.S. Department of Energy
Grant DE-FG02-91-ER-54109

Project Staff

Luigi Vacca, Professor Abraham Bers, Dr. Abhay K. Ram

As shown in *Progress Report No. 137*, the resonant minority ions mostly gain perpendicular energy from the fast Alfvén wave by localized kicks in phase space occurring at the resonant layer location. It has been observed experimentally that the resonant trapped particles' banana tips are very close to the resonance layer.²⁰ In this report, we provide a theoretical explanation for the occurrence of the resonant trapped ions' banana tips near the resonant layer. In addition, we describe the loss of the resonant trapped ions due to widening of their banana orbits as they are heated by the RF fields. The occurrence of the banana tips near the resonant layer can be explained in terms of diffusion in velocity space due to wave-particle resonance. In the case of ICRF heating, the increase in perpendicular energy is much greater than the increase in parallel energy

$$|\delta v_{\parallel}|_{\text{RF}}^2 < |\delta v_{\perp}|_{\text{RF}}^2. \quad (1)$$

The ion parallel velocity is a function of space for a single particle orbit. If we neglect the drifts, the parallel velocity can be written as

$$v_{\parallel} = \pm \left[\frac{2}{m} (E - \mu B_0 + \varepsilon \mu B_0) \right]^{1/2} \left(1 - k^2 \sin^2 \frac{\theta}{2} \right)^{1/2} \quad (2)$$

where k^2 is the trapping parameter given by

$$k^2 = \frac{2\varepsilon\mu B_0}{E - \mu B_0 + \varepsilon\mu B_0}. \quad (3)$$

E is the total energy, μ is the magnetic moment, and $\varepsilon = r/R_0$ where r is the minor radius and R_0 is the major radius. Trapped particles have trapping parameters greater than unity: $k^2 > 1$. The trapping parameter also yields the poloidal angle of the banana tips

$$\theta_{\text{tip}} = 2 \sin^{-1} \left(\frac{1}{k} \right). \quad (4)$$

It is evident from (4) that when k^2 increases, θ_{tip} decreases and vice versa. When the poloidal angle of the banana tip decreases, the trapped particle becomes more trapped. We show that this is exactly what happens when a trapped particle gains energy from the RF field. First, we establish a relationship for the increase in energy with increase in magnetic moment. Consistent with (1), the total increase in energy is equivalent to the total increase in perpendicular energy; thus

$$\delta\mu \sim \frac{\delta E}{B_{\text{res}}} \quad (5)$$

where B_{res} is the magnitude of the magnetic field at the resonance point. Using (3), the variation of k^2 yields

$$k^2 + \delta k^2 = \frac{2\varepsilon(\mu + \delta\mu)B_0}{D + \delta\mu(B_{\text{res}} - B_0 + \varepsilon B_0)} \quad (6)$$

where $D = E - \mu B_0 + \varepsilon\mu B_0 > 0$. After some algebra, we find

$$[1 + \delta\mu(B_{\text{res}} - B_0 + \varepsilon B_0)/D] \frac{\delta k^2}{k^2} = \frac{\delta\mu}{\mu} [1 - \mu(B_{\text{res}} - B_0 + \varepsilon B_0)/D]. \quad (7)$$

If $\delta\mu > 0$, then $\delta k^2 > 0$ if

$$[1 - \mu(B_{\text{res}} - B_0 + \varepsilon B_0)/D] > 0. \quad (8)$$

Manipulating inequality (8) yields equivalently

$$E - \mu B_{\text{res}} > 0. \quad (9)$$

²⁰ G.W. Hammett, *Fast Ion Studies of Ion Cyclotron Heating in the PLT Tokamak*, Ph.D. diss., Princeton University, 1986.

Equation (9) is satisfied for all trapped particles that intersect the resonance layer. When the trapped minority ion gains perpendicular energy, its banana tips move toward the resonance layer. If the minority ion orbit does not intersect the resonant layer, it does not interact with the wave, and, therefore, its banana tips do not move. This simplified model does not account for collisions and Doppler-shifted resonance which produces diffusion in parallel velocity. However, for highly energetic ions, collisions are rare and the ion moves eventually with its tips toward the resonant layer. Once the particle tips have reached the resonance layer, they can move along it if we then account for the parallel momentum exchanged with the wave. Collisional energy transfer from the energetic minority ions to bulk electrons and ions also induces a poloidal and radial displacement of their banana tips. The radial movement of the tips and the pitch-angle scattering occur on a slower time scale than the angular movement of the banana tips given by (7). In a strong RF-heating regime where pitch-angle scattering is not fast enough to make the resonant distribution function isotropic, most of the resonant ions become trapped with their banana tips in the resonance layer region. For this reason, the resonant ion distribution function is essentially comprised of trapped ions.

Loss of Resonant Banana Particles

Resonant trapped ions whose banana tips are on the resonant layer also have their banana widths increase as their energy increases with time. If the banana orbits have widths comparable to the tokamak minor radius, then the outer leg of the banana orbit touches the edge of the plasma and they become unconfined. This mechanism of transport differs from those previously provided on this subject.²¹ To study this effect, we focus on the resonant trapped particles that are barely confined. Our approach assumes that the loss of the barely confined particles takes place in a steady-state mode where the ion distribution function shape is practically unchanged. The steady-state scenario can be described by the lost, barely confined particles being continuously replaced by other resonant ions diffusing in phase-space, and being globally replaced by a source of heated minority ions.

We find that the radial displacement δx along the equatorial plane always increases with increasing magnetic moment and is larger for particles whose banana tips are close to the plasma's edge along the resonance layer. We find

$$\delta x = \quad (10)$$

$$\frac{1}{A_c^2} \frac{\delta \bar{v}^2 (1 + a_r/R_0)^2 - \delta \bar{\mu} (1 + a_r/R_0) + 2A_c (1 - x_0^2) \delta \bar{p}}{D(x_0, \theta_0)}$$

where $A_c = \mu_0 q I_{tor} / 4\pi m v_{th}$, $\bar{v}^2 = v^2/v_{th}^2$, $\bar{\mu} = 2B_0 \mu / m v_{th}^2$, $\bar{p} = A_c^2 x_{ip}^2$, $x = r/a_r$, a_r is the minor radius of the tokamak, and x_0, θ_0 are respectively the radial and poloidal coordinates of the banana tips. The denominator is given by

$$D(x_0, \theta_0) = 4(1 - x_0^2) + \left[-1 + \frac{a_r}{R_0} (x_0 \cos \theta_0 - 2) \right] \cdot \frac{(1 - x_0^2)^2}{[1 + (a_r/R_0)](1 - x_0 \cos \theta_0)} \quad (11)$$

The denominator of (10) is always positive for the trapped particles that intersect the resonant layer. The direction of the radial displacement δx is outward for a positive numerator and inward for a negative numerator. The changes in the phase-space variables caused by cyclotron resonance satisfy the following relations

$$\delta \bar{v}^2 = \frac{\delta \bar{\mu}}{h_{res}} + 2 |\bar{v}_{||}|_{res} \delta \bar{v}_{||} \quad (12)$$

where $h_{res} = 1 + (a_r/R_0) \cos(\theta)$ at the resonance location and

$$\delta \bar{p} = -h_{res} \delta \bar{v}_{||} \quad (13)$$

where the subscript res refers to the resonance location. The radial velocity of trapped minority ions due to a change in magnetic moment is given by

²¹ G.W. Hammett, *Fast Ion Studies of Ion Cyclotron Heating in the PLT Tokamak*, Ph.D. diss., Princeton University, 1986; L. Chen, J. Vaclavik, and G. Hammett, "Ion Radial Transport Induced by ICRF Waves in Tokamaks," *Nucl. Fusion* 28: 389 (1988).

$$\langle V_r \rangle = \langle \frac{\delta x}{\delta t} \rangle =$$

$$\frac{a_r}{A_c^2} \frac{\langle \delta \hat{\mu} \rangle \left[\frac{(1 + a_r/R_0)^2}{h_{\text{res}}} - (1 + a_r/R_0) \right]}{T_{\text{btrapp}} D(x_0, \theta_0)} \quad (14)$$

where we used the average change in radial coordinate in one poloidal period and let $\delta t = T_{\text{btrapp}}$, where T_{btrapp} is the poloidal bounce time for trapped particles. Also, $\langle \delta \hat{\mu} \rangle$ is the average change in magnetic moment that the particle experiences in one poloidal period. This velocity can be compared to the drift velocity of banana tips when the wave spectrum is asymmetric.²⁰ The radial velocity of trapped minority ions due to a change in magnetic moment is given by (14) where we used the

average change in radial coordinate in one poloidal period and let $\delta t = T_{\text{btrapp}}$. Also $\langle \delta \hat{\mu} \rangle$ is the average change in magnetic moment that the particle experiences in one poloidal period. This velocity can be compared to the drift velocity of banana tips when the wave spectrum is asymmetric

$$\left| \frac{\langle V_{\text{tip}} \rangle}{\langle V_r \rangle} \right| \sim \left| \frac{10N A_c^2 q_s D(x_0, \theta_0)}{(\omega_{c0} t_b)^2} \right|. \quad (15)$$

For instance, let's take $D \sim 3$ and $N \sim 10$; then this ratio is smaller than unity for typical tokamak parameters.²² In the case of small-width banana orbits, $D \ll 1$, the ratio in (15) is even smaller.

We can also compute the power lost by introducing a model distribution function for their resonant trapped ions:

$$f(x, \bar{v}) = \frac{N_{\text{res}}}{2\pi a R_0^2} g(y_n, y_T) (1 - x^2)^{y_n} \frac{M}{2\pi T_{\text{eff}}} e^{-Mv^2/2T_{\text{eff}}} \frac{2}{\sqrt{\pi}} \frac{\exp[-(\psi^2/\delta\psi^2)]}{\delta\psi} \quad (16)$$

where N_{res} is the total number of resonant trapped ions in the vicinity of resonant layer, y_n and y_T are the density and temperature profiles parameters,

T_{eff} is the minority tail temperature, ψ is the pitch-angle at the resonant layer, and

$$g(y_n, y_T) = \frac{1}{(1/\sqrt{2})[(60/9)(1/A_c^2)]^{3/4} \int_0^1 dx (1 - x^2)^{y_n + (3/4)(y_T - 2)}} \quad (17)$$

gives the proper normalization for $f(x, \bar{v})$. The distribution function is bi-Maxwellian in energy and pitch-angle. The spread in pitch-angle space $\delta\psi \sim \sqrt{\nu_{ii} \tau_s}$ is a function of pitch-angle scattering frequency ν_{ii} and drag time τ_s . The energy lost can be computed by estimating the number of particles that cross the plasma boundary in a poloidal period. The ratio of the maximum energy lost to the total minority energy content is

Maximum energy lost
Total energy content \sim

$$\frac{\int dV \int_{v_b^2 - \delta v_{\text{max}}^2}^{v_b^2} \int_{-\delta\psi}^{\delta\psi} d\psi dv 2\pi v^2 f mv^2/2}{\int dV \int_0^{v_b^2} \int_{-\delta\psi}^{\delta\psi} d\psi dv 2\pi v^2 f mv^2/2} \quad (18)$$

²² I.H. Hutchinson, et. al., "First Results From Alcator C-Mod," *Phys. Plasmas* 1: 1511 (1994).

where dV is the volume that comprises the resonant ions, $v_{\theta}^2 = 9A_c^2 v_{\theta}^2 / 4$, and δv_{\max}^2 is the positive kick in energy gained by a resonant particle in one semi-poloidal period. The power dependence in (18) is given by $T_{\text{eff}} = P_{\text{RF}} \tau_s / 3n_m$, where P_{RF} is the RF power density and n_m is the minority density. The range of the velocity space integral is over all particles that are deconfined due to RF; v_{θ}^2 is the energy of an ion which in the absence of P_{RF} is confined, but which in the presence of P_{RF} gains an energy δv_{\max}^2 that will deconfine it. The maximum kick in energy is computed by integrating the equation of motion in the vicinity of the plasma layer where most absorption takes place, using the results shown in *Progress Report No. 137*.

We numerically compute the power loss adopting the following tokamak parameters: minor radius $a = 0.30$ m, inverse aspect-ratio $a/R_0 = 1/3$, majority temperature is 1 KeV, and minority density is 10^{18} m^{-3} ; and we plot the power loss for three different values of the toroidal current I : 1.3 MA, 1.5 MA, and 2 MA, respectively. The result is shown in figure

10, where we can point out that the loss of the resonant minority ions is negligible at low powers, but becomes relevant at high powers, namely $P_{\text{RF}} > 3$ MW. The increase in energy loss due to an increase in RF power is substantial at low current (see the plot for $I = 1.3$ MA), because there are more energetic ions that touch the plasma edge. As is well known, an increased RF power injected into the plasma requires higher toroidal currents to keep the energetically-produced resonant ions confined.

The dependence of the energy loss on the toroidal current is due to A_c , which appears in the velocity integral limits. The explicit dependence of the fluxes on the total RF power is the new and main result of this report. We also point out that the same approach can be applied to the future study of resonating alpha particles confinement in a tokamak. Further details of this calculation and other aspects of ICRF heating are being written up in a forthcoming Ph.D. dissertation.²³

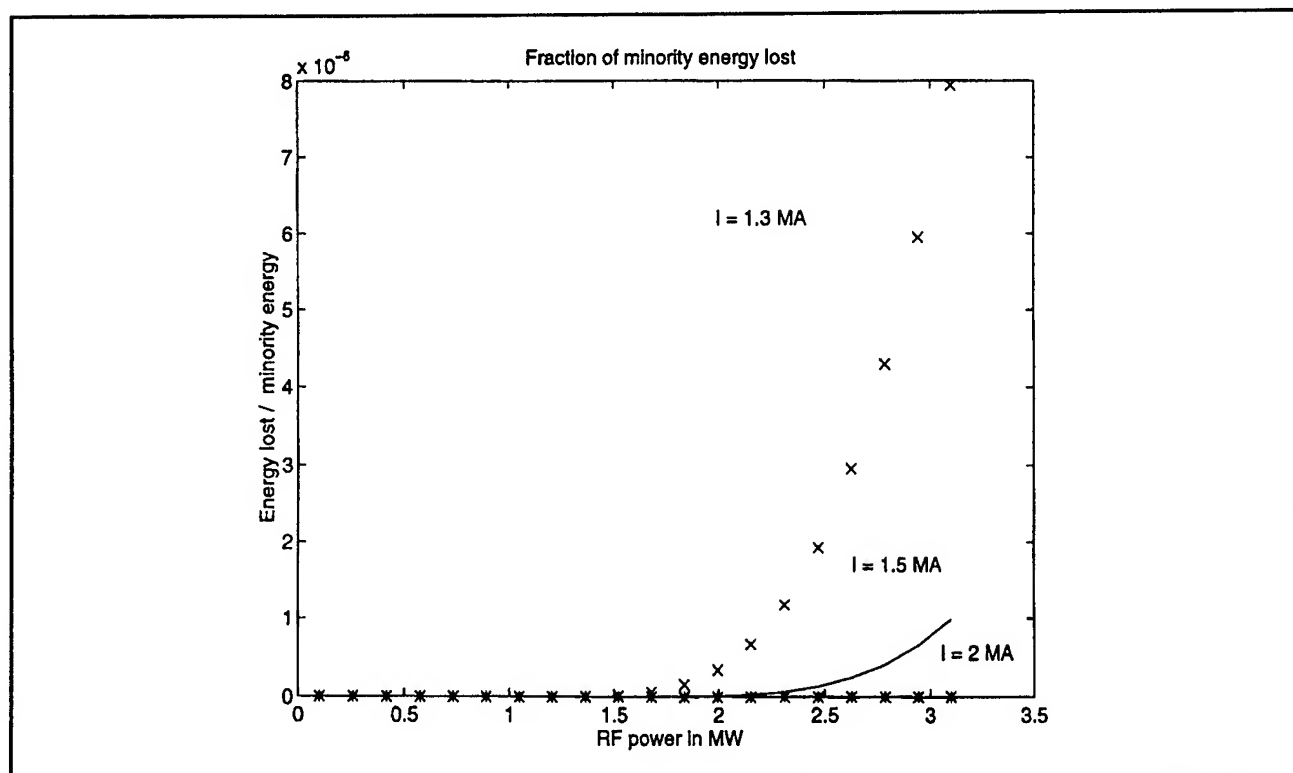


Figure 10. Ratio minority energy loss to the total energy of the minority species as function of the total RF power for standard Alcator C-Mod parameters²² and for three different values of the toroidal current. The full line refers to a toroidal current of 1.5 MA; the * line refers to a toroidal current of 2 MA, and the x line refers to a toroidal current of 1.3 MA.

²³ L. Vacca, *RF-Induced Transport of Resonant Minority Species in ICRF-Heated Tokamaks*, Ph.D. diss., Dept. of Nuclear Eng., MIT, 1996.

1.2.6 Plasma Wave Induced Stochasticity in a Magnetic Field

Sponsor

National Science Foundation
Grant ECS 94-24282

Project Staff

Felicesimo W. Galicia, Dr. Abhay K. Ram, Professor
Abraham Bers

In a magnetized plasma, the motion of a charged particle under the influence of an electrostatic wave that propagates across the magnetic field is a long-standing problem in chaotic dynamics whose detailed solution for various applications (e.g., plasma wave heating, particle acceleration) remains incomplete. Our recent work on this problem concentrated on the so-called web stochasticity analysis as a means of predicting the stochastic dynamics in this system.²⁴ Our current research has refocused efforts on the role that the Chirikov island overlapping condition can play in determining a threshold for stochasticity. The use of the Chirikov condition in the on-resonance case (the wave frequency $\omega = n\Omega$ where Ω is the cyclotron frequency) first appeared in the work of Fukuyama, et al.²⁵ They derived analytic thresholds for stochasticity valid for high harmonics ($n \gg 1$, where 1 is the action) and energies. Methods motivated by the Chirikov condition for the off-resonance case have been studied by Karney²⁶ and again, this work is valid for high harmonics and energies.

The goal of our current research is to determine a threshold for stochasticity valid for both the on- and off-resonance cases at low and high energies. To this end, our strategy has been to analyze previous analytical and computational work and to look for possible extensions and generalizations. The full Hamiltonian describing the system after appropriate transformations and normalizations has the form:

$$H = \frac{1}{T} + \varepsilon \sum_n J_n(\sqrt{2T}I) \cos(n\psi - \tau) \quad (1)$$

where T is the ratio of the frequency of the perturbing plasma wave to the cyclotron frequency and

ε is a dimensionless non-linearity parameter. At high harmonics and energies, expansions of the Bessel functions lead to tractable, approximate solutions complemented by results from computations;²⁶ unfortunately, these solutions are not applicable at lower energies and harmonics. Karney's method is to take an analytical expression for the threshold of primary island formation and to extend it to an upper bound for stochasticity in an ad hoc manner; numerical results are used to justify this extension. Karney's upper bound takes the form:

$$\varepsilon = \frac{\pi^{1/2} 2^{1/4} I^{3/4}}{4nT^{5/4}} \quad (2)$$

where n is the nearest integer to T . Also, by limiting the stochastic regime from below to those regions of action in phase space which have enough energy to be trapped by the perturbing wave, Karney determines a lower bound which takes the form:

$$\varepsilon = \frac{2I}{T} - \sqrt{\frac{8I}{T}} + 1. \quad (3)$$

A wave amplitude threshold for stochasticity (ε_{th}), as well as the action at which it sets in (I_{th}), may be found by the simultaneous solutions of (2) and (3).

A comparison of Karney's bounds to computer simulations is included in figures 11-16. Figure 11 is a surface plot of the upper bound in action of the stochastic region in phase space, as the non-linearity parameter ε and the frequency ratio T are varied where T is near 30. The upper bound is determined numerically by integrating the equations of motion and examining trajectories in phase space. Karney's work predicts an almost flat surface for such a plot. However, the surface in figure 11 is more complex. The surface shows more sensitivity to the nearness to resonance than that predicted by Karney. Figures 12-16 compare sections of the surface in figure 8 at constant T with Karney's threshold. The computer data is represented by the points and the predicted bounds are represented by the curves. These plots further support the need to increase the sensitivity of Karney's upper bound to the nearness to resonance.

²⁴ A. Bers, et. al., "Plasma Wave Interactions—RF Heating and Current Generation," *RLE Progress Report* 135: 184 (1992); 136: 240 (1993).

²⁵ A. Fukuyama, M. Momota, R. Itatani, and T. Takizuka, *Phys. Rev. Lett.* 28: 701 (1977).

²⁶ C.F.F. Karney, *Phys. Fluids* 21: 1584 (1978); 22: 2188 (1979).

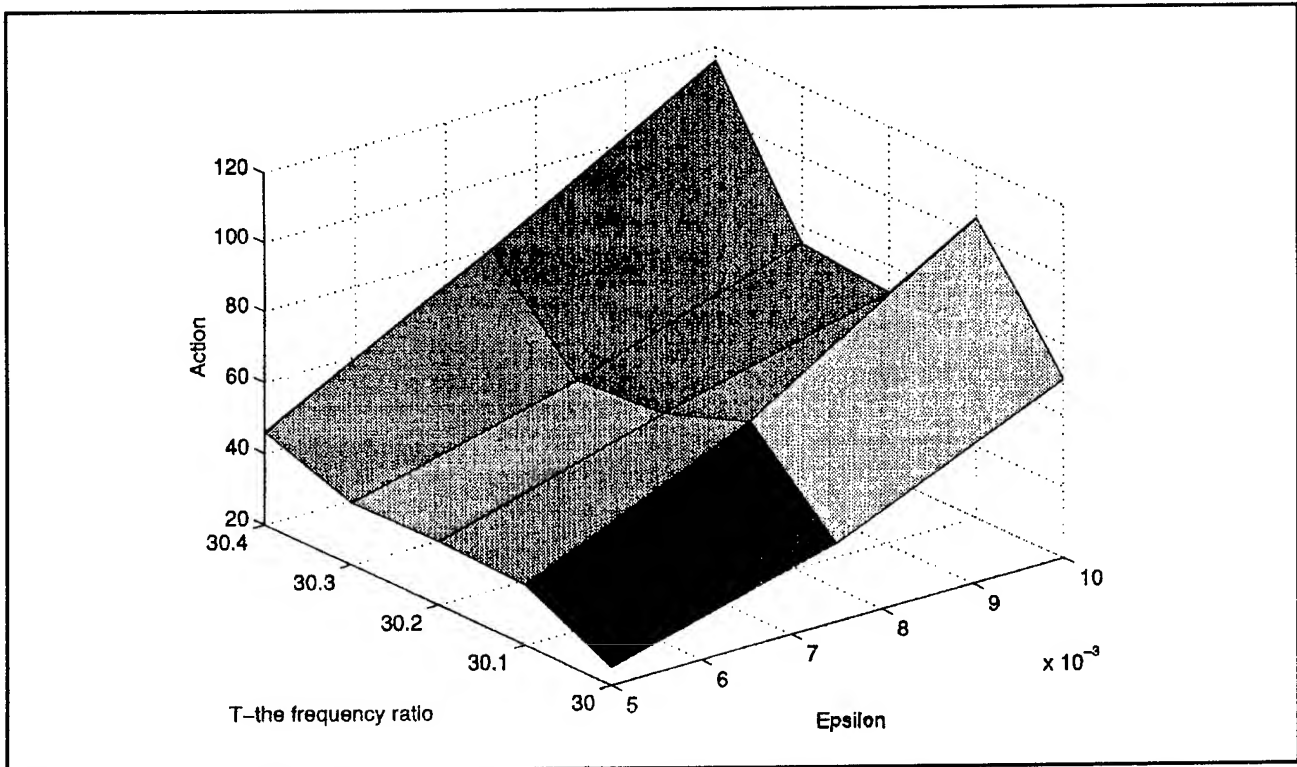


Figure 11. The numerically determined upper bound on the stochastic region in action as the frequency ratio and non-linearity parameter are varied for a frequency ratio near 30.

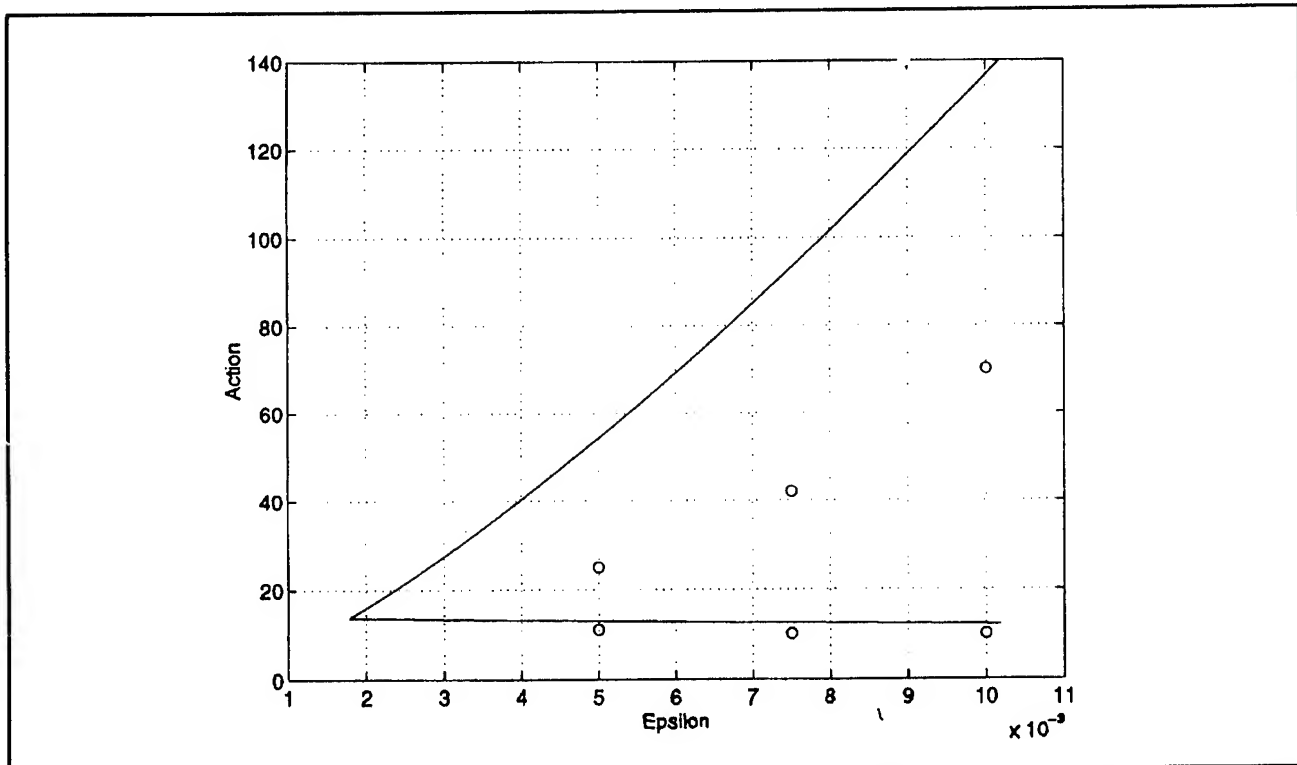


Figure 12. The numerically determined upper and lower bound on the stochastic region in action as the nonlinearity parameter is varied for a frequency ratio of 30.

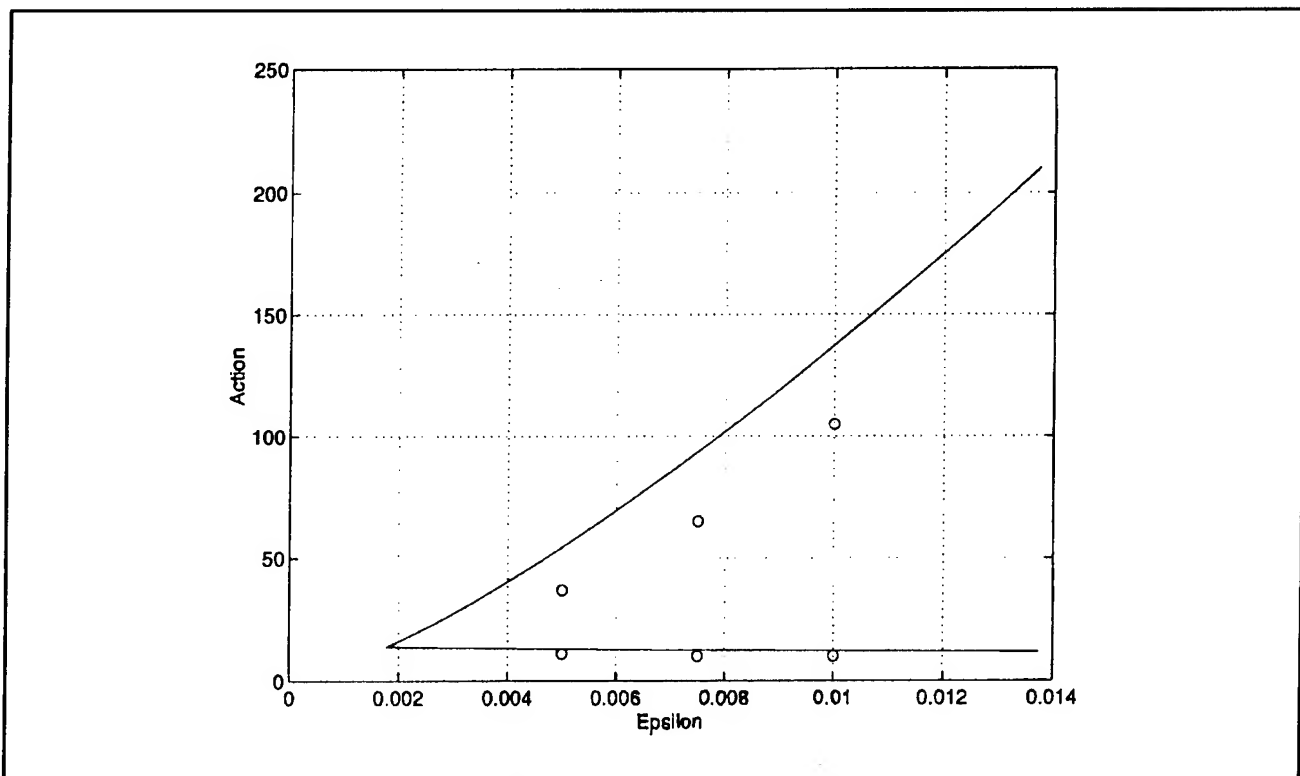


Figure 13. The numerically determined upper and lower bound on the stochastic region in action as the nonlinearity parameter is varied for a frequency ratio of 30.1.

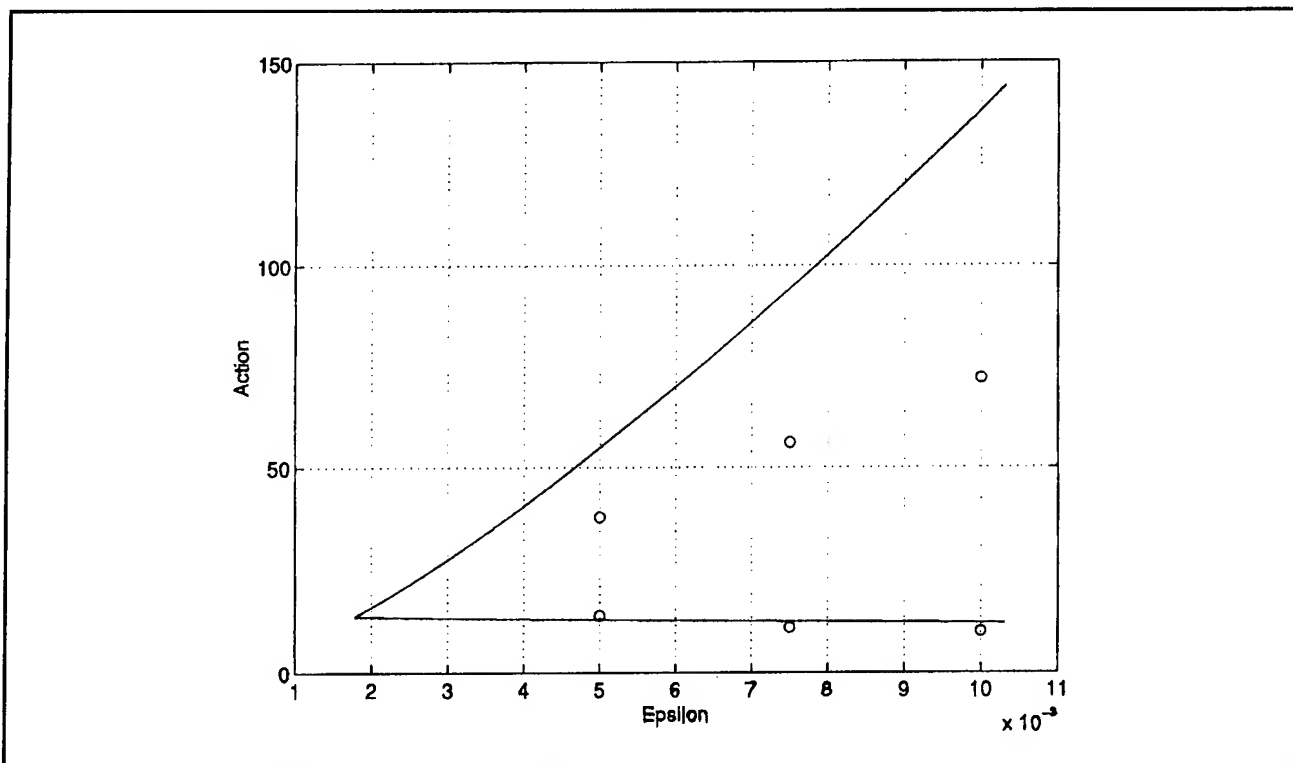


Figure 14. The numerically determined upper and lower bound on the stochastic region in action as the nonlinearity parameter is varied for a frequency ratio of 30.2.

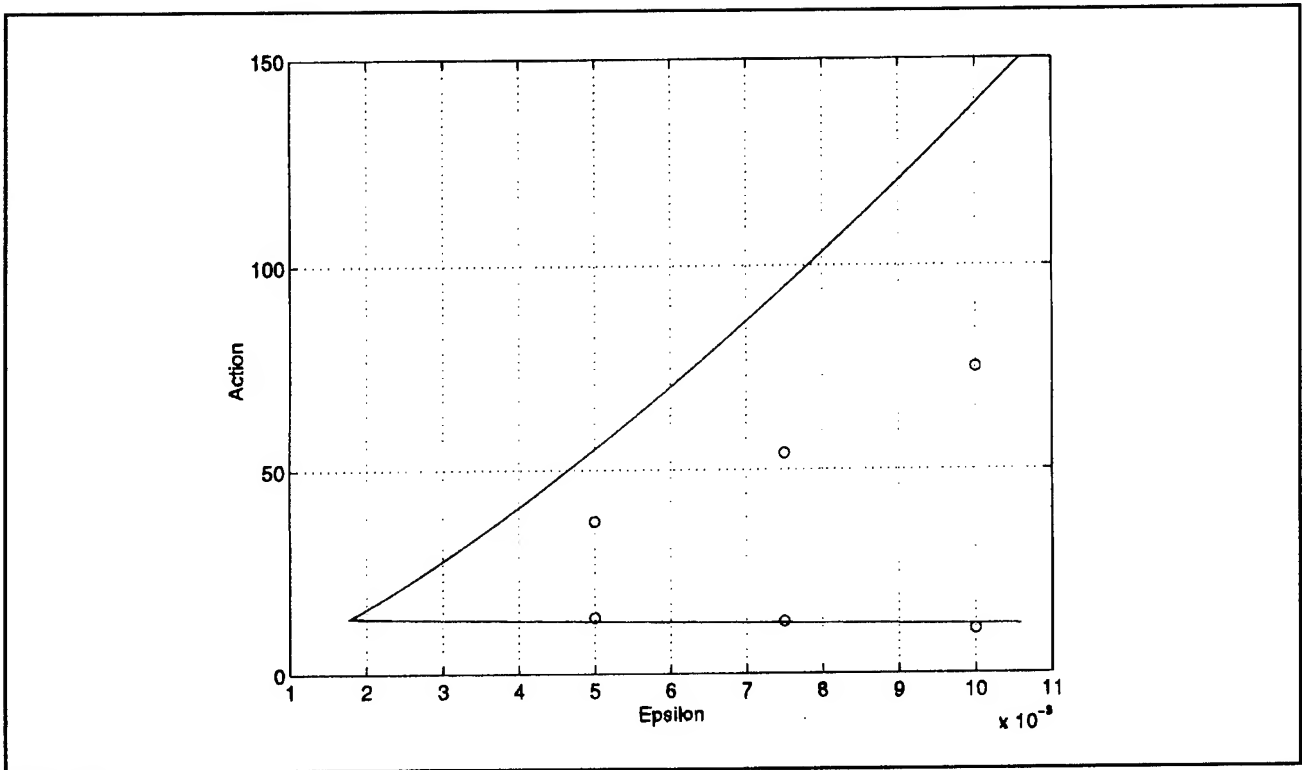


Figure 15. The numerically determined upper and lower bound on the stochastic region in action as the nonlinearity parameter is varied for a frequency ratio of 30.3.

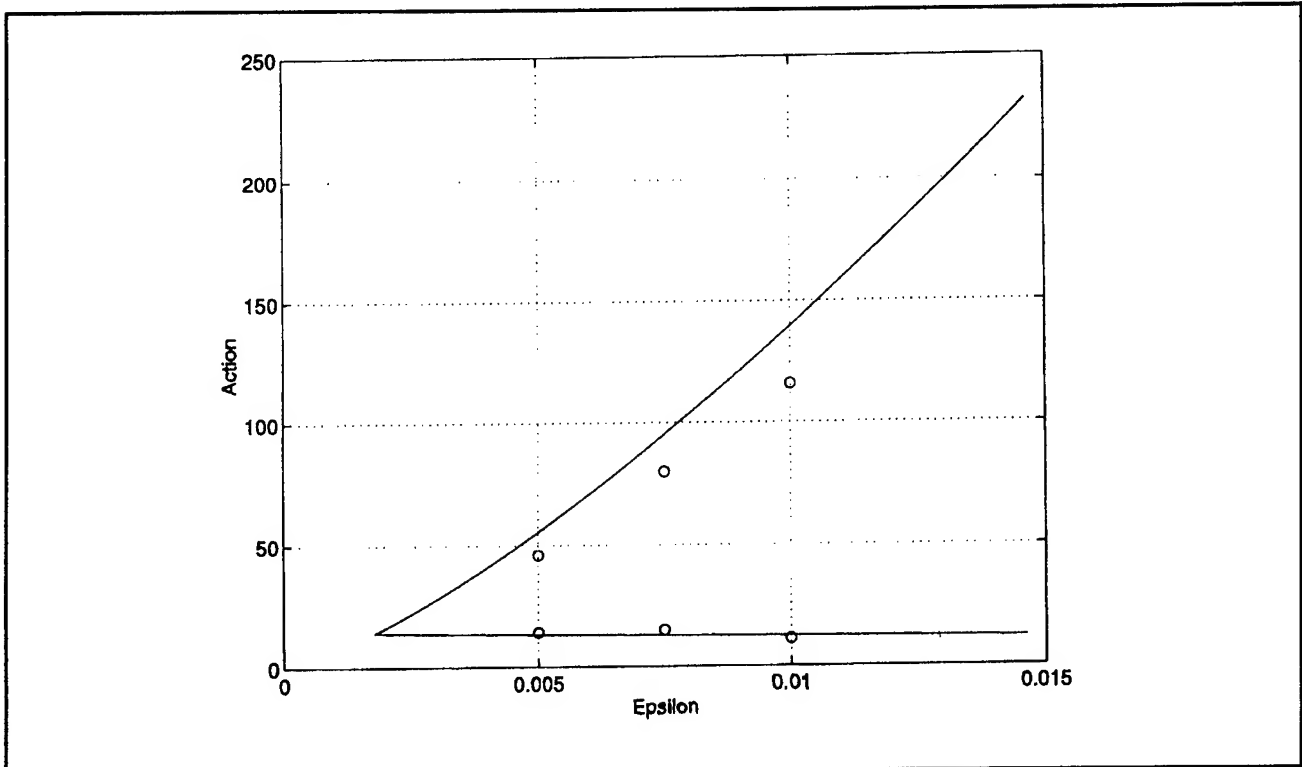


Figure 16. The numerically determined upper and lower bound on the stochastic region in action as the nonlinearity parameter is varied for a frequency ratio of 30.4.

Sagdeev and Zaslavsky²⁷ have provided some techniques which better motivate the expression derived by Karney for an upper bound and also make it possible to improve its performance as the nearness to resonance varies. In this work, the perturbation is separated into terms that oscillate on a fast time scale and those that oscillate on a slower time scale. The effects of the perturbation on the fast time scale are time averaged because only the averaged effects are seen at the time scale of island formation, and an effective fast potential is created. This potential, which includes some of the nonlinearity of the perturbation, is associated with a new unperturbed system, and a Chirikov condition may be found when this system is perturbed. The upper bound for stochasticity derived using this method is:

$$\varepsilon = \frac{\pi^{1/2} 2^{1/4} I^{3/4}}{\Delta n \cdot T^{9/4}} \quad (4)$$

where Δn is the number of terms that oscillate on the slower time scale. Notice that since n is the nearest integer to T , by choosing Δn to be 4 and $n=T$, this method gives a result equivalent to that of Karney (2). Further, the partition of the perturbation into fast and slow terms is somewhat arbitrary. The idea is to identify a group of terms near resonance as the slow terms. The interesting property of this method is that by making the number of terms that are averaged depend on the nearness to resonance of the original system, it appears that Karney's upper bound may be improved. Such work is currently in progress.

1.2.7 Publications

Bers, A., S.D. Schultz, and A.K. Ram. "Mode Conversion to Ion-Bernstein Waves of Fast Alfvén Waves with Finite Poloidal Wavenumber in Tokamak Geometries." *Bull. Am. Phys. Soc.* 40: 1705 (1995).

Fuchs, V., A.K. Ram, S.D. Schultz, A. Bers, and C.N. Lashmore-Davies. "Mode Conversion and Electron Damping of the Fast Alfvén Wave in a Tokamak at the Ion-Ion Hybrid Frequency." *Phys. of Plasmas* 2: 1637 (1995).

Lashmore-Davies, C.N., V. Fuchs, and A.K. Ram. "Strong Electron Dissipation by a Mode Converted Ion Hybrid (Bernstein) Wave." In *Proceedings of the 11th Topical Conference on Radio Frequency Power in Plasmas*, Palm Springs, California, May 17-19, 1995. Eds. R. Prater and V.S. Chan. New York: American Institute of Physics Conference Proceedings 355, 1995, pp. 277-280.

Ram, A.K. "Heating and Current Drive by Mode-Converted Ion-Bernstein Waves." Invited talk, in *Proceedings of the 11th Topical Conference on Radio Frequency Power in Plasmas*, Palm Springs, California, May 17-19, 1995. Eds. R. Prater and V.S. Chan. New York: American Institute of Physics Conference Proceedings 355, 1995, pp. 269-276.

Ram, A.K. "Heating and Current Drive by Mode-Converted Ion-Bernstein Waves." Report PFC/JA-95-18, MIT Plasma Fusion Center, Cambridge, Massachusetts, September 1995.

Ram, A.K., A. Bers, S.D. Schultz, and V. Fuchs. "Interaction of Mode-Converted Ion-Bernstein Waves With Electrons in Tokamaks." In *Proceedings of the International Sherwood Fusion Conference*, Incline Village, Nevada, April 3-5, 1995, Paper 2D17.

Ram, A.K. "Mode-Converted Ion-Bernstein Waves for Heating and Current Drive." *Bull. Am. Phys. Soc.* 40: 1828 (1995).

Ram, A.K., A. Bers, S.D. Schultz, V. Fuchs, A. Bécoulet, and B. Saoutic. "Mode-Converted Ion-Bernstein Waves in Tokamaks." In *Proceedings of the 22nd European Physical Society (EPS) Conference on Controlled Fusion and Plasma Physics*, Bournemouth, England, July 3-7, 1995, Volume 19C, Part IV, pp. 353-356.

Ram, A.K., A. Bers, S.D. Schultz, V. Fuchs, A. Bécoulet, and B. Saoutic. "Mode-Converted Ion-Bernstein Waves in Tokamaks." Report PFC/JA-95-20, MIT Plasma Fusion Center, Cambridge, Massachusetts, September 1995.

Ram, A.K., A. Bers, S.D. Schultz, V. Fuchs, A. Bécoulet, and B. Saoutic. "RF Wave Effects on the Neoclassical Electron Distribution Function in Tokamaks." In *Proceedings of the International Sherwood Fusion Conference*, Incline Village, Nevada, April 3-5, 1995, Paper 3C17.

²⁷ R.Z. Sagdeev and G.M. Zaslavsky, "Regular and Chaotic Dynamics of Particles in a Magnetic Field," in *Nonlinear Phenomena in Plasma Physics and Hydrodynamics*, ed. R.Z. Sagdeev (Moscow: Mir Publishers, 1986), p. 65.

Saoutic, B., A. Bécoulet, T. Hutter, D. Fraboulet, A.K. Ram, and A. Bers. "Mode Conversion Heating Experiments on Tore Supra." In *Proceedings of the 11th Topical Conference on Radio Frequency Power in Plasmas*, Palm Springs, California, May 17-19, 1995. Eds. R. Prater and V.S. Chan. New York: American Institute of Physics Conference Proceedings 355, 1995, pp. 71-74.

Schultz, S.D., A.K. Ram, and A. Bers. "RF Wave Effects on the Neoclassical Electron Distribution Function in Tokamaks." In *Proceedings of the 11th Topical Conference on Radio Frequency Power in Plasmas*, Palm Springs, California, May 17-19, 1995. Eds. R. Prater and V.S. Chan. New York: American Institute of Physics Conference Proceedings 355, 1995, pp. 263-266.

Schultz, S.D., A.K. Ram, and A. Bers. "RF Wave Effects on the Neoclassical Electron Distribution Function in Tokamaks." Report PFC/JA-95-19, MIT Plasma Fusion Center, Cambridge, Massachusetts, September 1995.

Schultz, S.D., A. Bers, and A.K. Ram. "RF Wave Effects on the Neoclassical Electron Distribution Function in Tokamaks." *Bull. Am. Phys. Soc.* 40: 1703 (1995).

Vacca, L., A. Bers, and A.K. Ram. "RF-Induced Transport of Resonant Minority Species in ICRF-Heated Tokamaks." *Bull. Am. Phys. Soc.* 40: 1706 (1995).

1.3 Physics of Thermonuclear Plasmas

Sponsor

U.S. Department of Energy
Grant DE-FGO2-91ER-54109

Project Staff

Professor Bruno Coppi, Dr. Augusta Airoidi, Dr. Giuseppe Bertin, Dr. Francesca Bombarda, Franco Carpignano, Dr. Giovanna Cenacchi, Marika Contos, William S. Daughton, Dr. Paolo Detragiache, Dr. Matteo Erba, Darin R. Ernst, Gianmarco M. Felice, MöH Kuang, Kevin Lewis, Dr. Riccardo Maggiora, Dr. Stefano Migliuolo, Dr. Francesco Pegoraro, Gregory E. Penn, Evan Reich, Marco Riccitelli, Caterina Riconda, Jeremy Roy, Dr. Suraj Salihu, Dr. Linda E. Sugiyama, George M. Svolos, Dr. Motohiko Tanaka

In this research program, we study the physics of magnetically confined plasmas in regimes relevant to present-day advanced experiments as well as to the planning of new experiments on fusion burning plasmas. The importance of providing an experimental proof of the process of ignition has been underlined²⁸ by the Panel on Fusion Research of PCAST: "Producing an ignited plasma will be a truly notable achievement for mankind and will capture the public's imagination. Resembling a burning star, the ignited plasma will demonstrate a capability with immense potential to improve human well-being. Ignition is analogous to the first airplane flight or the first vacuum-tube computer."

The Ignitor experiment, proposed by us in 1975, was first suggested and designed on the basis of the known physics of thermonuclear plasmas and present-day technology to reach ignition regimes. Thus, our group has recognized the importance of ignition even when its relevance was not universally acknowledged. ITER, a very large-scale experiment that has been studied more recently as an international undertaking to address the issue of ignition in large-volume, relatively low-density plasmas, has adopted in its design key features that were pioneered by the Ignitor program.

Construction of the Ignitor machine core, with technology based on MIT's Alcator program, is presently underway in Europe.

²⁸ PCAST, Fusion Review Panel, *PCAST Report* (Washington, D.C.: O.S.T.P., White House, 1995).

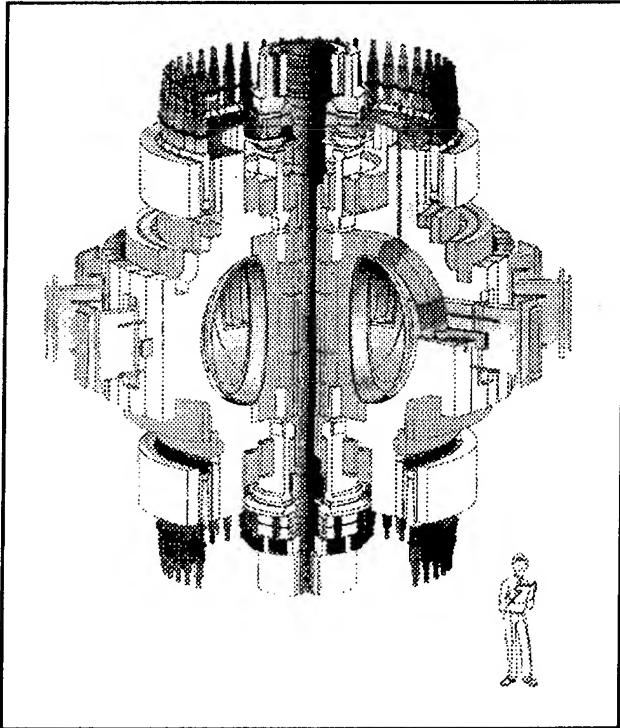


Figure 17. IGNITOR Ult machine.

At MIT, the Alcator C-Mod experiment combines the favorable features of an elongated plasma cross section with a high-magnetic field, to produce high-plasma currents and sustain high-plasma densities. Alcator C-Mod is being successfully operated and is producing novel results that are of interest to basic plasma physics and to fusion research in general. This machine has characteristics very similar to Megator, which we had studied in the early 1970s in order to produce multimegamperes plasma currents by combining high-magnetic fields, tight aspect ratios and elongated plasma cross sections. Megator was in fact considered a logical evolution of the Alcator program that we had initiated and developed.

There is an increasing body of experimental evidence supporting the elements that characterize the second stability region for finite β plasmas that we had discovered originally, including the good confinement characteristics of regimes with vanishing magnetic shear. Given their intrinsic value, we have followed closely these developments. These regimes can be explored with fusion burning plasmas by experiments of the Ignitor type.

In addition, we have studied Candor, a new machine concept for approaching the fusion burn

conditions of tritium-poor plasmas and in particular of D^3 - He mixtures or prevalent-deuterium plasmas (D-D "catalyzed"), where the fraction of fusion energy produced as neutrons is reduced relatively to the commonly considered D-T reactors. In particular, we have devoted considerable attention to the physics of those experiments that employ the high-field, high-current technologies developed for Ignitor and that exploit the favorable properties of the second stability regimes.

At this time, our research program follows two major avenues. First, the basic physical processes of thermonuclear plasmas (equilibrium, stability, transport, etc.) are being studied as they apply to existing or near-term experiments. In this effort, we collaborate with experimentalists and theorists from other research groups both in the United States, e.g., Columbia University, Phillips Laboratory, Princeton University, University of Texas, Lawrence Livermore Laboratory, and abroad, e.g., JET Laboratory, University of Turin, CNR of Milan, etc. This work also involves time-dependent simulations of the plasmas to be produced by the Ignitor-Ult experiment, with particular attention being focused on the evolution of spatial profiles of plasma current and temperature. Collaboration with our colleagues at the laboratories of E.N.E.A. (Italy), as well as in-house code development, plays a major role in this endeavor.

In the following we discuss some salient results of work completed or presently being carried out by members of our research group.

1.3.1 Feasibility of Ignition Experiments: Major Issues for Debate

As indicated earlier, the demonstration of ignition has been repeatedly recognized as the most important objective of fusion research, stressing the principle that "the initial model (experiment) need not resemble the one that is later commercialized; much of what would be learned in a tokamak ignition experiment would be applicable both to more advanced tokamak approaches and to other confinement concepts."²⁹ For ignition, there are difficult conditions to be met that include the macroscopic stability of the plasma column, the rate of thermal energy transport, the degree of plasma purity, the thermal loading on the first wall, the ability to survive major disruption events, etc. At typical DT ignition parameters, the electron collision frequency exceeds the ω_* -frequencies related to

²⁹ PCAST Report of the Fusion Review Panel (Washington, D.C.: O.S.T.P., White House, 1995).

the pressure gradients so that the modes producing magnetic reconnection are not of the (relatively benign) collisionless type. For reasons of confinement, the plasma current must be the maximum compatible with the applied toroidal field, corresponding to low values of the safety factor, (e.g., $q_a \approx 3$), for monotonic shear profiles, or be relatively low (e.g., $q_a \approx 6$) for a reversed shear configuration. In the case of low q_a , the ideal MHD stability against $m^0 = 1$ and coupled $m^0 = 2$ modes requires that β -poloidal be sufficiently low, such as $\beta_p < 0.3$. Since the central plasma pressure at ignition is prescribed within a rather well defined range, relatively high poloidal fields, B_p , are required. In the case of high q_a , the toroidal field B_T must also be sufficiently high, since there is a limitation on plasma size and on the minimum value of B_p that is acceptable for stability against ballooning modes. In all cases, the required fields are well above those permitted by present superconducting magnet technology.

Thus, the objective of ignition sustained over several (> 10) energy replacement times should be pursued by high-field, normal conducting magnets, and at first by compact experiments igniting at peak densities $n_{e0} \approx 10^{21} \text{ m}^{-3}$ and relatively low temperatures ($T_0 \approx 12 \text{ keV}$). Considering the collisional current equilibration time $\tau_1 \propto a^2 T^{3/2}$ as another reference for the duration of the ignited state (a is the plasma minor radius), it is clear that relatively small dimensions and low ignition temperatures are compatible with relatively short current pulses. The same argument applies for the density limit, which is commonly related to the average plasma current density and is higher at high fields and compact dimensions.

In the range of high-field machines that have been studied, from Ignitor ($R_0 \approx 1.32 \text{ m}$) to Candor ($R_0 \approx 2.5 \text{ m}$), the two sets of parameters chosen for construction are based on issues of cost versus benefits. Ignitor is suitable for D-T ignition while Candor is, in principle, capable of reaching D- ^3He burn conditions. The superconducting ITER device, as presently conceived and assuming that a field of 13 T can be achieved at the coils, does not satisfy macroscopic MHD stability conditions for internal modes, even with flattened pressure profiles when its reference plasma parameters are considered. The smaller "PCAST-machine" that employs normal-conducting magnets (at a cost $\sim 6\text{G}\$$) has a similar stability problem when its reference plasma parameters are analyzed.

1.3.2 Physics of Advanced, High-Magnetic Field Experiments

In identifying the optimal performance of an advanced experiment such as Ignitor, presently known constraints on the plasma parameters that can be achieved must be taken into account. These constraints are mutually linked. In particular, Ignitor can operate well within the known limitations for the particle density and the plasma pressure (beta limit). Detailed simulations of the plasma current ramp up and of plasma heating to ignition have been carried out. These are consistent with the engineering constraints of the machine design. A special updated version of the free boundary, 1 + 1/2D JETTO transport code has been employed to study and optimize these characteristics.

The plasma shape and position are controlled to achieve consistency with the reference magnetic confinement configurations, introducing also the first wall contour as a bound. The avoidance of the disruption boundaries in the (I, q_ψ) diagram is assured while taking the technical constraints on the poloidal coils (e.g., mechanical and thermal stresses) into account. Transport diffusion coefficients which lead to energy confinement times close to those predicted by "L-mode" scalings have been chosen. Special attention is being given to the influence of the parameters of the outermost region of the plasma column on the evolution of the current density.

1.3.3 Reversed Shear Operation for High-Field Ignition

The improvement of plasma confinement that has been observed during the operation of neutral beam heated tokamaks with nonmonotonic current and q profiles ("reversed shear") introduces the possibility of a new regime of D-T ignition at low density and very low fusion power in high field, magnetically confined plasmas. Reversed shear current profiles should be attainable with modest amounts of auxiliary heating, for discharges running at parameters that are well below the maximum design values that are intended to support full field ohmic or low-auxiliary-power ignition in such machines. In the reversed shear ignition scenario, the current ramp plays an important part in efficient plasma heating to ignition, as well as in establishing the current profile. Reversed shear conditions can be established part way into the initial current ramp-up phase of a discharge. Enhancement of the energy confinement during this part of the ramp provides the optimal heating path to ignition and minimizes the external heating requirement and the fusion power at ignition. The degree of shear

reversal decreases with time after the end of the current ramp, and particularly with the time spent at sub-ignition temperatures. The minimum q falls below two, but can easily be kept well above unity. Machines that can achieve high magnetic fields are likely to gain the greatest benefit from reversed shear ignition. Detailed examples of reversed shear scenarios have been studied for the Ignitor-Ult.³⁰

1.3.4 Low-Current Approach to Ignition

The "standard" path to achieve ignition conditions so far has been that of producing plasmas with the maximum current and poloidal field that are compatible with the applied toroidal field and the geometry of the adopted configuration (the low q_a approach.) The other approach that is motivated by recent experiments with reversed shear configuration is with relatively low currents and high fields corresponding to relatively high values of q_a (e.g., $q_a \approx 6$). While the first approach can be pursued with ohmic heating alone, the second one involves an auxiliary heating system that in the case of the Ignitor machine is ICRF. One of the advantages of this approach is that the onset of large scale internal modes can be avoided as $q(\psi)$ is kept above 1 over the entire plasma column. Since quite peaked density profiles are produced in the regimes where enhanced confinement is achieved, the α -particle power level at ignition (and, correspondingly, the thermal load on the first wall) can be reduced relative to the standard, low q_a approach. The possibility of reaching ignition in the reverse shear high q_a regime is considered and that it may be followed by a transition to the low q_a regime, assuring that the excitation of modes involving magnetic reconnection will not undermine the needed degree of confinement. Relevant numerical simulations include the use of the free boundary JETTO code, following the original analysis³¹ carried out by the Baldur Code.

1.3.5 Global Stability and Operational Regimes of Ignitor, ITER, and Alcator C-Mod

One of the primary requirements for an experiment capable of approaching ignition conditions is the macroscopic stability of the plasma column. A numerical analysis is carried for two proposed ignition experiments (Ignitor and ITER), concentrating on the stability of their confinement configuration for different plasma pressure and current profiles, using both the PEST and DCON codes (which involve the ideal MHD linearized approximation). Since, in both cases, the aspect ratio is tight ($R/a = 2.8$ and 2.9 , respectively), and the unwinding parameter $q(\psi)$ is less than unity over the inner half of the plasma column, unstable $n = 1$ modes arise (for which the $m = 1, 2$ poloidal harmonics prevail) and affect a major part of the plasma column ($0 \leq r \leq 3a/4 \leftrightarrow q(\psi) \leq 2$). Here we denote by ψ the normalized poloidal flux variable.

For profiles that are nearly flat up to the $q = 1$ surface and are represented by $p = p_0(1 - \psi^N)^{3/2}$ with $N > 3$, pressure driven modes, dominated by the $m = 2$ harmonic, may be found, depending on the value of $\beta_p = 2\mu_0 \langle p \rangle / B_p^2$. These modes are unstable for the reference parameters of operation of ITER ($B_T = 5.7\text{T}$, $n_0 = 1.5 \times 10^{20} \text{ m}^{-3}$, $T_0 = 20 \text{ keV}$), but are stable for those of Ignitor ($B_T = 13\text{T}$, $n_0 = 0.8 \times 10^{21} \text{ m}^{-3}$, $T_0 = 12 \text{ keV}$).

For relatively peaked profiles represented³² by $p = p_0(1 - \psi)^{3/2}$, the numerical analysis produces a stability threshold corresponding to extremely low values of β_p , but the validity of the linearized approximation ($|d\tilde{p}/dr| < |dp/dr|$, \tilde{p} = perturbed plasma pressure) breaks down for very small values of \tilde{p} , well before threshold. We consider the predicted instability meaningful when, for instance, $|\tilde{p}|_{BD} \leq 0.05p$, where $|\tilde{p}|_{BD}$ = value of $|\tilde{p}|$ for breakdown. The value of β_p for the ITER reference discharge leads to values of $|\tilde{p}|_{BD}$ exceeding this threshold while those for Ignitor are well below it.

We have also considered operating conditions corresponding to the reversed shear configuration, with reduced plasma currents ($q(a) \approx 6$). In this case, stability against ballooning modes become a concern in view of the low values of \bar{B}_p that can be produced (e.g., $\bar{B}_p \approx 0.5\text{T}$ in the case of ITER).

³⁰ B. Coppi, M. Nassi, and L.E. Sugiyama, *Phys. Scripta* 45: 112 (1992).

³¹ L.E. Sugiyama, PTP Report 95/03, MIT, 1995.

³² M. Rosenbluth et al., in *Plasma Physics and Controlled Fusion Research*, IAEA-CN-60/E-P-2 (Vienna: IAEA, 1995).

In order to assess the possibility of the onset of large scale sawtooth oscillations of the plasma column, the excitation of collisional $n=1$ modes involving magnetic reconnection is also considered. Thus we have analyzed 12 discharges obtained by Alcator C-Mod³³ with and without RF heating, all exhibiting sawtooth oscillations while ideal MHD stability is verified. Resistive $n=1$, $m=1$ modes are found to remain unstable according to the theory given in³⁴ (i.e., the relevant plasma parameters fall in the regions III-IV of the $\lambda_H - \omega_*$ parameter space).

1.3.6 Thermal Transport of Ohmic and ICRF Heated L-mode Plasmas in Alcator C-Mod

The observed similarity in the global thermal confinement between the ohmic and ICRF heated L-mode plasmas opens the possibility that thermal transport in the Alcator C-Mod machine may be described by one transport coefficient for both regimes. A modified form of a transport coefficient previously reported³⁵ has been used to simulate both ohmic and ICRF discharges over a wide range of parameters. Detailed simulations carried out by means of the BALDUR code reproduce the observed temperature profiles, loop voltage and energy confinement time of the Alcator C-Mod discharges. The coefficient D_e^{th} includes the constraint of profile consistency and is inspired by the properties of the so-called "ubiquitous" mode that can be excited in the presence of a significant fraction of trapped electrons; thus it includes a significant dependence on the electron pressure gradient. The resulting confinement time improves with the plasma current, in agreement with the observations, and contains only a weak dependence on density. In particular, the coefficient is of the form

$$D_e^{\text{th}} \propto \left(\omega_{pi} \frac{c^2 v_{ee}}{\omega_{pe}^2 V_{\text{the}}^2} \right)^{1/3} \frac{1}{enR} \beta_{pe}^* \quad (1)$$

where $\beta_{pe}^* = (8\pi p_e^* / B_0^2)$ and $p_e^* = a(dp_e/dr)_{\text{max}}$. It has been observed from both the experiment and the simulations that β_{pe} is roughly constant for ohmic discharges while it increases with P_H/P_{OH} for ICRF discharges, where P_H is the total heating power. Thus a natural transition between the ohmic and ICRF regimes is included in the coefficient through the pressure gradient dependence. The dependences on the main plasma parameters associated with this diffusion coefficient and the resulting global scalings have been studied and compared with the characteristics of L-mode discharges produced by the machine.

1.3.7 Energy Confinement in High-Field Experiments

In addition to the previously described work on the transport properties of Alcator C-Mod plasmas, which is based on the detailed spatial analysis of a relatively small number of discharges, a more extensive study of global confinement has been undertaken since the beginning of 1995. This also includes a comparison between C-Mod and the FTU machine in Frascati, the only two high-field devices in operation. Their results are especially significant in relation to some assumptions made for Ignitor.³⁶ The overall dimensions of the two machines are comparable, but they are characterized by some important differences: C-Mod has a D-shaped plasma and a close divertor, FTU is circular and has been operating with a poloidal limiter. Both machines use high-Z materials as plasma facing components.

These machines have been operating in a very similar range of parameters for ohmic plasmas (toroidal field $B_T \sim 5\text{T}$, electron density $n_e \sim 10^{20} \text{ m}^{-3}$, electron and ion temperature $T_e \leq T_i \sim 1 - 2 \text{ keV}$), but the energy confinement time seems to exhibit a substantially different behavior. On FTU, which is a circular machine, τ_e follows a neo-Alcator type of scaling, i.e., it increases with density and then saturates, while C-Mod shows a fairly strong positive dependence on the plasma current and a weak, but

³³ M. Porkolab et al., in *Plasma Physics and Controlled Fusion Research*, IAEA-CN-60/A-1-II-2 (Vienna: IAEA, 1995).

³⁴ B. Coppi et al., in *Plasma Physics and Controlled Fusion Research* (Vienna: IAEA, 1987), vol. 3, p. 397.

³⁵ B. Coppi, et al., in *Proceedings of the 21st EPS Conference on Contributions to Fusion and Plasma Physics*, Montpellier, France, 18B III 520 (1994).

³⁶ F. Bombarda, B. Coppi, W. Daughton, L. Sugiyama, M. Greenwald, A. Hubbard, J. Irby, C. Fiore, J.E. Rice, S. Wolfe, S. Golovato, and Y. Takase, International Sherwood Theory Conference, Incline Village, Nevada, 1995.

negative, dependence on n_e .³⁷ In ohmic conditions, our analysis shows that on C-Mod, the value of β_p is essentially constant, while on FTU, this is an inverse function of the plasma current. The analysis of some low elongation shots on C-Mod seems to indicate that elongation may be one of the responsible factors for the observed difference. Edge conditions can also effect the global plasma properties, particularly at very low densities, and the scrape-off layer parameters have also been compared. This analysis has confirmed the positive effect of current and elongation on confinement and the high density on plasma purity. Both the FTU and the Alcator C-Mod experiments agree on this for both limiter and divertor configurations, with the additional indication that high-Z first wall materials behave well even at relatively high power loads.

The results on confinement in plasma regimes where ohmic heating is prevalent, as well as at the transition from ohmic heating to injected heating conditions, are of particular interest for the Ignitor program. The results of C-Mod indicate that confinement does not degrade as collisionality decreases at values of β_p close to that for which Ignitor is designed to ignite.

Values of peak electron densities $n_e \approx 10^{21} \text{ m}^{-3}$ have again been obtained with pellet injection, and the successful ICRF heating of high-density plasmas has been demonstrated on C-Mod at power densities about equal to those of the Ignitor design. We have shown³⁸ that the values of the energy confinement time scaled from those obtained by C-Mod at the lowest collisionality are more than sufficient for ignition.

1.3.8 Recurrent and Random Explosive Events: Relevant Theoretical Models

There are events of relatively brief duration involving, for instance, accelerated or heated particles, excitation of fluctuations, radiation emission

that can be related to the onset of different kinds³⁹ of explosive instabilities and that can recur at regular intervals or randomly. An analytical model⁴⁰ is introduced, to represent these events, consisting of a set of nonlinear differential equations which involve a characteristic singularity. This corresponds to an explosive or quasi-explosive event for a "primary" factor (e.g., the population of heated or accelerated particles) or for the relevant plasma fluctuations that are excited when the primary factor exceeds an appropriate threshold value.

In the case where quasi-explosive events are periodically recurring, a noncanonical Hamiltonian is derived from which the equations for both the primary factor and the excited fluctuation amplitude can be derived. Significant examples of the numerical solution of these equations have been constructed. A comparison is made with the well known Volterra-Lotka equations and with previously considered equations producing sawtooth oscillations of the primary factor.⁴¹ None of these involve singularities and do not describe explosive events.

The random occurrence of this kind of events, involving the primary factor and the fluctuation level, is found by introducing a relatively small time-dependent component of the source of the driving factor or of the instability threshold for the fluctuation level, with a period that is not related to that of the original nonlinear equation. This case has also been illustrated by representative numerical solutions.

1.3.9 Importance of Radial Localization on the Interaction of Fusion Products with High-Frequency Modes

We investigate modes that can interact with high energy reaction products in fusion burning plasmas giving rise to instability for frequencies that correspond to harmonics of the energetic particles' cyclotron frequency. The corresponding modes in a homogeneous plasma would be classified as

³⁷ F. Bombarda, B. Coppi, W. Doughton, L. Sugiyama, C. Fiore, S. Golovato, M. Graf, M. Greenwald, A. Hubbard, J. Irby, B. LaBombard, E. Marmor, M. Porkolab, J.E. Rice, Y. Takase, and S. Wolfe, *Proceedings of the 22nd EPS Conference on Contributions to Fusion and Plasma Physics*, Bournemouth, United Kingdom, 1995; F. Bombarda, B. Coppi, C. Fiore, S. Golovato, M. Greenwald, A. Hubbard, J. Irby, E. Marmor, M. Porkolab, J.E. Rice, Y. Takase, and S. Wolfe, *Bull. Am. Phys. Soc.* 40: 1699 (1995).

³⁸ P. Detragiache, F. Bombarda, and B. Coppi, *Bull. Am. Phys. Soc.* 40: 1657 (1995).

³⁹ B. Coppi, M.N. Rosenbluth, and R.N. Sudan, *Ann. Physics* 55: 207 (1969); B. Coppi and A. Friedland, *Astr. J.* 169: 379 (1971).

⁴⁰ A.C. Coppi and B. Coppi, *Bull. Am. Phys. Soc.* 40: 1657 (1995).

⁴¹ B. Coppi, A. Taroni, and G. Cenacchi, *Plasma Physics and Controlled Nuclear Fusion* (Vienna: IAEA, 1979), vol. 1, p. 487; L. Chen, R. White, and M.N. Rosenbluth, *Phys. Rev. Lett.* 55: 1122 (1984); B. Basu and B. Coppi, *Phys. Plasmas* 2: 14 (1995).

Magnetosonic-Whistler modes. It is known that in a configuration with inhomogeneous magnetic field, density, and temperature, it is possible to find radially localized solutions,⁴² that we call "contained modes," for the perturbed field.

We study new localized solutions for the perturbed fields by solving the equations obtained by linearizing the extended MHD equations, including the Hall term. The main effects associated with this term are to break the symmetry in $\pm k_{\perp}$, and to include a Whistler-type term in the dispersion equation related to propagation in the direction of the equilibrium magnetic field. In a toroidal shell localized near the edge of the plasma, we find that contained modes exist only for positive values of K_{\perp} . We point out how the existence of this solution is essential that the resonant interaction of the considered modes with relatively few fusion products will yield a positive growth rate.⁴³

In fact, traveling modes in the radial direction would convect away the energy gained from the few resonating particles in too short a time to allow a significant increase of their amplitude.

1.3.10 Destabilization of Contained Interacting Modes by Fusion Products

The instability related to the interaction between high-frequency "contained modes" and the fusion products population in a toroidal configuration is being studied.⁴⁴ Emphasis is placed on the dependence of the growth rate on finite Larmor radius effects of the fusion products,⁴⁵ the characteristics of the particle distribution function,⁴⁶ and factors, such as the magnetic drift velocity and bounce-averaging,⁴⁷ related to the inhomogeneity of the magnetic field in a toroidal configuration. In particular, we find that a sufficient degree of anisotropy in the energetic particle distribution is required in order

to have a positive growth rate for realistic parameters.

Only a small region of phase space is involved in the resonant interactions associated with the considered modes. In the limit where the growth rate is larger than the bounce frequency (local approximation), we find unstable solutions for a class of trapped particles with large perpendicular velocities. Another evaluation of the growth rate γ is obtained in the case, that we consider realistic, where γ is comparable to the average bounce frequency of the interacting particles. We can solve for γ by integrating the linearized Vlasov equation over the unperturbed particle orbits and reducing the integrals through saddle-point approximations.

1.3.11 Nonlinear Saturation of the Parallel Velocity Shear Instability

Plasma flows in the direction parallel to the ambient magnetic field are nearly ubiquitous. They occur naturally in linear plasma columns (e.g., Q-machines) or in toroidal experiments under a variety of conditions. These flows are also observed in the near-Earth environment as solar wind is deflected by the bow shock and flows past the flanks of the magnetosphere. A shear in the flow (i.e., $\mathbf{B} \times \nabla V_{\parallel} \neq 0$) can lead to instabilities and spontaneous break-up of the flow. In driven systems, saturation by quasilinear processes such as relaxation of the velocity gradient is not realistic, thus one is led to consider other processes such as the coupling to a damped mode.

Linear stability analysis predicts two very distinct limits for the velocity shear problem. With relatively large values of the velocity gradient ($dV_{\parallel}/dx \sim V_{thi}/L_n$), a mode first found by D'Angelo⁴⁸ can occur. This mode is characterized by ($\gamma \gg \omega_i$) but is easily stabilized in the presence of significant density gradients. A new dissipative instability can occur for relatively low values of the velocity gra-

⁴² B. Coppi et al., *Phys. Fluids* 29: 4060 (1986).

⁴³ B. Coppi, in *Physics of High Energy Particles in Toroidal Systems*, eds. T. Tajima and M. Okamoto, (New York: AIP Press, 1993).

⁴⁴ B. Coppi et al., *Phys. Fluids* 29: 4060 (1986); B. Coppi, *Fusion Tech.* 25: 326 (1994).

⁴⁵ V.S. Belikov and Y.I. Kolesnichenkov, *Fusion Tech.* 25: 258 (1994); Y.P. Chen and S.T. Tsai, *Phys. Plasmas* 2: 3049 (1995).

⁴⁶ K.G. McClements et al., *Phys. Plasmas* 1: 1918 (1994).

⁴⁷ Y.P. Chen and S.T. Tsai, *Phys. Plasmas* 2: 3049 (1995); K.G. McClements et al., *Phys. Plasmas* 1: 1918 (1994); N.N. Gorelenkov and C.Z. Cheng, *Phys. Plasmas* 2: 1961 (1995).

⁴⁸ N. D'Angelo, *Phys. Fluids* 8: 1748 (1965).

dient as first suggested by Coppi.⁴⁹ The relevant dissipation can enter through a parallel ion viscosity or ion-neutral collisions. This mode is characterized by $(\omega_r - \omega_{*e} \gg \gamma)$ and is not stabilized by the presence of density gradients.

In our nonlinear analysis, we consider both the strongly growing D'Angelo mode and Coppi's weakly growing dissipative mode. A plane geometry including both density and velocity gradients is analyzed with two fluid equations. The linear stability of these modes is such that if a mode with wave number \vec{k} is unstable then so are all of its harmonics $(2\vec{k}, 3\vec{k}, \dots)$. The inclusion of FLR corrections in the fluid equations introduces a stability boundary in k -space so that we may consider a single linearly unstable eigenmode coupled to a linearly damped harmonic. For Coppi's weakly growing dissipative mode, this scheme results in saturation of the instability at weak to moderate levels, while in the strongly growing D'Angelo limit the scheme breaks down and does not saturate. Both analytical and numerical methods have been used.

1.3.12 Publications

- Basu, B., and B. Coppi. *Phys. Plasmas* 2: 14 (1995).
- Bombarda, F., B. Coppi, C. Fiore, S. Golovato, M. Greenwald, A. Hubbard, J. Irby, E. Marmor, M. Porkolab, J.E. Rice, Y. Takase, and S. Wolfe. *Bull. Am. Phys. Soc.* 40: 1699 (1995).
- Basu, B., and B. Coppi, "Bursting Processes in Plasmas and Relevant Nonlinear Model Equations." *Phys. Plasmas* 2: 1 (1995).
- Carpignano, F., B. Coppi, M. Nassi, and the Ignitor Project Group. "The Ignitor Machine: Construction of Prototypes." Interloan report (unpublished).
- Coppi, B. "Plasma Transport Barriers: Underlying Processes." Vienna: International Atomic Energy Agency. Forthcoming.
- Coppi, B. *Momentum Transport Modes in High Ion Temperature Regimes*. MIT/RLE Report PTP 95/01 1995, *Phys. Lett. A* 201: 66-69 (1995).
- Coppi, B. *Presentation to the PCAST Fusion Panel*. MIT/RLE Report PTP 95/02 (1995), presented to the panel in Washington D.C.
- Coppi, A.C., and B. Coppi. *Singular Non-linear Equations and Explosive Recurrent Events*. MIT/RLE Report PTP 95/04 (1995).
- Detragiache, P., F. Bombarda, and B. Coppi. *Bull. Am. Phys. Soc.* 40: 1657 (1995).
- Migliuolo, S. "Isotopic Effect in Transport and the Ubiquitous Mode." *Phys. Lett. A* 198: 341 (1995).
- Sugiyama, L.E. *Reversed Shear Ignition in a High Field Toroidal Experiment*. MIT/RLE Report PTP 95/03 (1995).
- Zakharov, L., F.M. Levinton, S.H. Batha, R. Budny, M.C. Zarnstorff, S. Migliuolo, and B. Rogers. "Onset and Stabilization of Sawtooth Oscillations in Tokamaks." In *Plasma Physics and Controlled Nuclear Fusion Research 1994* Vienna: I.A.E.A., 1995, paper CN-601 D-III-4.

Abstracts and Conference Presentations

- Airoldi, A., G. Cennachi, and B. Coppi. "Enhanced Confinement Conditions and the Ignitor Experiment." 1995 Annual Meeting of the APS, Division of Plasma Physics, Louisville, Kentucky, November 6-10, 1995.
- Bombarda, F., B. Coppi, W. Daughton, L. Sugiyama, C. Fiore, S. Golovato, M. Graf, M. Greenwald, A. Hubbard, J. Irby, B. LaBombard, E. Marmor, M. Porkolab, J.E. Rice, Y. Takase, and S. Wolfe. *Proceedings of the 22nd EPS Conference on Contributions to Fusion and Plasma Physics*, Bournemouth, United Kingdom, 1995.
- Bombarda, F., B. Coppi, W. Daughton, L. Sugiyama, M. Greenwald, A. Hubbard, J. Irby, C. Fiore, J.E. Rice, S. Wolfe, S. Golovato, and Y. Takase. International Sherwood Theory Conference, Incline Village, Nevada, 1995.
- Bombarda, F., B. Coppi, C. Fiore, S. Golovato, M. Greenwald, A. Hubbard, J. Irby, E. Marmor, M. Porkolab, J.E. Rice, Y. Takase, and S. Wolfe. "Transport Regimes in High Density Plasmas Produced by Alcator C-Mod." 1995 Annual

⁴⁹ B. Coppi, MIT Report *Plasma Phys. Contr. Fusion* 36: B107 (1994); J.M. Finn, *Phys. Plasmas* 2: 4400 (1995).

- Meeting of the APS, Division of Plasma Physics, Louisville, Kentucky, November 6-10, 1995.
- Bombarda, F., B. Coppi, W. Daughton, L. Sugiyama, M. Greenwald, A. Hubbard, J. Irby, C. Fiore, J. Rice, S. Wolfe, and B. LaBombard, "The Ignitor Experiment and Relevance of the Alcator C-Mod Confinement Results." International Sherwood Fusion Theory Conference, Incline Village, Nevada, April 3-5, 1995.
- Bonoli, P.T., M. Porkolab, L. Sugiyama, and C. Kessel. "Simulations of MHD Stable Operating Scenarios in the Tokamak Physics Experiment (TPX)." 1995 Annual Meeting of the APS, Division of Plasma Physics, Louisville, Kentucky, November 6-10, 1995.
- Carpignano, F., B. Coppi, M. Nassi, and the Ignitor Project Group. "Prototypes Construction in the Ignitor Program." 1995 Annual Meeting of the APS, Division of Plasma Physics, Louisville, Kentucky, November 6-10, 1995.
- Cennachi, G., B. Coppi, F. Ferro, M. Gasparotto, C. Rita, M. Roccella, and L. Lanzavecchia. "Plasma Evolution Scenarios in the Ignitor-Ult Experiment." 1995 Annual Meeting of the APS, Division of Plasma Physics, Louisville, Kentucky, November 6-10, 1995.
- Coppi, A.C., and B. Coppi. "'Explosive' Periodic Bursts and Generalized Bursting Equation." 1995 Annual Meeting of the APS, Division of Plasma Physics, Louisville, Kentucky, November 6-10, 1995.
- Coppi, B., and L.E. Sugiyama. "Collisionless Magnetic Reconnection." 1995 Annual Meeting of the APS, Division of Plasma Physics, Louisville, Kentucky, November 6-10, 1995.
- Coppi, B., P. Detragiache, and S. Migliuolo. "The Issue of Internal Modes in Ignition Experiments." 1995 Annual Meeting of the APS, Division of Plasma Physics, Louisville, Kentucky, November 6-10, 1995.
- Coppi, B., and L.E. Sugiyama. "Collisionless Magnetic Reconnection in Well-Confined Plasmas." International Sherwood Fusion Theory Conference, Incline Village, Nevada, April 3-5, 1995.
- Coppi, B., P. Detragiache, and S. Migliuolo. "The Issue of Internal Modes in Ignition Experiments." International Sherwood Fusion Theory Conference, Incline Village, Nevada, April 3-5, 1995.
- Daughton, W., and B. Coppi. "Anomalous Transport of Angular Momentum and Microscopic Dissipative Processes." 1995 Annual Meeting of the APS, Division of Plasma Physics, Louisville, Kentucky, November 6-10, 1995.
- Daughton, W., B. Coppi, L.E. Sugiyama, M. Greenwald, F. Bombarda, and Y. Takase. "Transport Simulations of the Alcator C-Mod Plasmas." International Sherwood Fusion Theory Conference, Incline Village, Nevada, April 3-5, 1995.
- Detragiache, P., F. Bombarda, and B. Coppi. "Recent Results on Confinement: Physics Basis of Ignitor." 1995 Annual Meeting of the APS, Division of Plasma Physics, Louisville, Kentucky, November 6-10, 1995.
- Ernst, D.R., B. Coppi, S.D. Scott, and The TFTR Group. "Transport Analysis of Rotating TFTR Plasmas and Modes Driven by Velocity Gradients." 1995 Annual Meeting of the APS, Division of Plasma Physics, Louisville, Kentucky, November 6-10, 1995.
- Gatto, R., D. Hua, and S. Migliuolo. "Analytical and Numerical Solutions of the Tearing Modes Linear Stability Equation." International Sherwood Fusion Theory Conference, Incline Village, Nevada, April 3-5, 1995.
- Lanzavecchia, L., B. Coppi, R. Andreani, M. Gasparotto, C. Rita, M. Roccella, G. Dalmut, R. Marabotto, G. Galasso, and I. Montanari. "Poloidal Field Coils Design for the Ignitor-Ult Experiment." 1995 Annual Meeting of the APS, Division of Plasma Physics, Louisville, Kentucky, November 6-10, 1995.
- Migliuolo, S. "Nonlinear and Nonlocal Dynamics of the Equatorial Spread-F." 1995 Annual Meeting of the APS, Division of Plasma Physics, Louisville, Kentucky, November 6-10, 1995.
- Migliuolo, S., J.P. Friedberg, J. Kesner, and J.J. Ramos. "Ideal MHD Analysis of TFTR Discharges." International Sherwood Fusion Theory Conference, Incline Village, Nevada, April 3-5, 1995.
- Park, W., G.Y. Fu, H.R. Strauss, and L. Sugiyama. "Multi-Level Numerical Simulation of Tokamak Plasmas." 1995 Annual Meeting of the APS, Division of Plasma Physics, Louisville, Kentucky, November 6-10, 1995.
- Penn, G., B. Coppi, and W. Daughton. "Transport Barrier in Very High Temperature Plasmas."

International Sherwood Fusion Theory Conference, Incline Village, Nevada, April 3-5, 1995.

Penn, G., and B. Coppi, "The Interaction of High Energy Particles with Modes near Harmonics of the Cyclotron Frequency." C. Riconda, 1995 Annual Meeting of the APS, Division of Plasma Physics, Louisville, Kentucky, November 6-10, 1995.

Penn, G., C. Riconda, and B. Coppi. "The Distribution of Fusion Products in a Tokamak Reactor, and Related Effects." 1995 Annual Meeting of the APS, Division of Plasma Physics, Louisville, Kentucky, November 6-10, 1995.

Porkolab, M., P.T. Bonoli, S. Golovato, J. Ramos, L. Sugiyama, Y. Takase, C. Kessel, and W. Nevins. "Advanced Tokamak Physics Scenarios in Alcator C-Mod." 1995 Annual Meeting of the APS, Division of Plasma Physics, Louisville, Kentucky, November 6-10, 1995.

Pravia, M., B. Coppi, W. Daughton, L. Sugiyama, F. Bombarda, M. Greenwald, and The Alcator C-Mod Team. "Transport Simulations of Alcator-C-Mod ICRF Plasmas." Annual Meeting of the APS, Division of Plasma Physics, Louisville, Kentucky, November 6-10, 1995.

Qu, Y.L., J.E. Rice, E.S. Marmor, and F. Bombarda. "X-Ray Observations of Toroidal Rotation in Alcator C-Mod Plasmas." 1995 Annual Meeting of the APS, Division of Plasma Physics, Louisville, Kentucky, November 6-10, 1995.

Rice, J.E., J.L. Terry, E.S. Marmor, and F. Bombarda. "X-Ray Observations of Up-Down Impurity Density Asymmetries in Alcator C-Mod Plasmas." 1995 Annual Meeting of the APS,

Division of Plasma Physics, Louisville, Kentucky, November 6-10, 1995.

Riconda, C., B. Coppi, and G. Penn. "Emission Above the Ion Cyclotron Frequency in a Nonhomogeneous Magnetic Field." International Sherwood Fusion Theory Conference, Incline Village, Nevada, April 3-5, 1995.

Sugiyama, L.E., and W. Park. "Two Fluid Studies of Low m , n Instabilities." 1995 Annual Meeting of the APS, Division of Plasma Physics, Louisville, Kentucky, November 6-10, 1995.

Sugiyama, L.E. "Two Fluid Studies of Tokamak Plasmas." MHD Workshop on the Beta Limit in Long Pulse Discharges, La Jolla, CA, September 11-14, 1995.

Sugiyama, L.E. "Reversed Shear Considerations for Ignition Experiments." MHD Workshop on the Effects of Reversed Shear on the Beta Limit, Princeton, New Jersey, December 14-15, 1995.

Sugiyama, L.E., and W. Park. "The Two Fluid Model and Stabilization of the $m = 1$, $n = 1$ Mode in a Tokamak." International Sherwood Fusion Theory Conference, Incline Village, Nevada, April 3-5, 1995.

Tajima, T., and B. Coppi. "Considerations on Plasma Transport Barriers." International Sherwood Fusion Theory Conference, Incline Village, Nevada, April 3-5, 1995.

Wang, Y., J. Rice, F. Bombarda, G. McCracken, E. Marmor, R. Granetz, J. Terry, B. Labombard, and M. Graf. "Impurity screening study of various Alcator C-Mod Plasmas." 1995 Annual Meeting of the APS, Division of Plasma Physics, Louisville, Kentucky, November 6-10, 1995.

Section 3 Electromagnetics

Chapter 1 Electromagnetic Wave Theory and Applications

Chapter 1. Electromagnetic Wave Theory and Applications

Academic and Research Staff

Professor Jin Au Kong, Dr. Kung Hau Ding, Dr. Robert T. Shin, Dr. Y. Eric Yang

Visiting Scientists and Research Affiliates

Dr. Fabio del Frate,¹ Dr. Minoru Ishikawa,² Dr. Arthur K. Jordan,³ Dr. Yasunori Kanamaru,⁴ Dr. Kevin O'Neill,⁵ Dr. Ligu Sun,⁶ Dr. Michael Tsuk⁷

Graduate Students

Jerome J. Akerson, Tza Jing Gung, Chih-Chien Hsu, Gregory T. Huang, Joel T. Johnson, Kevin Li, Christina Manolatu, Shih-En Shih, Prathet Tankuranun, Nayon Tomsio, Li-Fang Wang, Jun Yan, Chen-Pang Yeang, Yan Zhang

Undergraduate Students

Andrew Kao, Angel Martinez

Technical and Support Staff

Kit-Wah F. Lai

1.1 SIR-C Polarimetric Radar Image Simulation and Interpretation

Sponsor

National Aeronautics and Space Administration
Contract 958461

Project Staff

Professor Jin Au Kong, Dr. Kung Hau Ding, Dr. Robert T. Shin, Fabio del Frate, Dr. Ligu Sun, Chih-Chien Hsu, Joel T. Johnson, Shih-En Shih, Li-Fang Wang, Yan Zhang, Chen-Pang Yeang, Angel Martinez

This project investigates the use of spaceborne polarimetric radar measurements for monitoring, mapping, and retrieving the aboveground vegetation biomass. Fully polarimetric radar data obtained from the SIR-C/XSAR missions in April

and October 1994 over the Landes Forest in Southwestern France have been analyzed in detail.

In this work, we have collaborated closely with Dr. T. Le Toan's research group at the Center d'Etudes Spatiales de la Biosphere (CESBIO) of France. During the various flights of SIR-C/XSAR over the test site, extensive ground truth data has been collected by Dr. Le Toan's team. The data consists of an updated biomass map, which provides the location and ages of more than 50 stands of maritime pines, as well as the statistical information about the densities and sizes of trees and branches. In addition, a clear-cut map with some ground truth measurements including soil moisture and surface profiles is also available. These valuable descriptions provide the key input parameters for the theoretical pine forest scattering model. The acquired SIR-C data has been compared with the previous AIRSAR campaign (L- and C-band, fully

¹ Tor Vergata University, Rome, Italy.

² Sony Corporation, Tokyo, Japan.

³ U.S. Navy, Naval Research Laboratory, Washington, D.C.

⁴ Professor, Kanazawa Institute of Technology, Ishikawa, Japan.

⁵ U.S. Army, Cold Regions Research and Engineering Laboratory, Hanover, New Hampshire.

⁶ Chinese Academy of Sciences, Beijing, China.

⁷ Digital Equipment Corporation, Tewksbury, Massachusetts.

polarimetric, 40 degrees to 50 degrees), ERS-1 data (C-band, VV, 23 degrees), and JERS-1 data (L-band, HH, 35 degrees) to assure the consistency of measurement.

In the investigation of the application of SIR-C data to vegetated terrain classification and biomass inversion, the measured backscattering coefficients, the derived complex correlation coefficient of HH and VV polarizations as well as the ratio between cross- and co-polarization ratio, are fully utilized. A validated pine forest scattering model, which is based on radiative transfer theory with the specific branching structure of a pine tree taken into account, is used to interpret the SIR-C/XSAR polarimetric backscattering measurements from the Landes forest. The cross-polarization backscattering coefficients at L-band and the correlation between HH and VV backscattering returns at both L- and C-band are found to be most useful quantities for biomass retrieval. Bayesian classifications using data with known ground truth and theoretical simulation are applied to classify the forest for biomass up to 50 tons per hectare with the available data at this time (26 degrees of incident). With the use of the pine forest scattering model, biomass inversion has been shown to be feasible over a wider biomass range (up to 100 tons per hectare) for angles of incidence around 45 degrees. In addition to the analysis of SIR-C/XSAR data, we have refined our forest scattering model by taking into account the double scattering mechanism between trunk and branches which shows more effect on the cross-polarized backscattering return. We have also studied the collective scattering and absorption effects of clustered objects like the branches and leaves in a vegetative canopy. A new approach for studying the polarimetric response of various types of forest is also developed by using the L-systems technique to generate different kinds of plants.

1.2 Polarimetric Passive Remote Sensing

Sponsor

U.S. Navy - Office of Naval Research
Grant N00014-92-J-1616

Project Staff

Professor Jin Au Kong, Dr. Kung Hau Ding, Dr. Robert T. Shin, Chih-Chien Hsu, Joel T. Johnson, Li-Fang Wang, Jun Yan, Yan Zhang

This project investigates the application of fully polarimetric passive remote sensing techniques to the detection of sea surface wind direction using

air-borne or space-borne radiometers. The primary objectives are (1) to obtain a better understanding of how the third Stokes brightness parameter U is related to ocean wind direction, and (2) to develop a rough surface scattering model for realistic ocean surfaces that is required for the study of U. This brightness parameter U, which is not measured in conventional passive remote sensing, has recently been shown to respond to the azimuthal anisotropy of the observed medium and thus give information on the ocean wind direction. The calculation of the polarimetric brightness temperature of the ocean requires the use of rough surface scattering theory and a statistical model of the ocean surface. Our approach has been to use exact numerical methods, such as the extended boundary condition method and the method of moments, to insure accurate calculation of the polarimetric brightness temperature. Experimental verification of our models also plays an important role in the project. Through cooperation with U.S. Army Cold Regions Research and Engineering Laboratory (CRREL) and the Jet Propulsion Laboratory (JPL), experimental measurements were performed of periodic water surface polarimetric brightness temperature, and the results were found to be in good agreement with the theoretical predictions.

This project has established that U exists for a one-dimensional periodic surface and that it gives more information than conventional single polarization measurements at a single azimuthal angle. Values of U exceeding 30 K were measured at X and Ku band from a periodic water surface, and shown to indicate the azimuthal angle between the observation direction and the direction of surface periodicity. The Monte Carlo study of one-dimensional surfaces showed that U should be sensitive to variations in surface rms height or spectrum, and insensitive to variations in surface permittivity, and polar angle of observation. These results are promising for the use of U in satellite measurements.

The study of two-dimensional surface polarimetric brightness temperature showed that the properties of U observed in the one-dimensional case still hold in the two-dimensional deterministic surface case. U was found to indicate the azimuthal angle between the direction of observation and the directions of surface roughness and also to respond to the degree of surface anisotropy. This further strengthens the idea of using U for ocean wind remote sensing. The favorable comparison of the perfectly conducting surface model with measured ocean surface bistatic data indicates that the spectrum used for the ocean is a realistic one. The positive results of this project to data are expected to generate further interest in polarimetric techniques

for passive remote sensing and to lead to the development of future polarimetric passive systems for Earth remote sensing.

1.3 Theoretical Models for Microwave and Millimeter Wave Integrated Circuits with Anisotropic Materials

Sponsor

U.S. Navy - Office of Naval Research
Grant N00014-89-J-1019

Project Staff

Professor Jin Au Kong, Dr. Y. Eric Yang, Minoru Ishikawa, Professor Yasunori Kanamaru, Dr. Michael Tsuk, Jerry Ackerson, Kevin Li, Christina Manolatu, Andrew Kao

The scientific objective of this research is to develop computational models and techniques to deal with integrated circuits with anisotropic materials. The anisotropy could be naturally occurring or created artificially. The long-term goal is to evolve these models into inverse algorithms for speeding up the design process.

Part of this work involves macroscopic models of materials. To date, we have made stride in two areas: superconducting electronics and chiral media. In the case of chiral media, we studied the limitation of the Maxwell-Garnett mixing law and the weak-coupling approximation when they are applied to helix loaded dielectric materials. In the former case, the constitutive relation is obtained by modifying London's equations. Our formulation includes super-electron number density as a function of applied macroscopic current density, taking into consideration electron velocities distributions. This simplified model greatly facilitates the calculation of nonlinear resistance, inductance, and other quantities in superconduction electronic circuits.

We have also considered other composite structures that might be considered anisotropic at a larger scales. For example, the presence of multiple small apertures on a metal sheet will change the wave penetration properties. This structure is commonly seen in computer system enclosures. Our recent work took a semi-analytical approach by modeling the small apertures as interacting electric and magnetic dipoles. By using these dipoles in conjunction with finite-difference grids surrounding the interface, we save significant computation time without losing accuracy. A series of codes relating to apertures of various thickness and separation

have been developed. This work should be of great interest to equipment manufacturers since it provides them a quick tool to examine EMI compliance with the FCC regulations.

1.4 Three-Dimensional Time-Domain Analysis of Microstrip and Monolithic Millimeter/Submillimeter Wave Integrated Circuits

Sponsor

U.S. Navy - Office of Naval Research
Grant N00014-90-J-1002

Project Staff

Professor Jin Au Kong, Dr. Y. Eric Yang, Dr. Michael Tsuk, Minoru Ishikawa, Jerry Ackerson, Kevin Li, Nayon Tomsio, Andrew Kao

The scientific objective of this research is to understand the time-domain response in three-dimensional integrated hybrid microstrip circuits and for monolithic millimeter/submillimeter wave integrated circuits. These may include guiding structures, transitions and nonlinear terminations. The time-domain analysis serves as an effective tool leading towards engineering models for circuit design.

In certain conical structures, analytical techniques work well for modeling purposes. For example, recently a microwave network model of two parallel circular vias in a multilayer packaging was developed. This was achieved by replacing the via hole apertures with equivalent magnetic frill currents, the same used in cylindrical antenna theory. The circuit parameters are synthesized from the combination of even and odd mode equivalent circuits. Potential use of this model is for inclusion into CAD packages to reduce the complexity in circuit simulations.

With respect to numerical modeling, our attention has been on the recently developed "perfect matching layer" (PML) absorbing boundary condition. Parts of the study look into the PML as an artificial medium and investigate the "constitutive relation" of this medium, as well as the properties of propagating and nonpropagating plane waves at the PML interface. We observed that there is a systematic way to create a reflectionless interface, or PML "family". We also discovered that special constraints need to be placed on the matching layers in order to avoid numerical singularity when the core region of study is a multilayer medium. These discoveries allow us to move forward and comfortably apply the PML conditions to the analysis of dielectric waveguides.

1.5 Electromagnetic Modeling of Snow with Microstructures

Sponsor

U.S. Army Cold Regions Research and Engineering
Laboratory
Contract DACA89-95-K-0014

Project Staff

Professor Jin Au Kong, Dr. Y. Eric Yang, Dr. Kung Hau Ding, Dr. Kevin O'Neill, Shih-En Shih, Li-Fang Wang

On the ground, snow is a highly inhomogeneous medium consisting of mixture of ice particles, air, and liquid water. Seasonal snowpacks are also highly variable in time and space and are a very complex electromagnetic environment. To understand the influence of snow on the propagation of electromagnetic waves, we need to develop an appropriate method for studying the electromagnetic interaction with snow. The goal of this research is to develop a better understanding of (1) how the structure of inhomogeneities in snowcover will affect electromagnetic interaction, (2) how these effects can be parameterized, and (3) to quantify the effects of snow microstructure on millimeter wave backscattering signatures.

Our research strategy is based on the development of a more realistic microstructure model of snow and a rigorous technique for solving the electromagnetic scattering from snow terrain. In this work, we have used a sticky hard sphere (SHS) model to simulate the structure of grains of snow and the dense medium radiative transfer (DMRT) theory with the clustered particles as an electromagnetic scattering model of snow. The model which develops is then validated by comparing it with experimental snow data along with ground-truth measurements from past publications. The DMRT scattering model is further coupled to the snowpack physics model SNTHERM to interpret the diurnal variations of the millimeter wave radar returns from a series of experiments conducted by the University of Massachusetts at Amherst in March 1993.

The research performed during the period of June-December 1995 focused on the theoretical formulations and numerical simulations of electromagnetic wave propagation and scattering in media with adhesive scatterers, and their application to snowcover. Specifically, we have (1) investigated the electromagnetic wave interaction with snow microstructure based on the dense medium radiative transfer theory (DMRT) in conjunction with a clustered sphere model for snow grains; (2) interpreted the polarimetric snow measurements per-

formed by University of Massachusetts at Amherst in March 1993 and validated the proposed polarimetric radar clutter model of snow; and (3) developed a coupled model of DMRT and SNTHERM for predicting millimeter wave radar returns from snowcovers under various environmental condition.

1.6 Study of SAR Interferometry

Sponsor

Mitsubishi Corporation
Agreement Dated 8/31/95

Project Staff

Professor Jin Au Kong, Dr. Kung Hau Ding, Dr. Y. Eric Yang, Dr. Fabio del Frate, Chih-Chien Hsu, Li-Fang Wang, Yan Zhang

The SAR simulation model was recently expanded by adding a interferometric SAR (INSAR) capability. The major parts of INSAR algorithms include image interpolation and resampling, pixel registration, and phase unwrapping. INSAR provides a valuable means of generating topographical information from spaceborne radar images. Because our model simulates the physical mechanisms of radar scattering, it is a very useful tool to study the accuracy and sensitivity of different INSAR algorithms.

1.7 Inversion of Sea Ice Parameters

Sponsor

U.S. Navy - Office of Naval Research
Grant N00014-92-J-4098

Project Staff

Professor Jin Au Kong, Dr. Kung Hau Ding, Dr. Y. Eric Yang, Dr. Arthur K. Jordan, Dr. Kevin O'Neill, Chih-Chien Hsu, Shih-En Shih, Jun Yan, Chen-Pang Yeang, Yan Zhang, Andrew Kao, Angel Martinez

The scientific goals of this research are (1) to investigate the dependence of active and passive microwave measurements on sea ice parameters and (2) to develop practical reconstruction methods for retrieving sea ice parameters by remote electromagnetic measurements. In this project, we have developed theoretical forward scattering models for sea ice and snowcover which include their morphological structures and physical properties. The scattering model has taken into account the combined volume and surface scattering effects for the accurate prediction of microwave signatures. Com-

parison between model results and experimental measurements with ground truth has been carried out to validate the models. The analysis has confirmed the volume scattering contribution due to the sea ice inhomogeneities, such as brine and air bubble inclusions, to the electromagnetic response of sea ice. The coupled volume and surface scattering mechanism is important in the understanding of sea ice physical properties and the reconstruction of sea ice parameters. An improved model of snowcover with clustered grain structure has been developed. It shows that the attenuation due to scattering is significantly enhanced in snow media by the aggregated particles.

A novel electromagnetic inverse scattering theory using time-series backscatter measurements has been developed to reconstruct the evolution of sea ice thickness. The inversion theory is based on a parameter estimation algorithm where the developed and validated theoretical model is used as the direct scattering model to compute electromagnetic signatures from sea ice. A robust optimization technique is then applied as the inverse algorithm to retrieve the sea ice parameters iteratively. This algorithm has been applied to microwave scattering data from laboratory-grown saline ice, the reconstructed thickness growth agrees closely with measured sea ice thickness. This inverse scattering theory has also been useful in retrieving more sea ice parameters, for example the size and distribution of brine pockets simultaneously from microwave measurements.

1.8 Study of Radio Interference on ILS Category III Operations

Sponsor

U.S. Federal Aviation Administration
Grant 94-G-007

Project Staff

Professor Jin Au Kong, Dr. Y. Eric Yang, Jun Yan, Chen-Pang Yeang, Yan Zhang

Our emphasis is on the study of the effects of electromagnetic interference on the aircraft instrument landing system (ILS) Category IIIB (automatic (blind) landing operation). The objective is to gain a full understanding of radio interference on aircraft performance and to determine an acceptable level of interference for use in autoland certification. Previously, a computer package had been developed to assess the electromagnetic compatibility in ILS/MLS channel planning. It is proposed that this model is enhanced to include the industrial, scientific, and medical (ISM) sources in the interference

study. The aircraft automatic flight control system (AFCS) model will be integrated with the receiver model to simulate the effect of interference on autoland performance. Ultimately, a standard on acceptable exposure time of FM broadcast interference will be developed from the study.

Our research work to date has resulted in a generic ILS receiver signal model and a generic autoland system model. The former includes propagation model and account for the least-denominator performance of the current generation of airborne ILS receivers, as well as an extrapolated receiver model conforming to future specification that is aimed at reducing radio interferences. The latter accounts for both ends of aircraft dynamics—twin-engine small jets and four-engine jumbo jets—and with control mechanisms with and without inertial smoothing. Monte Carlo simulations of different operation environments are applied to study the statistical behavior of aircraft dynamic responses, from which the risk probability of catastrophic failure can be derived.

1.9 MMW Model for Three-Dimensional Radar Scattering from Targets and Background

Sponsor

DEMACO Corporation
Contract DEM-95-MIT-55

Project Staff

Professor Jin Au Kong, Dr. Dung Hau Ding, Dr. Robert T Shin, Dr. Y. Eric Yang, Tza Jing Gung, Prathet Tankuranun, Yan Zhang

In this study, we extended the theoretical model of microwave remote sensing EMSARS to millimeter wave applications, producing graphical user interface (GUI) based three-dimensional scanning radar and SAR simulation programs. The baseline scenarios include the effects of environments, hard targets, atmospheric absorption and scattering, and ground reflection. With X-window/Motif graphical user interface, this program allows us to access the GIS feature map and the elevation map, and given sensor specification to create realistic radar images. The user not only can display elevation maps and the feature map, but also can identify and highlight particular terrain features in the map. Furthermore, the user can modify the feature map to investigate how radar images will change. The K-distribution clutter statistics model and simple terrain shadowing effect is included, as is the effect of rough scattering.

1.10 Electromagnetic Waves in Complex Media

Sponsor

Joint Services Electronics Program
Contract DAAH04-95-1-0038

Project Staff

Professor Jin Au Kong, Dr. Robert T. Shin, Dr. Michael Tsuk, Dr. Y. Eric Yang, Joel T. Johnson, Christina Manolatu

This research is focused on theoretical studies of electromagnetic phenomena in complex media that will lead to applications in the modeling and analysis of realistic electronic systems. We concentrate our efforts on those characteristics that have major impacts on system behavior, in particular on electromagnetic interaction with detailed geometrical features and material properties.

Reduction of RF emission from electronic systems is becoming more critical these days as the lock rate of desktop computing systems increases. Most manufacturers still rely on empirical rules based on past experience for FCC-compliance in their design. The main reason for this is the absence of accurate design tools for the electromagnetic analysis of realistic electronic systems which are often very complicated. Recently, numerical techniques based on the time domain form of Maxwell's equations have received increased attention due to the accuracy of the results obtained and the inherent efficiency of time domain techniques for solving wideband problems, such as EMI problem.

Our research focuses on developing analytical techniques that will reduce the scope and complexity of numerical models. The modeling of metallic enclosure is a practical problem aimed at capturing the effect of finite conductivity using the time domain numerical technique with minimal impact on the computation time. This was done by deriving a simple iterative procedure for including this dependence from DC to above microwave frequencies in numerical simulations. This inclusion is important in the analysis of RF emission from an electronic system with metal enclosure, since the behavior near resonant frequencies of the metal enclosure will be significantly impacted without proper modeling of this effect.

1.11 Publications

Hara, Y., R.G. Atkins, S.H. Yueh, R.T. Shin, J.A. Kong, and R. Kwok. "Application of Neural Networks for Sea Ice Classification in Polarimetric SAR Images." *IEEE Trans. Geosci. Remote Sens.* 33(3): 740-748 (1995).

Li, K., M.A. Tassoudji, S.Y. Poh, M. Tsuk, R.T. Shin, and J.A. Kong. "FD-TD Analysis of Electromagnetic Radiation from Modules-on-Backplane Configurations." *IEEE Trans. Electromag. Compatibil.* 37(3): 326-332 (1995).

Oates, J.H., R.T. Shin, and M.J. Tsuk, "Small Aperture Modeling for EMI Applications Using the FDTD Technique." *J. Electromag. Waves Appl.* 9(1/2): 37-36 (1995).

Nghiem, S.V., R. Kwok, J.A. Kong, R.T. Shin, S.A. Arcone, and A.J. Gow. "An Electrothermodynamic Model with Distributed Properties for Effective Permittivities of Sea Ice." Submitted to *Radio Sci.*

Nghiem, S.V., R. Kwok, S.H. Yueh, J.A. Kong, C.C. Hsu, M.A. Tassoudji, and R. T. Shin. "Polarimetric Scattering from Layered Media with Multiple Species of Scatterers." *Radio Sci.* 30(4): 835-852, (1995).

Tsang, L., K.H. Ding, G. Zhang, C. Hsu, and J.A. Kong. "Backscattering Enhancement and Clustering Effects of Randomly Distributed Dielectric Cylinders Overlying a Dielectric Half Space Based on Monte Carlo Simulation." *IEEE Trans. Antennas Propag.* 43(5): 488-499 (1995).

1.11.1 Meeting Papers

Ding, K.H., S. E. Shih, Y. E. Yang, and J.A. Kong. "Scattering and Absorption of Electromagnetic Radiation by Bicontinuous Random Media." Paper presented at the Progress in Electromagnetics Research Symposium (PIERS), Seattle, Washington, July 24-28, 1995.

Gung, T.J., Y.E. Yang, C.C. Hsu, J.A. Kong, C. Kohler, T. Nguyen, and H. Nguyen. "MMW Radar Range Profile Simulation of Isolated Trees with Radiative Transfer Theory." Paper presented at the Progress In Electromagnetics Research Symposium (PIERS), Seattle, Washington, July 24-28, 1995.

- Hsu, C. C., J.A. Kong, J.C. Souyris, and T. LeToan. "Application of Radiative Transfer Modeling to the Polarimetric Backscattering of Forest." Paper presented at the Progress in Electromagnetics Research Symposium (PIERS), Seattle, Washington, July 24-28, 1995.
- Hsu, C.C., L. Wang, J.A. Kong, J.C. Souyris, T. Le Toan. "Theoretical Modeling for Microwave Remote Sensing of Forest." Paper presented at the International Symposium on Retrieval of Bio- and Geophysical Parameters from SAR Data for Land Applications, Toulouse, France, October 10-13, 1995.
- Johnson, J.T., J.A. Kong, R.T. Shin, and L. Tsang. "Monte Carlo Studies of Ocean Surface Scattering and Thermal Emission." Paper presented at the Progress in Electromagnetics Research Symposium (PIERS), Seattle, Washington, July 24-28, 1995.
- Le Toan, T., F. Ribbes, N. Floury, L. Wang, K.H. Ding, C.C. Hsu, and J.A. Kong. "On the Retrieval of Rice Crop Parameters from SAR Data." Paper presented at the International Symposium on Retrieval of Bio- and Geophysical Parameters from SAR Data for Land Applications, Toulouse, France, October 10-13, 1995.
- Li, K., J.T. Johnson, J.J. Akerson, R.T. Shin, and J.A. Kong. "Theoretical and Numerical Analysis of Berenger's PML." Paper presented at the Progress in Electromagnetics Research Symposium (PIERS), Seattle, Washington, July 24-28, 1995.
- Manolatu, C., J.T. Johnson, J.A. Kong, and R.T. Shin. "Mixing Laws for Helix Loaded Composite Media B." Paper presented at the Progress in Electromagnetics Research Symposium (PIERS), Seattle, Washington, July 24-28, 1995.
- Nghiem, S.V., R. Kwok, S.H. Yueh, J.A. Kong, C.C. Hsu, and K.H. Ding. "Variations in Polarimetric Backscattering of Saline Ice Grown under Diurnal Thermal Cycling Condition." Paper presented at the Progress in Electromagnetics Research Symposium (PIERS), Seattle, Washington, July 24 - 28, 1995.
- Shih, S.E., K.H. Ding, A.K. Jordan, C.C. Hsu, R.T. Shin, and J.A. Kong. "Electromagnetic Scattering Inversion using Bistatic Data." Paper presented at the Progress in Electromagnetics Research Symposium (PIERS), Seattle, Washington, July 24-28, 1995.
- Shih, S.E., K.H. Ding, S.V. Nghiem, C.C. Hsu, R.T. Shin, J.A. Kong, and A.K. Jordan. "Polarimetric Backscattering Signature of Laboratory Grown Saline Ice." Paper presented at the Progress in Electromagnetics Research Symposium (PIERS), Seattle, Washington, July 24-28, 1995.
- Shih, S.E., E. Yang, K.H. Ding, J.A. Kong, R.E. Davis, and K. O'Neill. "Discrete Scatter Modeling of Electromagnetic Scattering from Snow." Paper presented at the Progress in Electromagnetics Research Symposium (PIERS), Seattle, Washington, July 24-28, 1995. 24-28, 1995.
- Souyris, J.C., T. Le Toan, C.C. Hsu, and J.A. Kong. "Inversion of Forest Biomass using SIR-C/X-SAR Data." Paper presented at the International Symposium on Retrieval of Bio- and Geophysical Parameters from SAR Data for Land Applications, Toulouse, France, October 10-13, 1995.
- Souyris, J.C., T. Le Toan, Y. Zhang, C.C. Hsu, and J.A. Kong. "Inversion of Biomass with Polarimetric Data from SIR-C/X-SAR." Paper presented at the Progress in Electromagnetics Research Symposium (PIERS), Seattle, Washington, July 24-28, 1995.
- Tankuranun, P., K.H. Ding, C.F. Lee, R.T. Shin, and J.A. Kong. "Monte Carlo Simulation of Electromagnetic Wave Scattering by Randomly Buried Particles." Paper presented at the Progress in Electromagnetics Research Symposium (PIERS), Seattle, Washington, July 24-28, 1995.
- van Zyl, J., C. Dobson, J. Dozier, P. Dubois, D. Evans, J.A. Kong, T. Le Toan, J. Melack, E. Rignot, S. Saatchi, J.C. Shi, and F.T. Ulaby. "Preliminary Science Results from the SIR-C/XSAR Mission." Paper presented at the International Symposium on Retrieval of Bio- and Geophysical Parameters from SAR Data for Land Applications, Toulouse, France, October 10-13, 1995.
- Wang, L., K.H. Ding, C.C. Hsu, Y.E. Yang, and J.A. Kong. "Electromagnetic Scattering Model for Vegetation Based on L- Systems." Paper presented at the Progress in Electromagnetics Research Symposium (PIERS), Seattle, Washington, July 24-28, 1995.
- Wang, L., C.C. Hsu, J.A. Kong, J.C. Souyris, and T. Le Toan. "Inversion of Forest Biomass using Neutral Networks." Paper presented at the International Symposium on Retrieval of Bio- and Geophysical Parameters from SAR Data for

Land Applications, Toulouse, France, October 10-13, 1995.

Wang, L., J. T. Johnson, C.C. Hsu, J.A. Kong, J.C. Souyris, and T. Le Toan. "Application of Neural Networks to the Inversion of Geophysical Parameters." Paper presented at the Progress in Electromagnetics Research Symposium (PIERS), Seattle, Washington, July 24-28, 1995.

Yan, J., Y.E. Yang, and J.A. Kong. "Monte Carlo Technique for Random Rough Surface Scattering at Low Grazing Incidence Angles." Paper presented at the Progress in Electromagnetics Research Symposium (PIERS), Seattle, Washington, July 24-28, 1995.

Yeang, C.P., Y.E. Yang, Y. Zhang, and J.A. Kong. "Analysis of Intermodulation Interference to Instrument Landing System." Paper presented at the Progress in Electromagnetics Research Symposium (PIERS), Seattle, Washington, July 24-28, 1995.

Zhang, Y., Y.E. Yang, C.P. Yeang, and J.A. Kong. "Simulation of RF Interference Effect on Aircraft Automatic Landing System." Paper presented at the Progress in Electromagnetics Research Symposium (PIERS), Seattle, Washington, July 24-28, 1995.

Section 4 Radio Astronomy

Chapter 1 Radio Astronomy

Chapter 1. Radio Astronomy

Academic and Research Staff

Professor Bernard F. Burke, Professor David H. Staelin, Dr. Philip W. Rosenkranz, John W. Barrett

Graduate Students

Ian M. Avruch, Deborah J. Becker-Haarsma, William J. Blackwell, Carlos R. Cabrera-Mercader, Fronefield Crawford, Timothy J. Derksen, André B. Fletcher, Lori K. Herold-Jacobson, Charles A. Katz, Christopher B. Moore, Mark A. Rawizza, Michael J. Schwartz, Catherine S. Trotter-Wilson

Technical and Support Staff

Felicia G. Brady, Anne E. Conklin

1.1 Extragalactic Radio Source Studies

Sponsor

National Science Foundation
Grant AST 92-24191

Project Staff

Professor Bernard F. Burke, Ian M. Avruch, Deborah J. Becker-Haarsma, Fronefield Crawford, André B. Fletcher, Lori K. Herold-Jacobson

The research during the third year of the grant "Extragalactic Radio Astronomy" has been concentrated on (1) mapping and analysis of radio sources from the MIT-Green Bank (MG) and Parkes-MIT-National Radio Astronomy Observatory (PMN) surveys, (2) a statistical analysis of radio sources over the entire sky, (3) analysis of gravitational lensing, (4) a search for distant neutral hydrogen concentrations beyond redshift 5, and (5) the construction of a near-real-time correlator for the Japanese VSOP space VLBI mission in part with NASA support.

The radio source mapping and analysis has been carried out by Mr. Fletcher and Ms. Herold-Jacobsen, utilizing the extensive MIT database from VLA observations. Radio maps of approximately 4500 radio sources have been completed, and complementary optical observations of over 250 of these objects have been made with the MDM 1.3 m telescope. In the body of data so far, at least eight candidates for gravitational lensing have been identified.

Mr. Crawford has been investigating the isotropy of radio source distribution over the entire sky, using the 87 GB and PMN surveys. In particular, we are interested in seeing whether a dipole anisotropy appears in the distribution of radio sources on the sky. A dipole anisotropy would indicate local motion

with respect to the rest frame of radio sources and would complement dipole detections at other wavelengths (e.g., COBE). We have been investigating this possibility by splitting the sky into patches and measuring the source number density on these patches. We then compare the observed source number densities with the predictions of dipole models with various dipole directions and velocities. With this method we hope to statistically rule out the zero-motion (velocity = 0) model, thereby indicating that the Earth must be in motion with respect to a radio source rest frame.

In 1995 we made significant progress in the search for the time delay of gravitational lens 0957+561. This delay in the arrival time between the two images, when combined with knowledge of the lens geometry, is a measure of the angular diameter distance to the lens. The angular diameter distance can in turn be combined with a model of the lens structure and its redshift to yield a value for the Hubble constant. The time delay is found from the light curves of the A and B images, shown in the figure.

Monitoring observations continued at the VLA last year, making a total of 134 good quality observations at 5 GHz since we began the project in 1979. The monitoring has also included 8 GHz observations since 1990. During the summer of 1995, the B image increased in flux, following the increase of the A image flux in 1994. With the addition of this new feature to the light curves, we have increased our understanding of the structure function and other statistical properties of the underlying variation, and this has aided our search for the time delay.

Several types of statistical analysis have been done on the light curves, in an effort to resolve discussion in the literature of the best techniques for determining the delay from the data. Our best

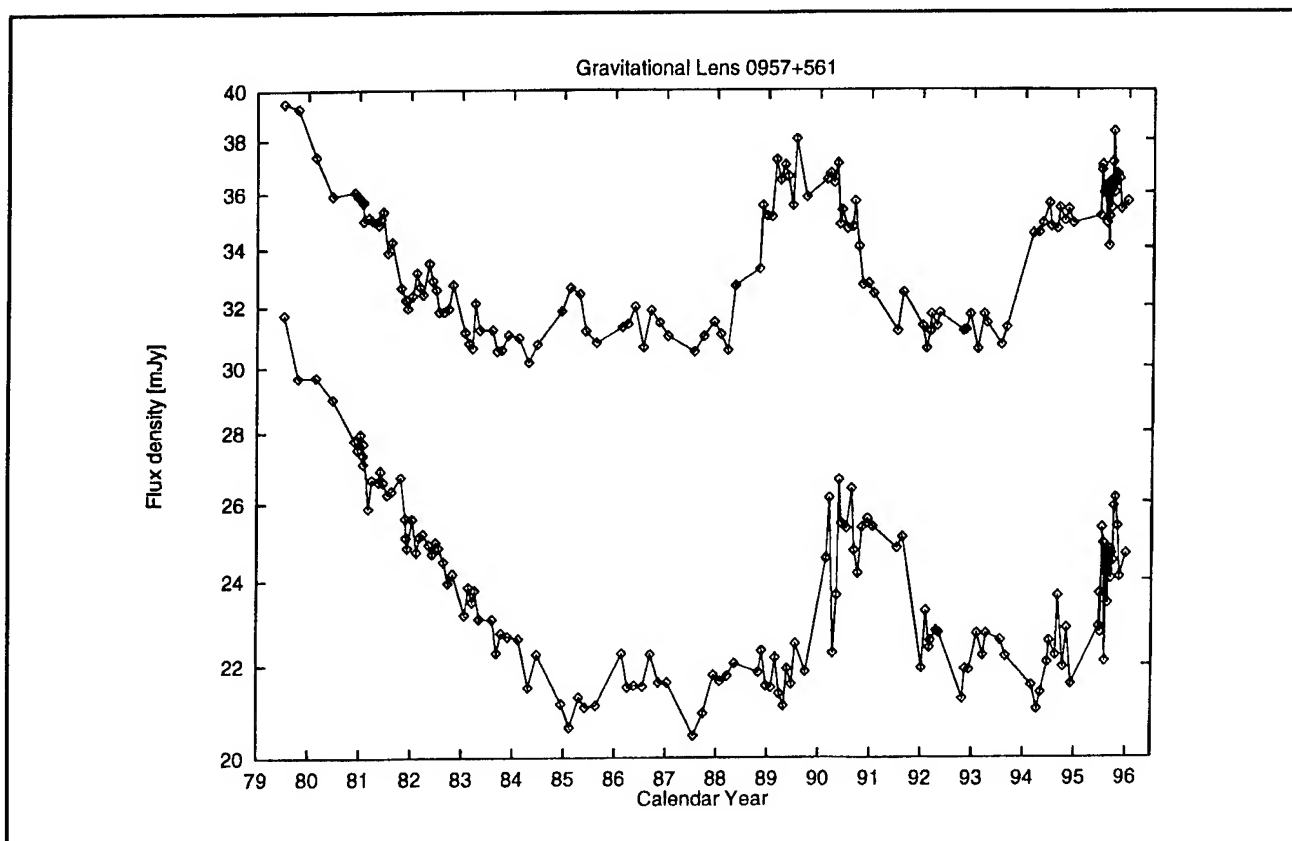


Figure 1.

result is from analysis of the data through December 1994 using the structure function method of Press, Rybicki, and Hewitt, yielding a time delay of 455 ± 16 days (68 percent confidence interval). While doing the analysis, we have learned that a poor choice of structure function can significantly alter the confidence interval but has little effect on the best-fit time delay. We now have a good fit for the structure function and feel that our confidence interval is a good measure of the uncertainty in our result. When this time delay is combined with mass models of the lens, we obtain H_0 in the range 25 to 85 $\text{km s}^{-1} \text{Mpc}^{-1}$, depending on the model and the measured velocity dispersion of the lensing galaxy.

The early hydrogen search is a collaboration between MIT, NAIC, and Harvard, in which we hope to observe neutral hydrogen $\lambda 21$ cm emission from massive proto-cluster clouds at redshift $z \sim 5$, the era of galaxy formation.

The search system, consisting of a dedicated feed on the world's largest radio telescope, a 4000 channel hybrid spectrometer, and control PC, has been running and gathering data since January 1995, although operation was interrupted for a few months during the very active hurricane season. Sensitivity is high compared to other radio telescopes, but the radio-frequency interference (RFI)

environment has deteriorated since the initial survey and limits our effective sensitivity. Some of this deterioration may be due to the extensive observatory upgrade underway, and some to the general increase in civilian and military traffic in the Caribbean. An assessment of the data indicates about 25 percent of our observing band is RFI-free most of the time, 10 to 30 percent is very strongly affected, and the balance is time-variable. We expect to salvage most of our data in post-processing and, with more integration time, make a detection.

In addition, members of this group have been planning for the design and construction of a near-real-time correlator for the upcoming VSOP space VLBI mission. This correlator will play a role in debugging the satellite before astronomical observations begin in January 1997.

The correlator will acquire digitized signals directly from both the ground radio telescope and the VSOP tracking station and store them on a PC. Once the data is stored, we will correlate the two streams quickly to see if there has been a detection of a test astronomical source. This will enable us to present feedback about the state of the satellite quickly, and any necessary adjustments can be made before the next satellite pass. The correlator

is expected to be completed in September 1996, close to the launch date of the satellite.

Presentations have included a talk at the URSI meeting in Boulder and displays at the AAS meeting in San Antonio, both in January 1996.

1.2 Algorithms for Advanced Microwave Sounding Unit Operational Use

Sponsor

MIT Lincoln Laboratory
Agreement BX-4975

Project Staff

Dr. Philip W. Rosenkranz, William J. Blackwell,
Michael J. Schwartz

This project provides scientific support to the National Oceanic and Atmospheric Administration (NOAA) for the advanced microwave sounding units A and B (AMSU-A, AMSU-B) which are scheduled for launch on NOAA polar-orbiting weather satellites starting in 1996 and also for improved instruments. The effort emphasizes development of atmospheric transmittance algorithms, estimation of surface emissivity and precipitation, issues related to instrument design and specification, and general retrieval methods.

Possible designs for a microwave sounder on a geosynchronous satellite are being explored. The absorption lines of atmospheric oxygen and water vapor between 118 and 425 GHz could be used to measure temperature and moisture profiles. With a two-meter diameter antenna, horizontal spatial resolution would range from 20 to 65 km at the sub-satellite point, depending on the frequency. However, the lines near the high end of this frequency band would be obscured by the water vapor absorption continuum within a few kilometers of the surface.

1.2.1 Publication

Rosenkranz, P.W. "A Rapid Atmospheric Transmittance Algorithm for Microwave Sounding Channels." *IEEE Trans. Geosci. Rem. Sens.* 33(5): 1135-1140 (1995).

1.3 Earth Observing System: Advanced Microwave Sounding Unit

Sponsor

National Aeronautics and Space Administration/
Goddard Space Flight Center
Grant NAS 5-31376

Project Staff

Professor David H. Staelin, Dr. Philip W. Rosenkranz, William J. Blackwell, Carlos R. Cabrera-Mercader, Michael J. Schwartz

The AMSU will provide microwave-band measurements to the atmospheric infrared sounder (AIRS), which will be a facility instrument on NASA's planned Earth observing system (EOS). This effort is directed toward developing algorithms for the retrieval of temperature and humidity profiles, precipitation, sea ice, land snow cover, and other parameters. The temperature and humidity profiles obtained from AMSU are intended to provide initial conditions for the AIRS infrared cloud-correction and profile retrieval algorithms. Work to date has focused on simulation efforts.

Uncertainty about the availability of a microwave moisture sounder for EOS motivated a study of low-cost alternative designs. One possible configuration would have two local oscillators at 118.75 and 183.31 GHz, with a total of seven channels derived from the IF passbands. Simulations of the retrieval performance showed accuracy comparable to the three-local-oscillator AMSU-B instrument. An added attractive feature of this design is the possibility of inferring the height of precipitation cells.

The possibility of combining AMSU and AIRS measurements in an optimum cloud-clearing algorithm was studied. The approach is to characterize the impact of clouds on the IR radiances by using both IR and microwave radiances to estimate cloud parameters. A weighted combination of nine AIRS spots is taken, with optimally chosen weights, to represent cloud-cleared radiance at 50-km resolution. It was found that reduction of noise through spatial averaging and use of all channels in profile retrievals were very desirable for good results.

1.3.1 Publications

Cabrera-Mercader, C.R., and D.H. Staelin. "Passive Microwave Relative Humidity Retrievals using Feedforward Neural Networks." *IEEE Trans. Geosci. Rem. Sens.* 33(6): 1324-1328 (1995).

Rosenkranz, P.W. "A Rapid Atmospheric Transmittance Algorithm for Microwave Sounding Channels." *IEEE Trans. Geosci. Rem. Sens.* 33(5): 1135-1140 (1995).

1.4 High-Resolution Passive Microwave Imaging of Atmospheric Structure

Sponsor

National Aeronautics and Space Administration/
Goddard Space Flight Center
Grant NAG5-10

Project Staff

Professor David H. Staelin, John W. Barrett, Dr. Philip W. Rosenkranz, Michael J. Schwartz

The major effort has involved evaluation of the atmospheric microwave transmittance spectrum. The data was obtained with the MIT Microwave Temperature Sounder (MTS), which is a dual-band radiometer incorporating an imaging spectrometer at 118 GHz and a tunable fixed-beam radiometer at 52-54 GHz. This instrument was flown on the NASA ER-2 high-altitude aircraft on a number of missions in 1993 and earlier.

The major challenge has been precise calibration of the MTS, partly because of the effects of radio frequency interference and other instrument irregularities. RF interference was removed from the images by taking advantage of its similar form in all frequency bands. In particular, the high-spatial-frequency structure of the interference contrasted strongly with the smooth character of the geophysical data in the most opaque channels. Calibration errors were removed by using external ambient temperature and liquid-nitrogen cooled black bodies, as well as the *a priori* brightness temperatures for zenith observations at high altitudes (~ 20 km) where the atmosphere is nearly transparent. Dual-mode behavior associated with an intermittent RF connection was calibrated by estimating the system state and then using appropriate coefficients. The two system states exhibited different channel band-pass characteristics, and this was also incorporated in data interpretation.

Preliminary examination of the data near 54 GHz and 118 GHz suggests that recent theoretical expressions based on laboratory data approximate true atmospheric transmittances within several percent, despite indications to the contrary published by others based on satellite data.

In addition, prior work was prepared and submitted for publication.

1.4.1 Publications

Schwartz, M.J., J.W. Barrett, P.W. Fieguth, P.W. Rosenkranz, M.S. Spina, and D.H. Staelin. "Observations of Thermal and Precipitation Structure in a Tropical Cyclone by Means of Passive Microwave Imagery near 118 GHz." *J. Appl. Meteorol.* 35(5): 671-678 (1996).

Spina, M.S., M.J. Schwartz, D.H. Staelin, and A.J. Gasiewski. "Application of Multilayer Feedforward Neural Networks to Precipitation Cell-Top Altitude Estimation." Submitted to *IEEE Trans. Geosci. Rem. Sens.*

1.5 Reduction of Variation

Sponsor

MIT Leaders for Manufacturing Program

Project Staff

Professor David H. Staelin, Timothy J. Derksen, Mark A. Rawizza

In a collaboration involving General Motors, Intel, and Kodak, Research Group 4 of the MIT Leaders for Manufacturing Program has defined a collaborative project focused on new methods for using data from data-rich manufacturing processes to better characterize the multivariate nature of those processes and their evolution, including sensitive detection of any erratic departures from normalcy. An efficient generic tool set and protocols for its use are being developed and tested on representative manufacturing processes.

The General Motors process is body-in-white assembly, and the metrics involve body shape. At Intel, the data involves integrated circuit manufacturing process parameters and the resulting circuit characteristics and dimensions. At Kodak, continuous film base manufacturing processes are being studied, and the metrics involve dimensions and optical properties. In all three cases, the number of measured parameters ranges from tens to hundreds, where each measurement set might be repeated hundreds of times or more, typically in a time sequential fashion. To protect the proprietary character of this manufacturing data, it has been encrypted for use on campus by removal of mean values, normalization of variances, and elimination of parameter labels. Since the objective of the research on campus is to develop efficient methods for uncovering hidden behavior, these steps are of no consequence. The implications of the uncov-

ered hidden behavior to the manufacturing process are explored within the proprietary envelope of each of the separate companies, often by their own employees.

This year, the focus has been on dimensionality reduction, accommodation of missing data, detection of outliers, and detection of surprises in time series data. The initial steps with each data set involve Karhounen-Loève transforms followed by process characterization in the resulting reduced-dimensionality space. Next, methods for removing predictable elements are explored, and the residuals are studied with linear and nonlinear techniques. Initial results indicate that many impor-

tant process variations hidden in the raw univariate data become evident in the reduced-dimension representations and reveal useful information.

Earlier work concerning sequential block design of experiments¹ was submitted for publication.

1.5.1 Publication

Koita, R., D.H. Staelin, and M. Rawizza. "Sequential Block Design Strategy for Two-Level Factorial Experiments." Submitted to *The 1995 Proceedings of the Section on Quality and Productivity*, American Statistical Association, 1995.

¹ R. Koita, *Strategies for Sequential Design of Experiments*. M.S. thesis, MIT, 1994.

Part III Systems and Signals

Section 1 Computer-Aided Design

Section 2 Digital Signal Processing

Section 1 Computer-Aided Design

Chapter 1 Custom Integrated Circuits

Chapter 2 Computer-Integrated Design and Manufacture
of Integrated Circuits

Chapter 1. Custom Integrated Circuits

Academic and Research Staff

Professor Jonathan Allen, Professor John L. Wyatt, Jr., Professor Srinivas Devadas, Professor Anantha P. Chandrakasan, Professor Jacob K. White, Professor Berthold K.P. Horn, Professor Hae-Seung Lee, Professor Martin A. Schmidt, Professor Stephen D. Senturia, Professor Chales G. Sodini, Dr. Robert C. Armstrong, Dr. Donald G. Baltus, Dr. Scott B. Dynes, Dr. Ichiro Masaki

Visiting Scientists and Research Affiliates

Daniel W. Engels, Dr. Andrew Lumsdaine,¹ Mark W. Reichelt,² Dr. Herre S.J. van der Zant

Graduate Students

Narayana R. Aluru, Jason R. Bergendahl, Michael T. Chou, Geoffrey J. Coram, Steven J. Decker, Michael S. Ehrlich, Ibrahim M. Elfadel, Farzan Fallah, Jeffrey C. Gealow, George I. Hadjiyiannis, Silvina Z. Hanono, Mattan Kamon, Stan Y. Liao, Robert G. McDonald, David R. Martin, Yehia M. Massoud, Ignacio S. McQuirk, José C. Monteiro, Keith S. Nabors, Ognen J. Nastov, Joel R. Phillips, Khalid Rahmat,³ Chin Hwee Tan, Johannes Tausch, Paul C. Yu

Technical and Support Staff

Susan E. Chafe, Dorothy A. Fleischer

1.1 Custom Integrated Circuit Design

Sponsors

IBM Corporation
MIT School of Engineering

Project Staff

Professor Jonathan Allen, Dr. Robert C. Armstrong, Dr. Donald G. Baltus, Dr. Scott B. Dynes, Michael S. Ehrlich, Robert G. McDonald, Chin Hwee Tan

The goal of this group includes the study of performance-directed synthesis of custom VLSI circuits. Nineteen-ninety-five was a transition year as many group members finished their projects and left MIT. Dr. Donald Baltus completed his doctoral dissertation on the design of systolic arrays.⁴ His dis-

sertation was one of two selected by MIT for submission to the annual ACM thesis prize competition, a significant recognition and honor. Chin Hwee Tan completed her SM thesis on transistor sizing for power minimization under a delay constraint⁵ and presented her research at the annual Workshop on Low-Power Design.⁶ Dr. Robert Armstrong completed his postdoctoral study on further refinement to the FICOM consistency maintenance CAD environment. Finally, Robert McDonald, who was developing a CAD system for the design of self-resetting CMOS circuits, has left MIT to apply these techniques in industry.

The major continuing effort has been the design and implementation of an interactive learning environment for VLSI design. There are two major components of this research. First, most of a major text has been developed for and utilized in MIT

¹ Notre Dame University, Notre Dame, Indiana.

² Mathworks, Natick, Massachusetts.

³ Hewlett-Packard Corporation.

⁴ D.G. Baltus, *Efficient Exploration of Affine Space-Time Transformations for Optimal Systolic Array Synthesis*, Ph.D. diss., Dept. of Electr. Eng. and Comput. Sci., MIT, 1994.

⁵ C.H. Tan, *Optimization of Power and Delay in VLSI Circuits Using Transistor Sizing and Input Order*, S.M. thesis, Dept. of Electr. Eng. and Comput. Sci., MIT, 1994.

⁶ C.H. Tan and J. Allen, "Minimization of Power in VLSI Circuits Using Transistor Input Ordering and Statistical Power Estimation," paper presented at the International Workshop on Low-Power Design, Napa, California, April 24-27, 1994.

subject 6.371 (Introduction to VLSI Systems) by Professor Jonathan Allen. This text, with its accompanying illustrations, has been well received for two semesters, and it continues to be extended and refined. The text will be converted to hypertext, and the figures will be realized in several formats. Simple illustrations, including photographs and graphs, will be digitized and represented as static figures. In addition, circuit schematics and layout will be represented in a CAD system environment so that users (students) can directly explore the behavior of the circuit. Thus, for example, when a student encounters a schematic diagram of a circuit in hypertext, control can be shifted directly to a circuit schematic editor.

In this environment, various input signals can be applied to the circuit, and results obtained immediately from a simulator with appropriate viewing software. In addition, the circuit schematic can be edited by the student (for example, transistor sizes can be modified), and the behavior of the resulting circuit studied and compared to other versions. It is believed that this ability to experiment directly with circuits is central to developing an understanding of large-voltage-swing (nonlinear) digital circuits. Tight coupling between the hypertext and the CAD system is central to the goals of this project.

Considerable effort has been devoted to the selection of an appropriate CAD environment. It must be small, fast, and inexpensive, yet with sufficient capability to serve the needs within this interactive learning environment. Both schematic and layout editors are required, and a circuit extraction (from layout) program is needed. A circuit simulator with viewing routines is also needed along with appropriate input-output interfaces.

For these requirements, the large, well-known CAD systems are inappropriate, and so significant effort was devoted to develop the FICOM design editing system, which was developed by Dr. Robert Armstrong to a point where it could be incorporated into the overall interactive learning environment system. Unfortunately, this effort was not successful. Attention is now focused on the use of a small, commercially available CAD system that can be readily learned and easily controlled from the hypertext. Experiments with a candidate system are now underway, and methods to couple the hypertext and CAD systems are under study. Dr. Scott Dynes, who has extensive multimedia design and programming experience, has joined the project as a postdoctoral associate. Graduate student Michael Ehrlich is contributing to the design of the system from a user perspective. Plans are to have an initial prototype of the system running by the fall of 1996, so that user feedback can be solicited and guidance for further development can be obtained.

1.2 Cost-Effective Hybrid Vision Systems for Intelligent Highway Applications

Sponsor

National Science Foundation
Grant MIP 94-23221

Project Staff

Professor Berthold K.P. Horn, Professor Hae-Seung Lee, Dr. Ichiro Masaki, Professor Martin A. Schmidt, Professor Charles G. Sodini, Professor John L. Wyatt, Jr., Jason R. Bergendahl, Geoffrey J. Coram, Steven J. Decker, Jeffrey C. Gealow, David R. Martin, Ignacio S. McQuirk, Paul C. Yu

1.2.1 Project Summary

The cost of machine vision systems is limiting their application. The goal of this project is to develop new cost-effective architectures for vision systems and to evaluate them for intelligent highway applications. We propose an advanced modular architecture as a way of improving the cost and performance of vision systems. We call this architecture the heterogeneous nanocomputer network because it consists of variety of functional modules. Some modules are application-specific integrated circuits (ASIC) chips for straight-forward early-vision processing while the others are highly programmable. The modules can be either analog, digital, or mixed signal. Examples of other modules include focal plane processors with visible light and an infrared imager. The heterogeneity provides a significant opportunity to lower the cost of each module by tailoring its architecture to a particular function with minimum constraints. Each functional module is called a nanocomputer because its computational silicon area is significantly smaller than a conventional microcomputer. Reducing module size is important for reducing total system cost. A small-grain architecture also provides greater flexibility for integrating modules. A network architecture is essential for integrating multiple modules without communication bottlenecks.

The next section details substantial progress on nine subprojects. Two image acquisition chips are under development: one for visible and the other for infrared lights. Please refer to sections 1.2.2 and 1.2.8 for more details. Two analog VLSI chips have both image acquisition and image processing functions (sections 1.2.4 and 1.2.10). We are developing two image processor chips (sections 1.2.3 and 1.2.5). An analog-to-digital conversion chip was

also developed (section 1.2.6). Two other projects are related to automotive applications and noise models for solid-state devices, respectively (sections 1.2.7 and 1.2.10).

1.2.2 Brightness Adaptive Imager with Analog and Digital Output

Graduate student Steven Decker, working with Professor Sodini, has been designing an imager to act as the front end of a modular vision system. The imager was originally designed with a 64×64 pixel array of pixels in a $1.75 \mu\text{m}$ CCD/CMOS technology, which was later expanded to a 256×256 array in a $0.8 \mu\text{m}$ CMOS process. Other features of the imaging chip include large fill factor, operating speed on the order of 1000 frames/sec, column parallel output, brightness adaptation capability, and 10-bit digital output. Static chip power at 1000 frames/second is estimated to be about 370 mW, 90 percent of which is dissipated by the on-chip A/D converters.

CCD and CMOS implementations of the wide dynamic range imager were compared, and the results presented at the 1995 IEEE Workshop on Charge-Coupled Devices and Advanced Image Sensors. It was concluded that the CMOS implementation had no significant disadvantages and would tend to have lower smear levels than a CCD implementation. Since commercially available CMOS processes have finer linewidths than available CCD/CMOS processes, a denser array is possible in the CMOS process.

A 256×256 CMOS imager was designed, laid out, and fabricated in the HP $0.8 \mu\text{m}$ process. Four issues were addressed in the design of the CMOS imager: pixel design, generation of the lateral overflow gate waveform, reduction of fixed-pattern noise, and analog-to-digital conversion.

A board was designed and constructed to test for basic functionality of the imager chip. The board allows the output from any single pixel in the array to be examined under realistic operating conditions. A different board will be required later to read data from the entire array.

An analysis of the sensitivity of the brightness adaptive algorithm was performed with Professor Wyatt. The goal of the analysis was to determine how much various mismatch sources in the pixel contribute to a mismatch in the voltage output from the pixel, given a desired compression ratio. Another goal was the determination of optimal barrier waveforms to minimize the effect of the mismatch terms. It was found that timing errors present a particularly important hazard. A separate analysis

was undertaken to determine the expected mismatch in CMOS pixels generally and find the extent to which correlated double sampling can compensate for them.

1.2.3 Analog versus Digital Approaches to Machine Vision Hardware

Graduate student David Martin, under the supervision of Professor Hae-Seung Lee, graduate student Steven Decker under the supervision of Professor Charles Sodini, and Dr. Ichiro Masaki are developing a stereo vision system in collaboration with Professors John Wyatt, Berthold Horn, and Jacob White. The goals of this project are twofold: (1) comparison of analog versus digital approaches, and (2) development of a practical stereo distance measurement system.

A case study to compare analog versus digital approaches is important in identifying what kinds of processing are suitable for analog implementation. An array processing function was chosen as the case for the comparison. The level of this function-definition is high enough for the generality of the result; and, at the same time, it is low enough to make the result independent from the algorithm. A hybrid analog/digital array processor chip is being developed as an example of the analog implementation. It will consist of an array of mixed signal processing elements which will work in an multi-instruction multidata (MIND) scheme. Each processing element will include a digital memory unit which will control an analog arithmetic unit and a data flow network. Examples of the digital array processors, for this comparison, include various schemes such as a pixel-parallel array processor architecture. With this scheme, a digital processing element is assigned for each pixel, and multiple processing elements work in a single-instruction multiple-data (SIMD) fashion.

In the first step, the vision algorithms that will run on the array processor were simulated to determine their accuracy and speed requirements. These simulations revealed that the algorithms could tolerate random errors of up to 10 percent as long as no information was lost from arithmetic overflow. In the second step, key circuits were designed, simulated, fabricated, and tested. As a result of these tests, it was determined that conventional analog circuits for arithmetic were too large and inaccurate for a general purpose arithmetic unit. Therefore, a novel analog arithmetic circuit was designed, simulated, and sent to MOSIS for fabrication. This new circuit essentially performs an A/D on a voltage and then immediately performs a D/A on the digital value. The output voltage is equal to the product of the

input voltage and the D/A reference voltage divided by the A/D reference voltage. Setting the reference voltages correctly allows the circuit to perform multiplication, division, addition, and subtraction.

The final processor cell is about 700 microns by 270 microns using Hewlett-Packard's 0.8 μm triple metal process. Simulations indicate that it can operate at about two million instructions per second and consumes about 2 mW of power at this speed. Two test chips have been fabricated through MOSIS and are now being tested. One test chip has a single processing cell, the other a 5 x 5 array.

1.2.4 A BiCMOS/CCD Focus-of-Expansion Chip for Estimating Camera Motion

Graduate student Ignacio McQuirk, working with Professors Berthold Horn and Hae-Seung Lee, has continued testing the real-time analog VLSI chip he designed for determining the direction of camera motion from time-varying image sequences. The approach assumes the presence of a camera moving through a fixed world with translational velocity. There is no restriction on the shape of the surfaces in the environment, only an assumption that the imaged surfaces have some texture, that is, spatial variations in reflectance. It is also assumed that the camera is stabilized so that there is no rotational motion. The focus of expansion (FOE) is the projection of the camera translation vector onto the image plane and gives the direction of camera. This location is the image point towards which the camera is moving and other image points appear to be expanding outward from.

The algorithm we use for estimating the FOE minimizes the sum of squares of the differences at every picture cell between the observed time variation of brightness and the predicted variation given the assumed position of the FOE. This minimization is not straightforward because the relationship between the brightness derivatives depends on the distance to the surface being imaged and that distance is not only unknown, but varies from picture cell to picture cell. However, image points where brightness is instantaneously constant play a critical role. Ideally, the FOE would be at the intersection of the tangents to the iso-brightness contours at these stationary points. In practice, image brightness derivatives are hard to estimate accurately given that the image itself is quite noisy. Hence the intersections of tangents from different stationary points may be quite scattered. Reliable results can nevertheless be obtained if the image contains many stationary points and the point is found that has the least weighted sum of squares of perpen-

dicular distances from the tangents at the stationary points. The chip itself calculates the gradient of this minimization sum, and the actual FOE estimation is performed by closing a feedback loop around it. The FOE chip has been implemented using an embedded CCD imager for image acquisition/storage and a row-parallel processing. A 64 x 64 version was fabricated through MOSIS in a 2 μm BiCMOS/CCD process with a design goal of 100 mW of on-chip power and a top frame rate of 1000 frames/second. Further algorithmic work also continues with Professor Wyatt to examine more robust, but more complex, algorithms which may also be suitable for implementation in analog VLSI.

A complete test setup for the chip was constructed. Current testing has moved into its final phase: examining the processed output of the FOE chip and using it in a closed loop manner to estimate the FOE in real time.

1.2.5 Integrated Computing Structure for Pixel-Parallel Image Processing

Graduate student Ignacio McQuirk, working with Professors Berthold Horn, and Jeffrey Gealow, working with Professor Sodini, have been developing an dense integrated processing element array to perform low-level real-time image processing tasks in the desktop computer environment. The layout pitch of one-bit-wide processing element logic is matched to the pitch of memory cells, maximizing the bandwidth between memory and logic and minimizing processing element area.

A two-dimensional network connects the processing elements. Control and data paths are distinct. The processing element array receives instructions from the controller, which is managed by the host computer. Analog images from a video camera or other source are converted to digital signals, then reformatted for processing using the processing element array. Output images from the array are converted to a format appropriate for subsequent use. Processing element logic is integrated with 128-bit DRAM columns in place of DRAM column decode logic.

To demonstrate the capability of the processing element array, execution of several low-level image processing tasks has been simulated. One of the investigated tasks is median filtering. The value of each output pixel is the median of all input values in a region centered at the output pixel. Median filtering eliminates spikes while maintaining sharp edges and preserving monotonic variations in pixel values. Operating at 10 MHz, the processing element array would perform a true 5 x 5 median filtering operation in less than 1 ms.

Circuit design and layout of the core processing element array has been completed. A compact logic implementation has been developed meeting the tight layout constraints imposed by pitch-matching memory and logic. Logic circuits operate with a low-voltage supply (2.5 V), minimizing power dissipation.

A completed integrated circuit design will soon be submitted for fabrication through MOSIS. A single device will provide a 64 x 64 block of processing elements. Expected typical power dissipation is 250 mW. Packaged chips will be used to build a complete image processing system. Sixteen chips may be employed to handle 256 x 256 images.

1.2.6 A Pipelined CMOS Analog-to-digital Conversion

Graduate student Paul Yu, working with Professor Hae-Seung Lee, has been working on various techniques of achieving low-power video-rate analog-to-digital conversion (ADC) using CMOS technology. A 2.5-V 12-b 5-MSample/s CMOS pipelined ADC is used as a vehicle to demonstrate efficient methods of power minimization for analog systems without sacrificing performance. One of the main power minimization techniques is a commutated feedback capacitor switching (CFCS) scheme that achieves 12-b resolution while using only 6-7 b accurate capacitor matching.

In a wide range of imaging applications, high-resolution, but medium accuracy are required. This requirement is due to the fact that human eyes, while sensitive to the difference in intensities between adjacent pixels, are quite insensitive to the absolute individual pixel intensities. Exploiting this relaxed requirement on absolute accuracy, an ADC with 12-b differential nonlinearity (DNL), only needs to have about 6-8 b of integral nonlinearity (INL). Similarly, signal-to-noise ratio (SNR), as opposed to signal-to-noise-and-distortion (SNDR) will be the primary target.

Fabricated in a 1.2 μm , double poly, double metal process in August 1994, the test chip was characterized from September 1994 to October 1995. We used a variety of characterization techniques including histogram and fast Fourier transform (FFT) tests. Maximum differential nonlinearity (DNL) of +0.63/-0.78 LSB at 5 MSample/s have been obtained. In July 1995, the conversion rate was pushed from 1 MHz to 5 MHz using reduced output swing logic. In August 1995, a discrete LC filter was designed and constructed to obtain a clean 2.2-MHz sine wave from an RF frequency synthesizer for FFT testing. At this near-Nyquist input frequency, a peak signal-to-noise ratio (SNR)

of 67.6 dB was obtained. The single-ended input capacitance of the ADC is only 1.0 pF. This is significantly lower than many previously reported video rate ADCs, especially those using the flash architecture.

1.2.7 Real-time Vision System for Automotive Applications

Graduate student Jason Bergendahl, under the supervision of Professor Berthold Horn and Dr. Ichiro Masaki, is developing a real-time machine vision system for stereo distance measurements in automotive applications. The basic approach differs substantially from those used by other stereo vision systems under development. First, the stereo distance measurements will rely on edge correlation between stereo pairs, instead of area correlation. The algorithm is greatly simplified to allow real-time performance at frame rate (30 frames/second) to be realized. Another important difference is that the distance measurements are based on sub-pixel disparity measurements between the stereo pairs, allowing for a compact camera arrangement that does not preclude accurate distance measurement.

The system, consisting of three miniature cameras and supporting image processing hardware, will be installed in a test vehicle for on-road trials. Thus, we will be able to directly evaluate the feasibility of vision-based adaptive cruise control under realistic highway conditions. We can also make meaningful performance comparisons between vision-based methods and millimeter wave radar approaches. Our goal is to demonstrate a stereo vision system with performance equal to that of millimeter-wave radar. However, unlike radar systems, a vision-based system may be expanded to provide additional functionality, such as lane tracking. To meet the computational demands of real-time machine vision at frame rate, commercially available image processing hardware and personal computers are used in our system.

The first phase of the project consisted of a thorough evaluation of candidate host systems to oversee the image acquisition and processing tasks. Desktop PCs, "luggable" PCs, laptop PCs, workstations, and VME systems were considered. The primary concern was availability of off-the-shelf plug-in hardware; however each candidate system was also evaluated for processing power, bus bandwidth, and portability. A Pentium-based desktop PC with PCI bus was selected to serve as the host system. This host's key advantage is the high sustainable data transfer rates (up to 133 MBytes/sec) between bus mastering PCI cards and the host.

In parallel with host selection, software development of simple stereo vision algorithms was begun. The objective was twofold: (1) to evaluate the performance of candidate algorithms, and (2) to estimate the capabilities of a workstation or PC for performing image processing without the aid of additional hardware. One software implementation of a simplified algorithm, performed by Gideon Stein, realized 6 Hz performance on a Silicon Graphics workstation. This result suggests that while image processing software is a useful tool for algorithm development, real-time performance with our algorithms requires that most computationally intensive image processing tasks be performed in hardware.

1.2.8 Uncooled Infrared Imager

The micromachined, uncooled infrared detector design which we are investigating consists of a thermally-isolated silicon island containing a bipolar transistor configured as a temperature sensing diode. The island is thermally isolated by suspending it several microns above the silicon chip surface and supporting it with thin silicon nitride tethers. A process technology is used which facilitates integration of electronics in the region surrounding the pixels. This technology employs silicon wafer bonding and has previously been demonstrated on micromachined pressure sensors and accelerometers.

A model to predict the sensitivity and noise of a single pixel has been developed utilizing standard lumped parameter thermal models and first order models for the temperature sensitivity of diodes. Using these models and some target performance specifications, a set of geometric parameters were determined. In some instances, the geometry had additional constraints imposed by the practical limitations of the technology. In particular, the minimum dimension of the pixel element is 5 micron, which was a conservative limitation imposed by the several micron step heights between the silicon island and the nitride tethers. While the current geometry is chosen to be conservative, more aggressive geometry can be attempted after the first prototype is fabricated and the limitations of the technology are understood. The total pixel size is 140 micron by 140 micron. The silicon nitride membrane is 1 micron thick, and the silicon island which contains the diode is 3 microns thick. The thermal conductivity is strongly influenced by the interconnect metal, which is made as thin as possible to reduce the conductivity. There is a trade-off against the increase in interconnect resistance, which impacts noise. The metal thickness was chosen to be 0.1 micron.

The process technology development plan we are pursuing involves several steps and leverages off previous technology which we have developed for integrated sensors. The process enhancements which are needed for the infrared detector are: silicon nitride membranes; diode processing on silicon islands; and metalization on the nitride and silicon island. The first step is to demonstrate the integrity of the nitride membranes through high temperature processes. The next step is to develop the metalization process with the required step coverage. The final step in process development will be the actual fabrication of the pixel elements.

1.2.9 Physically Correct Noise Models for Solid-State Devices

Noise imposes a fundamental limit to analog circuits, especially in low-power operation. Under the direction of Professor Wyatt, graduate student Geoffrey Coram has been studying nonlinear device noise models for agreement with fundamental physical theory. Accepted models for noise in nonlinear devices do not agree with thermodynamic principles. Mr. Coram is looking to resolve this discrepancy while maintaining consistency with experimental results.

In general, continuous-time Gaussian white noise is nonphysical, since it has an infinite variance. Poisson (i.e., shot noise) models give a more physical basis for accurate models. Probability theory tells us that Poisson processes can become Gaussian in the limit of numerous small jumps, and it is possible to derive Nyquist-Johnson thermal noise ($4 kTR$) as the limit of a Poisson-noise system.

We have recently shown that no Gaussian white-noise model can be physically correct for nonlinear devices—all such models predict circuit behavior that is contrary to thermodynamic principles. More importantly, we have also found a Poisson process model that agrees with thermodynamic theory. It accurately describes noise behavior of the pn junction and the subthreshold MOSFET at arbitrary bias points. Using the requirements of a Maxwell-Boltzmann equilibrium distribution and conformance with the Second Law of Thermodynamics, one can calculate the rates of the Poisson sources solely from the constitutive (current-voltage) relation for the device. This sort of nonlinear fluctuation-dissipation relation has been long sought in the literature.

This model accurately describes devices where the current results solely from thermal fluctuations over a barrier and/or from diffusion. It also fits the linear

resistor, with a pure drift transport mechanism. Professor Wyatt and Mr. Coram are now attempting to extend the model to the more general class of devices with both drift and diffusion.

1.2.10 Time-to-Collision Warning Chip

Under certain circumstances, it is possible to estimate the time-to-collision (TTC) from a time varying image. It would be useful to encapsulate an algorithm for doing this into a cheap camera, ideally with computation done on the chip that senses the image, or at least within the enclosure of the camera box itself. In this way, there is no need to move large volumes of image data from an image sensor to an image processor.

Such a device performs an extreme bandwidth compression: it has high bandwidth in (image sequence) and low bandwidth out (time-to-collision). This device could be outfitted with a cheap plastic lens and used as a warning system, aimed out the rear of a car into the two "blind spots" not easily visible in a driver's mirrors.

The key to recovering the time-to-collision is the realization that there are constraints between the brightness gradient (spatial derivatives of brightness) and the time derivative of brightness at a point in the image. These depend on the motion field, and the motion field in turn depends on the rigid body motion between the camera and the object being viewed.

We have formulated the problem using the (1) perspective projection equation, (2) motion field equation, and (3) constant brightness assumption. This leads to equations relating camera motion and image brightness gradients.

We have developed a least squares formulation that involves minimizing the sum of a set of error terms. The error terms are simply the differences between observed rates of change of brightness and predicted rates of change, based on the motion parameters and the scene description. The least squares problem does yield to a closed form solution, but this involves eigenvectors and eigenvalues. While these can be computed in digital or analog hardware, it is a difficult task.

Instead, we are now exploring an iterative method that alternately solves for the surface normal of the plane used to approximate the scene and the translational motion vector. This will be much easier to implement in either digital or analog hardware. We expect it to be fast enough despite the iterative nature of this method.

We will first explore a number of algorithmic alternatives on existing work stations using both real image sequences created under controlled conditions as well as synthetic sequences where the motion and shapes of objects are known exactly.

1.3 Computer-Aided Design Techniques for Embedded System Design

Sponsor

Defense Advanced Research Projects Agency/
U.S. Army Intelligence Center
Contract DABT63-94-C-0053

Project Staff

Professor Srinivas Devadas, George I. Hadjiyiannis,
Silvina Z. Hanono, Stan Y. Liao, Daniel W. Engels

1.3.1 Embedded Systems and Hardware/Software Codesign

One of the challenges of micro-architectural design is to harness the capabilities supplied by improved semiconductor processing. The advent of submicron processing allows for the integration of 5-10 million transistors on a single integrated-circuit (IC). One micro-architecture that effectively exploits the capability of the silicon integrates a micro-processor, digital-signal processor (DSP) or a micro-controller, with a ROM and an ASIC all in a single IC (figure 1). Micro-architectures of this style can currently be found in such diverse embedded systems as FAX modems, laser printers, and cellular telephones. To justify the design costs of such a product, as well as the utilization of such a level of integration, these embedded system designs must be sold in very large numbers and as a result, they are also very cost sensitive. The cost of the IC is most closely linked to the size of the IC, and that is derived from the final circuit area. It is not unusual for the single largest factor in the area of such ICs to be the ROM storing the program code for the microprocessor. In these embedded systems, the incremental value of using logic optimization to reduce the size of the ASIC is smaller because the ASIC circuitry is a relatively smaller percentage of the final circuit area. On the other hand, the potential for cost reduction through diminishing the size of the program ROM is great. There are also often strong real-time performance requirements on the final code, so there is a necessity for producing high-performance code as well.

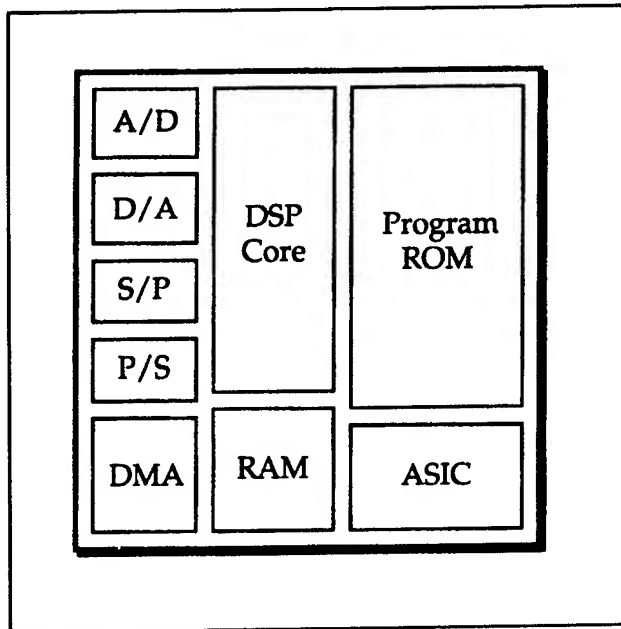


Figure 1. A typical embedded system.

In a hardware/software codesign flow for such an embedded system, the designer first determines which parts of the functionality of the system will be implemented in hardware and which parts in software. The designer then proceeds to design each of the hardware and software components. The system is simulated and evaluated with a hardware-software co-simulator. If the results of the simulation meet design specifications (e.g., correctness and timing constraints), then the design is accepted. Otherwise, the designer may re-partition the original algorithmic specification and iterate the same process. This is illustrated in figure 2.

Under this methodology, tools for *code generation* and *hardware-software co-simulation* are essential items in the designer's tool-box. Specifically, compilers for software written in high-level languages are indispensable in the design of embedded systems.

1.3.2 Reducing Code Size

A given target die size for an embedded system product may limit the size of the ROMs and therefore the size of the code. In many embedded system projects, the ROM space estimated at the beginning becomes insufficient later in the development phase or during maintenance. Designers usually have to work diligently to reduce the code size in order to avoid excessive design modification.

The traditional approach to these problems has been to write the embedded code in assembly language. As the complexity of embedded systems grows, programming in assembly language and optimization by hand are no longer practical or economical, except for time-critical portions of the program that absolutely require it. Recent statistics from Dataquest indicate that high-level languages (HLLs) such as C (and C++) are definitely replacing assembly language, because using HLLs greatly lowers the cost and time of development, as well as the maintenance costs of embedded systems. However, programming in a HLL can incur a code size penalty.

There are a number of reasons for this. One reason is that compiler optimization techniques have classically focused on code speed and not code density. Also, most available compilers optimize primarily for speed of execution. Although some optimizing transforms such as common sub-expression elimination can improve both speed and size at the same time, in many cases there is a speed-size trade-off. For example, subroutine calls take less space than in-line code, but are generally slower. Where execution speed is not critical, minimizing the code size is usually profitable. A second reason is that compiler-optimization techniques have typically been limited to approaches which can be executed quickly [$\leq O(n)$] because programmers require fast compilation times during development. For this reason the numerous NP-hard optimization problems associated with code optimization are rarely faced directly, as in computer-aided design, but are usually approached with simple linear-time heuristics.

Thus a central theme of our embedded system design project is that a new goal for code-optimization has emerged: The generation of the most dense code obtainable with the highest performance—within any reasonable compilation time. We have two important premises. First, the methodology required to generate this code will be most useful if it is retargetable—it can be easily changed to generate code for many different processors. Second, the methodology will require—in addition to traditional code optimizations—techniques analogous to the methodology employed in optimization of a circuit netlist than to traditional code-optimization. This does not imply that traditional Boolean logic-optimization techniques will be applied, but that the approach used commonly in logic optimization of attempting to define and achieve an optimal solution to a series of subproblems will be employed rather than applying a few heuristics in a top-down manner.

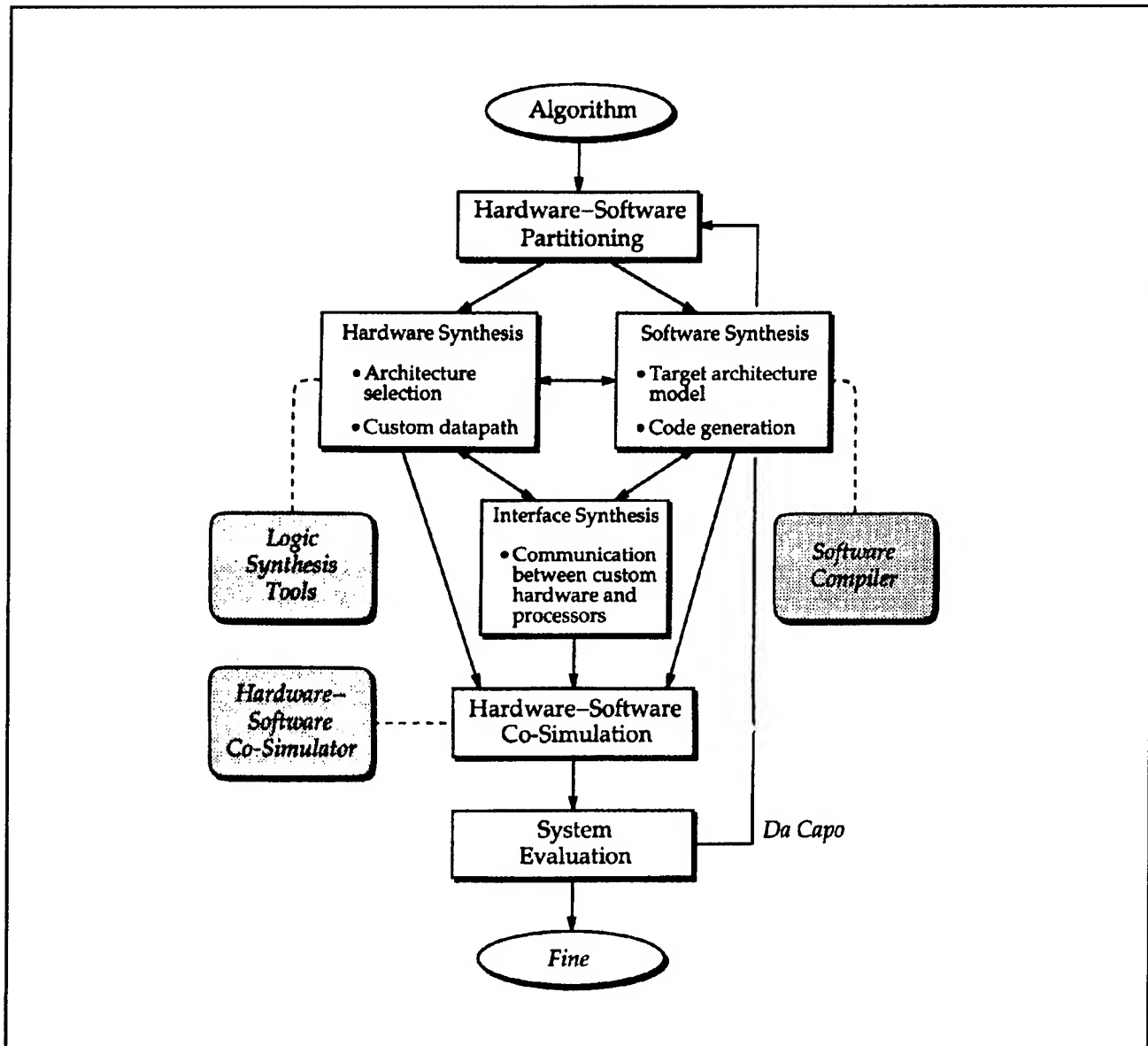


Figure 2. A hardware-software co-design methodology.

1.3.3 Experimental Compiler Framework

In our experimental framework, we use the SUIF Compiler as the front-end to translate source programs from C into the *Stanford University Intermediate Form*. (SUIF is the name of the compiler as well as the abbreviation for the intermediate form.) This project currently focuses on several optimization problems of the back-end. The overall compiler organization is illustrated in figure 3.

A program written in C is first translated into SUIF, which is a largely machine-independent representation of the program. Machine-independent optimizations, such as global common subexpression elimination and dead code elimination, are performed at this stage. Then, the program is trans-

lated via a *preliminary code generation* stage into another intermediate form called TWIF. The preliminary code generated is produced from a rule-based machine description written in OLIVE. OLIVE is a language for writing tree-matchers based on dynamic programming. If tree-covering for preliminary code generation is desired, OLIVE allows for compact specifications of code generators.

TWIF serves as a secondary intermediate form that captures some *machine-dependent* information such as most of the instruction set, while remaining largely *machine-independent* in form (e.g., call graph representation of the program and control-flow graph representation of the procedures). The purpose of this secondary intermediate form is to support optimizations which are to some extent

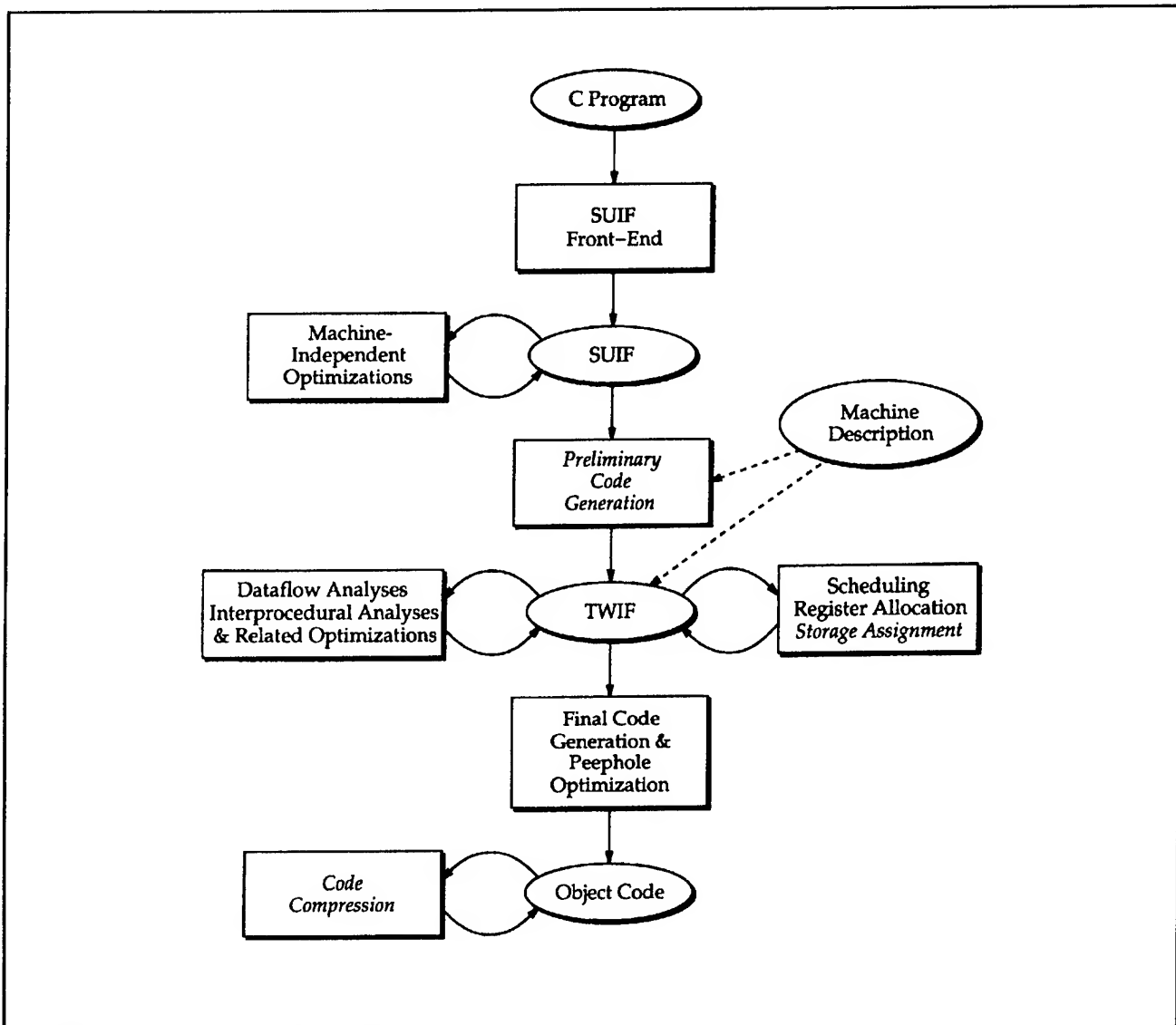


Figure 3. Overall compiler organization.

machine-dependent, but whose basic formulations and algorithms can be shared across a range of architectures. These optimizations include those based on global data-flow analyses, refinements to the schedule produced by the preliminary code generation phase, traditional register allocation, storage assignment, and interprocedural analyses and optimizations.

It is the task of the *final code generation* phase to translate macros and pseudo-instructions into actual target machine instructions. Also, because interprocedural analysis is performed in the TWIF intermediate form, this phase assumes the task of

resolving symbolic addresses of global variables and procedures as well. Along with this step, we can perform peephole optimizations to eliminate redundancy that may have been neglected in earlier phases or may have arisen from the translation of macros and pseudo-instructions. With peephole optimization the compiler attempts to find small sequences (using a sliding *peephole*) in the assembly or object code and either remove useless instructions in the sequences or replace the sequences with shorter ones. Finally, if further reduction in code size is desired, code compression can be applied to the object code.

1.4 VLSI Design for Low-Power Dissipation

Sponsors

Mitsubishi Corporation
National Science Foundation/
Young Investigator Award
Fellowship MIP 92-58376

Project Staff

Professor Srinivas Devadas, Professor Anantha P. Chandrakasan, Farzan Fallah, George I. Hadjiyiannis, José C. Monteiro

1.4.1 Design for Low Power

Average power dissipation has emerged as an important parameter in the design of general-purpose and application-specific integrated circuits.

Optimization for low power can be applied at many different levels of the design hierarchy. For instance, algorithmic and architectural transformations can trade off throughput, circuit area, and power dissipation; and logic optimization methods have been shown to have a significant impact on the power dissipation of combinational logic circuits.

It is important to develop optimization methods that are applicable to a broad class of circuits. To this end, we are developing a synthesis system capable of synthesizing low-power digital combinational and sequential circuits from high-level descriptions. Our recent work in this area is described in the section on scheduling. We are also issues involving the design of low-bandwidth protocols for remote terminals that can be implemented using low-power circuits. This work is described in the section on protocols.

1.4.2 Shutdown Techniques

It has been demonstrated at the gate and system levels that large power savings are possible merely by cutting down on wasted power—commonly referred to as power management. At the system level, this involves shutting down blocks of hardware that are not being used. Detection and shut down of unused hardware is done automatically in current generations of Pentium and PowerPC processors. The Fujitsu SPARClite processor provides software controls for shutting down hardware.

Graduate student José Monteiro applied power management techniques at the sequential logic and combinational logic levels in 1994. Application of power management at the gate level involves first identifying large portions of the circuit that frequently⁷ produce information that is either not essential for determining the values on the primary outputs, or information that could have been produced by much simpler hardware. Additional hardware is then added to the circuit that detects on a per-clock-cycle basis input conditions under which such a situation arises and shuts down the corresponding portions of the circuit for that clock cycle.

During 1995, Mr. Monteiro introduced power management into scheduling algorithms used in behavioral-level synthesis. Behavioral synthesis comprises of the sequence of steps by means of which an algorithmic specification is translated into hardware. These steps involve breaking down the algorithm into primitive operations and associating each operation with the time interval in which it will be executed (called operation scheduling) and the hardware functional block that will execute it (called hardware allocation). Clock-period constraints, throughput constraints, hardware resource constraints, and their combination make this a non-trivial optimization problem.

Decisions taken during behavioral synthesis have a far reaching impact on the power dissipation of the resulting hardware. For example, throughput-improvement by exploiting concurrency via transformations like pipelining and loop unrolling enables the hardware to be operated at lower clock frequencies and thereby at lower voltages. The lower supply voltage leads to a reduction in power dissipation.

Our work is centered around the observation that scheduling has a significant impact on the potential for power savings via power management. Based on this observation, we have developed a scheduling algorithm that is power-management-aware, i.e., it generates a schedule that maximizes the potential for power management in the resulting hardware. The algorithm operates under a user determined combination of throughput, cycle-time and hardware resource constraints. Starting from a high-level description, our implementation of the algorithm generates a logic implementation for the controller as well as the datapath corresponding to the power-management-aware schedule.

⁷ By "frequently," we mean for a large fraction of input vectors.

1.4.3 Protocols

The easiest way of reducing the power consumption of any computing device is to reduce the amount of computation it performs. A portable computer (hereafter called the terminal) can do just enough work to manage the input and output devices and defer all other computation to a separate cycle server (hereafter called the stationary cycle server or just cycle server for short) that will actually perform all the computationally intensive tasks. The terminal and the cycle server can be connected in such a fashion as to allow the terminal to transmit all input to the cycle server and the cycle server to transmit all output back. Then the cycle server can be made stationary, and therefore have an external power source. If the connection method is wireless, then the terminal becomes effectively a portable computer. Since the cycle server has an external power source, only the consumption of the terminal needs to be reduced. This becomes an easier task since the terminal can be designed to perform the minimal amount of computation necessary to manage the input and output devices. Nonetheless, to the user, the terminal appears to have all the processing power of the stationary cycle server.

The main problem with the above scheme is the bandwidth requirement between the terminal and the cycle server. Especially for color terminals this bandwidth can very easily become excessive. graduate student George I. Hadjiyiannis has developed a protocol for a wireless remote terminal which emphasizes low bandwidth and low power requirements. Rather than using a hardwired protocol, it was decided that general-purpose processor would be used, highly optimized for the task at hand. Thus, the terminal and its protocol would become infinitely flexible, allowing us to make use of better algorithms, new extensions to the X-server, and to make additions and modifications to the protocol at will. Then a more complex protocol was designed which reduces the bandwidth requirements while allowing the use of color. This was accomplished by giving the protocol the notion of higher level elements (for example, rectangles, polygons, lines, etc.), the protocol requires much less information to perform the same activities. For example, if the protocol had a notion of what a text character is, one would only need to send a command that identifies the character, its position, and the color to which it should be drawn, rather than sending a complex bitmap over the link.

Error correction and retransmission methods capable of dealing with burst error noise up to BERs of 10^{-3} were developed. The average bandwidth required by the protocol is 140 Kbits/sec for

8-bit color applications including the overhead for error correction.

1.4.4 Publications

Journal Articles

- Lin, B., and S. Devadas. "Synthesis of Hazard-Free Multilevel Logic Under Multiple Input Changes from Binary Decision Diagrams." *IEEE Trans. Comput.-Aided Des.* 14(8): 974-985 (1995).
- Monteiro J., S. Devadas, and A. Ghosh. "Retiming Sequential Circuits for Low Power." *Inter. J. High-Speed Logic*. Forthcoming.
- Monteiro J. and S. Devadas. "Techniques for Power Estimation and Optimization at the Logic Level: a Survey." *J. VLSI Signal Process.* Forthcoming.
- Monteiro J., S. Devadas, A. Ghosh, K. Keutzer, and J.K. White. "Estimation of Average Switching Activity in Combinational Logic Circuits Using Symbolic Simulation." *IEEE Trans. Comput.-Aided Des.* Forthcoming.
- Shen, A., S. Devadas, and A. Ghosh. "Probabilistic Manipulation of Boolean Functions Using Free Boolean Diagrams." *IEEE Trans. Comput.-Aided Des.* 14(1): 87-95 (1995).
- Tsui, C.-Y., J. Monteiro, M. Pedram, S. Devadas, A.M. Despain, and B. Lin. "Power Estimation Methods for Sequential Logic Circuits." *IEEE Trans. VLSI Syst.* 3(3): 404-416 (1995).

Conference Proceedings

- Devadas, S., and S. Malik. "A Survey of Optimization Techniques Targeting Low Power VLSI Circuits." Paper published in the *Proceedings of the 32nd Design Automation Conference*, San Francisco, California, June 1995, pp. 224-247.
- Liao, S., S. Devadas, K. Keutzer, S. Tjiang, and A. Wang. "Storage Assignment to Decrease Code Size." Paper published in the *Proceedings of the SIGPLAN Programming Language Design and Implementation Symposium*, Princeton, New Jersey, June 1995, pp. 186-195.
- Liao, S., S. Devadas, K. Keutzer, S. Tjiang, and A. Wang. "Code Optimization Techniques in Embedded DSP Microprocessors." Paper published in the *Proceedings of the 32nd Design*

Automation Conference, San Francisco, California, June 1995, pp. 599-604.

Liao, S., S. Devadas, K. Keutzer, and S. Tjiang. "Instruction Selection Using Binate Covering for Code Size Optimization." Paper published in the *Proceedings of the International Conference on Computer-Aided Design*, San Jose, California, November 1995, pp. 393-399.

Liao, S., S. Devadas, and K. Keutzer. "Code Density Optimization for Embedded DSP Processors Using Data Compression Techniques." Paper published in the *Proceedings of the 1995 Chapel Hill Conference on Advanced Research in VLSI*, Chapel Hill, North Carolina, March 1995, pp. 272-285.

Monteiro J., J. Rinderknecht, S. Devadas, and A. Ghosh. "Optimization of Combinational and Sequential Logic Circuits for Low Power Using Precomputation." Paper published in the *Proceedings of the 1995 Chapel Hill Conference on Advanced Research in VLSI*, Chapel Hill, North Carolina, March 1995, pp. 430-444.

Monteiro, J., and S. Devadas. "Techniques for the Power Estimation Sequential Logic Circuits Under User-Specified Input Sequences and Programs." Paper published in the *Proceedings of the International Symposium on Low Power Design*, Dana Point, California, April 1995, pp. 33-38.

1.5 Parallel Algorithms for Device Simulation

Sponsors

Defense Advanced Research Projects Agency/
U.S. Navy - Office of Naval Research
Contract N00014-94-1-0985
IBM Corporation
National Science Foundation
Grant MIP 91-17724

Project Staff

Dr. Andrew Lumsdaine, Mark W. Reichelt, Professor Jacob K. White, Professor Jonathan Allen

The growing importance of mixed circuit/device simulation, its enormous computational expense, as well as the increasing availability of parallel computers, have made the development of specialized, easily parallelized, algorithms for transient simulation of MOS devices necessary. In earlier work on the waveform overrelaxation device simulator (WORDS) program, the easily parallelized waveform relaxation (WR) algorithm was shown to be a computationally efficient approach to device transient simulation even on a serial machine. However, the WR algorithm typically requires hundreds of iterations to achieve an accurate solution.

To use WORDS in a mixed circuit/device simulator, we have been investigating ways of making WORDS more robust and efficient. We determined how to compute the terminal currents accurately using different timepoints at different mesh nodes. We also improved the timestep selection procedure by determining how to refine the timesteps as WR iterations proceed. Then we reduced the total computation by as much as a factor of 2 by using only a few coarse timesteps in early iterations. The more accurate electric field dependent mobility model was also implemented. Recent work on theoretical aspects of these methods have answered several long-standing questions about multirate stability.⁸

We found experimental evidence that WR using standard overrelaxation acceleration can produce oscillatory results and are investigating methods for eliminating this phenomenon. A frequency-dependent overrelaxation algorithm using lowpass filtering was developed, as well as a waveform

⁸ A. Lumsdaine, M. Reichelt, and J. White, "Accelerated Waveform Methods for Parallel Transient Simulation of Semiconductor Devices," *IEEE Trans. Comput.-Aided Des.*, forthcoming.

conjugate-direction approach.⁹ Experimental results indicate that both approaches reduce the number of waveform iterations required by more than a factor of seven. Finally, experimental results show that although the accelerated WR methods are as fast as the best of the standard algorithms for device transient simulation on a serial machine, WR algorithms are substantially faster on a parallel machine.⁹

1.6 Numerical Simulation of Short Channel MOS Devices

Sponsors

IBM Corporation
U.S. Navy - Office of Naval Research
Contract N00174-93-K-0035

Project Staff

Khalid Rahmat, Professor Dimitri A. Antoniadis,
Professor Jacob K. White

The model used in conventional device simulation programs is based on the drift-diffusion model of electron transport, and this model does not accurately predict the field distribution near the drain in small geometry devices. This is of particular importance for predicting oxide breakdown due to penetration by "hot" electrons. There are two approaches for more accurately computing the electric fields in MOS devices: one is based on adding an energy equation to the drift-diffusion model, and the second is based on direct solution of Boltzman's equation.

Energy-balance based simulation programs are limited in their ability to accurately predict hot-electron effects, and we have been investigating efficient techniques for solving the full Boltzman equation using a spherical-harmonics-based approach. We have implemented a Galerkin method for the solution of the Boltzmann equation which allows arbitrary order spherical harmonic expansions in momentum space. A self-consistent

solution is obtained by directly solving the Boltzmann and Poisson equations simultaneously. The boundary conditions and discretization methods necessary for the arbitrary order method have also been investigated. Results up to third order in one real space dimension show the importance of including harmonics beyond first order to accurately calculate the distribution function in high field regions.¹⁰

1.7 Coupled Simulation Algorithms for Microelectromechanical CAD (MEMCAD)

Sponsors

Analog Devices Corporation
Federal Bureau of Investigation
Contract J-FBI-92-196

Project Staff

Narayana R. Aluru, Mattan Kamon, Professor
Martin A. Schmidt, Professor Stephen D. Senturia,
Professor Jacob K. White

High fabrication costs and increasing microsensor complexity is making computer simulation of the realistic geometries necessary, both to investigate design alternatives and to perform verification before fabrication. At MIT, we are developing a microelectromechanical computer-aided design (MEMCAD) system to make it possible for microsensor designers to easily perform realistic simulations. Carefully selected commercial software packages have been linked with specialized database and numerical programs to allow a designer to easily enter a three-dimensional microsensor geometry and quickly perform both mechanical and electrical analysis. The system currently performs electromechanical analyses, such as calculating the capacitance versus pressure (or force) curve for both a square diaphragm deformed by a differential pressure, and can be used to calculate levitation forces in structures as complicated as a comb drive.¹¹

⁹ A. Lumsdaine and J. White, "Accelerating Waveform Relaxation Methods with Application to Parallel Semiconductor Device Simulation," *Numerical Functional Analysis and Optimization*, forthcoming; M. Reichelt, J. White, and J. Allen, "Optimal Convolution SOR Acceleration of Waveform Relaxation with Application to Parallel Simulation of Semiconductor Devices," *SIAM J. Sci. Stat. Comput.*, forthcoming.

¹⁰ K. Rahmat, J. White, and D. Antoniadis, "A Galerkin Method for the Arbitrary Order Expansion in Momentum Space of the Boltzmann Equation using Spherical Harmonics," *Proceedings of NUPAD V*, Honolulu, Hawaii, June 1994; K. Rahmat, J. White, and D.A. Antoniadis, "Solution of the Boltzmann Transport Equation in Two Real-Space Dimensions using a Spherical Harmonic Expansion in Momentum Space," *Proceedings of the International Electron Devices Meeting*, San Francisco, California, December 1994.

¹¹ X. Cai, P. Osterberg, H. Yie, J. Gilbert, S. Senturia, and J. White, "Self-Consistent Electromechanical Analysis of Complex 3-D Microelectromechanical Structures using a Relaxation/Multipole Method," *Int. J. Sensors Mater.*, forthcoming.

To support design of electromechanical structures, we are currently investigating two approaches to combining finite-element mechanical analysis with multipole-accelerated electrostatic analysis. The first method is the obvious relaxation algorithm and the second method is a more sophisticated surface/Newton generalized conjugate-residual scheme. By comparing the two methods, we have demonstrated both theoretically and by example that our surface/Newton-GCR algorithm is faster and more robust than the simpler relaxation scheme.¹² We have also been working on the multipole accelerated Galerkin implementation of our electrostatic analysis program FASTCAP. The motivation for this is that Galerkin is less sensitive to the mesh of the structure than the original collocation approach and, particularly with dielectric interfaces, yields more accurate results.¹³

We have also been investigating how to apply CAD to MEMS with the level of complexity of a practical, high-volume manufacturable sensor while avoiding computationally impractical models. Two methods were developed. One was a simple analysis method in which the ideal structure was assumed. This allowed prediction of the stability and the effects of structure misalignment on a surface-micromachined accelerometer. However, the simple method is limited because the actual structure has fabrication induced non-idealities, such as warpage, which can cause the simple method to be significantly in error. The second method discarded the ideal structure assumption and analyzed the non-ideal structure via a self-consistent analysis. This method is based on the calculation of an intermediate look-up table from which the electrostatic forces are obtained directly from the position of the moving mass, greatly reducing computation time and memory requirements in comparison to a standard self-consistent electromechanical analysis scheme. Using this lumped-model self-consistent scheme, we analyzed an Analog Devices, Inc. ADXL50 accelerometer including fabrication non-idealities (warpage, over-etching, residual stress, etc).¹⁴

Finally, in our latest work we investigate the coupling of fluid forces and mechanical deformation to add additional capabilities to our existing MEMCAD system. To gain more control over the underlying algorithms of the current MEMCAD system first, we are currently implementing an elastostatic solver to replace the commercial mechanical solver used in the MEMCAD system.

1.8 Numerical Techniques for Simulating Josephson Junction Arrays

Sponsors

Defense Advanced Research Projects Agency/
Consortium for Superconducting Electronics
Contract MDA 972-90-C-0021
National Defense Science and Engineering
Graduate Fellowship

Project Staff

Joel R. Phillips, Dr. Herre S.J. van der Zant, Professor Terry Orlando, Professor Jacob K. White

Vortices play a central role in determining the static and dynamic properties of two-dimensional (2-D) superconductors. Artificially fabricated networks of superconducting islands weakly coupled by Josephson junctions are model systems to study the behavior of vortices. Through simulation, we have discovered that the static properties of vortices in an array of Josephson junctions can be significantly influenced by magnetic fields induced by the vortex currents. The energy barrier for vortex motion is enhanced, nearly doubling for penetration depths on the order of a cell size. Moreover, we have found that correct calculation of the vortex current distribution, the magnetic moment, and the lower critical field require modeling mutual inductance interactions between all cell pairs in the array. To make numerical simulation of the system with all inductive effects computationally feasible, a novel FFT-accelerated integral equation solver was derived. This algorithm is sufficiently efficient to

¹² H. Yie, X. Cai, P. Osterberg, S. Senturia, and J. White, "Convergence Properties of Relaxation versus the Surface-Newton Generalized-Conjugate Residual Algorithm for Self-consistent Electromechanical Analysis of 3-D Micro-Electro-Mechanical Structures," *Proceedings of NUPAD V*, Honolulu, Hawaii, June 1994.

¹³ X. Cai, K. Nabors, and J. White, "Efficient Galerkin Techniques for Multipole-Accelerated Capacitance Extraction of 3-D Structures with Multiple Dielectrics," *Proceeding of the 16th Conference on Advanced Research in VLSI*, Chapel Hill, North Carolina, March 1995.

¹⁴ H. Yie, S.F. Bart, J. White, and S.D. Senturia, "Computationally Practical Simulation of a Surface-Micromachined Accelerometer with True Fabrication Non-idealities," *Proceedings of MEMS 95*.

allow Shapiro steps and the dynamics of row-switched states in large (500x500 cells) arrays.¹⁵

1.9 Efficient 3-D Interconnect Analysis

Sponsors

Defense Advanced Research Projects Agency
Contract DABT63-94-C-0053
Defense Advanced Research Projects Agency/
Consortium for Superconducting Electronics
Contract MDA 972-90-C-0021
Digital Equipment Corporation
IBM Corporation
MIT Lincoln Laboratory
National Defense Science and Engineering
Graduate Fellowship
Semiconductor Research Corporation
Contract SRC 95-SJ-558
U.S. Army
Contract DABT63-95-C-0088

Project Staff

Michael T. Chou, Mattan Kamon, Yehia M. Massoud, Keith S. Nabors, Joel R. Phillips, Johannes Tausch, Professor Jacob K. White

We have developed multipole-accelerated algorithms for computing capacitances and inductances of complicated 3-D geometries and have implemented these algorithms in the programs FASTCAP and FASTHENRY. The methods are accelerations of the boundary-element or method-of-moments techniques for solving the integral equations associated with the multiconductor capacitance or inductance extraction problem. Boundary-element

methods become slow when a large number of elements are used because they lead to dense matrix problems which are typically solved with some form of Gaussian elimination. This implies that the computation grows as n^3 , where n is the number of panels or tiles needed to accurately discretize the conductor surface charges.

Our new algorithms, which use generalized conjugate residual iterative algorithms with a multipole approximation to compute the iterates, reduces the complexity so that accurate multiconductor capacitance and inductance calculations grow nearly as nm where m is the number of conductors. For practical problems which require as many as 10,000 panels or filaments, FASTCAP and FASTHENRY are more than two orders of magnitude faster than standard boundary-element based programs.¹⁶ Manuals and source code for FASTCAP and FASTHENRY are available directly from MIT.

In our latest work, we have developed an alternative to the fast-multipole approach to potential calculation. The new approach uses an approximate representation of charge density by point charges lying on a uniform grid instead of by multipole expansions. For engineering accuracies, the grid-charge representation has been shown to be a more efficient charge representation than the multipole expansions. Numerical experiments on a variety of engineering examples arising indicate that algorithms based on the resulting "precorrected-FFT" method are comparable in computational efficiency to multipole-accelerated iterative schemes and superior in terms of memory utilization.¹⁷

¹⁵ J.R. Phillips, H.S.J. van der Zant, J. White, and T.P. Orlando, "Influence of Induced Magnetic Fields on Shapiro Steps in Josephson-junction Arrays," *Phys. Rev. B* 50(13): 9380-9386 (1994); J.R. Phillips, H.S.J. van der Zant, and T.P. Orlando, "Dynamics of Row-switched States in Josephson-junction Arrays," *Phys. Rev. B*

¹⁶ M. Chou, M. Kamon, K. Nabors, J. Phillips, and J. White, "Extraction Techniques for Signal Integrity Analysis of 3-D Interconnect," invited paper in *Proceedings of the Custom Integrated Circuits Conference*, CITY, May 1995, forthcoming; K. Nabors, F.T. Korsmeyer, F.T. Leighton, and J. White, "Multipole Accelerated Preconditioned Iterative Methods for Three-Dimensional Potential Integral Equations of the First Kind," *SIAM J. Sci. Stat. Comput.* 15(3): 713-735 (1994); M. Kamon and J.R. Phillips, "Preconditioning Techniques for Constrained Vector Potential Integral Equations, with Application to 3-D Magnetoquasistatic Analysis of Electronic Packages," *Proceedings of the Colorado Conference on Iterative Methods*, Breckenridge, Colorado, April 1994; M. Kamon, M.J. Tsuk, and J. White, "FASTHENRY: A Multipole-Accelerated 3-D Inductance Extraction Program," *IEEE Trans. Microwave Theory Technol.* 42(9): 1750-1758 (1994); M. Kamon, B. Krauter, J. Phillips, L. Pileggi, and J. White, "Two Optimizations to Accelerated Method-of-Moments Algorithms for Signal Integrity Analysis of Complicated 3-D Packages," paper published in the *Proceedings of the Fourth Topical Meeting on Electrical Performance of Electronic Packaging*, Portland, Oregon, October 1995, pp. 213-216; Y. Massoud and J. White, "Simulation and Modeling of the Effect of Substrate Conductivity on Coupling Inductance," *Proceedings of the International Electron Devices Meeting*, Washington, D.C., December 1994.

¹⁷ J.R. Phillips and J. White, "A Precorrected-FFT method for Capacitance Extraction of Complicated 3-D Structures," *International Conference on Computer-Aided Design*, Santa Clara, California, November 1994; J.R. Phillips and J. White, "Efficient Capacitance Extraction of 3D Structures Using Generalized Pre-corrected FFT methods," *Proceedings of the IEEE Third Topical Meeting on Electrical Performance of Electronic Packaging*, Monterey, California, November 1994, forthcoming; J.R. Phillips and J.K. White, "Precorrected-FFT Methods for Electromagnetic Analysis of Complex 3-D Interconnect and Packages," invited paper in *Progress in Electromagnetic Research Symposium*, Seattle, Washington, July 1995, forthcoming.

The precorrected-FFT method has another significant advantage over the multipole-based schemes, in that it can be easily generalized to some other common kernels. Preliminary results indicate that the precorrected-FFT method can easily incorporate kernels arising from the problem of capacitance extraction in layered media.¹⁸ More importantly, problems with a Helmholtz equation kernel have been solved at moderate frequencies with only a modest increase in computational resources over the zero-frequency case. An algorithm based on the precorrected-FFT method which efficiently solves the Helmholtz equation could form the basis for a rapid yet accurate full-wave electromagnetic analysis tool.¹⁹

In order to accurately compute the RC delay and cross-talk noise in complicated three-dimensional interconnects, it is necessary to numerically solve Maxwell's equation in the electro-quasistatic regime. It has been suggested that the analysis be performed by computing the time evolution of the electric field both inside and outside the conductors via a finite-difference discretization of Laplace's equation. While this method leads to a sparse matrix problem, it requires discretization of the entire physical domain and generates a large number of unknowns. More recently, a boundary-element approach based on Green's theorem was proposed, which performs the calculation using the same surface discretization used for ordinary capacitance extraction. However, this leads to dense matrix problems which are too expensive to solve directly. When the fast-multipole algorithm is applied to the iterative solution in the boundary-element method, we find that the small multipole errors are magnified to unacceptable levels due to the ill-conditioning in the steady-state problem.

We have formulated a new, mixed surface-volume approach, which requires both the conductor surfaces and interior volume be discretized. Given the

conductor surface potentials, Laplace's equation is solved independently inside each conductor via the finite-difference method to determine the internal current flow. The vector of internal and external currents cause charging of conductor surfaces, which is used to compute the time-rate of change of surface potentials via the boundary-element method. The interior problem is sparse and thus inexpensive to solve. The boundary-element problem is dense, but its solution can be accelerated by the fast-multipole algorithm to improve efficiency of the overall scheme. In this approach, accuracy is not affected by the ill-conditioning because the perturbed system has a physical analog close to the exact problem. Numerical experiments on realistic interconnect problems show that the new method can run twenty times faster and use two orders of magnitude less memory than using dense iterative methods.²⁰

1.10 Adaptive Gridding Techniques for Multipole-Accelerated Solution of Integral Equations

Sponsors

National Science Foundation
Grant MIP 91-17724
Semiconductor Research Corporation
Contract SRC-95-SJ-558

Project Staff

Michael T. Chou, F. Thomas Korsmeyer,²¹ Professor Jacob K. White

Finding computationally efficient numerical techniques for simulation of three dimensional structures has been an important research topic in almost every engineering domain. Surprisingly, the most numerically intractable problem across these

¹⁸ L.M. Silveira, I. Elfadel, J. White, M. Chilukuri, and K. Kundert, "Efficient Frequency-Domain Modeling and Circuit Simulation of Transmission Lines," *IEEE Trans. Components, Hybrids, Manufact. Technol.* Part B: Advanced Packaging, special issue on Electrical Performance of Electronic Packaging, 17(11): 505-513 (1994).

¹⁹ J. Phillips, "Error and Complexity Analysis for a Collocation-Grid-Projection plus Precorrected-FFT Algorithm for solving Potential Integral Equations with Laplace or Helmholtz Kernels," Second Place, Student Paper Competition, *Colorado Conference on Multigrid Methods*, April 1995.

²⁰ M. Chou and J. White, "A Multipole-Accelerated Boundary-Element Approach To Transient Simulations of Three-Dimensional Integrated Circuit Interconnect," *Proceedings of the IEEE Third Topical Meeting on Electrical Performance of Electronic Packaging*, Monterey, California, November 1994; M. Chou and J. White, "Transient Simulations of Three-dimensional Integrated Circuit Interconnect Using a Mixed Surface-Volume Approach," invited paper in *Progress in Electromagnetic Research Symposium*, Seattle, Washington, July 1995, forthcoming; M. Chou, T. Korsmeyer, and J. White, "Transient Simulations of Three-dimensional Integrated Circuit Interconnect using a Mixed Surface-Volume Approach," *Proceedings of the 32nd Design Automation Conference*, San Francisco, California, June 1995.

²¹ Research Staff, MIT Department of Ocean Engineering.

various disciplines can be reduced to the problem of solving a three-dimensional Laplace problem. Such problems are often referred to as potential problems. Examples of applications include (1) electrostatic analysis of sensors and actuators; (2) electro- and magneto-quasistatic analysis of integrated circuit interconnect and packaging; and (3) potential flow based analysis of wave-ocean structure interaction.

The recent development of extremely fast multipole-accelerated iterative algorithms for solving potential problems has renewed interest in integral equation formulations. In such methods, the fast multipole algorithm is used to implicitly construct a sparse representation of the dense matrix associated with a standard integral equation formulation, and this implicit representation is used to quickly compute the matrix-vector products required in a Krylov subspace based iterative method like GMRES. That the multipole-accelerated approach leads to practical engineering analysis tools has been demonstrated for electrostatic analysis of integrated circuit interconnect and packaging problems,²² as well as general Laplace problems.²³

We are extending our work on developing multipole-accelerated iterative methods for potential problems to address automatic error control, which is the key difficulty preventing such techniques from finding broader use in engineering applications. In particular, we will first investigate the straight-forward problem of how best to include higher-order boundary or volume elements. We are then planning to use such a result, along with other error estimation procedures, to perform automatic element refinement. The spatial hierarchy already introduced by the multipole algorithm and our use of a locally preconditioned iterative scheme make it possible to perform very efficient local element refinement and may even allow for an efficient variable element order scheme. Also, since we have been using realistic examples from a wide variety of

engineering disciplines, we will be able to determine the robustness of our procedures.

1.11 Coupled Circuit-Interconnect/Packaging Analysis

Sponsors

Defense Advanced Research Projects Agency
Contract DABT63-94-C-0053
Semiconductor Research Corporation
Contract SRC 95-SJ-558
U.S. Army
Contract DABT63-95-C-0088

Project Staff

Ibrahim M. Elfadel, Mattan Kamon, Joel R. Phillips, Michael T. Chou

To help support our work in interconnect analysis, we are developing algorithms for efficient SPICE-level simulation of elements with arbitrary frequency-domain descriptions, such as scattering parameters. That is, an element can be represented in the form of a frequency-domain model or a table of measured frequency-domain data. Our approach initially uses a forced stable decade-by-decade l_2 minimization approach to construct a sum of rational functions approximation, but the approximation has dozens of poles and zeros. This unnecessarily high-order model is then reduced using a guaranteed stable model order reduction scheme based on balanced realizations. Once the reduced-order model is derived, it can be combined with any inherent delay (for transmission line models) to generate an impulse response. Finally, following what is now a standard approach, the impulse response is efficiently incorporated in the circuit simulator SPICE3 using recursive convolution.²⁴

Reduced-order modeling techniques are now commonly used to efficiently simulate circuits combined

²² M. Chou and J. White, "A Multipole-Accelerated Boundary-Element Approach To Transient Simulations of Three-Dimensional Integrated Circuit Interconnect," *Proceedings of the IEEE Third Topical Meeting on Electrical Performance of Electronic Packaging*, Monterey, California, November 1994.

²³ M. Kamon, B. Krauter, J. Phillips, L. Pileggi, and J. White, "Two Optimizations to Accelerated Method-of-Moments Algorithms for Signal Integrity Analysis of Complicated 3-D Packages," paper published in the *Proceedings of the Fourth Topical Meeting on Electrical Performance of Electronic Packaging*, Portland, Oregon, October 1995, pp. 213-216.

²⁴ L.M. Silveira, I.M. Elfadel, J. White, M. Chilukuri, and K. Kundert, "An Efficient Approach to Transmission Line Simulation Using Measured or Tabulated S-parameter Data," paper published in the *Proceedings of the 31st Design Automation Conference*, San Diego, California, June 1994, pp. 634-639; L.M. Silveira, I. Elfadel, J. White, M. Chilukuri, and K. Kundert, "Efficient Frequency-Domain Modeling and Circuit Simulation of Transmission Lines," *IEEE Trans. Components, Hybrids, Manufact. Technol.* Part B: Advanced Packaging, special issue on Electrical Performance of Electronic Packaging, 17(11): 505-513 (1994); L.M. Silveira, M. Kamon, and J.K. White, "Algorithms for Coupled Transient Simulation of Circuits," *IEEE Trans. Components, Hybrids, Manufact. Technol.* Part B: Advanced Packaging, special issue on the Electrical Performance of Electronic Packaging, 18(1): 92-98 (1995).

with interconnect. Generating reduced-order models from realistic 3-D structures, however has received less attention. Recently we have been studying an accurate approach to using the iterative method in the 3-D magnetoquasistatic analysis program FASTHENRY to compute reduced-order models of frequency-dependent inductance matrices associated with complicated 3-D structures. This method, based on a Krylov-subspace technique, namely the Arnoldi iteration, reformulates the system of linear ODEs resulting from the FASTHENRY equation into a state-space form and directly produces a reduced-order model in state-space form. The key advantage of this method is that it is not more expensive than computing the inductance matrix at a single frequency. The method compares well with the standard Pade approaches; it may present some advantages because in the Arnoldi-based algorithm, each set of iterations produces an entire column of the inductance matrix rather than a single entry. If matrix-vector product costs dominate, then the Arnoldi-based algorithm produces a better approximation for a given amount of work.²⁵

1.12 Simulation Algorithms for Communication Circuits

Sponsors

Motorola Corporation
National Science Foundation
Grant MIP 91-17724

Project Staff

Ognen J. Nastov, Professor Jacob K. White

The determination of the steady-state distortion of clocked analog circuits such as switching filters and

phase-locked loops, using conventional circuit simulation techniques, is an extraordinarily computationally intensive task. This is because the period of the clock is orders of magnitude smaller than the required time interval to reach the steady-state. One approach to computing steady-state distortion is the mixed frequency-time method (MFT). This method is based on the observation that the node waveforms in a particular high-frequency clock cycle are similar to the node waveforms in the neighboring cycles. Therefore, this suggests that by calculating the solution accurately over a few selected clock cycles, a solution accurate over many cycles can be constructed.

We are developing a generalization of the MFT algorithm which can be used to calculate the steady-state and intermodulation distortion for analog circuits whose inputs are a sum of periodic signals at unrelated frequencies. For example, computing the intermodulation distortion of narrow-band amplifiers by traditional circuit simulation is very difficult. The maximum usable time step is much smaller than the period of the difference frequency of the two frequencies in the input signal. The period of the difference frequency is large since the two input frequencies are required to be close in order for the distortion products to be within the bandwidth of the amplifier. If the amplifier is high-Q, the required simulation time interval will be many times larger than the period of the difference frequency. At present, the key problem in applying MFT methods to large problems is finding efficient techniques to solve the large linear systems generated by these methods. We are investigating using a variety of preconditioned matrix-free iterative methods.²⁶ We are also exploring other possible extensions of the MFT ideas and their application to other nonlinear analog circuits that are difficult to simulate.

²⁵ L.M. Silveira, M. Kamon, and J. White, "Direct Computation of Reduced-Order Models for Circuit Simulation of 3-D Interconnect Structures," *Proceedings of the Third Topical Meeting on Electrical Performance of Electronic Packaging*, Monterey, California, November 1994; L.M. Silveira, M. Kamon, and J. White, "Efficient Reduced-Order Modeling of Frequency-Dependent Coupling Inductances associated with 3-D Interconnect Structures," *Proceedings of the European Design and Test Conference*, Paris, France, March 1995; L. Silveira, M. Kamon, and J. White, "Direct Computation of Reduced-Order Models for Circuit Simulation of 3-D Interconnect Structures," invited paper in *Progress in Electromagnetic Research Symposium*, Seattle, Washington, July 1995; L. Miguel Silveira, Mattan Kamon and Jacob K. White, "Efficient Reduced-Order Modeling of Frequency-Dependent Coupling Inductances associated with 3-D Interconnect Structures," *IEEE Trans. Components, Hybrids, and Manufact. Technol.* Part B: Advanced Packaging, special issue on Electrical Performance of Electronic Packaging, forthcoming; L.M. Silveira, M. Kamon and J. White, "Efficient Reduced-Order Modeling of Frequency-Dependent Coupling Inductances Associated with 3-D Interconnect Structures," *Proceedings of the 32nd Design Automation Conference*, San Francisco, California, June 1995, pp. 376-380; M. Chou and J. White, "Efficient Reduced-Order Modeling for the Transient Simulation of Three-dimensional Interconnect," *Proceedings of the International Conference on Computer Aided Design*, San Jose, California, November 1995, pp. 40-44; I.M. Elfadel, L.M. Silveira, and J. White, "Stability Criteria for Arnoldi-Based Model Order Reduction," *Proceedings of the IEEE Conference on Acoustics, Speech, and Signal Processing* (ICASSP '96), Atlanta, Georgia, May 1996, forthcoming.

²⁶ R. Telichevesky, K.S. Kundert, and J.K. White, "Efficient Steady-State Analysis Based on Matrix-Free Krylov Subspace Methods," *Proceedings of the Design Automation Conference*, San Francisco, California, June 1995.

1.12.1 Publications

- Cai, X., P. Osterberg, H. Yie, J. Gilbert, S. Senturia, and J. White. "Self-Consistent Electro-mechanical Analysis of Complex 3-D Micro-electromechanical Structures using a Relaxation/Multipole Method." *Int. J. Sensors Mater.* Forthcoming.
- Cai, X., K. Nabors, and J. White. "Efficient Galerkin Techniques for Multipole-Accelerated Capacitance Extraction of 3-D Structures with Multiple Dielectrics." *Proceeding of the 16th Conference on Advanced Research in VLSI*, Chapel Hill, North Carolina, March 1995.
- Chou, M., and J. White. "Efficient Reduced-Order Modeling for the Transient Simulation of Three-dimensional Interconnect." *Proceedings of the International Conference on Computer Aided Design*, San Jose, California, November 1995, pp. 40-44.
- Chou, M., M. Kamon, K. Nabors, J. Phillips, and J. White. "Extraction Techniques for Signal Integrity Analysis of 3-D Interconnect." Invited paper in *Proceedings of the Custom Integrated Circuits Conference*, CITY, May 1995. Forthcoming.
- Chou, M., and J. White. "Transient Simulations of Three-dimensional Integrated Circuit Interconnect using a Mixed Surface-Volume Approach." Invited paper in *Progress in Electromagnetic Research Symposium*, Seattle, Washington, July 1995. Forthcoming.
- Chou, M., T. Korsmeyer, and J. White. "Transient Simulations of Three-dimensional Integrated Circuit Interconnect using a Mixed Surface-Volume Approach." *Proceedings of the 32nd Design Automation Conference*, San Francisco, California, June 1995.
- Elfadel, I.M., L.M. Silveira, and J. White. "Stability Criteria for Arnoldi-Based Model Order Reduction," *Proceedings of the IEEE Conference on Acoustics, Speech, and Signal Processing (ICASSP '96)*, Atlanta, Georgia, May 1996, forthcoming.
- Kamon, M., B. Krauter, J. Phillips, L. Pileggi, and J. White. "Two Optimizations to Accelerated Method-of-Moments Algorithms for Signal Integrity Analysis of Complicated 3-D Packages." Paper published in the *Proceedings of the Fourth Topical Meeting on Electrical Performance of Electronic Packaging*, Portland, Oregon, October 1995, pp. 213-216.
- Lumsdaine, A., M. Reichelt, and J. White. "Accelerated Waveform Methods for Parallel Transient Simulation of Semiconductor Devices." *IEEE Trans. Comput.-Aided Des.* Forthcoming.
- Lumsdaine, A., and J. White. "Accelerating Waveform Relaxation Methods with Application to Parallel Semiconductor Device Simulation." *Numerical Functional Analysis and Optimization*. Forthcoming.
- Phillips, J.R., and J.K. White. "Precorrected-FFT Methods for Electromagnetic Analysis of Complex 3-D Interconnect and Packages." Invited paper in *Progress in Electromagnetic Research Symposium*, Seattle, Washington, July 1995, forthcoming.
- Phillips, J. "Error and Complexity Analysis for a Collocation-Grid-Projection plus Precorrected-FFT Algorithm for Solving Potential Integral Equations with Laplace or Helmholtz Kernels." Second Place, Student Paper Competition, *Colorado Conference on Multigrid Methods*, April 1995.
- Phillips, J.R., H.S.J. van der Zant, and T.P. Orlando. "Dynamics of Row-switched States in Josephson-junction Arrays." *Phys. Rev. B*
- Reichelt, M., J. White, and J. Allen. "Optimal Convolution SOR Acceleration of Waveform Relaxation with Application to Parallel Simulation of Semiconductor Devices." *SIAM J. Sci. Stat. Comput.* Forthcoming.
- Silveira, L.M., M. Kamon, and J.K. White, "Algorithms for Coupled Transient Simulation of Circuits." *IEEE Trans. Components, Hybrids, Manufact. Technol.* Part B: Advanced Packaging, special issue on the Electrical Performance of Electronic Packaging, 18(1): 92-98 (1995).
- Silveira, L.M., M. Kamon, and J. White. "Efficient Reduced-Order Modeling of Frequency-Dependent Coupling Inductances associated with 3-D Interconnect Structures." *Proceedings of the European Design and Test Conference*, Paris, France, March 1995.
- Silveira, L.M., M. Kamon, and J. White. "Direct Computation of Reduced-Order Models for Circuit Simulation of 3-D Interconnect Structures." Invited paper in *Progress in Electromagnetic Research Symposium*, Seattle, Washington, July 1995.

Silveira, L.M., M. Kamon, and J.K. White. "Efficient Reduced-Order Modeling of Frequency-Dependent Coupling Inductances associated with 3-D Interconnect Structures." *IEEE Trans. Components, Packaging, Manufact. Technol. Part B: Advanced Packaging*. Forthcoming.

Silveira, L.M., M. Kamon, and J. White. "Efficient Reduced-Order Modeling of Frequency-Dependent Coupling Inductances associated with 3-D Interconnect Structures." *Proceedings of the 32nd Design Automation Conference*, San Francisco, California, June 1995, pp. 376-380.

Telichevesky, R., K.S. Kundert, and J.K. White. "Efficient Steady-State Analysis Based on Matrix-Free Krylov Subspace Methods." *Proceedings of the Design Automation Conference*, San Francisco, California, June 1995.

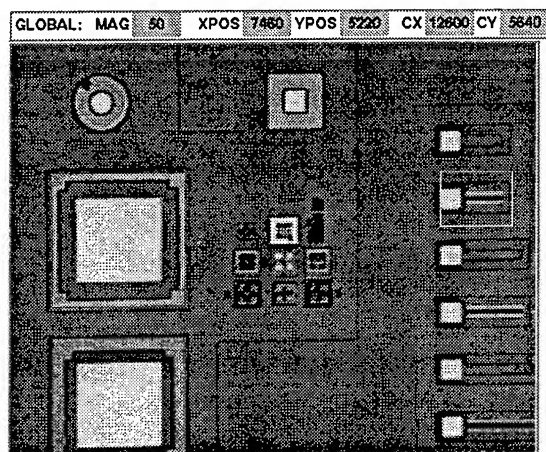
Yie, H., S.F. Bart, J. White, and S.D. Senturia. "Computationally Practical Simulation of a Surface-Micromachined Accelerometer with True Fabrication Non-idealities." *Proceedings of MEMS 95*, 1995.

Remote Microscope Interface

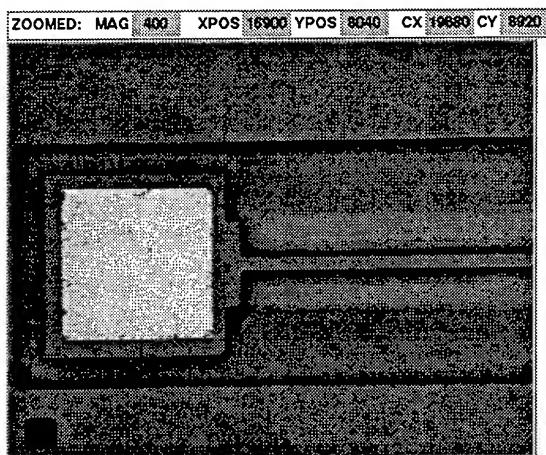
SET MAGNIFICATION	ACTION BUTTONS	Current Users
50X	grab	GARCON.MIT.EDU
100X	zoom	
200X	quit	
400X	cede	
1000X	G save	
	Z save	

SET POSITION	
CUR X	CUR Y

Console Window for controlling microscope



Global Window showing panoramic view at 50X



Zoomed Window showing image at 400X

Chapter 2. Computer-Integrated Design and Manufacture of Integrated Circuits

Academic and Research Staff

Professor Donald E. Troxel, Professor Dimitri A. Antoniadis, Professor Duane S. Boning, Linus F. Cordes, Gregory T. Fischer, Stanley B. Gershwin, Thomas J. Lohman, Michael B. McIlrath

Graduate Students

Asbjorn M. Bonvik, John C. Carney, Yonald Chery, Jarvis B. Jacobs, James T. Kao, Somsak Kittipiyakul, Jimmy Y. Kwon, William P. Moyne, Joseph E. Nemec, Nadir E. Rahman, Chantal E. Wright

Technical and Support Staff

Francis M. Doughty

2.1 Research Goals and Objectives

Sponsors

Defense Advanced Research Projects Agency/
U.S. Navy
Contract N00174-93-K-0035
Defense Advanced Research Projects Agency/
U.S. Army
Contract DABT 63-95-C-0088
Multisponsored Projects Industrial/
MIT Leaders for Manufacturing Program

2.1.1 The MIT Computer-Aided Fabrication Environment

The computer-aided fabrication environment (CAFE) is a software system being developed at MIT for use in the fabrication of integrated circuits and microstructures. The distinguishing feature of CAFE is that it can be used in all phases of process design, development, planning, and manufacturing of integrated circuit wafers. CAFE presently provides day-to-day support to research and production facilities at MIT with both flexible and standard product capabilities. This manufacturing software system is unique in the development of a process flow representation and its integration into actual fabrication operations. CAFE provides a platform for work in several active research areas, including technology (process and device) computer-aided design (TCAD), process modeling, manufacturing quality control, and scheduling.

Architecture

The CAFE architecture is a computer integrated manufacturing (CIM) framework for the deployment and integration of integrated circuit (IC) and process design and manufacturing software. CAFE uses an object oriented database model which is implemented in a layered manner on top of a relational database. Our database schema is based on GESTALT, an object oriented, extensible data model. GESTALT is a layer of abstraction which maps user defined objects onto existing database systems (e.g., a relational DBMS) and shields application programs from the details of the underlying database. The integration architecture includes the conceptual schema and models used to represent the IC manufacturing domain in CAFE and the user and programmatic interfaces to the various applications. Two important CAFE applications relate process simulation and actual wafer fabrication to the same process flow representation.

CAFE Applications

The fabrication of wafers with a process represented as a process flow representation (PFR) involves several steps. A suitable PFR for the specific process must be created and installed. Wafer lots must be created and associated with this specific PFR. These lots must then be "started" to create a task data structure which is isomorphic to the hierarchical structure of the PFR.

At this point, actual machine operations can be scheduled and reservations made for both machines and operators. Finally, the machine operations can be performed, instructions given to the operator and machines, and data collected from the operator or machine and entered into the database.

2.1.2 National Infrastructure for Networked Design and Prototyping

We are developing tools and infrastructure to enable virtual and physical prototyping of advanced microsystems. A "quasi-empirical" simulation approach requires data from select experiments to build accurate performance, reliability, and variation or statistical models. Parameters for these models must be determined and refined by multiple series of both simulations and repeated experiments. The validation of simulations produced by the computational prototyping tools can only be achieved by correlation of simulated results with actual experimental measurements. Advanced computational prototyping tools and methodologies will enable collaborative networked subsystem design and physical prototyping.

The infrastructure development will enable management of information required to specify processing, collect measurements, and retrieve results of remote processing and metrology. This infrastructure will support the timely conduct of the multitude of experiments to calibrate and validate simulations which are embodied in the computational prototyping of high performance integrated circuits.

Models and tools developed under this program, as well as both simulated and experimental data, will be collected into libraries and repositories and made available via network. This will provide convenient and effective access to research results as they become available and support collaborative subsystem design and physical prototyping.

2.1.3 CAFE at MIT Lincoln Laboratory

Project Staff

Gregory T. Fischer, Thomas J. Lohman, Professor Donald E. Troxel

MIT Lincoln Laboratory is using CAFE as the CIM system in their IC processing facility. Multiple lots are being processed daily via process flow representation (PFR) based fabrication. Lincoln has 100 percent of their wafers in this facility processed with PFR based fabrication.

It is now possible to view CAFE Help and Lab Manual text via the World Wide Web. Options have been added under the "Help" and "Help"/"Equipment Help" menus which will initiate a web browser to display the specified help text section.

2.2 Operating High Variability Manufacturing Systems

Project Staff

Asbjorn M. Bonvik

We present two factory control policies derived from optimal control considerations. Using sample factories distributed by Sematech, we compare the performance of these policies to other control strategies such as kanban and periodic lot release. We show that the policies designed for high variability environments have very attractive properties, including higher throughput than periodic release and much lower inventories than kanban.

Semiconductor manufacturing differs from many other manufacturing environments by the complexity and variability of its processes. A semiconductor process can be several hundred operations long, and the machines are relatively unreliable due to the leading edge technology involved. This makes semiconductor factories harder to control than other plants of comparable size.

We construct control policies by extending the structural properties found by optimal control formulations of smaller systems. This allows us to construct good, although not provably optimal, control schemes for large production systems.

In the following, we explain the structure of two such policies and contrast them with control policies that are commonly found in industry. We then report simulation results from datasets distributed by Sematech, representing actual semiconductor factories.

We have built a scheduling and simulation testbed integrated with the MIT CAFE computer-aided fabrication environment. This program can act as a factory floor dispatcher, where it recommends a daily schedule based on the factory state stored in the database. The program can also run in a simulation mode, where it will project long-term consequences of following a certain scheduling policy under various assumptions on lot releases and machine reliabilities. The main architectural components are (1) the data structures that represent the system state, (2) the front ends that create the initial state, (3) the system dynamics module that makes the state evolve in time, and (4) the control modules that make release and dispatch decisions.

In its simulation mode, the testbed can read the Sematech datasets instead of the CAFE database. This allows us to test out our scheduling approaches in other manufacturing systems than our own. The testbed does not currently support all

features found in the Sematech datasets. For instance, we do not simulate operator availability, scrap, or rework. Setups are simulated, but the scheduling policies tested do not make any attempt to optimize the setup sequence.

This leads to different production rates from our testbed than from the Delphi simulator also distributed by Sematech. On the other hand, we allow the scheduling modules to control the lot release rates to the fabrication, not just manipulate the dispatch decisions as appears to be the case with Delphi. Previous work has shown that the lot releases are a more important factor in fabrication performance than lot dispatch decisions on the shop floor.

2.3 A Distributed Discrete Event Simulation

Project Staff

Asbjørn M. Bonvik

Discrete event simulation is, almost by definition, a very CPU-intensive task. Some stochastic processes are represented by a program incorporating a pseudo-random number generator, and statistics are collected by executing the program. It may be necessary to run the simulation for a very long time to get good estimates of the performance measures of the actual system under study. For example, if one is studying a manufacturing system where machine failures are important to the overall behavior of the system, the simulation needs to cover a period with many failures of different lengths.

It is very hard to parallelize a discrete event simulation, because the commonly found algorithm maintains a centralized event list and a current simulation time, executing one event at a time. The current event may manipulate the list of future events, for instance by scheduling the end of some activity or the next instance of some event. When the current event is done, the event with the lowest activation time is taken out of the event queue, the simulation time is set to this value, and the event is executed. This essentially presumes a single thread of execution on a single processor.

On the other hand, because of statistical considerations, it is common to split a large simulation job into a batch of independent replications, where each replication is started from a different random number seed, everything else being the same. This is done to eliminate the dependency on a single sequence of pseudo-random numbers and to establish confidence intervals on the performance measures. This also gives a natural granularity for a

coarse-grained parallel or distributed computation: Distribute one replication to each processor, and designate one processor to collect the statistics emanating from the computation.

This is exactly what we did for a recent study of a small production system under various conditions. Our work had two phases: a screening phase where a large number of parameter settings had to be evaluated, and a refinement phase in which multiple replications were done of the best parameter settings to draw final conclusions. To do this efficiently, we constructed a distributed simulator architecture that ran on about one dozen Sun SparcStations, mainly SparcStation 10s. The computers used were the MTL machines, the machines at the Operations Research Center, and a single SparcStation 10 at the Norwegian Defence Research Establishment. After the actual study was completed, a Pentium 100 MHz PC running Linux was added to the architecture. This demonstrates that the architecture is not Sun-specific. Incidentally, the PC turned out to work approximately 20 percent faster than even a SparcStation 20, possibly because of faster I/O leading to less overhead when starting a client.

The software had three components: the discrete event simulation program itself, a client program that drove a single replication on some host, and the server program that organized the computation and collected statistics.

By using these programs, we successfully simulated about 6000 different cases. Most cases were run for a single replication of about 100 weeks of simulated time, but about 50 cases were selected for further scrutiny. This required 50 more replications of each case, for a total of about 8500 replications. We estimated this to take about three months of CPU time on a single SparcStation 2 such as hierarchy. Using our virtual supercomputer, the entire job was done in four days of real time. In addition, we did extensive model validation runs and a number of false starts before getting it right.

More speed is available by using more hosts. The approach is not limited to Sun computers, as our Pentium PC demonstrated. Anything that supports UNIX stream sockets can be used. This allows other fast computers to be added by the simple expedient of getting an account, recompiling the simulation for that machine type, and adding the host name to the server list of target hosts.

In conclusion, our approach gives supercomputer speed at very little cost. Suitable jobs for a similar scheme are very CPU-intensive with small memory and I/O requirements and have a structure such that fairly large pieces of the job can be computed

separately and the results assembled with little effort.

2.4 QUAN: A Language for the Schedule Of Repetitive Manufacturing Systems

Project Staff

Joseph E. Nemec

We propose the syntax for a language called Quan which allows for the expression of scheduling policies for repetitive manufacturing systems—systems which make multiples of single or several part types. We first develop a representation of the factory using an object-oriented approach similar to that of the one found in Stamatiopoulos.¹

In the course of doing so, we describe the physical objects in the factory, including such objects as machines, buffers, parts, and technicians, as well as the conceptual objects in a factory, including manufacturing cells, process flows, operations, process constraints, and material constraints.

2.4.1 Introduction

We propose a language that will allow for the expression of scheduling policies for repetitive manufacturing systems. We propose to use an object-oriented approach, using the software developed by Stamatiopoulos¹ as a basis.

In order to describe scheduling policies in the scheduler in a consistent manner, we must be able to express what constitutes the physical objects in the factory, such as machines, buffers, technicians, parts, as well as how these objects interact with each other, what their characteristics are, and other attributes. To this end, we define several representations; the factory representation (FR), the material representation (MR), the process representation (PR), the scheduling representation (SR), and the constraint representation (CR). Each will be described in detail.

In addition to the representations, we also have the state of the system. This is represented as the factory state (FS) and the materials state (MS).

With the complete definition of the factory at our disposal, we will then describe the quantity scheduling language (Quan), which will be interpreted by the scheduler. This language will allow for the expression of inventory control policies, such as Kanban or CONWIP,² or hybrids of such policies³ and production policies, such as FIFO, LIFO or preemptive processing.⁴

2.4.2 The General Model

Figure 1 shows the interaction between the various representations, the various states and the scheduler.

All of the representations, except the SR, are static. Once defined and internalized, they are not consulted anymore. They form the backbone of the manufacturing system. For example, it is assumed that once it has been defined that a certain operation can only be performed on a certain machine with certain operators, these constraints will not change. If, for example, more workers were trained to work a specific machine, then the representation of the factory must be updated to take this change into account. As such things do not happen instantaneously, but rather require time and effort, they are not of immediate concern to the scheduler.

The SR is continuously consulted by the scheduler. The scheduler, in making decisions, may have several possibilities for each machine. For example, we may make it a point of always running with a First-In First-Out unless we are badly backlogged, in which case we begin prioritizing certain part-types over others. This change in the factory state (i.e. the backlog) necessitates a reconsultation with the SR to determine appropriate actions.

The consultative process of the scheduler is illustrated in figure 2.

¹ M. Stamatiopoulos, *A Factory Representation as a Design Tool in a Computer Integrated Manufacturing Environment*, M.S. thesis, MIT, 1994.

² J.A. Buzacott, J. Shanthikumar, and J. George, *Stochastic Models of Manufacturing Systems*, (Englewood Cliffs, New Jersey: Prentice-Hall, 1993).

³ A.M. Bonvik, Y. Dallery, and S.B. Gershwin, "Approximate Analysis of Production Systems Operated by a CONWIP-finite Buffer Hybrid Control Policy," submitted for publication.

⁴ L. Kleinrock, *Queueing Systems, Volume 1: Theory* (New York: Wiley-Interscience, 1975).

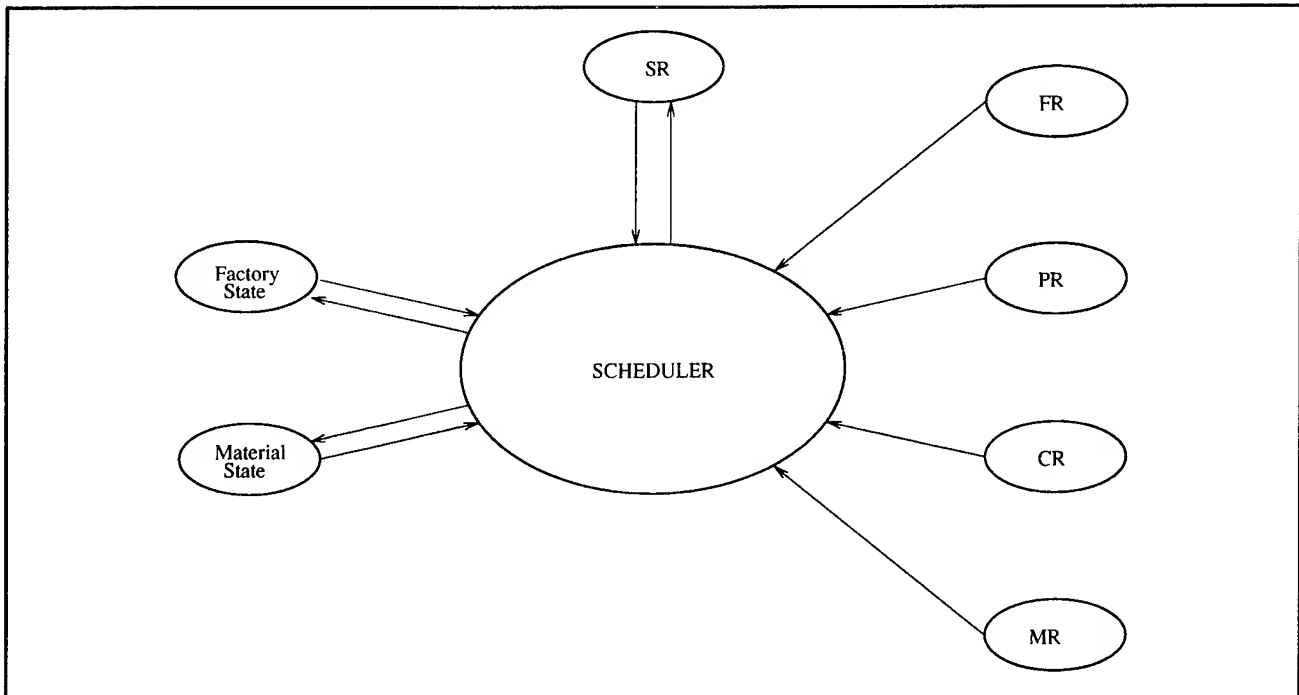


Figure 1.

2.5 Microsystems Factory Representation

Project Staff

Joseph E. Nemec

The microsystems factory representation (MFR) is a system that allows for the explicit representation of factories using an object oriented, C-like block structure programming language. It allows for the easy declaration of the attributes of various objects, and for fast and powerful editing of specific instances of the attributes defined. This document will describe the MFR through several examples, demonstrating its flexibility and power.

The MFR has three fundamental parts: the Schematic Representation, the Textual Representation, and the Textual Interpreter. The procedure for representing a factory in the MFR comes in two stages. In the first stage, the objects that are in the factory are declared. These include such classes of physical objects as machines, buffers, technicians, etc., as well as artificial constructions dependent on the structure of the factory chosen, such as cells. This collection of objects is known as the schema of the representation. This schema is compiled into the MFR Textual Interpreter by the MFR Schematic Interpreter.

In the second stage, the MFR textual representation of the factory, the representation of how the information about the factory is organized, is specified.

The syntax of the textual representation is dependent on the schema declared. The MFR Textual Interpreter is then used to parse the text, check for syntax errors, and create a representation of the factory in computer memory, or instantiate it into a data base.

The MFR schema is simply the collection of objects of different classes required to create an MFR textual representation of the factory. This is where the characteristics of such objects as machines or buffers are defined. For example, if the object we are creating is a machine class, we will want the class to have such attributes as mean time to fail and mean time to repair, failure modes, etc. The syntax of the schema representation is block-structured, like C. A programmer's manual for the schema may be found in Stamatopoulos.¹ The schematic is then compiled into the MFR Textual Interpreter using the MFR Schematic Interpreter.

The MFR textual representation describes how the objects defined in the schema are organized in the factory. Specifically, it declares how many of each object there are, their names, their locations, their specific attributes, etc. The textual representation allows for a hierarchical representation of the objects or a one-dimensional representation. We will see later that a hierarchical representation is preferred.

The MFR textual representation is then read by the MFR Textual Interpreter, which parses the text, performs consistency checks on the data and, creates

a representation of the MFR objects (those defined by the MFR schema above) in computer memory.

2.6 Run-by-Run: Interfaces, Implementation, and Integration

Project Staff

William P. Moyné

Run-by-run (RbR) control is a form of adaptive model based process control where recipe changes are performed between runs of the process. It is becoming popular in the area of VLSI processing but its acceptance has been hindered by integration issues. Existing systems cannot be replaced due to massive capital investments, so the RbR controller

must mesh with these systems without requiring large modifications. Two steps have been taken to ease this integration. First, an abstract data model has been developed for RbR control which can be easily communicated between dissimilar modules. Second, a three tier communication model has been developed to allow multiple levels of interaction with the RbR control module. These layers complement the underlying data model.

An RbR control server has been implemented to demonstrate the robustness of the communication model and data abstraction. This server provides RbR control to a variety of clients via TCP/IP network sockets. One of these clients is a graphical user interface that allows direct operation of the control algorithms. This can be a powerful tool when evaluating new control algorithms or testing equipment models. The interface contains a set of simulation, graphing, and archiving tools to aid in the testing and operation of the server. The controller has been integrated into a local computer integrated manufacturing (CIM) system, as well as a control framework being developed by The University of Michigan and SEMATECH.

In addition to interface issues, the control algorithms themselves have been enhanced to enable a variety of constraints and bias terms to be added to the models. The controller currently contains two control algorithms, but is designed to be expanded to include more algorithms as they are developed. Data needed for these new algorithms can be constructed using the data abstraction without disrupting existing modules. Implementation, interface, and integration barriers to the adoption of run-by-run control have been reduced by the definitions and demonstrations presented in this thesis.

2.7 Remote Fabrication of Integrated Circuits

Project Staff

Jimmy Y. Kwon

The computer-aided fabrication environment (CAFE) is a software system developed at MIT for use in all phases of integrated circuit fabrication. While still undergoing development and enhancements, CAFE provides day-to-day support to research and production facilities at MIT, with both standard and flexible product lines.

One of the limitations of the present CAFE system is that it is not a fully open system. An open system is one that is designed to accommodate components from various software applications and can be viewed from three perspectives: portability, inte-

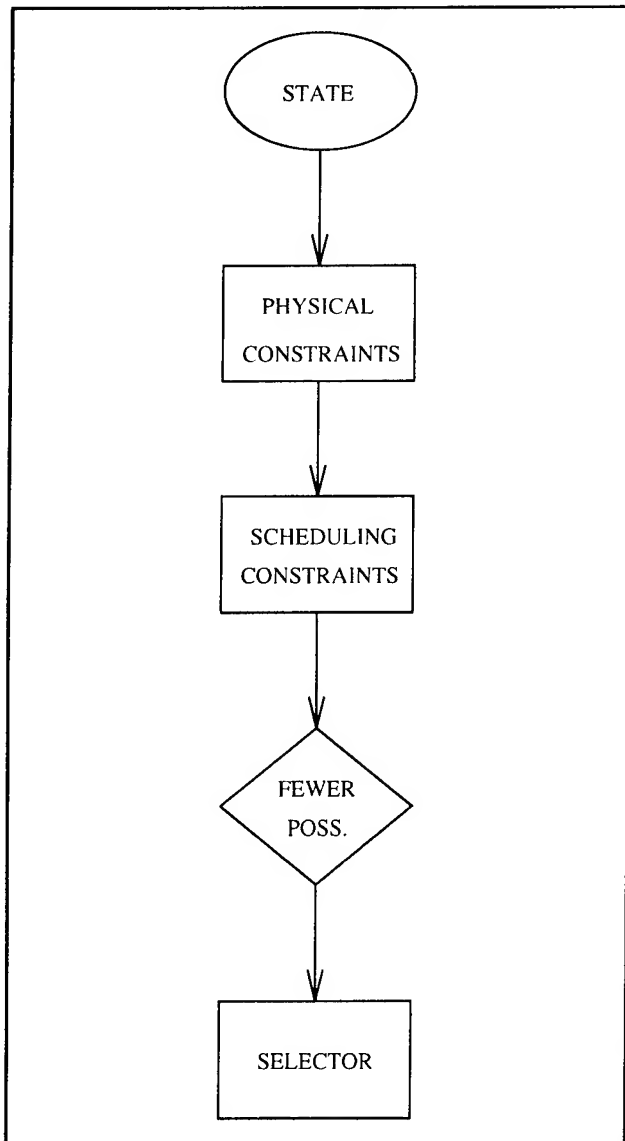


Figure 2.

gration, and interoperability. This document is concerned with the idea of interoperability between different computer integrated manufacturing (CIM) systems, and describes the extension to CAFE's architecture to support what is called remote fabrication.

With the goal of general interoperability between different CIM systems in mind, the virtual object manager is developed. The virtual object manager provides a framework for three key modules to support interoperability: the Object Management Module, the Export/Import Module, and the Remote Message Passing Module. Each of these modules are discussed and implemented for the CAFE platform.

Building upon the interoperability tools in the virtual object manager, application layer support is then developed for the specific task of remote fabrication in CAFE. The application modules and additional software tools are described, and together form the CAFE remote fabrication system, a prototype system providing remote fabrication capabilities. An example of a remote fabrication session is described, stepping the reader through CAFE's remote processing paradigm and showing how the various tools are used. In the form of a tutorial, the example starts with installing a process flow into the CAFE database and creating a lot of wafers. The operate-machine/next-operation processing cycle is then done using both local and remote machines, showing the interoperability features at work. When the processing cycle completes a traveller file is generated, summarizing the entire history of processing.

While this document describes and implements a remote fabrication system specifically for CAFE, it is hoped that this document brings into focus some of the issues involved in general interoperability between different CIM systems and provides a useful framework for future work.

2.8 Message Passing Tools for Software Integration

Project Staff

John C. Carney

As the base of developed software grows, software integration is becoming increasingly important. Many software systems are large and complex. Since rewriting the entire system is not generally possible, newly developed programs must be integrated into the existing system. It is the responsibility of the developer to not only write a new

program or tool, but to make it work within the existing environment.

There are several approaches to software integration. Programs within the Unix environment typically are integrated by operating on a common set of files. One program is used to create a file, another to process it, and perhaps yet another to analyze the results. Other approaches include program databases and remote procedure calls (RPCs). An alternative approach for software integration is through the use of a message passing system. The goal of the message passing system is to provide a method by which structured information may be exchanged between two or more running processes. These processes may possibly be running on a single workstation or on multiple workstations connected by a network.

While there are not many message passing systems in existence, the majority which do exist have been designed to be used for a special purpose or in a particular context. There are some general purpose message passing systems, however, these systems impose a fixed integration architecture and message format. A more flexible peer-to-peer approach to message passing has been developed. The peer-to-peer messaging system allows the software developer and integrator to completely design and choose the desired integration architectures and message formats.

The communications handling application tool suite (CHAT) has been developed and provides the programmer with a suite of libraries which can be used to integrate software programs using the peer-to-peer message passing approach. There are three libraries of routines, providing support for packaging data into messages, handling incoming messages, and application connection. All three libraries are implemented both in C and Tcl/Tk, a scripting language and toolkit for creating graphical user interfaces under X-Windows. The CHAT suite will allow arbitrary combinations and architectures of C programs and Tcl/Tk programs to exchange messages.

Libraries within the CHAT suite have been used to integrate a new factory display program into CAFE, MIT's computer-aided fabrication environment. CAFE is a software system for the use in the manufacture of integrated circuits, and provides day-to-day support for both research and production facilities at MIT. The factory display program is a graphical program which displays a map of a semiconductor manufacturing facility, including the machines and lots within the facility. The CHAT suite has also been used within other software integration efforts and plans have been made to use the libraries in future integration projects within

MIT's Computer Integrated Design and Manufacturing (CIDM) project.

2.9 Remote Microscope for Inspection of Integrated Circuits

Project Staff

James T. Kao

The remote microscope was developed at MIT as part of the computer integrated design and manufacturing project to aid in the remote fabrication of integrated circuits, and will allow a user to operate and view in "real time" an actual microscope located at a distant facility. We envision a growing trend in the semiconductor processing field for more collaboration and sharing of resources, so it will become important for researchers to have access to a telemicroscopy system like the one developed at MIT to perform remote inspections of semiconductor wafers.

The MIT remote microscope is extremely versatile; it operates over the internet and allows a user to run the graphical microscope interface on any ordinary UNIX workstation, thereby providing easy access to the microscope for researchers located throughout the world. The actual remote microscope utilizes readily available hardware as well, making the entire system very straightforward and economical to implement. To the best of our knowledge, the MIT remote microscope is the first telemicroscopy system to operate on the internet. The remote microscope also is original because it allows multiple users to view the microscope at the same time in a conference inspection, which should be very useful when geographically distant researchers wish to collaboratively inspect a wafer. The overwhelming response to the remote microscope has been very positive, as it was officially demonstrated in August 1995 between MIT and Stanford University during the annual TCAD symposium.

2.10 Semiconductor Manufacturing Process Flow Representation (PFR)

Project Staff

Michael B. McIlrath

2.10.1 Introduction

The process flow representation (PFR) and its integration into both design and fabrication operations is central to the CIDM program and the computer-aided fabrication environment (CAFE) software system.³ CAFE is currently being used at the semiconductor fabrication processing facilities of the MIT Microsystems Technology Laboratories, Lincoln Laboratories, and Case Western University. Activities in this area include both formal methods for process modeling and the practical application of process representation to process design and execution.

For high performance computing systems and other advanced technology, concurrence in the design of the product, manufacturing process, and factory is crucial. The goal is to achieve fully integrated design and manufacture, in which the boundary between design and manufacturing domains is eliminated: in particular, information from the manufacturing floor is continuously available from the earliest stages of process and device design onward. Conversely, the manufacturing process, developed concurrently with the product, continues to undergo design via improvement and modification while in production. Computer integrated design and manufacture (CIDM), therefore, requires a coherent manufacturing process representation capable of storing information from a variety of different knowledge domains and disciplines and supporting access to this information in a consistent manner. We believe that our general semiconductor process modeling framework organizes the complexity of this interrelated information and puts our process flow representation (PFR) on a sound footing by giving it clear semantics.

A high level conceptual model for describing and understanding semiconductor manufacturing processing is a crucial element of both the CIDM research program, and of software frameworks for TCAD and CIM, including the MIT computer-aided fabrication environment (CAFE). Initially a two-stage generic process step model was used, which described processing steps in terms of two independent components: an equipment-dependent, wafer-independent stage, which maps equipment settings to physical processing environments, and an equipment-independent, wafer-dependent stage, which relates physical environments to changes in the input wafers. Driven by the needs of process control and optimization research, including sophisticated modeling, design, and experimental model verification, our fundamental conceptual process model has evolved from the two-stage generic process model into one which is part of a more general process modeling framework, in which the

earlier two-stage model is a special case. Our approach to process representation for both TCAD and CIM is based on this general modeling framework for semiconductor processing. In this framework, state information (e.g., wafer, environment, and equipment state), and models, or transformations, that describe relationships between state descriptions, are formally identified and described. The purpose of this comprehensive framework is to enable an effective representation that can be used throughout the IC semiconductor process life-cycle, from early conception and design phases through fabrication and maintenance.

In the MIT CAFE system, the PFR is expressed in a textual (ASCII) format and then converted into Gestalt objects and loaded into the CAFE database. The textual language of the PFR is extensible, so that it can flexibly accommodate changes and extensions to both the underlying modeling methodology and the needs of specific applications. The object-oriented nature of the Gestalt database interface enables the convenient evolutionary development of CAFE software applications built around the PFR. The PFR allows process step descriptions to be "underdetermined"; for example, by expressing only the wafer-state change, making it possible to develop a process incrementally with increasing degrees of detail. In addition to expressing the fundamental concepts of wafer transformation within individual process steps, the PFR supports both hierarchical and parameter abstraction and embedded computation, thereby providing support for modular process design and development. Processes expressed in the PFR can be simulated using a variety of technology CAD tools; PFR extensibility allows the incorporation of both simulator-dependent and simulator-independent information. A simulation manager application uses the appropriate information in the PFR along with knowledge of specific simulators to invoke simulation tools and maintain simulation state.

2.10.2 Process Development and Execution

The PFR has been used to develop and execute all of the fabrication processing at MIT Lincoln Laboratory during the last three years. Over 500 fabrication runs have been completed with around forty lots in process at any given time. These lots represent a variety of technologies, including CCD, low power CMOS, and SOI. All the Lincoln facility processing uses CAFE and the CAFE PFR.

Additionally, at MIT the PFR is used for both baseline and research processing; in particular, in support of other computer integrated design and

manufacturing (CIDM) and MTL research activities including hot carrier reliability and extreme submicron technology design.

2.10.3 Design Rule Checking for Wafer Fabrication Using CAFE

We have developed an extensible and general framework for process design rule checking. A table-driven approach used is to check for rule constraints at each processing step, based on the current state of the wafers. By "wafer state" we refer not only to the simulated or measured process effects but also to the process history. The rule-checker can be used in two ways: on-line, to prevent unsafe operations from occurring during fabrication and during process.

2.11 Computer-Aided Technology Design

Project Staff

Professor Dimitri A. Antoniadis, Professor Duane S. Boning, Michael B. McIlrath, Nadir E. Rahman, Jarvis B. Jacobs

2.11.1 Introduction

The design of advanced integrated circuit microsystems is increasingly tightly linked to the design of both the component devices of the microsystem and the microfabrication process used in its manufacture. Traditionally, the devices and manufacturing process used in building integrated circuits are collectively called the technology. The objective of microsystems technology design is to devise a fabrication process sequence which yields structures with some desired characteristics. Actually, two design activities proceed in parallel: design of the device structures and the process to fabricate them. In general, design space for both is explored by the technology designer using a combination of physical experiments and numerical simulation.

The microsystem (circuit) designer typically views the technology through a very limited interface; usually, a set of process parameters, which describe electrical behavior of underlying structures (for example, resistance of polysilicon), and the design rules, which express the allowable manufacturing limits in geometrical terms (i.e., minimum line width). The high-level goal of this project area is the development of tools and methodologies for more fully integrating the technology design with

both the product design and the manufacture of integrated circuit microsystems.

2.11.2 Technology CAD Framework

Contemporary large-scale software system engineering emphasizes frameworks, wherein common structure and interface specifications enable both current and future software components to be integrated in a flexible and modular way. Frameworks have been particularly successful in the development of electronic circuit CAD systems. Software may be roughly divided into tools, such as a simulator, which perform some part of an application task, and services, such as a database, which provide some necessary support capability used by various tools.

With framework standards, reusable, interchangeable software components from various suppliers may be deployed in systems which comply with the standard. In the broad sense, a framework standard specifies:

1. data representations for the objects of discourse in the application domain and their semantics, and programmatic interfaces to those representations, and
2. architecture; that is, interactions among software components (tools and services), and how tools fit together to perform application tasks for the user.

Standards for CAD frameworks are currently being established by the CAD Framework Initiative (CFI), a broad organization of vendor and user companies which has expanded its scope to include technology CAD. Technology CAD (TCAD) framework components include programming representations for the fundamental objects of process and device CAD: the physical structures on the wafer, the manufacturing process, and the structure and behavior of the resulting devices. A TCAD framework standard should also specify how application software is structured to use these representations and the underlying software services in process and device design and simulation activities.

The problem of wafer representation can be divided into geometry (shapes of regions and their relations) and fields (variations of properties over a region). A wafer representation for two-dimensional simulation has been designed and prototyped and proposed through the CFI Semiconductor Wafer Representation (SWR) Working Group. Current research is focused on three-dimensional representations.

An information model for semiconductor manufacturing processes has been proposed through the CFI working group on semiconductor process representation (SPR). A pilot implementation of SPR is being built at TMA and an early version is in use in the Sematech Technology CAD Workbench.

2.11.3 Advanced Process Simulation and Design Environments

We are looking at higher-level architectural issues, such as the interrelationships between the framework data representations and the connection of compliant tools to achieve end-user design objectives. We are also investigating the larger questions of the relationship between frameworks for different related domains (e.g., circuit CAD and TCAD), and the integration of design frameworks into frameworks for computer integrated manufacturing (CIM).

Commercial one- and two-dimensional process simulators have been integrated into the CAFE system through a simulation manager interface to the process flow representation (PFR). Full two-dimensional physical simulation of the MIT CMOS baseline process and research processes have been performed from CAFE.

Through a description formalism for device structural and behavioral goals, we hope to be able to extend traditional process and device simulation further towards actual design. Such goals may be direct structural goals; e.g., junction depth, sidewall slope, or they may be electrical, mechanical, or thermal goals; e.g., threshold voltage or impact ionization current at a specified bias.

2.12 Modeling of Advanced Device Structures

Project Staff

Professor Dimitri A. Antoniadis, Keith M. Jackson, Jarvis B. Jacobs, Michael B. McIlrath, Nadir E. Rahman

The design of complex, scalable microsystems at the leading edge of technology requires a combination of theoretical understanding, numerical modeling, and experimental physical data. Atomistic, first principles models, while of great intrinsic value and an essential analytical tool, are not sufficient for designing large, high-performance systems. Designers need the means to examine the space of available technologies to match the specific requirements at hand and make appropriate engineering

tradeoffs in order to select from a range of technology variants.

In order to help meet this need, two ideas are being investigated: inverse modeling and knowledge-based simulation.

By inverse modeling, we mean the "reverse engineering" of process effects, not directly observable, via studies of experimental electrical measurements in combination with other directly observed or independently known data; e.g., physical process parameters. Through careful choice of physical experiments, inverse modeling can be used to calibrate forward models and provide technology designers with powerful tools for both understanding and design synthesis. Inverse modeling techniques can be used both to find device structures that meet desired performance criteria and to help map out the design space of a given process technology, whether the underlying physical phenomena are fully or only partially understood.

For example, the electrical performance and characteristics of extreme submicron, shallow junction transistors are critically dependent on the exact two- and three-dimensional shapes and locations of doped regions of the semiconductor. In such technologies, there is a trade-off between, for example, current drive and the device short-channel effects of drain-induced barrier lowering and punchthrough. Understanding the exact nature of the implant doping profiles is essential for design in the submicron regime.

However, fabrication of such shallow junction devices using preamorphization acceptor implants, e.g., indium, has made determination by forward simulation of the doping profile near the drain/source junctions more difficult. In the case of indium, the basic implant statistics and diffusion coefficients used in simulators are not as well-characterized as are the data for, e.g., boron and arsenic. Development and calibration of an adequate forward model by direct methods would require a large number of costly, difficult experiments, making aggressive exploitation of the technology prohibitively expensive.

Inverse modeling provides an alternative methodology to determine doping profiles. We have been exploring new methods for the determination of the two-dimensional doping profiles for a sub-0.1 micron MOSFET with super-steep retrograde channel doping and ultrashallow source/drain extension structure. Utilizing one-dimensional experimental doping profile data in combination with measured device electrical data, we have found that it is possible to generate a two-dimensional doping profile which matches the experimental

observations. To show that the resulting doping profile is unique, additional extracted doping profile data at the center of the channel for devices of differing channel lengths are incorporated into the analysis.

Knowledge-based simulation methods are being investigated in order to achieve full or partial automation of inverse modeling procedures. Knowledge-based simulation techniques combine numerical computing, symbolic computing, and formal reasoning methods. Through such techniques, the use of theoretical models, designer intuition, computational simulation experiments, and physical experiment data can be integrated in a systematic fashion.

Our approach is to develop applications that employ existing and new representations in computer-aided technology design; e.g., wafer, process, and device representations, and incorporate theoretical and experimenter knowledge bases, as a power assist to designers in the solution of specific problems. These applications create and evaluate computational experiments, calling on existing commercial or other simulators wherever possible.

Both heuristic and purely numerical methods can be used in conjunction with knowledge-based inferencing in order to drive simulations and suggest physical experiments needed for more data. Such techniques help designers gain insight into system and technology design problems and extend traditional process and device simulation towards actual design synthesis.

2.13 Semiconductor Process Repository

Project Staff

Professor Duane S. Boning, Michael B. McIlrath, William P. Moyne, Chantal E. Wright

The goal of this research task is to create a system to facilitate distributed process research and design. Such a system will allow users to retrieve and examine process flows from multiple process libraries across the network.

An experimental implementation of a networked semiconductor process repository has been demonstrated jointly with Stanford University, using the MIT CAFE database. Via the web, users can select from multiple process libraries, browse process catalogs within libraries, and examine specific processes in detail. Auxiliary software, now being implemented in the java programming language, enables users to assemble their own processes

graphically using repository processes as building blocks. Java is a cross-platform language; programs can be written that will run inside browsers that support java. We make use of the World Wide Web and the java programming language so that the system will be accessible to any potential user on the network. With java, we can produce a system that will not require any specialized software installation by the user. Java's capability of interaction with the network will allow our system to make available multiple, remote process libraries or databases.

Communication and usage of multiple databases requires a common data representation; our system will implement the current standard, the Semiconductor Process Representation. Conversion from the representations used by local systems (such as MIT's CAFE) will be necessary.

In the CAFE system used at the MIT Microsystems Technology Laboratories, process designers (students and staff) construct their own processes by combining process steps from a baseline with experimental processes or customized operations. For the repository, catalog and library (catalog container) objects were designed and implemented in the CAFE database. While the particular organization into libraries (experimental and baseline) and catalogs (thermal, etch, implant, etc.) in this initial repository implementation reflects current usage at MIT, it is not imposed by the design. Web service is provided via a database client program which creates and caches html pages.

Individual processes are presented according to the information model designed through the CAD Framework Initiative and Sematech working groups on process representation. The CAFE process representation is largely a subset of this information model; however, some interface translation is required. In addition to the standard process views effects, environment, equipment, and process (sequence), an encapsulated view accesses the corresponding CAFE process object directly, using a web common gateway interface program. In particular, this view allows examination of the dynamic usage of the process in the CAFE CIM system including current wafer lots, recent measurements, etc.

An optional, experimental feature under development is a web-integrated graphical process editor, adapted almost entirely from one in local use in CAFE. The editor software is written in java. Individual processes from the repository can be loaded into the editor via the web browser. Conversely, clicking on a process instance in the editor will bring the web page for that process from the repository into the browser.

2.14 Process Capabilities Database

Project Staff

Professor Duane S. Boning, Michael B. McIlrath

As semiconductor manufacturing becomes increasingly expensive, few institutions can maintain complete processing capability at the leading edge of research. We have built an information entry and retrieval system for data about university fabrication facilities collected by the Semiconductor Research Corporation (SRC). The system is accessible through the World Wide Web (WWW). Through a web-based query interface, remote users can find university facilities with particular fabrication capabilities and resources. Owners of remote fabs in the database can update information about their own facility.

2.15 National Infrastructure for Networked Design and Prototyping

The advanced computational prototyping tools and methodologies described above both depend upon and can be used to create an infrastructure for virtual and physical prototyping. The quasi-empirical simulation approach requires data from select experiments to build accurate performance, reliability, and variation or statistical models. Parameters for these models must be determined and refined by multiple series of both simulations and repeated experiments. The validation of simulations produced by the computational prototyping tools can only be achieved by correlation of simulated results with actual experimental measurements. Simulations based on the achieved calibrated models can then facilitate subsystem design and physical prototyping.

Some of these experiments may require specialized equipment which is unique or only available at few sites. For example, a suitable chemical mechanical planarization (CMP) machine may not be available at the primary site used by the simulation model developer; but all of the other processing equipment might be easily accessible. Thus, the timely conduct of repeated calibration experiments may be facilitated by local machine processing for all but one step, with that step being accomplished at a remote site.

Additionally, processing and metrology equipment for such experiments may well not be simultaneously available at a single site. Thus, appropriate metrology equipment may also be a scarce resource. The capture, exchange, and use of

experimental data both to develop models and to calibrate or validate these models can be greatly facilitated by utilization of emerging information technologies.

When multiple locations have the same processing or metrology equipment, the availability of such equipment will vary from site to site; and the timely completion of such experiments can be enhanced by arranging for the conduct of the experiment to be split across multiple sites. Furthermore, such experiments will invariably be complicated, requiring many splits.

Coordination of simulation, processing, and metrology resources will enhance collaborative efforts on subsystem design and subsequent physical prototyping. Models calibrated by experimental data collected at multiple sites can then be used at simulations making use of resources at multiple sites to facilitate the collaborative design of subsystems and the following physical prototyping.

It is also necessary to apply the best available computational prototyping capabilities, from MIT and elsewhere, to evaluate novel technology and microsystem architectures. This demands creation and use of the National Research Enterprise (NRE) to make possible distributed process and model repositories, computational tool executions, and collaborative design of experiments and microsystems. We will partner with Stanford University and other research sites to make the NRE a reality by extending our existing design and fabrication support systems to take advantage of National Information Infrastructure (NII) and high performance communications capabilities. The resulting infrastructure will thus support both computational and physical prototyping and greatly enhance the ability to explore new technologies and microsystems.

Our approach will be based on the use of the semiconductor process representation (SPR) as the vehicle with which to specify the change in wafer state goals, the treatment level parameters, the actual processing instructions, and the measurements to be made. The infrastructure that we propose will be designed to facilitate the accommodation of multiple CIM systems in operation across the country. Through the use of the SPR, simulation results will be unified with actual processing results. Thus, it is easier and more efficient to conduct experiments which can be used to validate the simulation results or, more usually, to calibrate the simulator so that the simulation results can be believable and, therefore, considerably more useful in the investigation of new process technology.

Remote fabrication is a technique that can improve the flexibility and efficiency of current integrated circuit fabrication technologies. Prototyping and experimentation can be much more robust, quicker, and more cost effective by providing the capability to perform different wafer processing and metrology steps at different facilities. Expensive and/or unique machines can be shared rather than duplicated. Wafers can be rerouted to different facilities upon protracted equipment failures. Currently, the process of remote fabrication is discontinuous and unorganized; there is no clean or structured way to exchange data or to provide feedback among multiple facilities.

The proposed development of remote simulation, fabrication, and inspection infrastructure will facilitate processing and experimental data interchange, remote inspection techniques, management of reporting mechanisms for assessing the current state of each experiment in progress, as well as collaborative microsystems design and physical prototyping.

2.16 Metal Reliability and Electromigration

Project Staff

Yonald Chery

As the minimum feature size of microelectronic devices continues to decrease, designing against failure inducing phenomena such as electromigration becomes increasingly important. Electromigration is current induced diffusion in metal interconnect. Electrons transfer momentum to metal atoms, causing an atomic flux in the direction of the electron flow. This effect is proportionally related to current density, which tends to rise as integration densities increase.

Recent research has demonstrated that interconnect reliability is strongly dependent not only on the interconnects current density stresses, but also on the distribution of the metal crystal grain sizes in the metal film from which the interconnect is patterned. Due to such microstructural inhomogeneities (e.g., the distribution of interconnect crystal grain sizes), flux divergences in the presence of current densities can occur. At such sites, the depletion of metal interconnect can form a void or accumulate and yield a short to some neighboring interconnect. Both effects can result in the eventual functional failure of some sub-circuit dependent on the failed metal interconnect.

Such physically-based, microstructural interconnect failure models make it possible to more accurately

predict electromigration induced failure. Prior to development of such models, one of the most popular mechanisms, such as Berkeley Technology Associates' BERT tool, required fabrication of test structures representative of one's design. Data collected from experiments on these structures is in turn used to calibrate a failure model. However, these newer models have the distinct advantage in that they are a function of process parameters (e.g. metal film grain size distribution), which provides design independence and eliminates the need for test structure fabrication.

Our current research goal involves the development of a computer-aided design tool to provide electromigration reliability feedback to the circuit designer. By using layout and circuit stimulus information along with these microstructure based reliability models, it is possible to compute the reliability distribution of the metal interconnect.

Research is well underway into investigating the requirements for an electromigration reliability CAD tool. Work has already begun on implementing our current tool framework. Our plan for a prototype electromigration tool consists of parsing layout files emitted from MAGIC to extract interconnect geometries. The next two phases involve deducing possible current directions. This information on the currents would be then used to tile the metal interconnection trees with a primitive set of microstructural electromigration geometry abstractions. At present, the abstraction set only provides a model for straight metal interconnect segments, but as further electromigration experiments are performed, other model primitives for interconnect shapes such as "L", "T"s, and "+" will be added. Once tiling the interconnect with these abstractions is performed and the current stresses and directions are known, the appropriate electromigration model can be used and a measure of failure computed.

Development of the first parsing phase of this tool is complete, and we expect to progress rapidly through the other prototype's modules. Concurrently with development efforts on this tool, experiments and further modification and development of an existing metal grain growth simulator is underway for understanding how to characterize different reliability of the different tiling geometry primitives. To develop a larger circuit designer, further work is needed to address the tool's computational efficiently.

2.17 RTFM: A Digital Design Lab Expert

Project Staff

Owen Wessling

This thesis describes the design and construction of the resource teaching framebased machine (RTFM), a knowledge based (or expert) system which helps users to debug and design systems. The RTFM system seeks to act in a more educational manner rather than as a direct problem solver, as it is intended for primary use within introductory digital design courses. The project, while seeking to help users with general problems when asked, is primarily based upon problems and questions students are likely to encounter in the 6.111: Introductory Digital Systems Laboratory class at MIT.

2.18 Publications

2.18.1 Journal Articles

Bonvik, A.M., and Y. Dallery, and S.B. Gershwin. "Approximate Analysis of Production Systems Operated by a CONWIP-finite Buffer Hybrid Control Policy." Submitted for publication.

2.18.2 Internal Publications

Bonvik, A.M., S.B. Gershwin, and D.E. Troxel. "Operating High Variability Manufacturing Systems." CIDM Memo 95-4. MIT, 1995.

Bonvik, A.M. "A Distributed Discrete Event Simulation, or How to Steal More CPU Cycles Than You Could Ever Imagine." CIDM Memo 95-6. MIT, 1995.

Carney, J.C. "Message Passing Tools for Software Integration." CIDM Memo 95-7 (May 1995).

Carney, J.C. "Message Passing Tools for Software Integration." CIDM Memo 95-11. MIT, 1995.

Fischer, G., and T. Lohman. "Error Handling within CAFE." CIDM Memo 95-1. MIT, 1995.

Kao, J. "Remote Microscope for Inspection of Integrated Circuits." CIDM Memo 95-5. MIT, 1995.

Kao, J. "Remote Microscope for Inspection of Integrated Circuits." CIDM Memo 95-10. MIT, 1995.

Kao, J., and D.E. Troxel. "MIT Remote Microscope." CAPAM Memo 95-1. MIT, 1995.

Kwon, J.Y. "Remote Fabrication of Integrated Circuits." CIDM Memo 95-3. MIT, 1995.

Kwon, J. "CAFE Remote Fabrication System—A Quick Step Guide to Remote Processing." CIDM Memo 95-8. MIT, 1995.

Kwon, J. "Remote Fabrication of Integrated Circuits—Software Support for the M.I.T. Computer Aided Fabrication Environment." CIDM Memo 95-9. MIT, 1995.

Moyne, W.P. "Run-by-Run Control: Interfaces, Implementation, and Integration." CIDM Memo 95-2. MIT, 1995.

Rahman, N. "A Survey of Existing Literature on Reverse Modeling of Field Effect Transistors." CAPAM Memo 95-3. MIT, 1995.

2.18.3 Meetings Papers

McIlrath, M. and D. Boning. "Process Repository." 1995 TCAD Symposium. *Hierarchical Technology CAD—Process, Device, and Circuits*. Stanford University, Palo Alto, California, August 10, 1995.

Tso, K., M. McIlrath, and D. Boning. "Fab Facilities Database." 1995 TCAD Symposium. *Hierarchical Technology CAD—Process, Device, and Circuits*. Stanford University, Palo Alto, California, August 10, 1995.

2.18.4 Theses

Carney, J.C. *Message Passing Tools for Software Integration*. S.M. thesis. Dept. of Electr. Eng. and Comput. Sci., MIT, 1995.

Jacobs, J. *Modeling of Electron Transport in Sub-100 nm Channel Length Silicon Mosfets*. Ph.D. thesis. Dept. of Electr. Eng. and Comput. Sci., May 24, 1995.

Kao, J. *Remote Microscope for Inspection of Integrated Circuits*. S.M. thesis. Dept. of Electr. Eng. and Comput. Sci., MIT, 1995.

Kwon, J.K. *Remote Fabrication of Integrated Circuits - Software Support for the M.I.T. Computer-Aided Fabrication Environment*. S.M. thesis. Dept. of Electr. Eng. and Comput. Sci., MIT, 1995.

Moyne, W.P. *Run-by-Run Control: Interfaces, Implementation, and Integration*. S.M. thesis. Dept. of Electr. Eng. and Comput. Sci., MIT, 1995.

Rahman, N. "Mosfet Drain/Source Doping Profile Extraction Using Inverse Modeling." Thesis proposal, Dept. of Electr. Eng. and Comput. Sci., Dec. 22, 1995.

Wessling, O.P. *RTFM: A Digital Design Lab Expert*. M. Eng. thesis. Dept. of Electr. Eng. and Comput. Sci., MIT, December 1995.

Section 2 Digital Signal Processing

Chapter 1 Digital Signal Processing Research Program

Chapter 2 Advanced Telecommunications and Signal Processing Program

Chapter 3 Combined Source and Channel Coding for High-Definition Television

Chapter 1. Digital Signal Processing Research Program

Academic and Research Staff

Professor Alan V. Oppenheim, Professor Arthur B. Baggeroer, Professor Gregory W. Wornell, Giovanni Aliberti

Visiting Scientists and Research Affiliates

Dr. Bernard Gold, Dr. Bruce R. Musicus,¹ Dr. S. Hamid Nawab,² Dr. James C. Preisig, Dr. Ehud Weinstein³

Graduate Students

Chalee Asavathiratham, Richard J. Barron, Soosan Beheshti, Stanley W. Brown, John R. Buck, Brian Chen, Alan E. Freedman, Andrew K. Halberstadt, Christoforos N. Hadjicostis, Steven H. Isabelle, Warren M. Lam, Junehee Lee, Jeffrey T. Ludwig, James M. Ooi, Haralabos C. Papadopoulos, Matthew J. Secor, Alan Seefeldt, Andrew C. Singer, Shawn M. Verbout, Kathleen E. Wage, Alex Che-Wei Wang

Technical and Support Staff

Margaret S. Beucler, Janice M. Zanganjori

1.1 Introduction

The field of digital signal processing grew out of the flexibility afforded by the use of digital computers in implementing signal processing algorithms and systems. It has since broadened into the use of a variety of both digital and analog technologies, spanning a broad range of applications, bandwidths, and realizations. The Digital Signal Processing Group carries out research on algorithms for signal processing and their applications. Current application areas of interest include signal enhancement, active noise cancellation, processing of speech, music and underwater acoustic signals, advanced beamforming for radar and sonar systems, and signal coding and transmission.

In some of our recent work, we have developed new methods for signal enhancement and noise cancellation with single or multisensor measurements. We have also been developing new methods for representing and analyzing fractal signals. This class of signals arises in a wide variety of physical environments and also has potential in problems involving signal design. We are also exploring potential uses of nonlinear dynamics and chaos theory of signal design and analysis. Another research emphasis is on structuring

algorithms for approximate processing and successive refinement.

In other research, we are investigating applications of signal and array processing to ocean and structural acoustics and geophysics. These problems require the combination of digital signal processing tools with a knowledge of wave propagation to develop systems for short time spectral analysis, wavenumber spectrum estimation, source localization, and matched field processing. We emphasize the use of real-world data from laboratory and field experiments such as the Heard Island Experiment for Acoustic Monitoring of Global Warming and several Arctic acoustic experiments conducted on the polar ice cap.

A major application focus of the group is in the area of communication systems and networks. One current area of activity involves developing new signal processing techniques for multi-user wireless communication systems. The intended applications range from mobile radio networks to indoor personal wireless systems to digital audio and television broadcast systems. Of special interest are broadband spread spectrum systems and code-division multiple access networks both for conventional and secure transmission.

¹ Bolt, Beranek, and Newman, Inc., Cambridge, Massachusetts.

² Associate Professor, Boston University, College of Engineering, Boston, Massachusetts.

³ Department of Electrical Engineering, Systems Division, Faculty of Engineering, Tel-Aviv University, Israel; adjunct scientist, Department of Applied Ocean Physics and Engineering, Woods Hole Oceanographic Institution, Woods Hole, Massachusetts.

Much of our work involves close collaboration with the Woods Hole Oceanographic Institution, MIT Lincoln Laboratory, and a number of high technology companies in the Boston Area.

1.2 Digital Audio Filter Design Using Frequency Transformations

Sponsor

U.S. Navy - Office of Naval Research
Grant N00014-93-1-0686

Project Staff

Chalee Asavathiratham, Dr. Paul Beckmann,⁴ Professor Alan V. Oppenheim

Audio filter design problems generally have a structure which is slightly different from that of conventional digital filter design problems. In audio filter specifications, frequency response is often specified on a logarithmic frequency scale. This is due to the fact that human auditory perception is more sensitive to low frequency resolution than to high frequency resolution. Similarly, the magnitude specification is usually specified in dB, which again stems from the way humans perceive differences in loudness. There is also a "just-noticeable" level of error. That is, at each frequency there is an allowable level of error within which the user cannot distinguish the output of the ideal from the approximated filter. One digital audio filter is equivalent to another if a listener cannot distinguish between the two different true frequency responses. In this thesis, by exploiting the special properties in audio filters and investigating the technique of frequency transformation, we seek to design a method which will yield filters with much shorter length than that resulting from conventional (for example, Parks-McClellan) design method. Specifically, we will study the all-pass frequency transformation, and its use to "warp" the frequency axis from a logarithmic scale to an approximately linear one. In taking the full benefit of "just-noticeable error," we will use McCallig's FIR filter design method, as opposed to the conventional one of Parks-McClellan. The benefit of the former is that it always guarantees that the output FIR filter is a filter of minimum length that meets the upper and lower "just-noticeable" error bound.

1.3 Channel Equalization for Self-Synchronizing Chaotic Systems

Sponsors

Lockheed Sanders, Inc.
Contract P.O. BY5561
U.S. Navy - Office of Naval Research
Grant N00014-93-1-0686
U.S. Air Force - Office of Scientific Research
Grant AFOSR 91-0034

Project Staff

Richard J. Barron, Professor Alan V. Oppenheim

There is great potential for self-synchronizing chaotic systems in communications. Typical transmission channels introduce distortion that significantly degrades synchronization of transmitter and receiver. The types of distortions include time-varying attenuation due to fading, scattering, etc., and modification of the spectral characteristics due to channel filtering and multipath effects. It is our goal to correct these channel effects to restore synchronization. We propose the use of the properties of the transmitted chaotic signals and the synchronization property of the receiver to estimate and compensate for the channel distortions.

1.4 Techniques for Enhancing the Performance of Communication Systems Employing Spread-Response Precoding

Sponsors

National Science Foundation
Grant MIP 95-02885
U.S. Navy - Office of Naval Research
Grant N00014-95-1-0834
Grant N00014-93-1-0686

Project Staff

Soosan Beheshti, Professor Gregory W. Wornell

In wireless communication systems, various coding schemes are used to improve transmission reliability over a fading channel. A spread-response precoder, even in the absence of a coder, not only is effective in correcting errors, but also effectively transforms a Rayleigh fading channel into a simpler quasi-Gaussian one.

⁴ Bose Corporation, Framingham, Massachusetts.

This research explores combining trellis coded modulation (TCM) with a spread-response precoding for transmission over a Rayleigh channel. We will assess the improvement yielded by the precoder in terms of system complexity, delay characteristics, and probability of error performance. We will also explore a multistage postcoder for use with spread-response precoding and assess the corresponding improved performance.

1.5 Active Noise Cancellation in Automobiles

Sponsors

U.S. Air Force - Office of Scientific Research
Grant AFOSR 91-0034
U.S. Navy - Office of Naval Research
Grant N00014-93-1-0686
Grant N00014-95-1-0834

Project Staff

Stanley W. Brown, Professor Alan V. Oppenheim

A fundamental goal of this research is to determine the feasibility of real-time active noise cancellation within the interior of an automobile. Active noise cancellation in a volume entails measuring the sound field at a finite number of microphone locations and using predictable characteristics of the acoustic noise to generate and transmit canceling signals from one or more speakers. The goal is to attenuate the noise at the sensors through destructive interference.

Using computer simulations on recorded road noise, we will assess the effectiveness of known algorithms, such as the estimate-maximize (EM), least-mean square (LMS), and optimal control approaches, in attenuating acoustic noise at a point within the car. An autoregressive-moving average (ARMA) model of the measured transfer function from car speaker to noise sensor represents the effect of car acoustics on the canceling signal.

1.6 Single Mode Excitation in the Shallow Water Acoustic Channel

Sponsor

MIT-WHOI Joint Graduate Program
in Oceanographic Engineering

Project Staff

John R. Buck, Professor Alan V. Oppenheim, Dr. James C. Preisig

For shallow water acoustics, the ocean acts as a waveguide, with sound propagation in the far field occurring almost entirely through a discrete set of normal modes. The goal of this research is to use a vertical source array to excite the underwater channel so that only one of these discrete modes is propagating at a specified reference location. While open loop solutions are analytically tractable, they require extensive and accurate environmental data. Our approach is to use feedback control to estimate the channel such that the pressure at a vertical hydrophone array at the reference location consists of only a single mode. Knowing that the propagating field consisted originally of only a single mode at this reference location, observers further downrange can treat the feedback array as a virtual single mode source. This will allow experiments to determine the nature of propagation and scattering of modes through features of the water column such as internal wave fields.

The feedback control algorithm explicitly estimates the transfer function between each source array element and each hydrophone in the feedback array for the frequency of excitation. These estimated transfer functions are used to compute the source array weighting that should give the desired pressure profile of a single mode at the feedback array. By moving the control location from the source array to the feedback array, we have reduced the degrees of freedom we are trying to control from a large continuum to a small discrete set of modes. Recently, we formulated the transfer function estimator as a Kalman filtering state estimation problem. This formulation provides a means of incorporating information about the temporal and spatial statistics of the channel variations into the estimator.

The algorithm has been tested in detailed simulations of realistic ocean environments. The simulated ocean environments were based on measurements of conditions on the South Continental Shelf region around Martha's Vineyard. These simulations indicated the feedback control approach performs much better than previous attempts using open loop control in environments

with range-varying bathymetry when no a priori knowledge of the environment is available. In addition to these simulated results, a series of scale-model experiments in a wave tank have demonstrated the algorithm performs robustly under the limitations imposed by real propagation with physical sources and receivers. The control algorithm was able both to obtain the desired pressure field and react to transients in the environment. These results make us optimistic that the algorithm should work for full-scale ocean experiments.

1.7 Efficient Communication Using Chaotic Systems

Sponsors

U.S. Air Force - Office of Scientific Research
Grant AFOSR 91-0034
U.S. Navy - Office of Naval Research
Grant N00014-95-1-0834

Project Staff

Brian Chen, Professor Gregory W. Wornell

This research explores the application of chaotic signals and systems for communication, with specific focus on discrete-time chaotic systems. Our main goals are to develop algorithms for estimating the state of chaotic systems under various forms of corruption and to investigate the potential role of these systems in communication applications such as modulation, coding, and deconvolution.

We have developed state estimation algorithms for chaotic sequences corresponding to so-called tent map dynamics in the presence of additive Gaussian noise, intersymbol interference, and multiple access interference and have evaluated their performance both analytically and empirically. In the additive white Gaussian noise case, the estimator is optimal under the maximum likelihood criterion, has a convenient recursive implementation, is asymptotically unbiased at high SNR, and has an error variance which decays exponentially with sequence length to a lower threshold which depends on the SNR. In the intersymbol interference case, we have developed three iterative algorithms and evaluated their performance empirically, considering the effects of sequence length, noise, and initialization. Finally, in the multiple access interference case, we have derived an optimal maximum likelihood estimator and the associated Cramer-Rao bound on the error variance. The estimator is asymptotically unbiased

at high SNR and has an error variance which depends on the particular tent map sequences.

We are currently investigating a modulation and coding system for transmission of analog sources in which the source data is encoded in the initial value of a tent map sequence. We are analyzing the performance of this so-called tent map coding system and are comparing it to the performance of other codes such as linear modulation codes and M-ary digital codes.

1.8 Signal Transmission and Recovery in Self-Synchronous Chaotic Systems

Sponsors

Lockheed Sanders, Inc.
Contract number P.O. BY5561
U.S. Navy - Office of Naval Research
Grant N00014-93-1-0686

Project Staff

Alan E. Freedman, Professor Alan V. Oppenheim

The goal of this project is to examine the extent to which it is possible to recover a transmitted signal, produced by a chaotic system and corrupted by an unknown filter present in the transmission channel. For self-synchronous chaotic systems, the uncorrupted transmission can drive an identical receiving system, and that drive signal can be exactly reproduced at the receiver. For small perturbations to the drive signal, the receiver will approximately synchronize to the transmitter. Measuring the energy in the error allows compensation for these perturbations, thus restoring the signal originally transmitted.

An algorithm will be developed in Matlab which will locate a compensating filter, ideally the inverse of the corrupting filter. Introducing this compensator at the receiver will cancel the corruption and restore the synchronization between the transmitter and receiver.

A successful algorithm for compensating for channel corruption would allow small perturbations such as speech signals to be masked beneath the chaotic signal with excellent opportunity for recovery at a receiving station; a receiver would need only achieve approximate synchronicity between the signal arriving and the reproduced output, and then subtract the two to recover the message being transmitted beneath the chaotic masking signal.

1.9 Algorithmic Structures for Signal Processing in Relation to the Rapid Prototyping of Application Specific Signal Processors

Sponsor

U.S. Navy - Office of Naval Research
Grant N00014-93-1-0686

Project Staff

Andrew K. Halberstadt, Professor Alan V. Oppenheim

Design and prototyping of signal processors must inherently take into account the structure of signal processing algorithms. Traditionally the signal processing community has relied heavily on a foundation of linear system theory and the associated tools of transform analysis. While this approach has formed the basis for many useful algorithms in a wide variety of applications over the last several decades, it has become increasingly clear that there are large classes of signal processing applications for which this basis is fundamentally inadequate. Many emerging classes of algorithms stem from new models and approaches, and current design tools and implementation structures are not necessarily well matched to these algorithms. The ARPA/Tri-Service Rapid Prototyping of Application Specific Signal Processors (RASSP) program is focused on dramatically improving the *process* by which digital signal processors are designed. Therefore, it is important that the RASSP tools and process be exercised and challenged by the demands of these new algorithms.

This research has two major goals. One is to identify and develop appropriate classes of emerging as well as more classical signal processing algorithms that are important but that the current RASSP tools and process cannot accommodate well. Classes of such algorithms may include, for example, interactive algorithms, algorithms oriented around partial differential equations, and certain types of multidimensional and multirate algorithms. These algorithms could have an impact on applications such as radar, sonar, geophysical processing, computed tomography, and biomedical ultrasound. A second

goal of this research is to provide specific input for a next generation of RASSP tools and process. One phase of this follows from having identified weaknesses in the currently available tools. Future work will consider how the tools need to be expanded and modified in order to make these new algorithms readily accessible to the designer of future signal processing systems.

1.10 Algebraic and Probabilistic Structure in Fault-Tolerant Computation

Sponsor

U.S. Navy - Office of Naval Research
Grant N00014-93-1-0686

Project Staff

Christoforos N. Hadjicostis, Professor George C. Verghese

The traditional approach towards fault-tolerant computation has been modular redundancy. Although universal and simple, modular redundancy is inherently expensive and inefficient in its use of resources. Recently developed algorithm based fault tolerance (ABFT) techniques offer more efficient fault coverage, but their design is specific to each application. A particular class of ABFT techniques involves the design of arithmetic codes that protect elementary computations. For the case of computations that can be represented as operations in a group, the recent doctoral thesis by Beckmann⁵ has shown how to obtain a variety of useful results and systematic constructive procedures.

In our research so far, we have been able to generalize this work to the case of computations occurring in semigroups and semirings⁶ and to outline a procedure that reflects such algebraically-based ABFT design into hardware. Currently, we are exploring extensions of our approach to sequences of "computations" associated with the evolution of dynamic systems in particular algebraic settings, such as linear systems over groups or rings, or finite automata and discrete-event systems. We also intend in future work to fold probabilistic models for failures and errors into the design and analysis of ABFT systems.

⁵ P.E. Beckmann, *Fault-Tolerant Computation Using Algebraic Homomorphisms*, RLE TR-580 (Cambridge: MIT Research Laboratory of Electronics, 1993).

⁶ C.N. Hadjicostis, *Fault-Tolerant Computation in Semigroups and Semirings*, RLE TR-594 (Cambridge: MIT Research Laboratory of Electronics, 1995).

1.11 Signal Processing Applications of Chaotic Dynamical Systems

Sponsors

AT&T Laboratories
Doctoral Support Program
Defense Advanced Research Projects Agency/
U.S. Navy - Office of Naval Research
Grant N00014-89-J-1489
Lockheed Sanders/U.S. Navy -
Office of Naval Research
Grant N00014-91-C-0125
U.S. Air Force - Office of Scientific Research
Grant AFOSR-91-0034
U.S. Navy - Office of Naval Research
Grant N00014-89-J-1489
Grant N00014-93-1-0686

Project Staff

Steven H. Isabelle, Professor A.V. Oppenheim

Researchers in areas ranging from animal behavior and medicine to economics and geophysics have found evidence of chaotic behavior in an enormous number of empirically gathered time series. Indeed, the sheer volume of apparently random phenomena which appear to have a deterministic explanation underscores the need for signal processing techniques specifically tailored to the unique characteristics of chaotic signals. In particular, because chaotic signals can generally be observed only indirectly, e.g., through some propagation channel or nonideal laboratory instrumentation, a signal's chaotic structure may be partially obscured by additive noise and convolutional distortion. Consequently, algorithms for reducing these distortions are an important component of signal processing systems for chaotic signals. This research explores effects of convolutional distortion on chaotic signals along with techniques for reducing such distortions.

In general, the limiting trajectory of a chaotic system will be a highly structured set in the state space, while the scalar output will appear erratic and unstructured. It is this "hidden" structure that makes the signal interesting and allows for a simple description. One measure of structure which has been used to characterize a chaotic signal is the fractal dimension of its strange attractor. We are examining the effect of convolution on fractal dimension and using these results to develop

deconvolution algorithms. The major challenge here is developing optimal computationally efficient techniques which are uniformly applicable to a broad class of chaotic signals.

1.12 Multiscale Signal Processing with Fractal Renewal Processes

Sponsors

National Science Foundation
Grant MIP 95-02885
U.S. Air Force - Office of Scientific Research
Grant AFOSR 91-0034
U.S. Navy - Office of Naval Research
Grant N00014-93-1-0686
Grant N00014-95-1-0834

Project Staff

Warren M. Lam, Professor Gregory W. Wornell

Point processes with fractal characteristics have a potentially important role to play in the modeling of numerous natural and man-made phenomena, ranging from the distribution of stars and planets in the universe to the arrival pattern of transmission errors in communication channels. However, in contrast to fractal waveforms, which have been explored in considerable depth,⁷ the development of efficient algorithms for synthesizing, analyzing, and processing fractal point processes has generally proven difficult, largely due to the lack of an adequate mathematical framework. In this work, we introduce a novel multiscale representation for fractal point processes and apply it to a number of practical signal processing problems involving such point processes.

Our study of fractal point processes is focused primarily on an important subclass called fractal renewal processes which possess a sense of stationarity as well as self-similarity. Recently, we have developed a multiscale representation whereby a fractal renewal process is viewed as the random mixture of a multiscale family of constituent Poisson processes.⁸ This decomposition facilitates the study of fractal renewal processes, as it allows exploitation of existing efficient algorithms for Poisson processes. Indeed, based on the multiscale framework, we have developed an efficient algorithm for synthesizing fractal renewal pro-

⁷ G.W. Wornell, "Wavelet-based Representations for the 1/f Family of Fractal Processes," *Proc. IEEE* 81: 1428-1450 (1993).

⁸ W.M. Lam and G.W. Wornell, "Multiscale Synthesis and Analysis of Fractal Renewal Processes," *Proceedings of the Sixth IEEE Digital Signal Processing Workshop*, October 1994, pp. 67-70.

cesses. In addition, we have successfully applied this framework to several practical detection and estimation problems including estimation of the fractal dimension of a point process and the recovery of a fractal renewal process from corrupted measurements. Application of this framework to other practical problems is currently being investigated.

1.13 Low-Complexity Receivers for Code Division Multiple Access Systems

Sponsors

Defense Advanced Research Projects Agency/
U.S. Navy
Contract DAAH04-95-1-0473
U.S. Air Force - Office of Scientific Research
Grant AFOSR 91-0034
U.S. Navy - Office of Naval Research
Grant N00014-93-1-0686

Project Staff

Junehee Lee, Professor Gregory W. Wornell

Code Division Multiple Access (CDMA) systems, in which different users are assigned distinct signature waveforms for modulating their messages, have many attractive characteristics for wireless communication applications. For example, CDMA systems are well-suited to scenarios where there is significant multipath fading or jamming, or where the users transmissions are intermittent in nature.

Because the transmissions of users in CDMA systems are typically only quasi-orthogonal, traditional CDMA receivers based on single-user detection strategies suffer from a near-far problem, whereby inter-user interference can severely limit performance. CDMA receivers based on multi-user detection strategies—in which all users are decoded jointly at a receiver—overcomes this problem, but typically at great cost in terms of computational complexity, particularly when large numbers of users are involved.

This research is aimed at developing and analyzing alternative receiver structures for CDMA systems that require substantially less computational complexity than traditional implementations of multi-user detection, but with minimal performance degradation. Several such algorithms are currently under investigation, including a variety based on iterative EM-type maximum likelihood estimation.

1.14 Approximate Signal Processing

Sponsor

U.S. Navy - Office of Naval Research
Grant N00014-93-1-0686

Project Staff

Jeffrey T. Ludwig, Dr. S. Hamid Nawab

In any given problem-solving domain, an algorithm, A, may be considered an approximation to another algorithm, B, provided A is more computationally efficient than B *by virtue* of A being designed to yield a lower quality answer than B. Such algorithms are said to carry out *approximate processing* with respect to the problem-solving domain under consideration. The need for such algorithms arises in applications with real-time constraints.

We have successfully applied approximate processing concepts to the area of low-power signal processing. Techniques for reducing power consumption have become important due to the growing demand for portable multimedia devices. We have developed an approach to the design of low-power frequency-selective digital filters based on the concepts of adaptive filtering and approximate processing. The technique uses a feedback mechanism in conjunction with well-known implementation structures for FIR and IIR digital filters. Our algorithm is designed to reduce the total switched capacitance by dynamically varying the filter order based on signal statistics. A factor of 10 reduction in power consumption over fixed-order filters has been demonstrated for the filtering of speech signals.

In previous research it has been demonstrated that approximate processing algorithms can be effective in the real-time analysis of music, speech, and synthetic signals. For example, approximations to the short-time Fourier transform (STFT) have been shown to retain prominent time-frequency characteristics of such signals while improving computational efficiency by an order of magnitude over FFT-based calculations of the exact STFT.

Our aim is to extend the development of formal structures for using approximate processing concepts in designing novel signal processing algorithms to areas such as time-frequency analysis, cepstral analysis, multipass analysis, adaptive beamforming, and image coding.

1.15 Tools for Decentralized Decision and Control with Application to Multiple Access Communications

Sponsors

Defense Advanced Research Projects Agency/
U.S. Navy
Contract DAAH04-95-1-0473
U.S. Air Force - Office of Scientific Research
Grant AFOSR 91-0034
U.S. Navy - Office of Naval Research
Grant N00014-93-1-0686
Grant N00014-95-1-0834

Project Staff

James M. Ooi, Professor Gregory Wornell

Decentralized decision-making is the problem of how more than one agent should make decisions when each agent has access to different information about the state of the system. Engineers have struggled with this problem with little progress for at least 25 years. In 1985, Tsitsiklis and Athans showed that the problem of finding optimal control laws for these problems is inherently difficult, explaining in part why so little progress had been made. Our goal is to develop and analyze easily computable bounds and computationally efficient protocols for this difficult problem. These tools can be applied to any problem that is recognized as one of decentralized decision-making, of which there are many. We will also explore the relationship between information structures and optimal performance. Finally, we plan to demonstrate the utility of our bounds and protocols on well-known difficult problems such as optimally controlling a multiple access communications channel.

1.16 Analysis and Applications of Systems Exhibiting Stochastic Resonance

Sponsors

U.S. Air Force - Office of Scientific Research
Grant AFOSR 91-0034
U.S. Navy - Office of Naval Research
Grant N00014-93-1-0686

Project Staff

Haralabos C. Papadopoulos, Professor Gregory W. Wornell

Stochastic resonance is a phenomenon encountered in certain bistable nonlinear systems (i.e., *systems with two stable points*) when driven by a periodic signal in noise. Specifically, these systems often display an enhancement of output signal-to-noise ratio (SNR) in a given input SNR regime. For this reason, such systems are appealing candidates for use in a variety of engineering contexts. In terms of signal analysis, such systems constitute potentially useful models for natural phenomena such as the regularity of appearance of earth's ice ages⁹ as well as for Detection Mechanisms in Certain Species, such as predator sensing by crayfish.¹⁰ In terms of signal synthesis, the induced SNR enhancement renders them attractive in a number of applications in signal communication and processing, such as robust communication and interference suppression. In order to exploit the phenomenon of stochastic resonance in such applications, there is a need for tools to analyze these systems in the presence of various forms and degrees of distortion.

One of the main directions of the proposed thesis is towards the development of novel techniques for analysis of dynamical systems exhibiting stochastic resonance, and considering their viability in various signal processing and communication contexts. In addition, the thesis explores the phenomenon of stochastic resonance in the context of general signal processing problems which includes signal detection, classification, and enhancement.

1.17 Distributed Digital Signal Processing Architectures for Approximate Processors

Sponsor

U.S. Navy - Office of Naval Research
Grant N00014-93-1-0686

Project Staff

Matthew J. Secor, Professor George C. Verghese, Dr. S. Hamid Nawab

⁹ R. Benzi, A. Sutera, and A. Vulpiani, "The Mechanism of Stochastic Resonance," *J. Phys. A*14: L453-L457 (1981).

¹⁰ J.K. Douglass, L. Wilkens, E. Pantazelou, and F. Moss, "Noise Enhancement of Information Transfer in Crayfish Mechanoreceptors by Stochastic Resonance," *Nature* 365: 337-340 (1993).

This research investigates the area of distributed digital signal processing (DDSP), studying the interactions among, and collective performance of, multiple approximate digital signal processors or processes. The approach we take is to study networks of digital signal processing (DSP) modules whose parameters and functionality can be varied to adapt to changes in specifications and constraints. The specifications that we focus on are ones that provide metrics or tolerances for various features of input and output quality (such as time- and frequency-resolution, quantization, probability of error), thus allowing the individual DSP modules to carry out what has come to be known as approximate processing. The flexibility allowed by approximate processing can be critical to accommodating constraints in a DDSP system. The constraints of interest involve such resources as cost, time, power, memory, and inter-processor communication. Our research includes modeling, the development of resource allocation and scheduling schemes, and simulation/testing (using University of California at Berkeley's Ptolemy system as a platform).

1.18 Sinusoidal Analysis-Synthesis

Sponsor

U.S. Navy - Office of Naval Research
Grant N00014-93-1-0686

Project Staff

Alan Seefeldt, Professor Alan V. Oppenheim

The use of a Sinusoidal Analysis-Synthesis (SAS) technique in the enhancement of speech corrupted by additive white noise is being examined. The SAS technique involves analyzing speech with the short time Fourier transform. Peaks in the magnitude spectrum of each frame are selected and matched from frame-to-frame in order to form sinusoidal tracks. The speech is then synthesized by interpolation through these tracks.

Currently, clean speech is being used as an aid in selecting sinusoidal tracks from noise-corrupted speech. Methods for smoothing these optimally-selected noisy tracks are being investigated. If satisfactory noise reduction can be achieved through this smoothing, methods for selecting tracks from

the noisy speech without any a priori information will be examined.

1.19 Signal Processing and Communication with Solitons

Sponsors

Defense Advanced Research Projects Agency/
U.S. Navy - Office of Naval Research
Grant N00014-89-J-1489
Lockheed Sanders/
U.S. Navy - Office of Naval Research
Contract N00014-91-C-0125
U.S. Air Force - Office of Scientific Research,
Grant AFOSR 91-0034
U.S. Navy - Office of Naval Research
Grant N00014-93-1-0686

Project Staff

Andrew C. Singer, Professor Alan V. Oppenheim

Traditional signal processing algorithms rely heavily on models that are inherently linear. This is predominantly due to the tractability of their analyses and the applicability of such techniques to the rich class of signals that can be represented with Fourier methods. Nonlinear systems that support soliton solutions enjoy many of the properties of linear systems, making them attractive from an engineering standpoint. Although nonlinear, these systems are solvable through a technique known as inverse scattering, which can be viewed as an analog of the Fourier transform. Soliton systems also possess a class of eigenfunctions, known as solitons, which satisfy a nonlinear form of superposition. As these systems evolve in time, their soliton solutions display interesting signal dynamics as multiple solitons interact. In this thesis, we explore some of the signal processing implications of the dynamics of soliton signals. We present new analog circuits that support soliton signals and can be used as natural modulators and demodulators for a variety of soliton communication applications. These circuit models play an important role in investigating the effects of noise on soliton behavior. Finally, the signal dynamics also provide a mechanism for simultaneously decreasing signal energy while potentially boosting detection and estimation performance.

1.20 Environmental Robustness in Automatic Speech Recognition

Sponsor

U.S. Navy - Office of Naval Research
Grant N00014-93-1-0686

Project Staff

Shawn M. Verbout, Professor Alan V. Oppenheim

As the technology in automatic speech recognition (ASR) becomes increasingly advanced, greater consideration is given to speech as a viable means of interaction between humans and machines. However, as more ASR systems become incorporated into real-world applications, greater attention must be devoted to making these systems robust with respect to changes in their operating environments. Although it is true that many modern speech recognizers can perform well in certain adverse environments when trained extensively under actual environmental conditions, even the most sophisticated ASR systems today are extremely sensitive to variations in these conditions, and must be carefully retrained for each new setting in which they are deployed.

In a given setting, a number of environmental factors can interfere with obtaining quality measurements of spoken language. In an office environment, for example, a spoken command intended for the recognizer can be corrupted by many different types of additive noise. Examples of noise sources in the workplace include background conversations, keyboard clicking, mechanical air circulation, and in general any movement of people, chairs, desk drawers, books, and paper. A noise source may produce sudden and transient interference, as in the case of a slamming door or a ringing telephone, or it may produce steady and persistent interference, as in the case of a humming computer fan or a buzzing overhead light.

The long-term objective of research in this area is to determine the signal processing technology required to maintain consistently good ASR performance in spite of possible changes in the recording environment. To improve the performance of an existing recognizer in the presence of additive noise, we have adopted a two-stage processing system in which: (1) the noisy input waveform is filtered to enhance the underlying speech, and (2) the enhanced waveform is analyzed by the recognizer in an attempt to decode the utterance.

In particular, our research has been directed at developing the first stage of this system for the case in which the physical parameters of the speaker are known in advance, but the parameters of the noise are unknown.

Both speech and noise are modeled as autoregressive processes over short time intervals; however, to account for the fact that the autoregressive parameters of these processes may change over time, each process is modeled globally using a Hidden Markov Model (HMM). The unknown HMM noise parameters are then computed iteratively such that the likelihood function over the entire utterance is eventually maximized. This iterative estimation is accomplished using the EM (Expectation-Maximization) algorithm, which is now a widely used mathematical tool for computing maximum likelihood estimates. As a by-product of this parameter estimation procedure, an optimum estimate of the underlying speech signal itself is generated, and hence may be subsequently used as input to the speech recognizer.

Important intermediate goals in this research will include quantifying the performance of an existing ASR system when the sensor measurements are preprocessed using the approach described above, and comparing this performance to that obtained using more standard adaptive filtering techniques.

1.21 Oceanographic Signal Processing

Sponsors

U.S. Navy - Office of Naval Research
Grant N00014-91-J-1628
University of California/Scripps Institute of Oceanography
Contract 1003-73-59

Project Staff

Professor Arthur B. Baggeroer

Our research programs involve application of signal and array processing to problems in ocean acoustics and geophysics. These applications require an understanding of both signal processing and wave propagation; moreover, most use data from laboratory or field experiments, so an appreciation of real world issues such as noise, sensor calibrations and modeling errors is needed. Several of the topics provide opportunities to participate in oceanographic cruises.

1.22 Acoustic Thermometry of Ocean Climate

The Heard Island Feasibility Test demonstrated that coded acoustic signal can be transmitted over 10,000 km ranges. This has led to the Acoustic Thermometry of Ocean Climate (ATOC) program by DARPA. A network of acoustic sources and receivers is being deployed in the Pacific this spring to monitor the ocean by measuring changes in acoustic travel times. These changes will be used to infer temperature changes.

1.22.1 Estimation of Normal Mode Amplitudes for Underwater Acoustics

Sponsor

University of California/Scripps Institute of Oceanography
Contract 1003-73-59

Project Staff

Kathleen E. Wage, Professor Arthur B. Baggeroer

The goal of this research is to develop array processing techniques for detection and estimation of broadband signals propagating in the low-order acoustic modes of the deep ocean. Normal modes are the eigenfunctions of the ocean waveguide and are useful to acousticians and oceanographers because the modal expansion coefficients contain valuable information about acoustic sources and the propagation medium. The objective of ocean acoustic tomography is to exploit the environmental dependence of signals, such as modes, in order to infer sound speed and temperature structure over large ranges. One goal of the ongoing Acoustic Thermometry of Ocean Climate (ATOC) project is to use modal phase and group velocity measurements in tomographic inversions. The purpose of our research is to develop methods of processing signals for experiments such as ATOC.

This work addresses two related signal processing problems. The first is the estimation of a time series of modal excitation coefficients based on measurements from a vertical hydrophone array. Since the modes form an orthonormal basis, similar to planewaves, computation of the mode coefficients is often referred to as modal beamforming.

We focus on robust adaptive methods of modal beamforming for broadband sources. An intriguing aspect of the waveform estimation problem is that it can be approached from the perspective of adaptive beamforming or of linear inverse theory. Both viewpoints provide valuable insights and indicate that this research is relevant to a broader class of signal processing problems.

The second aspect of this research concerns the detection of pulse arrivals in the mode waveforms and the estimation of mode travel times based on these arrivals. Although numerous researchers have proposed using modal group delay perturbations for tomographic inversions, very few have examined the signal processing required to determine the arrival times. In particular, tomographers have generally taken a naive approach to receiver design and have ignored possible effects of random phenomena such as internal waves. An objective of this work is to design optimal receivers for the modes which account for random fading and coupling as well as the intrinsic dispersion in the waveguide. Similar issues arise in the context of communication over fading dispersive channels. We hope to extend the concept of a diversity receiver for a single channel to the multidimensional mode estimation problem.

1.22.2 Detection and Estimation in Fractional Brownian Motion

Sponsor

U.S. Navy - Office of Naval Research
Grant N00014-93-1-0686

Project Staff

Alex Che-Wei Wang, Professor Gregory W. Wornell, Professor Arthur B. Baggeroer

The $1/f$ family of fractal processes models a wide range of statistically scale-invariant phenomena. One model for this class of processes is the fractional Brownian motion framework developed by Mandelbrot and Van Ness¹¹ However, many basic finite-interval detection and estimation problems in this framework have been mathematically intractable. This research explores using techniques of state variable random processes to investigate solutions to these problems.

¹¹ B.B. Mandelbrot and H.W. Van Ness. "Fractional Brownian Motions, Fractional Noises and Applications," *SIAM Rev.* 10: 422-436 (1968).

1.23 Publications

1.23.1 Journal Articles

Lam, W.M., and G.W. Wornell. "Multiscale Representation and Estimation of Fractal Point Processes." *IEEE Trans. Signal Process.* 43(11): 2606-2617 (1995).

Nawab, S.H., and E. Dorken. "A Framework for Quality Versus Efficiency Tradeoffs in STFT Analysis." *IEEE Trans. Signal Process.* 43(4): 998-1001 (1995).

Papadopoulos, H., and G.W. Wornell. "Maximum Likelihood Estimation of a Class of Chaotic Signals." *IEEE Trans. Info. Theory* 41(1): 312-317 (1995).

Winograd, J.M., and S.H. Nawab. "Incremental Refinement of DFT and STFT Approximations." *Signal Process. Lett.* 2(2): 25-27 (1995).

Wornell, G.W. "Spread-Signature CDMA: Efficient Multiuser Communication in the Presence of Fading." *IEEE Trans. Inform. Theory* 41(5): 1418-1438 (1995).

1.23.2 Conference Proceedings

Baggeroer, A.B., and H. Schmidt. "Cramer-Rao Bounds for Matched Field Tomography and Ocean Acoustic Tomography." *Proceedings ICASSP 95*, May 1995, vol. 5, pp. 2763-2766.

Buck, J.R., J.C. Preisig, M. Johnson, and J. Catipovic. "Monochromatic Single-Mode Excitation in Shallow Water Using Feedback Control." *Proceedings ICASSP 95*, May 1995, vol. 5, pp. 3107-3110.

Cuomo, K.M. "Systematic Synthesis Procedures for High-Dimensional Chaotic Systems." *Proceedings ISCAS Conference*, April 1995.

Hadjicostis, C.N. "Fault-Tolerant Computation in Semigroups and Semirings." International Conference on Digital Signal Processing, Limasol Cyprus, June 1995.

Halberstadt, A.K. "Application of Frequency-domain Polyphase Filtering to Quadrature Sampling." SPIE '95 Conference, San Diego, California, July 1995.

Isabelle, S.H., and G.W. Wornell. "Statistical Properties of One-Dimensional Chaotic Signals." *Proceedings ICASSP 95*, May 1995, vol. 2, pp. 1352-1355.

Lam, W.M., and G.W. Wornell. "Multiresolution Representations and Algorithms for Fractal Point Processes." IEEE Workshop on Nonlinear Signal and Image Processing, Halkidiki, Greece, June 1995.

Ludwig, J.T., S.H. Nawab, and A. Chandrakasan. "Low Power Filtering Using Approximate Processing for DSP Applications." *Proceedings of the Custom Integrated Circuit Conference*, May 1995.

Nawab, S.H., and J.M. Winograd. "Approximate Signal Processing Using Incremental Refinement and Deadline-Based Algorithms." *Proceedings ICASSP 95*, May 1995, vol. 5, pp. 2857-2860.

Oppenheim, A.V., K.M. Cuomo, R.J. Barron, and A.E. Freedman. "Channel Equalization for Communication with Chaotic Signals." Third Technical Conference on Nonlinear Dynamics, Mystic, Connecticut, July 1995.

Singer, A.C. "A New Circuit for Communication Using Solitons." IEEE Workshop on Nonlinear Signal and Image Processing, Halkidiki, Greece, June 1995.

Singer, A.C. "Signaling Techniques Using Solitons." Conference *Proceedings ICASSP 95*, May 1995, vol. 2, pp. 1336-1339.

Winograd, J.M., and S.H. Nawab. "A C++ Software Environment for the Development of Embedded Signal Processing." Conference *Proceedings ICASSP 95*, May 1995, vol. 4, pp. 2715-2718.

Winograd, J., J. Ludwig, S.H. Nawab, A. Chandrakasan, and A.V. Oppenheim. "Approximate Processing and Incremental Refinement Concepts." Second ARPA RASSP Conference, Washington, D.C., July 1995.

Winograd, J.M., and S.H. Nawab. "Mixed-radix Approach to Incremental DFT Refinement." SPIE '95 Conference, San Diego, California, July 1995.

Wornell, G.W. "Efficient Multiuser Communication in the Presence of Fading." *Proceedings of the IEEE International Symposium on Information Theory*, Whistler, Canada, September 1995.

Wornell, G.W. "A New Class of CDMA Systems for Fading Channels." IEEE Workshop on Information Theory, Multiple-Access, and Queuing, St. Louis, Missouri, April 1995.

1.23.3 Technical Reports

Hadjicostis, C.N. *Fault-Tolerant Computation in Semigroups and Semirings*. RLE Technical Report No. 594. Cambridge: MIT Research Laboratory of Electronics, 1995.

Isabelle, S.H. *A Signal Processing Framework for the Analysis and Application of Chaotic Systems*. RLE Technical Report No. 593. Cambridge: MIT Research Laboratory of Electronics, 1995.

1.23.4 Book

Wornell, G.W. *Signal Processing with Fractals: A Wavelet-Based Approach*. Englewood Cliffs, New Jersey: Prentice-Hall, 1995.

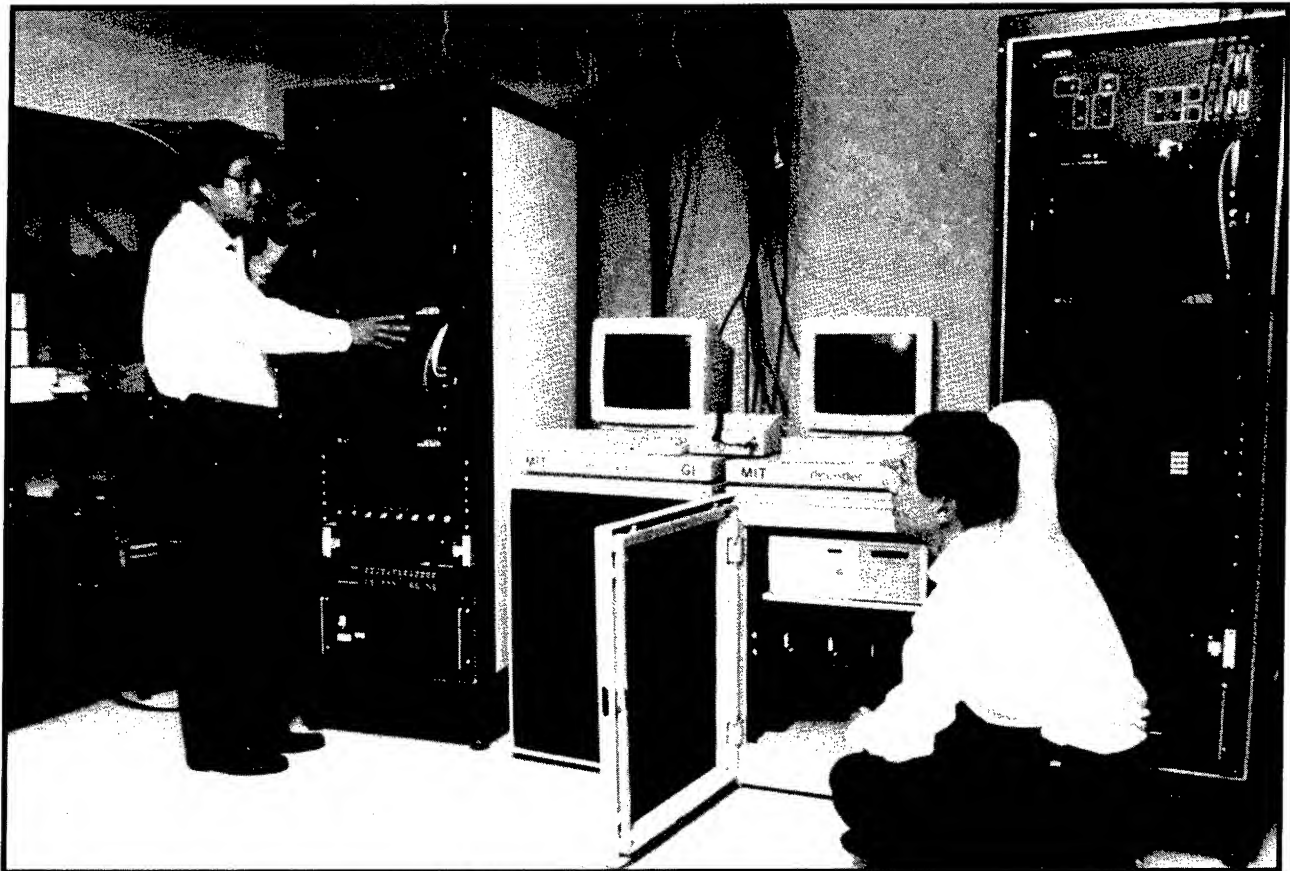
1.23.5 Theses

Brown, S.W. *A Feasibility Analysis of Single-Sensor Active Noise Cancellation in the Interior of an Automobile*. S.M. thesis. Dept. of Electr. Eng. and Comput. Sci., MIT, 1995.

Freedman, A.E., *Transmission Channel Compensation in Self-Synchronizing Chaotic Systems*. M.Eng. thesis. Dept. of Electr. Eng. and Comput. Sci., MIT, 1995.

Hadjicostis, C.N. *Fault-Tolerant Computation in Semigroups and Semirings*. M.Eng. thesis. Dept. of Electr. Eng. and Comput. Sci., MIT, 1995.

Isabelle, S.H. *A Signal Processing Framework for the Analysis and Application of Chaotic Systems*. Ph.D. diss. Dept. of Electr. Eng. and Comput. Sci., MIT, 1995.



Professor Jae S. Lim (left) and graduate student Julien Nicolas working with the channel compatible digiCipher system at the Advanced Television Test Center in Alexandria, Virginia.

Chapter 2. Advanced Telecommunications and Signal Processing Program

Academic and Research Staff

Professor Jae S. Lim

Visiting Scientists and Research Affiliates

M. Carlos Kennedy

Graduate Students

John G. Apostolopoulos, David M. Baylon, Shiufun Cheung, Raynard O. Hinds, Peter A. Monta, Eric C. Reed, Lon E. Sunshine, Carl Taniguchi, Chang Dong Yoo

Technical and Support Staff

Cindy LeBlanc, Denise M. Rossetti

2.1 Introduction

The present television system was designed nearly 50 years ago. Since then, there have been significant developments in technology, which are highly relevant to the television industry. For example, advances in the very large scale integration (VLSI) technology and signal processing theories make it feasible to incorporate frame-store memory and sophisticated signal processing capabilities in a television receiver at a reasonable cost. To exploit this new technology in developing future television systems, Japan and Europe established large laboratories, funded by government- or industry-wide consortia. The lack of this type of organization in the United States was considered detrimental to the broadcasting and equipment manufacturing industries, so in 1983 a consortium of American companies established the Advanced Television Research Program (ATRP) at MIT.

The major objectives of the ATRP are:

1. To develop the theoretical and empirical basis for the improvement of existing television systems, as well as the design of future television systems;
2. To educate students through television-related research and development and motivate them to undertake careers in television-related industries;

3. To facilitate continuing education of scientists and engineers already working in the industry;
4. To establish a resource center to which problems and proposals can be brought for discussion and detailed study; and
5. To transfer the technology developed from this program to the industries.

In the past, research areas of the program focused on a number of issues related to digital television design. As a result of this effort, significant advances have already been made, and these advances are likely to be included in the U.S. HDTV standard. Specifically, the ATRP group represented MIT in the Grand Alliance which consisted of MIT, AT&T, Zenith Electronics Corporation, General Instrument Corporation, David Sarnoff Research Center, Philips Laboratories, and Thomson Consumer Electronics. The Grand Alliance digital television system served as the basis for the advanced television (ATV) standard in the United States. This standard was formally recommended for adoption as the American ATV standard by the FCC's Advisory Committee on Advanced Television Service.

In addition to research on issues related to the design of digital television system, our program currently includes research on telecommunication issues and speech enhancement.

2.2 Signal Representations for Very-low-bit-rate Video Compression

Sponsors

Advanced Telecommunications Research Program
AT&T Fellowship

Project Staff

John G. Apostolopoulos

Video plays an important role in many of today's telecommunications applications, and it is expected to gain even greater importance in the near future with the advent of multimedia and personal communication devices. The large raw data rate of a video signal, together with the limited transmission capacity in many applications, necessitates compression of the video signal. A number of video compression algorithms have been developed for different applications from video-phone to high-definition television. These algorithms perform reasonably well at respective bit rates of 64 kb/s to tens of Mb/s. However, many applications in the near future, particularly those associated with portable or wireless devices, will most likely be required to operate at considerably lower bit rates, possibly as low as 10 kb/s. The video compression methodologies developed thus far are not applicable at such low bit rates. The goal of this research is to create efficient signal representations which can lead to acceptable video quality at these extremely low bit rates.

Conventional video compression algorithms may be described as block-based coding schemes; they partition each frame into square blocks and then independently process each block. Examples of these compression techniques include (1) block-based temporal motion-compensated prediction and (2) spatial block discrete-cosine transformation. Block-based processing is the basis for virtually all video compression systems today because it is a simple and practical approach to achieve acceptable video quality at the required bit rates. However, block-based coding schemes can not effectively represent a video signal at very low bit rates because the source model is extremely limited; block-based schemes inherently assume a source model of (translational) moving square blocks. However, a typical video scene is not composed of translated square blocks. In effect, block-based schemes impose an artificial structure on the video signal and then try to encode this structure, as opposed to recognizing the structure inherent to a particular video scene and attempting to exploit it.

The goal of this research is to develop signal representations that are better matches for the structure

that exists within a video scene. By identifying and efficiently representing this structure, it may be possible to produce acceptable video quality at very low bit rates. For example, since real scenes contain objects, a promising source model is two- or three-dimensional moving objects. This approach may provide a much closer match to the structure in a video scene than the aforementioned block-based schemes. Three fundamental issues that must be addressed for the success of this approach are (1) appropriate segmentation of the video scene into objects, (2) encoding of the segmentation information, and (3) encoding of the object interiors. In regard to the third issue, significant statistical dependencies exist in regions belonging to each object and must be exploited. Conventional approaches to encode arbitrarily shaped regions are typically simple extensions of the block-based approaches, and hence suffer from inefficiencies. A number of novel methods to efficiently represent the region interior have been developed.

2.2.1 Publications

Apostolopoulos, J.G., and J.S. Lim. "Representing Arbitrarily-shaped Regions - A Case Study in Overcomplete Representations." Paper presented at the IEEE International Conference on Image Processing, Washington, D.C., October 1995.

Apostolopoulos, J.G., and J.S. Lim. "Coding of Arbitrarily-Shaped Regions." Paper presented at the Conference on Visual Communications and Image Processing, Taipei, Taiwan, May 1995.

2.3 Optimal Transform Coefficient Selection for Images

Sponsors

Advanced Telecommunications Research Program
INTEL Fellowship

Project Staff

David M. Baylon

In many image coding schemes, compression is achieved by perceptual quantization and thresholding of data. In transform coding, thresholding of high-frequency, low-energy coefficients can lead to substantial compression while maintaining high image quality. However, in applications where it is desirable to optimize performance while keeping the rate or image quality constant, it becomes increas-

ingly important to select coefficients in a more optimal fashion. This research focuses on optimal transform coefficient selection in a rate-distortion framework using mean square error distortion.

Traditional threshold schemes which select coefficients based upon magnitude are very fast but do not guarantee to generate optimal solutions since consideration is not given to the bit rate requirement of encoding the selected coefficients. Previous convex hull methods are fast and typically yield optimal solutions when performed globally over the image but not when performed locally.

In this research, an algorithm is proposed for methodically deriving rate-distortion points by iteratively generating a set of convex hulls, from which a composite operational rate-distortion curve is generated. Although this "composite shell" method can be used for generating both globally and locally optimal rate-distortion points, the complexity of this approach is high. Therefore, a fast suboptimal approach is also proposed which is based upon a modified version of threshold selection. Simulations performed on some typical images using finely quantized DCT coefficients and separate coding of amplitudes and runlengths show that very good rate-distortion performance can be obtained using this fast algorithm while maintaining decoder-compatibility.

Current research is aimed at further improving performance by designing the analysis and synthesis filters to compensate for the distortion introduced by quantization and selection.

2.4 Biorthogonality in Lapped Transforms: A Study in Audio Compression

Sponsor

Advanced Telecommunications Research Program

Project Staff

Shiufun Cheung

The demand for high-quality audio in transmission systems such as digital audio broadcast (DAB) and high-definition television (HDTV), as well as commercial products such as the MiniDisc (MD) and the digital compact cassette (DCC), has generated considerable interest in audio compression schemes. The common objective is to achieve high quality at a rate significantly smaller than the 16 bits/sample used in current compact disc (CD) and digital audio tape (DAT) systems. We have been considering applications to HDTV; an earlier implementation,

the MIT audio coder (MIT-AC), is one of the systems that was considered for inclusion in the U.S. HDTV standard. In this research, we build upon our previous efforts by studying one important aspect of audio coder design: the short-time spectral decomposition.

In conventional audio coders, the short-time spectral decomposition serves to recast the audio signal in a representation that is not only amenable to perceptual modeling but also conducive to deriving transform coding gain. This decomposition is commonly achieved by a multirate filter bank, or equivalently, a lapped transform.

Towards the goal of improving the performance of audio compression schemes, we have formulated a biorthogonal cosine-modulated filter bank which is a generalization of Malvar's extended lapped transform (ELT). The ELT, a popular implementation of cosine-modulated filter banks, is of particular interest because it forms the major building block of signal decomposition schemes in many audio coders.

Conventional lapped transforms are designed to be orthogonal filter banks in which the analysis and synthesis filters are identical. Allowing the analysis and synthesis filters to differ leads to a biorthogonal transform which has more degrees of design freedom than its orthogonal counterpart. We have proven that the incorporation of biorthogonality into an M -channel ELT yields an increase of $M/2$ degrees of freedom. This additional flexibility allows the design of synthesis filter banks with improved sidelobe behavior which should be beneficial to audio coder performance.

2.4.1 Publication

Cheung, S., and J.S. Lim. "Incorporation of Biorthogonality into Lapped Transforms for Audio Compression." *Proc. ICASSP 5*: 3079-3082 (1995).

2.5 Multistage Video Compression

Sponsors

Advanced Telecommunications Research Program
AT&T Fellowship

Project Staff

Raynard O. Hinds

The television production and broadcasting process can be divided into three broad categories: produc-

tion, post-production, and broadcasting. During the production stage, the uncompressed television signal is acquired at a bit rate of 1.2 Gbits/sec. The video data will require further processing and editing before the final signal is transmitted to the consumer. Editing is done during the post-production stage where the television signal is manipulated and processed to produce special effects. During this stage, it is desirable to have a compressed representation of the signal to reduce the amount of storage required. The television signal must also be compressed for the final stage which consists of terrestrial broadcast to the consumer. The final two stages of the process require compressed representations. The requirements for the compression algorithm at each stage differ and may require the concatenation of separate algorithms. This research will consider a multistage compression algorithm to determine what problems may exist in its application to television broadcasting.

Post-production of video signals includes rearrangement of images, insertion of text and graphics, as well as temporal filtering for motion effects. In many cases, it is necessary to be able to access and manipulate any frame and insert it into the coded bit stream. This requires random access of frames in the compressed bit-stream. During this stage, there is further processing of the video signal, and it is necessary to keep the image at a quality sufficient for post-production.

For terrestrial broadcast, the television signal must achieve a bit rate of approximately 20 Mbits/sec to fit within the allocated 6 MHz channel. Thus, a high compression ratio is needed. For HDTV transmission a standardization process is taking place which will determine the algorithm applied at this stage to meet the requirements. The image representation at this stage will be fixed. The goal of this research is to find the best representation for the television signal at the first compression stage which meets the specified requirements above to deliver an acceptable image quality to the viewer.

2.5.1 Publications

Hinds, R.O., and T.N. Pappas. "An Adaptive Clustering Algorithm for Segmentation of Video Sequences." *Proc. ICASSP 4*: 2427-2430 (1995).

Pappas, T.N., and R.O. Hinds. "On Video and Audio Data Integration for Conferencing." *Proc. SPIE 2411*: 120-127 (1995).

2.6 Video Source Coding for High-Definition Television

Sponsor

Advanced Telecommunications Research Program

Project Staff

Peter A. Monta

Efficient source coding is the enabling technology for high-definition television over the relatively narrow channels envisioned for the new service (e.g., terrestrial broadcast and cable). Coding rates are on the order of 0.3 bits/sample, and high quality is a requirement. This work focuses on new source coding techniques for video relating to representation of motion-compensated prediction errors, quantization and entropy coding, and other system issues.

Conventional coders represent video with the use of block transforms with small support (typically 8 x 8 pixels). Such independent blocks result in a simple scheme for switching a predictor from a motion-compensated block to a purely spatial block; this is necessary to prevent the coder from wasting capacity in some situations.

Subband coders of the multiresolution or wavelet type have more desirable localization properties, lack "blocking" artifacts, and match better to motion-compensated prediction errors. Therefore, they complicate the process of switching predictors since the blocks now overlap. A novel predictive coding scheme is proposed in which subband coders can combine the benefits of good representation and flexible adaptive prediction.

Source-adaptive coding is a way for HDTV systems to support a more general imaging model than conventional television. With a source coder that can adapt to different spatial resolutions, frame rates, and coding rates, the system may then make tradeoffs among the various imagery types (for example, 60 frames/s video, 24 frames/s film, highly detailed still images, etc.). In general, this is an effort to make HDTV an image transport system rather than a least-common-denominator format to which all sources either must adhere or be modified to fit. These techniques are also applicable to NTSC to some extent; one result is an algorithm for improved chrominance separation for the case of "3-2" NTSC, that is, NTSC upsampled from film.

2.7 Improvement of MPEG by Position-dependent Encoding

Sponsors

Advanced Telecommunications Research Program
U.S. Navy - Office of Naval Research
NDSEG Graduate Fellowship

Project Staff

Eric Reed

In a typical MC-DCT compression algorithm, almost 90 percent of the available bit rate is used to encode the location and amplitude of the non-zero quantized DCT coefficients. Therefore efficient encoding of the location and amplitude information is extremely important. One novel approach to encoding the location and amplitude information of the non-zero coefficients is position-dependent encoding. Position-dependent encoding, in contrast to single-codebook encoding, exploits the inherent differences in statistical properties of the runlengths and amplitudes as a function of position.

Position-dependent encoding has been investigated as an extension to separate encoding of the runlengths and amplitudes and has proven to provide a substantial reduction in the overall bit rate compared to single-codebook methods. However, MPEG compression does not allow separate encoding of the runlengths and amplitudes. Therefore, this research involves developing a position-dependent extension to encode the runlengths and amplitudes jointly as a single event. Rather than having two separate codebooks for the runlengths and amplitudes, one two-dimensional codebook will be utilized. This method will be compared to conventional approaches as well as the position-dependent encoding approach using separate codebooks.

2.8 HDTV Transmission Format Conversion and the HDTV Migration Path

Sponsor

Advanced Telecommunications Research Program

Project Staff

Lon E. Sunshine

The current proposal for terrestrial HDTV broadcasting allows for several possible transmission

formats. Because production and display formats may differ, it will be necessary to convert between formats in an effective way. A key to this process is the de-interlacing process. Since HDTV will presumably move toward progressive display systems, it will be necessary to de-interlace nonprogressive source material. The research will consider topics relating to conversion among the six formats being proposed for the U.S. HDTV standard.

As HDTV evolves, it is probable that more transmission formats will be allowed. Furthermore, additional bandwidth may be allocated for some channels (terrestrial and/or cable). This research will consider the issues related to the migration of HDTV to higher resolutions. Backward compatibility and image compression and coding issues will be addressed.

2.9 Removing Degradations in Image Sequences

Sponsor

Advanced Telecommunications Research Program

Project Staff

Carl Taniguchi

The development of two-dimensional noise smoothing algorithms had been an active area of research since the 1960s. Many of the traditional algorithms fail to use the temporal correlation that exists between frames when processing image sequences. However, with the increasing speed of microprocessors and the rising importance of video, three-dimensional algorithms have not only become feasible, but also practical.

Developing three-dimensional median filters that are sensitive to motion is the first step in using the temporal correlation in images. Existing algorithms of this type effectively reduce to two-dimensional median filters under areas of the image undergoing motion. An improvement in the use of temporal correlation can be obtained by using a motion estimation algorithm before filtering the image with a three-dimensional median filter. Various median filters and motion compensation algorithms will be tested in the presence of noise.

Uniform processing of an image tends to unnecessarily blur areas of the image that are not affected by noise. In this case, a degradation detector may be of practical use.

2.10 Speech Enhancement

Sponsor

Maryland Procurement Office
Contract MDA904-93-C-4180

Project Staff

Chang Dong Yoo

The development of the dual excitation (DE) speech model has led to some interesting insights into the problem of speech enhancement. Based on the ideas of the DE model, a new speech model is being developed. The DE model provides more flexible representation of speech and possesses features which are particularly useful to the problem of speech enhancement. These features along with a variable length window are the backbone of the new speech model being developed.

Because the DE model does not place any restrictions on its characterization of speech, the enhancement system based on this model performs better than systems based on any of the previous speech models. While a model should be inclusive in its characterization, it should have some restrictions. Specifically, a speech model should pertain to speech. The DE model is somewhat unrestrictive

and simple in its characterization of speech. It is solely based on the separation of the voiced and unvoiced components. Whether it makes sense to represent a stop as a voiced and an unvoiced component is just one of many interesting issues which are being investigated. An extension of the DE model which deals with these issues better is currently being studied.

All model-based enhancement methods to date have been formulated on the premise that each segment of speech is stationary for a fixed window length. To improve the performance of the enhancement algorithm, this assumption of stationarity must be assured. In order to do so, a variable-length window should be used to capture varying durations of stationarity in the speech. There are several algorithms which adaptively detect changes in auto-regressive model parameters in quasi-stationary signals which have been successfully used in speech recognition. We propose to investigate some of these algorithms. The benefit from using a variable length window is two-fold: (1) it will allow better and "cleaner" separation of the voiced and unvoiced components, and (2) it will allow for a greater reduction in the number of characteristic parameters, such as the amplitudes of the voiced components and the LP coefficients of the unvoiced component.

Chapter 3. Combined Source and Channel Coding for High-Definition Television

Academic and Research Staff

Professor Emeritus William F. Schreiber

Graduate Students

Michael O. Polley, Susie J. Wee

Technical and Support Staff

Deborah S. Manning

3.1 Project Description

Sponsors

Research Laboratory of Electronics
Department of Electrical Engineering and
Computer Science

The purpose of this project is to develop a high-definition television (HDTV) system for terrestrial broadcasting. Under decisions previously made by the Federal Communications Commission, each current broadcaster will be given a second channel. This channel is to be used for HDTV, transmitting the same program as the standard NTSC channel in a procedure called simulcasting. Fifteen years after the commencement of high-definition broadcasting, NTSC is to go off the air, the original channels being returned to the FCC for reassignment. In many cases, the new assignments will be taboo channels not usable for NTSC because of interference. This obviously requires that the HDTV transmissions have excellent interference performance. Coverage must be comparable to what is now achieved with NTSC.

The system being developed in this project is intended to be more useful than the all-digital scheme that has evolved from the FCC process [the Grand Alliance (GA) system]. Its features have been chosen specifically to be acceptable to the various stakeholders including broadcasters, equipment manufacturers, program producers, regulatory authorities, and viewers. The most important performance factors are efficient use of spectrum, coverage versus quality, cost, and interoperability. In

addition, it must have a feasible transition scenario. We have concluded that all receivers need not have the same picture quality and that low-cost receivers must be available for less-critical applications. We have therefore designed a multiresolution (MR) system, in which a hierarchy of encoders of different price/performance can communicate with a hierarchy of decoders, also of varying cost and quality. As compared with the Grand Alliance system, the new scheme features:

1. Extended coverage, albeit at lower quality in the extra area,
2. Higher quality, albeit only in the central portion of the service area,
3. Comparable quality in a large portion of the service area,
4. Support for single-frequency networks (SFNs), which make the most efficient use of spectrum,¹
5. Support for less expensive receivers for less demanding applications, and
6. Automatic optimization of image quality as a function of signal quality and receiver complexity.

(The cost for features 1-3 is somewhat lower quality in a part of the service area.)

The multiresolution (MR) feature makes possible the design of cheaper receivers for small sizes and other noncritical applications. It also permits higher performance receivers to optimize their image

¹ SFNs make the signal level more uniform across the population of receivers by utilizing a cellular network of low-power transmitters, all operating in the same channel. The several signals sensed at each receiver appear to be ghosts, so very good ghost suppression is required.

quality as a function of received signal quality, thus improving spectrum utilization.

The MR feature is achieved using combined source and channel coding employing a pyramid technique. The coded video and audio data is divided into a number (typically 3 or 4) of data streams. The quality of the reconstructed video depends on the number of streams recovered and their signal-to-noise ratio. Thus the lowest stream provides a picture somewhat better than studio-quality NTSC to the least-expensive receivers and/or under poor reception conditions. The higher streams are used to enhance image quality. The streams are packaged by the channel coder so that the number recovered depends on the signal strength and receiver performance. The lowest quality level features standard MPEG-2 coding so that the cheapest receivers can use single-chip MPEG decoders.²

3.2 Technology

In the GA system, digital source coding is used to get very high compression, which is needed, in part, because all-digital channel coding does not make the best use of the analog channel capacity. Our system uses multiresolution hybrid analog/digital coding, which permits both high compression and efficient use of spectrum.

The source coder uses some MPEG features, but produces data in a form suitable for hybrid channel coding. This data is not all of one kind; some require essentially perfect transmission, and some can tolerate a certain amount of noise and distortion.

The channel coder uses spread spectrum and orthogonal frequency-division multiplex (OFDM),³ which, in combination, give good resistance to analog channel impairments and facilitate multiresolution operation. The coder transmits the more sensitive data digitally and the less sensitive data in analog form. The received signal "looks" simple to a low-performance receiver, while a high-performance receiver, with its more powerful decoder, "knows" where to look in the signal for the higher streams of data. These are recoverable at locations where the signal strength is higher and/or where the receiver is of better quality. Digital per-

formance is enhanced by extensive forward error correction. The simpler receivers are expected to be substantially cheaper than those used in the GA system, while the higher-performance receivers will be of comparable complexity and cost.

3.3 Current Status

By the end of 1995, the system simulation was nearly complete. Output sequences can be demonstrated after transmission through a simulated terrestrial channel showing the effect of noise and echoes on the digital and analog components of the signal. Three levels of resolution are attained at three different receiver CNRs. For details, see our chapter in *RLE Progress Report No. 137 (1994)*, including the first paper referenced at the end of the chapter. A small amount of work needs to be done on the source coder.

The channel coder work is complete and fulfills all our expectations for the system. One of the most important of these is the performance in the presence of echoes. Figure 1 shows the BER with several levels of echo as a function of CNR for a very simplified version of the channel coder. As can be seen, in distinction to the performance of conventional systems such as the Grand Alliance System, the performance of the new system actually *improves with large echoes*.

The echo performance of this system makes it suitable for use in SFNs without the use of directional antennas. In these systems, the conventional centralized transmitter is replaced by a cellular network of low-power transmitters, all emitting the same signal. Receivers, particularly with omnidirectional antennas, see a number of very strong "echoes." The channel coder that we have developed is the first, in my opinion, that is both practical in terms of computation and that performs well enough to be used in this way. SFNs permit much more efficient use of spectrum than conventional terrestrial broadcast systems because they effectively eliminate the effect of co-channel interference. The service area of each station is delimited by the location of the cellular transmitters, and it is only in a narrow region around the edge of the service area that two stations must compete for the same receivers.

² The Motion Picture Experts Group has promulgated an international all-digital standard for TV source coding, which has been adopted by many groups. Inexpensive coder and decoder chips are becoming available, which makes the use of MPEG coding very attractive.

³ OFDM was invented in the United States, but in recent years has been developed in Europe for digital audio broadcasting. It is also intended for use in digital TV terrestrial broadcasting in Europe. The coded form is referred to as COFDM.

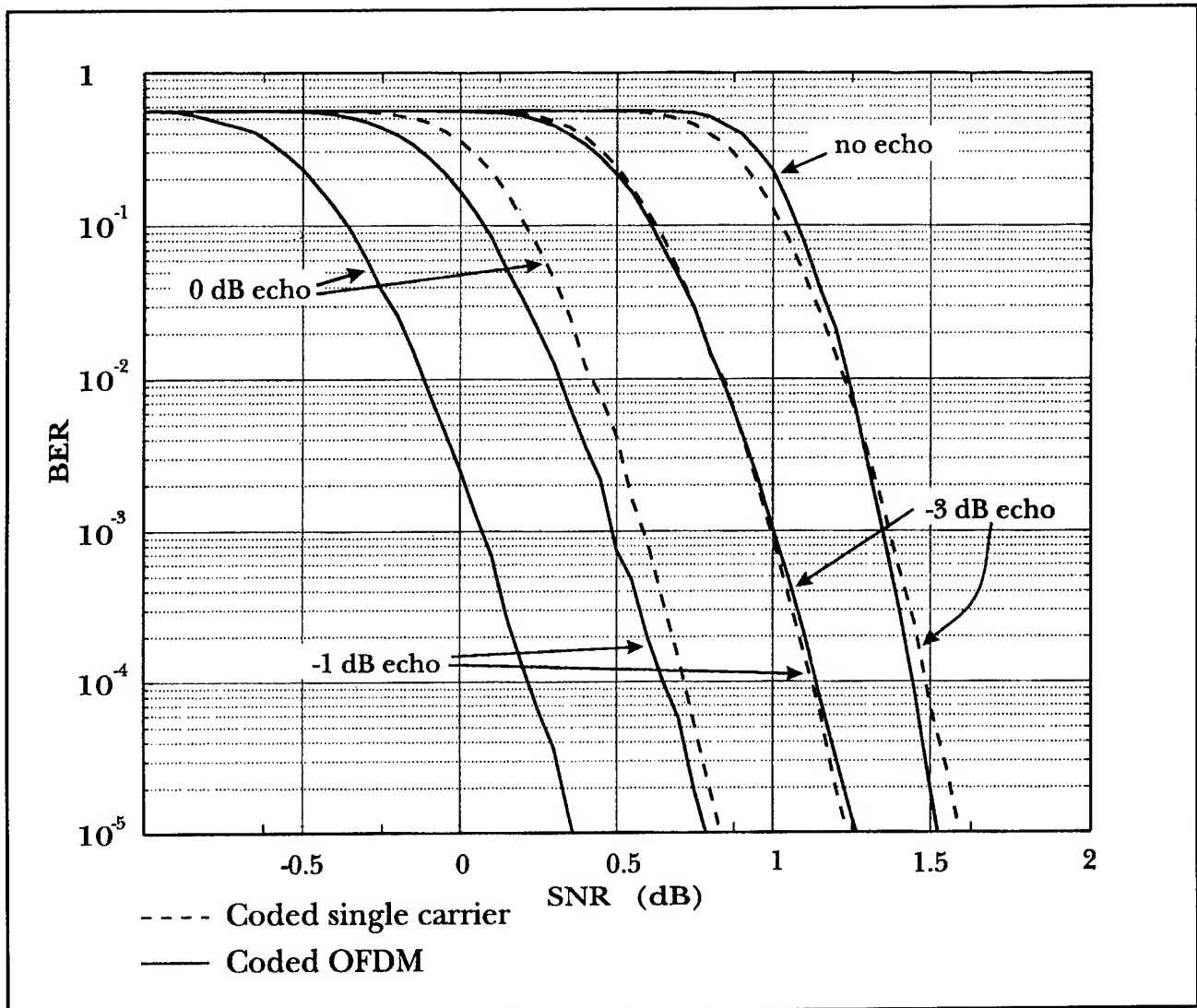


Figure 1. Comparison of single-carrier and OFDM concatenated coder performance for a single-echo channel as the echo power increases.

3.4 Publications

Polley, M.O., W.F. Schreiber, and S.J. Wee. "Comments on Transmission Techniques for Digital Terrestrial TV Broadcasting." *IEEE Commun. Mag.* 33(11): 22-25 (1995).

Schreiber, W.F. "A Unified Approach to Moving Image Coding for Most Media and Most Applications." *Sig. Proc.* 43: 305-321 (1995).

Schreiber, W.F. "Advanced Television Systems for Terrestrial Broadcasting: Some Problems and Some Proposed Solutions." *Proc. IEEE.* 83(6): 958-981 (1995).

Wee, S.J., M.O. Polley, and W.F. Schreiber. "A Scalable Source Coder for a Hybrid Transmission HDTV System." Paper published in the *Proceedings of the International Symposium on Multimedia Communications and Video Coding*, Brooklyn, New York, October 1995.

Part IV Bioelectronics

Section 1 Genetic Analysis

Section 1 Genetic Analysis

Chapter 1 Genosensor Technology Development

Chapter 1. Genosensor Technology Development

Academic and Research Staff

Dr. Daniel J. Ehrlich,¹ Dr. Mark A. Hollis, Dr. Dennis D. Rathman, Dr. Albert M. Young²

Graduate Students

Jeffrey T. Chiou

1.1 Introduction

The primary objective of our cooperative work with the Houston Advanced Research Center (HARC) is to develop a novel method for automated, low-cost, high-throughput DNA sequence analysis. The overall goal is to demonstrate laboratory prototypes that provide a substantial increase in speed over the conventional DNA sequencing methods now used in the biomedical, pharmaceutical, and agricultural industries.

The basic approach being taken is depicted in figure 1. In a hypothetical DNA sequencing test, a solution of single-stranded "target" DNA strands of identical but unknown sequence is washed onto a specialized microelectronic chip called a genosensor. The genosensor surface contains a large array of test sites, each site containing short pieces of single-stranded DNA known as "probes." These probes are chemically attached to the site. All probes in a given site are of like sequence, and the sequence for each site is unique on the chip. The target DNA strands will bond, or hybridize, very strongly to probes containing their exact Watson-Crick complement, but much less strongly to probes on other sites. The sites containing hybridized DNA are identified via electronic sensing on the chip, and this information is used by off-chip instrumentation to reconstruct the sequence of the target strands. MIT's role in this effort is to perform the design and fabrication of the genosensor chips.

1.2 Development of Genosensor Arrays for DNA Decoding

Sponsor

Houston Advanced Research Center
Contract HRC-HG00665-01

Project Staff

Dr. Daniel J. Ehrlich, Dr. Dennis D. Rathman, Dr. Mark A. Hollis

1.2.1 Genosensor Electronic-Detection Principle

The simplest electrical measurement that can be made at a test site to detect hybridization is probably a measurement of the change in local permittivity due to the addition of long target strands to the site. The complex permittivity $\epsilon' - j\epsilon''$ of an aqueous solution containing DNA exhibits a dispersion around a relaxation frequency which is a function of the size and conformation of the DNA molecule. A measurement of the capacitance and/or conductance between two electrodes in the solution over a range of frequency can therefore differentiate between a site that contains only short probe strands and one that contains long target strands hybridized to the probe strands. From these measurements the relative permittivity ϵ' , the dielectric loss ϵ'' , and the dissipation factor ϵ''/ϵ' can be obtained for the cell.

The ideal electrode structure in a test well consists of two parallel plates spaced so that the entire volume between them is filled by the hybridized DNA globules in aqueous solution. For the sizes of target DNA envisioned, this spacing ranges from approximately 200 to a few thousand angstroms. A

¹ MIT Whitehead Institute for Biomedical Research, Cambridge, Massachusetts.

² MIT Whitehead Institute for Biomedical Research, Cambridge, Massachusetts, and MIT Lincoln Laboratory, Lexington, Massachusetts.

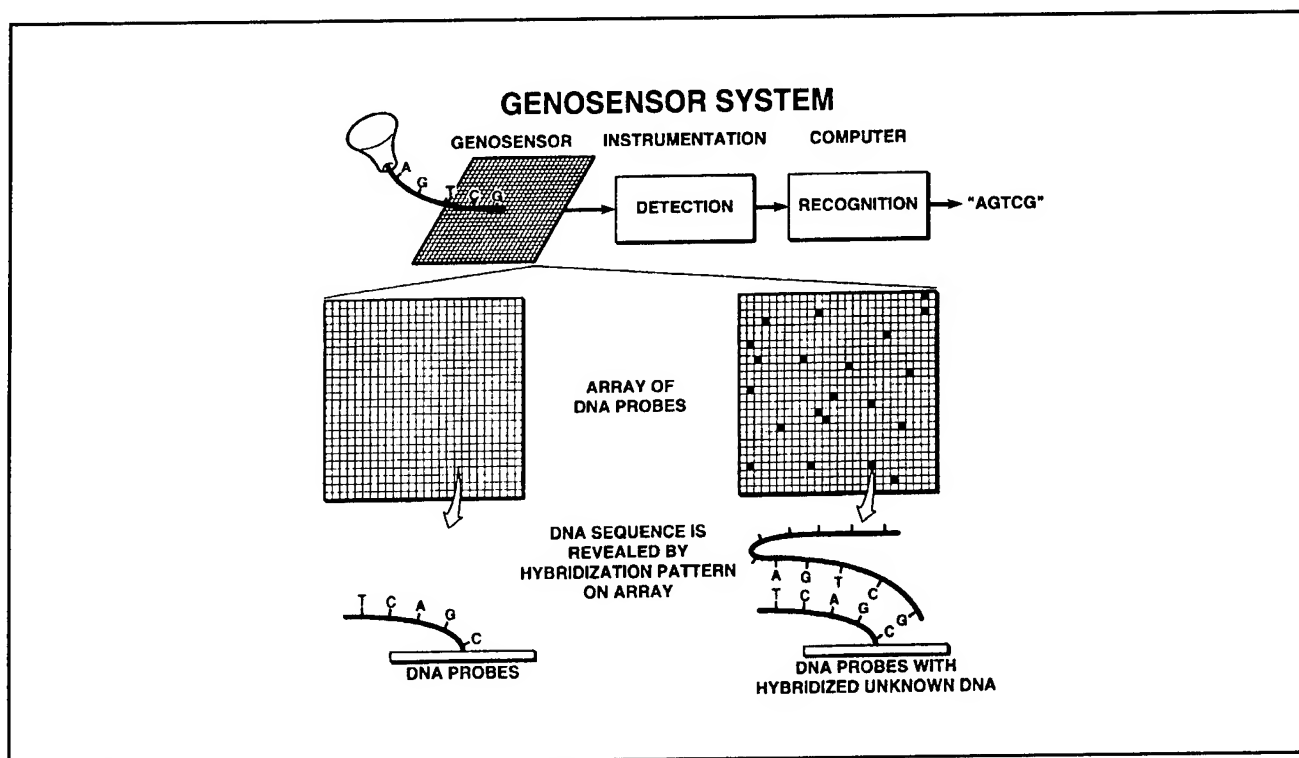


Figure 1. Conceptual genosensor system.

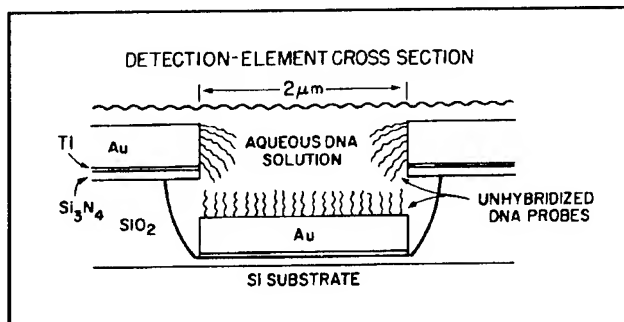


Figure 2. Electrode design for a permittivity genosensor. The unit cell shown is repeated many times across a test well to form an interdigitated test structure with the top Au electrodes connected to one access line and the bottom Au electrodes to the other.

practical, easily fabricated structure that approximates this ideal is an interdigitated design shown in figure 2. Fabricated by a combination of wet and dry etching with metal liftoff, this design can achieve the required spacings between the upper and lower electrodes at their edges. Devices having either Au or Pt electrodes have been fabricated, with Pt preferred for most applications. Figure 3 shows various aspects of completed genosensor devices.

1.2.2 Genosensor Fabrication Development

The primary emphasis of this grant is on the process development and feasibility exploration for the genosensor design of figure 2. For this chip, conventional 2- μm photolithography, wet and dry etching techniques, and electron-beam evaporation and liftoff processes are used to fabricate an interdigitated electrode structure in which the opposing electrodes are separated vertically. A second genosensor design has also been designed and fabricated where the interdigitated electrode structure has the electrodes separated, horizontally, in the same plane, as shown in figure 4.

During the past year, significant progress has been made in process development for both genosensor types. Yield and reproducibility of 6x6 passive arrays of various active-area sizes have in all cases been dramatically improved to greater than 90 percent. Problems related to the lift-off of the Pt device electrodes and interconnect lines have been solved. As detailed in last year's report, electrical measurements provided strong motivation to develop a buried-interconnect, or insulated-lead, process for both types of genosensor devices to eliminate potentially spurious signals generated by the uninsulated leads. The use of hard-baked polyimide as a second-layer dielectric deposited on the Pt electrode/interconnect structure was abandoned, because it produced inconsistent results due

to the apparent degradation of the layer after exposure to the DNA strand attachment chemistries.

For the planar electrode geometry of figure 4, the Pt electrodes are placed directly on a Si_3N_4 layer. This enables the use of a deposited CVD SiO_2 film (deposition temperature 425°C) as the covered-lead dielectric. Vias in the oxide to expose the active device electrodes can easily be etched without attacking the underlying nitride dielectric.

For the split-architecture electrode design illustrated in figure 2, the use of CVD SiO_2 for the covered-lead dielectric becomes more difficult because the bottom electrode sits on an etched SiO_2 surface. However, the lower oxide is thermally grown and has an etch rate in buffered HF that is approximately 10 times lower than the CVD oxide. This differential etch rate has enabled us to cover the device interconnects and subsequently remove this deposited oxide from the active device area without

significantly attacking the underlying thermal oxide and affecting the Pt electrode adhesion. We were prepared to incorporate spin-on glass as the covered-lead dielectric, since the differential etch rate compared to thermal oxide is much greater for spin-on glass than for our CVD oxide. However, this proved to be unnecessary.

For the 6x6 passive arrays, each device's input/output lead is completely isolated from adjacent devices. Ultimately, high-speed DNA sequencing will require the use of very large arrays of genosensor devices (e.g., 1024×1024). With limited space per chip for input/output pins, these large devices require the use of crossbar switching arrays where the sensor sites are connected in rows and columns, as shown in figure 5. The fabrication of such an array requires the development of a two-level metal, two-level dielectric process. The insulated-lead process described above is the first element required for the development of a crossbar

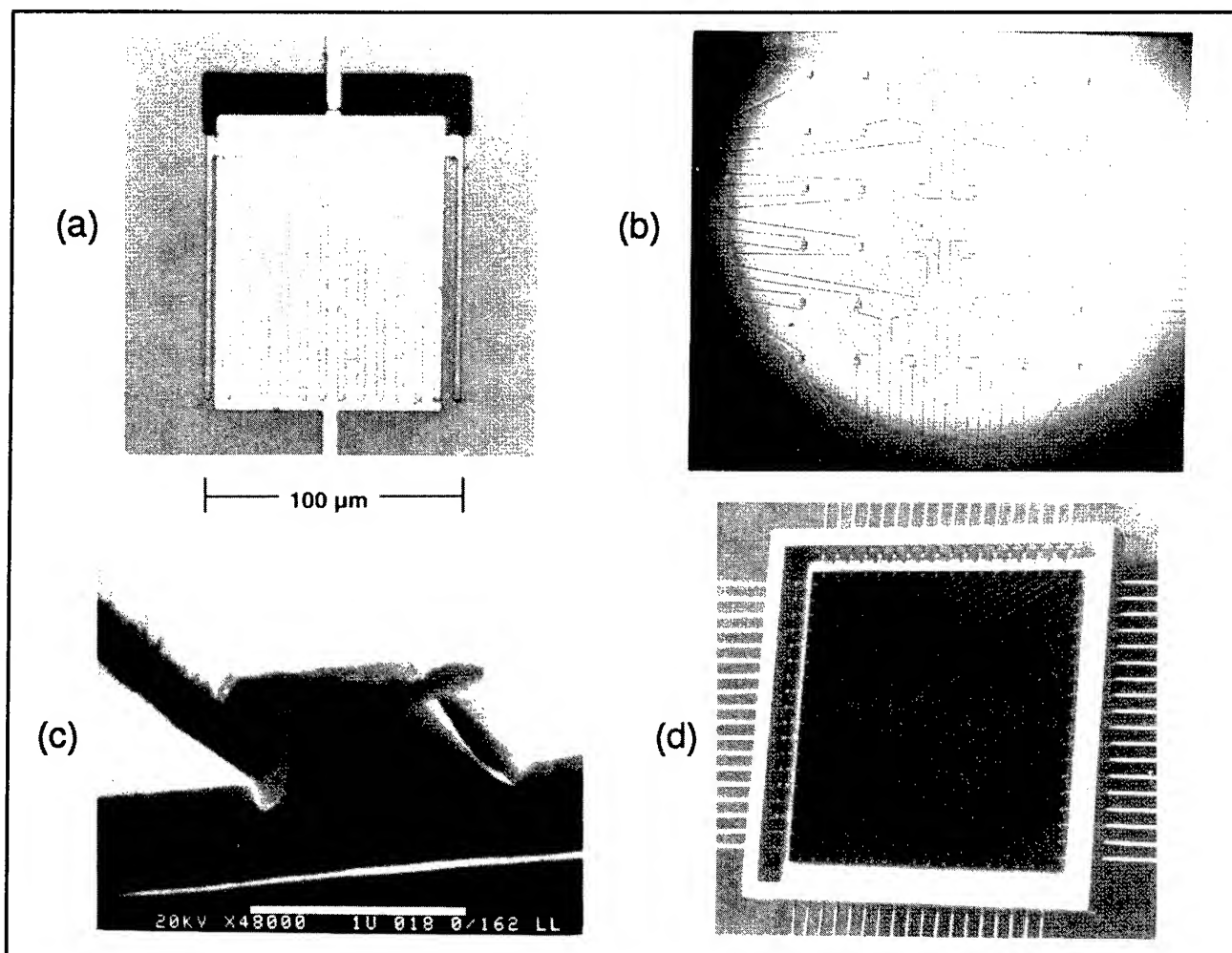


Figure 3. Collection of photographs showing various views of a complete genosensor device. (a) Top view of the standard $100\ \mu\text{m} \times 100\ \mu\text{m}$ single test cell. (b) Top view of the 6×6 passive array of test cells. (c) Scanning electron micrograph (SEM) closeup of the interdigitated electrode fingers. (d) Genosensor chip in electronic package.

switching array architecture. If the interdigitated electrodes and either the row or column feeds to the active cell are patterned as the first metal layer, the fabrication sequence of the crossbar switching array has only one additional step compared to the processing steps required for the buried-lead device. The leads are first covered over with the second-level dielectric (CVD oxide), and the active device area and contact pads are exposed by via-hole etching down to the first-level metal layer. Then, the second layer of metal can be lifted off and the device completed.

Figure 5 shows two views of the first 16x16 crossbar switching array genosensor, which was designed and completed this year utilizing the planar interdigitated device geometry. Also visible in the figure, along the array diagonal, are lines of open and short test structures for rf signal calibration. The 16x16 design layout and the admittance parameters for the active cell were determined from both experimental data and numerical simulations, in combination with an analysis of how the ultimate impedance-bridge measurements are obtained.

During the past year, we have delivered 22 packaged devices, as well as several unpackaged chips for DNA attachment experiments, to HARC for tests for this project. The devices are presently being characterized by HARC.

1.3 Microdetection Technology for Automated DNA Sequencing

Sponsor

Genometrix, Inc.
Contract GMX-GH00776-04

Project Staff

Dr. Daniel J. Erlich, Dr. Dennis D. Rathman, Dr. Mark A. Hollis

The primary emphasis of this effort is to complement the program described above by optimizing the electrode geometry for maximum sensitivity. Initial work for this contract began with the electrode configuration illustrated in figures 2 and 3. Subsequently, both experimental studies and theoretical modeling have shown a need to design and fabricate more aggressive electrode geometries, which are now being developed as described below.

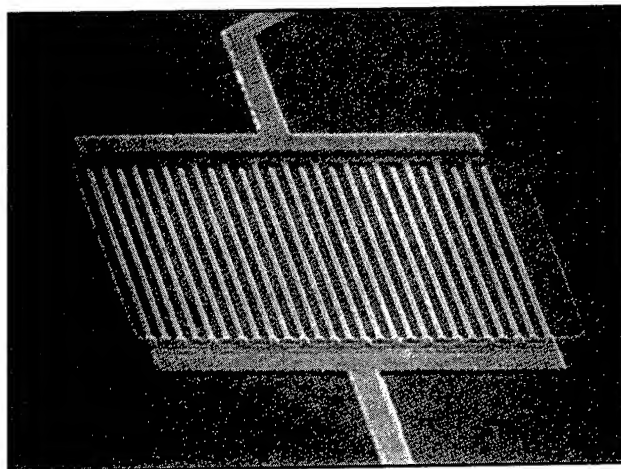


Figure 4. Interdigitated electrode structure where the electrodes are coplanar and non-self-aligned.

Measurements by our colleagues at HARC and Baylor College of Medicine have shown that DNA attachment is more easily achieved to SiO_2 or polysilicon than to Pt or Au. In fact, surface-attachment densities of DNA probes on oxide-coated polysilicon are typically one order of magnitude higher compared to the Pt electrodes of our conventional permittivity-chip designs. The exact reasons for this are not yet known but are probably related to (1) the different linker chemistries used for attachment, or (2) the strong ionic and polarization effects observed at liquid-metal interfaces. During the past year, we have completed and shipped several permittivity chips with polysilicon electrodes to Genometrix and HARC for test. For these first wafers, the polysilicon electrode fingers were patterned by dry etching using a conservative height-to-width aspect ratio for the electrode fingers.

In addition to the polysilicon coplanar design, two very aggressive self-aligned or split-architecture designs are being pursued using a Ti-Pt electrode metallization. These devices feature submicrometer-periodicity finger spacings in both the vertical and horizontal dimensions. The patterning of the electrodes is being done by a combination of laser interferometric lithography and reactive ion etching. A scanning electron micrograph of one of these devices is shown in figure 6. The electrode line-width and spacing is 160 nm, while the vertical separation of the interdigitated electrodes is approximately 200 nm. This geometry yields a 12.5 times improvement in the electrode density per cm^2 of device area. The fingers themselves are Si_3N_4 to a depth of 200 nm, where thermal oxide is exposed.

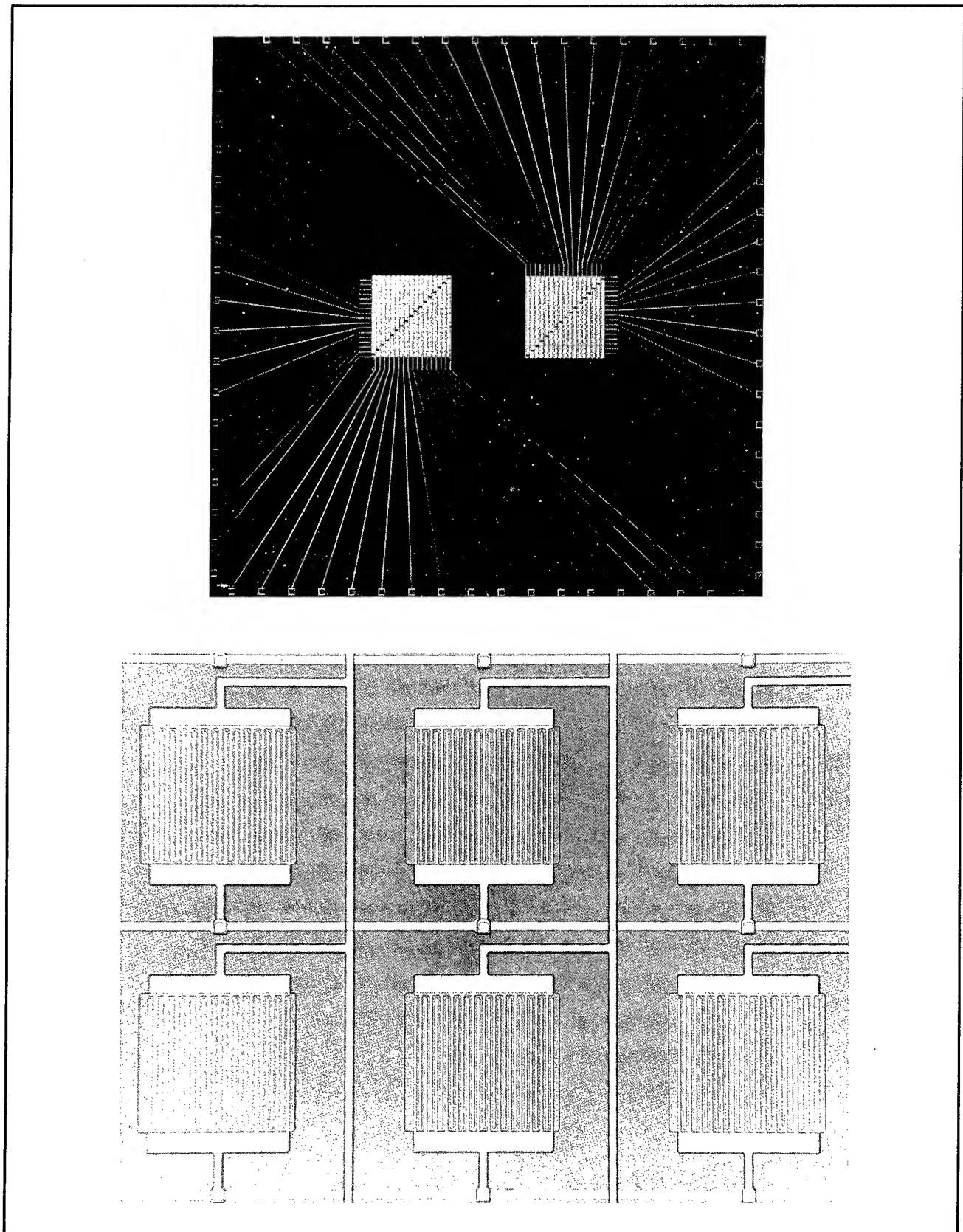


Figure 5. 16x16 crossbar array genosensors. (a)(top) Two arrays on a 1-inch silicon chip. (b)(bottom) Closeup of sensor sites.

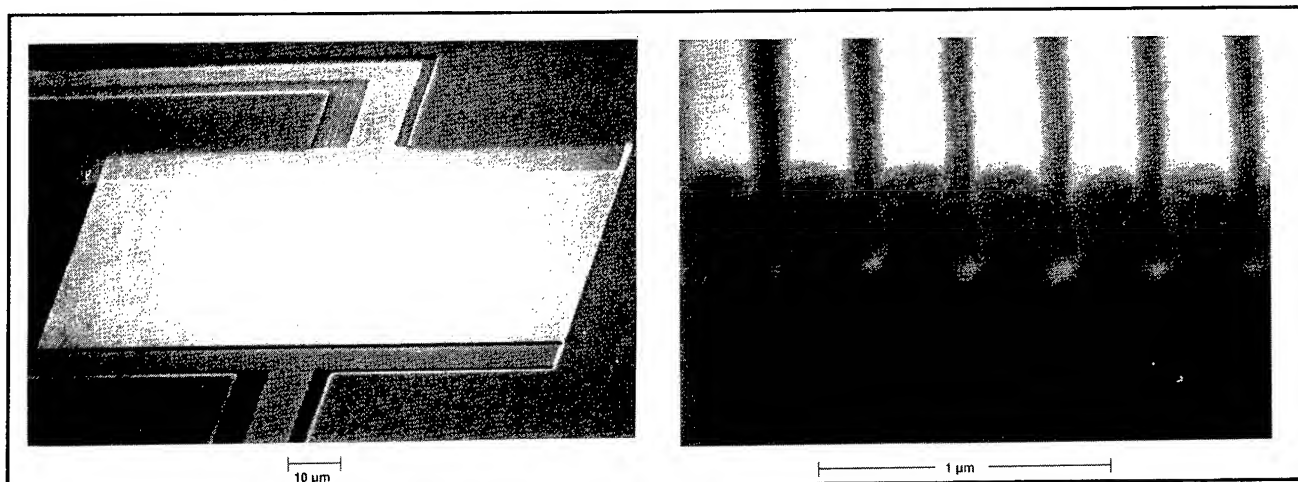


Figure 6. Submicrometer-periodicity genosensor. (a)(left) Overall view of sensor site. (b)(right) Closeup of electrode geometry. Note the 0.32- μm periodicity.

The use of oxide at the finger bottoms enables a slight undercut to be obtained by wet etching of the underlying oxide. It is anticipated that linker chemistries designed to attach either to the closely packed Pt electrodes or to the supporting dielectric posts would enable a substantial increase in probe density at the sensor site with a corresponding increase in detection sensitivity. An alternative submicrometer-spaced electrode geometry, shown in figure 7, is an array of 160-nm-diameter holes where the center-to-center spacing is 320 nm. Here, a continuous metal sheet (lower) forms one electrode and an upper layer of metal (perforated with the holes) forms the other electrode, with the

electrodes separated by a thin film of deposited CVD oxide. The fabrication of this electrode structure is accomplished by an extension of the laser interferometric technique where two perpendicular exposures are used. This technique has been greatly developed and refined through another ongoing program to produce small-geometry gated electron emitters for a variety of vacuum-microelectronics applications. The hole density for this closely packed geometry is 10^9 per cm^2 . As with the linear array design, the intended purpose of this aggressive approach is increased sensitivity. A number of submicrometer devices are expected to be delivered during the coming year.

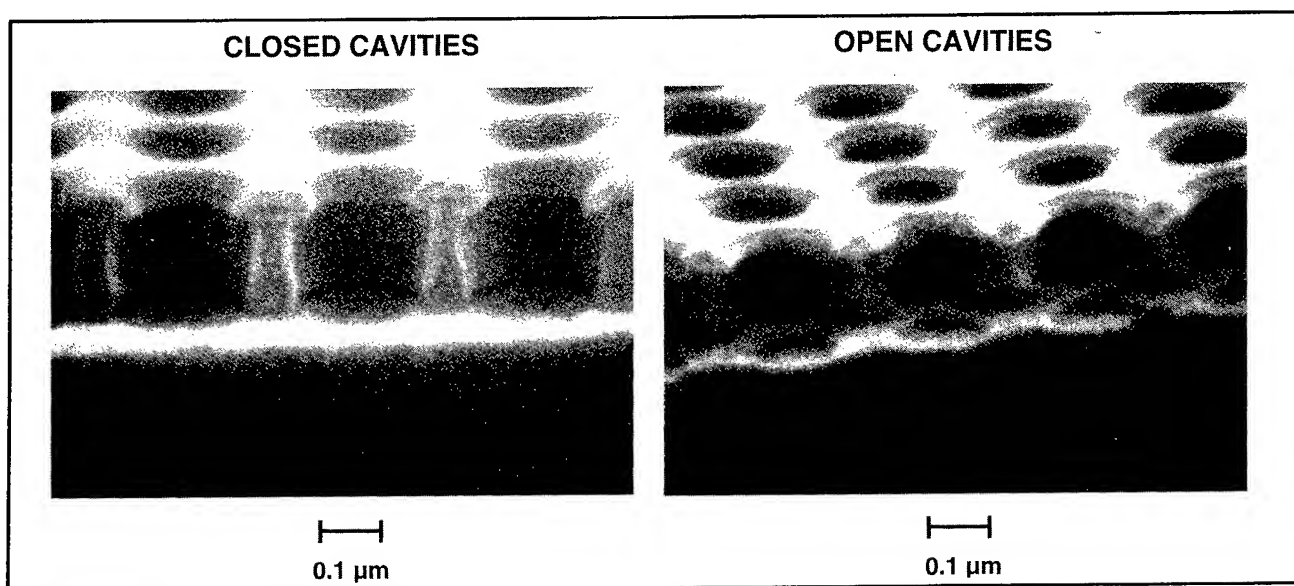


Figure 7. Alternate submicrometer-periodicity genosensor. The upper metal electrode is perforated with holes to allow DNA-probe attachment to the lower metal layer in the cavities.

1.4 Advanced MEMS for High-Throughput DNA Sequencing

Sponsor

National Institutes of Health
Grant 1-R01-HG01389

Project Staff

Dr. Daniel J. Ehrlich, Dr. Albert M. Young, Jeffrey T. Chiou

The goal of our program is to explore the opportunities that arise from using microelectromechanical systems (MEMS) to improve the throughput of automated DNA sequencing. This program is an outgrowth of similar work in microfluidic biodevices.

Microelectromechanical systems technology is the only readily available technology that offers the truly significant improvements in lane density needed for the Human Genome Project and the ability to satisfy long-term sequencing needs. In order to sequence a single human genome with 5x redundancy, we need to sequence at least 50,000,000 templates. To finish this project in three years would require 150 state-of-the-art instruments running continuously. Other technologies, such as capillary electrophoresis, may eventually reduce the number of instruments required to approximately 50. Although these methods may be considered technically feasible, they are costly, time-consuming, and fail to address parallelism, which is the most important requirement for future DNA sequencing applications.

In order to develop the technology and instrumentation needed to perform high-throughput DNA sequencing, we developed a technology base under ARPA funding covering the important subsystems used in DNA sequencing:

- Injection of linear polyacrylamide gel matrices;
- Piezoelectrically-driven droplet-injection for sample loading;
- Microfabrication of separation components in glass;
- Extension of microfabrication techniques to large-area plates; and
- Laser-induced fluorescence detection.

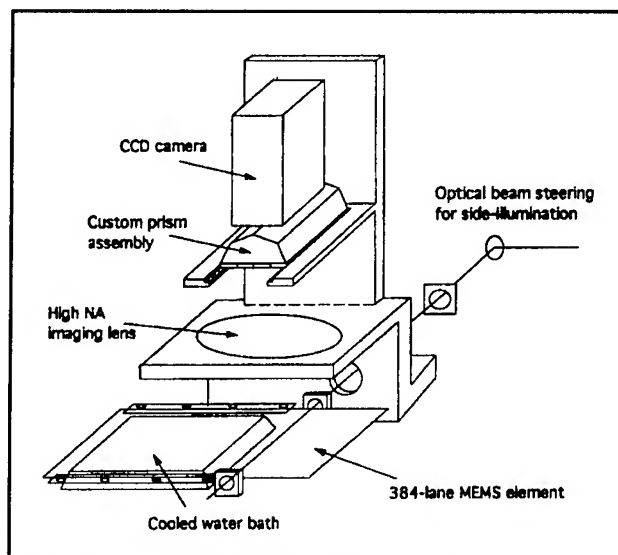


Figure 8. A schematic of the optical subsystem. Fluorescently-tagged DNA is to be electrophoresed from left to right. Important features to note are: (1) the micro-fabricated plates are held down against a thermal cooling bath; (2) side illumination is used to excite all lanes simultaneously, and (3) a prism is used to separate out the four fluorophores corresponding to the bases A, C, G, and T. The microfabrication design to be used is also of some interest.

In conjunction with our previously developed custom robotics hardware and software for XYZ manipulation and the automation of sample preparative processing being developed concurrently at the Whitehead Institute, we have generated a new design for MEMS-based DNA sequencing instrumentation which has recently been funded.

From a systems perspective, the basic instrument will involve the following elements:

- A DNA separation subsystem based on large-area MEMS fabrication technology;
- A CCD-based optical detection subsystem with interfacing to base-calling; and
- Automated sample-loading robotics.

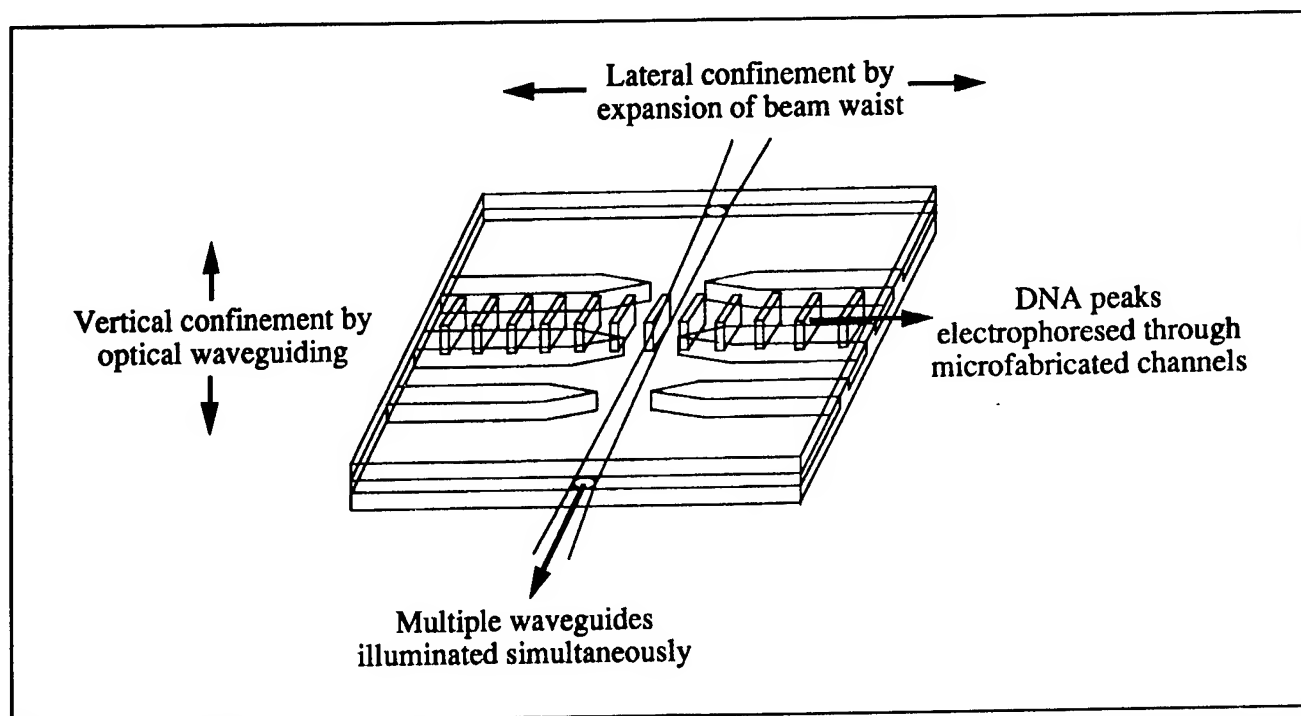


Figure 9. An enlarged schematic of the design for the illumination zone. In this schematic, DNA peaks again are being electrophoresed from left to right through the microfabricated channels. A small gap in the channels is fabricated to allow the excitation beam to pass through all lanes without interference from the glass sidewalls. Since the beam will be impinging on the structure at near-grazing incidence, the beam experiences a high degree of reflectivity from the gel-glass interface, and optical losses in the vertical direction are low. Confinement in the lateral direction is obtained by defocussing the waist out to a diameter of approximately $150\ \mu\text{m}$. Calculation of the beam confocal parameter shows there is very little beam spreading for this defocused case. However, the beam width is still tight enough to provide good resolution during the readout without having to resort to deconvolution methods.

Part V Language, Speech and Hearing

Section 1 Speech Communication

Section 2 Sensory Communication

Section 3 Auditory Physiology

Section 4 Linguistics

Section 1 Speech Communication

Chapter 1 Speech Communication

Chapter 1. Speech Communication

Academic and Research Staff

Professor Kenneth N. Stevens, Professor Jonathan Allen, Professor Morris Halle, Professor Samuel J. Keyser, Dr. Krishna K. Govindarajan, Dr. Helen M. Hanson, Dr. Joseph S. Perkell, Dr. Stefanie Shattuck-Hufnagel, Dr. Mario A. Svirsky, Dr. Alice Turk, Dr. Reiner Wilhelms-Tricarico, Dr. Yi Xu, Seth M. Hall

Visiting Scientists and Research Affiliates

Dr. Corine A. Bickley, Dr. Suzanne E. Boyce,¹ Dr. Anna Esposito,² Dr. Carol Espy-Wilson,³ Dr. Robert E. Hillman,⁴ Dr. Eva B. Holmberg,⁴ Dr. Caroline Huang,⁵ Dr. Harlan Lane,⁶ Dr. John I. Makhoul,⁷ Dr. Sharon Y. Manuel, Dr. Melanie L. Matthies,³ Dr. Pascal H. Perrier,⁸ Dr. David R. Williams,⁹ Jane W. Wozniak⁴

Graduate Students

Hwa-Ping Chang, Marilyn Y. Chen, Karen Chenausky, Harold Cheyne, Jeung-Yoon Choi, Michael Harms, David M. Horowitz, Mark A. Johnson, Hong-Kwang J. Kuo, Sharlene A. Liu, Kelly L. Poort, Walter Sun, Lorin F. Wilde

Undergraduate Students

Max Chen, Howard Cheng, Laura C. Dilley, Genevieve Lada, Zöe Park, Edward D. Semper, Hemant Tanaja

Technical and Support Staff

Peter C. Guiod, Glenn S. LePrell, D. Keith North,¹⁰ Arlene E. Wint

Sponsors

C.J. Lebel Fellowship
Dennis Klatt Memorial Fund
National Institutes of Health
Grant F32-DC00194
Grant F32-DC00205
Grant P01-DC00361¹¹
Grant R01-DC00075
Grant R01-DC00261¹¹

National Institutes of Health
Grant R01-DC00266¹¹
Grant R01-DC01291
Grant R01-DC01925
Grant R03-DC01721
Grant R29 DC02525
Grant T32-DC00038

¹ Delrina, Boston, Massachusetts.

² Department of Physics, Salerno University, Italy.

³ Boston University, Boston, Massachusetts.

⁴ Massachusetts Eye and Ear Infirmary, Boston, Massachusetts.

⁵ Altech Inc., Cambridge, Massachusetts, and Boston University, Boston, Massachusetts.

⁶ Department of Psychology, Northeastern University, Boston, Massachusetts.

⁷ Bolt, Beranek and Newman, Inc., Cambridge, Massachusetts.

⁸ Institut de Communication Parlé Grenoble, France.

⁹ Sensimetrics Corporation, Cambridge, Massachusetts.

¹⁰ Deceased February 9, 1995.

¹¹ Under subcontract to Massachusetts Eye and Ear Infirmary.

National Science Foundation
Grant INT 94-21146¹²
Grant IRI 89-05439¹³

1.1 Studies of Normal Speech Production

1.1.1 Speech Motor Control: Phonemic Goals and the Use of Feedback

Two oral presentations contained the following theoretical overview of speech motor control along with examples of supporting data from studies of articulatory-to-acoustic motor equivalence and changes in the hearing status of cochlear implant and NF2 patients.

Much of the information content in speech is conveyed by phonemic mechanisms, which consist of neuro-muscular synergisms that achieve segmental articulatory and acoustic goals. Some of the goals are determined by quantal (nonlinear) relations between articulation and sound. The goals may also be influenced by other principles, such as a compromise between sufficient perceptual contrast and economy of articulatory effort. This leads to the prediction that the goal definitions correspond to regions (as opposed to points) in acoustic and articulatory space. Thus the goals are characterized by some parameter variation, which is possible in part because listeners can understand variable speech. The speech motor control system includes a number of phonemic mechanisms, organized in a modular, hierarchical fashion.

When utterances are produced, sequences of goal specifications are converted to smooth, appropriately-timed articulatory movements by the control system, which takes into account the biomechanical properties of the articulators. To help keep acoustic variability within perceptually-acceptable limits, speech motor control mechanisms may include a strategy by which different parts of the vocal-tract area function are adjusted in a complementary ("motor equivalent") manner. This strategy takes advantage of the fact that for some sounds, a similar acoustic transfer function can be achieved with somewhat different area functions. The existence of such a strategy and the idea that speech motor programming is based in part on acoustic goals are supported by data that show motor equiv-

alent relations between lip and tongue constrictions in production of the sounds /u/, /r/ and /ɜ/. The strategy also implies that speech motor programming relies on the use of a robust internal model for feedforward control. The internal model represents relations between speech motor commands and the sound output.

Information about the relation between speech motor commands and the sound output is established during speech acquisition with the use of auditory feedback. The role of auditory feedback for speech production in adults is unclear, since the speech of people deafened as adults can remain intelligible for decades. However, their speech often develops abnormalities, indicating some role for auditory input in adult speech motor control. Studies of changes in speech production when postlingually-deafened patients receive cochlear implants have led us to hypothesize that auditory feedback has at least two functions in adult speech motor control. These are: (1) maintenance of the information represented in the internal model, and (2) monitoring the transmission channel to help make situation-dependent adjustments in "postural" settings of parameters that underlie average sound level, speaking rate, voice fundamental frequency, and vowel formants, which influence clarity and intelligibility. By inference, phonemic settings should be less labile than postural settings. Since phonemic settings and postural settings affect the same articulators, there can be interactions between them, but in some cases their changes can be observed separately.

1.1.2 Lip Protrusion Movements in Normal versus Clear Speech

A kinematic analysis of midsagittal movement (EMMA) data was performed for upper lip protrusion from /i/ to /u/ in /iku/, /ikku/ and /iktku/, produced by a speaker of American English. Utterances were embedded in a carrier sentence and spoken in four conditions: normal rate, normal rate and clear, fast rate, fast rate and clear. The results show several regularities across all conditions: (1) the delay between the protrusion onset and the acoustic onset of /u/ varies linearly with the vowel-to-vowel duration (VVD), /i/-end to /u/-onset, with a slope of 0.7; (2) the overlap between the protrusion movement and vowel /i/ decreases as VVD increases, with no significant differences between

¹² U.S.-India Cooperative Science Program.

¹³ Under subcontract to Boston University.

conditions for similar VVD values; (3) the relationship between the ratio of maximum velocity (V_{max}) to protrusion amplitude (Amp) and the movement duration (T) is constant: $V_{max}/Amp=c/T$; (4) the number of velocity peaks increases linearly with VVD. These regularities suggest that the same control strategy underlies the protrusion gesture, whatever the condition. However, for a given rate, clear tokens were produced with longer VVDs and larger protrusion amplitudes. For similar VVD values, fast clear tokens had larger values of V_{max} than normal tokens.

1.1.3 Physiological Modeling of Speech Production

For a computational finite element tongue model, a new finite element type was implemented experimentally, using Matlab and C subroutines. The code computes triquadratic interpolation of the displacements from 27 nodes per element, and a pressure field that is represented as linear function with four coefficients. All computations are vectorized. The total system of equations constitutes a mixed differential and algebraic system. The differential equations result from the dynamics of the system, and the purpose of the algebraic equations is to determine, for each element, four coefficients of a pressure field, such that each element's incompressibility condition is maintained. To solve the large system of equations, the previously used explicit method is being replaced by an implicit algorithm that is based on the conjugate gradient method.

One goal of the biomechanical vocal tract modeling is to emulate the morphological characteristics of individual speakers. For this purpose, MRI data are used to obtain data on the individual speaker, beginning with the extraction of vocal tract shapes (area functions). Software has been developed that loads three sets of MRI data, representing sagittal, coronal, and transversal series of slices of the oral and pharyngeal region of a subject who maintains an articulatory posture for a vowel or consonantal constriction. The spatial locations and spatial ranges of the three data sets are adjusted so that, at any spatial location, maximal similarity is achieved. The adjustment method is semi-automatic: initial values are set interactively using visual feedback; then an iterative search tries to maximize a quantitative measure of similarity (a binary correlation measure, formed as the relative number of equal bits in two thresholded images). The next stage extracts connected regions in the three-dimensional stacks of MRI images and eliminates the smallest (spurious) regions. For the final step, software has been implemented for regions growing in three dimensions and for hand-editing

binary images to aid the extraction of the vocal tract shapes. MRI data have been obtained on several speakers. Data from MRIs helps us to make substantial progress in obtaining high quality images.

1.1.4 Improvements in Facilities for Speech Production Research

A number of improvements were made in hardware and software facilities for gathering and analyzing data on articulatory movements. We received a new set of electronics for our EMMA system and new, smaller, pre-wired transducers. The new components were tested extensively, and a number of steps were taken to assure adequate performance. A new procedure was developed to facilitate the mounting of transducers on subjects' articulators. An interface box was designed and constructed to increase the channel capacity of the EMMA real-time display and eliminate interference between the real-time display and output voltages of the EMMA system. Improvements were also made in the functionality of the program for the EMMA real-time display. Several improvements were made in methods for taking and analyzing video recordings of subjects' lip areas. Additional algorithms were developed and used for the interactive, semi-automatic extraction of kinematic and timing data from movement signals.

1.2 Speech Research Relating to Special Populations

1.2.1 Speech Production of Cochlear Implant Patients

Intersyllabic Regulation of F_0 and SPL Both With and Without Auditory Feedback

Syllable-to-syllable fluctuation of F_0 and SPL were measured in readings of a passage by (1) four post-lingually deafened adults, recorded before and after they received cochlear implants, and (2) one adult with neurofibromatosis-2 (NF2), who was initially profoundly deaf in one ear and had a mild to moderate hearing loss in the other (aided). Three of the four cochlear implant users reliably reduced syllable-to-syllable fluctuation in F_0 and SPL following the activation of their speech processors. The fourth speaker began with and maintained the regularity achieved by the others post-activation. In recordings made following the onset of bilateral profound deafness, the NF2 subject showed increased syllable-to-syllable fluctuation in F_0 and SPL.

Results from another experiment¹⁴ in which multiple repetitions of vowels in an /hVd/ context were produced by cochlear implant users with their processors turned off and on, suggest that some subjects showed less token-to-token variability in *F0* and SPL with their processors turned on. The present results indicate that auditory feedback may also constrain the syllable-to-syllable variability of *F0* and SPL contours.

Acoustic and Articulatory Measures of Sibilant Production Both With and Without Auditory Feedback from a Cochlear Implant

The articulator positions of a subject with a cochlear implant were measured with an electro-midsagittal articulometer (EMMA) system both with and without auditory feedback available to the subject via his implant. Acoustic analysis of sibilant productions included specific measures of their spectral properties as well as the *F3* formant amplitude. More general postural characteristics of the utterances such as speech rate and sound level were also measured. Because of the mechanical and aerodynamic interdependence of the articulators, the postural variables must be considered before attributing speech improvement to the selective correction of a phonemic target with the use of auditory feedback. The tongue blade position was related to the shape and central tendency of the /š/. spectra; however, changes in the spectral contrast between /s/ and /š/. were not related to changes in the more general postural variables of rate and sound level. These findings suggest that the cochlear implant is providing this subject with important auditory cues that he can use to monitor his speech and maintain the phonemic contrast between /s/ and /š/.

1.2.2 Acoustic and Perceptual Effects of Endoscopic Nasal Surgery

Past research has shown that some modifications occur in the speech of patients who have undergone endoscopic nasal surgery. These changes have been measured in the spectra of nasal consonants and nasal vowels produced by these individuals. The measurements suggest that the surgery has two effects on the nasal vowels: an increased prominence of spectral peaks, due presumably to the decreased acoustic losses in the modified nasal cavity, and an enhanced influence of sinus resonances in the spectrum. Two of the nasal vowels

produced by the patients were excised from the speech and were presented to listeners, who compared the nasality in the vowels recorded pre- and post-operatively. The vowel /i/ was judged to be less nasal after the surgery and /æ/ sounded more nasal. A theoretical account of this result has been proposed in terms of the two abovementioned effects.

1.2.3 Speech Input for Dysarthric Computer Users

Previous work on this project has reported on the kinds of speech errors made by a group of dysarthric speakers. Errors or inconsistencies in production were especially prevalent for obstruent consonants. Within this class of sounds, the greatest difficulties were experienced for fricatives and affricates produced by forming a constriction with the tongue blade. One goal of this project is to facilitate interaction with computers by these individuals through the use of a speech recognizer. Based on a study of the characteristics of the speech sounds produced by each speaker, a list of words was selected for the speaker to control the computer. The words were designed to avoid the sounds that the speaker was unable to produce consistently. The percent error in recognition of these words for different speakers was 10-35 percent less than the error when the words were randomly selected.

1.2.4 Voice Source Analysis of Speakers with Vocal-Fold Nodules

The purpose of this research is to study the voice production mechanism in patients with vocal-fold nodules in an attempt to understand how they happen. Vocal-fold nodule formation has often been thought to be caused by voice misuse or abuse. This condition can cause partial or total loss of voice and often requires treatment with voice therapy and/or surgery.

Aerodynamic measures for a selected set of five female nodule patients and control subjects were studied and related to published data. The subjects were asked to speak at three levels of voice effort: comfortable, intermediate, and loud. In general, the nodule patients were found to be speaking louder when speaking at comfortable voice effort than the normals. They used increased transglottal pressure, and the glottal flow had a greater AC compo-

¹⁴ M.A. Svirsky, H.L. Lane, J.S. Perkell, and J.F. Wozniak, *J. Acoust. Soc. Am.* 92(3): 1284-1300 (1992).

nent, maximum flow declination rate, and minimum flow.

One nodule patient exhibiting high transglottal pressure and maximum flow declination rate was chosen for more detailed study. This patient had undergone voice therapy. The aerodynamic and acoustic properties of this patient's speech before and after voice therapy were compared, and in general showed a change toward more normal characteristics. Voice therapy appeared to reduce the transglottal pressure used by this patient and increase the speech intensity for a given pressure. The speech before therapy sometimes underwent large changes in amplitude during sustained vowel phonation, and spectral measures show that some of the low amplitude regions were more breathy in character or accompanied by diplophonia in severe cases when the voice "catches." All observations made have been on a small scale and need to be verified for other recordings for this subject as well as other patients who have the same voice pathology.

1.3 Studies of the Acoustics, Perception, and Modeling of Speech Sounds

1.3.1 Effects of Tracheal Resonances on Vowel Spectra

We often observe prominences in the spectra of vowels that are not attributable to natural frequencies of the vocal tract. These irregularities in the spectrum result from acoustic coupling, through the glottis, between the vocal tract and the trachea, and can be modeled as pole/zero pairs introduced into the transfer function between the glottal source and the output at the mouth. The amount of separation between a pole and a zero in such a pair depends on the size of the glottal opening, i.e., the glottal impedance. For different speakers, the average glottal area, and hence the magnitude of the glottal impedance may be different. Thus, tracheal resonances should be more evident in vowel spectra for individuals who phonate with a glottis that remains partially open throughout a glottal cycle. Such individuals are known to exhibit a greater high-frequency tilt in

the glottal spectrum and a greater first-formant bandwidth due to increased acoustic losses at the partially open glottis.

Theoretical analysis suggests that there are two kinds of acoustic evidence for acoustic coupling to the trachea: one is the presence of spectral prominences in addition to the prominences due to vocal-tract resonances, or formants, and the other is the disruption of prominences due to formants as they pass through frequency ranges of tracheal resonances. Acoustic data obtained from vowels produced by 22 female speakers were studied for such evidence of acoustic coupling to the trachea, and were examined in relation to acoustic measures of average glottal opening. The results show that when spectral measures indicate significant glottal openings, evidence for tracheal resonances appear in vowel spectra. The effect of the tracheal resonances on the spectrum is more pronounced for speakers who phonate with a greater average glottal opening.

1.3.2 Estimating the Effects of Acoustic Losses in the Nasal Cavity

Creation of a velopharyngeal opening during vowel production has two major acoustic consequences. One consequence is to shift the frequencies of the vocal-tract resonances or formants and to introduce additional resonances due to the nasal cavities or sinuses. Another influence is to create additional acoustic losses because of the relatively large area of the surfaces of the nasal passages. A theoretical examination of the influence of these losses on the bandwidth of the first formant has been carried out as part of an effort to develop acoustic measures of nasalization. The theory uses as a starting point published acoustic data on the transfer function of the nasal cavity. From these data, the impedance looking into the nasal cavity can be estimated, particularly the resistive component that accounts for the losses. This impedance is connected across the main vocal tract at about its midpoint. The effect of the resistive component of this impedance on the bandwidth of the first formant can then be calculated. The calculations show that the losses in the nasal cavity can lead to a 10 dB decrease in the amplitude of the first-formant peak when there is an appreciable velopharyngeal opening. This decrease in $F1$ amplitude is consistent with acoustic measurements comparing nasal and nonnasal vowels, although some variability in this measure is observed. Perceptual studies with synthetic speech have shown that this increased $F1$ bandwidth is a major contributor to the perception of nasality.

1.3.3 Lateral Consonants

As part of a continuing study of liquid consonants, we have been comparing the acoustic correlates of syllabic /**l**/ (in words like **buckle** and the unstressed syllable nucleus /o/ (in words like **bucko**). We have completed the analysis of several such utterances by four speakers. The principal findings from the analysis are a decreased prominence for the second formant and an increased prominence for the third formant for /**l**/ although there are individual differences in the magnitude of these effects. Perceptual experiments with synthetic speech show that both of these spectral changes are cues for syllabic /**l**/ with the second-formant bandwidth being the stronger cue. The increased *F2* bandwidth can be explained through the analysis of the behavior of models of /**l**/ production, which show that acoustic losses arise from airflow through a narrow constriction formed by the tongue blade.

1.4 Models of Lexical Representation and Lexical Access

1.4.1 Theoretical Background: Representation of Segments in the Lexicon

In a proposed model for lexical access that is under development, lexical items are stored in memory in terms of sequences of segments, each of which is specified as a set of features that are arranged in a hierarchical manner. We have proposed an arrangement of features in a tree-like structure that has three principal nodes which dominate nested sets of articulators. The root node at the top of the tree dominates the production of vowels. The next node in the hierarchy dominates the production of glides, and the lowest node (the supranasal node) dominates nodes designating articulators involved in the production of consonant sounds. The major class features [consonantal] and [vocalic] are specified by designating which of the three primary nodes is dominant. The remaining articulator-free features [continuant] and [strident] are distinctive only for consonants, and they are attached to the node designating the primary articulator for the consonant.

1.4.2 Identification of Landmarks

One component of a proposed model of lexical access is a procedure for locating a sequence of landmarks that identify times at which consonantal closures and releases are produced. The process of locating these landmarks also leads to specification of manner features such as [continuant] and [sonorant] for the consonants.

A consonantal landmark detector has been developed, and its performance has been evaluated for consonants in a variety of contexts, for speech in noise, and for telephone-quality speech. The detector showed relatively few errors for wideband noise-free speech but was more error-prone for consonants occurring in a context with a preceding stressed vowel and a following reduced vowel—a context in which the landmarks are less salient. The detection error rate rose significantly for a signal-to-noise ratio (with speech-shaped noise) of 10 dB or less and also more than doubled with telephone speech relative to wide-band noise-free speech. Improved performance was obtained if the landmark-finding algorithm was adjusted for the specific noise or band-limited condition.

The development of methods for locating consonantal landmarks is being extended to include the detection of landmarks for glide consonants. These consonants do not create abrupt discontinuities in the spectrum, and the landmarks are defined as points in the sound where the vocal tract is maximally constricted for the glide. Algorithms have been developed for locating local minima in amplitude and in first-formant frequency. These algorithms are being evaluated with several databases of utterances, including a group of sentences that have been designed specifically to evaluate landmark detection for glides in various phonetic contexts.

1.4.3 Automatic Measurement of Acoustic Correlates of Place of Articulation for Stop Consonants

In order to identify the distinctive features of a consonant, the acoustic signal must be characterized by an informative set of measurements, which can then be classified. Based on suggestions in the phonetics literature as well as theoretical analysis of consonant production, we have designed a set of acoustic measurements to extract information about the place of articulation of a stop or nasal consonant release. Algorithms were developed to collect four burst shape measurements at a stop release, two measurements of spectral change at a nasal release, and temporal samples of the first three

formant trajectories. These algorithms were designed and optimized manually, and then re-adjusted using a gradient descent algorithm to give minimum classification error on a large data set. Measurements were evaluated in the acoustic domain, and burst spectral measurements were also transformed to a related articulatory domain. Consonant and vowel-dependent shifts predicted by theory were observed in the mean and variance of the inferred articulatory variables.

1.5 Speech Production Planning and Prosody

Our work in speech production planning this year focused on three aspects of our goal of developing an integrated model of segmental and prosodic aspects of planning: (1) development of a corpus of tape-recorded speech errors with special focus on sublexical interaction errors between two sites in an utterance (e.g., phonemic spoonerisms such as "cry to teep" for "try to keep", and anticipatory/perseveratory substitutions such as "pound the focket" for "found the pocket"), and prosodic annotation of this corpus; (2) development and analysis of a corpus of professionally read, nonprofessionally read and spontaneous speech, with prosodic annotation, to permit analysis of glottalization and other phonetic markers of prosodic structure, and (3) continuing expansion and analysis of a prosodically labeled database of professional FM radio newscast speech. Results from analyses of these databases include:

1. Glottalization of vowel-initial syllables, previously shown to occur at prosodically significant locations in read speech, shows a similar pattern in spontaneous dialogues, occurring at the onset of intermediate intonational phrases as well as in conjunction with pitch accents. Although individual speakers differ substantially in their overall glottalization rate, each shows the same tendency to glottalize vowel-initial syllables more often at these prosodically significant locations.
2. Moreover, for most speakers a set of additional acoustic features often accompany this vowel-initial glottalization, including breathy onset, low amplitude and low F_0 . Re-analysis of tokens labeled as nonglottalized showed that these features can occur on their own at the onset of vowel-initial words. When they occur, it is at almost entirely at the same prosodically significant locations, i.e., at phrase onsets and prominent syllables. In conjunction with other work that is being reported from other laboratories,

these findings support the hypothesis that the onset of a prosodic constituent is strengthened.

3. Following up on earlier analyses of early pitch accent within late-stress words like "financial" and "Massachusetts", we found that early pitch accent occurs more consistently for alternating stress words like "Massachusetts" than for adjacent stress words like "financial". We are currently investigating the implications of this result for the role of branching foot structure in pitch accent assignment in English.

1.5.1 Progress in other Aspects of Speech Production Planning

1. We are transferring our corpus of 15,000 spoken errors from index cards to a computerized database, using a categorization system developed cooperatively with Merrill Garrett and Victoria Fromkin. The database will enable rapid searches for errors of certain types, facilitate the testing of large numbers of hypotheses to make it possible to share subsets of errors with the research community in presorted form, reducing the chances that error data will be miscategorized and misinterpreted.
2. We participated in the Workshop on Prosodic Transcription which preceded the International Congress of Phonetic Sciences in Stockholm in August 1995. We also began a collaborative effort which we hope will lead to an extension of our analysis of glottalization of vowel-initial syllables as a function of prosodic structure to examples in a prosodically labeled database of spoken German.

1.6 Development of Computer and Data Processing Facilities

We have completed the port of the Klatt Analysis Tools to the X11 environment and the integration of the Klatt speech synthesis utility, KLSYN, into the overall suite of Klatt Tools. This work completes a total integration of all the Klatt Tools used by the Speech Group into one seamless application package (called XKL), which is now available to the general research community in the X11 distributed graphics environment. Further ports of XKL have been done for the Sun and Silicon Graphics workstation environments, and a Project Athena port is in progress. The RLE Speech Group has continued to make increasing use of the new generation of very high performance RISC architecture UNIX workstations for signal analysis and biomechanical

modeling, as well as general purpose data analysis using MATLAB, PERL and the Entropics tool package. Work has begun on the migration of the speech physiology VAX-based real-time data acquisition and stimulus presentation hardware and software to a Pentium-based PC platform.

1.7 Publications

1.7.1 Published Papers

- Chen, M. "Acoustic Parameters of Nasalized Vowels in Hearing-impaired and Normal-hearing Speakers." *J. Acoust. Soc. Am.* 98 (5): 2443-2453 (1995).
- Dilley, L., and S. Shattuck-Hufnagel. "Variability in Glottalization of Word Onset Vowels in American English." *Proceedings of the International Congress of Phonetic Sciences*, Stockholm, Sweden, 1995, vol. 4, pp. 586-589.
- Hanson, H.M. "Individual Variations in Glottal Characteristics of Female Speakers." *Proceedings of the IEEE ICASSP*, Detroit, Michigan, 1995, vol. 1, pp. 772-775.
- Hanson, H.M., and K.N. Stevens. "Sub-glottal Resonances in Female Speakers and their Effect on Vowel Spectra." *Proceedings of the International Congress of Phonetic Sciences*, Stockholm, Sweden, 1995, vol. 3, pp. 182-185.
- Holmberg, E.B., R.E. Hillman, J.S. Perkell, and S. Goldman. "Comparisons Among Aerodynamic, Electroglossographic, and Acoustic Spectrum Measures of Female Voices." *J. Speech Hear. Res.* 38: 1212-1223 (1995).
- Lane, H., J. Wozniak, M.L. Matthies, M.A. Svirsky, and J.S. Perkell. "Phonemic Resetting vs. Postural Adjustments in the Speech of Cochlear Implant Users: An Exploration of Voice Onset Time." *J. Acoust. Soc. Am.* 98: 3096-3106 (1995).
- Liu, S.A. "The Effect of Vowel Reduction on Landmark Detection." *Proceedings of the International Congress of Phonetic Sciences*, Stockholm, Sweden, 1995, vol. 4, pp. 136-139.
- Manuel, S.Y. "Speakers Nasalize /ð/ after /n/, But Listeners Still Hear /ð/." *J. Phonetics* 23: 453-476 (1995).
- Manuel, S.Y., and K.N. Stevens. "Formant Transitions: Teasing Apart Consonant and Vowel Contributions." *Proceedings of the International Congress of Phonetic Sciences*, Stockholm, Sweden, 1995, vol. 4, pp. 436-439.
- Perkell, J.S., J. Manzella, J. Wozniak, M. Matthies, H. Lane, M. Svirsky, P. Guiod, L. Delhorne, P. Short, M. MacCollin, and C. Mitchell. "Changes in Speech Production Following Hearing Loss Due to Bilateral Acoustic Neuromas." *Proceedings of the International Congress of Phonetic Sciences*, Stockholm, Sweden, 1995, vol. 3, pp. 194-197.
- Perkell, J.S., M.L. Matthies, M.A. Svirsky, and M.I. Jordan. "Goal-based Speech Motor Control: A Theoretical Framework and Some Preliminary Data." *J. Phonetics* 23: 23-35 (1995). Also in *Disorders of Motor Speech: Assessment, Treatment, and Clinical Characterization*. Baltimore: Paul H. Brookes, 1995, pp. 27-42.
- Poort, K.L. "Stop Consonant Production: An Articulation and Acoustic Study." *Proceedings of the International Congress of Phonetic Sciences*, Stockholm, Sweden, 1995, vol. 3, pp. 444-447.
- Shattuck-Hufnagel, S. "Pitch Accent Patterns in Adjacent-stress vs. Alternating-stress Words in American English." *Proceedings of the International Congress of Phonetic Sciences*, Stockholm, Sweden, 1995, vol. 3, pp. 656-659.
- Shattuck-Hufnagel, S. "The Importance of Phonological Transcription in Empirical Approaches to Stress Shift vs. Early Accent." In *Papers in Laboratory Phonology IV: Phonology and Phonetic Evidence*. Eds. B. Connell and A. Arvaniti. Cambridge: Cambridge University Press, 1995, pp. 128-140.
- Sluijter, A.M.C., S. Shattuck-Hufnagel, K.N. Stevens, and V.J. van Heuven. "Supralaryngeal Resonance and Glottal Pulse Shape as Correlates of Stress and Accent in English." *Proceedings of the International Congress of Phonetic Sciences*, Stockholm, 1995, vol. 2, pp. 630-633.
- Stevens, K.N. "Models of Speech Production and Perception." In *European Studies in Phonetics and Speech Communication*. Eds. G. Bloothoof, V. Hazan, D. Huber, and J. Llisterri. The Hague: CIP-Gegeens Koninklijke Bibliotheek, 1995, pp. 52-57.
- Stevens, K.N. "Applying Phonetic Knowledge to Lexical Access." *Proceedings of the Fourth*

European Conference on Speech Communication and Technology, Madrid, Spain, 1995, vol. 1, pp. 3-1.

Wilde, L. "Quantifying Time-varying Spectra of English Fricatives." *Proceedings of the International Congress of Phonetic Sciences*, Stockholm, Sweden, 1995, vol. 4, pp. 120-123.

Wilhelms-Tricarico, R. "Physiological Modeling of Speech Production: Methods for Modeling Soft-tissue Articulators." *J. Acoust. Soc. Am.* 97(5): 3085-3098 (1995).

Wilhelms-Tricarico, R. and J.S. Perkell. "Biomechanical and Physiologically-based Speech Modeling." *Proceedings of the International Congress of Phonetic Sciences*, Stockholm, 1995, vol. 2, pp. 68-75.

Xu, Y. "The Effect of Emphatic Accent on Contextual Tonal Variation." *Proceedings of the International Congress of Phonetic Sciences*, Stockholm, Sweden, 1995, vol. 3, pp. 668-671.

1.7.2 Papers Accepted for Publication

Halle, M., and K.N. Stevens. "The Postalveolar Fricatives of Polish." *Festschrift for Osamu Fujimura*, Mouton de Gruyter. Forthcoming.

Hillman, R.E., E.B. Holmberg, J.S. Perkell, J. Kobler, P. Guiod, C. Gress, and E.E. Sperry. "Speech Respiration in Adult Females with Vocal Nodules." *J. Speech Hear. Res.* Forthcoming.

Lane, H., J. Wozniak, M.L. Matthies, M.A. Svirsky, J.S. Perkell, M. O'Connell, and J. Manzella. "Regularity of Fundamental Frequency and Amplitude Contours with and Without Auditory Feedback." *J. Acoust. Soc. Am.* Forthcoming.

Matthies, M.L., M.A. Svirsky, J.S. Perkell, and H. Lane. "Acoustic and Articulatory Measures of Sibilant Production with and without Auditory Feedback from a Cochlear Implant." *J. Speech Hear. Res.* Forthcoming.

Perkell, J.S. "Properties of the Tongue Help to Define Vowel Categories: Hypotheses Based on Physiologically-oriented Modeling." *J. Phonetics*. Forthcoming.

Perkell, J.S. "Articulatory Processes." In *Handbook of Phonetic Sciences*. Eds. W. Hardcastle and J. Laver. Oxford, England: Blackwell. Forthcoming.

Perkell, J.S., and M.H. Cohen. "Token-to-token Variation of Tongue-body Vowel Targets: The Effect of Context." *Festschrift for Osamu Fujimura*, Mouton de Gruyter. Forthcoming.

Shattuck-Hufnagel, S., and A. Turk. "A Tutorial on Prosody for Investigators of Auditory Sentence Processing." *J. Psycholinguistic Res.* Forthcoming.

Stevens, K.N. "Models of Speech Production." In *Handbook of Acoustics*, Ed. M. Crocker. New York: Wiley. Forthcoming.

Stevens, K.N. "Articulatory-acoustic-auditory Relationships." In *Handbook of Phonetic Sciences*. Eds. W. Hardcastle and J. Laver. Oxford, England: Blackwell. Forthcoming.

Stevens, K.N. "Critique: Articulatory-acoustic Relations and their Role in Speech Perception." *J. Acoust. Soc. Am.* Forthcoming.

Wilhelms-Tricarico, R. "Biomechanical and Physiologically-based Speech Modeling." *J. Phonetics*. Forthcoming.

1.7.3 Papers Submitted for Publication

Chen, M.Y. "Baseline Acoustic Correlates of English and French Nasalized Vowels." Submitted to *J. Acoust. Soc. Am.*

Dilley, L., S. Shattuck-Hufnagel and M. Ostendorf. "Glottalization of Vowel-Initial Syllables as a Function of Prosodic Structure." Submitted.

Hanson, H.M. "Glottal Characteristics of Female Speakers: Acoustic Correlates." Submitted to *J. Acoust. Soc. Am.*

Shattuck-Hufnagel, S. "Acoustic-phonetic Evidence for Prosodic Structure: A Review." An invited contribution to a festschrift.

Svirsky, M.A., K.N. Stevens, M.L. Matthies, J. Manzella, J.S. Perkell, and R. Wilhelms-Tricarico. "Tongue Surface Displacement during Obstruent Stop Consonants." Submitted to *J. Acoust. Soc. Am.*

Theses

- Chang, H.-P. *Speech Input for Dysarthric Computer Users*. Ph.D. diss. Dept. of Mechan. Eng., MIT, 1995.
- Chen, M.Y. *Acoustic Correlates of Nasality in Speech*. Ph.D. diss. Harvard-MIT Division of Health Sciences and Technology, 1995.
- Hanson, H.M. *Glottal Characteristics of Female Speakers*. Ph.D. diss. Division of Applied Sciences, Harvard University, 1995.
- Liu, S.A. *Landmark Detection for Distinctive Feature-Based Speech Recognition*. Ph.D. diss. Dept. of Electr. Eng. and Comput. Sci., MIT, 1995.
- Poort, K.L. *Stop Consonant Production: An Articulation and Acoustic Study*. S.M. thesis, Dept. of Electr. Eng. and Comput. Sci., MIT, 1995.
- Wilde, L.F. *Analysis and Synthesis of Fricative Consonants*. Ph.D. diss. Dept. of Electr. Eng. and Comput. Sci., MIT, 1995.

Section 2 Sensory Communication

Chapter 1 Sensory Communication

Chapter 1. Sensory Communication

Academic and Research Staff

Professor Louis D. Braid, Nathaniel I. Durlach, Professor Richard M. Held, Professor Anuradha M. Annaswamy, Dr. David L. Brock, Dr. Paul Duchnowski, Dr. Donald K. Eddington, Dr. Susan L. Goldman, Dr. Kenneth W. Grant, Dr. Julie E. Greenberg, Dr. Lynette A. Jones, Dr. Jeng-Feng Lee, Dr. Karen L. Payton, Dr. Matthew H. Power, Dr. William M. Rabinowitz, Dr. Christine M. Rankovic, Dr. Charlotte M. Reed, Dr. Wendelin L. Sachtler, Dr. J. Kenneth Salisbury, Dr. Kaoru Sekiyama, Dr. Barbara G. Shinn-Cunningham, Dr. Mandayam A. Srinivasan, Dr. Anne H. Takeuchi, Dr. Thomas E.v. Wiegand, Dr. David Zeltzer, Dr. Patrick M. Zurek, Merry A. Brantley, Andrew R. Brughera, Lorraine A. Delhorne, Dorrie Hall, Seth M. Hall, Coral D. Tassa

Visiting Scientists and Research Affiliates

Dr. G. Lee Beauregard, Dr. Kalman Glantz, Geoffrey L. Plant, Dr. Kouroush Saberi

Graduate Students

Walter A. Aviles, Maroula S. Bratakos, Douglas S. Brungart, Jyh-Shing Chen, Kiran Dandekar, Suvaranu De, Joseph G. Desloge, Jeffrey J. Foley, Eric M. Foxlin, Joseph A. Frisbie, Isaac Graaf, Rogeve J. Gulati, Rakesh Gupta, Chih-Hao Ho, Alexandra I. Hou, Louise Jandura, Owen D. Johnson, Steingrimur P. Karason, Jean C. Krause, Michael A. Leabman, Gregory G. Lin, Kinuku Masaki, Hugh B. Morgenbesser, Philip M. Nadeau, Michael P. O'Connell, John Park, Nicholas Pioch, Balasundara I. Raju, Christopher R. Richardson, John J. Rodkin, David W. Schloerb, Matthew G. Sexton, Nathan R. Shnidman, Jason Sroka, Hong Z. Tan, Kimberly J. Voss, Daniel P. Welker, Elron A. Yellin, John Yoon

Undergraduate Students

Stephen V. Baird, James H. Bandy, Susan E. Born, Erika N. Carmel, Frederick W. Chen, Gail Denesvich, Carmen Ho, Gabrielle Jones, Danielle G. Lemay, Rebecca F. Lippman, David C. Lossos, John J. Novak, T.H. Ogora, Jonathan Pfautz, Sudeep Rangaswamy, Frederick L. Roby, Jonathan R. Santos, Ranjini Srikanthiah, Lukasz A. Weber, Evan F. Wies

Technical and Support Staff

Ann K. Dix, David S. Lum, Eleanora M. Luongo, Francis G. Taylor

1.1 Introduction

The Sensory Communication Group is interested in understanding sensorimotor and cognitive processes and exploiting this understanding to solve practical problems in a variety of application domains. Our basic research is characterized by behavioral (psychophysical) experimentation and quantitative theoretical modeling. Facilities to support this research are developed as needed. Although some research is conducted on vision, most of the group's work is focused on audition or tacton. The main applications are concerned with aiding individuals who suffer from impaired hearing, developing improved human-machine interfaces for virtual environments and teleoperation (virtual reality), and the use of virtual environment technology for training. The main facilities of the group are associated with the psychoacoustics, touch (or haptics), and virtual environment laboratories.

In the following discussion, research is organized according to the sources of funding provided to our group. Thus, work on hearing and touch, and to a certain extent vision, is described in a variety of subsections in a variety of funding contexts.

1.2 Hearing Aid Research

Sponsor

National Institutes of Health
Grant RO1 DC00117

Project Staff

Professor Louis D. Braid, Dr. Paul Duchnowski, Dr. Karen L. Payton, Dr. Matthew H. Power, Dr. Christine M. Rankovic, Dr. Charlotte M. Reed, Dr. Patrick M. Zurek, Jeffrey J. Foley, Isaac Graaf, Jean C. Krause, T.H. Ogora, Jason Sroka

1.2.1 Specific Aims

Our long-term goal is to develop improved hearing aids for people suffering from sensorineural hearing impairments. Our efforts are focused on problems resulting from inadequate knowledge of the effects of various alterations of speech signals on speech reception by impaired listeners. Specifically, we seek to increase our knowledge of the fundamental limits to speech reception improvement achieved through speech processing.

Our aims are:

1. To assess the relative contribution of various functional characteristics of hearing impairments to reduced speech-reception capacity.
2. To evaluate the effect of the manner of speech articulation and variability in the production on speech reception by hearing-impaired listeners.
3. To develop and evaluate analytical models that can predict the effect of a variety of alterations of the speech signal on intelligibility.
4. To develop and evaluate signal processing techniques that might increase the effectiveness of hearing aids.

1.2.2 Characteristics of Sensorineural Hearing Impairment

Simulation of Sensorineural Hearing Loss

An accurate perceptual model of sensorineural hearing loss could assist clinicians and others who deal with hearing-impaired listeners to experience the effects of hearing impairment. It may also provide insight into the design of hearing aids intended to overcome these effects. Although there is no satisfactory model of sensorineural hearing

impairment, several *functional models* that allow listeners with normal hearing to experience the perceptual distortions and speech-reception problems of hearing-impaired listeners are emerging. Our past work¹ has documented the effectiveness of masking noise that elevates the tone-detection thresholds of normal-hearing listeners to those of listeners with hearing impairments in simulating limitations on speech-reception associated with the impairment. More recently, Duchnowski and Zurek² have shown that a type of multiband amplitude expansion proposed by Villchur³ is also capable of simulating these limitations. Both the noise and expansion simulations of hearing loss are addressed nominally at the minimal factors of audibility and abnormal loudness growth. These simulations differ both with respect to phenomenological realism and in the relation of the acoustic properties of processed stimuli to the normal listener's hearing. Moreover, they may differ with respect to secondary psychoacoustic variables. Our research helps determine the relative importance of these variables.

In previous work,⁴ we have shown that many of the perceptual effects of sensorineural hearing loss can be simulated for listeners with normal hearing using spectrally-shaped masking noise or multiband expansion amplification. Current research is exploring the use of these simulations to interpret the results of studies of signal processing techniques under consideration for use in hearing-aids. During the past year we applied the simulations to a popular two-band wide-dynamic range compression hearing aid that has been studied

-
- 1 P.M. Zurek and L.A. Delhorne, "Consonant Reception in Noise by Listeners with Mild and Moderate Hearing Impairment," *J. Acoust. Soc. Am.* 82: 1548-1559 (1987).
 - 2 P. Duchnowski and P.M. Zurek, "Villchur Revisited: Another Look at AGC Simulation of Recruiting Hearing Loss," *J. Acoust. Soc. Am.* 98: 3170-3181 (1995).
 - 3 E. Villchur, "Electronic Models to Simulate the Effect of Sensory Distortions on Speech Perception by the Deaf," *J. Acoust. Soc. Am.* 62: 665-674 (1977).
 - 4 P.M. Zurek and L.A. Delhorne, "Consonant Reception in Noise by Listeners with Mild and Moderate Hearing Impairment," *J. Acoust. Soc. Am.* 82: 1548-1559 (1987); P. Duchnowski and P.M. Zurek, "Villchur Revisited: Another Look at AGC Simulation of Recruiting Hearing Loss," *J. Acoust. Soc. Am.* 98: 3170-3181 (1995); S.V. DeGennaro and L.D. Braida, "Effects of Linear Amplification and Amplitude Compression on Sentence Reception by Listeners with Hearing Loss Simulated by Masking Noise," in *Modelling Sensorineural Hearing Loss*, ed. W. Jesteadt (Mahwah, New Jersey: L. Earlbaum Assoc., 1996); D.S. Lum and L.D. Braida, "DSP Implementation of a Real-Time Hearing Loss Simulator Based on Dynamic Expansion," in *Modelling Sensorineural Hearing Loss*, ed. W. Jesteadt. (Mahwah, New Jersey: L. Earlbaum Assoc., 1996).

recently.⁵ In our study, sentences in background noise were processed with either a dual-channel compression system or a linear amplification system and presented to the simulated normal listeners. The systems were implemented to employ the same cutoff frequency and gain functions as the aids used in the Moore et al. study.

Two normal hearing listeners were used to simulate the impairment of each of two hearing-impaired participants in the Moore et al. study. These participants were selected as having achieved relatively large gains from compression amplification relative to linear amplification. Each listener was tested with both the expansion and the additive noise simulations. The speech reception thresholds (SNR at which the listener scores 50 percent of the words correct) of the simulated normal listeners aided by both a compression system and a linear system were obtained. These SRTs were compared to the corresponding SRTs of the aided hearing-impaired individuals.

Although the small number of listeners tested does not allow for a statistical analysis of the results, some trends were observed in the performance of the simulated normals. First, linear amplification produced lower SRTs than amplitude compression in seven out of eight situations. This is in marked contrast with findings of Moore et al.: both hearing-impaired individuals had SRTs that were about 2 dB lower with compression than with linear processing. Second, SRTs were lower with the expansion simulation than with additive noise in seven of eight situations. A quantitative comparison of the SRTs in the two studies is not possible due to several differences in the experimental set-up, e.g., sentences presented monaurally in this study, but binaurally in the Moore et al. study.

Future work will focus on the discrepancy in the relative performance of linear amplification and compression amplification processing systems for listeners with real and simulated sensorineural hearing loss. We plan to implement the speech processing systems in real time to determine

optimal signal processing parameters for both systems. If linear amplification is found consistently to out-perform amplitude compression for the simulated normals, then we will attempt to identify the source of the discrepancy and investigate other methods of simulating the hearing loss.

1.2.3 Characteristics of the Speech Signal

Models of Speech Intelligibility

Models of speech intelligibility can help quantify those aspects of the speech signal that are essential for communication. Unlike the articulation index (AI),⁶ which bases predictions of speech intelligibility on the long-term power spectrum of speech, the speech transmission index (STI)⁷ bases predictions on the intensity modulation spectra for individual frequency bands. This distinction is fundamental to the understanding of the dependence of intelligibility on speaking mode. Whereas clear and conversational speech have roughly the same long-term spectrum,⁸ they are likely to have different modulation spectra because of differences in speaking rate and consonant-vowel energy (CV) ratios. Also the effects of reverberation and multiband amplitude compression on the speech signal are likely to be more evident in the intensity modulation spectra than in the power spectrum.

We are developing a method of calculating the Speech Transmission Index from measurements made on real speech waveforms. We have continued to develop techniques to remove noise-induced artifacts in speech envelope spectra. After several unsuccessful attempts to predict the artifacts and subsequently remove them, we chose to alter our approach. We investigated means to predict when the artifacts would dominate the envelope spectra and thus specify an upper modulation frequency limit for our spectra. We found that reliable Modulation Transfer Functions (MTFs) could be computed from speech envelope spectra if we computed the coherence function and used it to

⁵ B.C.J. Moore, J.S. Johnson, T.M. Clark, and V. Pluinage, "Evaluation of a Dual-Channel Full Dynamic Range Compression System for People with Sensorineural Hearing Loss," *Ear Hear.* 13: 349-370 (1992).

⁶ R.L. Dugal, L.D. Braida, and N.I. Durlach, "Implications of Previous Research for the Selection of Frequency-Gain Characteristics," in *Acoustical Factors Affecting Hearing Aid Performance and Measurement*, eds. G.A. Studebaker and I. Hochberg (New York: Academic Press, 1980).

⁷ T. Houtgast and H.J.M. Steeneken, "A Review of the MTF Concept in Room Acoustics and Its Use for Estimating Speech Intelligibility in Auditoria," *J. Acoust. Soc. Am.* 77: 1069-1077 (1985).

⁸ M.A. Picheny, N.I. Durlach, and L.D. Braida, "Speaking Clearly for the Hard of Hearing II: Acoustic Characteristics of Clear and Conversational Speech," *J. Speech Hear. Res.* 29: 434-446 (1986).

indicate a modulation frequency limit.⁹ A coherence criterion level of 0.8 was found to be appropriate for clear and conversational speech in noise. This same criterion level was also found to truncate reverberant speech envelope spectra in both speaking styles at appropriate modulation frequencies to remove the artifacts seen there.

We plan to compare the Speech Transmission Index (STI) computed from our truncated MTFs with those computed theoretically for the experimental conditions reported by Payton et al.¹⁰ In addition, we plan to compute the envelope spectra of amplitude compressed speech and amplitude compressed noisy speech. STIs derived from these amplitude compressed signals will be compared with intelligibility scores obtained for the same conditions.

1.2.4 Clear Speech

Although our previous studies¹¹ demonstrated that clear speech is generally more intelligible than conversational speech, it is also generally enunciated more slowly. This complicates the problem of determining what is responsible for the difference in intelligibility. Moreover, the degree to which the reduction in speaking rate is essential to clarity has not been established. To improve our understanding of the role of speaking rate in determining intelligibility, Krause¹² trained talkers with significant speaking experience to produce clear and conversational speech at slow, normal, and quick rates. In addition, each talker was provided feedback on intelligibility on a sentence by sentence basis in order to elicit the clearest possible speech at each speaking rate.

Intelligibility tests used nonsense sentences lacking in semantic context and were presented in a background of speech-spectrum noise. Key word scores indicated that clear speech was more intelligible than conversational speech at speaking rates up to roughly 200 wpm. When the speaking rate exceeded 200 wpm, the intelligibility of both clear and conversational speech declined, suggesting that there may be physiological limitations on clarity at high speaking rates. These results suggest that acoustical factors other than reduced speaking rate are responsible for the high intelligibility of clear speech.

We plan to characterize the acoustical differences between clear and conversational speech produced at the same speaking rate. Our new database of clear and conversational speech will be phonetically segmented and labeled. Several short-term acoustic differences between clear and conversational speech will be investigated for their effect on intelligibility. For example, the consonant-to-vowel ratios (CVR) found in clear speech are substantially greater than those in conversational speech.¹³ Recently, two studies have reported an intelligibility improvement due to artificial CVR increase for nonsense syllables presented to impaired listeners.¹⁴

1.2.5 Signal Processing For Hearing Aids

Frequency-lowering individuals who experience severe hearing losses at high frequencies typically experience difficulty understanding speech because they are unable to distinguish between consonants whose spectra differ primarily at these frequencies. Although there have been many attempts to use frequency lowering techniques to improve the audibility of these differences, few have produced net improvements in speech perception. Posen et

⁹ K.L. Payton and L.D. Braida, "Speech Modulation Transfer Functions for Different Speaking Styles," *J. Acoust. Soc. Am.* 98: 2982 (1995).

¹⁰ K.L. Payton, R.M. Uchanski, and L.D. Braida, "Intelligibility of Conversational and Clear Speech in Noise and Reverberation for Listeners with Normal and Impaired Hearing," *J. Acoust. Soc. Am.* 95: 1581-1592 (1994).

¹¹ M.A. Picheny, N.I. Durlach, and L.D. Braida, "Speaking Clearly for the Hard of Hearing II: Acoustic Characteristics of Clear and Conversational Speech," *J. Speech Hear. Res.* 29: 434-446 (1986); R.M. Uchanski, S. Choi, L.D. Braida, C.M. Reed, and N.I. Durlach, "Speaking Clearly for the Hard of Hearing IV: Further Studies of the Role of Speaking Rate," *J. Speech Hear. Res.*, forthcoming.

¹² J.C. Krause, *The Effects of Speaking Rate and Speaking Mode on Intelligibility*, S.M. thesis, Dept. of Electr. Eng. and Comput. Sci., MIT, 1995.

¹³ M.A. Picheny, N.I. Durlach, and L.D. Braida, "Speaking Clearly for the Hard of Hearing II: Acoustic Characteristics of Clear and conversational Speech," *J. Speech Hear. Res.* 29: 434-446 (1986).

¹⁴ A.A. Montgomery and R.A. Edge, "Evaluation of Two Speech Enhancement Techniques to Improve Intelligibility for Hearing-impaired Adults," *J. Speech Hear. Res.* 29: 434-446 (1986); S. Gordon-Salant, "Effects of Acoustic Modification on Consonant Perception by Elderly Hearing-impaired Subjects," *J. Acoust. Soc. Am.* 77: S106 (1986).

al.¹⁵ recently demonstrated that channel vocoding could be used to superimpose cues that enhanced the ability to make distinctions among such consonants at low frequencies where hearing is often less impaired. To facilitate future studies of this technique, Foley¹⁶ implemented Posen's vocoder system digitally using a Motorola DSP96002 DSP and Ariel DSP96 signal processing board suitable in one of our laboratory PCs. This implementation allows greater flexibility and precision in the selection of vocoder filters and the determination of speech levels, and also allows for monitoring and dynamic adjustment of processing parameters.

1.2.6 Publications

DeGennaro, S.V., and L.D. Braida. "Effects of Linear Amplification and Amplitude Compression on Sentence Reception by Listeners with Hearing Loss Simulated by Masking Noise." In *Modelling Sensorineural Hearing Loss*. Ed. W. Jesteadt. Mahwah, New Jersey: L. Earlbaum Assoc., 1996.

Duchnowski, P., and P.M. Zurek. "Vilchur Revisited: Another Look at AGC Simulation of Recruiting Hearing Loss." *J. Acoust. Soc. Am.* 98: 3170-3181 (1995).

Lum, D.S., and L.D. Braida. "DSP Implementation of a Real-Time Hearing Loss Simulator Based on Dynamic Expansion." In *Modelling Sensorineural Hearing Loss*. Ed. W. Jesteadt. Mahwah, New Jersey: L. Earlbaum Assoc., 1996.

Maxwell, J.A., and P.M. Zurek. "Feedback Reduction in Hearing Aids." *IEEE Trans. Speech Audio Proc.* 3: 304-313 (1995).

Payton, K.L., and L.D. Braida. "Speech Modulation Transfer Functions for Different Speaking Styles." *J. Acoust. Soc. Am.* 98: 2982 (1995).

Power, M.H., and L.D. Braida. "Consistency among Speech Parameter Vectors: Application to Predicting Speech Intelligibility." Submitted to *J. Acoust. Soc. Am.*

Rankovic, C.A. "Derivation of Frequency-gain Characteristics for Maximizing Speech Reception in Noise." *J. Speech Hear. Res.* 29: 434-446 (1995).

Uchanski, R.M., S. Choi, L.D. Braida, C.M. Reed, and N.I. Durlach. "Speaking Clearly for the Hard of Hearing IV: Further Studies of the Role of Speaking Rate," *J. Speech Hear. Res.* Forthcoming.

Theses

Foley, J.J. *Digital Implementation of a Frequency-Lowering Channel Vocoder*. M.Eng. thesis. Dept. of Electr. Eng. and Comput. Sci., MIT, 1996.

Krause, J.C. *The Effects of Speaking Rate and Speaking Mode on Intelligibility*, S.M. thesis, Dept. of Electr. Eng. and Comput. Sci., MIT, 1995.

1.3 Enhanced Communication for Speechreaders

Sponsor

National Institutes of Health
Grant RO1 DC02032

Project Staff

Professor Louis D. Braida, Dr. Paul Duchnowski, Dr. Susan L. Goldman, Dr. Matthew H. Power, Dr. Anne H. Takeuchi, Lorraine A. Delhorne, Dr. Charlotte M. Reed, Dr. Kaoru Sekiyama, Dr. Kenneth W. Grant, Maroula S. Bratakos, Frederick W. Chen, Joseph A. Frisbie, Gabrielle Jones, Danielle G. Lemay, Rebecca F. Lippman, Philip M. Nadeau, Matthew G. Sexton, Ranjini Srikantiah

1.3.1 Specific Aims

Although speechreading is an essential component of communications for the hearing impaired, under nearly all conditions the ability to communicate through speechreading alone is severely constrained. This is because many acoustic distinctions important to communication are not manifest visually. Supplements derived from the

¹⁵ M.P. Posen, C.M. Reed, and L.D. Braida, "The Intelligibility of Frequency-Lowered Speech Produced by a Channel Vocoder," *J. Rehab. Res. and Dev.* 30: 26-38 (1993).

¹⁶ J.J. Foley, *Digital Implementation of a Frequency-Lowering Channel Vocoder*, M.Eng thesis, Dept. of Electr. Eng. and Comput. Sci., MIT, 1996.

acoustic speech signal have been shown to improve speech reception markedly when the cues they provide are integrated with cues derived from the visible actions of the talker's face. Our long-term goal is to develop aids for individuals with hearing impairments so severe that their communication relies heavily on speechreading.

Our aims are:

1. To develop models of audiovisual integration to quantify how well supplementary signals are integrated with speechreading.
2. To develop and evaluate simplified acoustic signals that can be derived from acoustic speech by signal processing. Such signals would form the basis of new types of hearing aids for listeners with severe hearing impairments.
3. To develop systems for producing and displaying discrete speechreading supplements similar to the "Manual Cued Speech System" that can be derived from the acoustic signal by speech recognition technology. Such supplements would display streams of discrete symbols that would be derived automatically from acoustic speech and presented visually for integration with the speechreading signal.

1.3.2 Studies and Results

Supplements Based on Signal Processing

Acoustic supplements based on the amplitude envelopes of filtered bands of the acoustic speech signal have been shown to improve speech reception via speechreading in normal-hearing listeners.¹⁷ These supplements may also aid a range of hearing-impaired listeners because they place minimal demands on auditory capacities. The use of band envelopes requires only intensive and temporal resolution without the need to resolve fine spectral detail. Furthermore, envelopes can be easily extracted from continuous speech and transposed in frequency to fit the listener's best region of hearing.

Field Studies of Band-Envelope Supplements

These supplements consist of one or more tones whose frequency is in the audible area of the impaired listener and whose amplitude is modulated by the amplitude envelopes of one or more bands of the speech signal. To assess the effectiveness of these supplements in everyday situations, Nadeau¹⁸ programmed wearable DSP-based SiVo Aids¹⁹ to produce these supplements to listeners with severe to profound impairments. Seven impaired listeners who provided audiograms were screened; two of these were selected as likely to benefit more from the amplitude-envelopes than from their own aids (on the basis of data from listeners with normal hearing) and were provided with wearable SiVo aids. Each listener wore the aid for four weeks in each processing condition. Every two weeks the listeners received speechreading tests in the laboratory and completed the PHAB questionnaire to assess reaction to the aid. One listener received substantial benefit from the aid (word scores of 22 percent by speechreading alone, 38 percent for speechreading supplemented by her own aid, 51 percent for the two-tone configuration of the SiVo aid, and 55 percent for the one-tone configuration of the SiVo aid). Her reactions were sufficiently positive that she continues to use the SiVo aid in the one-tone configuration in preference to her own aid. The second listener also was able to make use of the envelope signals (word scores of 43 percent by speechreading alone, 47 percent for the two-tone configuration of the SiVo aid, and 55 percent for the one-tone configuration of the SiVo aid), but received greater benefit from her own hearing aid (a word score of 97 percent). Not surprisingly she has elected to continue using her own aid. A major limitation of this study, aside from the small number of listeners tested, is the inability of the SiVo aid to produce the two-tone signal at sufficiently high levels.

We are in the process of having the SiVo aids modified by their manufacturer, and are in the process of identifying a second set of impaired listeners. We plan to begin a second field trial during summer 1996 and a third six months later.

¹⁷ K.W. Grant, L.D. Braida, and R.J. Renn, "Single Band Amplitude Envelope Cues as an Aid to Speechreading," *Quart. J. Exp. Psych.* 43: 621-645 (1991); K.W. Grant, L.D. Braida, and R.J. Renn, "Auditory Supplements to Speechreading: Combining Amplitude Envelope Cues from Different Spectral Regions of Speech," *J. Acoust. Soc. Am.* 95: 1065-1073 (1994).

¹⁸ P.M. Nadeau, *Amplitude Envelope Cues as an Aid to the Speechreading of Impaired Individuals*, S.M. thesis, Dept. of Electr. Eng. and Comput. Sci., MIT, February 1996.

¹⁹ A. Faulkner, V. Ball, S. Rosen, B.C.J. Moore, and A. Fourcin, "Speech Pattern Hearing Aids for the Profoundly Hearing Impaired: Speech Perception and Auditory Abilities," *J. Acoust. Soc. Am.* 91: 2136-2155 (1992).

Supplements Based on Automatic Speech Recognition

Visual supplements related to the manual cued speech system used in the education of the deaf have been shown to improve speechreading dramatically. These supplements can be derived using the techniques of automatic speech recognition (ASR), a technology that has advanced rapidly during the past decade. Automatically generated cues would not require a speaker to be skilled in cue production, and so could assist a wider variety of individuals in everyday situations. Two major hurdles must be overcome to develop an effective automatic cueing system: the ASR technology used must provide cues with sufficient accuracy; and the cues must be displayed in a manner that can be integrated well with speechreading.

Simulations of Automatic Cueing Systems

Although previous studies of the reception of manual cued speech and the performance of ASR systems suggests that current technology may provide an adequate basis for the design of an automatic cueing system,²⁰ the effects of speech recognition errors and delays associated with the recognition process on cue reception and integration are not well understood.

To estimate the effects of such imperfections we are studying of the reception of simulated cued speech. This simulation is constructed using pre-recorded IEEE sentences that had been phonetically marked and labeled using the acoustic speech signal. Visual cues consisting of static images of the hand of the talker are dubbed onto these recordings. The nominal shapes and positions of the hands are those used in manual cued speech but there is no fluid articulation of movement. The determination of the cues to be superimposed is based on the rules of manual cued speech applied to (possibly) flawed phonetic labels. Three control conditions were included in the tests: SA (speechreading alone), MCS (manual cued speech), and PSC (cues derived from flawless phonetic labels). In the experimental conditions the phone sequence contained 0, 10, or 20 percent errors, with the error pattern corresponding to a Bernoulli process and with phone substitutions corresponding to our measurements of a real recognizer. We also studied the effect of delaying the superimposed cue relative to the facial image by 0-167 ms. A final test used cues derived from

the phone estimates produced by a state of the art phonetic recognizer trained on roughly 1000 sentences produced by the speaker of the sentences. The dubbed materials were presented to two groups of experienced young adult cue receivers.

The first group (four cue receivers) obtained average scores of 25 percent on SA, 78 percent on MCS, and 73 percent on PSC. Scores declined to 59 percent and 49 percent when cues were produced with phone error rates of 10 and 20 percent respectively. The effect of a small delay (0.03 sec) in cue production was negligible when the phone error rate was 20 percent. However scores declined to 37 percent when cues were produced with 20 percent phone errors and 0.1 sec of delay and to 35 percent when for cues produced with 10 percent phone errors and 0.17 sec of delay.

The second group (6 cue receivers, including three members of the first group) obtained slightly higher scores in the control conditions (36 percent with SA, 89 percent with MCS, and 81 percent with PSC). When tested under conditions of random cue delay (± 0.033 sec), their scores declined to 76 percent with no phone error, 69 percent with 10 percent phone errors, and 60 percent with 20 percent phone errors. This group was also tested on cues derived from the recorded acoustical speech signal by a real ASR system. Although 21 percent of the phones produced by the system were in error, word scores averaged 70 percent. Subsequent analyses indicated that the distribution of errors was different for the real recognizer than for the simulated error conditions, i.e., an excess of multiple phone errors occurring in single words.

For both groups of cue receivers differences between scores in the the MCS and PSC conditions were not statistically significant, indicating that subjects were relatively unaffected by the discrete nature of the cues, the faster speaking rate (150 wpm versus 100 wpm) and deviations between the articulated phone sequence and the phoneme sequence corresponding to the orthographic representation of the sentences. Also, while both groups were largely unaffected by superposition delays on the order of 30 ms (whether fixed or random), delays of 100 ms or more were detrimental. This indicates that practical automatic cueing systems must compensate for the delay associated with the time required for the recognition process.

Based on the results of our simulation studies, we have begun to design an real-time cueing system

²⁰ R.M. Uchanski, L.A. Delhorne, A.K. Dix, L.D. Braida, C.M. Reed, and N.I. Durlach, "Automatic Speech Recognition to Aid the Hearing Impaired. Prospects for the Automatic Generation of Cued Speech," *J. Rehab. Res. Dev.* 31, 20-41 (1994).

based on an automatic speech recognizer. This system is intended to facilitate future studies of the application of ASR technology to the automatic cueing application. The initial system is tailored to individual speakers and consists of three parts: the acoustic processor, the phonetic recognizer, and the cue display, each of which is implemented on a separate laboratory PC. The acoustic processor samples the speech waveform (which will be sensed initially by a close-talking microphone) and computes parameters of waveform segments at a frame rate of 100/sec. The speaker-dependent phonetic recognizer, which is based on the Entropic HTK software package, derives estimates of the phone sequence from these parameters. The cue display system buffers a sequence of images of the face of the talker, allowing for delays in the recognition process, superimposing pre-recorded images of the talker's hands with shapes and at positions corresponding to the recognized phone sequence.

We plan to continue our studies of the effects of cue imperfections on the reception of manual cued speech. We also plan to complete the initial development of our experimental automatic cueing system during the Summer of 1996 and to use it as the basis of these studies.

1.3.3 Publications

Takeuchi, A., and L.D. Braida. "Effect of Frequency Transposition on the Discrimination of Amplitude Envelope Patterns." *J. Acoust. Soc. Am.* 97: 453-460.

Takeuchi, A., and L.D. Braida. "Recognition of Envelope Patterns in the Presence of a Distractor: I. Effects of Correlation and Frequency Relation." *J. Acoust. Soc. Am.* 98: 135-141 (1995).

Takeuchi, A., and L.D. Braida. "Recognition of Envelope Patterns in the Presence of a Distractor: II. Effects of Dichotic Presentation and Unmodulated Distractors." *J. Acoust. Soc. Am.* 98: 142-147 (1995).

Theses

Bratakos, M.A. *The Effect of Imperfect Cues on the Reception of Cued Speech*. S.M. thesis, Dept. of Electr. Eng. and Comput. Sci., MIT, 1995.

Nadeau, P.M. *Amplitude Envelope Cues as an Aid to the Speechreading of Impaired Individuals*. S.M. thesis, Dept. of Electr. Eng. and Comput. Sci., MIT, 1996.

1.4 Cochlear Implants

Sponsors

National Institutes of Health
Contract P01-DC00361²¹
Contract N01-DC22402

Project Staff

Professor Louis D. Braida, Lorraine A. Delhorne, Dr. Donald K. Eddington, Dr. William M. Rabinowitz

Most people with profound hearing impairments have lost the ability to translate the acoustic energy of sound into electric signals carried to the brain by the auditory nerve. Cochlear implants bypass the impaired transduction mechanism and directly stimulate the auditory nerve via an electrode array implanted within the cochlea. Our research is directed at understanding the fundamental mechanisms of electroauditory stimulation and using that information to develop cochlear-implant systems for improved speech reception.

During the past year, work has involved initiation of studies on amplitude modulation discrimination and continuing evaluations of speech processors based on the continuous-interleaved-stimulation (CIS) strategy.²² Work in the latter area is described below (and is performed with collaborators listed in section 8 of the following chapter on (signal transmission in the auditory system).

In the latter part of 1994, a prototype portable processor (based on a DSP-56001) became available that could realize some CIS implementations. Two subjects with nine years of previous experience using the standard INERAID sound processor were fit with CIS systems that they have subsequently worn full-time. Measures of speech reception have been obtained longitudinally; all testing is

²¹ Subcontract from Massachusetts Eye and Ear Infirmary. Dr. Joseph P. Nadol, M.D., Principal Investigator.

²² B.S. Wilson, C.C. Finley, D.T. Lawson, R.D. Wolford, D.K. Eddington, and W.M. Rabinowitz, "Better Speech Reception with Cochlear Implants," *Nature* 352: 236-238 (1991).

performed without lipreading. With their INERAID systems, one subject (S1) is an average performer, and the other (S2) is a high performer.

Tests of consonant and vowel identification show learning effects for both subjects. With S1, initial scores with CIS were below INERAID values; over time, however, CIS performance increased and now exceeds INERAID values. S2 showed modest gains with CIS immediately, and further improvements over time. Consonantal feature analyses indicated that both subjects score highest for manner and voicing information and that scores with both CIS and INERAID are similar on these features. Score for place information is lower than that for manner and voicing, but increases with CIS (versus INERAID). This improved reception of place information provides important cues to enhanced perception of spectral shape, and it appears responsible for the overall increases in consonant recognition.

The ability to recognize words in sentences was tested in quiet and in noise. In quiet, S1 was tested with everyday sentences. He scored 36 percent (words correct) with his INERAID, dropped to 14 percent for his initial CIS evaluation, and increased to 70 percent over 24 weeks of CIS use. S2 was tested with more difficult, lower context sentences. He scored 62 percent with his INERAID and showed large and immediate gains with CIS scoring at, and then above, 95 percent.

Speech perception in noise was assessed by presenting sentences against a background of speech-spectrum-shaped noise at specified speech-to-noise ratios (RMS). At +8 dB S/N, S1 shows no gain with CIS (versus time or INERAID). For S2, high scores (above 80 percent) were obtained immediately with CIS; increases to near saturation (over 95 percent) occurred over several weeks of use. At a more difficult +2 dB S/N, a stronger learning effect was evident as performance increased from 35 percent at the time of fitting to about 60 percent after several weeks of use. Comparison to INERAID results indicates that S2's gains with CIS correspond to more than a 6 dB increase in noise tolerance (i.e., CIS at +2 dB exceeds INERAID at +8 dB). Furthermore, his CIS performance is only ~ 7 dB below that of normal-hearing listeners; this level of performance is remarkable, with interesting implications for understanding normal speech perception.

In summary, the data from both subjects show that substantial gains in speech reception have occurred in these CIS trials. The fact that these gains may not be immediate, as S1 clearly shows, reinforces the need for longitudinal studies with wearable

systems. Finally, although we focus on objective measures of speech reception, comments from the subjects indicate that these CIS processors also provide significant enhancements in environmental sound and music perception.

1.4.1 Publications and Conference Presentations

Rabinowitz, W.M., and D.K. Eddington. "Effects of Channel-to-Electrode Mappings on Speech Reception with the Ineraid Cochlear Implant." *Ear Hear.* 16: 450-458 (1995).

Rabinowitz, W.M., D.K. Eddington, J. Tierney, L.A. Delhorne, and M.E. Whearty. "Performance with Wearable CIS Processors." Conference on Implantable Auditory Prostheses, Asilomar, California, August 19-24, 1995.

Rabinowitz, W.M., D.K. Eddington, J. Tierney, and L.A. Delhorne. "Preliminary Evaluations of Cochlear Implantees using a Wearable CIS Processor." *J. Acoust. Soc. Am.* 97: 3346(A) (1995).

1.5 Tactile Communication of Speech

Sponsor

National Institutes of Health/National Institute on Deafness and Other Communication Disorders
Grant 2 R01 DC00126

Project Staff

Lorraine A. Delhorne, Gail Denesvich, Nathaniel I. Durlach, Seth M. Hall, Chih-Hao Ho, Dr. Geoffrey L. Plant, Dr. William M. Rabinowitz, Dr. Charlotte M. Reed, Dr. Mandayam A. Srinivasan, Hong Z. Tan, Jonathan R. Santos

This research is directed towards the development of effective tactual communication devices for individuals with profound deafness or deaf-blindness. Such devices would lead to improved speech reception, speech production, language competence, and awareness of environmental sounds for such individuals and would provide them with a sensory-aid option in addition to hearing aids and cochlear implants. At a more basic scientific level, this research contributes to increased understanding of speech communication, environmental-sound reception, tactual perception, manual sensing, display design, and sensory substitution.

Research in each of four project areas is described below.

1.5.1 Basic Studies of Hand Stimulation and Active Touch

Work in this area includes completion of a device for tactual stimulation, use of this display in studies of information-transfer, and experimental and theoretical work on the discrimination of thickness.

A multifinger positional display was designed to be capable of providing stimulation along a continuum from low-frequency, high-amplitude movements (kinesthetic stimulation) to high-frequency, low-amplitude vibrations (cutaneous stimulation). The device consists of three independent channels interfaced with the fingerpads of the thumb, the index finger and the middle finger. Stimuli from threshold to roughly 50 dB SL can be delivered throughout the frequency range from near DC to above 300 Hz.

With this display, absolute identification experiments were conducted using multicomponent stimuli formed by summing sinusoids from each of three frequency regions that evoked relatively distinct perceptual attributes. These signals were presented to any one or to all three of the digits. Information transfer with this set of signals at durations of 500 and 250 msec was roughly 6.6 bits, and decreased slightly (to 6.0 bits) at a duration of 125 msec.

Identification of stimuli from this set was also examined in a masking paradigm where the stimulus to be identified was preceded and followed by randomly selected signals (drawn from the same set). The optimal stimulus presentation rate was estimated to be approximately 3 items/sec regardless of stimulus duration, and the information-transfer rate was estimated to be approximately 13 bits/sec. This information-transfer rate is roughly the same as the rate achieved by Tadoma users in speech communication.

A study of thickness discrimination has been continued through experimental and theoretical work. An orderly set of results has been obtained on the discrimination of thickness for plastic and steel plates, indicating that the size of the jnd in mm is constant (at roughly 0.3 mm) when reference thickness exceeds some critical value (roughly 1 mm for plastic and 0.25 mm for steel). Below the critical value of reference thickness, the size of the jnd decreases sharply. The experimental results are interpreted in terms of the contributions of kinesthetic and cutaneous cues for bendable versus non-bendable plates and have been successfully modeled using a three-dimensional finite-method analysis of plate deformation.

1.5.2 Evaluation of Wearable Tactile Aids

Research in this area includes evaluation of deaf adult users of wearable tactile aids, tactile training programs with deaf children and adolescents, and development of training materials for use with the Tactaid 7 device.

Speech-reception testing has been conducted on two adults who routinely use the Tactaid 7 device in conjunction with hearing aids. Results indicate that improvements to speechreading provided by the tactile aid or hearing aid are comparable, and that their combined use may lead to small improvements over the use of either aid alone.

Speech-production training using the Tactaid 7 device was provided twice weekly over one year to an 18-year-old male who is congenitally deaf. Tapes of the subject producing /a/-C-/a/ syllables and common words in sentences were made pre- and post-training. The intelligibility of these utterances was examined in listening tests using normal-hearing subjects and indicated significant improvements in intelligibility for the post-training tokens.

Weekly tactile training sessions with three children fitted with the Tactaid 7 device in September 1993 are continuing on a weekly basis during the school year. The training addresses improving the childrens' speech production and speech perception skills using input from the tactile aid. A training program for adults has been developed. The program consists of 22 sessions which present both analytic and synthetic training materials using the Tactaid 7 device.

1.5.3 Development of Improved Tactual Supplements to Speechreading

Work in this area includes continued study of the differences in performance for auditory versus tactual presentation of a single-band envelope cue as a supplement to speechreading. In particular, investigation has continued into the relation between benefits to speechreading with the envelope cue and the psychophysical ability to detect changes in amplitude modulation of a 200-Hz carrier tone. In addition, performance on the reception of consonant segments has been measured in adult tactile aid users to determine the contribution of various features, including voicing, manner, and place, to improvements in speechreading through tactual input.

1.5.4 Study of the Reception of Environmental Sounds through Tactual Displays

Deaf users place a high value on the assistance provided by tactile aids in receiving and interpreting non-speech sounds in the person's environment. The reception of environmental sounds provides a sense of security and connection with the outside world and is associated with a sense of psychological well-being. To date, other researchers have shown relatively little concern about the reception and evaluation of environmental sounds through tactual aids. Our research will focus on development of a test tool for environmental-sound identification as well as on aspects of signal processing and display to enhance the reception of such sounds.

1.5.5 Publications

- Besing, J.M., C.M. Reed, and N.I. Durlach. "A Comparison of Auditory and Tactual Presentation of a Single-Band Envelope Cue as a Supplement to Speechreading." *Seminars in Hear.* 16: 316-327 (1995).
- Plant, G. "Training Approaches with Tactile Aids." *Seminars in Hear.* 16: 394-403 (1995).
- Reed, C.M. "Tadoma: An Overview of Research." In *Profound Deafness and Speech Communication*, pp. 40-55. Eds. G. Plant and K.-E. Spens. London: Whurr Publishers, 1995.
- Reed, C.M., L.A. Delhorne, N.I. Durlach, and S.D. Fischer. "A Study of the Tactual Reception of Sign Language." *J. Speech Hear. Res.* 38: 477-489 (1995).
- Reed, C.M., and L.A. Delhorne. "Current Results of a Field Study of Adult Users of Tactile Aids." *Seminars in Hear.* 16: 305-315 (1995).
- Tan, H.Z., and N.I. Durlach. "Manual Discrimination of Compliance Using Active Pinch Grasp: The Roles of Force and Work Cues." *Percept. Psychophys.* 57: 495-510 (1995).
- Tan, H.Z., N.I. Durlach, W.M. Rabinowitz, C.M. Reed, and J.R. Santos. "Reception of Morse Code through Motional, Vibrotactile, and Auditory Stimulation." *Percept. Psychophys.* Under revision.

Thesis

Denesvich, G. *Identification of Frequency and Amplitude through Cutaneous Stimulation*. S.B. thesis, Dept. of Electr. Eng. and Comput. Sci., MIT, 1995.

1.6 Multimicrophone Hearing Aids

Sponsor

National Institutes of Health
Grant 2 R01 DC00270

Project Staff

Andrew R. Brughera, Joseph G. Desloge, Dr. Julie E. Greenberg, Michael P. O'Connell, Dr. William M. Rabinowitz, Coral D. Tassa, Dr. Patrick M. Zurek

The goal of this research is to determine the improvements that can be made to hearing aids through the use of multiple microphones. In this work, we are developing algorithms for processing the signals from a head-worn microphone array for the primary goal of improving the intelligibility of speech (assumed to arise from a known direction) in the presence of noise and reverberation. Ideally, this intelligibility enhancement would be achieved without compromising the listener's ability to monitor and localize sound sources from all directions. In computer simulations, array processing algorithms are first implemented and evaluated in terms of signal-to-noise improvement. The most promising approaches are then implemented in real-time with wearable devices (tethered to a computer) in the laboratory for evaluation of speech reception in noise and sound localization by normal-hearing and hearing-impaired listeners.

Array signal processing is usually designed to form a single output signal. In the hearing-aid application, however, this design has to be modified. Such a system would not contain the information about the location of sound sources that is normally conveyed primarily by differences between the signals at the two ears. In addition to sound localization ability, binaural hearing provides a sensation of auditory space and improved speech reception in noise. In an attempt to provide the natural benefits of binaural hearing along with improvements from microphone array processing, we have been exploring ways of combining them.

In one project,²³ we explored designs of a fixed four-microphone array in which, by choice of a frequency-dependent parameter, directivity can be traded with fidelity of interaural time delay (the most important binaural cue). At one extreme in this trade, maximal directivity is achieved, while at the other extreme, the outermost microphone signals are simply passed to the two ears. In another project,²⁴ we employed a two-microphone adaptive binaural array, with the microphones worn at the ears.

The signal-processing structure that provided the best combination of intelligibility enhancement, localization performance, and implementation simplicity was one that employed a special case of the trade between directivity and interaural delay. This system results from consideration of psychoacoustic findings showing the importance of low-frequency cues for the binaural tasks of detection, localization, and speech reception. To reflect this importance the threshold tolerance on interaural delay error is set to zero below some cutoff frequency f_{cut} and to infinity above f_{cut} . The resulting system extracts the low-frequency parts of the signals below f_{cut} from the microphones nearest the ears and passes them to their respective outputs. The high-frequency parts of the outputs come from the single-channel output of the array processor.

Measurements with normal-hearing subjects using several microphone-array configurations showed the expected trade between intelligibility and sound localization as the cutoff frequency is varied. With f_{cut} near 700 Hz, both good localization and substantial intelligibility enhancement from array processing can be obtained.

These studies of binaural-output microphone arrays have been strongly encouraging. They indicate that the spatial filtering provided by array processing can be obtained without sacrificing the benefits of binaural hearing. This is especially true of fixed-processing systems, which achieve relatively little directivity at low frequencies. The success of the lowpass/highpass system suggests that a merger of directivity and binaural hearing can be accomplished in a way that is very simple, general (at least for arrays that have microphones near the ears), and flexible. By adjusting f_{cut} , a user could vary the spatial properties of the system from a

focused mode to an omnidirectional mode, depending on the listening condition.

1.6.1 Publications

Desloge, J.G., W.M. Rabinowitz, and P.M. Zurek. "Microphone-Array Hearing Aids with Binaural Output. I. Fixed-processing Systems." Submitted to *IEEE Trans. Speech Audio Proc.*

Welker, D.P., J.E. Greenberg, J.G. Desloge, and P.M. Zurek. "Microphone-Array Hearing Aids with Binaural Output. II. A Two-microphone Adaptive System." Submitted to *IEEE Trans. Speech Audio Proc.*

1.7 Hearing-Aid Device Development

Sponsor

National Institutes of Health
Contract N01 DC-5-2107

Project Staff

Merry A. Brantley, Lorraine A. Delhorne, Dr. Julie E. Greenberg, Michael A. Leabman, Dr. William M. Rabinowitz, Coral Tassa, Dr. Patrick M. Zurek

The overall objective of work under this new contract is to evaluate promising signal processing algorithms for hearing aids under realistic conditions. Progress toward this goal has begun with development of a laboratory-based signal-processing and testing system. Subsequent laboratory evaluations will select signal processing algorithms for implementation in wearable devices, which are being designed and built by Sensimetrics Corporation. Later in the project, field studies of hearing-impaired persons using this device will be conducted to evaluate the effectiveness of algorithms aimed at improving speech reception in background noise, preventing loudness discomfort, and increasing maximum gain without feedback.

1.8 Binaural Hearing

Sponsor

National Institutes of Health

²³ J.G. Desloge, W.M. Rabinowitz, and P.M. Zurek, "Microphone-Array Hearing Aids with Binaural Output. I. Fixed-Processing Systems," submitted to *IEEE Trans. Speech Audio Proc.*

²⁴ D.P. Welker, J.E. Greenberg, J.G. Desloge, and P.M. Zurek, "Microphone-Array Hearing Aids with Binaural Output. II. A Two-microphone Adaptive System," submitted to *IEEE Trans. Speech Audio Proc.*

Project Staff

Nathaniel I. Durlach, Dr. Patrick M. Zurek

The long-term goal of this program is (1) to develop an integrated, quantitative theory of binaural interaction that is consistent with psychophysical and physiological data on normal and impaired auditory systems, and (2) to apply our results to the diagnosis and treatment of hearing impairments. Psychoacoustic studies are currently being conducted on time-dependent mechanisms in lateralization of transient sounds.

1.9 Virtual Environment Technology for Training

Sponsors

U.S. Navy - Office of Naval Research/
Naval Air Warfare Center
Contract N61339-94-C-0087
Contract N61339-95-K-0014
Grant N00014-93-1-1399
Grant N00014-94-1-1079

Project Staff

Walter A. Aviles, James H. Bandy, G. Lee Beauregard, Dr. David L. Brock, Erika N. Carmel, Nathaniel I. Durlach, Rakesh Gupta, Dorrie Hall, Professor Richard M. Held, Alexandra I. Hou, Dr. Lynette A. Jones, Dr. Corrie Lathan, Dr. Jeng-Feng Lee, Hugh B. Morgenbesser, Jonathan Pfautz, Nicholas Pioch, Dr. Wendelin L. Sachtler, Dr. J. Kenneth Salisbury, David W. Schloerb, Dr. Barbara G. Shinn-Cunningham, Dr. Mandayam A. Srinivasan, Lukasz A. Weber, Dr. Thomas E.v. Wiegand, Evan F. Wies, Dr. David Zeltzer

The long-term goal of the virtual environment technology for training (VETT) program is to increase the cost-effectiveness of training through the development and application of virtual-environment technology. The multimodal, interactive, and immersive characteristics of VE systems, combined with their software reconfigurability and ability to generate situations (realistic or intentionally unrealistic) that are optimally matched to a variety of training tasks, strongly suggest that they have great potential for cost-effective training.

1.9.1 Research Testbed

The research testbed efforts have centered on (1) the further development of the VE training tested and (2) the use of this testbed to conduct training experiments.

Efforts in the first area include (1a) the development of improved software for the design and execution of simulations, (1b) the creation of an experimenter's interface for facilitating experimental research on the testbed, and (1c) the incorporation of the Virtual Workbench (described in *RLE Progress Report Number 137*) to serve as a front-end to the testbed for cases in which the task to be trained, or the experimental research to be performed, can be appropriately conceptualized in terms of a workbench metaphor. Efforts in the second area, include (2a) the completion of a baseline simulation for the officer of the deck (OOD) training task, incorporating models for the terrain, water, objects in the water, and the piloting team with which the OOD must interact. In addition to the submarine's visual and dynamic models, other water-bound objects include, geometric models of buoys, range markers, and adventitious marine traffic. The second work area also includes (2b) preliminary evaluations of the OOD simulation by domain experts. Finally, the primary objective of these development efforts, i.e., (2c) training experiments that make use of VE simulation, are currently in progress.

In the following paragraphs we focus on items (1b) and (2a).

Creation of an Experimenter's Interface

The experimenter's interface (EI) was designed to be a generalized top layer of software for facilitating research in a variety of experimental contexts. Development of the EI was guided by a review of the desirable characteristics of experimental systems, some of which include: providing a simple interface to a complex system, ensuring a consistent experimental procedure, enabling a consistent interface despite an evolving set of experimental software and hardware, and limiting the amount of programming overhead and redundant coding involved in data collection.

From the software developer's point of view, the ongoing creation of many different experimental systems means the development of a significant amount of redundant code. Any piece of software

²⁵ Subcontract from Boston University. Professor H. Steven Colburn, Principal Investigator.

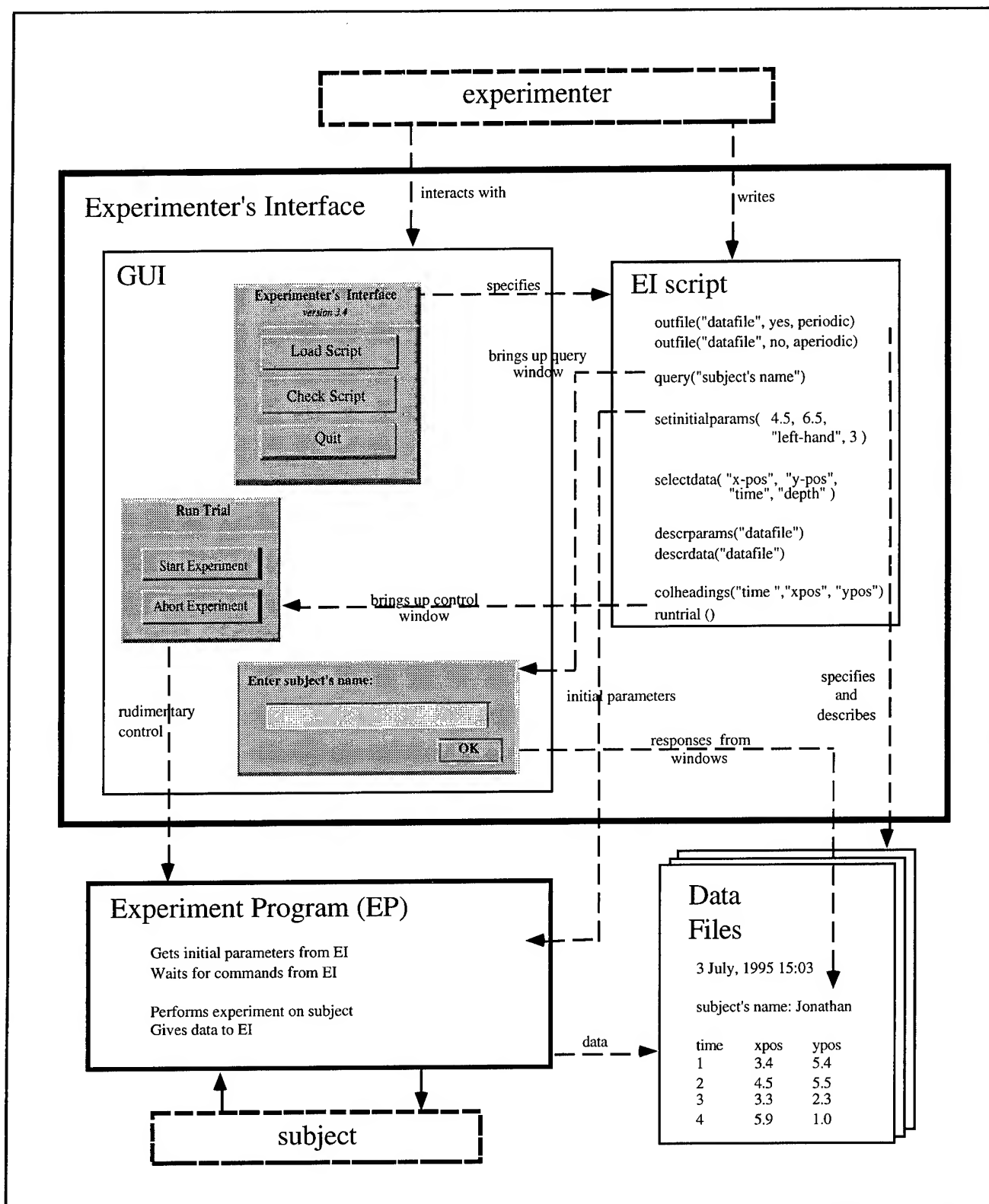


Figure 1. Schematic representation of the Experimenter's Interface. The Experimenter's Interface presents a uniform interface between the experimenter and the VE simulation that is presented to the subject, through the use of a standard set of script commands and a consistent Graphical User Interface. This approach facilitates the separation of simulation development from experimental design.

meant to drive an experiment has certain typical features. By using the EI for experiment specification, experiment control, and data collection, time and resources can be freed for other tasks. The EI also encourages lucid and consistent software design techniques since software engineers need to sufficiently modularize their code to efficiently utilize the EI interface. An additional advantage of using the EI is that more features will continue to be added over time, whereby it will evolve into a comprehensive top level interface for future experiments. Figure 1 depicts a schematic representation of the EI as currently used in the OOD experiments.

Completion of a Baseline Simulation for the OOD Task

In the OOD task, most information is received visually by observing the current configuration of shoreline and navigation aids relative to the submarine (see figure 2). Occasionally, verbal course information is sent by the chief navigator, and spoken acknowledgments of the OOD's commands are given by the helmsman. However, the OOD must be able to independently confirm the suggestions of the piloting team, and in addition, must be trained to perform this task independent of the piloting team in the event of on-board communication problems. Therefore, in the VE, the primary mode of output to the trainee is visual imagery, and spoken output to the trainee is secondary.

On the other hand, the OOD is only able to have an effect on the environment through a well-defined set of verbal commands that are issued to the helmsman. The implications for the VE system, then, are that the primary mode of input from the trainee is speech, which requires a speech recognition system and some degree of natural language understanding. Finally, tracking the head movements of the trainee is necessary to update the visual display from the appropriate point of view.

Creating a true-to-life model of every facet of this simulation in a single pass is an intractable undertaking. To facilitate software development, an evolutionary prototyping approach was employed in which a modular task analysis forms the framework from which incremental subtasks and added levels of detail can be derived. For example, it was decided that the first OOD simulator prototype would include the sequential task elements of centerline alignment, turning aid identification, and turn execution, while leaving secondary features such as water currents and moving traffic to be incorporated later.

Within these initial constraints, and in consultation with various domain experts, including submarine officers serving as instructors from the U.S. Navy Submarine School, the initial goals of the baseline simulation have been achieved. Overall, these officers showed considerable enthusiasm for the OOD simulator, including its potential for use as an on-board mission rehearsal system. We are currently in the process of analyzing results of the training experiments conducted with the completed baseline simulation, and are planning extensions to the experimental protocol.

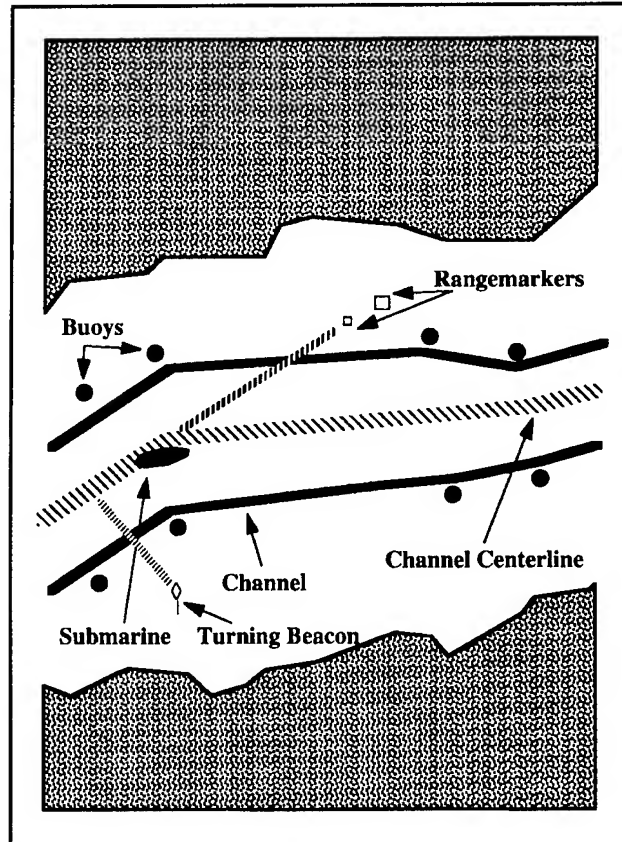


Figure 2. Map of channel to be navigated. The OOD's task in large measure is to verify the course of the ship as it negotiates the marked channel, using navigation aids such as buoys, which mark the channel boundaries, and rangemarkers, which are used to align the vessel with the channel centerline.

1.9.2 Sensorimotor Satellite

Work in the sensorimotor satellite involves research on human responses to alterations in sensorimotor loops associated with the use of virtual environment (VE) systems. Such alterations are likely to occur because of equipment limitations (resulting in unintended distortions, delays, or variability), or in some cases, because of deliberate attempts to emphasize

or de-emphasize certain features of a simulation in order to improve training efficiency.

During the past year, we have continued a series of experiments concerned with altered relations between seen and felt hand position in the plane facing the user and initiated a new series of experiments related to the perception of depth in VEs. In the first series of experiments, we have examined the effects of rotation on both closed-loop and open-loop movements of the hand, as well as compared the effects of rotation on velocity control to those on position control. In the second series of experiments, we have begun to examine (1) stereopsis and the effects of altered interpupillary distance on depth perception in VEs, (2) the

manner in which depth perception, achieved by means of motion parallax, degrades as temporal delay is increased, and (3) the effect of stereoscopic depth cues on brightness and contrast induction in VEs.

Most of these experiments were conducted using existing equipment such as the Sensorimotor Testbed and the Virtual Workbench, both previously described in *RLE Progress Report 137*. In order to perform the new motion parallax experiments, we have designed a device to passively limit an observer's head motion to a controlled maximum linear velocity. This system is constructed around a standard "bite bar" which can slide freely along a 20 cm track (see figure 3). In the experiments, the

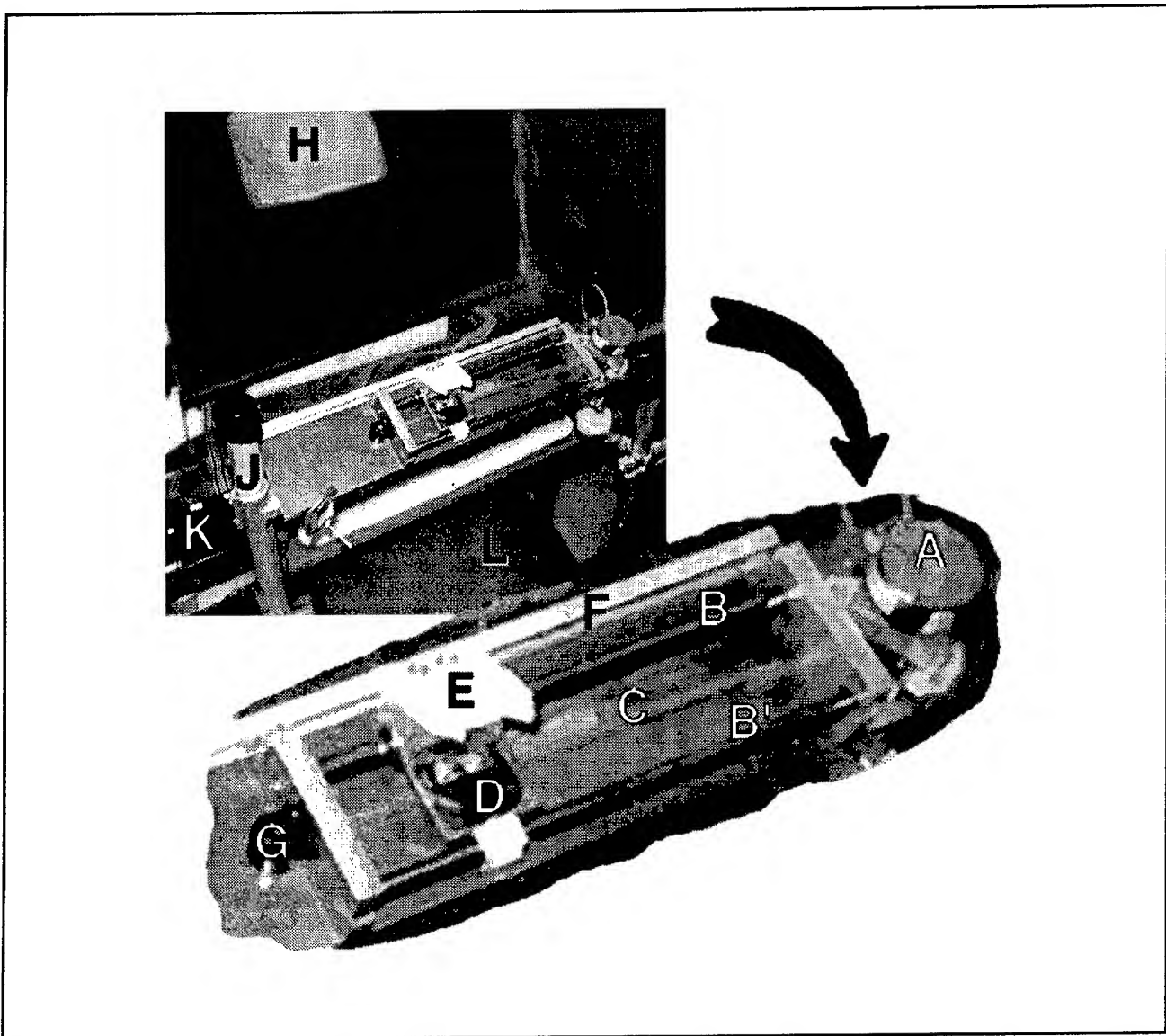


Figure 3. Motion Parallax Headguide. A: Magnetic particle brake; B: Guide rails; C: Toothed coupling belt; D: Carriage; E: Bite-piece; F: Precision linear potentiometer; G: Idler cog; H: CRT display screen; J: SpeedRail support framework; K: Interface control unit; L: Subject's seat.

observer's self-generated lateral motion can be limited through the frictional drag imparted by a servo-controlled magnetic particle brake. We are thus able to safely achieve changes in the velocity profile of the observer's viewpoint by completely avoiding components that are capable of generating motion on their own.

Subjects viewed a split-field random dot display, and their ability to identify the nearer field was measured. Changes in this ability were measured (discrimination thresholds) as a function of delay (between position measurement and display update), temporal quantization (of position readings and display writes), and spatial quantization (of position and display resolution). These measures have particular relevance with respect to limits on acceptable interprocess delays and the required resolution of VE tracking systems.

Figure 4 shows a plot of discrimination performance under various delay conditions. The data suggest

that degradation of depth perception is relatively small for delays of less than 167 msec. A precipitous increase in discrimination threshold occurs when delay increases beyond 200 msec. Current VE systems commonly exhibit tracker-to-display delays of under 100 msec (e.g., an SGI Onyx with a Polhemus FASTRAK head tracker can achieve delays in the 67 msec range while displaying scenes of nontrivial complexity). Thus, in the absence of additional degradations of temporal and spatial quantization, high-end VE performance lies within an adequate range to support depth perception from motion parallax. We are currently mapping out the effects of delays and temporal and spatial quantization, singly and in combination.

In general, the results being obtained in our research are being used both to support development of predictive models of human performance and to determine requirements for cost-effective VE interfaces.

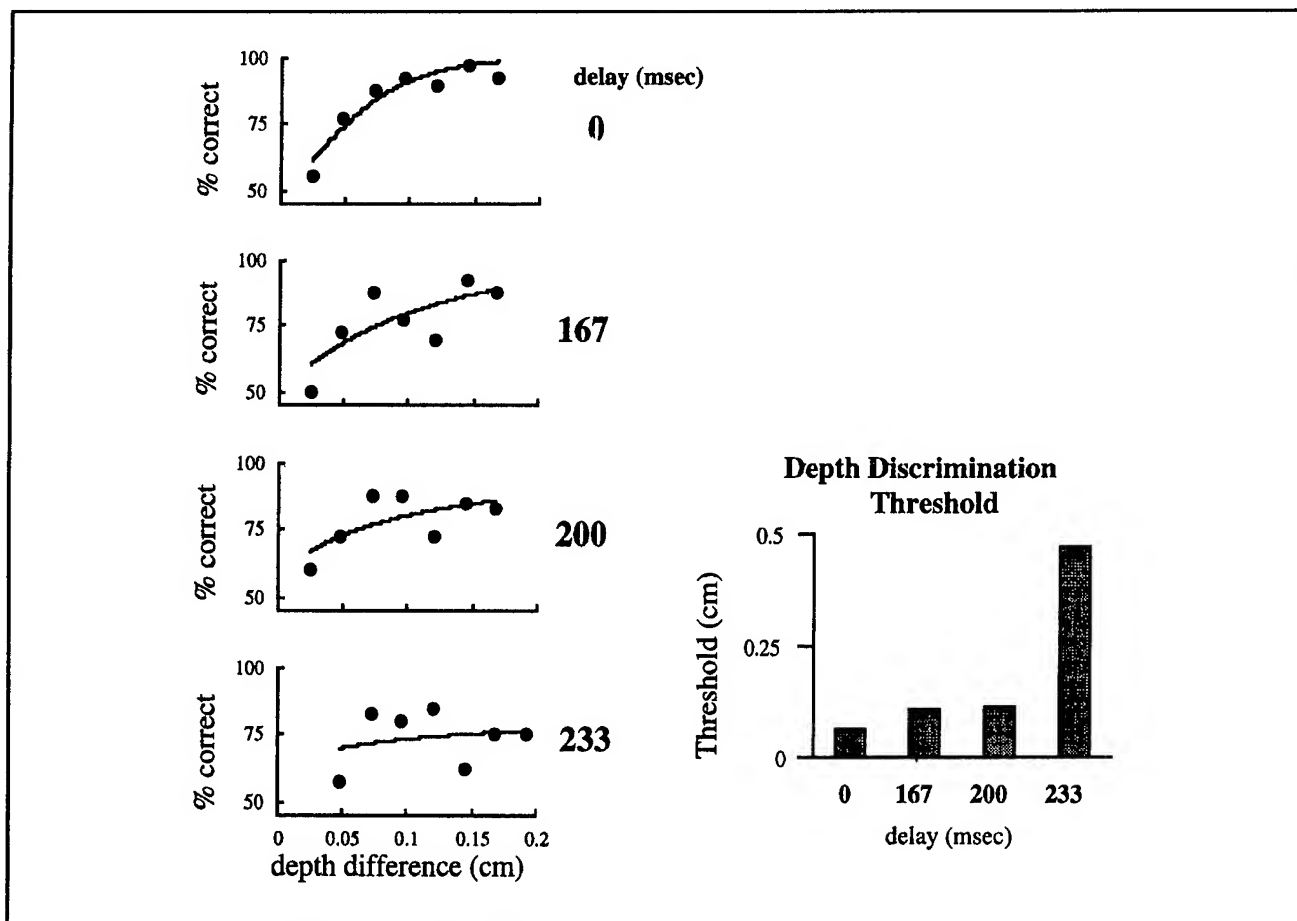


Figure 4. Results for four delay conditions. Left column: forty trials were run for each depth. The abscissa shows separation of the (virtual) surfaces in depth, while the percentage of trials on which the observer correctly indicated the location of the nearer surface is shown on the ordinate. Weibull functions fit to the data sets are shown as solid lines. Right column: thresholds for correct identification of the nearer surface, as estimated from the Weibull fits for the four different delay conditions.

1.9.3 Haptics Satellite

Over the past few years, we have developed device hardware and interaction software and performed psychophysical experiments pertaining to haptic interactions with virtual environments.²⁶ Two major devices for performing psychophysical experiments, the linear and planar graspers, have been fitted with additional sensors for improved performance. The linear grasper is now capable of simulating fundamental mechanical properties of objects such as compliance, viscosity, and mass during haptic interactions. Virtual wall and corner software algorithms were developed for the planar grasper, in addition to the simulation of two springs within its workspace. Another haptic display device developed previously, the PHANToM, has been used to prototype a wide range of force-based haptic display primitives. A variety of haptic rendering algorithms for displaying the shape, texture, and friction of solid surfaces have been implemented on the PHANToM. All the three devices have been used to perform psychophysical experiments aimed at characterizing the sensorimotor abilities of the human user and the effectiveness of computationally efficient rendering algorithms in conveying the desired object properties to the human user.

Human Sensorimotor Performance

We have completed a series of psychophysical experiments with the linear grasper designed to characterize human performance in the discrimination of fundamental mechanical properties of objects. These included several experiments that measured manual just noticeable difference (JND) in size, force, stiffness, viscosity, mass, velocity and acceleration.²⁷ We have also completed an analysis of the subjects' motor data during the discrimination of viscosity and mass. This analysis revealed that subjects used statistically the same initial temporal force profiles when manually discriminating these object properties. Based on this

observation, a mathematical model has been developed to show that this motor performance gives rise to different spatial variations of force and motion, depending on the mechanical property of the object being squeezed. From this model, relationships have been derived that enable predictions for the manual resolution of object properties to be made solely on the basis of force discrimination. A comparison of these predicted JND values with the actual JND results has led to the postulation of a single sensorimotor strategy capable of explaining the sensory and motor performance observed in all viscosity and mass experiments. This hypothesized strategy has been found not only to explain the observed motor and sensory data in these discrimination experiments, but it is also consistent with our previous work on the manual resolution of mechanical compliance.²⁸

Force Shading Algorithm

We have developed novel algorithms for the haptic display of shape, texture, and friction of solid surfaces using the PHANToM.²⁹ We have also performed psychophysical experiments to determine the effectiveness of such rendering algorithms in conveying the desired object properties to the human user. The results show that even when the user is exploring nominally flat surfaces, he can be made to feel as if he is interacting with a shaped and textured surface by appropriately varying the direction of the force reflected back to the user. These new algorithms, called "force shading," permit the mapping of a shape or texture onto a polygon, so that they may be used in haptic rendering in the same way that texture mapping and color shading are used in graphics rendering.

We have performed psychophysical experiments to determine the simplest polyhedral representation that is acceptable to the user as a smooth continuous surface. The PHANToM, which is a high performance haptic interface device developed as a

²⁶ M.A. Srinivasan, "Virtual Haptic Environments: Facts Behind the Fiction," *Proceedings of the Eighth Yale Workshop on Adaptive and Learning Systems*, Center for Systems Science, Yale University, New Haven, June 1994; M.A. Srinivasan, "Haptic Interfaces," in *Virtual Reality Scientific and Technical Challenges*, eds. N.I. Durlach and A.S. Mavor, Report of the Committee on Virtual Reality Research and Development, National Research Council (Washington, D.C.: National Academy Press, 1995); M.A. Srinivasan, "Haptic Interfaces: Hardware, Software, and Human Performance," *Proceedings of the NASA Workshop on Human-computer Interaction and Virtual Environments*, NASA Conference Publication 3320: 103-121 (1995).

²⁷ G.L. Beauregard, M.A. Srinivasan, and N.I. Durlach, "Manual Resolution of Viscosity and Mass," *Proceedings of the ASME Dynamic Systems and Control Division DSC-Vol. 57-2*: 657-662 (New York: ASME, 1995).

²⁸ H.Z. Tan, N.I. Durlach, G.L. Beauregard, and M.A. Srinivasan, "Manual Discrimination of Compliance Using Active Pinch Grasp: the Roles of Force and Work Cues," *Percept. and Psychophys.* 57(4): 495-510 (1995).

²⁹ H.B. Morgenbesser, *Force Shading for Shape Perception in Haptic Virtual Environments*, M.Eng. thesis, Dept. of Electr. Eng. and Comput. Sci., MIT, 1995.

part of the VETT project, was utilized for the experiments. It is capable of reflecting back three-dimensional force vectors within a three-dimensional workspace. In the first set of experiments in each trial, the user is asked to stroke the stylus of the PHANTOM over a continuous cylindrical surface and a polyhedral approximation to it (both are virtual surfaces). The polyhedral surface is associated with a force-shading scheme such that the subject can vary the effective average curvature of the polyhedral surface. The subject is asked to modify the force-shaded polyhedron until it perceptually matches the feel of the continuum surface. These experiments have been conducted for polyhedra with one to three faces approximating cylinders of several radii of curvature. The results show that the force-shading algorithm is successful in creating the illusion of a continuous surface and that the polyhedral surface needs to have a higher average curvature than that of the continuous cylinder that is its perceptual equivalent. In the second set of experiments, subjects manually explored the haptic display of various virtual polyhedral approximations of a circular cylindrical bump, with or without force shading. They then indicated the perceived shape by selecting one from a menu of shapes displayed on a computer monitor. Without force shading, the subjects accurately identified the polyhedral nature of the virtual bumps. With force shading, however, the subjects identified the polyhedral approximations as feeling closer to that of a smooth cylinder. The higher the number of polygons, the higher the percentage of trials in which the shape was identified with a smooth cylinder. The results from both experiments imply that the same polyhedral approximations to object shape used in visual displays can be used for haptic displays, provided the haptic renderer does the appropriate force-shading to make it feel continuous and smooth. Therefore, one can envision a data architecture for multimodal VEs where the core geometric information about object shapes relevant for the specific virtual environment of interest is independent of visual or haptic display modalities.

Visual-Haptic Interactions

Psychophysical experiments were also conducted with the planar grasper to investigate the influence of visual information on the perception of stiffness of virtual springs. In each trial, the subjects could manually press and feel the stiffness of two springs programmed to be side-by-side within the workspace of the planar grasper. At the same time, visual images of the springs were displayed on a computer monitor such that the amount of deformation of the spring that was pressed was displayed in real-time. The subjects were asked to judge which of the two springs was stiffer. The results showed that both in the absence of visual information (when the monitor was turned off) as well as when the visual displacement was exactly equal to the haptic displacement, the subjects were almost 100 percent correct in their judgements. However, when the visual displacement of the two springs were interchanged (i.e., for a given force applied by the subject, the visual displacement of the stiffer spring was equal to the haptic displacement of the softer spring and vice versa) the subjects were almost 100 percent wrong in their judgments. These and other experiments involving different scaling values between the visual and haptic displacements showed that in computing the stiffness of objects, when subjects have a choice of associating visual or haptic displacements with their haptic perception of force, they consistently choose the visual displacements, i.e., the visual information dominates over kinesthetic information in this context. An important implication for virtual environments is that by skewing the relationship between the haptic and visual displays, the range of object properties that can be effectively conveyed to the user can be significantly enhanced. For example, although the range of object stiffnesses that can be displayed by a haptic interface is limited by the force-bandwidth of the interface, the range perceived by the subject can be effectively increased by reducing or eliminating visual deformation of the object.

1.10 Training for Remote Sensing and Manipulation

Sponsor

U.S. Navy - Office of Naval Research
Subcontract 40167³⁰

Project Staff

Walter A. Aviles, Nathaniel I. Durlach, Francis G. Taylor, John Yoon, Dr. David Zeltzer

This project is concerned with a special type of remotely operated vehicle (ROV), namely, teleoperated minisubmarines. A few thousand such vehicles are currently operating around the world. They are used by oil companies to inspect and maintain offshore oil platforms, by various civil authorities to inspect underwater structures such as dams and sewage outflow pipelines, and by the U.S. Navy for undersea salvage and submerged mine counter measures (MCM).

The objective of the training for remote sensing and manipulation (TRANSOM) research program is to design, develop, and evaluate a prototype ROV pilot training and mission rehearsal system for a shallow-water MCM mission incorporating intelligent tutoring system (ITS) techniques within a virtual environment (VE). Such a system will benefit the efficiency of MCM operations, resulting in the preservation of life and property as well as significant cost savings in the training of operators. In addition, it is foreseen that the results of the proposed program will have applicability to ROV missions outside the MCM scenario and to other remote sensing and manipulation systems.

Five organizations are collaborating on this effort. Imetrix Corporation, Cataumet, Massachusetts, is the prime contractor, overseeing the overall effort, providing the ROV and control expertise, and serving as the main conduit for product transition. Our research group is providing the lead in human/machine interface research and VE technology. McDonnell Douglas Training Systems (MDTS), St. Louis, Missouri, is providing expertise in ITS design and leading the training transfer studies. Bolt Beranek and Newman, Inc., Cambridge MA, is developing the ITS and providing training research support. Finally, LRDC,

Pittsburgh PA, is providing training expertise in team interaction.

Work in the Sensory Communication Group is being conducted in three areas. This work is being implemented on SGI Indys acquired specifically for the TRANSOM program. We also make use of the SGI ONYX acquired for the VETT program.

(1) We have developed simulations of the ROV, the ocean bottom over which it operates, and the ROV control console. The ROV geometry model is based in specifications provided by Imetrix. ROV dynamics are simulated using a package developed at Imetrix and adapted for use in the VE developed at MIT. Validation and verification of this simulation software is currently getting underway.

(2) We have implemented a "developers' interface" that provides a rapid-prototyping environment for the development of intelligent VE tutoring components. This uses a Scheme language "front-end" to the SGI open Inventor Language.

(3) Prototypical part-task teaching components of the tutor have been integrated with the simulated ROV, the ROV console, and ocean elements as part of a joint effort with BBN and MDTs to identify effective training interventions.

1.11 Human and Robot Hands: Mechanics, Sensorimotor Functions and Cognition

Sponsor

U.S. Navy - Office of Naval Research
Grant N00014-92-J-1814

Project Staff

Dr. Mandayam A. Srinivasan, Dr. J. Kenneth Salisbury, Dr. Robert H. LaMotte,³¹ Dr. Robert D. Howe,³² Jyh-Shing Chen, Kiran Dandekar, Rogeve J. Gulati, Louise Jandura, Steingrimur P. Karason, Frederick L. Roby, Sudeep Rangaswamy

The premise of this University Research Initiative project is that the integrated study of human and robot haptics can provide complementary knowledge of the processes of prehension and manipulation. From the human side we wish to understand

³⁰ Imetrix Corporation.

³¹ Yale University School of Medicine, New Haven, Connecticut.

³² Harvard University, Cambridge, Massachusetts.

the basic mechanical, perceptual and strategic capabilities that lead to the dexterity and deftness we observe in human task performance. By studying the underlying competences that humans bring to bear on task performance we seek guidelines on how to better build robots. From the robotic side we wish to understand how mechanism and sensor design choices can best be made to maximize grasping and manipulative competences. By better understanding the mechanical demands of task performance we seek to understand the performance demands which underlie skillful human manipulation.

The main components of the research conducted under this project are (1) development of new hardware for robotic and human studies, (2) processing of robot sensor signals and task-level control of the devices, (3) investigation of the mechanics of human fingerpad-object contact, (4) experiments on human perception and control of forces using some of the devices, and (5) development of a computational theory of haptics that is applicable to both robots and humans. The subsections to follow provide descriptions of the results obtained mainly by the Human Haptics Group at the Touch Lab in RLE.

1.11.1 Biomechanics of Human Fingerpad-Object Contact

Although physical contact is ubiquitous in our interactions with objects in the environment, we do not yet understand the mechanistic phenomena occurring at the skin-object interface. The spatio-temporal distribution of mechanical loads on the skin at the contact interface is the source of all tactile information. These loads, specified as pressure, displacements, etc., depend on the geometrical and material properties of both the contacting entities, as well as the overall forces of interaction. The goals of this research are (1) to determine the growth and motion of contact regions and the associated force variations over time between the human fingerpad and carefully chosen transparent test objects whose microtexture, shape or softness is varied in a controlled manner, (2) Experimental measurement of the surface deformations of human fingertips under shaped indentors, and (3) Characterization of the mechanical properties of the human fingerpad. The results obtained are being used to gain a deeper understanding of the neurophysiological and psychophysical data we have already obtained for the same test objects.

To measure the *in vivo* surface deformations of the fingerpad under various tactile stimuli, we have designed a videomicroscopy system together with a

high precision tactile stimulator. The videomicroscopy system consists of a set of video zoom lenses attached to a high-resolution CCD camera, whose output can either be digitized into the computer system memory in real time at about 20 frames/s, or stored on a laserdisk at 30 frames/s for off-line digitization. The zoom lenses enable continuous variation of magnification, with the field of view covering the entire fingerpad, or just a few fingerprint ridges. The tactile stimulator is composed of a linear stepper motor with a microstepping drive. The motor is controlled by a 80386 PC, with a specified indentation velocity commanded by a 80486 PC via a digital link. To record the contact force, a strain gage based single degree of freedom force sensor is mounted on the motor to which a transparent test object can be attached for both biomechanical and psychophysical experiments. This method allows the force and video data to be synchronized and stored in the 80486 PC. With this setup, we are able to investigate how the skin-object contact region changes with indentation velocity and force. In active touch experiments the subject contacts a stationary specimen, whereas in passive touch experiments the stimulator moves the specimen to indent a stationary finger at a given velocity. High contrast images of the contact interface are achieved with coaxial and other fiberoptic lighting.

Videomicroscopy of the Fingerpad-object Contact Regions

Using the test facility described above, we have performed a set of experiments with human subjects to investigate the relationship between the contact force, contact area and compliance of the object. The experiments involved active indentation of transparent compliant rubber specimens and a glass plate with the subjects' fingerpads. Static video images of the contact regions were captured at various force levels and magnifications. In order to minimize the effects of non-uniform illumination, we implemented homomorphic image processing algorithms with or without image decimation. The processed images showed that contact regions consisted of discontinuous "islands" along each finger ridge, with clear distinction between contact and non-contact regions over the entire field of view.

Results show that for objects whose compliances are discriminable, even when the overall contact areas under a given contact force are the same, the actual contact areas can differ by a factor of two or more. The actual pressure distribution, which acts only within the discontinuous contact islands on the skin, will therefore be radically different for the objects. Consequently, a spatio-temporal neural code for object compliance emerges with far higher

resolution than an intensive code such as the average pressure over the overall contact area. These results are in agreement with our hypothesis that the neural coding of objects with deformable surfaces (such as rubber) is based on the spatio-temporal pressure distribution on the skin. This was one of the conclusions from our previous psychophysical, biomechanical and neurophysiological experiments.³³

Measurement of Surface Deformation of Human Fingerpads

The finite element models described previously need to be verified by comparing the experimentally observed skin surface deformations with those predicted by the finite element models under the same mechanical stimuli. The experimental data was obtained by indenting human fingerpads with several cylindrical and rectangular indentors and acquiring images of the undeformed and deformed fingerpad using the videomicroscopy setup.³⁴ Fine markers were placed on the fingerpad and the skin surface deformation was measured by tracking the displacements of the markers in the high resolution video images. The same experiment was simulated using the finite element models of the human fingertip and the displacements of corresponding points were compared with the experimental data. The displacements predicted by the multilayered 3D model matched the experimental data quite well.³⁵

Force Response of the Human Fingerpad to Indentation

A 2-DOF robot designed by Dr. Howe of the Harvard group was modified to serve as a "Tactile Stimulator" capable of delivering static and dynamic stimuli to the human fingerpad.³⁶

Three types of indentors (point, flat circular, and a flat plate) attached to the stimulator imposed a variety of constant velocity ramps (1 to 32 mm/s), depths of indentation (0.5 to 3mm), and sinusoids (0.25 mm to 0.5 mm amplitude; 0.125 to 16 Hz frequency) under displacement control (resolution ~ 20 microns). The resulting normal and shear forces were measured by a 2-axis force sensor (resolution ~ 10 mN). The results showed a pronounced nonlinear force-indentation depth relationship under both static and dynamic conditions, viscoelastic effects of force relaxation under constant depth of indentation, and hysteresis under sinusoidal displacements. There was wide variability in the magnitude of response for the five subjects who were tested, and their fingertip diameter or volume did not account for the observed variability.

A piecewise linear, lumped parameter model with spring and dashpot elements was developed to identify the mechanical parameters causing the nonlinear response. The model predictions with only one set of parameters for each subject matched the empirical data well under a wide variety of stimuli. The model represents a compact description of the data and will be used to verify and tune our finite element models of the fingertip.

Force Response of the Human Fingerpad to Shear Displacement

The 2-DOF Tactile Stimulator was also used to deliver shear displacement ramp (0.5 to 16 mm/sec for a total shear displacement of 7 mm) at various depths of indentation of the fingerpad (0.5 to 3 mm) by a flat, smooth Aluminum plate.³⁷ Only one subject has been tested so far under these stimuli, and the resulting data has been analyzed with a view towards fine tuning the experimental protocol and parameters. The results show that at each depth of indentation, the shear displacement initially caused increasing skin stretch and shear force, fol-

³³ M.A. Srinivasan and R.H. LaMotte, "Tactual Discrimination of Softness," *J. Neurophys.* 73(1): 88-101 (1995); M.A. Srinivasan and R.H. LaMotte, "Tactual Discrimination of Softness: Abilities and Mechanisms," in *Information Processing in the Somatosensory System*, eds. O. Franzen, R. Johansson, and L. Terenius. (Basel, Switzerland: Birkhauser Verlag AB, forthcoming).

³⁴ F.L. Roby, K. Dandekar, and M.A. Srinivasan, "Study of Fingertip Deformation Under Indentations by Circular and Rectangular Indentors," Report to the MIT Summer Research Program, 1994; F.L. Roby and M.A. Srinivasan, "Study of Fingertip Deformations Under Indentations by Circular Indentors," Report to the MIT Summer Research Program, 1995.

³⁵ K. Dandekar, *Role of Mechanics in Tactile Sensing of Shape*, Ph.D. diss., Dept. of Mech. Eng., MIT, 1995.

³⁶ R.J. Gulati, *Determination of Mechanical Properties of the Human Fingerpad, in vivo, using a Tactile Stimulator*, M.S. thesis, Dept. of Biomedical Eng., Boston University, 1995; R.J. Gulati and M.A. Srinivasan, "Human Fingerpad Under Indentation I: Static and Dynamic Force Response," *Proceedings of the 1995 Bioengineering Conference*, eds. R.M. Hochmuth, N.A. Langrana, and M.S. Hefzy, BED-29: 261-262 (1995).

³⁷ J.D. Towles and M.A. Srinivasan, "Frictional Properties of the Human Fingerpad," Report to the MIT Summer Research Program, 1994.

lowed by slipping of the plate across the skin surface. The shear force-shear displacement was almost linear and slip occurred at around 3 mm shear displacement at all velocities. Low velocities tended to cause stick-slip (as indicated by oscillatory shear force during slip), whereas the shear force decreased smoothly at higher velocities. At increasing depths of indentation, slip occurred at larger shear displacements, as is to be expected. The coefficient of static friction was obtained by measuring the slope of the normal and shear forces at the incipience of slip for a given shear velocity. To a first approximation it was found to be independent of shear velocity. More experiments on different subjects are being initiated.

1.11.2 Human Perception and Control

To quantify human perception and control of forces, we have conducted experiments under a wide variety of conditions: (1) Tracking of visual displays of static and dynamic force traces with a stationary fingerpad (isometric case), (2) Maintaining constant contact force on a moving robot end-effector (isotonic case), (3) sensing and control of torque applied on the shaft of an "Instrumented Screw Driver", and (4) Control of grasp forces on an "Active Instrumented Object". The data from each of these experiments have been analyzed with the viewpoint of developing engineering specifications of human haptic performance. Brief descriptions of each of the experiments and models described above are given in the sections below.

Isometric Force Tracking Ability of Humans

In the experimental setup, a human subject tracks visual images of force traces displayed on the monitor by applying appropriate normal forces through a fingerpad that is in contact with a force sensor.³⁸ In these experiments, the finger moves by only fractions of a mm, thus approximating isometric muscular contraction conditions. We had completed one set of experiments on such force tracking last year, and now we have expanded the range of target forces and their frequency. During tracking constant and sinusoidal force targets (three subjects with 3 trials per stimulus), the mean absolute error increased with constant force magnitude, target sinusoid frequency and amplitude. The

errors for a sinusoid of a given amplitude are 5 to 40 times higher than those for constant force targets with the same magnitude. Even at relatively low frequency of 2 Hz, the errors can be higher than 50 percent of the sinusoid amplitude at all amplitudes.

Isotonic Force Control Ability of Humans

We employed the high precision "Glass Smooth Actuator" to measure the ability of human subjects to maintain a constant force (0.1 to 0.8N) by pressing their fingerpads on the actuator's end effector while it was moving sinusoidally (2 to 16 degrees in amplitude; 0.5 to 16 Hz frequency).

During each trial, the robot maintained a constant position for the first 10 seconds, and during the first 8 seconds, the subjects tracked a constant target force displayed as a line on a monitor. The monitor screen was then blanked out, and after 2 seconds, the actuator started moving sinusoidally at a preprogrammed frequency and amplitude, but the subjects were asked to maintain the same force as before. All the subjects were able to perform the task with very little drift in mean force. However, the deviations from the mean were in phase with the actuator motion, and various error measures changed differently with stimulus parameters. The mean absolute error increased with frequency and amplitude almost linearly, but remained constant with respect to target force magnitude.

Torque Sensing and Control

The human ability to sense and control torque was investigated in experiments with the Instrumented ScrewDriver (ISD).³⁹ The ISD is comprised of a single shaft, which is supported by low friction bearings, and is connected to a reaction torque sensor and a magnetic particle brake. Angular position of the shaft is measured by an incremental optical encoder. In all cases the subjects grasped the handle of the ISD between the thumb and index finger of their dominant hand and turned the shaft clockwise for 180 degrees against a constant resistive torque applied by the magnetic particle brake. The magnitude of this resistive torque was varied across different trials. Two types of experiments were conducted: discrimination experiments to determine the human resolution in sensing

³⁸ M.A. Srinivasan and J.S. Chen, "Human Performance in Controlling Normal Forces of Contact with Rigid Objects," *Advances in Robotics, Mechatronics, and Haptic Interfaces*, DSC-49 (New York: ASME, 1993).

³⁹ L. Jandura and M.A. Srinivasan, "Experiments on Human Performance in Torque Discrimination and Control," in *Dynamic Systems and Control*, Vol. 1, ed. C.J. Radcliffe, DSC-55-1 (New York: ASME, 1994).

torque and control experiments to determine the human motor capability in controlling torque.

All torque discrimination experiments used a one-interval, two-alternative, forced-choice paradigm with no feedback to the subject. The reference torque value was 60 mN-m and the comparison values were equal to 5, 10, 20, and 30 percent of the reference torque. In addition, training runs were conducted with a comparison value of 50 percent of the reference torque until the subject response was 90 percent correct. The Just Noticeable Difference for torque was found to be 12.7 percent for the reference torque of 60 mN-m. During some of the trials, in addition to recording the stimulus and the subject's response, the resistive torque, the output of the torque sensor and the angular position of the shaft over time were also recorded. These data are used to make comparisons between the motor performance in the discrimination task and the control task.

For the control experiments, subjects were asked to maintain a constant angular velocity while turning against the constant resistive torque. The value of the angular velocity was up to the subject to choose, but they were asked to try and use the same value for each trial. Because of the physics of the ISD, attempting to maintain a constant angular velocity is directly related to attempting to apply and maintain a constant torque during shaft motion. The constant resistive torque values used were the same as for the discrimination experiments. As before, the resistive torque, the output of the torque sensor, and the angular position of the shaft were recorded over time. Comparison of the time profiles of angular velocity indicate that even when subjects were trying to maintain a constant angular velocity in the control experiments, their performance was not significantly better than when they were trying to discriminate the torques.

A curious phenomenon observed rather consistently in all of the data is the occurrence of peaks in the velocity and acceleration profiles at about 0.1 second intervals. To further investigate this observation, the power spectral density of the middle third of the angular velocity profile was calculated. Although there is some tendency for the discrimination PSDs to be single-peaked while the control PSDs are double-peaked, this was not observed consistently across all subjects. However, in all subjects, most of the frequency content was less

than about 15 Hz for both the discrimination and control experiments.

Passive Grasp Control of an Active Instrumented Object

Most of the investigations of human grasp control reported in the literature pertain to passive objects. In order to test the limitations of the human motor system in compensating for sudden disturbances, we fabricated an "Active Instrumented Object".⁴⁰ It mainly consisted of a pneumatic cylinder whose piston could expand or contract through the operation of computer controlled valves. A position sensor monitored the motion of the piston while two 2-axis force sensors measured the normal and shear forces applied by a subject's fingerpads on two circular plates when the object was held in a pinch grasp. The plate surfaces were either polished aluminum or sandpaper depending on the experiment. A visual display on a computer monitor indicated the force of pinch grasp the subjects were required to apply, and when subjects achieved it, after a random time-delay the object contracted suddenly (170 to 240 mm/s velocity; 19 mm displacement). When initial grasp forces were less than 1.8 N, the subjects dropped the object all the time (3 subjects; 10 trials per grasp force value per subject), whereas they held it in increasing number of trials as the grasp forces increased. No significant difference between aluminum and sand paper surfaces were observed. In one trial where there was a small slip, a perturbation in force applied by the thumb is seen at around 100 ms, but the object did not drop. In another trial where the object was dropped, oscillations in force applied by the middle finger began at 60 ms and those in force applied by the thumb began at about 80 ms. Both these oscillations continued until the object was dropped at about 100 ms.

A third order lumped parameter model of the finger was proposed and the parameters of the model corresponding to the stiffness and damping of the fingerpad and muscle together with finger mass were identified using the recorded force and displacement data. This model of the finger was shown to predict the experimental data quite well, indicating that the subjects' fingers are effectively passive during rapid haptic events that occur within 60 to 80 ms. This model also related the grasping performance of each subject to the strategy the subject used in the stiffness modulation of the finger muscles before each trial. Furthermore, the

⁴⁰ S.P. Karason and M.A. Srinivasan, "Passive Human Grasp Control of an Active Instrumented Object," *Proceedings of the ASME Dynamic Systems and Control Division*, DSC-57-2: 641-647, (New York: ASME, 1995).

identified parameters governing the passive dynamic properties of the fingers provide a starting point for more complex models which account for the active nature of the finger muscles.

1.11.3 Development of a Computational Theory of Haptics

Our research on computational theory of haptics is focused on developing a theoretical framework for studying the information processing and control strategies common to both humans and robots performing haptic tasks. For example, although the "hardware" of the tactile apparatus in humans and robots are different, they have the common feature of mechanosensors embedded in a deformable medium. Therefore the mechanistic analyses needed to solve the computational problem of coding (predicting sensor response for a given mechanical stimulus at the surface) and decoding (inferring the mechanical stimulus at the surface by suitably processing the sensor response) are sufficiently similar for human and robot tactile sensing systems that a theory common to both systems can be developed.

We first developed such a "computational theory" using a simplified 2D half-space model of the human or robot finger subjected to arbitrary pressure or displacement loading conditions normal to the surface, and gave explicit formulae for the coding and decoding problems.⁴¹ We have now expanded these results to a more general 3D half-space model where the load direction can be completely arbitrary.⁴² Explicit solutions for the coding problem are given and enable the selection of a useful set of relevant stimuli as well as the choice of sensors appropriate for maximizing the information about the stimulus on the skin surface. The solution of the decoding problem is also given, both for the idealized noise-free case and for the realistic case with measurement noise. For the latter, the solutions are shown to be numerically stable and optimal.

In our work during the previous years, we were successful in answering basic identification and control issues that arise during manipulation of compliant objects using compliant fingerpads.⁴³ In order to understand the fundamental aspects of these tasks, we have analyzed the problem of identification of compliant objects with a single finger contact, as well as under a two-finger grasp. Using lumped parameter models, we have carried out the identification of human and object parameters, using either force or displacement inputs to the rigid backing of the end-effector. Based on identified parameters, control strategies are developed to achieve a desired manipulation of the object in the workspace.

We have also modelled the dynamic interactions that occur between compliant end-effectors and deformable objects by a class of nonlinear systems.⁴⁴ It was shown that standard geometric techniques for exact feedback linearization techniques were inadequate. New algorithms were developed by using adaptive feedback techniques which judiciously employed the stability characteristics of the underlying nonlinear dynamics. In both theoretical and simulation studies, it was shown that these adaptive control algorithms led to successful manipulation. The theoretical results can be used to generate testable hypotheses for experiments on human or robot haptics.

1.11.4 Publications

Annaswamy, A.M., and M.A. Srinivasan. "The Role of Compliant Fingerpads in Grasping and Manipulation: Identification and Control." Chapter in a book to be published by the Institute of Mathematics. New York: Springer Verlag, forthcoming.

Beauregard, G.L., M.A. Srinivasan, and N.I. Durlach. "Manual Resolution of Viscosity and Mass." *Proceedings of the ASME Dynamic*

⁴¹ M.A. Srinivasan, "Tactile Sensing in Humans and Robots: Computational Theory and Algorithms," *Newman Laboratory Technical Report*, Department of Mechanical Engineering, MIT, 1988.

⁴² S.P. Karason, M.A. Srinivasan, and A.M. Annaswamy, "Tactile Sensing of Shape," *Proceedings of the Workshop Organized by the Center for Information Driven Mechanical Systems (CIDMS)*, Dept. of Mechanical Engineering, MIT, 1994.

⁴³ A.M. Annaswamy and M.A. Srinivasan, "A Study of Dynamic Interactions between Haptic Interfaces and Compliant Fingerpads," *Proceedings of the Motion Control Workshop*, Berkley, California, March 1994; A.M. Annaswamy and M.A. Srinivasan, "The Role of Compliant Fingerpads in Grasping and Manipulation: Identification and Control," Chapter in a book to be published by the Institute of Mathematics (New York: Springer Verlag, forthcoming).

⁴⁴ A.M. Annaswamy and D. Seto, "Object Manipulation Using Compliant Fingerpads: Modeling and Control," *ASME J. Dynamic Syst., Measure., Cont.* (1993).

Systems and Control Division. DSC-Vol. 57-2: 657-662. New York: ASME, 1995.

Dandekar, K., and M.A. Srinivasan. "A 3-dimensional Finite Element Model of the Monkey Fingertip for Predicting Responses of Slowly Adapting Mechanoreceptors." *Proceedings of the 1995 Bioengineering Conference*. Eds. R.M. Hochmuth, N.A. Langrana, and M.S. Hefzy. BED-29: 257-258 (1995).

Gulati, R.J., and M.A. Srinivasan. "Human Fingertip Under Indentation I: Static and Dynamic Force Response." *Proceedings of the 1995 Bioengineering Conference*. Eds. R.M. Hochmuth, N.A. Langrana, and M.S. Hefzy. BED-29: 261-262 (1995).

Karason, S.P., and M.A. Srinivasan. "Passive Human Grasp Control of an Active Instrumented Object." *Proceedings of the ASME Dynamic Systems and Control Division. DSC-57-2: 641-647. New York: ASME, 1995.*

LaMotte, R.H., C. Lu, and M.A. Srinivasan. "Peripheral Neural Representation of the Shapes and Orientations of Three-dimensional Objects Stroked Across the Monkey Fingertip." *Soc. Neurosci. Abstr.* 21: 1162 (1995).

LaMotte, R.H., C. Lu, and M.A. Srinivasan. "Tactile Neural Codes for Shapes and Orientations of Objects." In *Information Processing in the Somatosensory System*. Eds. O. Franzen, R. Johansson, and L. Terenius. Basel, Switzerland: Birkhauser Verlag AB. Forthcoming.

Roby, F.L., and M.A. Srinivasan. "Study of Fingertip Deformations Under Indentations by Circular Indentors." Report to the MIT Summer Research Program, 1995.

Srinivasan, M.A. "Haptic Interfaces." In *Virtual Reality Scientific and Technical Challenges*. Eds. N.I. Durlach and A.S. Mavor. Report of the Committee on Virtual Reality Research and Development. Washington, D.C.: National Academy Press, 1995.

Srinivasan, M.A. "Haptic Interfaces: Hardware, Software, and Human Performance." *Proceedings of the NASA Workshop on Human-computer Interaction and Virtual Environments*, NASA Conference Publication 3320: 103-121 (1995).

Srinivasan, M.A., and K. Dandekar. "An Investigation of the Mechanics of Tactile Sense Using Two Dimensional Models of the Primate Fingertip." *J. Biomech. Eng.* 118: 48-55 (1996).

Srinivasan, M.A., and R.H. LaMotte. "Tactual Discrimination of Softness." *J. Neurophys.* 73(1): 88-101 (1995).

Srinivasan, M.A., and R.H. LaMotte. "Tactual Discrimination of Softness: Abilities and Mechanisms." In *Information Processing in the Somatosensory System*. Eds. O. Franzen, R. Johansson, and L. Terenius. Basel, Switzerland: Birkhauser Verlag AB. Forthcoming.

Tan, H.Z., N.I. Durlach, G.L. Beauregard, and M.A. Srinivasan. "Manual Discrimination of Compliance Using Active Pinch Grasp: the Roles of Force and Work Cues." *Percept. Psychophys.* 57(4): 495-510 (1995).

Theses

Dandekar, K. *Role of Mechanics in Tactile Sensing of Shape*. Ph.D. diss., Dept. of Mech. Eng., MIT, 1995.

Gulati, R.J. *Determination of Mechanical Properties of the Human Fingertip, in vivo, Using a Tactile Stimulator*. S.M. thesis. Dept. of Biomedical Eng., Boston University, 1995.

Morgenbesser, H.B. *Force Shading for Shape Perception in Haptic Virtual Environments*. M.Eng. thesis. Dept. of Electr. Eng. and Comput. Sci., MIT, 1995.

1.12 Role of Skin Biomechanics in Mechanoreceptor Response

Sponsor

National Institutes of Health
Grant R01-NS33778

Project Staff

Dr. Mandayam A. Srinivasan, Kiran Dandekar, Balasundara I. Raju, Kimberly J. Voss, Suvranu De

When we touch an object, the source of all tactile information is the spatio-temporal distribution of mechanical loads on the skin at the contact interface. The relationship between these loads and the resulting stresses and strains at the mechanoreceptive nerve terminals within the skin plays a fundamental role in the neural coding of tactile information. Although empirical determination of the stress or strain state of a mechanoreceptor is not possible at present, mechanistic models of the skin and subcutaneous tissues enable generation of

testable hypotheses on skin deformations and associated peripheral neural responses. Verification of the hypotheses can then be accomplished by comparing the calculated results from the models with biomechanical data on the deformation of skin and subcutaneous tissues, and neurophysiological data from recordings of the responses of single neural fibers. The research under this grant is directed towards applying analytical and computational mechanics to analyze the biomechanical aspects of touch—the mechanics of contact, the transmission of the mechanical signals through the skin, and their transduction into neural impulses by the mechanoreceptors.

1.12.1 Determination of the Shape and Compressibility of the Primate Fingertip

The first step in performing mechanistic analyses of the primate fingertip (distal phalanx) is to determine its geometric and material properties. The three-dimensional (3D) external geometry of the primate fingertips was determined from accurate epoxy replicas of human and monkey fingertips. Using a videomicroscopy setup, we obtained images of orthographic projections of the epoxy replicas at various known orientations. The images were then digitized and processed to determine the boundary of the finger at each orientation. By combining the boundary data for all the different orientations, we were able to reconstruct the 3D external geometry of the fingertip.⁴⁵ We have reconstructed several human and monkey fingertips by using this method.

For mechanistic modeling of the human fingerpad, the Poisson's ratio, which is a measure of its compressibility, is required as an input to the mathematical models. The Poisson's ratio for the human fingerpad *in vivo* is unknown at present. In previous noninvasive experiments on human subjects, we have measured the change in volume of the fingerpad under static indentations with different

indentors.⁴⁶ Our results show that the compressibility of the fingertip increases with increases in both the depth of indentation and the contact area with the indenter. The highest change in fingertip volume was about 5 percent. We have also developed an experimental setup involving a computer controlled linear actuator for fingertip volume change measurements under dynamic conditions.⁴⁷ The results show that reductions in fingertip volume are in phase with stimulus variations, with an increase in their mean value over time. The volume changes during the ramp phase increase linearly with indenter displacement and are independent of velocity; during sawtooth stimulations, however, the nature of the hysteresis loops depend on velocity of indentation.

1.12.2 Fingertip Models and Finite Element Analysis

We have performed linear and nonlinear finite element analysis of a series of mechanistic models of the fingerpad under a variety of mechanical stimuli.⁴⁸

The models range from a semi-infinite medium to a 3D model based on the actual finger geometry, and composed of a homogeneous elastic material, a thick elastic shell containing a fluid or a multilayered medium. Simulations of the mechanistic aspects of neurophysiological experiments involving mapping of receptive fields with single point loads, determination of spatial resolution of two-point stimuli, and indentations by single bars as well as periodic and aperiodic gratings have been carried out for the 2D and 3D models. We have also solved the nonlinear contact problem of indentations by cylindrical objects and sinusoidal step shapes. The large number of numerical calculations needed even for the linear two dimensional models necessitated the use of the Cray-C90 at the NSF Pittsburgh Supercomputer Center.

⁴⁵ T.R.R. Perez, K. Dandekar, and M.A. Srinivasan, "Videomicroscopic Reconstruction of the Human Finger," Project report to the MIT Summer Science Research Program, 1992.

⁴⁶ M.A. Srinivasan, R.J. Gulati, and K. Dandekar, "In vivo Compressibility of the Human Fingertip," *Advances in Bioengineering*, ASME 22: 573-576 (1992).

⁴⁷ W.E. Babiec, *In vivo Volume Changes of the Human Fingerpad Under Indentors*, S.B. thesis, Dept. of Mech. Eng., MIT, 1994.

⁴⁸ M.A. Srinivasan and K. Dandekar, "Role of Fingertip Geometry in the Transmission of Tactile Mechanical Signals," *Advances in Bioengineering*, ASME 22: 569-572 (1992); M.A. Srinivasan and K. Dandekar, "An Investigation of the Mechanics of Tactile Sense Using Two Dimensional Models of the Primate Fingertip," *J. Biomech. Eng.* 118: 48-55 (1996); K. Dandekar and M.A. Srinivasan, "Tactile Coding of Object Curvature by Slowly Adapting Mechanoreceptors," in *Advances in Bioengineering*, ed. M.J. Askew, BED-28: 41-42 (New York: ASME, 1994); K. Dandekar and M.A. Srinivasan, "A 3-dimensional Finite Element Model of the Monkey Fingertip for Predicting Responses of Slowly Adapting Mechanoreceptors," *Proceedings of the 1995 Bioengineering Conference*, eds. R.M. Hochmuth, N.A. Langrana, and M.S. Hefzy, BED-29: 257-258 (1995); K. Dandekar, *Role of Mechanics in Tactile Sensing of Shape*, Ph.D. diss., Dept. of Mech. Eng., MIT, 1995.

The results show that the model geometry has a significant influence on the spatial distribution of the mechanical signals and that the elastic medium acts like a low-pass filter in causing blurring of the mechanical signals imposed at the surface. Multi-layered 3D models of monkey and human fingertips accurately predicted the surface deformations under a line load, experimentally observed by Srinivasan.⁴⁹ The same models predicted the experimentally observed surface deformations under cylindrical indentors as well. These 3D finite element models were used to simulate neurophysiological experiments involving indentation by rectangular bars, aperiodic gratings, cylindrical indentors and step shapes. Several strain measures at typical mechanoreceptor locations were matched with previously obtained neurophysiological data to determine the relevant mechanical signal that causes the receptors to respond. In all simulations, the strain energy density at the receptor location was found to be directly related to the static discharge rate of the slowly adapting afferents. In addition, strain energy density is a scalar that is invariant with respect to receptor orientations and is a direct measure of the distortion of the receptor caused by loads imposed on the skin. We have therefore hypothesized that the strain energy density at the receptor site is the relevant stimulus to the slowly adapting receptors.

In order to further improve the spatial resolution, a three-dimensional finite element model with high mesh density near the loading region has been developed. To model the internal geometry more accurately, we have investigated the use of magnetic resonance imaging (MRI) to visualize the internal structures of the fingerpad. In preliminary experiments, we have achieved a resolution of 300 microns/pixel. Efforts are underway to improve the resolution to 60 microns/pixel. Also, to account for the dynamic behavior of the fingertip, the models

are being enhanced to include viscoelastic effects. Once the models achieve sufficient spatial resolution and simulate temporal effects, they can be used to generate hypotheses on how the central nervous system might infer object shape from mechanoreceptor signals.

1.13 Peripheral Neural Mechanisms of Haptic Touch

Sponsor

U.S. Navy - Office of Naval Research
Grant N00014-88-K-0604

Project Staff

Dr. Mandayam A. Srinivasan, Professor Anuradha M. Annaswamy, Dr. Robert H. LaMotte

We have been collaborating with Dr. LaMotte of Yale University School of Medicine in conducting psychophysical and neurophysiological studies on the tactile perception of the microtexture, shape and softness of objects. We have shown that humans can detect extremely fine textures composed of 50 nanometers high parallel bars etched on plane glass plates.⁵⁰ Our neurophysiological recordings indicate that when such fine textures are stroked on the fingerpad skin, the fingerprint ridges vibrate and cause Pacinian Corpuscles to respond, thus enabling the detection of the microtexture.⁵¹

In studies of the tactile perception of shape, a series of two- and three-dimensional objects (e.g., cylinders, spheres, ellipsoids, and wavy surfaces) were pressed or stroked at various orientations across the fingerpads of anesthetized monkeys, and evoked responses in cutaneous mechanoreceptive primary afferent nerve fibers were recorded.⁵² Major geometrical properties of the

⁴⁹ M.A. Srinivasan, "Surface Deflection of Primate Fingertip Under Line Load," *J. Biomech.* 22(4): 343-349 (1989).

⁵⁰ R.H. LaMotte and M.A. Srinivasan, "Surface Microgeometry: Neural Encoding and Perception," in *Information Processing in the Somatosensory System*, eds. O. Franzen and J. Westman, *Wenner-Gren International Symposium Series* (New York: Macmillan Press, 1991).

⁵¹ M.A. Srinivasan, J.M. Whitehouse, and R.H. LaMotte, "Tactile Detection of Slip: Surface Microgeometry and Peripheral Neural Codes," *J. Neurophys.* 63(6) 1323-1332 (1990).

⁵² M.A. Srinivasan and R.H. LaMotte, "Encoding of Shape in the Responses of Cutaneous Mechanoreceptors," in *Information Processing in the Somatosensory System*, eds. O. Franzen and J. Westman, *Wenner-Gren International Symposium Series* (New York: Macmillan Press, 1991); R.H. LaMotte and M.A. Srinivasan, "Responses of Cutaneous Mechanoreceptors to the Shape of Objects Applied to the Primate Fingertip," *Acta Psychol.* 84: 41-51 (1993); R.H. LaMotte, M.A. Srinivasan, C. Lu, and A. Klusch-Petersen, "Cutaneous Neural Codes for Shape," *Can. J. Physiol. Pharmacol.* 72: 498-505 (1994); R.H. LaMotte, C. Lu, and M.A. Srinivasan, "Peripheral Neural Representation of the Shapes and Orientations of Three-dimensional Objects Stroked Across the Monkey Fingertip," *Soc. Neurosci. Abstr.* 21: 1162 (1995); R.H. LaMotte, C. Lu, and M.A. Srinivasan, "Tactile Neural Codes for Shapes and Orientations of Objects," in *Information Processing in the Somatosensory System*, eds. O. Franzen, R. Johansson, and L. Terenius (Basel, Switzerland: Birkhauser Verlag AB, forthcoming).

shapes were well represented in the spatio-temporal responses of SA and RA afferent fiber populations, particularly those of the SAs. The results show that the following hypothesis explains qualitatively all the data we have obtained until now: the depth of indentation and the change in curvature of the skin surface are encoded by the discharge rates of SAs; in addition, the velocity and the rate of change in skin surface curvature are encoded by the discharge rates of both SAs and RAs.

The intensive parameters of shapes, such as the magnitude of change in skin curvature produced by contact with the object surface were encoded in the discharge rates of SAs and RAs, but this neural code was also influenced by changes in stroke velocity. Spatial parameters of the response, such as the outline of the region of mechanoreceptor activity in the skin, encoded the size, shape and orientation of the 2-D outline of the object in contact with the skin. The third dimension of shape was represented best in the shape of the distribution of spatial discharge rates primarily in the SA fiber population. The shapes of the spatial discharge rates of RAs were more irregular and variable than those of SAs and exhibited poor or no representations of object shape. It was hypothesized that the distribution of slopes (in impulses/sec/mm) of the spatial discharge rate profile evoked by an object in the SA population encoded the distribution of curvatures on the surface of the object in contact with the skin. This is a neural code that is probably invariant with moderate changes in the parameters that govern contact conditions between the object and the skin, such as the contact force or orientation and velocity of its trajectory. Therefore, among the different possible geometric representations of the shape of objects, the intrinsic description, i.e., the surface curvature as a function of the distance along the surface, seems to be relevant for tactile sensing of shape.

Based on a theoretical analysis of the mechanics of contact, we have proposed a mechanism by which shapes of objects within contact regions are perceived through the tactile sense. The curvature of the skin surface under an object, which we know from differential geometry is approximated by the second spatial derivative of surface deflection, is

coded without differentiating (which is a noise enhancing process), but by exploiting its relationship to surface pressure. Pressure peaks occur where the depths of indentation and/or changes in the skin surface curvature are high. The skin effectively acts as a low-pass filter in transmitting the mechanical signals, and the mechanoreceptors respond to the blurred versions of the surface pressure distribution, thus encoding the shape of the object in terms of its surface curvatures.⁵³

We have also shown that the human discriminability of softness or compliance of objects depends on whether the object has a deformable or rigid surface.⁵⁴ When the surface is deformable, the spatial pressure distribution within the contact region is dependent on object compliance, and hence information from cutaneous mechanoreceptors is sufficient for discrimination of subtle differences in compliance. When the surface is rigid, kinesthetic information is necessary for discrimination, and the discriminability is much poorer than that for objects with deformable surfaces. The mechanistic data for rubber specimens indicates that the basis for the perception of softness of rubber-like objects is likely to be the spatio-temporal variation of pressure on the skin (or, equivalently the skin displacement and its derivatives). Neurophysiological data shows that the resulting responses from slowly adapting type I afferent population within the skin might encode the compliance of such objects.

1.14 Inertial Head Tracking

Sponsor

National Aeronautics and Space Administration
Grant NCC 2-771

Project Staff

Brian Clarkson, Nathaniel I. Durlach, Eric M. Foxlin, Owen D. Johnson, Christopher R. Richardson, John J. Rodkin, Nathan R. Shnidman

The objective of this effort is to develop a new head-tracking technology for HMD applications which offers large working volume, high fidelity, and unencumbered operation.

⁵³ M.A. Srinivasan and R.H. LaMotte, "Encoding of Shape in the Responses of Cutaneous Mechanoreceptors," in *Information Processing in the Somatosensory System*, eds. O. Franzen and J. Westman, *Wenner-Gren International Symposium Series* (New York: Macmillan Press, 1991).

⁵⁴ M.A. Srinivasan and R.H. LaMotte, "Tactual Discrimination of Softness," *J. Neurophys.* 73(1): 88-101 (1995); M.A. Srinivasan and R.H. LaMotte, "Tactual Discrimination of Softness: Abilities and Mechanisms," in *Information Processing in the Somatosensory System*, eds. O. Franzen, R. Johansson, and L. Terenius (Basel, Switzerland: Birkhauser Verlag AB, forthcoming).

Commercially available tracking systems suffer from a variety of limitations which restrict their use in human-machine interfaces. Mechanical trackers offer fast response times and good accuracy, but require physical attachment to the head which limits range of motion and user comfort. Optical methods are expensive, require a clear line-of-sight, and usually necessitate a trade-off between precision and working volume. Magnetic trackers (such as those available through Polhemus or Ascension Technologies) are reasonably priced, but have a small working volume and suffer from noise and magnetic field distortions caused by metallic objects. Finally, acoustic systems based upon a transmitted signal's time-of-flight are available at reasonable cost and offer a large working volume; however, their speed is limited by the speed of sound, and they are sensitive to acoustic interference.

Our system departs from prior art in head-tracking by relying on inertial sensors for its primary measurements. This offers the potential advantage of a self-contained head-mounted measurement device that does not rely on signals from other equipment in the lab. This makes possible large range and freedom from interference. The main difficulty with inertial systems is drift, which we correct with an inclinometer and compass. The orientation tracker therefore retains its large range and relative invulnerability to interference.

Due to the difficulty of tracking translational position by inertial means, the first two prototypes were designed to measure orientation only. In the past year, we have developed a hybrid 6-DOF tracking system which uses a Kalman filter to combine ultrasonic position updates with a 6-DOF inertial tracker. Other projects begun during the past year include development of a high performance inertial measurement unit (IMU) based on miniature dynamically-tuned gyroscopes and a low-cost ultra-miniature IMU based on solid state angular rate sensors and accelerometers.

1.14.1 Ultra-Miniature Solid-State Inertial Measurement Unit (IMU)

A third prototype of the MIT inertial tracker has been constructed which reduces the volume by a factor of three compared to the second prototype. The new sensor, based on state-of-the-art micro-machined angular rate sensors and accelerometers, has dimensions of $1 \times 1.24 \times 1.34$ inches and weighs 2.1 ounces. The biggest change to the design of the sensor assembly is that the fluid inclinometer was eliminated and replaced by a triad of orthogonal accelerometers which can determine

the gravimetric tilt regardless of attitude. In addition, the 2-axis fluxgate magnetometer was replaced with a much less bulky solid-state magnetometer. New interface circuitry was developed for the new sensor to interface it to the PC ISA bus for development and also to interface to a small microcontroller card for ultimate application in wearable and wireless VR systems.

To achieve this level of miniaturization, lower performance angular rate sensors had to be used. To compensate, more thorough methods of calibration were developed, making use of a servo-motor driven tilt table/rate table apparatus.

1.14.2 6-DOF Inertial Tracker

The largest effort during the past year has been to expand the tracking capabilities from 3-DOF to 6-DOF. In addition to providing all-attitude gravimetric tilt correction, the triaxial accelerometers in the new IMU were included for this purpose. Background reading and coursework have been completed in the field of strapdown inertial navigation to identify any existing theory that can be applied to the head-tracking problem. A hybrid 6-DOF tracking system has been designed which uses a Kalman filter to achieve efficient sensor data fusion of the signals from the three rate gyroscopes, three linear accelerometers, and an ultrasonic time-of-flight position triangulation system. The portion of the Kalman filtering algorithm which has been implemented so far enables improved estimation of orientation, which is vital to extracting linear acceleration in a confounding gravity field. The details of this Kalman filter have been submitted for publication in VRAIS96. Preliminary efforts in combining the ultrasonic position data with the double integrated acceleration data have shown promise of achieving the smoothness, update rate, and predictive capability of the accelerometers, with the accuracy of the ultrasonic system.

1.14.3 High-Performance IMU using Dynamically-Tuned Gyroscopes

To determine the ultimate accuracy that might be achieved by inertial body-trackers, we have begun to construct an IMU using today's state-of-the-art tactical-grade avionics technology which might represent the level of performance that will be achieved with tomorrow's low-cost micromachined technology. A final selection of a combination of 2-DOF DTGs and silicon servo-accelerometers has been made, and the development of the drive elec-

tronics for these sophisticated inertial instruments is well under-way.

1.14.4 Publication

Foxlin, E. "Inertial Head-Tracker Sensor Fusion by a Complementary Separate-Bias Kalman Filter." *Proceedings of VRAIS*, Santa Clara, California, March 30-April 3, 1996.

1.15 Supernormal Auditory Localization for Improved Human-Machine Interfaces

Sponsor

U.S. Air Force - Office of Scientific Research
Grant F49620-94-1-0236

Project Staff

Douglas S. Brungart, John Crouch, Nathaniel I. Durlach, Professor Richard M. Held, Gregory G. Lin, Kinuku Masaki, John Park, Dr. Barbara G. Shinn-Cunningham

This work constitutes a continuation of work described previously in *RLE Progress Reports 135* and *136*.

Research in this area conducted during the past year has focused on theoretical modeling of the results obtained on adaptation to altered azimuthal cues and on preliminary experimental work concerned with azimuthal coding of distance. Comments on each of these topics are contained in the following subsections.

1.15.1 Modeling of Adaptation to Transformed Azimuthal Cues

The most important accomplishment to date has been the development of a model capable of describing the experimental results for nearly all of the experiments performed so far. In particular, the model predicts the changes in both bias and resolution as subjects adapt to supernormal localization cues.

This model is significant for both sensorimotor adaptation and psychoacoustics. Its importance in the field of sensorimotor adaptation arises from two main facts. First, the model can make quantitative predictions of most aspects of performance over the time course of the adaptation process. Not only are most previous adaptation models qualitative rather than quantitative, but other models are generally restricted to describing only how mean performance

changes over time; no attention is given to how resolution varies over time. As such, the current model is more powerful than any existing model of sensorimotor performance found in the literature. Second, the necessary assumptions of the model have important implications for sensorimotor adaptation in general.

The model assumes that (1) subjects cannot adapt to nonlinear transformations of auditory localization cues, but instead adapt to a linear approximation of the imposed nonlinear transformation, and (2) given the linear constraint on adaptation, performance asymptotes to levels very close to the ideal levels achievable for the imposed nonlinear transformation. The fact that these assumptions allow the model to describe the results from the current experiments leads to a number of important questions about other sensorimotor adaptation studies. For instance, is it a general principle that humans cannot adapt to nonlinearities in sensorimotor rearrangement? Can it be shown that the failure of humans to completely adapt to other types of rearrangement is really a by-product of their inability to adapt to nonlinear transformations? How universal are the principles found in the current model? These questions are of great importance both for scientific understanding of sensorimotor adaptation and practical applications in which human subjects must adapt to sensorimotor rearrangements.

The importance of the model in the field of psychoacoustics arises from its ability to describe how performance evolves over time when subjects are provided with specific feedback or training that pushes them to interpret physical stimuli in new ways. No existing psychophysical models provide insight into how aspects of performance might change over time.

The current model incorporates ideas from the fields of sensorimotor adaptation and psychoacoustics to lead to a model that significantly adds to both areas. Whereas previous models of sensorimotor adaptation provided only qualitative descriptions of how one aspect of performance changed over time, previous psychophysical models provided detailed quantitative predictions of all aspects of performance at one point in time. The current model of adaptation to supernormal auditory localization cues provides quantitative predictions of all aspects of performance over time.

In the model, it was assumed that the range of stimuli attended to at any given time (determined by the slope relating mean response to acoustic stimulus) determined the amount of noise in the human perceptual system. For larger ranges of stimuli, noise increased, whereas for smaller stimulus

ranges, it decreased. In the model, as subjects adapted to supernormal cues, the range of stimulus values to which the subject attended also increased. This increase in range made the model predict a decrease in resolution over time for the same physical stimuli.

1.15.2 Distance Coding

It is well known that sound source distance is not well perceived naturally. Furthermore, very little effort has been made to explore the extent to which perception of distance could be substantially improved for use in acoustic displays by means of artificial coding.

We have completed an initial study concerned with subjects' abilities to identify various filter transfer characteristics,⁵⁵ using characteristics that we might use for coding distance. This work differs from past work performed at a variety of laboratories, including our own, on the perception of spectral shape⁵⁶ in that we are interested in selecting shapes and experimental paradigms related to the coding of distance rather than in modeling of cross-frequency intensity comparisons. In particular, in most cases our attention is focused on (1) transfer characteristics that are related (at least loosely) to those naturally encountered and that do not interfere too seriously with the perception of the transmitted signal (i.e., with the "message") and (2) the task of identification rather than discrimination. Our initial series of experiments examined absolute identification (AI) performance using the three-dimensional set of "single-echo" filters given by the following equations:

$$|S_{A, m, \tau}(\omega)|^2 = A^2 [1 + m^2 + 2m \cos(\omega\tau)]$$

$$\text{phase}[S_{A, m, \tau}(\omega)] = \tan^{-1} \left[\frac{-m \sin(\omega\tau)}{1 + m \cos(\omega\tau)} \right]$$

We have investigated the ability of listeners to perceive information encoded as the strength and delay of a single echo of the source. Although the work focused on how much information listeners

can extract when distance-like cues are presented rather than on the perception of distance per se, it is a first step toward developing simple but reliable distance cues for a virtual-environment system.

The most important result from these experiments was that the amount of information transfer (IT) was startlingly small. Whereas many unidimensional stimulus sets lead to an IT of 2 to 3 bits (and two-dimensional stimulus sets to an IT of 3-5 bits), in these experiments the value of IT obtained fell in the range of 0.2 - 2 bits. In general, these small values of IT appeared to result from two factors: (1) large JNDs in the variables m and τ and (2) lack of perceptual independence between m and τ (i.e., discrimination or identification of one variable increased substantially when the value of the other variable was randomized). Thus, it appears that encoding distance solely by means of the single-echo modulation parameters m and τ cannot lead to good distance resolution.

1.15.3 Publications

Shinn-Cunningham, B.G. "A Dynamic, Psycho-physical Model of Adaptation in Localization Experiments." *J. Acoust. Soc. Am.* 97(5): 3411 (1995).

Shinn-Cunningham, B.G., and A. Kulkarni. "Applications of Virtual Auditory Space." In *Virtual Auditory Space*. Ed. S. Carlile. New York: Landes Publishing Company. Forthcoming.

Shinn-Cunningham, B.G., H. Lehnert, G. Kramer, E.M. Wenzel, and N.I. Durlach. "Auditory Displays." In *Spatial and Binaural Hearing*. Eds. R. Gilkey and T. Anderson. New York: Erlbaum. Forthcoming.

Shinn-Cunningham, B.G., P.M. Zurek, E.R. Stutman, and R. Berkovitz. "Perception of Azimuth for Sources Simulated Using Two Loudspeakers in Natural Listening Environments." *Mid-Winter Meeting of the Association for Research in Otolaryngology*, St. Petersburg, Florida, February 4-8, 1996.

⁵⁵ D.S. Brungart, *Distance Information Transmission Using First Order Reflections*, S.M. thesis, Dept. of Electr. Eng. and Comput. Sci., MIT, 1994.

⁵⁶ D.M. Green, *Profile Analysis* (Oxford University Press, 1988); N.I. Durlach, L.D. Braida, and I. Ito, "Toward a Model for Discrimination of Broadband Signals," *J. Acoust. Soc. Am.* 62(4): 940-947 (1986); C.L. Farrar, C.M. Reed, Y. Ito, N.I. Durlach, L.A. Delhorne, P.M. Zurek, and L.D. Braida, "Spectral-shape Discrimination. 1. Results from Normal-hearing Listeners for Stationary Broadband Noises," *J. Acoust. Soc. Am.* 81(4) (1987).

1.16 Auditory Cues to Combat Spatial Disorientation

Sponsor

U.S. Air Force - Office of Scientific Research
Agreement with Brandeis University

Project Staff

Nathaniel I. Durlach, Professor Richard M. Held, Dr.
Barbara G. Shinn-Cunningham

Spatial disorientation (SD) in flight leads to the death of many flight crew members and wastes millions of dollars per year. Disorientation occurs because the aerial environment includes novel features to which our sensorimotor systems are not appropriately attuned.

In most past work directed towards correcting this problem, attention has focused primarily on the visual system, the vestibular system, and nonvestibular kinesthesia, as well as on interactions among these systems. In contrast, our work focuses on the possible use of auditory stimulation to alleviate SD problems.

To evaluate the efficacy of using auditory stimulation for this purpose, it is necessary to determine the extent to which and manner in which auditory perception is altered by acceleratory force fields. Although it is already known that certain illusory effects in audition can be induced by such fields (the audiogravic and audiogyral illusions), these effects have not yet been adequately characterized. Also, because such little previous research has been done in this area, it is possible that other important illusory affects also exist but have not yet been noted.

This research program is a collaborative effort by the Graybiel Spatial Orientation Laboratory at Brandeis University and the Sensory Communication Group of the Research Laboratory of Electronics at MIT. Whereas the former has personnel and facilities appropriate to the creation and study of acceleratory force fields, the latter has personnel and facilities appropriate to the study of audition.

The objectives of our work can be summarized as follows:

(1) Configure currently available equipment for providing accelerative forces and binaural audio in a manner suitable for studying the effects of such forces on auditory perception of azimuth (as well as auditory perception of pitch, loudness, and subjective duration);

(2) Make use of this facility to study how specified auditory perceptions are altered by application of various types of accelerative force fields (chosen to simulate the force fields encountered in aircraft flight);

(3) Construct a quantitative theoretical model to interpret the resulting data and to extend our ability to predict auditory function in non-1g force fields beyond the experimental conditions.

Work in the first eight months of the program (the period covered by this progress report) consisted of developing our experimental facilities and performing initial experiments examining how localization of a single sound source is affected by acceleratory force fields.

The initial experiments assessed changes in perceived localization of a sound in the azimuthal plane of the head during changes of the linear, gravito-inertial force field (G) in the head's azimuthal plane produced by centrifugation in a rotating room. Subjects were restrained in a bed, 2 m from the center of the rotating room, that kept the body's long axis in an Earth-horizontal plane and the interaural axis oriented along a radius of the room, right ear toward the center. Standard trials were 704 sec long. They involved 100 sec with the room stationary (normal 1 g condition), 152 sec of acceleration up to a speed that produced a G level two times the magnitude of normal g and tilted 60 deg toward the center of the rotating room, relative to normal g, 100 sec at this constant speed, 152 sec of deceleration and 200 sec with the room stationary again. In alternate trials, subjects set a sound to appear in the median plane of their head or set a joystick to indicate haptically the perceived median plane of the head. In sound localization trials, subjects listened to wide band noise gated at 4 Hz (50 percent duty cycle), spatialized with a Convolvotron II and played through earphones. The sound came on in a random location (azimuth) every 20 sec and the subject had 15 sec to set it to the apparent median plane of the head by adjusting a bidirectional switch that controlled the HRTF used by the Convolvotron. In haptic trials there was no sound except for a beep every 20 sec signaling the subject to set the joystick to coincide with head's perceived median plane.

Ten subjects participated in a series of three related experiments involving different G profiles. In the Experiment 1, the bed was flat, in an Earth-horizontal plane. Thus, when the room reached its dwell velocity, G was equal to 2 g in magnitude and was tilted 60 deg to the subject's right. Relative to the pre- and post-rotation periods, the average sound settings during rotation were 8.8 deg to right. (Put differently, subjects heard a physically constant

sound shift to the left during acceleration.) The shift developed gradually during acceleration. There was no evidence of a return to baseline (adaptation) during 100 sec of high G, and when the room decelerated auditory settings returned to pre-rotation baseline without overshoot or delay. Joystick settings were mirror symmetric to the sound settings, shifting to the left of baseline (Mean= 11.7 deg) during rotation. Thus, changes in both G magnitude and azimuthal orientation of G produce a change in the perceived, head-relative location of a constant auditory stimulus. The next two experiments showed that neither factor (magnitude or direction) alone is sufficient. In Experiment 2, the bed was pre-positioned to hold the subject's in a 60 deg right ear down position in 1 g so that during rotation the 2.0 g force field would be parallel to the median plane. There were no differences between auditory settings in 1.0 g with the body Earth horizontal and in 2.0 g with the body horizontal relative to the resultant G field. Thus, a change in G magnitude without change in G orientation is insufficient to alter auditory localization. Experiment 3 was run entirely in stationary, 1 g conditions. Subjects made auditory and haptic settings with the bed tilted to orientations between 75 deg left ear down and 75 deg right ear down, at 15 deg increments, in random order. There was no effect of tilt in 1 g on sound localization. Thus, a change in azimuthal orientation relative to the

normal 1 g field is not sufficient to produce an auditory localization shift. Head-relative changes in auditory localization do occur when G both increases in magnitude and tilts away from the median plane.

Supplementary observations confirmed and extended these observations. Experiment 4 confirmed the results of Experiment 1 with a different psychophysical technique. We provided a constant auditory stimulus throughout an entire 704 sec trial and asked subjects to point to the apparent location with the joystick. Four subjects perceived a 13 deg leftward shift with a time course similar that of the settings in Experiment 1. Perceived shift to the left of a constant sound is consistent with settings to the right of the perceived auditory midline. In Experiment 5, subjects were oriented with their left ear toward the center of the room in order to reverse, relative to Experiment 1, the direction of change in G orientation relative to the head during centrifugation. The results were that auditory settings were reversed relative to Experiment 1. In Experiment 6, we assessed whether auditory localization would remain constant during prolonged exposure to an augmented, tilted G field. During 10 minutes (as compared to 100 sec in Experiment 1) of exposure to a 2 g, 60 deg tilted field, there was no change in auditory or haptic settings relative to the median plane.

Section 3 Auditory Physiology

Chapter 1 Signal Transmission in the Auditory System

Chapter 1. Signal Transmission in the Auditory System

Academic and Research Staff

Professor Dennis M. Freeman, Professor Lawrence S. Frishkopf, Professor Nelson Y.S. Kiang, Professor William T. Peake, Professor William M. Siebert, Professor Thomas F. Weiss, Dr. Peter Cariani, Dr. Bertrand Delgutte, Dr. Donald K. Eddington, Dr. John J. Guinan, Jr., Dr. William M. Rabinowitz, Dr. Christopher A. Shera, Marc A. Zissman

Visiting Scientists and Research Affiliates

Dr. Robert D. Hall, Dr. Ruth Y. Litovsky, Dr. Sunil Puria, Michael E. Ravicz, Dr. John J. Rosowski, Joseph Tierney

Graduate Students

C. Cameron Abnet, Alexander J. Aranyosi, C. Quentin Davis, Scott B.C. Dynes, Benjamin M. Hammond, Shilpa M. Hattangadi, Gregory T. Huang, John R. Iversen, Laura K. Johnson, Sridhar Kalluri, Zohar Z. Karu, Christopher J. Long, Martin F. McKinney, Pankaj Oberoi, Mark N. Oster, Lisa F. Shatz, Janet L. Slifka, Konstantina M. Stankovic, Thomas M. Talavage, Su W. Teoh, Susan E. Voss

Undergraduate Students

Arash Lighvani, Christopher McKinney, Rosanne Rouf

Technical and Support Staff

Janice L. Balzer, David A. Steffens

1.1 Introduction

Research on the auditory system is carried out in cooperation with two laboratories at the Massachusetts Eye and Ear Infirmary (MEEI). Investigations of signal transmission in the auditory system involve the Eaton-Peabody Laboratory for Auditory Physiology. The Eaton-Peabody Laboratory's long-term objective is to determine the anatomical structures and physiological mechanisms that underlie vertebrate hearing and apply this knowledge to clinical problems. Studies of cochlear implants in humans are carried out at the MEEI Cochlear Implant Research Laboratory. Cochlear implants electrically stimulate intracochlear electrodes to elicit patterns of auditory nerve fiber activity that the brain can learn to interpret. The ultimate goal for these devices is to provide speech communication for the profoundly deaf.

1.2 Middle and External Ear

Sponsors

National Institutes of Health
Grant P01-DC-00119
Grant R01-DC-00194

Project Staff

Professor John J. Rosowski, Professor William T. Peake, Dr. Sunil Puria, Greg T. Huang, Michael E. Ravicz, Su W. Teoh, Susan E. Voss

1.2.1 Overall Goal

Our aim is to determine how the structure of the normal and pathological external and middle ear effects their acoustic and mechanical functions. To achieve this aim, we investigate the functions of the varied ear structures found in animals as well as measuring the function of normal and pathologic human middle ears. Acoustic and mechanical measurements are used to generate testable quantitative models of external and middle-ear function.

1.2.2 Middle-Ear Structure and Function

Last year, our studies of the structure and function of the middle-ears of different animals followed four paths: (1) tests of the common assumption that the cochlea responds to the difference in sound pressure at the two cochlear windows; (2) measurement of the acoustic function of an anatomically distinct section of the tympanic membrane, the *pars flaccida*; (3) an analysis of acoustic power flow through the external and middle ear in gerbils; and (4) a study of how the size of the ear affects middle-ear function. The first study confirmed that the window pressure difference is the primary cochlear input.¹ The second study resulted in the first demonstration of a role for *pars flaccida* in limiting the low-frequency response of the middle ear.² The third study, described in a paper which is forthcoming, demonstrated that the power-collection performance of the gerbil external and middle plays a large role in determining the overall shape of the gerbil audiogram. The fourth study compared middle-ear function in ears of similar structure, but greatly different size; the ears of house cats were compared with those of a lion. This work led to a quantitative rule relating skull length and middle-ear cavity function that was the subject of a meeting presentation.

Basic and Clinical Studies of the Human Middle Ear

Our work on human middle-ear function revolved around model analyses of surgical procedures used to reconstruct diseased middle ears. These studies led to three publications that presented surgical rules that could be used to improve the acoustic and mechanical function of diseased middle ears.

1.2.3 Publications

Journal Articles

Merchant S.N., J.J. Rosowski, and M.E. Ravicz. "Mechanics of Type IV and V Tympanoplasty. II. Clinical Analysis and Surgical Implications." *Am. J. Otol.* 16: 565-575 (1995).

Ravicz M.E., J.J. Rosowski, and H.F. Voigt. "Sound-power Collection by the Auditory Periphery of the Mongolian Gerbil *Meriones*

unguiculatus: II. External-ear Radiation Impedance and Power Collection." *J. Acoust. Soc. Am.* Forthcoming.

Rosowski J.J. and S.N. Merchant. "Mechanical and Acoustical Analyses of Middle-ear Reconstruction." *Am. J. Otol.* 16: 486-497 (1995).

Rosowski J.J., S.N. Merchant, and M.E. Ravicz. "Mechanics of Type IV and V Tympanoplasty. I. Model Analysis and Predictions." *Am. J. Otol.* 16: 555-564 (1995).

Voss S.E., J.J. Rosowski, and W.T. Peake. "Is the Pressure Difference Between the Oval and Round Windows the Effective Acoustic Stimulus for the Cochlea?" Submitted to *J. Acoust. Soc. Am.*

Meeting Paper

Rosowski J.J., W.T. Peake, G.T. Huang, and D.T. Flandermeyer. "Middle-ear Structure and Function in the Family *Felidae*." *Abstracts of the Eighteenth Midwinter Meeting of the Association for Research in Otolaryngology*, St. Petersburg, Florida, February 5-9, 1995, p. 5.

Theses

Teoh, S.W. *The Pars flaccida of the Gerbil Middle Ear*. S.M. thesis. Dept. of Electr. Eng. and Comput. Sci., MIT, 1995.

Voss, S.E. *The Cochlear Windows of the Cat*. S.M. thesis. Dept. of Electr. Eng. and Comput. Sci., MIT, 1995.

1.2.4 Cochlear Mechanisms

Sponsor

National Institutes of Health
Grant R01 DC00238

Project Staff

Professor Thomas F. Weiss, Professor Dennis M. Freeman, C. Cameron Abnet, Alexander J. Aranyosi, C. Quentin Davis, Shilpa M. Hattangadi, Laura K. Johnson, Zoher Z. Karu, Rosanne Rouf, Lisa F. Shatz, Janet L. Slifka

¹ S.E. Voss, *The Cochlear Windows of the Cat*, S.M. thesis, Dept. of Electr. Eng. and Comput. Sci., MIT, 1995.

² S.W. Teoh, *The Pars flaccida of the Gerbil Middle Ear*, S.M. thesis, Dept. of Electr. Eng. and Comput. Sci., MIT, 1995.

1.2.5 Using Video Microscopy to Measure Microscopic Motions

We have developed a video system to measure sound-induced motions of cochlear structures in the inner ear. The system uses a light microscope to project magnified images of cochlear structures onto a scientific grade CCD camera. Images from a series of focal depths are combined into a three-dimensional image that characterizes all of the structures in the cochlea including the basilar membrane, tectorial membrane, and sensory receptor (hair) cells. Stroboscopic illumination is used to obtain a sequence of three-dimensional images that are phase-locked to the audio-frequency hydrodynamic stimulus.

Development of Motion Detection Algorithms

Even after magnification by a light microscope, sound-induced motions of cochlear structures are smaller than the pixel spacing of a modern CCD camera. We have investigated two broad classes of algorithms for estimating subpixel displacements. The first class is based on optical flow and exploits relations between temporal and spatial derivatives of image brightness to estimate displacement. The second class is block-matching and determines translations between images by minimizing the difference between shifted versions of the original images. These two classes of algorithms were thought to be completely different, and the accuracy of subpixel estimates based on algorithms from the two classes have been reported to differ.³ However, we have proven that if you choose corresponding algorithms from the two classes, the estimators are identical.⁴ This insight has important consequences. Many properties of motion estimates are more easily understood when cast as an optical flow formulation; others are more easily understood when cast as block-matching. Furthermore, the computational costs for the two formulations are different. Knowing that the classes are equivalent allows one to capitalize on the strengths of each formulation.

Measurement of Sound-Induced Motion of Cochlear Structures

To characterize the relation between motion of a hair bundle and the overlying tectorial membrane, we analyzed motions of the structures in six planes of focus separated by $3\text{ }\mu\text{m}$.⁵ Displacements near the base of the hair bundle were larger than those near the tip (figure 1), which demonstrates that the hair bundle is rotating about its point of attachment to the hair cell. Displacements of the tectorial membrane were generally smaller than those of either the base or tip of the hair bundle. Furthermore, as distance from the base of the hair bundle increases, the motion shows increasing phase lag. In our 12 experiments to date, displacements of the tips and bases of hair bundles have been larger than those of the overlying tectorial membrane for frequencies throughout the lizard's auditory range. This result is consistent with the idea that inertial forces arising from the mass of the tectorial membrane and surrounding fluid tend to resist motion of the tectorial membrane.⁶ This result is not consistent with other theories that suggest that the tectorial membrane is a resonant structure.⁷ However, our results should be regarded as preliminary. Control experiments must be performed to assure that the cochlea is not damaged during experimentation.

The same data set used in the previous analysis can also be used to study mechanical events at the level of individual sensory hairs. The sinusoidal stimulus generates nearly sinusoidal motions of all the sensory hairs (top right panel of figure 2). To determine if there is relative motion between the sensory hairs, we applied our motion detection algorithm to estimate the motion of the right edge of the bundle and shifted the images to compensate for that motion. The resulting images show relative motions between sensory hairs (bottom right panel of figure 2). Motions of individual sensory hairs have been measured elsewhere,⁸ but only for hair

³ Q. Tian and M.N. Huhns, "Algorithms for Subpixel Registration," *Comput. Vision, Graphics Image Proc.* 35: 220-233 (1986).

⁴ C.Q. Davis, Z.Z. Karu, and D.M. Freeman, "Equivalence of Block Matching and Optical Flow Based Methods of Estimating Sub-pixel Displacements," *IEEE International Symposium for Computer Vision*, 1995, pp. 7-12.

⁵ D.M. Freeman and C.Q. Davis, "Using Video Microscopy to Characterize Micromechanics of Biological and Man-made Micromachines," *Solid-State Sensor and Actuator Workshop*, Hilton Head Island, South Carolina, June 2-6, 1996, forthcoming.

⁶ F. Mammano and R. Nobili, "Biophysics of the Cochlea: Linear Approximation," *J. Acoust. Soc. Am.* 93: 3320-3332 (1993).

⁷ J.B. Allen, "Cochlear Micromechanics: A Physical Model of Transduction," *J. Acoust. Soc. Am.* 68: 1660-1670 (1980).

⁸ R.K. Duncan, H.N. Hernandez, and J.C. Saunders, "Relative Stereocilia Motion of Chick Cochlear Hair Cells during High-frequency Water-jet Stimulation," *Aud. Neurosci.* 1: 321-329 (1995); R.B. MacDonald and D.P. Corey, "Stereocilia Bundles of the Bullfrog

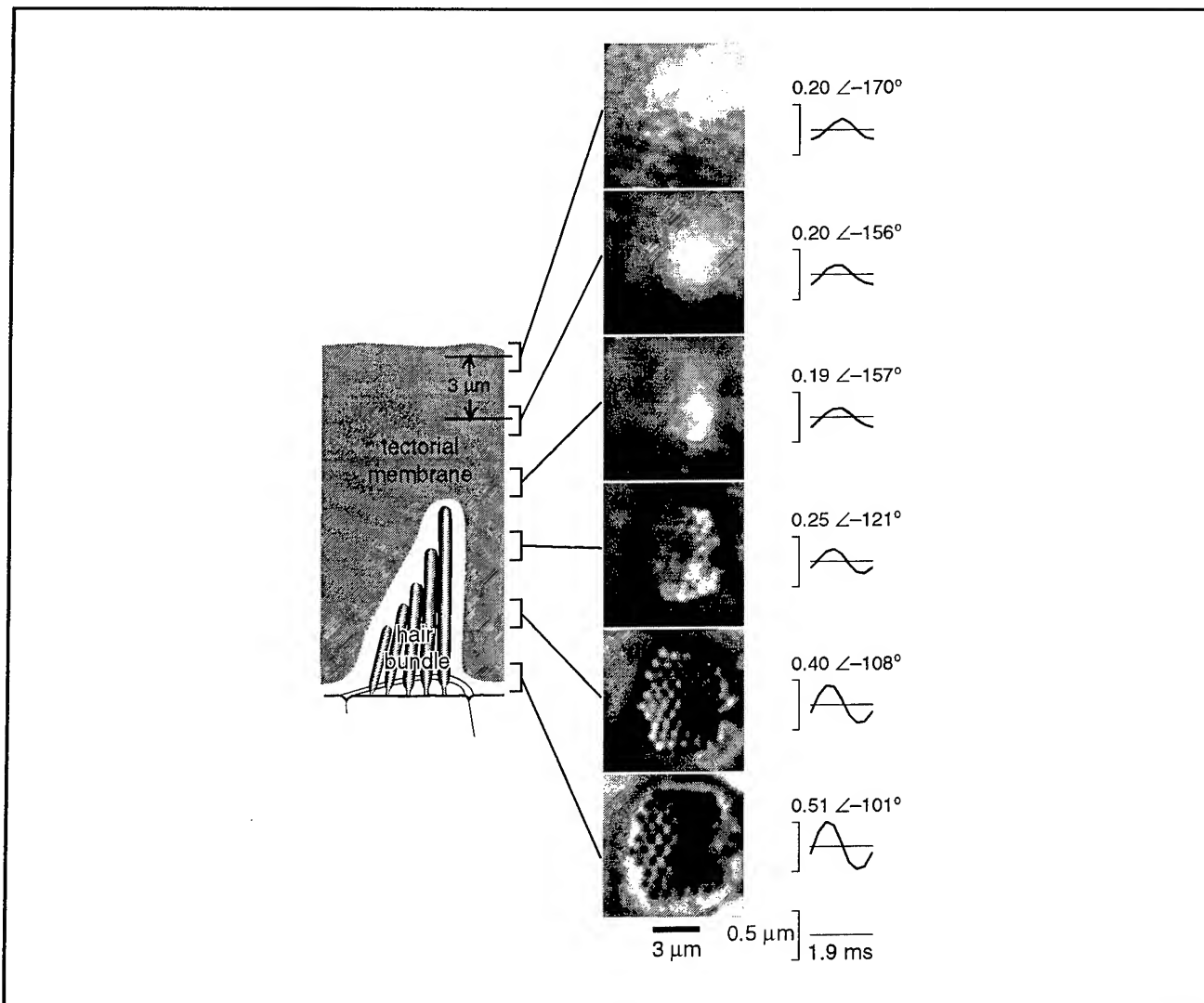


Figure 1. Sound-induced motions at six planes of focus through a hair bundle and overlying tectorial membrane. The intensity of the 513 Hz stimulus (115 dB SPL in the fluid adjacent to the basilar membrane) corresponds to approximately 89 dB SPL at the tympanic membrane. The left panel is a drawing of the hair bundle and overlying tectorial membrane. The center panels are images taken with our measurement system. Similar images acquired at eight different phases of the stimulus period were analyzed to quantify motion at the plane of each section. The waveforms (right panels) are the average horizontal displacements during one period of the stimulus. The numbers above each waveform give the peak-to-peak magnitude (in μm) and angle (in degrees) of the fundamental component of the displacement.

bundles that were stimulated with a water jet; the membranes through which natural stimuli are delivered had been removed.

Application of the Video System to Measure Man-Made Micromachines

Although originally developed to measure motions of cochlear structures, our video system has broader applications. Figure 3 shows results obtained for a man-made micromachine—a folded-

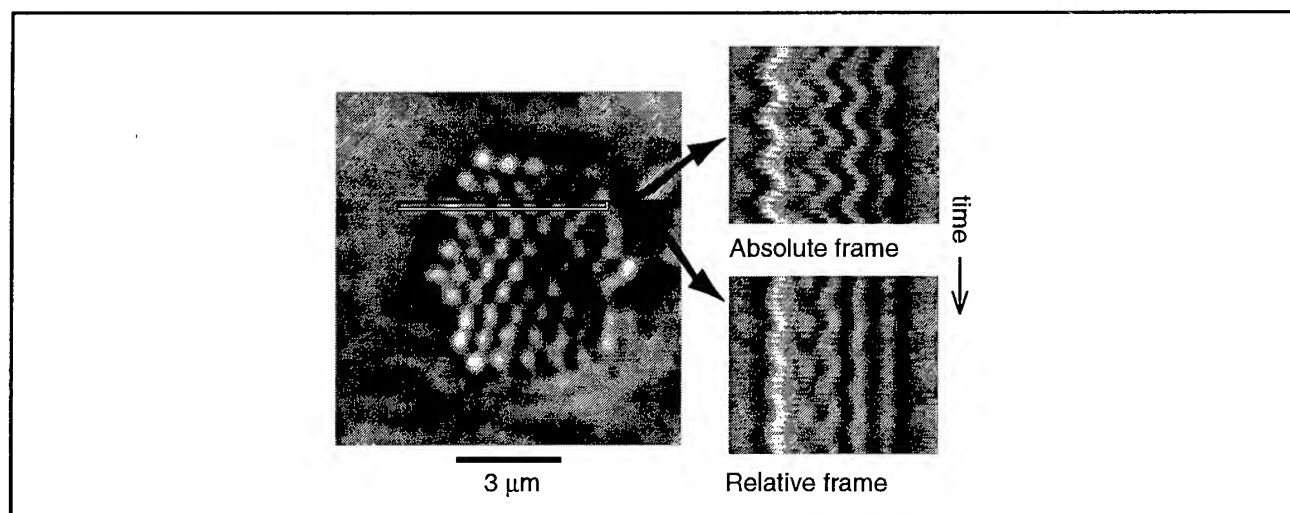


Figure 2. Motions of sensory hairs within a bundle. The left panel is an enlarged image of the hair bundle in figure 1, at a plane of section near the center of the bundle. The highlighted region was extracted from each of eight images acquired during eight evenly spaced phases of the stimulus period. The resulting regions were stacked one on top the next and repeated four times to generate the images in the right panels. The upper and lower right panels are similar, except that the images used to generate the lower panel were first shifted to cancel the motion of the right part of the hair bundle.

beam cantilever.⁹ This is a silicon structure that was fabricated by surface micromachining techniques. Using our measurement system, we measured motions of the shuttle in the horizontal direction and also in orthogonal directions. The motions in orthogonal directions represent failure modes for the device—failure modes that our motion measurement system can characterize. Characterizing failure modes can serve two important functions. First, it can help design engineers characterize and avoid failure modes. Second, the system may enable device fabricators to determine whether devices function properly before they are packaged. Such a system could even enable fabricators to correct minor problems using techniques such as laser trimming.

1.2.6 Material Properties of the Tectorial Membrane

Based on its biochemical composition and ultrastructure, the tectorial membrane (TM) is a polyelectrolyte gel. Such gels consist of macromolecules with ionizable fixed charges, small solutes (including ions), and water. Many of the

physicochemical properties of polyelectrolyte gels depend on the fixed charge concentration. For example, if the magnitude of the fixed charge concentration increases, mobile counterions will be drawn into the gel to maintain bulk electroneutrality. The increased concentration of mobile counterions represents an increase in osmotic pressure in the gel. Therefore water will flow into the gel and the gel will swell.

Knowledge about the pH dependence of charge groups in TM macromolecules can be used to test the importance of fixed charge in determining the material properties of the TM. If fixed charge density plays an important role, then changes in pH should result in predictable changes in TM volume. We have measured changes in the size and shape of the isolated TM of the mouse to changes in the pH of the surrounding bath.¹⁰ Altering the pH from 7 to a value between 5 and 11 caused changes of both the thickness and volume of the TM that were highly correlated; there was little change in surface area. Changes in thickness for pH between 6 and 9 were small: on the order of 1 percent. In basic solutions, swelling increased with pH: from <1 percent at pH 9 to 9 percent at pH 10 to 79 percent at pH 11. In mildly acidic solutions, thickness

⁹ D.M. Freeman and C.Q. Davis, "Using Video Microscopy to Characterize Micromechanics of Biological and Man-made Micromachines," Solid-State Sensor and Actuator Workshop, Hilton Head Island, South Carolina, June 2-6, 1996, forthcoming.

¹⁰ D.M. Freeman, S.M. Hattangadi, and T.F. Weiss, "Osmotic Responses of the Isolated Mouse Tectorial Membrane to Changes in pH," *Abstracts of the Nineteenth Midwinter Research Meeting of the Association for Research in Otolaryngology*, St. Petersburg, Florida, February 4-8, 1996.

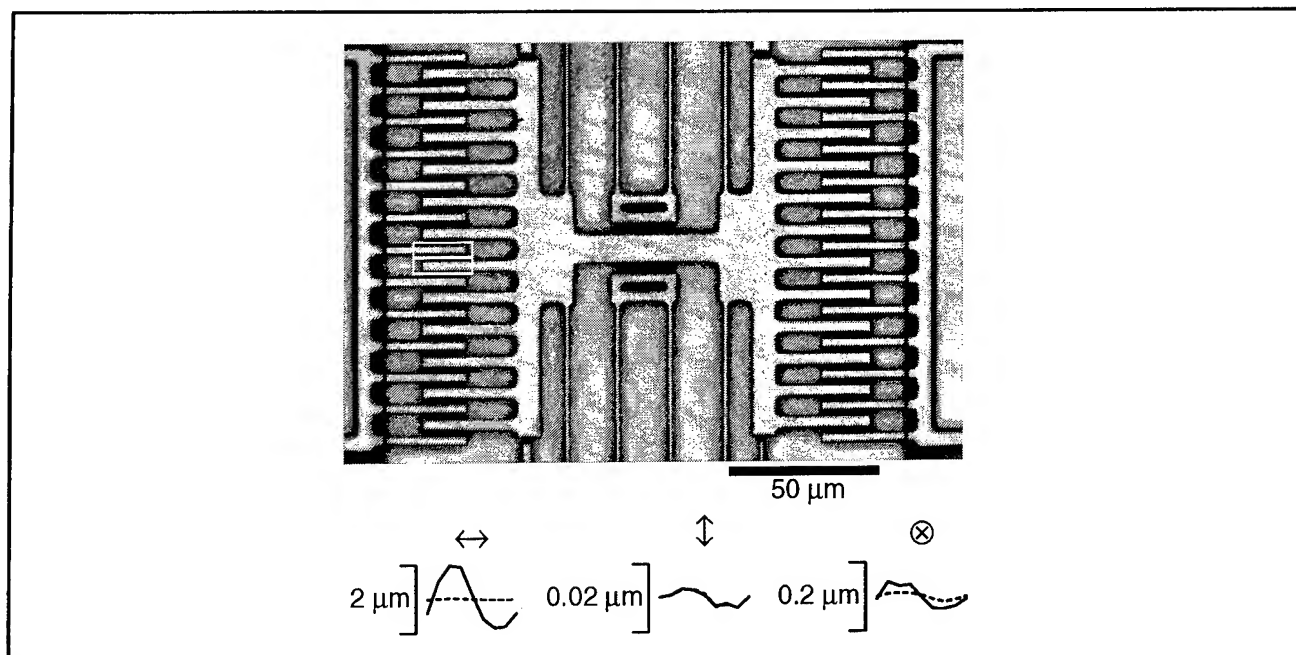


Figure 3. Motions of a folded-beam cantilever. The comb drive was stimulated with a 10 Hz sinusoidal voltage, 44 volts peak-to-peak with an 80 volt DC offset. Images such as the one shown here were obtained at 45 planes of focus with $0.45\ \mu\text{m}$ spacing to generate a three-dimensional image. Three-dimensional images were obtained at eight equally-spaced phases during the stimulus period. The portions of the images in the white boxes were analyzed to determine the motions of a stationary (top) and moving (bottom) tooth of the comb drive, shown in the three plots as dashed and solid curves, respectively. Displacements of the moving tooth were approximately $2\ \mu\text{m}$ peak-to-peak in the horizontal direction (left plot, solid line). Vertical motions (center plot, solid line) were about $5\ \text{nm}$ peak-to-peak, which is near the noise floor of our measurement system (without averaging). Motions orthogonal to the plane of focus were $0.08\ \mu\text{m}$ peak-to-peak for the moving tooth (right plot, solid line). Motions of the stationary tooth (dashed lines), which serve as control measurements to assess the stability of the measurement system, were 47 , 6 , and $26\ \text{nm}$ peak-to-peak in the horizontal, vertical, and out of the plane directions, respectively.

decreased to a local minimum of -1 percent near pH 6 which suggests that this is an isoelectric point of the TM. Thickness swelled in more acidic solutions, reaching a local maximum of 14 percent near pH 5.25. In solutions with very low pH (<4), the radial dimension and area of the TM decreased rapidly and monotonically while the thickness of the TM increased transiently and then decreased.

We have also measured osmotic responses of the mouse TM to isosmotic changes in the concentrations of sodium, potassium, and calcium in the bath.¹¹ Substitution of sodium for potassium as the predominant cation in the bath caused the TM to swell by an amount that depended on calcium concentration. Swelling was about 1 percent when the calcium concentration was $20\ \mu\text{mol/L}$ (similar to that of endolymph), 14 percent when the calcium

concentration was less than $7\ \mu\text{mol/L}$, and less than 1 percent when the calcium concentration was $2\ \text{mmol/L}$. Increasing calcium concentration without changing the predominant cation caused the TM to shrink. Decreasing calcium concentration by removal of calcium or by the addition of the calcium chelator EGTA caused the TM to swell.

To provide a conceptual framework for our measurements and to guide further experimental studies, we have analyzed the equilibrium behavior of an isotropic polyelectrolyte gel model of the TM.¹² The theory presumes that: (1) the gel is homogeneous and isotropic; (2) all ions in the gel are in electrodiffusive equilibrium with the bath ions; (3) the total charge density in the gel is zero; (4) the gel is in osmotic equilibrium with the bath; (5) the hydrodynamic pressure in the gel is proportional to

¹¹ D.M. Shah, D.M. Freeman, and T.F. Weiss, "The Osmotic Response of the Isolated, Unfixed Mouse Tectorial Membrane to Isosmotic Solutions: Effect of Na^+ , K^+ , and Ca^{2+} Concentration," *Hear. Res.* 87: 187-207 (1995).

¹² T.F. Weiss and D.M. Freeman, "Isotropic Polyelectrolyte Gel Model of the Tectorial Membrane," *Abstracts of the Nineteenth Midwinter Research Meeting of the Association for Research in Otolaryngology*, St. Petersburg, Florida, February 4-8, 1996.

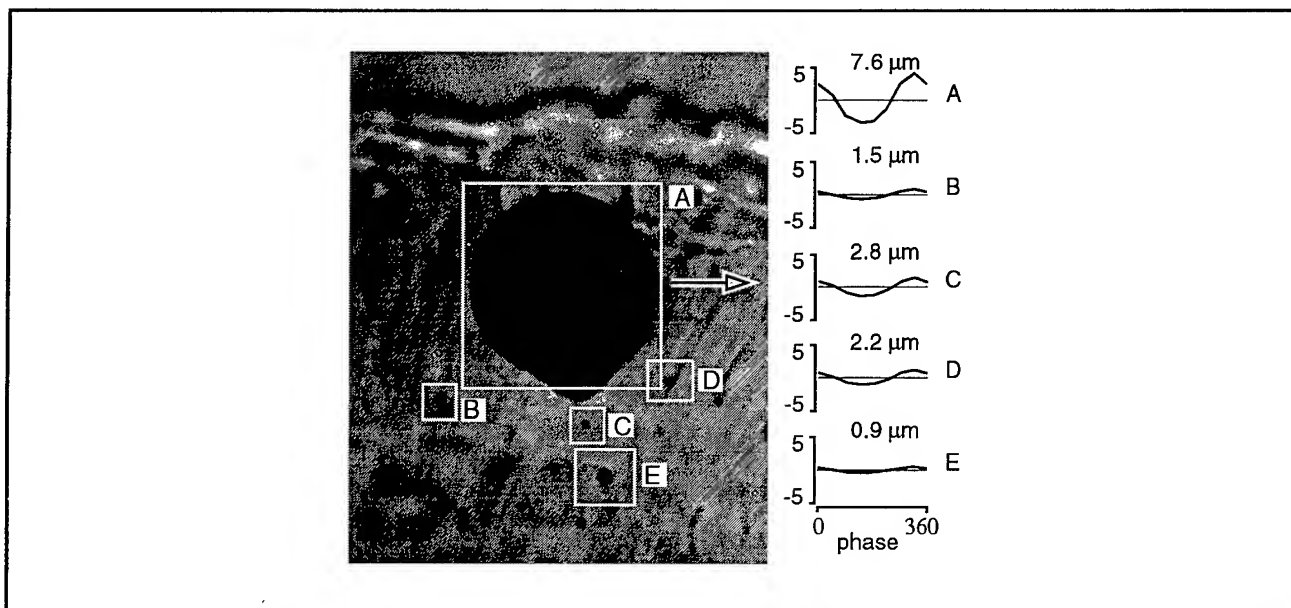


Figure 4. Image of an isolated mouse TM with a $50\ \mu\text{m}$ iron bead (region A) fixed to its surface. A force of $10\ \mu\text{N}$ at $10\ \text{Hz}$ is applied to the bead using electromagnets. The magnitudes of deformations for the five highlighted regions are plotted versus the phase of the force excitation. Positive deformations are in the direction of the arrow. The number above each plot indicates the peak-to-peak amplitude of deformation.

the volume increment; and (6) fixed charge groups in the gel are in chemical equilibrium with the mobile ions. Results demonstrate important properties of gels—including their ability to concentrate ions, generate an electrical potential, and swell. The model demonstrates how these properties are linked to the concentration of fixed charge in the gel. The model also allows us to predict the fixed charge concentration of the TM using previously published¹³ measurements of the electrical potential of the TM in solutions with different osmolarities. The resulting estimate is within a factor of three of estimates based on biochemical analyses.

1.2.7 Mechanical Properties of the Tectorial Membrane

We have developed a new method for applying calibrated forces to microscopic tissue samples. The forces generate deformation of the tissue that can be measured with video microscopy. The system has been applied to the investigation of the material properties of the TM, which are thought to play a key role in hearing.

The tectorial membrane of a mouse is isolated from the tissue that normally surrounds it and attached to

a glass slide. A small iron bead is then fixed to the surface of the tissue. An external magnetic field generates forces on the bead that are transmitted to the TM. The forces, parallel to the tissue surface, generate deformations of the tissue that provide information about its mechanical properties. Forces can be applied to different regions, in different directions, and at various frequencies to obtain information about the tissue's mechanical properties.

Figure 4 illustrates a typical result in which a $10\ \mu\text{N}$ force caused a $7.6\ \mu\text{m}$ displacement of the iron bead. This result indicates that the portion of the TM attached to the bead had an effective stiffness of $1.3\ \text{N/m}$. Parts of the TM near the iron bead also move, but the displacements decrease with distance from the bead with a space constant of approximately $10\ \mu\text{m}$. Both the space constant and effective stiffness are determined by (1) the material properties of the TM, (2) the geometry of the TM, and (3) the attachment of the TM to the glass slide. We are currently developing a mechanical model to quantify the importance of each of these factors. Results are important for understanding the role that the TM plays in determining the motions of hair bundles.

¹³ K.P. Steel, "Donnan Equilibrium in the Tectorial Membrane," *Hear. Res.* 55: 263-272 (1983).

1.2.8 Regulation of pH by Cochlear Hair Cells

As part of a project to quantify the mechanisms that regulate intracellular ion concentrations of hair cells, we are studying the regulation of hair cell pH. Since hair cells carry auditory information in the form of ionic signals, maintenance of the cells' ion concentrations is vital to their function in hearing. Maintenance of pH in particular is important for the function of many cellular enzymes, and it has recently been suggested that acoustic stimulation can affect hair cell pH.¹⁴

Hair cells in an in vitro preparation of the cochlea of the alligator lizard are loaded with the fluorescent dye BCECF, whose fluorescence intensity is a function of pH. Changes in dye fluorescence are measured using a video microscope and calibrated to estimate pH. Figure 5 illustrates results of an experiment in which 20 mM propionic acid is transiently added to the artificial perilymph bathing the cochlea. Because propionic acid permeates membranes quickly, the intracellular pH of hair cells decreases. However, during continued exposure to the acid, the intracellular pH gradually returns to a value near its starting value ($\tau \sim 5$ min). The subsequent removal of the acid triggers a similar transient increase in pH. Results in figure 5 are for just one cell. However, our fluorescence images simultaneously provide estimates of pH in all 50-100 cells in the image. The mean resting pH across cells in this experiment was 6.93 ± 0.16 ($n = 88$). Adding acid lowered the pH by 0.23 ± 0.04 , followed by recovery at an initial rate of 0.04 ± 0.01 pH units/min. Removing the acid caused the pH to rise by 0.42 ± 0.11 , then recover at an initial rate of 0.05 ± 0.02 pH units/min.

These results demonstrate that fluorescence microscopy can be used to characterize pH changes in cochlear hair cells of the alligator lizard. We are currently working on experiments to measure changes in fluorescence during acoustical stimulation—experiments that will directly assess the effect of acoustic stimulation on the regulation of intracellular pH.

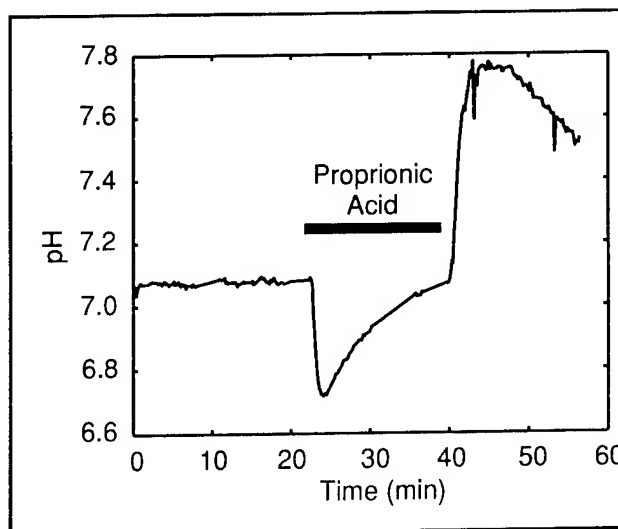


Figure 5. Change in intracellular pH as a function of time during perfusion of propionic acid. During the first interval of this experiment, the cochlea was bathed in artificial perilymph. During the second interval, which is indicated in this figure by the bar, 20 mM propionic acid was added to the bath. The perfusate in the third interval was the same as that in the first interval.

1.2.9 Publications

Journal Articles

Duncan, R.K., H.N. Hernandez, and J.C. Saunders. "Relative Stereocilia Motion of Chick Cochlear Hair Cells during High-frequency Water-jet Stimulation." *Aud. Neurosci.* 1: 321-329 (1995).

Shah, D.M., D.M. Freeman, and T.F. Weiss. "The Osmotic Response of the Isolated, Unfixed Mouse Tectorial Membrane to Isosmotic Solutions: Effect of Na^+ , K^+ , and Ca^{2+} Concentration." *Hear. Res.* 87: 187-207 (1995).

Published Meeting Papers

Davis, C.Q., Z.Z. Karu, and D.M. Freeman. "Equivalence of Block Matching and Optical Flow Based Methods of Estimating Sub-pixel Displacements." *IEEE International Symposium for Computer Vision*, 1995, pp. 7-12.

¹⁴ D. Ronan and E.A. Mroz, "Stability of Solute Composition in a Simple Hair-cell Model," *Abstracts of the Nineteenth Midwinter Research Meeting of the Association for Research in Otolaryngology*, St. Petersburg, Florida, February 4-8, 1996.

Meeting Papers Presented

Davis, C.Q., and D.M. Freeman. "Direct Observations of Sound-induced Motions of the Tecticular Lamina, Tectorial Membrane, Hair bundles, and Individual Stereocilia." *Abstracts of the Eighteenth Midwinter Research Meeting of the Association for Research in Otolaryngology*, February 1995, pp. 189.

Freeman, D.M., and T.F. Weiss. "Species Dependence of Osmotic Responses of the Tectorial Membrane: Implications of Structure and Biochemical Composition." *Abstracts of the Eighteenth Midwinter Research Meeting of the Association for Research in Otolaryngology*, February 1995, pp. 188.

Freeman, D.M., and C.Q. Davis. "Using Video Microscopy to Characterize Micromechanics of Biological and Man-made Micromachines." Solid-State Sensor and Actuator Workshop, Hilton Head Island, South Carolina, June 2-6, 1996. Forthcoming.

Shah, D.M., D.M. Freeman, and T.F. Weiss. "The Osmotic Response of the Isolated, Unfixed Mouse Tectorial Membrane: Effect of Na^+ , K^+ , and Ca^{2+} Concentration." *Abstracts of the Eighteenth Midwinter Research Meeting of the Association for Research in Otolaryngology*, February 1995, pp. 117.

1.3 Auditory Neural Processing of Speech

Sponsor

National Institutes of Health
Grant R01-DC02258
Grant T32-DC00038

Project Staff

Dr. Bertrand Delgutte, Dr. Peter Cariani, Benjamin M. Hammond, Sridhar Kalluri, Martin F. McKinney

The long-term goal of this project is to determine how speech is coded in brainstem auditory nuclei, particularly the inferior colliculus. In the past year, we have written a review of this research area and concentrated on three projects: (1) the neural representation of vowel formants; (2) the neural encoding of amplitude modulations in speech; and (3) functional models of cochlear nucleus neurons for speech processing.

We are continuing a collaborative study of the coding of vowel formants in the auditory nerve with

Dr. Tatsuya Hirahara from the NTT Basic Research Laboratories in Tokyo. Formant frequencies are important for vowel perception, yet their neural representation is poorly understood, particularly in the low frequency region where individual harmonics near the formant frequency are psychophysically resolved. Recent psychophysical results of Dr. Hirahara suggest that the phonetic boundary between certain vowels depends on the amplitude ratio of two "crucial" harmonics spanning the first-formant frequency (F_1). We are investigating the auditory representation of vowels by recording the activity of auditory-nerve fibers (ANFs) in anesthetized cats in response to /i/-e/ synthetic-vowel continua. For vowels with high fundamental frequencies (350 Hz), the crucial harmonics were directly represented in ANF responses, whereas the first formant frequency was not. Specifically, profiles of average discharge rate against characteristic frequency (CF) always showed local maxima at the frequencies of crucial harmonics rather than at F_1 . Furthermore, interspike intervals occurred at the periods of these harmonics rather than at the formant period ($1/F_1$). These findings lend support to the hypothesis put forth by Dr. Hirahara that the fine spectral structure near the first formant is important for vowel perception. This hypothesis is at variance with the widely-held view of vowel perception that vowel identity is based on the spectral envelope derived through wide-band spectral integration. Together, our physiological results and Hirahara's psychophysical findings argue for a new model of vowel perception in which crucial information about fine spectral structure would play a key role.

Speech shows intense vowels alternating with relatively weak consonants. This alternation results in pronounced amplitude modulations near 3-4 kHz that are important for speech understanding. As a first step toward understanding the neural encoding of these modulations, we measured modulation transfer functions (MTFs) and responses to speech utterances in ANFs of anesthetized cats. The ANF-MTF relates (as a function of modulation frequency) the modulation index of an AM stimulus to that of the neural response. ANF-MTFs were bandpass, with high frequency cutoffs in the range 200-700 Hz, reflecting the inability of ANFs to follow fast modulations. Low frequency cutoffs were typically between 3 and 50 Hz, indicating a reduction in the ability to follow slow modulations, consistent with adaptation. A three-stage model incorporating bandpass filtering, instantaneous compression, and the ANF-MTF simulated the envelope of responses to speech utterances. These results indicate that the MTF is useful for predicting neural responses to speech and this concept may also be useful for predicting the responses of central auditory neurons.

They further suggest that improved estimates of speech intelligibility in noise and reverberation might be developed by taking into account the MTFs of auditory neurons.

As a first step towards developing functional models of auditory neurons for speech processing, we are developing a model of onset responders in the cochlear nucleus (CN). These cells, which are characterized by a prominent peak at the onset of the stimulus in their tone-burst evoked peri-stimulus time (PST) histograms, are of particular interest because they respond to acoustic transients that are important in speech perception. Our single-node circuit model of onset cells receives model ANF inputs via excitatory synapses that are implemented by time-varying conductances. Onset PST histograms are obtained in model cells with short membrane time constants and many subthreshold synaptic inputs. By varying the number of model ANF inputs and the strength of these inputs, we can achieve various onset responses such as On-I and On-L as well as primary-like responses. However, the model fails to simulate the physiological observation that off-CF subthreshold tones enhance onset-cell responses to CF tones. This failure may be due to the asynchrony of AN inputs of different CF introduced by the traveling wave along the basilar membrane. We are examining simplified models to better identify the mechanisms that give rise to this cross-frequency summation.

1.3.1 Publications

Journal Articles

Cariani, P.A., and B. Delgutte. "Neural Correlates of the Pitch of Complex Tones. I. Pitch and Pitch Saliency." *J. Neurophys.* Forthcoming.

Cariani, P.A., and B. Delgutte. "Neural Correlates of the Pitch of Complex Tones. II. Pitch Shift, Pitch Ambiguity, Phase Invariance, Pitch Circularity, Rate Pitch and the Dominance Region for Pitch." *J. Neurophys.* Forthcoming.

Chapter in a Book

Delgutte, B. "Auditory Neural Processing of Speech." In *Handbook of Phonetic Sciences*. eds. W.J. Hardcastle and J. Laver. Oxford: Blackwell. Forthcoming.

Meeting Papers Presented

Hammond, B.M., and B. Delgutte. "Modulation Transfer Functions of Auditory-nerve Fibers: Measurements and Use in Predicting the Neural Response to Speech." *Abstracts of the Nineteenth Midwinter Research Meeting of the Association for Research in Otolaryngology*, St. Petersburg, Florida, February 4-8, 1996, p. 78.

Hirahara, T., P.A. Cariani, and B. Delgutte. "Representation of Low-frequency Vowel Formants in the Auditory Nerve." *Abstracts of the Nineteenth Midwinter Research Meeting of the Association for Research in Otolaryngology*, St. Petersburg, Florida, February 4-8, 1996, p. 80.

McKinney, M.F., and B. Delgutte. "Physiological Correlates of the Stretched Octave in Interspike Intervals of Auditory-nerve Fibers." *Abstracts of the Eighteenth Midwinter Research Meeting of the Association for Research in Otolaryngology*, St. Petersburg, Florida, February 1995, p. 175.

1.4 Binaural Interactions in Auditory Brainstem Neurons

Sponsor

National Institutes of Health
Grant P01-DC00119

Project Staff

Dr. Bertrand Delgutte, Dr. Ruth Y. Litovsky

The overall goal of this project is to characterize neural mechanisms for sound localization in the auditory midbrain. Studies conducted in the past year were aimed at comparing two possible neural codes for the location of sound sources: an average-rate code, and a temporal code. For this purpose, we made use of an existing data base on responses of inferior-colliculus (IC) neurons to "virtual space" stimuli. In this technique, closed acoustic systems are used to mimic the sound pressure waveforms produced in the ear canals of cats by sound sources originating from different directions. The specific stimulus used in these experiments was a 200-msec burst of pseudo-random broadband noise.

The sensitivity index d' was used to characterize the ability of single IC neurons to discriminate sound sources differing in virtual azimuth or elevation. This index makes it possible to compare psychophysical performance with that of an ideal

observer that would optimally process information available in neural responses. The sensitivity index was computed for two response measures: discharge rate averaged over the duration of the stimulus, and a small number (< 6) of principal components that concisely describe the temporal patterns of neural discharge for our stimuli.

For some neurons, d' based on average rates was within a factor of 2-3 of psychophysical performance over a narrow range of azimuths or elevations. Psychophysical performance could be approached over a broader range by selecting for each azimuth of elevation the neuron that gave the best performance. This finding suggests that psychophysical performance in discriminating the position of sound sources can be accounted for by average rate information available in a small fraction of the available pool of IC neurons.

For most neurons, performance based on the principal components was generally better than that based on average discharge rate, particularly when discharge rate showed a plateau as a function of azimuth or elevation. However, this advantage of the temporal code was minimal for the neurons that showed the best performance based on average rate alone. This result suggests that there would be little advantage in using a temporal code over a rate code for the location of sound sources at the level of the IC, except in conditions when average rate information from the most sensitive neurons would be degraded.

1.5 Electrical Stimulation of the Auditory Nerve

Sponsor

National Institutes of Health
Grant P01-DC00361

Project Staff

Dr. Bertrand Delgutte, Scott B.C. Dynes

The overall goal of this project is to study the physiological mechanisms of electrical stimulation of the cochlea to help design better processing schemes for cochlear implants. Experiments conducted last year were aimed at characterizing auditory-fiber correlates of interactions observed psychophysically when pulsatile electric stimuli are applied in rapid succession. Such interactions are likely to play an important role in the popular continuous interleaved sampling (CIS) speech processors. We are also evaluating Hodgkin-Huxley-like models of nerve membrane for the stimuli used in our experiments.

In our experiments conducted in anesthetized cats, a conditioner consisting of one or more pulses of equal amplitude, is used to modify the state of an auditory-nerve fiber. This conditioner is followed at various delays by a single pulse used to probe the state of the modified fiber. The neural threshold and dynamic range are measured for the probe pulse following various conditioners. Subthreshold conditioners result in a short period (< 1 msec) of sensitization, followed by a longer (4-5 msec) desensitization period. Sensitization decreases with increasing numbers of conditioning pulses. The neural dynamic range is increased during the sensitization period. Suprathreshold conditioners lead to a relative refractory period, with probe threshold resuming its resting value after 4 msec. There was no significant change in the relative refractory period as the number of pulses and interpulse intervals were varied. Following a suprathreshold conditioner, the dynamic range is decreased for short probe delays.

Modeling studies show that these experimental phenomena can be qualitatively reproduced using standard Hodgkin-Huxley-like models. Specifically, the Hodgkin-Huxley model of the squid giant axon and the Rothman-Manis-Young model of cochlear nucleus bushy cells provided simulations that were broadly consistent with the data. In contrast, models of mammalian systems (rat and rabbit sciatic nerve) provided poor simulations of the data, apparently because the time constants of their state variables are much quicker than those controlling cat auditory nerve fibers. A stochastic extension of the Hodgkin-Huxley model was developed in order to simulate the probabilistic character of neural responses. There was qualitative agreement between this stochastic model and the experimental data on how the dynamic range is affected by conditioning pulses.

It is clear that the type of temporal interactions we have studied must occur for present-day cochlear implant stimulation strategies. For a typical CIS processor, the interpulse interval for individual electrodes is less than 1 msec. The temporal interactions seen experimentally with sub- and suprathreshold conditioners last much longer, typically 4-5 msec. Moreover, the magnitude of the sensitization and desensitization due to temporal interactions are a significant fraction of the 12 dB perceptual dynamic range of human cochlear implant subjects.

Our finding that Hodgkin-Huxley-like models can simulate most of the experimental results suggests that the same models might be used to predict responses to the more complex stimuli produced by CIS processors. If so, it might be possible to use these models to determine the electrical stimulus

needed to produce a desired pattern of activity in the auditory nerve, and thereby help design improved processing schemes.

1.5.1 Publications

Meeting Papers Presented

Delgutte, B., and S.B.C. Dynes. "Implications of Auditory Neural Coding for Signal Processing in Cochlear Implants." Abstracts of the 1995 Conference on Implantable Auditory Prostheses, Asilomar, California, p. 1, 1995.

Dynes, S.B.C., and B. Delgutte. "Temporal Interactions of Electric Pulses in the Auditory Nerve: Experiments and Modeling." Abstracts of the 1995 Conference on Implantable Auditory Prostheses, Asilomar, California, p. 43, 1995.

Thesis

Dynes, S.B.C. *Discharge Characteristics of Auditory-nerve Fibers for Pulsatile Electrical Stimuli*. Ph.D. diss. Dept. of Physics, MIT, 1995.

1.6 Cochlear Efferent System

Sponsor

National Institutes of Health
Grant 2RO1 DC00235

Project Staff

Dr. John. J. Guinan, Jr., Christopher A. Shera, Konstantina M. Stankovic

Our aim is to understand the physiological effects produced by efferents in the mammalian inner ear including medial olivocochlear efferents, which terminate on outer hair cells, and lateral efferents, which terminate on auditory-nerve fibers.

During the past year, we have continued publishing our work on a class of vestibular primary afferent neurons that arise in the saccule and respond to sound at moderately high sound levels. A previously submitted paper was revised and published.¹⁵ A paper that summarized our results and pointed out that certain acoustically-evoked neck-muscle reflexes appear to be mediated by these acoustically responsive vestibular fibers was submitted for publication.¹⁶

In a recently submitted manuscript,¹⁷ we show that efferent inhibition of auditory-nerve fibers is largest at moderate to high sound levels, a finding that is unexpected with most current theories of the action of efferents. Previous work has shown that medial efferents can inhibit responses of auditory-nerve fibers to high-level sounds and that fibers with low spontaneous rates (SRs) are inhibited most. However, quantitative interpretation of these data was made difficult by effects of adaptation. To minimize systematic differences in adaptation, we measured efferent inhibition with a randomized presentation of both sound level and efferent stimulation. In anesthetized cats, we stimulated efferents with 200/s shocks and recorded auditory-nerve-fiber responses to tone bursts (0-100 dB SPL, 5 dB steps) at their characteristic frequencies. Below 50 dB SPL, efferent inhibition (measured as equivalent attenuation) was similar for all fibers with similar CFs in the same cat. At 45-75 dB SPL, low-SR and medium-SR fibers often showed inhibition that was much larger than at low sound levels. At 90-100 dB SPL, these fibers still had substantial inhibition even. Expressed as a fractional decrease in rate, at 90-100 dB SPL the inhibition was 0 percent, 6 percent and 13 percent for high-, medium- and low-SR fibers with the differences statistically significant. Finding the largest equivalent attenuations at 45-75 dB SPL does not fit with the hypothesis that medial-efferent inhibition is due solely to a reduction of basilar-membrane motion. The large attenuations, some over 50 dB, indicate that medial efferent inhibition is more potent than previously reported. During the past year we pre-

¹⁵ M.P. McCue and J.J. Guinan, Jr., "Spontaneous Activity and Frequency Selectivity of Acoustically Responsive Vestibular Afferents in the Cat," *J. Neurophys.* 74: 1563-1572 (1995).

¹⁶ M.P. McCue and J.J. Guinan, Jr. "Sound-Evoked Activity in Primary Afferent Neurons of the Mammalian Vestibular System," submitted to *Am. J. Otolaryng.*

¹⁷ J.J. Guinan, Jr., and K.M. Stankovic, "Medial Efferent Inhibition Produces the Largest Equivalent Attenuations at Moderate to High Sound Levels in Cat Auditory-nerve Fibers," submitted to *J. Acoust. Soc. Am.*

sented this work along with work comparing the time course of efferent effects.¹⁸

In work done with M.C. Liberman and S. Puria,¹⁹ we developed a method for measuring ipsilaterally-evoked efferent inhibition by measuring the time course of its effect on distortion-product otoacoustic emissions (DPOAEs). In anesthetized cats, the onset behavior of the DPOAE at 2f₁-f₂ produced by primary tones at frequencies f₁ and f₂ (f₁<f₂) was measured with temporal resolution finer than 70 msec. After the onset of the primary tones, the DPOAE adapted by as much as 6 dB for monaural stimulation and 10 dB when the primaries were presented binaurally. DPOAE adaptation consisted of a large, rapid component (time constant approximately 100 msec), and a small, slower component (time constant approximately 1000 msec). The rapid component disappeared when the olivocochlear bundle (OCB) was cut, whereas the slow adaptation persisted. The loss of rapid adaptation after OCB section was accompanied by a concomitant increase in the steady-state amplitude of the DPOAE. Thus, an intact OC reflex can significantly depress DPOAEs during routine measurements. Tests for the ipsilateral OC reflex based on the phenomenon of rapid adaptation should be both feasible and useful in human subjects. Also during the past year, a previously submitted paper has been revised and accepted.²⁰

Also during the past year, a chapter on "The Physiology of Olivocochlear Efferents" was submitted and accepted.²¹

1.6.1 Publications

Journal Articles

Guinan, J.J., Jr., and K.M. Stankovic. "Medial Efferent Inhibition Produces the Largest Equivalent Attenuations at Moderate to High Sound

Levels in Cat Auditory-nerve Fibers." *J. Acoust. Soc. Am.* Forthcoming.

Liberman, M.C., S. Puria, and J.J. Guinan, Jr. "The Ipsilaterally Evoked Olivocochlear Reflex Causes Rapid Adaptation of the 2f₁-f₂ DPOAE." Submitted to *J. Acoust. Soc. Am.*

McCue, M.P., and J.J. Guinan, Jr. "Spontaneous Activity and Frequency Selectivity of Acoustically Responsive Vestibular Afferents in the Cat." *J. Neurophys.* 74: 1563-1572 (1995).

McCue, M.P., and J.J. Guinan, Jr. "Sound-Evoked Activity in Primary Afferent Neurons of the Mammalian Vestibular System. Submitted to *Am. J. Otolaryngology*.

Puria, S., J.J. Guinan, Jr., and M.C. Liberman. "Olivocochlear Reflex Assays: Effects of Contralateral Sound on Compound Action Potentials vs. Ear-canal Distortion Products." *J. Acoust. Soc. Am.* 99: 500-507 (1996).

Chapter in a Book

Guinan, J.J., Jr. "The Physiology of Olivocochlear Efferents." In *The Cochlea*. Eds. P.J. Dallos, A.N. Popper, and R.R. Fay. New York: Springer-Verlag. Forthcoming.

Meeting Paper Presented

Guinan, J.J., Jr., and K.M. Stankovic. "Medial Olivocochlear Efferent Inhibition of Auditory-nerve Firing Mediated by Changes in Endocochlear Potential." *Abstracts of the Eighteenth Midwinter Research Meeting of the Association for Research in Otolaryngology*, February 1995, p. 172.

¹⁸ J.J. Guinan, Jr., and K.M. Stankovic, "Medial Olivocochlear Efferent Inhibition of Auditory-nerve Firing Mediated by Changes in Endocochlear Potential," *Abstracts of the Eighteenth Midwinter Meeting of the Association for Research in Otolaryngology*, St. Petersburg, Florida, February 1995, p. 172.

¹⁹ M.C. Liberman, S. Puria, and J.J. Guinan, Jr., "The Ipsilaterally Evoked Olivocochlear Reflex Causes Rapid Adaptation of the 2f₁-f₂ DPOAE," submitted to *J. Acoust. Soc. Am.*

²⁰ S. Puria, J.J. Guinan, Jr., and M.C. Liberman. "Olivocochlear Reflex Assays: Effects of Contralateral Sound on Compound Action Potentials vs. Ear-canal Distortion Products," *J. Acoust. Soc. Am.* 99: 500-507 (1996).

²¹ J.J. Guinan, Jr., "The Physiology of Olivocochlear Efferents," in *The Cochlea*, eds. P.J. Dallos, A.N. Popper, and R.R. Fay (New York: Springer-Verlag, forthcoming).

1.7 Interactions of Middle-Ear Muscles and Olivocochlear Efferents.

Sponsor

National Institutes of Health
Grant P01 DC00119

Project Staff

Dr. John J. Guinan, Jr.

Our aim is to determine the actions and interactions of the acoustically elicited middle-ear muscle reflexes and the olivocochlear efferent reflexes.

During the reporting period, we have begun a project aimed at determining the pathways of the medial olivocochlear efferents. For three reflexes which affect transmission of signals through the peripheral auditory system: the stapedius muscle, the tensor-tympani muscle, and the medial olivocochlear efferents, we know the locations of the effector neurons but not the locations of the brainstem interneurons neurons which relay information from the auditory nerve to the motoneurons. By selectively lesioning various areas in the cochlear nucleus with injections of kainic acid and monitoring the resulting changes in these reflexes, we hope to determine which areas of the cochlear nucleus contain interneurons which mediate these reflexes. Initial work shows that with kainic acid injections that destroy or damage substantial parts of the cochlear nucleus, the medial olivocochlear efferent acoustic reflex remains intact.

1.8 Cochlear Implants

Sponsor

National Institutes of Health
Grant P01-DC00361
Contract N01-DC22402

Project Staff

Dr. Donald K. Eddington, Dr. Robert D. Hall, Arash Lighvani, Christopher McKinney

The basic function of a cochlear prosthesis is to provide a measure of hearing to the deaf by using stimulating electrodes implanted in or around the cochlea to elicit patterns of spike activity on the array of surviving auditory-nerve fibers. By modulating the patterns of neural activity, these devices attempt to present information that the patient with the implant can learn to interpret. The spike activity patterns elicited by electrical stimulation depend on several factors: the complex, electrically heterogeneous structure of the cochlea, the geometry and

placement of the stimulating electrodes, the stimulus waveform, and the distribution of surviving nerve fibers. An understanding of how these factors interact to determine the activity patterns is fundamental to designing better devices and interpreting the results of experiments involving intracochlear stimulation of animal and human subjects.

As a first step toward achieving this understanding, we are developing a software model of the cochlea that predicts the distribution of potential produced by stimulation of arbitrarily placed, intracochlear electrodes. These potential distributions will be used as inputs that drive models of auditory-nerve fibers to compute neural activity patterns produced by intracochlear stimulation.

The initial model reported in previous *RLE Progress Reports* was formulated by digitizing sections of a human temporal bone with each spatial sample representing a specific tissue or fluid (e.g., bone, nerve, perilymph, membrane). Based on the material represented, each sample was assigned a resistivity and a finite difference technique was used to convert these data to a set of equations designed to represent the nonhomogeneous electrical structure of the cochlea. Current sources were added to the model at nodes representing the positions of the six intracochlear electrodes implanted in a number of deaf human subjects at the Massachusetts Eye and Ear Infirmary.

The human model has been tested by comparing the model predictions of intracochlear potential distributions computed for stimulation through a single electrode with intracochlear potentials measured at five unstimulated electrodes in human subjects when a sixth was stimulated. Model results predicted the asymmetric and, for some stimulation sites, nonmonotonically decreasing potentials measured in the human subjects.

While these initial tests are encouraging, the human model does not lend itself to comprehensive testing because of the restrictions placed on the location of electrodes and on the anatomical manipulations appropriate in human subjects. In order to provide wider latitude in testing, a similar model was implemented for the rat where the experimental subject can be sacrificed and the temporal bones quickly prepared for anatomical analysis.

The rat model is based on 105 histological sections, every fifth section of a series cut 5 μm thick and registered using 200- μm holes drilled in the embedded cochlea before sectioning. Outlines of cochlear structures were drawn on digital images using Image software with a resolution of 6.25 μm . Twenty-two different tissues or fluids were assigned

unique tags that could be converted to a specific resistance when the model was implemented.

Tests of the model were made in the rat by measuring the potential at four unstimulated electrodes when current was injected monopolarly (ipsilateral pinna reference) through a fifth and comparing the potentials with corresponding values predicted by the model. Stimuli were $10\text{-}\mu\text{A}$ sinusoidal pips. Potentials recorded between the intracochlear electrodes and the contralateral ear were averaged and measured peak-to-peak.

The five intracochlear Pt-Ir electrodes, implanted through holes in the capsule or through the round window, had cylindrical tips $100\text{ }\mu\text{m}$ -long. Their locations were determined in histological sections. Electrode implantation and all measurements were made in deeply anesthetized animals.

Figure 6 shows data from a single animal to illustrate three consistent features of the potentials recorded from 10 animals: (1) stimulation at apical sites produced large potentials with steep gradients; (2) stimulation at basal sites resulted in somewhat smaller potentials with flatter gradients; and (3) stimulus frequency, from 100 Hz to 10 kHz, had no significant effect on the amplitude of the recorded potentials, consistent with the assumption of no large capacitive effects of the tissues.

Histological evaluation of the cochleas revealed significant disturbance of tissues in the immediate vicinity of some electrodes (longitudinal extent less than 0.5 mm in most cases), indicating that predictions by the "normal" model might not be appropriate. The model was therefore modified to reflect abnormalities such as spiral ligament displacement and rupture of the basilar membrane.

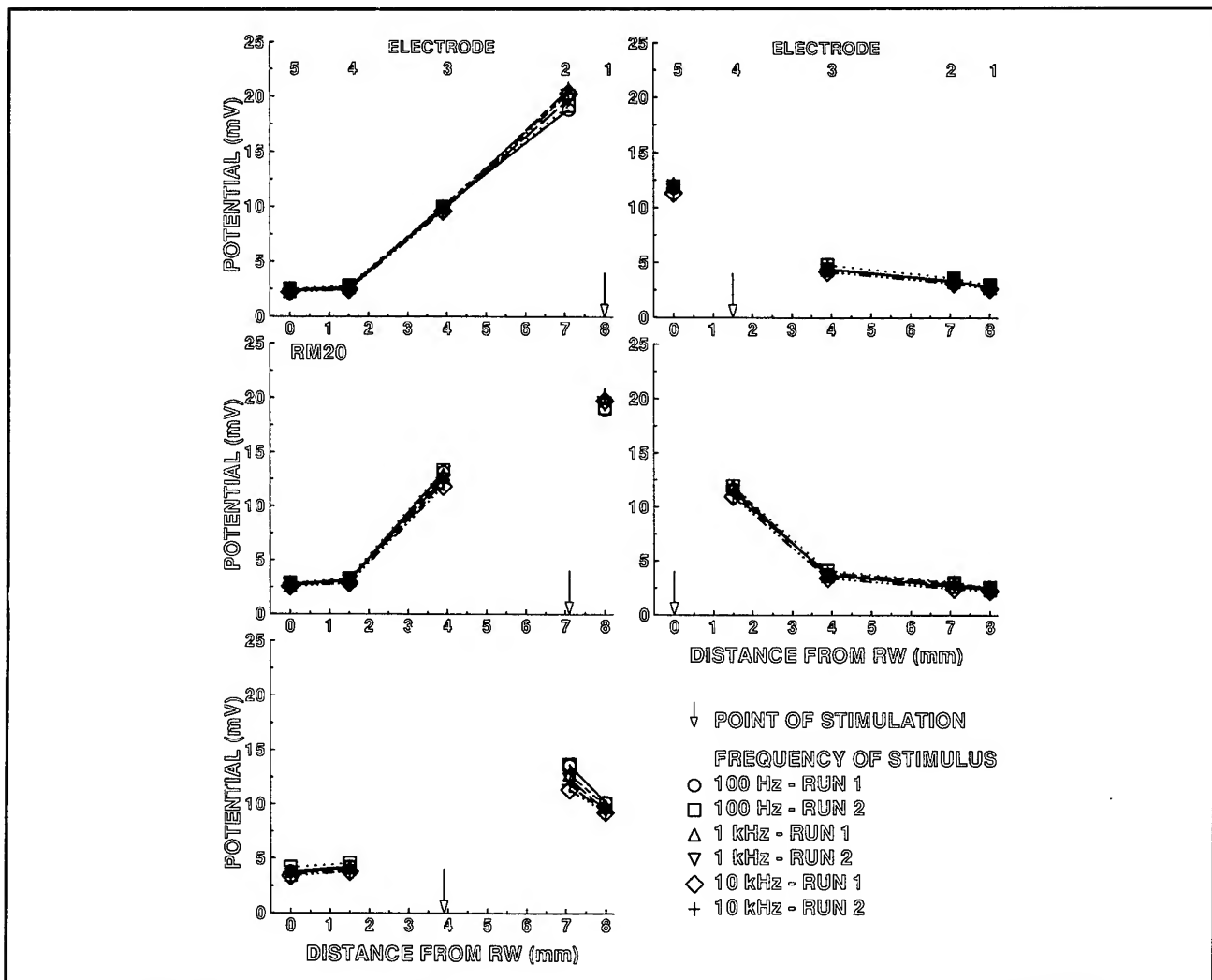


Figure 6. Cochlear potential measured at unstimulated, intracochlear electrodes (symbols) as a function of electrode position. The arrow in each panel shows the position of the stimulating electrode. The frequency of the sinusoidal stimuli are keyed by symbol.

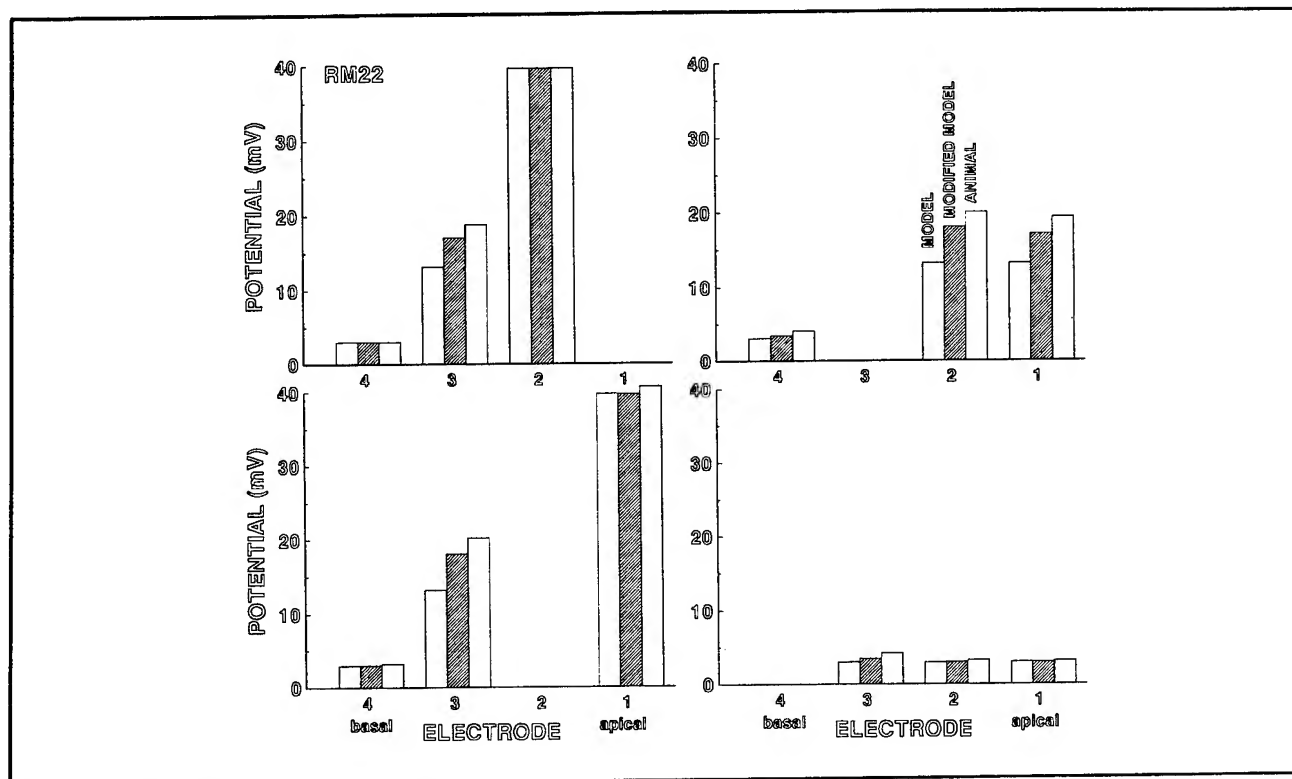


Figure 7. Normalized potentials measured at the unstimulated, intracochlear electrodes in a single rat and normalized potential predictions computed by the "normal" model and a model "modified" to represent the details of the animal's cochlear pathology. Data are not presented for electrode five because it was positioned outside the cochlea in this animal.

Figure 7 illustrates the general result that the potentials predicted by the "normal" and "modified" models for each rat did not differ by very much at the locations of the unstimulated electrodes. Where they were appreciably different, predictions of the modified model were nearly always closer to the potentials measured in the animals than were those of the normal model.

The modifications in the model did have a relatively large effect on the potential distributions, but were confined to the tissues and fluids in the immediate region of the stimulating electrode. This can be seen in figure 8, where scala media potentials predicted by the normal and modified models are plotted. Scala media potentials were selected for

this illustration because they represent the largest differences between the two models for this animal.

These initial results indicate that this electro-anatomical model of the rat's cochlea predicts with fairly good accuracy the potentials measured at unstimulated electrode sites. Manipulations of the model structure to more accurately reflect the cochlear pathology induced by the placement of intracochlear electrodes in five rat subjects led to significant improvements of the model predictions in most cases. In the next series of animal tests, we plan to measure potentials close to the stimulating electrode where (1) the potentials are relatively high, (2) the gradients are relatively steep, and (3) the model predicts the largest effects of cochlear pathology.

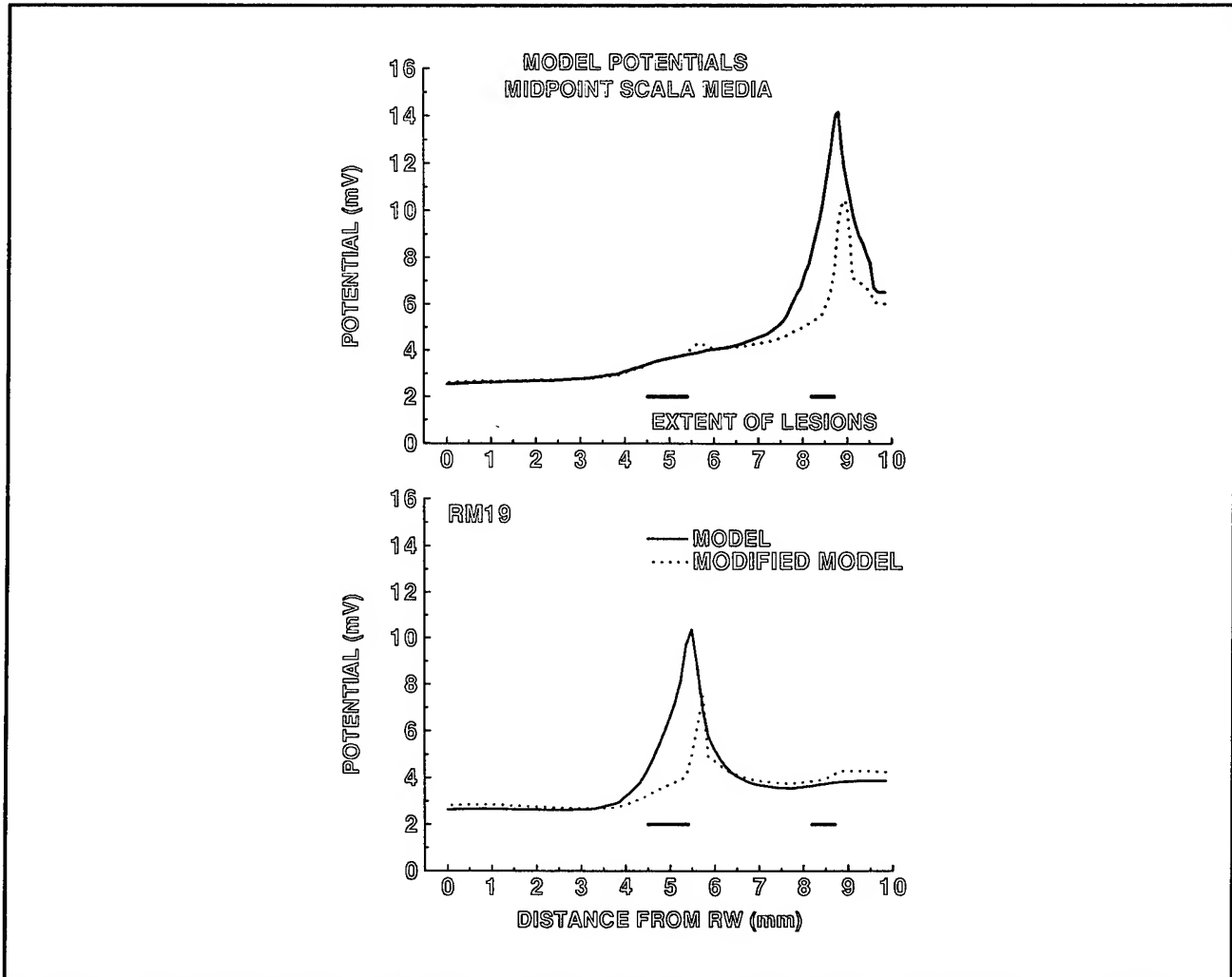


Figure 8. Scala media potentials predicted for the "normal" and "modified" models. Modifications of the model were made for sections included within the extent of the lesions as indicated.

Section 4 Linguistics

Chapter 1 Linguistics

Chapter 1. Linguistics

Academic and Research Staff

Professor Morris Halle, Professor Noam A. Chomsky

1.1 Introduction

The work of the Linguistics group is directed towards a better understanding of the mental capacities of human beings through the study of the nature, acquisition and use of language. Language is a uniquely human faculty: only humans appear to be capable of learning and using a language, and every normal human acquires knowledge of one or more languages.

We are trying to understand how this linguistic knowledge is represented in the speaker's mind. The central issues of linguistics research are:

1. What is the nature of linguistic knowledge? What do speakers of a particular language such as Latvian, Spanish or Walpiri know, and how does knowledge of one language resemble or differ from that of another language?
2. How do speakers acquire this knowledge?
3. How do speakers put this knowledge to use in producing and understanding utterances?
4. What are the physiological mechanisms that provide the material basis for storage, acquisition and utilization of linguistic knowledge?

Our ability to answer these questions differs considerably, and our research reflects these differences. At present, we have progressed further with regard to answering the questions posed by item one and have made less progress with item four. Currently, our research is heavily concentrated on issues concerned with the nature of the knowledge that characterizes fluent speakers of various languages. However, we are making a significant effort to solve the other questions also.

We are studying these topics along a number of parallel lines. Linguists have investigated the principles by which words are concatenated to form meaningful sentences. These principles have been the primary domain of inquiry into the disciplines of syntax and semantics. Phonology studies the sound structure of words while morphology examines the manner in which different languages combine different meaning-bearing units (specifically, stems, prefixes, suffixes and infixes) to form

words. The latter topic has attracted increasing interest in recent years and will probably become more prominent in our research efforts in the future.

1.2 Abstracts of Doctoral Dissertations

The following are abstracts of dissertations submitted in 1995 to the Department of Linguistics and Philosophy in partial fulfillment of the requirements for the degree of Doctor of Philosophy in Linguistics.

1.2.1 Null Subjects

Maria do Pilar Pereira Barbosa

Abstract

The goal of this thesis is to isolate the properties that characterize the languages that show a correlation between the possibility of dropping a subject and rich subject agreement morphology. I will propose an articulated structure for TP, which is meant to reflect, in binary terms, the relation established among the Speech time, the Reference time and the Event time, the basic primitives of tense in Reichenbachian theories of tense. I will suggest that TP is broken up into a projection of "Tense relative to the Event time" (T_E) and a projection of "Tense relative to the Speech time" (T_S). The former corresponds to the standard IP and is the locus of the Extended Projection Principle. Spec- T_S is an A'-position. In subordinate clauses, TP_S is selected by C. I will argue that the Null Subject Property is the result of the combination of the following two properties: overt V-to- T_E -to- T_S raising and a sufficiently rich bundle of nominal agreement features capable of checking off the Nominative Case feature of T_E and the EPP. The configuration of c-command established between the bundle of nominal features in T_S and an empty D in Spec- T_E will be argued to be essential to the Null Subject Property. Overt V-to- T_E -to- T_S raising will also be argued to be a property of a standard VSO language such as Irish. The differences between Irish and null subject Romance with respect to word

order will follow from the fact that Irish has no agreement inflection. T_E raising to T_S accompanied by subject raising to Spec- T_E P yields VSO order.

1.2.2 Morphosyntax: the Syntax of Verbal Inflection

Jonathan David Bobaljik

Abstract

This thesis investigates the interaction of the morphological process of verbal inflection with the syntactic process of verb movement and the distribution of the principal arguments.

In part I it is proposed that two apparently syntactic phenomena in the Germanic languages are accounted for by allowing the morphological component to filter syntactic derivations. First (chapter 1), it is proposed that the parametric variation in the licensing of the specifier of TP (an intermediate functional projection) can be derived from the verbal inflectional paradigms; certain morphological patterns require fusion, a requirement which in turn places restrictions on possible syntactic derivations. In Chapter 2 it is proposed that verbal inflection may take place via *morphological merger*, which requires *adjacency*. Syntactic operations which would disrupt the adjacency relation in the morphology are therefore blocked.

In part 2 the assumptions, common in the literature, which underlie the syntactic analyses in part I are reconsidered. In particular it is argued in chapter 3 that the base and derived positions of the principal arguments are stacked; that is, objects do not cross over subjects in moving to their derived position. In chapter 4 the view that floating quantifiers mark the positions of traces of their antecedents is challenged.

Part 3 attempts to salvage and extend the accounts of part 1 in light of the revised assumptions proposed in part 2. In chapter 5, I introduce the *Free Agr Parameter*, which states that languages vary with regard to the presence or absence of Agr-Phrases. The specifiers of Agr-Phrases are the derived positions for arguments as evidenced by object shift and other phenomena. It is also proposed that the presence or absence of an Agr head dominating Infl determines whether or not the verb raises out of the VP in nonverb-second environments, correctly predicting a further point of parametric variation in the Germanic languages. Chapter 6 investigates the possibility of pursuing these analyses while maintaining that the syntactic derivation cannot be filtered by the

morphophonological component(s). It is argued that this is possible, if the grammar admits of a process determining which copy of a moved element is pronounced. The morphological procedure determining which copy is pronounced is constrained by other morphological considerations, especially the adjacency condition on morphological merger investigated in chapter 2.

1.2.3 Nonverbal Predication and Head-Movement

Andrew Hay Carnie

Abstract

This thesis surveys the interaction between nonverbal predication in matrix clauses and processes of head-movement. Focusing mainly on the syntax of Modern Irish nominal predicates, it is claimed that matrix nonverbal predication can occur without any verbal support. When this happens, nonverbal predicates bear inflectional features directly and behave just like verbs with respect to processes of head-movement. In particular, it is claimed that nonverbal predicates raise through the inflectional complex to the highest inflectional head, just like verbal predicates in matrix VSO clauses.

It is also claimed that complex phrasal predicates are allowed to undergo head-movement, contra many standard assumptions. A new theory of phrase structure is proposed, where phrasal status (i.e., X-bar status) is determined by behavior of the phrase-marker involved, rather than the status determining the behavior. This derived notion of X-bar status is shown to account for a variety of phenomena from a variety of languages (such as construct state nominals in Celtic and Tagalog clitic placement).

The thesis also argues that the distribution of word order types from Irish copular clauses argues against a unified or single *be* analysis. It is claimed that at least two types of copular construction: a one placed predicative construction, and a two placed equative construction are present in the grammar. Structural asymmetries between the two arguments in equative constructions are shown to follow from their behavior with respect to theta marking.

Finally, a new analysis of Verb-Subject-Object (VSO) order is presented which accounts for a wide variety of phenomena, including nonverbal predicates, in the syntax of Modern Irish. This analysis makes use of verb raising, a split VP structure, and a new view of clausal architecture.

1.2.4 Indefinite Topics

Diana Cresti

Abstract

In this dissertation I investigate the phenomenon of what have come to be known as "specific" indefinites.

The atypical scope- and discourse-related properties of this kind of noun phrases have led researchers to posit a variety of recent analyses. I show that nothing special needs to be said about specific indefinites once we assume a pre-dynamic model of natural language which takes as a starting point the proposals of Kamp (1981) and Heim (1982) that indefinites are not inherently quantificational.

One core assumption of this dissertation is that indefinites that are interpreted as specific (or that otherwise exhibit atypical scopal properties) are always topic marked in the sense of von Stechow (1994) (but see also Diesing 1991). The phenomenon of topic marking is quite independent of specific indefinites and is generally the cause of existence presuppositions associated with quantificational noun phrases—which are argued not to be intrinsically presuppositional.

The presuppositions associated with topic marking are shown to follow the same projection patterns as standard presuppositional expressions; thus the semantic and pragmatic properties of specific indefinites are expected to exhibit a parallel behavior with respect to, e.g., presuppositions of the kind generated by definite noun phrases. The model proposed thus subsumes the apparently puzzling scope-taking options of indefinites under an independently available theory of syntax, semantics, and pragmatics. No recourse to task-specific devices is assumed.

The model proposed assumes a maximally constrained theory of syntax. Thus it is compatible with theories which assume the clause-boundedness of quantifier raising, including those models which assume that there is no independently occurring quantifier raising operation.

1.2.5 Subjects, Events and Licensing

Heidi Britton Harley

Abstract

While the notion of "subject" as a primitive of grammar is in some way encoded in most modern syntactic theories, the cluster of syntactic properties attributed to subjects is not a homogenous one. This thesis aims to precisely characterize certain of these properties, partially through an investigation of constructions where they fail to converge.

Two of these properties are of particular interest. First, the structural properties associated with "external arguments" are examined; that is, the question of where thematic subjects (as opposed to clausal subjects) are base-generated. Drawing on evidence from Japanese lexical causatives, a "split-VP" structure is argued for, in which external arguments (Agents, Causers) are generated in the specifier of a projection which marks the introduction of an event argument (hence termed EventP). Below EventP are case-checking positions for underlying objects and indirect objects (internal arguments) as well as the projection in which internal arguments are base-generated ("BaseP"). "Verbs" on this approach consist of a "Base" head in combination with an "Event" head, and the decomposition of verbal meaning into "primitives" such as CAUSE, HAVE or BE is assumed. In support, a correlation is drawn between the existence of the predicate "have" in a language and the possibility of a double object/double complement alternation, adducing evidence from Irish, Tagalog, and Diné, as well as Japanese, Georgian and English.

Secondly, the question of morphological nominative case is considered. Nominative marking on an NP is typically taken to be an indicator of subjecthood, nonetheless, there are constructions in which a nominative-marked argument appears to be in object position. Such nominative objects in Icelandic are examined in detail, and a mechanism for assigning morphological case is proposed which modifies standard assumptions about the strict connection of morphological case with structural position. Given such modification, the question of NP-licensing, is re-examined, with an eye to dispensing with abstract case entirely, the apparent effects of abstract case assignment (and, incidentally, Buzio's Generalization) are seen to be the result of the interaction of the mechanism governing morphological case assignment with the Extended Projection Principle.

1.2.6 Phrase Structure in Minimalist Syntax

Masatoshi Koizumi

Abstract

This thesis is a study of clause architecture within a theory of generative grammar. It discusses four major syntactic hypotheses that have crucial bearing on the design of phrase structure: the Agreement-based Case theory, the internal subject hypothesis (ISH), the uniform three-level X-bar theory, and a hypothesis about string vacuous head movement.

In chapters 2 through 4, I discuss object positions in three typologically and genetically different languages, i.e., English, Zarma, and Japanese, and argue that they all possess Object Agreement Phrases (A GRoP). A consideration of learnability suggests that the presence of A GRoP in these languages, particularly in Japanese, is not learnable from the data available to children. Thus, it is highly likely that UG is so construed that every language has AGR (the universal AGR hypothesis).

In chapter 5, I turn to subject positions. There is conflicting evidence regarding the base-position of the external argument. Some data indicate that the external argument originates in a position lower than its surface position, as is expected under the internal subject hypothesis. Other data suggest that the base-position of the external argument is outside the A GRoP and the VP that dominates the main verb and the internal arguments. If the ISH is correct in that all arguments of a predicate category (e.g., V) originate within the maximal projection of this category, then the apparently contradicting data suggest that there are two verbs, hence two VPs, in a single clause (the split VP hypothesis). One verb is above A GRoP, and the other is below A GRoP. The so-called external argument is an argument of the upper V, and "internal arguments" are arguments of the lower V.

Chapter 6 is concerned with X-bar theory. I argue, contrary to the wide held view, that some functional categories allow more than one specifier position within their projections (layered specifiers), and that the number of specifiers is different across categories. If this is correct, the X-bar schema as such cannot be a part of Universal Grammar, as already suggested in Fukui (1986) and others. Our claim, however, is crucially different from Fukui's (1986) in that the specifiers of functional categories do not necessarily (but sometimes do) "close off" their projections.

In chapter 7, I discuss string vacuous verb raising in head final languages. In particular, I present evidence that verbs in Japanese raise out of the VP in overt syntax. Its consequences are also explored to various aspects of syntactic theory such as the Proper Binding Condition, Kayne's (1994) Linear Correspondence Axiom, etc.

1.2.7 On the Temporal Interpretation of Noun Phrases

Renate Musan

Abstract

This thesis investigates the temporal interpretation of noun phrases. The leading questions throughout are the following: (1) Is the temporal interpretation of a noun phrase determined by the temporal interpretation of the rest of its clause? (2) What kind of further interactions take place between the interpretation of noun phrases and the temporal interpretation of the main predicate of a clause? The framework in which these questions are answered exploits an ontology that assumes individuals, stages of individuals, and kinds as basic entities. Determiner-quantification is argued to be quantification over stages of individuals rather than individuals in their whole temporal extendedness.

Chapter 1 provides a survey of the main topics of this thesis. It is argued that an account of the temporal interpretation of noun phrases must investigate at least two issues that are to be distinguished: the temporal location of individuals and the temporal location of predication times.

In chapter 2, the temporal location of individuals is explained as an effect of life-time presuppositions that are introduced by the lexical semantics of stage-level predicates and individual-level predicates, but not by a third type of predicate, existence-independent predicates. Life-time effects associated with individual-level predicates are captured as a pragmatic phenomenon in terms of Grice's Maxim of Informativity and related implicatures. In temporally specific contexts, life-time effects are neutralized. This is related to certain effects that topic-focus structure has on temporal interpretation.

Chapter 3 explains the temporal location of predication times associated with noun phrases. In contrast to previous research, it is argued that the temporal location of predication times of nouns depends on the temporal interpretation of the rest of the clause. The notions of "temporally dependent" and "temporally independent" noun phrases

are introduced. It is shown that the distribution of temporally dependent and temporally independent noun phrases involves the distinction between weak (or cardinal) and strong (or presuppositional) noun phrases as well as the distinction between existence-independent arguments and other arguments. This distribution is explained as a consequence of (1) determiner-quantification being analyzed as quantification over stages of individuals, (2) independently motivated mechanisms of implicit quantifier restriction, and (3) a particular account of weak and strong determiners. This account analyzes both types of determiners as restrictive quantifiers, and attributes differences between them to whether the noun is mapped at LF into the restrictive clause or into the nuclear scope of the determiner. The mechanisms introduced in this chapter are also applied to generic noun phrases, certain kind-denoting noun phrases, and to the distinction between object-related readings and event-related readings.

Chapter 4 deals with the semantics of certain types of noun phrase internal temporal modifiers, *in*-modifiers and *of*-modifiers. It is argued that *in*-modifiers are obligatory restrictors of quantifiers. Moreover, they impose constraints on the tense interpretation of their clause by activating the Upper Limit Constraint, which has also been used to explain certain aspects of the behavior of sequence-of-tense constructions and double-access constructions.

Chapter 5 offers a summary of results achieved in the preceding chapters and suggestions for future research.

1.2.8 Phonological Phrases: Their Relation to Syntax, Focus, and Prominence

Hubert Truckenbrodt

Abstract

This thesis investigates how phonological phrases are related to the syntactic representation, to focus, and to the representation of prominence. The proposal that is defended here is that among the three relevant basic entities represented by the grammar, syntactic constituency, prosodic constituency, and prominence, the grammar places a simple demand on each pair: (1) Syntactic phrases must be contained in phonological phrases. (2) Phonological phrases must have edgemoost phrasal prominence. (3) Syntactic phrases must contain phrasal prominence. These demands are taken to interact with one another as ranked and violable constraints, where variation among languages is expressed in terms of constraint reranking. Each relation is argued for separately. The effects of (1) (previously described as the role of government in phonological phrasing) are investigated on patterns of phrasing in the three Bantu languages Chi Mwi:ni, Chichewa, and Kimatumbi. The effects of (2), it is argued, can be seen most clearly in the effects of focus on phrasing, where Chichewa and Japanese will be discussed as examples. The effects of (3), finally, which have been discussed in different contexts as either a directionality parameter or the role of depth of embedding in the assignment of stress, will be argued to have desirable typological consequences that set (3) apart from some of its competitors. Jointly the constraints will be seen to derive an end-based typology of the kind familiar from work by Lisa Selkirk.

Appendices

Appendix A RLE Publications and Papers Presented

Appendix B Current RLE Personnel

Appendix C Milestones

Appendix D RLE Research Support Index

Appendix A. RLE Publications and Papers Presented

The first section of this bibliography includes papers and talks presented by RLE faculty, staff and students during 1995 and is in alphabetical order by conference name. Reprints of these papers may be obtained by contacting the authors directly.

Section 2 includes an alphabetical listing by author of journal articles that were published and accepted or submitted for publication. Book chapters by RLE authors are listed in section 3. Section 4 of this bibliography lists RLE general publications and technical reports, and section 5 is a list of RLE theses submitted during 1994. Theses and technical reports may be ordered from Document Services, MIT Libraries, Room 14-0551, 77 Massachusetts Avenue, Cambridge, Massachusetts 02139-4307; telephone (617) 253-5668; email: docs@mit.edu; fax: (617) 253-1690.

A.1 Meeting Papers

A.1.1 Papers Presented

Acoustical Society of America Meeting, St. Louis, Missouri, November 27-December 1, 1995.

Krause, J., and L.D. Braida. "The Effects of Speaking Rate and Speaking Mode on Intelligibility."

Acoustical Society of America Meeting, 129th, Washington, DC, May 30-June 3, 1995.

Dilley, L., and S. Shattuck-Hufnagel. "Individual Differences in the Glottalization of Vowel-Initial Syllables."

Perkell, J., M. Matthies, M. Svirsky, and R. Wilhelms-Tricarico. "Clarity Versus Effort in Speech Production: Initial Results of a Pilot Study." (poster presentation)

Rabinowitz, W.M., D.K. Eddington, J. Tierney, and L.A. Delhorne. "Preliminary Evaluations of Cochlear Implants Using a Wearable CIS Processor."

Shinn-Cunningham, B. "A Dynamic, Psycho-physical Model of Adaptation in Localization Experiments."

Wozniak, J., H. Lane, J. Manzella, J. Perkell, M. Matthies, M. Svirsky, M. O'Connell, and C. Mitchell. "Intersyllable Regulation of FO and SPL With and Without Auditory Feedback." (poster presentation)

American Astronomical Society Meeting, 185th, Tucson, Arizona, January 7-12, 1995.

Fletcher, A.B., S.R. Conner, and B.F. Burke. "First Results from 8.4 GHz VLA Imaging of 1800 Southern Sky Parkes-Mit-NRAO (PMN) Radio Sources."

Katz, C.A., J.N. Hewitt, C.B. Moore, and J.D. Ellithorpe. "The STARE Project: A Survey for Transient Astronomical Radio Emission." (poster session)

American Physical Society Meeting, San Jose, California, March 20-24, 1995.

Capaz, R.B., H. Lim, and J.D. Joannopoulos. "Ab initio Studies of the Initial Stages of GaN Growth on SiC."

Villeneuve, P.R. "Novel Applications of Photonic Band Gap Materials."

Wyss, R.A., F. Rana, Q. Hu, M.J. Rooks, and A. Furster. "Frequency Dependent Behavior of Photon-assisted Transport through a Planar Resonant Tunneling Transistor."

American Physical Society, Division of Plasma Physics Meeting, 37th Annual, Louisville, Kentucky, November 4-10, 1995.

Airoldi, A., G. Cennachi, and B. Coppi. "Enhanced Confinement Conditions and the Ignitor Experiment."

Bers, A., S.D. Schultz, and A.K. Ram. "Mode Conversion to Ion-Bernstein Waves of Fast Alfvén Waves with Finite Poloidal Wavenumber in Tokamak Geometries." (poster presentation)

Bombarda, F., B. Coppi, C. Fiore, S. Golovato, et al. "Transport Regimes in High Density Plasmas Produced by Alcator C-Mod."

Bonoli, P.T., M. Porkolab, L.E. Sugiyama, and C. Kessel. "Simulations of MHD Stable Operating Scenarios in the Tokamak Physics Experiment (TPX)."

- Carpignano, F., B. Coppi, M. Nassi, and the Ignitor Project Group. "Prototypes Construction in the Ignitor Program."
- Cennachi, G., B. Coppi, F. Ferro, M. Gasparotto, C. Rita, M. Roccella, and L. Lanzavecchia. "Plasma Evolution Scenarios in the Ignitor-Ult Experiment."
- Coppi, A.C., and B. Coppi. "'Explosive' Periodic Bursts and Generalized Bursting Equation."
- Coppi, B., and L.E. Sugiyama. "Collisionless Magnetic Reconnection."
- Coppi, B., P. Detragiache, and S. Migliuolo. "The Issue of Internal Modes in Ignition Experiments."
- Daughton, W., and B. Coppi. "Anomalous Transport of Angular Momentum and Microscopic Dissipative Processes."
- Detragiache, P., F. Bombarda, and B. Coppi. "Recent Results on Confinement: Physics Basis of Ignitor."
- Ernst, D.R., B. Coppi, S.D. Scott, and the TFTR Group. "Transport Analysis of Rotating TFTR Plasmas and Modes Driven by Velocity Gradients."
- Lanzavecchia, L., B. Coppi, R. Andreani et al. "Poloidal Field Coils Design for the Ignitor-Ult Experiment."
- Migliuolo, S. "Nonlinear and Nonlocal Dynamics of the Equatorial Spread-F."
- Park, W., G.Y. Fu, H.R. Strauss, and L.E. Sugiyama. "Multi-Level Numerical Simulation of Tokamak Plasmas."
- Penn, G., C. Riconda, and B. Coppi. "The Distribution of Fusion Products in a Tokamak Reactor, and Related Effects."
- Porkolab, M., P.T. Bonoli, S. Golovato, J. Ramos et al. "Advanced Tokamak Physics Scenarios in Alcator C-Mod."
- Pravia, M., B. Coppi, W. Daughton, L.E. Sugiyama, et al. "Transport Simulations of Alcator C-Mod ICRF Plasmas."
- Qu, Y.L., J.E. Rice, E.S. Marmor, and F. Bombarda. "X-ray Observations of Toroidal Rotation in Alcator C-Mod Plasmas."
- Ram, A., A. Bers, P. Bonoli, S.D. Schultz, V. Fuchs, A. Becoulet, and B. Saoutic. "Mode Converted Ion-Bernstein Waves for Heating and Current Drive." (talk)
- Ram, A., A. Bers, S.D. Schultz, and V. Fuchs. "Mode Conversion of Fast Alfvén Waves at the Ion-Ion Hybrid Resonance."
- Rice, J.E., J.L. Terry, E.S. Marmor, and F. Bombarda. "X-ray Observations of Up-Down Impurity Density Asymmetries in Alcator C-Mod Plasmas."
- Riconda, C., G. Penn, and B. Coppi. "The Interaction of High Energy Particles with Modes Near Harmonics of the Cyclotron Frequency."
- Schultz, S.D., A. Bers, and A.K. Ram. "RF Wave Effects on the Neoclassical Electron Distribution Function in Tokamaks." (poster presentation)
- Sugiyama, L.E., and W. Park. "Two Fluid Studies of Low m,n Instabilities."
- Vacca, L., A. Bers, and A.K. Ram. "RF-Induced Transport of Resonant Minority Species in ICRF-Heated Tokamaks." (poster presentation)
- Wang, Y., J.E. Rice, F. Bombarda, G. McCracken et al. "Impurity Screening Study of Various Alcator C-Mod Plasmas."
- American Society of Cell Biology Meeting*, Washington, DC, December 9-13, 1995.
- Boppart, S.A., M.E. Brezinski, B. Bouma, G.J. Tearney, E.A. Swanson, and J.G. Fujimoto. "In vivo Imaging of Developing Morphology Using Optical Coherence Tomography."
- American Statistical Associations Winter Conference*, Raleigh, North Carolina, January 5-8, 1995.
- Koita, R., and D.H. Staelin. "One-at-a-time Design Strategy for Two-level Factorial Experiments."
- Annual Meeting of the Division of Atomic, Molecular, and Optical Physics*, Toronto, Ontario, Canada, May 16-19, 1995.
- Ketterle, W. "Evaporative Cooling of Magnetically Trapped Sodium."
- Pritchard, D.E., M.S. Chapman, C.R. Ekstrom, T.D. Hammond, J. Schmiedmayer, A. Lenef, R. Rubenstein, and S. Wehinger. "Interferometry with Atoms and Molecules."
- Association for Research in Otolaryngology Meeting*, 18th Mid-Winter, St. Petersburg, Florida, February 5-9, 1995.
- Davis, C.Q., and D.M. Freeman. "Direct Observations of Sound-Induced Motions of the

- Reticular Lamina, Tectorial Membrane, Hair Bundles, and Individual Stereocilia."
- Delgutte, B. "Neural Correlates of Basic Psychophysical Functions."
- Freeman, D.M., and T.F. Weiss. "Species Dependence of Osmotic Responses of the Tectorial Membrane: Implications of Structure and Biochemical Composition."
- McKinney, M.F., and B. Delgutte. "Physiological Correlates of the Stretched Octave in Interspike Intervals of Auditory-Nerve Fibers."
- Rosowski, J.J., W.T. Peake, G.T. Huang, and D.T. Flandermeyer. "Middle-ear Structure and Function in Felidae."
- Shah, D.M., D.M. Freeman, and T.F. Weiss. "The Osmotic Responses of the Isolated, Unfixed Mouse Tectorial Membrane: Effect of Na^+ , K^+ , and Ca_2^+ Concentration."
- ARPA Rapid Prototyping of Application Specific Signal Processing*, Annual P.I. Meeting, Atlanta, Georgia, January 9-13, 1995.
- Oppenheim, A.V., G.W. Wornell, A. Chandrakasan. "Progress in Algorithms: Signal Processing with Chaos and Fractals."
- ARPA RASSP Conference*, Second, Washington, DC, July 1995
- Winograd, J., J. Ludwig, S.H. Nawab, A. Chandrakasan, and A.V. Oppenheim. "Approximate Processing and Incremental Refinement Concepts."
- ARPA Semi-Annual Microsystems Workshop*, Arizona, April 23-25, 1995.
- Devadas, S. "Code Optimization for Embedded DSP Processors."
- ASME International Mechanical Engineering Conference and Exposition*, San Francisco, California, November 12-17, 1995.
- Beauregard, G.L., M.A. Srinivasan, and N.I. Durlach. "The Manual Resolution of Viscosity and Mass."
- Karason, S., and M.A. Srinivasan. "Passive Human Grasp Control of an Active Instrumented Object."
- Colloquium on Quantum Electronics*, 25th Winter, Snowbird, Utah, January 3-5, 1995.
- Pritchard, D.E. "Atom Optics and Atom Interferometers."
- Conference on Advance Research in VLSI*, 16th, Chapel Hill, North Carolina, March 27-29, 1995.
- Cai, X., K. Nabors, J. White. "Efficient Galerkin Techniques for Multipole-Accelerated Capacitance Extraction of 3-D Structures with Multiple Dielectrics."
- Conference on Coherence and Quantum Optics*, Seventh, Rochester, New York, June 7-10, 1995.
- Lee, D., and N.C. Wong. "Quantum Phase Diffusion Noise Measurements in a cw Optical Parametric Oscillator."
- Pritchard, D.E. "Atom Interferometers and Atomic Coherence."
- Conference on Implantable Auditory Prostheses*, Asilomar, California, August 19-24, 1995.
- Rabinowitz, W.M., D.K. Eddington, J. Tierney, L.A. Delhorne, and M.E. Whearty. "Performance with Wearable CIS Processors."
- Conference on Ultrafast Transmission Systems in Optical Fibres*, Trieste, Italy, February 1995.
- Haus, H.A., F.I. Khatri, and W.S. Wong. "Soliton Interaction with Continuum."
- CLEO/QELS Conference on Lasers and Electro-Optics/Quantum Electronics and Laser Science Meeting*, Annual, San Francisco, California, November 1, 1995.
- Little, B.E., S.T. Chu, and H.A. Haus. "Micro-Ring Resonator Channel Dropping Filters."
- CLEO/QELS Conference on Lasers and Electro-Optics/Quantum Electronics and Laser Science*, Baltimore, Maryland, May 21-26, 1995.
- Boppart, S.A., M.R. Hee, J.G. Fujimoto, R. Birngruber, C.A. Toth, E.A. Swanson, C.P. Cain, G.D. Noojin, C.D. DiCarlo, W.P. Roach. "Dynamic Evolution and *in vivo* Tomographic Imaging of Laser-Induced Retinal Lesions Using Optical Coherence Tomography."
- Bouma, B., and J.G. Fujimoto. "Compact Gigahertz Repetition Rate Kerr-Lens Mode Locked $\text{Ti:Al}_2\text{O}_3$ Lasers Using Positive Dispersion."
- Darwish, A.M., G. Lenz, E. Ippen, G.Q. Le, J.P. Donnelly, S. Groves, and E. Swanson. "Frequency Conversion in Passive InGaAsP/InP Waveguides."
- Haus, H.A. "Squeezing in a Sagnac Fiber Loop."

- Haus, H.A., E.P. Ippen, W.S. Wong, F.I. Khatri, and K.R. Tamura. "Pulse Self-Ordering in Soliton Fiber Lasers."
- Lenef, A., M.S. Chapman, T.D. Hammond, J. Schmiedmayer, R. Rubenstein, E.T. Smith, and D.E. Pritchard. "Photon Scattering in an Atom Interferometer: Coherence Loss and Recovery."
- Lenz, G., E.T. Gellerman, E.P. Ippen, and K. Tamura. "Stretched-Pulse Mode-Locked Erbium-Fiber Laser Amplified by KCl:Ti Color-Center Crystals."
- Lenz, G., E.T. Ippen, J.M. Wiesenfeld, M.A. Newkirk, V. Koreu, and R.M. Jopson. "Anisotropy in the Ultrafast Nonlinear Response of Semiconductor Optical Amplifiers With Polarization-Intensive Gain."
- Nelson, L., K. Tamura, E.P. Ippen, and H.A. Haus. "Additive Pulse Mode-Rocked Thulium-Doped Fiber Ring Laser."
- Tearney, G.J., M.E. Brezinski, M.R. Hee, B. Bouma, J.A. Izatt, E.A. Swanson, J.F. Southern, and J.G. Fujimoto. "Optical Biopsy in Human Tissue Using Optical Coherence Tomography and Microscopy."
- Villeneuve, P.R., S. Fan, I. Kurland, J.C. Chen, and J.D. Joannopoulos. "Photonic Band Gap Structures and Devices."
- Design Automation Conference*, San Francisco, California, June 11-17, 1995.
- Chou, M., T. Korsmeyer, and J. White. "Transient Simulations of Three-dimensional Integrated Circuit Interconnect Using a mixed Surface-Volume Approach."
- Devadas, S., and S. Malik. "A Survey of Optimization Techniques Targeting Low Power VLSI Circuits."
- Liao, S., S. Devadas, K. Keutzer, S. Tjiang, and A. Wang. "Code Optimization Techniques for Embedded DSP Microprocessors."
- Silveira, L.M., M. Kamon, and J. White. "Efficient Reduced-Order Modeling of Frequency-Dependent Coupling Inductances Associated with 3-D Interconnect Structures."
- European Conference on Integrated Optics*, Delft, The Netherlands, 1995.
- Chen, J.C., H.A. Haus, S. Fan, and J.D. Joannopoulos. "Optical Filters from Photonic Band Gap Air Bridges."
- European Physical Society Conference on Controlled Fusion and Plasma Physics*, 22nd, Bournemouth, England, July 3-7, 1995.
- Ram, A.K., A. Bers, S.D. Schultz, V. Fuchs, A. Becoulet, and B. Saoutic. "Mode-Converted Ion-Bernstein Waves in Tokamaks."
- European Research Conferences on Bose-Einstein Condensation*, Mont Ste. Odile, France, June 16-21, 1995.
- Davis, K.B., M-O. Mewes, M.A. Joffe, M.R. Andrews, and W. Ketterle. "Evaporative Cooling of Sodium Atoms."
- Frontiers in Electronic Low-Dimensional Systems Workshop on High Frequency Experiments on Low-Dimensional Systems*, First, Weizmann Inst. Sci., Israel, November 1995.
- Hu, Q. "FIR Studies of Mesoscopic Devices."
- Geosynchronous Microwave Sounder Working Group Meeting*, Second, Washington, DC, December 6, 1995.
- Blackwell, W.J., and D.H. Staelin. "Temperature Retrieval Accuracy Stratified by Cloud Type and Atmospheric Moisture Content: Performance Analysis Using 50-425 GHz Bands."
- Gordon Research Conference on Atomic Physics*, Wolfboro, New Hampshire, July 2-7, 1995.
- Davis, K.B., M-O. Mewes, M.R. Andrews, and W. Ketterle. "Recent Progress in Evaporative Cooling of Sodium in a Modified Magnetic Trap." (poster session)
- Ketterle, W. "Evaporative Cooling of Sodium Atoms."
- Lenef, A., T.D. Hammond, M.S. Chapman, E. Smith, R.A. Rubenstein, J. Schmiedmayer, and D.E. Pritchard. "Applications of Atom Interferometry: Inertial Measurements, Molecules, and Index of Refraction of Gases."
- Pritchard, D.E. "Atom Interferometers."
- Gordon Research Conference on Lasers and Non-linear Optics*, Tilton, New Hampshire, July 30-August 4, 1995.
- Boivin, L., and H.A. Haus. "Quantum Cross-Phase Modulation."
- Bouma, B., and J.G. Fujimoto. "Compact Kerr Lens Modelocked Lasers." (poster session)
- Haus, H.A., W.S. Wong, and F.I. Khatri. "Continuum Generation by Perturbation of Soliton."

- Jones, D.J., H.A. Haus, E.P. Ippen, and C.R. Doerr. "Theory and Characterization of Asynchronous Modelocking."
- Lenz, G. "Femtosecond Studies of the Anisotropic in the Nonlinear Response of Semiconductor Optical Amplifiers with Isotropic Linear Gain."
- Haskins Laboratories*, New Haven, Connecticut, June 22, 1995.
- Perkell, J. "Acoustic Goals and Auditory Feedback in Speech Motor Control."
- Hearing Aid Research and Development Meeting*, Bethesda, Maryland, September 11-13, 1995.
- Desloge, J.G., D.P. Welker, W.M. Rabinowitz, and P.M. Zurek. "Microphone Array Hearing Aids with Binaural Output."
- Greenberg, J.E., and P.M. Zurek. "Evaluation of Adaptive Algorithm for Microphone-array Hearing Aids."
- Lum, D.S., and L.D. Braida. "A Psychoacoustic Comparison of Simulations of Sensorineural Hearing Loss Based on Dynamic Expansion and Additive Noise."
- Rabinowitz, W.M. "Noise Reduction." (invited introduction to session)
- Institute of Physics Annual Conference*, Telford, England, March 27-30, 1995.
- Fujimoto, J.G., M.R. Hee, G.J. Tearney, B.E. Bouma, M.E. Brezinski, E.A. Swanson, J. Schuman, and C.A. Puliafito. "Biomedical Imaging and Optical Biopsy Using Optical Coherence Tomography."
- International Astronomical Union Meeting 173: Conference On Astrophysical Applications of Gravitational Lenses*, Melbourne, Australia, July 9-14, 1995.
- Fletcher, A., B. Burke, S. Conner, L. Herold-Jacobson, D. Haarsma, F. Crawford, J. Cartwright, A. Cooray. "Preliminary VLA Snapshots of Southern Radio Sources from the Parkes-MIT-NRAO (PMN) Survey."
- Haarsma, D.B., J.N. Hewitt, B.F. Burke, and J. Lehar. "The VLA Light Curves of 0957+561, 1979-1994."
- Moore, C.B. and J.N. Hewitt. "Prospects for the Detection of Microlensing Time Delays."
- International Conference on Computer-Aided Design*, San Jose, California, November 6-9, 1995.
- Chou, M., and J. White. "Efficient Reduced-Order Modeling for the Transient Simulation of Three-Dimensional Interconnect."
- Liao, S., S. Devadas, and K. Keutzer. "Instruction Selection Using Binate Covering for Code Size Optimization."
- International Conference on Digital Signal Processing*, Limasol, Cyprus, June 1995.
- Hadjicostis, C.N. "Fault-Tolerant Computation in Semigroups and Semirings."
- International Conference on Electron, Ion, and Photon Beam Technology and Nanofabrication*, Phoenix, Arizona, May 30-June 2, 1995.
- Ferrera, J., M.L. Schattenburg, and H.I. Smith. "Analysis of Distortion in Interferometric Lithography."
- Moon, E.E., P.N. Everett, and H.I. Smith. "Simultaneous Measurement of Gap and Superposition in a Precision Aligner for X-ray Nanolithography."
- Savas, T.A., M.L. Schattenburg, J.M. Carter, and H.I. Smith. "Large-Area Achromatic Interferometric Lithography for 100 nm-Period Gratings and Grids With Novel Applications."
- Savas, T.A., S.N. Shah, M.L. Schattenburg, J.M. Carter, and H.I. Smith. "Achromatic Interferometric Lithography for 100-nm-period Gratings and Grids."
- Smith, H.I. "Maskless X-ray Projection Pattern Generator."
- Yang, I.Y., D.A. Antoniadis, and H.I. Smith. "Fabrication of Back-gated CMOS Devices Using Mixed and Matched Optical and X-ray Lithographies."
- International Conference on Intersubband Transitions in Quantum Wells: Physics and Applications*, Kibbutz Ginosar, Israel, October 1995.
- Hu, Q., J. Smet, B. Xu, and I. Lyubomirsky. "Far-infrared (THz) Lasers and Parametric Oscillators Using Coupled Double Quantum-well Structures."
- International Conference on Superlattices Microstructures and Microdevices*, Eighth, Cincinnati, Ohio, August 20-25, 1995.
- Sanders, G.D., C.J. Stanton, C.-K. Sun, B. Golubovic, and J.G. Fujimoto. "Theory of Carriers Gain Dynamics in InGaAs/GaAs Strained-layer Single-quantum-well Lasers."

International Congress of Phonetic Sciences, 13th, Stockholm, Sweden, August 13-19, 1995.

Dilley, L.C., and S. Shattuck-Hufnagel. "Variability in Glottalization of Word Onset Vowels in American English."

Hanson, H.M., and K.N. Stevens. "Sub-glottal Resonances in Female Speakers and Their Effect on Vowel Spectra."

Perkell, J., J. Manzella, J. Wozniak, M. Matthies, H. Lane, M. Svirsky, P. Guiod, L. Delhorne, P. Short, M. MacCollin, and C. Mitchell. "Changes in Speech Production Following Hearing Loss Due to Bilateral Acoustic Neuromas."

Wilhelms-Tricarico, R., and J.S. Perkell. "Towards a Physiological Model of Speech Production."

International Congress on Cochlear Implant, Third, Paris, France, April 27-29, 1995.

Svirsky, M.A. "Vowel Perception by Users of the Compressed Analog Stimulation Strategy: A Mathematical Model Including Temporal and Place-of-Stimulation Cues."

International Geoscience and Remote Sensing Symposium, Florence, Italy, July 10-14, 1995.

Schwartz, M.J., J.W. Barrett, P.W. Fieguth, P.W. Rosenkranz, M.S. Spina, and D.H. Staelin. "Observations of Thermal and Precipitation Structure in a Tropical Cyclone by Means of Passive Microwave Imagery near 118 GHz."

International HCIS Conference, Chicago, Illinois, August 1995.

Sanders, G.D., C.-K. Sun, B. Golubovic, J.G. Fujimoto, and C.J. Stanton. "Hot Carrier Effects in Femtosecond Gain Dynamics of InGaAs/AlGaAs Quantum Well Lasers."

International Semiconductor Device Research Symposium, Charlottesville, Virginia, December 5-8, 1995.

Rahman, A., G. de Lange, and Q. Hu. "Micro-machined Room-Temperature Microbolometers for Millimeter-Wave Detection."

International Sherwood Fusion Theory Conference, Incline Village, Nevada, April 3-5, 1995.

Bombarda, F., B. Coppi, W. Daughton, L. Sugiyama, M. Greenwald, A. Hubbard, J. Irby, C. Fiore, J. Rice, S. Wolfe, and B. LaBombard. "The Ignitor Experiment and Rel-

evance of the Alcator C-Mod Confinement Results."

Coppi, B., and L.E. Sugiyama. "Collisionless Magnetic Reconnection in Well-Confined Plasmas."

Coppi, B., P. Detragiache, and S. Niglinolo. "The Issue of Internal Modes in Ignition Experiments."

Daughton, W., B. Coppi, L.E. M. Greenwald, F. Bombarda, and Y. Takase. "Transport Simulations of the Alcator C-Mod Plasmas."

Gatto, R., D. Hua, and S. Migliuolo. "Analytical and Numerical Solutions of the Tearing Modes Linear Stability Equation."

Migliuolo, S., J.P. Friedberg, J. Kesner, and J.J. Ramos. "Ideal MMD Analysis of TFTR Discharges."

Penn, G., B. Coppi, and W. Daughton. "Transport Barrier in Very High Temperature Plasmas."

Ram, A.K., A. Bers, S.D. Schultz, and V. Fuchs. "Interaction of Mode-Converted Ion-Bernstein Waves with Electrons in Tokamaks."

Riconda, C., B. Coppi, and G. Penn. "Emission Above the Ion Cyclotron Frequency in a Non-homogeneous Magnetic Field."

Schultz, S.D., A. Bers, and A.K. Ram. "RF Wave Effects on the Neoclassical Electron Distribution Function in Tokamaks."

Sugiyama, L.E., and W. Park. "The Two Fluid Model and Stabilization of the $m=1$, $n=1$ Mode in a Tokamak."

Tajima, T., and B. Coppi. "Considerations on Plasma Transport Barriers."

International Symposium on Low Power Design, Dana Point, California, April 24-26, 1995.

Monteiro, J., and Devadas, S. "Techniques for the Power Estimation of Sequential Logic Circuits under User-Specified Input Sequences and Programs."

International Symposium on Retrieval of Bio- and Geophysical Parameters from SAR Data for Land Applications, Toulouse, France, October 10-13, 1995.

van Zyl, J., C. Dobson, J. Dozier, P. Dubois, D. Evans, J.A. Kong, T. Le Toan, J. Melack, E. Rignot, S. Saatchi, J.C. Shi, and F.T. Ulaby. "Preliminary Science Results from the SIR-C/X-SAR Mission."

- Hsu, C.C., L. Wang, J.A. Kong, J.C. Souyris, and T. Le Toan. "Theoretical Modeling for Microwave Remote Sensing of Forest."
- Le Toan, T., F. Ribbes, N. Floury, L. Wang, K.H. Ding, C.C. Hsu, and J.A. Kong. "On the Retrieval of Rice Crop Parameters from SAR Data."
- Souyris, J.C., T. Le Toan, C.C. Hsu, and J.A. Kong. "Inversion of Forest Biomass Using SIR-C/X-SAR Data."
- Wang, L., C.C. Hsu, J.A. Kong, J.C. Souyris, and T. Le Toan. "Inversion of Forest Biomass Using Neural Networks."
- International Symposium on Space THz Technology*, Sixth, California Institute of Technology, Pasadena, California, March 21-23, 1995.
- de Lange, G., B.R. Jacobson, A. Rahman, and Q. Hu. "Micromachines Millimeter Wave SIS-mixers."
- International Symposium: Auditory Physiology, Cochleopathies and Cochlear Implants*, Montevideo, Uruguay, May 2-5, 1995.
- Svirsky, M.A. "Signal Processing for Cochlear Implants."
- IEEE International Conference on Acoustics, Speech, and Signal Processing*, Detroit, Michigan, May 8-12, 1995.
- Cheung, S., and J.S. Lim. "Incorporation of Biorthogonality into Lapped Transforms for Audio Compression."
- Isabelle, S.H., and G.W. Wornell. "Statistical Properties of One-Dimensional Chaotic Signals."
- IEEE International Conference on Image Processing*, October 1995.
- Apostolopoulos, J.G., and J.S. Lim. "Representing Arbitrarily-shaped Regions—A Case Study in Overcomplete Representations."
- IEEE International Symposium on Computer Vision*, Coral Gables, Florida, November 21-23, 1995.
- Davis, C.Q., Z.Z. Karu, and D.M. Freeman. "Equivalence of Subpixel Motion Estimators Based on Optical Flow and Block Matching."
- IEEE International Symposium on Information Theory*, Whistler, British Columbia, Canada, September 18-22, 1995.
- Wornell, G.W. "Efficient Multiuser Communication in the Presence of Fading."
- IEEE Topical Meeting on Electrical Performance of Electronic Packaging*, Fourth, Portland, Oregon, October 2-4, 1995.
- Kamon, M., B. Krauter, J. Phillips, L.T. Pileggi, and J. White. "Two Optimizations to Accelerated Method-of-Moments Algorithms for Signal Integrity Analysis of Complicated 3-D Packages."
- IEEE Workshop on Information theory, Multiple Access and Queuing*, St. Louis, Missouri, April 19-21, 1995.
- Wornell, G. "A New Class of CDMA Systems for Fading Channels."
- IEEE Workshop on Nonlinear Signal and Image Processing*, Neos, Marmaras, Halkidiki, Greece, June 20-22, 1995.
- Lam, W.M., and G.W. Wornell. "Multiresolution Representations and Algorithms for Fractal Point Processes."
- Singer, A. "A New Circuit for Communication Using Solitons."
- IEEE/RSJ International Conference on Intelligent Robots and Systems*, Pittsburgh, Pennsylvania, August 5-9, 1995.
- Zilles, C.B., and J.K. Salisbury. "A Constraint-based God-object Method for Haptic Display."
- Joint Statistical Society Meeting*, Orlando, Florida, August 12-17, 1995.
- Koita, R., M. Rawizza, and D.H. Staelin. "Sequential Block Design Strategy for Two-Level Factorial Experiments."
- Mode Conversion and Current Drive Meeting*, Louisville, Kentucky, November 5, 1995.
- Ram, A.K., and A. Bers. "Propagation and Damping of Mode-Converted Ion-Bernstein Waves."
- Saoutic, B., A. Becoulet, A.K. Ram, and A. Bers. "Mode Conversion Heating—Tore Supra Experiments—Theory and Computations."
- Modeling Sensorineural Hearing Loss Meeting*, Boystown National Research Hospital, Omaha, Nebraska, June 10-11, 1995.
- Duchnowski, P., and P.M. Zurek. "Villchur Revisited: Another Look at Age Simulation of Recruiting Hearing Loss."

- MHD Workshop on the Beta Limit in Long Pulse Discharges*, La Jolla, California, September 11-14, 1995.
- Sugiyama, L.E. "Two Fluid Studies of Tokamak Plasmas."
- MHD Workshop on the Effects of Reversed Shear on the Beta Limit*, Princeton, New Jersey, December 14-15, 1995.
- National Association of Broadcasters Convention*, Las Vegas, Nevada, April 9-13, 1995.
- Lim, J.S. "System Overview—Advanced TV Technology."
- National Center for Integrated Photonics Workshop*, Santa Monica, California, February 2-3, 1995.
- Darwish, A.M., Lenz, G., Ippen, E.P. "Frequency Conversion in Passive InGaAsP/INP Waveguides."
- Haus, H.A. "Channel Dropping Filters and Progress in Their Fabrication."
- Neural Prosthesis Workshop*, 26th, Bethesda, Maryland, October 18-20, 1995.
- Eddington, D.K., and J. Tierney. "Compression Technique for Cochlear Implants."
- NATO Advanced Research Workshop on Future Trends in Microelectronics*, Ile de Bendor, France, July 1995.
- Hu, Q. "High-frequency (f-THz) Studies of Quantum-effect Devices."
- Optical Society of America Meeting*, Annual, Portland, Oregon, September 9-13, 1995.
- Ippen, E.P. "Ultrafast Science and Technology: How Fast? Which Way?"
- Particle Accelerator Conference*, Dallas, Texas, May 1-5, 1995.
- Catravas, P., R. Stoner, J. Blastos, D. Sisson, I. Mastovsky, G. Bekefi, X.J. Wang, and A. Fisher. "MIT Microwiggler for Free Electron Laser Applications."
- Volfbeyn, P., I. Mastovsky, G. Bekefi, I. Wilson, and W. Wuensch. "Experimental Studies of a CERN-CLIC 32.98 GHz High Gradient RF Accelerating Structure Driven by the MIT Free Electron Laser Amplifier."
- Progress in Electromagnetics Research Symposium (PIERS)*, Seattle, Washington, July 24-28, 1995.
- Chou, M., and J. White. "Transient Simulations of Three-dimensional Integrated Circuit Interconnect Using a Mixed Surface-Volume Approach."
- Ding, K.H., S.E. Shih, Y.E. Yang, and J.A. Kong. "Scattering and Absorption of Electromagnetic Radiation by Bicontinuous Random Media."
- Gung, T.J., Y.E. Yang, C.C. Hsu, J.A. Kong, C. Kohler, T. Nguyen, and H. Nguyen. "MMW Radar Range Profile Simulation of Isolated Trees with Radiative Transfer Theory."
- Hsu, C.C., J.A. Kong, J.C. Souyris, and T. LeToan. "Application of Radiative Transfer Modeling to the Polarimetric Backscattering of Forest."
- Johnson, J.T., J.A. Kong, R.T. Shin, and L. Tsang. "Monte Carlo Studies of Ocean Surface Scattering and Thermal Emission."
- Li, K., J.T. Johnson, J.J. Akerson, R.T. Shin, and J.A. Kong. "Theoretical and Numerical Analysis of Berenger's PML."
- Manolatu, C., J.T. Johnson, J.A. Kong, and R.T. Shin. "Mixing Laws for Helix Loaded Composite Media B."
- Nghiem, S.V., R. Kwok, S.H. Yueh, J.A. Kong, C.C. Hsu, and K.H. Ding. "Variations in Polarimetric Backscattering of Saline Ice Grown Under Diurnal Thermal Cycling Condition."
- Phillips, J.R., and J.K. White. "Precorrected-FFT Methods for Electromagnetic Analysis of Complex 3-D Interconnect and Packages."
- Shih, S.E., K.H. Ding, A.K. Jordan, C.C. Hsu, R.T. Shin, and J.A. Kong. "Electromagnetic Scattering Inversion Using Bistatic Data."
- Shih, S.E., K.H. Ding, S.V. Nghiem, C.C. Hsu, R.T. Shin, J.A. Kong, and A.K. Jordan. "Polarimetric Backscattering Signature of Laboratory Grown Saline Ice."
- Shih, S.E., E. Yang, K.H. Ding, J.A. Kong, R.E. Davis, and K. O'Neill. "Discrete Scatter Modeling of Electromagnetic Scattering from Snow."
- Silveira, L. M., M. Kamon, and J. White. "Direct Computation of Reduced-Order Models for Circuit Simulation of 3-D Interconnect Structures."
- Souyris, J.C., T. Le Toan, Y. Zhang, C.C. Hsu, and J.A. Kong. "Inversion of Biomass with Polarimetric Data from SIR-C/X-SAR."

- Tankuranun, P., K.H. Ding, C.F. Lee, R.T. Shin, and J.A. Kong. "Monte Carlo Simulation of Electromagnetic Wave Scattering by Randomly Buried Particles."
- Wang, L., J.T. Johnson, C.C. Hsu, J.A. Kong, J.C. Souyris, and T. Le Toan. "Application of Neural Networks to the Inversion of Geophysical Parameters."
- Wang, L., K.H. Ding, C.C. Hsu, Y.E. Yang, and J.A. Kong. "Electromagnetic Scattering Model for Vegetation Based on L-Systems."
- Yan, J., Y.E. Yang, and J.A. Kong. "Monte Carlo Technique for Random Rough Surface Scattering at Low Grazing Incidence Angles."
- Yeang, C.P., Y.E. Yang, Y. Zhang, and J.A. Kong. "Analysis of Intermodulation Interference to Instrument Landing System."
- Zhang, Y., Y.E. Yang, C.P. Yeang, and J.A. Kong. "Simulation of RF Interference Effect on Aircraft Automatic Landing System."
- Psychoacoustics, Speech, and Hearing Aid Symposium*, Bad Zwischenahn, Germany, August 31-September 5, 1995.
- Zurek, P.M., J.E. Greenberg, and W.M. Rabinowitz. "Prospects and Limitations of Microphone-Array Hearing Aids."
- Semiconductor Research Conference at Stanford*, Palo Alto, California, February 7-9, 1995.
- Chou, M. "SRC Review."
- Seminar at Washington University*, St. Louis, Missouri, May 25, 1995.
- Shapiro, J. "Laser Radar System Theory."
- Seventh International Conference on II-VI Compounds and Devices*, Edinburgh, Scotland, August 13-18, 1995.
- Ho, E., G.S. Petrich, and L.A. Kolodziejski. "Comparison of Hydrogen Passivation of ZnSe:N Using Gas Source and Conventional Molecular Beam Epitaxy."
- Special Seminar at University of Southern California Department of Aerospace Engineering*, Los Angeles, California, June 15, 1995.
- Schattenburg, M.L. "X-ray and XUV Transmission Gratings."
- SPIE International Society for Optical Engineering Conference*, San Jose, California, February 5-10, 1995.
- Birngruber, R., M.R. Hee, S.A. Boppart, J.G. Fujimoto, E.A. Swanson, C.A. Toth, C.D. DiCarlo, C.P. Cain, G.D. Noojin, and W.P. Roach. "In vivo Imaging Development Linear and Nonlinear Retinal Laser Effects Using Optical Coherence Tomography Correlation with Histopathological Finding."
- Brothers, L.R., and N.C. Wong. "Optical Frequency Comb Generation for Terahertz Difference-frequency Measurements."
- CiCarlo, C.D., S.A. Boppart, M.R. Hee, J.G. Fujimoto, D.A. Gagliano, E.A. Swanson, A.B. Cox, R.E. Amnotte, and W.P. Roach. "New Noninvasive Technique for Cataract Evaluation in the Rhesus Monkey."
- Hee, M.R., J.A. Izatt, S.A. Boppart, J.G. Fujimoto, E.A. Swanson, C.P. Lin, J.S. Schuman, C. Wong, and C.A. Puliafito. "Examination of the Retina With Optical Coherence Tomography."
- Lee, D., and N.C. Wong. "Tuning Characteristics of a CW Dual-Cavity KTP Optical Parametric Oscillator."
- Tearney, G.J., M.R. Hee, J.A. Izatt, B.E. Bouma, J.G. Fujimoto, M.B. Brezinski, J.F. Southern, R.R. Anderson, and E.A. Swanson. "Optical Coherence Tomography in Multiply Scattering Tissue."
- Wong, N.C. "New Applications of Optical Parametric Devices."
- SPIE/Advanced Signal Processing Algorithms*, San Diego, California, July 10-12, 1995.
- Halberstadt, A.K. "Application of Frequency-domain Polyphase Filtering to Quadrature Sampling."
- Winograd, J.M., and S.H. Nawab. "Mixed-radix Approach to Incremental DFT Refinement."
- Symposium on Combined Optical-Microwave Earth and Atmospheric Sensing*, Atlanta, Georgia, April 2-4, 1995.
- Staelin, D.H., and Kerekes, John F. "Combined Microwave and Optical Remote Sensing Techniques: A Review."
- Symposium on Luteractive 3D Graphics*, Monterey, California, April 9-12, 1995.
- Drucker, S., and D. Zeltzer. "CAMROID: A System for Implementing Intelligent Camera Control."
- Technical Conference on Nonlinear Dynamics*, Mystic, Connecticut, July 1995.

- Oppenheim, A.V., K.M. Cuomo, R.J. Barron, and A.E. Freedman. "Channel Equalization for Communication with Chaotic Signals."
- Topical Conference on Radio Frequency Power in Plasmas*, Eleventh, Palm Springs, California, May 15-19, 1995.
- Ram, A.K. "Heating and Current Drive by Mode-Converted Ion-Bernstein Waves."
- Schultz, S.D., A.Bers, and A.K. Ram. "RF Wave Effects on the Neoclassical Electron Distribution Function in Tokamaks."
- Trieste Conference on Ultrafast Processes in Spectroscopy*, Trieste, Italy, October 30-November 3, 1995.
- Fujimoto, J.G., G. Tearney, B. Bouma, S. Boppart, M. Hee, E.A. Swanson, C.A. Puliafito, and J. Schuman. "Biomedical Imaging and Optical Biopsy Using Optical Coherence Tomography."
- TCAD Symposium. Hierarchical Technology CAD—Process, Device, and Circuits*, Palo Alto, California, August 10, 1995.
- McIlrath, M., and D. Boning. "Process Repository."
- Tso, K., M. McIlrath, and D. Boning. "Fab Facilities Database."
- Virtual Reality World Meeting*, Stuttgart, Germany, February 20-26, 1995.
- Zeltzer, D. "Officer of the Deck: A Virtual Environment Training Application."
- Visual Communications and Image Processing Conference*, Taipei, Taiwan, May 23-26, 1995.
- Apostolopoulos, J.G., and J.S. Lim. "Coding of Arbitrarily-Shaped Regions."
- the 17th International Free Electron Laser Conference, New York, 1995.
- Baggeroer, A.B., and H. Schmidt. "Cramer-Rao Bounds for Matched Field Tomography and Ocean Acoustic Tomography." *Proceedings of the IEEE International Conference on Acoustics, Speech, and Signal Processing*, Detroit, Michigan, May 8-12, 1995.
- Beauregard, G.L., M.A. Srinivasan, and N.I. Durlach. "Manual Resolution of Viscosity and Mass." *Proceedings of the ASME Dynamic Systems and Control Division*.
- Buck, J.R., J.C. Preisig, M. Johnson, and J. Catipovic. "Monochromatic Single-Mode Excitation in Shallow Water Using Feedback Control." *Proceedings of the IEEE International Conference on Acoustics, Speech, and Signal Processing*, Detroit, Michigan, May 8-12, 1995.
- Cai, X., K. Nabors, and J. White. "Efficient Galerkin Techniques for Multipole-Accelerated Capacitance Extraction of 3-D Structures with Multiple Dielectrics." *Proceedings of the Chapel Hill Conference on Advanced Research in VLSI*, Chapel Hill, North Carolina, March 1995.
- Catravas, P., R. Stoner, and G. Bekefi. "Characteristics of the MIT Microwiggler for Free Electron Laser Applications." *Proceedings of the 17th International Free Electron Laser Conference*, New York, 1995.
- Chen, J., H. Haus, S. Fan, and J.D. Joannopoulos. "Optical Filters from PBG Air-Bridges." *Proceedings of the European Conference on International Optics*, Delft, The Netherlands, 1995.
- Chen, J.C., H.A. Haus, S. Fan, and J.D. Joannopoulos. "Optical Filters from Photonic Band Gap Air Bridges." *Proceedings of the Photonics Society of the Chinese-Americans Annual Meeting*, Baltimore, Maryland.
- Chou, M., M. Kamon, K. Nabors, J. Phillips, and J. White. "Extraction Techniques for Signal Integrity Analysis of 3-D Interconnect." *Proceedings of the Custom Integrated Circuit Conference*, May 1995.
- Chou, M., T. Korsmeyer, and J. White. "Transient Simulations of Three-dimensional Integrated Circuit Interconnect Using a Mixed Surface-Volume Approach." *Proceedings of the 32nd Design Automation Conference*, San Francisco, California, June 1995.
- Aggarwal, R.J., K.V. Shenoy, and C.G. Fonstad, Jr. "A Technology for Monolithic Integration of High-indium-fraction Resonant-tunneling Diodes with Commercial MESFET VLSI Electronics." *Proceedings of the Seventh International Conference on Indium Phosphide and Related Materials*, Sapporo, Japan, May 9-13, 1995.
- Babzien, M., I. Ben-Zvi, P. Catravas, J. Fang, A. Fisher, W. Graves et al. "Optical Diagnostics for the ATF Microundulator FEL." *Proceedings of*

- Courtney, M., H. Jiao, N. Spellmeyer, and D. Kleppner. "Quantum Chaos and Rydberg Atoms in Strong Fields." *Proceedings of the Drexel Conference*.
- Cuomo, K.M. "Systematic Synthesis Procedures for High-Dimensional Chaotic Systems." *Proceedings of ISCAS Conference*, April 1995.
- Dandekar, K., and M.A. Srinivasan. "A 3-dimensional Finite Element Model of the Monkey Fingertip for Predicting Responses of Slowly Adapting Mechanoreceptors." *Proceedings of the 1995 Bioengineering Conference*. Eds. R.M. Hochmuth, N.A. Langrana, and M.S. Hefzy.
- del Alamo, J.A., C.C. Eugster, Q. Hu, M.R. Melloch, and M.J. Roeks. "Electron Waveguide Devices." *Proceedings of the International Conference on Superlattices, Microstructures and Microdevices*, Eighth, Cincinnati, Ohio, August 20-25, 1995.
- deLange, G., B.R. Jacobson, and Q. Hu. "A Low-Noise Micromachined Millimeter-Wave Heterodyne Mixer with Nb Superconducting Tunnel Junctions." *Proceedings of the Workshop on Millimetre Waves Technology and Applications*, Noordwijk, The Netherlands, December 5-7, 1995.
- deLange, G., B.R. Jacobson, and Q. Hu. "A Low-noise Micromachined Millimeter-wave Heterodyne Mixer with Nb Superconducting Tunnel Junctions." *Proceedings of the European Space Agency Workshop on Millimeter Waves Technology and Applications*, Noordwijk, The Netherlands, December 1995.
- Devadas, S., and S. Malik. "A Survey of Optimization Techniques Targeting Low Power VLSI Circuits." *Proceedings of the 32nd Design Automation Conference*, San Francisco, California, June 1995.
- Gulati, R.J., and M.A. Srinivasan. "Human Fingertip Under Indentation I: Static and Dynamic Force Response." *Proceedings of the 1995 Bioengineering Conference*. Eds. R.M. Hochmuth, N.A. Langrana, and M.S. Hefzy.
- Hall, K.L., J.D. Moores, K.A. Rauschenback, W.S. Wong, E.P. Ippen, and H.A. Haus. "All-Optical Storage of a 1.25 kb Packet at 10 Gb/s." In *Conference on Lasers and Electro-Optics. OSA Technical Digest Series*, paper CPD 16. Washington, DC: Optical Society of America, 1995.
- Joannopoulos, J.D. "An Introduction to Photonic Crystals." *Proceedings of NATO ASI*, Crete, 1995.
- Joannopoulos, J.D. "The Almost-Magical World of Photonic Crystals." *Proceedings of the Seventh Brazilian Workshop on Semiconductor Physics*, Rio de Janeiro, Brazil, 1995.
- Karason, S.P., and M.A. Srinivasan. "Passive Human Grasp Control of an Active Instrumented Object." *Proceedings of the ASME Dynamic Systems and Control Division*.
- Koita, R., D.H. Staelin, and M. Rawizza. "Sequential Block Design Strategy for Two-Level Factorial Experiments." *Proceedings of the Section on Quality and Productivity, American Statistical Association*.
- Lashmore-Davies, C.N., V. Fuchs, and A.K. Ram. "Strong Electron Dissipation by a Mode Converted Ion Hybrid (Bernstein) Wave." *Proceedings of the 11th Topical Conference on Radio Frequency Power in Plasmas*, Palm Springs, California, May 17-19, 1995.
- Liao, S., S. Devadas, and K. Keutzer. "Code Density Optimization for Embedded DSP Processors Using Data Compression Techniques." *Proceedings of the Chapel Hill Conference on Advanced Research in VLSI*, Chapel Hill, North Carolina, March 1995.
- Liao, S., S. Devadas, K. Keutzer, and S. Tjiang. "Instruction Selection Using Binate Covering for Code Size Optimization." *Proceedings of the International Conference on Computer-Aided Design*, San Jose, California, November 1995.
- Liao, S., S. Devadas, K. Keutzer, S. Tjiang, and A. Wang. "Storage Assignment to Decrease Code Size." *Proceedings of the SIGPLAN Programming Language Design and Implementation Symposium*, Princeton, New Jersey, June 1995.
- Liao, S., S. Devadas, K. Keutzer, S. Tjiang, and A. Wang. "Code Optimization Techniques in Embedded DSP Microprocessors." *Proceedings of the 32nd Design Automation Conference*, San Francisco, California, June 1995.
- Liao, S., S. Devadas, K. Keutzer, S. Tjiang, and A. Wang. "Storage Assignment to Decrease Code Size." *Proceedings of the SIGPLAN Programming Language Design and Implementation Symposium*, Princeton, New Jersey, June 1995.

- Liu, S.A. "The Effect of Vowel Reduction on Landmark Detection." *Proceedings of the International Congress of Phonetic Sciences*, 13th, Stockholm, Sweden, August 13-19, 1995.
- Ludwig, J.T., S.H. Nawab, and A. Chandrakasan. "Low Power Filtering Using Approximate Processing for DSP Applications." *Proceedings of the Custom Integrated Circuit Conference*, May 1995.
- Lutwak, R., J. Holley, J. DeVries, and D. Kleppner. "Millimeter-Wave Measurement of the Rydberg Frequency." *Proceedings of the Fifth Symposium on Frequency Standards and Metrology*, Woods Hole, Massachusetts, October 15-19, 1995.
- Lyubomirsky, I., B. Xu, and Q. Hu. "THz Parametric Oscillators Using Coupled Double Quantum Wells." *Proceedings of the International Semiconductor Device Research Symposium*, Charlottesville, Virginia, December 5-8, 1995.
- Manuel, S.Y., and K.N. Stevens. "Formant Transitions: Teasing Apart Consonant and Vowel Contributions." *Proceedings of the International Congress of Phonetic Sciences*, 13th, Stockholm, Sweden, August 13-19, 1995.
- Monteiro, J., and S. Devadas. "Techniques for the Power Estimation Sequential Logic Circuits Under User-Specified Input Sequences and Programs." *Proceedings of the International Symposium on Low Power Design*, Laguna, California, April 23-26, 1995.
- Monteiro, J., J. Rinderknecht, S. Devadas, and A. Ghosh. "Optimization of Combinational and Sequential Logic Circuits for Low Power Using Precomputation." *Proceedings of the 1995 Chapel Hill Conference on Advanced Research in VLSI*, Chapel Hill, North Carolina, March 1995.
- Nawab, S.H., and J.M. Winograd. "Approximate Signal Processing Using Incremental Refinement and Deadline-Based Algorithms." *Proceedings of the IEEE International Conference on Acoustics, Speech, and Signal Processing*, Detroit, Michigan, May 8-12, 1995.
- Peng, L.H., and C.G. Fonstad, Jr. "Intersubband Transitions in Conduction Band Quantum Wells: The Role of Energy Band Gaps and Band Offsets." *Proceedings of the Seventh International Conference on Indium Phosphide and Related Materials*, Sapporo, Japan, May 9-13, 1995.
- Poort, K.L. "Stop Consonant Production: An Articulation and Acoustic Study." *Proceedings of the International Congress of Phonetic Sciences*, 13th, Stockholm, Sweden, August 13-19, 1995.
- Ram, A.K. "Heating and Current Drive by Mode-Converted Ion-Bernstein Waves." *Proceedings of the 11th Topical Conference on Radio Frequency Power in Plasmas*, Palm Springs, California, May 17-19, 1995.
- Ram, A.K., A. Bers, S.D. Schultz, and V. Fuchs. "Interaction of Mode-Converted Ion-Bernstein Waves with Electrons in Tokamaks." *Proceedings of the International Sherwood Fusion Conference*, Incline Village, Nevada, April 3-5, 1995.
- Ram, A.K., A. Bers, S.D. Schultz, and V. Fuchs. "RF Wave Effects on the Neoclassical Electron Distribution Function in Tokamaks." *Proceedings of the International Sherwood Fusion Conference*, Incline Village, Nevada, April 3-5, 1995.
- Ram, A.K., A. Bers, S.D. Schultz, V. Fuchs, A. Becoulet, and B. Saoutic. "Mode-Converted Ion-Bernstein Waves in Tokamaks." *Proceedings of the 22nd European Physical Society Conference on Controlled Fusion and Plasma Physics*, Bournemouth, England, July 3-7, 1995.
- Saoutic, B., A. Becoulet, T. Hutter, D. Fraboulet, A.K. Ram, and A. Bers. "Mode Conversion Heating Experiments on Tore Supra." *Proceedings of the 11th Topical Conference on Radio Frequency Power in Plasmas*, Palm Springs, California, May 17-19, 1995.
- Schultz, S.D., A.K. Ram, and A. Bers. "RF Wave Effects on the Neoclassical Electron Distribution Function in Tokamaks." *Proceedings of the 11th Topical Conference on Radio Frequency Power in Plasmas*, Palm Springs, California, May 17-19, 1995.
- Shattuck-Hufnagel, S. "Pitch Accent Patterns in Adjacent-stress vs. Alternating-stress Words in American English." *Proceedings of the International Congress of Phonetic Sciences*, 13th, Stockholm, Sweden, August 13-19, 1995.
- Silveira, L.M., M. Kamon, and J. White. "Efficient Reduced-Order Modeling of Frequency-Dependent Coupling Inductances Associated with 3-D Interconnect Structures." *Proceedings of the European Design and Test Conference*, Paris, France, March 1995.

- Singer, A.C. "Signaling Techniques Using Solitons." *Proceedings of the IEEE International Conference on Acoustics, Speech, and Signal Processing*, Detroit, Michigan, May 8-12, 1995.
- Sluijter, A.M.C., S. Shattuck-Hufnagel, K.N. Stevens, and V.J. van Heuven. "Supralaryngeal Resonance and Glottal Pulse Shape as Correlates of Stress and Accent in English." *Proceedings of the International Congress of Phonetic Sciences*, 13th, Stockholm, Sweden, August 13-19, 1995.
- Somerville, M.H., J.A. del Alamo, and W. Hoke. "A New Physical Model for the Kink Effect on InAlAs/InGaAs HEMTs." *Proceedings of the International Electron Devices Meeting*, Washington, DC, December 1995.
- Srinivasan, M.A. "Haptic Interfaces: Hardware, Software, and Human Performance." *Proceedings of the NASA Workshop on Human-computer Interaction and Virtual Environments*, NASA Conference Publication.
- Stevens, K.N. "Applying Phonetic Knowledge to Lexical Access." *Proceedings of the European Conference on Speech Communication and Technology*, Fourth, Madrid, Spain, 1995.
- Telichevesky, R., K.S. Kundert, and J. White. "Efficient Steady-State Analysis Based on Matrix-Free Krylov Subspace Methods." *Proceedings of the 32nd Design Automation Conference*, San Francisco, California, June 1995.
- Verghese, S., N. Zamdmer, E.R. Brown, A. Forster, and Q. Hu. "Correlation of Optical Pulses with a Low-Temperature-Grown GaAs Photoconductor." *Proceedings of the International Semiconductor Device Research Symposium*, Charlottesville, Virginia, December 5-8, 1995.
- Villeneuve, P.R., S. Fan, J.D. Joannopoulos, K.-Y. Lim, J.C. Chen, G.S. Petrich, L.A. Kolodziejski, and R. Reif. "Microcavities in Channel Waveguides." *Proceedings of a NATO Advanced Studies Institute of Photonic Band Gap Materials*, Elounda, Greece, June 1995.
- Wee, S.J., M.O. Polley, and W.F. Schreiber. "A Scalable Source Coder for a Hybrid Transmission HDTV System." *Proceedings of the International Symposium on Multimedia Communications and Video Coding*, Brooklyn, New York, October 1995.
- Wilde, L. "Quantifying Time-varying Spectra of English Fricatives." *Proceedings of the International Congress of Phonetic Sciences*, 13th, Stockholm, Sweden, August 13-19, 1995.
- Wilhelms-Tricarico, R., and J.S. Perkell. "Biomechanical and Physiologically-based Speech Modeling." *Proceedings of the International Congress of Phonetic Sciences*, 13th, Stockholm, Sweden, August 13-19, 1995.
- Winograd, J.M., and S.H. Nawab. "A C++ Software Environment for the Development of Embedded Signal Processing." *Proceedings of the IEEE International Conference on Acoustics, Speech, and Signal Processing*, Detroit, Michigan, May 8-12, 1995.
- Wong, N.C., B. Lai, P. Nee, and E. Mason. "Experimental Progress Toward Realizing a 3:1 Optical Frequency Divider." *Proceedings of the Fifth Symposium on Frequency Standards and Metrology*, Woods Hole, Massachusetts, October 15-19, 1995.
- Xu, Y. "The Effect of Emphatic Accent on Contextual Tonal Variation." *Proceedings of the International Congress of Phonetic Sciences*, 13th, Stockholm, Sweden, August 13-19, 1995.

A.2 Journal Articles

A.2.1 Published Journal Articles

- Agam, O., B.L. Altshuler, and A.V. Andreev. "Spectral Statistics: From Disordered to Chaotic Systems." *Phys. Rev. Lett.* 75: 4389 (1995).
- Aggarwal, R.J., and C.G. Fonstad. "High Peak-to-Valley Current Ratio InGaAs/AlAs RTTs on GaAs Using Relaxed InGaAs Buffers." *Electron. Lett.* 31: 75-76 (1995).
- Aggarwal, R.J., and C.G. Fonstad, Jr. "High Peak-to-Valley Current Ratio $\text{In}_{0.22}\text{Ga}_{0.78}\text{As}/\text{AlAs}$ RTDs on GaAs Using Relaxed $\text{In}_x\text{Ga}_{1-x}\text{As}$ Buffers." *Electron. Lett.* 31(1): 75-76 (1995).
- Andreev, A.V., and B.L. Altshuler. "Spectral Statistics Beyond Random Matrix Theory." *Phys. Rev. Lett.* 75: 902-905 (1995).
- Aucoin, R.J., and M.L. Schattenburg. "Optically-Matched Tri-Level Resist Process for Nanostructure Fabrication." *J. Vac. Sci. Technol. B* 13: 3007-3011 (1995).

- Bahl, S.R., J.A. del Alamo, J. Dickmann, and S. Schildberg. "Off-State Breakdown in InAlAs/InGaAs MODFETs." *IEEE Trans. Electr. Dev.* 42: 15-22 (1995).
- Bers, A., S.D. Schultz, and A.K. Ram. "Mode Conversion to Ion-Bernstein Waves of Fast Alfvén Waves with Finite Poloidal Wavenumber in Tokamak Geometries." *Bull. Am. Phys. Soc.* 40: 1705 (1995).
- Berthold, S., E. Zanoni, C. Canali, M. Pavesi, M. Pecchini, M. Manfredi, S.R. Bahl, and J.A. del Alamo. "Impact Ionization and Light Emission in InAlAs/InGaAs Heterostructure Field-Effect Transistors." *IEEE Trans. Electron. Dev.* 42: 752-759 (1995).
- Besing, J.M., C.M. Reed, and N.I. Durlach. "A Comparison of Auditory and Tactual Presentation of a Single-Band Envelope Cue as a Supplement to Speechreading." *Seminars in Hear.* 16(4): 316-327 (1995).
- Boivin, L. "The Sagnac Loop Squeezer at Zero Dispersion with a Response Time for the Kerr Nonlinearity." *Phys. Rev. A* 52(1): 754-766 (1995).
- Boivin, L. "Sagnac Loop Squeezer at Zero Dispersion with a Finite Response Time for Kerr Nonlinearity." *Phys. Rev. A* 52: 754 (1995).
- Bouma, B., G.J. Tearney, S.A. Boppart, M.R. Hee, M.B. Brezinski, and J.G. Fujimoto. "High Resolution Optical Coherence Tomographic Imaging Using a Modelocked Ti:Al₂O₃ Laser Source." *Opt. Lett.* 20(13): 1486-1488 (1995).
- Burkhardt, M., S. Silverman, H.I. Smith, D.A. Antoniadis, K.W. Rhee, and M.C. Peckerar. "Gap Control in the Fabrication of Quantum-Effect Devices Using X-ray Nanolithography." *J. Microelectron. Eng.* 27: 307-310 (1995).
- Cabrera-Mercader, C.R., and D.H. Staelin. "Passive Microwave Relative Humidity Retrievals Using Feedforward Neural Networks." *IEEE Trans. Geosci. Remote Sens.* 33(6): 1324-1328 (1995).
- Capaz, R.B., H. Lim, J.D. Joannopoulos. "Ab initio Studies of GaN Epitaxial Growth on SiC." *Phys. Rev. B* 51(24): 755-757 (1995).
- Capaz, R.B., K. Cho, and J.D. Joannopoulos. "Signatures of Bulk and Surface Arsenic Antisite Defects in GaAs(110)." *Phys. Rev. Lett.* 75(9): 1811-1814 (1995).
- Chapman, M.S., C.R. Ekstrom, T.D. Hammond, J. Schmiedmayer, B.E. Tannian, S. Wehinger, and D.E. Pritchard. "Near Field Imaging of Atom Diffraction Gratings: The Atomic Talbot Effect." *Phys. Rev. A* 51(1): R14-R17 (1995).
- Chapman, M.S., C.R. Ekstrom, T.D. Hammond, R.A. Rubenstein, J. Schmiedmayer, S. Wehinger, and D.E. Pritchard. "Optics and Interferometry with Na₂ Molecules." *Phys. Rev. Lett.* 74(24): 4783-4786 (1995).
- Chapman, M.S., T.D. Hammond, A. Lenef, J. Schmiedmayer, R.A. Rubenstein, E. Smith, and D.E. Pritchard. "Photon Scattering from Atoms in an Atom Interferometer: Coherence Lost and Regained." *Phys. Rev. Lett.* 75(21): 3783-3787 (1995).
- Chen, J.C., and K. Li. "Quartic Perfectly Matched Layers for Dielectric Waveguides and Gratings." *Microwave Opt. Tech. Lett.* 10(6): 319-323 (1995).
- Chen, M.Y. "Acoustic Parameters of Nasalized Vowels in Hearing-Impaired and Normal-Hearing Speakers." *J. Acoust. Soc. Am.* 98(5): 2443-2453 (1995).
- Cheung, S., and J.S. Lim. "Incorporation of Biorthogonality into Lapped Transforms for Audio Compression." *Proc. ICASSP* 5: 3079-3082 (1995).
- Cho, K., and J.D. Joannopoulos. "Tip-induced Modifications in Scanning Tunneling Microscopy and Atomic Force Microscopy." *Scan. Microscopy* 9(2): 381-386 (1995).
- Cho, K., and J.D. Joannopoulos. "Mechanical Hysteresis on an Atomic Scale." *Surf. Sci.* 328: 320 (1995).
- Coppi, B. "Momentum Transport Modes in High Ion Temperature Regimes." *Phys. Lett. A* 201: 66-69 (1995).
- Coppi, B. "Momentum Transport and Collective Modes in High Ion Temperature Regimes." *Phys. Lett. A* 201: 66-69 (1995).
- Courtney, M., H. Jiao, N. Spellmeyer, D. Kleppner, J. Gao, and J.B. Delos. "Closed Orbit Bifurcations in Continuum Stark Spectra." *Phys. Rev. Lett.* 74(9): 1538-1541 (1995).
- Courtney, M., N. Spellmeyer, H. Jiao, and D. Kleppner. "Classical, Semiclassical, and

- Quantum Dynamics in the Lithium Stark System." *Phys. Rev. A* 51(5): 3604-3620 (1995).
- Davis, K.B., M.-O. Mewes, and W. Ketterle. "An Analytical Model for Evaporative Cooling of Atoms." *Appl. Phys. B* 60: 155-159 (1995).
- Davis, K.B., M.-O. Mewes, M.R. Andrews, N.J. van Druten, D.M. Kurn, and W. Ketterle. "Bose-Einstein Condensation in a Gas of Sodium Atoms." *Phys. Rev. Lett.* 75(22): 3969-3973 (1995).
- Davis, K.B., M.-O. Mewes, M.A. Joffe, M.R. Andrews, and W. Ketterle. "Evaporative Cooling of Sodium Atoms." *Phys. Rev. Lett.* 74(26): 5202-5205 (1995).
- deLange, G., B.R. Jacobson, and Q. Hu. "Micro-machined Millimeter-wave SIS Mixers." *IEEE Trans. Appl. Supercond.* 5: 1087 (1995).
- DiFilippo, F., V. Natarajan, M. Bradley, F. Palmer, and D.E. Pritchard. "Accurate Atomic Mass Measurements from Penning Trap Mass Comparisons of Individual Ions." *Physica Scripta* T59: 144-154 (1995).
- Dougherty, D.J., F.X. Kartner, H.A. Haus, and E.P. Ippen. "Measurement of the Raman Gain Spectrum of Optical Fibers." *Opt. Lett.* 20(1): 31-33 (1995).
- Duchnowski, P., and P.M. Zurek. "Vilchur Revisited: Another Look at Automatic Gain Control Simulation of Recruiting Hearing Loss." *J. Acoust. Soc. Am.* 98(6): 3170-3181 (1995).
- Fan, S., J.N. Winn, A. Devenyi, J.C. Chen, R.D. Meade, and J.D. Joannopoulos. "Guided and Defect Modes in Periodic Dielectric Waveguides." *J. Opt. Soc. Am. B* 12: 1267 (1995).
- Fan, S., J.N. Winn, A. Devenyi, R.D. Meade, and J.D. Joannopoulos. "Guided and Defect Modes in Periodic Dielectric Waveguides." *J. Opt. Soc. Am. B* 12(7): 1267-1272 (1995).
- Fan, S., P.R. Villeneuve, and J.D. Joannopoulos. "Theoretical Investigation of Fabrication-Related Disorder on the Properties of Photonic Crystals." *J. Appl. Phys.* 78(3): 1415-1418 (1995).
- Fisher, P.A., E. Ho, J.L. House, G.S. Petrich, L.A. Kolodziejski, J. Walker, and N.M. Johnson. "p-Type and n-Type Doping of ZnSe: Effects of Hydrogen Incorporation." *J. Cryst. Growth* 150: 729-733 (1995).
- Furusaki, A., and K.A. Matveev. "Theory of Strong Inelastic Cotunneling." *Phys. Rev. B* 52: 16676 (1995).
- Furusaki, A., and K.A. Matveev. "Coulomb Blockade Oscillations of Conductance in the Regime of Strong Tunneling." *Phys. Rev. Lett.* 75: 709 (1995).
- Golubovic, B., J.P. Donnelly, C.A. Wang, W.D. Goodhue, and R.H. Rediker. "Basic Module for an Integrated Optical Phase Difference Measurement and Correction System." *IEEE Photonics Technol. Lett.* 7(6): 649-651 (1995).
- Grayson, M., D.C. Tsui, and M. Shayegan. "Far-Infrared Emission from Hot Quasi-One-Dimensional Quantum Wires in GaAs." *Appl. Phys. Lett.* 67: 1564 (1995).
- Griffith, M.R., A.E. Wright, R.D. Eckers, and B.F. Burke. "The Parkes-MIT-NRAO (PMN) Surveys: VI. Source Catalogue for the Equatorial Survey (covering $-9.5^\circ < \gamma < +10^\circ$)." *Astrophys. J. Suppl.* 97: 347 (1995).
- Guinan, J.J., Jr., and K.M. Stankovic. "Medial Olivocochlear Efferent Inhibition of Auditory-Nerve Firing Mediated by Changes in Endocochlear Potential." *Abstr. Assoc. Res. Otolaryngol.* 18: 172 (1995).
- Hall, K.L., J.D. Moores, K.A. Rauschenback, W.S. Wong, E.P. Ippen, and H.A. Haus. "All-Optical Storage of a 1.25 kb Packet at 10 Gb/s." *IEEE Photon. Technol. Lett.* 7: 1093 (1995).
- Hara, Y., R.G. Atkins, S.H. Yueh, R.T. Shin, J.A. Kong, and R. Kwok. "Application of Neural Networks for Sea Ice Classification in Polarimetric SAR Images." *IEEE Trans. Geosci. Remote Sens.* 33(3): 740-748 (1995).
- Haus, H.A. "From Classical to Quantum Noise." *J. Opt. Soc. Am. B* 12(11): 2019-2036 (1995).
- Haus, H.A., and M.J. Khan. "Gain-Distributed Feedback Filters." *J. Lightwave Technol.* 13(2): 261-274 (1995).
- Haus, H.A., K. Tamura, L.E. Nelson, and E.P. Ippen. "Stretched-Pulse Additive Pulse Mode-Locking in Fiber Ring Lasers: Theory and Experiment." *IEEE J. Quantum Electron.* 31(3): 591-598 (1995).
- Hee, M.R., C.A. Puliafito, C. Wong, J.S. Duker, E. Reichel, B.K. Rutledge, J.S. Schuman, E.A.

- Swanson, and J.G. Fujimoto. "Quantitative Assessment of Macular Edema with Optical Coherence Tomography." *Arch. Ophthalmol.* 113: 119-129 (1995).
- Hee, M.R., C.A. Puliafito, C. Wong, J.S. Duker, E. Reichel, J.S. Schuman, E.A. Swanson, and J.G. Fujimoto. "Optical Coherence Tomography of Central Serous Choroidopathy." *Am. J. Ophthalmol.* 120: 65-74 (1995).
- Hee, M.R., C.A. Puliafito, C. Wong, J.S. Duker, E. Reichel, J.S. Schuman, E.A. Swanson, and J.G. Fujimoto. "Optical Coherence Tomography of Macular Holes." *Ophthalmol.* 102: 746-748 (1995).
- Hee, M.R., J.A. Izatt, E.A. Swanson, D. Huang, J.S. Schuman, C.P. Lin, C.A. Puliafito, and J. G. Fujimoto. "Optical Coherence Tomography of the Human Retina." *Arch. Ophthalmol.* 113: 325-332 (1995).
- Hee, M.R., J.A. Izatt, E.A. Swanson, D. Huang, J.S. Schuman, C.P. Lin, C.A. Puliafito, and J.G. Fujimoto. "Optical Coherence Tomography for Micron-resolution Ophthalmic Imaging." *IEEE Eng. Med. Bio.* 14: 67 (1995).
- Hinds, R.O., and T.N. Pappas. "An Adaptive Clustering Algorithm for Segmentation of Video Sequences." *Proc. ICASSP* 4: 2427-2430 (1995).
- Ho, E., P.A. Fisher, J.L. House, G.S. Petrich, L.A. Kolodziejewski, J. Walker, and N.M. Johnson. "Hydrogen Passivation in Nitrogen- and Chlorine-Doped ZnSe Films Grown by Gas Source Molecular Beam Epitaxy." *Appl. Phys. Lett.* 66(9): 1062-1064 (1995).
- Holmberg, E.B., R.E. Hillman, J.S. Perkell, and S. Goldman. "Comparisons Among Aerodynamic, Electroglossographic, and Acoustic Spectrum Measures of Female Voices." *J. Speech Hear. Res.* 38: 1212-1223 (1995).
- Kastner, M.A., O. Klein, C. de Chamon, D. Tang, D.M. Abusch-Magder, U. Meirav, X.-G. Wen, and S.J. Wind. "Exchange Effects in Artificial Atoms." *J. Appl. Phys.* 34: 16 (1995).
- Ketterle, W. "Evaporative Cooling of Magnetically Trapped Sodium." *Bull. Am. Phys. Soc.* 40: 1269 (1995).
- Keyser, S.J., and K.N. Stevens. "Feature Geometry and the Vocal Tract." *Phon.* 11: 207-236 (1995).
- Khatr, F.I., J.D. Moores, G. Lenz, and H.A. Haus. "Models for Self-Limited Additive Pulse Mode-Locking." *Opt. Commun.* 114: 447-452 (1995).
- Klein, O., C. de Chamon, D. Tang, D.M. Abusch-Magder, X.-G. Wen, M.A. Kastner, and S.J. Wind. "Exchange Effects in an Artificial Atom at High Magnetic Fields." *Phys. Rev. Letts.* 74: 785 (1995).
- Lai, B., N.C. Wong, and L.K. Cheng. "Continuous-wave Tunable Light Source at 1.6 μm by Difference-frequency Mixing in CsTiOAsO₄." *Opt. Lett.* 20(17): 1779-1781 (1995).
- Lam, W.M., and G.W. Wornell. "Multiscale Representation and Estimation of Fractal Point Processes." *IEEE Trans. Signal Process.* 43(11): 2606-2617 (1995).
- LaMotte, R.H., C. Lu, and M.A. Srinivasan. "Peripheral Neural Representation of the Shapes and Orientations of Three-dimensional Objects Stroked Across the Monkey Fingerpad." *Soc. Neurosci. Abstr.* 21: 1162 (1995).
- Lane, H., J. Wozniak, M.L. Matthies, M.A. Svirsky, and J.S. Perkell. "Phonemic Resetting vs. Postural Adjustments in the Speech of Cochlear Implant Users: An Exploration of Voice Onset Time." *J. Acoust. Soc. Am.* 98: 3096-3106 (1995).
- Lenz, G., K. Tamura, H.A. Haus, and E.P. Ippen. "All Solid-State Femtosecond Source at 1.55 μm ." *Opt. Lett.* 20(11): 1289-1291 (1995).
- Li, K., M.A. Tassoudji, S.Y. Poh, M. Tsuk, R.T. Shin, and J.A. Kong. "FD-TD Analysis of Electromagnetic Radiation from Modules-on-Backplane Configurations." *IEEE Trans. Electro. Compatib.* 37(3): 326-332 (1995).
- Lim, H., K. Cho, I. Park, J.D. Joannopoulos, and E. Kaxiras. "Ab initio Study of Hydrogen Adsorption on Si(111)-(7x7) Surface." *Phys. Rev. B* 52(24): 231-237 (1995).
- Lin, B., and S. Devadas. "Synthesis of Hazard-Free Multilevel Logic Under Multiple Input Changes from Binary Decision Diagrams." *IEEE Trans. Comput.-Aided Des.* 14(8): 974-985 (1995).
- Little, B.E., and H.A. Haus. "A Variational Coupled-Mode Theory for Periodic Waveguides." *IEEE J. Quantum Electron.* 31: 2258 (1995).

- Manuel, S.Y. "Speakers Nasalize /o/ after /n/, but Listeners Still Hear /o/." *J. Phonetics* 23: 453-476 (1995).
- Martin, P.S., J.C. Chen, C.G. Fonstad, Jr., and H.A. Haus. "Application of the Spectral Index Method to Laser Diode Design." *IEEE J. Lightwave Technol.* 13: 569-574 (1995).
- Matveev, K.A. "Coulomb Blockade at Almost Perfect Transmission." *Phys. Rev. B* 51: 1743 (1995).
- Maxwell, J.A., and P.M. Zurek. "Reducing Acoustic Feedback in Hearing Aids." *IEEE Trans. Speech Audio Process.* 3(4): 304-313 (1995).
- McCue, M.P., and J.J. Guinan, Jr. "Spontaneous Activity and Frequency Selectivity of Acoustically Responsive Vestibular Afferents in the Cat." *J. Neurophysiol.* 74(4): 1563-1572 (1995).
- Migliuolo, S. "Isotopic Effect in Transport and the Ubiquitous Mode." *Phys. Lett. A* 198: 341 (1995).
- Moon, E.E., P.N. Everett, and H.I. Smith. "Immunity to Signal Degradation by Overlayers Using a Novel Spatial-Phase-Matching Alignment System." *J. Vac. Sci. Technol. B* 13: 2648-2652 (1995).
- Moore, J.D., K.L. Hall, S.M. LePage, K.A. Rauschenback, W.S. Wong, H.A. Haus, and E.P. Ippen. "20-GHz Optical Storage Loop/Laser Using Amplitude Modulation, Filtering, and Artificial Fast Saturable Absorption." *IEEE Photon. Technol. Lett.* 7: 1096 (1995).
- Nabors, K., F.T. Korsmeyer, F.T. Leighton, and J.K. White. "Multipole Accelerated Preconditioned Iterative Methods for Three-Dimensional Potential Integral Equations of the First Kind." *SIAM J. Sci. Stat. Comput.* 15(3): 713-735 (1995).
- Natarajan, V., F. DiFilippo, and D.E. Pritchard. "Squeezed States of Classical Motion in a Penning Trap." *Phys. Rev. Lett.* 74: 2855 (1995).
- Natarajan, V., F. DiFilippo, and D.E. Pritchard. "Classical Squeezing of an Oscillator for Subthermal Noise Operation." *Phys. Rev. Lett.* 74(15): 2855-2858 (1995).
- Nawab, S.H., and E. Dorken. "A Framework for Quality Versus Efficiency Tradeoffs in STFT Analysis." *IEEE Trans. Signal Process.* 43(4): 998-1001 (1995).
- Nelson, L.E., E.P. Ippen, and H.A. Haus. "Broadly Tunable Sub-500 fs Pulses from an Additive-pulse Mode-locked Thulium-doped Fiber Ring Laser." *Appl. Phys. Lett.* 67(1): 19-21 (1995).
- Nghiem, S.V., R. Kwok, S.H. Yueh, J.A. Kong, C.C. Hsu, M.A. Tassoudji, and R.T. Shin. "Polarimetric Scattering from Layered Media with Multiple Species of Scatterers." *Radio Sci.* 30(4): 835-852 (1995).
- Nuttall, W.J., D.Y. Noh, B.O. Wells, and R.J. Birgeneau. "Isothermal Melting of Near-monolayer Xenon on Single Crystal Graphite at 140K." *J. Phys. Condens. Matter* 7: 4337 (1995).
- Oates, J.H., R.T. Shin, and M.J. Tsuk. "Small Aperture Modeling for EMI Applications Using the FDTD Technique." *J. Electromag. Waves Appl.* 9(1/2): 37 (1995).
- Papadopoulos, H.C., and G.W. Wornell. "Maximum Likelihood Estimation of a Class of Chaotic Signals." *IEEE Trans. Inform. Theory* 41(1): 312-317 (1995).
- Pappas, T.N., and R.O. Hinds. "On Video and Audio Data Integration for Conferencing." *Proc. SPIE* 2411: 120-127 (1995).
- Peng, L.H., and C.G. Fonstad, Jr. "Spatial Confinement Effects on Type II Quantum Well Intersubband Transitions." *Appl. Phys. Lett.* 66: 1806-1808 (1995).
- Peng, L.H., and C.G. Fonstad, Jr. "Multiband Coupling Effects on Electron Quantum Well Intersubband Transitions." *J. Appl. Phys.* 77: 747-754 (1995).
- Perkell, J.S., M.L. Matthies, M.A. Svirsky, and M.I. Jordan. "Goal-based Speech Motor Control: A Theoretical Framework and Some Preliminary Data." *J. Phon.* 23: 23-35 (1995).
- Plant, G. "Training Approaches with Tactile Aids." *Seminars in Hear.* 16: 394-403 (1995).
- Polley, M.O., W.F. Schreiber, and S.J. Wee. "Comments on Transmission Techniques for Digital Terrestrial TV Broadcasting." *IEEE Commun. Mag.* 33(11): 22-25 (1995).
- Puliafito, C.A., M.R. Hee, C.P. Lin, E. Reichel, J.S. Schuman, J.S. Duker, J.A. Izatt, E.A. Swanson, and J.G. Fujimoto. "Imaging of Macular Dis-

- eases with Optical Coherence Tomography." *Ophthalmol.* 102: 217-229 (1995).
- Rabinowitz, W.M., and D.K. Eddington. "Effects of Channel-to-Electrode Mappings on Speech Reception with the Ineraid Cochlear Implant." *Ear Hear.* 16(5): 450-458 (1995).
- Rabinowitz, W.M., and D.K. Eddington, J. Tierney, and L.A. Delhorne. "Preliminary Evaluations of Cochlear Implantees Using a Wearable CIS Processor." *J. Acoust. Soc. Am.* 97: 3346A (1995).
- Ram, A.K. "Mode-Converted Ion-Bernstein Waves for Heating and Current Drive." *Bull. Am. Phys. Soc.* 40: 1828 (1995).
- Rauschenback, K.A., K.L. Hall, J.D. Moores, S.G. Finn, R.A. Barry, W.S. Wong, H.A. Haus, E.P. Ippen, and M. Haner. "Technologies for Ultra-High-Bit-Rate Time-Division-Multiplexed Networks." *OSA Photonics in Switching Digest* 12: 45 (1995).
- Reed, C.M., and L.A. Delhorne. "Current Results of a Field Study of Adult Users of Tactile Aids." *Seminars in Hear.* 16(4): 305-315 (1995).
- Reed, C.M., L.A. Delhorne, N.I. Durlach, and S.D. Fischer. "A Study of the Tactual Reception of Sign Language." *J. Speech Hear. Res.* 38: 477-489 (1995).
- Reichelt, M.W., J.K. White, and J. Allen. "Optimal Convolution SOR Acceleration of Waveform Relaxation with Application to Parallel Simulation of Semiconductor Devices." *SIAM J. Sci. Comput.* 16(5): 1137-1158 (1995).
- Ro, J.S., C.V. Thompson, and J. Melngailis. "Microstructure of Gold Grown by Ion-Induced Deposition." *Thin Solid Films* 258: 333-335 (1995).
- Rosenkranz, P.W. "A Rapid Atmospheric Transmittance Algorithm for Microwave Sounding Channels." *IEEE Trans. Geosci. Remote Sens.* 33(5): 1135-1140 (1995).
- Savas, T.A., S.N. Shah, M.L. Schattenburg, J.M. Carter, and H.I. Smith. "Achromatic Interferometric Lithography for 100 nm-Period Gratings and Grids." *J. Vac. Sci. Technol. B* 13(6): 2732-2735 (1995).
- Schmiedmayer, J., M.S. Chapman, C.R. Ekstrom, T.D. Hammond, S. Wehinger, and D.E. Pritchard. "Index of Refraction of Various Gases for Sodium Matter Waves." *Phys. Rev. Lett.* 74(7): 1043-1047 (1995).
- Schreiber, W.F. "Advanced Television Systems for Terrestrial Broadcasting: Some Problems and Some Proposed Solutions." *Proc. IEEE* 83(6): 958-981 (1995).
- Schreiber, W.F. "A Unified Approach to Moving Image Coding for Most Media and Most Applications." *Sig. Proc.* 43: 305-321 (1995).
- Schultz, S.D., A. Bers, and A.K. Ram. "RF Wave Effects on the Neoclassical Electron Distribution Function in Tokamaks." *Bull. Am. Phys. Soc.* 40: 1703 (1995).
- Schuman, J.S., M.R. Hee, C.A. Puliafito, C. Wong, T. Pedut-Kloizman, C.P. Lin, E. Hertzmark, J.A. Izatt, E.A. Swanson, and J.G. Fujimoto. "Quantification of Nerve Fiber Layer Thickness in Normal and Glaucomatous Eyes using Optical Coherence Tomography: A Pilot Study." *Arch. Ophthalmol.* 113: 586-596 (1995).
- Shah, D.M., D.M. Freeman, and T.F. Weiss. "The Osmotic Responses of the Isolated, Unfixed Mouse Tectorial Membrane: Effect of Na⁺, K⁺, and Ca₂⁺ Concentration." *Hear. Res.* 87: 187-207 (1995).
- Shapiro, J.H. "Phase Conjugate Quantum Communication with Optical Heterodyne Detection." *Opt. Lett.* 20(9): 1059-1061 (1995).
- Shapiro, J.H., and L. Boivin. "Raman-Noise Limit on Squeezing in Continuous-Wave Four-Wave Mixing." *Opt. Lett.* 20(8): 925-927 (1995).
- Shaw, J.A., J.B. Delos, M. Courtney, and D. Kleppner. "Recurrences Associated with Classical Orbits." *Phys. Rev. A* 52: 3695 (1995).
- Shen, A., S. Devadas, and A. Ghosh. "Probabilistic Manipulation of Boolean Functions Using Free Boolean Diagrams." *IEEE Trans. Comput.-Aided Des.* 14(1): 87-95 (1995).
- Shenoy, K.V., C.G. Fonstad, Jr., A.C. Grot, and D. Psaltis. "Monolithic Optoelectronic Circuit Design and Fabrication by Epitaxial Growth on Commercial VLSI GaAs MESFETs." *IEEE Photon. Tech. Lett.* 7: 508-510 (1995).
- Shinn-Cunningham, B.G. "A Dynamic, Psychophysical Model of Adaptation in Localization Experiments." *J. Acoust. Soc. Am.* 97(5): 3411 (1995).

- Shinn-Cunningham, B.G., P.M. Zurek, N.I. Durlach, and R.K. Clifton. "Cross-Frequency Interactions in the Precedence Effect." *J. Acoust. Soc. Am.* 98(1): 164-171 (1995).
- Smith, H.I. "100 Years of X-rays: Impact on Micro- and Nanofabrication." *J. Vac. Sci. Technol. B* 13(6): 2323-2328 (1995).
- Song, S., and S.G.J. Mochrie. "Attractive Step-step Interactions, Tricriticality, and Faceting in the Orientational Phase Diagram of Silicon Surfaces Between (113) and (114)." *Phys. Rev. B.* 51: 10068 (1995).
- Song, S., M. Yoon, and S.G.J. Mochrie. "Faceting, Tricriticality, and Attractive Interactions Between Steps in the Orientational Phase Diagram of Silicon Surfaces Between [113] and [5 5 12]." *Surf. Sci.* 334: 153 (1995).
- Song, S., S.G.J. Mochrie, and G.B. Stephenson. "Faceting Kinetics of Stepped Si(113) Surfaces: A Time-Resolved X-ray Scattering Study." *Phys. Rev. Lett.* 74(26): 5240-5243 (1995).
- Srinivasan, M.A., and R.H. LaMotte. "Tactual Discrimination of Softness." *J. Neurophys.* 73(1): 88-101 (1995).
- Stoner, R., and G. Bekefi. "A 70-Period High-Precision Microwiggler for Free Electron Lasers." *IEEE J. Quantum Electron.* 31(6): 1158-1165 (1995).
- Sun, C.-K., B. Golubovic, H.-K. Choi, C.A. Wang, and J.G. Fujimoto. "Femtosecond Investigations of Spectral Hole Burning in Semiconductor Lasers." *Appl. Phys. Lett.* 66(13): 1650-1652 (1995).
- Sun, C.-K., B. Golubovic, J.G. Fujimoto, H.K. Choi, and C.A. Wang. "Heterodyne Nondegenerate Pump-Probe Measurement Technique for Guided Wave Devices." *Opt. Lett.* 20: 210-212 (1995).
- Takeuchi, A.H., and L.D. Braida. "Effect of Frequency Transposition on the Discrimination of Amplitude Envelope Patterns." *J. Acoust. Soc. Am.* 97(1): 453-460 (1995).
- Tamura, K., E.P. Ippen, and H.A. Haus. "Pulse Dynamics in Stretched-pulse Fiber Lasers." *Appl. Phys. Lett.* 67(2): 158-160 (1995).
- Tan, H.Z., N.I. Durlach, G.L. Beauregard, and M.A. Srinivasan. "Manual Discrimination of Compliance Using Active Pinch Grasp: The Roles of Force and Work Cues." *Percep. Psychophys.* 57(4): 495-510 (1995).
- Taniguchi, N., A.V. Andreev, and B.L. Altshuler. "Statistics of Oscillator Strength in Chaotic Systems." *Europhys. Lett.* 29: 515 (1995).
- Taniguchi, N., B.S. Shastry, and B.L. Altshuler. "Random Matrix Model and Calogero-Sutherland Model: A Novel Current-Density Mapping." *Phys. Rev. Lett.* 75: 37 (1995).
- Tearney, G.J., M.E. Brezinski, B. Bouma, M.R. Hee, E.A. Swanson, J.F. Southern, and J.G. Fujimoto. "Determination of the Refractive Index of Highly Scattering Human Tissue Using Optical Coherence Tomography." *Opt. Lett.* 20(21): 2258-2260 (1995).
- Tearney, G.J., M.E. Brezinski, M.R. Hee, B. Bouma, J.A. Izatt, E.A. Swanson, J.F. Southern, R.R. Anderson, and J.G. Fujimoto. "Optical Coherence Tomography in Multiply Scattering Tissue." *SPIE Proc.* 2389: 29-34 (1995).
- Trias, E., J.R. Phillips, H.S.J. van der Zant, and T.P. Orlando. "Self-field Effects in Two Dimensional Nb Josephson-junction Arrays." *IEEE Trans. Appl. Superconduct.* 5: 2707 (1995).
- Tsang, L., K.H. Ding, G. Zhang, C. Hsu, and J.A. Kong. "Backscattering Enhancement and Clustering Effects of Randomly Distributed Dielectric Cylinders Overlying a Dielectric Half Space Based on Monte Carlo Simulation." *IEEE Trans. Antennas Propag.* 43(5): 488-499 (1995).
- Tsui, C.-Y., J. Monteiro, M. Pedram, S. Devadas, A.M. Despain, and B. Lin. "Power Estimation Methods for Sequential Logic Circuits." *IEEE Trans. VLSI Syst.* 3(3): 404-416 (1995).
- Turnbull, D.H. "Ultrasound Backscatter Microscope Analysis of Early Mouse Embryonic Brain Development." *Proc. Nat. Acad. Sci.* 92: 2239-2243 (1995).
- Vacca, L., A. Bers, and A.K. Ram. "RF-Induced Transport of Resonant Minority Species in ICRF-Heated Tokamaks." *Bull. Am. Phys. Soc.* 40: 1706 (1995).
- van der Zant, H.S.J., T.P. Orlando, and A.W. Kleinsasser. "One-dimensional Parallel Josephson-junction Arrays as a Tool for Circuit Diagnostics." *IEEE Trans. Appl. Superconduct.* 5: 3333-3336 (1995).

- van der Zant, H.S.J., T.P. Orlando, S. Watanabe, and S.H. Strogatz. "Kink Propagation in a Highly Discrete System: Observation of Phase Locking to Linear Waves." *Phys. Rev. Lett.* 74: 174-177 (1995).
- Vergheze, S., R.A. Wyss, T. Schapers, Q. Hu, A. Forster, M.J. Rooks. "Photon-assisted Transport Through Quantized Energy States in a Lateral Dual-gate Device." *Phys. Rev. B* 52(20): 14834-14838 (1995).
- Villeneuve, P.R., and J.D. Joannopoulos. "Tricks of the Light." *New Sci.* 26 (1995).
- Villeneuve, P.R., S. Fan, I. Kurland, J.C. Chen, and J.D. Joannopoulos. "Photonic Bandgap Structures and Devices." *QELS Tech. Digest Series* 15 (1995).
- Villeneuve, P.R., S. Fan, J.D. Joannopoulos, K.Y. Lim, G.S. Petrich, L.A. Kolodziejski, and R. Reif. "Air-Bridge Microcavities." *Appl. Phys. Lett.* 67(2): 167-169 (1995).
- Watanabe, S., S.H. Strogatz, H.S.J. van der Zant, and T.P. Orlando. "Resonant Steps in Parallel Josephson-junction Arrays: Parametric Instabilities of Whirling Modes." *IEEE Trans. Appl. Superconduct.* 5: 2698-2701 (1995).
- Watanabe, S., S.H. Strogatz, H.S.J. van der Zant, and T.P. Orlando. "Whirling Modes and Parametric Instabilities in the Discrete Sine-Gordon Equation: Experimental Tests in Josephson Rings." *Phys. Rev. Lett.* 74: 379-382 (1995).
- Wilhelms-Tricarico, R. "Physiological Modeling of Speech Production: Methods for Modeling Soft-tissue Articulators." *J. Acoust. Soc. Am.* 97(5): 3085-3098 (1995).
- Winograd, J.M., and S.H. Nawab. "Incremental Refinement of DFT and STFT Approximations." *Signal Process. Lett.* 2(2): 25-27 (1995).
- Wong, N.C. "Optical-to-microwave Frequency Chain Utilizing a Two-laser-based Optical Parametric Oscillator Network." *Appl. Phys. B* 61: 143-149 (1995).
- Wong, V.V., A. Yasaka, and H.I. Smith. "Resist Planarization Over Topography Using Ion Implantation." *J. Vac. Sci. Technol. B* 13(6): 2797-2800 (1995).
- Wong, V.V., J. Ferrera, J.N. Damask, T.E. Murphy, H.I. Smith, and H.A. Haus. "Distributed Bragg Grating Integrated-Optical Filters: Synthesis and Fabrication." *J. Vac. Sci. Technol. B* 13(6): 2859-2864 (1995).
- Wornell, G.W. "Spread-Signature CDMA: Efficient Multiuser Communication in the Presence of Fading." *IEEE Trans. Info. Theory* 41(5): 1418-1438 (1995).
- Wyss, R.A., C.C. Eugster, J.A. del Alamo, M.J. Rooks, M.R. Melloch, and Q. Hu. "Far-infrared Radiation-induced Thermopower in a Quantum Point Contact." *Appl. Phys. Lett.* 66(9): 1144-1146 (1995).
- Yang, I.Y., S. Silverman, J. Ferrera, K. Jackson, J.M. Carter, D.A. Antoniadis, and H.I. Smith. "Combining and Matching Optical, E-Beam and X-ray Lithographies in the Fabrication of Si CMOS Circuits with 0.1 and Sub-0.1 μm Features." *J. Vac. Sci. Technol. B* 13(6): 2741-2744 (1995).
- Zhao, Y., D.C. Tsui, M.B. Santos, and M. Shayegan. "Grating-Induced Cyclotron-Resonance Anomaly in GaAs/Al_{1-x}Ga_xAs Heterostructures." *Phys. Rev. B* 51: 174 (1995).

A.3 Books/Chapters in Books

- Boivin, L., C.R. Doerr, K. Bergman, and H.A. Haus. "Quantum Noise Reduction Using a Sagnac Loop with Positive Dispersion." In *Quantum Communications and Measurements*, pp. 489-496. Eds. V.P. Belavkin, O. Hirota, and R.L. Hudson. New York: Plenum Press, 1995.
- Chen, J.C., H.A. Haus, J.N. Winn, S. Fan, and J.D. Joannopoulos. "Wide Stop Band Optical Filters from Photonic Band Gap Air Bridges." In *Guided-Wave Optoelectronics: Device Characterization, Analysis, and Design*, pp. 477-483. New York: Plenum Press, 1995.
- Cho, K., and J.D. Joannopoulos. "The Devilish World of Surfaces." In *Toward Teraflop Computing and New Grand Challenge Applications.*, Eds. R.K. Kailia and P. Vashishta. Commack, New York: Nova Science Publishers, 1995.
- DiFilippo, F., V. Natarajan, M. Bradley, F. Palmer, and D.E. Pritchard. "Accurate Atomic Mass Measurements from Penning Trap Mass Comparisons of Individual Ions." In *Atomic Physics 14*. New York: American Institute of Physics, 1995.
- Haus, H.A., J.N. Damask, and M.J. Khan. "Distributed Feedback Channel Dropping Filters." In

- Guided-Wave Optoelectronics*, pp. 299-311. Eds. T. Tamir et al. New York: Plenum Press, 1995.
- LaMotte, R.H., C. Lu, and M.A. Srinivasan. "Tactile Neural Codes for Shapes and Orientations of Objects." In *Information Processing in the Somatosensory System*. Eds. O. Franzen, R. Johansson, and L. Terenius. Basel, Switzerland: Birkhauser Verlag AB, 1995.
- Orlando, T.P., H.S.J. van der Zant, J. White, E. Trias, and A.E. Duwel. "Measurements of Self-Field Effects in Arrays of Josephson Junctions." In *Macroscopic Quantum Phenomena and Coherence in Superconducting Arrays*. Eds. C. Giovannella and M. Tinkham. World Scientific, 1995.
- Reed, C.M. "Tadoma: An Overview of Research." In *Profound Deafness and Speech Communication*, pp. 40-55. Eds. G. Plant and K.-E. Spens. London: Whurr Publishers, 1995.
- Schmiedmayer, J., et al. "Atom and Molecule Interferometry with Separated Beams." In *Atom Interferometry*. Ed. P.R. Berman. New York: Academic Press, 1995.
- Shattuck-Hufnagel, S. "The Importance of Phonological Transcription in Empirical Approaches to Stress Shift vs. Early Accent." In *Papers in Laboratory Phonology IV: Phonology and Phonetic Evidence*, pp. 128-140. Eds. B. Connell and A. Arvaniti. Cambridge: Cambridge University Press, 1995.
- Shinn-Cunningham, B.G., and A. Kulkarni. "Applications of Virtual Auditory Space." In *Virtual Auditory Space*. Ed. S. Carlile. New York: Landes Publishing Company. Forthcoming.
- Shinn-Cunningham, B.G., H. Lehnert, G. Kramer, E.M. Wenzel, and N.I. Durlach. "Auditory Displays." In *Spatial and Binaural Hearing*. Eds. R. Gilkey and T. Anderson. New York: Erlbaum. Forthcoming.
- Srinivasan, M.A. "Haptic Interfaces." In *Virtual Reality Scientific and Technical Challenges*. Eds. N.I. Durlach and A.S. Mavor. Washington, DC: National Academy Press, 1995.
- Srinivasan, M.A., and R.H. LaMotte. "Tactual Discrimination of Softness: Abilities and Mechanisms." In *Information Processing in the Somatosensory System*. Eds. O. Franzen, R. Johansson, and L. Terenius. Basel, Switzerland: Birkhauser Verlag AB, 1995.
- Stevens, K.N. "Models of Speech Production and Perception." In *European Studies in Phonetics and Speech Communication*, pp. 52-57. Eds. G. Bloothoof, V. Hazan, D. Huber, and J. Llisterra. The Hague, The Netherlands: CIP-Gegeens Koninklijke Bibliotheek, 1995.
- van der Zant, H.S.J., T.P. Orlando, S. Watanabe, and S.H. Strogatz. "Nonlinear Dynamics of Discrete Josephson Rings." In *Macroscopic Quantum Phenomena and Coherence in Superconducting Arrays*. Eds. C. Giovannella and M. Tinkham. World Scientific, 1995.

A.4 RLE Publications

- RLE 45th Anniversary Brochure*. MIT, 1991. 72 pp. No charge.
- RLE currents* 8(1): (1996). "On the Road to Success with RLE Alumni Company Founders." 32 pp. No charge.
- RLE Progress Report 138*: January-December 1995. MIT, 1996. 500 pp. No charge.
- Bonvik, A.M. *A Distributed Discrete Event Simulation, or How to Steal More CPU Cycles Than You Could Ever Imagine*. CIDM Memo 95-6. MIT, 1995.
- Bonvik, A.M., S.B. Gershwin, and D.E. Troxel. *Operating High Variability Manufacturing Systems*. CIDM Memo 95-4. MIT, 1995.
- Carney, J.C. *Message Passing Tools for Software Integration*. CIDM Memo 95-7. MIT, 1995.
- Coppi, A.C., and B. Coppi. *Singular Non-linear Equations and Explosive Recurrent Events*. RLE PTP Report 95/04. MIT, 1995.
- Coppi, B. *Presentation to the PCAST Fusion Panel*. RLE PTP Report 95/02. MIT, 1995.
- Fischer, G., and T. Lohman. *Error Handling Within CAFE*. CIDM Memo 95-1. MIT, 1995.
- Hadjicostis, C.N. *Fault-Tolerant Computation in Semigroups and Semirings*. RLE TR-594. MIT, 1995.
- Isabelle, S.H. *A Signal Processing Framework for the Analysis and Application of Chaotic Systems*. RLE TR-593. MIT, 1995.

- Kao, J. *MIT Remote Microscope*. CAPAM Memo 95-1. MIT, 1995.
- Kao, J. *Remote Microscope for Inspection of Integrated Circuits*. CIDM Memo 95-5. MIT, 1995.
- Kwon, J.Y. *Remote Fabrication of Integrated Circuits*. CIDM Memo 95-3. MIT, 1995.
- Kwon, J.Y. *CAFE Remote Fabrication System—A Quick Step Guide to Remote Processing*. CIDM Memo 95-8. MIT, 1995.
- Kwon, J.Y. *Remote Fabrication of Integrated Circuits—Software Support for the MIT Computer Aided Fabrication Environment*. CIDM Memo 95-9. MIT, 1995.
- Moyne, W.P. *Run-by-Run Control: Interfaces, Implementation, and Integration*. CIDM Memo 95-2. MIT, 1995.
- Pioch, N.J. *Officer of the Deck: Validation and Verification of a Virtual Environment for Training*. RLE TR-596. MIT, 1995.
- Rahman, N. *A Survey of Existing Literature on Reverse Modeling of Field Effect Transistors*. CAPAM Memo 95-3. MIT, 1995.
- Ram, A.K. *Heating and Current Drive by Mode-Converted Ion-Bernstein Waves*. Plasma Fusion Center Report PFC/JA-95-18. MIT, 1995.
- Ram, A.K., A. Bers, S.D. Schultz, V. Fuchs, A. Becoulet, and B. Saoutic. *Mode-Converted Ion-Bernstein Waves in Tokamaks*. Plasma Fusion Center Report PFC/JA-95-20. MIT, 1995.
- Schultz, S.D., A. K. Ram, and A. Bers. *RF Wave Effects on the Neoclassical Electron Distribution Function in Tokamaks*. Plasma Fusion Center Report PFC/JA-95-19. MIT, 1995.
- Sugiyama, L.E. *Reversed Shear Ignition in a High Field Toroidal Experiment*. RLE PTP Report 95/03. MIT, 1995.
- S.M. thesis, Dept. of Electr. Eng. and Comput. Sci., MIT, 1995.
- Braun, E. *Elevated Temperature Stability of Gallium Arsenide Integrated Circuits*. S.M. thesis, Dept. of Electr. Eng. and Comput. Sci., MIT, 1995.
- Burkhardt, M. *Fabrication Technology and Measurements of Coupled Quantum Dot Devices*. Ph.D. diss., Dept. of Electr. Eng. and Comput. Sci., MIT, 1995.
- Carney, J.C. *Message Passing Tools for Software Integration*. S.M. thesis, Dept. of Electr. Eng. and Comput. Sci., MIT, 1995.
- Chang, H.-P. *Speech Input for Dysarthric Computer Users*. Ph.D. diss., Dept. of Mech. Eng., MIT, 1995.
- Chapman, M.S. *Photon Induced Coherence Loss in Atom Interferometry*. Ph.D. diss., Dept. of Physics, MIT, 1995.
- Chen, M.Y. *Acoustic Correlates of Nasality in Speech*. Ph.D. diss., Harvard-MIT Div. of Health Sci. and Technol., MIT, 1995.
- Cooray, A.R. *Optical Identification of Close Doubles and Gravitational Lenses from the MIT-Green Bank-VLA and the Parkes-MIT-NRAO-VLA 8.43*. S.B. thesis, Dept. of Physics, MIT, 1995.
- Courtney, M. *Rydberg Atoms in Strong Fields: A Testing Ground for Quantum Chaos*. Ph.D. diss., Dept. of Physics, MIT, 1995.
- Davis, K.B. *Evaporative Cooling of Sodium Atoms*. Ph.D. diss., Dept. of Physics, MIT, 1995.
- Denesvich, G. *Identification of Frequency and Amplitude Through Cutaneous Stimulation*. S.B. thesis, Dept. of Electr. Eng. and Comput. Sci., MIT, 1995.
- Duwel, A.E. *Underdamped Vortex Flow Devices*. S.M. thesis, Dept. of Electr. Eng. and Comput. Sci., MIT, 1995.
- Entin, I.A. *Magnetic Trapping of Neutral Sodium Atoms*. S.B. thesis, Dept. of Physics, MIT, 1995.
- Gulati, R.J. *Determination of Mechanical Properties of the Human Fingerpad, in vivo, Using a Tactile Stimulator*. S.M. thesis, Dept. of Mech. Eng., MIT, 1995.

A.5 Theses

- Aggarwal, R.J. *Design of Resonant-Tunneling Diodes for a GaAs Integrated SRAM*. Ph.D. diss., Dept. of Electr. Eng. and Comput. Sci., MIT, 1995.
- Ahadian, J.F. *Phosphide-based Optical Emitters for Monolithic Integration with GaAs MESFETs*.

- Hadjiyiannis, G.I. *A Low Power, Low Bandwidth Protocol for Remote Wireless Terminals*. S.M. thesis, Dept. of Electr. Eng. and Comput. Sci., MIT, 1995.
- Jacobs, J. *Modeling of Electron Transport in Sub-100 nm Channel Length Silicon MOSFETS*. Ph.D. diss., Dept. of Electr. Eng. and Comput. Sci., MIT, 1995.
- Kao, J.T. *Remote Microscope for Inspection of Integrated Circuits*. S.M. thesis, Dept. of Electr. Eng. and Comput. Sci., MIT, 1995.
- Kwon, J.Y. *Remote Fabrication of Integrated Circuits*. S.M. thesis, Dept. of Electr. Eng. and Comput. Sci., MIT, 1995.
- Lai, B.Y.F. *A Tunable Light Source at 1.6 μm by Difference-Frequency Mixing in Cesium Titanyl Arsenate*. S.M. thesis, Dept. of Electr. Eng. and Comput. Sci., MIT, 1995.
- Lee, D. *Optical Parametric Oscillators and Precision Optical Frequency Measurements*. Ph.D. diss., Dept. of Physics, MIT, 1995.
- Lenz, G. *Femtosecond Sources at 1.5 microns and Their Application for Time-Resolved Spectroscopic Studies of Semiconductor Devices*. Ph.D. diss., Dept. of Electr. Eng. and Comput. Sci., MIT, 1995.
- Li, K. *Finite Difference-Time Domain Analysis of Electromagnetic Interference and Radiation Problems*. Ph.D. diss., Dept. of Electr. Eng. and Comput. Sci., MIT, 1995.
- Liu, S.A. *Landmark Detection for Distinctive Feature-Based Speech Recognition*. Ph.D. diss., Dept. of Electr. Eng. and Comput. Sci., MIT, 1995.
- Morgenbesser, H.B. *Force Shading for Shape Perception in Haptic Virtual Environments*. M.Eng. thesis, Dept. of Electr. Eng. and Comput. Sci., MIT, 1995.
- Moyne, W.P. *Run by Run Control: Interfaces, Implementation, and Integration*. S.M. thesis, Dept. of Electr. Eng. and Comput. Sci., MIT, 1995.
- Patterson, S.G. *Quantum Intensity Noise Correlation in a Type-II Phase Matched Optical Parametric Oscillator*. S.M. thesis, Dept. of Electr. Eng. and Comput. Sci., MIT, 1995.
- Poort, K.L. *Stop Consonant Production: An Articulation and Acoustic Study*. S.M. thesis, Dept. of Electr. Eng. and Comput. Sci., MIT, 1995.
- Shah, S.N. *Free-Standing 100 nm Period Gratings Produced by Achromatic Holographic Lithography*. S.M. thesis, Dept. of Electr. Eng. and Comput. Sci., MIT, 1995.
- Shakeel, A. *Enhanced Squeezing in Homodyne Detection via Local-Oscillator Optimization*. S.M. thesis, Dept. of Electr. Eng. and Comput. Sci., MIT, 1995.
- Shenoy, K.V. *Monolithic Optoelectronic VLSI Circuit Design and Fabrication for Optical Interconnects*. Ph.D. diss., Dept. of Electr. Eng. and Comput. Sci., MIT, 1995.
- Slone, A.J. *Improved Remote Sensing Data Analysis Using Neural Networks*. S.B. thesis, Dept. of Electr. Eng. and Comput. Sci., MIT, 1995.
- Thompson, S.H., Jr. *Radio Frequency Induced Evaporative Cooling of Magnetically Trapped Neutral Sodium Atoms*. S.B. thesis, Dept. of Physics, MIT, 1995.
- Trias, E. *Inductance Effects in Two-Dimensional Arrays of Josephson Junctions*. S.M. thesis, Dept. of Electr. Eng. and Comput. Sci., MIT, 1995.
- Umminger, C.B. *Integrated Analog Focal Plane Processing for Automatic Alignment*. S.M. thesis, Dept. of Electr. Eng. and Comput. Sci., MIT, 1995.
- Voss, S.E. *Is the Pressure Difference Between the Oval and Round Window the Effective Acoustic Stimulus to the Inner Ear?* S.M. thesis, Dept. of Electr. Eng. and Comput. Sci., MIT, 1995.
- Wessling, O.P. *RTFM: A Digital Design Lab Expert*. M.Eng. thesis, Dept. of Electr. Eng. and Comput. Sci., MIT, 1995.
- Wilde, L.F. *Analysis and Synthesis of Fricative Consonants*. Ph.D. diss., Dept. of Electr. Eng. and Comput. Sci., MIT, 1995.
- Wong, V.V. *Fabrication of Distributed Feedback Devices Using X-ray Lithography*. Ph.D. diss., Dept. of Electr. Eng. and Comput. Sci., MIT, 1995.
- Wyss, R.A. *Far-infrared Radiation Response of Antenna-coupled Quantum-effect Devices*.

Appendix A. RLE Publications

Ph.D. diss., Dept. of Electr. Eng. and Comput. Sci., MIT, 1995.

Yasaka, A. *Feasibility Study of Spatial-Phase-Locked Focused-Ion-Beam Lithography*. S.M. thesis, Dept. of Mat. Sci. and Eng., MIT, 1995.

Yesley, P.S. *The Design and Testing of Novel, Spin-Flip, Zeeman Slowing Technique*. S.B. thesis, Dept. of Physics, MIT, 1995.

Appendix B. Current RLE Personnel

Director: Jonathan Allen

Associate Director: Daniel Kleppner

Professors

Jonathan Allen
Boris Altshuler
Dimitri A. Antoniadis
Arthur B. Baggeroer
Abraham Bers
Robert J. Birgeneau
Amar G. Bose
Louis D. Braid
Bernard F. Burke
Bruno Coppi
Srinivas Devadas
Shaoul Ezekiel
Clifton G. Fonstad, Jr.
Lawrence S. Frishkopf
James G. Fujimoto
Hermann A. Haus

Albert Hill¹
Erich P. Ippen
John D. Joannopoulos
Marc A. Kastner
Nelson Y.-S. Kiang
John G. King
Daniel Kleppner
Leslie A. Kolodziejski
Jin A. Kong
Patrick A. Lee
Jerome Y. Lettvin¹
Jae S. Lim
Alan V. Oppenheim
Terry P. Orlando
William T. Peake

Miklos Porkolab
David E. Pritchard
William F. Schreiber¹
Campbell L. Searle¹
Stephen D. Senturia
Jeffrey H. Shapiro
William M. Siebert¹
Henry I. Smith
Charles G. Sodini
David H. Staelin
Kenneth N. Stevens
Donald E. Troxel
Thomas F. Weiss
John L. Wyatt, Jr.
Henry J. Zimmermann¹

Associate Professors

Jesús A. del Alamo
Peter L. Hagelstein

Jacqueline N. Hewitt
Qing Hu

Simon G.J. Mochrie
Jacob K. White

Assistant Professors

Raymond C. Ashoori
Anantha P. Chandrakasan

Dennis M. Freeman

Wolfgang Ketterle
Gregory W. Wornell

Senior Research Scientists

Nathaniel I. Durlach

Joseph S. Perkell

Principal Research Scientists

Donald K. Eddington
John J. Guinan, Jr.
William M. Rabinowitz

Charlotte M. Reed
Philip W. Rosenkranz
J. Kenneth Salisbury

Mandayam A. Srinivasan
David Zeltzer
Patrick M. Zurek

¹ Professor Emeritus.

Research Scientists and Research Specialists

Giovanni Aliberti
John W. Barrett
Merry A. Brantley
Andrew R. Brughera
James M. Carter
Kyeongjae Cho
Jay H. Damask
Bertrand Delgutte
Lorraine A. Delhorne
Paul Duchnowski
David W. Foss
Julie E. Greenberg

Seth M. Hall
Thomas J. Lohman
David S. Lum
Ivan Mastovsky
Michael B. McIlrath
Stefano Migliuolo
Mark K. Mondol
Euclid E. Moon
Gale S. Petrich
Abhay K. Ram
Dennis D. Rathman

Robert H. Rediker
John J. Rosowski
Selim M. Shahriar
Stefanie Shattuck-Hufnagel
Linda E. Sugiyama
Francis G. Taylor
Pierre R. Villeneuve
Reiner Wilhelms-Tricarico
Ngai Chuen Wong
Y. Eric Yang
Majid Zandipour

Administrative Staff

Joseph F. Connolly
Virginia R. Lauricella
Barbara J. Passero

Gerrard F. Power
William H. Smith

Vicky-Lynn Taylor
Mary E. Young

Support and Technical Staff

Mary C. Aldridge
Janice L. Balzer
Felicia G. Brady
Margaret S. Beucler
Susan E. Chafe
Anne E. Conklin
John F. Cook
Carol A. Costa
Thomas L. DeFilippo
Ann K. Dix

Francis M. Doughty
Margaret A. Flaherty
Dorothy A. Fleischer
Donna L. Gale
Mary S. Greene
Peter C. Guidod
Maureen C. Howard
Cynthia Y. Kopf
Kit-Wah F. Lai
Cindy LeBlanc

Eleanora M. Luongo
Deborah S. Manning
Edward R. Murphy
Denise M. Rossetti
Maxine P. Samuels
Laura M. von Bosau
Arlene E. Wint
Janice M. Zaganjori
Mary J. Ziegler

Postdoctoral Fellows and Associates

Narayana R. Aluru
Gerald L. Beauregard
Brett E. Bouma
Gerhard De Lange
Kung-Hau Ding
Scott B. Dynes
James G. Goodberlet
Krishna K. Govindarajan
Timothy T. Grove

Byoung S. Ham
Helen M. Hanson
Steven H. Isabelle
Hong Jiao
Jeng-Feng Lee
Peter M. Osterberg
Fred L. Palmer
Anne Pepin
Matthew H. Power

Kourosh Saberi
Wendelin L. Sachtler
Barbara Shinn-Cunningham
Stephen P. Smith
Venkatapuram S. Sudarshanam
Hong Z. Tan
Johannes Tausch
Thomas E. Wiegand

Research Assistants

Charles C. Abnet
David M. Abusch-Magder
Joseph F. Ahadian
Anton Andreev
Michael R. Andrews

John G. Apostolopoulos
Mark A. Armstrong
Chalee Asavathiratham
Walter A. Aviles
Ian M. Avruch

David M. Baylon
Soosan Beheshti
Igor P. Bilinsky
William J. Blackwell
Roxann R. Blanchard

Luc Boivin
 Jeffrey K. Bounds
 Michael P. Bradley
 Louis R. Brothers
 Carlos R. Cabrera
 Rodrigo B. Capaz
 David J. Carter
 Palmyra E. Catravas
 Jyh-Shing Chen
 Brian Chen
 Yonald Chery
 Shiufun Cheung
 Cheewee Chew
 Jeffrey T. Chiou
 Jeung-Yoon Choi
 Patrick Chou
 Mike T. Chou
 Fronefield Crawford
 Ali Darwish
 Charles Q. Davis
 Suvranu De
 Timothy Denison
 Timothy J. Derksen
 Joseph G. Desloge
 Joel C. DeVries
 David J. Dougherty
 Erik K. Duerr
 Dallin S. Durfee
 Michael S. Ehrlich
 Alexander N. Ernst
 Farzan Fallah
 Shanhui Fan
 Maya S. Farhoud
 Juan Ferrera
 Siegfried B. Fleischer
 Andre B. Fletcher
 Eric M. Foxlin
 Andrea E. Franke
 Joseph A. Frisbie
 Alan I. Gale
 Boris Golubovic
 David Gosalvez
 Donald R. Greer
 Andrew E. Grumet
 Nitin Gupta
 Christoforos N. Hadjicostis
 George I. Hadjiyiannis
 Troy D. Hammond
 Silvina Z. Hanono
 Michael R. Hee
 Lori K. Herold
 Raynard O. Hinds

Chih-Hao Ho
 Easen Ho
 Jeffrey R. Holley
 David M. Horowitz
 Alexandra I. Hou
 Jody House
 Chih-Chien Hsu
 Gregory T. Huang
 Xiaohu Jiang
 Joel T. Johnson
 Mark A. Johnson
 David J. Jones
 Alkan Kabakcioglu
 Mattan Kamon
 James Kao
 Steingrimur Karason
 Zoher Z. Karu
 Charles A. Katz
 Sumanth Kaushik
 Mohammad J. Khan
 Farzana I. Khatri
 Glenn Koh
 Jean C. Krause
 Hong-Kwang J. Kuo
 Dan M. Kurn
 Warren M. Lam
 Craig Latimer
 Michael A. Leabman
 Junehee Lee
 Gilbert Leung
 Jung-Chi Liao
 Michael H. Lim
 Kuo-Yi Lim
 Jeffrey T. Ludwig
 Robert I. Lutwak
 Ilya Lyubomirsky
 Christina Manolatu
 Elisabeth A. Marley
 Paul S. Martin
 Elliott J. Mason
 Yehia M. Massoud
 Mitchell W. Meinhold
 Marc O. Mewes
 Jeremy M. Milikow
 Jose C. Monteiro
 Christopher B. Moore
 Nicole Y. Morgan
 William P. Moyne
 Thomas E. Murphy
 Philip M. Nadeau
 Ognen J. Nastov
 Phillip T. Nee

Lynn E. Nelson
 Joseph E. Nemec
 Michael P. O'Connell
 Haralabos C. Papadopoulos
 Ickjin Park
 Steven G. Patterson
 Gregory E. Penn
 Christopher N. Peters
 Jonathan D. Pfautz
 Arifur Rahman
 Nadir Rahman
 Balasundara I. Raju
 Monte J. Ramstad
 Farhan Rana
 Mark A. Rawizza
 Daniel J. Ripin
 Rosanne Rouf
 Richard A. Rubenstein
 Timothy A. Savas
 David W. Schloerb
 Michael J. Schwartz
 Matthew J. Secor
 Alan Seefeldt
 Matthew G. Sexton
 Lisa Shatz
 Shih-en Shih
 Andrew C. Singer
 Seungheon Song
 Neal W. Spellmeyer
 Lon E. Sunshine
 Xiaofeng Tang
 Guillermo J. Tearney
 Joseph Teja
 Erik R. Thoen
 Nayon Tomsio
 Catherine S. Trotter-Wilson
 Constantine Tziligakis
 Kimberly J. Voss
 Kathleen E. Wage
 Li-Fang Wang
 Emily L. Warlick
 William S. Wong
 Julie L. Wonus
 Bin Xu
 Chen-Pang Yeang
 Elron A. Yellin
 Chang D. Yoo
 John W. Yoon
 Charles X. Yu
 Noah D. Zamdmmer
 Yan Zhang

Teaching Assistants

John R. Buck
 Geoffrey J. Coram

Deborah B. Haarsma
 Caterina Riconda

Jennifer L. Stinn
 Susie J. Wee

Graduate Students

Laura E. Adams
 Jerome J. Akerson
 Alexander Aranyosi
 Richard J. Barron
 Stephen A. Boppart
 Douglas S. Brungart
 Erica N. Carmel
 Karen Chenausky
 Harold A. Cheyne
 William S. Daughton
 Steven J. Decker
 Lloyd D'Souza
 Tryn H. Eggen
 Eric J. Gaidos
 Felcissimo W. Galicia
 Matthew E. Grein
 Michael P. Harms
 Erik B. Iverson
 Steven G. Johnson
 Laura K. Johnson

Thomas C. Killian
 Somsak Kittipiyakul
 Chwen-yuen Ku
 Nicholas Laneman
 Daniel D. Lee
 Li Lee
 Gregory G. Lin
 Angel R. Martinez
 Ignacio S. McQuirk
 Ann W. Morgenthaler
 James M. Ooi
 John J. Park
 Anthony D. Patire
 Joel R. Phillips
 Constantinos Pitris
 Adam D. Polcyn
 Kelly L. Poort
 Eric C. Reed
 Diane E. Ronan
 Emmanuel Rousseau

Yakov Royter
 Jason M. Sachs
 Jay Sarkar
 Steven D. Schultz
 Hugh E. Secker-Walker
 Janet L. Slifka
 Mark H. Somerville
 Jason Sroka
 Konstantina Stankovic
 Susan Sujono
 Walter Sun
 Luigi Vacca
 Shawn M. Verbout
 Mark M. Visosky
 Che-Wei A. Wang
 Chen-Hsiang Yeang
 Mirang Yoon
 Michael J. Young
 Lee Zamir

Undergraduate Students

Marlon D. Abayan
 David E. Bakhsh
 Matthew D. Barnhart
 Christopher D. Bentzel
 Ronald Cao
 Max Chen
 Eugene F. Chow
 Erika Chuang
 Richard H. Conway
 David E. DiFranco
 Laura C. Dilley
 Joseph A. DiRusso
 Philip M. Hinz
 Darren S. Hsiung
 Everest W. Huang
 Raymond W. Hwang
 Julie Y. Ji
 Yan Jiao

Allen N. Jordan
 Genevieve K. Lada
 Daniele S. Lantagne
 Carol Y. Lee
 Arash Lighvani
 Samuel R. Madden
 David H. Manowitz
 Kinuko Masaki
 Mark A. Meier
 Adelaida D. Moranesu
 Zoe G. Park
 Jeffrey T. Pearlman
 Sara A. Perry
 Bahman Rabii
 Sudeep Rangaswamy
 Christopher R. Richardson
 Shira E. Rosenberg

Pietro Russo
 Jonathan R. Santos
 Michelle M. Scheer
 Edward D. Semper
 Yun-Ying Shi
 Nathan R. Shnidman
 Sarah M. Shore
 Adrienne H. Slaughter
 Snow C. Sudduth
 Shahram A. Tadayyon
 Matthew A. Tom
 Christiana Toutet
 Lukasz A. Weber
 Evan F. Wies
 Irene M. Wilson
 Chiann J. Yeh
 Adelaide Zhang

Visiting Scientists

Corine A. Bickley
 John R. Brandenberger
 Fabio Del Frate
 Daniel Ehrlich
 Daniel W. Engels
 Kalman I. Glantz
 William L. Hodge
 Mikhail S. Ioffe
 Minoru Ishikawa
 Arthur K. Jordan
 Jack Kotik

Ruth Y. Litovsky
 Brent E. Little
 Stefano Longhi
 Masayuki Matsumoto
 Shu Namiki
 Hamid Nawab
 Suzanne Neil
 Kevin O'Neill
 Karen L. Payton
 Pascal H. Perrier
 Geoffrey L. Plant

Yingyong Qi
 Marco Riccitelli
 Stanley J. Rosenthal
 Hannes J. Schmiedmayer
 Jean-Claude Souyris
 Gunter Steinmeyer
 Richard E. Stoner
 Ligu Sun
 George M. Svolos
 Motohiko Tanaka

Joachim S. Theilhaber
Christopher G. Townsend

Research Affiliates

John S. Barlow
Vladimir Barsukov
Giuseppe Bertin
Suzanne Boyce
Mark E. Brezinski
Frank S. Cardarelli
Shourov K. Chatterji
Steven Colburn
Theodore W. Ducas
Ibrahim M. Elfadel
Carol Y. Espy-Wilson
Patrick N. Everett
Paul D. Fiore
Ignacio Garcia-Otero
Gad Geiger
David J. Getty
Bernard Gold
Susan L. Goldman
Kenneth W. Grant
Thomas J. Green
Robert D. Hall
Katherine L. Hall
Philip R. Hemmer
Robert E. Hillman

Patrick E. Hoffman
Mark A. Hollis
Eva B. Holmberg
Caroline B. Huang
Robert J. Hull
Joseph A. Jarrell
Carlos Kennedy
John D. Kierstead
Harlan Lane
William H. Levison
John I. Makhoul
Sharon Y. Manuel
Melanie L. Matthies
Sumiko Miller
Martin Muendel
Victor A. Noel
Aniruddh D. Patel
Leonard L. Picard
James C. Preisig
Mara G. Prentiss
Christine M. Rankovic
Michael E. Ravicz
Stephen A. Raymond

Joseph F. Rizzo
John J. Rosowski
Christopher A. Shera
Robert T. Shin
Richard J. Solomon
Frank J. Stefanov-Wagner
David A. Steffens
Annie H. Takeuchi
Yvette J. Tenney
Joseph Tierney
Vivian E. Titus
Mark A. Tramo
Michael J. Tsuk
Alice E. Turk
Simon Verghese
Kenneth P. Wacks
Ehud Weinstein
Johannes W. Weis
Lorin F. Wilde
David R. Williams
Jane W. Wozniak
Jiqing Xia
Marc Zissman

Appendix C. Milestones

C.1 New Faculty and Staff

Merry A. Brantley was appointed as a research specialist in RLE's Sensory Communication Group, effective December 18, 1995. As a licensed and certified audiologist, she has worked at both the Brigham and Women's Hospital and Beth Israel Hospital in Boston. At RLE, Ms. Brantley, a graduate of California State University at Long Beach (BS'85), will participate in laboratory and field studies of prototype hearing aids. She is currently a doctoral candidate at Boston University.

Andrew R. Brughera was appointed as a research specialist in RLE's Sensory Communication Group, effective July 1, 1995. A graduate of Syracuse University (BS'86) and Boston University (MS'95), Mr. Brughera will provide electrical engineering and digital signal processing support to the group's hearing research laboratory.

Dr. Kyeongjae Cho (PhD'94), a postdoctoral associate in RLE's Surfaces and Interfaces Group, was appointed as a research scientist, effective October 1, 1995. Since joining RLE in 1990 as a research assistant, Dr. Cho's research has involved ab initio calculations on parallel supercomputer platforms. He will be continuing this work to perform realistic simulations of scanning tip microscopy on semiconductor surfaces.

Dr. Julie E. Greenberg (SM'89, PhD'94), a visiting scientist in RLE's Sensory Communication Group, was appointed as a research scientist, effective January 1, 1996. Dr. Greenberg joined RLE in 1989 as a graduate student and has conducted research on digital signal processing for multimicrophone hearing aids. She will continue to design, develop, and evaluate the microphone arrays for these devices.

David S. Lum (SB'94, MEng'95) was appointed as a research engineer in RLE's Sensory Communication Group, effective August 1, 1995. Since 1993, Mr. Lum has worked on various projects with the Sensory Communication Group as a student. In his current position, he will provide support to investigators using digital signal processing techniques to develop aids for the hearing impaired and the deaf. He will also assist in psychoacoustic evaluations of hearing loss simulations and the use of speech recognition to aid in speechreading techniques.

Francis G. Taylor (SB'89) was appointed as a research engineer in RLE's Sensory Communi-

cation Group, effective December 22, 1995. Mr. Taylor was previously a senior software developer for ConnectSoft in Bellevue, Washington. In his current position, he will perform computer system management and participate in the design and evaluation of simulation systems for virtual environment training programs.

Majid Zandipour was appointed as a research specialist in RLE's Speech Communication Group, effective February 20, 1996. He is currently a master's degree candidate in applied physics at the University of Massachusetts/Boston. Mr. Zandipour has served as laboratory supervisor in the school's psychology department for the last ten years. At RLE, he will provide engineering and technical support to investigators conducting research in speech motor control.

C.2 Promotions

Dr. Dennis M. Freeman (SM/EE'76, PhD'86) was promoted to Assistant Professor of Electrical Engineering, effective September 1, 1995. Professor Freeman joined RLE in 1978 as a research associate in the Auditory Physiology Group and was appointed a research scientist in 1986. His recent investigations have focused on the cochlear mechanisms by which acoustic stimuli are encoded into auditory nerve signals. He and his colleagues have developed microscopic photodetection methods and high-resolution image processing techniques to measure the motions and physical properties of inner ear structures. Since 1987, Professor Freeman has also been a research associate in otolaryngology at the Massachusetts Eye and Ear Infirmary.

Mark K. Mondol was appointed as a research engineer in RLE's Quantum-Effect Devices Group, effective February 22, 1996. A graduate of Lansing Community College (AAS'86), Mr. Mondol came to RLE in 1991 as a technician. He will be responsible for operating and maintaining the group's scanning electron-beam lithography system and focused ion-beam system.

Dr. Reiner Wilhelms-Tricarico was appointed as a research scientist in RLE's Speech Communication Group, effective September 1, 1995. Dr. Wilhelms-Tricarico joined RLE in 1993 as a research affiliate and postdoctoral associate. His research has focused on the simulation of the tongue's biomechanical behavior. Continuation of his

research will contribute to further understanding of phonological feature correlates and speech motor control. Dr. Wilhelms-Tricarico is a graduate of the University of Gottingen (BS'76, Diplom'81, ScD'87).

C.3 Retirements

Dr. William M. Siebert (SB'46, ScD'52), Ford Professor of Engineering, announced his retirement in 1995, after serving 45 years at MIT, 43 of those on the faculty. Professor Siebert came to RLE in 1950 as a research assistant. With an interest in network theory, he joined the staffs of RLE's Radar Group and Project Lincoln, the forerunner of Lincoln Laboratory. He was appointed to the MIT faculty in 1952 and became full professor in 1963. In recent work in RLE's Auditory Physiology Group, Professor Siebert has developed mathematical models for peripheral mechanical and neural structures in the auditory system.

C.4 Tenure

Dr. Srinivas Devadas, Associate Professor of Electrical Engineering and Computer Science, received tenure on July 1, 1995. Professor Devadas conducts research in the Circuits and Systems Group on the computer-aided design of very large-scale integrated (VLSI) circuits and systems. His work focuses on the synthesis for testability and the formal verification of VLSI circuits, providing circuit and system designers with high-quality circuit design tools.

Dr. Leslie A. Kolodziejski, Esther and Harold E. Edgerton Career Development Associate Professor in the Department of Electrical Engineering and Computer Science, received tenure on July 1, 1995. Professor Kolodziejski investigates II-VI and III-V materials in RLE's Materials and Fabrication Group. Since coming to the MIT from the Purdue University faculty in 1988, she has established an important ultrahigh vacuum facility for the epitaxial growth of II-VI and III-V semiconductor materials.

C.5 Awards and Honors

Dr. Hermann A. Haus, Institute Professor, was awarded the National Medal of Science by President Clinton on October 18, 1995. The medal, which is the United States' highest scientific honor, was also presented to seven other scientists. Professor Haus' was cited for his fundamental and

seminal research contributions to the fields of quantum electronics, noise, and ultrafast optics; and for his outstanding service to the engineering profession through teaching. His research in RLE's Optics and Devices Group involves quantum optics. His contributions to the field of laser optics have been applied to long-distance fiber-optic communications as well as laser medicine techniques and instrumentation for eye surgery. Professor Haus is widely recognized for his work on the generation of ultrashort optical pulses and developing the soliton method of signal transmission.

Dr. Jacqueline N. Hewitt (PhD'86), Class of 1948 Associate Professor of Physics, was announced the recipient of the 1995-1996 Harold E. Edgerton Award on May 17, 1995. MIT established the award in 1982 to recognize young faculty members for distinction in teaching, research, and service. With her colleagues in RLE's Radio Astronomy Group, she has identified several gravitational lens systems and has detected emissions from low-temperature main-sequence stars using very-long-baseline interferometry. Professor Hewitt received the award at ceremonies held during the American Physical Society meeting in San Jose, California, on March 20, 1995.

Dr. Daniel Kleppner, Lester Wolfe Professor of Physics and RLE's associate director, was awarded the 1995 James R. Killian, Jr. Faculty Achievement Award. Professor Kleppner's wide range of work in RLE's Atomic, Molecular, and Optical Physics Group focuses on atom interactions with static electricity, magnetic fields, and radiation.

Dr. Patrick A. Lee (BS'66, PhD'70), William and Emma Rogers Professor of Physics, received a 1995 J.S. Guggenheim Fellowship. Professor Lee, a principal investigator in RLE's Quantum-Effect Devices Group, was among 152 artists, scholars, and scientists selected for the award. During his fellowship, he plans to conduct research on a theory for high-temperature superconductors. Professor Lee's other research has included the investigation of physics in small devices, transport through quantum dots, and the quantum Hall effect in confined geometry.

Appendix D. RLE Research Support Index

- Advanced Telecommunications Research Program 351-355
- Analog Devices, Inc. 310-311
- AT&T Bell Laboratories 18, 352-353
- Ballistic Missile Defense Organization 211-214
- DEMACO 281
- Defense Advanced Research Projects Agency 7-16, 18, 29-35, 61, 68-73, 75-77, 105-109, 166-168, 303-306, 309-315, 319-333, 342-345,
- Digital Equipment Corporation 312-313
- Draper (Charles S.) Laboratory 229-235
- Electric Power Research Institute 143-150
- ENECO 143-150
- Genometrix, Inc. 368-370
- Hertz (Fannie and John) Foundation 7-8, 176-177
- Houston Advanced Research Center 365-368
- IBM Corporation 75-77, 297-298, 309-310, 312-313
- INTEL Corporation 352
- Joint Services Electronics Program 7-9, 21-27, 29-37, 47-57, 65-81, 83-102, 105-107, 116-128, 181-196, 217-235, 282-284
- Klatt (Dennis) Memorial Fund 377-386
- LeBel (C.J.) Foundation 377-386
- Lockheed Sanders, Inc. 338-342, 345
- Maryland Procurement Office 159-160, 356
- MIT Center for Materials Science and Engineering 111-115
- MIT Leaders for Manufacturing Program 290-291, 319-333
- MIT Lincoln Laboratory 40-42, 105-109, 138-142, 161-163, 171-175, 289, 312-313
- MIT Plasma Fusion Center 214-216
- MIT-Woods Hole Oceanographic Institution Joint Graduate Program 339-340
- Mitsubishi Corporation 280-281, 307-308
- Motorola Corporation 315
- National Aeronautics and Space Administration 73-75, 91-92, 166-168, 277-278, 289-290, 417-419
- National Center for Integrated Photonics Technology 29-42, 111-121
- National Institutes of Health 128-138, 371-372, 377-386, 389-401, 414-416, 425-441
- National Science Foundation 7-12, 16-18, 33-37, 42-44, 49-54, 59-63, 66-68, 97-102, 105-115, 123-124, 166-175, 191-196, 217-229, 235-240, 251-256, 260-265, 287-288, 298-302, 307-310, 313-315, 338-345, 377-386
- NTT Corporation 10
- Packard (David and Lucille) Foundation 96, 102
- Princeton University 248-251
- Semiconductor Research Corporation 65-68, 312-314
- Sloan (Alfred P.) Fellowship 235-240
- Texas Instruments 21-27
- U.S. Air Force - Office of Scientific Research 60-61, 79-82, 105-108, 116-139, 161-163, 201-206, 338-340, 342-345, 419-422
- U.S. Army - Cold Regions Research and Engineering Laboratory 281
- U.S. Army Research Office 29-33, 49-54, 66-68, 77-79, 84-85, 175-177, 229-240, 312-315
- U.S. Federal Aviation Administration 281
- U.S. Federal Bureau of Investigation 310-311
- U.S. Department of Energy 248-260, 265-274
- U.S. Navy 16-17, 68-73, 75-77, 96-102, 110-111, 124-138, 206-211, 217-221, 229-240, 243-247, 278-281, 310-311, 338-349, 401-414, 416-417
- University of California/Scripps Institute of Oceanography 346-347

Project Staff and Subject Index

Project Staff and Subject Index

A

Abnet, C. Cameron 425, 426
 Abusch-Magder, David M. 49
 Acoustic speech signals 393
 Acoustic Thermometry of Ocean Climate Program 347
 Acoustics
 Speech 381, 382
 Active noise cancellation 339
 Advanced microwave sounding unit 289
 Advanced Telecommunications Research Program 351—355
 Aggarwal, Rajni J. 7, 8
 Ahadian, Joseph F. 7, 9, 11, 15, 29, 38
 Aircraft automatic flight control system 281
 Airoidi, Augusta 243, 265
 Akerson, Jerome J. 277
 Akinwande, Akintunde I. 75
 Aldridge, Mary C. 105
 Aliberti, Giovanni 337
 Allen, Jonathan 297—317, 377
 Altshuler, Boris L. 47—48
 Aluru, Narayana R. 297, 310
 Andreev, Anton V. 47
 Andrews, Michael R. 217, 235
 Annaswamy, Anuradha M. 389, 416
 Antoniadis, Dimitri A. 75, 76, 79, 82, 310, 319, 327, 328
 Apostolopoulos, John G. 351, 352
 Aranyosi, Alexander J. 425, 426
 Asavathiratham, Chalee 337, 338
 Ashoori, Raymond C. 83, 95—102
 AT&T Bell Laboratories 108
 Atomic physics 217—240
 Atoms
 Structure in magnetic fields 217—226
 Aucoin, Richard J. 65, 91
 Audio filter design 338
 Auditory cues 421
 Auditory system 425—441
 Automobiles
 Active noise cancellation 339
 Aviles, Walter A. 389, 401, 408
 Avruch, Ian M. 287

B

Babzien, Marcus 243

Baggeroer, Arthur B. 337, 346—349
 Baird, Stephen V. 389
 Balzer, Janice L. 425
 Bandy, James H. 389, 401
 Barbosa, Maria do Pilar Pereira 445
 Barrett, John W. 287, 290
 Barron, Richard J. 337, 338
 Batchelor, Ken 243
 Baylon, David M. 351, 352
 Beauregard, G. Lee 389, 401
 Becker-Haarsma, Deborah J. 287
 Beckmann, Paul 338
 Beheshti, Soosan 337
 Bekefi, George 243
 Ben-Zvi, Ilan 243
 Bergendanl, Jason R. 297, 298
 Berman, David 65, 83, 95, 97
 Bers, Abraham 243, 248—265
 Bertin, Giuseppe 243, 265
 Beucler, Margaret S. 337
 Bickley, Corine A. 377
 Bilinsky, Igor P. 105, 124, 126
 Birgeneau, Robert J. 181—184
 Birngruber, Reginald 128
 Blackwell, William J. 287, 289
 Bobaljik, Jonathan David 446
 Boivin, Luc 105, 110
 Bombarda, Francesca 243, 265
 Boning, Duane S. 319, 327, 329, 330
 Bonvik, Asbjorn M. 319, 320, 321
 Boppart, Stephen A. 105, 128
 Born, Susan E. 389
 Bose-Einstein condensation 235
 Bouma, Brett E. 105, 124, 126, 128
 Bounds, Jeffrey K. 159
 Boyce, Suzanne E. 377
 Bradley, Michael P. 217, 226
 Brady, Felicia G. 243, 287
 Braid, Louis D. 389—422
 Brandenberger, John R. 217
 Brantley, Merry A. 389, 400, 483
 Bratakos, Maroula S. 389, 393
 Brezinski, Mark E. 105, 128
 Brock, David L. 389, 401
 Brodsky, Mikhail G. 95, 102
 Brookhaven National Laboratory 243, 246
 National Synchrotron Light Source 181, 191
 Brookhaven National Laboratory. 190
 Brothers, L. Reginald 159, 161
 Brown, Elliot 172
 Brown, Stanley W. 337, 339

Brughera, Andrew R. 389, 399, 483
 Brungart, Douglas S. 389, 419
 Buck, John R. 337, 339
 Buffer layers 33
 Bulsara, M.T. 8
 Burke, Bernard F. 287—291
 Burkhardt, Martin 59, 65, 69, 79

C

Cabrera-Mercader, Carlos R. 287, 289
 Cain, Clarence P. 128
 California Institute of Technology. Jet Propulsion Laboratory 278
 Canizares, Claude R. 91
 Capaz, Rodrigo B. 185
 Cariani, Peter 425, 433
 Carmel, Erika N. 389, 401
 Carney, John C. 319, 325
 Carnie, Andrew Hay 446
 Carpignano, Franco 243, 265
 Carter, David J. 59, 65, 79
 Carter, James M. 65, 66, 68, 69, 73, 75, 76, 84, 92
 Catravas, Palmyra E. 243
 Cenacchi, Giovanna 243, 265
 Center d'Etudes Spatiale de la Biosphere 277
 Chafe, Susan E. 297
 Chan, Ho Bun 95, 99
 Chandrakasan, Anantha P. 297, 307
 Chang, Hwa-Ping 377
 Channel-dropping filter 41
 Chaotic systems 338, 340, 342
 Chapman, Michael S. 217, 229
 Charles S. Draper Laboratory 105
 Chattevj, Shourov 138
 Chen, Brian 337, 340
 Chen, Chiping 243
 Chen, Frederick W. 389, 393
 Chen, Jerry C. 42, 105, 111
 Chen, Jyh-Shing 389, 408
 Chen, Marilyn Y. 377
 Chen, Max 377
 Chenausky, Karen 377
 Cheng, Howard 377
 Chery, Yonald 319, 331
 Cheung, Shiufun 351, 353
 Cheyne, Harold 377
 Chiou, Jeffrey T. 365, 371
 Cho, Kyeongjae 185, 483
 Choi, Jeung-Yoon 377
 Chomsky, Noam A. 445—449

Chou, Michael T. 297, 312, 313, 314
 Chou, Patrick 105
 Chun, Leo 105
 Circuit design 297—317, 319—333
 Clarkson, Brian 417
 Cochlear efferents 436, 438
 Cochlear implants 379, 396, 438
 Cochlear mechanisms 425—441
 Cohen, Aaron S. 95, 96
 Collective recoil 207
 Compound semiconductors 29
 Computer vision 298—303
 Computer-integrated design 319—333
 Conklin, Anne E. 287
 Contos, Marika 243, 265
 Cook, John F. i
 Coppi, Bruno 243, 265—274
 Coram, Geoffrey J. 297, 298
 Cordes, Linus F. 319
 Cornell University. Nanofabrication Facility 231
 Costa, Carol A. 217
 Coulomb blockade energy 55
 Courtney, Michael W. 217
 Crawford, Fronefield 287
 Cresti, Diana 447
 Crouch, John 419
 Cudjoe-Flanders, Charmaine A. 7, 29, 59
 Cutro, Janet A. 59
 Czachor, Marek L. 217, 229

D

Damask, Jay N. 29, 41, 65, 86, 90, 105, 115
 Dandekar, Kiran 389, 408, 414
 Dapkus, Daniel 10, 39
 Darwish, Ali M. 120
 Daughton, William S. 243, 265
 Davis, C. Quentin 425, 426
 Davis, Kendall B. 217, 235
 de Lange, Gerhard 165, 166
 De, Suvranu 389, 414
 Decker, Steven J. 297, 298
 del Alamo, Jesús A. 21—27, 168
 del Frate, Fabio 277
 Delgutte, Bertrand 425, 433, 434, 435
 Delhorne, Lorraine A. 389, 393, 396, 397, 400
 Denesvich, Gail 389, 397
 Derksen, Timothy J. 287, 290
 Desloge, Joseph G. 389, 399
 Detragiache, Paolo 243, 265
 Devadas, Srinivas 297, 303—309, 484
 DeVries, Joel C. 217, 221

DiCarlo, Cheryl D. 128
 DiFilippo, Frank 217, 226
 Digital signal processing 337—349, 357—359
 Dille, Laura C. 377
 Ding, Kung Hau 277, 278, 280, 281
 Dix, Ann K. 389
 DNA decoding 365
 DNA sequencing 365, 371
 Donnelly, Joseph 40
 Donoghue, John J. 201
 Dougherty, David J. 35, 105, 116, 118, 122
 Doughty, Francis M. 319
 Dresselhaus, Mildred S. 121
 Dual excitation speech model 356
 Ducas, Theodore W. 217, 221
 Duchnowski, Paul 389, 393
 Duerr, Erik 165, 166
 Durfee, Dallin S. 217, 235
 Durlach, Nathaniel I. 389—422
 Duwel, Amy E. 59, 60
 Dynes, Scott B.C. 425, 435

E

Earth observing system 289
 Eddington, Donald K. 389, 396, 425, 438
 Ehrlich, Daniel J. 365, 368, 371, 372
 Electromagnetic interactions 280
 Electromagnetic wave theory 277—284
 Electronic devices
 Quantum heterostructures 19
 Quantum-effect devices 65—94
 Superconducting transmission lines 59—63
 Superconductors 165—178
 X-ray lithography 65—94
 Electronic materials 7—19, 40
 (In,Ga)(As,P) 41
 (In,Ga)P 33, 38
 GaAs 35, 38
 II-VI 29, 35
 III-V 29, 35
 InGaAs 21
 InP 21
 Lattice-matched 33
 Semiconductors 191
 Silicon surfaces 191
 ZnSe 30, 33, 35
 ZnSe:Cl 30
 ZnSe:N 30
 Elfadel, Ibrahim M. 297, 314
 Engels, Daniel W. 297, 303
 Entin, Ilya 217, 235

Erba, Matteo 243, 265
 Ernst, Alexander N. 21
 Ernst, Darin R. 243, 265
 Esposito, Anna 377
 Espy-Wilson, Carol 377
 Evangelides, Stephen 108
 Evaporative cooling 235
 Everett, Patrick N. 65, 72
 Ezekiel, Shaoul 201—216

F

Fallah, Farzan 297, 307
 Fan, Shanhui 42, 185
 Fang, Jimmy 243
 Felice, Gianmarco 243, 265
 Feng, Shechao 169
 Ferrera, Juan 65, 66, 73, 84, 86, 115
 Fiber optics 105, 124, 160, 214
 FICOM design editing system 298
 Field-effect transistors
 InGaAs 21
 InP 21
 Fischer, Gregory T. 319, 320
 Fisher, Alan 243
 Fitzgerald, Eugene A. 8
 Flaherty, Margaret A. 65
 Fleischer, Dorothy A. 297
 Fleischer, Siegfried B. 105, 116, 121, 124
 Fleming, Robert C. 65, 73, 91
 Fletcher, André B. 287
 Fleury, Marc 105, 138
 Foley, Jeffrey J. 389
 Fonstad, Clifton G., Jr. 7—19, 38
 Foresi, James S. 65
 Forrest, Steven 10, 38
 Foss, David W. i
 Föster, Arno 171
 Foxlin, Eric M. 389, 417
 Franke, Andrea E. 65, 69
 Free electron laser 243
 Freedman, Alan E. 337, 340
 Freeman, Dennis M. 425, 426, 483
 Fresnel drag 215
 Frisbie, Joseph A. 389, 393
 Frishkopf, Lawrence S. 425
 Fuchs, Vladimir 243, 248, 260
 Fujimoto, James G. 105, 124—138
 Furusaki, Akira 55
 Fusion 214
 Fusion reactors 265

G

Gale, Donna L. 105
 Galicia, Felicísimo W. 243, 260
 Garrison, David 217, 226
 Gas source molecular beam epitaxy 29—44
 Gealow, Jeffrey C. 297, 298
 Gellerman, Werner 118
 Genetic analysis 365—372
 Genosensor technology 365—372
 Gershwin, Stanley B. 319
 Glantz, Kalman 389
 Glicofridis, Paul I. 95
 Gold, Bernard 337
 Goldhaber-Gordon, David J. 49
 Goldman, Susan L. 389, 393
 Golubovic, Boris 124, 126
 Goodberlet, James G. 105, 138
 Goodhue, William D. 10, 13
 Govindarajan, Krishna K. 377
 Graaf, Isaac 389
 Grand Alliance digital television system 351
 Grant, Kenneth W. 389, 393
 Graves, William 243
 Gravitational lenses 287
 Grayson, Patrick 159, 161
 Greenberg, Julie E. 389, 399, 400, 483
 Greene, Mary i
 Greer, Donald R. 159, 161
 Grein, Matthew 105
 Grimson, W. Eric L. 161
 Grove, Timothy 201
 Guinan, John J., Jr. 425, 436, 438
 Guiod, Peter C. 377
 Gulati, Rokeva J. 389, 408
 Gung, Tza Jing 277, 281
 Gunshor, R.L. 30
 Gupta, Rakesh 389, 401

H

Hadjicostis, Christoforos N. 337, 341
 Hadjiyiannis, George I. 297, 303, 307
 Hagelstein, Peter L. 105, 138—157
 Halberstadt, Andrew K. 337, 341
 Hall, Dorrie 389, 401
 Hall, Katherine L. 40
 Hall, Robert D. 425, 438
 Hall, Seth M. 377, 389, 397
 Halle, Morris 377, 445—449
 Hammond, Benjamin M. 425, 433
 Hammond, Troy D. 217, 229, 235

Hands 398, 408—417
 Hanono, Silvina Z. 297, 303
 Hanson, Helen M. 377
 Haptics 408—417, 421
 Harley, Heidi Britton 447
 Harms, Michael 377
 Hattangadi, Shilpa M. 425, 426
 Haus, Hermann A. 41, 86, 90, 105—124, 125, 243, 484
 HDTV 351—355, 357—359
 Head-tracking technology 417
 Heard Island feasibility test 347
 Hearing 389—401, 419, 425—441
 Binaural 400
 Hearing aids 389—401
 Hearing-impaired individuals 389—401
 Hee, Michael R. 105, 128
 Held, Richard M. 389, 401, 419, 421
 Hemmer, Philip R. 201
 Herold-Jacobson, Lori K. 287
 Heteroepitaxy 29, 33, 35
 Heterointerfaces 35
 Heterostructures 7—27
 Hewitt, Jacqueline N. 484
 High-definition television 351—355, 357—359
 Hill, Marc 65
 Hillman, Robert E. 377
 Hinds, Raynard O. 351, 353
 Hinz, Philip M. 217, 235
 Ho, Carmen 389
 Ho, Chih-Hao 389, 397
 Ho, Easen 29, 30, 33
 Hodge, William 105, 138
 Holley, Jeffrey R. 217, 221
 Hollis, Mark A. 365—371
 Holmberg, Eva B. 377
 Horn, Berthold K.P. 298
 Horowitz, David M. 377
 Hoshino, Isako 7, 18
 Hou, Alexandra I. 389, 401
 House, Jody L. 29, 30, 33, 35, 122
 Howe, Robert D. 408
 Hsu, Chih-Chien 277, 278
 Hu, Qing 165—178
 Huang, Caroline 377
 Huang, Everest W. 217, 235
 Huang, Gregory T. 277, 425
 Human-machine interfaces 401, 408, 417, 419

I

IBM Corporation
 Thomas J. Watson Research Center 67

Ignitor-Ult experiment 265
 Iisuka, Norio 7, 17
 Ilic, Ljubomir M. 217, 226
 Image processing 337—349, 357—359
 Instrument landing system 281
 Integrated circuits 279, 297—298, 319—333
 Computer vision 298, 303
 Computer-aided design 297—317, 319—333
 Low-power dissipation 307
 Low-power embedded system 303, 309
 Manufacturing processes 319—333
 VLSI 7—19, 29—44
 VLSI computer-aided design 297—317
 Intelligent highway systems 167, 298—303
 Interferometry
 Atom wave 229
 International Laser Center 126
 Ions
 Mass spectrometry 226
 Ippen, Erich P. 35, 44, 105—124, 125, 126
 Isabelle, Steven H. 337, 342
 Ishikawa, Minoru 277
 Iversen, John R. 425

J

Jackson, Keith M. 65, 75, 76, 328
 Jacobs, Jarvis B. 319, 327, 328
 Jandura, Louise 389, 408
 Jiao, Hong 217
 Joannopoulos, John D. 42, 185—189
 Johnson, Joel T. 277, 278, 282
 Johnson, Laura K. 425, 426
 Johnson, Mark A. 377
 Johnson, Owen D. 389, 417
 Jones, David J. 105
 Jones, Gabrielle 389, 393
 Jones, Lynette A. 389, 401
 Jordan, Allen 229
 Jordan, Arthur K. 277

K

Kalluri, Sridhar 425, 433
 Kamon, Mattan 297, 310, 312, 314
 Kanamaru, Yasunori 277
 Kannam, P. 16
 Kao, Andrew 277
 Kao, James T. 319, 326
 Karason, Steingrimur P. 389, 408
 Karu, Zoher Z. 425, 426

Kastner, Marc A. 49—54
 Katz, Charles A. 287
 Katz, Daniel P. 201
 Kennedy, M. Carlos 351
 Ketterle, Wolfgang 217, 235—240
 Keyser, Samuel J. 377
 Khan, Mohammed J. 105, 111, 115
 Khatri, Farzana I. 105, 108
 Kiang, Nelson Y.S. 425
 Kierstead, John D. 201
 Kittipiyakul, Somsak 319
 Klatt analysis tools 383
 Klein, Olivier 49
 Kleppner, Daniel 217—226, 484
 Koizumi, Masatoshi 448
 Kokorowski, David A. 217, 229
 Kolodziejski, Leslie A. 7, 9, 15, 29—44, 84, 115, 122, 124, 484
 Kong, Jin Au 277—284
 Kopf, Cynthia Y. 105
 Korsmeyer, F. Thomas 313
 Krause, Jean C. 389
 Kuang, MòH 243, 265
 Kuo, Hong-Kwan J. 377
 Kurn, Dan M. 217, 235
 Kwon, Jimmy Y. 319, 324

L

Lada, Genevieve 377
 Lai, Kit-Wah F. 277
 Lam, Warren M. 337, 342
 LaMotte, Robert H. 408, 416
 Lane, Harlan 377
 Laser cooling 235
 Laser retinal injury 128
 Lasers 7—19, 84, 105—157
 EUV 138—142
 Fiberoptic 105, 124
 III-V 38
 Medical 128
 Soft x-ray 138—142
 Solid-state 124
 Lathan, Corrie 401
 Le Toan, T. 277
 Leabman, Michael A. 389, 400
 LeBlanc, Cindy 351
 LeBlanc, William M. 95, 96
 Lee, Dicky 159, 161
 Lee, Hae-Seung 298
 Lee, Jeng-Feng 389, 401
 Lee, Junehee 337, 343

Lee, Patrick A. 55—57, 484
 Lemay, Danielle G. 389, 393
 Lenef, Alan L. 217, 229
 Lenz, Gadi 105, 116, 118, 124
 LePrell, Glenn S. 377
 Leung, Gilbert 159, 161
 Lewis, Kevin 243, 265
 Lexical access 382—383
 Li, Kevin 277
 Liao, Stan Y. 297, 303
 Lighvani, Arash 425, 438
 Lim, Jae S. 351—356
 Lim, Kuo-Yi 29, 42
 Lim, Michael H. 65, 68, 69, 84, 86, 115
 Lin, Charles P. 128
 Lin, Gregory G. 389, 419
 Linguistics 445—449
 Lippman, Rebecca F. 389, 393
 Litovsky, Ruth Y. 425, 434
 Little, Brent E. 105, 111, 115
 Liu, Sharlene A. 377
 Lohman, Thomas J. 319, 320
 Long, Christopher J. 425
 Lopatnikova, Anna 29, 30
 Lossos, David C. 389
 Ludwig, Jeffrey T. 337, 343
 Lum, David S. 389, 483
 Lumsdaine, Andrew 297, 309
 Luo, Jiafu 12
 Luongo, Eleanora M. 389
 Lutwak, Robert I. 217, 221
 Lyszczarz, Theodore M. 49
 Lyubomirsky, Ilya 165, 176

M

Maggiora, Riccardo 243, 265
 Magnetic trapping 235
 Makhoul, John I. 377
 Mankiewicz, Paul M. 49
 Manning, Deborah S. 357
 Manolatos, Christina 277, 282
 Manuel, Sharon Y. 377
 Marley, Elisabeth A. 29, 40, 41, 84
 Martin, David R. 297, 298
 Martin, Debra L. 181
 Martin, Paul S. 7, 16
 Martinez, Angel 277
 Masaki, Ichiro 297, 298
 Masaki, Kinuku 389, 419
 Mason, Elliot J. 159
 Mass flow measurement 215

Massachusetts Eye and Ear Infirmary 425
 Massachusetts General Hospital 129
 Massoud, Yehia M. 297, 312
 Mastovsky, Ivan 243
 Matthies, Melanie L. 377
 Matveev, Konstantin 55
 McIlrath, Michael B. 319, 326—331
 McKinney, Christopher 425, 438
 McKinney, Martin F. 425, 433
 McKinnon, Rita C. i
 McQuirk, Ignacio S. 297, 298
 Medical lasers 128
 Meinhold, Mitchell W. 65, 77
 Melloch, Michael R. 79, 82, 168, 172, 175
 Mervis, Juliet 201
 Mewes, Marc-O. 217, 235
 Microwave sounding 289
 Microwiggler 243
 Middle ear 425—441
 Muscles 438
 Migliuolo, Stefano 243, 265
 Mikhailov, Viktor P. 105, 124
 Mikkelsen, J.M. 7, 15
 Milikow, Jeremy M. 29, 40, 41
 Millimeter-wave devices 166
 MIT Artificial Intelligence Laboratory 161
 MIT Center for Material Science and
 Engineering 44
 MIT Laboratory for Information and Decision
 Systems 161
 MIT Lincoln Laboratory 10, 75, 108, 129, 161,
 320, 337
 MIT Microelectronics Fabrication Laboratory 44
 MIT Microsystems Technology Laboratory 44
 MIT-Green Bank surveys 287
 Mochrie, Simon G.J. 181, 191—196
 Molecule cooling 206
 Mollenauer, Linn 108
 Mondol, Mark K. 65, 69, 483
 Monta, Peter A. 351, 354
 Monteiro, José C. 297, 307
 Moon, Euclid E. 65, 68, 72
 Moore, Christopher B. 287
 Morgan, Nicole Y. 49
 Morgenbesser, Hugh B. 389, 401
 Moyne, William P. 319, 324, 329
 Muendel, Martin H. 105, 138
 Multiple quantum-well structures 174
 Murphy, Edward 65, 69
 Murphy, Thomas E. 65, 84, 86, 90, 115
 Musan, Renate 448
 Musicus, Bruce R. 337

N

Nabors, Keith S. 297, 312
 Nadeau, Philip M. 389, 393
 Namiki, Shu 105, 110
 Nasalization 380
 Nastov, Ognen J. 297, 315
 National Oceanic and Atmospheric
 Administration 289
 National Radio Astronomy Observatory 287
 Nawab, S. Hamid 337, 343, 344
 Nee, Phillip T. 159
 Nelson, Lynn E. 105, 116
 Nemec, Joseph E. 319, 322, 323
 New England Eye Center 132
 Nonlinear optics 159
 Nonlinear waves in plasmas 247
 Noojin, Gary D. 128
 Normal speech 378
 North, D. Keith 377
 Novak, John J. 389
 Nurmikko, A.V. 30
 Nyman, Bruce 108

O

O'Connell, Michael P. 389, 399
 O'Meara, Margaret 55, 185
 O'Neill, Kevin 277, 280
 Oberoi, Pankaj 425
 Ocean temperatures 347
 Oceanographic signal processing 346
 Odoardi, Angela R. 7, 29, 59
 Ogora, T.H. 389
 Ooi, James M. 337, 344
 Ophthalmic laser surgery 128
 Oppenheim, Alan V. 337—349
 Optical coherence tomography 128—138
 Optical communication 21, 159—163
 Devices 7—19
 Optical computing 201
 Optical data storage 211
 Optical force 206
 Optical physics 201—216
 Optics 105—157
 Fiber 214
 Nonlinear 159
 Opto-electronics 38, 105—157, 161
 OPTOCHIP 38
 Orlando, Terry P. 59—63, 79, 82, 311
 Oster, Mark N. 425
 Otoacoustic emissions 436

P

Palmer, Fred L. 217, 226
 Pan, Janet L. 7, 16
 Pant, Amrit R. 217
 Papadopoulos, Haralabos C. 337, 344
 Park, Ickjin 185
 Park, John 389, 419
 Park, Zöe 377
 Parkes-MIT-National Radio Astronomy Observatory
 surveys 287
 Passero, Barbara i
 Passive waveguides 41
 Patterson, Steven G. 7, 9, 15, 29, 38, 159
 Payton, Karen L. 389
 Peake, William T. 425
 Pegoraro, Francesco 243, 265
 Penn, Gregory E. 243, 265
 Pepin, Anne 65, 82
 Perkell, Joseph S. 377—386
 Perrier, Pascal H. 377
 Petrich, Gale S. 7, 9, 15, 29—44
 Pevzner, Boris 121
 Pfautz, Jonathan 389, 401
 Phase transitions 181
 Phase-conjugation 201
 Phillips, Joel R. 297, 311, 312, 314
 Photonic bandgap 42
 Photonic devices 40, 41
 Pierre, Darren M. 243
 Pioch, Nicholas 389, 401
 Plant, Geoffrey L. 389, 397
 Plasma fusion 143
 Plasma physics 243—274
 Induced stochasticity and chaos 247
 Nonlinear waves in plasmas 247
 RF heating and current drive in tokamak
 plasmas 247
 Space and astrophysical plasma dynamics 247
 Thermonuclear plasmas 265
 Polley, Michael O. 357
 Poort, Kelly L. 377
 Porter, Jeanne M. 65, 92
 Power, Matthew H. 389, 393
 Prasad, Sheila 7, 11
 Preisig, James C. 337, 339
 Prentiss, Mara G. 201
 Princeton University 10, 38
 Pritchard, David E. 217, 226—235
 Process flow representation 319—333
 Psaltis, Demetri 12
 Psychoacoustics 389—422
 Puria, Sunil 425

Q

Quantum studies 49, 55, 95—102, 201—216, 217
 Chaos 47, 217
 Computation 150
 Heterostructures 7—19
 Optics 105—157, 159
 Point contacts 168
 Statistics 47, 235
 Qui, Joe 243

R

Rabinowitz, William M. 389, 396, 397, 399, 400, 425
 Radar 21
 Laser 161
 Radar scattering 281
 Radio astronomy 287—291
 Radio interference 281
 Rahman, Arifur 165, 166
 Rahman, Nadir E. 319, 327, 328
 Rahmat, Khalid 297, 310
 Raju, Balasundara I. 389, 414
 Ralston, Richard 166
 Ram, Abhay K. 243, 248—265
 Ramstad, Monte J. 181
 Rana, Farhan 165, 168
 Rangaswamy, Sudeep 389, 408
 Rankovic, Christine M. 389
 Rathman, Dennis D. 365, 368
 Ravicz, Michael E. 425
 Rawizza, Mark A. 287, 290
 Rediker, Robert H. 159
 Reed, Charlotte M. 389, 393, 397
 Reed, Eric C. 351
 Reich, Evan 243, 265
 Reichelt, Mark W. 297, 309
 Reif, L. Rafael 42
 Relativistic electron beams 243
 Remote sensing 277—279
 Remotely operated vehicles 408
 Riccitelli, Marco 243, 265
 Richardson, Christopher R. 389, 417
 Riconda, Caterina 243, 265
 Ripin, Daniel 217, 226
 Roach, W.P. 128
 Roby, Frederick L. 389, 408
 Rodkin, John J. 389, 417
 Rohwedder, Bernd S. 217, 229
 Rooks, Michael J. 168, 171, 172
 Rosenband, Till P. 217, 235

Rosenkranz, Philip W. 287, 289—291
 Rosowski, John J. 425
 Rossetti, Denise M. 351
 Rouf, Rosanne 425, 426
 Roy, Jeremy 243, 265
 Royter, Yakov 7, 13, 15
 Rubenstein, Richard A. 217, 229
 Rusinkiewicz, Szymon M. 217, 226
 Rydberg atoms 217, 221

S

Saberi, Kouroush 389
 Sachtler, Wendelin L. 389, 401
 Salihu, Suraj 243, 265
 Salisbury, J. Kenneth 389, 401, 408
 Santos, Jonathan R. 389, 397
 Savas, Timothy A. 65, 73, 92, 105
 Schäpers, Thomas 171
 Schattenburg, Mark L. 65, 73, 91, 92
 Scheer, Michelle M. i
 Schloerb, David W. 389, 401
 Schmidt, Martin A. 297, 298, 310
 Schmiedmayer, H. Jörg 217, 229
 Schreiber, William F. 357—359
 Schultz, Steven D. 243, 248, 251, 254
 Schwartz, Michael J. 287, 289, 290
 Schweizer, Mark R. 59, 82
 Scripps Institute of Oceanography 346, 347
 Secor, Matthew J. 337, 344
 Seefeldt, Alan 337, 345
 Segalov, Zvi 243
 Sekiyama, Kaoru 389, 393
 Semiconductors 185—196
 Compound 21, 29—44
 II-VI 30, 33
 III-V 33
 Single-electron transistors 49
 Semper, Edward D. 377
 Sensimetrics Corporation 400
 Sensorimotor satellite 403
 Sensory aids 396, 438
 Sensory communication 389—422
 Senturia, Stephen D. 297, 310
 Sestok, Charles K. 217
 Sexton, Matthew G. 389, 393
 Shah, Satyen 65, 73
 Shahriar, Selim M. 201—214
 Shakeel, Asif 159
 Shapiro, Jeffrey H. 159—163
 Shattuck-Hufnagel, Stefanie 377—386
 Shatz, Lisa F. 425, 426

Shaver, David C. 49
 Shenoy, Krishna V. 7, 12, 38
 Shera, Christopher A. 425, 436
 Shih, Shih-En 277, 280
 Shin, Robert T. 277, 278, 281, 282
 Shinn-Cunningham, Barbara G. 389, 401, 419, 421
 Shnidman, Nathan R. 389, 417
 Siebert, William M. 425, 484
 Signal processing 7, 337—349, 351—355, 396, 438
 Fractals 342
 Silevitch, Daniel M. 95, 96
 Silverman, Scott E. 65, 66, 75
 Singer, Andrew C. 337, 345
 Single-electron spectroscopy 95—102
 Slifka, Janet L. 425, 426
 Smith, Edward T. 217, 229
 Smith, Henry I. 41, 65—94, 97, 115
 Smith, Stephen P. 201, 214—216
 Sodini, Charles G. 297, 298
 Sokolinski, Ilia 59, 65, 79
 Somerville, Mark H. 21
 Song, Seungheon 191
 Speech communication 377—386, 397
 Speech perception 381—382
 Speech processing 346, 356
 Speech reception 389
 Speech recognition systems 346
 Speechreading 393
 Spellmeyer, Neal 217
 Squeezing 201
 Srikantiah, Ranjini 389, 393
 Srinivasan, Mandayam A. 389, 397, 401, 408, 414, 416
 Sroka, Jason 389
 Staelin, David H. 287, 289—291
 Stankovic, Konstantina M. 425, 436
 Stanton, Christopher 126
 Stapedius 438
 Steffens, David A. 425
 Steinmeyer, Günter 105, 118, 124
 Stevens, Kenneth N. 377—386
 Stoner, Richard 243
 Streetman, Ben 176
 Strogatz, S. 59
 Sudarshanam, Venkatapuram S. 201
 Sugiyama, Linda E. 243, 265
 Sun, Liguu 277
 Sun, Walter 377
 Sunshine, Lon E. 351, 355
 Superconducting devices 59—63, 165—178
 Superconducting magnet quench 214
 Surface studies 181—184
 Semiconductors 185—189, 196

Svilan, Vjekoslav 59
 Svirsky, Mario A. 377
 Svolos, George M. 243, 265
 Swanson, Eric A. 128

T

Tachikawa, Masami 7, 11, 15
 Tactile communication 397
 Tactile information 408—417, 421
 Tadoma method 397
 Takeuchi, Anne H. 389, 393
 Talavage, Thomas M. 425
 Tan, Hong Z. 389, 397
 Tanaja, Hemant 377
 Tanaka, Motohiko 243, 265
 Tang, Xiao-feng 29, 42
 Taniguchi, Carl 351, 355
 Taniguchi, Nobuhiko 47
 Tankuranun, Prathet 277, 281
 Tassa, Coral D. 389, 399, 400
 Tausch, Johannes 297, 312
 Taylor, Francis G. 389, 408, 483
 Tearney, Guillermo J. 105, 128
 Television
 High-definition 355
 Television research
 High-Definition 351—359
 Teoh, Su W. 425
 Tessmer, Stuart 95, 96
 Theilhaber, Joachim 243, 254, 260
 Thermonuclear plasmas 265
 Thoen, Eric R. 105
 Thompson, Carl V. 75
 Thompson, Stanley H. 217, 235
 Tierney, Joseph 425
 Tolk, Norman 126
 Tomsio, Nayan 277
 Toth, Cynthia A. 128
 Touch 398, 408—417
 Training for remote sensing and manipulation program 408
 Trías, Enrique 59, 60
 Trotter-Wilson, Catherine S. 287
 Troxel, Donald E. 319—333
 Truckenbrodt, Hubert 449
 Tsuk, Michael 277, 282
 Tufts University, School of Medicine 132
 Turk, Alice 377
 Tziligakis, Constantine 105, 124

U

U.S. Army Cold Regions Research and Engineering Laboratory 278
 Ullschmied, Jiri 243
 Underwater acoustics 339, 346, 347
 University of Massachusetts, Amherst 280
 University of Southern California 10, 39

V

Vacca, Luigi 243, 248, 256
 van der Zant, Herre S.J. 59, 60, 61, 297, 311
 van Druten, Nicolaas J. 217, 235
 Vanderbilt University 126
 Verbout, Shawn M. 337, 346
 Verghese, George C. 341, 344
 Verghese, Simon 165, 171, 172
 Vestibular system 436
 Viadyananthan, Praveen T. 7, 9, 11, 15
 Villeneuve, Pierre 42, 185
 Virtual environment technology 401, 408, 417, 419, 421
 Visible emitters 30
 Vision chip project 298—303
 Vitesse Corporation 38
 VLSI computer-aided design 297—317
 VLSI technology 351
 von Bosau, Laura 243
 Voss, Kimberly J. 389, 414
 Voss, Susan E. 425

W

Wage, Kathleen E. 337, 347
 Wang, Alex Che-Wei 337, 347
 Wang, Hao 7, 12, 15
 Wang, Li-Fang 277, 278, 280
 Wang, Xi-Jie 243
 Warde, Cardinal 12
 Warlick, Emily L. 29, 30, 33
 Watanabe, S. 59
 Waveguides 42
 Wavelength division multiplexing 211
 Weather satellites 289
 Weber, Lukasz A. 389, 401
 Wee, Susie J. 357
 Weiner, Miriam 243
 Weinstein, Ehud 337
 Weiss, Thomas F. 425, 426
 Welker, Daniel P. 389

Wells, Barry 181
 Wessling, Owen 332
 Whan, Chagarn B. 59, 61
 White, Jacob K. 61, 297, 309—317
 Wiegand, Thomas E.v. 389, 401
 Wies, Evan F. 389, 401
 Wilde, Lorin F. 377
 Wilhelms-Tricarico, Reiner 377, 484
 Williams, David R. 377
 Willsky, Alan S. 161
 Wind, Shalom 49
 Wint, Arlene E. 377
 Wong, Ngai C. 159, 161
 Wong, Vincent V. 65, 68, 69, 84, 86
 Wong, William S. 105, 107, 108
 Woods Hole Oceanographic Institution 337, 339
 Wornell, Gregory W. 337, 338—346, 347
 Wozniak, Jane W. 377
 Wright, Chantal E. 319, 329
 Wurtele, Jonathan S. 243
 Wyatt, John L., Jr. 297, 298—303
 Wyss, Rolf A. 165, 168, 171

X

X-ray generation 207
 Xu, Bin 165, 175
 Xu, Yi 377

Y

Yakubo, Kou 169
 Yan, Jun 277, 278, 281
 Yang, Isabel Y. 65, 68, 69, 75, 76
 Yang, Y. Eric 277, 280, 281, 282
 Yasaka, Anto 65, 75
 Yeang, Chen-Pang 277, 281
 Yellin, Elron A. 389
 Yesley, Peter S. 217, 235
 Yoo, Chang Dong 351, 356
 Yoon, John 389, 408
 Yoon, Mirang 191
 Young, Albert M. 365, 371
 Young, Michael J. 181
 Yu, Charles 105, 110
 Yu, Paul C. 297, 298

Z

Zaganjori, Janice M. 337

Zamdmer, Noah D. 165, 172
Zandipour, Majid 483
Zeidenberg, Lisa 21, 65
Zeltzer, David 389, 401, 408
Zhang, Yan 277, 278, 281
Zhitenev, Nikolai 95, 102
Ziegler, Mary J. i
Zissman, Marc A. 425
Zurek, Patrick M. 389, 399